THE JOURNAL OF
PHYSICAL CHEMISTRY

VOLUME 70, NUMBER 4 APRIL 15, 1966

Donnan Equilibria in Polystyrenesulfonate Gels

by Richard L. Gustafson

Rohm & Haas Company, Research Division, Philadelphia, Pennsylvania 19137 *(Received December 27, 1965)*

Measurements of sorption of HCl, NaCl, NaI, NaH_2PO_4, $CaCl_2$, and $LaCl_3$ by the appropriate ionic forms of two polystyrenesulfonate gels, Amberlite XE-100 and Amberlite IR-120, have been carried out in 0.02–4 *m* solutions at 25°. Mean molal activity coefficients, $\gamma_{\pm}^{*} = \gamma_{\pm}^{r} e^{\pi \bar{V}/\nu RT}$, of the various electrolytes in the resin phase have been calculated after suitable corrections have been made for occlusion of solution on the surface of the resin. Values of $\gamma_{\pm}^{*}$ decrease with decreasing ionic strength, in accordance with the theoretical predictions of Katchalsky and Lifson, except in the case of the dihydrogen phosphate ion. The values of $\gamma_{\pm}^{*}$ decrease in the orders NaI > NaCl > NaH_2PO_4 and NaCl > $CaCl_2$ > $LaCl_3$, which are the orders obtained in aqueous solutions of the same salts.

Introduction

A number of investigators have studied the electrolyte sorption characteristics of ion-exchange resins as a function of the external concentration in a variety of acid, base, and salt systems.[1-12] They have found that, as the external concentration decreases, the mean molal activity coefficient of the electrolyte in the resin phase also decreases, in contrast to the behavior observed in aqueous solutions of strong electrolytes in which activity coefficients approach unity at infinite dilution. However, as has been pointed out by other workers,[13-16] it is possible that the decreases in the values of the activity coefficients (which are calculated by the use of the modified Donnan relationship) with decreasing solution concentration are caused by occlusion of electrolyte on the bead surfaces and by sorption of co-ions by resin impurities. Hence, some of the electrolyte which is found to be present in the resin phase actually is a component of the solution phase. The relative contribution of such an error naturally increases as the concentration of electrolyte in the external solution decreases, thus producing the observed effect.

(1) W. C. Bauman and J. Eichhorn, *J. Am. Chem. Soc.*, **69**, 2830 (1947).

(2) H. P. Gregor, F. Gutoff, and J. I. Bregman, *J. Colloid Sci.*, **6**, 245 (1951).

(3) H. P. Gregor and M. H. Gottlieb, *J. Am. Chem. Soc.*, **75**, 3539 (1953).

(4) C. W. Davies and G. D. Yeoman, *Trans. Faraday Soc.*, **49**, 968 (1953).

(5) J. S. Mackie and P. Meares, *Proc. Roy. Soc.* (London), **A232**, 485 (1955).

(6) G. J. Hills, P. W. M. Jacobs, and N. Lakshminarayanaiah, *ibid.*, **A262**, 257 (1961).

(7) K. A. Kraus and G. E. Moore, *J. Am. Chem. Soc.*, **75**, 1457 (1953).

(8) M. H. Gottlieb and H. P. Gregor, *ibid.*, **76**, 4639 (1954).

(9) F. Nelson and K. A. Kraus, *ibid.*, **80**, 4154 (1958).

(10) J. Danon, *J. Phys. Chem.*, **65**, 2039 (1961).

(11) N. Lakshminarayanaiah, *J. Polymer Sci.*, **A1**, 139 (1963).

(12) R. L. Gustafson, *J. Phys. Chem.*, **67**, 2549 (1963).

In the present study, measurements of sorption of HCl, NaCl, NaI, NaH_2PO_4, $CaCl_2$, and $LaCl_3$ by the appropriate forms of Amberlite XE-100, a polystyrenesulfonate resin which has been cross-linked with 4.8% divinylbenzene (DVB) and Amberlite IR-120, a similar resin containing 8.0% DVB, have been carried out in 0.02–4 *m* solutions at 25°. Corrections have been made for the amounts of electrolyte occluded on the bead surfaces, and mean molal activity coefficients of electrolytes in the resin phase have been calculated.

Experimental Section

Resins. Samples of 20–30 mesh Amberlite XE-100 and Amberlite IR-120 polystyrenesulfonate resins which contain 4.8 and 8.0% divinylbenzene (DVB), respectively, were placed in glass columns and treated three times with alternate washings with 1 *M* HCl and 1 *M* NaOH. After exhaustive treatment with the NaOH the resins were washed until the pH of the effluent was equal to that of the influent. Approximately 5 ml of resin was taken for each experiment. The capacities of the resins were determined by conversion of the resins to the hydrogen form, washing with water, displacement of the hydrogen ions by treatment with 1 *M* NaCl, and titration of the effluent with standard NaOH to a phenolphthalein end point. After the capacity determinations, some of the samples were converted to the calcium and lanthanum forms by exhaustive treatment with the corresponding chloride salts.

Equilibrations and Swelling Measurements. The resin samples, approximately 7 mequiv in capacity, were equilibrated for several days with 0.01–3 *m* HCl, NaCl, NaI, NaH_2PO_4, $CaCl_2$, and $LaCl_3$ solutions at 25°. The measurements of resin volumes were carried out pycnometrically, and determinations of the weights of swollen resin were made after centrifugation in a manner similar to that described by Gregor, *et al.*[17] The amount of water imbibed by each resin sample was calculated by difference.

Measurements of Imbibed Electrolyte. The imbibed salts were eluted from the resins by 15–20 washings with deionized water whose resistance was greater than 10^6 ohms, and the solutions were made to the desired volumes. Chloride and iodide determinations were carried out coulometrically with the use of an Aminco-Cotlove chloride titrator. Phosphate analyses were carried out colorimetrically by the method of Rockstein and Herron.[18]

Some of the eluted salt is present in a liquid film at the surfaces of the beads and must not be included in the calculation of imbibed electrolyte. Corrections for the amount of salt in the liquid film, and in any internal cracks or voids, were determined on the basis of measurements of sorption of disodium indigodisulfonate from 0.003 *M* aqueous solutions. It was assumed that, because of Donnan exclusion of the divalent dye anion, a negligible amount of dye enters the gel phase. Rough calculations, made without consideration of activity coefficients, show that the dye concentration in the gel phase will be in the order of 10^{-7} *m*. Known quantities of resin were contacted with the dye solutions for 1–2 hr, after which time the resin phases were separated by centrifugation under the same conditions as those employed for all of the experiments, *i.e.*, 3000 rpm for 10 min. After the resin samples were weighed, the dye was eluted with water, the resulting solutions were made to 100 ml in a volumetric flask, and the dye concentrations were determined spectrophotometrically at a wavelength of 605 mμ. With the knowledge of the densities and dye concentrations of the solution phase and the volumes of the resins, it was possible to calculate the volumes of solution occluded on the resin surface. See Table I.

Table I: Solution Occluded on Resin (ml/mequiv)

	IR-120	XE-100
	0.00694	0.00557
	0.00732	0.00541
	0.00729	
	0.00763	
Av	0.00730 ± 0.00018	0.00549 ± 0.00008

The results given in Table I correspond to occluded volumes of 0.0286 ± 0.0007 and 0.0132 ± 0.0002 ml/ml of bead in the cases of IR-120 and XE-100, respectively. The greater occlusion by IR-120 is caused by the presence of a greater percentage of surface cracks and fissures in this material. The above corrections apply only to fully swollen resins. The volumes of solution occluded by resins which were equilibrated in salt solutions were calculated by multiplying the above values by a factor equal to the ratio of the surface area of the partially swollen bead to that of the completely swollen resin. It is assumed that the film thickness is equivalent in the salt and dye solutions. The final calculations of activity coefficients are not seriously affected by

(13) D. H. Freeman, *J. Phys. Chem.*, **64**, 1048 (1960).

(14) E. Glueckauf and R. E. Watts, *Nature*, **191**, 904 (1961).

(15) E. Glueckauf and R. E. Watts, *Proc. Roy. Soc.* (London), **A268**, 339 (1962).

(16) E. Glueckauf, *ibid.*, **A268**, 350 (1962).

(17) H. P. Gregor, K. M. Held, and J. Bellin, *Anal. Chem.*, **23**, 620 (1951).

(18) M. Rockstein and P. W. Herron, *ibid.*, **23**, 1500 (1951).

Table II: Values of Mean Molal Activity Coefficients, $\gamma_{\pm}^*$, for Electrolytes in Styrene–DVB Gels at 25°

m^s	$\gamma_{\pm}^s$	m_C^r	m_A^r	$\gamma_{\pm}^*$
		HCl–XE-100		
1.010	0.811	3.75	0.1863	0.98
0.493	0.757	3.37	0.0538	0.88
0.197	0.767	3.14	0.0110	0.82
0.0993	0.796	3.09	0.0031	0.81
		NaCl–XE-100		
3.275	0.737	6.84	1.201	0.84
2.151	0.676	5.63	0.672	0.75
1.043	0.655	4.55	0.233	0.66
0.521	0.677	4.02	0.0791	0.63
0.210	0.729	3.67	0.0179	0.60
0.1039	0.778	3.58	0.0055	0.58
		NaI–XE-100		
3.37	1.032	7.56	1.488	1.04
2.25	0.855	5.99	0.798	0.88
1.04	0.740	4.62	0.242	0.73
0.533	0.725	4.07	0.0814	0.67
0.207	0.750	3.70	0.0161	0.64
0.107	0.785	3.61	0.0048	0.64
0.0521	0.818	3.55	0.00176	0.54
0.0209	0.869	3.50	0.00050	0.43
		NaH_2PO_4–XE-100		
3.69	0.300	6.08	0.775	0.51
2.11	0.365	5.17	0.469	0.49
1.00	0.468	4.34	0.1894	0.52
0.488	0.566	3.91	0.0702	0.53
0.197	0.675	3.61	0.01816	0.52
0.0983	0.745	3.52	0.00587	0.51
0.0501	0.820	3.46	0.00193	0.50
0.0210	0.869	3.42	0.00040	0.49
		$CaCl_2$–XE-100		
1.636	0.655	3.33	1.233	0.99
1.070	0.513	2.84	0.711	0.77
0.525	0.449	2.44	0.293	0.63
0.256	0.461	2.25	0.123	0.58
0.1001	0.518	2.14	0.0403	0.54
0.0523	0.575	2.11	0.0191	0.52
0.0258	0.643	2.09	0.0083	0.50
0.01068	0.725	2.06	0.0028	0.48
		$LaCl_3$–XE-100		
0.246	0.268	1.784	0.237	0.38
0.1140	0.306	1.724	0.1110	0.36
0.0451	0.419	1.680	0.0445	0.39
0.0228	0.482	1.677	0.0234	0.37
0.01129	0.5554	1.672	0.0122	0.34
0.00453	0.650	1.666	0.0051	0.31
		NaCl–IR-120		
1.024	0.655	6.83	0.1189	0.74
0.509	0.679	6.51	0.0392	0.68
0.203	0.732	6.27	0.00831	0.65
0.1009	0.778	6.21	0.00306	0.57
0.0504	0.820	6.18	0.00136	0.45
0.0204	0.872	6.17	0.00067	0.28
		NaH_2PO_4–IR-120		
1.084	0.456	6.70	0.0952	0.62
0.529	0.556	6.52	0.0358	0.61
0.208	0.670	6.29	0.0073	0.65
0.1041	0.740	6.24	0.0020	0.69

small changes in the occluded volume. For instance, a 3% error in this quantity will change a value of $\gamma_{\pm}^*$ for NaI sorption by XE-100 from 1.037 to 1.039 in a 3.4 m solution and, in the most sensitive case studied, $\gamma_{\pm}^*$ changed from 0.435 to 0.442 in a 0.02 m NaI solution. These errors are small relative to the large variations of $\gamma_{\pm}^*$ which are observed with changes in ionic strength in many cases.

Results

Donnan Equilibria. Mean molal activity coefficients of the various salts in the resin phase were calculated by the use of the equation

$$\gamma_{\pm}^* = \gamma_{\pm}^r e^{\pi \bar{V}/\nu RT} = \left[\frac{m_C^s (m_A^s)^{\nu_A} (\gamma_{\pm}^s)^{\nu}}{m_C^r (m_A^r)^{\nu_A}}\right]^{1/\nu}$$

Here m refers to molality, superscripts r and s refer to resin and solution phases, respectively, $\bar{V}$ is the partial molar volume of the electrolyte, C and A represent the cationic and anionic component, respectively, ν_A is the number of anions produced by dissociation of 1 mole of electrolyte, and ν is the total number of anions plus cations produced by such dissociation. Values of activity coefficients of the electrolytes were taken from data tabulated by Harned and Owen[19] except in cases in which the concentration was less than 0.1 m. Here, values were calculated by the use of the Debye–Hückel expression

$$\log \gamma_{\pm} = -\frac{Az^+z^-\mu^{1/2}}{1 + \mathring{a}B\mu^{1/2}}$$

where

$$A = \frac{e^3}{2.303(DkT)^{3/2}}\sqrt{\frac{2\pi N}{1000}} = 0.509$$

and

(19) H. S. Harned and B. B. Owen, "The Physical Chemistry of Electrolytic Solutions," 3rd sd, Reinhold Publishing Corp., New York, N. Y., 1958.

$$B = \left(\frac{8\pi Ne^2}{1000DkT}\right)^{1/2} = 3.29 \times 10^7 \text{ at } 25°$$

The following values of $\mathring{a}$ (in centimeters), the distance of the closest approach, were employed: NaCl, 4.4×10^{-8}; NaI, 4.4×10^{-8}; NaH_2PO_4, 4.4×10^{-8}; $CaCl_2$, 5.2×10^{-8}; and $LaCl_3$, 6.5×10^{-8}. The values of $\gamma_\pm$*, which are presented in Table II, include the contribution from the pressure–volume term which is of unknown but presumably small magnitude.

The values of the resin phase activity coefficients in Table II decrease with decreasing ionic strength, except in the experiments involving sorption of NaH_2PO_4. In the latter case, the values of $\gamma_\pm$* in the XE-100 resin remain essentially constant throughout the entire range and actually increase with decreasing concentration in the more highly cross-linked IR-120. As was mentioned earlier, several investigators have shown that, as the external electrolyte concentration approaches zero, the mean molal activity coefficient of the sorbed electrolyte in the resin phase decreases markedly. Freeman[13] has shown that constant activity coefficients may be calculated if appropriate corrections are made for the electrolyte which is assumed to be occluded on the bead surfaces and in resin fissures and also for that which is sorbed by resin impurities. In the present case, an overcompensation may have been made for the amount of occluded electrolyte, for, in the case of NaCl sorption by XE-100, the amount of salt which was calculated to be occluded was slightly greater than the total amount of salt present in the resin in 0.05 and 0.02 *m* solutions. Nevertheless, the calculated values of $\gamma_\pm$* decrease with decreasing ionic strength, indicating that the observed effect is not produced by a failure to recognize the contribution of surface occlusion or adsorption by impurities. The theoretical treatments of Katchalsky and Lifson[20] and Katchalsky and Michaeli[21] predict such a decrease in the activity coefficient of electrolyte in the resin phase with decreasing concentration, although quantitative agreement has not been found by a number of workers.[5,6,11,12]

The values of the activity coefficients in the resin phases decrease in the order NaI > NaCl > NaH_2PO_4 and NaCl > $CaCl_2$ > $LaCl_3$, which are the same orders which are observed in aqueous solutions of the same salts. It is not surprising that the ions which form ion pairs of the Bjerrum type most extensively in aqueous solution should be involved to the greatest degree in ionic interactions in the polyelectrolyte gel.

Data concerning the swelling of the various forms of Amberlite XE-100 are shown in Figure 1. As the activity coefficients and osmotic coefficients decrease in the order NaI > NaCl > NaH_2PO_4, the swelling of the resin increases in the order NaI < NaCl < NaH_2PO_4. The volume of resin also decreases in the order Na > Ca > La. Whereas the degree of swelling of the sodium and calcium salts of Amberlite XE-100 increases with decreasing ionic strength in the usual manner, that of the lanthanum salt is virtually independent of the ionic strength of the external solution. This lack of response of the resin to changes in the osmotic pressure of the external solution is probably produced by the extremely high coulombic attraction (between fixed ions and counterions) which is sufficient to prevent swelling or shrinking.

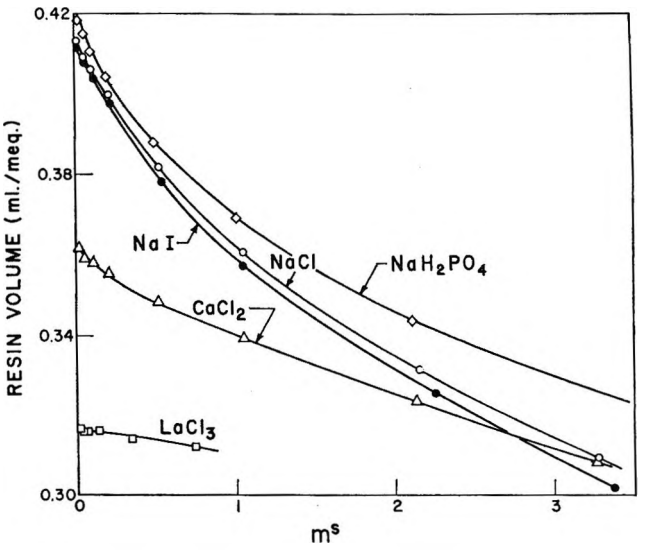

Figure 1. Plots of resin volume *vs.* external salt concentration for various forms of Amberlite XE-100.

Discussion

In view of the results of this paper, it is of interest to compare the values of activity coefficients of NaCl in various types of resin systems. Such data have been obtained from several sources and are shown in Table III. All results obtained from Gustafson and Lirio[12,22] are based on data which have been corrected for the effects of surface occlusion. Of the various systems for which data are available, the greatest degree of salt sorption, and hence the lowest values of the activity coefficients, is found in the polymethacrylic acid resin. The high degree of ionic interaction in this case is probably produced by the close proximity of functional groups along the polymer chains, relative to that which is found in polystyrene or phenol–formaldehyde polymers. In order to reduce the greater electrostatic po-

(20) A. Katchalsky and S. Lifson, *J. Polymer Sci.*, **11**, 409 (1953).
(21) A. Katchalsky and I. Michaeli, *ibid.*, **15**, 39 (1955).
(22) J. A. Lirio and R. L. Gustafson, unpublished results.

tential in the polymethacrylate systems, more electrolyte is imbibed than in the other systems. In the cases of the Amberlite resins, in which surface occlusion effects have been taken into account, the values of $\gamma_{\pm}^*$ obtained in quaternary ammonium resin (IRA-400, -401, -410, and -411) are less than those obtained in the sulfonic systems, despite the fact that the distances between charged groups are approximately equivalent for the two resins. Similar results were shown by Gregor and Gottlieb[3,8] who found that values of $\gamma_{\pm}^*$ for KCl in polystyrenesulfonate–10% DVB resins were somewhat higher than those obtained in polystyrenebenzyldimethylethanolammonium–8% DVB resins. The two systems are quite different in the sense that, whereas the sodium and chloride ions are counterions and co-ions in the case of the cation exchanger, the roles of the ions are reversed in the case of the anion-exchange resin. The lack of a self-consistent picture may be shown by comparison of data obtained for the Amberlite anion-exchange resins and Dowex 1-X10. Whereas activity coefficients of 0.49–0.52 were obtained in a 1 *m* medium in the case of the four former resins, which vary over a considerable range in moisture and cross-linker content, a much higher value of 0.69 may be interpolated from the Dowex 1-X10 data of Nelson and Kraus[9] at the same concentration.

Although the contents of the present paper lend support to the view that the extent of ion pairing in the resin phase increases as the concentration in the external phase decreases, an unambiguous solution to the problem of electrolyte sorption has not yet been attained. Freeman, *et al.*,[23] have recently measured the uptake of KCl and $MgCl_2$ by low cross-linked (2% DVB) cation and anion exchangers by the use of a technique which circumvents the problems associated with the presence of the liquid film and have found rather constant values of $\gamma_{\pm}^*$ over a 0.002–0.26 *m* concentration range. It would appear that simultaneous measurements by the Freeman technique and by the conventional method on a series of resin systems would be invaluable in attempting to resolve the problem. Hopefully, identical results will be obtained by the two methods. Armed with undisputedly valid data, the final step should involve a search for a theoretical treatment of co-ion uptake which will be in satisfactory agreement with the experimental data over a wide range of salt concentration and resin composition.

Table III: Values of Mean Molal Activity Coefficients for NaCl in Various Resin Systems

Resin	m_{NaCl}	$\gamma_{\pm}^*$	Ref
Polymethacrylic acid–5% DVB	1.0	0.55	12
	0.40	0.43	12
	0.10	0.30	12
	0.020	0.20	12
Amberlite IRA-400[a]	1.02	0.52	22
Amberlite IRA-401[a]	1.03	0.52	22
Amberlite IRA-410[b]	1.02	0.49	22
Amberlite IRA-411[b]	1.03	0.50	22
Dowex 1-X10[a]	2.24	0.73	9
	0.91	0.68	9
	0.25	0.52	9
	0.100	0.39	9
	0.050	0.29	9
	0.010	0.09	9
Amberlite XE-100	1.04	0.66	*c*
	0.52	0.63	*c*
	0.21	0.60	*c*
	0.104	0.58	*c*
Amberlite IR-120	1.02	0.74	*c*
	0.51	0.68	*c*
	0.20	0.65	*c*
	0.101	0.57	*c*
	0.050	0.45	*c*
	0.020	0.28	*c*
Phenol-formaldehyde–sulfonate	1.02	0.63	11
	0.51	0.54	11
	0.101	0.37	11
	0.0100	0.09	11

[a] Polystyrenebenzyltrimethylammonium chloride–DVB.
[b] Polystyrenebenzyldimethylethanolammonium chloride–DVB.
[c] This work.

(23) D. H. Freeman, V. C. Patel, and T. M. Buchanan, *J. Phys. Chem.*, 69, 1477 (1965).

On the Transfer of Energy between a Gas and a Solid

by H. Shin

Department of Chemistry, University of Nevada, Reno, Nevada 89507 *(Received May 6, 1965)*

An analytical expression of the thermal accommodation coefficient is presented for a Morse potential. The effect of the attractive force between an incident particle and a lattice atom is found to be extremely important in controlling the magnitude of the accommodation coefficient, but in general the theoretical values are significantly smaller than experimental values. By considering the contribution of adsorbed particles on the energy transfer, a physically realistic expression of the thermal accommodation coefficient for theoretical calculations is expressed as $\alpha = f_{pp}\alpha_{pp} + f_{ps}\alpha_{ps}$, where α_{ps} and α_{pp} are the accommodation coefficients for the collision of the incident particles with the lattice atom and with the adsorbed particles, respectively, and where f_{ps} and f_{pp} are the fractions of sites unoccupied and occupied by these gas particles, respectively. It is shown that the discrepancy can be substantially reduced if this expression is used in the theoretical calculation of accommodation coefficients. The Ne–W, He–Pt, and Ar–Pt systems are chosen for numerical illustrations.

1. Introduction

The possible existence of a discontinuity of temperature between the surface of vessel and a gas at a different temperature was first experimentally demonstrated by von Smoluchowski.[1] He explained it as due to the decreased length of the free paths in the immediate neighborhood of the surface, and to the imperfect equalization of temperature on collision between gas particles (atoms or molecules) and the atoms of the solid. The effect is specified in terms of the accommodation coefficient, α, introduced by Knudsen.[2] Since then, many investigations[3-6] have made important contributions to the growth of chemistry and physics at gas–solid interfaces, both in the development of experimental apparatus and techniques and in the formulation of refined theory. In spite of the concentration of effort in this area for more than half a century, some of the long-recognized problems, such as wide discrepancies between theoretical predictions and experimental values of the accommodation coefficient, have been only partly solved and new problems have been raised.

Jackson and Howarth[7,8] formulated the accommodation coefficient by considering the interaction between gas atoms and the normal modes of the crystal lattice, and assuming only single quantum transition, eq 1.1,

$$\alpha_{ps} = \frac{3}{\nu_m^3}\int_0^{\nu_m} \frac{(h\nu/kT)^2\nu^2 d\nu}{\exp(h\nu/kT) - 1} \times \int_0^{\infty} P(E)\exp(-E/kT)\frac{dE}{kT} \quad (1.1)$$

where ν_m is the Debye frequency of the solid, $P(E)$ is the vibrational transition probability per collision, and E is the initial translational energy of the relative motion. The subscript ps denotes the accommodation coefficient for the interaction of the incident particles with the solid atoms.

In general $P(E)$ appears as a complicated function of E and ν, and the analytical evaluation of α_{ps} with such a $P(E)$ has not been possible. A number of

(1) M. von Smoluchowski, *Ann. Physik*, **64**, 101 (1898).

(2) M. Knudsen, *ibid.*, **34**, 593 (1911); **6**, 129 (1930).

(3) For an extensive list of references, see M. Kaminsky, "Atomic and Ionic Impact Phenomena on Metal Surfaces," Academic Press Inc., New York, N. Y., 1965, Chapter 6.

(4) H. Y. Wachman, *Am. Rocket Soc. J.*, **32**, 2 (1962).

(5) D. M. Gilbey, *Phys. Chem. Solids*, **23**, 1453 (1962).

(6) F. O. Goodman, *ibid.*, **24**, 1451 (1963); also see references therein.

(7) J. M. Jackson and A. Howarth, *Proc. Roy. Soc.* (London), **A142**, 447 (1933).

(8) Also, see recent articles P. Feuer, *J. Chem. Phys.*, **39**, 1311 (1963); **40**, 2810 (1964).

years ago Devonshire[9] obtained, assuming the interaction potential to be a Morse type of the form $U(r) = D[\exp(-r/a) - 2\exp(-r/2a)]$, the vibrational transition probability as eq 1.2

$$P(E) = 16\left(\frac{\pi^3}{\hbar}\right)\left(\frac{a^2\mu^2}{m}\right)\times \nu\frac{\sinh(2\pi\eta a)\sinh(2\pi\eta' a)}{[\cosh(2\pi\eta' a)-\cosh(2\pi\eta a)]^2}\frac{(A+A')^2}{AA'} \quad (1.2)$$

where

$$\eta = \frac{2(2\mu E)^{1/2}}{\hbar};\quad \eta' = \frac{2[2\mu(E+h\nu)]^{1/2}}{\hbar};\quad E' = E + h\nu;$$
$$A = |\Gamma(-d + i\eta + 1/2)|^2;$$
$$A' = |\Gamma(-d + i\eta' + 1/2)|^2;$$
$$d = \frac{2a(2\mu D)^{1/2}}{\hbar};\quad \hbar = \frac{h}{2\pi}$$

μ is the reduced mass of the system and m is the mass of solid atom. Using this expression he evaluated eq 1.1 by numerical integrations for the assumed values of a and D and showed the possibility of fitting the calculated α_{ps} values to experiments by adjusting a and D.

Obviously, any attempt to integrate eq 1.1 explicitly with $P(E)$ given by eq 1.2 will fail because of the complicated dependences of the integrand on E and ν. If $D = 0$, then we can represent the interaction potential by a purely repulsive form $U(r) = A\exp(-r/a)$. For this potential, the transition probability for the one-quantum transition is known to be[10]

$$P(E) = 16\left(\frac{\pi^3}{\hbar}\right)\left(\frac{a^2\mu^2}{m}\right)\nu\frac{\sinh(\pi\eta a)\sinh(\pi\eta' a)}{[\cosh(\pi\eta' a)-\cosh(\pi\eta a)]^2} \quad (1.3)$$

Even with this expression, the explicit evaluation of α_{ps} appears to be impossible. However, when $\pi\eta a >> 1$ and $\pi\eta' a >> 1$, we obtain Landau's classical result[11] by expanding the exponent of eq 1.3 in a series of $h\nu/E$, eq 1.4. This equation holds approximately for

$$\alpha_{ps}^{L} = \frac{3}{32m\mu^{1/2}}\left(\frac{8\pi T}{k}\right)^{3/2}\left(\frac{\hbar}{a\Theta}\right)^3;\quad \Theta = \frac{h\nu_m}{k} \quad (1.4)$$

helium at low temperatures, but the simplifications introduced in the evaluation are found to be not valid in many real systems.[9] For example, for helium on tungsten, this expression is valid in the range $10°K < T < 24°K$. Furthermore, the effect of the attractive force is not considered in obtaining eq 1.4. In general, these theoretical calculations of accommodation coefficients will be least reliable when interactions are strong (*i.e.*, when use of perturbation theory is inapplicable) and when collision times are comparable to the characteristic times of the degrees of freedom being excited.

The Morse potential has also been used in Goodman's purely classical approach[6] in which the lattice atom is assumed to be at rest during the entire interaction and the interaction force is expressed as a known function of time. The final expression of α_{ps} is then evaluated using electronic computer technique, but the final expression is shown to be valid for a small α_{ps} ($<<1$) and small ratio of mass of gas atom to mass of lattice atom ($<<1$).

It should be emphasized that these numerical integrations, however, have the disadvantage of giving only particular solutions to specific problems just as any experiment would do. It might be possible, when a number of calculations have been performed, to deduce analytical generalizations which are now hard to see because of the mathematical complexities involved. However, analytical solutions, even if they are approximate, will give detailed information on the dependences of the final solutions on relevant physical parameters; *e.g.*, the dependence of α_{ps} on the potential parameters, temperature, masses, etc., in the present case. Such solutions are therefore of great importance in the present system in showing the generality of theories and in comparing theories and experiments.

The purpose of the present paper is to elucidate quantitatively the discrepancies between theoretical and experimental values of accommodation coefficients in terms of (i) the effect of the attractive force between incident particles and lattice atoms and (ii) the contribution of adsorbed particles on the solid surface in transferring energy between a gas and a solid. For this purpose we analytically solve eq 1.1 for the Morse potential and show the detailed dependence of α_{ps} on the attractive force, the potential range parameter, and temperature. The energy transfer *via* the collision of incident particles with adsorbed particles is discussed in terms of classical dynamics. We only consider weakly adsorbed particles.

2. Interaction of Incident Particles with Solid Atoms

When we consider a one-dimensional motion of the collision system in a potential field of $V(x,r)$, where r is the distance between the center of mass of the incident particle and the equilibrium position of the oscillator (the surface atom) and x is the displacement of

(9) A. F. Devonshire, *Proc. Roy. Soc.* (London), **A158**, 269 (1937).
(10) J. M. Jackson and N. F. Mott, *ibid.*, **A107**, 703 (1932).
(11) L. Landau, *Physik Z. Sowjetunion*, **8**, 489 (1935).

the oscillator from its equilibrium position, the *over-all* interaction energy can be expressed as $V(x,r) = U(r) - xF(r)$, where $F(r)$ is the perturbing force. Suppose initially the gas particle–solid atom system is in internal state i, and the gas particles collide with relative motion characterized by an energy E. If the transition i → f takes place, then the final state of energy is characterized by a new energy E' ($>E$). In terms of Zener's quantum mechanical treatment,[12] the probability of the transition i → f can be expressed in the form shown in eq 2.1, where $\psi(E,r)$ and $\psi(E',r)$

$$P(E) = \frac{8\mu \mathbf{x}_{if}^2}{\hbar^2(EE')^{1/2}}\left[\int_{-\infty}^{\infty}\psi(E,r)F(r)\psi(E',r)dr\right]^2 \quad (2.1)$$

are the wave functions of the initial and final states of the collision system, respectively. The quantity $\mathbf{x}_{if}$ is the matrix element of x taken between the unperturbed initial and final states of the oscillator.

When we substitute eq 2.1 into eq 1.1, the accommodation coefficient can be written as eq 2.2. The

$$\alpha_{ps} = \frac{96\pi^2\mu}{(\nu_m kT)^3}\int_0^{\infty}\int_0^{\nu_m}\frac{\nu^4\mathbf{x}_{if}^2\exp(-E/kT)}{[\exp(h\nu/kT) - 1](EE')^{1/2}} \times \left[\int_{-\infty}^{\infty}\psi(E,r)F(r)\psi(E',r)dr\right]^2 d\nu dE \quad (2.2)$$

interaction energy and perturbing force between the incident gas particle and the surface atom are assumed to be the Morse potential and $F(r) = \gamma(dU/dr)$, where γ is a dimensionless constant, respectively.

We now introduce the WKB semiclassical wave functions[13] to evaluate the r integral in eq 2.2 explicitly, *i.e.*, $P(E)$.

$$\psi(E,r) = \frac{c_i}{[U(r) - E]^{1/4}}\exp\left[\frac{1}{\hbar}\int_E^{U(r)} \times \{2\mu[U(r) - E]\}^{1/2}\left(\frac{dr}{dU}\right)dU\right] \quad (2.3)$$

$$\psi(E',r) = \frac{C_f}{[U(r) - E']^{1/4}}\exp\left[-\frac{1}{\hbar}\int_{E'}^{U(r)} \times \{2\mu[U(r) - E']\}^{1/2}\left(\frac{dr}{dU}\right)dU\right] \quad (2.4)$$

where c_i and c_f are constants evaluated as $|U(r \to \infty) - E|^{1/4}$ and $|U(r \to \infty) - E'|^{1/4}$, respectively. The function dr/dU is obtained as, in the region of strong interaction, eq 2.5. When this expression is

$$\frac{dr}{dU} = -\frac{a}{U}\left[1 - \left(\frac{D}{U}\right)^{1/2} + \frac{1}{2}\left(\frac{D}{U}\right)^{3/2} + \dots\right] = -\frac{1}{U}\sum_{i=0}^{\infty}\beta_i U^{-i} \quad (2.5)$$

$$i = 0, 1/2, 3/2 \dots$$

introduced in eq 2.3 and 2.4, the final form of $P(E)$ may be written as eq 2.6. In this solution the expression $\mathbf{x}_{if} = \hbar/(2mh\nu)^{1/2}$ is introduced.

$$P(E) = 16\gamma^2\pi^3a^2\left(\frac{\mu^2}{m\hbar}\right)\nu \times \exp\left[\frac{(2\mu\pi)^{1/2}}{\hbar}\sum_{i=0}^{\infty}\sum_{n=1}^{\infty}\beta_i(-h\nu)^n \times \frac{\Gamma(-1/2 + i + n)}{n!\Gamma(1 + i)}E^{1/2-i-n}\right] \quad (2.6)$$

Therefore, the accommodation coefficient can be written as eq 2.7, where $K = 16\gamma^2\pi^3a^2\mu^2/m\hbar$ and the

$$\alpha_{ps} = \frac{12\pi^2K\hbar^2}{(\nu_m kT)^3}\int_0^{\infty}\int_0^{\nu_m}\frac{\nu^5}{[\exp(h\nu/kT) - 1]} \exp\left[-\frac{E}{kT} + \frac{(2\mu\pi)^{1/2}}{\hbar}\sum_i\sum_n(\dots)\right]d\nu dE \quad (2.7)$$

double summation is given in eq 2.6. The double summation, which is the exponent of $P(E)$, is explicitly obtained as

$$\frac{-2\pi^2a(2\mu)^{1/2}}{E^{1/2}}\left\{\left[1 - \frac{2}{\pi}\left(\frac{D}{E}\right)^{1/2} + \frac{2}{3\pi}\left(\frac{D}{E}\right)^{3/2} + \dots\right]\nu - \frac{\pi\hbar}{2E}\left[1 - \frac{4}{\pi}\left(\frac{D}{E}\right)^{1/2} + \dots\right]\nu^2 + \dots\right\}$$

By expanding $\exp\{[(2\mu)^{1/2}\pi^3a\hbar/E^{3/2}][1 - (4/\pi)(D/E)^{1/2}]\nu^2\}$ as an infinite series, the ν integral can be given in a form that is integrable analytically. In the evaluation a further simplification is found if we introduce

$$\exp(h\nu/kT) - 1 = (h\nu/kT)[1 + 1/2(h\nu/kT) + 1/6(h\nu/kT)^2 + \dots]$$

With these series the accommodation coefficient finally appears in the form given in eq 2.8, where c's are the

$$\alpha_{ps} = \frac{6\pi K\hbar}{\nu_m^3(kT)^2}\int_0^{\infty}\int_0^{\nu_m}\nu^4\left(1 + \sum_{j=1}^{\infty}c_j\nu^j\right) \exp\left(-\frac{E}{kT} - g\nu\right)d\nu dE \quad (2.8)$$

ν-independent coefficients from the above expansions and are given in Appendix I, and where

$$g = \frac{2\pi^2a(2\mu)^{1/2}}{E^{1/2}}\left[1 - \frac{2}{\pi}\left(\frac{D}{E}\right)^{1/2} + \frac{2}{3\pi}\left(\frac{D}{E}\right)^{3/2} + \dots\right]$$

(12) C. Zener, *Phys. Rev.*, 37, 556 (1931).

(13) L. Landau and E. M. Lifshitz, "Quantum Mechanics," Pergamon Press Ltd., London, 1959, pp 178–183.

Note that in g the coefficient of $(D/E)^2$ is zero and the terms containing $(D/E)^{5/2}$ and higher orders may, for practical purposes, be neglected. In order to obtain the explicit solution of eq 2.8, we first perform the integration over normal modes and then the energy transfer between the collision partners.

From eq 2.8 the ν integral contains infinitely many terms, but as will be seen below only first few terms are needed in the final solution of α_{ps}. The complete result of the ν integral is in the order of decreasing magnitude

$$\int_0^{\nu_m} \nu^4\left(1 + \sum_{j=1}^{\infty} c_j\nu^j\right)\exp(-g\nu)\mathrm{d}\nu = \frac{24}{g^5} + \frac{24\phi}{g^5} - \exp(-g\nu_m)\left[(1+\phi)\sum_{i=0}^{4}\theta_i\nu_m{}^i + \sum_{i=5}^{\infty}\rho_i\nu_m{}^i\right] \quad (2.9)$$

where

$$\phi = \frac{5c_1}{g} + \frac{30c_2}{g^2} + 2.10\times 10^2\frac{c_3}{g^3} + 1.68\times 10^3\frac{c_4}{g^4} + 1.51\times 10^4\frac{c_5}{g^5} + 1.51\times 10^5\frac{c_6}{g^6} + 1.66\times 10^6\frac{c_7}{g^7} + \cdots$$

The coefficients θ's and ρ's are given in Appendix II. In this expression ϕ is small compared to unity, and the third part containing $\exp(-g\nu_m)$ may be neglected.

The E integral can be therefore separated into three parts. Both I_2 and I_3 contain infinitely many terms;

$$I_E = 24\int_0^{\infty} g^{-5}\exp(-E/kT)\mathrm{d}E + 24\int_0^{\infty} g^{-5}\phi\times\exp(-E/kT)\mathrm{d}E - \int_0^{\infty}(1+\phi\Sigma\theta_i\nu_m{}^i + \Sigma\rho_i\nu_m{}^i)\times\exp(-E/kT - g\nu_m)\mathrm{d}E = I_1 + I_2 + I_3$$

however, I_3 is insignificant while in I_2 only the first term of ϕ, which is $-5\pi\hbar/kTg$, is important. For example, in the Ne–W system $I_2/I_1 = 0.08$–0.05 over the temperature range from 100 to 300°K. Thus a satisfactory expression for the E integral is

$$I_E = I_1 + I_2' = 24\int_0^{\infty} g^{-5}\exp(-E/kT)\mathrm{d}E - (120\pi\hbar/kT)\int_0^{\infty} g^{-6}\exp(-E/kT)\mathrm{d}E$$

With the expansions of g^{-5} and g^{-6} in power series in $(D/E)^i$, where $i = 0, {}^1/_2, 1, {}^3/_2 \ldots$, the analytical solution of the E integral finally gives the accommodation coefficient as eq 2.10, where

$$\alpha_{ps} = \left[\left(\frac{190.89\gamma^2}{\pi m\mu^{1/2}}\right)\left(\frac{T}{\pi k}\right)^{3/2}\left(\frac{\hbar}{a\Theta}\right)^3\right]\times\left[1 + \sum_m^{\infty} a_m\left(\frac{D}{kT}\right)^m\right] - \left[\left(\frac{190.89\gamma^2}{\pi m\mu^{1/2}}\right)\left(\frac{T}{\pi k}\right)^{3/2}\left(\frac{\hbar}{a\Theta}\right)^3\right]\times\left[\frac{3\hbar}{a\pi^{3/2}}\left(\frac{2}{mkT}\right)^{1/2}\right]\left[1 + \sum_m^{\infty} b_m\left(\frac{D}{kT}\right)^m\right] \quad (2.10)$$

$$m = {}^1/_2,\ 1,\ {}^3/_2,\ 2,\ {}^5/_2 \ldots$$

where

$$a_{1/2} = \frac{32}{3\pi^{3/2}};\quad a_1 = \frac{24}{\pi^2};\quad a_{3/2} = \frac{16}{3\pi^{3/2}}\left(\frac{28}{\pi^2} - \frac{1}{3}\right);\quad a_2 = \frac{32}{3\pi^2}\left(\frac{28}{\pi^2} - 1\right);\quad a_{5/2} = \frac{64}{15\pi^{5/2}}\times\left(\frac{504}{\pi^3} - \frac{100}{3\pi} - \frac{1}{15}\right)\cdots$$

$$b_{1/2} = \frac{5}{\pi^{1/2}};\quad b_1 = \frac{28}{\pi^2};\quad b_{3/2} = \frac{1}{2\pi^{1/2}}\left(\frac{112}{\pi^2} - 1\right);\quad b_2 = \frac{28}{3\pi^2}\left(\frac{36}{\pi^2} - 1\right);\quad b_{5/2} = \frac{8}{12\pi^{3/2}}\times\left(\frac{1008}{\pi^3} - \frac{163}{3\pi} - \frac{1}{15}\right)\cdots$$

Thus we have succeeded in obtaining the explicit solution of α_{ps} given by eq 2.2, which has not been possible by previous workers. The second term results from the contribution of the leading term of I_2 and is smaller than the first term by a factor of $\sim(3\hbar/a\cdot\pi^{3/2})(2/mkT)^{1/2}$. Equation 2.10 can be readily reduced to the case of a simple repulsive interaction, *e.g.*, the interaction with $U(r) = D\exp(-r/a)$

$$\alpha_{ps}{}^* = \left[1 - \frac{3\hbar}{a\pi^{3/2}}\left(\frac{2}{mkT}\right)^{1/2}\right]\alpha_{ps}{}^{**}$$

where

$$\alpha_{ps}{}^{**} = \left(\frac{190.89\gamma^2}{\pi m\mu^{1/2}}\right)\left(\frac{T}{\pi k}\right)^{3/2}\left(\frac{\hbar}{a\Theta}\right)^3$$

We now note that $\alpha_{ps}{}^{**}$ is very close to $\alpha_{ps}{}^{L}$. Note

$$\frac{\alpha_{ps}{}^{L}}{\alpha_{ps}{}^{**}} = 1.0844$$

that the essential difference between eq 1.4 and 2.10 for the purely repulsive interaction is the extension of the integral over ν to infinity in the former, but this is valid only for low temperatures. From the above ratio, it can be seen that this extension overestimates α_{ps} by a factor of 1.0844. However, the correct comparison between these two treatments should be made in terms of the ratio

$$\alpha_{ps}{}^{L}\Big/\left[1 - \frac{3\hbar}{a\pi^{3/2}}\left(\frac{2}{mkT}\right)^{1/2}\right]\alpha_{ps}{}^{**}$$

where the second term in the square brackets is in general less than 0.10 as will be seen below. Therefore, Landau's purely classical treatment overestimates α_{ps} for the pure repulsive interaction by 10–15% compared to the present work.

The summations in $(D/kT)^m$ are due to the effect of the attractive energy $-2D\exp(-r/2a)$ acting between the collision partners. The convergence of the summations becomes rather slow at low temperatures or for large D values; however, the signs of the terms start to alternate beyond $(D/E)^3$ and a numerical test shows that the contribution of these terms is very small compared to the first six or seven terms.

It should be pointed out that although we have ignored the contribution of I_3 in the E integral, its evaluation is not difficult. In this integral the exponential part is $\exp(-E/kT - g\nu_m)$, in which $\exp(-g\nu_m)$ increases with E as $\exp(-\text{const}/E^{1/2})$, whereas $\exp(-E/kT)$ decreases as E increases. Therefore, the integral has the maximum value at $E = E^*$, and an asymptotic evaluation of I_3 can be made using the Laplace integral method.[14]

3. Numerical Illustration of α_{ps}

Equation 2.10 is the explicit solution of α_{ps} formulated originally as eq 2.2. The solution is obtained without approximations other than the use of the WKB semiclassical wave functions, which assumes that the translational motion is essentially classical. In recent papers[15-18] the applicability of the semiclassical method in many actual cases has been discussed. We should note, however, that the final result does not contain smaller terms, namely $(I_2 - I_2')$ and I_3 of the E integral (this aspect will be quantitatively discussed below).

Devonshire evaluated eq 2.2 for the Morse potential numerically and found in the Ne–W system an excellent agreement with Roberts' experimental values[19] when the potential parameters are assumed as $D = 493$ cal/mole and $a^{-1} = 1.484 \times 10^8$ cm^{-1}, taking the characteristic temperature of tungsten to be 205°. We have applied our explicit formula, eq 2.10, with these parameters assuming $\gamma = 1$, which is Devonshire's case. The calculated values of α_{ps} are shown in Figure 1 along with Devonshire's numerical and Roberts' experimental results. Other experimental values are also shown. The excellent agreement between eq 2.10 and Devonshire's is seen. Unlike the gas phase collision, in this comparison it is important to note that the consideration of the D-dependent terms in eq 2.10 is so important

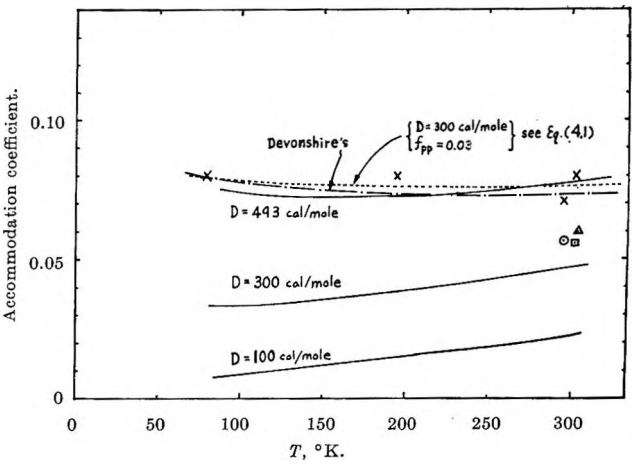

Figure 1. Comparison of the present approach with Devonshire's results for Ne–W; $a^{-1} = 1.484 \times 10^1$ cm^{-1}, $\Theta = 205$°K. Roberts' experimental values are shown by ×. Other experimental values are ⊙, A. B. van Cleave, *Trans. Faraday Soc.*, **34**, 1174 (1938); △, G. W. Spivak and A. A. Zaitzev, *Compt. Rend. Acad. Sci. USSR*, **2**, 118 (1935); ⊡, J. L. Morrison and J. K. Roberts, *Proc. Roy. Soc.* (London), **A173**, 1 (1939).

that the D summation is no longer plays a role as corrections, but it is the predominant part of α_{ps}. For example, at 100°K we obtain $\alpha_{ps}{}^{**} = 0.0018$ while the D summation in the first part of eq 2.10 is 43.4209, so that the first part becomes $0.0018(1 + 43.4209) = 0.0799$. In the second part, the factor $(3\hbar/a\pi^{3/2})\cdot(2/mkT)^{1/2}$ is 0.0588 and the D summation is 55.3657; the second part is then $(0.0018)(0.0588)(1 + 55.3657) = 0.0057$, which is significantly smaller than the first part. This part represents the contribution of the leading part of I_2 in the E integral; therefore, the remaining part of I_2 and I_3 may be neglected. (Here we are showing seemingly unnecessary numerical procedures to obtain α_{ps}; however, we do this because the sources of these values are important in refinement of the theoretical treatment.) From these two parts, the over-all value of the accommodation coefficient is 0.0740. Devonshire's value at 100°K is 0.0775. Both theoretical results are in complete agreement at 200°K. At 295°K $\alpha_{ps}{}^{**} = 0.0094$, and after the introduction of the D-dependent terms we

(14) A. Erdelyi, "Asymptotic Expansion," Dover Publications, New York, N. Y., 1956, pp 36–39.

(15) D. Rapp, *J. Chem. Phys.*, **32**, 735 (1960).

(16) T. L. Cottrell and J. C. McCoubrey, "Molecular Energy Transfer in Gases," Butterworth and Co. (Publishers) Ltd., London, 1961, Chapter 6.

(17) B. Widom, *Discussions Faraday Soc.*, **33**, 37 (1962).

(18) H. Shin, *J. Chem. Phys.*, **42**, 1739 (1965).

(19) J. K. Roberts, *Proc. Roy. Soc.* (London), **A129**, 146 (1930); **A135**, 192 (1932); **A142**, 518 (1933).

find $\alpha_{ps} = 0.0776$, which is somewhat larger than Devonshire's value, 0.0735. Roberts' experimental value at this temperature is 0.07. For the purely repulsive interaction, we have $\alpha_{ps}^* = 0.0017$ and 0.0094 at 100 and 295°K, respectively, which are too small compared to either the above results or Roberts' experimental values. From this it is then obvious that the attractive energy plays a major role in bringing the incident particles to the proximity of the surface for an effective energy transfer. Using the explicit solution of α_{ps}, we are therefore able to reproduce Devonshire's results obtained from numerical integrations. Although both results agree with Roberts' experimental values quite satisfactorily, it does not validate the use of eq 2.2 for the discussion of inelastic collisions at a gas–solid interface, because such an agreement is found only after adjusting the potential parameters. Since α_{ps} is sensitively dependent on a and D, any change in the magnitudes of these parameters will give a serious variation in the final results. For example, if we take $a^{-1} = 2.0 \times 10^8$ cm^{-1}, $D = 493$ cal/mole, and $\Theta = 205$°K, then $\alpha_{ps} = 0.1893$ at 100°K, which is seriously larger than the above results of Devonshire and Roberts. The chosen value, $D = 493$ cal/mole, may be large for the present interaction system. In Figure 1 we therefore also show the calculated values of α_{ps} for $D = 300$ and 100 cal/mole. The curves are significantly lowered from the case with $D = 493$ cal/mole. Although the examples are not exhaustive, this in itself, quite aside from any other approximation which may enter, means that we could never hope to calculate accommodation coefficients which are in agreement with experiments for a physically realistic collision at a gas–solid interface using α_{ps}, *i.e.*, considering the ps collision alone.

If the quantum mechanical formulation of α_{ps} is correct and simplifying approximations in its solution are satisfactory, then we must look for other sources which may contribute to the energy transfer rather than adjusting the potential parameters in α_{ps}. It may be mentioned that assumptions made in most theoretical treatments are important to point out at this stage. The temperature difference $\Delta T = T_{gas} - T_{surface}$ is assumed to be zero in the above formulation, whereas the experimental results were obtained for $\Delta T > 0$. In Roberts' experiment it has been noted that $\Delta T = 10$ to 30°, so that if we use T_{gas} in α_{ps} the calculated values can increase by factors of 1.10–1.30 at 100°K and by 1.04–1.10 at 300°K. In the present discussion we consider the experimental values which are obtained with the condition $T_{surface} >> \Delta T$. Equation 2.2 is formulated assuming only single quantum transition. Strachan[20] attempted to include a superposition of higher-order transitions in place of the single transition. He used the complete Morse function without expanding it in powers of the vibrational amplitude and found that, within the domain of applicability of the first-order perturbation theory used, the multiplet transitions are extremely improbable.

In his purely classical approach similar to that used by Landau,[11] Rapp,[15] and Turner and Rapp,[21] Goodman[6] showed that the attractive part of $U(r)$ has a negligible effect on the values of the accommodation coefficients. In the purely classical limit $\hbar \to 0$; the only important part of $U(r)$ is the repulsive term $D \exp(-r/a)$ so that this argument can be accepted. However, at low temperatures the interaction of a neutral gas with a solid surface can never be adequately described without the attractive forces. Even in the high-temperature inelastic collision systems, it has been shown that the attractive forces play important roles in controlling the over-all values of the vibrational transition probability and the total inelastic cross sections.[17,22,23] Goodman chose $a^{-1} = 3.2 \times 10^8$ cm^{-1} and $D = 440$–450 cal/mole as the "realistic" potential parameters in the Ne–W system, and obtained $\alpha_{ps} = 0.051$, 0.041, and 0.040 at 100, 200, and 300°K, respectively, which are in satisfactory agreement with Thomas' experimental results.[24] The characteristic temperature was taken to be 330°K, which is much larger than the value used in the above calculation. If we employ these "realistic" parameters, then the present formula, eq 2.10, results in $\alpha_{ps} = 0.1460$, 0.1383, and 0.1528 at the three corresponding temperatures, but these values are larger than Goodman's (or Thomas') results by a factor of ~3. However, it should be remembered that the present formula is derived from the assumption of a one-dimensional model. If we use a three-dimensional model but assume that the field is dependent only on the interaction coordinate of the incident particle and the lattice atom, so that the motion parallel to the surface is unchanged, then we can introduce the factor $^1/_2$ in eq 2.10. Even with this factor, the present results are still larger than Goodman's.

In the latter work the chosen parameters are seem to be large in the Ne–W case. Since there is no reliable experimental data for a and D for the W–W

(20) C. Strachan, *Proc. Roy. Soc.* (London), **A158**, 591 (1937).

(21) R. E. Turner and D. Rapp, *J. Chem. Phys.*, **35**, 1076 (1961).

(22) E. E. Nikitin, *Opt. i Spektroscopiya*, **6**, 141 (1959); *Opt. Spectry.* (U.S.S.R.), **6**, 93 (1959); *Discussions Faraday Soc.*, **33**, 14, 90 (1962).

(23) H. Shin, *J. Chem. Phys.*, **42**, 59 (1965).

(24) The experimental results are cited in Goodman's paper[6] as a private communication from L. B. Thomas.

interaction system at present, it is not possible to obtain accurate values of the parameters. In view of this difficulty, we show our results for D = 440, 300, and 100 cal/mole and $a^{-1} = 3.2 \times 10^8$, 2.5×10^8, and 2.0×10^8 cm^{-1} in Figure 2. Except the top three curves, which stand for D = 440 cal/mole, $a^{-1} = 3.2 \times 10^8$ cm^{-1}; D = 300 cal/mole, $a^{-1} = 3.2 \times 10^8$ cm^{-1}; and D = 440 cal/mole, $a^{-1} = 2.5 \times 10^8$ cm^{-1}, all curves are significantly lower than both Roberts' and Thomas' results. On the other hand, it is obvious that by adjusting these parameters we can produce an excellent agreement between the present approach and the experiments.

In both Figures 1 and 2, it may be noticed that the calculated values display a minimum when D is large (*i.e.*, 493 cal/mole in Figure 1 and 440 cal/mole in Figure 2), which is in accordance with Thomas' experiment.[6,24] The minimum occurs at ~170°K.

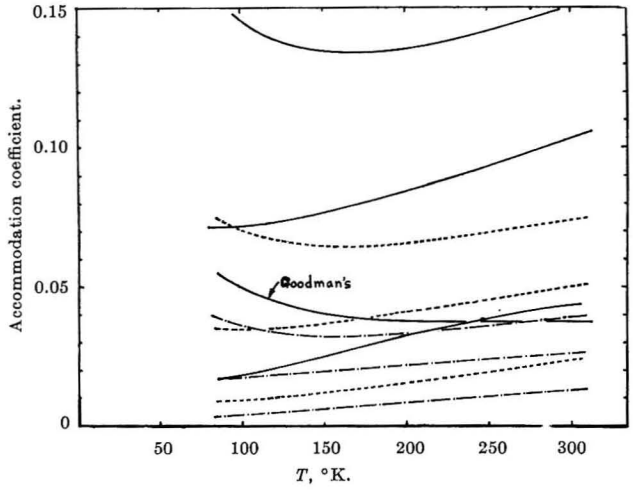

Figure 2. Calculated α_{ps} for Ne–W: ———, $a^{-1} = 3.2 \times 10^8$ cm^{-1}; – – – –, $a^{-1} = 2.5 \times 10^8$ cm^{-1}; and –·–·–, $a^{-1} = 2.0 \times 10^8$ cm^{-1}. The three curves for each a^{-1} represent from the top D = 440, 300, and 100 cal/mole, respectively. Goodman's numerical result is also shown. Θ = 330°K.

4. Interaction of Incident Particles with Adsorbed Particles and Discussion

In practice it is difficult to measure accommodation coefficients with a *clean* surface. Even if we started with such a surface, some of the incident particles will adsorb during the experimental runs. Especially for the earlier work, we must assume that the experimental values for supposedly *clean* surfaces actually refer to surfaces with a slight gas coverage. In such a system the incident particles then interact either with the lattice atoms or the adsorbed particles (adparticles), which are in general weakly adsorbed with small energies of adsorption and are at $T_{surface}$. The incident particle can have a finite lifetime on the surface before it returns to the gas phase, and during this lifetime it can interact with other incident particles. In the quantum mechanical treatment it has been assumed that the duration of a collision between the incident particle and the solid atom is of the same order of magnitude as for the collision of two particles in the gas phase. However, this assumption is not necessary, if we use the quantum mechanical result, α_{ps}, for the collisions in which this condition is strictly valid. It can be said that as far as the ps collisions are concerned, the basic formulation of α_{ps} given in eq 2.2 is satisfactory in practice (see ref 5).

Thus the above consideration leaves out the interaction of incident particles with the adparticles and with the particles which are staying on the surface temporarily for their finite lifetimes. At a thermal equilibrium the average number of these *temporarily* adsorbed particles may be assumed constant so that we can consider them as parts of the adsorbed particles.

The interaction between the incident particles and the adparticles can also participate in transferring energy. If the particles are weakly adsorbed, they can readily transport energy from the solid surface to the incident particles or from the incident particles to the surface. If they are strongly bound to the surface, they are less free to oscillate in the force field of the surface, so that they play less effective roles in transferring energy compared to the former case. There are a number of experiments in which accommodation coefficients are known to increase when the surface is covered with gas particles.[25] We briefly discuss some of these experimental results.

In Roberts' experiment[19] for Ne–W at 295°K, the accommodation coefficient is 0.07 when the surface is initially degassed but probably slightly covered with Ne during the run. On the other hand, it is 0.17 when the surface is covered with monatomic hydrogen gas. If we use eq 2.2 for the theoretical calculation of α_{ps} with D = 493 cal/mole and $a^{-1} = 1.484 \times 10^8$ cm^{-1}, obviously it is impossible to obtain the latter value.

Blodgett and Langmuir,[26] using a tungsten filament in H_2 at 0.2 mm, found $\alpha_{exptl} = 0.54$ above 1000°K, but found at lower temperatures α_{exptl} as low as 0.14. At high temperatures the filament was supposed to be clean in their work, while at lower temperatures it was covered with a film of adsorbed hydrogen. However, the lowering of α_{exptl} by an adsorbed gas film

(25) See Tables 6.3.1.1A-C of ref 3.

(26) K. B. Blodgett and I. Langmuir, *Phys. Rev.*, **40**, 78 (1932).

is hard to understand. In this system, since the adsorption is a chemisorption type,[27] many molecules can be adsorbed at higher temperatures, thus leading to more frequent collisions of adsorbed molecules with free molecules. Furthermore, hydrogen chemisorption is normally dissociative; therefore, the system will also involve the adsorbed atom-free molecule collisions. These processes are more effective in transferring energy compared to the gas molecule–lattice atom interaction, and lead to larger α_{exptl} at high temperatures. In fact, in experiments by Michels[28] and Roberts,[19] it was found that the α_{exptl} values are increased by adsorbed gas molecules on the tungsten surface.

Spivak[29] considered the accommodation coefficients of Ar and Ne on pure metal surfaces of W and on surfaces of W covered with films of O, H, and N. He observed a marked effect of adsorbed films on the accommodation coefficients.

Eggleton and Tompkins[30] showed the time variation of the accommodation coefficient for Ne on an iron surface on admission of 3×10^{-4} mm of hydrogen. They found that the accommodation coefficient is almost constant (0.045) until the admission of hydrogen. Upon the admission at $t = 26$ min it rapidly increased to a saturation value of $\sim$0.10, which they explained as the result of the formation of a complete monatomic hydrogen layer on the surface.

At 329.7°K Wachman[31] obtained the result that the accommodation coefficient for He–W is 0.020 for the initially degassed surface, and is 0.045 for the surface covered with deuterium. Such a change has also been reported for diatomic molecules. With the surface covered with gas, von Ubisch[32] found $\alpha_{\text{exptl}} = 0.357$ for H_2-W at 373.1°K, which may be compared with 0.143 at 400°K obtained by Blodgett and Langmuir[26] with the initially degassed surface.

Since these experiments were carried out at different conditions, it is not possible to make any quantitative comparison. However, all these results indicate significant increases in accommodation coefficients when the solid surface is covered with gases. In order to include the role of these adparticles in the theoretical calculation of accommodation coefficients we now consider the collision of the incident particles with the adparticles, which we denote the pp collision. The over-all accommodation coefficient can be then expressed in the form[33] given in eq 4.1, where f_{ps} and f_{pp}

$$\alpha = f_{\text{ps}}\alpha_{\text{ps}} + f_{\text{pp}}\alpha_{\text{pp}} \tag{4.1}$$

are the fraction of the unoccupied sites and occupied sites of the surface by the adparticles, respectively. This expression does not consider the case in which the solid surface is initially contaminated by some other impurity gases. In such a case an additional term(s) similar to $f_{\text{pp}}\alpha_{\text{pp}}$ may be introduced, but it is possible with extreme precautions to eliminate almost entirely the contamination of the surface so that only particles adsorbed during the experimental runs are needed to be considered. Note that the adparticles and the incident particles are identical, except the former particles are in the force field of the surface.

For the explicit formulation of α_{pp} we assume that the adparticles, which are now at the temperature of the surface, are weakly bound to the surface, that the interaction between the collision partners is impulsive along the line of oscillation of the adparticle, and that whenever the adparticle attains a momentum greater than or equal to $(2MD)^{1/2}$ it dissociates from the surface, where M is the mass of the particle.

Let p_1 and p_2 be the momenta of the adparticle and incident particle, respectively. Then, analogous to the collision of the incident particle with the surface atom, we consider the ratio, R, where p_2' is the momentum of the recoiled particle. If the collision system involves only one impact, the ratio R is unity since at each impact the momenta p_1 and p_2 are interchanged. If it involves two impacts, on the other hand, the ratio is zero. For a collision system of the present type it has been shown[34] that the momenta are always interchanged if $p_1 > p_2$, regardless of the initial phase of the adparticle, so that the amount of energy transferred is $|p_2^2 - p_1^2|/2M$. And, if $p_1 < p_2$, the adparticle which is initially in a certain interaction range on the surface results in the interchange. That is, for these two possible cases the probability of the transition p_1 to p_2 per collision is 1 and p_1/p_2, respectively. Therefore, the probability of the pp collision which results in $R = 1$ is

$$(P|R = 1) = \begin{cases} 1, & p_1 > p_2 \\ p_1/p_2, & p_1 < p_2 \end{cases} \tag{4.3}$$

$$R = \frac{p_2'^2 - p_2^2}{p_1^2 - p_2^2} \tag{4.2}$$

With the above collision model, this probability repre-

(27) G. Halsey, *Advan. Catalysis*, **4**, 259 (1952).

(28) W. C. Michels, *Phys. Rev.*, **52**, 1067 (1937).

(29) G. V. Spivak, *Khim. Referat. Zh.*, **3**, 15 (1940); *Chem. Abstr.*, **36**, 3995 (1942).

(30) A. E. J. Eggleton and F. C. Tompkins, *Trans. Faraday Soc.*, **48**, 738 (1952).

(31) Y. H. Wachman, Ph.D. Thesis, University of Missouri, 1957.

(32) H. von Ubisch, *Appl. Sci. Res.*, **A2**, 364, 403 (1949–1950).

(33) H. Shin, *J. Chem. Phys.*, **42**, 3442 (1965).

(34) H. Shin, *J. Phys. Chem.*, **68**, 3410 (1964).

sents the collision which may be considered as one in which a very large force acts for very short time so that we are no longer restricted to the adiabatic collision which is assumed in the formulation of the quantum mechanical forms. It is also important to note that eq 4.3 explicitly considers the effect of the double-impact collision on energy transfer.

The accommodation coefficient α_{pp} may be formulated by integrating $(P|R = 1)$ over physically permissible values of p_1 and p_2. After integrating $(P|R = 1)$ over the initial momentum state of the adparticles, we then integrate over the final state, $0 < p_2 < (2MD)^{1/2}$. The final result is

$$\alpha_{pp} = 1 - \exp(-D/kT) + \frac{\pi}{2}\Phi[(D/kT)^{1/2}] - \pi^{1/2}\int_0^{(D/kT)^{1/2}} \Phi(y)\exp(-y^2)dy \quad (4.4)$$

where

$$\Phi(s) = \frac{2}{\pi^{1/2}}\int_0^s \exp(-x^2)dx$$

The integral in eq 4.4 may be evaluated by a numerical procedure. When $(D/kT)^{1/2} \to \infty$, its limiting value is 0.4430. On the other hand, for small values of D/kT it can be ignored in comparison with other terms. For example, when $D/kT = 0.01$, the integral is 0.0111. However, in the following calculation we explicitly include this term.

From eq 4.1 with eq 2.10 and 4.4, we calculate α for Ne–W for several different surface coverages. The energy D = 300 and 100 cal/mole, the range parameter $a^{-1} = 2.5 \times 10^8$ cm^{-1}, and the modern value $\Theta = 330$°K are chosen, and the results are shown in Figures 3a and b. These figures show the important role of the pp collision, *i.e.*, $f_{pp}\alpha_{pp}$, in controlling the over-all value of α. Even with $f_{pp} = 0.01$, α for D = 300 cal/mole is increased by a factor of 1.5 over α_{ps} at 100°K. With this D value, the 3% coverage results in $\alpha \simeq \alpha_{exptl}$. *This case is also shown in Figure 1 for comparison.* The accommodation coefficient α with $f_{pp} = 0$ for D = 300 cal/mole is 0.0327, 0.0386, and 0.0464 at 100, 200, and 300°K, respectively, while with $f_{pp} = 0.03$ the result is 0.0783, 0.0756, and 0.0779 at these temperatures; therefore, the surface coverage of 3% increases α by factors of 2.4, 2.0, and 1.7, respectively, compared to the base-surface case.

In Table I, we show α for various f_{pp} values for the He–Pt and Ar–Pt systems, along with the experimental values. In He–Pt at 77.4°K, $\alpha_{exptl} = 0.090$. When we choose D = 60 cal/mole and $a^{-1} = 2.0 \times 10^8$ cm^{-1}, $\alpha_{ps} = 0.0178$. The characteristic

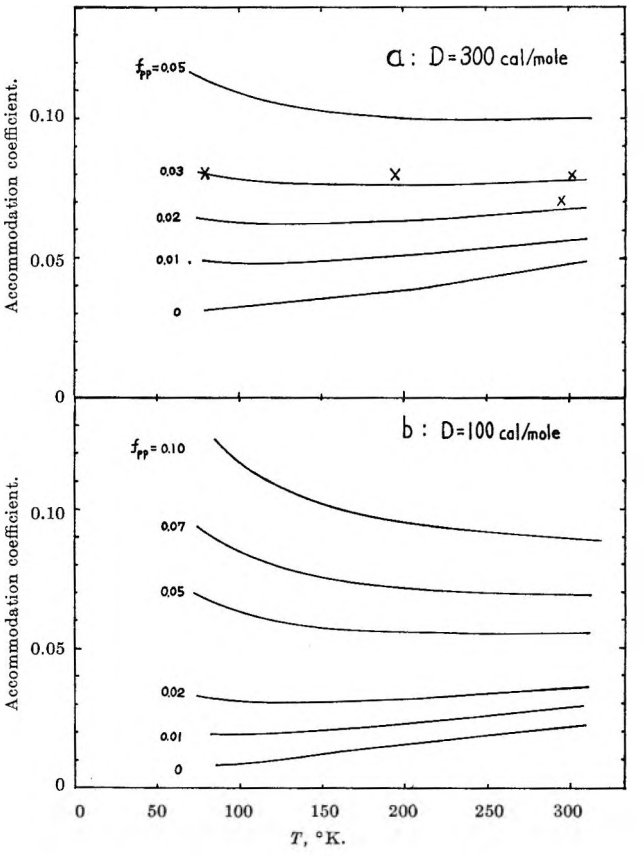

Figure 3. Calculated results of $\alpha = f_{pp}\alpha_{pp} + f_{ps}\alpha_{ps}$ for Ne–W for various surface coverages: $a^{-1} = 2.5 \times 10^8$ cm^{-1}, Θ = 330°K. (a) D = 300 cal/mole. (b) D = 100 cal/mole.

temperature is taken to be 230°K. For the 7% coverage, $\alpha = 0.0857$. At 273.2°K for the same parameters, $\alpha_{ps} = 0.0579$, while with 3% coverage eq 4.1 gives $\alpha = 0.0733$. The experimental value is 0.071. In the Ar–Pt system the experimental accommodation coefficients are large. For example, $\alpha_{exptl} = 0.869$ at 312°K and 0.648 at 405°K. However, α_{ps} are in general much smaller than these values as shown in Table I. Again, by introducing the term $f_{pp}\alpha_{pp}$ we can obtain α which are in good agreement with these experimental results, but in this system we must consider significant surface coverages in order to fit with the results. If we assume $a^{-1} = 4.0 \times 10^8$ cm^{-1} and D = 300 cal/mole, $\alpha = 0.6172$ for 10% coverage and 0.6587 for 20% coverage at 405°K, while the experimental result is 0.648. On the other hand, if $a^{-1} = 4.0 \times 10^8$ cm^{-1} and D = 200 cal/mole, $\alpha = 0.6251$ for $f_{pp} = 0.50$, and if $a^{-1} = 3.0 \times 10^8$ cm^{-1} and D = 400 cal/mole, $\alpha = 0.6229$ for $f_{pp} = 0.40$. It may be noted that α is proportional to the surface coverage so that the increase in α continues until the completion of the surface coverage, which is

Table I: Calculated Values of the Accommodation Coefficient for He–Pt and Ar–Pt for Various f_{pp}

System	T, °K	$10^{-8}a^{-1}$, cm^{-1}	D, cal/mole	α_{ps}	α_{exptl} at T, °K	f_{pp}	α
He–Pt	77.4	2.0	60	0.0178	0.090[a]	0.03	0.0469
						0.05	0.0665
						0.07	0.0859
						0.10	0.1152
He–Pt	273.2	2.0	60	0.0579	0.071[a]	0.01	0.0630
						0.03	0.0733
Ar–Pt	312	3.0	400	0.2688	0.8695[b]	0.03	0.2968
						0.10	0.3623
						0.40	0.6430
						0.60	0.8302
Ar–Pt	312	4.0	400	0.6372	0.8695[b]	0.01	0.6428
						0.03	0.6541
						0.10	0.6938
						0.20	0.7506
						0.40	0.8640
Ar–Pt	405	3.0	400	0.3094	0.6487[b]	0.01	0.3172
						0.05	0.3485
						0.10	0.3877
						0.20	0.4661
						0.40	0.6229
						0.50	0.7014
Ar–Pt	405	4.0	200	0.4335	0.6487[b]	0.03	0.4450
						0.10	0.4718
						0.20	0.5101
						0.30	0.5840
						0.50	0.6251
						0.60	0.6635
Ar–Pt	405	4.0	300	0.5758	0.6487[b]	0.05	0.5965
						0.10	0.6172
						0.20	0.6587

[a] P. Rolf, *Phys. Rev.*, 65, 185 (1944). [b] L. B. Thomas and R. E. Brown, *J. Chem. Phys.*, 18, 1367 (1950).

approximately in accordance with the work of Eggleton and Tompkins.[30]

In the above numerical illustration, although the choice of D and a is still arbitrary, it strongly represents an important role of the adparticles in transporting energy and thus affecting on the over-all values of accommodation coefficients. Therefore, when the information regarding surface coverages is quantitatively known, *e.g.*, from adsorption isotherm data, it should be possible to make a major refinement to the "conventional" theoretical treatment of the energy transfer at a gas–solid interface, in terms of the important role of the adparticles. Since both the incident and adsorbed particles are identical in the present model, they will interchange their energies completely at each impact. As mentioned above, the partners can suffer either one or two impacts before the incident particle recedes from the surface; therefore, the incident particle will be either excited or unexcited (but *not* deexcited) if the adparticle is initially in a higher energy state, which is the case of the collision of a cold gas with a hot surface, in general. Thus, the adparticles can be very effective in transferring energy from the surface lattice to the gas. The lattice atoms are in general heavy and tightly bound parts of the surface, so that only a small amount of energy is lost per collision, *i.e.*, α_{ps} is in general a small quantity. (In such a case the use of the perturbation theory should be a satisfactory approach.)

In summary, it may therefore be stated that any theoretical consideration of the energy transfer at a gas–solid interface should explicitly consider the role of adparticles. Without this consideration the theoretical accommodation coefficients will be always small com-

pared to the experiments and it will be impossible to interpret or to find agreements with experimental results, which contain in practice the contribution of adparticles even if we have started the experiment with a *clean* surface. It may again be emphasized that the attractive force between the collision partners plays an important role in the calculation of α_{ps}; *i.e.*, α_{ps} is sensitively dependent on the assumed form of the attractive term of $U(r)$.

We finally point out that it would be premature to discuss quantitatively the theoretical significance of α_{pp} for diatomic and polyatomic gases, because our formulation does not explicitly consider the detailed internal motion of adparticles. Also, the present formulation of α_{pp} cannot be applied to the collision of the incident particles with the *strongly* adsorbed particles. However, the present study may be considered as the next logical step in the investigation of such systems, and the model for the pp collision can be expected to remain qualitatively correct.

Acknowledgment. The support of the Petroleum Research Fund of the American Chemical Society is gratefully acknowledged.

Appendix I

The coefficients c's in eq 2.8 are

$$c_1 = -\frac{\pi\hbar}{kT};\quad c_2 = \frac{1}{3}\left(\frac{\pi\hbar}{kT}\right)^2 + \frac{\pi^3 a\hbar(2\mu)^{1/2}}{E^{3/2}} \times \left[1 - \frac{4}{\pi}\left(\frac{D}{E}\right)^{1/2}\right];\quad c_3 = \frac{1}{3}\left(\frac{\pi\hbar}{kT}\right)^3 - \frac{\pi^4\hbar^2 a(2\mu)^{1/2}}{kTE^{3/2}} \times \left[1 - \frac{4}{\pi}\left(\frac{D}{E}\right)^{1/2}\right];\quad c_4 = \frac{1}{3}\left(\frac{\pi\hbar}{kT}\right)^2\left(\frac{\pi^3 a\hbar}{E^{3/2}}\right)(2\mu)^{1/2} \times \left[1 - \frac{4}{\pi}\left(\frac{D}{E}\right)^{1/2}\right] + \frac{\mu\hbar a^2\pi^5}{2E^3}\left[1 - \frac{4}{\pi}\left(\frac{D}{E}\right)^{1/2}\right]^2;\quad c_5 = \frac{1}{3}\left(\frac{\pi\hbar}{kT}\right)^3\left(\frac{\pi^3 a\hbar}{E^{3/2}}\right)(2\mu)^{1/2}\left[1 - \frac{4}{\pi}\left(\frac{D}{E}\right)^{1/2}\right] - \frac{\pi^7\hbar^3\mu a^2}{E^3 kT} \times \left[1 - \frac{4}{\pi}\left(\frac{D}{E}\right)^{1/2}\right]^2;\quad c_6 = \frac{1}{3}\left(\frac{\pi\hbar}{kT}\right)^2\left(\frac{\pi^6\mu\hbar^2 a^2}{E^3}\right) \times \left[1 - \frac{4}{\pi}\left(\frac{D}{E}\right)^{1/2}\right];\quad c_7 = \frac{1}{3}\left(\frac{\pi\hbar}{kT}\right)^3\left(\frac{\pi^6\mu a^2\hbar^2}{E^3}\right) \times \left[1 - \frac{4}{\pi}\left(\frac{D}{E}\right)^{1/2}\right]\cdots$$

Appendix II

The coefficients θ and ρ in eq 2.9 are

$$\theta_0 = \frac{24}{g^5};\quad \theta_1 = \frac{24}{g^4};\quad \theta_2 = \frac{12}{g^3};\quad \theta_3 = \frac{4}{g^2};\quad \theta_4 = \frac{1}{g};$$

$$\rho_6 = 3.32 \times 10^5\frac{c_7}{g^7} + 3.02 \times 10^4\frac{c_6}{g^6} + 3.02 \times 10^3\frac{c_5}{g^5} + 3.36 \times 10^2\frac{c_4}{g^4} + 42\frac{c_3}{g^3} + 6\frac{c_2}{g^2} + \frac{c_1}{g};\quad \rho_6 = 5.54 \times 10^4\frac{c_7}{g^6} + 5.04 \times 10^3\frac{c_6}{g^5} + 5.04 \times 10^2\frac{c_5}{g^4} + 56\frac{c_4}{g^3} + 7\frac{c_3}{g^2} + \frac{c_2}{g};\quad \rho_7 = 7.92 \times 10^3\frac{c_7}{g^5} + 7.20 \times 10^2\frac{c_6}{g^4} + 72\frac{c_5}{g^3} + 8\frac{c_4}{g^2} + \frac{c_3}{g};\quad \rho_8 = 9.90 \times 10^2\frac{c_7}{g^4} + 90\frac{c_6}{g^3} + 9\frac{c_5}{g^2} + \frac{c_4}{g};\quad \rho_9 = 1.10 \times 10^2\frac{c_7}{g^3} - 10\frac{c_6}{g^2} + \frac{c_5}{g};\quad \rho_{10} = 11\frac{c_7}{g^2} + \frac{c_6}{g};\quad \rho_{11} = \frac{c_7}{g}\cdots$$

The Thermodynamic and Physical Properties of Beryllium Compounds. IX. The Free Energy of Formation of Beryllium Hydroxide(g)[1]

by Jay Blauer, Michael A. Greenbaum, and Milton Farber

Maremont Corporation, Rocket Power, Inc., Research Laboratories, Pasadena, California *(Received May 11, 1965)*

An intensive study of the surface effects on the equilibrium $BeO(c) + H_2O(g) = Be(OH)_2(g)$ has been made at four temperatures in the range 1567 to 1808°K. The equilibrium is extremely sensitive to the surface area of the crystalline beryllium oxide. The data have been interpreted and extrapolated to yield a free energy of formation at 298°K of -158.4 ± 0.7 kcal/mole for gaseous $Be(OH)_2$.

Introduction

The reaction

$$BeO(c) + H_2O(g) = Be(OH)_2(g) \qquad (1)$$

has been subjected to several investigations in recent years in an effort to obtain a definitive value for the heat of formation of $Be(OH)_2(g)$. Grossweiner and Seifert[2] reported a value of 41.5 kcal/mole for the enthalpy change of reaction 1 at 1673°K. Young[3] obtained a value of 42.46 ± 0.40 kcal/mole for the same quantity at 1700°K. Both of these studies were transpirations carried out at atmospheric pressures and high flow rates (>100 cc/min). The gas–solid contact time for Young's work was the larger by a factor of 3. Because of the relatively short contact times employed by both investigators, coupled with non-attainment of equilibrium under such conditions encountered in this laboratory, a new investigation of this reaction was undertaken using a molecular flow technique.

Experimental Section

The beryllia used in these studies (obtained from Brush Beryllium Co.) had a minimum purity of 99.5% and consisted of irregular particles having dimensions in the range of 0.5 to 3 mm. Several runs were also made with samples consisting of cylindrical tubes having dimensions of 4-cm length, 5-mm o.d., and 3-mm i.d. These samples were used only in a few vapor pressure studies. Samples of beryllia of known weight were placed in an alumina combustion boat which in turn was placed in an alumina furnace tube having an inside diameter of 2.5 cm. The furnace used in this study was a Leco tube furnace with automatic temperature controls. The automatic controller maintained the temperature to ±5°. The temperature was established by means of a Leeds and Northrup optical pyrometer. The pyrometer was calibrated against a standardized platinum–rhodium thermocouple the bead of which was imbedded in beryllia.

After the system had been evacuated, gaseous, distilled water was admitted through a very fine metering valve. The transpired products were collected in a cold trap cooled by liquid nitrogen. The total pressure in the system never exceeded 300 μ as determined by means of a Veeco thermocouple gauge. The extent of reaction was found to be independent of water pressure; as a consequence, no attempt was made to calibrate the pressure sensor.

At the end of each run, the boat was removed from the furnace and allowed to cool in a desiccator over dehydrated $CaCl_2$. The sample of beryllia was removed from the boat and weighed separately. The boat itself showed no weight loss. The amount of water that passes through the system was determined by weighing the vessel from which the water was admitted into the system (a 50-ml, vacuum-tight, round-bottomed flask). The duration of the runs varied

(1) This work was supported by the Air Force Rocket Propulsion Laboratory, Research and Technology Division, Edwards Air Force Base, Calif., Air Force Systems Command, U. S. Air Force.

(2) L. I. Grossweiner and R. L. Seifert, *J. Am. Chem. Soc.*, 74, 2701 (1952).

(3) W. A. Young, *J. Phys. Chem.*, 64, 1003 (1960).

from 24 to 100 hr. In all cases, the time was well in excess of that required to establish equilibrium.

Blank runs were made at each temperature to determine the weight losses from the BeO samples due to causes other than reaction with water. These losses would include errors due to possible $BeO–Al_2O_3$ compound formation resulting in a nonquantitative transfer of particles of sample to the balance pan.

Treatment of Data

The theory of the low-pressure molecular flow reaction method for obtaining equilibrium data has previously been described.[4]

If only $Be(OH)_2(g)$ is formed under the experimental conditions considered, it is possible to show on the basis of the theory of molecular flow[4] that the following equation describes the conditions holding at equilibrium

$$K_p = \frac{(M_{Be(OH)_2})^{1/2}}{(M_{H_2O})^{1/2}} \frac{\Gamma_{BeO}}{\Gamma_{H_2O}} \quad (2)$$

The symbols appearing in eq 2 have the following definitions: K_p is the equilibrium constant, $M_{Be(OH)_2}$ and M_{H_2O} are the molecular weights of $Be(OH)_2$ and H_2O, respectively, Γ_{BeO} is the number of moles of BeO which react with water in unit time and pass from the cell, and Γ_{H_2O} is the number of moles of H_2O that pass through the cell unreacted in unit time.

It was found that the apparent equilibrium constant is markedly influenced by changing the surface area or, equivalently, the weight of the BeO sample. This effect seems to be best described by an equation of the form

$$\frac{1}{K_p} = \frac{1}{K^0_p} + \frac{J}{W} \quad (3)$$

where K^0_p is the value of K_p (the apparent equilibrium constant) extrapolated to a condition of infinite surface area, J is a constant, and W is the sample weight. It is of interest to note that this empirical expression can be derived directly from an equation derived from theory by Farber[5] and Motzfeldt[6] to relate equilibrium pressures in an effusion cell to the measured pressures. Their expression was of the form

$$P_m = \frac{P_e}{1 + \frac{A}{a\alpha}} \quad (4)$$

where P_m and P_e are the measured and equilibrium pressures, respectively. A is the effective area of the orifice (a constant dependent only on the tube diameter and its length in the present case), a is the surface area of the sample, and α is the accommodation coefficient (*i.e.*, the surface area necessary for reaction is related directly to the accommodation coefficient).

If eq 3 were fitted directly to the experimental data, the greatest statistical weight would be given to samples of low weight. Since the greatest weight losses were obtained for samples of large weight, it becomes desirable to rearrange eq 3 in an effort to redistribute these statistical weights. As a consequence, the equation was fitted to the data in the form

$$\frac{W}{K_p} = J + \frac{W}{K^0_p} \quad (5)$$

It was found that within experimental error, the blank correction was directly proportional to the sample size. The dependence of the blank correction upon the sample size has been plotted for a temperature of 1808°K in Figure 1. As a consequence, only one blank was made at most temperatures, the corresponding sample blanks being computed from the pertinent weights.

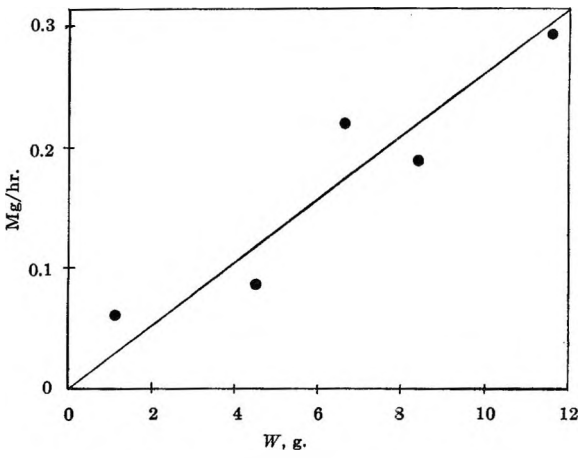

Figure 1. Effect of sample size upon the blank correction at 1808°K.

Results and Discussion

The experimental data are tabulated in Table I. In an effort to deduce the nature of the reaction occurring between BeO and H_2O under the experimental conditions, data were taken for samples of fixed surface area and various pressures at each of two temperatures. The following equation was fitted to the resulting data at each temperature.

$$\log \overset{*}{\Gamma}_{BeO} = C + X \log \Gamma_{H_2O} \quad (6)$$

(4) M. Farber and J. Blauer, *Trans. Faraday Soc.*, 58, 2090 (1962).
(5) M. Farber and A. J. Darnell, *J. Chem. Phys.*, 25, 526 (1956).
(6) K. Motzfeldt, *J. Phys. Chem.*, 59, 139 (1955).

Table I: Experimental Transpiration Data

Run no.	T, °K	Γ^*_{BeO} × 10^5, moles/hr	Γ_{H_2O} × 10^2, moles/hr	W, g	10^3K_p
18	1567	0.491	2.69	11.2095	0.283
19	1567	0.476	4.25	5.9260	0.173
20	1567	0.357	4.96	3.2763	0.211
25	1639	1.41	2.93	14.5424	0.743
26	1639	1.33	4.20	10.1212	0.489
27	1639	0.950	2.99	5.2182	0.491
28	1639	0.497	2.90	2.8150	0.265
30	1639	0.573	2.52	4.0140	0.351
46	1707	0.713	2.53	0.7252	0.436
47	1707	2.17	2.38	3.0576	1.41
48	1707	2.29	2.22	5.7744	1.59
49	1707	1.79	2.27	4.7664	1.22
50	1707	1.66	2.35	3.2169	1.09
51	1707	1.61	2.44	1.4268	1.02
52	1707	0.600	2.66	0.4647	0.349
4	1808	6.93	3.79	11.4216	2.82
5	1808	0.940	0.580	11.3784	2.50
6	1808	2.90	1.43	11.3670	3.13
7	1808	4.23	2.40	11.3453	2.72
9	1808	2.58	1.77	6.2805	2.25
10	1808	2.30	2.58	2.7120	1.38
11	1808	2.18	4.52	1.0896	0.745

where log Γ^*_{BeO} is the loss of BeO corrected for the blank. The results of this analysis indicate a value of X of 1.04 ± 0.07 over the whole temperature range indicating that $Be(OH)_2$ is the major gaseous product formed. The theoretical slope is 0.5 for the competing reaction to form the monohydroxide; if a dimer or trimer of $Be(OH)_2$ were formed, the resulting slopes would be 2 or 3, respectively.

$$BeO(c) + {}^1/_2H_2O(g) = BeOH(g) + {}^1/_4O_2(g) \quad (7)$$

When eq 4 is cast into the form given by eq 3, the following result is obtained

$$\frac{1}{K_p} = \frac{1}{K^0_p} + \left(\frac{J'A}{K^0_p}\right)\frac{1}{W} \quad (8)$$

where J' is the conversion factor giving the relationship between the surface area of the sample and its weight. Accordingly, it is of interest to compare the products of J and K^0_p for the various temperatures as a test for the temperature dependence of $(J'A/\alpha)$. The values of these products are shown in the last column of Table II. The results indicate that, contrary to what is expected, the product K^0_pJ shows a very marked negative temperature dependence. Some of this effect can be ascribed to other kinetic effects which remove the system further from equilibrium as the temperature is lowered. The data taken at 1707°K show that the value of J is markedly dependent upon the nature of the apparatus; however, it is comforting to note that the resulting value of K^0_p falls within its proper range when compared with the values obtained at the other temperatures.

Equation 5 was fitted to the data at each temperature by the method of least squares; the results are tabulated in Table II. The free energy changes for reaction 1 were computed by means of the relation

$$\Delta F_r = -RT \ln K^0_p \quad (9)$$

The resulting free energies of formation were computed from these values and tabulated free energy data for $H_2O(g)$ and BeO(c). Interpolation within the most recent estimated heat capacity and entropy data[7] permits the estimation of the heat of formation of gaseous $Be(OH)_2$. The results of these calculations are listed in Table III. The resulting free energy of formation at 1705°K (average temperature) for $Be(OH)_2(g)$ is found to be −119.5 ± 0.7 kcal/mole. At 298°K this becomes −158.4 ± 0.7 kcal/mole. The error is the computed standard deviation accounting for the error incurred on averaging as well as the error arising from surface effects. It must be admitted that this is a tentative result as it is based upon uncertain heat capacity data for $Be(OH)_2$.

Table II: Effect of Sample Surface Area upon the Apparent Equilibrium Constant from Eq 5

T, °K	$10^{-3}J$, g	$10^3K^0_p$	$10^3K^0_p$, g
1567	25.9 ± 1.4	0.81 ± 0.11	20.8
1639	7.71 ± 3.9	1.07 ± 0.44	8.2
1707	1.07 ± 0.28	2.03 ± 0.21	2.2
1808	0.53 ± 0.27	3.97 ± 0.41	2.1

Estimated entropies[7] have been used to convert these data to the enthalpy changes for reaction 1. Tabulated enthalpies[7] for $H_2O(g)$ and BeO(c) have been used to interpret the data in terms of the heat of formation of $Be(OH)_2(g)$. Interpolation within the estimated heat capacity data[7] have been used to reduce the resultant heats of formation to a temperature of 298°K. The results of all of these computations are listed in Table III. The resulting third-law heat of formation of $Be(OH)_2(g)$ at 298°K is −165.9 ± 0.7 kcal/mole. It is to be admitted that this value is only tentative as no experimental data concerning

(7) "JANAF Thermochemical Tables," USAF Contract AF 33 (616)-6149, Advanced Research Projects Agency, Washington 25, D. C.

Table III: Thermodynamic Properties of the Reaction: $BeO(c) + H_2O(g) = Be(OH)_2(g)$

T, °K	ΔF_T, kcal/mole	$\Delta F_f[Be(OH)_2(g)]$, kcal/mole	ΔH_T, kcal/mole	$\Delta HF_f[Be(OH)_2(g)]$, kcal/mole	$\Delta H_{f,298}[Be(OH)_2(g)]$, kcal/mole
1567	22.2 ± 0.4	122.9 ± 0.4	33.8 ± 0.4	−170.3 ± 0.4	−165.7 ± 0.4
1639	22.3 ± 1.3	116.0 ± 0.4	34.4 ± 1.3	−170.5 ± 1.3	−165.0 ± 1.3
1707	21.0 ± 0.4	118.8 ± 0.4	33.5 ± 0.4	−171.4 ± 0.4	−165.8 ± 0.4
1808	19.9 ± 0.4	120.0 ± 0.4	33.0 ± 0.4	−171.8 ± 0.4	−166.2 ± 0.4

the entropy of $Be(OH)_2$, spectroscopic or otherwise, are available at the present time.

Although data were obtained at only four temperatures, a second-law calculation was made. The results indicate a heat of formation and entropy at 1705°K for $Be(OH)_2(g)$ of −166.4 ± 7 kcal/mole and 92.6 ± 4 cal/deg mole, respectively. The errors reported here represent the result of a complete analysis of variance of all of the data in Table I. Interpolation within the estimated heat capacity data[6] was used to extrapolate these values to a temperature of 298°K. The resultant heat and entropy are −161 ± 7 kcal/mole and 92.6 ± 4 cal/deg mole, respectively. The bulk of the uncertainty in the second-law values can be attributed to the very small number of temperatures considered. However, the length of time necessary to obtain equilibrium data at a given temperature made it impractical to extend the study. The entropy value reported here is the first experimentally determined one for this species. Additional data points will be necessary to establish this important value to a considerably higher order of precision and accuracy than is possible now.

Since the gas–solid contact time in the work of Young[3] was approximately triple that of Grossweiner and Seifert,[2] it is more likely that Young's work corresponds more nearly to equilibrium. As a consequence, the most critical comparison must be made between this work and that of Young.

Since the BeO samples used in both this work and that of Young consisted of irregular particles having dimensions between 0.5 and 3 mm, the most obvious comparison to make is between the results for samples of roughly equivalent weight. All of Young's results are based on samples of BeO having weights of approximately 0.7 g. A reference to Table I shows that only one experimental run was made for a sample approximately this size; *i.e.*, run 46 corresponds to a weight of 0.7252 g. At 1707°K Young's data gives a value of 3.12×10^{-4} for the equilibrium constant for reaction 1. The value obtained for run 46 at this same temperature is 4.36×10^{-4}. This seems in very good agreement when one considers the differences in the

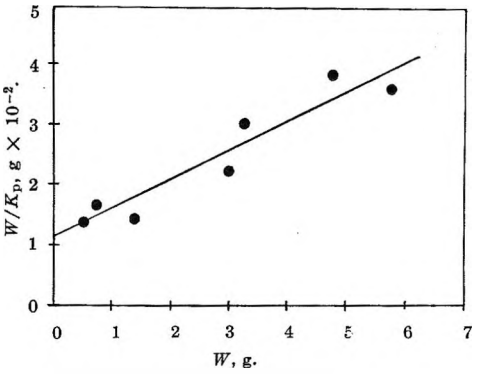

Figure 2. Effect of surface area upon the apparent equilibrium constant at 1707°K, from a plot of eq 5.

experimental techniques. Since the equilibrium value for K_p obtained at 1707°K is 2.03×10^{-3}, it follows that a neglect of surface effects leads to a 465% error in the equilibrium constant and an error of 5.2 kcal in the resulting calculated heat of formation of $Be(OH)_2(g)$. Comparisons at other temperatures could be made, but these would involve extrapolations outside the range of the experimental data with large resultant uncertainties. It must be admitted that this comparison is crude due to the fact that no direct comparison could be made of the actual surface conditions of the samples used in the two studies.

While it is to be admitted that the extreme pressure of 300 μ is at the upper limits at the range of pressure generally encountered in molecular flow, it is felt that the linearity of Figure 2 over the whole pressure range lends some credence to the analysis given. The largest error incurred in the assumption of molecular flow would be to cause all values of K^0_p to be high by a factor of 1.55, well within the stated uncertainty of the second-law analysis, which is the value of the factor

$$\left(\frac{M_{Be(OH)_2}}{M_{H_2O}}\right)^{1/2}$$

Summary

On the basis of the results reported here, it can be seen that the surface area effects in the reaction of BeO(s) and $H_2O(g)$ are very important. On the basis

of the results obtained, however, a definitive value for the ΔF_r for this reaction can be considered established from which tentative values for the ΔH_f and $S°$ of BeOH(g) can be obtained.

Measurement of Reaction Rate by Competitive Removal of Reactant

by George B. Smith and George V. Downing, Jr.

Merck Sharp & Dohme Research Laboratories, Division of Merck & Co., Inc., Rahway, New Jersey
(Received May 17, 1965)

Measurement of reaction rate ordinarily involves either quantitative chemical analysis or measurement of some physical property during reaction. A method has been devised in which the quantitative measurement is measurement of time. The technique is useful in measurement of rates of reactions with half-lives of about 1 min. Rate constants can be evaluated if the kinetic behavior of the system is known. The method has been illustrated by the reactions of thiosulfate with methyl chloroacetate, methyl bromoacetate, and methyl iodoacetate.

Introduction

Classical methods of determining the rates of reaction involve removing samples at definite times and analyzing them for one or more of the reactants and products. Variations of this technique in which some property such as conductance, optical rotation, or absorbance is monitored continuously have greatly facilitated the determination of kinetic data. However, in general, these have been applied to relatively slow reactions, often by diluting the reactants. Special techniques must be used when the time required to sample or make a measurement is a significant part of the total reaction time. In the case of very fast reactions, elegant techniques have been developed. The intermediate case, in which the half-life of the reaction is on the order of a few minutes, is a difficult one because sampling or measurement time is a significant part of the total, and the very fast techniques are not easily applied.

The method described here is related to the "clock" reactions[1] in which the rate constant is calculated from the time required for the generation of an amount of product equal to a known amount of a second reagent which reacts very rapidly with the product. In the method used in this work, competition is established for one of the reactants according to the scheme

$$A + B \xrightarrow{k} C \qquad \text{(reaction under study)}$$

$$R(t) + A \xrightarrow{\text{fast}} \text{products}$$

R is generated electrochemically and reacts with A as fast as it is generated. The net result is that A is removed by two reactions, and the time required to remove all of A is a measure of the rate of the reaction under study. The time at which all of A is removed is determined by detecting the presence of R.

To illustrate the method the reaction of thiosulfate with methyl bromoacetate, which has previously

$$CH_2BrCOOCH_3 + S_2O_3^{2-} \longrightarrow CH_2(S_2O_3)COOCH_3^- + Br^-$$

been investigated by La Mer and Kamner,[2] was chosen. They analyzed aliquots of the reaction by adding excess iodine and back-titrating with thiosulfate. In the

(1) G. S. Forbes, H. W. Estill, and O. J. Walker, *J. Am. Chem. Soc.*, 44, 97 (1922).

(2) V. K. La Mer and M. E. Kamner, *ibid.*, 53, 2832 (1931).

Table I: Data for $\tau/\tau_B = (1/C) \ln (C + 1)$. First-Order Reaction: $C = k\tau_B$. Pseudo-First-Order Reaction: $C = kB\tau_B$

τ/τ_B	C	τ/τ_B	C	τ/τ_B	C	τ/τ_B	C
0.01	600	0.26	8.7	0.51	2.4	0.76	0.69
0.02	290	0.27	8.2	0.52	2.3	0.77	0.65
0.03	170	0.28	7.8	0.53	2.2	0.78	0.61
0.04	120	0.29	7.3	0.54	2.1	0.79	0.58
0.05	90	0.30	6.9	0.55	2.0	0.80	0.54
0.06	71	0.31	6.5	0.56	1.90	0.81	0.50
0.07	58	0.32	6.1	0.57	1.81	0.82	0.47
0.08	49	0.33	5.8	0.58	1.73	0.83	0.44
0.09	42	0.34	5.5	0.59	1.66	0.84	0.40
0.10	36	0.35	5.2	0.60	1.58	0.85	0.37
0.11	32	0.36	5.0	0.61	1.51	0.86	0.34
0.12	28	0.37	4.7	0.62	1.44	0.87	0.31
0.13	25	0.38	4.5	0.63	1.38	0.88	0.28
0.14	23	0.39	4.3	0.64	1.31	0.89	0.26
0.15	21	0.40	4.1	0.65	1.25	0.90	0.23
0.16	18.6	0.41	3.9	0.66	1.19	0.91	0.21
0.17	17.0	0.42	3.7	0.67	1.13	0.92	0.18
0.18	15.6	0.43	3.5	0.68	1.07	0.93	0.16
0.19	14.4	0.44	3.3	0.69	1.02	0.94	0.13
0.20	13.3	0.45	3.2	0.70	0.96	0.95	0.11
0.21	12.3	0.46	3.0	0.71	0.91	0.96	0.09
0.22	11.4	0.47	2.9	0.72	0.86	0.97	0.06
0.23	10.7	0.48	2.8	0.73	0.82	0.98	0.04
0.24	10.0	0.49	2.7	0.74	0.78	0.99	0.02
0.25	9.3	0.50	2.5	0.75	0.73	1.00	0.00

present work the same reaction was carried out in the titration cell of a coulometer. The reaction was initiated by addition of thiosulfate to a solution of the ester. At the same time addition of iodine generated at constant current was started. Thiosulfate was depleted by reaction with ester and reaction with iodine simultaneously. Rate of reaction of thiosulfate with iodine was constant and equal to the rate at which iodine was generated because the thiosulfate reaction with iodine is very rapid. The end point was observed with the appearance of free iodine (disappearance of thiosulfate), and the time at which the end point occurred was a measure of the thiosulfate–ester reaction rate. Second-order rate constants for reactions of thiosulfate with methyl chloroacetate, methyl bromoacetate, and methyl iodoacetate were measured.

Theory

Suppose that during the second-order reaction of A and B a further constant rate of disappearance K is imposed on A. Then

$$-\frac{dA}{dt} = kAB + K \tag{1}$$

where A and B represent concentrations of the corresponding species, and k is the second-order rate constant. For the pseudo-first-order case with B present in large excess, the integrated form of eq 1 is easily obtained.

$$t = \frac{1}{kB} \ln\left(\frac{kA_0B + K}{kAB + K}\right) \tag{2}$$

where A_0 is the initial concentration of A. The time τ required for A to disappear is

$$\tau = \frac{1}{kB} \ln\left(\frac{kA_0B}{K} + 1\right) \tag{3}$$

The rate K can be expressed as the quotient of A_0 and the blank time τ_B, which is the time required for A to disappear when B is absent.

$$K = \frac{A_0}{\tau_B} \tag{4}$$

From eq 3 and 4

$$\frac{\tau}{\tau_B} = \frac{1}{C} \ln (C + 1) \tag{5}$$

where $C \equiv kB\tau_B$. The rate constant can thus be calculated from the experimental quantities B, τ_B, and

Table II: Data for Second-Order Reaction Where $f = kA_0\tau_B$: Equivalent Amounts

τ/τ_B	f	τ/τ_B	f	τ/τ_B	f	τ/τ_B	f
0.01	20,000	0.26	19.4	0.51	3.5	0.76	0.79
0.02	4,000	0.27	17.9	0.52	3.3	0.77	0.74
0.03	2,000	0.28	16.4	0.53	3.1	0.78	0.70
0.04	1,000	0.29	15.0	0.54	2.9	0.79	0.65
0.05	640	0.30	13.8	0.55	2.8	0.80	0.60
0.06	440	0.31	12.8	0.56	2.6	0.81	0.56
0.07	330	0.32	11.9	0.57	2.5	0.82	0.52
0.08	250	0.33	11.0	0.58	2.3	0.83	0.48
0.09	190	0.34	10.2	0.59	2.2	0.84	0.44
0.10	154	0.35	9.6	0.60	2.1	0.85	0.40
0.11	126	0.36	9.0	0.61	1.97	0.86	0.37
0.12	105	0.37	8.4	0.62	1.86	0.87	0.34
0.13	89	0.38	7.8	0.63	1.76	0.88	0.31
0.14	76	0.39	7.3	0.64	1.66	0.89	0.28
0.15	66	0.40	6.8	0.65	1.57	0.90	0.24
0.16	57	0.41	6.4	0.66	1.48	0.91	0.21
0.17	50	0.42	6.0	0.67	1.39	0.92	0.19
0.18	44	0.43	5.6	0.68	1.31	0.93	0.16
0.19	39	0.44	5.3	0.69	1.23	0.94	0.14
0.20	35	0.45	5.0	0.70	1.16	0.95	0.11
0.21	32	0.46	4.7	0.71	1.09	0.96	0.09
0.22	29	0.47	4.4	0.72	1.03	0.97	0.06
0.23	26	0.48	4.2	0.73	0.97	0.98	0.04
0.24	23	0.49	3.9	0.74	0.91	0.99	0.02
0.25	21	0.50	3.7	0.75	0.85	1.00	0.00

τ/τ_B. Equation 5 is also the solution for a first-order reaction with $C \equiv k\tau_B$.

The function τ/τ_B has been evaluated for chosen values of C. Values of C corresponding to τ/τ_B between 0.01 and 1.00 at intervals of 0.01, obtained by graphical interpolation are shown in Table I.

The case of the second-order reaction with equal initial concentrations has also been developed. In this case

$$B = A + Kt \tag{6}$$

where A is the concentration of the reactant which is removed at constant rate. Then

$$\frac{dA}{dt} = kA(A + Kt) + K \tag{7}$$

With the changes of variable $\alpha = A/A_0$ and $t' = t/\tau_B$ eq 7 becomes

$$-\frac{d\alpha}{dt'} = 1 + f\alpha^2 + f\alpha t' \tag{8}$$

where $f \equiv kA_0\tau_B$. Times $\tau' = \tau/\tau_B$ required for α to become zero have been calculated with a computer for various values of f. Values of f corresponding to τ/τ_B from 0.01 to 1.00 at intervals of 0.01, obtained by graphical interpolation, are given in Table II.

Of course, relative reaction rates for any mechanism can be observed as relative end point times without evaluating rate constants.

Experimental Section

Materials. Merck reagent grade potassium iodide and sodium thiosulfate, conforming to ACS specifications, were used. Matheson Coleman and Bell methyl chloroacetate, bp 128–130°, and methyl bromoacetate, bp 38–39° (10 mm), were used as purchased. Methyl iodoacetate was prepared as follows. Equal volumes of ethyl ether and 40% KOH in water were mixed and cooled in an ice bath. N-Nitrosomethylurea was added to make diazomethane. The ether layer containing the diazomethane was decanted and dried with KOH pellets. An ether solution of iodoacetic acid was mixed with an excess of diazomethane in ether to form methyl iodoacetate, and the ether was removed by vacuum distillation. The pale yellow product, $n^{27.2}D$ 1.5167, had an infrared spectrum in chloroform with a single carbonyl band.

Purity of the esters was demonstrated by vapor phase chromatography with a Burrell Kromo-Tog Model K2,

equipped with a thermal conductivity detector. The column was 2.5 m long and 6 mm in i.d., packed with 20% DC-200 on Gas Chrom Z, −80 + 100 mesh. Helium carrier flow rate was 60 ml/min, and column temperature was 115°. Retention times of 3, 5, and 9 min were observed for the chloro, bromo, and iodo esters, and purities by area per cent were 99.99, 99.97, and 99.0%, respectively. Impurities were not identified.

Procedure. Reaction rates were measured with a Fisher Coulomatic Titrimeter. The titration cell (reaction vessel) was a 250-ml beaker equipped with a magnetic stirrer. Platinum electrodes were used to generate iodine externally from 1 *M* KI solution in a buret using a delivery tip with an internal electrode (Sargent S-29703). Iodine was generated at constant current of 5 ma, and an electric clock in the circuit indicated the generating time. The presence of free iodine at the end point was detected by polarized platinum electrodes as a "dead stop" end point.

Distilled water, 150 ml, containing 1 vol % methanol, was placed in a 250-ml beaker, and the temperature of the liquid was adjusted to 25.0°. The methanol was used to dissolve the esters. The beaker was placed on the titrimeter, and flow of KI solution from the buret at about 1 ml/min was started. The solution was titrated to an initial end point to provide a slight excess of iodine to which the following runs were titrated. Ester was then added in high excess to the amount of thiosulfate to be titrated. At the initial reaction time sodium thiosulfate solution was added, and the generating current and clock were started. The titration time τ was observed and compared with the blank time τ_B obtained similarly in the absence of ester. Amounts of thiosulfate were used to make τ_B about 4 min. Rate constants corresponding to observed values of τ/τ_B were obtained from Table I.

Results and Discussion

The present method is useful in measurement of reaction rates as opposed to mechanism elucidation. The method is particularly suited for measurement of reaction rates of related compounds in a given reaction. Rate constants can be evaluated if the rate law is known.

La Mer and Kamner[2] showed that reaction of thiosulfate and methyl bromoacetate in water at 25° is second order and free from side reactions. Second-order rate constants have been evaluated in the present work on the basis of this prior knowledge.

Experimental data and calculations are summarized in Table III. Each run includes successive titrations of three portions of thiosulfate in the same solution of excess ester at 25.0°. The ester used in each run is shown in Table III along with ester molarity B, titration time τ, τ/τ_B, $C = kB\tau_B$ corresponding to τ/τ_B from Table I, and finally the value for the second-order rate constant measured in each titration. Blank times τ_B obtained from four titrations of thiosulfate in absence of ester were 215.4, 217.6, 217.2, and 214.9 sec. The average time of 216.3 sec was used in the calculations.

Volume of reaction mixtures increased slightly throughout each run as potassium iodide solution flowed from the buret into the beaker, and ester concentration decreased accordingly. Ester molarities used in the calculations are concentrations at half-time of each titration. Salt concentration also increased during each run to about 0.1 *M* after the third titration.

In each run the rate constants for titrations 1, 2, and 3 are the same. This shows that rate is independent of salt concentration, as reported by LaMer and Kamner. Second-order behavior is verified by the fact that the observed rate constant for reaction of methyl bromoacetate is independent of ester concentration in the range 0.033 to 0.136 *M*. LaMer and Kamner reported values of 0.21 to 0.25 M^{-1} sec^{-1} for this rate constant at 25 ± 0.01°, in agreement with the present data. They used lower ester concentrations and followed reactions for several hours.

With the apparatus used an interval of about 2 sec was required for iodine generated externally to pass into the reaction mixture. This was the source of the most important error in the rate measurement. During the 2-sec interval thiosulfate reacted with ester but not with iodine. As a result of the time delay titration times increased, and observed rate constants were slightly low. Reproducibility of rate constant values was about ±5%.

This method should find use in a variety of applications. Addition of a reagent at constant rate can be accomplished conveniently by electrochemical means, as in the present example. Also, mechanical devices can be arranged to deliver liquids at constant flow rate. Detection of end points can be done in many ways, depending on the application.

This kinetic method offers several distinct advantages. First, the method is most accurate in measurement of rates of reactions with half-lives about 1 min. Such rates are often difficult to measure by analysis of aliquots during reaction or by observation of physical parameters. It should be noted, however, that the method as applied here is not useful for rate measurements of very slow or very fast reactions. Second, rate data are obtained rapidly. Rates are determined

Table III: Summary of Data and Calculations

Run	Ester	Titration	B, M	τ, sec	τ/τ_B	$C = kB\tau_B$	k, M^{-1} sec^{-1}
1	Methyl chloroacetate	1	0.414	195.0	0.902	0.23	0.0026
		2	0.403	193.5	0.895	0.24	0.0028
		3	0.395	194.3	0.898	0.23	0.0027
2	Methyl bromoacetate	1	0.0342	130.4	0.603	1.56	0.21
		2	0.0334	133.3	0.616	1.47	0.20
		3	0.0326	135.1	0.625	1.41	0.20
3	Methyl bromoacetate	1	0.0345	133.9	0.619	1.45	0.19
		2	0.0337	133.1	0.615	1.48	0.20
		3	0.0328	134.6	0.622	1.43	0.20
4	Methyl bromoacetate	1	0.0683	100.9	0.466	2.94	0.20
		2	0.0667	101.4	0.469	2.91	0.20
		3	0.0651	104.1	0.481	2.79	0.20
5	Methyl bromoacetate	1	0.0683	97.4	0.450	3.20	0.22
		2	0.0667	100.0	0.462	2.98	0.21
		3	0.0651	101.6	0.470	2.90	0.21
6	Methyl bromoacetate	1	0.135	69.0	0.319	6.1	0.21
		2	0.132	71.6	0.331	5.8	0.20
		3	0.129	75.1	0.347	5.3	0.19
7	Methyl bromoacetate	1	0.136	68.4	0.316	6.3	0.21
		2	0.132	70.9	0.328	5.8	0.20
		3	0.130	74.1	0.343	5.4	0.19
8	Methyl iodoacetate	1	0.0195	150.5	0.696	0.99	0.23
		2	0.0189	150.4	0.695	0.99	0.24
		3	0.0186	153.0	0.707	0.93	0.23

by titration times of a few minutes. Third, a wide range of rate constants can be measured conveniently for cases such as second-order reactions by variation of initial concentrations. The second-order rate constants for reactions of thiosulfate with methyl bromoacetate and methyl iodoacetate are about 100 times larger than the rate constant for methyl chloroacetate. This was determined without difficulty by using different concentrations of the esters. In the present example, methyl bromoacetate was used in 3000-fold excess to initial thiosulfate. This means that a rate constant 3000 times larger could have been measured with about the same accuracy if ester equivalent to initial thiosulfate were used, without changing initial thiosulfate concentration or generating current. Table II would be used in that case instead of Table I.

Acknowledgments. The authors wish to express their appreciation for the assistance of Dr. I. Schoenewaldt in the preparation of methyl iodoacetate and Mr. M. Zirrith in the computation of the table for the second-order reaction with equimolar initial concentrations.

Polarographic Relationships Suggested by an Asymptotically Correct Solution to Matsuda's Integro-Differential Equation

by George H. Duffey, W. Patrick Rahilly, and Russell B. Kidman

Department of Physics, South Dakota State University, Brookings, South Dakota 57006
(Received June 28, 1965)

Matsuda's integro-differential equation characterizes the rate at which an electroactive substance diffuses to a mercury drop. However, it is an integral law, admitting various invalid sequences of concentration distributions besides valid ones. We have employed a sequence which is correct when rate of growth of the drop is negligible. The resulting nonlinear differential equation was integrated numerically for various initial states of depletion. Dimensionless reduced variables were defined, and a procedure for estimating diffusion coefficients and initial depletions from experimental data was worked out. Empirical equations for the variation of the diffusion layer parameter and the diffusion current with time were based on the theoretical results.

Introduction

In polarographic determinations, one exploits the concentration polarization that develops near a small electrode whenever the applied voltage is sufficient to cause appreciable faradaic reaction of a dilute solute. To avoid effects of contamination, one forms the electrode of mercury flowing dropwise out of a small capillary tube. The surface at which the reaction occurs thus grows periodically from that of the nascent drop to that of the separating drop.

When the voltage is high enough, the solute reacts as fast as it reaches the mercury surface, and the polarization is fully developed. The corresponding faradaic current is called the *diffusion current* because it depends on the rate of diffusion of the species to the interface. A small residual current also contributes to the observed flow of charge.

Now, growth in area of the surface causes the diffusion current to vary from a very small value to a relatively large quantity during the lifetime of each drop. The theory of this variation has been developed by many workers.[1-12] In general, the later treatments have produced small changes in the formula that Heyrovsky and Ilkovic[1] derived. The important alterations were first introduced by Lingane and Loveridge[3] and by Strehlow and von Stackelberg.[4]

Matsuda's work[7] is said to be as nearly definitive as any.[9] However, he uses functions which cannot represent the concentration variation exactly even when rate of growth of the drop is negligible. Besides employing truncated series, he assumes that depletion develops only in a boundary layer of thickness δ' about the growing drop. He also chooses the initial conditions so that the drop begins its life in a uniform solution. Markowitz and Elving,[11] on the other hand, have introduced corrections for an initially depleted layer into the procedure of Lingane and Loveridge.

In our work, we have employed a function which

(1) D. Ilkovic, *Collection Czech. Chem. Commun.*, **6**, 498 (1934); *J. Chim. Phys.*, **35**, 129 (1938).

(2) D. MacGillavry and E. K. Rideal, *Rec. Trav. Chim.*, **56**, 1013 (1937).

(3) J. J. Lingane and B. A. Loveridge, *J. Am. Chem. Soc.*, **72**, 438 (1950).

(4) H. Strehlow and M. von Stackelberg, *Z. Elektrochem.*, **54**, 51 (1950).

(5) T. Kambara and I. Tachi, *Bull. Chem. Soc. Japan*, **25**, 284 (1952).

(6) J. Koutecky, *Czech. J. Phys.*, **2**, 50 (1953).

(7) H. Matsuda, *Bull. Chem. Soc. Japan*, **26**, 342 (1953).

(8) W. Hans, W. Henne, and E. Meurer, *Z. Elektrochem.*, **58**, 836 (1954).

(9) J. M. Markowitz and P. J. Elving, *Chem. Rev.*, **58**, 1047 (1958).

(10) D. J. Macero and C. L. Rulfs, *J. Am. Chem. Soc.*, **81**, 2944 (1959).

(11) J. M. Markowitz and P. J. Elving, *ibid.*, **81**, 3518 (1959).

(12) I. M. Kolthoff and K. Izutsu, *ibid.*, **86**, 1275 (1964).

does reduce to the exact solution (in the approximation that it is spherically symmetric) when the growth rate is negligible. Furthermore, we have allowed for various initial depletions.

Basic Analysis

The rate of diffusion of the reducible (or oxidizable) species to a dropping-mercury electrode is governed by the equation

$$\frac{\partial C}{\partial t} = \frac{1}{r^2}\frac{\partial}{\partial r}\left(Dr^2\frac{\partial C}{\partial r} - \frac{\gamma}{3}C\right) \tag{1}$$

to the approximation that the field is spherically symmetric about the center of the drop. Here the origin is located at the center, while C is concentration of the species out distance r, D is its diffusion coefficient, and t is the time. γ is related to radius r_0 of the drop by the relationship

$$r_0^3 = \gamma t \tag{2}$$

One can derive this diffusion equation from the postulate that diffusion occurs with respect to the solvent, which is here moving outward.

Following Matsuda, we multiply both sides of eq 1 by r^2dr, integrate, and reduce to get

$$\frac{\partial}{\partial t}\int_{r_0}^{\infty} r^2(C_0 - C)dr = Dr_0^2\left(\frac{\partial C}{\partial r}\right)_{r=r_0} \tag{3}$$

where C_0 is the concentration in the bulk of the solution. Equation 3 expresses the *conservation rule* that the rate at which the pertinent species is depleted in unit solid angle of solution equals the rate at which it diffuses inward to the corresponding part of the electrode.

However, since eq 1 imposes a similar conservation rule on diffusion of the solute among successive infinitesimal layers of solvent, it is much more restrictive. Now, Matsuda reintroduced some of the lost detail by employing boundary conditions at $r = r_0$ based on eq 1. However, a similar amount of information can be reintroduced by replacing his series with the proper function.

Thus, consider a drop of fixed radius r_0 initially in homogeneous solution of concentration C_0. Suppose the polarizing potential is applied at $t = 0$, without allowing the drop to grow. From Crank's book,[13] we find the concentration would vary radially so that

$$C_0 - C = C_0\frac{r_0}{r}\operatorname{erfc}\frac{r - r_0}{\sqrt{(4Dt)}} \tag{4}$$

However, in the polarographic cell, each drop begins its life in a small volume of depleted solution left behind by the previous drop. Also, the capillary shields a small area of the drop. On the other hand, growth of the drop pushes each spherical layer of the solvent outward, increasing its area and decreasing its thickness. This movement lowers the distance between neighboring radial positions and so increases the concentration gradient.

The first two influences exist from birth of the drop while the third cumulates with its growth. Transient effects associated with formation of the drop also exist. These include variation in mass rate of flow from the capillary and early nonsphericity of the drop.

The net effect of the influences existing from the beginning is an extra depletion about the electrode. This may be allowed for by increasing $\sqrt{(4Dt)}$ in formula 4. In general, the change required varies with the radius of the drop, $r_0 = (\gamma t)^{1/3}$, and so with t. On the other hand, the gradient steepening caused by growth of the drop is allowed for by decreasing $\sqrt{(4Dt)}$ in the formula. This correction also depends on t.

So we write

$$C_0 - C = C_0\frac{r_0}{r}\operatorname{erfc}\frac{\sqrt{\pi}(r - r_0)}{2\theta} \tag{5}$$

and let the conservation rule determine θ as a function of t. In effect, we are assuming the concentration to vary with r as it does at some time about a fixed spherical electrode of radius r_0. Thus, C approaches C_0 asymptotically as r increases; no arbitrary thickness δ' need be introduced. Furthermore, one can show that this concentration expression satisfies eq 1 on the inner boundary where $r = r_0$. Matsuda[7] put a similar limitation on both of his series.

Differentiating eq 5, setting $r = r_0$, and changing signs, we obtain the formula

$$\left(\frac{\partial C}{\partial r}\right)_{r=r_0} = C_0\left(\frac{1}{r_0} + \frac{1}{\theta}\right) \tag{6}$$

for concentration gradient at the surface of the drop. This goes into the right side of eq 3. For the left side, we substitute concentration reduction (5) into the integrand and carry out the indicated operations. The resulting limitation on θ is

$$\frac{d}{dt}(2r_0^2\theta + r_0\theta^2) = \pi Dr_0^2\left(\frac{1}{r_0} + \frac{1}{\theta}\right) \tag{7}$$

Integration of a reduced form of this equation will be discussed later.

The function θ so obtainable determines gradient $(\partial C/\partial r)_{r=r_0}$ by eq 6. Through the definitions of dif-

(13) J. Crank, "The Mathematics of Diffusion," Oxford University Press, London, 1956, p 98.

fusion coefficient D and faraday $\mathfrak{F}$, this gradient determines the diffusion current

$$i = n\mathfrak{F}D4\pi r_0^2\left(\frac{\partial C}{\partial r}\right)_{r=r_0} \tag{8}$$

Parameter n is the number of electrons lost (or gained) by the electrode per molecule of electroactive species reacting.

Matsuda's seven-term series[7] for $C_0 - C$ yields a formula like eq 6, but with $3/\delta'$ appearing in place of $1/\theta$. So the diffusion layer thickness δ' produces the same gradient at $r = r_0$ and thence diffusion current as 3θ. Substituting 3θ for δ' in the nonlinear differential equation which Matsuda obtained from the series yields the result

$$\frac{\mathrm{d}}{\mathrm{d}t}(2r_0^2\theta + r_0\theta^2) = \frac{28}{9}Dr_0^2\left(\frac{1}{r_0} + \frac{1}{\theta}\right) \tag{9}$$

This differs from eq 7 only in the first factor on the right side. Because the fraction 28/9 is close to π, the difference is small.

Introducing Dimensionless Variables

Note that parameter γ is constant to the approximation that the rate of mass flow from the capillary is fixed. Furthermore, D is constant to the approximation that the immediate environment of a diffusing ion does not change with distance from the electrode or with depletion. Since the initial concentration of the electroactive species is small, depletion should have little effect. In addition, the rate of mercury flow from the capillary is kept nearly constant.

Consequently, we take γ and D to be constant and employ eq 2 to eliminate r_0 from the differential equations. Then the dimensionless variables

$$\bar{t} = \frac{D^3}{\gamma^2}t \qquad \bar{\theta} = \frac{D}{\gamma}\theta \tag{10}$$

are introduced in order that our numerical work may suffice for various values of γ and D. Thus, eq 7 and 9 are transformed to

$$\frac{\mathrm{d}}{\mathrm{d}\bar{t}}(2\bar{t}^{2/3}\bar{\theta} + \bar{t}^{1/3}\bar{\theta}^2) = c\bar{t}^{2/3}\left(\frac{1}{\bar{t}^{1/3}} + \frac{1}{\bar{\theta}}\right) \tag{11}$$

where c is π for our equation and 28/9 for Matsuda's.

Because $\bar{\theta}$ is proportional to the diffusion layer thickness δ' of Matsuda, we call $\bar{\theta}$ the *diffusion layer parameter*. Variable $\bar{t}$, on the other hand, is proportional to time t and so is called the *reduced time*.

The integral on the left side of eq 3 measures how much reducible (or oxidizable) material has been removed from unit solid angle about the drop. To the approximation that the concentration reduction follows eq. 5, this integral equals

$$\frac{1}{\pi}(2r_0^2\theta + r_0\theta^2)C_0 \tag{12}$$

at any given time, as we saw in the derivation of eq 7. The corresponding expression in Matsuda's derivation is

$$\frac{9}{28}(2r_0^2\theta + r_0\theta^2)C_0 \tag{13}$$

However, since the quantity

$$\bar{Y} = 2\bar{t}^{2/3}\bar{\theta} + \bar{t}^{1/3}\bar{\theta}^2 \tag{14}$$

whose derivative appears on the left side of eq 11 is proportional to expressions 12 and 13, it is approximately proportional to the depletion about the electrode. We call it the *reduced depletion*.

Theoretical Predictions

If each falling drop carried all of its diffusion layer with it, as Matsuda assumed, then the concentration about a given drop would nearly coincide with that given by eq 4 when t was small. Since $\bar{\theta}$ is defined by eq 10 and 5, the diffusion layer parameter would vary roughly as $\bar{t}^{1/2}$. So an expansion of $\bar{\theta}$ in powers of $\bar{t}^{1/6}$, starting with a $\bar{t}^{1/2}$ term, might then be valid.[7]

However, if any of the depleted volume remains about the nascent drop, the expansion would not be valid. For then, $\bar{Y}$ must be different from 0 at $\bar{t}$ equal to 0. This is possible in eq 14 only if $\bar{\theta}$ is infinite. So, if one traces a plot of $\bar{\theta}^2$ against $\bar{t}$ backward in time, one finds that it approaches the $\bar{\theta}^2$ axis asymptotically as $\bar{t}$ goes to 0, and curves of $\bar{\theta}^2$ starting from different intermediate points must approach each other asymptotically as $\bar{t}$ becomes small.

Furthermore, as $\bar{t}$ increases, the curves should eventually come together again, for the electroactive species diffuses faster to the electrode from the less depleted solutions, depleting them faster. Therefore, the greatest separation between any two curves occurs at an intermediate time.

In carrying out each integration, we began in this intermediate region, where neighboring curves were well separated. Runge–Kutta fourth-order computations[14] were then executed at sufficiently small intervals in both temporal directions. For the final computations, the reduced depletion was the dependent variable.

(14) P. J. Davis and I. Polansky in "Handbook of Mathematical Functions," M. Abramowitz and I. A. Stegun, Ed., U. S. Government Printing Office, Washington, D. C., 1964, p 896.

Table I: Variation of $\bar{\theta}^2$ with $\bar{t}$ Implied by Eq 11 for Various Initial Conditions[a]

Reduced time, $\bar{t}$	Run 1	Run 2	Run 3	Run 4	Run 5	Run 6
0	∞	∞	∞	∞	∞	0
1.000×10^{-9}	1.8×10^{-5}	1.5×10^{-5}	1.2×10^{-5}	7.7×10^{-6}	1.69×10^{-6}	1.3×10^{-9}
3.50×10^{-9}	8.5×10^{-6}	7.1×10^{-6}	5.3×10^{-6}	3.2×10^{-6}	5.63×10^{-7}	4.8×10^{-9}
1.000×10^{-8}	3.8×10^{-6}	3.1×10^{-6}	2.2×10^{-6}	1.29×10^{-6}	1.92×10^{-7}	1.37×10^{-8}
2.00×10^{-8}	2.05×10^{-6}	1.63×10^{-6}	1.15×10^{-6}	6.45×10^{-7}	1.062×10^{-7}	2.76×10^{-8}
4.00×10^{-8}	1.036×10^{-6}	8.24×10^{-7}	5.81×10^{-7}	3.36×10^{-7}	8.90×10^{-8}	5.53×10^{-8}
6.00×10^{-8}	7.06×10^{-7}	5.68×10^{-7}	4.12×10^{-7}	2.57×10^{-7}	1.036×10^{-7}	8.31×10^{-8}
8.00×10^{-8}	5.58×10^{-7}	4.57×10^{-7}	3.45×10^{-7}	2.34×10^{-7}	1.253×10^{-7}	1.109×10^{-7}
1.000×10^{-7}	4.83×10^{-7}	4.05×10^{-7}	3.18×10^{-7}	2.33×10^{-7}	1.497×10^{-7}	1.388×10^{-7}
1.500×10^{-7}	4.21×10^{-7}	3.73×10^{-7}	3.19×10^{-7}	2.66×10^{-7}	2.15×10^{-7}	2.09×10^{-7}
2.00×10^{-7}	4.29×10^{-7}	3.95×10^{-7}	3.56×10^{-7}	3.19×10^{-7}	2.83×10^{-7}	2.79×10^{-7}
3.00×10^{-7}	5.11×10^{-7}	4.90×10^{-7}	4.66×10^{-7}	4.44×10^{-7}	4.22×10^{-7}	4.19×10^{-7}
4.50×10^{-7}	6.87×10^{-7}	6.73×10^{-7}	6.59×10^{-7}	6.45×10^{-7}	6.31×10^{-7}	6.30×10^{-7}
6.00×10^{-7}	8.81×10^{-7}	8.72×10^{-7}	8.62×10^{-7}	8.52×10^{-7}	8.42×10^{-7}	
7.00×10^{-7}	1.016×10^{-6}	1.008×10^{-6}	9.99×10^{-7}	9.91×10^{-7}	9.83×10^{-7}	
8.00×10^{-7}	1.152×10^{-6}	1.145×10^{-6}	1.138×10^{-6}		1.124×10^{-6}	
9.00×10^{-7}	1.290×10^{-6}		1.278×10^{-6}		1.265×10^{-6}	
1.000×10^{-6}	1.428×10^{-6}		1.418×10^{-6}		1.407×10^{-6}	

[a] Coefficient c was taken to be π in the integrations.

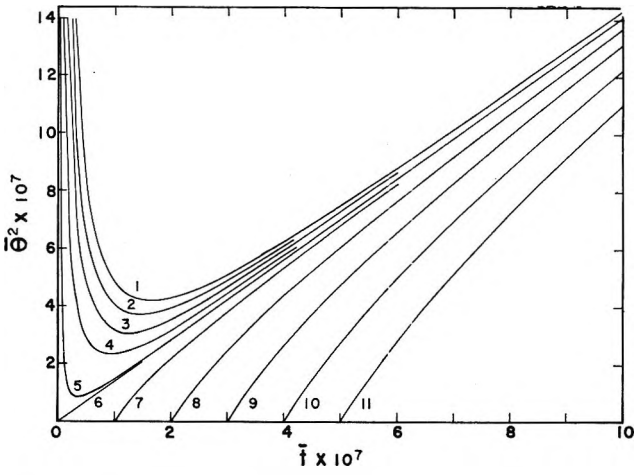

Figure 1. Variation of the square of the diffusion layer parameter with reduced time for various initial conditions.

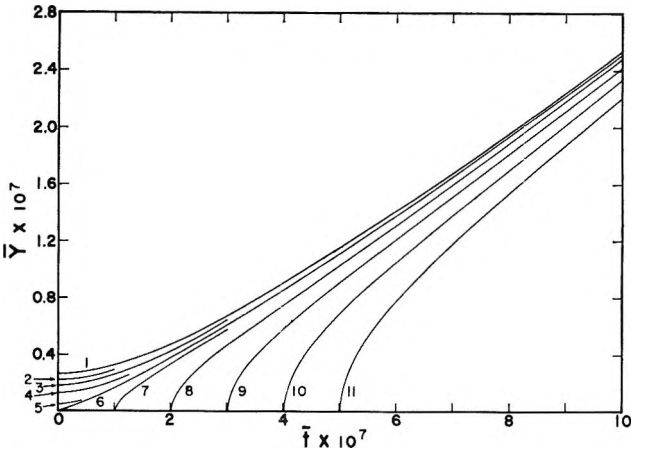

Figure 2. Variation of the reduced depletion with reduced time for the various runs.

A few of the results so obtained appear in Tables I through IV. All of the tabulated results are for $c = \pi$, that is, for our equation. Plots of these appear in Figures 1 and 2. Note how the curves are identified by the run number.

Now, the reduced depletion at the instant the drop falls divided into the extrapolated value at $\bar{t} = 0$ for the same run

$$f = \frac{\bar{Y}_{\text{initial}}}{\bar{Y}_{\text{final}}} \qquad (15)$$

yields the extent of depletion about the nascent drop as a fraction of the final depletion. Runs 6–11 describe possibilities when no initial depletion exists. In each case, electrolysis begins at a different stage in the growth of the drop.

Treating Experimental Data

In fitting experimental data to the appropriate integrated results, one has a problem. The diffusion coefficient to use is not known. Consequently, the reduced quantities $\bar{\theta}^2$ and $\bar{t}$ have to be calculated with

Table II: Reduced Depletion $\bar{Y}$ for Pertinent Entries in Table I

Reduced time, $\bar{t}$	Run 1	Run 2	Run 3	Run 4	Run 5	Run 6
0	2.636×10^{-8}	2.297×10^{-8}	1.860×10^{-8}	1.319×10^{-8}	4.283×10^{-9}	0
1.500×10^{-7}	3.887×10^{-8}	3.644×10^{-8}	3.357×10^{-8}	3.053×10^{-8}	2.734×10^{-8}	2.689×10^{-8}
3.00×10^{-7}	6.751×10^{-8}	6.602×10^{-8}	6.434×10^{-8}	6.266×10^{-8}	6.102×10^{-8}	6.080×10^{-8}
4.50×10^{-7}	1.026×10^{-7}	1.015×10^{-7}	1.004×10^{-7}	9.925×10^{-8}	9.816×10^{-8}	9.801×10^{-8}
6.00×10^{-7}	1.410×10^{-7}	1.402×10^{-7}	1.393×10^{-7}	1.385×10^{-7}	1.377×10^{-7}	1.376×10^{-7}
7.00×10^{-7}	1.679×10^{-7}	1.672×10^{-7}	1.655×10^{-7}	1.658×10^{-7}	1.651×10^{-7}	1.650×10^{-7}
8.00×10^{-7}	1.957×10^{-7}	1.951×10^{-7}	1.944×10^{-7}	1.938×10^{-7}	1.932×10^{-7}	1.931×10^{-7}
9.00×10^{-7}	2.242×10^{-7}	2.236×10^{-7}	2.231×10^{-7}	2.225×10^{-7}	2.219×10^{-7}	2.219×10^{-7}
1.000×10^{-7}	2.533×10^{-7}	2.528×10^{-7}	2.523×10^{-7}	2.518×10^{-7}	2.513×10^{-7}	2.512×10^{-7}

Table III: Square of Diffusion Layer Parameter, $\bar{\theta}^2$, at Various Times Following Given Starting Conditions

Reduced time, $\bar{t}$	Run 7	Run 8	Run 9	Run 10	Run 11
1.000×10^{-7}	0				
2.00×10^{-7}	2.20×10^{-7}	0			
3.00×10^{-7}	3.83×10^{-7}	2.50×10^{-7}	0		
4.00×10^{-7}	5.34×10^{-7}	4.40×10^{-7}	2.66×10^{-7}	0	
5.00×10^{-7}	6.81×10^{-7}	6.09×10^{-7}	4.76×10^{-7}	2.75×10^{-7}	0
6.00×10^{-7}	8.25×10^{-7}	7.68×10^{-7}	6.61×10^{-7}	5.00×10^{-7}	2.82×10^{-7}
7.00×10^{-7}	9.69×10^{-7}	9.21×10^{-7}	8.32×10^{-7}	6.99×10^{-7}	5.18×10^{-7}
8.00×10^{-7}	1.112×10^{-6}	1.071×10^{-6}	9.96×10^{-7}	8.82×10^{-7}	7.28×10^{-7}
9.00×10^{-7}	1.255×10^{-6}	1.219×10^{-6}	1.154×10^{-6}	1.055×10^{-6}	9.21×10^{-7}
1.000×10^{-6}	1.398×10^{-6}	1.366×10^{-6}	1.308×10^{-6}	1.221×10^{-6}	1.103×10^{-6}

various D values at pertinent times. However, a simple computer program suffices for carrying out the calculations.

In getting the necessary relationships, we combine eq 2, 6, and 8

$$\theta = \frac{n\mathfrak{F}DC_0 4\pi\gamma^{2/3}t^{2/3}}{i - n\mathfrak{F}DC_0 4\pi\gamma^{1/3}t^{1/3}} \tag{16}$$

Then we introduce the reduced current

$$\bar{\imath} = \frac{i}{4\pi n\mathfrak{F}C_0\gamma} \tag{17}$$

ant the dimensionless variables $\bar{t}$ and $\bar{\theta}$ with eq 10 and obtain

$$\bar{\theta} = \frac{\bar{t}^{2/3}}{\bar{\imath} - \bar{t}^{1/3}} \tag{18}$$

Into the program one puts i, t, and the various possible D values. Out come the corresponding $\bar{\theta}^2$ and $\bar{t}$ values.

Now, from Figure 1, we see that at any high $\bar{t}$, the square of the diffusion layer parameter, $\bar{\theta}^2$, varies little from run to run. So we examine the computed $\bar{\theta}^2$ values for this region and choose the D that makes them lie along a likely curve in the bundle. Then points for lower reduced times are plotted, and the choice is checked. If necessary, a corrected D is chosen, and the steps are repeated.

Since they seemed to be the most detailed available, the data of Taylor, Smith, and Cooter[15] were used in testing the procedure. Indeed, when the diffusion coefficient was chosen as

$$D = 7.65 \times 10^{-6} \text{ cm}^2 \text{ sec}^{-1} \tag{19}$$

the points fit run 3 as illustrated in Figure 3. This choice is to be compared with the value 7.2×10^{-6} cm^2 sec^{-1} which the cadmium ion exhibits in infinitely dilute solution.[16]

(15) J. K. Taylor, R. E. Smith, and I. L. Cooter, *J. Res. Natl. Bur. Std.*, **42**, 387 (1949).

(16) I. M. Kolthoff and J. J. Lingane, "Polarography," 2nd ed, Interscience Publishers, Inc., New York, N. Y., 1952, p 52.

Table IV: Variation of $\bar{Y}$ with $\bar{t}$ for Entries in Table III

Reduced time, $\bar{t}$	Run 7	Run 8	Run 9	Run 10	Run 11
1.000×10^{-7}	0				
2.00×10^{-7}	3.335×10^{-8}	0			
3.00×10^{-7}	5.802×10^{-8}	4.649×10^{-8}	0		
4.00×10^{-7}	8.326×10^{-8}	7.528×10^{-8}	5.792×10^{-8}	0	
5.00×10^{-7}	1.093×10^{-7}	1.031×10^{-7}	9.069×10^{-8}	6.827×10^{-8}	0
6.00×10^{-7}	1.362×10^{-7}	1.311×10^{-7}	1.212×10^{-7}	1.048×10^{-7}	7.787×10^{-8}
7.00×10^{-7}	1.638×10^{-7}	1.595×10^{-7}	1.512×10^{-7}	1.380×10^{-7}	1.181×10^{-7}
8.00×10^{-7}	1.921×10^{-7}	1.883×10^{-7}	1.812×10^{-7}	1.709×10^{-7}	1.538×10^{-7}
9.00×10^{-7}	2.210×10^{-7}	2.177×10^{-7}	2.114×10^{-7}	2.017×10^{-7}	1.878×10^{-7}
1.000×10^{-6}	2.504×10^{-7}	2.474×10^{-7}	2.418×10^{-7}	2.332×10^{-7}	2.211×10^{-7}

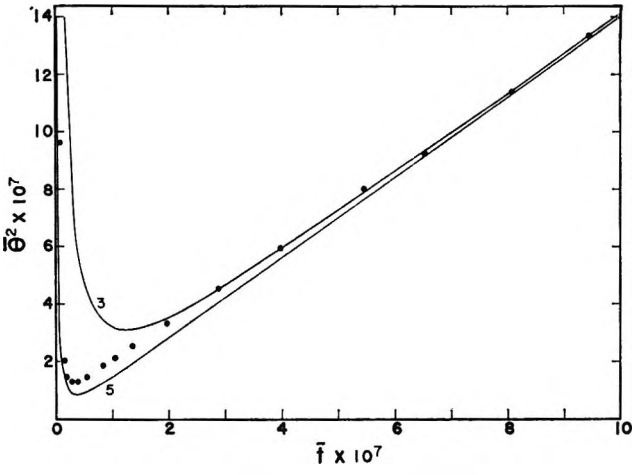

Figure 3. Comparison of points calculated from data of Taylor, Smith, and Cooter[15] with theoretical curves.

Our choice of D is upheld by the good agreement between experiment and theory when $\bar{t} > 2.5 \times 10^{-7}$. However, when it is less, the experimental points fall under curve 3. Indeed, they parallel curve 5 down to its minimum. We interpret this deviation as due to failure of eq 5 as an approximation when $\bar{t} < 2.5 \times 10^{-7}$. Nevertheless, the experimental data could be fitted over any limited range in this region by one of the theoretical curves. Furthermore, the sharp rise in $\bar{\theta}^2$ at small times has empirical support.

Because there is close agreement over the range $2.5 \times 10^{-7} < \bar{t} < 9.5 \times 10^{-7}$ and because the approximations should be better at higher $\bar{t}$ values, we presume that the calculated $\bar{Y}$ when the drop falls is valid. The initial $\bar{Y}$ can only be estimated, however.

We begin with an experimental point near $\bar{t} = 2.5 \times 10^{-7}$, where the calculated $\bar{Y}$ should still be good. From eq 11 and 14 we write

$$\frac{d\bar{Y}}{d\bar{t}} = c\bar{t}^{2/3}\left(\frac{1}{\bar{t}^{1/3}} + \frac{1}{\bar{\theta}}\right) \tag{20}$$

Then we integrate this equation roughly, putting in the empirical variation of $\bar{\theta}$, from the lowest nondeviating experimental point down to $\bar{t} = 0$. With the data of Taylor, Smith, and Cooter,[15] we found that $\bar{Y}_{initial}$ was approximately 0.14×10^{-7}, whence

$$f = 0.06 \tag{21}$$

Useful Approximate Formulas

Interestingly enough, the experimental points in Figure 3 fall close to the straight line

$$\bar{\theta}^2 = 0.74 \times 10^{-7} + 1.325\bar{t} \tag{22}$$

except for $\bar{t} < 0.4 \times 10^{-7}$. While this line does not represent the slight curvature in both the empirical and the theoretical curves when $2.5 \times 10^{-7} < \bar{t} < 10 \times 10^{-7}$, it does represent the much greater shift of the points up from the curve for no initial depletion.

Putting formula 22 back into eq 18 and solving for the instantaneous current in terms of the conventional quantities used in polarographic work, we obtain

$$i = 31{,}563nDCm^{1/3}t^{1/3} + \frac{713.8nD^{1/2}Cm^{2/3}t^{2/3}}{(1.74 \times 10^{-17}m^2/D^3 + t)^{1/2}} \tag{23}$$

To the approximation that the relationship between $\bar{\theta}^2$ and $\bar{t}$ is universal, eq 23 applies to other systems for which fraction f is about 6%.

From Figure 1 we see that increasing the extent of initial depletion causes the theoretical points to be shifted upward. The intercept of the approximating line would be increased, and its slope would be decreased. On the other hand, the straight-line approxi-

mation to the theoretical curve for no initial depletion is

$$\bar{\theta}^2 = 1.400\bar{l} \quad (24)$$

whence

$$i = 31{,}563nDCm^{1/3}t^{1/3} + 694.4nD^{1/2}Cm^{2/3}t^{1/6} \quad (25)$$

Equation 23 is simpler than the other formulas[11] that do allow for an initial depleted layer. Equation 25 is like the modified Ilkovic equation, but with somewhat different numerical factors.

Discussion

When we choose the diffusion coefficient D which allows the empirical $\bar{\theta}^2$ to lie on the theoretical $\bar{\theta}^2$ curve at high $\bar{l}$ values, we are in effect calculating D from diffusion currents near the maximum. This procedure is recommended because the approximations are best in this region. Other authors,[12] using other equations, have similarly calculated D from the maximum current instead of from the average current.

On the other hand, we believe that the entire curve, from birth of the drop to its fall, must be considered in estimating fraction f. First, one sets limits on f by observing the theoretical curves which bracket the empirical points. Thus, the points from Taylor, Smith, and Cooter's data generally fall between curve 3 and a curve not plotted which we did determine. Obtaining $\bar{Y}$ for the final $\bar{t}$ and dividing it into the initial $\bar{Y}$ along the upper curve yields $f = 0.080$, while along the lower curve we get $f = 0.026$. Then one can integrate approximately eq 20 along the empirical points to get a better value. Our final result, $f = 0.060$, was rounded off in eq 21. Compare this with the value $f = 0.2$ obtained by Markowitz and Elving[11] by another procedure.

Acknowledgments. During early phases of this research, Russell B. Kidman held a National Science Foundation Cooperative Fellowship. Later, the other two authors received some support from National Science Foundation Grant GP-4646.

Relations Among Vibrational Frequencies of Isotopically Substituted Molecules and the Determination of Force Constants. II. The One-Dimensional Case

by Julian Heicklen

Aerospace Corporation, El Segundo, California *(Received June 29, 1965)*

There are some additional relations among vibrational frequencies in addition to those previously described for the special case in which only one Cartesian coordinate of any atom is involved in the motion. This situation applies for all motions of linear molecules and the out-of-plane motions of planar molecules. There are $m(m-1)/2$ relations, in addition to the product rules, among the vibrational frequencies of $m+1$ isotopic molecules, in which nonequivalent atoms are substituted.

In an earlier communication,[1] the general relationships were derived that exist among vibrational frequencies of molecules which have symmetrically equivalent atoms isotopically substituted. It was also pointed out that, in general, it is necessary to substitute isotopically all but one set of equivalent atoms to determine the force constant matrix completely.

It is interesting to note that there are some other relations in addition to those previously described for the special case in which only one Cartesian coordinate of any atom is involved in the motion. This situation applies for all motions of linear molecules and the out-of-plane motions of planar molecules. There are $m(m-1)/2$ relations, in addition to the product rules, among the vibrational frequencies of $m+1$ isotope molecules, in which nonequivalent atoms are substituted. It can also be demonstrated that for these "one-dimensional" cases, the most general valence force constant matrix attainable by isotopic substitution can be obtained from fewer substituted molecules than needed for the general case in which two or three of the Cartesian coordinates of any atom participate in the motion. In particular, it is only necessary to substitute isotopically $n-2$ atoms to determine the stretching force constants of linear molecules; $n-3$ atoms for the bending force constants of linear molecules; and $n-4$ atoms for the out-of-plane force constants of planar molecules.

In the following discussion, all atoms will be considered nonequivalent. If there should be equivalent atoms, then the relationships existing among them, as described in ref 1, would also have to be taken into account. The problem to be examined is that of $m+1$ isotopic molecules, each with n atoms of which m have been isotopically substituted. The one-dimensional vibration problem is considered in the coordinate system in which the first m coordinates are the external Cartesian coordinates of the m isotopically substituted atoms, and the remaining $n-m$ coordinates are the normal coordinates of the submolecule associated with the $n-m$ unsubstituted atoms. This coordinate system and its associated force constant matrix have the peculiarity that both the coordinates and force constants are functions of the atomic masses, but only of the unsubstituted atoms. Consequently, neither the coordinates system nor the force constant matrix is altered by the isotopic substitution, yet the number of nonzero force constants is reduced to a minimum. The G and F matrices are

$$G = \begin{bmatrix} \mu_1 & 0 & \cdots & 0 & 0 & \cdots & 0 \\ & \mu_2 & \cdots & 0 & 0 & \cdots & 0 \\ & & \cdot & \cdot & \cdot & \cdot & \cdot \\ & & \cdot & \cdot & \cdot & \cdots & \cdot \\ & & & \cdot & \cdot & \cdot & \cdot \\ & & & \mu_m & 0 & \cdots & 0 \\ & & & & 1 & \cdots & 0 \\ & & & & & \cdot & 0 \\ & & & & & \cdot & \cdot \\ & & & & & \cdot & \cdot \\ & & & & & & 1 \end{bmatrix}$$

(1) J. Heicklen, *J. Chem. Phys.*, **36**, 721 (1962).

$$F = \begin{bmatrix} F_{1,1} & F_{1,2} & \cdots & F_{1,m} & F_{1,m+1} & \cdots & F_{1,n} \\ & F_{2,2} & \cdots & F_{2,m} & F_{2,m+1} & \cdots & F_{2,n} \\ & & \cdot & \cdot & \cdot & \cdot & \cdot \\ & & \cdot & \cdot & \cdot & \cdots & \cdot \\ & & \cdot & \cdot & \cdot & \cdot & \cdot \\ & & & F_{m,m} & F_{m,m+1} & \cdots & F_{m,n} \\ & & & & F_{m+1,m+1} & 0 & 0 \\ & & & & & \cdot & 0 \\ & & & & & \cdot & \cdot \\ & & & & & \cdot & \cdot \\ & & & & & & F_{n,n} \end{bmatrix}$$

where the μ_i are the reciprocal masses of the substituted atoms.

For the $m + 1$ molecules, there are $(m + 1)n$ frequencies, whereas there are only $(m + 1)n - m(m + 1)/2$ unique force constants. Clearly, $m(m + 1)/2$ relationships must exist among the frequencies of all the molecules. Of these, m relationships are the product rules and the remaining $m(m - 1)/2$ are new relationships not previously known to exist. The number of new relations is one-half the number of zeros in the F matrix.

In any general coordinate system, there are $n(n + 1)/2$ unique force constants. Therefore, it is necessary for $m = n - 1$ to determine the general force field. However, this includes the force constants associated with translation and rotation. Since the translations and rotations can always be factored out with a corresponding reduction in the rank of the matrix, then it is sufficient to substitute fewer atoms.

In particular for the stretching vibrations of linear molecules (one translation, no rotations), the rank is reduced by one, and if $n - 2$ atoms are isotopically substituted, then the F matrix is completely determined. Thus, for HCN (with three stretching force constants) the original molecule gives two relationships, and the remaining relationship can be found by substituting any one of the three atoms. (This statement corrects the erroneous requirement concerning HCN in ref 1 where it was stated that it is necessary to substitute two atoms. That statement was based on the general rule and would have been correct if HCN were nonlinear.) The simplest nontrivial example of the rule occurs with a linear molecule containing five atoms, *e.g.*, O=C=C=C=S. There are 10 stretching force constants. Three molecules (two isotopically substituted atoms) gives 12 frequencies. However, there are three relationships (two product rules and one additional relationship) so that it is necessary to substitute isotopically another atom to completely specify the F matrix.

Associated with the bending vibrations of linear molecules are a rotation and a translation. Thus, it is only necessary to substitute $n - 3$ atoms to specify the force constants. For a triatomic molecule, the rule is immediately seen to be correct inasmuch as no isotopes are needed to compute the bending force constant.

For the out-of-plane motions of planar molecules, there are two rotations and a translation. Thus, if $n - 4$ atoms are isotopically substituted, the F matrix is determined. For example, the out-of-plane force constants of

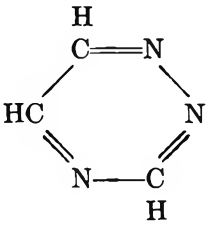

can be found by substituting any five atoms.

Acknowledgment. The author wishes to thank Mrs. Barbara Peer for assistance with the manuscript, and Professor Bernard Kirtman for useful suggestions.

Appendix

To illustrate the coordinate transformation from external Cartesian coordinates, X to the coordinate system used in this note (called S), consider the stretching motions of a linear triatomic molecule for which only one atom is substituted (referred to as atom one). For the purpose of simplicity, the translation is retained as a vibration. Then

$$X = \begin{pmatrix} X_1 \\ X_2 \\ X_3 \end{pmatrix} \qquad G_X = \begin{pmatrix} \mu_1 & 0 & 0 \\ 0 & \mu_2 & 0 \\ 0 & 0 & \mu_3 \end{pmatrix}$$

$$F_x = \begin{pmatrix} F_{11}^x & F_{12}^x & F_{13}^x \\ F_{12}^x & F_{22}^x & F_{23}^x \\ F_{13}^x & F_{23}^x & F_{33}^x \end{pmatrix}$$

and

$$S = \begin{pmatrix} S_1 \\ S_2 \\ S_3 \end{pmatrix} = \begin{pmatrix} 1 & 0 & 0 \\ 0 & L_{22} & L_{23} \\ 0 & L_{32} & L_{33} \end{pmatrix} \begin{pmatrix} X_1 \\ X_2 \\ X_3 \end{pmatrix}$$

and

$$G_s = \begin{pmatrix} \mu_1 & 0 & 0 \\ 0 & 1 & 0 \\ 0 & 0 & 1 \end{pmatrix} \qquad F_s = \begin{pmatrix} F_{11}^s & F_{12}^s & F_{13}^s \\ F_{12}^s & F_{22}^s & 0 \\ F_{13}^s & 0 & F_{33}^s \end{pmatrix}$$

The coordinates S_2 and S_3 are the normal coordinates of the submolecule consisting of atoms 2 and 3. In

particular, $F_{11}^s = F_{11}^x$, and F_{22}^s and F_{33}^s are the two roots of the equation

$$F_{22}^s, F_{33}^s = \frac{\{\mu_2 F_{22}^x + \mu_3 F_{33}^x \pm \sqrt{(\mu_2 F_{22}^x + \mu_3 F_{33}^x)^2 - 4[\mu_2\mu_3 F_{22}^x F_{33}^x - \mu_2\mu_3 (F_{23}^x)^2]}\}}{2}$$

Thus F_{11}^s, F_{22}^s, and F_{33}^s are functions only of the force constants in external Cartesian coordinates and the unsubstituted masses. The solutions for the L matrix elements are

$$L_{32}^2 = (F_{22}^x - m_2 F_{22}^s)/(F_{33}^s - F_{22}^s)$$

$$L_{23}^2 = (F_{33}^x - m_3 F_{33}^s)/(F_{22}^s - F_{33}^s)$$

$$L_{22}^2 = m_2 - (F_{22}^x - m_2 F_{22}^s)/(F_{33}^s - F_{22}^s)$$

$$L_{33}^2 = m_3 - (F_{33}^x - m_3 F_{33}^s)/(F_{22}^s - F_{33}^s)$$

where m_1, m_2, and m_3 are the atomic masses. Again it can be seen that the L matrix elements are functions only of the force constants in external coordinates and the masses of the unsubstituted atoms. The remainder of the F_s matrix elements is

$$F_{12}^s = (L_{32} F_{13}^x - L_{33} F_{12}^x)/(L_{23} L_{32} - L_{22} L_{33})$$

$$F_{13}^s = (L_{23} F_{12}^x - L_{22} F_{13}^x)/(L_{23} L_{32} - L_{22} L_{33})$$

Again these elements are not functions of m_1. Consequently, the F_s matrix has fewer nonzero force constants than F_x, yet these force constants are not changed by the isotopic substitution of atom one.

Heats of Mixing of Aqueous Electrolytes. II. Alkaline Earth Halides[1]

by R. H. Wood and Henry L. Anderson

Department of Chemistry, University of Delaware, Newark, Delaware *(Received July 6, 1965)*

The heats of mixing of the alkaline earth halides at constant total ionic strength have been measured at 25° in the concentration range of 0.1 to 2.0 *m*. The heats of mixing were quadratic in mole fraction. The magnitudes of the interaction parameters, RTh_0, were found to be much smaller and to depend more strongly on concentration than those of the alkali metal halides. The heats of mixing of the chloride–bromide ions were found to be relatively independent of the common cation, even with a common cation of a different valence. This result indicates that like-charged pair interactions are more important than triplet interactions in determining the heats of mixing and supports Friedman's application of Mayer's ionic solution theory to mixed electrolytes. The common cation mixings were all endothermic. The cross-square rule was verified for the reciprocal mixture of $MgCl_2$–$CaBr_2$. A set of general equations which allows the prediction of the total excess free energy and relative apparent molal heat content of any multicomponent mixture of electrolytes of the same charge type from the knowledge of only the thermodynamic properties of the component pure electrolyte and common-ion mixed electrolyte solutions was derived.

Introduction

In order to have a better understanding of the thermodynamic properties of aqueous electrolyte solutions, a more detailed knowledge of the nature of ionic interactions in solution is needed. In the first communication of this series,[2] the utility of measuring heats of mixing at constant ionic strength to investigate these interactions has been discussed. The heats of mixing of the alkali metal halides and nitrates at constant ionic strength at 25° in the concentration range 0.1 to 1 *m* were interpreted as being in good agreement with Friedman's treatment of mixed electrolyte solutions.[3]

The heats of mixing of a wide variety of 1–1 electrolytes at 1 total ionic strength and 25° have been measured by Young, *et al.*[4,5] Their results show that the heat of mixing is independent of the common ion and are in good agreement with Friedman's theory. Several observations are made in their work which are not generally deduced from Friedman's theory. (1) In the presence of a common ion, the heat of mixing of cations (30 to −50 cal/kg of solvent) is much larger than the heat of mixing of anions (~1 cal/kg of solvent). (2) The cations fall into two groups, (H^+, Li^+, and Na^+) and (K^+, Rb^+, Cs^+), and in the presence of a common ion, the enthalpy of mixing of ions of the same group is positive and ions of opposite groups is negative. (3) For reciprocal salt pairs, the sum of the heats of common ion mixings equals the sum of the heats of noncommon-ion mixings (cross-square rule).

It is the purpose of the present work to test the generality of the conclusions drawn from the studies of the 1–1 electrolyte mixtures by measuring the heats of mixing of some polyvalent electrolyte solutions of the same charge type. The systems chosen for this investigation were the alkaline earth halides.

The results of the present study suggested the derivation of a set of general equations based on Friedman's mixed electrolyte theory. The resulting equations

(1) The authors acknowledge support by the Office of Saline Water, U. S. Department of the Interior, Contract No. 14-01-0001-431.

(2) R. H. Wood and R. W. Smith, *J. Phys. Chem.*, 69, 2974 (1965).

(3) H. L. Friedman, *J. Chem. Phys.*, 32, 1134 (1960).

(4) (a) T. F. Young and M. B. Smith, *J. Phys. Chem.*, 58, 716 (1954); (b) T. F. Young, Y. C. Wu, and A. A. Krawetz, *Discussions Faraday Soc.*, 24, 27, 7780 (1957).

(5) Y. C. Wu, M. B. Smith, and T. F. Young, *ibid.*, 69, 1868, 1873 (1965).

allow the prediction of the excess free energy and relative apparent molal heat content of any multicomponent mixture of electrolytes of the same charge type from the knowledge of only the thermodynamic properties of the component pure electrolyte solutions and the common ion mixtures.

Experimental Section

1. Preparation and Analysis of Stock Solutions. Stock solutions (1–3 *m*) of $MgCl_2$, $MgBr_2$, $CaCl_2$, $CaBr_2$, $SrCl_2$, and $BaCl_2$ were prepared and stored in polyethylene bottles. The $MgCl_2$, $CaCl_2$, and $BaCl_2$ solutions were prepared directly from their Mallinckrodt AR (ACS) grade salts. The $CaBr_2$ and $MgBr_2$ solutions were prepared from Mallinckrodt AR (ACS) grade 48% HBr with $CaCO_3$ and MgO, respectively. The $SrCl_2$ stock solution was prepared from Mallinckrodt AR grade $SrCO_3$ and Fisher reagent grade 37% HCl. In the preparation of the salt solutions from the carbonates and oxide, the resultant slightly acidic solutions had a yellow or reddish brown color and gave positive Fe(III) tests with KSCN. Each of the solutions was treated with its carbonate or oxide and filtered. The colorless filtrates gave negative Fe(III) tests. All of the solutions were adjusted to give pH values ranging from 4 to 6 so as to suppress hydrolysis. The solutions prepared from the carbonates were refluxed for several hours to ensure that all of the CO_2 had been expelled. The $MgCl_2$ and $MgBr_2$ stock solutions were standardized by EDTA titration.[6] The $CaCl_2$ and $CaBr_2$ stock solutions were standardized by Mg–EDTA substitution titrations.[6] The $SrCl_2$ and $BaCl_2$ stock solutions were standardized by AgCl gravimetric analyses. The concentrations of all stock solutions were determined to within 0.1% (mean standard deviation of from four to six determinations). The stock solutions were analyzed for Na, K, Mg, Ca, Sr, and Ba ion impurities. In most cases the ion impurities were determined flame photometrically,[7] with a Beckman DU spectrophotometer Model 2400 with flame attachment using an oxygen–hydrogen flame,[8] and the blue sensitive phototube[9] by the semi-internal standard method. The magnesium and barium ion impurities in the case of the calcium chloride, calcium bromide, strontium chloride, and barium chloride were determined using Titan yellow and sulfate turbidity tests.[7] Except for the $SrCl_2$ (0.59 and 1.0 mole % for stock solutions I and II, respectively) the total cation impurities were less than 0.15 mole % in all of the stock solutions.

2. Procedure. The heat of mixing experiments were performed at constant ionic strength over the concentration range of 0.1 to 1 *m* at 25.03° in an isothermal differential calorimeter (sensitivity = 2×10^{-6}). For a description of the calorimeter and the experimental procedure see ref 2.

3. Treatment of Data and Results. The experimental data were fitted to the equation[2]

$$\Delta H_m \text{ (cal/kg of solvent)} = RTI^2y(1 - y)[h_0 + (1 - 2y)h_1] \quad (1)$$

and the results recorded in Table I (y is the mole fraction of the salt with the largest formula weight). Three major sources of error were accounted for in estimating the uncertainty of RTh_0 in Table I. The heat of mixing due to ion impurities was estimated for each mixture. In addition, the heat of dilution or concentration due to the ionic strength uncertainty in the standardization of the stock solutions, and the calorimetric precision were calculated for each experiment. The total error of RTh_0 was estimated by taking the square root of the sum of the squares of these three errors. The calorimetric precision was the controlling factor in the dilute solution experiments whereas in the 1 *m* experiments the calorimetric precision was of the same order of magnitude as the inherent errors of the stock solutions.

Discussion

From the study of Wood and Smith[2] it was concluded that RTh_0 for common-ion mixtures of the alkali metal halides and nitrates showed no strong concentration dependence. This was interpreted as indicating that triplet and higher order interactions are relatively small. In the present results, RTh_0 decreases considerably with decreasing concentration. This indicates that triplet interactions are more important in these salts. This is to be expected because of the increased charge on the cations. If these interactions are the result of just triplet interactions, it should be possible to use an equation of the form

$$RTh_0 = BI + CI^{3/2} \quad (2)$$

to represent the data.[2,10,11] The results indicate that triplet interactions alone cannot explain the data.

The heats of mixing of the alkaline earth cations are on the average much smaller than the heats of mixing

(6) H. A. Flaschka, "EDTA Titrations," Pergamon Press Inc., New York, N. Y., 1959.

(7) "Reagent Chemicals," American Chemical Society Specifications, 1960, ed by Applied Publications, American Chemical Society, Washington, D. C., 1961.

(8) An oxygen–acetylene flame was used for the magnesium analyses.

(9) A red-sensitive phototube was used for the potassium analyses.

(10) G. Scatchard and S. S. Prentiss, *J. Am. Chem. Soc.*, **56**, 2315, 2320 (1934).

(11) G. Scatchard, *ibid.*, **83**, 2636 (1961).

Table I: Parameters for Heat of Mixing Equations

Mixture	I	N^a	$RTh_0{}^b$	$RTh_1{}^b$	$\Delta H_{m,y=0.5}{}^c$
$MgCl_2$–$CaCl_2$	3	8	1.55 ± 0.04	0.09 ± 0.04	3.50
$MgCl_2$–$SrCl_2$	3	7	3.84 ± 0.05	0.18 ± 0.03	8.65
	2	15	3.63 ± 0.03	0.17	3.63
	1	11	3.3 ± 0.2	0.2 ± 0.2	0.82
	3/5	15	3.1 ± 0.5		0.27
$MgCl_2$–$BaCl_2$	3	19	8.26 ± 0.05	0.89 ± 0.04	18.59
	2	12	8.00 ± 0.06	0.8 ± 0.1	8.00
	1	15	6.7 ± 0.3		1.67
	3/5	8	4.5 ± 0.5		0.41
	3/10	12	5 ± 1		0.12
$CaCl_2$–$SrCl_2$	3	15	0.28 ± 0.01		0.64
$CaCl_2$–$BaCl_2$	3	9	3.59 ± 0.10	0.3 ± 0.2	8.07
$SrCl_2$–$BaCl_2$	3	11	1.47 ± 0.05	0.08 ± 0.04	3.32
$MgBr_2$–$CaBr_2$	3	12	1.22 ± 0.04	0.14 ± 0.04	2.76
$MgCl_2$–$MgBr_2$	3	8	1.81 ± 0.03	0.05 ± 0.03	4.08
	2	15	1.57 ± 0.03		1.57
$CaCl_2$–$CaBr_2$	3	10	1.96 ± 0.03		4.42
$MgCl_2$–$CaBr_2$	3	11	8.29 ± 0.07	0.24 ± 0.03	18.66
	2	12	7.30 ± 0.06	0.20 ± 0.08	7.30
	1	7	5.8 ± 0.4		1.44
	3/5	8	5.1 ± 0.3		0.46
$MgBr_2$–$CaCl_2$	3	13	−1.70 ± 0.02	0.14 ± 0.03	−3.83

[a] N is the number of experiments. [b] Units are cal/kg of solvent/ional[2] (see eq 1). [c] Units are cal/kg of solvent.

of the alkali metal cations. Since the ionic strength does not have a strong influence on determining the relative magnitude of the interaction constant, we can compare the average heat of mixing of 1 m common-ion alkali metal halide solutions (20 cal/kg of solvent) with the average heat of mixing of 1 m common ion alkaline earth halide solutions (7 cal/kg of solvent).

In most cases the absolute value of RTh_0 decreases with decreasing concentration; therefore, when the comparison is made at the same ionic strength, the differences in the two average heats of mixing will be even greater. This is in accord with the qualitative expectation that the higher the charge on the ions, the less they will interact with ions of the same charge.

The heats of mixing of the alkaline earth cations in the presence of a common anion were all endothermic. Young, Wu, and Krawetz[4b] have shown that by classifying the alkali metal cations into two groups, the sign of the heat of mixing can be predicted. They classified the ions according to size (large or small) and suggested that solvent structure about the ions may also be important. All of the alkali cations in the group containing H^+, Li^+, and Na^+ are small, structure-making ions according to the model of Frank and Evans.[12] The group containing the large ions, K^+, Rb^+, and Cs^+ are all structure-breaking ions. The alkaline earth cations are all small, structure-making ions. Thus, the prediction of the sign of the heat of mixing according to the correlation of Young, *et al.*, can be extended to include the alkaline earth cations. Unfortunately, the mixtures studied to date are not capable of showing the relative importance of structural properties and sizes of the ions.[13]

For common ion mixtures, Wu, Smith, and Young[5] found the heat of mixing to be relatively independent (±10%) of the common ion. The heats of mixing of the chloride and bromide ions in the presence of the common magnesium and calcium ions (4.08 and 4.42 cal/kg of solvent, respectively) show fair agreement with this principle. However, those mixtures containing KNO_3, a salt having considerable ion-pair character,[14,15] deviate substantially from this conclusion. Thus, it is not surprising that the heats of mixing of the magnesium and calcium ions in the presence of the common chloride and bromide ions (3.50 and 2.76 cal/kg of solvent, respectively) deviate from this principle. In order to extend this principle, one can compare the chloride–bromide heats of mixing in the presence of common alkali metal and alkali earth cations. Assuming pairwise interactions to be the

(12) H. S. Frank and M. W. Evans, *J. Chem. Phys.*, **13**, 507 (1945).

(13) A future communication will report the results of the heats of mixing of a large variety of anions and cations designed to test the relative importance of ionic radii and structural properties.

(14) C. W. Davies, *Trans. Faraday Soc.*, **23**, 354 (1927).

(15) R. A. Robinson and C. W. Davies, *J. Chem. Soc.*, 574 (1937).

major interactions, the cation interactions cancel and one can write the relation for a common ion mixture

$$\Delta H_m = m_{Cl} m_{Br} R T h_{Cl-Br} \quad (3)$$

where h_{Cl-Br} is a function of ionic strength. Therefore, to compare the heat of mixing of the chloride–bromide mixtures in the presence of a common alkali metal cation with that of a chloride–bromide mixture in the presence of a common alkaline earth cation, one obtains at constant ionic strength

$$\Delta H_m{}^{2-1} = {}^4/_9 \Delta H_m{}^{1-1} \quad (4)$$

To make the comparison, 0.80 cal/kg of solvent[4b] was taken for the heat of mixing chloride and bromide ions in the presence of an alkali metal cation at unit ionic strength. The heat of mixing chloride and bromide ions in the presence of common alkaline earth cations was not measured at unit ionic strength. However, a value was estimated (0.33 cal/kg of solvent) by extrapolation from measurements made at 3 and 2 total ionic strength for the $MgCl_2$–$MgBr_2$ mixture. From eq 4, one predicts ΔH_m for the $MgCl_2$–$MgBr_2$ mixture to be 0.36 cal/kg of solvent. This rather good agreement is considered to be additional confirmation of the conclusions of Wood and Smith[2] that pairwise interactions are the major contributor to the heat of mixing. The division of interactions into either pair interactions with their ionic atmospheres or triplet interactions is arbitrary at finite concentrations. The distinction proposed in the above comparison is that, if the third ion has no specific effect, it is most convenient to call it part of the ion atmosphere. If the interactions vary only slightly with the common ion, it is most convenient to assign the major part of the interaction to a pair with its ion atmosphere and to account for the small differences by invoking triplet interactions. In the majority of cases where comparisons are possible, a change in anion (even to a different charge type) does not change the interaction by more than 10% and in the case of mixing chloride and bromide, the interaction is the same in the presence of either Li^+, Na^+, K^+, Mg^{2+}, or Ca^{2+} to within about 10%.

General Equations

One of the major aims of research on mixed electrolyte solutions is the prediction of the properties of mixed electrolyte solutions from as few parameters as possible. The present results suggested the derivation of a simple equation for the enthalpy and excess free energy of a mixture of any number of electrolytes, provided they are all of the same charge type. The equations are based on only the knowledge of the thermodynamic properties of common-ion mixtures and pure electrolyte solutions. The mixtures are formed by mixing solutions at constant ionic strength, to give a resulting solution containing 1 kg of solvent. Thus energy units will be in calories per kilogram of solvent.[16]

One can write the expression

$$G^E{}_{Mix} = \sum_{i,j} y_{R_i} y_{X_j} G^E{}_{R_iX_j} + \Delta_m G^E \quad (5)$$

where $G^E{}_{Mix}$ is the total excess free energy per kilogram of solvent of an aqueous electrolyte mixture containing cations $(R_1,\ldots,R_i,\ldots)$ and anions $(X_1.,..,X_j,\ldots)$; $G^E{}_{R_iX_j}$ is the total excess free energy per kilogram of solvent of the component pure electrolyte R_iX_j; y_{R_i}, etc. is the component ion mole fraction $= m_{R_i}/\sum_k m_{R_k}$; $\Delta G^E{}_m$ is the total excess free energy per kilogram of solvent of mixing the single component solutions at constant ionic strength. It will be seen that the component rule governing this expression will allow the calculation of $\Delta G^E{}_m$ from the knowledge of only common-ion mixings. This is true because this component rule essentially equates the plus–minus pairwise interactions in the final mixture and in the component pure electrolyte solutions since the amount of pure electrolyte is proportional to the product of the cation and anion mole fraction in the final mixture.[17] To show that this is indeed true, one can use Friedman's application of Mayer's ionic cluster expansion.[3] Friedman's theory is based on constant molar ionic strength and constant water activity, while the present calculations are based on constant total molal ionic strength and pressure. The nature of the correction terms needed to equate the two methods of calculation are mostly due to the difference in concentration scales. Since it has been shown that these corrections are fairly small for 1–1 electrolytes,[3] we will proceed by neglecting them.

Thus eq 18.20 of Friedman[18] can be rewritten for the case of mixing several electrolytes as

$$\Delta G^E{}_m \simeq \Delta G^E{}_m\,(y_{R_1} \cdots y_{R_i}, y_{X_1} \cdots y_{X_j}, I) = \sum_{u \geq 2} B_u(I)\,\Delta_m C^u(y_{R_1} \cdots y_{R_i}, y_{X_1} \cdots y_{X_j}, I) \quad (6)$$

where $\Delta G^E{}_m$ is the excess free energy of mixing all the electrolytes per kilogram of solvent and $B_u(I)$ is a cluster integral and $\Delta_m C^u(y,I)$ is a concentration set.[18] When this equation is used to calculate $\Delta G^E{}_m$ in eq 5

(16) H. L. Friedman, *J. Chem. Phys.*, 32, 1351 (1960).

(17) This is the component rule suggested as reasonable by Prof. Scatchard in ref 11.

(18) H. L. Friedman, "Ionic Solution Theory," Interscience Publishers Inc., New York, N. Y., 1962.

it is found that the oppositely charged pair interactions cancel. If the integrals in eq 6 are identified with the experimental measurements on common-ion mixings and if all interactions higher than triplets are neglected and like-charged triple ion interactions are neglected, the resultant equation is

$$\Delta G^{E}_{m} = {}^{1}/_{2}RT^{2}[\Sigma y_{R_h} y_{R_i} y_{X_j} g^{X_j}{}_{R_h R_i} + \Sigma y_{X_j} y_{X_k} y_{R_i} g^{R_i}{}_{X_j X_k}] \quad (7)$$

where

$$g^{X_j}{}_{R_h R_i} = [B^{hi} - B^{hh} - B^{ii}] + I[B^{hij} - B^{hhj} - B^{iij}]$$

$$g^{R_i}{}_{X_j X_k} = [B^{jk} - B^{jj} - B^{kk}] + I[B^{ijk} - B^{iik} - B^{jjk}]$$

and ΔG^{E}_{m} is in calories per kilogram of solvent. By combining the interactions of $g^{X_j}{}_{R_1 R_2}$ with $g^{X_j}{}_{R_2 R_1}$ etc., one can rewrite eq 7 to give

$$\Delta G_{m}{}^{E} = RTI^{2}\left[\sum_{h>i} y_{R_h} y_{R_i} y_{X_j} g^{X_j}{}_{R_h R_i} + \sum_{j>k} y_{X_j} y_{X_k} y_{R_i} g^{R_i}{}_{X_j X_k}\right] \quad (8)$$

Thus, it is seen from this relation that ΔG^{E}_{m} is calculated from the weighted average of the interactions of all of the cations in the presence of all of the anions plus the weighted average of the interactions of all of the anions in the presence of all of the cations. The weighting factors are the respective ion mole fractions (y_{R_h}, y_{X_j}, etc.). The interaction parameter $g^{X_j}{}_{,R_h R_i}$ etc. include both pairwise and triplet interactions. The only terms neglected are those involving the interactions of three like-charged ions. The reason for not including these terms is that they contribute asymmetry to the equations. Experimentally, it is known that the asymmetry is very small.[2,4b] Therefore, only common-ion mixtures are needed to calculate ΔG^{E}_{m}.

Analogous equations can be written for the relative apparent molal heat content of a mixed electrolyte solution

$$\phi_{L}{}^{Mix} = \Sigma y_{R_i} y_{X_j} \phi_{L}{}^{R_i X_j} + 1/m \quad \Delta H_{m} \quad (9)$$

where

$$\Delta H_{m}\ (\text{cal/kg}) = RTI^{2}\left[\sum_{h>i} y_{R_h} y_{R_i} y_{X_j} h^{X_j}{}_{R_h R_i} + \sum_{j>k} y_{X_j} y_{X_k} y_{R_i} h^{R_i}{}_{X_j X_k}\right] \quad (10)$$

Wirth, Lindstrom, and Johnson have given an equation for the excess volume of a mixture containing four ions.[19] If the higher terms in their equations (those involving k') are neglected, it can be shown that their equation is of the same form as eq 9. The present derivation shows how the arbitrary division of volumes among the ions can be avoided, gives a physical reason for the interactions, and includes symmetrical mixtures of any number of electrolytes.

As an example of the use of the general equations, an equation for calculating the relative partial molal heat content of a solution containing ${}^{4}/_{3}$ moles of Ca^{2+}, ${}^{2}/_{3}$ mole of Mg^{2}, ${}^{10}/_{3}$ moles of Cl^{-}, and ${}^{2}/_{3}$ mole of Br^{-} in 2 kg of water will be given. Applying eq 9 and 10 to this mixture gives

$$\phi_{L}{}^{Mix} = y_{Ca^{2+}} y_{Cl^{-}} \phi_{L}{}^{CaCl_2} + y_{Ca^{2+}} y_{Br^{-}} \phi_{L}{}^{CaBr_2} + y_{Mg^{2+}} y_{Cl^{-}} \phi_{L}{}^{MgCl_2} + y_{Mg^{2+}} y_{Br^{-}} \phi_{L}{}^{MgBr_2} + \frac{RTI^{2}}{m}[y_{Ca^{2+}} y_{Mg^{2+}} y_{Cl^{-}} h^{Cl^{-}}{}_{Mg^{2+},Ca^{2+}} + y_{Ca^{2+}} y_{Mg^{2+}} y_{Br^{-}} h^{Br^{-}}{}_{Mg^{2+},Ca^{2+}} + y_{Cl^{-}} y_{Br^{-}} y_{Ca^{2+}} h^{Ca^{2+}}{}_{Cl^{-},Br^{-}} + y_{Cl^{-}} y_{Br^{-}} y_{Mg^{2+}} h^{Mg^{2+}}{}_{Cl^{-},Br^{-}}]$$

where $I = 3$, $m = 1$, $y_{Ca^{2+}} = {}^{2}/_{3}$, $y_{Mg^{2+}} = {}^{1}/_{3}$, $y_{Cl^{-}} = {}^{5}/_{6}$, and $y_{Br^{-}} = {}^{1}/_{6}$. The common-ion interaction parameters from Table I are $RTh^{Cl^{-}}{}_{Mg^{2+},Ca^{2+}} = 1.55$, $RTh^{Br^{-}}{}_{Mg^{2+},Ca^{2+}} = 1.22$, $RTh^{Mg^{2+}}{}_{Cl^{-},Br^{-}} = 1.81$, and $RTh^{Ca^{2+}}{}_{Cl^{-},Br^{-}} = 1.96$. The result $\phi_{L}{}^{Mix}$ is in calories per mole of salt and there are 2 moles of salt in the 2 kg of water.

The cross-square rule[4b] has been verified for a large number of alkali metal halides and nitrates at unit ionic strength by Wu, Smith, and Young[5] and over the concentration range of 0.1 to 0.5 total ionic strength by Wood and Smith.[2] The present results allow the first test of this relation for a 2–1 electrolyte mixture. The reciprocal salt mixture of $MgCl_2$–$CaBr_2$ yielded

$$\Sigma\square = \Delta H_{m}(MgCl_2\text{–}CaCl_2) + \Delta H_{m}(CaCl_2\text{–}CaBr_2) + \Delta H_{m}(MgBr_2\text{–}CaBr_2) + \Delta H_{m}(MgCl_2\text{–}MgBr_2) = 14.76 \text{ cal/kg of solvent}$$

$$\Sigma\times = \Delta H_{m}(MgCl_2\text{–}CaBr_2) + \Delta H_{m}(MgBr_2\text{–}CaCl_2) = 14.83 \text{ cal/kg of solvent}$$

Thus, within experimental error one can conclude that the cross-square rule is valid for this system.

It can be shown that the cross-square rule is a specific case of the general equations. Consider the reciprocal mixture of MX–NY at constant total ionic strength and $y_{MX} = y_{NY}$. Then from eq 9 and 10 we can write

(19) H. E. Wirth, R. E. Lindstrom, and J. N. Johnson, *J. Phys. Chem.*, **67**, 2339 (1963).

$$\phi_L^{MXNY} = {}^1/_4\phi_L^{MX} + {}^1/_4\phi_L^{MY} + {}^1/_4\phi_L^{NX} + {}^1/_4\phi_L^{NY} + \frac{RTI^2}{m}[{}^1/_8h_{MN}^{X} + {}^1/_8h_{MN}^{Y} + {}^1/_8h_{XY}^{M} + {}^1/_8h_{XY}^{N}] \quad (11)$$

This equation is independent of the manner in which the mixture was formed. There are two paths possible for forming the mixture

$$\phi_L^{MXNY} = {}^1/_2\phi_L^{MX} + {}^1/_2\phi_L^{NY} + \Delta H_m^1 \quad (12)$$

$$\phi_L^{MXNY} = {}^1/_2\phi_L^{MY} + {}^1/_2\phi_L^{NX} + \Delta H_m^2 \quad (13)$$

Combining eq 11, 12, and 13, one obtains

$$\Delta H_m^1 + \Delta H_m^2 = \frac{RTI^2}{4m}[h_{MN}^{X} + h_{MN}^{Y} + h_{XY}^{M} + h_{XY}^{N}]$$

or

$$\Sigma\times = \Sigma\square$$

where $\Sigma\times = \Delta H_m(MX + NY) + \Delta H_m(MY + NX)$ and $\Sigma\square = \Delta H_m(MX + NX) + \Delta H_m(MY + NY) + \Delta H_m(MX + MY) + \Delta H_m(NX + NY)$.

Acknowledgment. The authors are grateful for many helpful discussions with Dr. Ronald W. Smith concerning this work.

The Influence of Amino Acid Side Chains on the Free Energy of Helix-Coil Transitions[1]

by George Némethy,

The Rockefeller University, New York, New York

S. J. Leach, and Harold A. Scheraga

Department of Chemistry, Cornell University, Ithaca, New York *(Received July 15, 1965)*

Because of steric factors, the presence of side chains affects the relative stability of the α-helical (or other folded structures) and the random coil form of polypeptides and polyamino acids. (1) The entropy of unfolding depends on the nature of the side chain, because the freedom of internal rotation of the backbone in the random coil form is diminished by the presence of long or bulky side chains. ΔS_{conf}, the entropy of unfolding per residue is about 2.5 eu smaller for amino acids with unbranched side chains and about 5 eu smaller for valine and isoleucine than for glycine. These values refer to unfolding from any rigid structure, not only the α-helix; they were calculated on the basis of excluded volumes due only to steric interactions. (2) The freedom of internal rotation of the side chain itself can change during the unfolding process. This effect contributes about 0.5 eu to ΔS_{conf} in the α-helix-to-random coil process. In the unfolding of some other structures, this entropy contribution may be negative if the side chain is less restricted in these structures than it is, on the average, in the random coil. (3) Although valine and isoleucine are classed as non-α-helix-forming amino acids, they can be accommodated in α-helixes by rotating the side chains out of the potential minima for internal rotation. This has a destabilizing effect on the α-helix amounting to about $\Delta H = 0.76$ kcal/mole per residue.

Introduction

When the stability of the α-helix or the thermodynamic parameters for the helix-to-random coil transition (or similar transformations) of a polypeptide chain are considered, the gain in entropy is usually evaluated merely from changes in the freedom of rotation of the peptide backbone, disregarding the nature or the influence of the side chains. We wish to point out that the presence of the side chains can have a profound effect on the stability of the α-helix or other folded structures. Their influence is manifested in several ways. (1) The extent of freedom of rotation of the backbone itself in an unfolded state depends very strongly on the nature of the side chains. (2) The freedom of rotation around single bonds in the side chain is variable, depending on the conformation of the backbone. (3) In some backbone conformations (such as the α-helix), bulky side chains may be forced into positions not corresponding to minima for rotation around the single bonds in the side chain, while these minima are accessible in other conformations; this results in a destabilization of certain folded structures.

The considerations presented here apply not only to the α-helix-to-random coil transition, but also to the unfolding from any (regular or irregular) structure, in which the peptide residues have been constrained to a definite conformation, to a state in which there are more degrees of conformational freedom.

(1) This work was supported by a research grant (AI-01473) from the National Institute of Allergy and Infectious Diseases of the National Institutes of Health, U. S. Public Health Service, and by a research grant (GB-2238) from the National Science Foundation.

Discussion

1. Number of Conformations Available to the Peptide Backbone in the Unfolded State. For the estimation of the entropy of unfolding of the polypeptide chain in the helix–random coil conversion, the expression

$$\Delta S_{conf} = R \ln z^n \qquad (1)$$

is used generally, where n is the number of residues in the polypeptide and z is the number of conformations available to each residue in the unfolded state.[2,3] The number z has always been taken to be the same for every residue. Values such as six[2] or eight[3] per residue are often used to represent the number of *accessible* minima of the potential functions for rotation around the two single bonds (N–C^α and C^α–C′) of the polypeptide chain, assuming all minima to be of equal energy.

In recent work on the steric effects in polypeptides, it has been shown[4–6] that the conformational freedom of the peptide backbone in the random coil state is strongly dependent on the nature of the side chain (Figure 1).[7–9] Therefore, ΔS_{conf} will vary for various amino acids because z is variable.

If one could make a reliable estimate of the total number of minima and of their positions with respect to the angles of rotation around the N–C^α and C^α–C′ single bonds, denoted by ϕ and ψ, respectively, it would be possible to derive a value of z for each amino acid, utilizing the conformational maps[4–6,10] which indicate the sterically accessible ranges of rotational angles; *i.e.*, one would count the number of potential minima falling into sterically allowed regions of the conformational maps (*cf.* Table IIIB of ref 4). However, the positions of the angles of rotation corresponding to potential minima for internal rotation are in doubt, and it is not even certain whether three- or sixfold potential functions of rotation[4,11,12] should be used. As an even more serious objection, it has been increasingly recognized lately that the potential functions for rotation around the N–C^α and the C^α–C′ bonds most likely have very shallow minima, of depth ≈ 1 kcal/mole or less.[13,14] With shallow minima, the polypeptide chain is not restricted to isolated rotational positions. Therefore, calculations based on eq 1 are not valid unless z is reinterpreted as a purely empirical parameter selected to give ΔS_{conf} of the required magnitude, instead of being the number of allowed positions of the residue in the polypeptide chain.

For an exact evaluation of ΔS_{conf}, one would have to perform a statistical mechanical averaging over the entire range of rotational angles (*i.e.*, the entire conformational map[4–6,10]), taking into account the energies of steric interactions, rotational potentials, and other possible interactions.

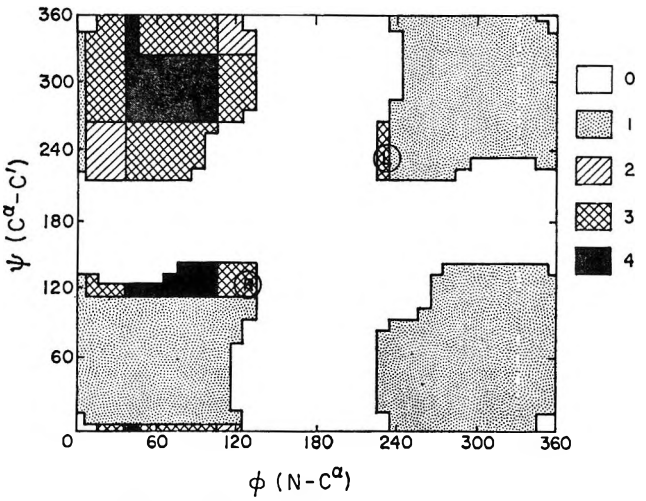

Figure 1. Allowed areas of the steric map for various dipeptides.[6,7] In area 0 no conformations are allowed. Conformations in areas 1 to 4 are allowed for glycyl glycine, in areas 2 to 4 for glycyl-L-alanine, in areas 3 to 4 for higher straight chain homologs, while only area 4 is allowed for glycyl-L-valine and glycyl-L-isoleucine. The circles marked R and L indicate the location of the right- and left-handed α-helix on the steric map.

Because of the shallowness of the rotational potential functions, it seems that steric effects are the most im-

(2) J. A. Schellman, *Compt. Rend. Trav. Lab. Carlsberg, Sér. Chim.*, **29**, 230 (1955).

(3) W. Kauzmann in "The Mechanism of Enzyme Action," W. D. McElroy and B. Glass, Ed., Johns Hopkins University Press, Baltimore, Md., 1954, p 70.

(4) G. Némethy and H. A. Scheraga, *Biopolymers*, **3**, 155 (1965).

(5) G. N. Ramachandran, C. Ramakrishnan, and V. Sasisekharan, *J. Mol. Biol.*, **7**, 95 (1963).

(6) S. J. Leach, G. Némethy, and H. A. Scheraga, *Biopolymers*, in press.

(7) A standard system of conventions for the description of polypeptide conformations has been adopted recently.[8] The standard conventions have been followed in this paper for the symbols ϕ, ψ, and χ, denoting angles of rotation, and for the arrangement of the conformational maps in Figures 1 and 3. They differ from the system used in earlier publications.[6,9]

(8) J. T. Edsall, P. J. Flory, J. C. Kendrew, A. M. Liquori, G. Némethy, G. N. Ramachandran, and H. A. Scheraga, *Biopolymers*, **4**, 130 (1966); *J. Biol. Chem.*, in press; *J. Mol. Biol.*, **15**, 339 (1966).

(9) S. J. Leach, G. Némethy, and H. A. Scheraga, unpublished data.

(10) J. A. Schellman and C. Schellman in "The Proteins," Vol. II, 2nd ed, H. Neurath, Ed., Academic Press, Inc., New York, N. Y., 1964, p 1.

(11) S.-I. Mizushima and T. Shimanouchi, *Advan. Enzymol.*, **23**, 1 (1961).

(12) L. Pauling and R. B. Corey, *Proc. Natl. Acad. Sci. U. S.*, **37**, 729 (1951).

(13) R. A. Scott and H. A. Scheraga, *J. Chem. Phys.*, **42**, 2209 (1965).

(14) D. A. Brant and P. J. Flory, *J. Am. Chem. Soc.*, **87**, 2791 (1965).

portant local factor in restricting the range of allowed conformations of a peptide residue.[15] Therefore, *as a first approximation*, the entropy of unfolding for various amino acids can be estimated from steric interactions alone. The latter require that atoms do not approach each other closer than given van der Waals contact distances. Assuming fixed van der Waals contact distances, *i.e.*, replacing the atoms by hard spheres, the ranges of sterically allowed conformations have been calculated for various amino acids.[4-6] Although the hard-sphere assumption is an approximation, the boundaries of the allowed regions correspond satisfactorily to the boundaries of favored, *i.e.*, low-energy, regions calculated with more elaborate methods.[14,16,17]

If one assumes that all conformations within the sterically allowed regions are equiprobable, the area of the allowed regions provides a measure of the conformational freedom of each residue. This assumption must also be recognized as an approximation, since interaction energies differ for various conformations in the allowed regions. However, these differences are not well established yet, since the exact shapes of the potential surfaces[14,16] are not known, due to the uncertainties of various parameters entering into their calculation. Within these limitations, the energy calculations available so far[14,16,17] seem to indicate that the potential surface inside the allowed regions is relatively flat, so that one can replace it with a uniformly flat surface as a first approximation.

If γ_Y is the allowed relative area in a conformational map[6] for the amino acid residue Y when it is part of a polypeptide chain in the random coil state (γ is normalized, *i.e.*, $\gamma = 1$ for the entire conformational map), and γ_h is the relative area in the conformational map assigned to a definite restricted conformation, such as the α-helix, the entropy of unfolding per residue is given by

$$\Delta S_{conf} = R \ln \frac{\gamma_Y}{\gamma_h} \quad (2)$$

Although a well-defined conformation is represented by a single point on the conformational map, a small, finite area γ_h must be assigned to any real conformation.[9,18]

The determination of a numerical value of γ_h for the α-helix or for other regular structures would require an analysis of the vibrational freedom of these structures. Such an elaborate analysis is beyond the scope of the present communication and, therefore, calculations are restricted to the determination of the *relative entropies* of unfolding, ΔS_{rel}, of various residues, Y, as compared with glycine, according to

$$\Delta S_{rel} = \Delta S_{conf}(Y) - \Delta S_{conf}(gly) = R \ln \frac{\gamma_Y}{\gamma_{gly}} \quad (3)$$

The values of γ_Y, determined by us earlier[6] from the allowed areas on the steric map (Figure 1), and the calculated values of ΔS_{rel} are summarized in Table I.

The values of ΔS_{rel} given in Table I apply not only to the α-helix–random coil transition, but to any transformation leading to "random coil" states from a polypeptide conformation in which the backbone has been constrained to a single choice. For this reason, ΔS_{rel} is included even for those amino acids whose polymers cannot form an α-helix,[19] *e.g.*, valine and isoleucine.

Table I: Estimates of the Backbone Contribution to the Entropy of Unfolding of Polypeptides for Various Amino Acid Residues Relative to That of Glycine (the Effects of the Side Chains Are Considered Here Only Insofar As They Affect the Freedom of the Backbone)

Amino acid Y	Side chain (carbon skeleton)	γ_Y[a]	ΔS_{rel}, eu
Glycine	...	0.52	0
Alanine[b]	C^β	0.16	−2.4
Higher straight chain homologs[c,d]	C^β–C^γ C^β–C^γ–C^δ C^β–C^γ–C^δ–C^ϵ	0.14	−2.7
Leucine	C^β–$C^\gamma<^{C^\delta}_{C^\delta}$	0.11	−3.1
Valine, isoleucine[c]	$C^\beta<^{C^\gamma(-C^\delta)}_{C^\gamma}$	0.046	−4.8
Threonine	$C^\beta<^{O^\gamma}_{C^\gamma}$	0.06	−4.3

[a] See ref 6; *cf.* Figure 1 of this paper. [b] The data for alanine also hold for aspartic acid and asparagine.[6] [c] Addition of carbon atoms beyond the C^γ atom (without branching) causes no further restriction of the freedom of rotation of the backbone.[6] [d] The data in this line also hold for glutamic acid, glutamine, and tyrosine.[6]

The presence or absence of side chains can alter the entropy of unfolding of a rigid structure (such as the

(15) Only interactions between adjacent residues are to be considered here (except in section 3). Steric interactions also can occur between nonadjacent residues. Their occurrence and their importance in proteins have been discussed elsewhere;[4] their presence does not affect significantly the conclusions reached in this section.

(16) K. D. Gibson and H. A. Scheraga, *Biopolymers*, in press.

(17) P. de Santis, E. Giglio, A. M. Liquori, and A. Ripamonti, *Nature*, **206**, 456 (1965).

(18) S. Lifson and A. Roig, *J. Chem. Phys.*, **34**, 1963 (1961).

(19) S. M. Bloom, G. D. Fasman, C. de Lozé, and E. R. Blout *J. Am. Chem. Soc.*, **84**, 458 (1962).

α-helix) by several entropy units, as shown in Table I. Although the difference between individual amino acid residues is small (except for valine and isoleucine), the effect can become an important stabilizing or destabilizing factor for polyamino acids, in which an identical contribution is made by each residue. The large value of ΔS_{conf} for glycine destabilizes any helix or other ordered structure composed entirely or largely of glycine, as compared with other amino acids. For example, this factor causes a poly-L-alanine α-helix to be more stable than a polyglycine one would be.

2. Number of Conformations Available to an Amino Acid Side Chain. The freedom of internal rotation around bonds in side chains can also change as a result of the helix–coil transition or a similar unfolding process.

In the absence of competing interactions, atoms in side chains occupy potential minima for internal rotation, located in the staggered position of the atoms.[13,20] For hydrocarbons, these minima are given by a threefold potential function.[21] However, due to steric restrictions, not all three conformations (*i.e.*, minima) are accessible to a side chain attached to a peptide residue. In contrast to the polypeptide backbone, the potential minima for hydrocarbons are well defined, with potential barriers of 3 kcal/mole or more.[13] Therefore, it is justified to consider the side chains as restricted to the positions of rotational minima, in order to illustrate the arguments presented in this section. The effect of allowing rotation of the side chain out of the potential minima will be discussed in section 3.

In analogy with eq 2, the extent of freedom of a side chain in the *unfolded* state, $\bar{y}$, can be estimated to a *first approximation* with the aid of eq 4, in which $\bar{y}$ represents the average number of positions available to the side chain and y is the number of positions available for a given backbone conformation characterized by ϕ, ψ. This number can then be used to determine ΔS_{sc}, the contribution of the side-chain conformations to the entropy of unfolding of the polypeptide, as shown in eq 5. Here y_h is the number of allowed minima in the particular *folded* state considered.

$$\bar{y} = \frac{\iint y \, d\phi d\psi}{\iint d\phi d\psi} \tag{4}$$

$$\Delta S_{sc} = R \ln \frac{\bar{y}}{y_h} \tag{5}$$

With the hard-sphere approximation, as used in section 1, the allowed regions of Figure 1 subdivide into areas in each of which y is a constant, as shown in Figures 2 and 3. If $\gamma' \equiv \iint d\phi d\psi$ is normalized to

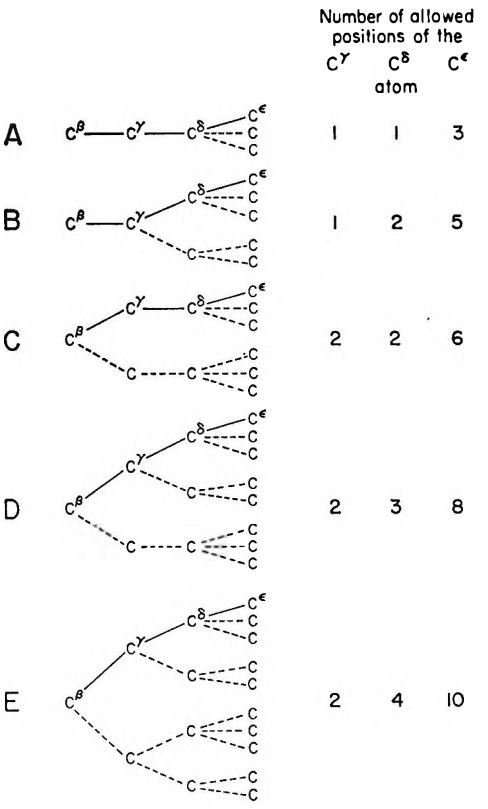

Figure 2. Schematic representation of the restriction of the freedom of rotation of an *unbranched* four-carbon side chain for various backbone conformations. In the diagrams, the dashed lines and symbols represent y, the *number of sterically allowed conformations* of the side chain, *i.e.*, the number of allowed positions of the atoms considered. The letters A to E refer to the areas marked similarly in Figure 3, and indicate where each of the sets of allowed conformations of this figure may occur.

$\gamma' = 1$ for the entire sterically allowed region (*i.e.*, for areas 3 and 4 of Figure 1 for unbranched hydrocarbon side chains), eq 4 reduces to

$$\bar{y} = \sum_i y_i \gamma_i' \tag{6}$$

where i is an index denoting the various areas into which Figure 3 is divided.

For a C^β–C^γ side chain, y is simply the number of allowed positions of the C^γ atom in each area of Figure 3. For larger side chains, y is the number of allowed conformations for the *entire* side chain, and is not obtained additively from the number of rotational minima of each bond considered separately. This qualification is necessary because the number of

(20) J. C. Kendrew, *Brookhaven Symp. Biol.*, 15, 216 (1962).

(21) Bonds next to aromatic rings possibly have six minima;[6] the S–S bond of disulfide has two minima.[4] These will not be discussed here.

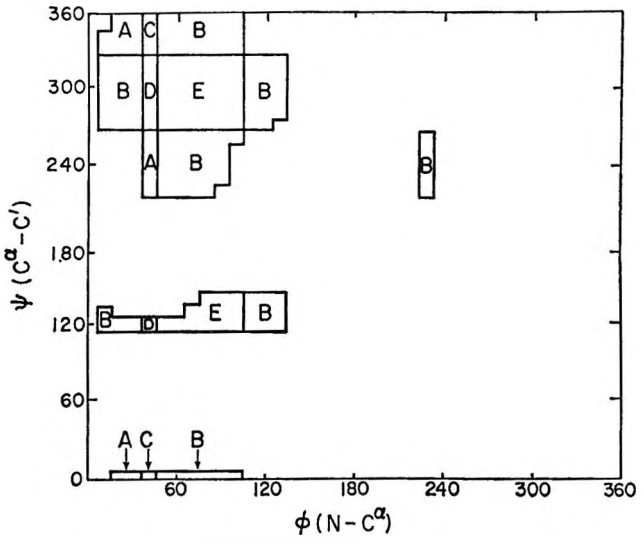

Figure 3. Steric map for a dipeptide having a C^{β}–C^{γ}–C^{δ}–C^{ϵ} side chain, with indication of the extent of freedom of rotation of the side chain bonds in the allowed area. The following code indicates y, the total number of allowed positions for the various atoms of the side chain (*cf.* Figure 2): A: 1 allowed position for C^{γ}, 1 for C^{δ}, 3 for C^{ϵ} (8%); B: 1 allowed position for C^{γ}, 2 for C^{δ}, 5 for C^{ϵ} (58%); C: 2 allowed positions for C^{γ}, 2 for C^{δ}, 6 for C^{ϵ} (2%); D: 2 allowed positions for C^{γ}, 3 for C^{δ}, 8 for C^{ϵ} (4%); E: 2 allowed positions for C^{γ} 4 for C^{δ}, 10 for C^{ϵ} (28%). The numbers in parentheses indicate $100\gamma'$, the percentage of the total allowed area for each class.

positions allowed for a given atom in the side chain depends on the conformation of the preceding part of the side chain. This is illustrated in Figure 2 which shows the allowed conformations and y values for unbranched side chains of various lengths, up to four C atoms. As an example, a comparison of areas B and C indicates why the side chain has to be treated as a single unit in determining y. In area B, C^{γ} has only one allowed position, but C^{δ} has two allowed positions so that $y = 2$ for the C^{β}–C^{γ}–C^{δ} side chain. In area C, C^{γ} has two allowed positions, but only one position of the C^{δ} atom is allowed for each of the two conformations of the C^{γ} atom, so that y is still 2, etc.

Combinations of conformations which are not listed in Figure 2 do not occur, because of steric interactions.[22] The regions of the steric map, in which the various sets of conformations of Figure 2 occur, are indicated in Figure 3. The data on which the two figures are based have been derived earlier[6] for a set of van der Waals contact distances adopted for studies of steric effects.[6,9] For another selection of contact distances, the boundaries in Figure 3 might change slightly.

The areas, given by γ' (normalized as described earlier) for each possible value of y, are shown in Table II for each of the unbranched hydrocarbon side chains having two to four carbon atoms, together with the values of $\bar{y}$ and ΔS_{sc}, calculated from eq 5 and 6. The table also indicates the extent to which the conformational freedom of the side chain is reduced by the steric effects of the adjacent backbone; in the absence of steric interactions, the number of conformations of a side chain having n bond rotations would be 3^n, *i.e.*, 3, 9, and 27 for the three side chains discussed, while the highest possible actual values of y in Table II are 2, 4, and 10. The calculations are also valid for side chains in which heteroatoms (O, N, or S) occur. In some cases, the values of γ' for some of the areas might change because of differences in the van der Waals radii of the atoms. However, it has been shown[6] that steric maps for such side chains are nearly identical with those for hydrocarbon side chains. Therefore, the numbers in Table II would be altered only slightly.

Because the C^{γ} atom is restricted to a single rotational position of the side chain in the α-helical conformation, but is less restricted in the random coil, its presence makes a *positive* contribution to the entropy of unfolding, amounting to $\Delta S_{sc} = 0.58$ eu. In longer side chains, the *average* number of allowed positions of the C^{δ} and C^{ϵ} atoms per allowed position of the C^{γ} atom in the random coil is nearly the same as the number of their allowed positions in the α-helix. Therefore, their additional contribution to ΔS_{sc} for the α-helix-to-random coil transition is nearly zero.

If the transition to the random coil takes place from a restricted conformation in which the side chain has much freedom of rotation (such as pleated sheet structures, β-keratin, etc., which lie in areas D and E, respectively, of Figure 3), transformation into a random coil may actually *decrease* the *average* number of allowed conformations of the side chain, resulting in a *negative* entropy contribution. This effect would contribute to the stabilization of a pleated sheet over the random coil for polyamino acids having long unbranched side chains. However, this conclusion holds only for residues in the pleated sheet conformation in the absence of nonlocal steric interactions. As was pointed out to us by one of the referees of this paper, the freedom of rotation of side chains may be restricted severely in pleated sheet structures in which the interlocking of side chains in adjacent layers acts as a constraint. Even in single pleated sheets, there are close contacts

(22) Since we are interested here only in the number of allowed conformations of the side chains and not in the actual positions of the allowed minima, we do not distinguish in Figure 3 between areas in both of which, say, the C^{γ} atom has one allowed minimum, but for which the spatial orientation of the atom in the minima is different.

Table II: Estimates of the Contribution of Side Chains to the Entropy of Unfolding of Polypeptides for Unbranched Side Chains of Various Lengths

Side chain	y_h for the α-helix[a]	Fraction of allowed area,[b] γ', where y side-chain conformations are allowed[c]					$\bar{y}$[d]	ΔS_{sc},[e] eu
C^γ	1	y	1	2				
		γ'	0.66	0.34			1.34	0.58[f]
C^γ–C^δ	2	y	1	2	3	4		
		γ'	0.08	0.60	0.04	0.28	2.52	0.44
C^γ–C^δ–C^ϵ	5	y	3	5	6	8	10	
		γ'	0.08	0.58	0.02	0.04	0.28	6.39	0.47

[a] As seen from Figure 3 where both the right- and the left-handed α-helix fall into an area labeled B (*cf.* Figure 1). [b] Normalized to the sterically allowed region for residues with unbranched hydrocarbon side chain; *i.e.*, $\gamma' = 1$ for areas 3 + 4 in Figure 1. [c] See Figures 2 and 3 for the construction of this column. [d] Calculated from data in the previous column, using eq 6. [e] Calculated from data in the previous column, using eq 5. [f] However, for unfolding into the "random coil" from a folded structure in which $y_h = 2$ (*e.g.*, from the pleated sheet), $\Delta S_{sc} = -0.79$ eu.

between side chains in adjacent polypeptide chains[23] which, besides allowing the formation of hydrophobic bonds,[23] restrict the freedom of rotation of the side chains. For these reasons, this effect may not appear in the layered pleated sheet structures, and ΔS_{sc} may be the same as calculated for the α-helix.

The arguments of the preceding paragraphs and the estimations of ΔS_{sc} are all based on the assumption that the allowed areas of the steric maps are all equivalent, *i.e.*, that all allowed values of ϕ and ψ are equally probable for the random coil. Actually, the probability of occupancy of various ϕ, ψ points on the conformational map is not uniform, depending on the details of the conformational free energy, invalidating eq 6 in a higher approximation. Already, the side-chain effect discussed in this section in itself would change the probability distribution over the conformational map; the larger freedom of the side chains in areas D and E of Figure 3 causes a preference for these conformations over those lying in areas A, B, or C. This would increase ΔS_{sc} but decrease ΔS_{conf} slightly due to the change from uniform probability distribution over the entire area. For this reason, it is not strictly proper to treat the two contributions to the entropy separately, since they are interdependent and ought to be determined in a single, combined calculation. However, in the present study, it was worthwhile to separate them to point out the origin and the relative importance of the two effects.

In this section, only the effect of the backbone atoms in a *dipeptide* upon the freedom of rotation of the side chain has been considered.[6] In a long helical polyamino acid, *i.e.*, in the presence of more than a complete turn of a helix, some side chains are even more severely restricted in their freedom of rotation[4] because of the presence of the next turn of the helix.[9] Such additional restrictions can make the value of ΔS_{sc} slightly more positive than shown here.

3. Energy Requirement for α-Helix Formation in the Presence of Bulky Side Chains. Poly-L-valine and poly-L-isoleucine cannot form an α-helix because of steric hindrance, as shown both by experiment[19] and by theory.[6] On the other hand, several isolated valyl and isoleucyl residues occur within α-helical regions in myoglobin.[20] A valyl or isoleucyl residue can be placed in a conformation corresponding to the α-helix if the side chain is rotated out of a position for a rotational minimum around the C^α–C^β bond. The energy required to do this appears as a positive ΔH contribution to the free energy of formation of the helix.[24] In helical sequences, such as those in myoglobin, an occasional valyl or isoleucyl residue can be accommodated because the unfavorable enthalpy is compensated by the over-all free energy of stabilization of the α-helix. However, in poly-L-valine or poly-L-isoleucine, each residue would contribute this positive ΔH to the free energy of formation of the α-helix; this apparently is sufficient to render the formation of the helix thermodynamically unfavorable.

By using the methods developed for the calculation of steric interactions in peptides,[4,6] we have found[9] that a rotation away from a potential minimum

(23) G. Némethy and H. A. Scheraga, *J. Phys. Chem.*, 66, 1773 (1962).

(24) An equivalent description would be that some atoms must approach each other to a distance less than the normal van der Waals contact distance, which also would result in a positive ΔH contribution. The actual value of ΔH is a combination of the two effects, *i.e.*, of some rotation and some close approaches such that the over-all unfavorable free energy change for the two distortions is minimized.

around the C^{α}–C^{β} bond by about 15° is sufficient to allow the formation of either a left- or right-handed α helix (keeping the van der Waals contact distances constant).[25] Assuming that the rotation can be described by a sinusoidal potential function having three minima, the energy required for this rotation can be estimated using

$$U_{rot} = (1/2)U_0(1 + \cos 3\chi) \quad (7)$$

Very little information is available about the value of U_0 appropriate in this case. Volkenstein[26] quotes an estimate of 5.2 kcal/mole for the height of the barrier nearest to the lowest minimum for rotation around the central C–C bond in 1,1,2,2-tetramethylethane, the closest analog of the bond considered here. This value was substituted[27] in eq 7, giving $\Delta H = 0.76$ kcal/mole. Although this is not a large quantity, it is apparently sufficient to disrupt the poly-L-valine α-helix. Therefore, one can conclude that the intrinsic stability of the α-helix is less than 0.76 kcal/mole per residue, under the conditions of the experimental studies.[19]

Conclusions

Specific steric effects due to the presence of various side chains can affect the stability of helices or other folded polypeptide structures. The effects influence both the entropy and the enthalpy of unfolding, and can alter the free energy of unfolding by 0 to 2 kcal/mole per residue. These effects are particularly important for polyamino acids where they should be taken into account in comparative studies of conformational stabilities. The effects may be less important in polypeptides of mixed amino acid composition, but even there, minor changes in the amino acid composition may result in the stabilization or destabilization of ordered structures of marginal thermodynamic stability.

(25) In contrast to the calculations presented in sections 1 and 2, the estimates discussed in this section refer not to a dipeptide but to a side chain present on a completed turn of the helix.

(26) M. V. Volkenstein, "Configurational Statistics of Polymeric Chains," Interscience Publishers Inc., New York, N. Y., 1963, p 108.

(27) Since the substituents on the two C atoms are not identical, a pure sinusoidal potential function is no longer strictly applicable. Because we are considering here small deviations from the minimum, it was felt that the use of eq 7 is a good approximation.

A Kinetic Study of Vanadate Polymerization in Aqueous Solution[1]

by M. P. Whittaker,[2] J. Asay,[3] and E. M. Eyring

Department of Chemistry, University of Utah, Salt Lake City, Utah *(Received July 15, 1965)*

Temperature-jump relaxation times have been observed in basic aqueous solutions of Na_3VO_4 and have been attributed to the equilibria

$$(VO_2)(OH)_2^- + (VO_2)(OH)_3^{2-} \underset{}{\overset{k_D}{\rightleftharpoons}} (VO_2)_2(OH)_5^{3-}$$

and

$$(VO_2)(OH)_3^{2-} + (VO_2)_2(OH)_5^{3-} \overset{k_T}{\rightleftharpoons} (VO_2)_3(OH)_6^{3-} + 2OH^-$$

The values for the rate constants at 25° in 0.5 M ionic strength aqueous solution were found to be $k_D = 3.1 \times 10^4\ M^{-1}\ sec^{-1}$ for the dimerization and $k_T = 5 \times 10^2\ M^{-1}\ sec^{-1}$ for the formation of the trimeric species.

While the polyanions of vanadium (V) are well known, there is little information available regarding their rate of formation. In fact, the rate of formation of the low molecular weight polyanions has been described as being "immeasurably fast."[4] This suggests that a relaxation-rate study of these polyanion equilibria similar to one previously undertaken with the polyborate system[5] should prove interesting.

Stability constants of the species present in basic aqueous solutions of sodium vanadate, Na_3VO_4, have been reported by Ingri, Brito, and Sillén.[6,7] The choice of species made by these authors in dilute solutions has been confirmed recently by Howarth and Richards.[8] At 25° and 0.5 M ionic strength these are given by eq 1–3, where, for example $\beta_1 = [VO_2(OH)_2^-][OH^-][VO_2(OH)_3^{2-}]^{-1}$. The relative importance of the concentrations of the various vanadate species over the 7.5 to 10.0 pH range is depicted in Figure 1.

$$VO_2(OH)_3^{2-} \rightleftharpoons VO_2(OH)_2^- + OH^- \qquad (\log \beta_1 = -6.0 \pm 0.1) \quad (1)$$

$$2VO_2(OH)_3^{2-} \rightleftharpoons (VO_2)_2(OH)_5^{3-} + OH^- \qquad (\log \beta_2 = -3.18 \pm 0.05) \quad (2)$$

$$3VO_2(OH)_3^{2-} \rightleftharpoons (VO_2)_3(OH)_6^{3-} + 3OH^- \qquad (\log \beta_3 = -10.42 \pm 0.04) \quad (3)$$

Experimental Section

A vanadate stock solution was prepared by dissolving Matheson Coleman and Bell purified sodium vanadate in distilled water. The concentration of the stock solution was determined by reducing the V^{5+} to V^{4+} by bubbling SO_2 through the solution and titrating the resulting V^{4+} back to V^{5+} with a standard permanganate solution.[9] The resulting colorless solution was very basic and upon acidification turned a light yellow-orange which faded over a period of days. The yellow color has been attributed to the formation of decavanadic acid.[10–12] All solutions were allowed

(1) Work supported in part by the National Institute of Arthritis and Metabolic Diseases, Grant AM-06231, and by the University of Utah research fund.

(2) This is an essential portion of a thesis submitted to the Chemistry Department, University of Utah, in partial fulfillment of the requirements of a Doctor of Philosophy Degree.

(3) National Science Foundation undergraduate research participant.

(4) H. Remy, "Treatise on Inorganic Chemistry," Part II, Elsevier Publishing Co., New York, N. Y., 1956, p 100.

(5) J. L. Anderson, E. M. Eyring, and M. P. Whittaker, *J. Phys. Chem.*, **68**, 1125 (1964).

(6) N. Ingri and F. Brito, *Acta Chem. Scand.*, **13**, 1971 (1959).

(7) F. Brito, N. Ingri, and L. G. Sillén, *ibid.*, **18**, 1557 (1964).

(8) O. W. Howarth and R. E. Richards, *J. Chem. Soc.*, 864 (1965).

(9) I. M. Kolthoff and P. J. Elvings, "Treatise on Analytical Chemistry," Vol. 8, Part II, Interscience Publishers, Inc., New York, N. Y., pp 223, 224.

(10) K. F. Jahr, L. Schoepp, and J. Fuchs, *Z. Naturforsch.*, **14b**, 469 (1959).

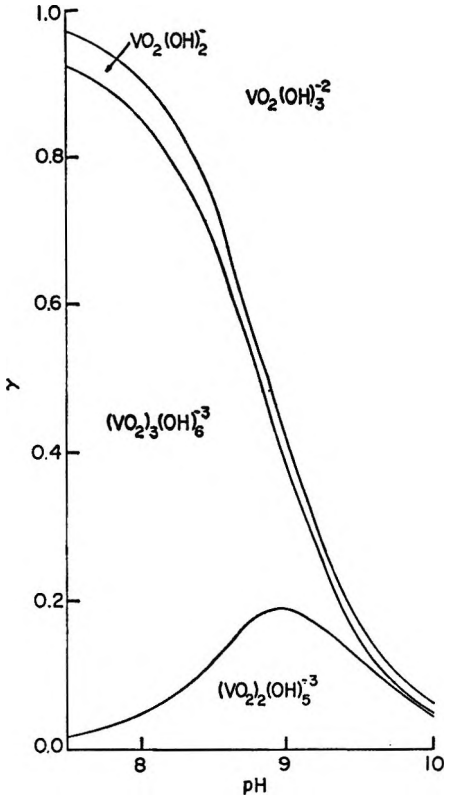

Figure 1. Distribution of vanadium between different ions in 0.5 *M* ionic strength medium (adjusted with NaCl) when total Na_3VO_4 concentration C_0 = 0.008 *M* at 25° calculated from the equilibrium constants of Ingri and Brito. At a given pH, the fraction of vanadium, γ, present as a given ion is represented by the length of a vertical line segment falling between curves.

to stand for 3 days after the yellow color had completely faded to ensure that this slow reaction had gone to completion. The pH of the sample solution was adjusted with Wasco reagent grade NaOH and measured with a Radiometer TTT-1 titrimeter. The ionic strength, μ, of each sample was made 0.5 *M* by addition of Wasco reagent grade sodium chloride. A single-beam temperature-jump apparatus of the type described by Hammes and Steinfeld[13] was used to perturb the vanadate equilibria. A temperature jump of ~10° (*i.e.*, from 15 to ~25°) was effected. The relaxation times were obtained from the photographed exponential oscilloscope traces by looking for linearity in semilogarithmic plots of vertical deflection, *i.e.*, relative light absorbance, *vs.* time. Since the mono-, di-, and tripolyvanadates are colorless, an acid–base indicator, either phenolphthalein or *o*-cresol red depending upon the pH of the solution, was coupled with the vanadate equilibria. The analyzing wavelength of light directed through the sample cell was 552 mμ for the experiments using phenolphthalein and 560 mμ when *o*-cresol red was used. A single relaxation time, in the 10-μsec to 0.1-sec time range accessible to our apparatus, was observed for solutions having a pH in the range 7.5 to 9.0. Two closely spaced relaxation times were observed for solutions having a pH of 9.5 or 10.0.

Calculations

The following simple, though not necessarily unique, mechanism is consistent with the known equilibrium constants and our kinetic data.

$$A \underset{k_{-1}}{\overset{k_1}{\rightleftharpoons}} HA + OH$$

$$K_1 = \frac{(HA)(OH)}{A} = 1 \times 10^{-6} \quad (4)$$

$$A + HA \underset{k_{-2}}{\overset{k_2}{\rightleftharpoons}} B$$

$$K_2 = \frac{B}{A(HA)} = 6.61 \times 10^2 \quad (5)$$

$$A + B \underset{k_{-3}}{\overset{k_3}{\rightleftharpoons}} C + 2OH$$

$$K_3 = \frac{C(OH)^2}{(A)(B)} = 5.75 \times 10^{-8} \quad (6)$$

$$HIn + OH \underset{k_{-4}}{\overset{k_4}{\rightleftharpoons}} In$$

$$K_4 = \frac{In}{(HIn)(OH)} = 2.5 \times 10^4, 3.2 \times 10^5 \quad (7)$$

where OH $\equiv$ OH^-, A $\equiv$ $VO_2(OH)_3^{2-}$, HA $\equiv$ $VO_2(OH)_2^-$, B $\equiv$ $(VO_2)_2(OH)_5^{3-}$, C $\equiv$ $(VO_2)_3(OH)_6^{3-}$, HIn and In represent the two forms of the acid–base indicator, and K_4 = 2.5 × 10^4 for phenolphthalein and 3.2 × 10^5 for *o*-cresol red. Italicized symbols indicate concentration.

Reactions involving only the addition or removal of a proton or hydroxide ion are known to be very fast.[14] Therefore, making the safe assumption that the relaxation times of the first and fourth equilibria are both much shorter than those of the second and third, we write eq 8 and 9. Now, upon making the substitution

(11) R. P. Mitra and A. K. Banerjee, *J. Sci. Ind. Res.* (India), **B20**, 129 (1961).

(12) F. J. Rossotti and H. S. Rossotti, *Acta Chem. Scand.*, **10**, 957 (1956).

(13) G. G. Hammes and J. I. Steinfeld, *J. Am. Chem. Soc.*, **84**, 4639 (1962).

(14) H. Diebler and M. Eigen, *Z. Physik. Chem.* (Frankfurt), **20**, 299 (1959).

$$\frac{dB}{dt} = k_2A(HA) + k_{-3}C(OH)^2 - k_{-2}B - k_3(AB) \quad (8)$$

$$\frac{dC}{dt} = k_3(AB) - k_{-3}C(OH)^2 \quad (9)$$

$B = \bar{B} + \Delta B$, etc., and noting that

$$\frac{d(\bar{B} + \Delta B)}{dt} = \frac{d\Delta B}{dt} \quad (10)$$

$$\frac{d\bar{B}}{dt} = 0 =$$

$$k_2\bar{A}(\overline{HA}) + k_{-3}\bar{C}(\overline{OH})^2 - k_{-2}\bar{B} - k_3(\bar{A})(\bar{B}) \quad (11)$$

and $\Delta A\,\Delta(HA) \sim 0$, etc., we obtain

$$\frac{d\Delta B}{dt} = (k_2\overline{HA} - k_3\bar{B})\Delta A + k_2\bar{A}\Delta HA + 2k_{-3}(\overline{OH})\bar{C}\Delta OH + k_{-3}(\overline{OH})^2\Delta C - (k_{-2} + k_3\bar{A})\Delta B \quad (12)$$

Arguing similarly, eq 9 becomes

$$\frac{d\Delta C}{dt} = k_3\bar{B}\Delta A + k_3\bar{A}\Delta B - 2k_{-3}(\overline{OH})\bar{C}\Delta OH - k_{-3}(\overline{OH})^2\Delta C \quad (13)$$

The conservation relations are

$$\Delta A + \Delta HA + 2\Delta B + 3\Delta C = 0 \quad (14)$$

$$3\Delta A + 2\Delta HA + 5\Delta B + 6\Delta C + \Delta OH + \Delta In = 0 \quad (15)$$

$$\Delta HIn = -\Delta In \quad (16)$$

$$K_1\Delta A = \overline{HA}\Delta OH + \overline{OH}\Delta HA \quad (17)$$

$$K_4\overline{OH}\Delta HIn + K_4\overline{HIn}\Delta OH = \Delta In \quad (18)$$

Considerable simplification of our subsequent notation can be achieved by introducing the functions α and β.

$$\alpha = \frac{K_4\overline{HIn}}{1 + K_4\overline{OH}} \quad (19)$$

$$\beta = \frac{\overline{HA}}{\overline{OH}} + (1 + \alpha)\left(1 + \frac{K_1}{\overline{OH}}\right) \quad (20)$$

We then have

$$\Delta A = -\frac{1}{\beta}\left[\frac{\overline{HA}}{\overline{OH}} + 2(1 + \alpha)\right]\Delta B - \frac{1}{\beta}[3(1 + \alpha)]\Delta C \quad (21)$$

$$\Delta OH = \left(1 - \frac{K_1}{\overline{OH}}\right)\left(\frac{1}{\beta}\right)\Delta B + \frac{3}{\beta}\Delta C \quad (22)$$

$$\Delta HA = -\frac{1}{\beta}\left[\frac{\overline{HA}}{\overline{OH}} + \frac{2K_1}{\overline{OH}}(1 + \alpha)\right]\Delta B + \frac{3(1 + \alpha - \beta)}{\beta}\Delta C \quad (23)$$

Substituting eq 21, 22, and 23 in (12) and (13), we obtain

$$\frac{d\Delta B}{dt} = \left(k_2\left\{-\frac{\overline{HA}}{\beta}\left[\frac{\overline{HA}}{\overline{OH}^2} + 4(1 + \alpha) + \frac{\overline{HA}}{K_1} + \beta\frac{\bar{A}}{\bar{B}}\right]\right\} + k_3\left\{\frac{1}{\beta}\left[\bar{B}\left(\frac{\overline{HA}}{\overline{OH}} + 2(1 + \alpha)\right) + \frac{2}{K_3}\bar{C}(\overline{OH} - K_1) - \beta\bar{A}\right]\right\}\right)\Delta B + \left(k_2\left\{\frac{1}{\beta}[-3(1 + \alpha)\overline{HA} + 3(1 + \alpha - \beta)\bar{A}]\right\} + k_3\left\{\frac{1}{\beta}\left[3(1 + \alpha)\bar{B} + \frac{\overline{OH}}{K_3}(6\bar{C} + \beta\overline{OH})\right]\right\}\right)\Delta C \quad (24)$$

$$\frac{d\Delta C}{dt} = k_3\left\{-\frac{1}{\beta}\left[\bar{B}\left(\frac{\overline{HA}}{\overline{OH}} + 2(1 + \alpha)\right) + \frac{2\bar{C}}{K_3}(\overline{OH} - K_1) - \beta\bar{A}\right]\right\}\Delta B + k_3\left\{-\frac{1}{\beta}\left[3(1 + \alpha)\bar{B} + \frac{\overline{OH}}{K_3}(6\bar{C} + \beta\overline{OH})\right]\right\}\Delta C \quad (25)$$

Rewriting eq 24 and 25 in terms of $X_1 \equiv \Delta B$ and $X_2 \equiv \Delta C$, we have

$$\dot{X}_1 = Y_{11}X_1 + Y_{12}X_2 \quad (26)$$

and

$$\dot{X}_2 = Y_{21}X_1 + Y_{22}X_2 \quad (27)$$

Making the substitutions

$$X_1 = a_{11}e^{-\lambda_1 t} + a_{12}e^{-\lambda_2 t} \quad (28)$$

and

$$X_2 = a_{21}e^{-\lambda_1 t} + a_{22}e^{-\lambda_2 t} \quad (29)$$

we obtain two identical secular equations either of which leads to the quadratic formula

$$\frac{1}{\tau_{1,2}} = -\frac{Y_{11} + Y_{22}}{2}\left\{1 \mp \sqrt{1 - \frac{4(Y_{11}Y_{22} - Y_{12}Y_{21})}{(Y_{11} + Y_{22})^2}}\right\} \quad (30)$$

where τ_1 and τ_2 are relaxation times.

Results and Discussion

Making use of experimentally determined relaxation times, eq 30 was solved on an IBM 7044 computer for the corresponding values of k_2 and k_3. The results in

Table I indicate no significant pH dependence of k_2. As illustrated in Table II, good agreement between experimental and theoretical relaxation times is obtained at several concentrations covering a range of pH values using $k_2 = 3.1 \times 10^4\ M^{-1}\ \text{sec}^{-1}$ and $k_3 = 5 \times 10^2 M^{-1}\ \text{sec}^{-1}$.

Table I: Average Rate Constants Calculated from Experimental Relaxation Times and Eq 30 for Vanadate Polymerization as a Function of pH

pH	$10^{-4}k_2$, M^{-1} sec^{-1}	$10^{-2}k_3$, M^{-1} sec^{-1}
7.5	3.1	...
8.0	3.4	...
8.5	3.1	...
9.0	3.1	...
9.5	2.9	5
10.0	2.7	5

Table II: Comparison of Theoretical and Experimental Relaxation Times with the Former Calculated Using $k_2 = 3.1 \times 10^4$ and $k_3 = 5 \times 10^2$

pH	C_0, M	τ_2, msec Obsd	τ_2, msec Calcd	τ_3, msec Obsd	τ_3, msec Calcd
10.0	0.02	1.6	1.9	7.1	5.9
10.0	0.01	2.2	2.8	10.0	9.3
10.0	0.008	3.0	2.9	11.5	11.2
10.0	0.006	3.5	3.0	15.0	13.7
10.0	0.004	3.5	3.0	17.0	16.7
9.5	0.01	3.3	3.7	~20	18.8
9.5	0.008	6.1	4.8	~20	20.1
9.0	0.02	3.0	2.9	...	30.3
9.0	0.01	5.1	4.3	...	47.1
9.0	0.008	4.7	4.9	...	52.0
9.0	0.006	5.3	5.8	...	63.1
8.5	0.02	5.3	6.2	...	90.2
8.5	0.01	6.4	6.2	...	157.0
8.5	0.008	7.6	8.1	...	156.0
8.5	0.006	8.8	8.3	...	189.0
8.5	0.004	12.0	10.0	...	255.0
8.0	0.02	10.2	9.7	...	567.0
8.0	0.01	10.3	11.6	...	700.0
8.0	0.008	10.5	12.2	...	818.0
8.0	0.006	11.0	12.8	...	992.0
7.5	0.01	14.8	14.6	...	5360
7.5	0.008	15.6	14.9	...	6190
7.5	0.006	16.0	15.4	...	7510
7.5	0.004	14.6	16.0	...	8370

The experimental fact that two relaxation times can be observed only at pH 9.5 and 10.0 can easily be explained by noting the theoretical values for τ_3 listed in the last column of Table II. These predicted relaxation times for pH values less than 9.5 are too long to be measured reliably with our temperature-jump apparatus.

The conclusion reported earlier[15] that the over-all rate constants for dimerization of uranyl ion ($k_2 = 116\ M^{-1}\ \text{sec}^{-1}$) and for the dimerization of vanadate ion are similar was based on preliminary vanadate kinetic data and is now clearly seen to be incorrect. The difference is more than two powers of ten. In fact, the dimerization of vanadate is markedly faster than that of either uranyl or chromate ion ($1.8\ M^{-1}\ \text{sec}^{-1}$).[16] It would be interesting to compare the values of the activation parameters ΔH^* and ΔS^* for the vanadate dimerization with those for uranyl dimerization

$$2UO_2^{2+} + 2H_2O \underset{}{\overset{k_2}{\rightleftharpoons}} (UO_2)_2(OH)_2^{2+} + 2H^+ \quad (31)$$

which we have recently determined[17] to be $\Delta H^* \cong +17$ kcal/mole and $\Delta S^* \cong +7$ cal/mole deg in 0.5 M ionic strength aqueous solution (from $k_2 = 32.2\ M^{-1}\ \text{sec}^{-1}$ at 15° and $k_2 = 116\ M^{-1}\ \text{sec}^{-1}$ at 25° and the equilibrium data of Baes and Meyer[18]). Such a comparison will not be possible until the temperature dependence of the equilibrium constants of the vanadate system is reported.

We should note too, in passing, that although the uranyl perchlorate equilibrium data of Rush and Johnson[19] ruled out our use[15] of this uranyl dimerization reaction, eq 32 yields[17] $k_2' = 6.4 \times 10^4\ M^{-1}\ \text{sec}^{-1}$ at

$$UO_2^{2+} + UO_2OH^+ + H_2O \underset{}{\overset{k_2'}{\rightleftharpoons}} (UO_2)_2(OH)_2^{2+} + H^+ \quad (32)$$

25° very much like that reported above for vanadate dimerization. Since eq 32 more closely resembles the presently proposed vanadate dimerization reaction 5 than does (31), the possibility of a common rate-determining step such as the removal of a coordinated water molecule in such dimerizations remains a matter of conjecture.

Acknowledgment. The authors wish to thank John L. Haslam for his help in preparing the computer program.

(15) M. P. Whittaker, E. M. Eyring, and E. Dibble, *J. Phys. Chem.*, **69**, 2319 (1965).

(16) J. N. Swinehart and G. W. Castellan, *Inorg. Chem.*, **3**, 278 (1964).

(17) M. P. Whittaker, Doctoral Dissertation, University of Utah, 1966.

(18) C. F. Baes, Jr., and N. J. Meyer, *Inorg. Chem.*, **1**, 378 (1962).

(19) R. M. Rush and J. S. Johnson, *J. Phys. Chem.*, **67**, 821 (1963).

Adsorption Isotherms and Heats of Adsorption by Frontal Analysis Chromatography

by R. A. Beebe, P. L. Evans, T. C. W. Kleinsteuber, and L. W. Richards

Department of Chemistry, Amherst College, Amherst, Massachusetts 01002 (*Received July 15, 1965*)

Adsorption isotherms down to low coverages have been determined by frontal analysis chromatography for systems containing the carrier gas, one of the gases N_2, Ar, O_2, CO, or C_2F_6, and either carbon black or bone mineral. Isosteric heats of adsorption q_{st} have been calculated from these isotherms. The same systems have been studied previously by the pulse method in this laboratory and thus the q_{st} from the two methods can be compared. It is found that the pulse method gives values of q_{st} which are too low for Type II isotherms and too high for Type III isotherms, and an equation is derived which explains these results. The pulse method should give correct results for linear isotherms. The frontal analysis data were taken in such a way that lack of instantaneous equilibrium or temperature fluctuations of moderate duration at the adsorbate front, or a strongly nonlinear isotherm, would not introduce errors into the results.

Introduction

Gas–solid chromatography has been used by a considerable number of investigators as a means of determining heats of adsorption. In much of the work the pulse technique has been employed. Gale and Beebe[1] applied this method to several gas–solid systems for which calorimetric data on the heats of adsorption were available from previous work in this laboratory. These authors, as well as others, have discussed some of the approximations which are necessary in using the method. A number of pertinent journal references to the pulse technique, for gas–solid systems, are given in the above publication; additional references are included here.[2-6] A considerable body of work leading to heats of solution has been done for gas–liquid systems. Typical references are given here.[7,8]

Because of the shortcomings of the pulse technique, especially for those systems in which the isotherm fails to obey Henry's law at low coverage, it is important to survey the advantages of the frontal analysis method of chromatography. Pertinent references for this latter method are cited herein.[9-11]

In the present work, we have applied the frontal analysis method to some of the same gas–solid systems previously studied by Gale and Beebe using the pulse method. It then becomes possible to compare the heats of adsorption obtained from both chromatographic techniques as well as from calorimetry for the same adsorption systems.

In the frontal analysis method we obtain the adsorption isotherms at low coverage at several temperatures and from these data we calculate the heats of adsorption by means of the Clapeyron–Clausius relationship. Furthermore, a knowledge of the isotherms is useful in assessing the applicability of the pulse method because linearity of the isotherm is a major necessary condition

(1) R. L. Gale and R. A. Beebe, *J. Phys. Chem.*, **68**, 555 (1964).

(2) H. W. Habgood, *Ann. Rev. Phys. Chem.*, **13**, 259 (1962). See ref 118–130 and 162 and the text accompanying them.

(3) G. C. Chirnside and C. G. Pope, *J. Phys. Chem.*, **68**, 2377 (1964).

(4) R. D. Oldenkamp and G. Houghton, *ibid.*, **67**, 597 (1963).

(5) A. V. Kiselev, E. A. Paskonova, R. S. Petrova, and K. D. Shcherbakova, *Zh. Fiz. Khim.*, **38**, 161 (1964).

(6) H. Knozinger and H. Spannheimer, *J. Chromatog.*, **16**, 1 (1964).

(7) D. H. Everett and C. T. H. Stoddart, *Trans. Faraday Soc.*, **57**, 746 (1961).

(8) D. L. Peterson and F. Helfferich, *J. Phys. Chem.*, **69**, 1283 (1965).

(9) S. J. Gregg and R. Stock in "Gas Chromatography 1958," D. H. Desty, Ed., Butterworth and Co. Ltd., London, 1958, pp 90–98.

(10) P. E. Eberly, Jr., *J. Phys. Chem.*, **65**, 1261 (1961).

(11) H. G. Lutrick, K. C. Williams, and R. W. Maatman, *J. Chem. Educ.*, **41**, 93 (1964).

in deriving the heats of adsorption by the pulse technique.

In the present paper, we include a derivation of a modification of eq 4 to fit those cases in which the isotherms deviate from linearity. This modified equation should tell us the direction in which the heat of adsorption by the pulse method in nonlinear systems may be expected to deviate from the more accurate data of the frontal analysis method.

Experimental Section

Procedure. There are two somewhat different procedures which have been used for obtaining adsorption isotherms from frontal analysis chromatography. One of these, which can only be used when the adsorbate front or the elution tail is not sharp, involves the quantitative measurement of the shape of the front or tail. It is then feasible to calculate a portion of the adsorption isotherm from a single chromatographic experiment.[9,10] The other procedure, which is used when the adsorbate front is relatively sharp, is to measure the retention time of the front and then calculate the corresponding point on the isotherm. The first of these methods is clearly dependent on the assumption that equilibrium is approached rapidly and that there are no important temperature changes in the adsorption or desorption processes. Unless special care is exercised, the second method may be dependent on these assumptions though perhaps to a lesser degree.[12] It is possible to take a point of view which renders such assumptions unnecessary and this is described in the following paragraphs.

In the frontal analysis method which we used, carrier gas is passed through the column until a steady state is reached. Then a steady flow of adsorbate is introduced into the carrier, and since the flow rates are known, it is possible to calculate how much adsorbate is carried into the column in any time interval. Similarly, if the concentration of the adsorbate in the gas coming out of the column is measured as a function of time, the measured total flow rate can be used to calculate the amount of adsorbate which comes out of the column in any time interval. The amount of adsorbate remaining in the column is then the difference between these results.

By doing a similar experiment with a nonadsorbed gas, it is possible to determine how much of the adsorbate in the column is in the gas phase. Then a subtraction gives the amount which is adsorbed on the solid surface. Since in the steady state the partial pressure of the adsorbate over the column is known, these experiments serve to determine a point on the isotherm.

If these measurements are begun when the adsorbate flow is started and *continued until the column reaches a steady state,* then the details of the processes by which the steady state is achieved are of no concern. Temperature fluctuations attending the passage of the adsorbate front through the column, a slow approach to equilibrium, a strongly nonlinear isotherm, or channeling, eddies, and diffusion in the gas flow can only serve to change the length of time required to reach the steady state. They cannot change the properties of this steady state. Therefore, in principle it is possible to determine points on adsorption isotherms by gas chromatography without making any assumptions about the importance of these effects.

In practice, the detectors for measuring the concentration of adsorbate flowing out of the column are susceptible to drift, so there is a limit to the slowness with which the adsorbate concentration can change in the final approach to the steady state. However, in the work reported here the steady state was approached sufficiently rapidly that recorder drift was not a problem.

For the adsorbate pressure we used the average of the partial pressure at the entrance of the column P_i and at the exit P_o. In the case of a linear isotherm this can be shown to be a very good approximation even when the pressure drop down the column is large. With the aid of the expression of James and Martin[13] for the pressure at any point in the column, an integration can be carried out to calculate the total amount of adsorbate in the column at the steady state. The result is that a uniform pressure P as given by

$$P = {}^2/_3 P_o \frac{P_i^3/P_o^3 - 1}{P_i^2/P_o^2 - 1} \approx \frac{P_i + P_o}{2} \qquad (1)$$

(which is also the familiar pressure correction to the retention time) will cause the same amount to be adsorbed in the steady state, and therefore is the correct pressure to use in the calculations.

Materials. In the present work we have chosen three adsorbents as column materials; the one, bone mineral (Ossar-500°), typefies a strongly polarizing surface, and the others (Graphon and Sterling MT-G) have nonpolarizing surfaces. These materials have been described in earlier publications from this laboratory.[1,14] The bone mineral (Ossar-500°) was in all cases degassed in the column in a stream of dry helium at 500° before use. The degassing temperature was not at all critical in the case of the carbon adsorbents; the temperature

(12) A. I. M. Keulemans, "Gas Chromatography," 2nd ed, Reinhold Publishing Corp., New York, N. Y., 1959, p 206.

(13) A. T. James and A. J. P. Martin, *Biochem. J.*, **50**, 679 (1952).

(14) J. M. Holmes, D. H. Davies, W. J. Meath, and R. A. Beebe, *Biochemistry*, **3**, 2019 (1964).

used here was approximately 200°. The columns were those which had actually been employed in the earlier work by the pulse method.[1]

The helium carrier gas was purified by passage through a system of traps cooled in liquid air. All adsorbate gases were of prepurified quality supplied by the Matheson Co.

Apparatus. In the chromatograph, a Gow-Mac katharometer was used with a Leeds and Northrup Speedomax recorder which at maximum sensitivity produced a full-scale deflection per millivolt input. Flow control of the helium carrier gas was maintained by a constant differential type flow controller (Moore Products Co.) in conjunction with a needle valve and the flow rate of the effluent helium or adsorbate–helium mixture was conveniently measured by a soap bubble flow meter. Hydrogen was used as a nonadsorbed gas in measuring the dead time of the chromatograph.

The adsorbate gas was stored in glass flasks of large volume and at a pressure sufficiently in excess of atmospheric pressure to produce the desired small rate of injection into the helium stream through the capillary tube indicated in Figure 1. The injector system was calibrated for each gas by measuring the flow rate of the adsorbate as a function of the pressure head, between the two ends of the capillary, which was measured by means of a differential manometer. Capillaries of appropriate internal diameter and length were used for the different gases.

The withdrawal of adsorbate gas during a single experiment led to a small decrease in the pressure in the bulb and to a correspondingly small decrease in the flow rate of the adsorbate during the experiment. We estimated the error introduced by this decrease. In the least favorable case (strong adsorption, nonlinear isotherm), N_2 on Ossar-500, the uncertainty in the partial pressure due to this decrease in the flow rate amounts to $\pm 1.5\%$. This would result in an error no greater than $\pm 0.7\%$ for any single point on the isotherm. (See error discussion below.) In calculating the heats of adsorption q_{st} from the isotherms this error is reduced to 0.2% due to the fact that all isotherms are affected in the same direction.

The column temperature used in the present work for the several gas–solid systems ranged from −95° up to 5°. These temperatures were produced and maintained by one of two methods. The first method employed a solid–liquid slush of organic substances of appropriate freezing points. A partial list of these cold-bath liquids is given in Table I of the paper by Gale and Beebe.[1] A second method made use of the cryostat described by Graham.[15] This latter method had the advantage that any selected bath temperature below

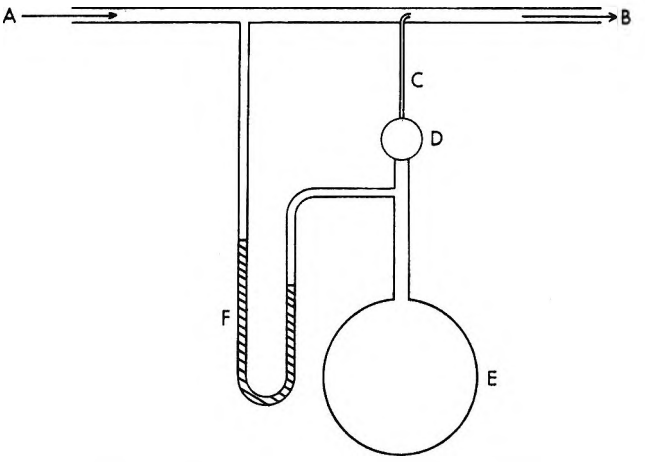

Figure 1. Schematic diagram of the gas injection system (not drawn to scale): A, carrier gas stream; B, carrier plus adsorbate gas stream; C, capillary tube; D, special valve with no dead space between valve and capillary C; E, adsorbate gas storage volume; F, differential manometer.

that of the room could be realized without depending on the availability of an organic liquid of a specified freezing point.

Sources of Errors. We carried out a thorough analysis of the errors involved, based on reasonable assumptions on the accuracy of our original measurements. As this is a conventional procedure, we do not feel that we ought to reproduce the calculations here. It seems worthwhile, however, to discuss the importance of the individual error sources and to point out some conclusions which may help to improve the accuracy of future similar experiments.

The retention time measurements were, in almost all systems, the major source of inaccuracy in the isotherms. Because we obtain the retention time as the difference between the observed retention time and the dead time, it is of great importance to make the observed retention time large compared to the dead time. This objective can be attained most easily by selecting a low column temperature; this increases the observed retention time without increasing the dead time appreciably.

The size of the difference between the temperatures T_i and T_j, at which the isotherms are measured, influences the accuracy of the heats of adsorption q_{st} in a twofold manner. First, the relative error due to the factor $(1/T_i - 1/T_j)$ decreases with increasing $(T_i - T_j)$; second, the relative error of $\ln p_i - \ln p_j$ also decreases with increasing $(T_i - T_j)$.

The inaccuracies due to the measurement and varia-

(15) D. Graham, *J. Phys. Chem.*, **66**, 1815 (1962).

tion of the column temperature and of the flow rate of the carrier gas plus adsorbate mixture become important only if the error due to the retention time is small (*e.g.*, less than 2%).

At first sight it is surprising that the error due to the measurement of the flow rate of the adsorbate is of minor importance in most cases. The flow rate of the adsorbate enters as a factor into the computation of the partial pressure of the adsorbate, and this factor[16] is also used in computing the volume of adsorbate adsorbed on the column. As a result of this, an error in the measurement of the adsorbate flow would affect the partial pressure and the volume adsorbed in the same direction. Consequently, the error cancels out if the adsorption isotherm is linear and its effect is greatly reduced if the isotherm is nonlinear. We found that the error introduced because of the water vapor pressure of the soap solution of the soap bubble flow meter is negligible.

The most important consideration in achieving a minimum error in the q_{st} value, obtained from the continuous flow data, is the selection of an optimum set of column temperatures. The temperature intervals should be as large as is practicable, and the highest temperature used should be low enough still to result in a large ratio of the retention time to the dead time.

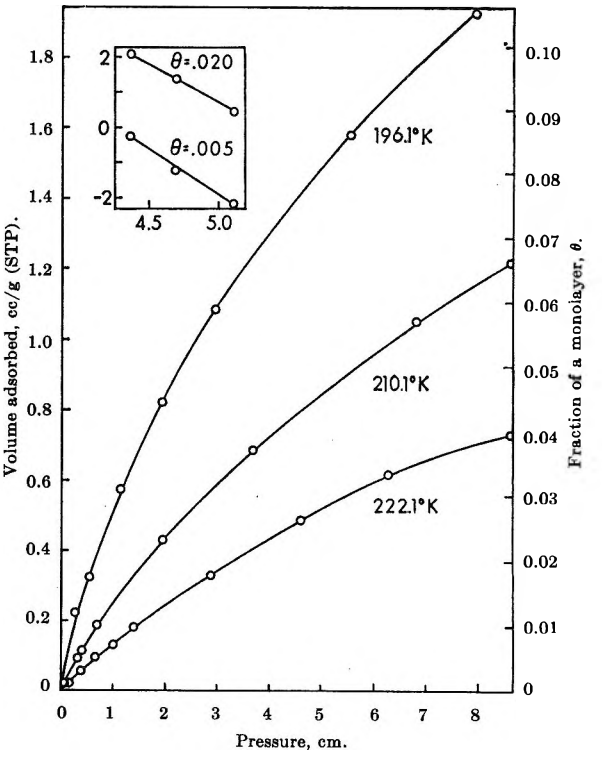

Figure 2. Type II isotherms at low coverage from continuous flow chromatography: N_2 on Ossar-500°. Inset gives plot of ln p (ordinates) *vs.* $10^3/T$ (abscissas).

Results

In the present work, adsorption data have been determined by the frontal analysis technique for nitrogen, argon, and carbon monoxide on Ossar-500°, for nitrogen, argon, and oxygen on the Graphon carbon black, and for nitrogen and C_2F_6 on Sterling MT-G carbon black.

The Isotherms. The isotherms for N_2 and Ar on Ossar-500° and C_2F_6 on Sterling MT-G are plotted in Figures 2–4. These are representative of the three isotherm types encountered in the present work.

The following observations can be made concerning the isotherms for the various gas-solid systems considered here.

(1) The isotherms for N_2 and for CO on Ossar-500° at all temperatures and coverages studied show a marked deviation from linearity which is well *outside* the estimated limits of error. These isotherms are concave to the pressure axis (BDDT Type II).[17]

(2) For N_2 and Ar on Graphon carbon black, there is a small but demonstrable deviation from linearity (BDDT Type II) in the isotherms at the lowest temperatures employed in each case (−95.7 to −96.0°), but in the slightly higher temperature range from −76 to −85° any apparent deviation from linear isotherms is *within* the limits of error.

(3) The isotherms for Ar–Ossar-500° and O_2–Graphon all conform to linearity; *i.e.*, they obey Henry's law *within* the limits of error.

(4) In the case of N_2 and C_2F_6 on Sterling MT-G at all coverages and temperatures studied there is a marked departure from linearity, well *outside* the limits of error. These isotherms are *convex* to the pressure axis (BDDT Type III).

The Heats of Adsorption. The isosteric heat of adsorption q_{st} as defined by eq 2 has been calculated from the isotherm data. Plots of ln p *vs.* $1/T$ are given in

$$q_{st} = -R\left(\frac{\partial \ln P}{\partial(1/T)}\right)_V \qquad (2)$$

Figure 5 and as insets in Figures 2–4, and the derived heats for the three Ossar systems are given in Figure 6. The heats of adsorption together with error estimates for all systems studied here are given in Table I.

In the case of the system N_2–Ossar, the conditions

(16) $V_{ads} = t_R \times F[273.1/T][(760 + P/2)/760]$, where V_{ads} is the volume adsorbed (STP), F is the flow rate of the adsorbate, T is the temperature of the column in °K, and P is the pressure drop in the column.

(17) S. Brunauer, L. S. Deming, W. E. Deming, and E. Teller, *J. Am. Chem. Soc.*, 62, 1723 (1940).

Table I

System	Frontal analysis method: Temperature range, °K	Coverage, θ	q_{st}, kcal/mole	Pulse method q_{st}, kcal/mole	Isotherm type
N_2–Ossar	196–222	0.001	5.97 ± 1.5%	5.3	Type II
		0.002	5.95 ± 1.5%		
		0.004	6.03 ± 1.5%		
		0.008	5.97 ± 1.5%		
		0.010	5.84 ± 1.5%		
		0.020	5.52 ± 1.5%		
		0.040	5.35 ± 1.5%		
		0.060	5.3 ± 2.5%		
Ar–Ossar	187–208	0.0025–0.025	2.7 ± 9%	2.5	Linear
CO–Ossar	266–278	0.005	8.4 ± 3.5%	...	Type II
		0.010	7.9 ± 3.5%		
		0.015	7.7 ± 3.5%		
		0.020	7.7 ± 3.5%		
		0.030	7.8 ± 3.5%		
N_2–Graphon	178–197	0.0005–0.004	3.2 ± 5%	2.7	Type II–linear
Ar–Graphon	179–197	0.001–0.003	2.9 ± 7%	2.7	Type II–linear
O_2–Graphon	177–197	0.0003–0.003	2.6 ± 6%	2.7	Linear
N_2–MT-G	172–189	0.003–0.015	2.1 ± 12%	2.4	Type III
C_2F_6–MT-G	221–261	0.02–0.15	4.6 ± 2.5%	4.9	Type III

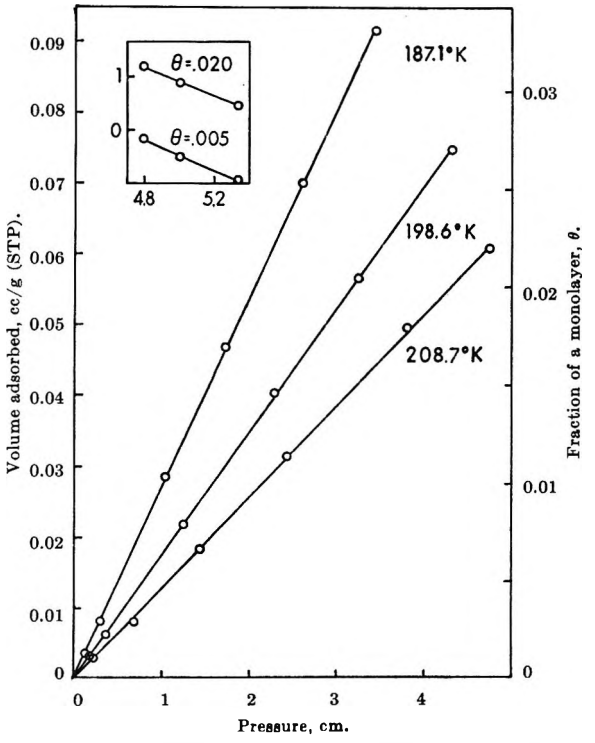

Figure 3. Linear isotherms at low coverage from continuous flow chromatography: Ar on Ossar-500°. Inset gives plot of ln p (ordinates) *vs.* $10^3/T$ (abscissas).

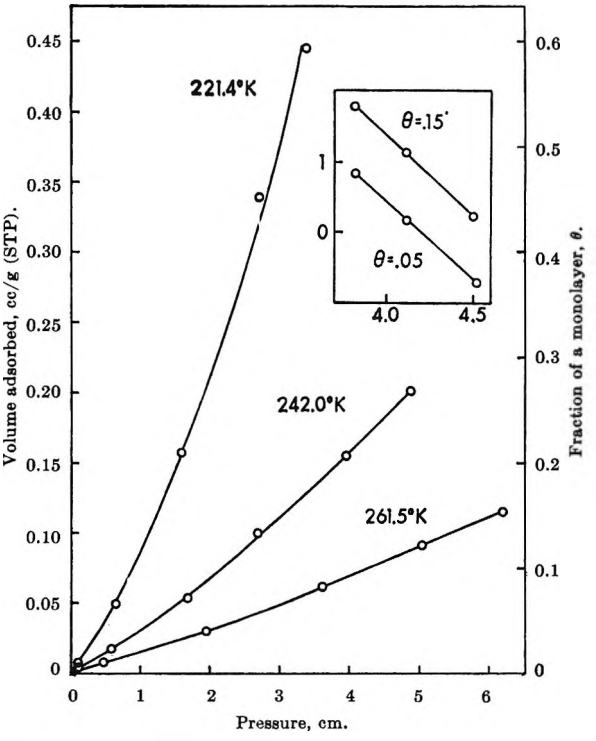

Figure 4. Type III isotherms from continuous flow chromatography: C_2F_6 on Sterling MT-G carbon black. Inset gives plot of ln p (ordinates) *vs.* $10^3/T$ (abscissas).

selected for the continuous flow study were particularly favorable; this is reflected in a low value of the estimated error of less than ±0.2% in the resultant heats of adsorption. It is seen from the inset of Figure 2 that the points read off the isotherms, at the arbitrarily selected coverages indicated, fall nicely on a straight

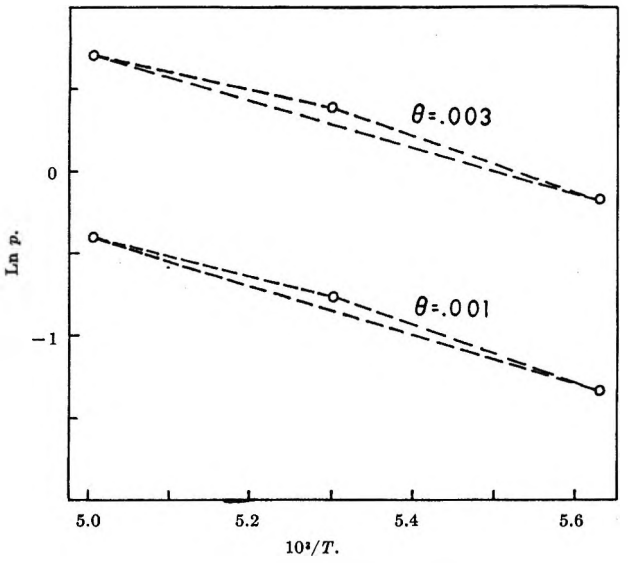

Figure 5. Plots of ln p *vs.* $10^3/T$ for N_2 on Graphon carbon black.

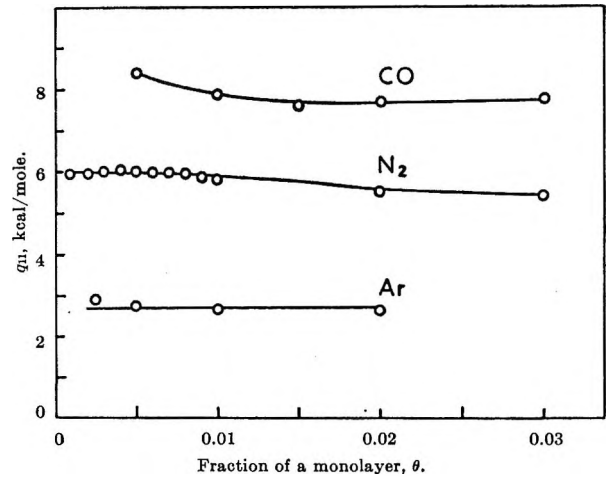

Figure 6. Isosteric heats of adsorption derived from continuous flow gas–solid chromatography: N_2, Ar, and CO on Ossar-500°.

line. The slope of this line bears a linear relation to q_{st}, the isosteric heat of adsorption. In this case there was a marked variation in the slope as a function of coverage which was reflected in decreasing q_{st} values as θ increased. This relationship is brought out in Figure 6 and in Table I. A decrease in q_{st} with coverage was shown also by the system CO–Ossar. In all other systems under consideration here, there was no significant change in q_{st} with θ outside the estimated limits of error. For this reason we have included in Table I only the range of coverage rather than specific values of θ, except in the cases of N_2 and CO on Ossar.

In all cases except N_2–Ossar the estimated error runs considerably higher than ±0.2%; in fact, the error for N_2–MT-G is as high as 12%. As a result, there may be a considerable scatter of points in the ln p *vs.* $1/T$ plot, as seen for instance in Figure 5 for the system N_2–Graphon. In this case the heats of adsorption q_1, q_2, and q_3 were calculated from the slopes of the dotted lines for the three temperature intervals indicated. The weighted mean value $\bar{q}_{st}$ was then found, with appropriate attention to the estimated errors E_1, E_2, and E_3 in each of the values q_1, q_2, and q_3. This procedure is based on the relationship

$$\bar{q}_{st} = \left(\sum_{i=1}^{3} \frac{1}{E_i^2} q_i\right) \Big/ \left(\sum_{i=1}^{3} \frac{1}{E_i^2}\right) \tag{3}$$

If the three points of a ln p *vs.* $1/T$ plot do fall on a single straight line, this may be merely fortuitous depending on how the isotherms were drawn through the experimental points. The important factor to bear in mind here is the final estimate of the over-all error in the q_{st} determination.

The most commonly used relation for calculating q_{st} from the dependence of the retention time t_R of an adsorbate pulse on temperature is

$$\frac{d \ln t_R}{d(1/T)} = \frac{q_{st}}{R} \tag{4}$$

Here t_R is the length of time it takes the maximum of the adsorbed gas pulse to be eluted minus the time required to elute a nonadsorbed gas pulse. All experiments are done at the same flow rate (or else the retention volume is used in place of t_R) and usually with the same size pulse of adsorbate.

Equation 4 can easily be shown to be valid if the adsorption isotherm is linear. It is the purpose of this section to deduce the sign and estimate the magnitude of the error in the value of q_{st} obtained from eq 4 if the adsorption isotherm is not linear.

To help to visualize the problem, let us assume for the moment that a system with an isotherm like that shown in Figure 7 is being studied. When the adsorbate pulse first enters the column its pressure might be given by point a. As the pulse travels down the column it spreads out and therefore the pressure at the peak maximum becomes smaller. By the time the pulse leaves the column the peak pressure decreases to some value given by the point b. For the isotherm shown, the fraction of the adsorbate adsorbed is larger at point b than at point a, and therefore the pulse slows down as it moves through the column. It is this slowing down which makes the interpretation of the retention time difficult. However, it would be possible to find some point c such that the retention time for the front of a

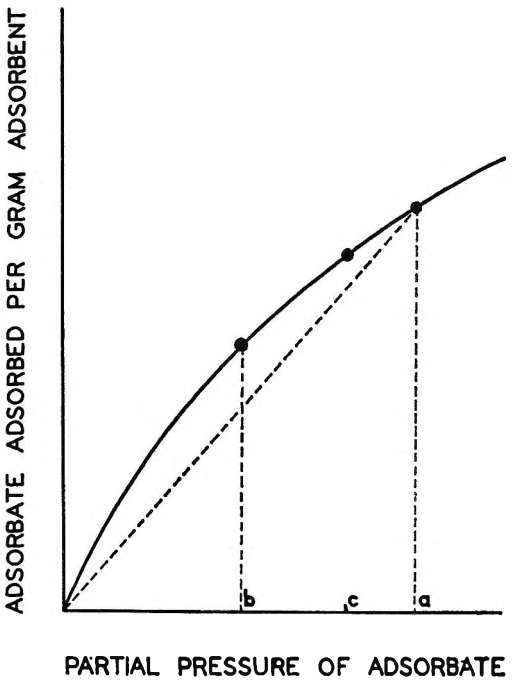

Figure 7. A sample of adsorption isotherm.

continuous flow of adsorbate at pressure c would be the same as the retention time for the pulse which starts at pressure a.

This same thing can be done for other temperatures T', T'', etc., obtaining points a′, b′, and c′; a″, b″, and c″; etc., where the points for each temperature are related as above. Now it is assumed that if the same size pulse is always used so that $a = a' = a'' = \ldots$, then it is at least *approximately* true that the same pressure $c = c' = c'' = \ldots$ should be used in each of the equivalent continuous flow experiments. To the extent that this assumption is weak, the following analysis is weak. (If the isotherm is linear, all fronts and peaks will have the same retention time at a given temperature and the following analysis becomes exact.)

A series of experiments at several temperatures, but with one pulse size, would yield a corresponding series of retention times. The above assumption implies that the same retention times for each temperature could be obtained from a series of experiments using the frontal analysis technique and only one adsorbate pressure. Therefore, in the two cases a plot of $\ln t_R$ *vs.* $1/T$ would appear exactly the same. In the series of frontal analysis experiments, t_R is directly proportional to V, the volume of adsorbate adsorbed per gram of adsorbent. Furthermore, the experiments are done with the adsorbate gas pressure held constant. Therefore

$$\frac{\partial \ln t_R}{\partial(1/T)} = \left(\frac{\partial \ln V}{\partial(1/T)}\right)_P \qquad (5)$$

This can be related to the isosteric heat of adsorption by a calculus identity, giving

$$\frac{\partial \ln t_R}{\partial(1/T)} = -\left(\frac{\partial \ln V}{\partial \ln P}\right)_T \left(\frac{\partial \ln P}{\partial(1/T)}\right)_V = \frac{P}{V}\left(\frac{\partial V}{\partial P}\right)_T \frac{q_{st}}{R} \qquad (6)$$

where use has been made of the definition of q_{st} in eq 2. Equation 6 differs from eq 4 by the inclusion of the additional factor $(P/V)(\partial V/\partial P)_T$. If the adsorption isotherm is linear, this factor is unity and we have succeeded in deriving eq 4.

If the isotherm is not linear, then the factor will be greater or less than unity and the q_{st} determined by the pulse method will be correspondingly too large or too small. If the shape of the isotherm and the surface coverage at which the pulse experiments are being done are known, then the magnitude of the error can be estimated by taking the ratio of the slope of the isotherm $(\partial V/\partial P)_T$ to the slope of the line from the isotherm to the origin V/P.

Discussion

In the systems under consideration here, there is no evidence for a slow approach to a steady state behind the adsorbate front, so the procedure described in the experimental section appears to be valid. However, since some of the isotherms are not linear, it is to be expected that the pulse and frontal analysis methods might give different heats of adsorption as predicted by eq 6. To verify this, we shall compare[18] data for the systems N_2–Ossar, Ar–Ossar, and C_2F_5–Sterling MT-G as representative examples. The isotherms for these three gas–solid systems, shown in Figures 2, 3, and 4, are seen to be Type II, linear, and Type III, respectively.

(18) In making this comparison of the q_{st} values obtained by the two methods we must call attention to certain qualifications.

(1) The values of coverage θ given in Table I may be accepted with considerable confidence since they depend on a direct comparison of the moles of gas adsorbed on the column with the moles of gas necessary to give an adsorbed monolayer on the column. This latter quantity is determined from the weight and specific surface area of the adsorbent in the column with the use of the accepted molecular cross section of 16.2 A^2 for nitrogen in the adsorbed monolayer. The BET method is employed here.

Unfortunately, in the pulse method no such direct determination of θ is possible. This problem is discussed in the earlier publication from this laboratory.[1] It seems reasonable to take an average of the $\theta_{f\max}$ and $\theta_{l\max}$ values given in Table V of the above publication. As a result of this uncertainty in the θ values of the pulse method, we cannot be sure that we are considering equal coverages in comparing the two methods. This problem is of importance only where there is a substantial change in q_{st} with coverage as in Figure 6 for the systems N_2 and CO on Ossar.

(2) We have given estimates of the specific percentages of error in the isotherms and in the derived q_{st} values of the present research. It is not practicable for us to make similarly detailed error analysis of the results obtained by the pulse method. In reviewing the earlier work we conclude that the upper limit of error was of the order of ±5%.

Since the isotherm in the case of Ar–Ossar is linear, we may expect that q_{st} as derived by the pulse method[1] will be correct. The values 2.7 and 2.5 kcal/mole, as obtained by the two methods, are in agreement within the estimated limits of experimental error which in the case of this system is rather high. Thus eq 4 is satisfactory in this case.

The isotherm for N_2–Ossar is seen from Figure 2 to be distinctly nonlinear (Type II). The correction term $(P/V)\ (\partial V/\partial P)_T$ in eq 6 would be greater than 1.0 in this case and thus the q_{st} value of Gale and Beebe calculated without the correction would be too low. It is seen from Table I that the value of q_{st} by the pulse method at low coverage is 5.3 as compared with about 6.0, at $\theta < 0.01$, obtained in the present research. Fortunately, the error in the present determination of q_{st} is very low (*ca.* 2%) for the N_2–Ossar system. Thus the prediction of the relative values of q_{st} obtained by the two chromatographic methods is substantiated here.[16]

The isotherm for C_2F_6–Sterling MT-G in Figure 4 is nonlinear in the opposite sense to that of Figure 2, being concave to the pressure axis (Type III). In this case eq 6 leads to the conclusion that the q_{st} value of Gale and Beebe would be too high. From Table I we see that this is indeed true with 4.9 kcal by the pulse method and 4.6 kcal by the present method. Here again we have a relatively low error (2.6%) and the difference between the two above q_{st} values is well outside the limits of error.[16]

The other gas–solid systems are not represented in Figures 2, 3, and 4, but the q_{st} data are given in Table I. Among these systems, only in the case of O_2–Graphon was a linear isotherm observed at each of the three temperatures used. The nature of the isotherms is indicated in the extreme right-hand column of Table I. Where the isotherms were linear at certain temperatures but Type II at lower temperatures, the designation Type II–linear is given.

The system CO–Ossar yields distinctly Type II isotherms and excessively high q_{st} values. Unfortunately, we have no data for this system by the pulse method. When these data become available, we would predict that the resulting q_{st} values would be too small by a substantial amount, unless one makes the correction given in eq 6.

The significance of the variation in the heats of adsorption of CO and the elementary gases N_2, O_2, and Ar when adsorbed on polarizing surfaces such as the Ossar-500° or on the nonpolarizing carbon blacks has been discussed by Gale and Beebe[1] and more recently by Smith and Ford.[19] It is rather remarkable to find, as we do, a q_{st} value as high as 8.0 kcal/mole for CO on Ossar since Smith and Ford found by calorimetry the low value 2.4 for this gas on Sterling MT-G. This wide spread in the q_{st} values on different adsorbents underscores the importance of the polarizability of the adsorbate in combination with a strongly polarizing surface. Of course CO, unlike N_2, has a small permanent dipole and this contributes even more strongly to a higher q_{st} value on the polarizing surface of Ossar-500°. It is also noted that the q_{st} value for CO obtained chromatographically may serve as a convenient and useful probe in assessing the polarizing power of a given surface.

All the chromatographic data obtained in this laboratory by the two methods employing the pulse technique[1] and that of frontal analysis, give qualitative support to the prediction of eq 6 within the estimated error limits. However, it is noted that any differences in the two methods do not exceed a figure of approximately 15%. In our opinion, the systems N_2–Ossar and C_2F_6–MT-G represent rather extreme cases of Type II and III adsorption, respectively, at low coverage. Thus we may make the observation that the chromatographic pulse method of getting at q_{st} data is not excessively in error even if one does not make the correction included in eq 6. Because of the convenience in operation, the pulse method still has merit as a means of getting rough q_{st} values which may be useful in many situations.

Acknowledgments. Our gratitude is due to the National Science Foundation and to the National Institutes of Health for financial support of this work.

(19) W. R. Smith and D. G. Ford, *J. Phys. Chem.*, 69, 3587 (1965).

Cross-Phenomenological Coefficients. III. Studies on Electroosmosis

by R. P. Rastogi and K. M. Jha

Department of Chemistry, University of Gorakhpur, Gorakhpur, India *(Received July 27, 1965)*

The electroosmotic permeability of conductivity water through sintered Pyrex glass has been measured for varying magnitudes of potential difference, $\Delta\phi$, at 35°. Measurements have also been made for electroosmotic pressure differences per unit potential difference which have been found to be constant up to 60 v. Measurements on electroosmosis show that the cross-phenomenological coefficient is also constant up to 60–70 v. Experiments for the direct test of phenomenological equations have been performed. The temperature dependence of cross-phenomenological coefficients has also been studied. The results appear to be consistent with the classical theory of electroosmosis.

Introduction

Linear phenomenological laws are used as axioms in thermodynamics of irreversible processes.[1-4] However, direct experimental tests of linear phenomenological laws when two or more forces are involved have not been attempted so far. These laws are valid within a certain range and it is of considerable interest to know this range. Further, very little information is available regarding the cross-phenomenological coefficients.[5,6] The objects of this paper are (i) to ascertain the magnitude of cross-phenomenological coefficients in electroosmosis of water through sintered glass, (ii) to study its dependence on temperature and potential difference, and (iii) to test the validity of linear phenomenological equation in this case, and to assess its range of validity.

The phenomenon of electroosmosis has been chosen for detailed study because various electrokinetic effects which are related to phenomenological coefficients can be studied experimentally. However, experimental difficulties are known to be considerable.[7] It may be remarked that the experimental studies recorded in the paper are the first of their kind.

Phenomenological Equations for Electrokinetic Phenomena

The expression for entropy production, σ at temperature T (°K), for electrokinetic phenomena can be written in the form[1]

$$T\sigma = J\Delta P + I\Delta\phi$$

The fluxes are the volume flow, J, and the current I. The forces are, respectively, the pressure difference ΔP and the potential difference, $\Delta\phi$. The linear phenomenological equations are consequently written as

$$J = \frac{L_{11}}{T}\Delta P + \frac{L_{12}}{T}\Delta\phi \quad (1)$$

$$I = \frac{L_{21}}{T}\Delta P + \frac{L_{22}}{T}\Delta\phi \quad (2)$$

where L_{ik} $(i, k = 1, 2)$ are called the phenomenological coefficients. When $i \neq k$, the coefficients are called cross-phenomenological coefficients. When $\Delta\phi = 0$

$$J = \frac{L_{11}}{T}\Delta P \quad (3)$$

From Poisseuille's law, flow through n capillaries is given by

$$J = \frac{dV}{dt} = \frac{\pi r^4 \Delta P n}{8\eta l} \quad (4)$$

(1) K. G. Denbigh, "The Thermodynamics of Steady State," Methuen and Co. Ltd., London, 1958.

(2) S. R. de Groot and P. Mazur, "Non-equilibrium Thermodynamics," North-Holland Publishing Co., Amsterdam, 1961.

(3) I. Prigogine, "Introduction to Thermodynamics of Irreversible Process," Interscience Publishers, Inc., New York, N. Y., 1961.

(4) D. G. Miller, *Chem. Rev.*, **60**, 15 (1960).

(5) R. P. Rastogi, R. L. Blokhra, and R. K. Agarwal, *Trans. Faraday Soc.*, **60**, 1386 (1964).

(6) R. P. Rastogi, R. C. Srivastava, and K. Singh, *ibid.*, **61**, 854 (1965).

(7) H. R. Kruyt, "Colloid Science," Vol. 1, Elsevier Publishing Co., Amsterdam, 1952.

where V is the volume of the liquid flowing through the capillaries, r is the radius of the capillary, η is the viscosity of the liquid, and l is the length of the capillary. Comparing eq 3 and 4 it follows that

$$L_{11} = \frac{n\pi r^4}{8\eta l}T \tag{5}$$

Similarly, when $\Delta P = 0$

$$I = \frac{L_{22}}{T}\Delta\phi \tag{6}$$

but from Ohm's law $I = \Delta\phi/R$, where R is the resistance. On comparing eq 6 with Ohm's law, we find that

$$L_{22} = \frac{T}{R} \tag{7}$$

Ohm's law has a very large domain of validity; *i.e.*, L_{22} is independent of $\Delta\phi$ up to a very high value of $\Delta\phi$. The extent to which L_{22}/T depends upon temperature is largely governed by the temperature dependence of R which is generally given by

$$R = R_0 + \alpha T + \beta T^2 + \gamma T^3 + \ldots$$

where R_0, α, β, and γ are constants.

As long as the flow does not become turbulent and the Reynolds number is not greater than 1000, Poisseuille's law remains valid and hence L_{11}/T remains constant up to a fairly high value of ΔP.

Thus, whereas we find that we have reasonably reliable information regarding the limits up to which L_{11} and L_{22} are independent of the corresponding forces, we do not have any information about L_{21} or L_{12}.

From eq 1 it follows that when $\Delta P = 0$

$$(J)_{\Delta P=0} = \frac{L_{21}}{T}\Delta\phi \tag{8}$$

where $(J)_{\Delta P=0}$ is called the electroosmotic velocity. The quantity L_{12}/T may be called the electroosmotic permeability. It is clear that measurements of electroosmotic velocity for various values of $\Delta\phi$ at a constant temperature can directly yield the value of L_{12}.

In the same fashion, when $\Delta\phi = 0$

$$(I)_{\Delta\phi=0} = L_{21}\frac{\Delta P}{T} \tag{9}$$

where $(I)_{\Delta\phi=0}$ is called the streaming current. Measurements of streaming current for various values of ΔP would directly yield the value of L_{21}.

From eq 1 it follows that when $J = 0$

$$(\Delta P)_{J=0} = -\frac{L_{12}}{L_{11}}\Delta\phi \tag{10}$$

where $(\Delta P)_{J=0}$ is the electroosmotic pressure.

Equation 1 can be written as

$$(J)_{\text{total}} = (J)_{\Delta\phi=0} + (J)_{\Delta P=0} \tag{11}$$

where $(J)_{\text{total}}$ is the resultant flow. The three quantities involved in eq 11 can be directly and simultaneously measured and hence the equation can be conveniently tested.

Experimental details for the measurement of L_{12}, $(J)_{\text{total}}$, $(J)_{\Delta\phi=0}$, $(J)_{\Delta P=0}$ and electroosmotic pressure are given below.

Experimental Section

Membrane. Sintered Pyrex glass was used as membrane. The G_4 variety was chosen to get maximum value of electroosmotic pressure, since according to the classical theory of electrokinetic phenomena it is inversely proportional to the square of the radius of the capillary. It may be noted that it is difficult to get a single capillary with a radius equal to that of the pores of sintered Pyrex. Since the electroosmotic velocity depends directly on the fourth power of the radius, it would tend to decrease when pore size is reduced. Fortunately, this factor is compensated for the case of sintered Pyrex since it acts as a bundle of capillaries and the amount of liquid flowing is multiplied by the number of such capillaries.

Treatment of the Membrane. The disk was cleaned with boiling hot nitric acid followed by steaming from either side and washing with filtered boiling hot, deionized water several times. The washing with the deionized water was continued until the disk was practically free from acid. This was ensured by noting the conductivity of the washings. It was then dried in an electrically controlled air oven at a temperature of 180° for a period of 3–4 hr. Before starting the experiments, boiling hot deionized water which was previously filtered was sucked three or four times from either side of the disk to ensure the wetting of the maximum number of pores. Prior to starting the experiment, the conductivity of the washing was checked once again. The apparatus was then filled with freshly degassed and filtered deionized water and kept in an air thermostat for 45 min to attain the temperature of the bath. The fluctuation in the thermostat was of the order of ±0.05°.

Material. Fresh distilled water was twice distilled over potassium permanganate. The specific conductivity of the deionized water was of the order of (1.2–3) $\times 10^{-6}$ ohm^{-1} cm^{-1}. The specific conductivity was measured by an ac conductivity bridge based on Jones' design.[8]

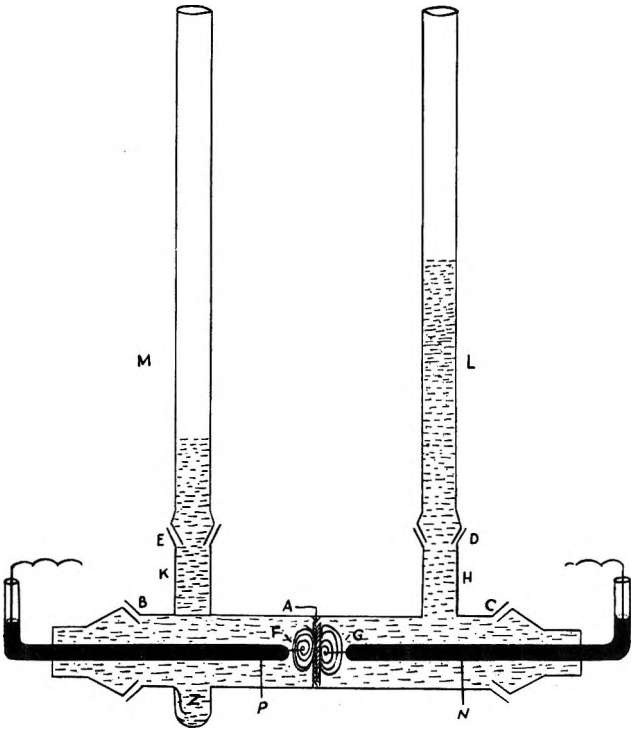

Figure 1. Apparatus for the measurement of electroosmotic pressure difference and electroosmotic permeability.

Source of Emf. An electronically variable voltage supply was used as a source of emf. The strength of the current drawn was in the range of 2–5 ma. This greatly facilitated the reduction of polarization. In order to maintain the consistency of the voltage during the run, a voltage stabilizer was connected in series. Fluctuations in the voltage were of the order of 2–5%.

Electrode. Silver–silver chloride electrodes did not work well. Hence, spiral-type platinum electrodes were used which were kept pressed against the two sides of the sintered disk, covering the maximum area of the disk.

Measurement of Electroosmotic Permeability and Electroosmotic Pressure Difference. Apparatus. The apparatus used for the measurement of electroosmosis is shown in Figure 1. The central part consisted of a Pyrex tube 30 cm long and 2.5 cm in diameter with a sintered glass disk, A, fixed in the middle. The tube had two female joints, B and C, at the ends. Platinum wires, F and G, were fixed to two standard male joints as shown in Figure 1 through tubes P and N. The electrical contact was made with mercury. The length of the wires was adjusted in such a way that when the standard joints were kept in position, the spiral ends of these just pressed the disk. The central tube, BAC, had two side tubes, H and K. The latter was joined at Z. The tubes H and K had standard joints D and E, respectively. The tubes L and M each of 1.138-cm diameter were kept parallel. When the liquid in the limbs L and M was the same, a constant dc voltage was supplied. The rise of water level in L or M at different time intervals was noted with a vernier telescope. Time was measured with the help of a stop watch reading up to 0.1 sec. The measurements were made for voltages varying from 10 to 120 v.

If X is the rise in the water column in one limb, the fall in the other tube would be to the same extent. The volume rate of flow would be given by $A\mathrm{d}X/\mathrm{d}t$, where A is the cross-sectional area of the tube. Now according to eq 1

$$A\left(\frac{\mathrm{d}X}{\mathrm{d}t}\right) = L_{11}\frac{\Delta P}{T} + L_{12}\frac{\Delta\phi}{T} \tag{12}$$

In the beginning of the experiment, $\Delta P = 0$ and electroosmotic flow predominates which is instantaneous; hence

$$(J)_{\Delta P=0} = A\left(\frac{\mathrm{d}X}{\mathrm{d}t}\right) \tag{13}$$

Expressed differently, in the initial stages the rise of the water column would be entirely due to electroosmosis, and the rate of rise would be constant at constant temperature when voltage is kept constant. Thus when X is plotted against time, the limiting slope is $L_{12}\ \Delta\phi/TA$ from which the magnitude of L_{12} can easily be determined. The method is quicker and more convenient than the conventional methods. One typical plot of X against t is given in Figure 2. Another way of getting the same information from the same set of data is as follows. ΔP would be equal to $2X\rho g$ where ρ is the density of the fluid and g is the acceleration due to gravity so that

$$A\left(\frac{\mathrm{d}X}{\mathrm{d}t}\right) = \frac{L_{11}}{T}(2X\rho g) + L_{12}\frac{\Delta\phi}{T} \tag{14}$$

Equation 14 can be integrated, but the integrated form is of little value from the point of view of the analysis of the data. However, since for a particular value of $\Delta\phi$ the second factor would be constant at constant temperature even if L_{12} depends upon $\Delta\phi$, one can plot $\mathrm{d}X/\mathrm{d}t$ against $2X$, and a straight line should be obtained ($\mathrm{d}X/\mathrm{d}t$ can be determined graphically either directly or by finding a suitable analytical equation for the curve). The slope of this straight line would give the value of ordinary permeability and the intercept would be L_{12}. It is difficult, however, to estimate the value of $\mathrm{d}X/\mathrm{d}t$ with precision. Hence, ac-

(8) G. Jones and R. C. Joseph, *J. Am. Chem. Soc.*, **50**, 1049 (1928).

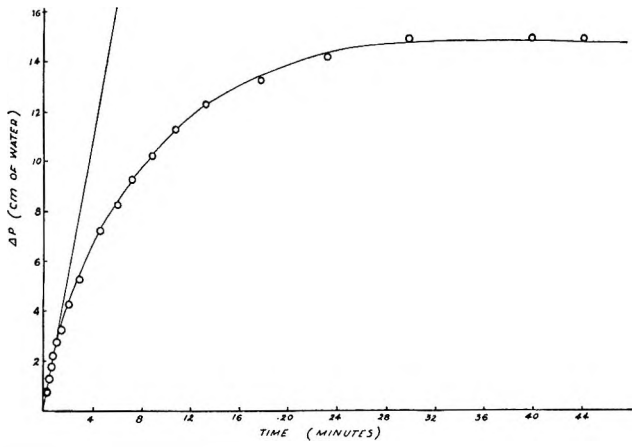

Figure 2. Plot of ΔP as a function of time in a typical experiment.

curate values of ordinary and electroosmotic permeability cannot be obtained, but they are useful as rough correlations.

In order to study the temperature dependence of L_{12}, measurements of electroosmotic velocity were made at different temperatures for $\Delta\phi = 70$ v. The results are recorded in Table III.

The electroosmotic pressure difference was measured with a similar apparatus. The steady-state value of $(\Delta P)_{J=0}$ was measured with a vernier telescope for various values of $\Delta\phi$. The steady state was usually attained in 2–3 hr.

Measurement of the Ordinary Permeability. In order to have information about the magnitude of L_{11} and the domain of validity of Poisseuille's law in the region under study, careful studies of ordinary permeability were undertaken.

The measurements for the ordinary permeability of deionized water through the disk were carried out in two different ways using essentially the same apparatus as was used for measuring electroosmotic permeability in order to assess the influence of capillary active forces on fluid flow in the present case. In one case, the flow was measured in a capillary by noting the movement of the water–air meniscus, while in the other the flow was measured by noting the mass of water that came out of the capillary in a certain time interval. We will call the former the volume-flow method and the latter the mass-flow method. The amount collected in a definite interval of time was weighed and the amount flowing per unit time was thus calculated.

The experiments were repeated using a capillary of 4.323×10^{-2}-cm radius instead of the Pyrex disk.

Blank experiments were performed by inducing the streaming potential to zero. These showed that the effect of the streaming potential on ordinary permeation is negligible. In other words, $(J)_{\Delta\phi=0}$ is equal to $(J)_{I=0}$.

Test of Linear Phenomenological Equations. Experiments were performed in order to test the range of validity of eq 1. The experimental setup was quite similar to that described above. It was modified to have simultaneous values of $(J)_{\text{total}}$, $(J)_{\Delta P=0}$ and $(J)_{\Delta\phi=0}$. For convenience the flow rates in these experiments were measured by noting the time taken by the water–air meniscus to move through a definite distance in the exit capillary, the cross-sectional area of which was 2.78×10^{-2} cm^2.

Reproducibility and Sources of Errors

The following factors are likely to affect the reproducibility of the results for ordinary and electroosmotic permeability.

Incomplete Wetting of the Disk. The rate of flow of liquid depends upon the number of capillaries available for the transmission of the liquids; hence, if all the capillaries are not wet, poor reproducibility would be expected. Prior suction of boiling hot deionized water from both the sides of the disk several times ensured wetting of maximum number of the capillaries. This treatment also minimized the number of air bubbles in the capillaries.

Blocking of the Capillaries. If periodic blocking and opening of the capillaries in the sintered glass disk were to occur, reproducibility would be badly affected. Blocking is mainly due to suspended impurities, and opening of the capillaries is due to the force of the flowing liquid. In order to avoid this, carefully filtered deionized water was used. Care was also taken so that no suspended impurities were introduced during the run.

Cleanliness of the Disk. Since ordinary flow is affected by the presence of grease in the pores, its use was avoided. Further, since inorganic impurities affect the ζ potential, which in turn affects electroosmotic flow, only deionized water was used.

Action of Water on Glass Membrane. This is a very serious source of error and affects the reproducibility tremendously. Even with the use of carefully purified water after filtration, the permeability of the sintered glass disk was found to vary with time. The permeability could be reasonably reproducible only when the disk was subjected to the specific treatment described earlier. The reason for this behavior is not definitely known.[9] The following reasons have been ascribed: (a) chemical action, and (b) swelling. The evidence, although very meager, is perhaps in favor of the for-

(9) H. George, "Properties of Glass," Reinhold Publishing Corp., New York, N. Y., 1954.

mer. Consequently, experiments had to be devised which could be finished in a short period of time.

Polarization of Electrodes. Due to evolution of gases at the electrodes, there is the likelihood of bubbles sticking to the sides of the capillaries, thus causing significant errors in precisely knowing the actual height of water column in the tube. This was, however, minimized by using freshly boiled conductivity water for the filling of the apparatus, and currents of very small magnitude (of the order of 2–5 ma).

The conductivity of the water used was checked before and after the experiments. The per cent change in the conductivity of deionized water, on the average, for a run of shorter duration (up to 2 min) in which we were only interested in the measurement of the electroosmotic velocity, is given below. The increase in conductivity for the measurements up to 80 v was of the order of 5%, whereas for 90 v and beyond, the increase was more than 20%. It is thus apparent that in the measurement of electroosmotic velocity up to 80 v, where the change in specific conductivity is only 5%, very small amounts of electrode products are formed. This is confirmed by the good reproducibility of observations with the same sample of water.

In the measurements of electroosmotic pressure difference where each run is of comparatively longer duration (2–3 hr) the per cent change in conductivity was as follows. In experiments with voltages varying from 10 to 50 v, the increase in the specific conductivity was of the order of 7.5%, but when the voltage was further increased to 70 v, there was a 20% increase in the specific conductivity. For 90 v, there was a threefold increase in the specific conductivity.

Heating of the Fluid in the Pores. Since the magnitude of the current passed was of the order of 2–5 ma only, and since the duration of the experiment was very short for the electroosmotic velocity measurements, the chances of heating were very small. If $\Delta\phi$ = 100 v, time = 120 sec, the heat produced for 5 ma current would equal 60 joules. Since the amount of water in the main tube (BAC) is about 150 cc, the maximum temperature rise during the whole course of one single experiment would only be approximately 0.1°. However, if local heating takes place, the viscosity should go down and the electroosmotic permeability should be higher.

For experiments of longer duration involving the study of the electroosmotic pressure difference, the effect of heating may have been significant. It was assumed that the field on the disk was uniform in spite of the shape of the electrodes.

Results

Results are given in Tables I to V and represented in Figures 2, 3, 4, and 5. The standard deviations from the mean are recorded along with the data.

Table I: Electroosmotic Velocity and Cross-Phenomenological Coefficients for Water at 35°

$\Delta\phi$, v	Volume flow,[a] cc sec^{-1} × 10^2	L_{12}/T,[a] cc sec^{-1} v^{-1} × 10^4
10	0.66 ± 0.04	6.6 ± 0.40
20	1.40 ± 0.10	7.0 ± 0.50
30	2.13 ± 0.06	7.1 ± 0.20
40	2.84 ± 0.16	7.1 ± 0.40
50	3.65 ± 0.18	7.3 ± 0.36
60	4.08 ± 0.21	6.8 ± 0.35
70	4.83 ± 0.14	6.9 ± 0.20
80	5.60 ± 0.10	7.0 ± 0.13
90	4.70 ± 0.70	5.2 ± 0.8
100	5.20 ± 0.40	5.2 ± 0.4
110	4.60 ± 0.30	4.2 ± 0.3
120	5.70 ± 0.20	4.8 ± 0.2

[a] The values recorded are the mean for five runs corresponding to each value of $\Delta\phi$.

Table II: Test for Linear Relation for Purely Hydrodynamic Flow

	Method of experiment	Slope or L_{11}/T,[a] g sec^{-1} dyne^{-1} cm^2	Intercept,[a] g sec^{-1}
Disk	Volume flow	1.59×10^{-6}	2.64×10^{-3}
Disk	Mass flow	1.54×10^{-6}	0.40×10^{-3}
Capillary	Volume flow	1.22×10^{-5}	7.62×10^{-3}
Capillary	Mass flow	1.15×10^{-5}	1.44×10^{-3}

[a] The values recorded were obtained by the method of least squares.

Table III: Temperature Dependence of L_{12}/T[a]

Temp, °K	Membrane I L_{12}/T × 10^4	Membrane I L_{12}/T × 10^6	Membrane II L_{12}/T × 10^4	Membrane II L_{12}/T × 10^6
303	3.9 ± 0.2 (5)	4.06		
308	4.4 ± 0.2 (4)	4.23		
313	5.1 ± 0.2 (6)	4.55		
318	5.4 ± 0.2 (7)	4.50	3.4 ± 0.1 (5)	2.84
323	5.8 ± 0.2 (6)	4.53	3.5 ± 0.3 (6)	2.73
328			3.7 ± 0.2 (3)	2.73
333			3.9 ± 0.2 (4)	2.72
	Av 4.37 ± 0.18		Av 2.75 ± 0.04	

[a] The figures in the parentheses indicate the number of readings.

Table IV: Electroosmotic Pressure Difference for Water at 35°[a]

$\Delta\phi$, v	$(\Delta P)_{J=0}$, cm of water	$L_{12}/T \times 10^4$, cc sec^{-1} v^{-1}	$L_{11}/T \times 10^3$, cc sec^{-1} dyne^{-1} cm^2	$(\Delta P/\Delta\phi)_{J=0} \times 10$	$L_{12}L_{11} \times 10^2$
10	5.05 ± 0.15	6.6 ± 0.4	1.59×10^{-6}	5.05 ± 0.15	4.15 ± 0.26
20	10.08 ± 0.20	7.0 ± 0.5	1.59×10^{-6}	5.04 ± 0.10	4.40 ± 0.32
30	16.00 ± 0.44	7.1 ± 0.2	1.59×10^{-6}	5.33 ± 0.14	4.47 ± 0.12
40	20.33 ± 0.36	7.1 ± 0.4	1.59×10^{-6}	5.08 ± 0.09	4.47 ± 0.26
50	25.46 ± 0.58	7.3 ± 0.4	1.59×10^{-6}	5.09 ± 0.13	4.59 ± 0.26
60	31.40 ± 1.50	6.8 ± 0.35	1.59×10^{-6}	5.23 ± 0.25	4.28 ± 0.23
70	39.70 ± 1.00	6.9 ± 0.20	1.59×10^{-6}	5.67 ± 0.14	4.34 ± 0.12
80	46.60 ± 1.30	7.0 ± 0.13	1.59×10^{-6}	5.82 ± 0.16	4.40 ± 0.08
90	55.15 ± 1.00	5.2 ± 0.8	1.59×10^{-6}	6.13 ± 0.11	3.27 ± 0.52

[a] The values recorded in columns 2 and 3 are mean of five readings corresponding to each value of $\Delta\phi$ and those in column 4 were determined by the method of least squares.

Table V: Direct Test of Linear Phenomenological Equations[a]

Disk no.	ΔP, cm of water	Rate of permeation, cm sec^{-1}			
		$(J)_{\Delta\phi=0}$	$(J)_{\Delta P=0,\ \Delta\phi=50V}$	$(J)_{total}$, exptl	$(J)_{total}$ sum of columns 3 and 4
1	15	0.27 ± 0.02 (10)	0.39 ± 0.02 (10)	0.63 ± 0.02 (10)	0.066 ± 0.04
1	106	1.95	0.39	2.24	2.34
1	114.5	2.08 ± 0.13 (2)	0.39 ± 0.02 (2)	2.47 ± 0.16 (2)	2.47 ± 0.15
2	88.5	4.46 ± 0.22 (6)	1.33 ± 0.06 (6)	5.74 ± 0.19 (6)	5.79 ± 0.28
3	106	1.53	0.31	1.70	1.83
3	114.5	1.59 ± 0.08 (2)	0.31 ± 0.01 (2)	2.00 ± 0.09 (2)	1.90 ± 0.09
4	106	2.27	0.46	2.78	2.73
4	114.5	2.46	0.45	2.94	2.91
5	126	0.46 ± 0.04 (4)	0.15 ± 0.005 (4)	0.62 ± 0.04 (4)	0.61 ± 0.05
6	106	2.68 ± 0.26 (2)	0.62 ± 0.03 (2)	3.30 ± 0.29 (2)	3.30 ± 0.29

[a] The figures in the parentheses indicate number of readings.

Discussion

Test for Linear Relation for Flow in the Absence of Potential Difference. A detailed verification of the linear relation between pressure difference and the isothermal fluid flow in the absence of potential difference was necessary because the present investigation basically involves a study of liquid flow through the small capillaries of the disk.

Volume flow per second and mass flow in grams per second are plotted against the pressure difference in Figures 3 and 4. For the sake of comparison, the volume flow has also been converted into mass flow by multiplying the volume by the density of water at 35°.

Straight lines are obtained in both the cases but these do not pass through the origin. The values of the intercepts, obtained by the method of least squares, were 2.64×10^{-3} g sec^{-1} for volume flow and 0.4×10^{-3} g sec^{-1} for mass flow. It may be noted that these are different.

In order to have a further check on the existence of the intercept, similar experiments for volume flow and mass flow were carried out with a single glass capillary. When the corresponding data are plotted in the above manner, the intercept in the case of volume flow is found to be 7.62×10^{-3} g sec^{-1} as compared to 1.44×10^{-3} g sec^{-1} in the case of mass flow. The magnitude of uncertainty of the slope and the intercept was 5 to 6% as obtained by statistical considerations. The result for the two cases has been compared in Table II.

Since the straight lines do not pass through the origin, Poisseuille's relation apparently is not obeyed. The reason for the occurrence of intercepts may be ascribed to the kinetic energy[10,11] of the flowing liquid through

(10) F. H. Newman and G. F. C. Searle, "The General Properties of Matter," Edward Arnold (Publishers) Ltd., London, 1957, Chapter VII.

(11) F. Daniels, J. Williams, P. Bender, R. Alberty, and C. D. Cornwell, "Experimental Physical Chemistry," McGraw-Hill Book Co., Inc., New York, N. Y., 1962, Chapter VIII.

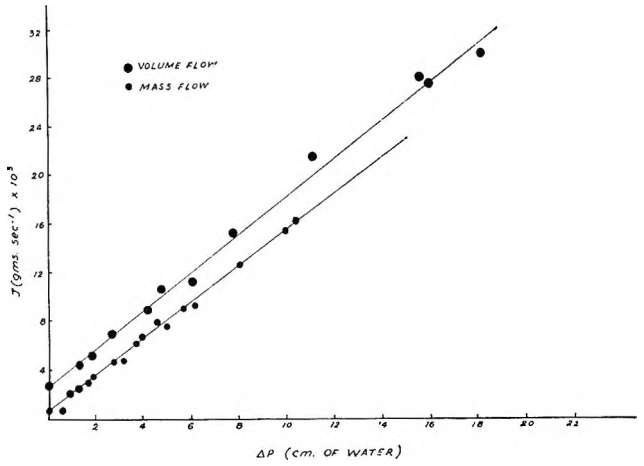

Figure 3. Test of Poiseulle's law for flow through Pyrex sinter.

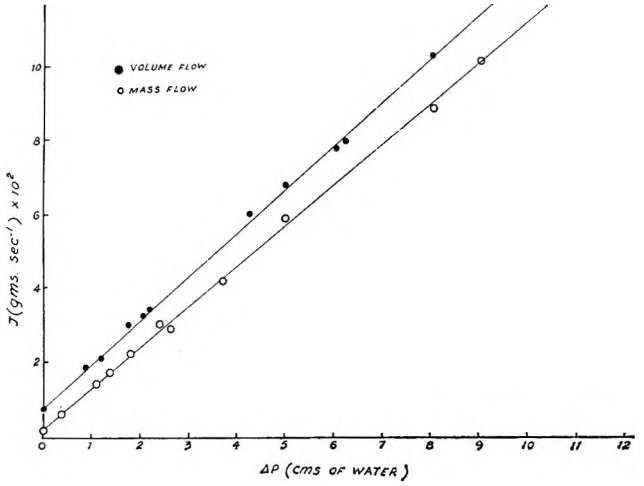

Figure 4. Test of Poiseulle's law for flow through a single capillary.

the disk or a single glass capillary, which is unaccounted for in the Poisseuille's equation.

It is important to note that although the slope for volume flow and mass flow is identical within experimental error, the intercepts differ considerably. It appears that capillary forces are primarily responsible for this discrepancy. In the case of mass flow, the capillary forces are utilized in the formation of the drops at the outlet, and consequently the intercept has a smaller value.

The apparatus for electroosmotic velocity measurements and electroosmotic pressure difference measurements were so designed that the use of capillary was avoided. Hence the influence of capillary-active forces is entirely negligible when the pressure difference developed is considerable. It was thus ensured that the fluid satisfied the linear relation. However, the rate of flow was measured in capillaries for the test of the linear phenomenological relations. Since $(J)_{\text{total}}$ and $(J)_{\Delta\phi=0}$ involve the same amount of error on this account, the conclusions are unaffected. The values of L_{11}/T were estimated by the method of least squares.

Electroosmotic Velocity. When the electroosmotic flow is plotted against $\Delta\phi$, a straight line passing through the origin is obtained within experimental error. The behavior of the disk near about 100 v becomes ambiguous.

When the voltage is increased beyond 70 v, the value of L_{12}/T shows a decreasing tendency. This may be due to decrease in the value of ζ potential caused by the appearance of an increasing amount of ions due to electrolysis. The conductivity measurements of deionized water in the apparatus before and after the experiment confirm the existence of ionic species. At $\Delta\phi$ = 70 to 110 v, the specific conductivity of water was found to increase from 5 to 30%.

Temperature Dependence of L_{12}/T. According to the classical theory of electroosmosis[7]

$$\frac{L_{12}}{T} = \frac{D\zeta S}{4\pi\eta l} \tag{15}$$

where D is the dielectric constant of the medium, ζ is the ζ potential at the interface, S is the area of the cross section of the capillary, η is the viscosity of the medium, l is the length of the capillary, and T is the temperature in degrees absolute. Equation 15 shows that L_{12}/T should depend on the temperature since the dielectric constant D and the viscosity η depend on temperature.[12] The manner in which L_{12}/T depends on temperature, however, is not very clear. From the experiment,

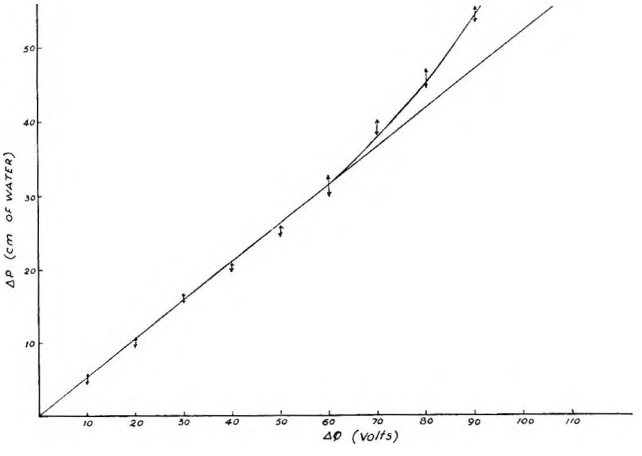

Figure 5. Electroosmotic pressure difference at various voltages.

(12) R. A. Robinson and R. H. Stokes, "Electrolyte Solutions," Butterworth and Co. Ltd., London, 1959.

however, it appears that L_{12}/T has a tendency to increase with temperature. A rearrangement of the above equation shows that the quantity $(L_{12}/T)(\eta/D)$ should be independent of temperature for the same system. Table III confirms this point.

Electroosmotic Pressure Difference. When $(\Delta P)_{J=0}$ is plotted against $\Delta\phi$, a smooth curve is obtained which passed through the origin. This may be treated as a straight line at least in the region up to 60 v as shown in Figure 5. Up to 60 v the conductivity of deionized water used in the experiment changes only by 7.5% during a single run. At higher voltages, however, the conductivity of deionized water changes by 2–3-fold the original value for a single run. In all probability the ζ potential at the glass–water interface changes due to the appearance of ionic species in greater concentration. This would affect the value of L_{12}/T. We have seen earlier that at higher voltages L_{12}/T has a tendency to decrease. Let us consider Table IV, where the experimental values of $(\Delta P/\Delta\phi)_{J=0}$ have been compared with L_{12}/L_{11} by using the experimentally determined values of L_{12}/T and L_{11}/T. Up to 60 v, there is moderate agreement between the experimental and the theoretical values considering the uncertainty involved. The agreement is not improved even when a kinetic energy correction (which is of the order of 0.01) is made.

Test of Linear Phenomenological Equation. Table V records the values of $(J)_{\Delta P=0}$, $(J)_{\Delta\phi=0}$, and $(J)_{\text{total}}$ in simultaneous sets of experiments for a new set of disks. It is found that the directly observed value of $(J)_{\text{total}}$ agrees with that calculated from eq 11 within experimental error. It confirms the linear phenomenological eq 1 in the range of study.

Acknowledgment. K. M. J. is thankful to the authorities of Bhagalpur University, Bhagalpur, India, for the grant of leave for study purposes. The investigation is supported by Indian Council of Scientific and Industrial Research, New Delhi, India.

Adsorption of Phosphoramidates on Iron

by J. E. Berger and E. Wittner

Shell Oil Company, Research Laboratory, Wood River, Illinois *(Received August 2, 1965)*

Phosphoramidates and phosphonamidates were adsorbed from dilute isooctane solution onto iron powder. Adsorption was rapid and appears tc be monomolecular. In competitive adsorption experiments, carboxylic acids or phosphoric acids prevented deposition of neutral phosphoramidates on the iron surface. During long-term adsorption experiments, phosphoramidates containing $-NH_2$ or $-NHR$ moieties hydrolyze at the iron surface by the scission of one ester bond. Phosphoramidates derived from secondary amines were not observed to undergo surface hydrolysis at 25°. In homogeneous hydrolysis experiments with both acidic and basic media, hydrolysis rates of the phosphoramidates were in the same order as in iron-powder adsorption experiments.

Introduction

Lubricants often depend on small quantities of polar additives for controlling wear and corrosion: although use of such agents is widespread, it is not fully understood how they function. There is general agreement that effective additives must adsorb at the metal–oil interface as a necessary first step. Zisman and co-workers[1] showed that carboxylic acids and strong amines adsorb tenaciously at oil–metal interfaces; these types of compounds resemble many additives found in lubricants. Daniel[2] has discussed both the speed and strength of adsorption of polar molecules at the hydrocarbon–metal interface. Although quantitative adsorption experiments at ordinary temperatures reveal that many polar organic compounds deposit about a monolayer on metal surfaces,[3] examination of wear scars in mechanical equipment indicates that up to 300 monolayers might be present.[4] These findings imply that adsorption is only a first step which precedes reactions between polar lubricant additives and metals. Slow reactions between carboxylic acids and iron surfaces in anhydrous systems at ordinary temperatures have been reported.[3,5]

The behavior of neutral phosphoramidates is germane because these polar compounds adsorb readily on metal surfaces and because the changes which these species undergo in anhydrous systems are indicative of the reactions occurring at metal surfaces even under mild conditions.

Experimental Section

Derivatives of phosphoramidic acid, $(HO)_2P(O)NH_2$, were prepared by heating gradually 1 mole of phosphorus oxychloride and 2 moles of the appropriate phenol to 250° and maintaining the mixture at this temperature for periods ranging up to 10 hr. The resulting chlorides were isolated by vacuum distillation in yields of 50 to 70%. Benzene solutions containing 1 mole of acid chloride were added dropwise to benzene solutions which contained 2 moles of amine at a temperature of 5°. Reaction mixtures then were refluxed. After cooling, amine hydrochloride was filtered from the system. Filtrates were water washed, dried, and freed of solvent; crystalline products were recrystallized repeatedly from *n*-hexane but compounds which were oils were not purified further.

Derivatives of chloromethylphosphonamidic acid, $ClCH_2P(O)(OH)NH_2$, were prepared from chloromethylphosphonodichloridate; 1 mole of a phenol and 1 mole of this acid chloride were allowed to react as described earlier. The resulting acid chlorides were vacuum distilled and converted to amides in the

(1) W. C. Bigelow, D. L. Pickett, and W. A. Zisman, *J. Colloid Sci.*, 1, 513 (1946).

(2) S. G. Daniel, *Trans. Faraday Soc.*, 47, 1345 (1951).

(3) D. C. Walker and H. E. Ries, Jr., *J. Colloid Sci.*, 17, 789 (1962).

(4) E. H. Loeser, R. C. Wiquist, and S. B. Twiss, *ASLE Trans.*, 2, 199 (1960).

(5) J. E. Berger, *J. Phys. Chem.*, 69, 2598 (1965).

manner described above. Some properties of these phosphoramidates and phosphonamidates are shown in Tables I and II. The structures for phosphoramidates and phosphonamidates are illustrated by I and II, respectively.

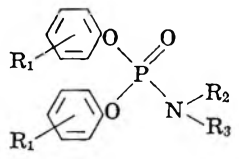

I

R_1 = H, CH_3, or C_9H_{19}
R_2 = H, C_2H_5, C_3H_7, or $C_{12}H_{25}$
R_3 = H or C_2H_5

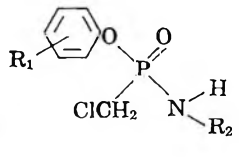

II

R_1 = CH_3 or C_9H_{19}
R_2 = H or C_2H_5

Table I: Some Properties of Amides Derived from Phosphorus Acids

Compd	No.	Mp, °C	Spectral data[a] E, l. mole^{-1} cm^{-1}	λ, A
Diphenyl N,N-diethylphosphoramidate	I	56–57	1070	2635
Diphenyl N-propylphosphoramidate	II	53–54	1065	2635
Bis(nonylphenyl) phosphoramidate[b]	III	Oil	1175	2665
Bis(*o*-cresyl) N-laurylphosphoramidate[c]	IV	59–60	1005	2645
Bis(*o*-cresyl) N-ethylphosphoramidate	V	72–73	1015	2645
Nonylphenyl chloromethylphosphonamidate[b]	VI	Oil	593	2665
o-Cresyl N-ethylchloromethylphosphonamidate	VII	40–41	521	2655
Diphenyl phosphoramidate[d]	VIII	150–151	...	...
Bis(*o*-cresyl) N-methylphosphoramidate[e]	IX	75–76	...	...

[a] Measured in isooctane at 25°. [b] Prepared by adding gaseous ammonia to the corresponding acid chloride in benzene solution. [c] Recrystallized from methanol. [d] Prepared by adding gaseous ammonia to the phosphorochloridate in chloroform solution. The product was insoluble in chloroform at room temperature and after filtration it was separated from by-product ammonium chloride by extraction with refluxing chloroform. It was not purified further. [e] The phosphonochloridate was added to a mixture of benzene and 40% aqueous methylamine.

Di-*n*-butylphosphoramidate (Aldrich Chemical Co.), octadecylamine (Matheson Coleman and Bell), Ortholeum 162 (mixture of mono- and dilauryl phosphate, Du Pont), and stearic acid (Eastman White Label) were used as received. Nonylphenoxyacetic acid (Geigy Chemical Co.) was refined by repeatedly washing with water a hexane solution of the acid. The dried hexane layer was freed of solvent and subjected to two vacuum distillations. Isooctane (Phillips Reagent) was percolated through a column packed with silica gel immediately before solutions were prepared; solvent treated in this manner contained 12 ppm of water or less.

Table II: Elemental Analyses of Amides

Compd	% C Calcd	% C Found	% H Calcd	% H Found	% N Calcd	% N Found	% P Calcd	% P Found
I	63.0	62.8	6.56	6.82	4.6	4.8	10.2	10.3
II	61.9	62.3	6.19	6.60	4.8	4.9	10.7	10.8
III	71.8	71.3	9.67	9.83	2.8	2.4	6.2	6.2
IV	70.1	...	8.98	9.06	3.2	3.2	7.0	7.0
V	63.0	63.3	6.56	6.47	4.6	4.9	10.2	10.4
VI	58.0	57.0	8.15	8.43	4.2	4.3	9.4	9.0
VII	48.5	48.5	6.06	6.11	5.7	5.5	12.5	11.7
VIII	57.9	...	4.82	4.96	5.6	5.3	12.5	12.6
IX	61.9	60.6	6.19	6.33	4.8	4.8	10.7	11.0

Iron-powder adsorption experiments involved breaking an ampoule (containing a known amount of washed and out-gassed iron powder) under the surface of a known volume of a solution of known concentration. Changes in solute concentration were monitored by ultraviolet spectroscopy. Film balance measurements were made with a heavily waxed brass trough fitted with a hanging glass slide attached to a torsion wire. Equipment and procedures for film-balance and iron-powder adsorption experiments have been described in detail previously.[5] Table I contains molar absorptivities for phosphoramidates and phosphonamidates in isooctane solution; all systems obeyed Beer's law in the concentration range employed.

Iron powder (Mallinckrodt No. 5321) employed in most of this work exhibited an area of 1.08 m^2/g when measured by the BET method[6] using noble gases. If nonylphenoxyacetic acid was used as a reference adsorbate,[5] an area of 0.937 m^2/g was found. The latter value was used in all calculations.

Results and Discussion

At 25°, phosphoramidates and phosphonamidates adsorb rapidly from isooctane solution onto iron powder. Some typical results are shown for compounds III–V in Figure 1. It was not possible to withdraw samples earlier than 1 min but even this short adsorption interval was sufficient for the systems to be at or near their equilibrium levels. Others[3,5] also have observed rapid deposition of polar additives on metals from non-

(6) S. Brunauer, P. H. Emmett, and E. Teller, *J. Am. Chem. Soc.*, **60**, 309 (1938).

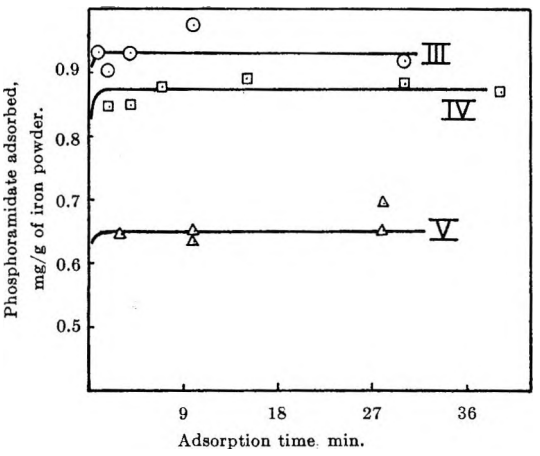

Figure 1. Adsorption of phosphoramidates from isooctane by iron powder at 25°. Labels refer to compounds listed in Table I. All concentrations are about 2m*M*.

polar solvents. Compounds of Figure 1 include those whose equilibrium adsorption levels (expressed as milligrams per gram of iron) are the highest and the lowest of the phosphoramidates studied. When the adsorption level is expressed in this manner, the amount adsorbed is roughly proportional to molecular weight of the compound. Table III illustrates this and shows that adsorption levels of phosphoramidates expressed as moles per gram of iron are reasonably constant. Estimated molecular areas calculated with the assumption of complete coverage of iron having an area of 0.937 m^2/g are shown in column 5. With the exception of compound II, molecular areas are in reasonable agreement; this may be taken as evidence that pendant alkyl groups on ester or amide moieties exert only a secondary influence on the area occupied by adsorbed phosphoramidates. In this series of compounds, alkyl substituents on the aromatic rings range from C_0 to C_9; amide nitrogens carry from zero to 12 carbons. Since estimated molecular areas do not depend markedly on the size of alkyl substituents, it seems reasonable to expect adsorption of the same portion of the phosphoramidate molecule in each instance.

Attempts were made to determine molecular areas of phosphoramidates with a film balance. Meaningful results were not obtained with compounds I, II, and V because they are slightly soluble in water. Compound III, with nonylphenyl substituents, yielded the force–area isotherm shown in Figure 2. Film collapse appears to occur at pressures from 18 to 20 dynes/cm which corresponds to a minimum molecular area of 70 to 80 A^2. Results depicted in Figure 2 should be compared with the results of Ries who found a minimum molecular area of about 45 A^2 for tri-*p*-cresyl phosphate and about 93 A^2 for tri-*o*-xenyl phosphate.[7] When extrapolated to zero pressure, both these phosphates exhibit areas of about 95 A^2.

Table III: Adsorption of Phosphoramidates by Iron Powder

Compd	Mol wt	Adsorption level, mg/g of Fe	Adsorption level, μmoles/g of Fe	Molecular area, A^2
I	305	0.58	1.9	83
II	291	0.68	2.3	67
III	501	0.93	1.9	84
IV	445	0.87	2.0	77
V	305	0.65	2.1	73

Because the phosphoramidates generally yielded flat adsorption *vs.* time plots, it was possible to construct unambiguous isotherms of concentration change. A series of isooctane solutions containing different concentrations of compound I, for example, was prepared and each solution was subjected to iron-powder adsorption experiments. When the adsorption level was plotted as a function of equilibrium concentration, a constant deposition level of 0.58 mg of phosphoramidate/g of iron was observed for equilibrium concentrations greater than 0.7 m*M*. Initial concentrations as high as 5.0 m*M* were used in this series of experiments.

The behavior of phosphoramidates in competition with other polar, adsorbable species was studied by using isooctane solutions containing two solutes in iron-powder adsorption experiments. For each series of experiments, one solute carried a chromophoric group while the other solute selected was transparent in the ultraviolet region of interest. Results of competitive adsorption experiments involving compound IV are illustrated in Figure 3. The presence of an equimolar quantity of octadecylamine reduced the adsorption of this phosphoramidate by about 10%, but the presence of equimolar quantities of stearic acid or Ortholeum 162 (a mixture of mono- and dilauryl phosphates) virtually excluded the phosphoramidate from the metal surface. Concentrations of each solute were about 2 m*M* in these experiments.

Since carboxylic or phosphoric acids appear to prevent adsorption of phosphoramidates, it was of interest to employ ultraviolet-absorbing acids and transparent amides in the reverse experiment. It might be expected that phosphoramidates would have negligible influence on the adsorption of acids by iron powder. Figure 4 presents data obtained in competitive adsorption experiments involving nonylphenoxyacetic acid (NPA) and di-*n*-butylphosphoramidate. In this

(7) H. E. Ries, Jr., and H. D. Cook, *J. Colloid Sci.*, 9, 535 (1954).

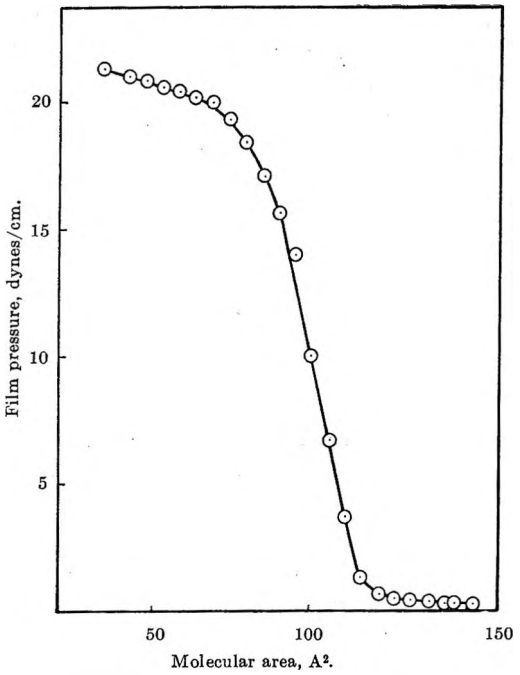

Figure 2. Force–area isotherm for bis(nonylphenyl) phosphoramidate on 0.5 *M* aqueous KCl at 25°.

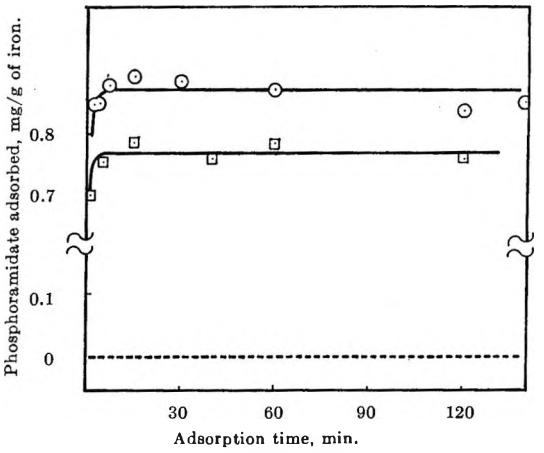

Figure 3. Competitive adsorption from isooctane by iron powder at 25°: O, bis(*o*-cresyl) N-laurylphosphoramidate (IV); □, compound IV plus octadecylamine; ———, compound IV plus stearic acid or Ortholeum 162. All concentrations are about 2 m*M*.

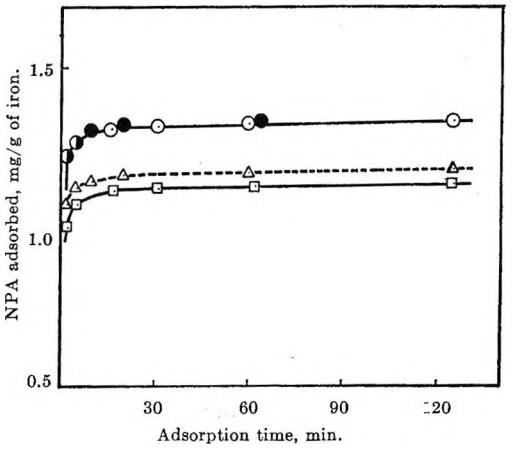

Figure 4. Competitive adsorption from isooctane by iron powder at 25°: O, nonylphenoxyacetic acid (NPA); □, NPA plus dibutylphosphoramidate; △, NPA plus water-washed dibutylphosphoramidate. All concentrations are about 2 m*M*; shaded and open circles represent duplicate experiments.

series of experiments, NPA was the chromophore and the amide was transparent in the ultraviolet region of interest. The upper curve shows the adsorption characteristic of NPA alone; the lower curve illustrates the deposition of NPA in the presence of di-*n*-butylphosphoramidate (both solutes about 2 m*M* in isooctane). A 15% reduction of NPA adsorption by iron was unexpected and prompted analysis of the di-*n*-butylphosphoramidate. A significant amount of strongly acidic contaminant (2 wt % assuming the acid to be orthophosphoric) was found in the amide. Water washing removed 70% of this unidentified acidic species, and a second competitive adsorption experiment involving NPA and water-washed di-*n*-butylphosphoramidate produced the middle curve in Figure 4. Reduction of acidic contamination in the amide causes adsorption of NPA to proceed more easily; this point was not pursued further.

Although the phosphoramidates and phosphonamidates of Table I have similar adsorption properties, differences emerge in their desorption characteristics. These differences first became apparent in long-term experiments involving adsorption of compounds I and II from isooctane solutions by iron powder. Ultraviolet spectra of 24-hr adsorption samples showed small amounts of phenol in aliquots containing compound II; no phenol could be detected with samples containing compound I. Subsequently, other phosphoramidates derived from mono-N-alkylamines or from ammonia were found to liberate phenol during long iron-powder adsorption experiments: identical solutions of these amides stored in glass out of contact with iron powder failed to show evidence of free phenol even when water was added to the systems. Precautions were taken, however, to exclude water from long-term iron-powder adsorption runs. Qualitatively, it appeared that phosphoramidates derived from ammonia produced phenols more readily and in larger amounts than did mono-N-alkylphosphoramidates.

Adsorption–desorption experiments were conducted in an attempt to measure the quantity of phenol

liberated by representative phosphoramidates which contained zero, one, and two N-alkyl substituents. Some of these results are contained in Table IV which deals with adsorption from isooctane of compounds I and II. In these experiments, adsorption was allowed to proceed for 1 hr—an interval sufficient for attaining equilibrium (see Figure 1). Iron powder then was filtered from the system and fresh isooctane (100 ml) was added to the iron; about one-third of the N,N-diethyl derivative was desorbed although negligible N-propylamide was displaced. A small quantity of phenol appeared in the supernatant solvent from

Table IV: Adsorption and Desorption of Phosphoramidates

	I. $(PhO)_2P(O)N(C_2H_5)_2$	II. $(PhO)_2P(O)NH(C_3H_7)$
Amount adsorbed,[a] mg/g of Fe	0.58	0.68
% of phosphoramidate desorbed intact by isooctane rinse at 25°[c]	36	0[b]
% of phosphoramidate desorbed intact by refluxing isooctane	0	0[b]
Moles of phenol liberated per mole of amide adsorbed	0.1	0.9

[a] Using 20 g of iron powder with a surface area of 0.937 m^2/g.
[b] Phenol identified in supernatant isooctane.

compound II. Heating the desorption systems to the reflux temperature failed to desorb intact any of compounds I or II although additional phenol was observed in the experiment with compound II. Finally, a 10-mg quantity of stearic acid was added to each of the refluxing systems; this step liberated a small amount of phenol from compound I but produced a relatively large quantity of phenol from the system containing compound II.

Iron powder used with compound II initially carried 13.6 mg of adsorbed diphenyl N-propylphosphoramidate: hydrolysis of one ester group would be expected to produce 4.4 mg of phenol. The total phenol liberated in the various desorption steps with compound II was estimated by ultraviolet spectroscopy to be 4.1 mg. Nearly all the phenol appeared in the stearic acid desorption sequence; about one-tenth as much phenol was produced by compound I.

Phosphoramidates synthesized from ammonia liberate phenol readily under the conditions used in adsorption experiments. This fact was demonstrated by adsorbing compound III from isooctane onto a different supply of iron of low surface area. After an adsorption interval of 150 min, 60 g of this iron carried a total of 14.4 mg of bis(nonylphenyl) phosphoramidate; if monohydrolysis is assumed, this quantity of adsorbate would yield 6.3 mg of nonylphenol. Following the adsorption step, the coated iron was removed from the system and washed at 25° with 300 ml of isooctane; the wash liquid was found to contain 5.8 mg of nonylphenol. Stearic acid displacement experiments were carried out at 25° (for 15 min) and at 100° (for 1 hr): additional quantities of nonylphenol amounted to 0.8 and 0.3 mg, respectively. No soluble, iron-containing species were found in these systems.

It appears that phosphoramidates adsorb on iron but that those compounds derived from ammonia or primary amines undergo facile hydrolysis at the metal surface. Somewhat similar reactions were described by Fowkes, *et al.*,[8] in a publication dealing with clay-catalyzed decomposition of dieldrin and endrin.

Some homogeneous hydrolysis experiments in both acidic and basic solutions were performed with several phosphoramidates and phosphonamidates. Compound II, for example, was hydrolyzed in mildly alkaline aqueous dioxane to yield phenol (which was identified by means of its crystalline tetrabromo derivative). Further, Van Wazer[9] reports similar results with diphenyl phosphoramidate. Hydrolysis of this compound with concentrated aqueous sodium hydroxide yields disodium orthophosphoramidic acid; hydrolysis with ammonium hydroxide produces the monoammonium salt of monophenyl orthophosphoramidic acid.

Compounds I, II, and VIII are diphenyl orthophosphoramidates derived from a secondary amine, a primary amine, and ammonia, respectively. Relative rates of hydrolysis of these compounds in alkaline, refluxing isopropyl alcohol are indicated in Figure 5. Initial concentrations of phosphoramidate and NaOH were about equal; aliquots were analyzed by titrating residual NaOH. In this reaction medium, phosphoramidates hydrolyze with increasing ease as the number of alkyl substituents on the nitrogen atom decreases.

Similarly, refluxing in a solvent mixture of 70 vol % dioxane and 30 vol % water which was 0.1 *N* in NaOH showed that those phosphoramidates derived from ammonia were more susceptible to degradation than

(8) F. M. Fowkes, H. A. Benesi, L. B. Ryland, W. M. Sawyer, E. S. Loeffler, E. B. Folckemer, M. R. Johnson, and Y. F. Sun, *J. Agr Food Chem.*, 8, 203 (1960).

(9) J. R. Van Wazer, "Phosphorous and Its Compounds," Vol. I Interscience Publishers, Inc., New York, N. Y., 1958, p 831.

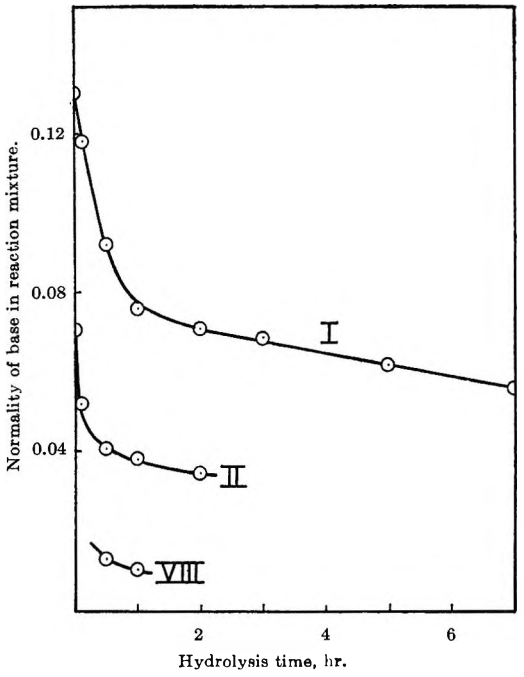

Figure 5. Hydrolysis of phosphoramidates in refluxing alkaline isopropyl alcohol. Labels refer to compounds in Table I.

those derived from primary amines. In the phosphoramidate series, compounds having $-NH_2$ moieties (III and VIII) are about 90% hydrolyzed in 5 min, but derivatives of primary amines (IV, V, and IX) suffer only about 65 to 80% hydrolysis in 15 min. Acid-catalyzed hydrolysis experiments gave similar results: phosphoramidates derived from ammonia suffer more rapid decomposition than those containing alkyl substituents on the nitrogen atom. Diphenyl N,N-diethylphosphoramidate did not hydrolyze under the conditions chosen for these experiments (a refluxing mixture of 25% water and 75% dioxane containing 0.05 mole of H_2SO_4/l.).

The effects of acidic impurities on the tribochemistry of tricresyl phosphate have been discussed by Godfrey[10] and by Klaus and Bieber.[11] These workers demonstrate that some of the observed surface chemical properties of neutral species, such as tricresyl phosphate, can be due to minor amounts of acidic contaminants. Barcroft and Daniel[12] have reported detailed studies of the action of neutral phosphate esters in which they suggest that esters adsorb on metals and then decompose *via* a hydrolytic mechanism. Results of experiments described in this paper support the view that strongly adsorbable species can be generated *in situ* at the oil–metal interface through a mechanism which involves hydrolysis.

Conclusions

Phosphoramidates and phosphonamidates adsorb rapidly from isooctane solution onto iron powder. Molecular areas of adsorbed phosphoramidates vary from about 70 to about 80 A^2 and are consistent with the area estimated for bis(nonylphenyl) phosphoramidate in film-balance experiments. The degree of coverage of iron powder by phosphoramidates is not influenced by concentration in the range from 1 to 5 mM/l. These observations indicate formation of reasonably perfect monolayers. In competitive adsorption experiments, carboxylic acids or phosphoric acids can prevent deposition of neutral phosphoramidates on the iron surface.

In long-term adsorption experiments, phosphoramidates derived from ammonia or primary amines hydrolyze at the iron surface; apparently one ester bond breaks to liberate phenol. Although the phenol can be detected in isooctane solution, the acidic fragment of the phosphoramidate remains adsorbed at the metal–hydrocarbon interface. Phosphoramidates containing the $-NR_2$ group do not undergo surface hydrolysis in iron–isooctane systems at 25°. Homogeneous hydrolysis experiments confirm that secondary amines yield phosphoramidates which are more resistant to hydrolysis than those derived from ammonia or primary amines.

(10) D. Godfrey, *ASLE Trans.*, 8, 1 (1965).
(11) E. E. Klaus and H. E. Bieber, *ibid.*, 8, 12 (1965).
(12) F. T. Barcroft and S. G. Daniel, *J. Basic Eng.*, 87, 761 (1965)

Radiolysis of the Crystalline Alkaline Earth Bromates by Cobalt-60 γ-Rays[1]

by J. W. Chase and G. E. Boyd

Oak Ridge National Laboratory, Oak Ridge, Tennessee 37831 *(Received August 9, 1965)*

The anhydrous crystalline alkaline earth bromates were radiolyzed by ^{60}Co γ-rays to decompositions exceeding 1 mole %. Bromate ion was decomposed to oxygen gas and bromite, hypobromite, and bromide ions, which were observed when the irradiated crystals were dissolved in alkaline aqueous solutions. Evidence was obtained suggesting that BrO_2 also was produced and stabilized in the crystal lattice. The bromate ion decomposition and the yields of oxidizing fragments increased nonlinearly with the dose. Bromide ion and oxygen gas yields increased linearly with dose for small doses, but at larger doses the *rate* of formation of bromide increased and then became constant, while the rate of oxygen gas production decreased slightly. The bromite ion yield initially was strongly dose dependent, but subsequently it became essentially independent of the dose. The rate of formation of hypobromite ion increased from a vanishingly small value at low doses to a maximum and then approached zero at large doses. The data were consistent with the hypothesis that bromide ion, bromite ion, oxygen gas, and possibly BrO_2 were formed directly by the dissociation of excited BrO_3^- ions, whereas hypobromite and some bromide ions were formed *via* precursors. Recombination reactions reconstituting bromate ion also occurred.

This study of the radiolysis of the anhydrous alkaline earth bromates was undertaken to elucidate further the effect of the crystalline environment on the decomposition of bromate ion by ^{60}Co γ-rays. Significant differences in radiation stability have been shown to exist between the various alkali metal bromates,[2] and it was expected that differences between the alkaline earth compounds would be observed. Differences in the stability of the molecular bromate ion in the alkaline earth salts from that in the alkali metal bromates also were expected based on observations previously made with the nitrates[3] and perchlorates.[4] The alkaline earth bromates have been shown to be less stable thermally than the alkali metal salts,[5] and their hydrates at room temperature to be more stable.

Experimental Section

The hydrated alkaline earth bromates (City Chemical Corp.) were purified by several recrystallizations from ethanol–water mixtures. The anhydrous compounds were prepared by heating (*ca.* 125°) the purified salts in a vacuum oven until a constant weight was reached. Thermogravimetric analysis confirmed that all water was removed. The weighing bottles holding the dehydrated salts were capped immediately upon removal from the vacuum oven and were stored away from light over a desiccant. Each preparation was analyzed for alkali metal, alkaline earth, and bromide ion impurities (Table I). A satisfactory preparation of anhydrous $Mg(BrO_3)_2$ could not be obtained because of its excessive thermal decomposition on drying. Heating the salt under vacuum for *ca.* 24 hr at 105° to obtain a completely anhydrous product yielded more than 800 ppm of bromide ion. Accordingly, the radiolysis for large doses only could be measured without a large blank correction.

Approximately 3–5-g amounts of the purified crystalline salts were transferred in dry nitrogen to cylindrical

(1) Presented before the Division of Physical Chemistry, 150th National Meeting of the American Chemical Society, Atlantic City, N. J., Sept 1965. Research sponsored by the U. S. Atomic Energy Commission under contract with Union Carbide Corp.

(2) G. E. Boyd, E. W. Graham, and Q. V. Larson, *J. Phys. Chem.*, 66, 300 (1962).

(3) J. Cunningham and H. G. Heal, *Trans. Faraday Soc.*, 54, 1355 (1958).

(4) L. A. Prince and E. R. Johnson, *J. Phys. Chem.*, 69, 359 (1965).

(5) J. W. Chase, to be published.

Table I: Purity of the Anhydrous Alkaline Earth Bromates (All Values in ppm by Weight)

Impurity	$Mg(BrO_3)_2$[a]	$Ca(BrO_3)_2$	$Sr(BrO_3)_2$	$Ba(BrO_3)_2$
Li^+	<2	<0.5	<5	<2
Na^+	15	81	3.3	6
K^+	<5	7	29	<5
Rb^+	<5	<2	<3	<5
Cs^+	<5	<2	<3	<5
Mg^{2+}	...	<2	<20	<30
Ca^{2+}	9	...	<1	7.8
Sr^{2+}	<3	28	...	28
Ba^{2+}	<30	31	175	...
Br^-	67.4	20.3	14.3	4.2

[a] Not anhydrous; contained *ca.* 5% H_2O.

glass vials, dried under vacuum, and closed off with Bakelite screwtop caps which were sealed with wax. Irradiations were conducted at constant geometry in a ^{60}Co γ-ray source, where the equilibrium temperature was *ca.* 35° and the dose rate was 1.61×10^{18} ev g^{-1} min^{-1}.

Dose rates were measured with Fricke dosimeter solutions as described by Boyle.[6] A molar absorbancy index at 25° of 2220 at 3030 A and $G(Fe^{III}) = 15.6$ were used in the calculations. The dose rate in each of the salts was estimated by multiplying the rate in the dosimeter solution by the ratio of the energy absorption mass attenuation coefficients at 1.25 Mev for the compound and the solution, respectively. The required (μ_a/ρ) coefficients for each of the compounds were derived as the average of the coefficients for the constituent elements weighted in proportion to the abundance of each element by weight in the compound.

Chemical analyses for radiolytic products were performed on aqueous solutions of the irradiated crystals. Previously described[7] microtitration procedures were employed in the measurements of the bromate ion decomposition and the production of bromide ion and oxidizing fragments. The yields of hypobromite and bromite were determined with a new, superior procedure involving micropotentiometric titration with arsenite in the absence and the presence of osmium tetroxide.[8] Our earlier determinations[7] of these species using the methods of Hashmi and of Chapin are believed to have given low values for the amounts of bromite present. The presence of BrO^- in alkaline aqueous solutions of irradiated $Sr(BrO_3)_2$ was demonstrated also by spectrophotometric measurements, which showed the ultraviolet absorption band of hypobromite at 330 mμ.

Oxygen yields were measured by gas chromatography. Irradiations in these instances were made under vacuum, and the radiolytic gas was collected in a closed system after dissolving the crystals in deaerated water. The strontium salt was considerably more resistant to crystal rupture than $Ca(BrO_3)_2$. Gas was detected above the latter before dissolution for doses as small as 0.12×10^{23} ev mole^{-1}, and above $Sr(BrO_3)_2$ for doses of *ca.* 1.0×10^{23} ev mole^{-1}. The amount of gas above the calcium salt was approximately five times that above the strontium bromate at large doses. Small amounts of $N_2(g)$ were observed in all the irradiations, suggesting either the occlusion of air by the crystals or a slight in-leakage during the chromatographic analysis. The observed quantities of $N_2(g)$ were used as a basis for correcting the $O_2(g)$ yield for contamination by atmospheric oxygen. No $H_2(g)$ was seen except with massive doses (15×10^{23} ev mole^{-1}), where 100-ev yields of 0.001 and 0.003 were found for $Ca(BrO_3)_2$ and $Sr(BrO_3)_2$, respectively. Very small amounts of bromine vapor were detected over $Sr(BrO_3)_2$ crystals irradiated under vacuum to a very large dose (81×10^{23} ev mole^{-1}).

Experimental Results and Discussion

The experimentally measured yields were converted to a "per mole of BrO_3^- ion" basis to facilitate intercomparisons between the various salts and with previous results on the radiolysis of the alkali metal bromates. The variation of the yields for the production of oxidizing fragments, bromide ion, oxygen gas, and for bromate decomposition with dose is given in Figures 1–3; estimated initial 100-ev yields (*i.e.*, G_0 values) are listed in Table II. The radiolysis of BrO_3^- ion occurred to a significantly greater extent in $Ca(BrO_3)_2$ than in $KBrO_3$ (*viz.*, $G_0 = 2.4$ *vs.* 1.3), and to a greater extent in $Sr(BrO_3)_2$ than in $RbBrO_3$ ($G_0 = 2.9$ *vs.* 2.3). The data for $Mg(BrO_3)_2$ are incomplete because of the difficulties mentioned earlier; however, BrO_3^- ion in this salt was appreciably more decomposed than in $NaBrO_3$, where $G_0 = 1.4$. Decomposition in $Ba(BrO_3)_2$, however, was distinctly less than in $CsBrO_3$, and the radiolytic stabilities of the alkaline earth bromates varied less from the lightest to the heaviest member studied than did those for the alkali metal salts.

The data for $Ba(BrO_3)_2$ were complicated by the fact that its radiolysis increased with the temperature at which it was vacuum dried prior to irradiation (Table

(6) J. W. Boyle, *Radiation Res.*, 17, 427 (1962).
(7) G. E. Boyd and Q. V. Larson, *J. Phys. Chem.*, 69, 1413 (1965).
(8) T. Andersen and H. E. L. Madsen, *Anal. Chem.*, 37, 49 (1965).

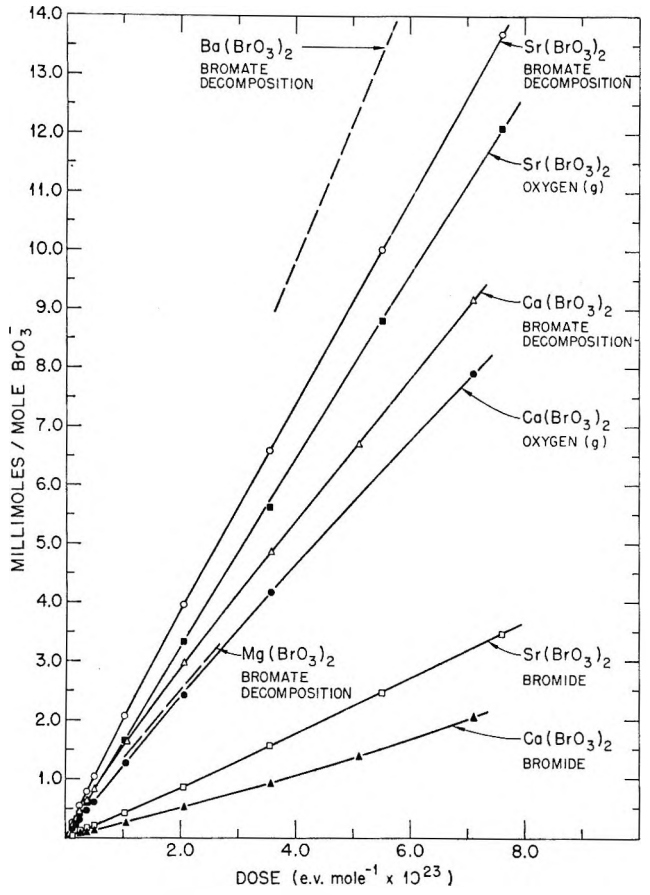

Figure 1. Radiolysis of the alkaline earth bromates by ^{60}Co γ-rays.

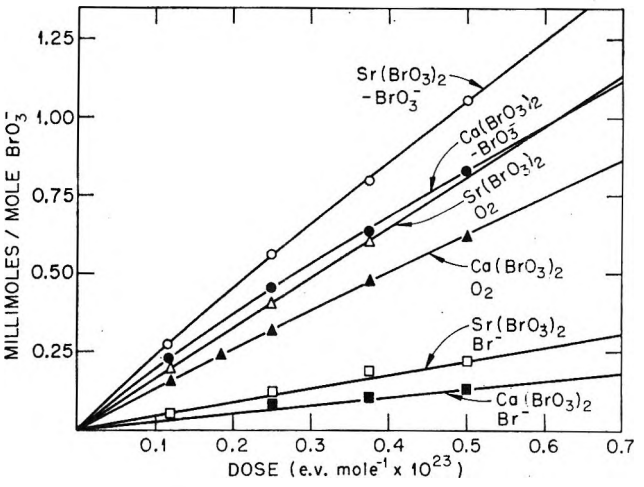

Figure 2. Radiolysis of calcium and strontium bromates at low doses.

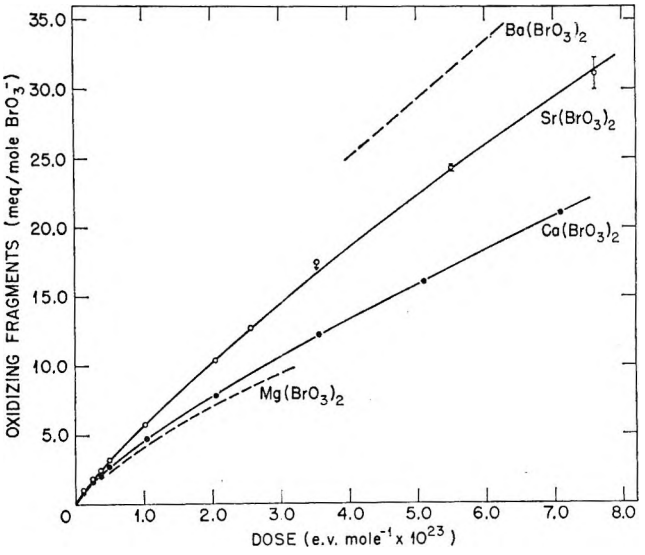

Figure 3. Production of oxidizing fragments in the radiolysis of the alkaline earth bromates by ^{60}Co γ-rays.

Table II: Initial 100-ev Yields for Radiolytic Products of the Crystalline Alkaline Earth Bromates at 35°

	$Ca(BrO_3)_2$	$Sr(BrO_3)_2$
$G_0(-BrO_3^-)$	2.36	2.87
$G_0(Br^-)$	0.33	0.51
G_0("Ox")	2.03	2.36
$G_0(O_2)$	1.51	1.96

III). The data plotted in Figures 1 and 3 for the barium salt were for preparations dried at *ca.* 120°, the temperature at which the calcium and strontium salts also were dried. Thermogravimetric analysis showed that $Ba(BrO_3)_2$ above 100° is anhydrous; therefore, a solid-state phase change was suspected. Support for this view was given by X-ray powder diffraction patterns, which revealed mixtures of different compositions to be present at each of the drying temperatures indicated. Differential thermal analysis (dta) also suggested that a phase transformation occurred whose rate appeared to reach a maximum at *ca.* 180°. No phase changes were detected in the anhydrous calcium and strontium bromates by dta, and the radiolysis of each of these salts was independent of the drying temperature. Data on the radiolysis of BrO_3^- ion in salts dried at 200° shown in Table III were taken in an earlier study.[2] It may be seen that they are consistent with the measurements on other preparations dried at lower temperatures.

The data of Figures 1 and 2 show that the decomposition of bromate ion increased nonlinearly with dose at small doses and then approached linearity for doses greater than 2×10^{23} ev mole^{-1}. The order of stability was: Mg > Ca > Sr > Ba, and the yields of oxidizing fragments, bromide ion, and oxygen were:

Table III: Dependence of the Radiolysis of Anhydrous $Ba(BrO_3)_2$ upon Drying Temperature (Dose for All Measurements 4.90×10^{23} ev mole^{-1})

Drying temp, °C	BrO_3^- decomposition, mmoles/mole of BrO_3^-	Oxidizing power, mequiv/mole of BrO_3^-
86	8.03[a]	14.65[a]
105	8.35[a]	17.26[a]
120	11.92[a]	28.96[a]
	11.75[b]	28.49[b]
170	14.28[b]	37.40[b]
~200	15.2[c]	...

[a] Preparation no. 1. [b] Preparation no. 2. [c] Data from ref 2.

Ba > Sr > Ca > Mg. The *rate* of production of bromide ion became progressively larger with increasing dose after an initial nearly linear yield–dose dependence. This behavior suggested that part of the bromide found in the irradiated crystals was formed either through thermal or radiolytic decomposition of intermediates. The production of O_2(g) in $Sr(BrO_3)_2$ was linear with dose within experimental error up to 15.5×10^{23} ev mole^{-1}; with $Ca(BrO_3)_2$ there was a slight but definite nonlinear yield–dose dependence for doses as small as 0.12×10^{23} ev mole^{-1}.

The dose dependence of the production of oxidizing fragments in $Ca(BrO_3)_2$ and $Sr(BrO_3)_2$ (Figure 3) and of bromite ion in irradiated $CsBrO_3$ (Figure 4)[9] contrasts with the yields for O_2(g) and Br^- ion in that saturation or "steady-state" concentrations of the former were approached at large doses. It, therefore, was necessary to assume that either a decomposition and/or a recombination reaction of a thermal or radiolytic nature acted to remove the oxidizing fragments. If O_2(g) were produced in the same decompositions which led to bromide ion, a similar dose dependence of the yields for these two products would have been expected. The fact that the O_2(g) yield actually was less than expected on this hypothesis indicated that a reaction which consumed oxygen occurred in the crystal. The observation that the yield of bromite ion became constant at large doses (Figure 4) suggested that this reaction was[10]

$$BrO_2^- + O \longrightarrow BrO_3^- \qquad (A)$$

The virtually linear dependence of the O_2(g) yield on dose may be explained if the oxygen atoms required in (A) were supplied predominantly by the decomposition of hypobromite

$$BrO^- \longrightarrow Br^- + O \qquad (B)$$

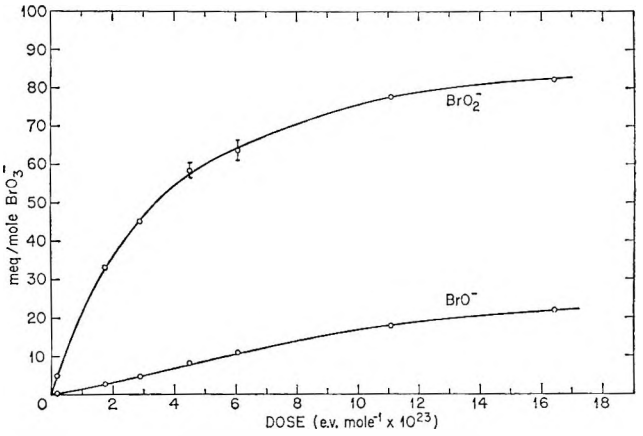

Figure 4. Yield of BrO_2^- and BrO^- in the radiolysis of crystalline $CsBrO_3$ by ^{60}Co γ-rays (hypobromite ion yield curve is convex to dose axis below 6×10^{23} ev mole^{-1}).

The effect of temperature upon the yields in crystalline $CsBrO_3$ as well as isothermal and isochronal annealing experiments with irradiated crystals of the cesium salt[7] have shown that thermal decomposition of the oxidizing fragments and thermally activated recombination reactions occur in the absence and in the presence of radiation. Hypobromite ion is known to be quite unstable and to break down to give Br^- and O_2(g); bromite is relatively stable and may be implicated as one of the fragments which reacted with oxygen to reconstitute bromate ion. Results from isothermal anneals of the oxidizing fragments produced in $Sr(BrO_3)_2$ are given in Table IV. Heating the irradiated crystals, as in the case of irradiated $CsBrO_3$, caused the removal of some of the oxidizing fragments by a reaction which was quite rapid initially followed by a much slower process. In addition, the amount of BrO_3^- ion decomposed decreased. If thermal decomposition to Br^- ion only had occurred, the BrO_3^- ion decomposition would have remained constant. Consequently, a back-reaction converting oxidizing fragments to BrO_3^- ions must have taken place. The changes observed on heating irradiated $Sr(BrO_3)_2$ may be explained by assuming a recombination reaction of BrO_2^- with oxygen (eq A) and a thermal decomposition of BrO^- to yield Br^- ion (eq B).

The dependence of the yield of hypobromite ion on dose (Figure 4) indicates that this species was not a

(9) BrO_2^- and BrO^- yields also were obtained with $Sr(BrO_3)_2$, but not to a dose sufficiently large to give a "steady-state" concentration. However, the shapes of the yield–dose curves were quite similar to those for $CsBrO_3$.

(10) The oxygen atoms consumed in eq A are assumed to have been formed by the thermal decomposition of oxidizing fragments. Reaction with radiolytically produced O atoms may have occurred to a minor extent, however.

Table IV: Isothermal Annealing (125°) of Oxidizing Fragments Produced in Crystalline $Sr(BrO_3)_2$ by ^{60}Co γ-Rays (Dose = 5.5×10^{23} ev mole^{-1})

Time of heating, hr	Oxidizing power, mequiv/mole of BrO_3^-	Bromate decomposition, mmoles/mole of BrO_3^-
0	24.5	10.2
0.5	21.4	9.92
1	20.2	(8.83)
2	(21.1)	9.91
3	(21.0)	9.73
5	19.2	9.51
8	18.8	9.90
16	18.8	9.52
30	18.5	9.47
46	18.9	9.76

primary radiolysis product of BrO_3^- ion. At small doses the BrO^- yield was zero within experimental error, but subsequently it increased in a manner similar to that observed with bromide ion. However, in contrast to the Br^- ion yield, at large doses (*i.e.*, >10 $\times 10^{23}$ ev mole^{-1}), the yield of hypobromite became independent of dose. The yield of BrO^- also showed a distinct temperature dependence: at −196° and a dose of 1.75×10^{23} ev mole^{-1}, the amount produced in $CsBrO_3$ was 40% smaller than at room temperature. In contrast, the yield of BrO_2^- was changed by only *ca.* 5%, as expected for a species formed by a direct process. Analogous observations have been made in the radiolysis of $KClO_4$, where hypochlorite was found but not as a primary radiolytic product.[11] The lack of a dependence of the BrO^- yield on dose at large doses (*i.e.*, "steady-state" BrO^- ion concentration) may be understood if this ion decomposed thermally at the same rate as it was formed from a precursor.[12]

Information as to the nature of the precursor of hypobromite ion may be inferred from the average oxidation number, $\bar{Z}$, of bromine in the oxidizing fragments. The ratio of the measured "total oxidizing power" (mequiv g^{-1}) of the radiolyzed crystals (Figure 3) to the mmoles g^{-1} of bromine contained in the fragments as estimated from the difference in the bromide ion and bromate decomposition yields (Figure 1) gives the average change in oxidation number, $\bar{Z} + 1$, involved in the complete reduction of the fragments. The dependence of $\bar{Z}$ (mequiv mmole^{-1}) on the extent of bromate ion radiolysis is shown in Figure 5. Initially, $\bar{Z}$ was greater than 3.5, but this decreased rapidly, followed by a gradual decrease to an apparent limiting value of *ca.* 2.0. Although the latter value corresponds to an equimolar mixture of BrO_2^- and BrO^- ions, a

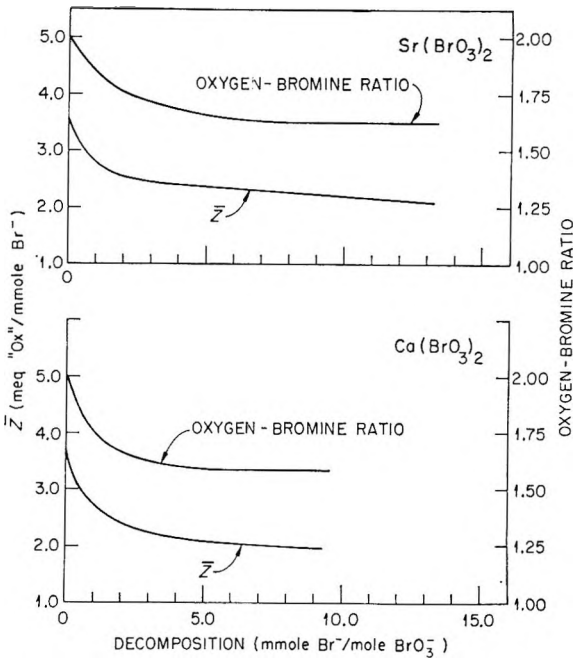

Figure 5. Oxidation number and oxygen–bromine ratio of an average oxidizing fragment as a function of bromate decomposition.

value greater than 3.5 requires that species of higher oxidation number also be present in small amounts. These species appeared to be quite unstable thermally; it seemed logical to suppose that they might have been the free radicals, BrO_2 and BrO_3.

Indirect evidence that the species BrO_2 was an intermediate in the radiolysis may be found by estimating the average amount of oxygen in the oxidizing fragments. The stoichiometric composition of an "average fragment" was computed from the difference between the amount of O_2(g) expected (assuming 1.5 moles of gas released per BrO_3^- ion decomposed) and the amount of O_2(g) measured experimentally divided by the amount of bromine in the fragments. As may be seen (Figure 5) as the decomposition increased, the composition of an "average fragment" in $Ca(BrO_3)_2$ decreased from $BrO_{2.0_0}$ to $BrO_{1.6_0}$ and in $Sr(BrO_3)_2$ from $BrO_{2.0_1}$ to $BrO_{1.6_3}$. If only BrO_2^- and BrO^- had been formed initially, the composition would have been less than the $BrO_{2.0}$ observed; if only BrO_2^- were produced, the observed stoichiometry would have obtained, but $\bar{Z}$ would have been too small; if BrO_3 were formed, both $\bar{Z}$ and the observed average ratio of oxygen to bromine would have been too small. Accordingly, it was assumed that the oxidizing

(11) L. A. Prince and E. R. Johnson, *J. Phys. Chem.*, 69, 377 (1965).

(12) No evidence was found for the thermal or the radiolytic decomposition of BrO_2^- to form BrO^-.

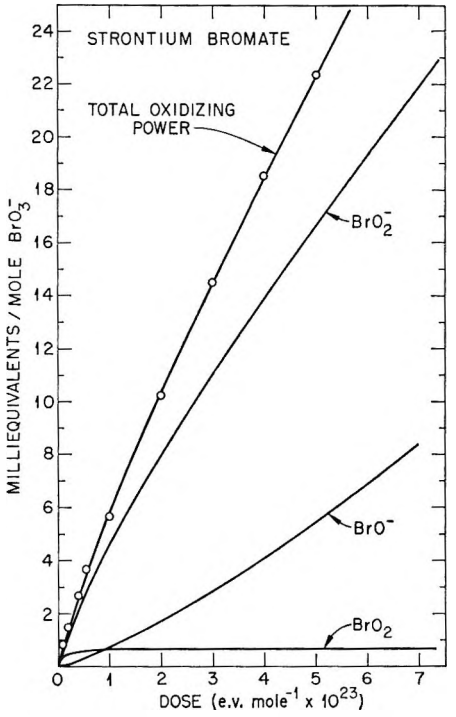

Figure 6. Calculated oxidizing fragment yields as a function of dose (curve for total oxidizing power from experimental measurements in Figure 3; note similarity of dose dependence of BrO^- and BrO_2^- yields to those observed in Figure 4).

power of the irradiated crystals could be attributed to three species, BrO_2, BrO_2^-, and BrO^-. The data of Figures 1 and 3 for $Ca(BrO_3)_2$ and $Sr(BrO_3)_2$ were "smoothed" with a computer program, and values of $\bar{Z}$ and O:Br were calculated for interpolated doses. These values served to establish two equations relating the fraction of each oxidizing species present, and, with a "material-balance" equation, algebraic solutions for the percentages of BrO_2, BrO_2^-, and BrO^- were obtained. The concentrations of these species then were found from the known concentrations of bromine in all the oxidizing species. The dependence of the calculated yields expressed as mequiv mole^{-1} on the radiation dose in $Sr(BrO_3)_2$ is shown in Figure 6, and the variation of the 100-ev yields estimated from Figure 6 are shown in Figure 7. A check on the calculations was afforded by stoichiometry

$$G(O_2) = {}^1/_2G(BrO_2) + {}^1/_2G(BrO_2^-) + G(BrO^-) + {}^3/_2G(Br^-) \quad (C)$$

Thus, for a dose of 0.1×10^{23} ev mole^{-1}, $G(O_2)_{calcd} = 1.96$ compared with the experimental value of 1.95. The oxidizing power yield also may be estimated from the calculated concentrations of BrO_2, BrO_2^-, and BrO^-; thus, for a dose of 0.1×10^{23} ev mole^{-1}, the

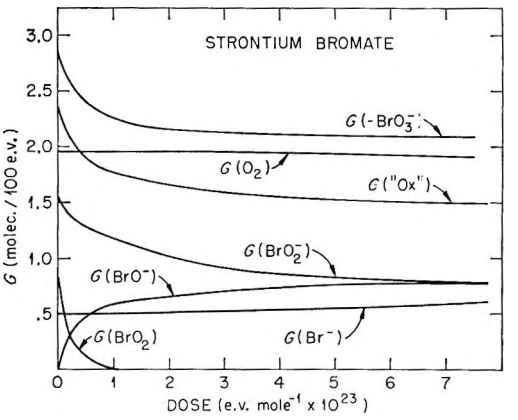

Figure 7. Dose dependence of 100-ev yields for $Sr(BrO_3)_2$ (values for BrO_2, BrO_2^-, and BrO^- were calculated).

estimated oxidizing power was 0.82_1 and the experimental value was 0.82_0 mequiv mole^{-1}.

The foregoing treatment shows that the assumption of one additional radiolytic species, BrO_2, is sufficient to account for all of the observed radiolytic yields. It also must be assumed that BrO_2 was stabilized within the crystal and that when the crystal was dissolved, BrO_2 reacted with arsenite to produce Br^- ion. The presence of species such as BrO_3 or BrO_4^- was not required. The necessary yields of BrO_2 appear to be quite small and relatively unimportant except for small doses. A direct identification of this species in the irradiated crystal, however, remains to be obtained.[13,14]

The following radiolytic mechanism summarizes the state of our knowledge of the radiolysis of bromate ion at this time

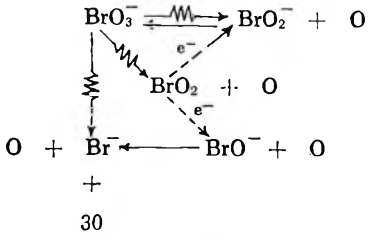

In this mechanism BrO_2 is assumed to capture a secondary electron and dissociatively deexcite to give BrO^- ion and an oxygen atom, or, alternatively, BrO_2^-. The species BrO_2^-, BrO^-, and BrO_2 all reach "steady-state" concentrations at large absorbed doses, and the radiolysis of BrO_3^- ion then goes effectively to Br^-

(13) The assumption of BrO_2 does not seem unreasonable as, in the radiolysis of $KClO_3$, ClO_2 is reported to be formed (*cf.* ref 14) and also in the radiolysis of the alkali metal and alkaline earth perchlorates (*cf.* ref 4).

(14) H. G. Heal, *Can. J. Chem.*, **37**, 979 (1959).

ion and oxygen gas. A mechanism analogous to the above will describe the radiolytic decomposition of $KClO_3$ by X-rays[14] to form $O_2(g)$, ClO_2^-, ClO_2, ClO^-, and Cl^-.

The Effect of the Properties of Solvents of Various Dielectric Constants and Structures on the Photoionization of the Leucocarbinols and Leucocyanides of Malachite Green, Crystal Violet, and Sunset Orange and Related Phenomena

by Edward O. Holmes, Jr.

Hughes Research Laboratories, Malibu, California *(Received August 12, 1965)*

Photoionization occurs only in solvents whose dielectric constant is greater than 4.7. Malachite green leucocyanide shows 100% photoionization in three straight-chain alcohols but less in chlorinated hydrocarbons; hence, a "chemical factor" is present. The photoionization of the leucocyanides of crystal violet and sunset orange in absolute alcohol are reported. The average λ_{max} and absorbance ratios of malachite green leucocyanide were determined in various solvents after various treatments. The anomalous photochemical behavior of malachite green carbinol in ethyl alcohol is interpreted on the basis of two forms, one of which is nonphototropic. The absorption bands of crystal violet, malachite green, and sunset orange ions are related to structure.

I. Historical

The reason for the choice of this problem is that in 1957 the author[1] published a paper on the degree of photoionization of malachite green leucocyanide (MGLC) in solvents consisting of mixtures of two of the following: (1) *n*-hexane, (2) 1,2-dichloroethane, and (3) 1,1-dichloroethane. It was discovered that photoionization increased with increasing dielectric constant of the solvent. Very little photoionization occurred at values below 4.5, but above this value photoionization increased rapidly. Although the dipole moment of the solvent increased at the same time, it was felt that the effect was due largely to increasing dielectric constant (ϵ).

Sporer[2] states that "the dielectric constant is not the sole criterion for photoionization...." Hence, it seemed both interesting and worthwhile to undertake an investigation to determine whether or not a "chemical factor," also, might not be influential, and to learn something about its nature.

II. Qualitative Results

To begin with, solutions of malachite green leucocyanide (MGLC) in solvents of various dielectric constants were made up and irradiated with ultraviolet light transmitted through a Pyrex filter. It was noted whether or not photoionization occurred by visually observing the appearance of the characteristic color of the carbonium (MG^+) ion.

It was found that photoionization began with solvents whose dielectric constants were in the range ϵ = 4.5–4.7, except for diethyl ether where no photoioniza-

(1) E. O. Holmes, Jr., *J. Phys. Chem.*, **61**, 434 (1957).

(2) A. H. Sporer, *Trans. Faraday Soc.*, **57**, 983 (1961).

Table I: Qualitative Results on Photoionization of Malachite Green Leucocyanide in Solvents of Various Dielectric Constants

Name	Dielectric constant (ϵ)	Dipole moments, D.	Photo-ionization[a]	Remarks
Cyclohexane	2.05	0	−	
n-Hexane	1.85	0	−	
Dioxane	2.20	0	−	
Carbon tetrachloride	2.24	0	−	
Tetrachloroethylene	2.30	0	−	
Benzene	2.28	0	−	
Diethyl ether	4.335	1.27 in benzene	−	Blue fluorescence
Trichloroacetic acid	4.6	1.1	−	Dimer
Chloroform	4.8	1.11 in benzene	+	
n-Butylamine	5.3	1.40	−	Unusual yellow, fades
Glacial acetic acid	6.15	1.74	+	Stable color
α-Chlorotoluene	7	1.85	+	Stable 25 days
Chlorocyclohexane	7.6	2.3	+	
1,2-Dichloroethane	9.9	1.89	+	
1,1-Dichloroethane	10.23	2.07	+	
Chloroacetic acid	12.3	1.524	+	
1-Hexanol	13.3	1.64	+	
Cyclohexanol	15	1.9	+	
t-Butyl alcohol	15.8	1.66	+	
1-Butanol	17.8	1.62	+	
Isopropyl alcohol	18.3	1.6	+	
Isopropyl alcohol	18.3	1.75	+	
Methyl ethyl ketone	18.3	2.79	+	
n-Propyl alcohol	20.1	1.69	+	
Acetone	21	2.89	+	Stable 25 days
Ethyl alcohol	24.3	1.69	+	
Dimethylformamide	36.7	3.5	+	Fast reversal
Methanol	37.2	1.7	+	
Acetonitrile	38	3.9	+	
Water	78	1.84	+	*b*
Ethylene carbonate	85.1	4.87	+	
Formamide	109	3.2	+	
n-Methylformamide	182.4	...	+	
Hexylamine[c]		1.32–1.59 in benzene	−	
Methyl sulfoxide[c]	...	4.3	+	Color fades in 2 hr
Trichloroacetonitrile[c]	...	2.0	−	Slight yellow through Pyrex, ppt with quartz ultraviolet

[a] + = occurs; − = does not occur. [b] See quantitative results where $N_{H_2O} = 0.98$ (N_{H_2O}, mole fraction of water). [c] These cannot be positioned as complete data are not available.

tion occurred but a strong blue fluorescence was observed.

Table I gives a complete list of the various solvents tried and the results obtained.

III. Preparations

A. Malachite Green Leucocyanide. It was found quite impossible to prepare malachite green leucocyanide directly free from contamination by the carbinol. Hence a new method of purification was devised that gave a pure product quickly and easily. The impure malachite green leucocyanide was prepared by treating a solution of 2 g of malachite green oxalate (Eastman) in 1 l. of water with another solution containing 2 g of potassium cyanide in an equal volume of water. After allowing the precipitate to settle for 2 hr, the crude leucocyanide was removed by filtration and washed with water.

It was then dissolved in benzene and shaken in a separatory funnel with a dilute solution of potassium cyanide, twice, to convert a maximum amount of oxalate to the leucocyanide. Then, the carbinol remaining as an impurity was extracted by shaking the benzene layer with a very dilute water solution of hydrochloric acid. This was repeated several times until the acid solution was colorless. Finally, the remaining acid was extracted from the benzene layer by shaking with water.

The benzene layer was now bright yellow. This color was easily removed by treatment with animal charcoal. Following filtration, the benzene solution was evaporated on a hot plate until crystallization began. Now three to four times the volume of *n*-hexane was added and the resulting solution was evaporated slowly until white crystals started to form. On cooling, a large crop of pure white crystals, mp 188°, resulted which was dried in a vacuum pistol at the temperature of boiling chloroform. Recrystallization from hexane showed no change in color or melting point.

B. Malachite Green Carbinol. The crude carbinol was made similarly to the crude leucocyanide, using sodium hydroxide in place of potassium cyanide. In this case, purification by extraction with acid was not applicable owing to the ease of reaction of the carbinol with the slightest trace of acid.

A great deal of effort was expended in the purification of the crude product to get colorless crystals with the same melting point. The melting points of crystals obtained by various methods varied from 102 to 121° and the crystal form from needles to hexagonal dendrites from the same *n*-hexane solution, depending solely on the rate of crystallization.

Many of our preparations were light green. It was found that the color could be completely removed by dissolving these in ether. The solution was now water-white. *n*-Hexane was added and the carbinol crystallized from this solvent. The crystals were dried as usual in a vacuum pistol in subdued light but frequently turned green again.

Table V will show that the physical properties were the same regardless of crystal form and melting point. Others[3] have reported this variation in melting point and crystal form.

C. Preparation of Crystal Violet Leucocyanide and Carbinol. The cyanide was prepared in a manner similar to that of the malachite green leucocyanide and had a melting point of 283°. In the preparation of the carbinol, we experienced the same type of difficulties as with malachite green carbinol but finally succeeded in obtaining crystals that were very pale purple and melted with decomposition at about 189°.

D. The Preparation of Sunset Orange[4] *Carbinol and Leucocyanide.* The preparation of the carbinol is adequately described by Walba and Branch.[5]

To prepare the leucocyanide, the carbinol was converted to the dye by dissolving in ether and shaking with dilute hydrochloric acid solution. After separating the layers, the water layer containing the dye was treated with an aqueous solution of potassium cyanide. As no precipitation occurred, a concentrated solution of sodium hydroxide in water was added drop by drop until a heavy, finely divided precipitate was formed and the solution became colorless. The precipitate, largely the leucocyanide, was extracted with ether several times. The ether layer was then extracted with dilute hydrochloric acid many times until both the ether layer and the water layer were colorless. Now the excess acid was removed by extracting the ether layer with water. It was found that the addition of an equal volume of *n*-hexane to the ether layer facilitated the extraction with acid.

The ether–hexane layer that now contained the leucocyanide free from carbinol was evaporated to dryness at room temperature with the aid of a jet of dry nitrogen and yielded long brown needlelike crystals which, after drying at the temperature of boiling chloroform, gave a melting point of 160°.

This product, in solution in absolute alcohol, produced no color when treated with hydrochloric acid, showing that this leucocyanide, like those of crystal violet and malachite green, is not acid sensitive and, in addition, that it contained no carbinol.

IV. Procedure

As our initial objective was to ascertain whether or not there was a "chemical factor" in addition to the dielectric constant of the solvent that affected the degree of photoionization, we proceeded in the following manner.

Two series of solvents were chosen in which the variation in structure followed, as far as possible, a regular pattern, and all the members possessed a relatively high degree of purity. The first series consisted of ethyl, *n*-propyl, and *n*-butyl alcohols and the second of 1,6-dichlorohexane, 1,2-dichloroethane, 1,1-dichloroethane, and chloroform.

Solutions of malachite green carbinol in the various

(3) V. Villinger and E. Kopelschini, *Ber.*, 45, 2916 (1912).

(4) Name assigned by author for the N-dimethylaminotriphenylmethyl cation: E. O. Holmes, Jr., *J. Phys. Chem.*, 62, 884 (1958).

(5) H. Walba and G. E. K. Branch, *J. Am. Chem. Soc.*, 73, 3347 (1951).

Table II[a]

Solute		Solvent: EtOH	*n*-PrOH	*n*-BuOH	1,6-Dichlorohexane	1,2-Dichloroethane	1,1-Dichloroethane	$CHCl_3$
Malachite green carbinol								
Original solution	λ_{max}	264	265	265	...	268	268	...
Corresponding	*A*	0.76	0.68	0.88	...	0.72	0.76	...
x band on addition of excess HCl	λ_{max}	622	624	624	627	622	622	622
	A	2.37	2.33	2.35	2.41	2.27	2.43	1.04
x band on max irradiation, no HCl	λ_{max}	620	623	624	625	263	622	622
	A	1.95	0.95	0.65	1.83	1.60	1.70	1.48
% photoionization		82	41	28[b]	77	70	70	?
Malachite green leucocyanide								
Original solution	λ_{max}	272	272	272	...	...	274	274
	A	0.91	1.06	1.05	...	...	0.67	0.96
x band, excess HCl, then max irradiation	λ_{max}	622	623	625	625	630	622	610
	A	2.38	2.35	2.30	1.6	2.1	0.48	0.08
% photoionization		100	100	98	66	92	20	8

[a] All wavelengths are in millimicrons; all concentrations were converted to 2.17×10^{-5} *M*. [b] See section on detailed discussion.

pure solvents were made as nearly as possible to the same concentration (2.17×10^{-5} *M*, for comparison with earlier work by the author at this concentration[1,4]) and the ultraviolet spectra were obtained on a Cary 14 spectrophotometer. Then a minute amount of hydrochloric acid (about 20×10^{-5} *M*) was added to convert all the carbinol into the ionic form (MG^+), and now the visible as well as the ultraviolet spectrum was scanned. A second trace of hydrochloric acid was added, and the range was rescanned as a check on the first run.

Another portion of the same solution was irradiated with a PEK-200 super high-pressure mercury arc lamp through a Pyrex filter and a layer of water to remove wavelengths below 290 mμ and heat. The irradiations were repeated until maximum values were obtained for the peak of the strongest band (λ_{max} 622 mμ x band). By dividing this maximum value by that of a solution of the carbinol of corresponding concentration, which had been completely converted by acid into the carbonium ion (MG^+), and multiplying by 100, the percentage photoionization was calculated.

A similar radiation procedure was used with the leucocyanide except that previous to irradiation an excess of hydrochloric acid was added to prevent any reverse reaction. The same procedures were used in the cases of the carbinols and leucocyanides of crystal violet and sunset orange.

The results are tabulated in Tables II–IV.

Table III[a]

		Crystal violet: Carbinol	Crystal violet: Leucocyanide	Sunset orange: Carbinol	Sunset orange: Leucocyanide
Original	λ_{max}	264	272	262	269
	A	...	1.53	0.43	0.49
x band with excess HCl, then max irradiation	λ_{max}	589	...	465[b]	...
	A	2.35	...	0.29	...
x band with excess HCl, then max irradiation	λ_{max}	...	589	...	465[b]
	A	...	2.37	...	0.31
% photoionization		...	101	...	100+[c]

[a] All wavelengths are given in millimicrons; solutions are in absolute ethanol. [b] Considered by the author to be the y band. [c] Reverse reaction was so fast that it was impossible to measure (see section on flash photolysis).

Table IV

Solute[a]	Mole fraction of water	λ_{max}, mμ (*A*)	λ_{max}, mμ (*A*), after addition of acid	Dielectric constant (ε)
Malachite green leucocarbinol	0	263 (0.76)	624 (2.37)	24.3
Malachite green leucocarbinol	0.76	261 (0.59)	622 (2.25)	62[b]
Malachite green leucocarbinol	0.98	255 (0.42)	618 (1.62)	75[b]
Malachite green leucocarbinol	0.98	After 12-min irradiation *A* = 1.18; photoionization 73%		

[a] In ethanol–water. [b] Computed assuming linearity.

V. Discussion of Results

Table II presents the data necessary for the calculation of the percentage photoionization of both malachite green leucocarbinol and leucocyanide in various solvents according to the method described in part IV.

It may be seen that the photoionization of the carbinol varies irregularly in all the solvents used. On the other hand, that of the cyanide is 100% or close to it (estimated error 2%) in the three alcohols used. However, in the four other solvents used (all chlorinated hydrocarbons) the leucocyanide shows a distinct "chemical factor" related to the positions of the chlorine atoms in the molecule.

When the chlorine atoms are at the end of the chain, as in 1,2-dichloroethane, the photoionization is a maximum, namely, 92%, but when they are adjacent on the same carbon atom, as in 1,1-dichloroethane, it is only 20%. This is most interesting as the dielectric constants of the two are 9.9 and 10.23, and their dipole moments are 1.89 and 2.07, respectively—very close to each other.

Earlier results by the author[1] under quite different conditions of irradiation showed a difference in the same direction but not so great (3:2).

The value of 66% for the photoionization in 1,6-dichlorohexane may be attributed to the greater separation of the two chlorine atoms in the molecule although there remains the possibility that a lower dielectric constant (not yet determined) might be partially responsible.

The low degree of photoionization in chloroform solution is the result of its dielectric constant being so very close to the marginal value ($\epsilon = 4.54$–7, see Table I).

Table III is similar in structure to Table II and gives the results of the photoionization of crystal violet leucocyanide (100%) and sunset orange leucocyanide (100+%) in absolute alcohol. Nothing unusual was experienced in the case of the crystal violet. However, in the case of sunset orange the average value for the absorbance of the y band produced photochemically from the leucocyanide (0.31 at 465 mμ, SO^+, having no x band), came out larger than the corresponding value (0.29) for the same band from conversion of the same concentration of the carbinol into the colored ion (SO^+) photochemically, an obviously impossible result.

The source of trouble seemed to be in the acid conversion. In half of the runs, the absorbance values of the peaks for the y bands (465 mμ) went through a maximum; in the other half, they reached a constant value as acid was added in the most minute amounts. In every case, the value was lower than that obtained with photoionization of the leucocyanide. Even here trouble was enhanced by a reverse reaction that could not be prevented by the addition of acid before irradiation, as was possible with crystal violet and malachite green. More knowledge, which was gained on the unusual behavior of sunset orange by flash photolysis, will be presented in a following section.

In order to determine the degree of photoionization in a transparent stable medium of high dielectric constant such as water, it was necessary to dilute alcoholic solutions of the solute by slowly adding water. In this way we were able to attain a mole fraction of water (equal to 0.98) so large that the solute molecules were in an environment closely approximating that of water.

Table IV gives the results obtained showing the values of λ_{max} and absorbancy with changing environment. The first line in Table IV is taken from Table II to facilitate comparison. It is interesting to note how much the values of λ_{max} and absorbancies change as the proportion of water is increased. This is not surprising as the partial molal values of the physical properties of water–alcohol vary unevenly and to a considerable extent, and surely affect the optical properties.

Table IV gives only one determination of the photoionization of malachite green leucocyanide—that in which the proportion of water was the greatest (N_{H_2O} 0.98). This was made at standard concentration (2.17×10^{-5} M). Allowance for change in volume of solution on mixing of the two components had to be made in all cases.

The fact that the solution with the highest proportion of water which has a dielectric constant about three times as great as pure ethyl alcohol is only 73% photoionized is added evidence of the influence of a "chemical factor," and considering all the results in the Tables II–IV, the author feels that he has established beyond the question of a doubt that "the dielectric constant is not the sole criterion for photoionization."[2]

The Anomalous Behavior of Malachite Green Leucocarbinol. On account of the wide variation in the melting points and crystal forms of malachite green leucocarbinol (*cf.* part III B) and the unusual phototropic behavior of the low and high melting forms (Table V, part I), a special effort was made to interpret these differences.

Table V contains the average values of several determinations with each of the forms. Infrared spectra on the solid forms in potassium bromide and also in liquid carbon tetrachloride solution showed no differences between them.

In search for a criterion that would be most significant in revealing any differences in the photochromic properties, it was decided to determine the initial rate of increase of the absorbance of the x band peak

Table V[a]

	Sample A	Sample B
Part I. Average Initial Values		
Mp, °C	103	121
A	0.75	0.75
Corresponding λ_{max} of peak, mμ	266	265
Corresponding x band peak after addition of acid, mμ	624	625
A of x band peak after addition of acid	2.32	2.35
Part II. Value after Irradiation to Pseudo-Stationary State In Visible Region		
λ_{max} of x band peak, mμ	623	622
% photoionization based on absorbancy increase of x band	31	23
Fading rate of peak value (A decrease/min av A of interval) (concn 1.55×10^{-5} M)	−0.008/0.3	−0.22/0.3
Initial photolysis rate at start (zero time) increase in A of x band/min at 2.17×10^{-6} M)	0.95	0.57
In Ultraviolet Region		
A at λ_{max} at pseudo-stationary state	0.49	0.42
% photolysis based on above value	42	41
% decrease in absorbance on addition of acid	33	32
λ_{max} after irradiation and acid, mμ	251	254
Corresponding A	0.23	0.23
Portion of A attributable to h band peak	0.15	0.15
A that could be attributed to dimethylaniline if it is assumed that one molecule of malachite green leucocarbinol is photolyzed so as to produce two molecules of DMA (above)	0.08	0.08

[a] All values adjusted to a concentration of 2.17×10^{-5} M of carbinol in n-butyl alcohol, unless otherwise stated.

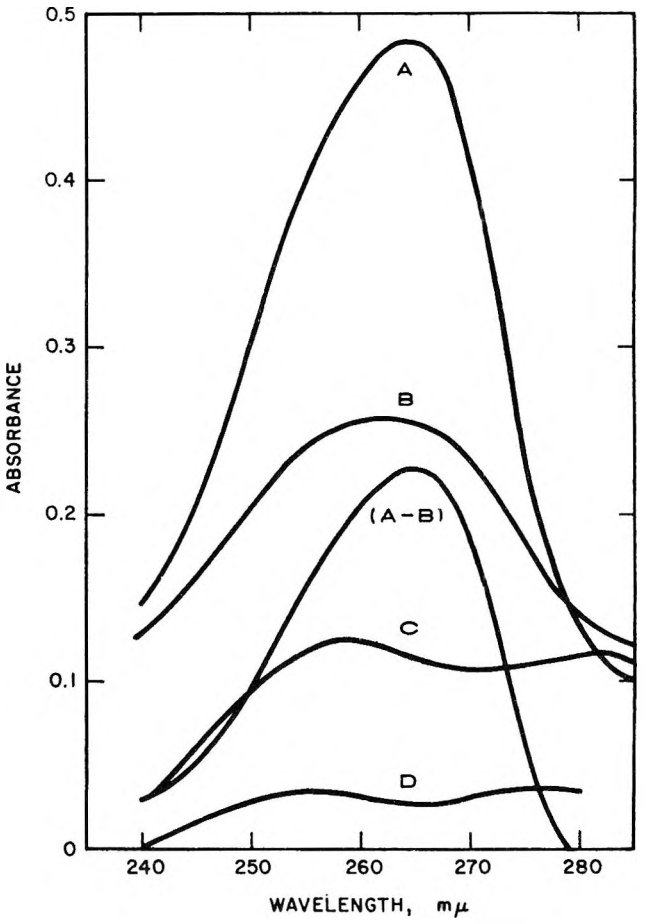

Figure 1. Malachite green leucocarbinol in n-butyl alcohol (1.32×10^{-5} M): A, original solution; B, at pseudo-photostationary state; A-B, difference of above curves; C, after addition of excess HCl; and D, contribution of h band (computed).

(624 mμ). Under these conditions, all the carbinol is present and there is no appreciable reverse reaction. To obtain these data, extrapolation methods were used. Preliminary results, although not precise, indicated a very large difference in the initial rates of the two forms.

In order to be sure that each sample received exactly the same amount of light, a simple apparatus was devised that we named the "spin-rotor," whereby the contents of four test tubes could be irradiated in a beam of light while being rotated at about 200 rpm. All solutions of malachite green leucocarbinol in n-butyl alcohol were diluted to exactly the same concentration. Checks using the same solution in all four test tubes gave excellent results. Measurements in the visible spectrum (Table V, part II) show the lower melting form to have about 50% greater rate of photoionization than the higher, which is so far beyond the limit of any possible experimental error that it was considered quite significant.

The balance of the data in Table V was obtained in the following manner. To illustrate the various steps we are introducing Figure 1 which gives the absorbance curves of a typical run. To begin with, the absorbance and corresponding λ_{max} in the ultraviolet of the original solutions of the carbinols were measured immediately after the solutions were made up (curve A). Then a minute amount of hydrochloric acid was added to convert all the carbinol into the ionic form, and all absorbances were measured throughout the spectrum. More acid was added as a check on these values (Table V, part I, lines 4 and 5). Next, another portion of the same solution was irradiated successively

until what appeared to be a stationary state was reached. However, in nine cases out of ten the absorbance of the x band peak rose to a maximum and then started to decrease so that we termed the maximum to be a "pseudo-stationary state" (curve B, Figure 1). The rate of the reverse (thermal) reaction for this band peak was now determined by allowing the chart of the Cary to run while the instrument remained at a constant wavelength. As soon thereafter as possible, the λ_{max} and absorbancies in the ultraviolet were read, and frequently the recovery rate of the latter was determined. Finally, excess hydrochloric acid was added and all absorbancies and values were measured again (curve C, Figure 1).

VI. Interpretation of Results

As our primary object is to find and interpret, if possible, any differences in photochemical behavior between the low- and high-melting forms of the carbinol, we will begin with the 50% (70% from preliminary runs) difference in the initial rate of formation of the carbonium ion MG^+.

Neither the ultraviolet nor the infrared spectra showed any evidence of impurities that might be responsible. Hence, it appears that in solution the carbinol molecules exist in two types of clusters, one having different photochromic properties than the other. Some basis for this assumption is the recent work of Ericks and others, who have discovered that triphenylmethyl perchlorate ionic crystals[6a] (and also those of *p*-roseaniline perchlorate[6b]) contain benzene rings surrounding the methyl carbon atom which resemble right-handed and left-handed overlapping propeller blades. Now if this arrangement were present in the carbinol crystals and gave two different types of clusters on solution, one having, for example, more of the left-handed form than of right, a difference in photochemistry would undoubtedly be observed.

A second phenomenon that seemed most unusual was the difference between the measured and the calculated rates at the "pseudo-stationary state." It was possible to measure the rate of decrease of absorbance of the peak of the x band (623 mμ), as already mentioned. Now at the stationary state, the rate of decrease of absorbance and its rate of increase must be equal and opposite.

From the initial rate of increase of the x band at zero time of $0.95\Delta A$/min (Table V, part II, line 4) and the absorbancies of the MGOH at the start and at the stationary state (0.75 and 0.49 for sample A), it should be possible to calculate the rate of formation of the carbonium ion MG^+ assuming that the latter value (λ_{max} of curve B in Figure 1) truly represents the amount of photolyzable MGOH. Hence, the calculated rate of the stationary state is $(0.49/0.75)\cdot 0.95 = 0.62$, which, corrected for concentration differences, is 0.44. This is 55 times as large as the measured rate ($-0.008/0.3$). This must mean that in the photostationary state there is not nearly so much photoionizable carbinol as one would assume. Although these figures are approximate, the difference is so enormous that it cannot be due to experimental error and suggests that there must be a form of carbinol that can not be photoionized but yet reacts with acid to form the MG^+ represented by curve C (Figure 1) and the ultraviolet data in Table V, part II. The possibility that its curve B might be due to the butyl ether of malachite green formed in the solution itself is ruled out by the fact that the ether can be photoionized to the extent of 72%.

We checked our basic assumption by integrating the area under several absorption curves and found it proportional to the absorption at λ_{max} in the concentration range used above to within a few per cent.

Curve A-B in Figure 1 might be considered the absorption curve of the photoionized carbinol. Its λ_{max} is slightly to the right of that of curve B and much to the right of curve C which leads us to surmise that curve A is a composite curve.

The final results on samples A and B seem to be the same but this is not surprising as now there remains only the absorbance of the photoproducts and that due to the h band in this far-ultraviolet region (see part VII).

We regret that it is impossible to give an unequivocable interpretation of the rather conflicting data but are strongly inclined to believe that two forms of carbinol are present (possible three) with distinctly different photochromic properties, when dissolved in butyl alcohol. Moreover, the facts that crystals that are initially white and, while protected from light, heat, and water and carbon dioxide, eventually turn green and that the low-melting form converts into a higher melting form while its melting point is being taken lead us to believe that the ultimate stable form is a green ionic crystal and that the carbinol tends to go through the following transitions: low-melting form → high-melting form → green ionic crystal.

Results with Flash Photolysis. (a) The reason that no photoionization is observed visually when our solutes are irradiated in a solvent of no dipole moment and low dielectric constant, such as hexane or dioxane, might be that there is a reverse reaction of extreme

(6) (a) A. H. G. De Mosquita, C. H. Mac Gillavry, and K. Ericks, *Acta Cryst.*, **18**, 437 (1965); (b) unpublished results.

Table VI: λ_{max} and Absorbance Ratios for x, y, and g Bands of MG^+

Solvent	Previous treatment: HCl added initially	Previous treatment: Irradiated	Previous treatment: HCl added after irradiation	λ_{max}, mμ: Band x	λ_{max}, mμ: Band y	λ_{max}, mμ: Band g	Absorbance ratios: Band x	Absorbance ratios: Band y	Absorbance ratios: Band g
Malachite Green Carbinol									
Ethyl alcohol	X			622	427	317	1	0.19	0.18
	X			622	427	319	1	0.19	0.18
Ethyl alcohol–water (mole fraction water 0.76)				622	428	320	1	0.20	0.19
Ethyl alcohol–water (mole fraction water 0.98)				618	425	311	1	0.21	0.19
n-Butyl alcohol	X			624	430	318	1	0.23	0.22
1,2-Dichloroethane	X			622	430	318	1	0.19	0.17
Ethyl alcohol		X		622	426	318	1	0.19	0.20
n-Propyl alcohol	X	X		624	428	319	1	0.19	0.18
n-Butyl alcohol		X	X	623	434	320	1	0.19	0.21
1,2-Dichloroethane		X		623	430	319	1	0.21	0.15
1,1-Dichloroethane		X	X	623	430	318	1	0.18	0.18
Chloroform		X		620	428	318	1	0.21	0.19
Malachite Green Cyanide									
Ethyl alcohol		X		620	428	319	1	0.17	0.17
Ethyl alcohol		X	X	622	428	318	1	0.19	0.19
n-Propyl alcohol		X	X	623	428	318	1	0.19	0.19
n-Propyl alcohol	X	X		624	428	319	1	0.19	0.19
n-Butyl alcohol		X		624	430	318	1	0.19	0.18
Mean (12 best values)				622.4	428.5	319.0	1	0.19	0.185

rapidity. To answer this question a solution of malachite green leucocyanide in *n*-hexane was examined by flash photolysis with a xenon lamp using a 360-joule input and a filter that transmitted in the range 230–400 mμ. The result showed less than 0.1% conversion with a reverse reaction of about 4 sec, or virtually nothing. The same leucocyanide in *p*-dioxane showed even less photoionization.

(b) With malachite green leucocyanide dissolved in absolute ethyl alcohol we obtained 100% photoionization just as previously reported with successive irradiation from our mercury lamp. Flash photolysis is surely much quicker and more convenient.

Malachite green carbinol gave 82% photoionization—exactly the same amount as with the slower and more cumbersome method of successive irradiations.

(c) When the reverse reaction is very rapid, as with sunset orange leucocyanide and carbinol, flash photolysis is absolutely necessary. As was done in the former cases, the apparatus was standardized and checked with an acid solution of the carbinol whose absorbance was adjusted to unity, at maximum of the 465-mμ band.

A solution of the carbinol was flash irradiated using a 106-joule discharge three times in succession a few seconds apart. The results showed 76, 76, and 70% photoionization. With still another portion of the solution, 180-joule inputs were used, and we waited after each successive flash until the absorbance returned to zero, which rquired only a few minutes. The results were 82.5, 52, and 26% photoionization. Hence, it is observed that, although there is very little decomposition of the carbinol owing to the irradiation, the reverse reaction forms a product that cannot be photoionized.

Using a solution of sunset orange leucocyanide in absolute ethyl alcohol of the same concentration as above, successive flashes using 106 joules showed 103, 28, and 11% photoionization. The solution was allowed to fade completely before the last two.

VII. Comparison of λ_{max} of Band Peaks and Ratio of Absorbancies

In addition to our search for a "chemical factor," we were interested in the effects of various solvents on the position of the peaks of the various absorption bands and the ratios of the corresponding absorbancies of the peaks of the bands of the malachite green carbon-

ium ion. Data gathered from various runs are presented in Table VI which shows solvents, acid treatment, and irradiations used in each case.

A remarkable constancy was found. The average of 12 determinations of the λ_{max} of the three principal bands are 622.4, 428.5, and 319.0 mμ with absorbancy ratios of 1, 0.19, and 0.185, regardless of the nature of the solvent, irradiation time, or added HCl. The greatest deviation from this average was exhibited by a solution of malachite green leucocyanide in *n*-butyl alcohol to which an excess of acid had been added. The λ_{max} values were 624, 430, and 318 mμ and absorbance ratios, 1, 0.23, and 0.22.

VIII. The Relation of the Absorbance Bands to Structure of the Carbonium Ions of Crystal Violet, Malachite Green, and Sunset Orange in Absolute Alcohol

Considerable previous work[7] has been done relating maximum absorbancies and corresponding wavelengths to structure. However, it does not appear that those of the three closely related ions, CV^+, MG^+, and SO^+, have been considered in view of the new short-wave band (the n band not previously reported).

Table VII gives the data and frequency relations. Inasmuch as our interpretation will deviate somewhat from the previous, we have not adhered strictly to the older notation. No attempt has been made to locate the positive charge on the ion, and the ring systems have been written in conventional manner fully realizing that the true structure of the ion is uncertain and must be represented by several resonance structures.

Table VII, in which the frequency ratios are compared, shows that the x, g, and h bands are closely related and belong to the same system. Making the conventional assumption, the band of lowest frequency, the x band, of the crystal violet ion (CV^+) is the result of an induced dipole along the longest dimension of the molecule, namely, through ring 1 and either of the 2 rings--the quinoid ring and a dimethylaniline ring. The correspondence of the peak frequencies of the g band and h band is so close to those of dimethylaniline itself that we feel that dipoles induced in each of the 2 rings in the ion are responsible for these.

Table VII reveals that the ratios of the frequencies of the x band and g band peaks for the ions CV^+ and MG^+ (1) within each ion—1.95 and 1.95—and (2) between the two ions—1.05 and 1.04—are almost identical, so that these bands should result from the same induced dipoles as above—rings 1 and 2 for the x band, and ring 2 for the g band in the malachite green ion. Furthermore, the fact that the absorbance of the g band peak for the MG^+ is so close to half its value in CV^+ strongly suggests this relation. The same is true for the h band.

The ion of sunset orange (SO^+) has no x band because there is no dimethylaniline ring present. Table

Table VII

Ion	Band	λ_{max}, mμ	A (2.17×10^{-5} M)	Frequency $\times 10^{-14}$
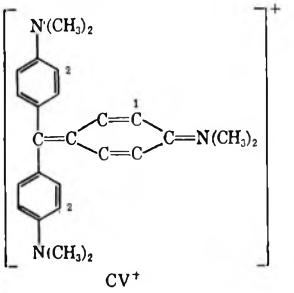 CV^+	x	589	2.35	5.10
	y	...	...	...
	g	305	0.93	9.84
	h	251	0.56	12.0
	n	...	...	...
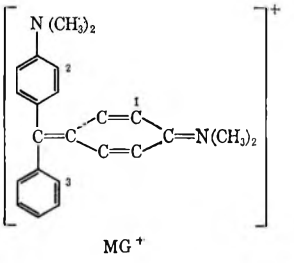 MG^+	x	622	2.35	4.82
	y	428	0.44	7.0
	g	318	0.423	9.44
	h	251	0.195	12.0
	n	236	0.23	12.7
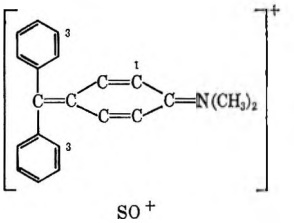 SO^+	x	...	...	...
	y	463	0.29	6.48
	g	345	0.07	8.70
	h	264	0.18	11.4
	n	255	0.14	11.8

Ion Ratios of Frequencies of λ_{max} for Same Ion

Band	$\frac{g}{x}$	$\frac{h}{g}$	$\frac{n}{y}$
CV^+	1.93	1.22	...
MG^+	1.93	1.27	1.81
SO^+	...	1.31	1.82

Ion Ratios of Frequencies of Corresponding λ_{max} Compared between Different Ions

	x	g	h	y	n
$\frac{MG^+}{CV^+}$	1.05	1.04	1.00	...	...
$\frac{SO^+}{MG^+}$	...	1.08	1.05	1.08	1.08

(7) G. N. Lewis and M. Calvin, *Chem. Rev.*, **25**, 273 (1939); G. N. Lewis and D. Lipkin, *J. Am. Chem. Soc.*, **64**, 2801 (1942); G. N. Lewis and J. Bigeleisen, *ibid.*, **65**, 520 (1943); **65**, 2170 (1943); H. Walba and G. E. K. Branch, *ibid.*, **73**, 3347 (1951).

VII shows a close relation of the frequencies of the y, g, and n bands (all 1.08) of this ion to those of the MG^+ ion. Now the n band, that of highest frequency may be attributed to the dipoles induced in the benzene rings present (3 rings), as the peak frequency of this band is within the range of those of benzene itself.

In the three ions, the h and g bands do not appear to have such a close relationship. However, they appear in closer relationship in the CV^+ and MG^+ ions than in the MG^+ and SO^+ ions. Regarding the n band that is common to both ions, we feel that in the MG^+ ion it is the result of the strong 250-mμ band in the dimethylaniline structure, whereas in the SO^+ ion it originates from a new dipole set up through the two benzene structures (3–3).

To explain the presence of the very weak g band in the SO^+ ion we must assume that there remains a small amount of resonance character of dimethylaniline associated with the quinoid ring itself.

The identical values for the ratio of the frequencies of n and y bands in the MG^+ and the SO^+ ions (1.81 and 1.82) and the ratio of the frequencies of the corresponding λ_{max} values between the y and n bands between these ions (1.08 and 1.08) lend strong support to the arguments presented above.

Acknowledgments. The author desires to express his gratitude to Dr. George Smith, Director of the Hughes Research Laboratory, for his invitation to use the facilities of the laboratory for the investigations herein described, and to Dr. J. David Margerum, who proposed my association with the laboratory and made space, supplies, and equipment available. In addition, he is further indebted to Dr. Margerum for all flash-photolysis determinations and valuable suggestions and to Dr. Robert Brault for assistance and advice in the preparation of the pure organic compounds used and infrared determinations.

Chemistry of Crystalline Aluminosilicates. I. Factors Affecting the Formation of Zeolite A

by George T. Kerr

Socony Mobil Oil Company, Inc., Research Department, Central Research Division Laboratory, Princeton, New Jersey *(Received August 12, 1965)*

The rate of formation of zeolite A is proportional to the quantity of crystalline zeolite present in the reaction system. The period during which crystal formation can be observed is preceded by an induction period which is probably the time required for formation of nuclei. The induction period can be eliminated by the addition of zeolite A to the reaction mixture at the beginning of the reaction. The formation of nuclei and the formation of zeolite crystals both result from the reaction of some species dissolved in the liquid phase (sodium hydroxide solution) of the reaction mixture and derived from the amorphous substrate. The rate of formation of zeolite A is increased as the concentration of alkali in the aqueous phase is increased. As the volume of the aqueous phase is increased, at a constant alkali concentration, the induction period is decreased with little change in the absolute rate of reaction. A mechanism is proposed which explains most of the experimental observations.

Synthesis of a variety of crystalline aluminosilicates of the zeolite group has been the subject of a series of publications by Barrer and co-workers during the past 20 years.[1] Highly significant contributions to this field were made by Milton, Breck, and co-workers in the discovery of a new synthetic zeolite, zeolite A,[2] and a synthetic zeolite isostructural with faujasite, zeolite X.[3] Barrer, especially, has studied a number of variables which determine the compositions and crystal structures of zeolites prepared synthetically. Flanigen and Breck conducted a kinetic study on the growth of zeolites A and X; their publication does not contain experimental details.[4]

The research reported here was directed toward understanding the mechanism of zeolite formation. To this end, the synthesis of sodium zeolite A afforded a convenient reaction for studying the kinetics of zeolite growth. This zeolite can be prepared at 100° and atmospheric pressure, and reaction is usually complete in several hours or less. X-Ray diffraction analysis or vapor phase adsorption measurements can serve to determine the quantity of zeolitic product present in the solid phases of the reaction mixtures.

Experimental Section

Reagents. Reagent grade sodium aluminate and sodium hydroxide were used throughout this work. The sodium aluminate contained 40–41 wt % Al_2O_3 and 36–37 wt % Na_2O. Tetraethyl orthosilicate was obtained from Carbide and Carbon Chemicals Co.

Apparatus. Zeolite A was synthesized in either 1-l. or 1.5-l. four-neck, round-bottom glass flasks fitted with a stirrer, water-cooled reflux condenser, and a thermometer. All reactions were conducted at reflux temperatures, 100 ± 2°; heat was supplied directly to the

(1) For example, (a) R. M. Barrer, *Trans. Faraday Soc.*, 40, 555 (1944); (b) R. M. Barrer, J. W. Baynham, F. W. Bultitude, and W. M. Meier, *J. Chem. Soc.*, 195 (1959); (c) R. M. Barrer and P. J. Denny, *ibid.*, 971 (1961).

(2) (a) R. M. Milton, U. S. Patent 2,882,243 (1959); (b) D. W. Breck, W. G. Eversole, R. M. Milton, T. B. Reed, and T. L. Thomas, *J. Am. Chem. Soc.*, 78, 5963 (1956); (c) T. B. Reed and D. W. Breck, *ibid.*, 78, 5972 (1956).

(3) (a) R. M. Milton, U. S. Patent 2,882,244 (1959); (b) D. W. Breck, W. G. Eversole, and R. M. Milton, *J. Am. Chem. Soc.*, 78, 2338 (1956).

(4) E. M. Flanigen and D. W. Breck, presented at the 137th Meeting of the American Chemical Society, Division of Inorganic Chemistry, Cleveland, Ohio, April 1960; Abstracts, p 33-M.

reaction mixtures with mantles. The same electrically powered stirrer was used throughout these crystallizations, thus assuring reasonably constant stirring speeds.

Preparation of Amorphous Substrate. Throughout this study the zeolite was prepared from reaction mixtures consisting of an amorphous sodium aluminosilicate substrate contacted with aqueous sodium hydroxide solutions, rather than by the usual method.[2a] This procedure made available a stock of amorphous substrate of fixed composition and thus eliminated a possibly critical variable from these studies. The amorphous substrate was prepared as follows. In a 5-l. four-neck flask, fitted with a stirrer and reflux condenser, was placed a solution of 530 g of sodium aluminate and 87.5 g of sodium hydroxide in 1880 ml of water. After the solution was heated to boiling, 490 g of tetraethyl orthosilicate was added with stirring. Stirring was continued throughout the course of the reaction. Initially the boiling point of the mixture was 100°, but as the reaction proceeded, the temperature decreased and finally remained constant at 82 to 84°, at which point the following reaction was complete.

$$NaAlO_2 + x(C_2H_5O)_4Si + 2xH_2O \xrightarrow{NaOH} Na(Al_2 \cdot xSiO_2) + 4xC_2H_5OH$$

The water and/or hydroxyl groups in the inorganic product are not included in the equation. The rate of the reaction must be carefully controlled; reaction times of at least 1 hr are preferred. For reaction times of less than 1 hr a dark brown by-product was observed, probably a polymeric sodium ethoxypolysilicate, which was exceedingly difficult to remove from the inorganic product. The reaction rate was easily controlled by varying the stirring rate, since tetraethyl orthosilicate is not miscible with the aqueous solution. At completion of reaction the inorganic, amorphous product was collected on a Büchner funnel, washed with about 3 l. of water, and partially air dried. Upon ignition at 1100°, this material yielded a solid residue amounting to 46 wt % of the initial sample. Elemental analysis indicated this solid had the following composition, on a water-free basis: 45.2 mole % SiO_2, 27.4 mole % Al_2O_3, and 27.4 mole % Na_2O. The empirical formula of this substrate, calculated on the water-free basis, was $Na(AlO_2 \cdot 0.82SiO_2)$ compared with $Na(AlO_2 \cdot SiO_2)$ for completely dehydrated sodium zeolite A. Thus, reaction mixtures consisting of this material and sodium hydroxide solution contain some excess sodium aluminate relative to the composition of sodium zeolite A.

Sampling for Kinetic Studies. For kinetic studies of the growth of zeolite A, zero time was defined as the time of mixing of the solid amorphous substrate and the aqueous phase. At prearranged times after commencement of reaction, aliquot portions of the reaction mixture were filtered and the solid residue was washed with water. The time of sampling was taken as the time at which one-half of the liquid portion of the sample had passed through the filter. The solid samples were then purged with either nitrogen or air for at least 3 hr at 350–400°. Prolonged purging under these conditions had no further measurable effect on the sample. The weight per cent zeolite in the water-free samples was determined by X-ray diffraction or water sorptive capacity. The amorphous substrate had no crystallinity according to X-ray diffraction and no water sorptive capacity after purging with air or nitrogen at 350–400°.

The Autocatalysis of Zeolite A Growth. Zeolite A was prepared, using 35.0 g of amorphous substrate and 700 ml of 1.0 *M* NaOH solution. The entire mixture was permitted to react to completion; this required 4 hr (see Figure 1). Then 35.0 g of additional amorphous substrate was added to the reaction mixture of crystalline zeolite A and mother liquor. The time of addition of the second portion of amorphous solid served as zero time for a rate study, samples being collected at regular intervals and analyzed in the usual manner.

Experimental Evidence of Growth from Solution. Two filters were used: the first (A) contained 35.0 g of the amorphous solid; the second (B) contained 8.0 g of anhydrous sodium zeolite A. The solvent, 1.4 *N* sodium hydroxide solution, was circulated by means of two pumps. The solution was first passed through funnel A to yield a solution of the amorphous sodium aluminosilicate. This solution was then passed through funnel B where crystallization occurred owing to the influence of the crystalline sodium aluminosilicate. (The liquid passing from the filter should be depleted of the active species and capable of dissolving more of the amorphous phase on passage back into funnel A.) The liquid was kept close to 100° by heating each round-bottom filter flask with a mantle and by retaining most of the solvent in these flasks. In this fashion a total of about 80 l. of solvent was passed through each funnel. After about 4 hr, nearly all of the amorphous solid had been dissolved from funnel A. One pump failed at this point. The lumpy residue in funnel A weighed 1.5 g after ignition. The zeolite collected in funnel B weighed 19.5 g after purging; water sorption analysis indicated this zeolite to be approximately 100% type A. Approximately 90% of the amorphous substrate was converted into zeolite.

Results

In Figure 1 the curve labeled "control" illustrates the results of a typical kinetic experiment for the formation

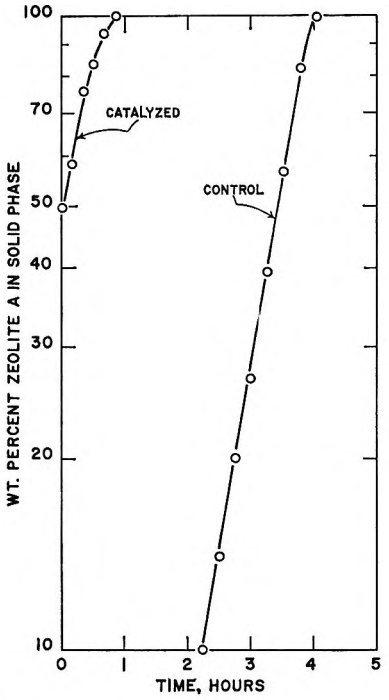

Figure 1. Control and catalyzed growth of zeolite A.

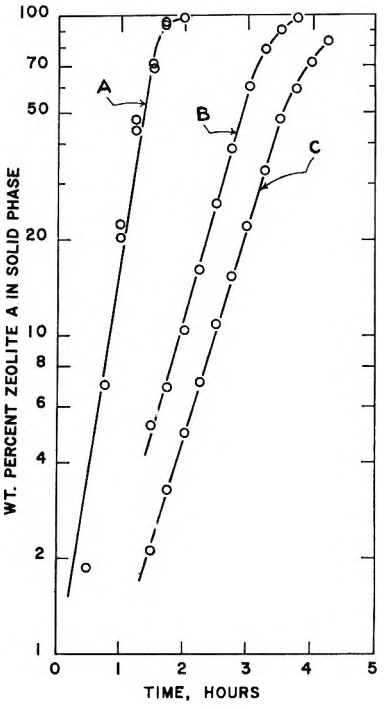

Figure 2. Effect of solution variables on the growth of zeolite A: A, 500 ml, 1.5 *M* NaOH; B, 1000 ml, 1.0 *M* NaOH; and C, 500 ml, 1.0 *M* NaOH.

of zeolite A. The rate of formation of crystalline product is thus seen to approximate closely first-order kinetics with respect to the quantity of crystalline zeolite present.

$$\frac{dZ}{dt} = KZ \qquad (1)$$

where Z = per cent of zeolite in solid phase at time t and K is a proportionality constant. The equation for the straight-line portion of the "control" curve is

$$\ln Z = Kt + \ln Z_0 \qquad (2)$$

where Z_0 is Z at $t = 0$, and K is the slope of the line. Ordinarily in zeolite A growth, Z_0 can be determined only by extrapolation of the straight line, and the value found for Z_0 probably is not real. Addition of known amounts of crystalline zeolite to reaction mixtures at $t = 0$, however, imparts reality to Z_0 and thereby permits a test of the validity of eq 2. The results of the tests are also shown in Figure 1, in the curve labeled "catalyzed." The major difference between the experiments whose results are presented in this figure is that in the "catalyzed" experiment zeolite A is present at $t = 0$ in an amount equal to the weight of amorphous substrate used. It is therefore evident that the time required for conversion of amorphous solid to crystalline solid can be decreased by adding crystalline zeolite to the reaction mixtures.

In Figure 2 are curves showing the effects of solution concentration and volume on the growth of zeolite. The absolute rate of formation of zeolite increases as the concentration of the sodium hydroxide solution increases. At constant concentration, the volume of the alkaline solution has little effect on the absolute rate of crystal growth. However, with an increase in volume of solution, a decrease in induction time is observed which strongly indicates that spontaneous nucleation occurs from species in solution. The ratio of total number of nuclei should be 2/1 for the 1000-ml reaction compared with the 500-ml reaction after the same period of time. Consequently, the ratio of the per cent conversion of amorphous solid to zeolite A should be 2/1 for these reactions at any time after growth begins and before conversion is complete. The ratio of the Z values for the 1000- and 500-ml experiments during most of the crystallization lies between 2.0/1 and 2.5/1.

Discussion

The various experimental results can be explained by a simple hypothesis: amorphous solid dissolves rapidly in the alkaline solution to form a soluble active species. The concentration of this species remains constant during most of the growth period but decreases sometime during the last half, as the amorphous substrate is depleted. This depletion explains the decrease in the

slope of the curves near completion of reaction. The rate-determining step is the reaction of the soluble species with nuclei or zeolite crystals to yield zeolitic product.

$$\text{amorphous solid} \xrightarrow{\text{fast}} \text{soluble species}$$

$$\text{soluble species} + \text{nuclei (or zeolite crystals)} \xrightarrow{\text{slow}} \text{zeolite A}$$

This sequence of reactions states that the rate of formation of zeolite is a function of the quantity of nuclei or zeolite A crystals present in the system and is also dependent on concentration of active soluble species, [S].

$$\frac{dZ}{dt} = k[S] \qquad (3)$$

Hence, in eq 1 and 2, K contains a concentration term, $K = k[S]$. The concentration of the active species in solution would be expected to depend upon the concentration of sodium hydroxide in the liquid phase and to remain constant during most of the growth period. Although the quantitative relation between the concentration of hydroxide ion and [S] has not been reported, the effect of hydroxide ion was also observed by Flanigen and Breck, who stated that crystal growth is "catalyzed" by excess hydroxide.[4]

According to the proposed mechanism, it should be possible to (1) dissolve a small portion of amorphous substrate in sodium hydroxide solution, (2) filter the solution from the amorphous solid, and (3) effect crystallization of the soluble species by contacting the solution with crystalline zeolite. In a sequence of these incremental steps, the amorphous material should ultimately be completely dissolved and converted to zeolite. Time is an important factor in the success of the scheme. The amorphous material must be dissolved and converted to zeolite before the species in solution undergo nuclei formation. The results of this type of experiment strongly indicate that solution of the amorphous substrate takes place during formation of zeolite A crystals. The nature of the dissolved species is unknown and admittedly may be colloidal particles rather than simple molecular or ionic species.

Conclusions

The observation that zeolite A crystals serve as growth centers for further zeolite A formation explains the finding of Flanigen and Breck, who reported the sudden, rapid growth of zeolite A crystals.[4] However, these workers stated, "There is no significant solution of the solid phase during crystallization." They also stated that crystal growth occurs in the solid phase. The results reported here indicate that a direct solid–solid transformation of amorphous substrate to crystalline product does not occur.

The various rate curves presented here apply only to the particular stock of amorphous substrate used in these studies. The absolute rates of growth and the induction times will depend upon the particular amorphous material used. Indeed, amorphous gels prepared *in situ* from sodium silicate, sodium aluminate, and, in some cases, added sodium hydroxide usually have a shorter induction period and higher rates of growth than does the amorphous substrate used in the present studies. Nonetheless, numerous studies using a variety of amorphous substrates have indicated that the findings of the study reported here are at least qualitatively applicable to other substrates. It was necessary to use an arbitrary standard stock of substrate to determine, at least semiquantitatively, the effect of the crystallization variables reported here. The proposed mechanism, derived from these semiquantitative relationships, is generally applicable to any zeolite A preparation.

A Study of Stepwise Adsorption[1]

by Bruce W. Davis[2] and Conway Pierce

Department of Chemistry, University of California, Riverside, California *(Received August 20, 1965)*

Isotherms are reported for adsorption of C_2H_5Cl, $CHCl_3$, $CFCl_3$, and C_6H_6 on a uniform graphite surface. At low reduced temperatures (p_0 is below 5 torr) all except benzene have a vertical phase change in the submonolayer region of the isotherm and a sharp second-layer step, both due to lateral interactions. The benzene isotherms show little evidence for any lateral interaction forces between molecules. It is concluded that stepped isotherms are to be expected for uniform surfaces provided the reduced temperature is sufficiently low and the adsorbate has lateral interactions.

It is generally recognized that adsorption isotherms for a uniform surface have a different shape than those for a heterogeneous surface. Lateral interactions between adsorbate molecules cause the isotherm to be convex to the pressure axis below V_m and to show steps for filling of successive layers. Under certain conditions these steps may have vertical regions where a phase change is occurring.

Previous studies of such stepped isotherms have concentrated on either the first layer or the multilayer region; none has covered both regions for the same isotherm. The purpose of the present study is to investigate the whole isotherm for selected systems, in an attempt to define the conditions that lead to stepwise adsorption and phase changes as a layer fills.

Experimental Section

The adsorption line, designed to cover a pressure range from 10^{-5} torr to 1 atm, was similar to the one used by Pierce and Ewing.[3] A 5.11-g sample of graphitized carbon black (Sterling MT) used in the previous study was the adsorbent. The nitrogen area[4] was 9.45 m^2/g, based on $\sigma(N_2) = 20$ A^2, or 7.65 m^2/g if $\sigma(N_2)$ was taken as 16.2 A^2. The following adsorbates were used: C_2H_5Cl, U.S.P. grade, purified by treatment with sulfuric acid and distillation *in vacuo;* $CHCl_3$, spectroquality reagent, packaged under an inert atmosphere and distilled into the system under vacuum; $CFCl_3$, E. I. du Pont de Nemours[5] Freon 11 (The analysis showed "no detectable impurities." It was distilled directly from the storage cylinder into the adsorption system and redistilled *in vacuo.*); and C_6H_6, reagent grade, distilled *in vacuo* and dried over potassium alloy.

Temperature Control. A very constant temperature near 195°K was obtained by powdered Dry Ice, used without added solvent. Other temperatures required were obtained by liquid–solid mixtures of various organic compounds: isopropyl bromide, 184°K; chloroform, 210°K; mesitylene, 221°; 2-octanol, 238°K; and 2-octanone, 251°K.

Frozen sticks of the compounds were added to the bath as required to maintain the temperature, with occasional hand stirring. Condensation of water vapor into the cold bath was prevented by a rubber-dam cover as previously described.[3] Frequent measurements are made of the bath temperature by means of the p_0 pressure reading.

Experimental Procedure. The organic vapors used were so highly soluble in the stopcock grease (Apiezon T) that major difficulties were encountered by (1) loss of vapor by solubility in the grease and (2) small air leaks owing to failure of the grease as it was softened by the dissolved vapors. It was necessary to regrease the stopcocks frequently and to use routinely the following procedure in the low-pressure region of all

(1) Presented before the Division of Colloid and Surface Chemistry at the 148th National Meeting of the American Chemical Society, Chicago, Ill., Sept 1964.

(2) Based on the doctoral dissertation submitted by B. W. Davis, June 1964.

(3) C. Pierce and B. Ewing, *J. Am. Chem. Soc.*, **84**, 4070 (1962).

(4) C. Pierce and B. Ewing, *J. Phys. Chem.*, **68**, 2562 (1964).

(5) Provided through the courtesy of Dr. E. B. Cooper, Plastics Division, Du Pont Co.

isotherms. Each dose of vapor was measured in the McLeod gauge portion of the line, then admitted to the sample. When the pressure became constant, the valve to the sample tube was closed and the gauge portion of the line was pumped briefly to remove any residual air that may have leaked into the system. (The amount of vapor removed in pumping was subtracted from the original amount of the dose.) The valve to the sample was then opened and vapor was desorbed into the gauge until the pressure became constant. This reading was taken as the equilibrium pressure.

Admittedly this procedure is open to some question as to whether the reading obtained at very low pressures is the true equilibrium pressure. The consistency of the data, however, leads us to believe that the values obtained are reliable; in the vertical portion of the isotherms we find that pressures in different runs, each started with a freshly outgassed sample, agree closely with one another. By comparison, the previous ethyl chloride isotherm of Pierce and Ewing,[3] where the gauge was not pumped prior to measuring the equilibrium pressure for each dose, did not show the vertical region we now find but instead it had a finite slope in this region. The difference is, we believe, due to a small amount of air leakage into the system during the long time required to measure the first 10–15 points of the isotherm. Any such leakage is, of course, cumulative if the gauge portion of the line is not pumped between successive points.

As a final check on the accuracy of the cumulative doses admitted to the sample, a material balance was made at the conclusion of a run by desorbing the vapor into a weighed charcoal bulb (at Dry Ice temperature) and weighing the total amount recovered. In all such tests the recovered weight of vapor agreed closely with the sum of the individual doses added. (Usually it was greater by 1% or less.) This test served both to check on the accuracy of the calibrations of line volumes and to show that no appreciable amount of vapor was lost by solution in stopcock grease.

Temperatures and saturation pressures for the isotherms measured are given in Table I.

Thermal Transpiration. Since the sample bulb was below room temperature, it was necessary to apply a correction to the measured pressures to obtain the equilibrium pressure in the sample bulb. This was done by application of an equation developed by Liang.[6] The parameters of this equation were later improved by Bennett and Tompkins,[7] who wrote it in the form

$$1 - R = \frac{p_2 - p_1}{p_2} = \frac{1 - R_0}{\alpha_{He}(\varphi_g X)^2 + \beta_{He}\varphi_g X + 1} \quad (1)$$

where $R = p_1/p_2$; p_1 = pressure at sample temperature, T_1; p_2 = pressure at gauge temperature, T_2; $X = p_2 d$, where d is the inside diameter, in millimeters, of the lead tube to the sample; $R_0 = (T_1/T_2)^{1/2}$; and α_{He}, β_{He}, and φ_g are parameters experimentally determined for helium and the gas in question (see ref 6 and 7 for experimental details).

Instead of evaluating these parameters experimentally for each vapor, we have used theoretical equations of Mason, Evans, and Watson,[8] based on the viscosity, η, and the mass per molecule, m, to compute them. This gives

$$\alpha_{He} = \frac{m_{He}}{48kT\eta_{He}^2} \quad (2)$$

$$\beta_{He} = \left(1 + \frac{2\pi}{3}\right)\left(\frac{3\alpha_{He}}{4\pi}\right)^{1/2} \quad (3)$$

$$\varphi_g = \frac{\eta_{He}}{\eta_g}\left(\frac{m_g}{m_{He}}\right)^{1/2} \quad (4)$$

Values of the computed parameters of the Liang equation for our adsorbates and the gas viscosities (taken from plots of log η *vs.* $1/T$) on which they are based are summarized in Table II. These, with our tube diameter of 1.77 mm, gave correction factors, R, as high as 0.8 to 0.9 for some measurements.

Table I

Adsorbate	Temp, °K	p_0, torr
C_2H_5Cl	184.3	1.10
C_2H_5Cl	195.5	3.41
C_2H_5Cl	210.1	12.5
$CHCl_3$	220.9	1.71
$CHCl_3$	238.5	6.94
$CFCl_3$	195.3	1.91
C_6H_6	238.4	1.19
C_6H_6	250.6	3.84

Results and Discussion

Ethyl Chloride. Isotherms for three temperatures are shown in Figure 1. The experimental points are from several independent determinations.

The low-pressure isotherms (A) on the enlarged scale show the same type of first-layer phase change as

(6) S. C. Liang, *J. Phys. Chem.*, **57**, 910 (1953).

(7) M. J. Bennett and F. C. Tompkins, *Trans. Faraday Soc.*, **53**, 185 (1957).

(8) E. A. Mason, R. B. Evans, and G. W. Watson, *J. Chem. Phys.*, **38**, 1808 (1963).

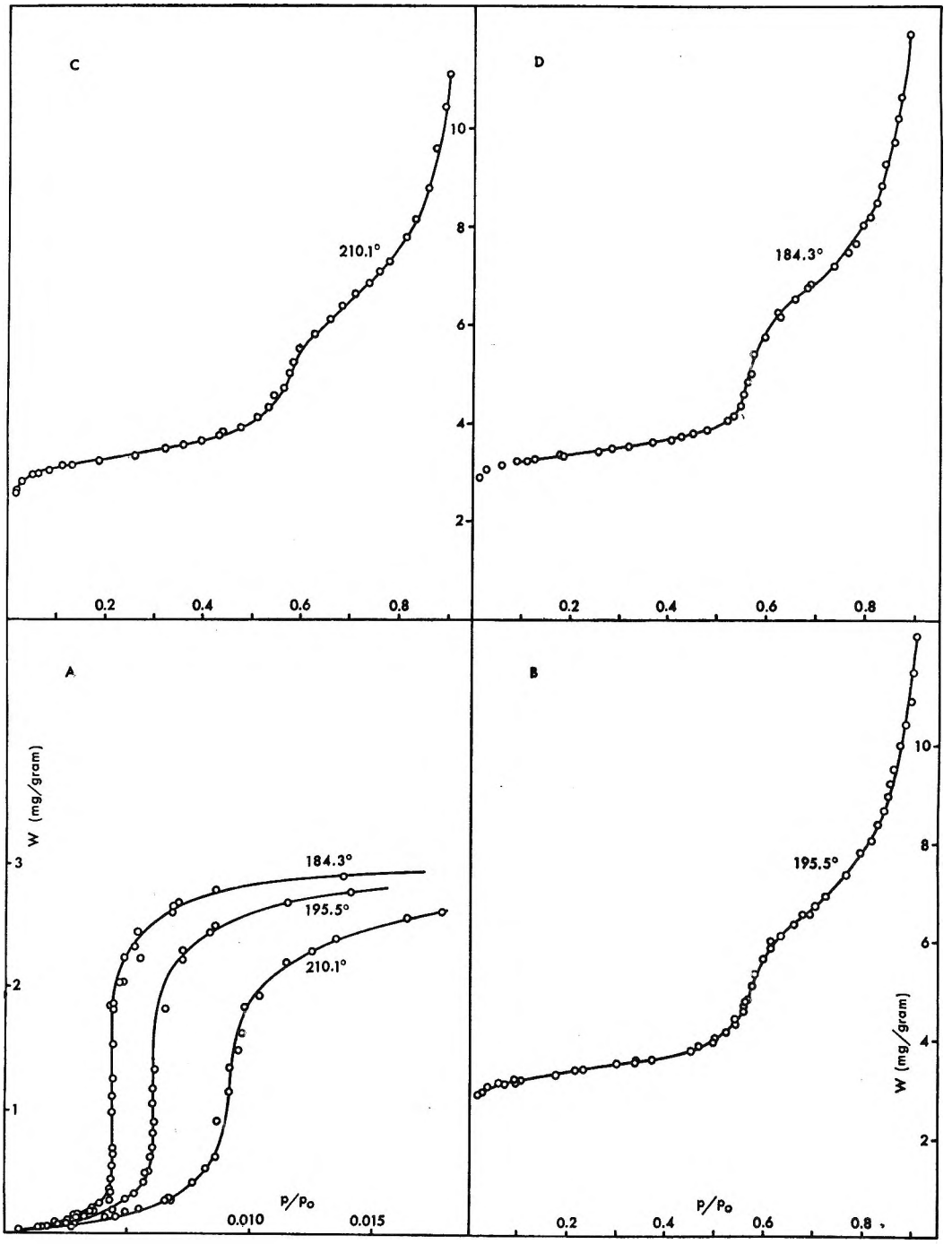

Figure 1. Ethyl chloride isotherms on MTg.

reported by Ross and associates,[9] Fisher and McMillan,[10] and Graham[11] for adsorption of krypton and various organic vapors on alkali halide crystals and on graphitized carbon blacks. There appears to be no question that on a highly uniform surface and at sufficiently low temperature the vertical discontinuity is real. That others have not observed similar phase changes is probably due to three reasons: (1) lack of a sufficiently uniform surface, (2) failure to take precautions to avoid a small amount of leakage at the

(9) S. Ross and J. P. Olivier, "On Physical Adsorption," Interscience Publishers, Inc., New York, N. Y., 1964; W. E. Machin and S. Ross, *Proc. Roy. Soc.* (London), **A265**, 455 (1962).

(10) R. B. Fisher and W. G. McMillan, *J. Chem. Phys.*, **28**, 549 (1953).

(11) D. Graham, *J. Phys. Chem.*, **62**, 1210 (1958).

Table II: Parameters for Thermal Transpiration Correction[a,b]

Vapor	T, °K	R_0	η_g, μp	α_{He}	β_{He}	φ_g	Ref
C_2H_5Cl	184.3	0.785	83.6	1.73	1.99	8.40	*c, d*
	195.5	0.809	85.3	1.64	1.93	8.40	
	210.1	0.838	87.7	1.52	1.86	8.34	
N_2	77.4	0.509	122	3.08	2.65	3.23	*c*
$CHCl_3$	220.9	0.859	88.9	1.46	1.82	11.3	*c, e*
	238.5	0.893	92.3	1.35	1.76	11.1	
$CFCl_3$	195.3	0.809	92.6	1.64	1.93	11.2	*f*
C_6H_6	238.4	0.892	68.2	1.35	1.76	12.2	*c*
	250.6	0.915	69.8	1.28	1.71	12.1	

[a] The quantities η, α_{He}, β_{He}, and φ_g are calculated for an *average* temperature $\bar{T} = (T + 300)/2$ where T is the sample bulb temperature and 300°K is the assumed room temperature. [b] The viscosity of helium (in micropoises) was calculated from $\log \eta_{He} = 0.6789 + 0.6567 \log T$. [c] "International Critical Tables," Vol. V, McGraw-Hill Book Co., Inc., New York, N. Y., 1926, p 2. [d] R. H. Tomlinson and E. A. Flood, *Can. J. Res.*, B26, 48 (1948). [e] H. Braune and R. Linke, *Z. Physik. Chem.*, A148, 203 (1930). [f] A. F. Benning and W. H. Markwood, Jr., *Refrig. Eng.*, **37**, 245 (1939).

stopcocks of the system, and (3) measurements at too high a temperature.

In common with others who have reported phase changes in isotherms at more than one temperature we find that (1) the height of the vertical region increases as the temperature is lowered, (2) the relative pressure at which the vertical region appears increases with increase in temperature, and (3) above a "critical temperature" the vertical rise disappears. These characteristics of the phase changes have been observed for isotherms taken at temperatures both below the normal freezing point of the adsorbate and above the freezing point.

Inspection of isotherms that exhibit a phase-change region shows that of the adsorbents studied to date the graphitized carbon blacks and boron nitride, whose surface lattice is almost identical with that of graphite,[9] have the most uniform surfaces known. All of the isotherms reported for alkali halide crystals have a slight concave portion for the initial adsorption, an indication of some surface heterogeneity. Our isotherms in Figure 1A and those of Ross and associates[9] for P33g show no evidence of any initial concave portion but instead a Henry's law region where the amount adsorbed is proportional to the pressure.

A steep second-layer step is shown in all three isotherms of Figures 1B, C, and D at a relative pressure near 0.6. The existence of such discrete layer steps was predicted by Halsey[12] and by Hill[13] before they were first observed experimentally by Polley, Schaeffer, and Smith,[14] who found that as a carbon black sample is progressively heated, the isotherm changes from a BET type to one with successive layer steps. Since then numerous studies have been made of stepped isotherms, in particular by Halsey[15] and associates. All of their isotherms that show steps are at temperatures below the normal freezing point of the adsorbate. The ethyl chloride steps of Figures 1B, C, and D occur at temperatures far above the normal freezing point. The general shape of the ethyl chloride steps is like those for isotherms at subfreezing temperatures but, unlike the latter,[15] the ethyl chloride isotherms for different temperatures do not cross one another at each tread and each step. Also the ethyl chloride isotherms do not show a distinct third-layer step, as is found for some of the rare gases. At a relative pressure where this step might be expected there probably is some capillary condensation between particles.

As expected, the second-layer step is steepest at the lowest temperature. At still higher temperature it completely disappears, as shown in a previous ethyl chloride isotherm at 0°.[3]

The ethyl chloride second-layer step has no vertical phase-change region at the lowest temperature which gave sufficient vapor pressure for making the measurement. Prenzlow and Halsey[15] report an almost vertical region in the second-layer step for argon on P33g at 64.38°K and estimate that the critical region for a phase change is near this temperature. They did not investigate the first-layer region in detail.

Chloroform. Isotherms for two temperatures are shown in Figure 2. The low-pressure region shows a phase change at 221°K but this is absent or nearly so

(12) G. D. Halsey, Jr., *J. Chem. Phys.*, 16, 931 (1948); see also *J. Phys. Chem.*, 57, 646 (1953).

(13) T. L. Hill, *J. Chem. Phys.*, 15, 767 (1947).

(14) M. H. Polley, W. D. Schaeffer, and W. R. Smith, *J. Phys. Chem.*, 57, 469 (1953).

(15) See, in particular, C. F. Prenzlow and G. D. Halsey, Jr., *ibid.*, 61, 1158 (1957); J. R. Sams, Jr., G. Constabaris, and G. D. Halsey, Jr., *ibid.*, 66, 2154 (1962).

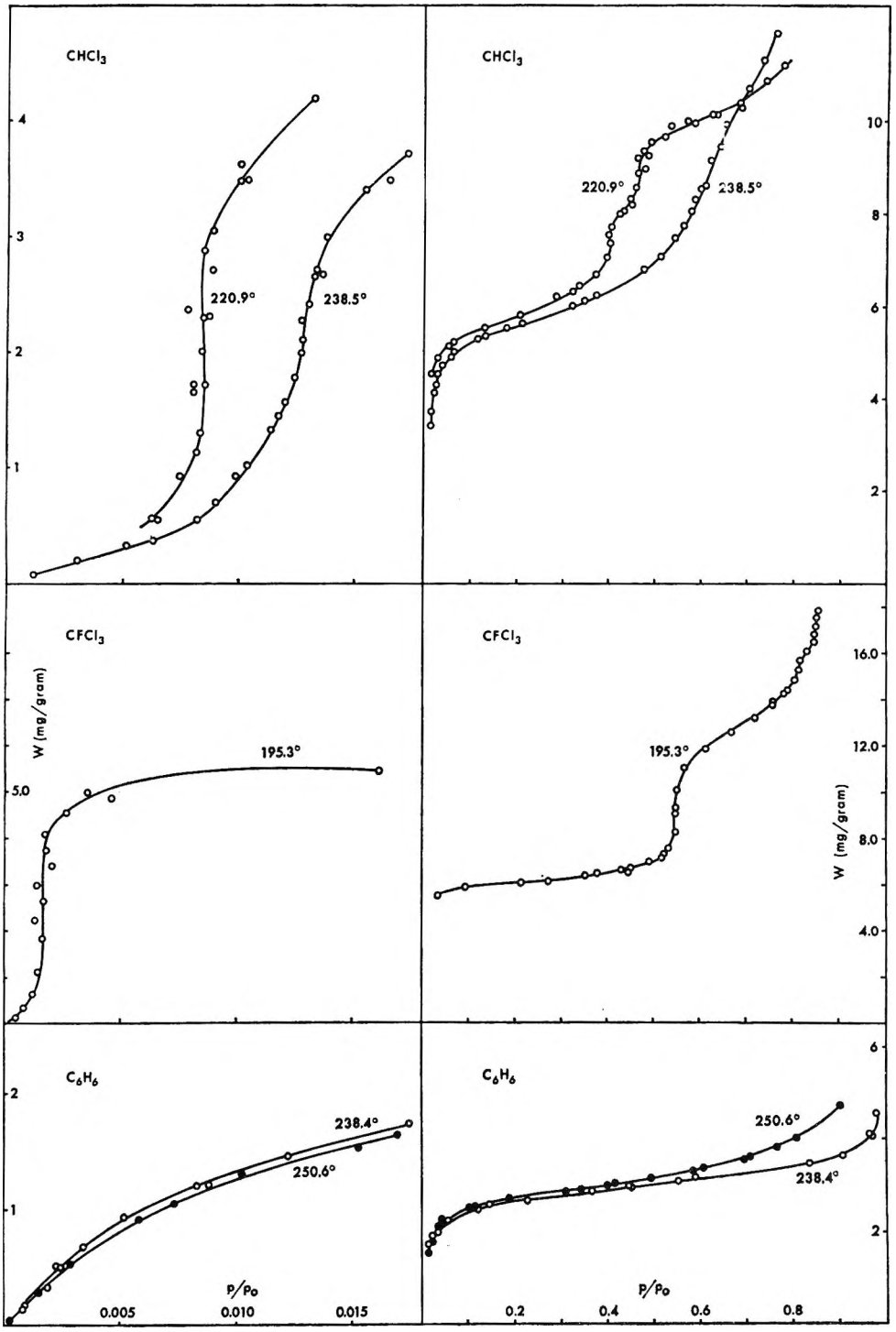

Figure 2. Isotherms of $CHCl_3$ (upper), $CFCl_3$ (middle), and C_6H_6 (bottom) on MTg.

at 238°K. A second-layer step is found in the 221° isotherm but this step disappears at the higher temperature. The 221° step has two nearly vertical portions, for which we have no satisfactory explanation. In general, the tread between the steps is not so flat as that for the ethyl chloride isotherms.

An unusual feature of the $CHCl_3$ isotherms, not previously observed for other adsorbates at temperatures above the bulk freezing point, is the pronounced crossover at about 11 mg/g adsorbed.

Trichlorofluoromethane. An isotherm at 195.3°K is shown in Figure 2. So much difficulty was en-

countered because of extreme solubility in stopcock grease that only one temperature was investigated. The low-pressure isotherm is in good agreement with the 194.7°K isotherm of Machin and Ross.[9] There is a long vertical region at a relative pressure near 0.0017, in agreement with their value.

Beyond V_m there is a sharp second-layer step, with a very flat tread between $\theta = 1$ and $\theta = 2$. The second-layer step terminates at about twice the amount adsorbed in the first layer, and there is a very slight indication (whether true or not we cannot say) of a third-layer step terminating at about $3V_m$. The second-layer step has an almost vertical region which suggests that a phase change is occurring.

Benzene. Data of Isirikyan and Kiselev[16] for adsorption of benzene on a graphitized carbon black at room temperature indicate that there is apparently very little lateral interaction between adsorbate molecules. It was felt to be of interest to include C_6H_6 isotherms in the study, for comparison with the other adsorbates which do have strong lateral interactions. In order to reach sufficiently low vapor pressures to make the results comparable with those for the other adsorbates, it was necessary to use temperatures far below the freezing point of bulk benzene.

Isotherms at 238 and 251°K are shown in Figure 2. As expected from the isotherm and heats of adsorption given by Isirikyan and Kiselev, the low-pressure isotherms show no apparent indication of any lateral interactions—the isotherms are the Langmuir type, concave to the p axis from the start. Also, as expected, the isotherms in the submonolayer region lie very close to one another, an indication that the net heat of adsorption is low, as reported by Isirikyan and Kiselev.

A totally unexpected phenomenon was found in the higher pressure region. The two isotherms cross near V_m and thereafter there is less adsorption in the multilayer region at the lower temperature than at the higher one.[17] At no measurable pressure did the isotherms cross one another again. The shapes of the isotherms in this region are quite different from the isotherm of Isirikyan and Kiselev at 293°K. They find, above the freezing point, what appears to be normal BET multilayer adsorption.

A suggested explanation of this unusual behavior is that the first layer is held tightly to the surface with the molecules flat, as somewhat rigid disks. To form a second layer below freezing temperatures, molecules must build on somewhat as in a surface layer of solid crystals. As shown by Cox,[18] molecules in the unit cell of solid benzene are tilted with respect to one another. Thus, the adsorbed molecules held flat may act as "imperfect crystals." According to this view, formation of the second layer is facilitated when thermal agitation and the disorder of the surface layer are increased by rise in temperature.

The situation appears to be quite different for adsorption of rare gas molecules at temperatures below their freezing points. Perhaps there is some of the "imperfect crystal" effect that inhibits formation of a second layer, but here the surface layer is probably not greatly unlike a crystal layer in structure and a second layer can start at quite low relative pressure. The manner in which these rare gas isotherms cross one another at each tread and each step may, however, be somewhat related to an imperfect crystal effect in the successive layers.

Heats and Entropies. Differential heats of adsorption (q_{st}) for benzene, chloroform, and ethyl chloride are shown in Figure 3A. Dotted lines give heats of vaporization for bulk adsorbate, computed from p_0 values.

The q_{st} curves for benzene and chloroform were computed in the usual manner from isotherms at two temperatures. Consequently they give average values over the temperature range. A more exact computation was made for ethyl chloride by using isotherms at three temperatures and taking the slopes of the isosteres at 195°K. This curve is the first one we know of that shows the differential heat for adsorption at a phase-change region.

The heat curve for chloroform is different from any previously published. For most adsorbates the differential net heat drops to near zero after completion of the first layer, then shows a low peak as the second layer forms. The chloroform curve drops to about 1.2 kcal/mole past V_m, then rises to about 2 kcal/mole for the second layer (whether the dual peak for the second layer is real or not we cannot tell from present data). The net heat drops to a negative value only after the second layer is completed, and it remains negative as the third layer is adsorbed.

(16) A. A. Isirikyan and A. V. Kiselev, *J. Phys. Chem.*, **65**, 601 (1961).

(17) The relative pressures used in the isotherm plots are based on p_0 values as measured for the reference state, pure solid. Formerly the isotherms taken below the normal freezing temperature were plotted with relative pressures based on supercooled liquid, but most data given today used the measured value for the pure adsorbates regardless of its physical state. The authors prefer this usage because molecules adsorbed at a relative pressure of 1 must be in the same condition as those in bulk adsorbate at that temperature. This does not imply that adatoms at relative pressure below 1 are in the same state as those of bulk adsorbate; in fact, at $\theta < 1$ the adatoms are in neither liquid nor solid state for any temperature, since they cannot have the same number of nearest neighbors as in the bulk state. Replotting of the data with relative pressures based on supercooled liquid gives isotherms that do not cross one another, but instead they practically coincide in the relative pressure region 0.1 to 0.4.

(18) E. G. Cox, *Rev. Mod. Phys.*, **30**, 159 (1958).

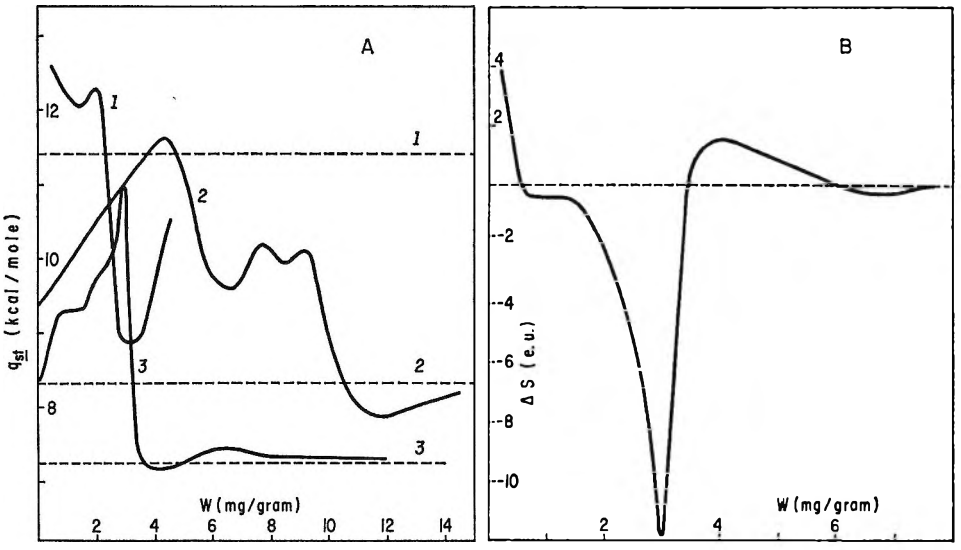

Figure 3. (A) Isosteric heats for benzene (1), chloroform (2), and ethyl chloride (3). (B) Differential entropy for ethyl chloride adsorption at 195°K. The reference state is pure liquid.

This behavior for chloroform suggests that adsorption in the second layer is aided by the presence of first-layer molecules (as if there were a vertical interaction) but that formation of a third layer is hindered by substrate molecules. A possible explanation is that molecules in the first layer are oriented with H atoms sticking up and that second-layer molecules orient in the opposite direction.

Benzene isotherms at two temperatures are so close together that a small uncertainty exists in the computation of q_{st}. For this reason we cannot tell whether the small peak at V_m is real or due to an experimental error in the isotherms. The general shape of the heat curve, however, is thought to be correct. We find, like Isirikyan and Kiselev[16] that the net heat of adsorption in the first layer is quite small. The total heat at 244°K is, however, some 2 kcal/mole larger than their value at 293° K. Since our reference state is pure solid and theirs is pure liquid, our net heats become negative past V_m while theirs do not. The large negative net heat in the second layer is much greater than Prenzlow and Halsey[15] find for argon, where the reference state is also pure solid. In fact, their heat curves for argon are much more like our ethyl chloride than our benzene curve.

The detail in the q_{st} curve for ethyl chloride makes it possible to determine quite precisely the partial molal entropy change for transfer of vapor from bulk liquid to adsorbed film at 195°K. A plot of the values is shown in Figure 3B. An interesting feature of the ΔS curve is that the entropy of adsorbate molecules at the first-layer phase change is approximately the same as that of molecules in bulk liquid. The remainder of the entropy curve is much like that given by Prenzlow and Halsey for argon, with a sharp minimum near V_m, a positive region as the second layer fills, and a gradual approach to zero in the multilayer region.

Cross Sections of Adsorbate Molecules. As pointed out by others,[15] a unique assignment of V_m from adsorption isotherms on uniform surfaces is not possible. A BET plot, which for isotherms on nonuniform surfaces gives a reproducible value, is not applicable to any stepped isotherm. One can only make estimates of V_m based upon point B, step heights, the maximum in the net heat curve, the minimum in the partial molal entropy curve, etc., as a best guess. These

Table III

Vapor	T, °K	V_m, mg/g	Method
C_2H_5Cl	184	3.2	Point B
	195	3.1	Point B
	210	2.9	Point B
	195	2.9	Max q_{st} curve
	195	3.0	Min ΔS curve
$CHCl_3$	221	5.2	Point B
	238	5.0	Point B
$CFCl_3$	195	5.5	Point B
C_6H_6	238, 251	2.3–2.6	Point B
	293	2.5	Isirikyan and Kiselev, BET
	244	2.6	Midpoint steep region of q_{st} curve

empirical methods lead to the estimates shown in Table III for the adsorbates used in this study.

The various methods give for each adsorbate values that fall fairly close to one another, which can be used to estimate the cross-section areas provided a standard area is assigned to the adsorbent, MTg. In a previous paper[4] it was estimated by data for various adsorbates that the area of MTg is 9.1 ± 0.4 m^2/g. An area of 9.1 ± 0.4 m^2/g gives the cross sections in Table IV.

Table IV

Vapor	V_m, mg/g	V_m, μmole/g	A^2/ molecule
C_2H_5Cl	3.0	46.5	32 ± 2
$CHCl_3$	5.1	42.7	36 ± 2
$CFCl_3$	5.5	40.0	38 ± 2
C_6H_6	2.5	32.0	47 ± 2

In view of these areas for $CHCl_3$ and $CFCl_3$ it appears that both molecules are oriented on the carbon surface with the three Cl atoms down, as previously assumed on other grounds by Ross and Olivier.[9] Such an arrangement is consistent with scale models of the molecules also. If we assume a close hexagonal packing on the surface, the area per molecule is related to the equilibrium distance, d, between centers by eq 5. Using

$$\text{area} = \frac{\sqrt{3}}{2}d^2 \qquad (5)$$

the cross sections listed in Table IV gives d = 6.4 A for $CHCl_3$ and 6.6 A for $CFCl_3$. A circumscribed circle about a scale model oriented with the Cl atoms down has a diameter of about 6.6 A; arrangement of the model with an H or F atom plus two Cl atoms down gives circumscribed circles of smaller diameter. These distances indicate an arrangement with center-to-center distance large enough to permit the adsorbed molecule to rotate on the surface.[19]

Our estimates of V_m for $CHCl_3$ and $CFCl_3$ are appreciably smaller than the ones computed by Machin and Ross[9] for adsorption of these molecules on P33g Using point-B values for nitrogen isotherms of 1.74 ml/g (data of Isirikyan and Kiselev[16]) for MTg and 2.87 ml/g for P33 (data of Prenzlow and Halsey[15]), the V_m values given by Machin and Ross are converted to corresponding amount for MTg. This gives V_m on MTg for $CHCl_3$ = 5.9 mg/g and V_m on MTg for $CFCl_3$ = 6.8 mg/g. Comparison with the isotherms of Figure 2 shows that these values fall far above point B of the isotherms (the Machin and Ross isotherms were not carried to completion of the monolayer but the V_m values were computed from the adsorption in the submonolayer region).

Conclusions

The present data, along with those of others, permit some tentative conclusions regarding adsorption isotherms for uniform surfaces. Unfortunately, however, the only truly uniform surfaces yet studied are the graphitized carbon blacks and boron nitride[9,20] (as noted previously, alkali halide crystals of quite high uniformity have been prepared but all show some degree of heterogeneity). It is recognized, therefore, that conclusions based on adsorption by a graphite surface may later prove to be in part related to properties of the graphite lattice. (1) All adsorbates studied to date except one, benzene, show marked lateral interaction effects. (2) At temperatures sufficiently low, lateral interaction forces cause adsorption to occur in discrete steps for successive layers. (3) The formation of stepped isotherms is highly sensitive to temperature. Thermal agitation may smear out steps and cause the isotherm to change to a BET type-II S shape. This effect is strikingly shown in the chloroform isotherms of Figure 2, where a change from 220.9 to 238.5°K causes both first- and second-layer steps to disappear completely. It is the reduced rather than the absolute temperature that is important. Thus, ethyl chloride isotherms are stepped at 195°K whereas nitrogen isotherms show no steps at 78°K. In general, stepped isotherms are observed at temperatures sufficiently low that p_0 is of the order of 1–10 torr, but argon isotherms have been shown[15] to have steps at temperatures where p_0 is much higher. One might even expect a stepped isotherm to occur at room temperature for a vapor whose p_0 value is 1–10 torr if such measurements were possible experimentally.

Acknowledgments. This research was supported in part by a grant from the Petroleum Research Fund administered by the American Chemical Society. Grateful acknowledgment is hereby made to the donors of this fund.

(19) See N. N. Avgul, A. V. Kiselev, and I. A. Lygina, *Trans. Faraday Soc.*, 59, 2113 (1963).

(20) R. A. Pierotti, *J. Phys. Chem.*, 66, 1810 (1962).

Conformations of Isotactic Polyalkyl Acrylates in Solution Determined by Nuclear Magnetic Resonance

by Tsuneo Yoshino, Yoshikazu Kikuchi, and Jiro Komiyama

Basic Research Laboratories, Toyo Rayon Company, Kamakura, Kanagawa, Japan *(Received August 23, 1965)*

Nuclear magnetic resonance spectra of isotactic polymethyl acrylate-β-d_1 and isotactic polyisopropyl acrylate-β-d_1 showed two triplets corresponding to two kinds of β protons. From the peak separations in the respective triplets, the conformations of the polymers dissolved in various solvents were determined by using the *trans* and *gauche* coupling constants obtained from trimethyl *cis*-hexahydrotrimesate. Probabilities of the polymers having *trans*, *gauche*, and the other *gauche* forms were found to be about 0.5 and in the ranges of 0.3–0.2 and 0.2–0.3, respectively, depending on the solvent used.

Introduction

Much information about dimensions and shapes of polymers in solution has been obtained by means of light scattering, viscosity measurement, etc. It may be preferable to interpret these data in terms of microscopic structures of polymers.

X-Ray diffraction[1] and infrared spectroscopy[2] have been used to determine the conformation in solids but have not been used successfully for similar studies on polymers in solution.

Since Bovey, *et al.*,[3] applied nmr spectroscopy for the determination of the configurations (stereoregularity) of polymers in 1959, much work has been done in the field. However, only a few nmr studies are reported[4] on the conformations (isomeric forms caused by the rotation about single bonds) of polymers.

The aim of the present work is to investigate the conformation of isotactic polymethyl and polyisopropyl acrylates in solution by nmr spectroscopy, which is expected to be a powerful tool to determine the conformation since the spin-coupling constant between α and β protons depends upon the dihedral angle of the CH bonds.

In the isotactic acrylate polymer, there are two sets of equivalent β protons, and they give a complicated spectrum due to the coupling between geminal β protons as well as between α and β protons.[5] Elimination of the coupling between geminal β protons is desired to obtain the unequivocal and accurate value of the coupling constant between α and β protons. Deuteration of one of the geminal β protons is a method to meet this purpose[6] since the spin-coupling constant becomes 0.15 when one of the protons is substituted with a deuteron.

The observable vicinal coupling constants of the deuterated polymer are averaged with weight over the t, g, and g' forms shown in Figure 1 since the rotation about the single bond is rapid as far as nuclear magnetic resonance is concerned. Probabilities of the polymers having these three forms can be estimated from the observed vicinal coupling constant if the coupling constants in *trans* and *gauche* arrangements are known. The *trans* and *gauche* coupling constants are obtainable from the spectrum of trimethyl *cis*-hexahydrotrimesate as model compound, in which the rotation about the single bonds of the ring is a negligible process.

(1) G. Natta and P. Corradini, *J. Polymer Sci.*, **39**, 29 (1959).

(2) G. Natta and G. Zerbi, Ed., *ibid.*, **C7**, 3, 224 (1964).

(3) F. A. Bovey, G. V. D. Tiers, and G. Filipovich, *ibid.*, **38**, 73 (1959).

(4) F. A. Bovey, *et al.*, *J. Chem. Phys.*, **42**, 3900 (1965); T. M. Conner and K. A. McLauchlan, *J. Phys. Chem.*, **69**, 1888 (1965).

(5) C. Schuerch, *et al.*, *J. Am. Chem. Soc.*, **86**, 4481 (1964).

(6) Schuerch, *et al.*,[5] interpreted the complicated spectrum of nondeuterated isotactic polyisopropyl acrylate regarding that the two vicinal coupling constants are equal to each other. Analysis of the simplified spectra of deuterated polymers, however, gave unequal values for these vicinal coupling constants as seen in a later part of this paper.

Experimental Section

Preparation of Monomer and Model Compounds. (*1*) *Methyl Acrylate-β-d_1.* A mixture of acetylene and deuterium chloride, prepared from thionyl chloride and heavy water, was passed through a column packed with active charcoal treated with an alcoholic solution of mercuric chloride. The reaction temperature was 100–180°. The resulting gas mixture was trapped after it was passed through sodium hydroxide solution and water. Unreacted acetylene was removed from the mixture by distillation. The portion distilled out in a temperature range of −17 to −10° was collected, passed through sodium hydroxide solution and water, and then dried with calcium chloride. Vinyl chloride-*trans*-β-d_1 thus obtained was introduced under stirring to a flask containing tetrahydrofuran, newly polished magnesium, a small quantity of ethyl bromide, and a trace of iodine. After completion of the reaction, the Grignard solution thus obtained was poured onto a mixture of Dry Ice and ether and was then hydrolyzed to give acrylic acid-β-d_1. By refluxing with methanol, sulfuric acid, and a trace of hydroquinone, the acid was converted to methyl acrylate-β-d_1, which was proved not to contain any other isomers and impurities by nmr inspection. The molar ratio γ of the *trans*-β-d_1 to *cis*-β-d_1 isomer was found to be $^3/_2$ by nmr measurement.

(*2*) *Isopropyl Acrylate-β-d_1.* Acrylic acid-β-d_1 was refluxed with isopropyl alcohol, sulfuric acid, hydroquinone, and benzene, which was added to remove the water formed through the reaction by making use of the fact that benzene makes an azeotropic mixture with isopropyl alcohol and water. The nmr spectrum of the isopropyl acrylate-β-d_1 showed that it did not contain any other isomers and impurities except benzene and that $\gamma = {}^3/_2$.

(*3*) *Dimethyl cis- and trans-Hexahydroisophthalates.* Isophthalic acid in glacial acetic acid was hydrogenated over freshly prepared rhodium oxide catalyst at 40–50° (130–90 atm). *cis*- and *trans*-hexahydroisophthalic acids thus obtained were separated through their calcium salts.[7] The acids were esterified with diazomethane.

(*4*) *Trimethyl cis-Hexahydrotrimesate.* Trimesic acid in ethanol was hydrogenated in the same way as mentioned above. The resulting hexahydrotrimesic acid was recrystallized from water. The nmr spectrum proved it to be pure *cis*-hexahydrotrimesic acid. The acid was esterified with diazomethane.

Polymerization. (*1*) *Isotactic Polymethyl Acrylate-β-d_1.* Lithium aluminum hydride (0.14 g) was introduced to an ampoule, which was then immersed in a Dry Ice–methanol bath. After the air in the ampoule was replaced by nitrogen, toluene (25 ml) was added to the ampoule. It was kept standing for 10 min, and then a mixture of methyl acrylate-β-d_1 (8 ml) and toluene (23 ml) was added with a syringe through a rubber tube connected with the ampoule. After it was sealed, the ampoule was kept in the Dry Ice–methanol bath for 20 hr. The polymerization mixture was poured onto 100 ml of methanol containing 10% of hydrochloric acid, and polymer was extracted with chloroform. After the chloroform was removed, the polymer was again dissolved in benzene and freeze dried.

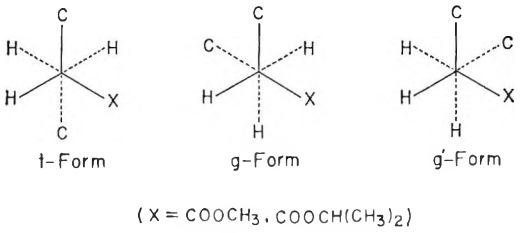

Figure 1. Isomeric forms due to rotation about a single bond.

(*2*) *Isotactic Polyisopropyl Acrylate-β-d_1.* A toluene solution (8 ml) of phenylmagnesium bromide (8 mole % of monomer) was placed under nitrogen in an ampoule cooled with Dry Ice–methanol. A mixture of monomer (1 ml) and toluene (5 ml) was added by a syringe to the ampoule, which was then kept in a Dry Ice–methanol bath for 24 hr. Polymer precipitated by petroleum ether (bp 30–70°) was dried after washing with dilute hydrochloric acid and water.

Nmr Spectral Measurement. A Varian HR-100 spectrometer was employed to record the spectra of monomer, polymer, and model compounds. Measurement was done at room temperature, and the concentration of all solutions measured was about 0.1 g/ml.

Nmr Spectra and Interpretation

Isotactic Polymethyl and Polyisopropyl Acrylate-β-d_1. In Figure 2 is shown a typical spectrum of the α and β protons of isotactic polymethyl acrylate-β-d_1.[8] The spectrum of isotactic polyisopropyl acrylate-β-d_1 is not shown here since it resembles very closely the spectrum given in Figure 2. The lowest field signal corresponds to the α protons, and the remaining two triplets correspond to the β-protons. The lower field triplet corresponds to the β protons (H_A) oriented

(7) G. A. Haggis and L. N. Owen, *J. Chem. Soc.*, 399 (1953).

(8) Here "isotactic" is referred to the placement of the COOR groups. The polymers prepared from the monomers with $\gamma = {}^3/_2$ are considered to be almost random with respect to the CHD groups: T. Yoshino and K. Kuno, *J. Am. Chem. Soc.*, **87**, 4404 (1965). However, it may be realized that the placement of the CHD groups is not concerned with the conclusions in this paper.

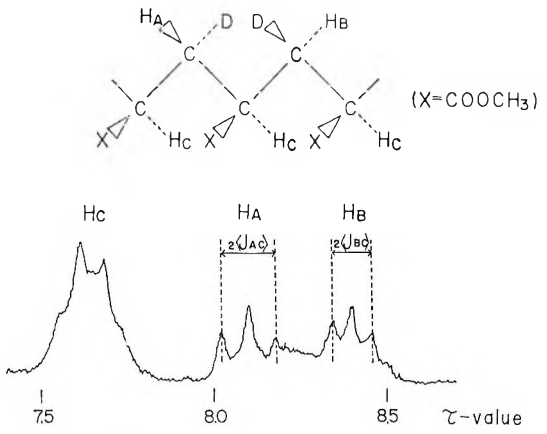

Figure 2. Spectrum of the α and the β protons of isotactic polymethyl acrylate-β-d_1 in methyl formate.

trans to the α protons (H_C) for the hypothetical *trans* zigzag skeletal conformation.[9] The higher field one is the signal of the other β protons (H_B). The β protons couple mainly with the vicinal α protons, and more distant couplings may be neglected. The steric relation of any of the β protons to one of the vicinal α protons is just the same as the relation to the other vicinal α proton when averaged over all conformations. We may, therefore, interpret each of the β-proton multiplets as the A part of the AC_2 system or the B part of the BC_2 system, and then the separation of the outer peaks of the triplet is shown to be equal to twice the vicinal coupling constant ($\langle J_{AC} \rangle$ or $\langle J_{BC} \rangle$) in the second-order approximation.

In Table I are listed the chemical shifts (σ) of the β protons and the spin-coupling constants of the polymers dissolved in various solvents. In all of the measurements it may be noted that the peak separations in the H_A triplet are larger than those of the H_B triplet.

Table I: Chemical Shifts (in τ Values) and Spin-Coupling Constants (in cps) of β Protons of Isotactic Polyalkyl Acrylates-β-d_1

Polymer	Solvent	σ_A	σ_B	$\langle J_{AC} \rangle$	$\langle J_{BC} \rangle$
Polymethyl acrylate-β-d_1	Chloroform	8.07	8.45	7.2	5.9
	Methyl formate	8.10	8.39	8.1	5.6
	Benzene	7.86	8.33	7.4	5.5
Polyisopropyl acrylate-β-d_1	Chloroform	8.15	8.50	7.2	5.3
	Methyl formate	8.11	8.43	7.5	5.9
	Benzene	7.77	8.22	7.7	6.0

Trimethyl cis-Hexahydrotrimesate. Of the two conceivable conformations shown in Figure 3, the one with three axial methoxycarbonyl groups can be neglected because of larger steric hindrance.

Since geminal, *trans*, and *gauche* coupling constants are known to be about 12, 12, and 3 cps, respectively,[10] the equatorial and the axial methylene protons (H_A and H_B) and the methine protons (H_C) are expected to give two triplets (each with 3 cps peak separations) separated by 12 cps, a quartet with peak separations of about 12 cps, and three triplets (each with 3 cps peak separations) separated by 12 cps, respectively. It is expected that the axial methylene protons appear at higher field by several tens of cycles than the equatorial protons[11] and that the methine protons, which are located near the negative methoxycarbonyl groups, appear at lower field than the axial methylene protons.

On the basis of this consideration, the observed signals of the trimethyl *cis*-hexahydrotrimesate were assigned as shown in Figure 4. The present assignments are also supported by the decoupled spectra shown in Figure 5.

Several solvents were employed for the spectral measurements of this compound. The coupling constants J_{AB}, J_{AC}, and J_{BC} were obtained from these spectra, regarding the signals of H_A, H_B, and H_C as the A and B parts of the ABC_2 system[12] and the C part of the A_2B_2C system, respectively. The values obtained are shown in Table II. It may be noted that the solvents have influence on the chemical shifts but little on the spin-coupling constants.

Dimethyl trans-Hexahydroisophthalate. The two protrons H_1 and H_2 of the methylene group located between α carbons are expected to give a single multiplet because chemical shifts of H_1 and H_2 are averaged by rapid inversion of the ring, and the inverted form is the same as the original one. The triplet at τ 8.01 in the observed spectrum (Figure 6) was ascribed to H_1 and H_2 because the position is nearly the same as the mean of the chemical shifts of the axial and the equatorial methylene protons of trimethyl *cis*-hexahydrotrimesate. The spectrum of H_1 and H_2 was analyzed as the A part of the A_2B_2 system. The separation of the outer peaks of the triplet is equal to $(J'_t + 3J'_g)/2$, where J'_t is the coupling constant between the A and B protons in the axial–axial arrange-

(9) T. Yoshino, M. Shinomiya, and J. Komiyama, *J. Am. Chem. Soc.*, **87**, 387 (1965).

(10) H. S. Gutowsky and C. Juan, *J. Chem. Phys.*, **37**, 120 (1962).

(11) L. M. Jackman, "Application of Nuclear Magnetic Resonance Spectroscopy in Organic Chemistry," Pergamon Press Ltd., London, 1959, Chapter 7.

(12) J. A. Pople, W. G. Schneider, and H. J. Bernstein, "High-resolution Nuclear Magnetic Resonance," McGraw-Hill Book Co., Inc., New York, N. Y., 1959, Chapter 6.

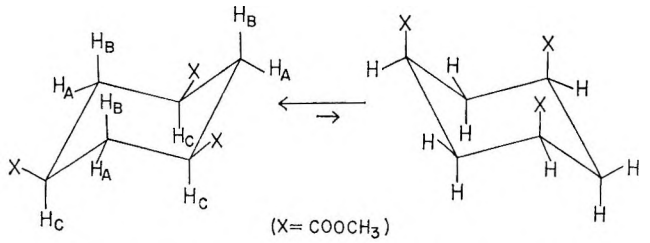

Figure 3. Conformations of trimethyl *cis*-hexahydrotrimesate.

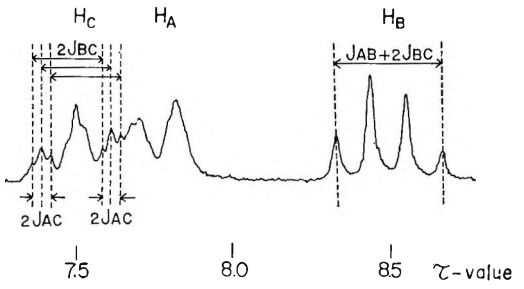

Figure 4. Spectrum of the methylene and the methine protons of trimethyl *cis*-hexahydrotrimesate.

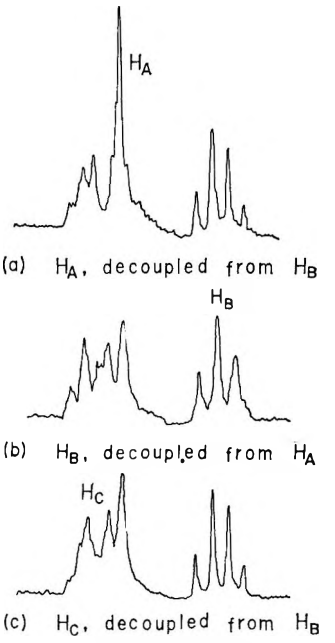

Figure 5. Decoupled spectra of trimethyl *cis*-hexahydrotrimesate.

ment, and J'_g is that in the axial–equatorial or equatorial–equatorial arrangement.

Conformations of Isotactic Acrylate Polymers in Solution

The observed coupling constants $\langle J_{AC} \rangle$ and $\langle J_{BC} \rangle$ may be expressed in terms of the probabilities (P_t, P_g, and $P_{g'}$) that the chain has the t, g, and g' forms, and the coupling constants J_t and J_g between α and β protons in *trans* and *gauche* arrangements, respectively

$$\langle J_{AC} \rangle = P_t J_t + P_g J_g + P_{g'} J_g \quad (1)$$

$$\langle J_{BC} \rangle = P_t J_g + P_g J_t + P_{g'} J_g \quad (2)$$

$$P_t + P_g + P_{g'} = 1 \quad (3)$$

Transforming these equations, one obtains the expressions for the probabilities

$$P_t = (\langle J_{AC} \rangle - J_g)/(J_t - J_g) \quad (4)$$

$$P_g = (\langle J_{BC} \rangle - J_g)/(J_t - J_g) \quad (5)$$

$$P_{g'} = [J_t + J_g - (\langle J_{AC} \rangle + \langle J_{BC} \rangle)]/(J_t - J_g) \quad (6)$$

The values of J_t and J_g may be transferred from trimethyl *cis*-hexahydrotrimesate: $J_t = J_{BC}$ and $J_g = J_{AC}$. Substituting the values of $\langle J_{AC} \rangle$ and $\langle J_{BC} \rangle$ (Table I) into eq 4–6, one obtains the probabilities P_t, P_g, and $P_{g'}$ (Table III).

The t form has the largest probability of around 50%, the g form about 30%, and the g' form about 20%, except for polymethyl acrylate-β-d_1 in benzene and polyisopropyl acrylate-β-d_1 in chloroform. It should be emphasized that the g' form for which little attention has been paid has rather larger probability.

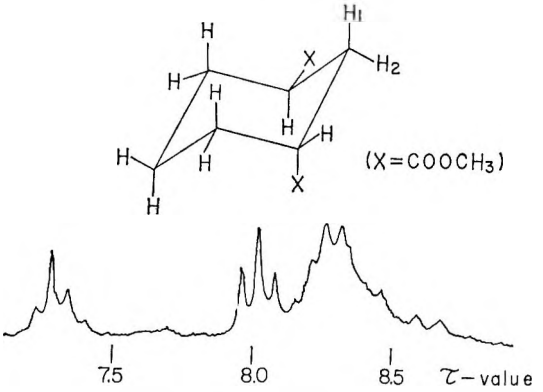

Figure 6. Spectrum of the methylene and the methine protons of dimethyl *trans*-hexahydroisophthalate.

Table II: Chemical Shifts (in τ Values) and Spin-Coupling Constants (in cps; Signs Are Neglected) of Trimethyl *cis*-Hexahydrotrimesate

Solvent	σ_A	σ_B	σ_C	J_{AB}[a]	J_{AC}	J_{BC}
Chloroform	7.69	8.45	7.51	14.9	3.1	12.1
Methyl formate	7.79	8.54	7.46	14.6	3.3	12.3
Methanol	7.74	8.55	7.46	13.3	3.3	12.0

[a] The value of J_{AB} is less accurate than those of J_{AC} and J_{BC} because the former was obtained from the large separation $J_{AB} + 2J_{BC}$ between the outermost peaks of the H_B signal.

Table III: Conformations of Acrylate Polymers Dissolved in Various Solvents

Polymer	Solvent	P_t	P_g	$P_{g'}$
Polymethyl acrylate-β-d_1	Chloroform	0.48	0.33	0.19
	Methyl formate	0.53	0.29	0.18
	Benzene	0.47	0.25	0.28
Polyisopropyl acrylate-β-d_1	Chloroform	0.46	0.24	0.30
	Methyl formate	0.47	0.29	0.24
	Benzene	0.49	0.30	0.21

Discussion

In the preceding section it was mentioned that the probability of the polymers having the g' form is rather large. This was also confirmed by the following experimental results.

The nmr spectra of dimethyl glutarate and its solutions in benzene, methyl formate, carbon tetrachloride, and chloroform were observed. The separations of the outer peaks of the triplet corresponding to α protons were measured and listed in Table IV. The separation is given by $P'_t(J''_t - J''_g)/2 + (J''_t + 3J''_g)/2$, where P'_t is the probability that the chain CH_2–CH_2–CH_2–$COOCH_3$ has the *trans* zigzag form, and J''_t and J''_g are the coupling constants in *trans* and *gauche* arrangements, respectively. This expression has the maximum value $J''_t + J''_g$ when $P'_t = 1$. The observed value of 14 cps in Table IV gives the lower limit of $J''_t + J''_g$ since P'_t is smaller than unity in reality. The probability of finding the g' form of the polymer is given by eq 6. The value of $\langle J_{AC} \rangle + \langle J_{BC} \rangle$ is, for example, 12.9 cps for isotactic polymethyl acrylate-β-d_1 in benzene. The denominator may be about 9 cps, the error of which is at most 1 cps. By assuming $J_t + J_g = J''_t + J''_g$, $P_{g'}$ is concluded to be larger than 0.1.

Table IV: Outer Peak Separation (in cps) of the α Proton Triplet of Dimethyl Glutarate

		Chloroform	Methyl formate	Benzene	Carbon tetrachloride
Separation	14.0	13.6	13.9	12.3	13.6

Further support for the presence of the g' form is this. If one neglects the g' form, $\langle J_{AC} \rangle + \langle J_{BC} \rangle$ is equal to $J_t + J_g$, which is considered to be independent of solvent species as stated before, in contrast to the observed change of $\langle J_{AC} \rangle + \langle J_{BC} \rangle$ with solvents.

Calculation of the probabilities was made by using the values of spin-coupling constants obtained from the model compound. Transferability of coupling constants will be discussed below.

The observed values of the spin-coupling constants of *cis*-hexahydrotrimesic acid in methanol, J_{AC} = 3.2 cps and J_{BC} = 12.4 cps, are very close to those of trimethyl ester in methanol (Table II). This indicates that the slight change of the structure has little influence on the *trans* and *gauche* coupling constants. The similar situation was found for the *trans*-hexahydroisophthalic acid. The separation of the triplet at τ 8.03 of the acid in methanol was 5.8 cps. This should be compared with 5.9 cps of the ester in methanol. Besides these, the values of *trans* and *gauche* coupling constants in the trimesate are very close to those[10] of [2.2]metacyclophane obtained by Gutowsky and Juan (J_t = 12.3 cps, J_g = 3.2 cps, and J_g' = 4.0 cps).

Surface Chemical Displacement of Organic Liquids from Solid Surfaces[1]

by Marianne K. Bernett and W. A. Zisman

U. S. Naval Research Laboratory, Washington, D. C. 20390 *(Received September 7, 1965)*

An investigation has been made of the various factors operative in the displacement by organic liquid compounds of a bulk layer of any nonaqueous liquid from a solid surface. Although solid surfaces used in the experiments were SAE 1020 steel and borosilicate glass, the results are readily extended to other solids. The nonaqueous pure liquids displaced were selected so as to cover a wide surface-tension range and included *n*-hexadecane, *ar*-dibromoethylbenzene, tricresyl phosphate, and propylene carbonate. A large number of well-defined displacing agents were investigated, of which the most efficient proved to be those for which an optimum balance could be achieved between low surface tension, high equilibrium spreading pressure, and good solubility with respect to the organic substrate to be removed. Agents which were particularly effective for long-lasting or permanent displacement were certain classes of highly fluorinated organic compounds and low-molecular weight dimethyl silicones. Low surface tension polar hydrocarbon derivatives, such as the 1-alkanols, were effective for temporary displacement. The several mechanisms operative in liquid–liquid displacement from solid surfaces have been investigated and are discussed. It is shown that these results and generalizations include earlier results on water-displacing agents as a special (and extreme) case.

Introduction

Comparatively little has been published on the spreading of liquids over solid surfaces previously coated with a thin layer of a different liquid. Baker and Zisman[2] studied many solid hydrophilic surfaces coated with a thin layer of water and found that certain types of pure organic liquids were able not only to spread rapidly on the water but also to displace it from the solid. In each instance the organic liquid had a hydrophobic–hydrophilic (or amphipathic) molecular structure. The most effective compounds were somewhat soluble in water and had large initial spreading coefficients on water (or high equilibrium spreading pressures). When a drop of such an organic liquid was placed gently on the surface of the water-coated solid surface, it spread rapidly on the water surface, a hole formed in the water layer, and it grew in diameter while exposing a dry surface of area Σ. Ultimately Σ attained a maximum value Σ_{max} which was a function of the mass and constitution of the drop of the water-displacing liquid. It was shown that some water-displacing liquids deposited a hydrophobic film on the exposed solid surface such that after the water layer had been displaced it would not respread. By the addition of a suitable solute, any water-displacing liquid could be made to behave in that way.

Baker[3–5] subsequently prepared emulsions of hydrocarbon solvents in water which were effective in displacing thin layers of oils from solid surfaces. By the successive applications of oil and water-displacing agents, Baker, Singleterry, and Zisman[6–9] developed the theory and practice for an economic and efficient proc-

(1) Presented before the Colloid and Surface Chemistry Division at the 150th National Meeting of the American Chemical Society in Atlantic City, N. J., Sept 16, 1965.

(2) (a) H. R. Baker and W. A. Zisman, "Water Displacing Fluids and Their Application to Reconditioning and Protecting Equipment," U. S. Naval Research Laboratory Report C-3364, Oct 4, 1948, Washington, D. C.; (b) H. R. Baker and W. A. Zisman, U. S. Patent 2,647,839 (1953).

(3) H. R. Baker and P. B. Leach, "Salvage of Flooded Electrical Equipment," U. S. Naval Research Laboratory Report 5316, June 16, 1959, Washington, D. C.

(4) H. R. Baker, U. S. Patent 3,078,189 (1963).

(5) H. R. Baker, U. S. Patent 3,167,514 (1965).

(6) H. R. Baker, P. B. Leach, C. R. Singleterry, and W. A. Zisman, "Surface Chemical Methods of Displacing Water and/or Oils and Salvaging Flooded Equipment," Part I, U. S. Naval Research Laboratory Report 5606, Feb 23, 1961, Washington, D. C.

ess for salvaging equipment previously damaged by water and/or smoke.

In the past decade investigations of surface activity in nonaqueous liquid systems and of the surface chemistry of fluorocarbon derivatives have established that (a) surfaces of close-packed adsorbed perfluoromethyl groups have the lowest surface energies known at ordinary temperatures[10-15] and (b) suitably constituted fluorocarbon derivatives are the most effective compounds for depressing the surface tensions of *any* nonfluorocarbon liquids at such temperatures.[16-23] This report will present our recent work using the above-mentioned concepts to demonstrate the existence of agents capable of displacing a great variety of organic liquids from solid surfaces.

For the effective displacement of water from solid surfaces, Baker, Singleterry, and Zisman[2a,6,8,9] found that the essential properties were some solubility of the agent in water and a large value of either the Harkins initial spreading coefficient, $S_{b/a}$[24,25]

$$S_{b/a} = \gamma_a - (\gamma_b + \gamma_{b'a'}) \quad (1)$$

or the equilibrium spreading pressure, $F_{b/a}$,[26] where

$$F_{b/a} = \gamma_a - \gamma_{a'} \quad (2)$$

Here, γ_a and γ_b are the surface tensions of the liquid a to be displaced and the displacing liquid b, respectively, and $\gamma_{b'a'}$ is the interfacial tension of b and a, the prime superscripts indicating that a is saturated with b and *vice versa*.

Therefore, we sought at first to find a somewhat soluble pure liquid compound b which when placed on the surface of the organic liquid a to be displaced would exhibit the largest possible values of $S_{b/a}$ (or $F_{b/a}$). Inspection of eq 1 reveals that if liquid b is to be effective in displacing liquid a it should have a surface tension (γ_b) as much below γ_a as possible. This is obvious when a and b are such that the interfacial tension ($\gamma_{a'b'}$) is small when compared with either γ_a or γ_b. Where a and b are somewhat soluble, Pound's interfacial tension rule[27,28] reveals that $\gamma_{a'b'}$ will be small or negligible. Equation 2 shows that $F_{b/a}$ will be greater, the smaller the value of $\gamma_{a'}$, *i.e.*, the greater the surface tension depressant ability of b when dissolved in a. Since certain types of fluorocarbon derivatives are now known to be the most efficient surface tension depressants,[16,17,21,23] any liquid member of such a homologous family of compounds was assumed to be suitable as the displacing liquid b. However, the maximum spreading pressure of b on a and the optimum liquid-displacing effect would be determined by some upper and lower limits to the allowable solubility of b in a. For the sake of brevity, we will refer hereafter to liquid b as the oil-displacing "agent" and to liquid a as the displaced "oil."

Experimental Conditions, Materials, and Techniques

In the experiments described here, the approach was essentially the same as that used to observe the water-displacing properties of organic compounds.[2-9] We first investigated the ability of many pure compounds to displace each of a selected group of pure organic liquids from clean, smooth, horizontal plates of steel and glass; however, as we will show later, the results can be extended readily to other solids. In order to ensure solid surfaces free from chemisorbed organic matter, panels of SAE 1020 cold-rolled steel 15.0 cm long and 7.5 cm wide were polished with No. 4/0 sandpaper and then rinsed repeatedly with ACS grade

(7) H. R. Baker, P. B. Leach, and C. R. Singleterry, "Surface Chemical Methods of Displacing Water and/or Oils and Salvaging Flooded Equipment," Part II, U. S. Naval Research Laboratory Report 5680, Sept 19, 1961, Washington, D. C.

(8) H. R. Baker, C. R. Singleterry, and W. A. Zisman, "Surface Chemical Displacement of Water and/or Oils from Solid Surfaces and Application to Salvaging Equipment after Flood or Fire," to be published.

(9) H. R. Baker, C. R. Singleterry, and W. A. Zisman, "Factors Affecting Surface-Chemical Displacement of Bulk Water from Solid Surfaces," presented to the Division of Colloid and Surface Chemistry, 150th National Meeting of the American Chemical Society, Atlantic City, N. J., Sept 16, 1965.

(10) H. W. Fox, E. F. Hare, and W. A. Zisman, *J. Colloid Sci.*, **8**, 194 (1953).

(11) F. Schulman and W. A. Zisman, *J. Am. Chem. Soc.*, **74**, 2123 (1952).

(12) E. F. Hare and W. A. Zisman, *J. Phys. Chem.*, **59**, 335 (1955).

(13) H. W. Fox, E. F. Hare, and W. A. Zisman, *ibid.*, **59**, 1097 (1955).

(14) E. G. Shafrin and W. A. Zisman, *ibid.*, **64**, 519 (1960).

(15) W. A. Zisman, Advances in Chemistry Series, No. 43, American Chemical Society, Washington, D. C., 1964, p 1.

(16) H. M. Scholberg, R. A. Guenthner, and R. I. Coon, *J. Phys. Chem.*, **57**, 923 (1953).

(17) G. B. Blake, A. H. Albrecht, and H. G. Bryce, American Chemical Society Division of Petroleum Chemistry, General Papers, No. 32, 1954, pp 131-142.

(18) A. H. Ellison and W. A. Zisman, *J. Phys. Chem.*, **63**, 1121 (1959).

(19) N. L. Jarvis and W. A. Zisman, *ibid.*, **64**, 150 (1960).

(20) N. L. Jarvis and W. A. Zisman, *ibid.*, **64**, 157 (1960).

(21) M. K. Bernett, N. L. Jarvis, and W. A. Zisman, *ibid.*, **66**, 328 (1962).

(22) M. K. Bernett and W. A. Zisman, *ibid.*, **65**, 448 (1961).

(23) N. L. Jarvis and W. A. Zisman, "Encyclopedia of Technology," Kirk-Othmer, Interscience Division, John Wiley and Sons, New York, N. Y., in press.

(24) W. D. Harkins and A. Feldman, *J. Am. Chem. Soc.*, **44**, 2665 (1922).

(25) W. D. Harkins, *Chem. Rev.*, **29**, 385 (1941).

(26) A. Cary and E. K. Rideal, *Proc. Roy. Soc.* (London), **A109**, 328 (1928).

(27) J. R. Pound, *J. Phys. Chem.*, **30**, 791 (1926).

(28) D. J. Donahue and F. E. Bartell, *ibid.*, **56**, 480 (1952).

Table I: Behavior of Oil-Displacing Agents on Steel Substrates at 25°

Agent				Behavior on displacement of oil			
Compound	γ, dynes/cm	d, g/ml	Bp, °C (mm)	Hexadecane[a]	ar-Dibromoethylbenzene[b]	Tricresyl phosphate[c]	Propylene carbonate[d]
Fluorinated Esters							
Perfluorooctyl ethanesulfonate	19.1	1.709	100 (2.8)	Good	Excellent	Good	Good
Hexyl perfluorobutyrate	19.2	1.231	74 (20)	Excellent	Excellent	Excellent	Excellent
Bis(perfluorooctyl)-α-n-dodecenyl succinate	19.4	1.484	185 (0.3)	...	...	Good	Good
Bis(perfluorooctyl) 3-methylglutarate	19.5	1.689	145 (0.5)	Good	Good	Good	Good
Bis(perfluorohexyl) 3-methylglutarate	19.7	1.539	115 (0.5)	Good	Good	Good	Good
1,2,3-Trimethylolpropane tris(perfluorobutyrate)	21.4	1.614	120 (0.2)	Fair	Fair	Good	Good
Bis(ω-hydrogen perfluoroheptyl) 3-methylglutarate	25.6	1.648	147 (0.5)	Poor	Poor	Good	Good
Bis(ω-hydrogen perfluoroheptyl) phenylsuccinate	25.9	1.640	165 (0.25)	Inactive	Poor	Fair	Fair
Bis(ω-hydrogen perfluoroheptyl) phenylglutarate	26.2	1.654	180 (0.5)	Inactive	Poor	Fair	Fair
ω-Hydrogen perfluoroheptyl hydrogen-3-methylglutarate	26.4	1.557	143 (0.5)	Inactive	Poor	Fair	Fair
$C_7F_{15}CONH(CH_2)_3\overset{+}{N}(CH_3)_2(CH_2)_2COO^-$	...	1.5	Viscous	Fair	Good	Good	Good
Silicones							
Bis(t-butoxy)bis(perfluorooctoxy)silane	18.4	1.525	108 (0.3)	Good	Good	Good	Good
Bis(t-butoxy)-bis(ω-hydrogen perfluoroheptoxy)silane	20.8	1.474	125 (0.3)	Good	Good	Fair	Fair
Silicone DC 200, 0.65 poise	15.9	0.761	100	Fair[e]	...	...	Fair
Silicone DC 200, 1.0 poise	17.4	0.818	152	Fair[e]	...	...	Fair
Silicone DC 200, 1.5 poises	18.0	0.853	192	Fair[e]	...	...	Fair
Silicone DC 200, 2.0 poises	18.7	0.873	230	Fair[e]	...	...	Fair
Silicone DC 200, 3.0 poises	19.2	0.900	70–100 (0.5)	Good	Good	...	Fair
Fluorosilicone QF 1-0065	25.7	1.24	...	Inactive	Poor	Poor	Poor
Fluorocarbons							
$C_3F_7[CF_2CF(CF_3)]_2Cl$	15.1	1.915	134	Fair	...	Poor	Fair
$C_3F_7[CF_2CF(CF_3)]_{3A}F$	16.3	1.992	115 (98)	Fair	Fair	...	Good
$C_3F_7[CF_2CF(CF_3)]_{4A}F$	17.8	...	143 (95)	Fair	Fair	...	Good
$\{C_3F_7[CF_2CF(CF_3)]_{2A}\}_2$	18.5	1.996	127 (10)	Poor	...	...	...
FCD − 330	20.2	1.996	...	Poor	Fair	Fair	Inactive

[a] γ 27.0 dynes/cm, d 0.775 g/ml, and bp 287°. [b] γ 38.2 dynes/cm, d 1.738 g/ml, and bp ~260°. [c] γ 40.4 dynes/cm and bp ~410° dec. [d] γ 41.4 dynes/cm, d 1.198 g/ml, and bp ~240°. [e] Area recovered after 15 min.

benzene. The borosilicate (Pyrex) plates of the same dimensions were soaked for 1 hr in a hot sulfuric acid–nitric acid (ratio 1:2) bath and then were rinsed repeatedly with distilled water. All specimens were dried in a clean oven at 100° for several hours. Each test plate was mounted on a leveling table with the plane face horizontal and then covered to a depth of 0.2 mm ± 1.0% with the oil or organic liquid to be displaced. Unless stated otherwise, a 0.01-ml ± 1.0% drop of the oil-displacing agent was delivered gently to the wet surface from a freshly flamed platinum wire tip, and the speed, extent, and mode of spreading and oil displacement were observed where necessary through a low-power lens. During these observations each panel was completely enclosed and observed through a glass cover plate to avoid disturbances by dust or air currents. This precaution was helpful also in observing the behavior of the more volatile oil-displacing agents. Unless indicated otherwise, all experiments were conducted at 25° and 50% relative humidity.

Organic liquids displaced from the panels are listed in the first row of Table I, and the pure liquid compounds used to displace them are given in the first column. The former liquids were selected to cover a wide range in surface tensions at 25° and a promising variety of chemical compositions. Each organic liquid

Table II: Behavior of Aliphatic 1-Alkanols as Oil-Displacing Agents at 25°

Agent				Oil					
				Hexadecane[a]			Propylene carbonate[b]		
Compound	γ_b, dynes/cm	d, g/ml	Substrate	$\Sigma_{max/mole}$, cm² × 10^{-4}	t_{max}, min	Area condition	$\Sigma_{max/mole}$, cm² × 10^{-4}	t_{max}, min	Area condition
Ethanol	22.3	0.785	Steel	1.5	Imm[c]	...	4.2	Imm[c]	...
			Pyrex	1.5	Imm	...	3.7	Imm	...
Butanol-1	23.9	0.810	Steel	2.8	Imm	...	6.5	Imm	Moist
			Pyrex	0.9	Imm	...	2.8	1	Dry
Pentanol-1	24.9	0.814	Steel	2.7	1	Dry	4.5	1	Moist center
			Pyrex	4.9	1	Center drop	11.6	1	Moist center
Hexanol-1	24.9	0.819	Steel	1.0	Imm	...	1.5	2	Center drop
			Pyrex	7.3	1	Dry	5.2	1	Center drop
Heptanol-1	26.2	0.822	Steel (4/0[d])	1.1	1	Moist	2.8	3	Center drop
			Steel (400A[d])	0.7	1	...	...	...	...
			Nickel (4/0[d])	1.3	1	...	...	...	...
			Nickel (α-Al_2O_3[d])	6.2	5	...	...	...	...
			Soda-lime glass	6.5	5	...	...	...	...
			Pyrex	7.6	5	Dry	2.8	1	Center drop
Octanol-1	26.9	0.825	Steel	Inactive		...	0.8	5	Large drop
			Pyrex	Inactive		...	0.8	1	Large drop
Nonanol-1	27.4	0.827	Steel	Inactive		...	1.4	10	Large drop
			Pyrex	Inactive		...	0.2	1	All drop
Decanol-1	27.4	0.833	Steel	Inactive		...	2.3	15	Large drop
			Pyrex	Inactive		...	0.4	5	All drop
Undecanol-1	28.1	0.833	Steel	Inactive		...	1.7	30	Large drop
			Pyrex	Inactive		...	1.7	5	Large drop
Dodecanol-1	28.7	0.831	Steel	Inactive		...	1.8	60	Large drop
			Pyrex	Inactive		...	1.8	5	Large drop

[a] γ_a 27.0 dynes/cm and d 0.775 g/ml. [b] γ_a 41.1 dynes/cm and d 1.198 g/ml. [c] Immediate. [d] Surface finish.

or oil-displacing agent, however previously prepared and purified, was finally purified by being percolated slowly at room temperature through an adsorbent column of activated alumina and Florisil just prior to each experiment in order to remove any traces of polar adsorbable impurities.

Surface tensions were measured by the ring method with a du Noüy tensiometer (6-cm circumference platinum ring), using the corrections of Harkins and Jordan[29] for conventional liquids and the corrections of Fox and Chrisman[30] for liquids of high density and low surface tension. The solubility of an oil-displacing agent in an oil was obtained by measuring the surface tension of a progressively more concentrated solution and by finding that point in the surface tension *vs.* concentration curve at which an additional quantity of solute did not further depress the surface tension.

The equilibrium spreading pressure ($F_{b/a}$) was calculated from eq 2.

General Conditions for "Oil" Displacement from Metal Substrates

Observations made of the various materials on steel panels revealed distinctive patterns of oil-displacement behavior which were dependent upon several parameters. Baker, Singleterry, and Zisman[2-9] had observed that maximum water displacement was a function of the solubility of the agent in water, the initial spreading coefficient (or else the equilibrium spreading pressure) on water, and the speed of spreading. The present investigation showed that displacement of the oil by the agent was determined by its solubility in the oil, the difference ($\gamma_a - \gamma_b$) in the surface tension of the agent and the oil, and the volatility of the agent. Table I lists the fluorinated esters, silicon-containing compounds, and halogenated hydrocarbons examined as oil-displacing agents, along with selected physical constants and a qualitative statement of the oil-displacement characteristics observed. Table I reveals that the most efficient oil-displacing liquids had an appreciably smaller surface tension (γ_b) than that of the

(29) W. D. Harkins and H. F. Jordan, *J. Am. Chem. Soc.*, **52**, 1751 (1930).

(30) H. W. Fox and C. H. Chrisman, Jr., *J. Phys. Chem.*, **56**, 284 (1952).

Table III: Behavior of Fluorinated 1-Alkanols as Oil-Displacing Agents at 25°

Agent				Oil					
				Hexadecane[a]			Propylene carbonate[b]		
Compound	γ_b, dynes/cm	d, g/ml	Substrate	$\Sigma_{max/mole}$, cm² × 10^{-4}	t_{max}, min	Area condition	$\Sigma_{max/mole}$, cm² × 10^{-4}	t_{max}, min	Area condition
Perfluoroethanol	19.5	1.374	Steel	0.6	1	Small drop	9.1	Imm[c]	Dry
			Pyrex	0.6	1	Small drop	3.4	Imm	Dry
Perfluorobutanol-1	17.2	1.600	Steel	2.1	1	Small drop	29.5	1	Droplets
			Pyrex	1.5	1	Small drop	19.6	Imm	Dry
Perfluorohexanol-1	17.4	1.686	Steel	1.4	5	Large drop	83.8	2	Droplets
			Pyrex	6.7	1	Small drop	17.0	1	Center drop
Perfluorooctanol-1	17.0	1.734	Steel	5.3	30	Large drop	152.0	5	Droplets
			Pyrex	10.4	1	Large drop	21.9	1	Center drop
ω-Hydrogen perfluoropropanol-1	26.0	1.485	Steel	0.2	5	Large drop	11.2	20	Droplets
			Pyrex	0.2	5	Large drop	6.7	Imm	Dry
ω-Hydrogen perfluoropentanol-1	23.5	1.665	Steel	0.3	5	Large drop	30.6	30	Droplets
			Pyrex	1.1	5	Large drop	26.2	5	Dry
ω-Hydrogen perfluoroheptanol-1	22.7	1.753	Steel	1.0	5	Large drop	107.0	60	Dry
			Pyrex	1.0	5	Large drop	107.9	60	Dry

[a] γ_a 27.0 dynes/cm and d 0.775 g/ml. [b] γ_a 41.1 dynes/cm and d 1.198 g/ml. [c] Immediate.

oil displaced (γ_a); however, solubility in the oil as well as other physical properties were also involved. Furthermore, it was observed that oil displacement proceeded at various speeds, and the resulting cleared area could be (a) perfectly dry and clean, (b) covered with a thin layer of oil, or (c) showing a combination of both properties in various proportions.

Oil Displacement by Agents Having Polar Functional Groups

Effect of Homology and Molecular Weight of Displacing Agent. In Tables II and III are given the observations made on the homologous series of liquid 1-alkanols, perfluoro-1-alkanols, and ω-monohydrogen perfluoroalkanols when a drop of each is placed on a 0.2-mm layer of hexadecane or propylene carbonate covering a steel or Pyrex panel. In these experiments certain spreading properties were measured with a precision of ±2%. These are Σ_{max}, the maximum value of the approximately circular area of oil displaced by 0.01 ml of displacing agent, and t_{max}, the time required to attain Σ_{max}. For more meaningful comparison of the various agents, Σ_{max} was calculated in terms of area displaced by 1 mole of the agent; this value was designated as $\Sigma_{max/mole}$ and is used in the tables and figures. In addition, a brief remark was added to describe the ultimate condition of the cleared solid surface. When the molecular weights (M) in the homologous series of perfluoro alcohols were plotted against $\Sigma_{max/mole}$ (as represented in Figure 1 for propylene carbonate), it was found that $\Sigma_{max/mole}$ increased with M, the slope becoming steeper with higher values of M. The family of ω-hydrogen perfluoroalkanols behaves similarly at high values of M, but the lower members were not as efficient as the lower perfluoroalkanols in displacing the propylene carbonate. In contrast to the fluorinated alcohols, the lower 1-alkanols were less effective in displacing propylene carbonate, and when M exceeded 100, became essentially ineffective. Whereas the surface tensions of the perfluoroalkanols decrease with increased molecular weight, the opposite occurs in the family of 1-alkanols (see Figure 2). Hence, $\Sigma_{max/mole}$ can be directly related to $\gamma_a - \gamma_b$, the difference in surface tension of the oil and the displacing agent. The interfacial tension $\gamma_{b'a'}$ is smaller than the surface tension (γ_a) of the organic liquid; it decreases as the solubility of the agent increases, and it approaches zero at infinite solubility. Thus, the value of $\gamma_{b'a'}$ can be neglected in eq 1, so that ($\gamma_a - \gamma_b$) becomes equal to the initial spreading coefficient $S_{b/a}$ and also approximates the spreading pressure $F_{b/a}$. Plots of $\Sigma_{max/mole}$ against ($\gamma_a - \gamma_b$) are given in Figure 3 for each of the three homologous series of alcohols when placed on specimens coated with propylene carbonate or with *n*-hexadecane. For comparison purposes, results obtained on specimens coated with water are also included. Displacement of propylene carbonate or of hexadecane by the same agent made it evident that greater oil-displacing ability was observed the higher the surface tension of the oil. It was also evident that the fluoro alcohols were more effective in displacing liquids than were the 1-alkanols.

Another measure of the efficiency of the oil-displacing agent is t_{max} which is plotted in Figure 4 against

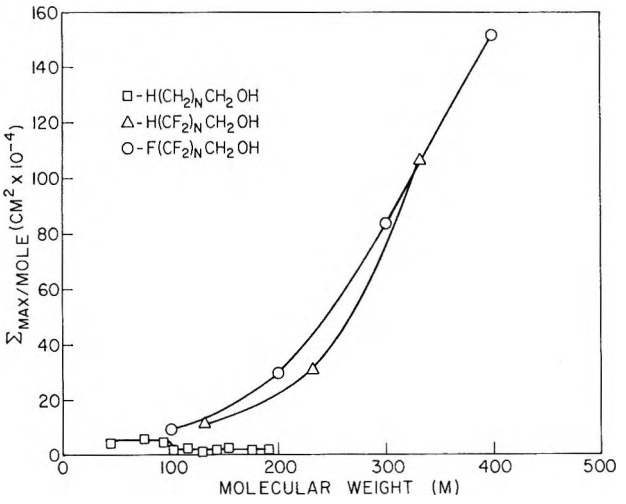

Figure 1. Effect of molecular weight of oil-displacing agent on maximum area displaced of propylene carbonate (substrate steel).

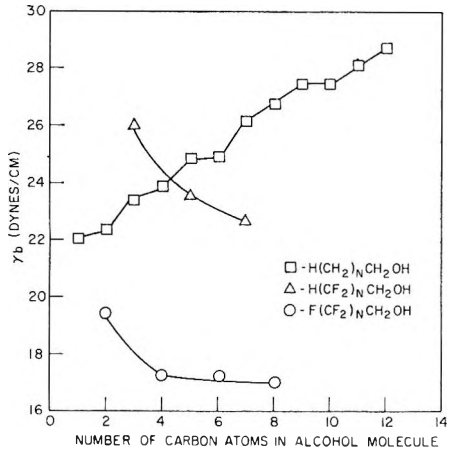

Figure 2. Surface tensions of 1-alkanols at 25°.

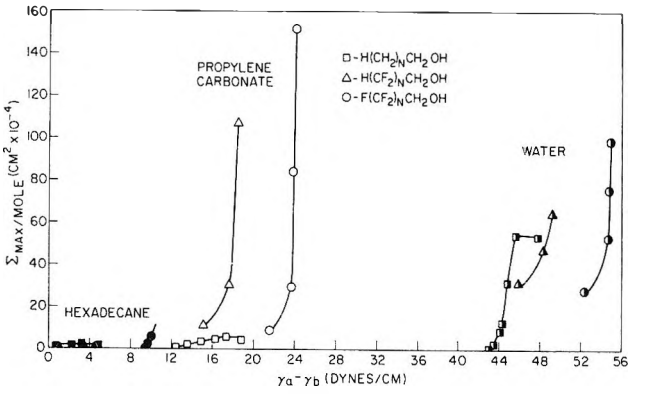

Figure 3. Effect of surface tension difference of liquid and agent on maximum area displaced of liquid (substrate steel).

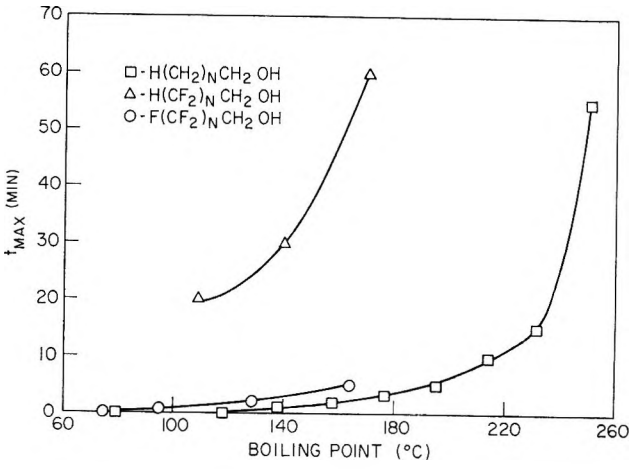

Figure 4. Effect of boiling point on time necessary to reach maximum area when 1-alkanols are spread on propylene carbonate (substrate steel).

the boiling point of the agent. As in any homologous series, an increase in the molecular weight raises the boiling point and lowers the vapor pressure. The increase in t_{max} of Figure 4 may be regarded as the result of the decrease in the vapor pressure of the agent or a lower rate of agent diffusion in the oil.

Effect of Solubility of Displacing Agent in Oil. The effectiveness of water-displacing agents was found by Baker, Singleterry, and Zisman[2-9] to be roughly proportional to the solubility in water. This is reasonable because in each homologous series of such agents, higher water solubilities correspond to lower molecular weights, higher volatilities, higher rates of spreading, and higher equilibrium spreading pressures. In order to observe the effect of agent solubility in oil-displacing mechanisms, we examined several agents having large differences in solubility in oils of nearly equal surface tensions. *ar*-Dibromoethylbenzene (Alkazene 42) and propylene carbonate, which have surface tensions at 25° of 38.2 and 41.1 dynes/cm, respectively, are two such oils. Here, the value of $\gamma_a - \gamma_b$ of the oil-displacing agent with respect to each oil is nearly the same and, therefore, of negligible influence. Any difference in oil-displacing properties must then necessarily be due to solubility properties only. Table IV summarizes the results obtained with these oils. For purposes of comparison, the results observed on displacing hexadecane (γ_a = 27.0 dynes/cm) are also given in Table IV. Where the solubility of the agent (for example, that of any fluorinated alcohol) is greater in propylene carbonate than in *ar*-dibromoethylbenzene, the value of $\Sigma_{max/mole}$ is always greater; where the agent solubility is in reverse order (1-decanol or the methyl silicones are examples), $\Sigma_{max/mole}$ is always

Table IV: Effect of Solubility, Spreading Pressure, and Surface Tension Difference on Behavior of Oil-Displacing Agents

Agent	Oil[a]	Solubility, moles/l.	$\gamma_a - \gamma_b$, dynes/cm	$F_{b/a}$ dynes/cm	$\Sigma_{max/mole}$, cm² × 10^{-4}	t_{max}, min	Composition of residual mound[a]
Perfluorobutanol-1	P	>2	23.9	17.6	29.5	1	P + some alkanol[b]
	B	Insol	21.0	8.0	11.7	30	B (center)
	H	<0.02	9.8	0.6	2.1	1	H (ridge)
Perfluorooctanol-1	P	>1	24.1	21.7	152.0	5	P + alkanol[b]
	B	Insol	21.2	11.9	29.1	30	B (center)
	H	<0.01	10.0	0.6	5.3	30	H (ridge)
ω-Hydrogen perfluoro-heptanol	P	Sol	18.4	12.9	107.0	60	No remains
	B	Insol	15.5	8.9	26.5	60	B (center)
	H	<0.02	4.3	0.3	1.0	5	Alkanol (center)
Butanol-1	P	Sol	17.2	16.4	6.5	Imm[c]	...
	B	Sol	14.3	12.8	5.8	Imm	...
	H	Sol	3.1	1.8	2.8	Imm	Alkanol + some H (moist)
Decanol-1	P	<0.3	13.7	12.5	2.3	5	P (center)
	B	Sol	10.8	10.5	24.2	10	B + alkanol (ridge)
	H	...	0.2	...	Inactive	...	...
Dimethyl silicone (DC 200, 0.65 poise)	P	Insol	25.2	2.4	15.1	1	P (center)
	H	Sol	11.1	8.7	41.7	1	...
Dimethyl silicone (DC 200, 3.0 poises)	P	Insol	21.9	4.8	49.5	60	P (center)
	B	Sol	19.0	18.8	307.6	60	Silicone + some B (ridge)
	H	Sol	7.8	6.8	174.2	60	...

[a] P = propylene carbonate; B = *ar*-dibromoethylbenzene; H = hexadecane. [b] Ridge during displacement process. Final $\Sigma_{max/mole}$ dry. [c] Immediate.

greater for *ar*-dibromoethylbenzene than for propylene carbonate.

The influence of solubility is even more striking in the case of the two methyl silicone fluids, because each is insoluble in propylene carbonate but soluble in hexadecane. Values of $\gamma_a - \gamma_b$ for the two methyl silicones are 25.2 and 21.9 dynes/cm with respect to propylene carbonate, and only 11.1 and 7.8 dynes/cm with respect to hexadecane. Yet the corresponding values of $\Sigma_{max/mole}$ are only 15.1 and 49.5 cm² × 10^{-4} for propylene carbonate, and 49.5 and 174.2 cm² × 10^{-4} for hexadecane. A comparison of the values of $\Sigma_{max/mole}$ for the same two methyl silicones spread on *ar*-dibromoethylbenzene as well as on hexadecane, in both of which these silicones are soluble, reveals that $\Sigma_{max/mole}$ increased with $\gamma_a - \gamma_b$. Thus, if the oil solubilities of the displacing agents are approximately the same, the dominant variable is the value of $\gamma_a - \gamma_b$.

In miscible systems, $\gamma_{a'}$ approaches γ_b, and thus $F_{b/a}$ approaches $\gamma_a - \gamma_b$; when the agent is insoluble, however, the value of $F_{b/a}$ is small as compared to $\gamma_a - \gamma_b$. The relationship is thus shown to be more simple between $F_{b/a}$ and $\Sigma_{max/mole}$ than that between $\gamma_a - \gamma_b$ and $\Sigma_{max/mole}$ (compare the methyl silicones in Table IV). Thus, under these circumstances both the equilibrium spreading pressure of $F_{b/a}$ and the oil solubility of the agent are the principal factors determining the oil displacement; furthermore, $F_{b/a}$ decreases with the solubility of the agent in the organic liquid.

Effect of Volatility of Displacing Agent. In those systems where $\gamma_a - \gamma_b$ is large and the oil-displacing agent has a high vapor pressure, the drop of the agent does not have to be in direct contact with the oil in order to cause oil displacement. When a drop of any of the fluorinated alcohols or fluorocarbons was held just above the surface of the oil-coated panel, the vapor molecules of the agent adsorbed on the liquid surface creating a large enough local surface tension gradient to cause formation of a growing hole in the oil layer. The oil-displacing action continued as long as the drop was held above the oil. The area cleared of oil grew to a maximum size which was larger the nearer the drop of agent was held relative to the panel and the higher its vapor pressure. When the suspended drop was removed to a great distance, the displaced oil flowed back over the cleared area to cover it completely once more. Thus, the attractive forces between the solid surface and the vapor molecules of the agent were not strong enough, for the systems studied, to promote irreversible adsorption on the solid surface

of an oleophobic monolayer (one on which no oil respreading could occur).

When the suspended drop of the agent was placed on the cleared area of the solid, it continued to cause displacement of the oil if insoluble in it, but $\Sigma_{max/mole}$ was less than the value observed when the agent was placed directly on the oil layer to be displaced. When the agent was soluble in the oil to be displaced, Σ attained about the same maximum as that caused by an insoluble agent, but it thereafter gradually diminished in size; it was concluded that some of the agent was dissolving in the oil around the cleared periphery.

Mechanisms of Oil Displacement. A. Oil-Soluble Agent. Several mechanisms participated in the displacement of oils by liquid organic agents, but their relative importance depended upon the experimental conditions. Of special importance was the oil solubility of the displacing agent. When a drop of an oil-soluble spreadable agent was placed on the surface of a layer of organic liquid not over a few tenths of a millimeter thick, it dissolved as it spread (Figure 5a). Since the surrounding area of the liquid had a higher surface tension than the oil solution in the immediate vicinity of the spreading oil drop, a localized and large surface tension gradient developed which was equivalent to a large spreading pressure directed radially and outwards. The result was a flow of the surface layer of the liquid in the same direction. The so-called Marangoni effect[31-33] is the same radial pressure effect occurring on the surface of water. The movement of the spreading surface film dragged along the bulk oil immediately beneath it,[34,35] and therefore the local, radial, outward movement of the oil tended to form a circular depression of the oil level with a central mound (see Figure 5b), which resulted because the radial gradient in surface tension must be greatest at the periphery of the drop and least at the center. The greater the rate of spreading of the agent, the deeper the circular depression. However, during this spreading process the agent continued to dissolve in the central oil mound and contacted the solid–oil interface to adsorb as a monolayer. This solution process also caused continued spreading of the central mound and eventually its disappearance leaving a circular hole in the oil layer and so exposing the dry surface of the solid.

Whenever the oil-spreading movement was sufficiently rapid, inertial effects of the flowing oil mass were manifested. An annular oil ridge usually appeared around the central spreading drop which eventually broke up into a circular array of oil mounds (see Figure 5c). Such a break-up process is familiar evidence of the characteristic instability of a toroidal

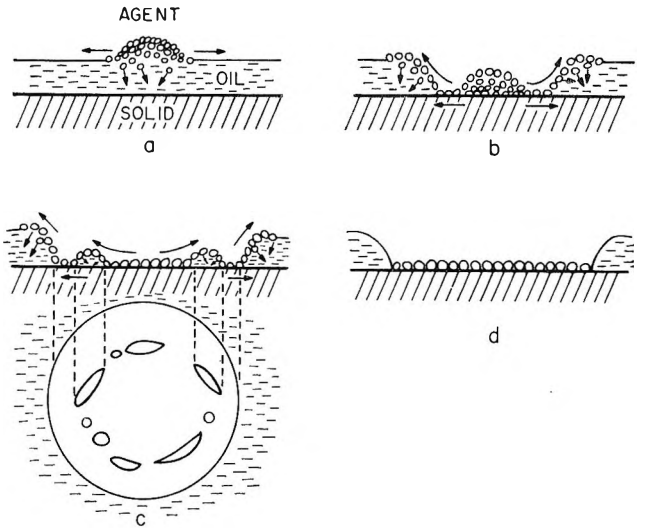

Figure 5. Displacement mechanism by agent soluble in oil ($\gamma_a - \gamma_b$ is large).

liquid mass which is striving to minimize its surface energy. Infrared analysis of the resulting drops of residual liquid revealed that it consisted of the oil and a low concentration of the dissolved agent (see last column of Table IV). The rate at which the oil ridge broke up into discrete oil mounds depended upon the density, viscosity, and surface tension of the oil, and also on the molecular weight, viscosity, and volatility of the agent. For example, an oil-displacing agent of relatively high volatility and low surface tension (such as perfluorobutanol) would spread in a minute on propylene carbonate while piling up a well-defined oil ridge which subsequently broke up into a modest number of oil mounds. When the oil-displacing agent had such a chemical structure as to be strongly adsorbed on the solid surface to form an oleophobic film, a completely dry surface area, exhibiting a large and characteristic contact angle with a drop of the oil, remained exposed after the spreading process had been completed (see Figure 5d).

If the oil-displacing agent exerted a low spreading pressure (*i.e.*, if γ_b was only slightly less than γ_a), the central oil mound did not disappear, but changed into a thin residual layer of oil which in turn usually retracted slowly to leave a disk-shaped bare area on

(31) J. Thompson, *Phil. Mag.*, [4] 10, 330 (1855).

(32) L. E. Scriven and C. V. Sternling, *Nature*, 187, 186 (1960).

(33) W. D. Bascom, R. L. Cottington, and C. R. Singleterry, Advances in Chemistry Series, No. 43, American Chemical Society, Washington, D. C., 1964, p 335.

(34) S. E. Bressler and D. C. Talmud, *Physik. Z. Sowjetunion*, 4, 864 (1933).

(35) J. H. Schulman and T. Teorell, *Trans. Faraday Soc.*, 34, 1337 (1938).

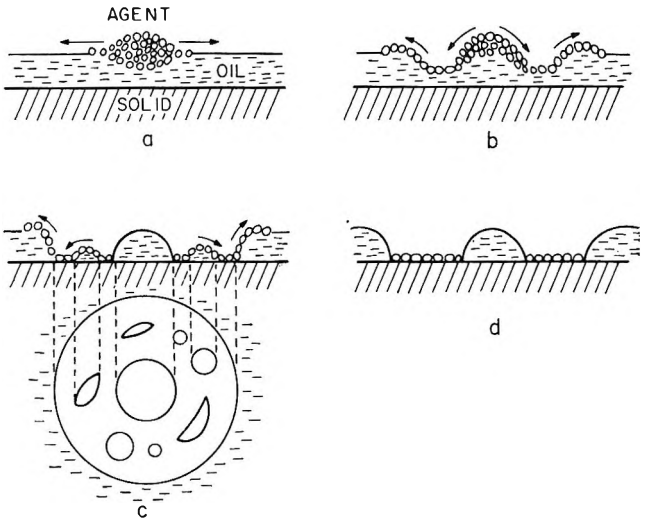

Figure 6. Displacement mechanism by agent insoluble in oil ($\gamma_a - \gamma_b$ is large).

which were located a few scattered drops of oil. Some examples of such behavior are given in Table IV. Since γ_b was only a little less than γ_a, any residual adsorbed film of agent modifying the solid surface imparted to the solid a critical surface tension of wetting (γ_c) only slightly lower than γ_a. Thus the contact angle of the residual film of oil had to be small. Although the bulk oil had been swept back vigorously in the initial spreading process, the residual oil layer retracted slowly, but completely, until a dry oleophobic surface remained.

B. Oil-Insoluble Agent. When the agent was insoluble in the oil upon which it spread, several new and interesting stages appeared in the oil-displacement process. If $\gamma_a - \gamma_b$ was large, the drop of agent spread rapidly and radially over the surface of the oil (Figure 6a). An oil hole was not created immediately below the area of original contact, but instead a widening circular dry band appeared (Figure 6b). Where the agent had become adsorbed on the dry solid surface, an oleophobic monolayer remained which prevented the oil from respreading. Thus, an oil disk remained in the center, surrounded either by a thinner circular oil layer or by a dry annulus which in turn was surrounded by a thin toroidal mound of oil (see Figure 6c). Somewhat later the thin oil layer often broke up to form a number of small scattered drops. Under any condition the residual thin film of oil retracted into the large center mound or into the displaced bulk liquid (Figure 6d). Infrared analysis showed that the residual oil mounds consisted of the pure oil only (Table IV), as would be expected because of the insolubility of agent and oil.

An example of effective oil displacement for an insoluble system in which $\gamma_a - \gamma_b$ is small is that of ω-hydrogen perfluoroheptanol and *n*-hexadecane (Table IV). When a drop of the alcohol was placed upon the layer of hexadecane, it first remained there in the shape of a lens. After about 2 to 3 min, the drop completely sank through the oil layer and, on contacting the solid–oil interface, spread radially over this interface, displacing the hexadecane through adsorption on the solid as a monolayer of ω-hydrogen perfluoroheptanol. At the site of initial contact, there remained a drop of pure displacing liquid (Table IV). The alkanol drop displaced the oil by a combination of gravitational, hydrodynamic, and surface chemical mechanisms. The effect of gravity is significant because the densities at 25° of hexadecane and of the alcohol are 0.775 and 1.753 g/ml, respectively. As the lens traveled through the oil, its lower surface assumed a concave configuration. On reaching the solid–oil interface, it displaced the oil beneath but entrapped a layer of hexadecane between it and the solid below the center region of the drop; only the periphery of the lens was in actual contact with the solid, and spreading of the alcohol started at that site. An oil layer several thousand angstroms thick may have been present initially trapped beneath the bulk alcohol drop. Baker, Bascom, and Singleterry[36] have made similar observations in their study on water drops approaching solid–oil interfaces.

Effect of Injecting Agent at Solid–Oil Interfaces. In order to understand better the mechanisms involved, several systems were studied by injecting the displacing agent below the oil layer in direct contact with the solid–oil interface.

A. When a drop of an oil-soluble agent was deposited directly at the solid–oil interface, the results were the same as though the drop were deposited at the oil–air interface, since the agent was able to reach the solid–oil interface through solution in the oil. In such a system, monolayer formation at the solid–oil interface is the dominant mechanism rather than viscous drag, as in the case of agent spreading at the air–oil interface.

B. When a drop of an oil-insoluble agent was deposited directly at the solid–oil interface, a different mechanism was operative. After the drop of agent contacted the solid–oil interface, it spread radially along that interface, depositing a monolayer on the solid and dragging the layer of oil immediately above it toward the periphery. In consequence, the oil layer became thinner. If the critical surface tension γ_c

(36) H. R. Baker, W. D. Bascom, and C. R. Singleterry, *J. Colloid Sci.*, **17**, 477 (1962).

of the modified solid–oil interface was sufficiently low and the oil not too viscous, a hole formed at the site of the drop from which the oil retracted spontaneously to leave a dry solid surface area coated with an oleophobic film. When the oil could not be carried fast enough toward the periphery of the spreading drop, it retracted into droplets with well-defined, nonzero contact angles. In systems where $\gamma_a - \gamma_b$ was small, the rate of spreading was slow.

These experiments revealed that the net oil displacement we had observed was the resultant of two processes: (a) the Marangoni effect on an organic liquid–air interface, and (b) the additional effect of the permeation of the agent through the oil layer to adsorb as an oleophobic film at the solid–oil interface and its effect on destabilizing the thin layer of oil adhering to the solid.

Oil Displacement by Agents Free of Polar Functional Groups

Monolayer adsorption of the agent is easily understood, for the polar–nonpolar displacing agents mentioned thus far always contained an adsorbable functional polar group which adsorbed at the solid–oil interface exposing, in the case of the fluorinated alcohols, the fluorocarbon (or organophobic) portion of the molecule to the oil. The metal surface coated with close-packed fluorinated paraffin chains became a surface of low free energy for which γ_c was much smaller than γ_a; therefore, it became oleophobic to the oil displaced. When the polar agents were unfluorinated, as was true of the fatty alcohols, the solid surface was coated by the terminal methyl groups of the oriented paraffin chains. If the value of γ_c of the resulting film-covered surface was not appreciably lower than γ_a, oil displacement was only temporary; *i.e.*, the oil (such as hexadecane) spread back eventually as the alcohol disappeared to recover the cleared area. If γ_a was higher than γ_c, as in the case of liquids such as *ar*-dibromoethylbenzene, tricresyl phosphate, or propylene carbonate, then permanent oil displacement occurred, but the areas displaced were small and some remained partially covered by oil.

Agents free of polar functional groups, such as the perfluoroalkanes and chloroperfluoroalkane prepared by Hauptschein, *et al.*,[37] were also found capable of permanently displacing oil from a steel plate. Thus some adsorption at the solid–oil interface must have occurred. It is pertinent to note here that adsorption of even a nonpolar compound occurs readily at metal–air interfaces through the polarization induced by the surface forces emanating from the metal.[38] In displacing oils the perfluoroalkanes behaved somewhat differently than the other agents. The peripheral front of the oil-displacing drop advanced in an irregular waving manner; *i.e.*, a small section was cleared but immediately was recovered by the oil and an adjacent section was cleared; this one, in turn, was recovered by the oil and the initial section was cleared. This wavering advance continued for long periods of time until evaporation of the drop. When the oil-coated steel panel was fully exposed to the atmosphere rather than covered by a glass plate, the waving action was enhanced, and the final $\Sigma_{max/mole}$ was smaller. Oil displacement by these compounds was thus primarily the result of surface tension gradient of the agent in the oil layer and the high volatility of the agent.

Bascom, Cottington, and Singleterry[33] had found that in a mixture of hydrocarbons, the constituents of high volatility, since they are capable of lowering the surface tension of the mixture, would increase the rate of spontaneous liquid spreading. An analogous but somewhat modified process occurred in the present study. The rate of spreading of these highly volatile nonhydrophilic agents was very rapid. Since adsorption at the solid–oil interface did not take place readily, the oil of higher surface tension respread over the solid surface, but it was displaced in turn by the highly volatile and therefore better spreading compound of lower surface tension. This dynamic process continued until evaporation of the agent in excess of the adsorbed fraction was completed and equilibrium conditions had been reached. The ease and efficiency of oil displacement were thus dictated by $\gamma_a - \gamma_b$ and the difference in volatility of oil and displacing agent.

Oil Displacement by Dimethyl Silicones

The volatile open-chain dimethyl silicone fluids, when used as oil-displacing agents, behaved similarly to the perfluoroalkanes. Specimens of high volatility displaced the oil rapidly, but eventually the oil respread over the area; the rate and completeness of rewetting depended upon $\gamma_a - \gamma_b$. As the molecular weight of the silicones increased, and therefore the volatility decreased, $\Sigma_{max/mole}$ increased (Figure 7); eventually the film remained adsorbed on the solid, making the surface oleophobic, even with respect to oils of such low γ_a as hexadecane (Table IV). In systems such as these, the vapor pressure of the agent plays a significant part in the oil-displacement mechanism as was proven by the contraction to smaller values of $\Sigma_{max/mole}$ when the systems were exposed to the open atmosphere.

(37) M. Hauptschein, M. Braid, and F. E. Lawlor, *J. Am. Chem. Soc.*, 79, 6248 (1957).

(38) K. W. Bewig and W. A Zisman, *J. Phys. Chem.*, 68, 1804 (1964).

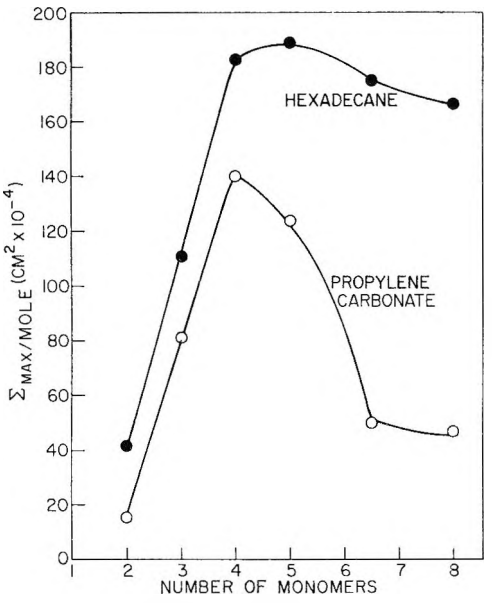

Figure 7. Effect of degree of polymerization of dimethyl silicones on maximum area displaced of oil (substrate steel).

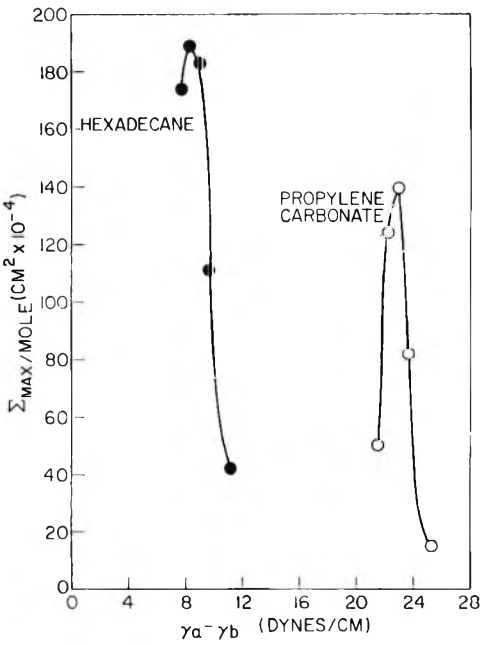

Figure 8. Effect of surface tension difference of oil and dimethyl silicones on maximum area displaced of oil (substrate steel).

Figure 7 shows the effect of degree of polymerization of the dimethyl silicones on the extent to which they displace hexadecane and propylene carbonate. $\Sigma_{max/mole}$ was greatest in either case for the tetramer and pentamer, which apparently combine the optimum features of volatility and molecular weight; silicones of lower molecular weight were too volatile to be efficient, whereas those of higher molecular weight were too viscous. Higher solubility of the silicone in the hexadecane than in propylene carbonate accounted for the larger $\Sigma_{max/mole}$ obtained by displacement from hexadecane than from propylene carbonate (see Table IV). Results in Figure 8 also confirmed the conclusions about the effect of solubility on oil displacement, as evidenced by the larger $\Sigma_{max/mole}$ observed with hexadecane, although the surface tension differences between the silicones and hexadecane were much smaller than those between the silicones and propylene carbonate. The smaller $\Sigma_{max/mole}$ with increasing $\gamma_a - \gamma_b$ were again the manifestations of the high viscosity of the high molecular weight silicones.

These observations were made using the linear dimethyl silicones. Studies carried out with cyclic[39] and branched dimethyl silicones led to essentially the same results and showed the same trends.

Oil Displacement from Other Solids

The same series of experiments on oil-coated borosilicate (Pyrex) glass panels resulted in essentially the same oil displacement phenomena observed with steel panels. In Tables II and III will be found the results obtained on Pyrex substrates for drops of aliphatic and fluorinated alcohols placed on hexadecane and propylene carbonate. Usually, the values of $\Sigma_{max/mole}$ caused by the aliphatic alcohols on Pyrex were approximately the same or slightly larger than those on steel. The fluorinated alcohols displaced areas of hexadecane which were equal to, or slightly larger than, those on steel and areas of propylene carbonate which were smaller. Similar experiments using hexanol, heptanol, perfluorooctanol, and the tetramer of dimethyl silicone to displace hexadecane from copper, aluminum, nickel, and nichrome resulted in the same values of $\Sigma_{max/mole}$ as those on steel, when the metals were given the same surface treatment. $\Sigma_{max/mole}$ was somewhat higher for borosilicate glass and soda-lime glass, which behaved alike.

The effect of surface roughness on $\Sigma_{max/mole}$ was observed by comparing results on nickel, metallographically polished to a smooth mirror finish with Linde α-Al_2O_3 fine abrasive, with those on soda-lime and borosilicate glass, when hexadecane was displaced by hexanol and heptanol. $\Sigma_{max/mole}$ on the smooth mirror-finish nickel surface equalled those on the two glass surfaces. When a steel surface was roughened to a 400A Tri-M-Ite paper finish, $\Sigma_{max/mole}$ displaced by hexanol, heptanol, and perfluorooctanol from hexa-

(39) M. J. Hunter, J. F. Hyde, E. L. Warrick, and H. J. Fletcher, *J. Am. Chem. Soc.*, 68, 667 (1946).

decane were decreased slightly over those obtained by a 4/0 emery paper surface finish. Some of these results obtained are listed in Table II. The differences in $\Sigma_{max/mole}$ shown in Tables II and III thus are most likely attributable to the differences in surface roughness between steel and borosilicate glass. Hence, the mechanisms of oil displacement and the final condition of the cleared solid surfaces were essentially independent of the chemical, but dependent upon the physical nature of the solid surface as long as the critical surface tension of wetting of the solid was high enough to permit spreading of the oil. Studies by Levine and Zisman[40] and Cottington, Shafrin, and Zisman[41] of the physical properties of adsorbed aliphatic alcohol monolayers at the glass–air and steel–air interfaces concluded that the adhesion of the alcohol polar group to glass and steel were about the same. Our observations were in agreement with theirs.

It has been shown that the mechanism involved in liquid–liquid displacement is not strongly dependent on the nature of the underlying solid surface. The bulk of the oil is displaced by any suitable agent without a specific solid–liquid interaction. Only when the agent molecules reach the oil monolayer adsorbed at the solid surfaces does it have to compete with the oil molecules for the available adsorption sites. Thus liquid–liquid displacement can apply to any solid surface for which there is not an extremely unfavorable competitive adsorption situation. For example, such an unfavorable situation would occur if the adjacent monolayer of oil (or liquid to be displaced) is chemisorbed on the solid.

General Conclusions

This investigation has extended our knowledge of the surface-chemical displacement of water from solid surfaces, to the displacement of *any* liquid from such surfaces. This method of displacing oil films relates to physically adsorbed films; it is not concerned with the displacement of chemisorbed films. It is concluded that: (a) The most suitable liquid displacement agents are polar–nonpolar compounds capable of adsorbing readily at the solid–oil interface. Certain nonpolar compounds can also act as displacing agents, but their efficiencies are not as high. (b) It is preferable that the nonpolar portion of the molecule of the displacement agent be a long aliphatic chain for maximum cohesion between adjacent molecules in the adsorbed monolayer; for maximum organic liquid displacing ability (oleophobicity) the aliphatic chain should be fully fluorinated. (c) For optimum results the liquid displacing agent should have a large initial spreading coefficient on the liquid to be displaced. (d) The agent should also exhibit a high equilibrium spreading pressure. For achievement of the two preceding properties it is necessary that the displacing agent (i) have a surface tension as low as possible when compared to that of the oil to be displaced and (ii) a high solubility in the oil to be displaced, and (iii) be efficient in depressing the surface tension of the oil to be displaced. (e) High volatility (high vapor pressure) is advantageous when the agent must displace the oil rapidly; where long-lasting oleophobicity of the area cleared of oil is more important than speed, compounds of low volatility (but high solubility) are more suitable. (f) Low-molecular weight dimethyl silicones (dimers, trimers, and tetramers) are also good displacing agents for liquids in which they are highly soluble. (g) The results presented here (for example, Figures 3, 5, and 6) include the previous conclusions of Baker, Singleterry, and Zisman[2–9] on water displacement.

(40) O. Levine and W. A. Zisman, *J. Phys. Chem.*, **61**, 1068, 1188 (1957).

(41) R. L. Cottington, E. G. Shafrin, and W. A. Zisman, *ibid.*, **62**, 513 (1958).

The Rates of Decomposition of Chemically Activated Propylene[1]

by J. W. Simons,

Department of Chemistry, New Mexico State University, University Park, New Mexico 88070

B. S. Rabinovitch, and F. H. Dorer

Department of Chemistry, University of Washington, Seattle, Washington 98105 *(Received September 13, 1965)*

The decomposition of chemically activated propylene formed by the addition of methylene to ethylene has been studied. Decomposition into H + allyl is characterized by a looser complex than that found earlier for decomposition of $RCH_2CH{=}CH_2$ into R + allyl. This behavior is compared with that in related systems. Decomposition into CH_3 + vinyl also occurs as a minor reaction. The combination rate of allyl radical with H atoms is intermediate between those of alkyl radicals and of alkenes with H atoms.

Introduction

The study of the reaction kinetics of chemically activated species[2] has been extended recently to the decomposition of alkenes.[3] In the latter work it was shown that the decomposition into allyl plus alkyl radicals by butene-1, pentene-1, hexene-1, and several other higher alkenes, produced by the isomerization of various substituted cyclopropanes, proceeded at a rate suggestive of only a semiloose activated complex. To express it otherwise, the recombination rate of allyl and alkyl radicals does not involve as loose a complex as that for recombinations of alkyl radicals of comparable size[4] which proceed with a specific rate, $k \sim 0.1z$, where z is the specific collision rate; instead, the value $5 \times 10^{-3}z$ was found.

In a recent study of the collisional deactivation of vibrationally excited cyclopropane,[5] it was found that the decomposition of the resultant chemically activated isomerization product, propylene, became significant at low pressures. It seemed of considerable interest to compare this decomposition reaction, $CH_3CH{=}CH_2 \rightarrow H + \cdot CH_2CH{=}CH_2$, with that of the higher alkenes; as is well known,[6] the rate of association of H plus alkene (or the reverse decomposition) differs considerably in character from the analogous reaction of methyl, or other alkyl radicals, with alkenes. In the present work, more-detailed low-pressure data and a quantitative treatment of the decomposition of chemically activated propylene produced by the reactions of methylene radicals with ethylene are reported. Both ketene and diazomethane have been used as sources of methylene radicals.

Experimental Section

The experimental procedure and analysis was the same as that described previously.[5,7] Product identification and analysis was made by glpc and mass spectrometry.

Toward the end of the work, it was discovered that the pentene-1 analyses in both the ketene and diazomethane systems included a contribution from an unidentified compound having the same retention time as pentene-1 on the analytical column employed. Calibration runs ruled out allene, 1,3-butadiene, and other pentene isomers as the unknown. The glpc peak cor-

(1) This work was supported by the National Science Foundation and Office of Naval Research through the University of Washington.

(2) (a) B. S. Rabinovitch and R. W. Diesen, *J. Chem. Phys.*, **30**, 735 (1959); (b) B. S. Rabinovitch and M. C. Flowers, *Quart. Rev.* (London), **18**, 122 (1964); (c) B. S. Rabinovitch and D. W. Setser, *Advan. Photochem.*, **3**, 1 (1964).

(3) F. H. Dorer and B. S. Rabinovitch, *J. Phys. Chem.*, **69**, 1952 (1965).

(4) (a) A. Shepp and K. O. Kutschke, *J. Chem. Phys.*, **26**, 1020 (1957); (b) G. Z. Whitten and B. S. Rabinovitch, *J. Phys. Chem.*, **69**, 4348 (1965).

(5) (a) J. W. Simons, B. S. Rabinovitch, and D. W. Setser, *J. Chem. Phys.*, **41**, 800 (1964); (b) D. W. Setser, B. S. Rabinovitch, and J. W. Simons, *ibid.*, **40**, 1751 (1964).

(6) E. W. R. Steacie, "Atomic and Free Radical Reaction," Reinhold Publishing Corp., New York, N. Y., 1954.

(7) J. W. Simons and B. S. Rabinovitch, *J. Phys. Chem.*, **68**, 1322 (1964).

responding to pentene-1 was collected from a number of lower pressure runs and was reanalyzed on a boiling point column which resolved the two peaks. This analysis showed that at least two-thirds of the original peak was pentene-1.

Results and Discussion

Analytical and Other Errors. The maximum error in the rate constant for propylene decomposition, due to the error in pentene-1 analysis, corresponds to only ~20% if all correction is omitted.

Small amounts of ethane, propane, and *n*-butane impurities in the ketene and, especially, diazomethane precursors could cause an overestimate of the rate, particularly at higher pressures, but becoming less important at low pressures. In fact, a very high value of the ratio, ethane/butane, in the diazomethane system is most easily explained as due to ethane impurity. It is felt that the most reliable measure of the experimental rate was obtained at limitingly low pressures; the higher pressure rate constants are considered unreliable.

Ketene–Ethylene System. In Figure 1 the variation of the product composition with pressure is shown for ketene photolysis at ~3200 A in ~1:10 admixture with ethylene. The observed products and their variations with pressure are adequately explained by the mechanism scheme

$$CH_2CO \xrightarrow{3200\ A} {}^1CH_2 + CO \quad (1)$$

$${}^1CH_2 + C_2H_4 \longrightarrow \text{propylene}^* \quad (2a)$$

$$\longrightarrow \nabla^* \quad (2b)$$

$$\nabla^* \xrightarrow{k_a} \text{propylene}^* \quad (D) \quad (3a)$$

$$\xrightarrow{\omega} \nabla \quad (S) \quad (3b)$$

$$\text{propylene}^* \xrightarrow{k_H} H + \text{allyl} \quad (D_h) \quad (4a)$$

$$\xrightarrow{\omega} \text{propylene} \quad (S_h) \quad (4b)$$

followed by

$$H + C_2H_4 \longrightarrow C_2H_5 \quad (5)$$

$$C_2H_5 + \text{allyl} \longrightarrow \text{pentene-1} \quad (6a)$$

$$\longrightarrow C_2H_6 + C_2H_4 \quad (6b)$$

$$\longrightarrow C_2H_4 + C_3H_6 \quad (6b')$$

$$CH_3 + \text{allyl} \longrightarrow \text{butene-1} \quad (6c)$$

$$2C_2H_5 \longrightarrow n\text{-butane} \quad (7a)$$

$$\longrightarrow C_2H_6 + C_2H_4 \quad (7b)$$

$$CH_3 + C_2H_5 \longrightarrow C_3H_8 \quad (8a)$$

$$\longrightarrow CH_4 + C_2H_4 \quad (8b)$$

$$2CH_3 \longrightarrow C_2H_6 \quad (9)$$

$$2(\text{allyl}) \longrightarrow C_6H_{10} \quad (10)$$

where the asterisk indicates internal vibrational energy in excess of that required for a decomposition reaction and ω is assumed to be equal to the collision frequency ($\omega = 1.52 \times 10^8 p$ (cm) $\sec^{-1}$; see ref 5). The possible origin of the methyl radicals (eq 6c, 8, and 9) in methylene radical systems has been considered previously.[4b] This source is not important in ethylene systems and reactions 6c, 8, and 9 are insignificant here; they will be considered again later.

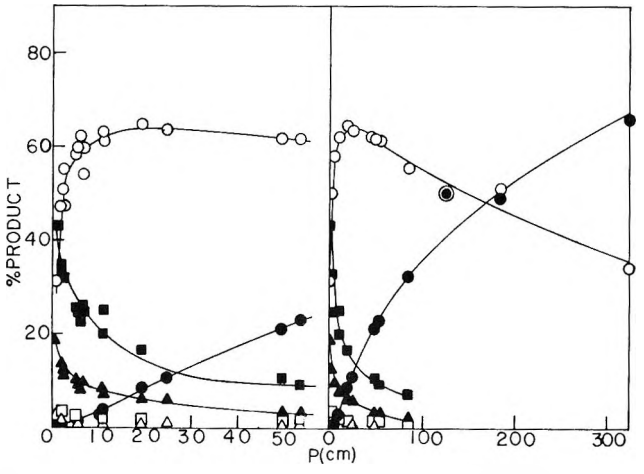

Figure 1. Variation of product percentages with pressure in the ketene–ethylene system: ○, propylene; ●, cyclopropane; ■, pentene-1; ▲, *n*-butane; □, butene-1; △, ethane.

Reactions 3a and 3b are more correctly represented by multistep processes but simple, single-step representations are sufficient for present purposes. Reactions 1–3b and 4b have been discussed in detail previously for this system. Apart from complications due to the presence of triplet methylene, they quantitatively explain the ∇ and propylene variations in Figure 1 down to a pressure of ~10 cm.[5,8] At lower pressures, propylene decomposition by eq 4a becomes important and explains, *via* reactions 5–7b, the decreasing propylene and increasing pentene-1, ethane, and *n*-butane yields with decreasing pressure as indicated in Figure 1. The small, relatively constant percentage of butene-1 is presumably due to secondary reaction of methylene radicals with propylene, mainly.

Reaction 5 scavenges H atoms in this system. The

(8) H. M. Frey and G. B. Kistiakowsky, *J. Am. Chem. Soc.*, **79**, 6373 (1957); B. S. Rabinovitch, E. Tschiukow-Roux, and E. W. Schlag, *ibid.*, **81**, 1081 (1959).

activation energy for addition to the double bond is low (~2 kcal mole^{-1})[9] and the ethylene is present in large excess over other species in the system. The reverse recombination reaction, H + allyl, is unimportant because of the small steady-state concentration of allyl radicals relative to ethylene. Reactions 6 and 7 are the logical subsequent reactions of ethyl radicals in view of the relatively high activation energy (~8 kcal/mole) for addition of ethyl radicals to ethylene.[10] The disproportionation reactions, 6b and 6b′, amount to only 14% of the recombination reaction 6a.[11]

The ratio of ethane to *n*-butane, as shown in Figure 2 for this system, is virtually pressure independent and has the average value 0.12 ± 0.03. This ratio is quite close to the accepted value[6] of the disproportionation/recombination ratio for ethyl radicals. This lends support to the proposed mechanism and, together with negligible propane production, to the absence of reactions 8 and 9.

The ratio of *n*-butane/pentene-1 as a function of pressure, shown in Figure 3, is virtually pressure independent. It is known that a small amount of the pentene-1 may be formed on photolysis of methylene precursors.

Unfortunately, no search was made for hexadiene (reaction 10) in the products. Estimation of the amount of decomposition may be made either on the basis of H atom-derived products, or of allyl radical-derived products. The former basis is used immediately below, and for this reason other disproportionation reactions of allyl need not be listed in the scheme.

On the basis of the mechanism, the specific rate of decomposition of propylene* in this system is

$$k_H = \omega D_h / S_h \qquad (I)$$

where the amount of decomposition is D_h = 2(ethane + *n*-butane) + 1.14(pentene-1); the amount of stabilization is S = propylene. Values of k_H are given in Table I. Part of the variation of k_H with pressure is due to the energy dispersion of the activated molecules.[5] The lowest pressure results are considered as more reliable for the reasons described earlier. In addition, the perturbation of the system due to the concomitant formation of triplet methylene[3,7] tends to zero at low pressure. The listed value for p = 0, k_{H0}, is the zero-pressure extrapolated value.

Ketene–Ethylene–Helium Systems. The product composition as a function of pressure for ketene photolysis (~3200 A) in ketene:ethylene:helium mixtures of 1:10:167, on a collision basis, is shown in Figure 4. The ratios of ethane/*n*-butane and *n*-butane/pentene-1 are shown in Figures 2 and 3, respectively. These

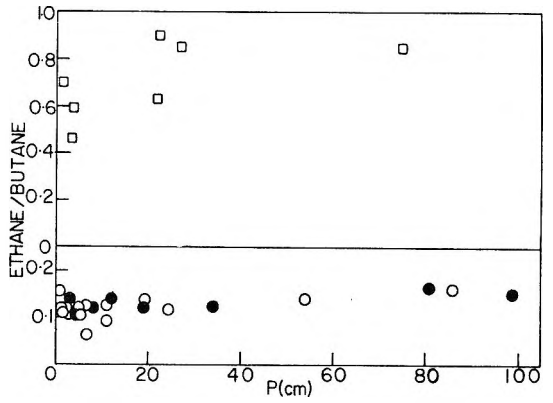

Figure 2. Variation of the ethane/*n*-butane ratio with pressure in the various systems: □, diazomethane–ethylene; ○, ketene–ethylene; ●, ketene–ethylene–helium (latter pressures are reduced by one-third for graphing convenience).

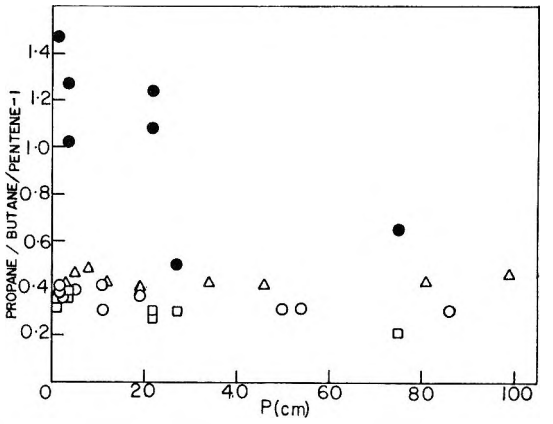

Figure 3. Variation of the ratio, propane/*n*-butane, and of *n*-butane/pentene-1 with pressure in the various systems; open symbols are *n*-butane/pentene-1 ratios; ○, ketene–ethylene; △, ketene–ethylene–helium (pressures are reduced by one-third for graphing convenience); □, diazomethane–ethylene; ●, propane/butane ratio in diazomethane–ethylene system.

results are similar in all respects to those for the ketene–ethylene system except that decomposition of propylene* in the present system occurs at much higher total pressures. This result is consistent with an interpretation of inefficient collisional deactivation of propylene* by helium relative to ethylene; similar behavior was obtained earlier for ∇* deactivation where a total inefficiency of 0.21 was found.[5a]

(9) K. R. Jennings and R. J. Cvetanović, *J. Chem. Phys.*, **35**, 1233 (1961); R. Klein and M. S. Scheer, *J. Phys. Chem.*, **65**, 375 (1961); K. Yang, *J. Am. Chem. Soc.*, **84**, 719 (1962).

(10) M. Miyoshi and R. K. Brinton, *J. Chem. Phys.*, **36**, 3019 (1962); D. G. L. James and E. W. R. Steacie, *Proc. Roy. Soc.* (London), **A244**, 289 (1958).

(11) D. G. L. James and G. E. Troughton, *Chem. Commun.*, 94 (1965).

Table I: Experimental Rate Constants (sec^{-1}) for Propylene Decomposition in the Lower Pressure Region (25°)

						Ketene–ethylene system							
p, cm	10.9	10.8	6.6	6.6	6.0	5.4	5.0	2.3	2.1	1.8	1.8	0.64	(0)
$k_H \times 10^{-8}$	11.9	10.5	9.3	7.8	6.3	6.5	6.5	3.5	3.9	3.9	3.9	2.8	2.3
						Ketene–ethylene–helium system							
p, cm			57		34		23		15		9.5		(0)
p, cm (cor)			11.9		7.1		4.8		3.2		2.0		
$k_H \times 10^{-8}$			123		70		49		53		32		13
$k_H \times 10^{-8}$ (cor)			25.9		14.7		10.3		11.1		6.7		2.7
						Diazomethane–ethylene system							
p, cm		22		22		3.4		3.4		1.3		(0)	
$k_H \times 10^{-8}$		12.1		11.6		6.8		7.3		4.4		3	
$k_c \times 10^{-8}$		4.9		5.4		2.2		2.6		1.9		1.5	

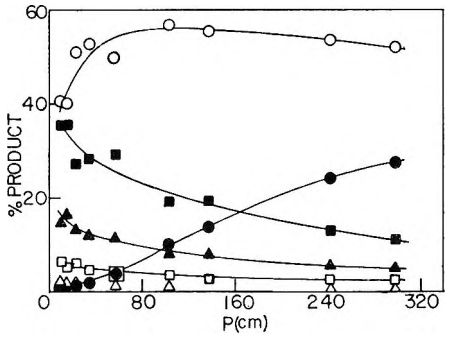

Figure 4. Variation of product percentages with pressure in the ketene–ethylene–helium system; symbols are identical with those in Figure 1.

Values of k_H calculated for this system by eq I are given in Table I. A rather large dependence of k_H on pressure is observed, and probably for the same reason as in the ketene–ethylene system. The zero pressure value, only, is accepted and the nominal value 13×10^8 sec^{-1} becomes 2.7×10^8 sec^{-1}, with use of β. The agreement with the pure system is good. Some formation of triplet methylene due to the presence of the inert gas helium occurs, but at this dilution amounts to only ~7%.[12]

Diazomethane–Ethylene System. The product composition as a function of pressure for diazomethane photolysis (~4300 A) in 1:20 admixture with ethylene is shown in Figure 5. An important difference between these results and those for the ketene systems is the inversion of the amount of butene-1 relative to butane with decreasing pressure. It is believed that this results from propylene* decomposition to give vinyl radicals, in addition to allylic C–H rupture, in this higher energy system. The following additional reactions are proposed to explain the products and their variation with pressure

$$\text{propylene}^* \xrightarrow{k_c} CH_3 + \text{vinyl} \quad (4c)$$

$$C_2H_5 + \text{vinyl} \longrightarrow \text{butene-1} \quad (6d)$$

$$\longrightarrow C_2H_6 + C_2H_2 \text{ or } 2C_2H_4 \quad (6e)$$

The rise in propane product by reaction 8 at lower pressures is consistent with reaction 4c.

The ratio of ethane/*n*-butane (Figure 2) is larger than that for the ketene systems. This is consistent with an increased importance of reaction 9 which follows reaction 4c. However, the increase also reflects some ethane impurity in the diazomethane. The data in this system are the most inaccurate and least reliable.

The ratio of *n*-butane/pentene-1 shown in Figure 3 is not greatly different from that for the ketene systems. This is as expected since the introduction of methyl

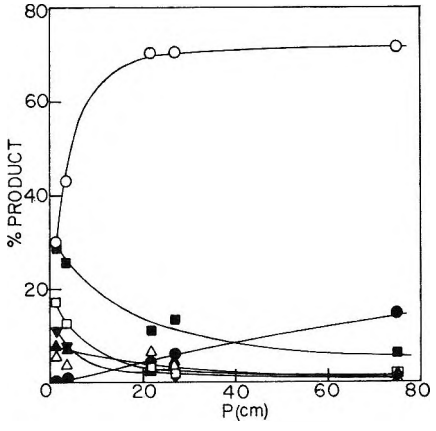

Figure 5. Variation of product percentages with pressure in the diazomethane–ethylene–system; symbols are the same as in Figure 1 with ▼, for propane, in addition.

(12) H. M. Frey, *J. Am. Chem. Soc.*, **82**, 5947 (1960); R. F. W. Bader and J. I. Generosa, *Can. J. Chem.*, **43**, 1631 (1965).

and vinyl radicals from reaction 4c would not affect this ratio greatly.

The ratio of propane/*n*-butane, given in Figure 3, increases markedly with decreasing pressure, as expected from the increasing relative importance at lower pressures of reaction 4c followed by reaction 8. Experimental values of k_H and k_c were calculated by eq I, where D_H = 1.14(pentene-1) + 2.24(*n*-butane) + 0.5(butene-1) + 1.06(propane), and D_c = 2 [ethane–0.12(*n*-butane)] + 0.5(butene-1) + 1.06(propane), and are given in Table I for various pressures. In the above expressions the ethane from disproportionation of ethyl radicals was taken to be 0.12 of the *n*-butane and the butene-1 was assumed to result equally from ethyl + vinyl and from methyl + allyl. The ethane from methyl radical recombination (reaction 9) was taken to be the measured excess over that resulting from ethyl radical disproportionation (0.12 × *n*-butane). Removal of ethyl by (6e) was simply ignored relative to reaction 6d which is itself an estimate.

The data in this system are very sparse at low pressures and k_{H0} is only semiquantitative in nature; also, D_c is based on CH_3-derived products, only, and various reactions of vinyl and allyl are not listed.

Thermochemistry and Energetics. The relevant thermochemical quantities for the following discussion are given in Table II.

The value of the critical energy, E_0, for reaction 4a can be obtained within reasonable limits from the values in Table II and the resonance energy of the allyl radical. It is assumed that the activation energy for the combination reaction is zero. Although this may not be correct, it is certainly not in error by more than ~1 kcal mole^{-1}. Estimates of the allylic resonance energy have been discussed recently[13] and the more reliable of these are encompassed by the limits of 12–14 kcal mole^{-1}. This range of allylic resonance energies, coupled with the range of 95–97 kcal mole^{-1} for the primary C–H dissociation energy in propane, gives values ranging from 81 to 85 kcal mole^{-1} for D_0^0(C–H) in propylene; the mean of 83 kcal should be representative.

A value of E_0 for reaction 4c can be obtained within reasonable limits from the data in Table II, again assuming zero activation energy for the recombination reaction for simplicity. Now $D_0^0(CH_3—CH=CH_2)$ is given by

$$\Delta H_f^\circ{}_0(CH_3) + \Delta H_f^\circ{}_0(CH=CH_2) - \Delta H_f^\circ{}_0(CH_3CH=CH_2)$$

where

$$\Delta H_f^\circ{}_0(CH_3) = D_0^0(CH_3—H) + \Delta H_f^\circ{}_0(CH_3) - \Delta H_f^\circ{}_0(H) = 34.3\text{–}35.3 \text{ kcal mole}^{-1}$$

and

$$\Delta H_f^\circ{}_0(CH=CH_2) = D_0^0(CH_2=CH—H) + \Delta H_f^\circ{}_0(C_2H_4) - \Delta H_f^\circ{}_0(H) = 64.8\text{–}67.8 \text{ kcal mole}^{-1}$$

which gives a range 90.6–94.6 kcal mole^{-1} for E_0 of reaction 4c; the mean value of 93 will be accepted as representative; From the mean value, it is seen that vinylic C–C rupture requires about 10 kcal mole^{-1} more energy than allylic C–H rupture.

The average energies of excitation, $\langle E^* \rangle$, of propylene* are 8.2 kcal mole^{-1} greater in these systems than those of cyclopropane* (Table II), which previous estimates have placed at ~103 kcal mole^{-1} for ketene photolysis at 3200 A[5a,14] and ~110 kcal mole^{-1} for diazomethane photolysis at 4300 A.[14,15] (These values are appropriate for use with a strong collision value for ω and allow for the actual collisional inefficiency.)[5] Then $\langle E \rangle$ are 111 and 118 kcal, respectively, and the average excess energy $\langle E^+ \rangle$ for allylic C–H rupture in propylene* has the representative value of 28 kcal mole^{-1} for the ketene system and 35 kcal mole^{-1} for the diazomethane system. For vinylic C–C rupture, $\langle E^+ \rangle$ is

Table II: Gaseous Heats of Formation and Bond Dissociation Energies at 0°K (kcal mole^{-1})[a]

	$\Delta H_f^\circ{}_0$	D_0^0(R–H)
H	51.7	
Methane	−16.0	102.5 ± 0.5[b]
Propane		96 ± 1 (prim)[c]
Ethylene	14.5	104 ± 2[d]
Propylene	8.5	
Cyclopropane	16.7[e]	

[a] Unless otherwise specified, values are taken from F. D. Rossini, API, "Selected Values of Physical and Thermodynamic Properties," 1953. [b] A median of the values given in *a* and by J. A. Kerr and A. F. Trotman-Dickenson, "Strengths of Chemical Bonds," "Handbook of Chemistry and Physics," 46th ed, Chemical Rubber Publishing Co., Cleveland, Ohio, 1965. [c] A median of the values in *b* for propane and ethane at 0°K. [d] An average of the values determined by A. G. Harrison and F. P. Lossing, *J. Am. Chem. Soc.*, **82**, 519 (1960), and by A. F. Trotman-Dickenson and G. J. O. Verberke, *J. Chem. Soc.*, 2580 (1961). [e] The 298°K value [J. W. Knowlton and F. D. Rossini, *J. Res. Natl. Bur. Std.*, **43**, 113 (1949)] converted to 0°K.

(13) (a) H. M. Frey and D. C. Marshall, *J. Chem. Soc.*, 3891 (1962); (b) D. M. Golden, K. W. Egger, and S. W. Benson, *J. Am. Chem. Soc.*, **86**, 5416 (1964), and references therein.

(14) D. W. Setser and B. S. Rabinovitch, *Can. J. Chem.*, **40**, 1425 (1962).

(15) F. H. Dorer and B. S. Rabinovitch, *J. Phys. Chem.*, **69**, 1973 (1965).

Table III: Theoretical Values of $k_{H\langle E\rangle}$ (sec^{-1}) for Various Complexes and Values of E_0

E_0, kcal $mole^{-1}$	81	84	81	84	A[a]
$\langle E\rangle$, kcal $mole^{-1}$	111	111	118	118	...
Model I	2.4×10^8	8.5×10^7	9.3×10^8	3.7×10^8	...
II_{300}	1.2×10^8	4.7×10^7	5.2×10^8	2.1×10^8	1.8×10^{14}
II_{150}	4.6×10^8	1.6×10^8	1.8×10^9	7.1×10^8	6.0×10^{14}
II_{75}	...	6.0×10^8	...	...	2.4×10^{15}
III	1.6×10^{10}	6.2×10^9	...	...	7.6×10^{15}
Expt		2.5×10^8		3.0×10^8	

[a] Calculated frequency factor at 750°K for the relation $k = Ae^{-E_0/RT}$; *i.e.*, this is *not* the "Arrhenius" factor.

Table IV: Frequency Assignments for Propene Decomposition by CH Rupture

Motion[a]	Molecule	I	II_{300}[b]	II_{150}[b]	II_{75}	III[c]
C-H str	3090					
	3013					
	2954 (2)					
	2992					
	2933	...	...	...	...	...
HCH bend	1474	150 (2)	300 (2)	150 (2)	75 (2)	allyl rot (2)
	1378					
	1443					
	1419					
C=C str	1652	1400	1400	1400	1400	1400
HC=C bend	1298					
	1172					
C—C=C bend	428	600	375	375	375	375
C—C str	920	1200	1300	1300	1300	1300
CH_3 wag	912					
HCC bend	578		375	375	375	375
	963		900	900	900	900
	991	700	700	700	700	700
	1045	963	925	925	925	925
CH_3 rot	225	450	500	500	500	500

[a] Only the changes made in the molecule assignment to form the complexes are indicated. [b] The subscript indicates the frequency assignment for the rupturing HCH bends. [c] Assuming a 120° angle for symmetrical allyl radical ($\sigma = 2$).

18 kcal $mole^{-1}$ for ketene and 25 kcal $mole^{-1}$ for diazomethane.

The excess energies for H rupture are less than the 40 and 47 kcal $mole^{-1}$ excess for cyclopropane isomerization.[4,14] In the latter case, it has been shown that the experimental values of k_a (eq 2b) can be adequately compared to the theoretical value of $k_{\langle E\rangle}$ because the system is relatively monoenergetic; the same assumption is still adequate here. In the comparison of $k_{\langle E\rangle}$ with k_{H0} we may keep in mind the fact that the value of E appropriate for the low-pressure regime is smaller than $\langle E\rangle$, although still within the limits of experimental uncertainty.

RRKM Rate Calculations

Accurate theoretical calculations of k_H, the rate of decomposition by H rupture, have been made in the manner described previously.[3] The frequency assignment for the propylene molecule used was that of Sverdlov;[16] however, the methyl torsion frequency was lowered from his assignment to 225 cm^{-1}, in accord with similar assignments made earlier[17] (Table IV).

(16) I. M. Sverdlov, *Proc. Acad. Sci., U.S.S.R.* (*Chem. Sec.*), **106**, 80 (1956).

(17) M. J. Pearson and B. S. Rabinovitch, *J. Chem. Phys.*, **42**, 1624 (1965).

Table V

	C—C=C	C=C=C	C≡C—C	C—C—C·
		·H addition		
E_a, kcal mole^{-1}	1.5[a]	1.5[a,k]	Very small or zero[b]	~0[b]
P[c]	$\sim 10^{-3}$[a,d]	$\lesssim 10^{-3}$[d,k]	$\gtrsim 0.015$[d]	~ 0.25[b,d]
		·CH_3 addition		
E_a, kcal mole^{-1}	7–8[e]	5.7[f]	<2	Very small or zero[g]
P[c]	$\sim 10^{-3}$[g,h]	$\lesssim 10^{-3}$[f,i]	$\lesssim 10^{-3}$[d]	0.1[d,j]

[a] See ref 10. [b] Estimated. [c] This quantity is the collision yield if $E_a = 0$. [d] For $E_a = 0$. [e] See ref 20. [f] A. Rajbenbach and M. Szwarc, *Proc. Roy. Soc.* (London), **A251**, 394 (1959); estimated here relative to isooctane;[11] [g] See ref 4a. [h] For E_a = 7–8 kcal. [i] For E_a = 5.7 kcal. [j] See ref 4b. [k] T. T. Kassal and M. Szwarc, *J. Phys. Chem.*, **68**, 381 (1964).

Calculations were made for several activated complex models (Table IV). Complex II is the preferred model. The C–H bending frequencies of 150 and 300 cm^{-1} in alternative complex II models conform to the assignments used successfully for H-atom addition to alkenes, or the reverse H-atom split-off from alkyl radicals to give H + alkene.[17,18] A reaction path degeneracy of three is included in the calculations. Complex I differs from II in what turned out to be an accidental fashion. Complex III is that for a loose Gorin-type model and simply represents an unrealistic extreme.

Table III gives the calculated rates for several assumed values of the total level of excitation and of the critical energy, E_0. The values of thermal frequency factors corresponding to the models are also included for illustrative purposes.

Comparison of the calculations with the experimental values yields some interesting ideas. A loose complex (Model III) is seen to give too fast a rate, but this model is known to be defective in general and to yield rates that are too high.[4b] At an energy of 110.5 kcal, which for ketene corresponds closely to the energy appropriate to k_{H0}, model II_{150} gives a slightly low rate, *i.e.*, is a little too tight, for E_0 = 84 kcal and gives a little too high a rate for E_0 = 81 kcal, *i.e.*, is a little too loose. This model thus seems to yield a good representation of this system. Model II_{300} yields consistently low rates. Model II_{75} yields a rate which is somewhat too high.

For the diazomethane system, model II_{300} yields a rate at an energy of 118 kcal which is a little too low for E_0 = 84 kcal; the rate for E_0 = 81 kcal is a little high, however, and thus this model is a good representation of this system. However, as measured, k_{H0} is here only around 20% higher than the value in the ketene system, whereas the difference to be expected for more accurate data is much larger.[5] In addition, the lowest possible value of k_H deducible from the experiments has been used so that model II_{300} is actually on the tight side.

By contrast with the above deductions, a suitable theoretical model for higher alkene-1 compounds was shown earlier[3] to be much tighter. A qualitative difference thus exists between the decomposition rate and association of H plus allyl, and the analogous reactions involving R plus allyl, where R is methyl, ethyl, etc. For the methyl case, a suitable activated complex was found in which several molecular bendings were reduced by one-fourth;[3] this model would now be *too loose* with the present energetics: Dorer and Rabinovitch used a value of the allylic resonance energy of 12 rather than 13 kcal and, in addition, assumed an activation energy for recombination of 2 kcal mole^{-1}; for the present allylic energetics, their model would have to be further tightened, and their calculated P factor for recombination, in the expression $k_{rec} = Pz$, should be reduced from 5×10^{-3} to $\lesssim 10^{-3}$. By contrast, the P factor for recombination of H + allyl in a thermal room temperature system is calculated to be $\gtrsim 1.5 \times 10^{-2}$ on the basis of model II_{150}. This leads to the comparison at 25° shown in Table V.

For the recombination of lower alkyl radicals, A and B, Trotman-Dickenson[19] has shown that the "rule of 2," $[R^2_{AB}/(R_{AA}R_{BB})]^{1/2} \simeq 4^{1/2} = 2$, where 2 is a symmetry factor ratio, holds well. Heller and Gordon[20] have measured this ratio for the reactions of isopropyl and allyl mixtures and find the somewhat higher value, $6.5^{1/2}$, at room temperature. Obviously,

(18) J. H. Current and B. S. Rabinovitch, *J. Chem. Phys.*, **38**, 783 (1963).

(19) J. A. Kerr and A. F. Trotman-Dickenson, *Progr. Reaction Kinetics*, **1**, 105 (1961).

(20) C. A. Heller and A. S. Gordon, *J. Chem. Phys.*, **42**, 1262 (1965).

the ratio permits at least partial cancellation of "abnormal" behavior on the part of allyl radical.

Decomposition into Methyl and Vinyl Radicals

The decomposition of propylene by reaction 4c proceeds half as fast as H rupture (Table II). The critical energy, $E_0 = 93$ kcal, is 10 kcal higher than the value for allyl formation. Thus, the decomposition into methyl plus vinyl radicals, and hence the reverse recombination, evidently corresponds to a looser activated complex than that which characterizes the allyl reaction; the vinyl radical is closer to methyl or ethyl radical behavior in this respect. The higher entropy of activation for vinyl production compensates in part for the unfavorable energetics relative to allyl formation. It is of interest to note that the decomposition of Hg-photosensitized propylene has been found to occur in the proportions of bond rupture, C–C/C–H $\simeq$ 0.1 (2537 A)[21] and C–C/C–H $\simeq$ 0.06 (1849 A).[20]

In conclusion, it seems plausible that the rates of recombination of other delocalized radicals, *e.g.*, benzyl, should also be lower than those of alkyl radicals, and the more so for a pair of such resonance-stabilized radicals.

(21) M. Avrahami and P. Kebarle, *J. Phys. Chem.*, 67, 354 (1963).

Thermodynamic Study of Solid Solutions of Uranium Oxide. I. Uranium Oxide–Thorium Oxide[1]

E. A. Aitken, J. A. Edwards, and R. A. Joseph

General Electric Company, Nuclear Materials and Propulsion Operation, Cincinnati, Ohio
(Received September 20, 1965)

The activity of uranium dioxide in solid solutions of $U_yTh_{1-y}O_{2+x}$ was measured by the transpiration method. The partial pressure of UO_3 gas in a carrier gas of dry air was obtained and related to the thermodynamic activity of UO_2 in the solution according to the equation

$$UO_2(\text{in solid soln}) + {}^1/_2O_2(g) \rightleftharpoons UO_3(g)$$

The activity of UO_2 was found to decrease with an increase in thorium oxide content. The decrease was much greater if the solid solution contained interstitial oxygen. By means of an integral method for three-component systems, the UO_2 activity was calculated at the stoichiometric composition from published oxygen activity data and the measured UO_2 activity of a nonstoichiometric composition. The stoichiometric solid solution was found to be ideal in the region of 1300°. The effect of interstitial oxygen which caused negative departure from ideality was explained in terms of localized interaction of the interstitial oxygen with the uranium ion. The free energy of formation data gave a predicted composition, consistent with X-ray diffraction results, for precipitation of U_3O_8 phase from the solid solution at 0.2 atm of oxygen.

Introduction

Uranium dioxide dissolves appreciable amounts of the group III and group IV oxides if the solute cation radius is similar to that of the uranium ion. Among the group IV oxides, ThO_2 and stoichiometric UO_2[2-4] form a complete series of solid solutions which obey Vegard's law. Solid solutions[5] of urania–thoria also may take up oxygen interstitially. This first decreases the lattice parameter until the oxidation number of the uranium reaches about 5.0 and then increases it at higher oxidation numbers. The composition containing interstitial oxygen is limited to the region below $MO_{2.32}$ regardless of the U/Th ratio. For uranium cation fractions above 0.59, the solid solution precipitates U_3O_8 when it is heated in air above 1000°.[6] Other than the diffraction results and some oxygen activity data[5,7-9] on selected compositions, little else is known about the thermodynamic behavior of urania–thoria solid solutions. Since Vegard's law is obeyed and there is mutual solubility, we might expect stoichiometric solid solutions to be nearly ideal. Vapor pressure measurements of the uranium dioxide component provide a direct means of determining its

(1) This paper originated from work sponsored by the Fuels and Materials Development Branch, Atomic Energy Commission, under Contract AT(40-1)-2847.

(2) W. Trezebiatowsky and P. W. Selwood, *J. Am. Chem. Soc.*, **72**, 4504 (1950).

(3) E. Slowinski and E. Elliot, *Acta Cryst.*, **5**, 768 (1952).

(4) W. Lambertson, M. Mueller, and F. Gunzel, *J. Am. Ceram. Soc.*, **36**, 397 (1953).

(5) L. E. J. Roberts, "Nonstoichiometric Compounds," Advances in Chemistry Series, No. 39, American Chemical Society, Washington, D. C., 1963, p 69.

(6) (a) F. Hund and G. Niessen, *Z. Elektrochem.*, **56**, 972 (1952); (b) J. Handwerk, L. Abernathy, and R. Bach, *Am. Ceram. Soc. Bull.*, **36**, 99 (1957).

(7) S. Aronson and J. Clayton, *J. Chem. Phys.*, **32**, 1749 (1960).

(8) "Uranium Dioxide: Its Properties and Applications," J. Belle, Ed., U. S. Government Printing Office, Washington, D. C., 1961, p 293.

(9) L. E. J. Roberts, L. E. Russell, A. G. Adwick, A. J. Walter, and M. H. Rand, P/26 UK Geneva Conference of Peaceful Uses of Atomic Energy, Vol. 28, 1958, p 215.

activity since gaseous UO_3 volatilizes from the solution in oxidizing atmospheres above 1000°.[10] The vaporization process may be visualized from eq 1.

$$U_yTh_{1-y}O_{2+x} + \frac{3\delta}{2}O_2(g) \rightleftharpoons \delta UO_3(g) + U_{y-\delta}Th_{1-y}O_{2+x} \quad (1)$$

If δ is small, the amount of gas removed does not significantly change the composition of the solution, and the uranium dioxide activity may be determined from the partial pressures of UO_3 and O_2 gas in equilibrium with the solution. Since a fixed oxygen pressure is required to maintain the UO_3 pressure constant, the transpiration method is a convenient one in that air can be used as the carrier gas. High oxygen pressures, however, result in excess oxygen in the solid solution and the activity of UO_2 cannot be determined directly at the stoichiometric composition $U_yTh_{1-y}O_2$. Fortunately, we know, approximately, the variation of the oxygen activity as a function of excess oxygen, which allows us to calculate the uranium dioxide activity at the stoichiometric composition. Using the activity measurements of two of the components in the system we can delineate more clearly the mixing behavior of the urania–thoria solid solution.

Experimental Section

The transpiration apparatus used for measuring the UO_3 partial pressure consisted of a dense, gas-tight muffle of Al_2O_3 (Morganite) in a Pt–Rh wire-wound furnace capable of achieving temperatures of 1600°. A rhodium boat containing a powder (−325 mesh) of the solid solution was placed in the hot zone of the muffle and dry carrier gas was passed over the boat and exhausted through a small hole in a platinum condenser. The carrier gas saturated with uranium oxide vapors passed through the platinum condenser where the uranium oxide vapor condensed and then through a flowmeter. The platinum collector was leached after the run (1–100 hr) and the number of moles of uranium collected was determined fluorometrically. The UO_3 partial pressure was determined from the ratio of the moles of uranium collected to the moles of air multiplied by the absolute pressure which in all cases was 1 atm. The technique and system were calibrated by measuring the vapor pressure over U_3O_8 powder at 1300° in air. The results were within 20% of the work reported by others;[10,11] the relative standard deviation was about 50%. The flow rate was varied between 50 and 200 cc/min for several of the solid solutions studied. In all cases the UO_3 partial pressure was insensitive to the flow rate, an indication that the carrier gas was saturated. Most measurements were taken at flow rates between 90 and 130 cc/min. The temperature was measured with an optical pyrometer sighted on the sample and the end of the collector tube. Thermocouples placed in the charge gave readings which differed by less than 5° from the temperatures read optically. The solid solutions were prepared by blending the oxide powders (−325 mesh), heating the blended powders in air at 1850°, and then impact-milling the product to −325 mesh powder. About 10 g of charge was used and the net loss of uranium determined by chemical analysis was <1% after 20 measurements with the powder. The powder was checked for homogeneity and completeness of reaction by X-ray diffraction before measurement.

The UO_3 pressure was measured first at 1200° and then at successively higher temperatures up to 1600° and then again at 1200°. No significant changes in the volatility occurred as a result of the temperature cycle. After the partial pressure measurements were completed, the charge was held at 1300° for 24 hr in the carrier gas and then quenched to room temperature in the carrier gas. The oxygen to uranium ratio was determined after this treatment by dissolution in hot phosphoric acid under nitrogen followed by titration with Ce(IV) solution to obtain the per cent U(IV). The total U was obtained by titration of a portion of the solution which had been passed through a lead reductor.

Results

Table I summarizes the compositions used and results obtained in this study. The partial pressure data were reduced to equation form by least-squares fit of the Clausius–Clapeyron equation (2), where P is the pressure in atmospheres and T is the temperature in degrees Kelvin. The enthalpy and entropy of sublimation were calculated from the constants B and A, respectively, and are listed in Table I along with the standard deviation. The average scatter in the partial pressure values about the least-squares line was about 50%. For $UO_{2.61}$ (composition 1) the results of Alexander[11] were used since his measurements were more extensive and covered a wider range of temperatures. $UO_{2.61}$ is the stable composition of the U_3O_{8-x} phase at 1300° in air. The results for $UO_{2.61}$

$$\ln P = A - B/T \text{ (1200 to 1600°)} \quad (2)$$

(10) R. J. Ackerman, R. J. Thorn, C. A. Alexander, and M. Tetenbaum, *J. Phys. Chem.*, **64**, 350 (1960).

(11) C. A. Alexander, Doctoral Dissertation, The Ohio State University, 1961.

Table I: Compositions and Results of Urania–Thoria Solid Solutions Used in Transpiration Studies between 1200 and 1600°

No.	Compn in air at 1300°	O/U	Total no. of measurements	B	A	Heat of sublimation, cal/mole Value	Heat of sublimation, cal/mole Std dev	Entropy of sublimation, cal/mole °K Value	Entropy of sublimation, cal/mole °K Std dev
1	$UO_{2.61}$[11]	2.61	..	42,455	15.72	84,354	...	31.23	...
2	$U_{0.5}Th_{0.5}O_{2.24}$	2.47	15	42,568	15.20	84,580	1400	30.20	0.85
3	$U_{0.25}Th_{0.75}O_{2.13}$	2.52	11	39,808	13.02	79,100	800	25.87	0.45
4	$U_{0.20}Th_{0.80}O_{2.10}$	2.51	11	37,313	11.43	74,143	1500	22.71	0.95
5	$U_{0.063}Th_{0.94}O_{2.03}$	2.43	11	33,198	8.32	65,960	1900	16.53	1.2

composition are required later in the calculation of the UO_2 activity. The uranium oxide content of the solid solutions was kept below 0.59 to prevent precipitation of a U_3O_8 phase.

Discussion of Results

Activity of UO_2. In this section, various thermodynamic properties of the solid solution calculated from the experimental results are compared at 1300°. The solid solution, $U_yTh_{1-y}O_{2+x}$, contains three components, UO_2, ThO_2, and O_2. The oxygen activity is readily determined from the oxygen partial pressure, which in this study was maintained constant at 0.2 atm. The activity of UO_2 was calculated according to eq 3, where $P_{UO_3}(1,0)$ is the pressure of UO_3 over

$$a_{UO_2}(y,x) = \frac{P_{UO_3}(y,x)}{P_{UO_3}(1,0)}\left[\frac{P_{O_2}(1,0)}{P_{O_2}(y,x)}\right]^{1/2} \quad (3)$$

$UO_{2.00}$ at unit activity. Since the U_3O_{8-z} phase (specifically[11] $UO_{2.61}$ at 1300° and 0.2 atm of O_2) is the stable composition in air at 1300°, the partial pressure of UO_3 for pure $UO_{2.00}$ had to be determined indirectly from reactions 4–6.

$$UO_{2.61}(s) + \frac{0.39}{2}O_2(g) \rightleftharpoons UO_3(g) \quad (4)$$

$$UO_{2.00}(s) + \frac{0.61}{2}O_2(g) \rightleftharpoons UO_{2.61}(s) \quad (5)$$

$$UO_{2.00}(s) + \frac{1}{2}O_2(g) \rightleftharpoons UO_3(g) \quad (6)$$

Reaction 4 gives

$$\frac{P_{UO_3}(UO_{2.61})}{(P_{O_2})^{0.39/2}} = K_4$$

and reaction 6 gives

$$\frac{P_{UO_3}(1,0)}{(P_{O_2})^{1/2}} = K_6$$

Since $K_6 = K_5K_4$, we obtain eq 7, where ΔG_5 is the

$$P_{UO_3}(1,0) = P_{UO_3}(\text{for } UO_{2.61})(P_{O_2})^{\frac{0.61}{2}} \exp\left(-\frac{\Delta G_5}{RT}\right) \quad (7)$$

change in free energy on oxidation of one mole of $UO_{2.00}$ to $UO_{2.61}$ at 1300°. This free-energy change was evaluated over the composition range using $\bar{G}_{O_2}$, $\bar{H}_{O_2}$, and $\bar{S}_{O_2}$ values of Roberts and Walter,[12] Aronson and Belle,[13] and Blackburn[14] in the single-phase region between $UO_{2.00}$ and $UO_{2.25}$ and the corresponding values of Aronson and Belle,[13] Blackburn,[14] and Anthony, *et al.*,[15] for the two-phase region between $UO_{2.25}$ and $UO_{2.61}$. These sources are essentially in agreement with each other. Transforming the partial molar quantities to the integral quantities we obtain, respectively, for the free energy, enthalpy, and entropy of oxidation of $UO_{2.00}$ to $UO_{2.61}$, −7.62, −22.5 kcal/gfw of U, and −9.6 eu/gfw of U. The numerical values for UO_3 pressure over $UO_{2.61}$ at 1300° in air reported by Ackermann, *et al.*,[10] and by Alexander[11] are, respectively, 1.35×10^{-5} and 1.25×10^{-5} atm, which agree within experimental error with the average value of 1.15×10^{-5} atm obtained in this work. By using the latter value in eq 7 the reference pressure, $P_{UO_3}(1,0)$, becomes 8.3×10^{-5} atm with an uncertainty of about 20%.

In the third column of Table II, the activity of UO_2 in the solid solution may be examined as a function of y at constant oxygen activity, $a_{O_2} = 0.2$. Since the excess oxygen is present in the solid solution, the question arises whether the decrease in UO_2 activity with decreasing y is strongly influenced by the excess oxygen. Application of the Gibbs–Duhem relation for three-component systems enables one to calculate the change in the activity of one component owing to

(12) L. E. J. Roberts and A. J. Walter, *J. Inorg. Nucl. Chem.*, **22**, 213 (1961).

(13) S. Aronson and J. Belle, *J. Chem. Phys.*, **29**, 151 (1958).

(14) P. E. Blackburn, *J. Phys. Chem.*, **63**, 897 (1959).

(15) A. M. Anthony, R. Kiyoura, and T. Sata, *Compt. Rend.*, **255**, 1606 (1962).

changes in composition of a second component if all other variables in the system are held constant. Of the several methods by which activity corrections can be made in three-component systems, the method derived by Wagner[16] seemed appropriate.

Table II: Summary of UO_2 Activity in $U_yTh_{1-y}O_{2+x}$ in 0.2 Atm O_2 at 1300°

Composition y	Excess oxygen x_0	Activity at $x = x_0$	Correction factor	Activity at $x = 0$	Activity coefficient at $x = 0$
(0.52)[a]	(2.27)		(5.5)		
0.50	2.24	0.091	5.5	0.5	1.0
(0.29)[a]	(2.17)		(4.4)		
0.25	2.13	0.061	3.9	0.24	0.96
0.20	2.10	0.059	3.4	0.20	1.0
(0.06)[a]	...		(1.3–1.5)		
0.06	2.032	0.036	1.4	0.05	0.83

[a] Parentheses identify specific compositions at which correction of the UO_2 activity was calculated. Correction values at other compositions were obtained by interpolation.

Following his approach we choose ThO_2, O_2, and UO_2 to be, respectively, the first, second, and third components. It is convenient to set

$$p = \frac{n_2}{n_1 + n_2 + n_3}; \quad y = \frac{n_3}{n_1 + n_3}$$

with this terminology Wagner's eq 1–81 becomes

$$RT \ln \frac{a_{UO_2}(y,p)}{a_{UO_2}(y,0)} = \int_0^{p_0} \left[\frac{\bar{G}_{O_2}}{(1-p)^2} + (1-y)\frac{\partial}{\partial y}\frac{\bar{G}_{O_2}}{(1-p)^2} \right]_y dp - \frac{p\bar{G}_{O_2}(\text{at } p_0)}{1-p} \quad (8)$$

p_0 represents the mole fraction of excess molecular oxygen at the oxygen pressure of 0.2 atm. Since $p = (x/2)/[1 + (x/2)]$, eq 8 transforms to (9). The limit of

$$RT \ln \frac{a_{UO_2}(y,x_0)}{a_{UO_2}(y,0)} = \int_0^{x_0} \left[\bar{G}_{O_2} + (1-y) \times \frac{\partial \bar{G}_{O_2}}{\partial y} \right]_y \frac{dx}{2} - \frac{x_0}{2}\bar{G}_{O_2}(\text{at } x_0) \quad (9)$$

integration, x_0, is the amount of excess oxygen per mole of cation in equilibrium with 0.2 atm of oxygen gas at 1300°. $\bar{G}_{O_2}$ (at x_0) is RT ln (0.2) or −5.0 kcal/mole of O_2 for all values of y. The integral is evaluated for a constant value of y. If $\bar{G}_{O_2}$ is known as a function of x for particular values of y, the UO_2 activity change can be determined; the attainable accuracy, however, is limited somewhat because of the difficulty of evaluating derivatives of the partial molar functions.

Partial molar functions of oxygen obtained from several sources[5,7-9] were collected and plotted over the ranges of x and y. Although the data are not complete, it is evident that the most significant parameter which influences these functions is the oxygen to uranium ratio which we define as $2 + x'$, where $x' = x/y$. This trend appears to hold for $y > 0.20$ and for all values of x except possibly near the limit of the integration, $x = 0$. The limit, $x = 0$, corresponds to U(IV) and x_0 corresponds to approximately U(V) over most values of y. Over $0 \leq x \leq x_0$, $\bar{G}_{O_2}$, $\bar{H}_{O_2}$, and $\bar{S}_{O_2}$ may be represented as nearly linear functions of x or x' for a given y as shown in Table III. These relationships were obtained by plotting the available data as a function of x' and drawing the best straight line. Since the data were obtained at temperatures a few hundred degrees below 1300°, $\bar{H}_{O_2}$ and $\bar{S}_{O_2}$ were assumed to be temperature independent and $\bar{G}_{O_2}$ was estimated at 1300° by adding a correction term of $-\Delta T\bar{S}_{O_2}$. These functions were selected at values of y near the compositions used in the transpiration study. The functions at $y = 0.06$ are approximate since data existed for only two values of x'. As x' approaches zero, it is expected that the partial molar free energy will become rapidly more negative at all values of y similar to observations made by Markin and Roberts[17] for UO_2. Since this change occurs over narrow ranges of x' (~0.002) the contribution to the integral should be small and nearly equivalent for all y. Thus, it seems reasonable to evaluate eq 9 using linear relations of $\bar{G}_{O_2}$, $\bar{H}_{O_2}$, and $\bar{S}_{O_2}$ as a function of x'.

Table III: Partial Molar Free Energy, Enthalpy, and Entropy Relations as a Function of Excess Oxygen at 1300°

Compn y	$\bar{G}_{O_2}$, kcal/mole	$\bar{H}_{O_2}$, kcal/mole	$\bar{S}_{O_2}$, eu
0.52[7]	$86x' - 49$	$-54.6x' - 70$	$-78.5x' - 14$
0.29[7]	$74x' - 42$	$-24.4x' - 67$	$-86x' - 13$
0.06[5]	$19x' - 13$	*Ca.* −44	*Ca.* −22

Roberts[5] has shown for constant $x' = 0.175$ that the partial molar enthalpy exhibits only small variations with y until $y < 0.20$ and the entropy changes sharply only when $y < 0.05$. He attributes this behavior to local trapping of the excess oxygen because strong reaction occurs with uranium ion neighbors nearby.

(16) C. Wagner, "Thermodynamics of Alloys," Addison-Wesley Publishing Co., Reading, Mass., 1952, p 19.

(17) T. L. Markin and L. E. J. Roberts, Symposium on Thermodynamics of Nuclear Materials, May 1962, International Atomic Energy Agency, Vienna, 1962, p 701.

If this is so, then the partial molar quantities to a first approximation would be determined uniquely by x' and not x. The empirical equations in Table III for a given region of y would vary with y only as x' varies with y. Therefore, $\bar{G}_{O_2} = C(x/y) + D$ and $\partial\bar{G}_{O_2}/\partial y = -Cx/y^2$, where C and D are the coefficients to the linear equation in Table III.

If we replace; $\bar{G}_{O_2}$ and $\partial\bar{G}_{O_2}/\partial y$ (in eq 9) with these algebraic expressions and evaluate, the right-hand side reduces to $-Cx_0^2/4y^2$. The coefficient, C, will be different for various values of y. Dividing $-Cx_0^2/4y^2$ by RT and solving, we get

$$a_{UO_2}(y,0) = \exp\left(\frac{Cx_0^2}{4y^2}\Big/RT\right)a_{UO_2}(y,x_0)$$

The exponential term is listed in the fourth column of Table II as a correction factor.

Evaluation of eq 9 by graphical determination of $\bar{G}_{O_2}$ and $\partial\bar{G}_{O_2}/\partial y$ indicates that the correction factor at $y = 0.06$ is probably higher than the value of 1.3 obtained algebraically. Because of the paucity of data the correction factor at $y = 0.06$ is more uncertain. Graphical evaluation at other values of y give correction factors which are in reasonable agreement with the values obtained algebraically.

The activity coefficient for UO_2 listed in the last column of Table II is obtained by dividing $a_{UO_2}(y,0)$ by y. The activity coefficients within experimental error are essentially unity over the range of y which indicates that the stoichiometric solid solution is nearly ideal. Nonideal behavior in the activity of UO_2 is attributed almost completely, therefore, to the excess oxygen. This is consistent with Roberts' suggestion that the excess oxygen atoms interact strongly with the uranium ions in the solid solution, while the thorium ions are principally a diluent.

Enthalpy and Entropy of Mixing. Some indication of solid solution behavior can be obtained from the enthalpy and entropy of sublimation but with less accuracy than from the activity data. Ideal solutions have no enthalpy of mixing and the entropy of mixing is random. If the heats of mixing are caused only by reactions between uranium ions and excess oxygen, then the presence of ThO_2 is secondary and the partial reactions 10 and 11 should be equivalent to the total reaction 12. Thus, $\Delta H_{12} = \Delta H_{10} + \Delta H_{11}$. ΔH_{11} is

$$UO_{2.00}(\text{in } ThO_2) + \frac{x'_0}{2}O_2(g) = UO_{2+x_0'}(\text{in } ThO_2) \quad (10)$$

$$UO_{2+x_0'}(\text{in } ThO_2) + \frac{1 - x'_0}{2}O_2(g) = UO_3(g) \quad (11)$$

$$UO_2 + \frac{1}{2}O_2(g) = UO_3(g) \quad (12)$$

the enthalpy of sublimation from a particular solid solution shown in Table I. ΔH_{10} is obtained from the integral

$$\left\{\int_0^{x_0}\bar{H}_{O_2}\frac{dx_0}{2y}\right\}_{y=\text{constant}}$$

where the algebraic expression for $\bar{H}_{O_2}$ is listed in Table III. ΔH_{12} is obtained from the sum of enthalpy of sublimation of UO_3 from $UO_{2.61}$ and the enthalpy of oxidation of 1 mole of $UO_{2.00}$ to $UO_{2.61}$, which was listed earlier as -22.5 kcal/gfw of U. The enthalpy of sublimation for $UO_{2.61}$ from Table I is 84.3 ± 2 kcal/gfw of U, making $\Delta H_{12} = 61.8 \pm 2$ kcal/gfw of U. Table IV compares the calculated sum of ΔH_{10} and ΔH_{11} with ΔH_{12}, and it is apparent that there is reasonable agreement over the range of y. The deviation is largest at $y = 0.06$ but within experimental error.

Table IV: Enthalpy Comparison for Reactions 10, 11, and 12 (kcal)[a]

y	ΔH_{10} (±2)	ΔH_{11} (±2)	$\Delta H_{10} + \Delta H_{11}$ (±3)	ΔH_{12} (±2.0)
0.52	(−20.9)			
0.50	−20.9	84.6	63.7	61.8
0.29	(−18.2)			
0.25	−17.3	79.1	61.8	61.8
0.20	−16.5	74.1	57.6	61.8
0.06	(−9.5)			
0.06	∼−9.5	66.0	∼56.5	61.8

[a] Numbers in parentheses are calculated from data of ref 5 and 7; intermediate values were estimated by interpolation.

The entropy relations between reactions 10, 11, and 12 should be similar to the enthalpy relation except for an added configurational term because of the random distribution of thorium and uranium atoms. Again, if the entropy change upon adding excess oxygen occurs because of its localization with uranium ions, then $\Delta S_{10} + \Delta S_{11} = \Delta S_{12} + R \ln y$. Evaluating these terms in a similar manner as the enthalpy terms, we compare the last two columns in Table V. Again there is substantial agreement within experimental error except at $y = 0.06$.

These arguments based on enthalpy and entropy considerations are not inconsistent with the activity results, which together with the knowledge that the stoichiometric solid solution obeys Vegard's law indicates that the solution is ideal at 1300° when stoichio-

Table V: Entropy Comparison for Reactions 10, 11, and 12 (entropy units)[a]

y	ΔS_{10} (±1.0)	ΔS_{11} (±0.7)	$\Delta S_{10} + \Delta S_{11}$ (±1.5)	$\Delta S_{12} + R \ln y$ (±2.0)
0.52	(−8.4)			
0.50	−8.4	30.2	21.8	20.2
0.29	(−8.6)			
0.25	−8.2	26.0	17.8	18.8
0.20	−7.6	22.7	15.1	18.4
0.06	(−4.7)			
0.06	−4.7	16.5	11.8	16.1

[a] Numbers in parentheses are calculated from data of ref 5 and 7; intermediate values were estimated by interpolation.

metric. When excess oxygen is present, negative departure from ideality occurs which is caused principally by the localized interaction of oxygen interstitials with the uranium ions.

Total Free Energy vs. Composition. Ackermann, *et al.*,[18] list the standard free energy of formation of ThO_2(s) as follows.

$$\Delta G_f^\circ(ThO_2) = -296{,}000 + 46.38T(2000\text{–}3000^\circ K) \text{ cal/gfw of Th}$$

Assuming that the free-energy equation is valid to 1573°K

$$\Delta G_f^\circ(ThO_2 \text{ at } 1573^\circ K) = -223{,}040 \text{ cal/gfw of Th}$$

Alexander[11] recently derived the standard free energy equation for $UO_{2.61}$(s) as

$$\Delta G_f^\circ(UO_{2.61}) = -279{,}700 + 48.48T(1300\text{–}1800^\circ K) \text{ cal/gfw of U}$$

from which we obtain at 1573°K

$$\Delta G_f^\circ(UO_{2.61} \text{ at } 1573^\circ K) = -203{,}440 \text{ cal/gfw of U}$$

Since ΔG for oxidation of $UO_{2.0}$ to $UO_{2.61}$ is −7620 cal/gfw of U at 1573°K, we get by subtraction

$$\Delta G_f^\circ(UO_{2.0} \text{ at } 1573^\circ K) = -195{,}820 \text{ cal/gfw of U}$$

The standard free energies of formation have an absolute accuracy of only 2000 cal/mole.

Assuming that the stoichiometric solid solution is ideal, the total free energy of formation of the solution is calculated from eq 13. The free-energy curve as a

$$\Delta G_f^\circ(y,0) = y\Delta G_f^\circ(UO_2) + (1-y)\Delta G_f^\circ(ThO_2) + R[y \ln y + (1-y)\ln(1-y)] \quad (13)$$

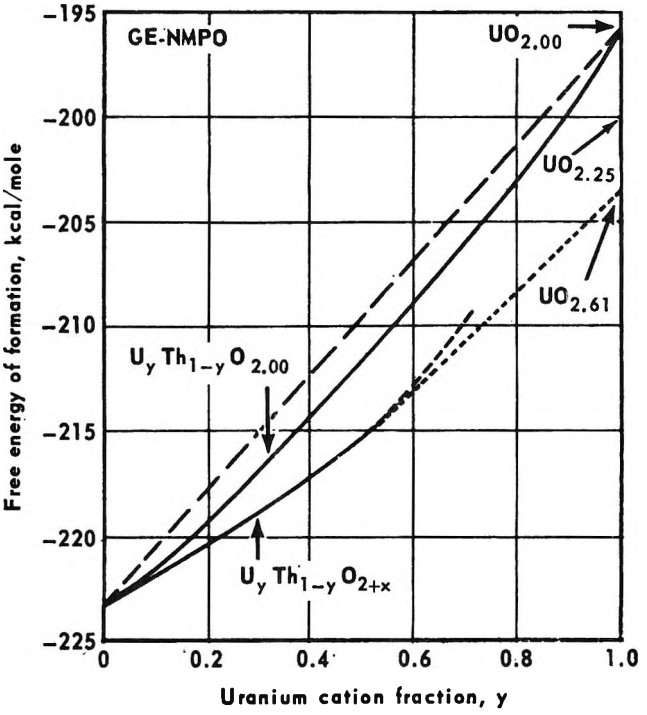

Figure 1. Free energy of formation of $U_yTh_{1-y}O_2$ at 1300°.

function of composition, y, is shown in Figure 1. From the integral

$$\left\{\int_0^{x_0} \tilde{G}_{O_2} \frac{dx}{2}\right\}_y$$

the free-energy change between $\Delta G_f^\circ(y,0)$ and $\Delta G_f^\circ(y,x_0)$ is obtained for various values of y. If we use the equations for $\tilde{G}_{O_2}$ in Table III, the free-energy change on oxidation to the nonstoichiometric solid solution in equilibrium with 0.2 atm of O_2 at 1300° is, respectively, −6.9, −5.9, and −1.9 kcal/gfw of U for y values of 0.52, 0.29, and 0.06. Using these values for the free energy of formation, we can draw a curve in Figure 1 for the nonstoichiometric solid solution. For $y > 0.5$ the curve must extend upward and approach ΔG_f° ($UO_{2.25}$) because no further oxygen can be added to the fluorite phase without precipitating $UO_{2.61}$.

$\Delta G_f^\circ(UO_{2.61})$ and $\Delta G_f^\circ(UO_{2.25})$ are shown as points at the right-hand side of Figure 1. There is no known solubility of thorium oxide in U_3O_{8-z} phase; therefore, the minimum in the free energy *vs.* composition for $UO_{2.61}$ occurs at $y = 1$. If we draw a dashed straight line from the value for $UO_{2.61}$ and tangent to the nonstoichiometric curve, the point of tangency occurs in the vicinity of $0.5 > y > 0.6$. For y larger than the

(18) R. J. Ackermann, E. G. Rauh, R. J. Thorn, and M. C. Cannon, *J. Phys. Chem.*, 67, 762 (1963).

point of tangency, precipitation of $UO_{2.61}$ would occur. This is in agreement with the results obtained from X-ray diffraction measurements.[6]

Acknowledgment. The authors wish to acknowledge the technical contributions of S. F. Bartram, K. M. Bohlander, H. S. Edwards, and E. A. Schaefer.

Thermodynamic Study of Solid Solutions of Uranium Oxide. II. Uranium Oxide–Yttrium Oxide[1]

by E. A. Aitken and R. A. Joseph

General Electric Company, Nuclear Materials and Propulsion Operation, Cincinnati, Ohio
(Received September 20, 1965)

The activity of uranium dioxide in solid solutions of $U_yY_{1-y}O_{2-x}$ along a selected composition line was measured by the transpiration method. The partial pressure of UO_3 gas in a carrier gas of air (0.2 atm of O_2) or CO_2–CO mixture was obtained between 1200 and 1700° and related to the UO_2 activity of the solid solution according to the equation

$$UO_2(\text{in solid soln}) + {}^1/_2O_2(g) \rightleftharpoons UO_3(g)$$

A large negative departure from Raoult's law was obtained at 1300°. The UO_2 activity measured at two different oxygen partial pressures differed significantly. However, if the solid solution was visualized as a pseudobinary mixture of UO_{2+x} and $YO_{1.5}$, the effect of oxygen pressure on the activity could be largely eliminated. The results could then be expressed according to a binary regular solution model with an attractive interaction energy term of about 41 kcal. The linear relation between log activity coefficient and $(1 - y)^2$ appeared to be independent of the average valence and the degree of anion deficiency. Examination of the enthalpy and entropy of vaporization indicated that the regular solution model did not properly describe the enthalpy and entropy changes on mixing; however, qualitatively these differences were largely the result of volume changes on mixing, which the regular solution model ignores. Additions of ZrO_2 to solid solutions of uranium oxide–yttrium oxide caused an increase in UO_2 activity but no change was observed with ThO_2 additions.

Introduction

A previous study[2a] of UO_2–ThO_2 solid solutions showed that the UO_2 activity followed Raoult's law provided the compound was stoichiometric with respect to oxygen to metal ratio [constant U(IV)]. If the average uranium valence was increased by accommodating excess oxygen, interstitially, a negative departure from ideal behavior was observed. To understand further the effect of valence changes on UO_2 activity, solid solutions of UO_{2+x}–Y_2O_3 were studied. These two oxides are not completely miscible but there is

(1) This paper originated from work sponsored by the Fuels and Materials Development Branch, Atomic Energy Commission, under Contract AT(40-1)-2847.

(2) (a) E. A. Aitken, J. A. Edwards, and R. A. Joseph, *J. Phys. Chem.*, **70**, 1084 (1966); (b) S. F. Bartram, E. F. Juenke, and E. A. Aitken, *J. Am. Ceram. Soc.*, **47**, 171 (1964).

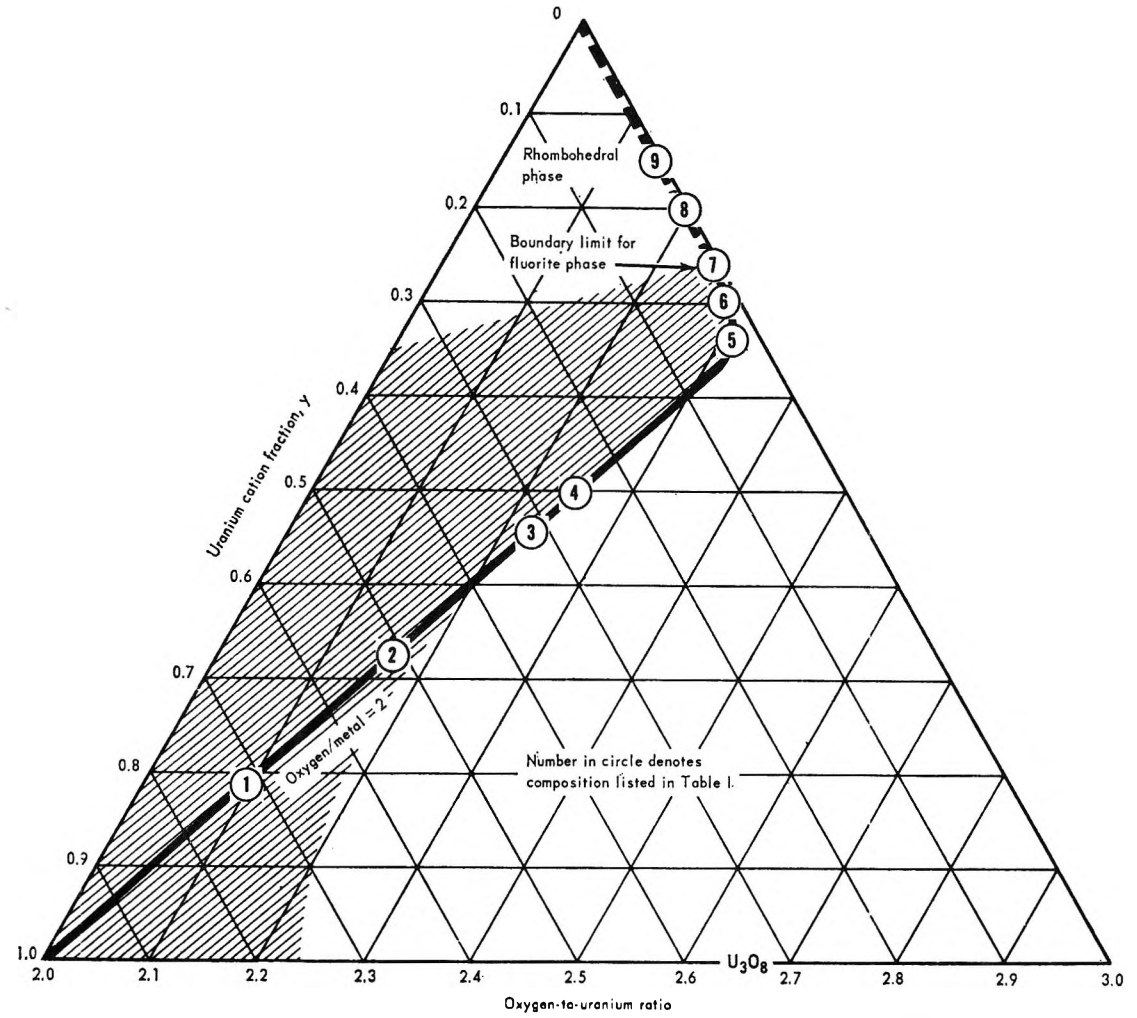

Figure 1. Partial diagram of the UO_2–UO_3–Y_2O_3 system in the 1000 to 1500° temperature region showing the location of the yttria–urania compositions used in the transpiration studies.

an appreciable range of solubility convenient for studying the change in UO_2 activity with composition.[2b] In particular, solid solutions of composition $U_yY_{1-y}O_{2.00}$ can be obtained at reasonable oxygen partial pressures. At a fixed O/M ratio, the average valence of the uranium increases to compensate for the addition of the lower valent yttrium atom. By working along a composition line of fixed oxygen to metal ratio, we can compare the effect of a lower valent cation on the uranium dioxide activity with that obtained for the stoichiometric UO_2–ThO_2 solutions. Further, ThO_2 and ZrO_2 can be dissolved appreciably in $U_yY_{1-y}O_{2.00}$ compositions without change in the average valence, and their effect on UO_2 activity can be determined.

Uranium–Yttrium–Oxygen Systems.[2b] In this three-component system, the uranium valence varies between four and six depending on the oxygen partial pressure. The solid solutions form either a defected fluorite structure or compounds which are small distortions of this structure. The structure is easily made nonstoichiometric by incorporation of oxygen interstitials or vacancies. The stable range of the fluorite phase in the temperature region of 1000 to 1500° is shown approximately by the shaded area of Figure 1. The compositions studied in this paper are shown along the line drawn in the figure. The portion of the line between $1 > y > 0.33$ indicates that the compositions are at a constant oxygen to metal ratio of 2.0. The compositions which fall along this line segment can be maintained by heating in CO_2–CO mixtures for $1 > y > 0.50$ and in 0.2 atm of oxygen for $0.5 > y > 0.33$. If $y > 0.5$, a U_3O_8 phase precipitates, when heated in 0.2 atm of oxygen, and the system contains two phases. The U_3O_8 phase has a negligible solubility for yttrium oxide.

For $0.33 > y > 0.25$, the fluorite phase is stable in 0.2 atm of oxygen, but it is oxygen deficient since the uranium atoms have reached their maximum oxidation state. At $y < 0.33$, the composition line in Figure 1 changes at $y < 0.33$ to correspond to the condition of maximum valence. Below $y = 0.25$ the fluorite phase is not stable and the compositions are two-phase mixtures between $0.25 > y > 0.14$ and $0.14 > y > 0$. The compound at $y = 0.14$ is a rhombohedral phase and is a member of a family of compositions with the general formula $U_yY_{1-y}O_{1.71}$ where $0.25 > y > 0.14$.

Below $y = 0.14$, the body-centered cubic structure of Y_2O_3 (type C) is observed. This structure dissolves a small amount of uranium oxide at low oxygen partial pressures, but in 0.2 atm of oxygen the solubility is negligible.

Experimental Section

The transpiration method was used to measure the vapor pressure of UO_3 gas in equilibrium with the solid solution according to eq 1. From the measured partial

$$UO_{2+x'}(\text{in soln}) + \frac{1-x'}{2}O_2(g) \rightleftharpoons UO_3(g) \quad (1)$$

pressures of oxygen and uranium trioxide, the activity of uranium dioxide was calculated as a function of the uranium content. The apparatus and experimental procedure were described previously.[2a] The carrier gas was dry air except for a few compositions where a dry CO_2–CO mixture was used to avoid precipitation of a U_3O_8 phase from the solid solution.

The CO_2/CO ratio was varied at each temperature of measurement to maintain a constant O_2 partial pressure ($10^{-5.66}$ atm). Gas chromatographic analysis of the effluent confirmed that the CO_2/CO ratios were changed insignificantly on passing through the transpiration apparatus.

The solid solutions were prepared by blending the oxide powders (−325 mesh), treating them in air at 1850°, and then impact milling the reaction product to −325 mesh powder. A charge of about 10 g was used, and the net loss of uranium determined by chemical analysis was <1% after 20 measurements with the powder. Compositions above 70 mole % UO_2 were treated in hydrogen for 24 hr at 1700° to retain a single-phase composition. The treated powders were checked for homogeneity and completeness of reaction by X-ray diffraction before measurement. The oxygen to uranium ratio of the solid solution was determined after the transpiration measurements using a method described previously.[2a]

Results

Table I summarizes the compositions used and results obtained in this study. The partial pressure of UO_3 is expressed by the constants A and B in the form of the Clausius–Clapeyron equation (2), where P

$$\ln P = A - B/T \ (1200\text{–}1700°) \quad (2)$$

is the pressure in atmospheres and T is the temperature in degrees Kelvin. The enthalpy and entropy of vaporization have been calculated from the constants B and A, respectively, and are listed in Table I along with their standard deviations obtained by statistical analysis of the deviations from the least-squares line. The statistically derived error in a few cases is unusually low, which is believed to be accidental. The average scatter in the partial pressure values about the least-squares line is about 50%. The compositions listed in Table I are grouped in three categories. The first category of six compositions was within the solubility range of the fluorite lattice. The second category, compositions 7–9, were two-phase mixtures involving the rhombohedral phase of composition UY_6O_{12}. The vapor pressure measurements for compositions 7 and 8 represent the state of equilibrium on the uranium-rich side of the rhombohedral composition, and the yttria-rich side is represented by results from composition 9. Any further decrease of the uranium content produces more of the Y_2O_3 phase which in 0.2 atm of O_2 contains a negligible amount of uranium oxide. The last category of compositions was carried out to measure the effect on the UO_3 pressure of adding Th(IV) and Zr(IV) ions to the yttria solid solution at fixed uranium to yttrium ratio. Additions of these ions cause a variation in lattice size without changing appreciably the oxygen to metal ratio.

Discussion of Results

A. Binary Oxide. Activity and Activity Coefficients. The compositions of the binary oxide, $U_yY_{1-y}O_{2-x}$, listed in Table I follow along two line segments as shown in Figure 1. One line segment ranges from $1.0 > y > 0.33$ where the oxygen to metal ratio is 2.0 ($x = 0$). The other, with the oxygen to uranium ratio nearly constant at 3.0, ranges from $0 < y < 0.33$, requiring that $x = (1 - 3y)/2$.

The activity of the UO_2 component of the solid solution was calculated from the UO_3 partial pressure, using eq 3. $P°_{UO_3}$ and $P°_{O_2}$ refer to the pressures in equilibrium with $UO_{2.00}$, the reference state.

$$a_{UO_2} = \frac{P_{UO_3}}{P°_{UO_3}}\left[\frac{P°_{O_2}}{P_{O_2}}\right]^{1/2} \quad (3)$$

Table I: Compositions and Results of Urania, Thoria, Yttria, and Zirconia Solid Solutions used in Transpiration Studies between 1200 and 1700°

No.	Compositions in air at 1300°	O/U[a]	Fluorite lattice parameter	Total no. of measurements	B	A	Heat of sublimation, cal/mole Value	Heat of sublimation, cal/mole Std dev	Entropy of sublimation, cal/mole °K Value	Entropy of sublimation, cal/mole °K Std dev
1	$U_{0.81}Y_{0.19}O_{2.002}$[b]	2.12	5.423	5	37,202	7.59	73,930	2300	15.08	1.4
2	$U_{0.67}Y_{0.33}O_{2.00}$[b]	2.25	5.383	4	29,253	2.65	58,130	4100	5.27	2.5
3	$U_{0.54}Y_{0.46}O_{2.002}$[b]	2.43	5.354	4	38,185	7.57	75,880	1900	15.04	1.2
4	$U_{0.5}Y_{0.5}O_{2.005}$	2.51	5.35	15	38,190	11.03	76,000	3700	21.95	2.3
5	$U_{0.33}Y_{0.67}O_{0.98}$	2.93	5.32	10	48,900	14.57	97,310	3700	28.99	2.1
6	$U_{0.29}Y_{0.71}O_{1.90}$	2.86	5.32	6	47,990	12.85	95,500	5000	25.57	3.1
7	$U_{0.25}Y_{0.75}O_{1.84}$	2.85	5.34 + trace rhombohedral	13	46,010	11.86	91,560	3100	23.60	1.8
8	$U_{0.20}Y_{0.80}O_{1.80}$	2.98	5.32 + rhombohedral	14	44,910	11.02	89,370	3900	21.93	2.2
9	$U_{0.14}Y_{0.86}O_{1.70}$	2.93	Rhombohedral	14	54,130	13.91	107,720	5600	27.68	3.0
10	$U_{0.32}Y_{0.36}Th_{0.32}O_{1.99}$	2.53	5.458	11	38,863	11.09	77,220	1900	22.03	1.1
11	$U_{0.16}Y_{0.18}Th_{0.66}O_{1.99}$	2.49	5.515	12	40,773	12.29	81,020	2600	24.42	1.6
12	$U_{0.26}Y_{0.49}Zr_{0.25}O_{2.00}$	2.95	5.275	31	46,860	14.40	93,250	2800	28.66	1.6
13	$U_{0.27}Y_{0.24}Zr_{0.49}O_{2.03}$	2.57	5.23	15	35,530	10.36	70,700	1100	20.62	0.70
14	$U_{0.14}Y_{0.29}Zr_{0.57}O_2$		5.20	11	47,085	15.09	93,590	3100	30.00	1.9

[a] The oxygen to uranium ratio was determined by chemical analysis after heating in the carrier gas for 24 hr at 1300° and quenching to room temperature in the carrier gas. These values were used to calculate the oxygen to metal ratio of the solid solution, assuming that the valences of the other cations are Y(III), Zr(IV), and Th(IV). [b] These compositions were run in CO_2–CO mixture. Results are reported from measurements at 1300 and 1400° only.

Table II: Summary of Thermodynamic Activities in $U_yY_{1-y}O_{2-x}$ at 1300°

No.	y	$2-x$	P_{O_2}, atm	a_{UO_2}	γ_{UO_2}	$a'_{UO_{2+x'}}$	$\gamma'_{UO_{2+x'}}$
1	0.81	2.00	$10^{-5.66}$	3.98×10^{-1}	5.16×10^{-1}	2.0×10^{-1}	2.47×10^{-1}
2	0.67	2.00	$10^{-5.66}$	4.44×10^{-1}	7.5×10^{-1}	1.06×10^{-1}	1.58×10^{-1}
3	0.54	2.00	$10^{-5.66}$	2.10×10^{-1}	4.34×10^{-1}	1.8×10^{-2}	3.34×10^{-2}
4	0.50	2.00	0.2	2.19×10^{-2}	4.92×10^{-2}	2.19×10^{-2}	4.38×10^{-2}
5	0.33	1.98	0.2	8.34×10^{-4}	2.94×10^{-3}	8.34×10^{-4}	2.52×10^{-3}
6	0.29	1.90	0.2	2.67×10^{-4}	1.04×10^{-3}	2.67×10^{-4}	9.2×10^{-4}
7	0.25	1.84	0.2	3.49×10^{-4}	1.55×10^{-3}	3.49×10^{-4}	1.4×10^{-3}
8	0.20[a]	1.80	0.2	3.04×10^{-4}	1.35×10^{-3}	3.04×10^{-4}	1.21×10^{-3}
9	0.14	1.70	0.2	1.56×10^{-5}	1.19×10^{-4}	1.56×10^{-5}	1.11×10^{-4}

[a] Two-phase mixture; the mole fractions for calculating the activity coefficient were the same as the composition for $y = 0.25$.

For a temperature of 1300° in 0.2 atm of oxygen, $P^\circ_{UO_3}$ is 8.0×10^{-5} atm which was calculated previously[2a] by the authors from data in the literature. If we separate the binary oxide into components UO_2, O_2, and $YO_{1.5}$, the mole fraction of UO_2 becomes

$$X_{UO_2} = \frac{y}{\left[1 - \frac{x}{2} + \frac{1-y}{4}\right]} \qquad (4)$$

remembering that $x = 0$ for $y > 0.33$ and $x = 1 - 3y/2$ for $y < 0.33$. The value of the denominator in (4) is between 1.0 and 1.15 for all y. The activity coefficient is obtained by dividing (4) into (3). The activity and activity coefficient of the UO_2 components at 1300° are listed in the fifth and sixth column of Table II. A large negative deviation from Raoults' law is apparent from the results.

The UO_2 activities of the first three compositions which were obtained at low oxygen pressures (CO_2–CO mixture) appear to be inconsistent with the results obtained in 0.2 atm. For instance, compositions 3 and 4 have about the same uranium and oxygen content but their UO_2 activities differ by an order of mag-

nitude. This difference could be attributed to the change in activity of oxygen. If we use the Gibbs–Duhem equation,[3] the change in activity of UO_2 from the change in activity of oxygen is given by

$$\ln a_{UO_2}(y,x_2) - \ln a_{UO_2}(y,x_1) = \int_{x_1}^{x_2} \frac{x}{2} \frac{\partial \ln a_{O_2}}{\partial x} dx \quad (5)$$

where the limits of integration are determined by the particular oxygen activities used in the transpiration study.

The x values for compositions 3 and 4 (Table I) are both small, but the composition heated in 0.2 atm of oxygen appears to have a slight oxygen excess ($x_1 = -0.005$) compared to composition 3 which is essentially stoichiometric ($x_2 = 0$). Thus, the range of integration will be very narrow. The relation between a_{O_2} and x is not known and therefore the integral cannot be evaluated, but from inspection of the phase diagram,[2b] it would seem that the derivative term in eq 5 is large and most certainly negative. This means that the UO_2 activity will increase because of a small decrease in the oxygen to metal ratio. Since composition 4 has a slight oxygen excess ($x = -0.005$), its corrected UO_2 activity would be brought into closer agreement with composition 3.

Solutions which exhibit a negative departure from Raoult's law frequently behave according to a regular solution model.[4] In a regular solution, an energy term, Ω, is introduced to account for the interactions between the components. The configurational entropy, however, is assumed to remain random in spite of the interactions. It can be shown for a regular solution that the activity coefficient, γ_i, for component i will behave according to eq 6, where X_i is the mole fraction of i. Ω, in general, may vary with composition but frequently it is constant.

$$\log \gamma_i = \Omega(1 - X_i)^2 \quad (6)$$

Inspection of column 5 in Table II shows that γ_{UO_2} determined at the low oxygen partial pressure does not change much with composition but it does change according to eq 6 for compositions determined in 0.2 atm of O_2. As explained above, these differences arise because we have a three-component system and one cannot ignore the effect of changes in oxygen activity on the activity of other components. If the U–Y–O system could be viewed as a pseudo-binary system, for instance, a mixture of molecular units of $UO_{2+x'}$ and $YO_{1.5}$, we show below that a general relationship independent of oxygen pressure can be obtained.

Visualizing the solid solution as a pseudo-binary mixture does not appear to be entirely without justification based on the behavior of UO_2 activity in UO_2–ThO_2–O solid solutions.[2a] In this system, negative departures from ideality were observed when excess oxygen was present in the solution. The degree of departure, however, was much smaller than the departure indicated by the UO_2–$YO_{1.5}$–O system. Therefore, the major interaction probably is between $UO_{2+x'}$ and $YO_{1.5}$ and not between the excess oxygen and UO_2. The effect of changes in oxygen to uranium ratio, while significant, are relatively small. As a pseudo-binary system, we then redefine the activity, a', and activity coefficient, γ', by eq 7 and 8. The activity, a', differs from a_{UO_2} because of the change in the exponent of the ratio of oxygen pressures. The mole fractions of $UO_{2+x'}$ and UO_2 are essentially the same, differing at most only by 15%. Therefore, the compositions measured at low oxygen pressure will be affected most by the redefined activity. As shown in Table II, a' and γ' determined at the low pressures are now in closer agreement with a' and γ' at 0.2 atm of oxygen. In Figure 2 is shown the relationship between log γ' and y according to eq 6. The results obtained at low oxygen pressures give values which are parallel to and only slightly below the line determined from γ' values obtained at high oxygen pressures. It is surprising that a linear relation between log γ' and y applies even at low values of y where the lattice either has become anion deficient or has transformed to the compound, UY_6O_{12}. The points at $(1 - y)^2 = 0.56$ represent the activity of solution at the boundary on the uranium rich side of the phase region between $U_{0.25}Y_{0.75}O_{2-x}$ and YU_6O_{12}. From Figure 2, we obtain a value of Ω of -5.70 which corresponds to an attractive interaction energy (between the molecular units of $UO_{2+x'}$ and $YO_{1.5}$) at 1300° of about 41 kcal/gfw of U. This value is unusually high when compared to interaction energies obtained for fused salt solutions,[5] but it is reasonable in comparison to the relative lattice energies between oxide solid solutions and typical fused salt systems.

$$a' = \frac{P_{UO_3}}{P^\circ_{UO_3}} \left(\frac{P^\circ_{O_2}}{P_{O_2}}\right)^{\frac{1-x'}{2}} \quad (7)$$

$$\gamma' = \frac{a'}{y} \quad (8)$$

It is difficult to describe physically the interaction between $UO_{2+x'}$ and $YO_{1.5}$. γ' follows regular solu-

(3) C. Wagner, "Thermodynamics of Alloys," Addison-Wesley Publishing Co., Reading, Mass., 1952, p 19.

(4) R. A. Swalin, "Thermodynamics of Solids," John Wiley and Sons, Inc., New York, N. Y., 1962, p 115.

(5) M. Blander, "Molten Salt Chemistry," Interscience Publishing Co., Inc., New York, N. Y., 1964, p 166.

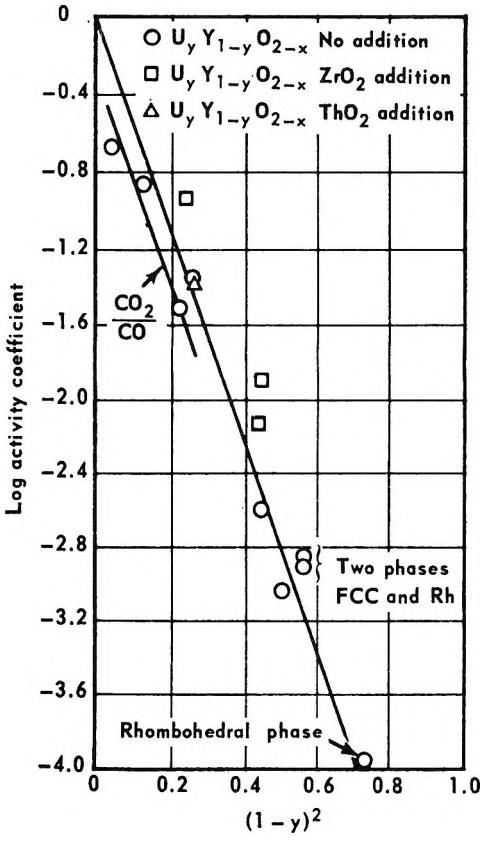

Figure 2. Log activity coefficient *vs.* $(1 - y)^2$ for $U_yY_{1-y}O_{2-x}$ at 1300°.

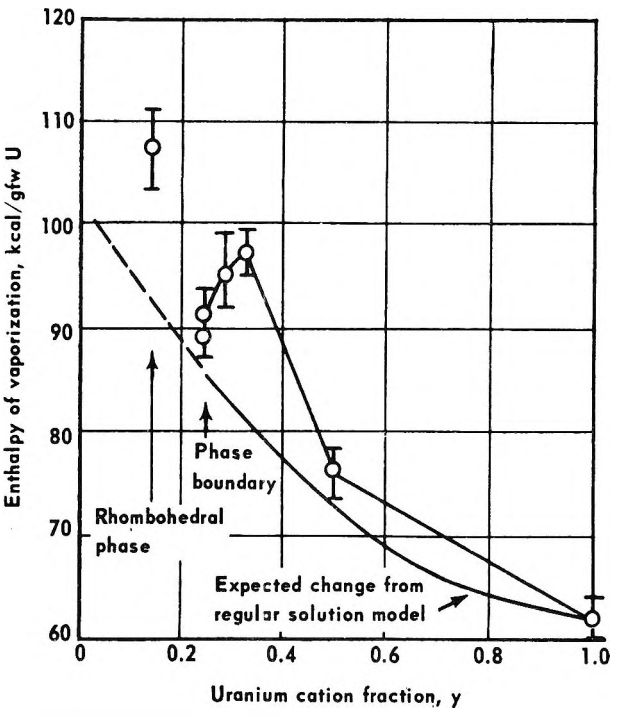

Figure 3. The enthalpy of the vaporization for $U_yY_{1-y}O_{2-x}$ solid solutions.

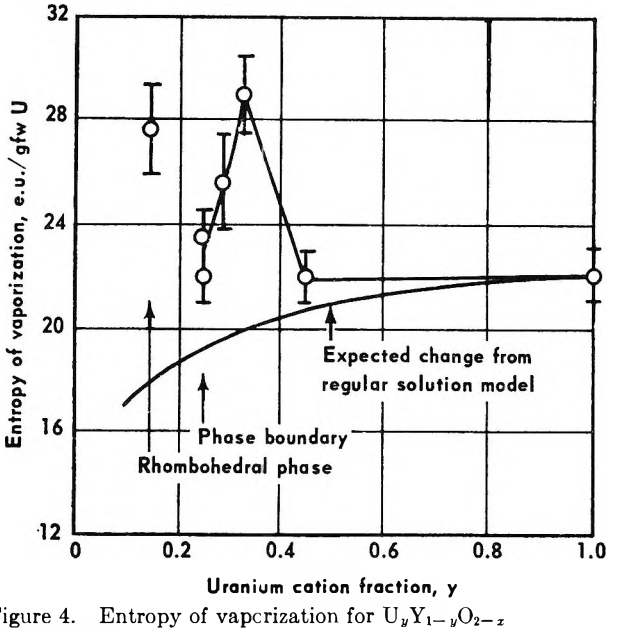

Figure 4. Entropy of vaporization for $U_yY_{1-y}O_{2-x}$ solid solutions

tion predictions in composition regions where the uranium valence is variable, where it is constant, where the oxygen sublattice is full or deficient. It would seem then that the interaction energy arises from a progressively stronger ionic association of oxygen ions around the uranium ion as the lattice is diluted by Y ions. The interaction can arise from an increased charge on the uranium ion or from a preferential occupation of anion lattice sites near the uranium.

Enthalpy and Entropy of Mixing. The trends in the enthalpy and entropy of mixing may be inferred from the changes in the enthalpy and entropy of vaporization relative to the corresponding values at $y = 1$. ΔH_{vap} and ΔS_{vap} are listed in Table I. ΔH_{vap} and ΔS_{vap} for pure UO_2 determined previously[2a] are shown in Figures 3 and 4, respectively. In spite of the lower accuracy of the measured ΔH_{vap} and ΔS_{vap}, it is apparent that the trends of ΔH_{vap} and ΔS_{vap} with y depart significantly from the predictions of a regular solution model. From eq 6, the predicted ΔH_{vap} should obey eq 9, and similarly for a regular solution model, ΔS_{vap} should obey eq 10. These relations

ΔH_{vap}(solid solution) −

$$\Delta H_{vap}(UO_2, y = 1) = -\Omega(1 - y)^2 \quad (9)$$

ΔS_{vap}(solid solution) −

$$\Delta S_{vap}(UO_2, y = 1) = +R \ln y \quad (10)$$

appear as curves shown in Figures 3 and 4. The measured ΔH_{vap} indicates that the interaction energy

is stronger than that calculated from eq 9 in the region $0.5 < y < 0.33$. From Figure 4, it is also apparent that the ΔS_{vap} has increased also in the same region. In the region $0.25 < y < 0.33$, there is a rapid decrease in both ΔH_{vap} and ΔS_{vap}. These results indicate that the regular solution approximation is not followed and the interactions tend to be stronger than the activity data would indicate. Moreover, the solid solution has a lower entropy than would be predicted.

In Figure 5, we show the variation in lattice parameter as a function of y. A large negative volume of mixing is indicated and the molar volume is a minimum at $y = 0.33$, which coincides with maxima in the ΔH_{vap} and ΔS_{vap} plots.

The connection between volume changes and entropy or enthalpy changes in solutions has been discussed by Hildebrand and Scott.[6] Because regular solution theory assumes a constant volume of mixing and the experimental data are obtained at constant pressure, corrections for the volume change will affect the enthalpy and entropy terms to the first order. A negative volume change will cause the enthalpy of mixing to increase and the entropy to decrease from the corresponding values expected in a constant volume of mixing. On the other hand, volume changes will affect the free-energy terms (*i.e.*, activity, activity coefficient) only to the second order. Therefore, the activity coefficient can be expected to be relatively insensitive to volume changes in mixing. The absence of any unusual departure from linearity of the results shown in Figure 2 tends to confirm this reasoning.

Free Energies of Formation. The free energies of formation of the solid solution along the composition line shown in Figure 1 were calculated from the partial pressure measurements and the free energies of formation of $UO_{2.61}$ (U_3O_8) and Y_2O_3(s).

The standard free-energy equation[7] for $UO_{2.61}$ is

$$\Delta G_f^\circ(UO_{2.61}) = -297{,}700 + 48.48T \qquad (11)$$

If we use the results of Alexander,[7] the standard free-energy equation for UO_3(g) near 1573°K is

$$\Delta G_f[UO_3(g)] = -202{,}080 + 20.79T \qquad (12)$$

The standard free energy equation for UO_2(s) near 1573°K obtained from eq 11 and the integral heats and entropy for oxidation[2a] of UO_2 to $UO_{2.61}$ is

$$\Delta G_f^\circ[UO_2(s)] = -259{,}640 + 40.56T \qquad (13)$$

The standard free energy of formation of Y_2O_3 was calculated from recent heat capacity data of Pankratz, King, and Kelley[8] and previously published heats of formation[9] and entropies[10] of formation for Y_2O_3 and corresponding values for the elements.[11]

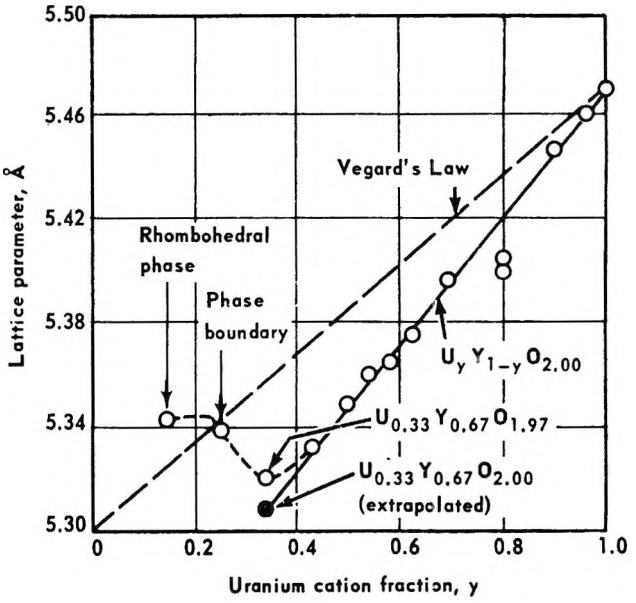

Figure 5. Room-temperature lattice parameter of $U_yY_{1-y}O_{2-z}$ solid solutions.

Near 1573°K, the linear free energy equation is

$$\Delta G_f^\circ(Y_2O_3(s)) = -459{,}800 - 70.17T \qquad (14)$$

From (12) and (14) and the partial pressure relation of composition 9 in Table I, we obtain for eq 15 the

$$yUO_3(g) + (1 - y)YO_{1.5}(s) \rightleftharpoons U_yY_{1-y}O_{1.71}(s) \qquad (15)$$

free energy of formation for the rhombohedral phase which occurs at $y = 0.14$

$$\Delta G_f^\circ(\text{rhomb}) = -241{,}270 + 36.98T \text{ cal/mole of cation}$$

Using ΔG_f°(rhomb) and the UO_3 partial pressure for composition 8, we obtain for eq 16 the ΔG_f° of the solid

$$U_{0.14}Y_{0.86}O_{1.71}(s) + UO_3(g) \rightleftharpoons U_yY_{1-y}O_{1.875} \qquad (16)$$

solution at the phase boundary ($y = 0.25$).

(6) J. H. Hildebrand and R. L. Scott, "Regular Solutions," Prentice-Hall, Inc., Englewood Cliffs, N. J., 1962, p 104.

(7) C. A. Alexander, Doctoral Dissertation, The Ohio State University, 1961.

(8) L. B. Pankratz, E. G. King, and K. K. Kelley, U. S. Bureau of Mines Report of Investigations, No. BM-RI-6033, Mines Bureau, Pittsburgh, Pa., 1962.

(9) E. J. Huber, C. E. Holley, and E. L. Head, *J. Phys. Chem.*, 61, 497 (1957).

(10) E. F. Westrum and B. H. Justice "Rare Earth Research," J. F. Nachman and C. E. Lundin, Ed., Gordon and Breach, New York, N. Y., 1962, Paper No. 13.

(11) D. R. Stull and G. C. Sinke, "Thermodynamic Properties of the Elements," American Chemical Society, Washington, D. C., 1956.

$\Delta G_f°$(solid solution at $y = 0.25$) =

$$-247{,}819 + 37.91T$$

B. Effect of ThO_2 and ZrO_2 Additions. The solid solution $U_yY_{1-y}O_{2.00}$, $1 > y > 0.25$, can dissolve appreciable amounts of ThO_2 and ZrO_2. Substitution of these additives leaves the oxygen sublattice filled and maintains a constant oxygen to metal ratio. The thorium additive increases the lattice volume and the zirconium additive decreases the volume. The change in UO_3 partial pressure as a result of these additives was measured (see compositions 10 to 14 in Table I). If we plot the activity coefficient at 1300° in Figure 2 at the corresponding y values based on U and Y content only, then we find that there is a significant increase in the activity for the zirconium oxide additions which decreased the lattice volume by 7%, and no change for the thorium oxide additions, which increased lattice by 9%.

The fact that no change in activity results from the thorium oxide addition seems compatible with the indication suggested earlier that the interaction is principally the result of oxygen grouping or polarization away from the yttrium ion toward the uranium. The thorium ion having the same average valence in the lattice does not perturb the oxygen position relative to the uranium. The zirconium ion, because it is smaller, shrinks the lattice which in turn may induce strain energies leading to less interaction. This is supported by the fact that the enthalpy of vaporization for the zirconium oxide containing solid solutions listed in Table I appear smaller than the corresponding enthalpies for compositions without zirconium oxide. This same general behavior has been reported for fused salts having different ion sizes.[5] Thus, dissolving the large uranium cation in a smaller lattice increases its activity.

Summary

A strong negative departure from ideality was observed for the activity of UO_2 in solid solutions of UO_2–$YO_{1.5}$–O, which was much larger than was observed with UO_2–ThO_2–O solid solutions. It would appear, therefore, that interaction energies between molecular units involving the two cations are high when the valence of the cation diluent is less than that for uranium, *i.e.*, yttrium and the rare earth ions. The extension of this observation to divalent ions needs confirmation, however. Diluting a urania–yttria solid solution with cations of the same valence as that of the solvent does not cause significant changes in UO_2 activity unless strain energies are significant because of too large a difference in ion size of the cations, *i.e.*, Zr and U.

A regular solution model is appropriate for expressing the relationship between activity coefficients and composition but enthalpy and entropy of the solution indicate a more complex relationship because of their greater sensitivity to volume changes. The components which give rise to the interaction energy are difficult to define but it appears that visualizing the solid solution as a pseudo-binary mixture of $UO_{2+z'}$ and $YO_{1.5}$ offers some simplifying features in that the dependence of the activity coefficient, γ', on the oxygen activity can be minimized.

Radiolysis and Energy Transfer in the Adsorbed State

by J. G. Rabe, Birgit Rabe, and A. O. Allen

Chemistry Department, Brookhaven National Laboratory, Upton, New York 11973 *(Received September 22, 1965)*

The radiolysis of azoethane adsorbed on various solids was studied as an indicator of the energy-transfer processes occurring within the solids and at the surface. On the insulators SiO_2, MgO, and various alkali halides considerable decomposition occurred, which was assumed to result from energy transfer to the adsorbed molecules. The semiconductors ZnO, TiO_2, NiO, and graphite gave little or no sensitization, as expected, since the available quantum energy should not be much larger than the band gap. Some phenomena peculiar to the MgO system are described and are attributed to closer coupling between excited states of the solid and of the adsorbed molecules than occurs in other systems. A chemical method is described for determination of the number of negative color centers in an irradiated sample of alkali halide. The decomposition of azoethane occurring on contact with irradiated solids was studied and is discussed. In radiolysis, a considerable decrease in yield of decomposition of adsorbed azoethane with increase in the total dose was generally found and was attributed to hindrance of energy transfer by radiation-produced defects.

The study of radiolysis of substances in a state of adsorption on chemically inert supports[1-4] has shown clearly that excitation energy, delivered to the solids from the radiation, can move to the surface and cause decomposition of the adsorbate. The yield of the decomposition depends very strongly on the properties of the solid. These radiolytic processes can serve as a tool for the study of excitation in solids and may perhaps indirectly shed useful light on the fundamental processes occurring in surface-catalyzed reactions. The organic molecule may be regarded as an indicator of the processes of energy migration which are occurring in the solid support. In the present work, we chose as adsorbate azoethane, $(C_2H_5)_2N_2$, since it readily decomposes to nitrogen which is easily separated and measured. Small yields of hydrogen and methane, which are measured together with the nitrogen, serve as indicators of other modes of decomposition which probably require more energy than needed for the production of nitrogen.

The quantum of energy available for delivery to the adsorbed molecule is not likely to be larger than the energy gap between the ground state and conduction band in the solid. One object of the present study was to see if a correlation existed between the yield of decomposition of the organic molecules and the size of the band gap in the solid support. It was hoped that the yields of the processes would lead to some idea of the distance over which excitation energy can migrate without dissipation in solids. A preliminary account of this work appeared as a Communication to the Editor.[5]

Experimental Section

Azoethane, synthesized by the method of Renaud and Leitsch,[6] was purified by pouring it through a column of activated alumina, followed by gas chromatography on diethylene glycol. The purity was better than 99.8%.

The solids were prepared and were outgassed by heating under vacuum, as shown in Table I. The sample preparations were carried out in a grease-free system using metal and Teflon valves. Azoethane was measured as vapor in a calibrated volume and was condensed onto the solid in a glass ampoule fitted with a break-seal and sealed off under vacuum.

The irradiations were all made at 23° with cobalt-60

(1) J. M. Caffrey, Jr., and A. O. Allen, *J. Phys. Chem.*, 62, 33 (1958).

(2) J. W. Sutherland and A. O. Allen, *J. Am. Chem. Soc.*, 83, 1040 (1961).

(3) R. R. Hentz, *J. Phys. Chem.*, 68, 2889 (1964).

(4) Yu. A. Kolbanovskii, L. S. Polak, and E. B. Shlekhter, *Dokl. Akad. Nauk SSSR*, 136, 147 (1961).

(5) J. G. Rabe, B. Rabe, and A. O. Allen, *J. Am. Chem. Soc.*, 86, 3887 (1964).

(6) R. Renaud and L. C. Leitsch, *Can. J. Chem.*, 32, 545 (1954).

Table I: Preparation and Properties of Solids

Name	Sp surface, m^2/g	Starting material	Heated in air: Temp, °C	Heated in air: Time, hr	Outgassed: Temp, °C	Outgassed: Time, hr
SiO_2 gel A	775[a]	14–20 mesh gel[b]	...	...	450	65
SiO_2 gel B	500[a]	SiO_2 gel A	800	16	450	65
MgO 600	(~100)[c]	Basic $MgCO_3$[b]	600	16	450	16
MgO 800	29[a]	Same	800	16	450	16
MgO 1140	29[a]	Same	140	16	450	16
ZnO	...	$ZnCO_3$[d]	600	16	400	16
NiO	...	Pptd $NiCO_3$	380	4	525	16
TiO_2	...	(*b*)	...	...	430	16
Graphite	3.9[e]	(*f*)	...	...	800	16
NaCl	4.7[a]	Ground in mortar 45 min,[g] sieved to −300 mesh	...	...	130	16
NaF	8[a]	As received[d]	...	...	130	16
LiF	12[a]	As received[b]	...	...	130	16
KI	5.1[a]	Same treatment as NaCl[g]	...	...	130	16

[a] Determined by BET method, using nitrogen. [b] Fisher Scientific Co. [c] Estimated from the reports of R. M. Dell and S. W. Weller, *Trans. Faraday Soc.*, **55**, 2203 (1959); **59**, 470 (1963); and R. I. Razouk and R. Sh. Mikhail, *Actes Congr. Intern. Catalyse, 2e, Paris, 1960*, 2, 2023 (1961). [d] Baker and Adamson Chemical Corp. [e] Determined by the supplier. [f] National Carbon Co. [g] Baker Analyzed.

γ rays at a dose rate of about 0.25 Mrad/hr. Total doses ranged from 0.25 to 40 Mrads. The fraction of azoethane decomposed was less than 1% in the great majority of the runs. After irradiation, the ampoule was sealed to the vacuum line, the break-seal was opened, and the permanent gas fraction was pumped (by a Toepler pump) through a liquid nitrogen trap into a McLeod gauge; the gas was then transferred to the gas chromatograph for analysis. Separation was accomplished over a 4-m column of Linde Molecular Sieve 5A at room temperature with argon as carrier gas. The sample was passed successively through a thermal conductivity detector (for measurement of hydrogen and nitrogen) and a flame ionization detector (for measurement of methane). Gas volumes were determined from peak heights as calibrated with known samples; the total amount of gas was always checked against the amount determined in the McLeod gauge, and the results to be acceptable had to agree within 2%. No attempt was made to determine decomposition products other than the permanent gases.

To determine the amount of electrons trapped as color centers in irradiated salt samples, the ampoule containing the salt was opened to the vacuum system by the break-seal, and previously degassed water or aqueous solution was poured into the salt. The apparatus was agitated by hand until all of the salt was dissolved. The hydrogen gas produced was then pumped out and measured in the McLeod gauge and again in the gas chromatograph.

Results

Radiolysis of pure liquid azoethane gave $G(N_2) = 3.69$, $G(H_2) = 0.46$, $G(CH_4) = 0.076$.

Most of the present results are represented by graphs showing the amount of product formed per unit amount of solid, by a constant dose of radiation, as a function of the amount of azoethane present per unit amount of solid (here called the "coverage").

It is assumed that the azoethane covers the available surface with reasonable uniformity and that to form a monolayer would require about 4 μmoles of azoethane/m^2. All of the present data were obtained at coverages of less than one monolayer. On many graphs we have plotted the amount of product that would be expected to result from energy absorbed directly by the organic material from the radiation, assuming that the energy is taken up in the two phases in proportion to their electron fractions and that the specific energy yield G is the same as for the pure liquid organic compound. This quantity is indicated on the graphs as the "liquid line." Of course, the assumptions of energy partition between phases, and equal efficiency as between the liquid state and the adsorbed state, should not be expected to hold exactly, but an amount of product more than twice that given by the liquid line presumably provides an indication that energy taken up by the solid is being transferred to the adsorbate and is utilized for its decomposition.

Figure 1 shows the nitrogen obtained at a dose of 2 Mrads on various alkali halides. Some yields obtained on silica gel at 1.5 and 5.9 Mrads are shown for com-

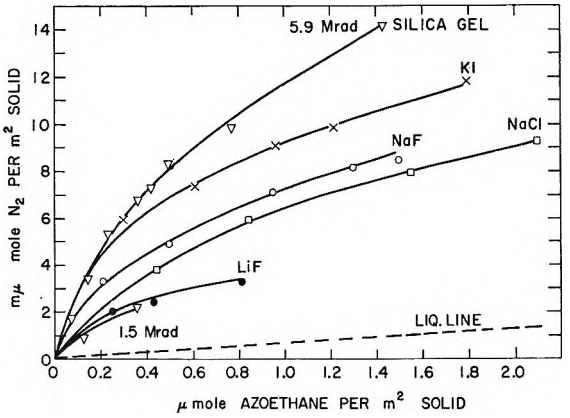

Figure 1. Nitrogen production from azoethane on alkali halides at 2 Mrads and on silica gel A at 1.5 and 5.9 Mrads.

parison. Figure 2 shows nitrogen yields obtained at 5.9 Mrads in the two preparations of silica gel, on three preparations of MgO, and on graphite. It is seen that the efficiency of energy transfer is similar at very low coverages for the salt, silica, and magnesia; as the coverage is increased, the yield of product per molecule of azeoethane present rapidly decreases with the first two solids but remains constant up to much higher coverage for the magnesia, so that much higher total yields are obtained with the latter substance. The curves for the magnesia remain linear up to a sudden maximum, beyond which the yield suddenly declines, showing that above a certain coverage additional amounts of adsorbate protect the material already there against radiolytic decomposition—a phenomenon not found with the other solids.

Figure 3 shows some results obtained with nickel oxide, zinc oxide, and titanium dioxide, expressed here as amount of product obtained per unit weight of solid, rather than unit surface as in the preceding graphs. As may be seen by comparing the results with the liquid lines shown, the yields in these semiconducting oxides are much smaller than in the insulating substances. Indeed the zinc oxide is seen to exert a definite protective effect for the azoethane with respect to decomposition to nitrogen although the yield of hydrogen appears to be somewhat increased. (This hydrogen might however arise from adsorbed water or surface hydroxide groups, rather than from the azoethane.) The band gap in MgO is 8.7 ev,[7] in the alkali halides it is thought to be around 10 ev,[8] and it is probably equally as high in silica, while the corresponding quantity in ZnO is only 3.2 ev,[9] in TiO_2 3 ev,[9] in NiO probably about the same, and in graphite close to zero.[9] Thus, as expected, the insulators show a large transfer of energy to the

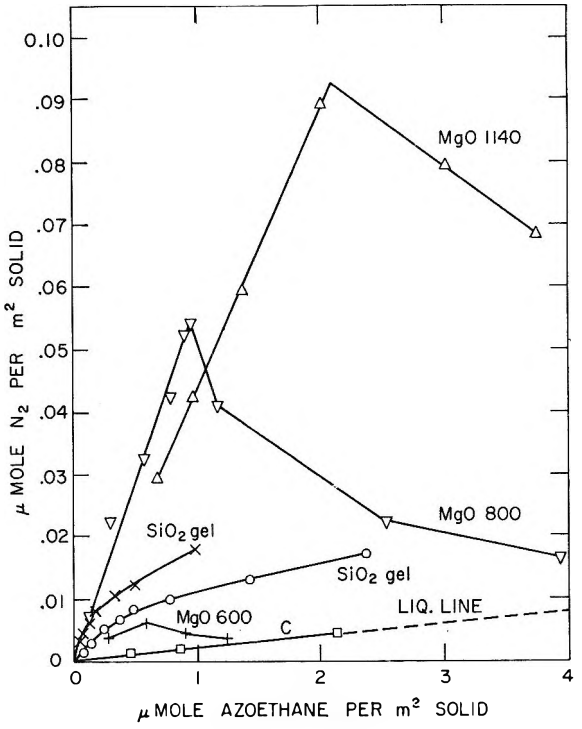

Figure 2. Nitrogen produced from azoethane on various solids at 5.9 Mrads. The points for graphite (labeled C) coincide with the liquid line.

adsorbate, while the semiconductors give a relatively small effect.

The magnesium oxide data at 5.9 Mrads are shown in more detail in Figure 4. The same data were given in our preliminary publication.[5] At low coverages the yields of methane and nitrogen are practically equal although on the other solids the methane yield was much smaller than the nitrogen, usually by a factor of 10 or more. However, on magnesia the methane reaches its maximum at a lower coverage than does nitrogen. There is some indication for the 800° preparation that a maximum may also be reached at extremely low coverages for the hydrogen yield. The energy transfer is seen to attain higher values, the higher the calcination temperature of the MgO. Figure 5 shows the radiolysis of a saturated and an unsaturated hydrocarbon on MgO. In both cases the evolution of hydrogen is suppressed by the presence of MgO although the formation of methane seems to be somewhat sensitized. Figure 6 shows the results of irradiating mixtures of azoethane and 2-methylpentane.

(7) G. H. Reiling and E. B. Hensley, *Phys. Rev.*, 112, 1106 (1958).
(8) J. H. Schulman and W. D. Compton, "Color Centers in Solids," The Macmillan Co., New York, N. Y., 1962, p 6.
(9) W. C. Dunlap, Jr., "An Introduction to Semiconductors," John Wiley and Sons, Inc., New York, N. Y., 1957.

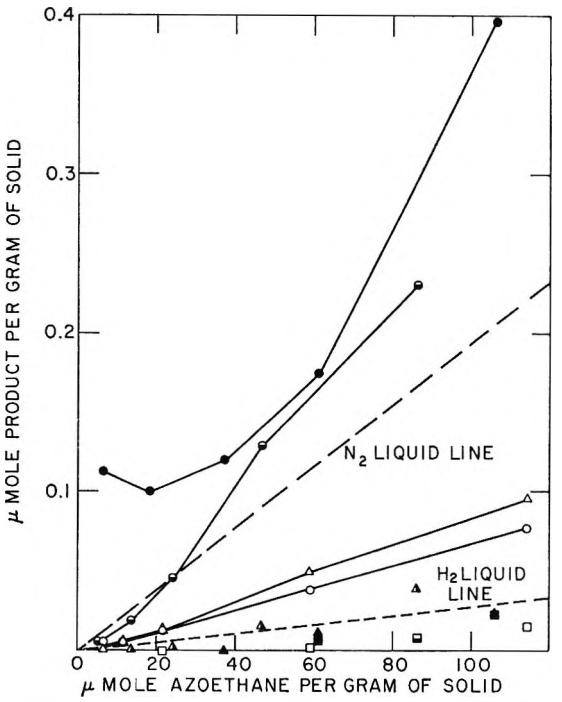

Figure 3. Products from azoethane on semiconducting oxides: open symbols, ZnO; half-filled symbols, TiO_2; solid symbols, NiO; circles, N_2; triangles, H_2; squares, CH_4.

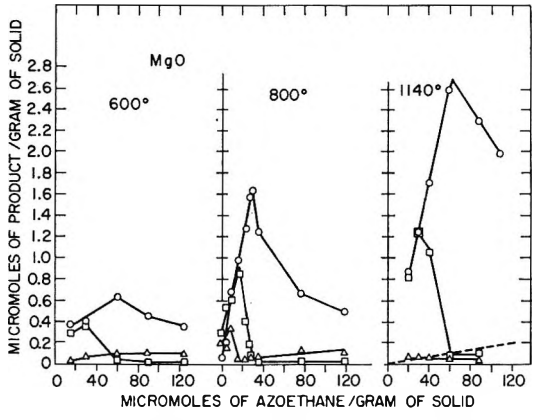

Figure 4. Products from azoethane radiolysis at 5.9 Mrads on MgO heated to different temperatures.

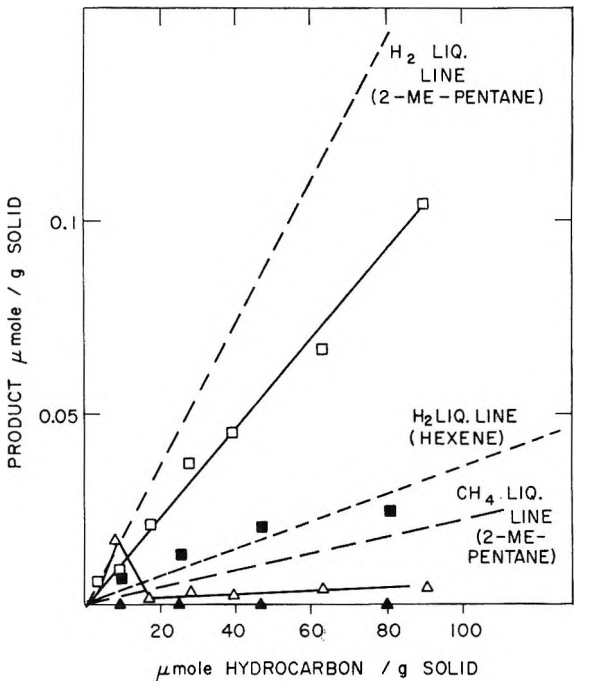

Figure 5. Hydrocarbon radiolysis on MgO 800. Hexene-1 at 4.4 Mrads; 2-methylpentane at 5.9 Mrads: squares, CH_4; triangles, H_2; open symbols, 2-methylpentane; solid symbols, hexene-1.

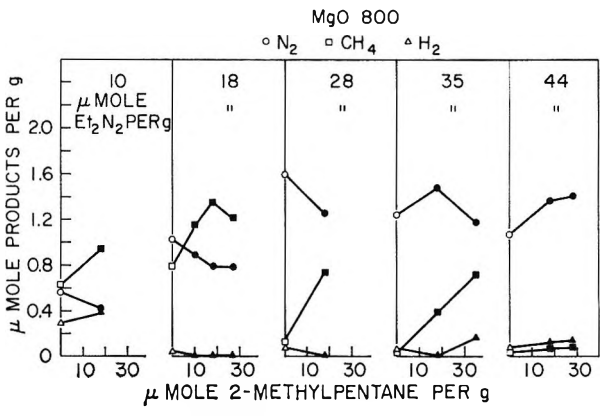

Figure 6. Product yields from mixtures of azoethane and 2-methylpentane on MgO 800 at 5.9 Mrads.

The methylpentane caused a reduction of the nitrogen yield, compared to that obtained with the azoethane present alone, when the azoethane coverage was low; but at high coverages, beyond the maximum in the nitrogen yield curve, adding methylpentane tended to cause an increase in the nitrogen yield. Thus, the effect of adding methylpentane was similar to the effect of decreasing the amount of azoethane present.

Figure 7 shows the effect of total dose on the specific energy yield of nitrogen, $G(N_2)$, for different coverages on silica gel. There is a marked decrease of the yield with increasing dose. Figure 8 shows the effect of total dose for MgO, which is seen to behave in this respect quite similarly to the silica. Figure 9 shows that a similar effect occurs for the yield of total gas on sodium chloride.

Irradiated salt must contain an equal number of negative and positive centers, usually referred to as "trapped electrons" and "trapped holes," respectively. When irradiated salt is dissolved in water, one might expect the trapped electrons to react to yield hydrogen

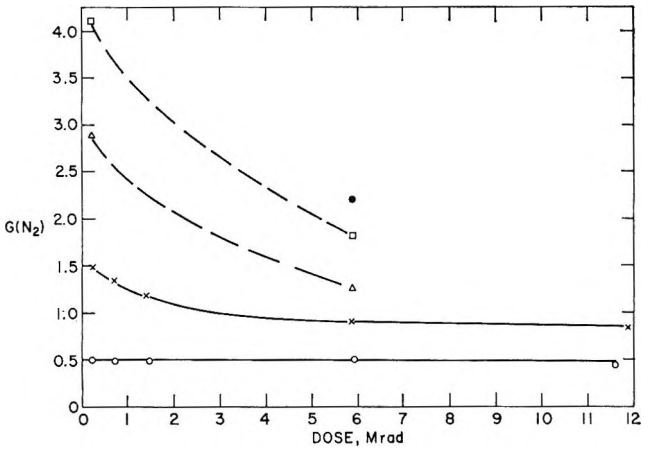

Figure 7. Effect of total dose on the yield of nitrogen $G(N_2)$ (in molecules per 100 ev delivered to the total system of solid plus adsorbate) from azoethane on silica gel A. μmoles of azoethane/g of solid: O, 105; ×, 284; △, 598; □, 1100; ●, 1810.

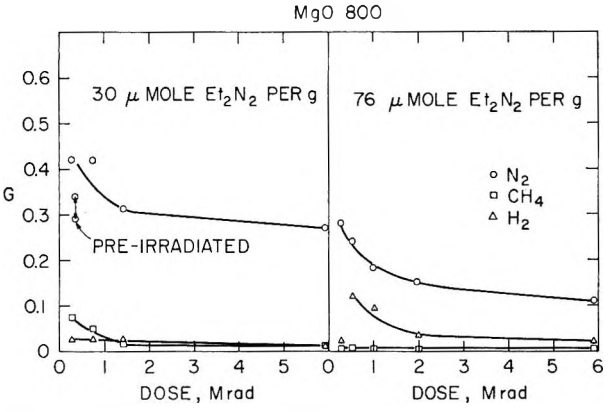

Figure 8. Effect of total dose on product yields from azoethane on MgO 800.

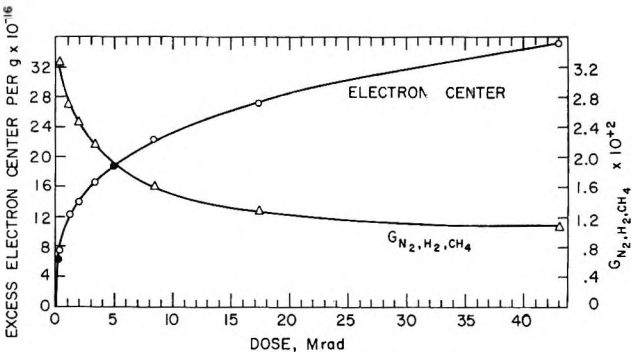

Figure 9. Effect of total dose on the excess yield of permanent gas (right-hand scale) from azoethane adsorbed on NaCl (10 μmoles/g) (yield corresponding to "liquid line" has been subtracted from total yield) and dose effect on the number of negative centers in the irradiated salt as determined by the hydrogen formed on dissolution in an acid aqueous solution containing 3 M ethanol: solid circles, salt irradiated under vacuum without adsorbate; open circles, irradiated in presence of azoethane.

atoms or solvated electrons, while the holes should yield OH, Cl, or other oxidizing radicals. The oxidizing and reducing radicals would then be expected to combine to a great extent with one another. Some hydrogen gas should form by combination of reducing radicals with one another, but its amount should be less than half the amount of trapped electrons present. If some acid and a sufficient concentration of an organic substance such as ethanol were added to the water, however, we would expect that all the negative centers would be rapidly converted to hydrogen atoms, which would then react with the alcohol to form a molecule of H_2 and an organic radical, while all the positive centers would eventually react with the alcohol to abstract hydrogen, forming H_2O or HCl and another alcohol radical. Thus, when sufficient ethanol is present, a yield of hydrogen gas should be obtained that would serve as a measure of the number of electrons trapped in the salt. Figure 10 shows the hydrogen yields obtained when 1 g of irradiated sodium chloride was dissolved in acid solutions containing different amounts of ethanol. The yield is seen to reach a constant value at ethanol concentrations above 2 M. These determinations were made routinely using 0.1 M H_2SO_4 and 3 M ethanol. Different samples of ground Baker Analyzed NaCl, irradiated separately to the same dose, gave hydrogen yields reproducible to within 5%, provided the bottles in which the salt was obtained bore the same lot number. Samples from different lots might differ as much as 20%.

A saturated solution of hydrogen sulfide in water was found to give the same yield of hydrogen as the acidic alcohol solution, as was expected, since each negative center would form an H atom which would then abstract H from an H_2S molecule to give a molecule of hydrogen. An acidic alcohol solution saturated with oxygen was tried and was expected to give a yield of hydrogen peroxide equal to that of the hydrogen formed in the absence of oxygen, provided that reactive negative and positive centers were present in equal numbers. It was thought that each center whether negative or positive should either react directly with oxygen to give a radical HO_2 or with the alcohol to give an alcohol radical which in its turn would react with oxygen to give HO_2. Two HO_2 radicals would then react together to give a molecule of peroxide. In fact, the yield of peroxide found was only 70% of the yield of hydrogen produced in the absence of oxygen. The difference may be due in part to the low

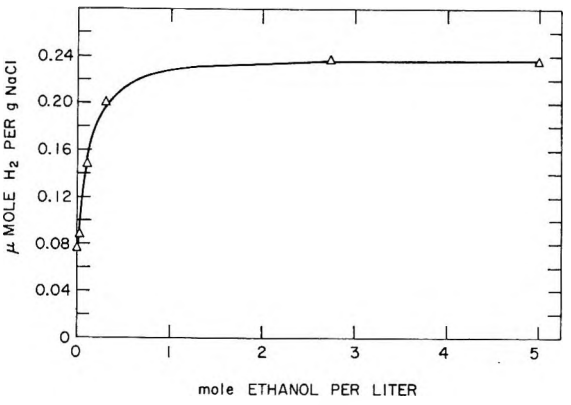

Figure 10. Effect of ethanol concentration on hydrogen formed when NaCl, irradiated to 2 Mrads, was dissolved in 0.1 N H_2SO_4.

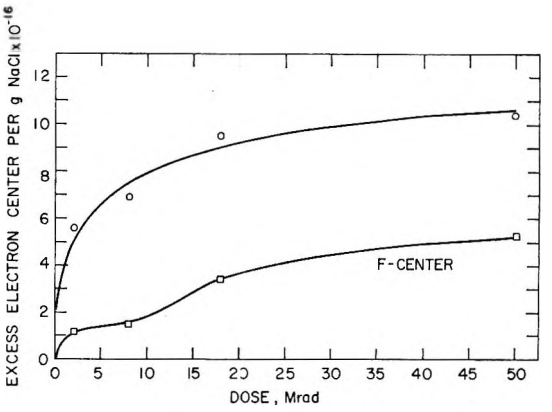

Figure 11. Total negative centers of irradiated salt, as determined by hydrogen evolution, and F centers determined optically, by assuming 0.9 oscillator strength.

solubility of oxygen in concentrated salt solution and also perhaps to the fact that some of the negative centers determined in this way are really hydride ions which are not accompanied by an equal number of reactive positive centers.

It might be expected that the number of trapped electrons indicated by this method should be nearly equal to the number of F centers produced by radiation in the solid. To test this point, we irradiated single-crystal specimens of NaCl, cleaved from large synthetic crystals obtained from the Harshaw Co., and determined the number of F centers present from the area under the F band in the absorption spectrum, assuming an oscillator strength of 0.9. These crystals, carefully protected from light and mechanical strain, were then dissolved in the acidic alcohol solution, and the resulting hydrogen yields were determined. Figure 11 shows that the total hydrogen yield was much greater than the number of F centers present. A similar large discrepancy was shown to exist between the F center concentration and the hydrogen yield from an additively colored crystal prepared in sodium metal vapor by the method of van Doorn.[10] The spectra of these crystals all showed a peak at 1900 A, the position reported in the literature for the U band. At low doses in our irradiated crystals, the U band actually appeared larger than the F band though it became relatively smaller at higher doses. The U band is supposed to indicate the presence of hydride ion H^- in the crystal, probably derived from radiation decomposition of impurity OH^- ions or perhaps from traces of occluded water or hydrogen. Continued irradiation is known to cause the decomposition of the hydride ion into a trapped electron (F center) plus an interstitial hydrogen atom.[11] One would expect, on dissolution in the alcohol solution, to obtain one molecule of hydrogen by reaction of this hydrogen atom with the alcohol, while the original hydride ion would react with water to give only one molecule of hydrogen. Thus, the difference between the total hydrogen yield and the number of F centers should, at high doses, remain constant and equal to the number of hydride ions present at low dose.

Figure 9 shows that radiolysis of adsorbed azoethane decreases with dose in approximately the same way that the number of electron centers increases with dose, in the case of sodium chloride. A plausible assumption is that in all cases the decrease in decomposition yield with dose results from a decreasing efficiency of energy transfer within the solid, owing to the buildup of radiation-produced defects.

When the solids were first irradiated under vacuum and then azoethane was added without further irradiation, small yields of gas were noted, amounting to a few per cent of the quantity that would have been produced had the azoethane been present throughout the irradiation. Silica gel is colored blue under irradiation. It was noted by Kohn[12] that this blue color could be bleached simply by the addition of various gases to the system. We observed that irradiated silica gel would lose its color when azoethane vapor was added to it, while small quantities of nitrogen were formed at the same time. When a limited quantity of azoethane vapor was let into a tube containing irradiated silica gel at room temperature, only the gel at the top of the column was bleached; apparently no

(10) C. Z. van Doorn, *Rev. Sci. Instr.*, **32**, 755 (1961).

(11) C. J. Delbecq, B. Smaller, and P. H. Yuster, *Phys. Rev.*, **104**, 599 (1956).

(12) H. W. Kohn, *Nature*, **184**, 630 (1959).

Table II: Preirradiation Effects in Sodium Chloride

Preirradn dose, Mrads	Irradn dose, Mrads	Products, nmoles/g of solid: N_2	H_2	CH_4	ΣN_2, H_2, CH_4	Σ_{cor} for liq line[a]	Σ_{cor} for preirradn[b]	$G(N_2 + H_2 + CH_4)$[c]	Electron center/g of solid, nmoles
2.0	...	6.7	0.06	0.24	7.0	...	...	...	230
17.25	...	13.2	0.21	1.01	14.4	...	...	...	451
...	2.01	52.0	5.8	2.8	60.6	51.5	51.5	0.0247	...
2.00	2.00	49.0	4.7	2.2	55.9	47.1	40.1	0.0193	...
17.25	2.00	47.2	4.1	2.0	53.3	44.5	30.1	0.0145	...

[a] "Liquid line" yield is subtracted from the preceding column. [b] Amount produced during preirradiation is subtracted from preceding column. [c] Based on the numbers in the preceding column.

azoethane penetrated to the lower parts of the column. Figure 12 shows the approximate fraction of silica gel decolorized by different amounts of added azoethane, along with the quantities of nitrogen simultaneously produced. The amount of nitrogen is, within the experimental uncertainty, proportional to the amount of decolorization. The nitrogen produced here is about 9% of what would be formed, had the azoethane been present during the irradiation. When similar experiments were tried with MgO 800, the amount of gas formed was much smaller and appeared to be approximately constant at about 0.015 μmole/g, independent of the amount of azoethane added although with the silica gel the gas formed was almost proportional to the amount of azoethane added.

Table II shows the results of similar experiments on sodium chloride, with further experiments in which additional irradiation was given after the azoethane was added to the preirradiated salt. It is seen that the gas formed on adding the azoethane to the preirradiated salt has a much lower ratio of hydrogen to nitrogen than that formed when the azoethane is present during irradiation. The table shows that the amount of gas formed during the irradiation is considerably less when the solid has been preirradiated than when it is fresh. This effect was also demonstrated for MgO, as shown in Figure 8. Table II also shows that the amount of decomposition on samples of salt preirradiated with different doses is proportional to the number of negative centers present (as shown by the amount of hydrogen generated when the salt is dissolved in the acid solution of alcohol). It seems reasonable that the decomposition of the azoethane should be accompanied by bleaching of color centers located near the surface although the surface is so small that the fractional decrease in total color centers present in the salt is too small to be noticed. The quantity of nitrogen shown in the upper two rows of Table II corresponds to a yield of one molecule for

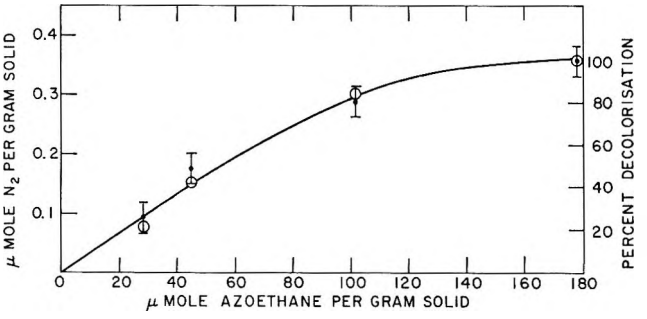

Figure 12. Per cent decolorization and amount of N_2 formed when azoethane is put on silica gel A, irradiated to 6 Mrads under vacuum.

each negative center lying within 30 A of the surface (if the centers are uniformly distributed). Since essentially the entire volume of silica gel lies within this distance of the surface, it is consistent to find that the silica gel is bleached quickly and completely.

Discussion

The interpretation of data on such complicated systems, involving processes, the basic nature of which is unclear, must be tentative at best. Much more experimentation will be required to confirm any proposed models. For instance, we determine, among the decomposition products of azoethane, only the permanent gases, as we believe it more valuable to obtain yields of a few products under a wide range of environmental conditions than to obtain a more nearly complete product spectrum with less variation in conditions. Yet we cannot be sure that study of the yields of other products might not have led to a different picture.

The data all seem consistent with a picture in which energetic entities, which might be electrons, holes, or excitons, are produced in the solid by radiation, migrate to the surface with a probability which is higher the more perfect the solid lattice, and transfer their energy to the adsorbed molecules which then

have a certain probability to undergo various modes of decomposition. This picture is consistent with the finding that the yields on MgO increased with increasing calcination temperature of the oxide, which is known[13] to be associated with increasing perfection of the crystal lattice.

Such a result emphasizes the basic difference between radiolysis and heterogeneous catalysis. A catalyst is generally spoiled by treatments that tend to eliminate lattice imperfections. In radiolysis the activation energy is supplied from outside, and the problem is to get it to the point of reaction; in catalysis the reaction arises spontaneously from the field of force resulting from a peculiar specific arrangement of atoms in the system.

As remarked above, we incline to the opinion that the decrease in yield with increasing dose results from hindrance to energy transfer by radiation-produced imperfections in the solids. The most effective imperfections are no doubt the new vacancies and interstitials which are known to be produced by X-rays, probably as a result of multiple ionizations arising from inner-shell excitation of atoms in the solid. We cannot tell whether the presence of color centers (trapped electrons and holes) may also hinder energy transfer.

A possible alternative explanation for the dose effect is that radiolysis products on the surface could act as inhibitors to further reaction. Another possibility is that energy transfer to adsorbate molecules is favored at certain active sites; molecules on these sites will tend to decompose first, and if the decomposition products remain on these sites, preventing other molecules from migrating to them, the decomposition yield should decrease with time. However, the data of Table II and Figure 9 show that in the case of NaCl a given dose of radiation is about as effective in lowering the energy transfer when applied to the solid before the adsorbate is introduced as when the adsorbate is present throughout the irradiation. The effect must be on the solid itself. It could be thought that radiation actually destroys active sites, or potential active sites, by annealing out or breaking up peculiar surface structures. This idea is plausible in the case of the oxides, where OH groups on the surface may play a role in the adsorbate decomposition, but does not seem likely in the case of alkali halides.

It may seem paradoxical that build-up of radiation-produced defects should decrease the decomposition yield, while on the other hand the presence of color centers causes decomposition of added materials with no direct exposure at all of these materials to radiation. When a solid is irradiated, most of the electrons and holes recombine, but a few are trapped at lattice vacancies, at other defects, and at points on the surface. Though these traps appear optically to be several volts in depth, it is well known that slight straining of the lattice, such as caused by relatively gentle jarring of the crystals, will distort some of the traps enough to free some of the electrons and holes, thereby decreasing the concentration of color centers. A similar strain is produced near the surface of a crystal by the mere physical adsorption of vapor molecules on the surface[14] because the change in surface energy is sufficient to change appreciably the equilibrium separation of ions in the surface layer. Hence, adsorption frees some of the electrons and holes trapped near the surface of an irradiated solid, and some of them will interact with the adsorbing molecules and may cause decomposition if sufficient energy is made available. This differs from the interaction at the surface of excited entities generated directly by radiation since the latter should on the average carry more energy than those released from traps. An indication of the difference is the relatively smaller amount of the higher energy product hydrogen, relative to nitrogen, generated from azoethane on contact with irradiated salt, as compared to the corresponding yields formed during irradiation (Table II).

The radiolysis of materials adsorbed on MgO follows a different pattern from that found for any of the other mineral supports tried, which include[1,2] various oxides, silicates, and alkali halides. Except for MgO, the curve showing the yield of decomposition products as a function of coverage ordinarily rises at a continually decreasing rate, bends over gradually, and becomes parallel to the "liquid line" after the first monolayer is complete. On MgO, the curve, instead of gradually bending over, remains straight, up to a certain coverage, after which it abruptly falls and reaches a relatively very low value by the time the monolayer is complete. The maximum in these yield–coverage curves is reached at very different coverages for different individual products of the radiolysis. A further peculiarity of MgO is shown in the profound effects on the yields of particular products at low coverages. Thus, with hydrocarbons on MgO the yield of hydrogen was almost completely suppressed while that of methane was increased. For azoethane, the percentage of methane in the permanent gas fraction was an order of magnitude higher on MgO than on any other solid, or in the liquid state.

(13) R. Fricke and J. Lueke, *Z. Elektrochem.*, **41**, 174 (1935); R. M. Dell and S. W. Weller, *Trans. Faraday Soc.*, **55**, 2203 (1959).

(14) D. J. C. Yates, *Advan. Catalysis*, **12**, 265 (1960).

One may ask first why with most materials these curves bend over gradually. One possibility is that the range of action of an excitation produced in the solid is quite large; that is, a molecule adsorbed on the solid has a certain probability of receiving energy from an event occurring anywhere within a considerable distance although this probability may not be very large. Then as additional molecules are added to the surface, even though they may be at considerable distances from the first molecule, they will compete for the energy coming from a given event in the solid, and the probability of a given molecule becoming decomposed will continually decrease with increasing coverage. A model of this type would predict a hyperbolic dependence of yield on coverage, typical of competition kinetics. A second possibility is that, even if the adsorbed molecules only communicate with a rather small volume in the solid, additional molecules added to the surface go on at random or show some tendency to cluster together. Then competition for the energy will occur only between molecules lying close together, but the proportion of molecules occurring in such close pairs or groups will increase as the coverage increases, approaching unity exponentially. Such a model would lead to an exponential dependence of yield (corrected for liquid line) on coverage. Actually, a fair fit to the data can be made with either a hyperbolic or exponential type of expression. Probably both effects are present in most cases.

Since MgO shows no gradual change in the slope, we must conclude that neither condition holds in this case. First, the molecules must be drawing energy from a rather restricted volume of solid; and, second, as they go on the solid, they must be spaced so that no two molecules are located very close together. Although we have no evidence that chemisorption is occurring in any of our experiments, we must assume that in the neighborhood of a molecule adsorbed on MgO the force of attraction for a second molecule is somewhat reduced, so that molecules effectively tend to repel one another on the surface to the extent of keeping a respectful distance away from each other. The marked enhancement of yields of certain decomposition products and suppression of others shows that electronic excitations within the lattice must activate surface states of the solid which interact with excited states of the adsorbed molecules in very specific ways. Thus, in the case of azoethane, electronic excitation within the magnesia activates a surface state which communicates its energy to a specific excited state of the molecule that results in splitting of the relatively strong C–C bond. Most modes of excitation of this molecule split the weak C–N bond, resulting in the formation of nitrogen gas and not of methane. In hydrocarbons, excitation by direct absorption of energy usually gives rise to states which lead to the breaking of a C–H bond with ultimate formation of hydrogen gas. On MgO these states, which have rather high energy, are in communication with surface states of somewhat lower energy so that this mode of decomposition is suppressed. Instead, other modes of decomposition giving rise to breakage of C–C bonds, which have somewhat lower energy, are favored.

Now we have to suppose that when a certain degree of coverage is attained, the distance between the molecules becomes comparable to the geometrical extent of the surface excitation which is responsible for the formation of a decomposition product and which presumably includes orbitals belonging both to the adsorbed molecule and to the magnesium and oxygen atoms nearby. When the second molecule comes close enough to distort the orbital of that excited state of the first molecule which leads to formation of a particular decomposition product, then this excited state will be quenched, its energy presumably divided between the two molecules, and decomposition in this particular mode will no longer be possible. In general, we might expect that those states of higher energy which are required to break the strongest bonds in the molecule would tend to have the most extended orbitals. In fact, it is found that hydrogen, which requires the most energy for its formation from azoethane, reaches a maximum in its yield at a very low coverage; methane reaches its maximum at a higher coverage; and nitrogen, which requires the least energy, reaches its peak at the highest coverage.

When hydrocarbon is added to the surface which already contains adsorbed azoethane at a fairly high coverage, the decomposition yield of the azoethane products, nitrogen and methane, is increased, as though the amount of azoethane had been decreased. A probable explanation is that the hydrocarbon molecule, which has a tendency to deliver energy to the surface states, intervenes between two azoethane molecules which would otherwise share the energy. The energy cannot flow so readily into the hydrocarbon molecule and hence remains in the azoethane molecule, which decomposes.

The yield of nitrogen per molecule of azoethane on MgO at 5.9 Mrads is 20 times that from liquid azoethane, while the total yield of permanent gas (N_2 + H_2 + CH_4) is about 50 times that of the liquid. The region in the crystal from which energy communicates to the adsorbed molecule may then be assumed to have a mass at least 20–50 times that of the azoethane molecule or (density of MgO = 3.65) a volume

of 800–2000 A^3. This would correspond to a cubic volume 9.3–12.6 A on a side—not much greater than the length of the azoethane molecule, which would be about 8.3 A if it lay in a stable configuration but stretched out to get maximum contact with the surface.

Some features of the data remain unsatisfactorily explained. Thus, it is not clear why, in Figure 7, the effect of dose on G should be small at low coverage. Again, on comparing MgO 800 with MgO 1140, the yields at low coverage are nearly the same, showing equally good energy transfer. Why should the maximum yields then be so different? Though the present model seems to fit the major qualitative features of the data, a great deal obviously remains to be learned about the fundamental processes occurring in the radiolysis of heterogeneous systems.

Acknowledgments. The surface-area determinations by the BET method were performed on his apparatus with the permission of R. N. Dietz, who also supplied valuable advice and assistance in carrying out the measurements and calculations. Preparation of the large single crystals and measurement of their absorption spectra were carried out for us by R. L. Warasila. Throughout the work we have profited by frequent discussions with Dr. Paul Levy of the physics department. The chemical method for determination of negative centers in salt originated from discussions we held with Drs. A. Appleby and W. A. Seddon. J. G. R. was supported by a NATO research fellowship during most of the time in which this work was carried out. This research was performed under the auspices of the U. S. Atomic Energy Commission.

Shift of Nuclear Magnetic Resonance Signal Caused by Micelle Formation.

II. Micelle Structure of Mixed Surfactants[1]

by Hideo Inoue[2] and Toshio Nakagawa

Shionogi Research Laboratory, Shionogi & Co., Ltd., Fukushima-ku, Osaka, Japan *(Received September 27, 1965)*

This study deals with the nmr spectra of mixed solutions of ω-phenylpentyltrimethylammonium bromide and ω-phenyloctyltrimethylammonium bromide; they differ from each other only in the alkyl chain length. An increase in the total concentration of the surfactants beyond the cmc causes upfield shifts of the proton signals of phenyl, N^+-methyl, and methylene groups. In the concentration region above the cmc the phenyl proton signal splits into two peaks, each of which shifts to a higher field at different rates with an increase in total concentration. Intensities of these peaks measured at several mixing ratios of the two surfactants indicate that the signal at the higher field is due to the surfactant of longer alkyl chain length. These facts suggest that surfactant molecules are exchanged rapidly between the micelles and the bulk water phase. The compositions of mixed micelles and of the water phase are determined by examining the shifts of phenyl protons and assuming rapid exchange, and several rules governing the formation of mixed micelles are proposed. These results are in agreement with predictions derived from statistical thermodynamics.

Introduction

In a preceding paper[3] the shift of the nmr signal for a series of ω-phenylalkyltrimethylammonium bromides in deuterium oxide solutions of increasing concentration was examined. The signal of the phenyl protons remained at the same position until the critical micelle concentration (cmc) was reached. It then began to shift to a higher magnetic field at the cmc and approached a definite position. This ultimate position depended upon the length of the alkyl chain connecting the phenyl group and the nitrogen atom in a surfactant molecule. The longer the chain length, the higher this position.

This behavior was interpreted as follows. In the concentration range below the cmc, all phenyl groups are distributed homogeneously in the aqueous medium and show a signal at a relatively low field. Micelles are formed at the cmc, and the phenyl groups in a micelle experience a large diamagnetic anisotropy arising from the other phenyl groups in the same micelle.[4-6] If there were no exchange (or slow exchange) of surfactant molecules between the micelle and the bulk water phase, a second signal would appear at a higher field besides that of the monomolecularly dispersed surfactant. Because of a rapid exchange, however, only a single averaged shift is observed in reality; a sharp singlet appears at the weight-averaged position between those expected for monomolecular surfactant and micellar surfactant. With a further increase in concentration this single peak shifts upfield, since the fraction of surfactant in the micelle increases. At extremely high concentrations, the signal approaches the position where the signal of the phenyl protons in a completely micellar environment would appear. With an increase in the alkyl chain length, the propor-

(1) Presented in part at the 150th National Meeting of the American Chemical Society, Atlantic City, N. J., Sept 1965.

(2) To whom inquiries should be addressed: Eastern Regional Research Laboratory, U. S. Department of Agriculture, Philadelphia, Pa.

(3) T. Nakagawa and H. Inoue, 4th International Congress on Surface Active Substances, Brussels, Sept. 1964, Vol. BIV, p 11.

(4) J. A. Pople, W. G. Schneider, and H. J. Bernstein, "High-resolution Nuclear Magnetic Resonance," McGraw-Hill Book Co., Inc., New York, N. Y., 1959.

(5) S. I. Chan, M. P. Schweizer, P. O. P. Ts'o, and G. K. Halmkamp, *J. Am. Chem. Soc.*, **86**, 4182 (1964).

(6) E. S. Hand and T. Cohen, *ibid.*, **87**, 133 (1965).

tion of surfactant molecules in a micelle increases at a given molar concentration,[7] and therefore each phenyl group is surrounded, on the average, with more benzene rings. This also results in an upfield shift of the phenyl proton signal.

These results and interpretation suggest the possibility that some important information may be obtained about the structure of a mixed micelle if the concentration dependence of the phenyl proton signal is examined with a mixture of two surfactants of the above type. As explained later, this seems really the case. Comparing the results obtained with different mixing ratios, we suggest several rules governing the formation of mixed micelles.

Experimental Section

The surfactants used were ω-phenylpentyltrimethylammonium bromide (PA) and ω-phenyloctyltrimethylammonium bromide (OA) ($C_6H_5(CH_2)_nN^+(CH_3)_3Br^-$, n = 5 and 8, respectively).[7] High purity of these compounds was verified by surface tension measurements, where a plot of the surface tension of each surfactant against the logarithm of concentration showed no minimum at the cmc. The two surfactants were mixed in mole ratios of 1:0, 3:1, 1:1, 1:3, and 0:1. For each mole ratio a solution containing about 400 mg of the total surfactant/ml was prepared by dissolving the mixture in deuterium oxide containing a small amount of 1,4-dioxane as an internal reference. After the nmr spectra were recorded, the first solution was diluted with deuterium oxide to give a concentration that was 0.8 or 0.7 of the original one. The resulting solution was measured and diluted repeatedly until the final concentration reached about 2 mg/ml.

The nmr spectra were recorded on a Varian A-60 spectrometer operating at the room temperature of around 30°. Chemical shifts were measured in cycles per second from an internal reference, 1,4-dioxane.[8] The error of measuring the distance between the dioxane peak and the phenyl peak was within 1 cps.

Results

In Figure 1 is shown a typical spectrum of an equimolar mixture of PA and OA. In this work our concern is mainly directed to the phenyl proton signals appearing at low field. In an aqueous solution containing both surfactants, the phenyl proton signal, which is a sharp singlet below the cmc, splits into two peaks in the concentration region above the cmc. These peaks shift upfield at different rates with increase in concentration. Relative intensities of these peaks measured at several mixing ratios reveal that the peak at the higher field is due to the phenyl group

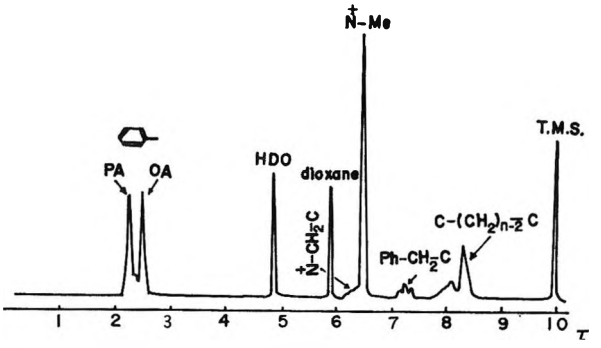

Figure 1. The nmr spectrum of a mixture of ω-phenylpentyltrimethylammonium bromide (PA) and ω-phenyloctyltrimethylammonium bromide (OA) in deuterium oxide: total concentration, 15 g/100 ml; mole ratio of PA to OA = 1:1.

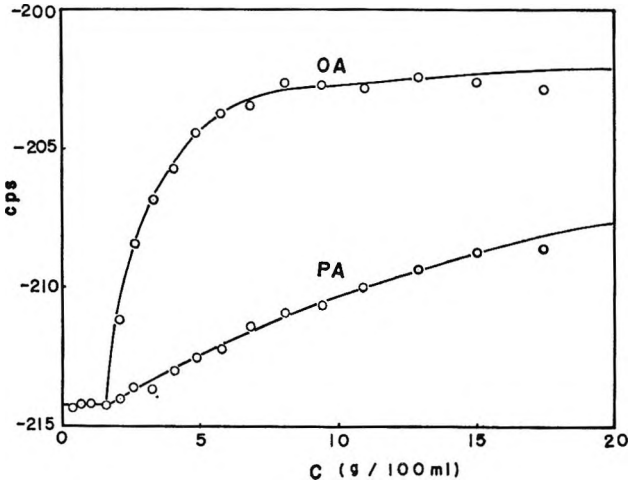

Figure 2. The shifts of phenyl proton signals as a function of the total concentration: PA:OA = 1:1.

of OA while that at lower field is due to that of PA. The shifts of phenyl proton signals with reference to 1,4-dioxane are illustrated in Figure 2 as a function of the total concentration of the equimolar mixture. Similar curves were obtained for mole ratios 3:1 and 1:3. The curves for pure PA and pure OA have been shown in the previous paper.[3]

With increasing concentration both phenyl proton signals approach asymptotically to definite but different positions for different mole ratios. The composition of a mixed micelle at a sufficiently high con-

(7) H. Inoue, H. Jizomoto, K. Horiuchi, and T. Nakagawa, in preparation.

(8) Chemical shifts were also observed from an external reference, tetramethylsilane. However, it is not possible at this time to apply a bulk-susceptibility correction to the observed chemical shifts since the magnetic susceptibilities of PA and OA have not yet been measured. Therefore, a change in the chemical shifts with reference to an external standard is not discussed in this paper.

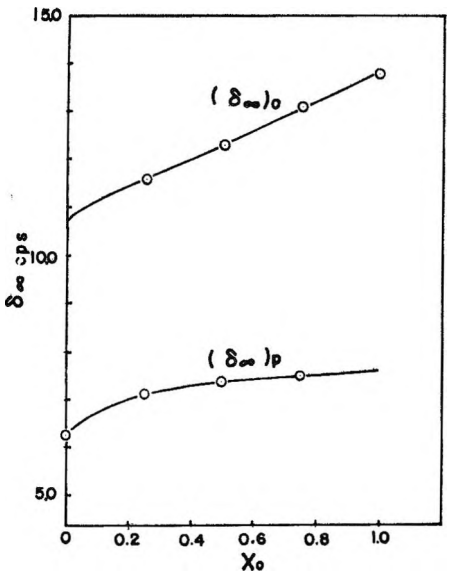

Figure 3. Plots of $(\delta_\infty)_P$ and $(\delta_\infty)_O$ against the mole fraction of OA, X_O.

centration is believed to be almost identical with the mole ratio of the mixture because the amount of monomolecularly dispersed surfactant is negligibly small as compared with that of micellar surfactant. Therefore, the values of the two asymptotes may be regarded as the chemical shift of phenyl protons of PA, $(\nu_m)_P$, and that of OA, $(\nu_m)_O$, both in the mixed micelle whose composition is the same as the mixture. Let ν_w be the chemical shift of phenyl protons below the cmc of the same mixture, then $(\delta_\infty)_P = (\nu_m)_P - \nu_w$ and $(\delta_\infty)_O = (\nu_m)_O - \nu_w$ express the changes which occur in the resonance frequencies of phenyl protons of PA and of OA when these molecules are displaced from the water phase into the mixed micelle of a given composition. In Figure 3, $(\delta_\infty)_P$ and $(\delta_\infty)_O$ are plotted against the mole fraction of OA species, X_O. By interpolation or extrapolation one can estimate $(\delta_\infty)_P$ and $(\delta_\infty)_O$ at any mole fraction of OA.

Calculation of Micelle Composition

Supposing a mixture whose mole ratio of PA to OA is p to q, we shall explain first how to calculate the compositions of the mixed micelle and of the coexisting aqueous phase. The chemical shifts of the phenyl protons of OA are measured at several concentrations at a constant ratio of the two surfactants, and we subtract from these values the chemical shift of the phenyl protons below the cmc to obtain a series of $(\delta)_O$ values. The value of $(\delta_\infty)_O$ at the mole fraction $X_O = q/(p + q)$ is obtained from Figure 3 and used to compute $(\delta/\delta_\infty)_O$ values at these concentrations.

If the mole fraction of OA in the mixed micelle were the same as that of the mixture, X_O, each $(\delta/\delta_\infty)_O$ could be regarded as the ratio of OA in a micellar state to the total OA. However, this is not the case in reality. By assuming $(\delta/\delta_\infty)_O$ thus obtained and $(\delta/\delta_\infty)_P$ computed in a similar manner to be zero-order approximations, the concentrations in moles per liter of total solution of the micellar PA and OA at a given total concentration c (grams per liter) can be evaluated by the formulas

$$\left(\frac{c}{M_P}\right)\left(\frac{pM_P}{pM_P + qM_O}\right)\left(\frac{\delta}{\delta_\infty}\right)_P \text{ and } \left(\frac{c}{M_O}\right)\left(\frac{qM_O}{pM_P + qM_O}\right)\left(\frac{\delta}{\delta_\infty}\right)_O \quad (1)$$

respectively, where M_P is the molecular weight of PA and M_O is that of OA. Now, the mole fraction of OA in a mixed micelle at the concentration c is calculated by the equation

$$(X_O)_1 = \frac{(\delta/\delta_\infty)_O}{(\delta/\delta_\infty)_O + (p/q)(\delta/\delta_\infty)_P} \quad (2)$$

For the mole fraction of PA in the same mixed micelle eq 3 is derived. Generally $(X_O)_1$ thus obtained is not

$$(X_P)_1 = \frac{(\delta/\delta_\infty)_P}{(q/p)(\delta/\delta_\infty)_O + (\delta/\delta_\infty)_P} = 1 - (X_O)_1 \quad (3)$$

equal to X_O. In this case the above-described procedure is repeated to obtain $(X_O)_2$ and $(X_P)_2$ by the use of $(\delta_\infty)_O$ and $(\delta_\infty)_P$ read from Figure 3 at the mole fraction $(X_O)_1$ instead of those read at X_O. This procedure is reiterated until $(X_O)_n$ agrees with $(X_O)_{n-1}$. In this way a self-consistent value $(X_O)_{mic}$ is obtained for the mole fraction of OA in the mixed micelle at the given concentration.

Using the self-consistent values of $(\delta/\delta_\infty)_O$ and $(\delta/\delta_\infty)_P$, one can calculate the concentrations in grams per 100 ml of total solution of OA and PA in a micellar state, $(C_O)_{mic}$ and $(C_P)_{mic}$, by eq 1. Subtraction of these quantities from the total concentration of each surfactant yields the concentrations of monomolecularly dispersed surfactants, $(C_O)_{mono}$ and $(C_P)_{mono}$. The mole fraction[9] of monomolecular OA in the water phase can then be calculated by eq 4. In Figure 4 are shown

$$(X_O)_{mono} = \frac{(C_O)_{mono}}{(C_O)_{mono} + (C_P)_{mono}(M_O/M_P)} \quad (4)$$

(9) The term "mole fraction" of monomolecular OA ($(X_O)_{mono}$, as defined in eq 4) is not a true mole fraction of the total aqueous solution. We call this a mole fraction in order to allow a comparison of the composition of the mixed micelle on a water-free basis with that of the molecularly dispersed phase.

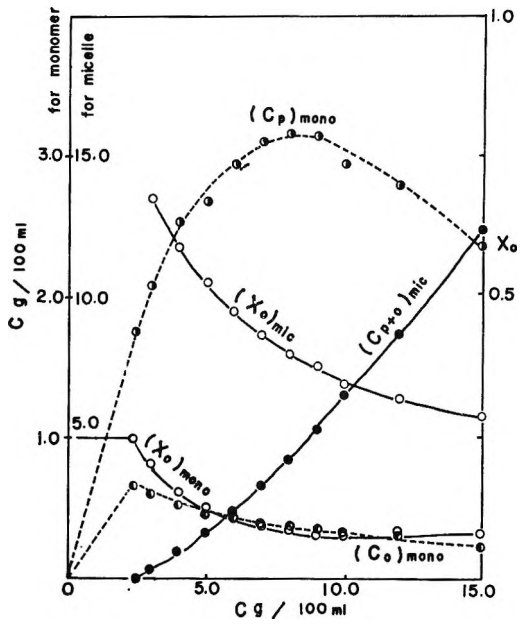

Figure 4. Composition changes in the mixed micelle and the water phase as a function of the total concentration: PA:OA = 3:1.

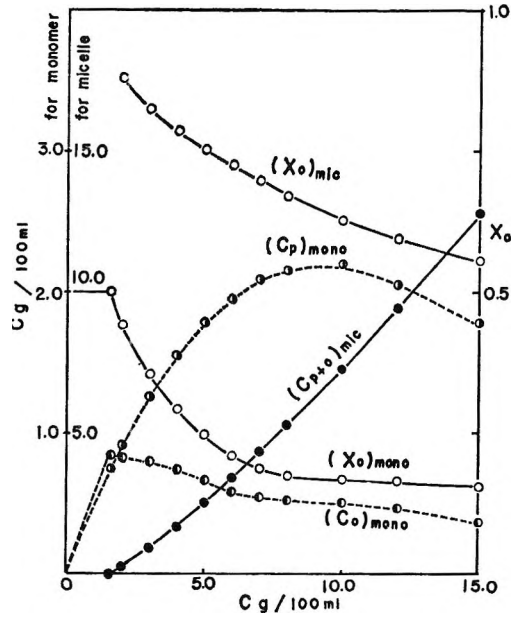

Figure 5. Composition changes in the mixed micelle and the water phase as a function of the total concentration: PA:OA = 1:1.

$(X_O)_{mic}$, $(C_{P+O})_{mic} = (C_P)_{mic} + (C_O)_{mic}$, $(C_O)_{mono}$, $(C_P)_{mono}$, and $(X_O)_{mono}$ at the mole ratio of PA:OA = 3:1 against the total concentration. Similar curves are presented in Figures 5 and 6 for the cases of PA:OA = 1:1 and 1:3, respectively.

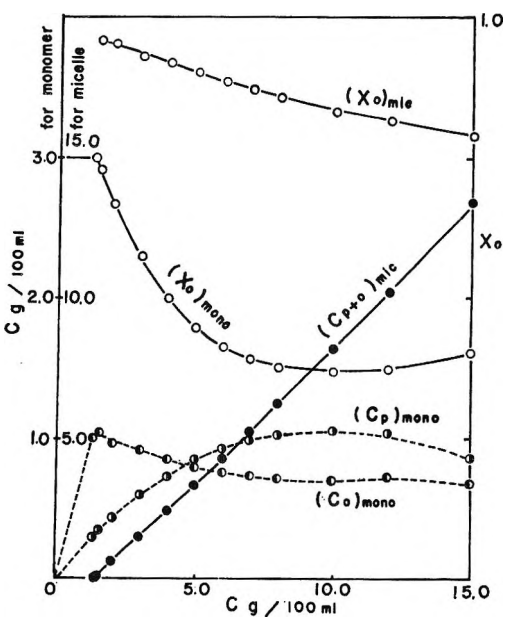

Figure 6. Composition changes in the mixed micelle and the water phase as a function of the total concentration: PA:OA = 1:3.

Discussion

In the above-mentioned calculation it is tacitly assumed that both surfactants show a phenyl proton signal as a singlet at the weight-averaged position between those expected for monomolecular and micellar states. This assumption has been supported by much evidence in regard to solutions of a single component.[3] As shown schematically in Figure 7, the circumstances are substantially the same for a mixture of two surfactants as far as the rapid exchange of surfactant molecules is assumed: we have no reason to consider that the exchange might be hindered in a solution of a mixture.

At any ratio of PA to OA below the cmc a difference is hardly noticeable in the phenyl proton chemical shifts of the PA and OA. On the other hand, the chemical shift of phenyl protons of OA molecules in the mixed micelle is at a higher field than that of PA in the same micelle.[10] Moreover, the ratio of the micellar molecules to the molecularly dispersed molecules for PA is generally different from that of OA. As a result of these effects combined, the signals of PA and OA appear at different positions (*cf.* Figure 7-II).

The surfactants used in this work, PA and OA, are

(10) The reason for this difference is not clear at present. As a possible explanation, it may be suggested that the loci of phenyl groups in the micelle might be statistically different between these two surfactants.

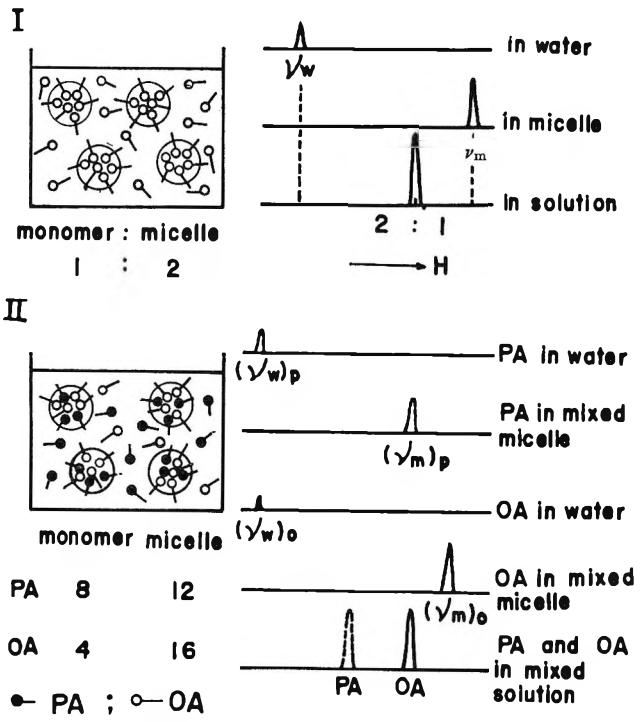

Figure 7. A schematic illustration of nmr signals of phenyl protons in aqueous solutions of surfactant PA and/or OA: I, a single surfactant (PA or OA) in solution above the cmc; II, two surfactants in solution above the cmc.

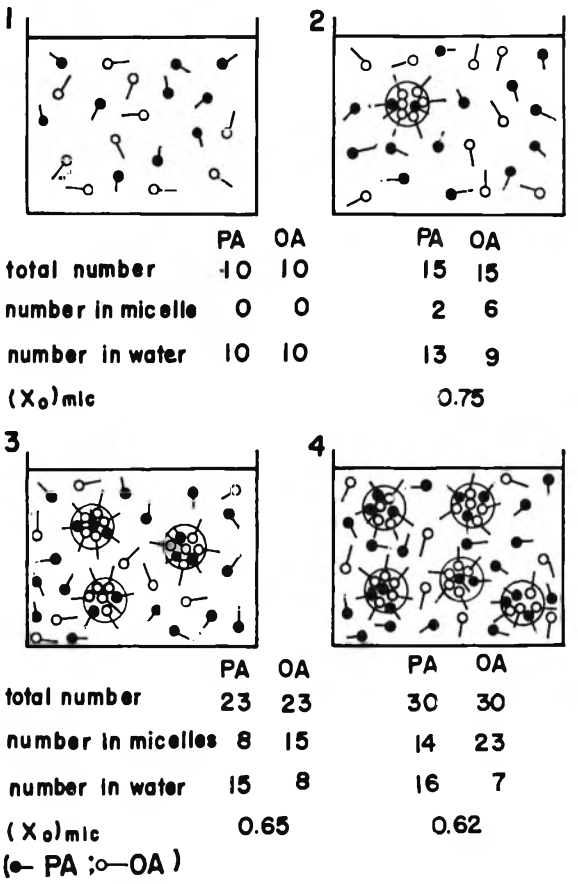

Figure 8. A schematic illustration of mixed solutions of surfactants PA and OA. The total concentration increases from 1 to 4: PA:OA = 1:1.

of the same class; they differ only in length of the alkyl portion of the lipophilic group. We may discuss the general features of a surfactant mixture, regarding PA as a representative of a more hydrophilic component and OA as one of a more lipophilic component. Several features evident from Figures 4–6 are the following. (1) The concentration of molecularly dispersed molecules of the more lipophilic component $(C_O)_{mono}$ increases with an increase in the total concentration until the cmc is reached, and thereafter decreases monotonically. (2) The concentration of molecularly dispersed molecules of the more hydrophilic component $(C_P)_{mono}$ continues to increase monotonically to a far higher concentration (9 or 10 g/100 ml), then falls gradually because of the volume effect; at such high concentrations, the volumes of micelles and of bound water captured by micelles occupy a considerable portion of the whole solution. This results in a diminution of free water which serves as the solvent for monomolecular surfactant. (3) The concentration of micellar surfactants $(C_{P+O})_{mic}$ is zero below the cmc and increases almost linearly with the total concentration above the cmc. (4) The mole fraction of lipophilic component in a micelle $(X_O)_{mic}$ decreases from the highest value at the cmc and approaches the mole fraction of the mixture. (5) The mole fraction of lipophilic component in the water phase $(X_O)_{mono}$ must be, of course, equal to the mole fraction of the mixture until the cmc is reached. Above the cmc, it decreases asymptotically to some definite value. (6) The cmc of a mixture lies somewhere between the cmc's of the components. (7) The degree of the above features depends upon the mole ratio of the mixture.

For ready comprehension, the structure changes of micelle and of coexisting water phase are illustrated schematically in Figure 8. The number of molecules associated in the mixed micelle is provisionally assumed because it is impossible to determine the association number from the nmr spectra alone.

On the basis of statistical thermodynamics, T. N. has discussed previously the solution structure of a mixture of two nonionic surfactants which differed from each other only in the alkyl chain length and calculated the structure as a function of the mole ratio of the components and the total concentration.[11]

(11) T. Nakagawa, *Shionogi Kenkyusho Nempo*, 8, 805 (1958).

The calculated results for the mixtures of methoxydodecaoxyethylene caprate and methoxydodecaoxyethylene laurate showed all seven features described above. At that time, the structure changes could not be verified experimentally because of the lack of suitable techniques, although the cmc's calculated agreed fairly well with the experimental results. The system considered then differs from the present one in that the former is a mixture of nonionic surfactants while the latter is of cationic surfactants. It may be said, however, that the solution behavior predicted for the mixture of two surfactants has been substantiated by the nmr technique.

Mysels and Otter[12] have measured the conductivity of solutions of pure sodium decyl and dodecyl sulfates and their mixtures in the region of the cmc, and their results on the composition of mixed micelles are quite similar to those obtained here.

Some comments are worthy of mention. In the present study, the formation of mixed micelles is presumed as an established fact. This assumption cannot be proven by the nmr data alone, and the spectra might be interpretable under the alternative assumption that each component forms micelles composed of a single species. This latter assumption is, however, rendered untenable by electrophoretic experiment. Hoyer and Marmo[13] have shown that a single moving boundary was observed in mixed solutions of decyl- and dodecyltrimethylammonium chlorides and of dodecyl- and tetradecyltrimethylammonium chlorides. These facts indicate that the two components associate to form a mixed micelle in an aqueous solution.

Both the N^+-methyl and the methylene nmr signals shifted upfield like the phenyl proton signal with an increase in the total concentration. However, quantitative measurement of these shifts is difficult because of the following reasons. (1) The maximum shifts of proton signals were 3 and 7 cps for methylene and N^+-methyl groups, respectively. These values are so small that the mixed micelle structure cannot be derived quantitatively from them. (2) The proton signal of the N^+-methyl group overlapped with that of the N^+-methylene group. Therefore, it is difficult to measure precisely its resonance frequency on a Varian A-60 spectrometer. (3) The shape of the signal of the methylene protons was diffuse as shown in Figure 1, and thus the determination of the resonance position of methylene protons is accompanied by a large error.

Sodium 4,4-dimethyl-4-silapentane-1-sulfonate (DSS) has been recommended as an internal standard for an aqueous solution.[14] The molecular structure of this compound suggests that it may interact with a surfactant to form a kind of mixed micelle because it contains both a lipophilic and a hydrophilic group in the same molecule. The methyl proton signal of DSS, which is an adequate reference in other solutions, may no longer serve as such in a surfactant solution.[6] Moreover, the use of DSS is undesirable because complicated electrical interactions with cationic surfactants are expected in our system.

It was said by Hand and Cohen[6] that water itself could serve as a more satisfactory standard in an aqueous solution containing an aromatic compound. However, the peak due to water protons is sensitive to temperature and shifts to a higher field upon addition of a surfactant such as sodium alkyl sulfate.[15]

The proton signal of 1,4-dioxane has been widely used as an internal reference.[16,17] It was determined by nmr spectroscopy that the solubility of dioxane in the deuterium oxide phase was about twice as large as that in the butylbenzene phase when dioxane was dissolved into an equivolume mixture of the two liquids by vigorous shaking. Calculations based on such an experiment indicate that the amount of dioxane solubilized in the mixed micelle is probably small as compared with that dissolved in water until the total concentration of surfactants becomes 10 to 15 g/100 ml. Dioxane seems to be useful as an internal standard, at least in lower concentrations, and was therefore used in the present work as an internal standard.

For the sake of comparison, the chemical shift of phenyl protons was measured also with reference to the water signal. When plotted against the total concentration, the resulting curve showed a similar shape to that obtained with 1,4-dioxane, with, however, somewhat greater scatter of the points.

Acknowledgment. The authors are indebted to Mr. K. Aono for running the nmr spectra.

(12) K. J. Mysels and R. J. Otter, *J. Colloid Sci.*, 16, 462 (1961).

(13) H. W. Hoyer and A. Marmo, *J. Phys. Chem.*, 65, 1807 (1961).

(14) G. V. D. Tiers, Abstracts, 137th National Meeting of the American Chemical Society, Cleveland, Ohio, April 1960, p 17R.

(15) J. Clifford and B. A. Pethica, *Trans. Faraday Soc.*, 60, 1483 (1964).

(16) R. A. Y. Jones, A. R. Katritzky, J. N. Murrell, and N. Sheppard, *J. Chem. Soc.*, 2576 (1962).

(17) T. Nakagawa and K. Tori, *Kolloid-Z.*, 194, 143 (1964).

The Heats of Decomposition of Some More Boron Hydrides[1]

by Stuart R. Gunn and John H. Kindsvater

Lawrence Radiation Laboratory, University of California, Livermore, California *(Received September 30, 1965)*

The heats of decomposition of decaborane-14, decaborane-16, and hexaborane-12 have been measured calorimetrically by explosion in mixtures with stibine at 150, 130, and 25°, respectively. Derived standard heats of formation of the gases at 25° are, for $B_{10}H_{14}$, +4.4 kcal mole^{-1}, in excellent agreement with previous results by other methods; and for $B_{10}H_{16}$ and B_6H_{12}, +34.8 and +26.5 kcal mole^{-1}, respectively, in good agreement with calculations from previously derived thermochemical bond energies.

The heats of decomposition of B_2H_6,[2] B_2D_6,[3] and B_4H_{10}, B_5H_9, B_5H_{11}, and B_6H_{10}[4] have previously been measured in this laboratory by exploding the gases in mixtures with stibine in a calorimeter. Prosen and co-workers have measured the heats of decomposition of B_2H_6,[5] B_5H_9,[5] and $B_{10}H_{14}$[6] by pyrolysis in a furnace enclosed in a calorimeter. Results of the two methods for B_2H_6 and B_5H_9 are in agreement if the reasonable assumption is made that the energy of the amorphous boron produced is different in the two types of experiments. A set of bond energies was derived[4] which is reasonably consistent with all the heats of formation except for $B_{10}H_{14}$. Accordingly, a calorimeter capable of operation at higher temperatures was developed to permit measurements of this compound by the stibine explosion method.

In recent years several other higher boron hydrides have been prepared; their heats of decomposition can be determined by the present method provided that they undergo little decomposition in an hour or so as pure gases at a temperature where the vapor pressure is *ca.* 0.1 atm or more. The upper temperature limit is probably between 150 and 200°, imposed by the rapid pyrolysis of stibine. In the present work, the method has been extended to $B_{10}H_{16}$ and B_6H_{12}.

Experimental Section

The aneroid copper-block calorimeter described elsewhere[7] was used, with an oil thermostat at the elevated temperatures. Thermistors were used for the $B_{10}H_{14}$ work at 150° and a copper thermometer for $B_{10}H_{16}$ at 130° and B_6H_{12} at 25°.

The reaction cells, about 90 cc in volume, were Pyrex tubes 2.8 cm o.d., 20 cm long, with a 1-mm i.d. thick-walled capillary passing through the top axially, extending inside to the center of the cell and above the cell extending 16 in. upward to a stopcock and ball joint, which were just above the thermostat lid. Tungsten leads were sealed through the top of the cell. For the $B_{10}H_{14}$ runs and the first few $B_{10}H_{16}$ runs a platinum fuse, 0.002 in. in diameter and 1 to 2 cm long, was mounted at the end of the capillary inside the cell; this was fired with a 24-v storage battery. For the remaining work, the tungsten wires were crossed in springing contact at the same position and sparked with a 0.1-μf condenser charged to 1000 v.

The firing leads were No. 36 copper for a length of 5 in. above the cell and then No. 26 to the outside of the calorimeter. A heater of about 150 ohms of No. 35 manganin was wrapped bifilarly on the outside of the cell and covered with cellophane tape. The current leads were 5 in. of No. 36 copper above the cell and then No. 26 outward; potential leads were attached 2.5 in. above the cell and consisted first of 2.5 in. of No. 36 copper and then No. 26.

For the $B_{10}H_{14}$ and $B_{10}H_{16}$ work, the capillary and leads were surrounded by a copper rod 0.75 in. in diameter, 7 in. long, with a slot which was closed by a copper

(1) This work was performed under the auspices of the U. S. Atomic Energy Commission.

(2) S. R. Gunn and L. G. Green, *J. Phys. Chem.*, 65, 779 (1961).

(3) S. R. Gunn and L. G. Green, *J. Chem. Phys.*, 36, 1118 (1962).

(4) S. R. Gunn and L. G. Green, *J. Phys. Chem.*, 65, 2173 (1961).

(5) E. J. Prosen, W. H. Johnson, and F. Y. Pergiel, *J. Res. Natl. Bur. Std.*, 61, 247 (1958).

(6) W. H. Johnson, M. V. Kilday, and E. J. Prosen, *ibid.*, A64, 521 (1960).

(7) S. R. Gunn, *Rev. Sci. Instr.*, 35, 183 (1964).

bar taped in place over the capillary when assembled. The lower end of the rod was 6 in. above the top of the cell. A heater was wrapped on its surface, and its temperature was maintained equal to that of the oil bath by a differential thermocouple, amplifier, and controller. This served to eliminate the effect of varying heat conduction along the leads and capillary and to heat stibine entering the cell. The space between the cell and the copper rod, around the capillary and leads in the calorimeter well, was stuffed loosely with tissue paper to minimize convective heat transfer.

A weighed sample of the borane was condensed in the cell through a side arm, which was then sealed off. With $B_{10}H_{14}$ and $B_{10}H_{16}$ an equal amount of xenon was added to the cell. The purpose of this was to prevent condensation of decaborane in the short length of cool capillary below the stopcock. Calculation indicated that in the interval—about 1 hr—between placing the cell in the calorimeter and performing the reaction, diffusion of borane through the xenon in the capillary would be negligible. With B_6H_{12}, one-tenth to one-third as much xenon was added, serving only to separate the borane from the stopcock grease.

In performing the runs, the cell was placed in the calorimeter and heated to 0.3–0.5° below the bath temperature. A weighed bulb of stibine was connected to the cell through a linkage communicating with the vacuum system. The temperature foredrift was recorded. The stibine was kept frozen with liquid nitrogen, to minimize absorption in the stopcock grease, until a few minutes before reaction. It was then warmed to room temperature and admitted to the linkage. The cell stopcock was opened for 3 or 4 sec and closed, and the stibine remaining in the linkage was condensed in the weighing bulb, which was later reweighed. With $B_{10}H_{14}$ and $B_{10}H_{15}$, firing was performed immediately after admitting the stibine; it was not possible to wait a few minutes to permit better mixing of the gases as was done with lower boranes at 25° because of rapid decomposition of the stibine at the higher temperatures. After the reaction, the calorimeter was calibrated twice by introduction of about the same amount of electrical energy. After the run, the hydrogen was pumped off through liquid nitrogen traps and measured. Mass spectrometric analysis for xenon in the hydrogen was performed in all cases, but none was ever found.

Commercial $B_{10}H_{14}$ was purified by two sublimations at room temperature. Analysis of the melting curve[8] indicated a purity of 99.87 mole %, and this may be low, since some discoloration occurred when the sample was melted into the melting point bulb and possibly during the melting point measurement. The material was handled in a drybox; samples were sealed in small bulbs and weighed. These bulbs were then sealed in side arms attached to the reaction cells, and the system was reevacuated overnight. Then the bulb was broken and the decaborane sublimed into the cell.

$B_{10}H_{16}$ was prepared as described by Lipscomb's group[9,10] and purified by trap-to-trap sublimation and use of a low-temperature fractional sublimation column. Purified samples were stored overnight in bulbs with strips of gold foil to reduce mercury contamination. Vapor pressure measurements were well fitted by the following equations. These imply a

$$\log p_{mm} = 10.357 - 3103/T \quad (40\text{–}81°)$$

$$\log p_{mm} = 7.959 - 2254/T \quad (81\text{–}126°)$$

melting point of *ca.* 81°; this is consistent with a poor melting-curve analysis of a less pure sample. Only a small amount of noncondensable gas was evolved in the vapor pressure apparatus during several hours in the higher temperature region. X-Ray diffraction analysis of the purified material showed the known structure of $B_{10}H_{16}$ and no other lines; estimated sensitivity for $B_{10}H_{14}$, the most likely impurity, was 5%. Calorimetric samples were weighed in a U tube with greased stopcocks.

B_6H_{12} was prepared as described by Gaines and Schaeffer[11] and purified by gas–liquid partition chromatography.[12] The infrared spectrum agreed with those previously reported.[11,12] An elemental analysis of a sample pyrolyzed 15 min at 800° gave 99 ± 1% of theoretical hydrogen and 101 ± 1% theoretical boron. A sample showing a vapor pressure of 20 mm at 0° gave a molecular weight of 79 (calcd, 76.96). The compound appeared to be adequately stable as a gas, giving only traces of hydrogen upon standing 1 hr at room temperature. Calorimetric samples were weighed as a gas in 100-cc bulbs with greaseless valves.

Results

The calorimetric program for each of the three boron hydrides consisted of a comparison of two series of runs. In one, stibine was introduced into a cell containing boron hydride and xenon and was exploded. In the other, stibine was introduced into a cell containing a larger amount of xenon, comparable to the

(8) S. R. Gunn, *Anal. Chem.*, **34**, 1292 (1962).

(9) R. Grimes, F. E. Wang, R. Lewin, and W. N. Lipscomb, *Proc. Natl. Acad. Sci. U. S.*, **47**, 996 (1961).

(10) R. N. Grimes and W. N. Lipscomb, *ibid.*, **48**, 496 (1962).

(11) D. F. Gaines and R. Schaeffer, *Inorg. Chem.*, **3**, 438 (1964).

(12) C. A. Lutz, D. A. Phillips, and D. M. Ritter, *ibid.*, **3**, 1191 (1964).

sum of boron hydride and xenon in the other series, and exploded. In this manner some possible systematic errors, such as absorption of stibine in stopcock grease, errors in weighing stibine, etc., could be made to cancel.

The millimoles of SbH_3 given in Tables I–VI represents the weight loss of the stibine bulb; this will be designated a. Part of this, a', is trapped in the bore of the stopcock at the top of the reaction cell and is assumed not to decompose significantly before the hydrogen determination is performed. The volume of the bore is 0.05 cc. The factor a'/a is calculated from the temperature of the calorimeter (since the stopcock

Table I: SbH_3 Runs at 150°

mmoles of Xe	mmoles of SbH_3	mmoles of H_2	H_2, % of theory	q, cal	Q, kcal mole^{-1}
0.4	2.639	3.952	99.91	91.84	35.03
0.4	2.611	3.911	99.94	90.65	34.95
0.8	2.488	3.723	99.84	86.39	35.02
			Av. 99.90		35.00

remains essentially at room temperature) and the ratio, r, of stibine introduced to boron hydride plus xenon originally in the cell; it ranges from 0.0006 to 0.0011. A larger amount, a'', in the 0.4-cc capillary volume above the cell explodes but does not contribute heat to the calorimeter. This volume is assumed to be at the calorimeter temperature, and hence the factor a''/a is calculated from r only; it ranges from 0.0050 to 0.0060. The hydrogen produced is designated c, and the per cent of theoretical H_2, Y, in Tables I, III, and V is given by

$$Y = (2/3)[c/(a - a')] \quad (1)$$

The heat of explosion per mole of SbH_3, Q, uncorrected for compressional heat, is then

$$Q = q/[Y(a - a' - a'')] \quad (2)$$

where q is the observed heat, corrected for fuse energy in the earlier work. Subtracting RT to correct for the pV compressional heat of entering stibine, changing the sign, and adding $0.5RT$ to convert from constant volume to constant pressure, the heat of explosion of stibine is given by

$$\Delta H = -(Q - 1.5RT) \quad (3)$$

although this function is not needed for calculating the borane runs.

In the boron hydride runs, Tables II, IV, and VI, a' and a'' are calculated as before, and for each run the amount of heat due to SbH_3 is calculated by rearrangement of eq 2

$$q_{SbH_3} = QY(a - a' - a'') \quad (4)$$

where the values of Q and Y used are the averages from the preceding tables. The amount of boron hydride, B_mH_n, decomposed, d, is calculated from

$$d = 2[c - 1.5Y(a - a')]/n \quad (5)$$

The per cent boron hydride decomposed is d/b, b being the millimoles of boron hydride determined by weighing. The decomposition energy of the $B_{10}H_{14}$ and $B_{10}H_{16}$ is then calculated from

$$\Delta E = (q - q_{SbH_3})/d \quad (6)$$

This implicitly assumes that hydrogen not liberated is present as the unchanged original boron hydride, or an energetically equivalent form; one check upon this is whether ΔE varies systematically with d/b, which normally varies directly as a/b.

The results for $B_{10}H_{14}$ are given in Tables I and II. For the SbH_3 only runs, ΔH is -33.74 kcal mole^{-1}. Using our value[2,7] of -34.68 kcal mole^{-1} for ΔH_{298} and enthalpy data for SbH_3 from Sunderam[13] and for antimony and hydrogen from Stull and Sinke[14] we calculate -33.93 kcal mole^{-1} for ΔH_{423}. There are two possible mechanisms to explain the discrepancy. First, and more probably, the entering stibine may not be fully heated in the upper part of the calorimeter; the deficiency in ΔH corresponds to stibine entering the cell at 133° instead of 150°. Experiments in which air was admitted to a similar cell at 150° indicated a temperature deficiency of 15°. Secondly, a significant amount of stibine might be decomposed in the capillary while entering the cell. In either event, the effect would tend to be similar in the decaborane runs.

In the $B_{10}H_{14}$ runs about two-thirds of the hydrogen deficiency was evolved by flaming the cells to the softening point of Pyrex. This could be either unchanged decaborane or higher polymeric hydrides; lower volatile hydrides would have escaped from the cell and are thus indicated to be rather low in amount. There is no significant trend of ΔE with the percentage of decomposition. Accordingly we take the average, 4.8 kcal mole^{-1}, for ΔE_{423} of the reaction

$$B_{10}H_{14}(g) \longrightarrow 10B(am) + 7H_2(g) \quad (7)$$

(13) S. Sunderam, *Can. J. Phys.*, **39**, 370 (1961).

(14) D. R. Stull and G. C. Sinke, "Thermodynamic Properties of the Elements," Advances in Chemistry Series, No. 18, American Chemical Society, Washington, D. C., 1956.

Table II: $B_{10}H_{14}$ Runs at 150°

mmoles of Xe	mmoles of $B_{10}H_{14}$	mmoles of SbH_3	mmoles of H_2	q_{tot}, cal	q_{SbH_3}, cal	$-q_{B_{10}H_{14}}$, cal	% $B_{10}H_{14}$ decompd	ΔE, kcal mole^{-1}
0.2	0.160	2.653	4.970	91.62	92.22	0.60	88.9	4.2
0.2	0.193	2.627	5.112	90.44	91.31	0.87	87.2	5.2
0.3	0.318	2.522	5.373	86.61	87.63	1.02	71.7	4.5
0.3	0.331	2.517	5.433	86.41	87.45	1.04	71.8	4.4
0.4	0.419	2.401	5.607	81.51	83.40	1.89	68.6	6.6
0.4	0.429	2.422	5.748	82.83	84.13	1.30	70.6	4.3

Table III: SbH_3 Runs at 130°

mmoles of Xe	mmoles of SbH_3	mmoles of H_2	H_2, % of theory	q, cal	Q, kcal mole^{-1}
0.6	2.328	3.483	99.83	80.27	34.76
0.6	2.497	2.734	99.77	86.95	35.13
0.5	2.594	3.865	99.41	89.45	34.90
0.5	2.689	4.020	99.74	93.29	34.99
0.5	2.633	3.928	99.53	91.06	34.96
0.5	2.652	3.957	99.55	92.05	35.08
0.5	2.603	3.888	99.65	90.38	35.06
			Av. 99.64		34.98

In the $B_{10}H_{16}$ runs, about half of the missing hydrogen was liberated by flaming the cells. Again, there is no significant trend of ΔE with the percentage of decomposition; the average is -26.0 kcal mole^{-1} for ΔE_{403} of the reaction

$$B_{10}H_{16}(g) \longrightarrow 10B(am) + 8H_2(g) \qquad (8)$$

Converting to constant pressure, ΔH_{403} is -20.4 kcal mole^{-1}. Estimating $H_{403} - H_{298}$ for $B_{10}H_{16}$ to be 5.67 kcal mole^{-1}, slightly more than $B_{10}H_{14}$ and slightly less than twice B_5H_9,[15] ΔH_{298} is 23.8 kcal mole^{-1}. Converting to crystalline boron and changing the sign, $\Delta H_f°(B_{10}H_{16}(g))$ is $+34.8$ kcal mole^{-1}.

Table IV: $B_{10}H_{16}$ Runs at 130°

mmoles of Xe	mmoles of $B_{10}H_{16}$	mmoles of SbH_3	mmoles of H_2	q_{tot}, cal	q_{SbH_3}, cal	$q_{B_{10}H_{16}}$, cal	% $B_{10}H_{16}$ decompd	ΔE, kcal mole^{-1}
0.35	0.184	2.656	5.390	96.71	92.00	4.71	96.7	26.5
0.2	0.231	2.597	5.685	95.76	90.00	5.76	97.8	25.5
0.3	0.275	2.552	5.892	95.03	88.39	6.64	94.6	25.5
0.26	0.291	2.503	5.825	93.54	86.68	6.86	89.7	26.3
0.3	0.311	2.476	...	93.38	85.74	7.64	(88)	27.9
0.35	0.387	2.407	6.304	91.43	83.32	8.11	87.5	24.0
0.4	0.444	2.298	...	89.80	79.54	10.26	(86)	26.8

Converting to constant pressure, ΔH_{423} is 9.84 kcal mole^{-1}. Using the enthalpy data of Evans, Prosen, and Wagman[15] for boron and decaborane and of Stull and Sinke[14] for hydrogen, ΔH_{298} is calculated to be 6.65 kcal mole^{-1}. Converting from our form of B(am)[4] to B(c) by subtracting 1.1 kcal (g-atom of B)$^{-1}$, the standard heat of decomposition is -4.4 kcal mole^{-1} and $\Delta H_f°(B_{10}H_{14}(g))$ is $+4.4$ kcal mole^{-1}.

Results for $B_{10}H_{16}$ are given in Tables III and IV. The SbH_3 only runs scattered more than usual, and hydrogen yields were also exceptionally low. The final result for ΔH_{403}, -33.78 kcal mole^{-1}, compared with the calculated value of -34.04 kcal mole^{-1}, corresponds to a temperature deficiency of 23°.

Table V: SbH_3 Runs at 25°

mmoles of Xe	mmoles of SbH_3	mmoles of H_2	H_2, % of theory	q, cal	Q, kcal mole^{-1}
0.2	1.678	...	(99.9)	59.02	35.38
0.2	1.641	2.459	99.90	57.80	35.44
0.2	1.693	2.534	99.78	59.49	35.39
0.2	1.387	2.085	100.2	48.70	35.21
			Av. 99.90		35.36

(15) W. H. Evans, E. J. Prosen, and D. D. Wagman, "Thermodynamic and Transport Properties of Gases, Liquids, and Solids," McGraw-Hill Book Co., New York, N. Y., 1959, p 226.

Table VI: Heat of Decomposition of B_6H_{12} at 25°

mmoles of Xe	mmoles of B_6H_{12}	mmoles of SbH_3	mmoles of H_2	q_{tot}, cal	q_{SbH_3}, cal	$q_{B_{10}H_{16}}$, cal	% B_6H_{12} decompd	$-\Delta E$, kcal mole^{-1}
0.03	0.210	2.022	4.176	75.94	71.04	4.90	91.1	23.3
0.1	0.298	1.770	4.255	68.70	62.13	6.57	89.7	22.0
0.04	0.168	1.118	2.567	42.75	39.25	3.50	89.5	20.8
0.03	0.209	1.331	3.110	51.25	46.75	4.50	89.1	21.5
0.02	0.213	1.278	...	49.31	44.87	4.44	(90)	20.8
0.06	0.214	0.899	2.503	35.84	31.58	4.26	90.0	19.9

Results for B_6H_{12} are given in Tables V and VI. The SbH_3 only runs give a value of -34.47 kcal mole^{-1} for ΔH_{298}, compared with a best value of -34.68 kcal mole^{-1}.

For the runs with B_6H_{12}, unlike the other two boron hydrides, there is no trend of the percentage of the borane decomposed, as indicated by the hydrogen yield, with the borane:stibine ratio in the initial mixture. Flaming the cells in all cases evolved about one-fourth of the missing hydrogen. It was finally found, for runs 4–6, that the traps between the cell and the gas buret had caught two fractions, subsequently separated, measured, and identified by infrared spectrometry as B_5H_9 and B_2H_6 in a mole ratio of approximately 2:1 and a total amount roughly corresponding to the missing hydrogen. Accordingly, ΔE in Table III is calculated from the weight of B_6H_{12} measured, $q_{B_6H_{12}}/n_{B_6H_{12}}$; the average, -21.4 kcal mole^{-1}, is assumed to represent ΔE of the reaction

$$B_6H_{12}(g) \longrightarrow 5.4H_2(g) + 5.4B(am) + 0.1B_5H_9(g) + 0.05B_2H_6(g) \quad (9)$$

Converting to constant pressure, ΔH_3 is -18.7 kcal mole^{-1}; using $\Delta H_f(B(am)) = +1.1$ kcal mole^{-1}, $\Delta H_f°(B_5H_9(g)) = +15.0$ kcal mole^{-1}, and $\Delta H_f°(B_2H_6) = +6.5$ kcal mole^{-1}, $\Delta H_f°(B_6H_{12})$ is calculated to be $+26.5$ kcal mole^{-1}.

If all the B_6H_{12} were assumed to have decomposed to the elements, $\Delta H_f°(B_6H_{12})$ would be calculated as $+25.0$ kcal mole^{-1}; if it were assumed that 90% decomposed and the remainder were unchanged, $\Delta H_f°$ would be $+27.4$ kcal mole^{-1}. If the missing 10% of hydrogen is assumed to remain all as B_5H_9 or all as B_2H_6, $\Delta H_f°$ becomes $+26.6$ or $+26.3$ kcal mole^{-1}, respectively. Only if the hydrogen remains in a thermochemically much more stable form does the calculated $\Delta H_f°(B_6H_{12})$ change much from that obtained by assuming reaction 3; even if it is all present as solid $B_{10}H_{14}$, $\Delta H_f°$ is calculated to be $+23.1$ kcal mole^{-1}.

Discussion

The over-all uncertainty in the three standard heats of formation obtained in the present work may be estimated as *ca.* ± 2 kcal mole^{-1}, aside from an additional uncertainty in the heat of conversion of amorphous to crystalline boron which affects the absolute values of heats of formation but not calculations of heats of interconversion of boranes.

Decaborane-14 is the most stable of the boron hydrides; this is reflected in the relatively low percentages of decomposition achieved with it in the present work. It is, indeed, the only hydride having a positive heat of decomposition which has been successfully decomposed in this laboratory by the stibine explosion method; however, the large value of ΔS of course makes ΔG negative. Johnson, Kilday, and Prosen[6] obtained -15.8 ± 1.4 kcal mole^{-1} for $\Delta H_f°(B_{10}H_{14}(c))$, and Galchenko, Timofeev, and Skuratov[16] obtained -14.0 ± 1.0 kcal mole^{-1}, both by pyrolysis methods. Using $+18.6$ kcal mole^{-1} for the heat of sublimation,[14] these values become $+2.8$ and $+4.6$ kcal mole^{-1} for $\Delta H_1°(B_{10}H_{14}(g))$, in excellent agreement with the present result. Thus, as previously observed,[4] $B_{10}H_{14}$ does not fit well in a thermochemical bond-energy scheme with the lower boranes.

The decaborane-16 molecule consists of two pyramidal B_5H_8 groups, having essentially the structure of B_5H_9 with the apical terminal hydrogen removed, joined by a B–B bond at the apical borons. Hence, one might expect the heat of the reaction

$$2B_5H_9(g) \longrightarrow B_{10}H_{16}(g) + H_2(g) \quad (10)$$

to be closely equal to E(H–H) + E(B–B) − 2E(B–H), which from the previously recommended set of bond energies[4] is -1.2 kcal. However, from the presently obtained heats of formation, ΔH_{10} is $+4.8$ kcal mole^{-1}. In view of possible perturbations of the skeletal shape

(16) G. L. Galchenko, B. I. Timofeev, and S. M. Skuratov, *Dokl. Akad. Nauk SSSR*, **142**, 1077 (1962).

and electronic distribution of the two B_5H_8 groups, this 6-kcal discrepancy is probably not surprising.

From the nmr spectrum, Gaines and Schaeffer[11] deduced the most probable structure of B_6H_{12} to be 4212 in terms of Lipscomb's formulations.[17] From our previous set of bond energies[4] this leads to a calculated heat of atomization of 1411.7 kcal mole^{-1} and a standard heat of formation of +24.8 kcal mole^{-1} (not +14.7 kcal mole^{-1} as given by Gaines and Schaeffer), in excellent agreement with the present experimental result.

Gaines and Schaeffer observed a base-catalyzed decomposition of gaseous hexaborane-12 to give predominantly a mixture of pentaborane-9 and diborane-6 in a mole ratio of roughly 2:1. We observed the same to be one apparent course of decomposition in the stibine explosions. The calculated value of the heat of the rearrangement reaction, ΔH_{11}, is -8 kcal mole^{-1}.

$$B_6H_{12}(g) \longrightarrow B_5H_9(g) + {}^1/_2B_2H_6(g) \qquad (11)$$

Acknowledgments. We thank Leroy G. Green for assistance in the $B_{10}H_{14}$ work, Vernon G. Silveira for performance of the X-ray analyses, and Professor W. N. Lipscomb for providing additional information concerning the $B_{10}H_{16}$ preparation.

(17) W. N. Lipscomb, "Boron Hydrides," W. A. Benjamin, Inc., New York, N. Y., 1963.

Color Centers and Hydrogen–Deuterium Exchange in γ-Irradiated Silica–Alumina Catalysts

by George F. Shipman

Socony Mobil Oil Co., Inc., Central Research Division Laboratory, Princeton, New Jersey
(Received October 4, 1965)

Diffuse reflectance spectroscopy has been used to observe the spectrum of a γ-irradiated silica–alumina catalyst. Intense absorption is observed in the range of 200 to 700 mμ. The intensity of the absorption increases steadily with dose up to a dose of about 12×10^{20} ev/g. At doses greater than this only small changes in optical absorption are observed. The H_2–D_2 exchange activity induced by γ irradiation increases in a manner similar to that of the optical absorption. However, experiments in which the γ-irradiated catalyst was treated with O_2 or thermally annealed prior to exchange rate measurements indicate that there is little direct relationship between the number of color centers and H_2–D_2 exchange activity. For instance, exposure of a γ-irradiated silica–alumina to 100 torr of O_2 pressure at 25° did not cause any loss in optical absorption intensity but did reduce the exchange activity sixfold. Thermally annealing the irradiated catalyst at 150° caused a 22-fold decrease in the optical absorption but did not affect the exchange rate. An attempt was made to measure the number of sites active in the exchange reaction but this was unsuccessful.

Introduction

In recent years, a number of studies[1-5] have shown that radiation alters the adsorptive and catalytic properties of oxide catalysts. In many cases radiation also produces color centers. Cohen[6,7] and others[8] have shown that for quartz these color centers are related to the substitutional aluminum impurity, and O'Brien and Pryce[9] have shown that in quartz the color centers are due to positive holes trapped by oxygen atoms adjacent to aluminum. Boreskov, *et al.*,[10] suggest that the color centers in silica gel are similar to those in quartz. Kohn and Taylor[11] have observed that in silica gel the radiation-induced color and H_2–D_2 exchange activity parallels the concentration of aluminum. They concluded that, although there may be a relationship between the number of color centers and activity, it was also possible that these were independent consequences of irradiation.

This article describes experiments made to investigate the relationship between the radiation-induced color centers and H_2–D_2 exchange activity of a silica–alumina cracking catalyst.

Experimental Section

Apparatus. Measurements of the color centers induced by irradiation of the silica–alumina were made by diffuse reflectance spectroscopy. The theory and general technique has been discussed elsewhere.[12,13]

(1) H. Kohn and E. H. Taylor, *J. Phys. Chem.*, **63**, 500 (1959).

(2) H. Kohn and E. H. Taylor, *ibid.*, **63**, 966 (1959).

(3) H. Kohn and E. H. Taylor, *J. Catalysis*, **2**, 32 (1963).

(4) J. H. Lunsford and T. W. Leland, Jr., *J. Phys. Chem.*, **66**, 2591 (1962).

(5) E. H. Taylor and J. A. Wethington, Jr., *J. Am. Chem. Soc.*, **76**, 971 (1954).

(6) A. J. Cohen, *J. Chem. Phys.*, **25**, 908 (1956).

(7) A. J. Cohen, *Phys. Chem. Solids*, **13**, 321 (1959).

(8) J. H. E. Griffiths, J. Owen, and I. M. Ward, *Nature*, **173**, 439 (1954).

(9) M. C. M. O'Brien and M. H. L. Pryce, "Defects in Crystalline Solids," The Physical Society, London, 1955, p 88.

(10) G. K. Boreskov, V. B. Kazanskii, Yu A. Mishchenko, and G. B. Pariiski, *Dokl. Akad. Nauk SSSR*, **157**, 693 (1964).

(11) H. Kohn and E. H. Taylor, *Actes Congr. Intern. Catalyse*, 2e, Paris, 1960, [II] 1461 (1961).

(12) R. J. H. Clark, *J. Chem. Educ.*, **41**, 488 (1964).

(13) G. Kortüm, W. Braun, and G. Herzog, *Angew. Chem. Intern. Ed. Engl.*, **2**, 333 (1963).

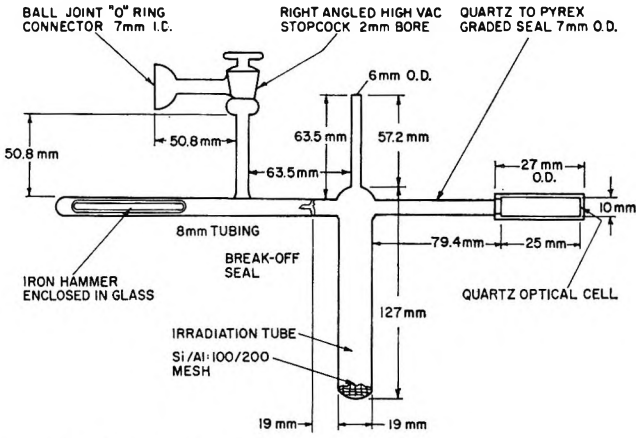

Figure 1. Irradiation cell.

Spectra were recorded using a Perkin-Elmer Model 13U spectrophotometer with a special diffuse reflectance attachment.

The cell used for degassing, irradiation, and spectral observations is shown in Figure 1. Matched quartz spectral cells were used throughout the investigation.

The chromatographic unit used for the separation and analysis of mixtures of H_2, HD, and D_2 has been described previously.[14] Before use, both H_2 and D_2 were purified by a Model CL Serfass hydrogen purifier.

The catalyst samples were degassed in a furnace which consisted of a brass block containing wells of approximately the same dimensions as the cells. The block was heated by a hot plate and the temperature was controlled to within 5°.

An oil diffusion pump was used for degassing the catalysts. Dynamic pressures of 10^{-6} torr, measured with a Bayard–Alpert ionization gauge, were obtained.

For studying the effect of ultraviolet light on γ-irradiated catalysts, a General Electric germicidal lamp, G18T6, having 90% of its output in the 2537-A line, was used.

Chemicals. The silica–alumina cracking catalyst used in this study was a conventional silica–alumina for which methods of preparation have been described.[15] The particular sample used had a surface area of 400 m^2/g, a pore volume of 0.433 cc/g and an alumina content of 10.0%. Iron in the amount of 0.030% was the major impurity. Prepurified hydrogen and 99 mole % deuterium obtained from the Matheson Co., Inc., East Rutherford, N. J., were used. The deuterium contained 1% HD, and, because this could not be easily removed, analyses were corrected for it.

Procedure. 1. Preparation and Measurement. A catalyst sample of about 0.3 g was weighed into an irradiation cell (see Figure 1) and placed in the well furnace at 465°. The sample was ignited in air for 6 to 20 hr. (The air ignition removes hydrocarbon contaminants that are adsorbed in handling.) At the end of the air ignition period, the cell was connected to the vacuum system and evacuated for 24 hr at 465°. Finally, the cell was sealed. Pressures just prior to sealing were 10^{-6} to 10^{-7} torr. Separate samples were used for each experiment.

The catalyst sample was transferred to the quartz optical cell, and a baseline spectrum of the degassed catalyst was recorded. For this measurement a portion of the catalyst, identically treated in a matched cell, was placed in the reference beam. After transferring the catalyst to be examined back to the irradiation tube, it was irradiated with a 2000-curie cobalt-60 pencil. Following the irradiation, the tube was cooled in liquid nitrogen while the quartz optical cell was heated. This was necessary to anneal out radiation-induced coloring of the quartz. When the optical cell was cool, the catalyst was transferred back to the quartz cell and the spectrum was recorded, again using the unirradiated portion of the same catalyst in the reference beam.

To determine the exchange rate, the catalyst was transferred back to the irradiation tube and cooled to the desired temperature, usually −120°. The cell was connected to a vacuum manifold by the ball-joint O-ring connector and evacuated to 10^{-6} torr. Finally, the vacuum manifold was pressurized to approximately 150 torr with a 50:50 mixture of H_2–D_2 and the seal was broken. The stopcock was then closed and, after a measured time, the gas was analyzed for the amount of HD present by a gas chromatographic technique.[14]

2. Dosimetry. The γ-ray dose was measured with a ceric sulfate dosimeter placed in the same experimental geometry used for the irradiation of catalyst samples. Doses were corrected for the difference in density between the ceric sulfate solution and the catalyst and for the decay of the cobalt-60 source. Dose rates were of the order of 2×10^{20} ev/g hr.

3. Bleaching and Annealing. In several experiments the effects of ultraviolet light, oxygen, and heat on the irradiated samples of catalyst were studied as follows.

a. Ultraviolet. After degassing and γ irradiation, the catalyst sample was transferred to the quartz optical cell and exposed to the ultraviolet lamp for 22 hr. The catalyst sample was mixed continuously during the ultraviolet irradiation by rotating the

(14) G. F. Shipman, *Anal. Chem.*, **34**, 877 (1962).

(15) M. M. Marisic (to Socony-Vacuum Oil Co.), U. S. Patent 2,384,946 (Sept 18, 1945).

entire cell. After 22 hr of ultraviolet irradiation, the spectrum and exchange rates were measured.

b. Oxygen Pretreatment. Following γ irradiation, the catalyst samples were exposed to various pressures of pure dry oxygen for 60 min. The oxygen was then pumped off and the spectrum and exchange rates were measured. The oxygen used was dried by passing it through a tower of anhydrous magnesium perchlorate, and purified by passing it through a liquid nitrogen trap.

c. Thermal Annealing. Irradiated samples of silica–alumina were annealed in a drying oven at various temperatures for 22 hr. Following annealing the spectrum and exchange rates were measured.

Results and Discussion

(A) Effects of Radiation on the Optical Absorption of Silica–Alumina. Irradiation of degassed silica–alumina produces a black to brownish purple color in the catalyst, and, as expected, the diffuse reflectance spectrum shows strong absorption throughout the visible region (curve 1, Figure 2). The catalyst, after irradiation, absorbs strongly from 300 to 700 mμ with an apparent maximum at 425 mμ. Upon adsorption of H_2 at 25°, the optical absorption is decreased, and two bands at 395 and 550 mμ are observable (curve 3, Figure 2). Boreskov, *et al.*,[10] observed that in an irradiated silica gel containing traces of aluminum, a band at 550 mμ and the sextet in the epr spectrum disappeared upon adsorption of H_2 at 25°. They concluded that the adsorption of H_2 and catalytic isotopic exchange took place on the same sites. In the irradiated silica–alumina catalyst, the intensity of the absorption at 550 mμ decreases by a factor of 14 upon adsorption of H_2 at 25° (Figure 2). However, there is little evidence to indicate that these color centers are the sites active in H_2–D_2 exchange.

The intensity of the absorption at 550 mμ in silica–alumina varies with the degassing conditions used. A sample evacuated at 465° shows 17 times more relative absorbance at 550 mμ than does a sample evacuated at 25°. Possibly, the formation of the color centers during irradiation depends upon the prior removal of oxygen or water, creating defects that serve as traps for electrons and/or holes. To test this possibility an irradiated sample of silica–alumina catalyst was exposed to 100 torr of oxygen at 25° for 1 hr. The relative absorbance at 550 mμ changed only from 0.25 to 0.23 (Table I). This decrease is not any greater than found upon annealing under vacuum at 25° for 24 hr. When the irradiated catalyst was exposed to water vapor, however, the optical absorption band disappeared immediately, and no spectral difference between sample and reference was observed.

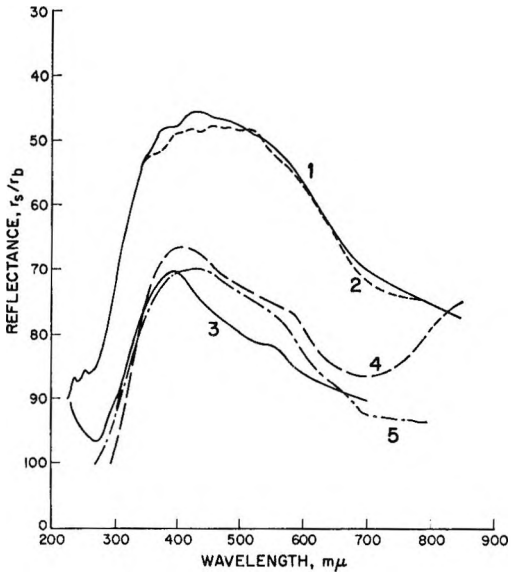

Figure 2. Reflectance of γ-irradiated silica–alumina: (1) γ irradiated to a dose of 2.0×10^{20} ev/g; (2) exposed to 100 mm of oxygen at 25°; (3) exposed to 100 mm of hydrogen at 25°; (4) annealed 22 hr at 150°; and (5) irradiated with ultraviolet light for 22 hr at 25°.

The absorption at a given wavelength for the irradiated silica–alumina catalyst increases with radiation dose and then ceases to increase further at a dose between 12 and 20×10^{20} ev/g (Figure 3). This suggests that the electrons and/or holes formed during the irradiation are stabilized at defects existing prior to the irradiation. If the radiation *produced* defects

Table I: Effect of O_2 on H_2–D_2 Exchange Rate Constant and Optical Absorption of Silica–Alumina Irradiated with γ Rays (Dose, 2×10^{20} ev/g)

Sample treatment	Rate constant, $10^2 k$, hr^{-1} M^{-2}		Relative absorbance (λ 550 mμ)	
	Prior to O_2 treatment	After O_2 treatment	Prior to O_2 treatment	After O_2 treatment
Control[a]	13.5	...	0.34	...
12 torr of O_2 at 25° for 1 hr	...	3.3	0.32	0.28
12 torr of O_2 at 25° for 1 hr	...	1.9	0.28	0.26
102 torr of O_2 at −120° for 1 hr	...	2.3	0.28	0.26
102 torr of O_2 at 25° for 1 hr	...	1.1	0.25	0.23

[a] Separate samples of catalyst used for the control and for each O_2 treatment.

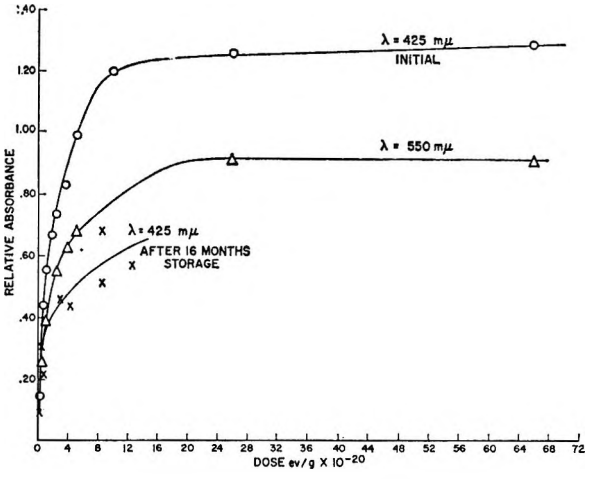

Figure 3. Variation of relative absorbance with dose for silica–alumina. $A_{rel} = (1 - R)^2/R(2 + R)$, where R = reflectance for normally incident light.

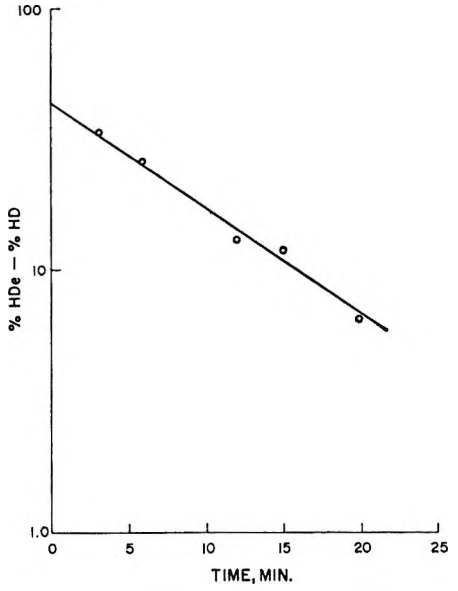

Figure 4. Variation of H_2–D_2 exchange rate with time over γ-irradiated silica–alumina: temperature, −120°; dose, 3.1 × 10^{19} ev/g.

that acted as trapping centers, optical absorption would be expected to increase continuously with dose. This suggestion is supported by the observation that the optical absorption of the γ-irradiated catalyst also depends upon how long it has aged since initial synthesis. As shown in Figure 3, the absorbance at 425 mμ is roughly a factor of 2 lower after a 16-month storage interval. Evidently storage leads to a decrease in the number of defects that can act as trapping centers or a slow thermal annealing of trapped entities.

(*B*) *H_2–D_2 Exchange over Irradiated Silica–Alumina.* The H_2–D_2 exchange reaction has been used quite frequently to study catalytic systems.[1,2,4,11,16] For optical studies, the exchange reaction is ideal because molecularly adsorbed H_2 and D_2 do not absorb in the spectral region of interest. This is not true of many organic reactions in which the adsorption of products leads to colored species on the surface, obscuring the optical bands in the solid.

Duffield and Calvin[17] have shown that, for a homogeneous system, the appearance rate of an isotope in an exchange reaction will be first order in distance from equilibrium regardless of the actual kinetics of the exchange reaction. This is also observed for the heterogeneous H_2–D_2 exchange reaction as shown in Figure 4, in which the HD appearance rate is first order through three half-lives.

The first-order reaction rate constant increases with temperature (Figure 5). In fact, the activity of irradiated catalyst was so high that rate measurements at 25° could not be made. Assuming an Arrhenius relationship, the apparent activation energy for the radiation-induced exchange reaction is about 1.4 kcal/mole. This value of the activation energy was used to compute the exchange rate at 25° of the irradiated silica–alumina, and this rate was then compared with the exchange rate at 25° of the unirradiated silica–alumina (Table II). The data in Table II show that irradiated silica–alumina is 78 times as active for exchange at 25° as unirradiated silica–alumina.

Table II: H_2–D_2 Exchange Rate Constant of γ-Irradiated and Unirradiated Silica–Alumina (Dose, 2 × 10^{20} ev/g)

Temp, °C	H_2–D_2 exchange rate constant, 10^2k, hr^{-1} M^{-2}	
	Irradiated	Non-irradiated
−120	11 (obsd)	0.0 (obsd)
25	102 (calcd)	1.3 (obsd)

Although the data points scatter, the exchange rate appears to increase with dose in a manner similar to the optical absorption (Figure 6). The scatter is most probably caused by the transfer operations described under experimental procedure. Small amounts of the irradiated catalysts are left behind in the regions of the reactor that are not cooled during the rate measurements. Because the activity of the irradiated catalyst is nine times as great at 25° as at −120°, traces of the catalyst in the noncooled portions of

(16) S. W. Weller and S. G. Hindin, *J. Phys. Chem.*, **60**, 1507 (1956).
(17) R. B. Duffield and M. Calvin, *J. Am. Chem. Soc.*, **68**, 557 (1946).

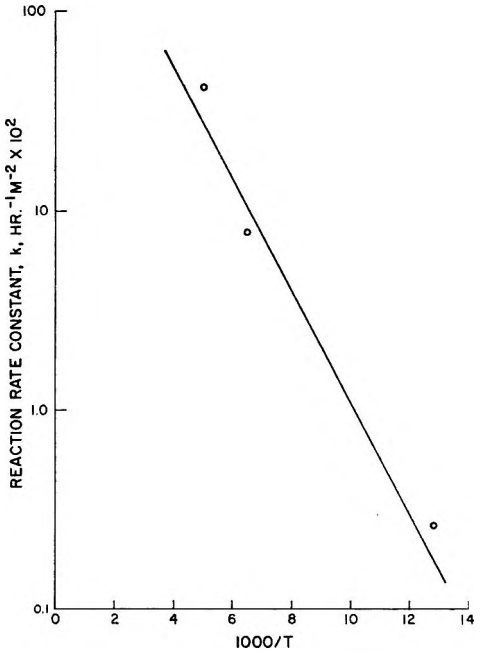

Figure 5. Variation of the first-order rate constant, k, with temperature: dose, 3.1 $\times$ 10^{20} ev/g.

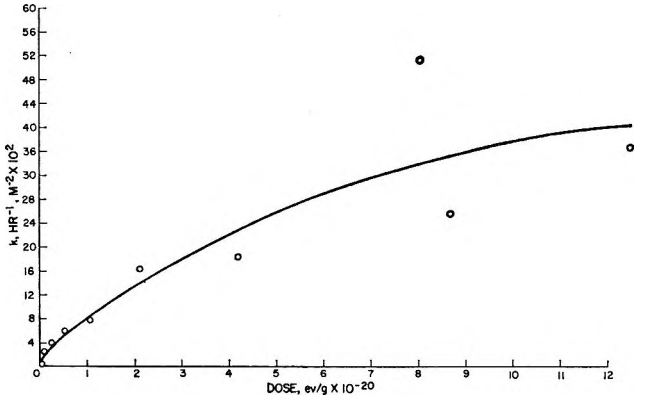

Figure 6. Variation of exchange rate constant with dose for silica–alumina.

the reactor can cause significant errors in the rate. These rate measurements were made early in the research. In later experiments, the noncooled portions of the reactor were annealed prior to the rate measurement. This variation of both exchange rate and optical absorption with dose suggested that the exchange rate and concentration of color centers might be related. To learn more of this possible relationship, experiments were made in which, following the γ irradiation but prior to the exchange rate measurements, the catalyst was treated with ultraviolet light, with oxygen, or was thermally annealed at various temperatures.

The effects of these treatments upon the spectrum of an irradiated silica–alumina are shown in Figure 2. Ultraviolet light and thermal annealing decrease the radiation-induced optical absorption to about the same extent. Oxygen has little effect.

Oxygen does have a significant effect on the exchange rate, however, decreasing it by a factor of 6 (Table I). So, indeed, does the ultraviolet light; it reduces the exchange activity by a factor of 4 (Table III). Evidently, the 5-ev photons are sufficient to cause depopulation of the traps. However, within the scatter of the experimental points, annealing an irradiated silica–alumina at 150° for 22 hr *does not* lower the exchange rate, even though the relative absorbance is decreased 22-fold (Table IV). At 200° the exchange rate constant drops by a factor of 6, but the absorption is barely measurable. It appears that if there is any correlation between the number of color centers and exchange activity, it is far from the approximately linear relationship that might be expected. The increase in the exchange rate observed upon annealing at 100 and 125° appears real, but no satisfactory explanation for this has been found.

Table III: Effect of Ultraviolet Radiation on H_2–D_2 Exchange Rate Constant and Optical Absorption of γ-Irradiated Silica–Alumina (Dose, 2.0 $\times$ 10^{20} ev/g)

	10^2k, hr^{-1} M^{-2}	Relative absorbance 425 mμ	550 mμ
γ irradiated only	13	0.38	0.32
	15	0.41	0.30
	12	0.51	0.40
γ irradiated, then ultraviolet irradiated	4.4	0.04	0.03
	2.5	0.02	0.01
	2.6	0.02	0.03

On the assumption that hydrogen can be irreversibly adsorbed at a catalytic site and subsequently participate in the exchange reaction, as depicted below, an attempt was made to determine the number of exchange sites in an irradiated catalyst. (S represents a catalytic site.) First an irradiated catalyst was pretreated with H_2. After pumping off the excess

$$H_2 + 2S \longrightarrow 2HS \text{ or } SH_2, \text{ etc.}$$

$$HS + D_2 \rightleftharpoons \begin{matrix} & D & \\ & \diagup\ \diagdown & \\ H & & D \\ & \diagdown\ \diagup & \\ & S & \end{matrix} \longrightarrow SD + HD$$

Table IV: Effect of Annealing Temperature on k and Relative Absorbance (Dose before Annealing Treatment Was 2×10^{20} ev/g)

Temp, °C	10^2k, $hr^{-1}\ M^{-2}$	Relative absorbance 425 mμ	Relative absorbance 550 mμ
25	14	0.41	0.30
	13	0.47	0.37
	10	0.45	0.29
100	22	0.11	0.05
125	20	0.07	0.05
150	16	0.02	0.007
	15	0.01	0.007
	13	0.02	0.01
200	2.3	0.001	0.001
	2.8	0.001	0.001
250	0.02	0.001	0.0004
	0.04	0.001	0.002

H_2, D_2 was admitted, and the gases were analyzed for HD. The number of exchange sites was then assumed to be one-half the number of HD molecules observed. The chromatographic method of analysis can detect 0.5 mole % HD in the presence of 99 mole % deuterium. For a test temperature of −120° and a deuterium pressure of 90 torr at this temperature, the total number of molecules present in the cell was 1.7×10^{20}. Therefore, the number of HD molecules that can be detected is 8.5×10^{17}, corresponding to 4.3×10^{17} sites. Unfortunately, the analysis is limited because the purified D_2 contains 1% HD. To overcome this limitation, larger samples of catalyst (2 g) were used in the experiment instead of the usual 0.3 g. All other conditions were kept the same. In two such experiments no HD above the blank value was observed. Evidently, (1) the number of sites at which exchange occurs is less than about 2×10^{17} sites/g, or (2) hydrogen remaining adsorbed on the irradiated catalysts after pumping does not participate in the exchange.

An experiment similar to the one just described, but omitting the pretreatment with H_2, was made to establish if any of the residual hydrogen remaining after degassing was involved in the exchange under the conditions used. No HD was observed. Most of the exchange evidently occurs among the molecules admitted to the system during exchange measurements.

The possibility that the irradiated cell contributed to the exchange process was tested by carrying an empty cell through the whole process. No exchange was observed at a test temperature of 25° and a reaction period of 120 min.

Summary and Conclusions

Although both the optical absorption and exchange activity increase in a similar manner upon γ irradiation, there appears to be little or no relationship between the number of color centers and the exchange activity. Either the sites at which exchange occurs do not absorb in the region of the spectrum studied or the radiation-induced sites responsible for exchange are too few to be measurable with diffuse reflectance spectroscopy.

The Adsorption of Ethylene on a Series of Near-Faujasite Zeolites Studied by Infrared Spectroscopy and Calorimetry

by J. L. Carter, D. J. C. Yates, P. J. Lucchesi, J. J. Elliott, and V. Kevorkian

Process Research Division and Analytical Research Division, Esso Research and Engineering Company, Linden, New Jersey *(Received October 6, 1965)*

The adsorption of ethylene (at room temperature) on a series of ion-exchanged synthetic near-faujasites has been studied by infrared spectroscopy and by microcalorimetry. It has been found that the nature of the adsorption of the ethylene is dependent on the nature of the exchangeable cations. In particular, the heats of adsorption of the ethylene have been related to changes in the frequency of the double bond vibration of the adsorbed molecules. It has also been found that in all cases except that of Cd–X and Ag–X the ethylene is relatively weakly held, as the adsorbed gas can be readily removed by evacuation at room temperature. By means of an assignment of the probable symmetry of the adsorbed ethylene, and of the half-widths of the bands of the adsorbed molecules, it has been shown that, except for Ag–X, all of the adsorbed molecules are freely rotating. In addition, very striking changes have been found in the intensity of the CH stretching bands of adsorbed ethylene. With Cd–X, no CH stretching bands could be detected. With Ag–X, the same bands have a very high intensity.

I. Introduction

Relatively little work has been reported[1-4] on the infrared spectra of molecules adsorbed on zeolites. This is surprising, as most zeolites have such a large surface area that quite intense bands owing to adsorbed molecules can readily be obtained. One of the most intriguing properties of zeolites is their ability to retain their aluminosilicate structure intact while the metallic cations, needed to ensure over-all electrical neutrality, are changed by ion exchange. This change of cation has been shown, in a number of cases, to produce marked changes in the physical properties of zeolites. For example, a synthetic near-faujasite, designated by its makers as sieve X, will admit molecules with critical dimensions up to 9 A when sodium is the cation but only molecules smaller than about 8 A when calcium is the cation.[5] However, as well as changing physically the effective size of openings in such zeolites, it is quite probable that specific interactions could exist between the cations and the adsorbed molecules.

Such an effect has been found with ethylene. A series of ion-exchanged near-faujasites have been prepared and it has been found that very specific interactions occur between ethylene and the cations. These effects have been demonstrated both spectroscopically and thermodynamically.

II. Experimental Section

Materials. The adsorbent used in this study was powdered Linde Na-13X (Lot No. 13961) zeolite (containing no binder), which has a near-faujasite structure.[6] Details of these preparations and of the methods used to put the powders in a form suitable for spectroscopic examination have been given in an earlier publication.[4] No particular problems were encountered with Ag–X. It was not shielded from light during preparation or handling, but was stored in the dark.

(1) G. J. C. Frohnsdorff and G. L. Kington, *Proc. Roy. Soc.* (London), **A247**, 469 (1958).

(2) H. A. Szymanski, D. N. Stamires, and G. R. Lynch, *J. Opt. Soc. Am.*, **50**, 1323 (1960).

(3) L. Bertsch and H. W. Habgood, *J. Phys. Chem.*, **67**, 1621 (1963).

(4) J. L. Carter, P. J. Lucchesi, and D. J. C. Yates, *ibid.*, **68**, 1385 (1964).

(5) "Molecular Sieves Bulletin," Linde Co., Tonawanda, N. Y.

(6) R. M. Barrer, F. W. Bultitude, and J. W. Sutherland, *Trans. Faraday Soc.*, **53**, 1111 (1957).

The ethylene was obtained from the Matheson Co., Inc., and was stated to be 99.5% pure. It was purified by freezing and evacuating at 77°K before use.

Apparatus and Procedure. Infrared Measurements. The infrared portion of this study was done using a cell and vacuum system that has previously been described.[7] The samples were evacuated at room temperature and the temperature was raised slowly to 100°. When the pressure was in the region of 10^{-4} torr, the temperature was again increased slowly to 450°. Evacuation was continued at 450° until the pressure was about 5×10^{-6} torr. The cell stopcock was then shut, the sample was cooled to room temperature, and its infrared spectrum was recorded. A dose of ethylene was then admitted to the sample cell and the spectrum was again recorded.

The ethylene pressure in all experiments was between 9.1 and 11.5 cm. After this, the gaseous ethylene and any weakly adsorbed ethylene were removed from the cell by evacuation for 5 min at room temperature. The spectrum was then recorded again. In some cases the sample was heated to a higher temperature, while evacuating, to remove the more strongly adsorbed ethylene, and after cooling to room temperature the spectrum was again recorded.

Calorimetric Measurements. The experimental equipment and technique used were essentially the same as that described earlier,[8] except for small modifications. The constant-temperature bath was a multiple-wall type and consisted of five concentric steel cylinders separated from each other by insulation. The centermost cylinder contained a solid stainless steel block with two holes. One hole accommodated the calorimeter, which had three iron–constantan thermocouples spot-welded to the trays and the other, the three thermocouple reference junctions. This constant-temperature bath had no moving parts and could be used from room temperature to 600° with a temperature control of ±0.001°. The samples were outgassed as described earlier.[8] About 14 mm of helium was then added to the calorimeter to speed the transfer of the heat of adsorption to the surroundings. If helium were not added, the time required for the heating–cooling curve to return to its initial position of thermal equilibrium would be extremely long. Electrical calibrations were made under the same conditions, before and after each dose, to ensure that correct allowances could be made for heat losses from the sample.

The heats of adsorption were measured at 50° and the cross-sectional area of the ethylene molecule was assumed to be 22 A².

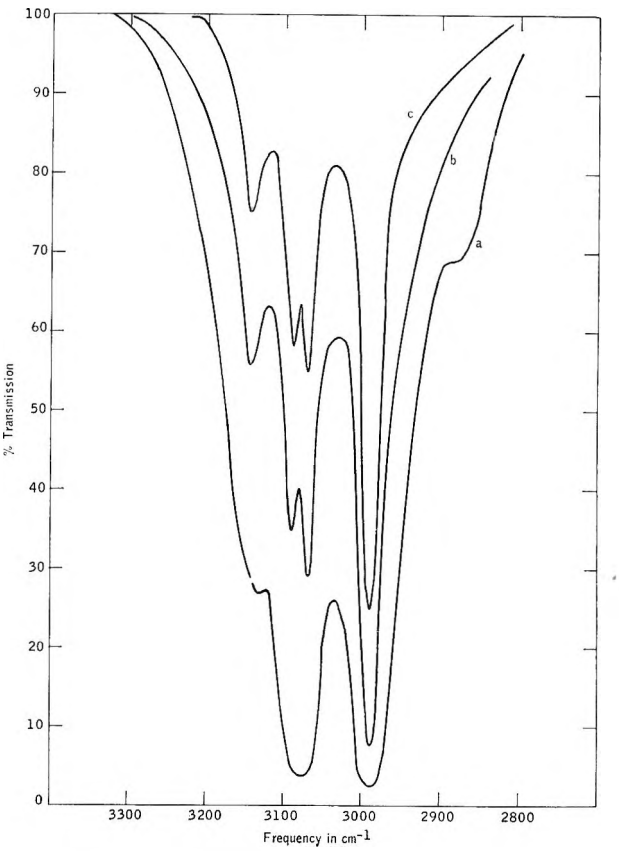

Figure 1. Spectra of ethylene adsorbed on Ag–X: (a) with 10.9 cm of ethylene in the cell, (b) after evacuation for 5 min at room temperature, and (c) evacuation for 15 min at 100°.

III. Results

(*a*) *Infrared Measurements.* Because of the variable background spectra of the zeolites, all spectra have been replotted from the original recordings and are presented in transmission in Figures 1 to 9. Figure 1 shows the CH stretching bands of ethylene adsorbed on Ag–X, and Figure 2 shows the C=C stretching bands (ν_2) and the two CH_2 deformation bands (ν_3 and ν_{12}). The notation followed here is that of Herzberg.[9] The ethylene was strongly held on this zeolite, and spectra are also given after desorption. Figures 3 and 4 show the data obtained with Cd–X. The CH stretching bands are shown in Figure 3, and ν_2, ν_3, and ν_{12} in Figure 4. As with silver, the ethylene was strongly held, and data are given on Figure 4 for various degrees of desorption. For all of the zeolites studied, the ν_{12} band of the adsorbed molecules could not be determined

(7) D. J. C. Yates and P. J. Lucchesi, *J. Chem. Phys.*, **35**, 243 (1961).

(8) V. Kevorkian and R. O. Steiner, *J. Phys. Chem.*, **67**, 545 (1963).

(9) G. Herzberg, "Infrared and Raman Spectra of Polyatomic Molecules," D. Van Nostrand, Inc., Princeton, N. J., 1945.

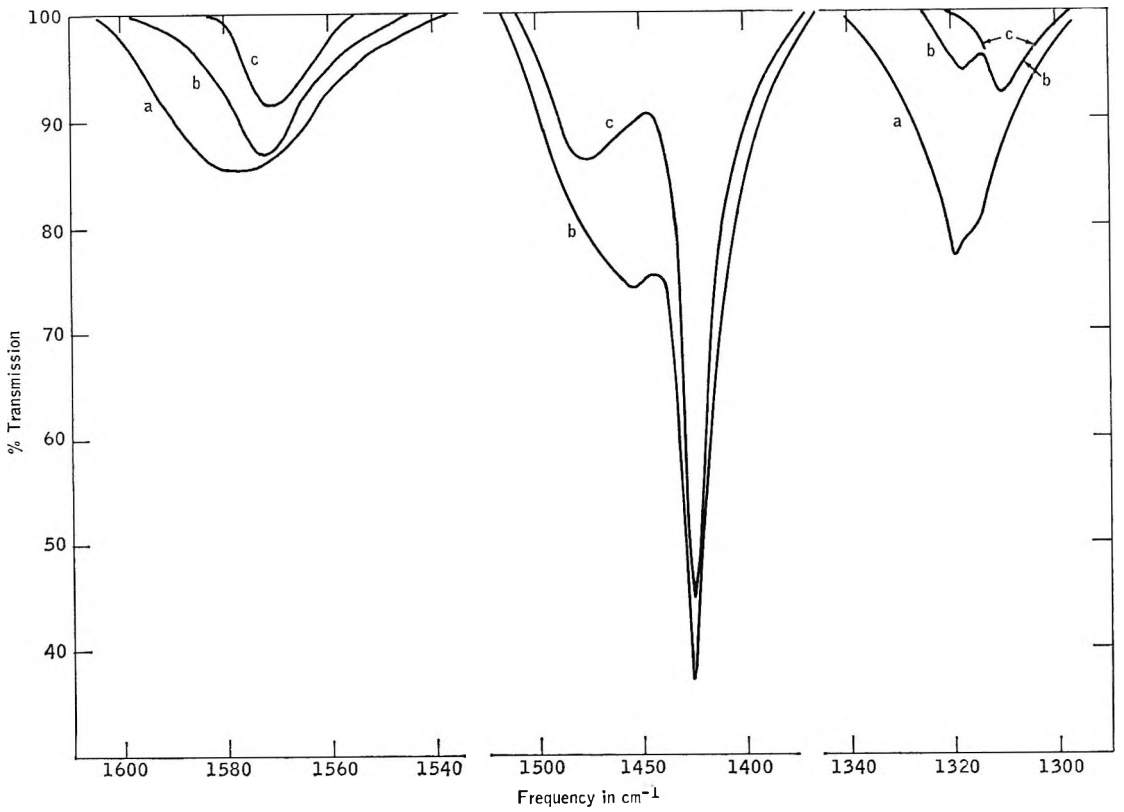

Figure 2. Spectra of ethylene adsorbed on Ag–X: (a) with 10.9 cm of ethylene in the cell, (b) after evacuation for 5 min at room temperature, (c) evacuation for 15 min at 100°. Half-widths for the 1570-cm^{-1} band are 21 cm^{-1} for (b) and 15 cm^{-1} for (c); for the 1310-cm^{-1} band, 9 cm^{-1} for (c); for the 1425-cm^{-1} band, 14 cm^{-1} for (b) and 12.5 cm^{-1} for (c).

when the gaseous ethylene was present owing to overlapping by the strong ν_{12} band of the gas.

Spectra are given for the alkali metal substituted near-faujasites, lithium, sodium, and potassium, in Figures 5, 6, and 7, respectively. In all cases, in addition to the CH stretching bands, the ν_2 and ν_3 bands are shown. All the adsorbed molecules were quite weakly held, as they could be removed by 5-min evacuation at room temperature. Results for barium are shown in Figure 8. The same bands are given as for the alkali metal zeolites, as the ethylene was also weakly adsorbed on this sample. The adsorbed phase was all removed by evacuation for 5 min at room temperature.

With calcium, in contrast, the ethylene was slightly more strongly held, some of the adsorbed species remaining on the surface after evacuation for 5 min at room temperature (Figure 9). All the adsorbed species were removed after evacuation for 15 min at 100°. Although the presence of the ν_{12} vibration in the adsorbed molecules could be clearly detected after the gaseous ethylene was removed at room temperature, the presence of two bands (between 1450 and 1475

Table I: Slit Widths (SW, in mm) and Resolution (Res, in cm^{-1}) Used for All Samples

Sample	At 1330 cm^{-1}		At 1600 cm^{-1}		At 2800 cm^{-1}		At 2900 cm^{-1}		At 3000 cm^{-1}	
	SW	Res	SW	Res	SW	Res	SW	Res	SW	Res
Ag–X	1.05	1.8	0.62	1.7	3.0	12.6	2.35	10.6	1.7	8.3
Cd–X	1.05	1.8	0.62	1.7	3.5	14.7	2.8	12.6	2.1	10.3
Li–X	1.05	1.8	0.62	1.7	2.9	12.2	2.2	9.9	1.6	7.8
Na–X	0.80	1.4	0.48	1.3	2.0	8.4	1.5	6.7	1.1	5.4
K–X	1.24	2.1	0.77	2.1	3.3	13.8	2.6	11.7	1.95	9.5
Ba–X	1.24	2.1	0.77	2.1	3.0	12.6	2.35	10.6	1.7	8.3
Ca–X	1.05	1.8	0.62	1.7	3.2	13.4	2.5	11.2	1.85	9.1

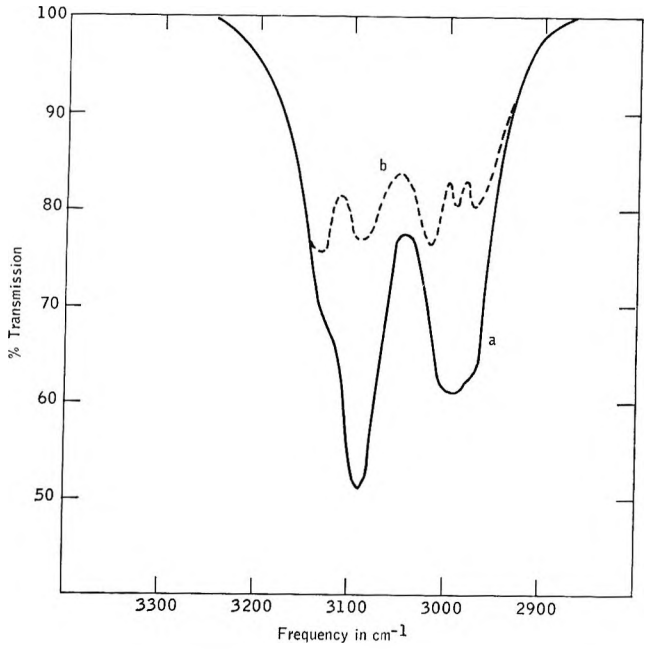

Figure 3. Spectra of ethylene adsorbed on Cd–X: (a) gas plus adsorbed phase, with 9.5 cm of ethylene in the cell; (b) gas phase only in the cell (no Cd–X present), ethylene pressure 10.1 cm. Slit widths for spectrum b are the same as those used for spectrum a. After spectrum a was measured, the gas phase was removed by evacuation for 5 min at room temperature. No bands due to adsorbed ethylene were detected in the 2900–3200-cm^{-1} region.

cm^{-1}) in the spectrum of the evacuated Ca–X made it very difficult to determine accurately the ν_{12} of the adsorbed molecules. However, the band seems to be at about 1455 cm^{-1}. Table I gives details of the slit width and resolution used for all the samples.

(*b*) *Calorimetric Measurements.* The values of the heat of adsorption of ethylene, as a function of coverage, on a number of the samples used in this study are presented in Table II. The coverages used were less than 0.12, and the number of ethylene molecules adsorbed in all cases was considerably less than the number of cations present (Table III). The highest pressure used was 1.2 cm, considerably less than in the infrared experiments. The low coverage used probably explains the constancy of ΔH for a given zeolite as a function of coverage, as at all coverages there was an excess of cations present. However, there is a wide variation in ΔH values as the cation is varied. Both these facts indicate that, for each zeolite, the heats of adsorption are primarily due to ethylene–cation interactions, rather than to ethylene–aluminosilicate interactions.

The above is in agreement with the conclusions drawn from the infrared spectra. It is found that there

Table II: Heats of Adsorption of Ethylene on Zeolites

Zeolite	Coverage	ΔH, kcal/mole	
Ag–X	0.006	18.9	
	0.028	17.3	Av 18.1
	0.052	18.2	
Cd–X	0.012	15.0	
	0.037	15.5	
	0.059	14.7	Av 14.9
	0.078	14.3	
Na–X	0.027	9.6	
	0.077	8.3	Av 8.6
	0.124	7.8	
Ba–X	0.034	6.6	
	0.048	10.0	Av 8.3
Ca–X	0.029	8.2	
	0.060	9.3	Av 9.1

Table III: Relation between Maximum Number of Moles of Ethylene Adsorbed and the Moles of Cations in the Heat of Adsorption Experiments

Cation	Cation, moles × 10^4 [a]	Total ethylene adsorbed, moles × 10^4
Ag	39.8	4.96
Cd	25.1	4.21
Na	60.2	4.37
Ba	23.6	2.43
Ca	30.7	3.71

[a] Per gram of dehydrated zeolite.

Table IV: Relation between Heats of Adsorption and Relative Ease of Desorption of Ethylene on Zeolites

Zeolite	Av heat of adsorption, kcal/mole	Desorption data (from infrared spectra)
Ag–X	18.1	Not removed by evacuation at 200°
Cd–X	14.9	Removed by evacuation at 200°
Na–X	8.6	Removed by evacuation at room temperature

is good agreement between the relative ease of desorption, as measured from the infrared spectra, and the heats of adsorption (Table IV). It follows that the heat of adsorption should be related to changes in the infrared spectra of adsorbed ethylene. Such a rela-

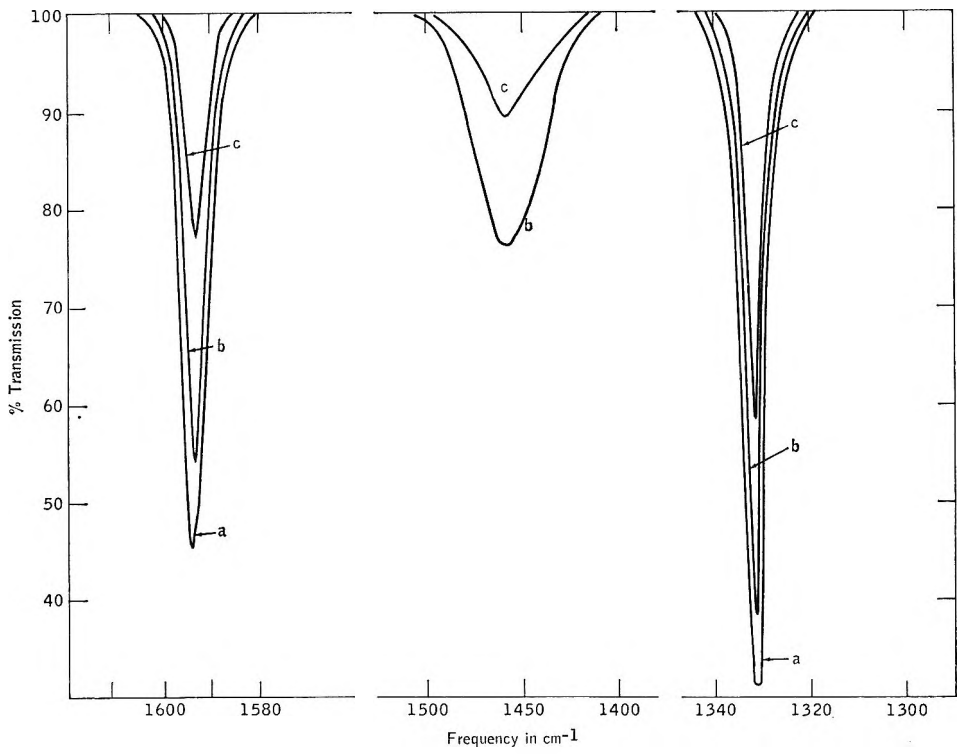

Figure 4. Spectra of ethylene adsorbed on Cd–X: (a) with 9.5 cm of ethylene in the cell, (b) after evacuation for 5 min at room temperature, (c) evacuation for 15 min at 100°. Half-widths for the 1594-cm^{-1} band are 5 cm^{-1} for (a), 4 cm^{-1} for (b), and 5 cm^{-1} for (c); for the 1331-cm^{-1} band, 4 cm^{-1} for (a) and (b), and 3 cm^{-1} for (c); for the 1460-cm^{-1} band, 40 cm^{-1} for (b) and 30 cm^{-1} for (c).

tion has been found (Figure 10), and the significance of this relation will be discussed in detail in another section.

IV. Discussion

Interpretation of Spectra. (*a*) *General Effects.* There are some features of the spectra which are common to all the zeolites, and these will be discussed first. In all cases, despite the obviously weak forces holding the ethylene to some of the zeolites, the normally forbidden ν_2 and ν_3 vibrations are quite strong bands. Table V contains details of the shifts, peak intensities, and half-widths of these two bands for all samples. These experiments were all conducted at room temperature, or slightly above, while ethylene boils at 169°K. Under these conditions, the vapor pressure of ethylene is in the region of 60 atm. At temperatures so far removed from the boiling point of ethylene, physical adsorption does not normally take place. However, the spectra very clearly indicate that the molecules are adsorbed as ethylene (*e.g.*, the presence of the double bond C=C stretching vibration, ν_2) so that dissociative adsorption, characteristic of strong chemisorption, is not occurring. Hence, the interaction between C_2H_4 and these zeolites can be described as weak chemisorption (or strong physical adsorption). Even for quite weak physical adsorption, such as occurs with methane on silica, the surface forces render permitted certain forbidden vibrations,[10] so that it is not surprising that the same effect is found for weak chemisorption. The presence of ν_2 and ν_3 bands is thus to be expected. It is of interest to note that even the weak perturbations occurring in liquid ethylene are enough to cause ν_2 and ν_3 to be infrared active.[11] However, in the more symmetrical environment of the crystal, ν_2 and ν_3 are again forbidden.

The absence of combination bands, however, is unexpected. Ethylene has two very prominent combination bands in its spectrum ($\nu_7 + \nu_8$) and ($\nu_6 + \nu_{10}$), the former being classed as very strong in the liquid phase by Brecher and Halford.[11] Their spectra show that, for liquid and crystalline ethylene, the $\nu_7 + \nu_8$ combination band has almost 100% absorption. In fact, this band is as intense, or more so, than the fundamental CH_2 deformation band (ν_{12}) in the condensed phases. In all of our experiments, a careful

(10) N. Sheppard and D. J. C. Yates, *Proc. Roy. Soc.* (London), **A238**, 69 (1956).

(11) C. Brecher and R. S. Halford, *J. Chem. Phys.*, **35**, 1109 (1961).

Table V: Characteristics of Adsorption-Induced Bands of Ethylene Adsorbed on Near-Faujasite Zeolites

	ν_2 band				ν_3 band			
Cation	Peak position, cm^{-1}	Shift from gaseous ν_2, cm^{-1}	Half-width, cm^{-1}	Apparent peak, optical density	Peak position, cm^{-1}	Shift from gaseous ν_3, cm^{-1}	Half-width, cm^{-1}	Apparent peak, optical density
Ag[a]	1578	−45	...	...	1320	−22	...	...
Ag[b]	1572	−51	21	0.060	1318	−24	...	...
					1310	−32	...	...
Ag[c]	1571	−52	15	0.038	1310	−32	9	0.035
Cd[a]	1594	−29	5	0.345	1331	−11	4	0.515
Cd[b]	1594	−29	4	0.28	1331	−11	4	0.418
Cd[c]	1594	−29	5	0.115	1331	−11	3	0.225
Li[a]	1614	−9	8	0.027	1340	−2	4	0.100
Na[a]	1613	−10	7	0.047	1339	−3	4	0.114
K[a]	1615	−8	7	0.117	1340	−2	6	0.240
Ba[a]	1612	−11	8.5	0.130	1339	−3	5	0.236
Ca[a]	1610	−13	6	0.055	1339	−3	4	0.190
Ca[b]	1610	−13	5	0.027	1339	−3	3.5	0.088

[a] Spectra taken with gaseous ethylene in contact with the zeolites. For pressures, see the captions of figures. [b] After evacuation for 5 min at room temperature. [c] After evacuation for 15 min at 100°.

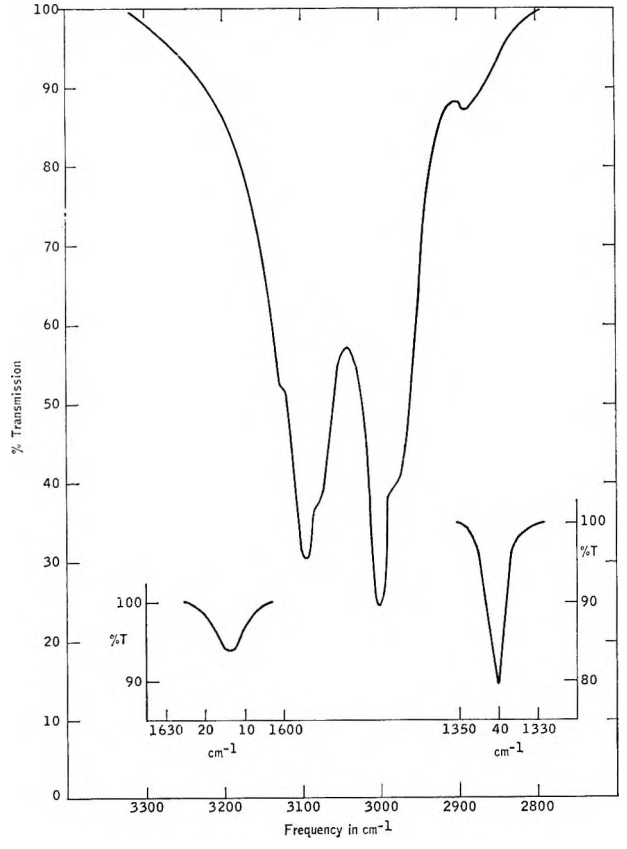

Figure 5. Spectra of ethylene (10.3 cm) adsorbed on Li–X.

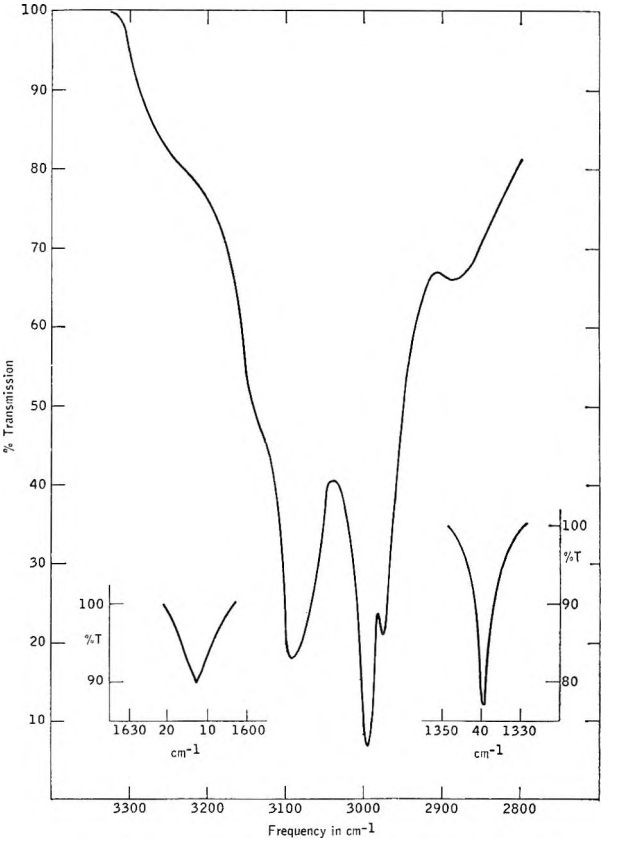

Figure 6. Spectra of ethylene (11.5 cm) adsorbed on Na–X.

search was made to try to locate these combination bands, but they could not be found. Bands of greater than 5% intensity would certainly have been detected.

To interpret these results, it is important to consider the symmetry of the adsorbed ethylene. In the gas phase, ethylene has the symmetry described by the

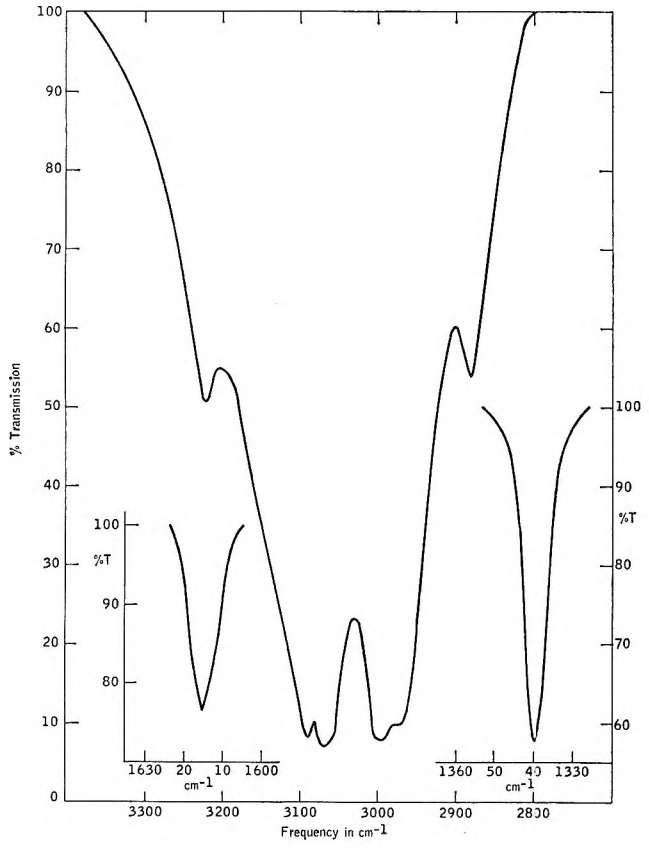

Figure 7. Spectra of ethylene (10.3 cm) adsorbed on K–X.

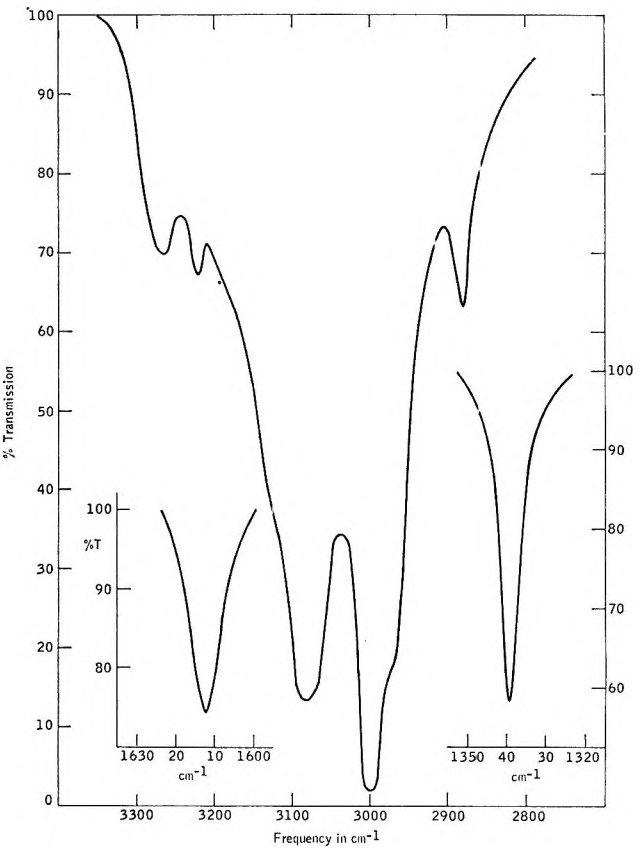

Figure 8. Spectra of ethylene (9.1 cm) adsorbed on Ba–X.

point group D_{2h}. In view of the relation found between the heat of adsorption and the shift in the C=C stretching vibration, ν_2 (Figure 10), it seems very likely that the ethylene is held to the surface by a bond between the π electrons and the cation. The nature of this bonding will be discussed in more detail later, in connection with the results on the silver zeolite. If this is the correct mode of attachment, the symmetry of the ethylene–cation complex is most probably that described by the point group C_{2v}. Even for nonspecific adsorption of ethylene, *i.e.*, silica at low temperatures, if it is adsorbed with its principal plane parallel to the surface,[10] its symmetry will also become C_{2v}. It should be noted that under these conditions the ethylene molecules are in an environment which is quite different from that of liquid and solid ethylene. The adsorbed molecules are subjected to a perturbing force oriented at a known angle to one "side" of the molecule. In the liquid, the ethylene environment is that produced by a random averaging of forces from all directions, while in the solid the ethylene is subjected to oriented perturbing forces. The ν_6 vibration in ethylene, when the ethylene has the C_{2v} point group, now has species A_2 rather than B_{1g}, ν_7 now has species A_1, ν_8 has B_1, and ν_{10} has B_2. The combinations $\nu_6 + \nu_{10}$ and $\nu_7 + \nu_8$, in the C_{2v} situation, both have B_1 symmetry. As a consequence, the same combinations are allowed, by the selection rules, despite the change in symmetry.

The reason for the absence of combination bands in the spectra of adsorbed ethylene must be sought elsewhere. In particular, the detailed motion of the hydrogen and carbon atoms in the ethylene–cation complex must be considered. The ν_6 vibration is expected to be almost unaffected by the formation of the carbon–cation bond. However, ν_7, ν_8, and ν_{10} vibrations are all likely to have their frequencies greatly changed by the formation of the carbon–cation bonds. It is probable that ν_7 is the most affected and ν_8 the least affected. These changes in frequency may put the combination bands into inaccessible (less than 1250 cm^{-1}) regions of the spectrum. In any case, there appear to be no rules enabling one to predict the intensity of combination bands in the gas phase,[12] let alone in the adsorbed phase.

(*b*) *Specific Effects.* Both from the heats of ad-

(12) B. L. Crawford, private communication.

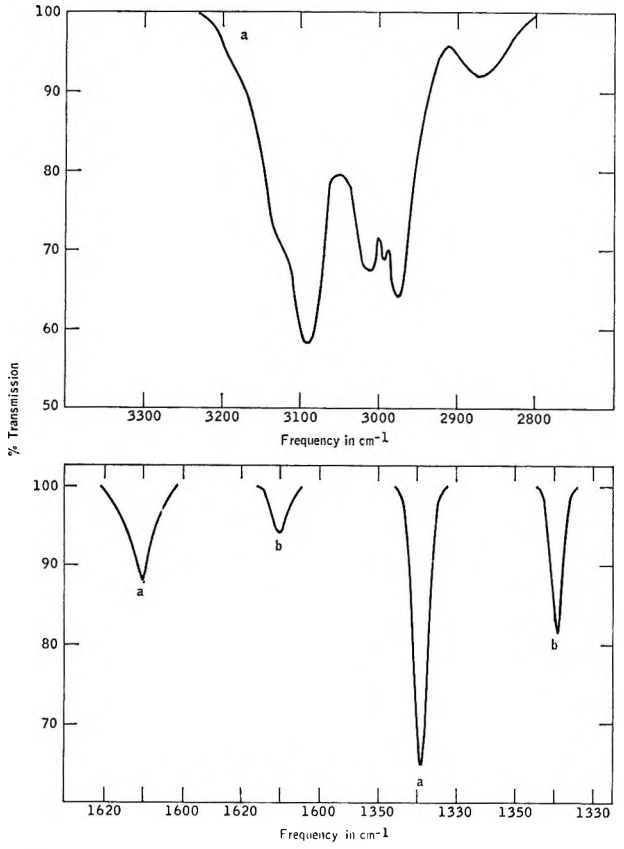

Figure 9. Spectra of ethylene adsorbed on Ca–X: (a) with 10.7 cm of ethylene in the cell, (b) after evacuation for 5 min at room temperature.

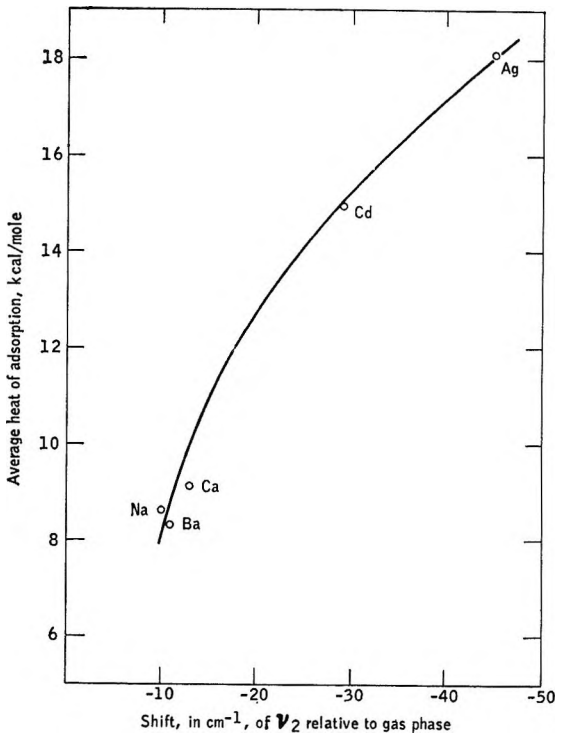

Figure 10. Relation between the average heat of adsorption of ethylene and the shift in the double bond stretching frequency (ν_2) as a function of the exchangeable cation in near-faujasites.

sorption and the spectroscopic evidence of reversibility the ethylene is relatively weakly held on the majority of the zeolites examined. These are lithium, sodium, potassium, and barium, where all the adsorbed ethylene was removed by 5-min evacuation at room temperature. With calcium (Figure 9) some ethylene is left adsorbed after evacuation at room temperature, but it was all removed after evacuation at 100°. With cadmium (Figures 3 and 4), the ethylene was even more strongly held, evacuation at 200° being necessary to remove all the adsorbed species. With silver (Figures 1 and 2), which held the ethylene most tenaciously, a temperature above 200° was needed to remove all the ethylene.

The group of zeolites which hold the ethylene most weakly will be considered first. In the case of bands corresponding to the ν_2 and ν_3 vibrations of gaseous ethylene, the bands of the adsorbed molecules can be quite accurately measured, as these vibrations are inactive in the gas phase. For the whole CH stretching region and for the asymmetric CH_2 deformation band (ν_{12}) the spectra are complicated considerably by the presence of the gaseous ethylene. However, the ethylene pressure was in all cases close to 10 cm, and the spectra obtained with the same cell filled with the same pressure of ethylene are shown in Figure 3, using slits of similar width to those used while measuring the zeolitic spectra. It will be seen that the most intense band in the gas has an absorption of about 25%. Hence, the gaseous ethylene contributes relatively little intensity to the CH stretching region for the sodium, potassium, and barium samples.

Now we will consider the zeolites on which the ethylene is most strongly adsorbed, namely the Cd–X and Ag–X. The spectra of these materials are shown in Figures 1–4 and the half-band width ($\Delta\nu_{1/2}$) values are given in the legends of the figures and in Table V. Considering the Cd zeolite first (Figure 4), it is of interest to note the rather large $\Delta\nu_{1/2}$ value (40 cm^{-1}) of the 1460-cm^{-1} band (corresponding to ν_{12} in gaseous ethylene). This should be compared with the very narrow bands (ν_2 and ν_3) at 1594 and 1331 cm^{-1}, which both have half-widths close to 4 cm^{-1}. If we assume that the adsorbed molecule–cation complex has C_{2v} symmetry, *i.e.*, its principal axis is perpendicular to the plane of the molecule and runs through the cation and the center of the double bond, then the 1460-cm^{-1} band is of species B and the other two are of

species A. The direction of the change in dipole of a vibration of species A is perpendicular to the surface plane in which the cation is situated, while in contrast the direction of the dipole change for species B is parallel to the surface. For ethylene rotating around the C_2 axis, the vibration which has a dipole change parallel to the surface would be modulated, giving broad bands, while the vibration having a dipole change along the axis of rotation would not be modulated, giving narrow bands. The spectra of Figure 4 thus establish that the adsorbed ethylene is indeed rotating.

The high intensity of the two narrow bands of species A is related to the motion of the delocalized π electrons during each of the two vibrations. First, consider the 1594-cm^{-1} band. This band is primarily due to the stretching of the C=C bond, the π electrons of which are strongly polarized toward the cation. As this bond stretches and contracts, there will be an oscillating motion of these electrons toward and away from the cation. The large dipole moment accompanying such a motion could account for the high intensity of the band. Secondly, for the 1331-cm^{-1} band, which is primarily a CH deformation mode, the orbital following which accompanies such a vibration[13] will result in a change in the hybridization of the C=C double bond. This will again result in an in-phase motion of the π cloud perpendicular to the surface.

It is of interest to note from Figures 5–9 that all the other zeolites, with the exception of Ag–X, have narrow ν_2 and ν_3 bands and broad ν_{12} bands. It follows that it is very likely that the adsorbed ethylene is rotating in these cases also. As far as the freedom of the rotation is concerned, no fine structure was resolved in the 1460-cm^{-1} band on Cd–X. This lack of discrete structure does not necessarily mean that the adsorbed species is not freely rotating, as vibration of the molecule against the surface could interrupt the rotation.[10]

However, the most interesting feature of the spectra of ethylene adsorbed on Cd–X is the absence of any bands in the CH stretching region after removal of the gaseous ethylene. There seems to be no precedent for the absence of the normally strong CH stretching bands in ethylene, while the normally forbidden CH deformation and CC stretching bands (ν_3 and ν_2) are the strongest peaks in the spectrum. The only other case where it has been observed is Ca–X (Figure 9). Here, after evacuation for 5 min at room temperature, fairly strong bands remain at 1339 and 1610 cm^{-1} (curve b), but no CH stretching bands could be detected. There does not appear to be any plausible explanation for this extreme effect. Relatively small effects have been found by Dows and co-workers,[14-16] who observed a variation in intensity (factors between 2 and 3) of the infrared-active bands of ethylene and benzene on going from the gaseous to the solid state. In a recent review of infrared intensities[17] it was considered that the results obtained by Dows are very disturbing, as the intensity changes are far greater than can be accounted for by dielectric changes or by the expected magnitudes of intermolecular perturbations. As our intensity changes are probably at least two orders of magnitude larger than those reported by Dows, they can be considered to be correspondingly more disturbing. In addition, the variations in the work reported here are between two forms of ethylene both in the same phase—the adsorbed phase.

The spectra of ethylene on Ag–X are somewhat different from that on Cd–X. There are at least two different sites upon which the ethylene is adsorbed. This is most clearly shown by the ν_3 band in Figure 2. With the gas present (curve a) the band is at 1320 cm^{-1}, with a shoulder at lower frequency. After the evacuation at room temperature, two bands are present (1318 and 1310 cm^{-1}). Finally, after evacuation at 100° only the 1310-cm^{-1} band remains. These two types can be called moderately and strongly held species. The frequencies of the moderately held species are fairly close to those of ethylene on the Cd–X, although shifted to somewhat lower frequencies. The strongly held species are at lower frequencies than the moderately held species.

It is illustrative to compare the half-width of the bands of the strongly held species on silver with the corresponding bands found on cadmium. The most striking feature is the large reduction in $\Delta\nu_{1/2}$ of the ν_{12} bands, from 30 to 12.5 cm^{-1}. This immediately suggests that adsorbed ethylene is no longer rotating around the C_2 axis and that some force secondary to the donor $\pi \rightarrow Ag^+$ bond is holding the molecule rigidly in place.

In order to explain the stability of silver ion–olefin complexes, Dewar[18] suggested that the bond formed between these moieties was made up of two components. These were the overlap of the filled π orbitals of the olefin with the vacant 5s orbital of the silver ion, and the overlap of the filled 4d orbitals of the silver ion with the vacant π^* orbitals of the olefin. Whether in our case the σ bond is composed of the overlap of π–5s orbitals or, as illustrated in Figure 11, the overlap of

(13) C. A. Coulson, "Valence," 2nd ed, Oxford University Press, London, 1961, p 232.

(14) G. M. Wieder and D. A. Dows, *J. Chem. Phys.*, **37**, 2990 (1962).

(15) J. L. Hollenburg and D. A. Dows, *ibid.*, **37**, 1300 (1962).

(16) D. A. Dows and A. L. Pratt, *Spectrochim. Acta*, **18**, 433 (1962).

(17) D. Steele, *Quart. Rev.* (London), **18**, 21 (1964).

(18) M. J. S. Dewar, *Bull. Soc. Chim. France*, **18**, C71 (1951).

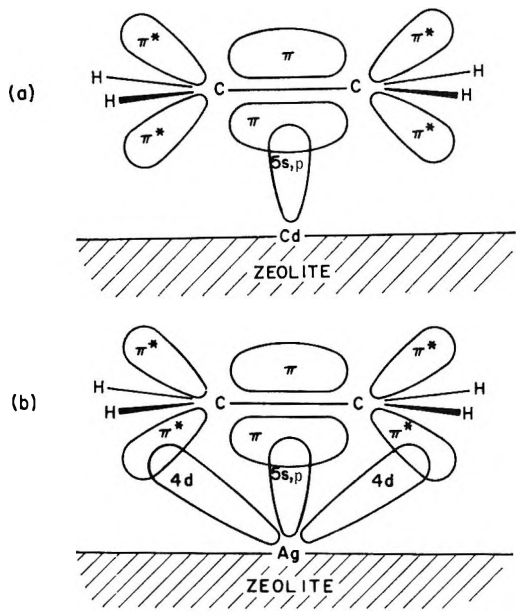

Figure 11. Schematic diagram showing the spatial arrangement of the orbitals involved in the bonding between ethylene and (a) Cd–X and (b) Ag–X.

the π orbital with a 5s,p hybrid is not certain. In our case, the silver ion occupies a fixed position in the zeolite lattice. It follows that any discussion of the orbitals involved in forming the olefin complex must, of necessity, rest upon some knowledge of the orbitals involved in the interaction between the silver ion and its neighboring atoms within the zeolite lattice. This interaction is not known, hence the bonding illustrated in Figure 11 can only be a hypothesis. However, it does appear more probable that the σ bond involves a hybrid 5s,p orbital rather than a pure 5s orbital, for the latter would place critical spatial and angular restrictions upon the now unhybridized 5p orbitals and hence upon their ability to participate in the interaction between the silver ion and its lattice neighbors.

The concept of back-donation of d electrons into the olefin π^* orbital appears to explain all of the features of the Ag–X spectrum. Because the silver ion is fixed in a crystal lattice, it is reasonable to assume that the d orbitals of the silver are also directionally fixed in space. Hence any strong interaction between these orbitals and the π^* orbital of the olefin would effectively prevent the olefin from rotating around the C_2 axis. The strength of such interaction compared to that of the σ bond is not known, though it has been suggested that they could well be of the same order of magnitude.[19]

From the legends of Figures 2 and 4 it will be seen that the $\Delta\nu_{1/2}$ of the A species for Ag–X are now larger than those for the A species of Cd–X. It should also be noted that the B species with Ag–X are broader than the A species for Cd–X. This can also be understood by the assumption that the d orbitals of silver that are participating in the complex are directionally fixed in space. Thus, the torsional mode that has now replaced the free rotation mode around the C_2 axis will now modulate both A and B species, for any motion away from the equilibrium position will result in a movement of d electrons which will have components parallel and perpendicular to the C_{2v} axis. This will modulate both the A and B species, but, of course, not to anything like the degree to which the B species was modulated by rotation of ethylene on Cd–X.

The concept of back-donation also explains the reduction in the intensity of the A-species bands for silver as compared to cadmium. For cadmium, the high intensity is due to the component of the dipole change parallel to the C_2 axis that originates in the motion of the electrons in the $\pi \rightarrow$ 5s,p donor bond. With silver, this component will still exist, but there will be an additional component parallel to the C_2 axis that originates from the motion of the electrons in the d$\rightarrow\pi^*$ donor bond (Figure 11). This latter dipole will be in phase with that from the $\pi \rightarrow$ 5s,p bond, but it will be in the opposite direction. Thus, to some degree, these components parallel to the C_2 axis will cancel, and thus we expect to find an over-all reduction in the intensity of the A species bands for Ag–X, compared to Cd–X.

It is possible that the difference between cadmium and silver in their ability to back-donate 4d electrons to the π^* orbitals of ethylene lies in their difference in ionic radii. Cadmium, a divalent ion, has an ionic radius of 0.98 A, compared to 1.26 A for the monovalent silver. This suggests that the filled 4d orbitals of cadmium do not reach sufficiently far out in space to overlap effectively, whereas those of silver do. However, it should be stressed that we do not know the distance between the adsorbed C_2H_4 and the Ag and Cd cations.

As the moderately held ethylene on Ag–X is removed to a considerable extent by evacuation at room temperature, it is more likely that these molecules are rotating than are the strongly held species. Unfortunately, it is not possible to determine whether or not the moderately held species are rotating, as the half-widths of the bands of these molecules are very difficult to measure accurately.

It should be noted that some of the simplicity of the spectra obtained with Cd–X may be due to the divalent nature of cadmium and the monovalent nature

(19) S. P. McGlynn, *Chem. Rev.*, 58, 1113 (1958).

of silver. For Na–X, there are at least two distinct positions of the Na^+ ions,[20] one in the bridge position and one in the cage position. Some of the ions were not located in that work, but more recent data[21] have shown the location of all the monovalent ions. Possibly, there are three distinct positions of Ag^+ ions, only two of which can adsorb ethylene. With Cd–X, there are only half as many cations per unit cell, and it is possible that only two of the above positions are occupied and that only one of these can adsorb ethylene. This could explain the extreme narrowness and constant frequency of the two A species lines on Cd–X (Figure 4).

In striking contrast to the spectra of ethylene adsorbed on Cd–X, the CH stretching bands of ethylene on Ag–X are extremely strong. It follows that it is most unlikely that the variations in CH stretching intensity are related to the energies of adsorption of the ethylene, as in both these cases the ethylene is strongly held to the zeolite. This is also shown by the fact that adsorbed ethylene on sodium, potassium, and barium zeolites has strong CH stretching bands and in all cases the adsorbed material can be readily removed by a short evacuation.

(*c*) *Relation between Spectroscopic Data and Heat of Adsorption.* Figure 10 shows that there is a well-defined relationship between the heat of adsorption of ethylene on a given zeolite and the shift in the double bond stretching frequency (ν_2) in the adsorbed ethylene. In all cases, the ν_2 vibration is found at lower frequencies than in the gas phase. Shifts to lower frequency are commonly observed[9] on going to condensed phases from the gas phase, but are usually smaller than are found in this work with Cd–X and Ag–X. For instance, in gaseous ethylene ν_2 is at 1623 cm^{-1}, decreasing to 1621 cm^{-1} in the liquid and to 1616 cm^{-1} in the crystal.[11] Frequencies for ν_2 lower than that of crystalline ethylene are found for ethylene adsorbed on the majority of the near-faujasites used in this work (Li, Na, K, Ba, and Ca). The heats of adsorption of ethylene on these zeolites, in agreement with the above shifts, are considerably higher (about 8–9 kcal/mole) than the heat of liquefaction. The heat of liquefaction of ethylene is 3.2 kcal/mole. Comparison with data obtained recently by Habgood,[22] using a gas chromatographic technique, is satisfactory. His isosteric values for Na–X and Ba–X (8.4 and 9.6 kcal/mole) are close to ours, but he reports a high value for Ca–X (19 kcal/mole). However, it is stated that the gc values for ΔH with Ca–X are uncertain.[22] The values for Ag–X are lower than we found, but it seems clear that the isosteric technique is only measuring the heat of adsorption of the more weakly held ethylene in the Ag–X lattice. In contrast, values of ΔH for mainly the strongly held ethylene were directly measured calorimetrically in our work.

With Ag–X and Cd–X, in contrast, the shift in ν_2 is much larger, and the heat of adsorption is much larger (double in the case of Ag–X). This shows directly that the ethylene is interacting with the zeolite *via* the double bond.

In this connection, the work of Quinn and Glew[23] on coordination compounds of olefins with silver salts is of interest. With ethylene and silver fluoroborate, a decrease in ν_2 of 38 cm^{-1} was observed for the $Ag\text{-}BF_4\text{-}2C_2H_4$ complex. This shift was observed relative to the ν_2 vibration of ethylene dissolved in carbon tetrachloride. Studies of the complexes of other olefins with silver fluoroborate showed that there was a linear relation between the enthalpy of formation of the complex and the shift in the double bond stretching frequency. In our work on the interaction between ethylene and the Ag^+ ions in zeolite X, a decrease of 52 cm^{-1} was observed for the most strongly held ethylene (Table V). It follows that the silver–ethylene complex formed on zeolite X should be more stable than the ethylene–silver fluoroborate complex. A similar observation of the stability of the C_2H_4—Ag–X species has been reported by Habgood,[22] who showed that some ethylene remained adsorbed at 100°. A more striking illustration of the stability of ethylene adsorbed on Ag–X is shown by the fact that some ethylene remained adsorbed after evacuation at 200° (Table IV). With this increased stability in the zeolite case, there is a corresponding increase in the shift of ν_2—14 cm^{-1} more than with silver fluoroborate. It is considered that, in view of the different ethylene environments in a solid complex such as that formed with silver fluoroborate and the surface complex formed with Ag–X, the differences in the ethylene ν_2 frequencies between these complexes are in qualitative agreement with the differences in stability. We have been unable to find any infrared data on Cd–olefin complexes for comparison with Cd–X data.

Acknowledgment. We wish to thank Dean B. L. Crawford, Jr., of the University of Minnesota, for helpful discussions on some spectroscopic aspects of this work.

(20) L. Broussard and D. P. Shoemaker, *J. Am. Chem. Soc.*, **82**, 1041 (1960).

(21) L. Broussard, private communication.

(22) H. W. Habgood, *Can. J. Chem.*, **42**, 2340 (1964).

(23) H. W. Quinn and D. N. Glew, *ibid.*, **40**, 1103 (1962).

Reactions of Tritium Atoms with Tritium-Labeled Isopropyl Radicals at 63°K[1]

by K. W. Watkins and H. C. Moser

Department of Chemistry, Kansas State University, Manhattan, Kansas *(Received October 11, 1965)*

DT, tritiated propene, and tritiated propane were obtained as products of reactions of tritium atoms with a solid mixture of propene-d_6 and isopentane (mole ratio 1:1000) at 63°K. These products are interpreted as having resulted from disproportionation and combination reactions of T atoms with i-C_3D_6T radicals. Disproportionation to combination ratios, k_d/k_c, for tritium atom reactions with i-C_3H_6T and i-C_3D_6T radicals at 63°K were determined to be 3.55 ± 0.05 and 3.05 ± 0.10, respectively. These ratios were used to calculate a value of 1.2 for the hydrogen–deuterium kinetic isotope effect, k_H/k_D, in the disproportionation reaction. The similarities of H atom–alkyl radical and alkyl–alkyl radical disproportionation and combination reactions are discussed.

Introduction

Reactions of hydrogen atoms with solid propene have been studied in our laboratory[2,3] and by others.[4-7] The atoms were produced by the atomization of molecular hydrogen at an incandescent tungsten filament in each case except one in which a microwave discharge was used. Under conditions where the hydrogen atoms reacted before reaching thermal equilibrium with solid propene at 77°K, hydrogen atom abstraction and nonterminal addition occurred along with terminal addition.[2] When the hydrogen atoms were thermalized to the temperature of the solid propene by collisions with helium, hydrogen atom addition to the terminal carbon appeared to be the only initial reaction.[2,3] In the presence of helium all of the products were explained by the disproportionation and combination reactions of isopropyl radicals.

Klein, Scheer, and Kelley[8] have recently demonstrated that a *sec*-butyl radical, produced by the addition of a hydrogen atom to *cis*-2-butene, can be trapped in 3-methylpentane long enough so that it reacts with another hydrogen atom before diffusing to another butyl radical. The products which they observed indicated that, in addition to the combination of a hydrogen atom and a *sec*-butyl radical, a little known reaction, hydrogen atom–alkyl radical disproportionation, also occurred. Heller and Gordon previously observed this type of reaction in the gas phase for ethyl[9] and isopropyl radicals.[10]

In the present paper the results of tritium atom reactions with tritium-labeled isopropyl radicals are reported. From measurements of the hydrogen yield new evidence in support of hydrogen atom–alkyl radical disproportionation is presented. Also, we have measured the disproportionation to combination ratios for T + i-C_3H_6T and for T + i-C_3D_6T at 63°K.

Experimental Section

Most of the experimental apparatus and techniques have been described,[11] including the reaction vessel.[2] The bath temperature of 63°K was obtained by using a slush of liquid and solid nitrogen. The slush was easily prepared by lowering the vapor pressure of nitrogen over the liquid nitrogen with a vacuum pump.

Films composed of 0.5 μmole of propene (Matheson CP grade) or propene-d_6 (99%, Volk Radiochemical

(1) From the Ph.D. Thesis of K. W. Watkins, Kansas State University, 1965. Work performed under Contract AT(11-1)584 with the U. S. Atomic Energy Commission.

(2) H. B. Yun and H. C. Moser, *J. Phys. Chem.*, 67, 2806 (1963).

(3) H. B. Yun and H. C. Moser, *ibid.*, 69, 1059 (1965).

(4) R. Klein, M. D. Scheer, and J. G. Waller, *ibid.*, 64, 1247 (1960).

(5) Y. P. Lomanov, A. N. Ponomarev, and V. L. Tal'roze, *Kinetika i Kataliz*, 3, 49 (1962).

(6) A. N. Ponomarev, *ibid.*, 4, 859 (1963).

(7) C. G. Hill, Jr., R. C. Reid, and M. W. P. Strandberg, *J. Chem. Phys.*, 42, 4170 (1965).

(8) R. Klein, M. D. Scheer, and R. Kelley, *J. Phys. Chem.*, 68, 598 (1964).

(9) C. A. Heller and A. S. Gordon, *J. Chem. Phys.*, 36, 2648 (1962).

(10) C. A. Heller and A. S. Gordon, *J. Phys. Chem.*, 64, 390 (1960).

(11) K. W. Watkins and H. C. Moser, *ibid.*, 69, 1040 (1965).

Co.) diluted with 500 μmoles of isopentane (99+%, Matheson Coleman and Bell) were treated with T atoms produced by the atomization of T_2 (pressure, 1×10^{-3} torr) at a hot tungsten filament. All reactions reported here were performed in the presence of 0.05 torr of helium (Airco assayed reagent grade). Tritium-containing products were counted by an ionization chamber placed in the effluent stream of a gas chromatograph. This technique allowed a complete analysis on as little as 2×10^{-6} μmole of products. The reaction times were from 5 to 15 sec for a filament temperature of 2025°K. During an average reaction, 2×10^{-4} μmole of tritium-labeled products was produced.

After the reaction, carrier (H_2 or D_2) was added, and the hydrogen products containing tritium (HT, DT, and T_2) were collected on Molecular Sieve 5A at 77°K. These products were separated by gas chromatography using a 6-ft column of moderately activated alumina at 77°K.[12]

The T_2 used in these experiments was obtained by separation from a sample containing a mixture of HT, T_2, and DT (~1%) which had been purified by diffusion through a heated palladium thimble. Separation of HT, T_2, and DT was performed by the alumina column, and the T_2 was trapped from the helium stream on Molecular Sieve 5A at 77°K. The molecular sieve trap was then attached to the vacuum system, and while maintaining the molecular sieve at 77°K, the helium was pumped off. Upon warm-up the T_2 expanded into the vacuum system and was used for production of tritium atoms.

Results

The products of tritium atom reactions with films of pure propene-d_6 and highly diluted propene-d_6 are shown in Table I. Each of the values represents an average from four reactions. Standard deviations are indicated. Smaller standard deviations were obtained if the per cent DT was left out of the averages. Table II compares the propene and propane products from light and perdeuterated propene. Yields of HT from T atom reactions with C_3H_6 are not reported because some HT was always formed as a product even in the C_3D_6 experiments which indicated that the HT could not be considered to result exclusively from reactions with C_3H_6. In experiments where the hydrogen yield (DT) was used as a measure of the T atom–isopropyl radical disproportionation reaction, C_3D_6 instead of C_3H_6 was used in order to eliminate the experimental difficulty owing to the formation of HT from parts of the system other than the hydrocarbon film. Thus, any DT formed by the reaction of T atoms with the C_3D_6 film could be considered to have originated only from reactions at the film.

Table I: Products of Reactions of Moderated Tritium Atoms with Solid Propene-d_6 at 63°K[a]

	% T in products	
	Film composition	
Product	100% propene-d_6	0.1% propene-d_6 in isopentane
DT	5.0 ± 0.4	36.9 ± 2.8
C=C—C	40.2 ± 2.4	35.5 ± 2.0
C—C—C	41.1 ± 1.2	27.5 ± 0.9
C—C—C |	13.6 ± 0.8	0
C—C—C		
C=C—C/	1.0	1.3
C—C—C		

[a] Conditions: filament temperature, 2025°K; 0.05 torr of helium moderator; and 10^{-3} torr of purified T_2.

Table II: Products of Reactions of Moderated Tritium Atoms with Propene and Propene-d_6 in Isopentane at 63°K

	% T in products[a]	
	Film composition	
Product	0.1% C_3D_6	0.1% C_3H_6
C=C—C	55.9 ± 1.2	59.7 ± 0.6
C—C—C	44.1 ± 1.2	40.3 ± 0.6
C—C—C |	0	0
C—C—C		
C=C—C/	1.27 ± 0.04	1.48 ± 0.02
C—C—C		

[a] Does not include DT or HT.

Discussion

Reactions of Atoms and Radicals. The hydrocarbon products shown in Table I from reactions of moderated tritium atoms with a film of pure propene-d_6 at 63°K are consistent with previous work and evidently result from isopropyl radical disproportionation and combination. Labeled isopropyl radicals were formed from tritium atom addition to propene.

When propene-d_6 was highly diluted with isopentane, the per cent of isopropyl radical dimer, 2,3-dimethylbutane, fell to zero and the per cent DT became equal to that of labeled propene to within experimental error. This effect resulted from changing two experimental conditions: (1) the concentration of propene and (2) a change of the film composition to reduce

(12) E. H. Carter, Jr., and H. A. Smith, *J. Phys. Chem.*, 67, 1512 (1963).

diffusion. Because of the small concentration of propene in the mixed film, isopropyl radicals are formed much farther apart than they are in a pure propene film. Also, the diffusion of isopropyl radicals in or on isopentane is probably slower than in pure propene, and the isopropyl radicals cannot diffuse to each other before encountering a tritium atom. The absence of 2,3-dimethylbutane from the products shows that isopropyl–isopropyl reactions did not occur. Under these conditions isopropyl radicals reacted only with tritium atoms. The products can be explained by reactions 1–4.

$$T + C_3D_6 \xrightarrow{k_1} CD_3CDCD_2T \quad (1)$$

$$T + i\text{-}C_3D_6T \xrightarrow{k_2} C_3D_5T + DT \quad (2)$$

$$T + i\text{-}C_3D_6T \xrightarrow{k_3} C_3D_6 + T_2 \quad (3)$$

$$T + i\text{-}C_3D_6T \xrightarrow{k_4} C_3D_6T_2 \quad (4)$$

These experiments with C_3D_6 represent the first quantitative measurement of the hydrogen formed from H atom–alkyl radical disproportionation. If all of the labeled propene is formed by reaction 2, then an equal quantity of DT must be formed. The data in Table I show that within experimental error DT and propene were formed in equal amounts. Thus, good evidence was obtained for tritium atom–isopropyl radical disproportionation.

Consecutive reactions of tritium atoms with product propene molecules were not evident. The product distributions used to calculate the averages in Table II did not vary, even though the tritium incorporated into the products varied over a range of 85-fold for C_3H_6 and a range of sixfold for C_3D_6. If consecutive reactions were important, the per cent labeled propene should have decreased as more tritium was incorporated into products.

Lomanov, Ponomarev, and Tal'roze[5] observed the formation of HD when deuterium atoms were treated with solid isobutene at 77°K and attributed HD formation to reaction 5. However, the activation energy

$$D + t\text{-}C_4H_8D \longrightarrow t\text{-}C_4H_7D_2 + H \quad (5)$$

requirements are too large for this reaction to occur between atoms and radicals thermalized to 77°K, whereas hydrogen atom–alkyl radical disproportionation, if it is similar to alkyl radical disproportionation, would require essentially no activation energy and could easily occur at 77°K. Also, the equivalent yields of DT and propene reported here would not be expected from reaction 5, which does not form an olefin product.

Disproportionation to Combination Ratio. The ratio of disproportionation to combination (k_d/k_c) is

$$\frac{k_d}{k_c} = \frac{k_2 + k_3}{k_4} \quad (6)$$

The ratio of tritium in propene to tritium in propane, propene(T)/propane(T), was used to calculate k_d/k_c. The ratio k_2/k_4 was taken as

$$\frac{k_2}{k_4} = \frac{2\text{propene(T)}}{\text{propane(T)}} \quad (7)$$

Multiplication by 2 corrects for the occurrence of two tritium atoms in propane(T). Since k_3 results in nonlabeled propene, it could not be measured. The value k_3 was assumed to be $^1/_5k_2$ since there are five deuterium atoms and one tritium atom that can be transferred randomly in disproportionation if isotope effects are neglected. The ratio of disproportionation to combination was calculated from eq 8. For T + i-C_3H_6T, k_d/k_c was calculated to be 3.55 ± 0.05, while for T + i-C_3D_6T, k_d/k_c was calculated as 3.05 ± 0.10.

$$\frac{k_d}{k_c} = \frac{k_2}{k_4} + \frac{^1/_5k_2}{k_4} = \frac{2(^6/_5)\text{propene(T)}}{\text{propane(T)}} \quad (8)$$

An estimate of the hydrogen–deuterium kinetic isotope effect, k_H/k_D, on the disproportionation reaction was obtained from values of k_d/k_c for T + i-C_3H_6T and T + i-C_3D_6T. The rate of combination, k_c, was assumed to be the same for both radicals. This amounts to neglecting a possible inverse secondary isotope effect. The primary isotope effect was calculated as follows.

$$\frac{k_H}{k_D} \cong \frac{k_d/k_c(T + i\text{-}C_3H_6T)}{k_d/k_c(T + i\text{-}C_3D_6T)} \cong 1.2 \quad (9)$$

The effect of isotopic substitution on k_d/k_c is very small and shows that neglecting an isotope effect in calculating k_d/k_c is a reasonable approximation.

Comparison of Radical–Radical and Hydrogen Atom–Radical Reactions. Hydrogen atom–alkyl radical disproportionation and combination exhibit several similarities to alkyl–alkyl radical disproportionation and combination. In both cases small hydrogen kinetic isotope effects on disproportionation were observed at 63°K. In alkyl–alkyl radical reactions this effect was considered to support the concept of a "loose" transition state for disproportionation.[3,11] A loose association of the H atom and the alkyl radical in the transition state for disproportionation is also proposed here. In both cases the rate of disproportionation increases relative to combination as the temperature decreases, indicating that the activation energy for combination (E_c) is higher than the activation energy for disproportionation (E_d). Using the values k_d/k_c = 0.2 for deuterium atom–isopropyl radical reactions at

361°K[9] and k_d/k_c = 3.55 for tritium atom–isopropyl radical reactions at 63°K, an activation energy difference of $E_c - E_d$ = 0.43 kcal/mole was calculated. This calculation was done by making the assumption that the k_d/k_c ratio is dependent exclusively upon the temperature and is not affected by a change in the phase. A small activation energy difference of 0.42 kcal/mole with combination having the higher activation energy would also explain the difference in k_d/k_c values for isopropyl radical disproportionation and combination at 373 and 77°K, 0.64[13] and 5.5, respectively. The value of k_d/k_c of 0.8 for ethyl radicals at 63°K[11] is consistent with the gas phase value of 0.13 at 273°K[14] for an activation energy difference of $E_c - E_d$ = 0.3 kcal/mole which is essentially the same dependence that was first reported in the gas phase.[14] Other small activation energy differences of the same magnitude with $E_c - E_d$ have been reported for isopropyl–isopropyl and *sec*-butyl–*sec*-butyl radical disproportionation and combination.[8]

(13) C. A. Heller and A. S. Gordon, *J. Phys. Chem.*, 60, 1315 (1956).
(14) P. S. Dixon, A. P. Stefani, and M. Szwarc, *J. Am. Chem. Soc.*, 85, 2551 (1963).

A Study of Some Concentration Cells with Liquid Ion-Exchanger Membranes

by O. D. Bonner and David C. Lunney[1]

Department of Chemistry, University of South Carolina, Columbia, South Carolina *(Received October 11, 1965)*

Concentration potentials of cells in which two aqueous electrolyte solutions are separated by a liquid ion exchanger (an oil phase with ion-exchange properties) have been measured for aqueous NaCl, NH_4Cl, and $CaCl_2$ solutions, using organic solutions of dinonylnaphthalenesulfonates as the liquid exchangers, for aqueous HCl solutions using General Mills Aliquat 336 and Humko Kemamine Q-1902-C exchangers, and for *p*-toluenesulfonic acid solutions, using Humko Kemamine Q-1902-C exchanger. The behavior of the cells is analogous to that of concentration cells with solid ion-exchange membranes; their failure to reach the theoretical potential for cells with ideally permselective membranes is explained by considering the solubility of the exchanger in the aqueous phase and transport of water across the organic phase by hydrated ions. Activity coefficients were calculated from data obtained for *p*-toluenesulfonic acid, and they agree well with activity coefficients determined isopiestically.

Introduction

The electrochemical properties of cells of the type

electrode	electrolyte solution 1	ion-exchange membrane	electrolyte solution 2	electrode

have been studied intensively since about 1935, but very little attention has been given to cells in which the membrane is a liquid ion exchanger (an organic solution of a water-insoluble ionogen). In 1953 and 1954 Bonhoeffer, Kahlweit, and Strehlow[2] reported potentials of concentration cells in which two aqueous LiCl solutions were separated by an oil phase consisting of quinine hydrochloride in quinoline. The observed potentials fell far short of those obtainable with conventional ion-exchange membranes. In 1964, Sollner and Shaen[3] reported that they had obtained concentra-

(1) National Science Foundation Graduate Fellow.
(2) K. F. Bonhoeffer, M. Kahlweit, and H. Strehlow, *Z. Elektrochem.*, 57, 614 (1953); *Z. Physik. Chem.* (Frankfurt), 1, 21 (1954).

tion potentials within several tenths a millivolt of the theoretical values for cells using benzene, xylene, and nitrobenzene as solvents for Rohm and Haas Amberlite LA-2 anion exchanger in the chloride form.

The work described here was initially undertaken for the purpose of developing a cell suitable for the measurement of activity coefficients of high molecular weight disulfonic acids; conventional ion-exchange membranes were unsuitable for this application because of their small pore sizes. Sollner, *et al.*,[4,5] for example, have described membranes of graded porosity prepared by adsorbing polyelectrolytes on collodion films. Their least porous membranes have excellent permselectivity but will hold back molecules larger than urea, while membranes with sufficiently large pores for our application have poor permselectivity. Liquid ion exchangers, however, can admit very bulky ions, and their permselectivity is very high for electrolytes which are much more soluble in the aqueous phase than in the organic phase.

Experimental Section

Liquid Cation-Exchanger Materials. Sodium dinonylnaphthalenesulfonate (NaDNNS) was prepared by adding sodium hydroxide in ethanol to the sulfonic acid in heptane as received from King Organic Chemical Co. until the solution was strongly basic. The heptane–sulfonate solution was separated by adding a large quantity of water. The heptane layer was washed four or five times with water, and the heptane was evaporated. The product was then weighed and dissolved in *o*-dichlorobenzene to make a stock solution. Ammonium dinonylnaphthalenesulfonate (NH_4DNNS) was similarly prepared from the sulfonic acid and alcoholic ammonia solution.

Calcium dinonylnaphthalenesulfonate ($Ca(DNNS)_2$) was prepared by equilibrating a heptane solution of the acid with several portions of 1 *M* $CaCl_2$ solution; the heptane layer was shaken with a saturated solution of $Ca(OH)_2$ to ensure complete conversion. The heptane layer was then washed and evaporated by the same method used for the sodium and ammonium sulfonates. In all instances, the washing effectively removed all water-soluble materials from the organic phase.

Liquid Anion-Exchanger Materials. Liquid anion exchangers were prepared from General Mills Aliquat 336 and from Kemamine Q-1902-C, manufactured by the Humko Chemical Division of National Dairy Products Co.

Aliquat 336 was furnished as a mixture of crystals and syrupy solution in toluene and 2-propanol. This was diluted with toluene, washed five times with distilled water to remove 2-propanol, and evaporated under vacuum with a rotary evaporator in a hot water bath. The resulting syrup was diluted with *o*-dichlorobenzene to make a stock solution.

Humko Kemamine Q-1902-C is a white, waxy solid consisting of dialkyldimethylammonium chlorides in which the alkyl groups contain from 20 to 22 carbons. It is almost insoluble in heptane, nitrobenzene, *o*-dichlorobenzene, and toluene at room temperature, but is very soluble in chloroform. To prepare the chloride exchanger the solid was dissolved in chloroform, washed twice with about 1 *M* HCl to ensure complete conversion to the chloride, then washed four to five times with water to remove excess HCl. The resulting stock solution contained about 10% Kemamine chloride.

Kemamine Q-1902-C was converted to the *p*-toluenesulfonate by dissolving it in chloroform and shaking the solution with portions of 1 *M* aqueous *p*-toluenesulfonic acid until the sulfonic acid picked up no detectable chloride. The chloroform layer was then washed with distilled water and used as a stock solution.

Solvents for Exchanger Solutions. The primary purity criterion for solvents used in this work was low conductivity and freedom from water-soluble impurities. Commercial *p*-dichlorobenzene was purified by passing it through a column of activated alumina and storing it over alumina; this reduced its conductivity to less than 10^{-9} ohm^{-1} cm^{-1}. Nitrobenzene was purified by distilling it, storing it over activated alumina, and washing it four or five times with distilled water immediately before use, or by washing undistilled nitrobenzene four or five times with saturated aqueous sodium bicarbonate,[6] four or five times with water, and passing it through a column of activated alumina. These methods produced nitrobenzene with a conductivity between 1.3 and 2 $\times$ 10^{-9} ohm^{-1} cm^{-1} (wet). Commercial chloroform was used without purification since its conductivity was only 2.5 $\times$ 10^{-9} ohm^{-1} cm^{-1}.

Exchanger solutions were prepared by diluting the stock solutions to the desired concentrations, washing four or five times with distilled water, and separating the emulsified organic layer. Used exchangers were recovered by repeating the washing and separation procedure.

(3) K. Sollner and G. M. Shaen, *J. Am. Chem. Soc.*, **86**, 1901 (1964).

(4) C. W. Karr, R. McClintock, and K. Sollner, *J. Electrochem. Soc.*, **109**, 251 (1962).

(5) M. H. Gottlieb, R. Neihof, and K. Sollner, *J. Phys. Chem.*, **61**, 154 (1957).

(6) J. B. Ezell, unpublished doctoral dissertation, University of South Carolina.

Aqueous Solutions. The most concentrated solution of each chloride was prepared by weight from the carefully dried salt, then used as a stock solution for preparation of the more dilute solutions. All of the chlorides were Baker and Adamson reagent grade and were subjected to no purification except drying.

Acid solutions were prepared by weight from stock solutions whose concentrations had been determined by titrating three weighed aliquots with freshly standardized NaOH solution. The most concentrated solution of each acid was then used as a stock solution to prepare the more dilute solutions, except for 10^{-4} *m* solutions, which were made from the 0.01 *m* solutions. Baker and Adamson CP hydrochloric acid was used without purification. Matheson Coleman and Bell *p*-toluenesulfonic acid was found to be sulfate free and was also used without purification.

Electrodes. Silver–silver chloride electrodes were made by a method similar to that of Bonner and Smith.[7] Platinum wires sealed in soft-glass tubing were washed with concentrated nitric acid and rinsed well with distilled water, then plated for 6–12 hr in 0.2 *M* $NaAg(CN)_2$ solution at a current density of about 10 ma/cm^2. The plated wires were washed with dilute ammonia and soaked in distilled water, then anodized in 1 *M* HCl at about 5 ma/cm^2 for 30–45 min. The completed electrodes were stored in distilled water or dilute HCl and were usually reliable for 6 weeks or more.

Two matched Beckman glass electrodes with mercury internals were used for the HCl and *p*-toluenesulfonic acid measurements. They were calibrated against a silver–silver chloride electrode in HCl solutions from 10^{-3} to 1.0 *m;* the corrections obtained were applied to the data reported herein for HCl and *p*-toluenesulfonic acid. The correction for 10^{-4} *m* HCl was obtained by extrapolating the calibration curve.

Electrical Measurements. Cell potentials were measured with a Beckman Research pH meter, which is reproducible to ±0.05 mv and has an absolute accuracy of ±0.37 mv over its 1500-mv span. The cell was contained in a shielded box maintained at 25.0° by an air thermistor and control amplifier. In initial experiments, attempts were made to use static cells, but these exhibited extremely poor performance because of the surface-active nature of the materials. The cell described below in which all surfaces were continually renewed was necessary to give reproducible results.

The Cell. The cell used in this work is shown in Figure 1. The liquid ion exchanger flowed from 1.5-mm capillaries C into the aqueous solutions contained in two polyethylene beakers B. The fine glass frit

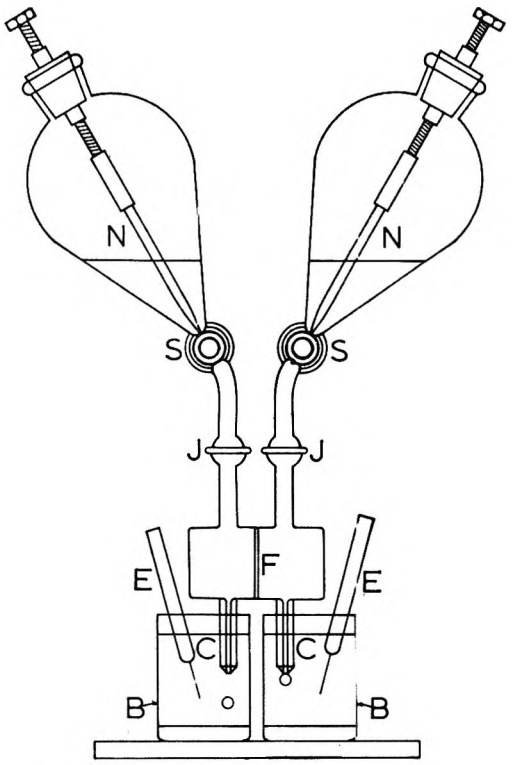

Figure 1. Flowing cell for liquid ion exchangers.

F across the lower compartment allowed the drop rates to be independently adjusted with the two needle valves N, while maintaining a low-resistance electrical path through the cell. The reservoirs were ordinary pear-shaped separatory funnels attached by the ball joints J. The beakers rested on a laboratory jack which allowed them to be lowered to clear the capillaries; the electrodes E were held in clamps attached to the jack platform. When both beakers contained identical solutions, the cell developed an asymmetry potential (about 1 mv), but it was usually reproducible. The effect of the asymmetry was canceled by repeating each emf reading several times and interchanging the two beakers after each reading until two pairs of readings were reproduced within ±0.2 mv. When glass electrodes were used, this procedure also canceled the emf arising from their differing asymmetry potentials (about 5 mv). It was found that the following conditions must be met to obtain a sharp interface (no emulsion) and thus proper operation of the cell.

(1) The capillaries must be rendered hydrophobic to prevent water from wetting their inner walls. They were treated with Siliclad silicone and coated with Dow-Corning silicone grease dissolved in methylene chloride. If the inner walls of the capillaries were

(7) O. D. Bonner and L. L. Smith, *J. Phys. Chem.*, 64, 261 (1960).

allowed to become wet with water, a large unreproducible asymmetry potential developed, and the cell emf became too noisy to be readable.

(2) The capillary tips must be ground at an angle as shown in Figure 1 and rendered hydrophobic to encourage the formation of well defined drops. This was not critical for the anion exchangers but was indispensable for cation exchangers; failure to form clean drops of cation exchanger produced noisy, unreproducible potentials.

The cell worked well with drop rates ranging from the 2 drops/sec to 1 drop/10 sec. The emf usually oscillated as drops separated from the capillary tips, but the amplitude of the oscillation was below 0.1 mv for cation exchangers when the cell was operating properly. Anion exchangers were in general noisier because the drops did not separate cleanly from the capillaries but wet the external conical tips; this caused a sharp pulse of several tenths of a millivolt as each drop fell, after which the emf would return to its former value. The input of the Beckman Research pH meter is shunted by a 0.001-μf capacitor which charged during the pulses and discharged slowly through the high resistance of the cell, so a very slow drop rate (about 1 drop/10 sec) was used to ensure that the emf could return to its equilibrium value between drops.

Anion exchangers were also slower to reach constant potentials than cation exchangers. With cation exchangers the potential usually reached its equilibrium value within about 5 min, while anion exchangers required as long as 30 min to reach a constant potential.

Results and Discussion

Concentration potentials obtained with the cell in Figure 1 for NaCl, NH_4Cl, and $CaCl_2$ solutions are given in Figure 2. In every case silver–silver chloride electrodes were used, and the cation exchanger was the corresponding dinonylnaphthalenesulfonate in 50% nitrobenzene–50% *o*-dichlorobenzene by volume; the exchanger concentration was 0.02 *M*. Activity coefficients for KCl tabulated by Pitzer and Brewer[8] were used for NH_4Cl up to 0.1 *m* because the activity coefficients of KCl and NH_4Cl are almost identical up to 2.0 *m*.[9] Activity coefficients for 0.003 and 0.03 *m* $CaCl_2$ were obtained by interpolation.

Data obtained for HCl with glass electrodes and anion exchangers are shown in Figure 3. The theoretical potentials shown were calculated from activity coefficients tabulated by Robinson and Stokes.[10] Solvents used for the anion exchangers were *o*-dichlorobenzene for Aliquat 336 and 50% chloroform–50% nitrobenzene by volume for Kemamine Q-1902-C.

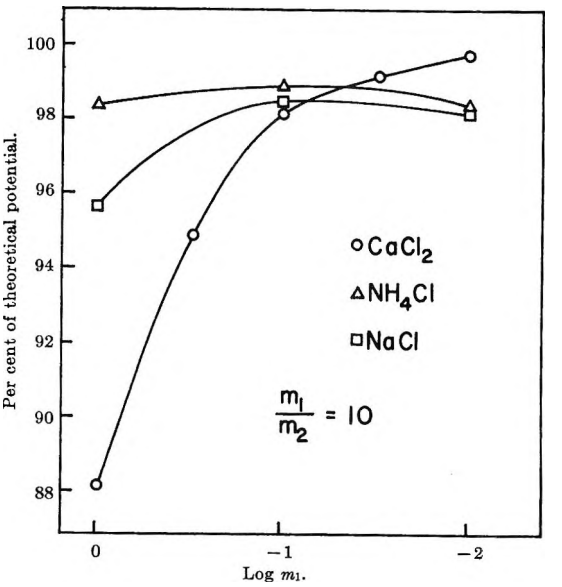

Figure 2. Concentration potentials obtained with dinonylnaphthalenesulfonate cation exchangers.

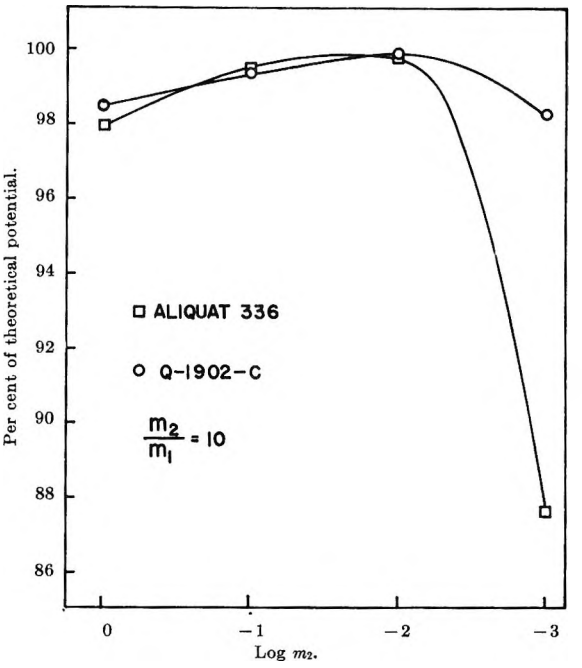

Figure 3. Concentration potentials obtained for HCl solutions with anion exchangers.

These solvents were chosen because of their relatively high dielectric constants and low solubility in water

(8) G. N. Lewis and M. Randall, "Thermodynamics," revised by K. S. Pitzer and L. Brewer, 2nd ed, McGraw-Hill Book Co., Inc., New York, N. Y., 1961.

(9) B. F. Wishaw and R. H. Stokes, *Trans. Faraday Soc.*, **49**, 27 (1953).

(10) R. A. Robinson and R. H. Stokes, "Electrolyte Solutions," Academic Press Inc., New York, N. Y., 1959.

except in the case of chloroform, a choice necessitated by the virtual insolubility of Kemamine Q-1902-C in our usual solvents.

In discussing our results we shall use the quasi-thermodynamical approach of Scatchard.[11] For any cell with a transference across a membrane he writes

$$\frac{\mathcal{E}F}{RT} = \frac{\mathcal{E}^\circ_\alpha F}{RT} - \frac{\mathcal{E}^\circ_\omega F}{RT} - \sum \nu_{i\alpha} \ln a_{i\alpha} - \sum \nu_{i\omega} \ln a_{i\omega} - \sum \int_\alpha^\omega t_i \mathrm{d} \ln a_i \quad (1)$$

where the subscripts α and ω refer to the left and right compartments, respectively, and a_i is the activity of species i; $\nu_{i\alpha}$ and $\nu_{i\omega}$ are the number of moles of species i produced at the left and right electrodes and t_i is the number of moles of species i transported from left to right when 1 faraday of negative charge flows reversibly from left to right in the external circuit. $\mathcal{E}^\circ_\alpha$ and $\mathcal{E}^\circ_\omega$ are the standard electrode potentials of the left and right electrodes, $\mathcal{E}$ is the cell potential, F is the faraday, and R and T are the gas constant and the temperature, respectively. It can be shown that for a cation-exchanger membrane with electrodes reversible with respect to the anion equation (1) is equivalent to

$$\mathcal{E}F = -RT\left(\frac{1}{z_M} - \frac{1}{z_X}\right) \ln \frac{m_\omega \gamma_\omega}{m_\alpha \gamma_\alpha} + RT \frac{n_M(A + B)}{55.5 z_M} \times (m_\omega \phi_\omega - m_\alpha \phi_\alpha) - \frac{z_M + z_X}{(A + B) z_M} \int_\alpha^\omega t_X \mathrm{d}\mu_{M_A X_B} \quad (2)$$

where m_α and m_ω are the molalities of the electrolyte $M_A X_B$ in the left and right compartments; z_M and z_X are the ionic charges of the cation and anion; n_M is the hydration number of the cation in the organic phase and the γ's and ϕ's are mean activity coefficients and osmotic coefficients, respectively.

The first term in eq 2 is the theoretical emf for an ideally permselective membrane, the second term is a correction for water transport, and the third term is a correction for leakage of coion. We would expect the error due to water transport to be large at high concentrations and to go in the order $Ca^{2+} > Na^+ > NH_4^+ \approx Cl^-$; examination of Figures 2 and 3 shows that this is indeed the case. The error due to leakage is probably negligible in the data reported here. Sollner and Shaen[2] have reported that the ionic selectivities of the liquid anion exchanger Amberlite LA-2 range from 100,000 to 400,000 for aqueous solutions of alkali metal salts; this indicates that the effect of the integral in eq 2 should be negligibly small compared to other errors, even if our exchanger is a great deal less selective than Sollner's. For electrolytes which are appreciably soluble in the organic phase, however, the liquid exchanger membrane would leak, and the integral would then be significant.

The sources of error thus far discussed are common to both solid and liquid ion-exchanger membranes. There are two additional errors present in liquid exchangers: the effects of solubility of the exchanger and those of the organic solvent in the aqueous phases. The effect of the organic solvent on the activities of aqueous electrolytes is not predictable from any simple theoretical treatment; the error can be minimized, however, by using solvents with very low solubility in water. The effect of exchanger solubility can be treated more rigorously. Let us consider the cell

$$\mathrm{Ag,AgX} \left| \begin{matrix} \mathrm{MX}(m_\alpha) \\ \mathrm{MR}(m_\alpha^*) \end{matrix} \right| \begin{matrix} \mathrm{MR\ in} \\ \mathrm{organic} \\ \mathrm{solvent} \end{matrix} \left| \begin{matrix} \mathrm{MX}(m_\omega) \\ \mathrm{MR}(m_\omega^*) \end{matrix} \right| \mathrm{AgX,Ag}$$

We assume that both aqueous solutions are in equilibrium with the organic phase, so that the chemical potential of the organic salt MR is the same in all three phases. Ignoring transport of water and X^- ions yields

$$\begin{aligned} \mathcal{E}F &= -(\mu_{X\omega} - \mu_{X\alpha}) - \int_\alpha^\omega t_R \mathrm{d}\mu_R - \int_\alpha^\omega t_M \mathrm{d}\mu_M \\ &= -(\mu_{X\omega} - \mu_{X\alpha}) - (\mu_{M\omega} - \mu_{M\alpha}) - \int_\alpha^\omega t_R \mathrm{d}\mu_{MR} \\ &= -RT \ln \frac{a_{MX\omega}}{a_{MX\alpha}} - \int_\alpha^\omega t_E \mathrm{d}\mu_{MR} \end{aligned}$$

Since the chemical potential of MR is the same in all three phases, the integral is zero. We now assume that the presence of a low concentration of MR in the aqueous solutions does not change the activity coefficients of the ions M^+ and X^-. If MR is regarded as being completely ionized in aqueous solutions, we obtain

$$a_{M\alpha} = \gamma_{M\alpha}(m_\alpha + m_\alpha^*) \qquad a_{M\omega} = \gamma_{M\omega}(m_\omega + m_\omega^*)$$

$$a_{MX\alpha} = \gamma_\alpha^2 m_\alpha^2 \left(1 + \frac{m_\alpha^*}{m_\alpha}\right) \qquad a_{MX\omega} = \gamma_\omega^2 m_\omega^2 \left(1 - \frac{m_\omega^*}{m_\omega}\right)$$

where γ_α and γ_ω are mean activity coefficients of MX. The cell potential now becomes

$$\mathcal{E} = -\frac{2RT}{F} \ln \frac{m_\omega \gamma_\omega}{m_\alpha \gamma_\alpha} - \frac{2RT}{F} \ln \frac{\left(1 + \frac{m_\omega^*}{m_\omega}\right)}{\left(1 + \frac{m_\alpha^*}{m_\alpha}\right)} \quad (3)$$

The first term is the theoretical potential, and the

(11) G. Scatchard, *J. Am. Chem. Soc.*, **75**, 2853 (1953).

second term is a correction for solubility of the exchanger.

We would expect this correction to increase rapidly in dilute solutions. This is seen in the HCl data obtained with Aliquat 336 (Figure 3). For $10^{-3}/10^{-2}$ m HCl the error is only 0.1%; for $10^{-4}/10^{-3}$ m HCl it increases to more than 12%. Furthermore, the observed potential for $10^{-4}/10^{-3}$ m HCl decreased with time as the aqueous solutions became saturated with the exchanger. The relatively high solubility of Aliquat 336 in water is also indicated by the fact that the conductivity of the *o*-dichlorobenzene-exchanger solution decreased by about 25% when it was washed four times with water.

Studies of the Kemamine anion exchanger and HCl were quite promising, however, and encouraged an attempt to measure activity coefficients for a sulfonic acid. *p*-Toluenesulfonic acid was chosen for the first attempt because its activity coefficients have been accurately determined isopiestically down to 0.1 m.[12] The results obtained with Kemamine Q-1902-C are shown in Table I. The exchanger solvent was 50% chloroform–50% nitrobenzene by volume.

Table I: Concentration Potentials for *p*-Toluenesulfonic Acid Obtained with Kemamine Q-1902-C in 50% $C_6H_5NO_2$–50% $CHCl_3$[a]

m_1/m_2	Obsd emf, mv
0.0001/0.001	126.91
0.001/0.01	115.56
0.003/0.03	112.73
0.01/0.10	110.00
0.03/0.30	106.33
0.001/0.003	56.06
0.003/0.01	59.26
0.01/0.03	53.38
0.03/0.10	56.69
0.10/0.30	49.82

[a] Exchanger conductivity, 9.3×10^{-5} ohm^{-1} cm^{-1}.

The activity coefficients reported in Table II were calculated from the data in Table I by choosing 0.003 m as a reference concentration, calculating the potentials for all other solutions against the reference (using every possible sum of experimental emf values and averaging the results), and plotting the function[8]

$$\frac{\mathcal{E}}{118.3} - \log \frac{m}{m'} = \log \gamma - \log \gamma'$$

where m' and γ' are the molality and mean activity coefficient for the 0.003 m reference solution, respectively. Extrapolation of this function to $m = 0$ gives the value of γ'. The extrapolation was taken along the Debye–Hückel limiting slope, which is equivalent to assuming that *p*-toluenesulfonic acid obeys the limiting law up to 0.003 m. This procedure is justified by the fact that the curve between 0.003 and 0.01 m deviates only minutely from the limiting slope. Points for 0.001 and 0.0001 m solutions were ignored in making the extrapolation because their inclusion would have led to grotesque deviations from the limiting law. The high potentials observed for solutions below 0.003 m are probably attributable to the effect of the organic solvent of the exchanger on the activity of *p*-toluenesulfonic acid in the aqueous phases since all the other sources of error lead to potentials lower than the theoretical. This is predicated on the assumption that we have written the cell reaction correctly, *i.e.*, that current is carried only by the *p*-toluenesulfonate ion. If an appreciable fraction of current were carried by a dimer with a single negative charge, the observed emf would be higher than the value calculated from our assumed cell reaction. Attempts to apply the method described here to measurement of activity coefficients of disulfonic acids may not be feasible because of inability to specify a unique cell reaction, *i.e.*, if the acid HSO_3RSO_3H dissociates incompletely, so that some current is carried by the ion $HSO_3RSO_3^-$.

Table II: Activity Coefficients of *p*-Toluenesulfonic Acid

	−Log	Emf data		Isopiestic data[12]	
m	γ	γ	ϕ	γ	ϕ
0.003	0.0279	0.938	...	...	...
0.01	0.0495	0.892	...	...	...
0.03	0.0754	0.841	...	...	...
0.10	0.1195	0.759	0.923[a]	0.759	0.922
0.30	0.1483	0.667	0.894[a]	0.660	0.887

[a] Calculated by graphical integration of $1 - \phi = -(1/m)\int m d \ln \gamma$

In summary, we believe that we have described a method of some potential usefulness in measuring activity coefficients of bulky electrolytes for which cells with solid ion-exchange membranes would be unsuitable. At the present stage, however, great care must be exercised in the choice of the exchanger and solvent, and data are reliable only over the approximate range $3 \times 10^{-1} > m > 3 \times 10^{-3}$.

(12) O. D. Bonner, G. D. Easterling, D. L. West, and V. F. Holland, *J. Am. Chem. Soc.*, 77, 242 (1955).

Acknowledgments. The authors gratefully acknowledge the assistance of Charles F. Jumper and William J. Sutton, who did the preliminary work on this problem. The project was partially supported by the Atomic Energy Commission under Contract No. AT-(40-1)-1437.

Boron Isotope Exchange between Boron Fluoride and Its Alkyl Halide Complexes. II.[1] Infrared Spectrum of Boron Fluoride–Methyl Fluoride Complex

by Ryohei Nakane and Toshiyuki Ōyama

The Institute of Physical and Chemical Research, Bunkyo-ku, Tokyo, Japan *(Received October 15, 1965)*

The infrared spectra of liquid $B^{10}F_3$, $B^{11}F_3$, CH_3F, $B^{10}F_3 \cdot CH_3F$ complex, and $B^{11}F_3 \cdot CH_3F$ complex are observed in the region from 400 to 4000 cm^{-1}. The isotopic data are used to calculate the theoretical equilibrium constant for boron isotope exchange between gaseous boron fluoride and its methyl fluoride complex. The calculated values are found to agree fairly well with observed values.

Previously, one of the authors found that, for boron isotope exchange, the equilibrium constant is much smaller between gaseous boron fluoride and weak boron fluoride complexes in the liquid form than between gaseous boron fluoride and strong boron fluoride complexes in the liquid form. Namely, with boron fluoride–alkyl halide complexes[1] or boron fluoride–alkyl halide–alkylbenzene 1:1:1 addition oriented π complexes,[2] which exist only at low temperatures, the constant is much smaller than with boron fluoride–ether complexes which are stable even at room temperature. The known infrared spectra of gaseous boron fluoride[3] and liquid boron fluoride–ether complexes[4] were used to calculate the theoretical equilibrium constant for boron isotope exchange. In the present work, the infrared spectrum of liquid boron fluoride–methyl fluoride complex was observed at low temperatures and the equilibrium constants, observed and calculated from isotopic data of infrared spectrum, were compared.

Experimental Section

For the measurements of infrared spectra at low temperatures a cell as shown in Figure 1 was made. The specimen to be studied was introduced into the space between two KRS-5 plates (1 cm diameter by 5 mm thick) A and A′, between which spacer B of Teflon was inserted to give a space of about 0.05 mm thickness. The two KRS-5 plates were firmly held in brass holder C with two Teflon gaskets D and D′ for vacuum tightness. The cryostat was a stainless steel dewar with two KRS-6 plate windows (2 cm diameter by 3 mm thick), E and E′. The thickness,

(1) Part I: R. Nakane, O. Kurihara, and A. Natsubori, *J. Phys. Chem.*, **68**, 2876 (1964).

(2) R. Nakane, A. Natsubori, and O. Kurihara, *J. Am. Chem. Soc.*, **87**, 3597 (1965).

(3) J. Vanderryn, *J. Chem. Phys.*, **30**, 331 (1959).

(4) A. A. Palko, G. M. Begun, and L. Landau, *ibid.*, **37**, 552 (1962); G. M. Begun and A. A. Palko, *ibid.*, **38**, 2112 (1963); G. M. Begun, W. H. Fletcher, and A. A. Palko, *Spectrochim. Acta*, **18**, 655 (1962).

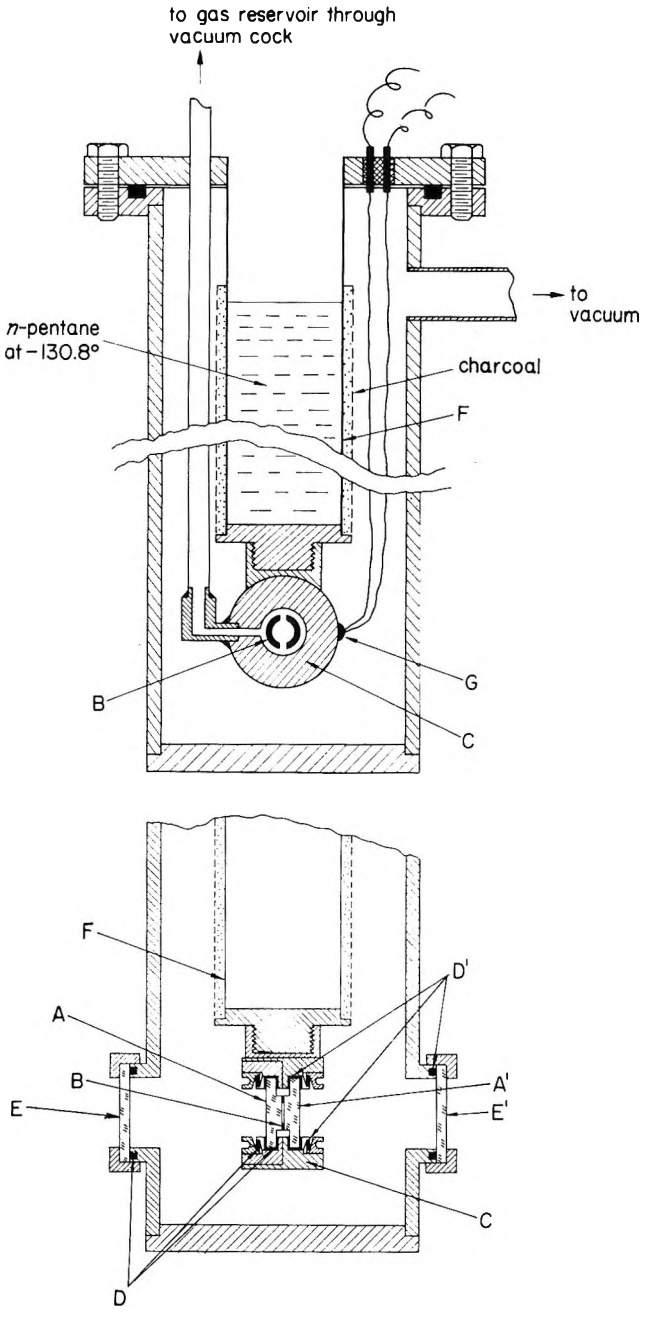

Figure 1. Low-temperature absorption cell.

3 and 5 mm, of KRS plates, though detrimental to infrared work, was necessary to assure the strength of the plates.

Experiments were made as follows. After evacuating the cryostat to dewar vacuum, liquid nitrogen was poured into center tube F of the cell, the outer surface of which was coated with charcoal to hold dewar vacuum for a long time. The specimen gases were then introduced one after another through a vacuum cock into the cell and solidified in holder C. When *n*-pentane at its melting point (−130.8°) was poured into tube F, the solid specimen in C melted, and at this instant the thermocouple G attached on the outer surface of C indicated approximately −105°. The cell window was placed directly in the radiation path of a Perkin-Elmer Model 521 grating infrared spectrometer.

Enriched $B^{10}F_3$ was obtained by multiplying boron isotope exchange between boron fluoride gas and boron fluoride–anisole complex; it was analyzed as 95 atom % B^{10}.[5] In place of enriched $B^{11}F_3$, normal boron fluoride was used. Methyl fluoride was prepared from methyl tosylate by reaction with potassium fluoride.[6]

Results and Discussion

The infrared spectra of liquid $B^{10}F_3$, $B^{11}F_3$, CH_3F, $B^{10}F_3 \cdot CH_3F$ complex, and $B^{11}F_3 \cdot CH_3F$ complex were observed in the region from 400 to 4000 cm^{-1}.

Our infrared spectrum of liquid boron fluoride agreed fairly well with the known infrared spectrum of solid boron fluoride[7] as shown in Table I and Figure 2. Hence the 1416-cm^{-1} frequency in liquid $B^{11}F_3$ can be assigned to B–F antisymmetric stretch. In liquid $B^{11}F_3 \cdot CH_3F$ complex the absorption band was observed at 1424 cm^{-1} as shown in Table II and Figure 3. In the region from 1000 to 1424 cm^{-1}, no frequency other than the frequency of combination ($\nu_1 + \nu_4$) in boron fluoride and of CH_3 rock was observed. On the other hand, the B-F antisymmetric frequencies in $B^{11}F_3 \cdot CH_3OCH_3$ complex[3] and $B^{11}F_4^-$ ion[8] were observed at 1177 and 1216 cm^{-1} for the former and near 1050 cm^{-1} for the latter. Therefore, the 1424-cm^{-1} frequency in $B^{11}F_3 \cdot CH_3F$ complex is assigned to the B–F antisymmetric stretch and no BF_4^- ion is contained in liquid $BF_3 \cdot CH_3F$ complex. The change in frequency with complex formation was not observed in the BF_3 in-plane bending band. The out-of-plane bending band in liquid $B^{11}F_3$ was observed at 661 cm^{-1}, but in liquid $B^{11}F_3 \cdot CH_3F$ complex no band was observed there, and a new band was observed at 617 cm^{-1} which can be assigned to out-of-plane bending band in liquid $B^{11}F_3 \cdot CH_3F$ complex. The intensity of the band in the complex is higher than that in liquid BF_3. The B–F symmetric stretching frequency, which is not infrared active, was not observed.

(5) R. Nakane and T. Watanabe, *Dōitai To Hōshasen*, **2**, 273 (1959).

(6) W. F. Edgell and L. Parts, *J. Am. Chem. Soc.*, **77**, 4899 (1955).

(7) D. A. Dows, *J. Chem. Phys.*, **31**, 1637 (1959).

(8) (a) J. Goubeau and W. Bues, *Z. Anorg. Allgem. Chem.*, **268**, 221 (1952); N. N. Greenwood, *J. Chem. Soc.*, 3811 (1959); G. L. Coté and H. W. Thompson, *Proc. Roy. Soc.* (London), **A210**, 217 (1951); (b) B. P. Susz and J. J. Wuhrmann, *Helv. Chim. Acta*, **40**, 722 (1957); (c) D. Cook, S. J. Kuhn, and G. A. Olah, *J. Chem. Phys.*, **33**, 1669 (1960).

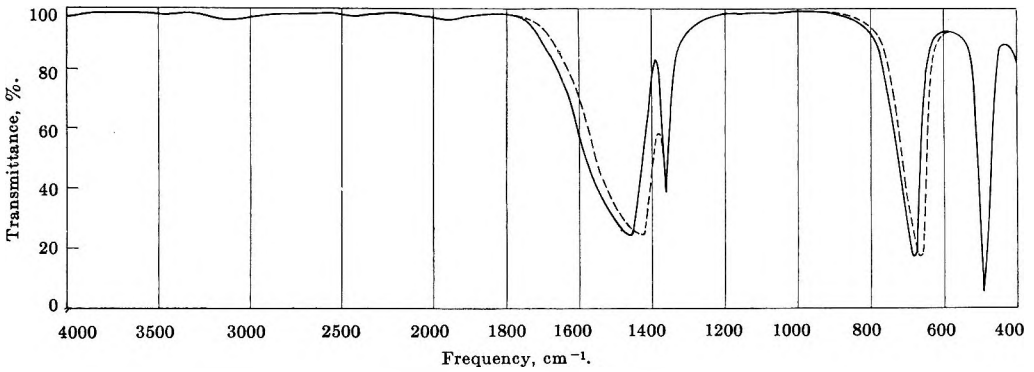

Figure 2. Infrared spectrum of liquid boron fluoride: ———, $B^{10}F_3$; - - - - - - -, $B^{11}F_3$.

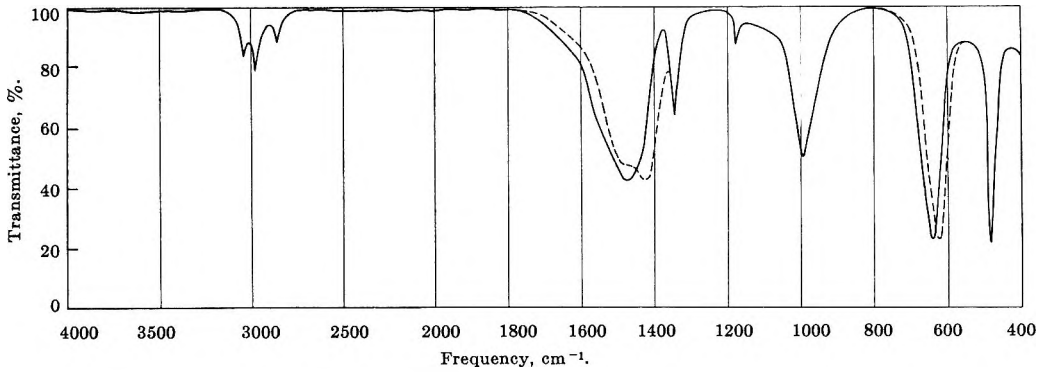

Figure 3. Infrared spectrum of liquid boron fluoride–methyl fluoride complex: ———, $B^{10}F_3 \cdot CH_3F$ complex; - - - - - - -, $B^{11}F_3 \cdot CH_3F$ complex.

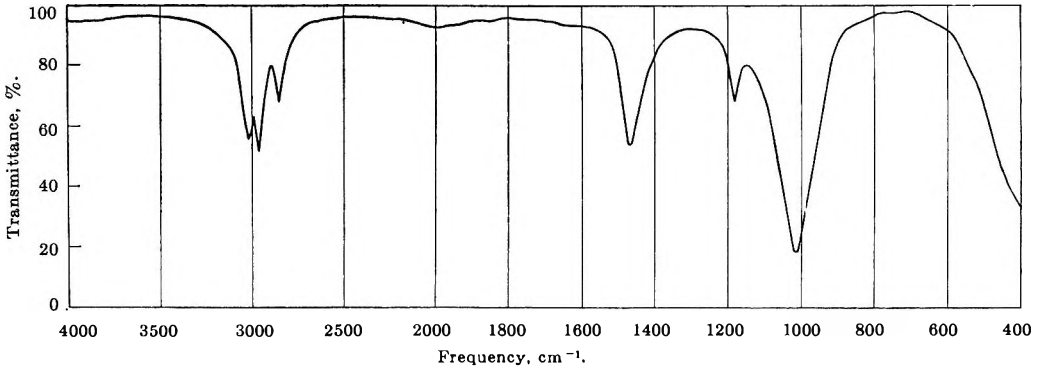

Figure 4. Infrared spectrum of liquid methyl fluoride.

The infrared spectrum of liquid methyl fluoride agreed fairly well also with the known spectrum of gaseous methyl fluoride[9] as shown in Table III and Figure 4. Thus, the bands observed at 1013, 2966, and 3018 cm^{-1} in liquid methyl fluoride are assigned to C–F, C–H symmetric, and C–H antisymmetric stretches, respectively. In both liquid isotopic complexes, these bands were observed at 990, 2980, and 3046 cm^{-1}, which shows that the C–F force constant becomes slightly lower and the C–H force constant becomes slightly higher when methyl fluoride forms the complex with boron fluoride; there was no boron isotope effect on these force constants. The change in frequencies of the CH_3 bend and the CH_3 rock in methyl fluoride with complex formation was not distinct.

The values of the equilibrium constant for boron isotope exchange were calculated from infrared spectra data, obtained on boron fluoride–methyl fluoride com-

(9) E. F. Barker and E. K. Plyler, *J. Chem. Phys.*, **3**, 367 (1935).

Table I: Vibrational Frequencies of Gaseous, Liquid, and Solid BF_3 (cm^{-1})

Gaseous BF_3[a]		Liquid BF_3[b]		Solid BF_3[c]		
B^{10}	B^{11}	B^{10}	B^{11}	B^{10}	B^{11}	Assignment
888	888	...	...	876–880	876–880	ν_1, B–F stretch (sym)
718.23	691.45	685	661	658	632	ν_2, BF_3 out-of-plane bend
1504.8	1453.9	1467	1416	1457	1405	ν_3 (2), B–F stretch (antisym)
482.0	480.4	489	487.5	474–484	472–483	ν_4 (2), BF_3 in-plane bend

[a] See ref 3. [b] This work. [c] See ref 7.

Table II: Vibrational Frequencies and Band Assignments for Liquid $BF_3 \cdot CH_3F$ Complex (cm^{-1})

$B^{10}F_3 \cdot CH_3F$	$B^{11}F_3 \cdot CH_3F$	Assignment
489	487.5	BF_3 in-plane bend
638	617	BF_3 out-of-plane bend
990	990	C–F stretch
1182	1182	CH_3 rock
1351	1350	Combination band (ν_1 + ν_4 of BF_3)
1475	1424	B–F stretch (antisym)
...	(1451)	(CH_3 bend)
...	(1483)	(CH_3 bend)
2863	2863	CH_3 bend (overtone)
2980	2980	C–H stretch (sym)
3046	3046	C–H stretch (antisym)

Table III: Vibrational Frequencies of Gaseous and Liquid CH_3F (cm^{-1})

Gaseous CH_3F[a]	Liquid CH_3F[b]	Assignment
1048.2	1013	C–F stretch
1195.5	1182	CH_3 rock
1475.3	1464	CH_3 bend (sym)
1471.1		CH_3 bend (antisym)
2861.6	2860	CH_3 bend (overtone)
2964.5	2966	C–H stretch (sym)
2982.2	3018	C–H stretch (antisym)

[a] See ref 9. [b] This work.

plex and gaseous boron fluoride, by the use of the formulas given by Urey[10] and Bigeleisen and Mayer,[11] assuming that there is no boron isotope shift of the B–F symmetric stretching frequency in the complex as in gaseous boron fluoride. It was found that the equilibrium constant depends mostly on the boron isotope shift of the BF_3 out-of-plane bending frequency. The calculated values of the constant were in fair agreement with the observed as shown in Table IV. Thus, the BF_3 out-of-plane bending frequency in a weak boron fluoride complex will become lower as the density of localized electrons on the vacant orbital of boron atom and hence the polarity of complex becomes higher, causing the equilibrium constant to become larger.

Table IV: Equilibrium Constants for Boron Isotope Exchange between Gaseous BF_3 and Liquid $BF_3 \cdot CH_3F$ Complex

Temp, °C	Equil constant, K	
	Calcd	Obsd[a]
−95	1.020	1.020
−112	1.023	~1.026

[a] See ref 1.

In a previous work,[1] one of the authors assumed that the B–F antisymmetric stretching frequency in boron fluoride decreases and the structure of boron fluoride deforms slightly from planar towards tetrahedral when boron fluoride forms the weak complexes with alkyl halides and that this change results in the increase of values of the equilibrium constant for boron isotope exchange. However, the above assumption was found mistaken. When liquid boron fluoride is dissolved in liquid methyl fluoride, a lone pair of electrons of the fluorine atom in the methyl fluoride is partially localized on the vacant orbital of the boron atom, causing (a) the force constant of BF_3 out-of-plane bend to become lower, (b) the B–F force constant to become slightly higher, (c) the C–F force constant to become slightly lower, and (d) the C–H force constant to become slightly higher. The B–F antisymmetric stretching frequency, which degenerates doubly in the uncoordinated boron fluoride molecule, is split into two by the destruction of the molecular symmetry in the $BF_3 \cdot CH_3OCH_3$ complex, but not in the $BF_3 \cdot CH_3F$ complex. Hence, in the latter weak complex the weakening of the B–F bond does not occur and the

(10) H. C. Urey, *J. Chem. Soc.*, 562 (1947).

(11) J. Bigeleisen and M. G. Mayer, *J. Chem. Phys.*, **15**, 261 (1947).

boron fluoride retains the planar structure. The increase of the values of the equilibrium constant for boron isotope exchange in the weak boron fluoride complex system results from the lowering, not of the B–F force constant, but of the force constant of the BF_3 out-of-plane bend. As for the weakening of the C–F bond, it is very small and the methyl carbon retains a tetrahedral geometry. Thus, the ionic carbonium form is absent in the weak boron fluoride complex as in $CH_3Cl \cdot SbCl_5$ complex.[12]

Acknowledgment. The authors wish to thank Mr. Teruo Kurihara for helpful advice on the infrared analyses.

(12) H. M. Nelson, *J. Phys. Chem.*, **66**, 1380 (1962).

Competitive–Consecutive Reactions in the Photochemical Chlorination of *p*-Xylene

by Paolo Beltrame, Sergio Carrà, and Sandro Mori

Istituto di Chimica fisica, Università di Milano, Italy *(Received October 18, 1965)*

A kinetic study of the side-chain chlorination of *p*-xylene was carried out in CCl_4 solution at 30 and 50° under ultraviolet irradiation. Seven products from monochloro- to hexachloro-*p*-xylene were detected and determined by gas chromatography. On the basis of a system of kinetic equations first order with respect both to chlorine and to the organic compounds, relative rate constants, referred to the specific rate of *p*-xylene chlorination, were evaluated. A solution of the set of kinetic equations was obtained such as to give reagent and products concentrations as functions of the chlorination degree. Employing the values of the relative rate constants (at 50°), a good fit was obtained of calculated curves of concentrations *vs.* chlorination level and observed values. Taking into account statistical factors, relative rate factors, f_r, for attack of chlorine atoms to single C–H bonds were derived. The f_r values prove that mainly the negative inductive effect of chlorine substituents governs the rates of the reactions. A comparison is made of the relative rates constants at 30 and 50°.

The formal kinetics of complex reaction systems has been the object of extensive mathematical research;[1,2] however, the proposed calculation schemes have been applied to relatively few cases, for lack of experimental data.

A suitable reaction system is the side-chain chlorination of alkylbenzenes. The simple case of toluene has been examined by several authors, particularly by Haring and Knol.[3] A xylene, for instance, the *para* isomer that we have chosen, can on principle give the pattern of competitive–consecutive reactions shown in Scheme I.

(1) J. Wei and C. D. Prater, *Advan. Catalysis*, **13**, 203 (1962), and references cited therein.

(2) N. M. Rodiguin and E. N. Rodiguina, "Consecutive Chemical Reactions," D. Van Nostrand Co., Inc., New York, N. Y., 1964.

(3) H. G. Haring and H. W. Knol, *Chem. Process Eng.*, **45**, 560, 619, 690 (1964); **46**, 38 (1965).

Scheme I

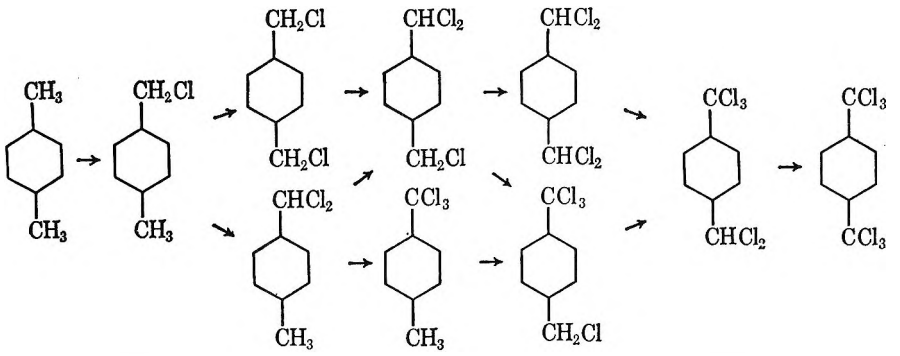

No mention has been found in the literature about α,α,α-trichloro-*p*-xylene, $\alpha,\alpha,\alpha,\alpha'$-tetrachloro-*p*-xylene, and $\alpha,\alpha,\alpha,\alpha',\alpha'$-pentachloro-*p*-xylene. The other compounds in Scheme I are known, some having been prepared by direct chlorination, others by indirect methods, but no thorough kinetic study of this system has been done so far.

The present paper, following a preliminary communication,[4] is devoted to the kinetics of *p*-xylene direct side-chain chlorination in CCl_4 solution under ultraviolet irradiation. According to the analysis of the reacting system it has been possible to neglect two terms in Scheme I, therefore obtaining the simplified Scheme II. Two indexes are attributed to each compound in Scheme II: the letter is for general use, while the number shall be employed for the mathematical treatment from eq 6 on.

Scheme II

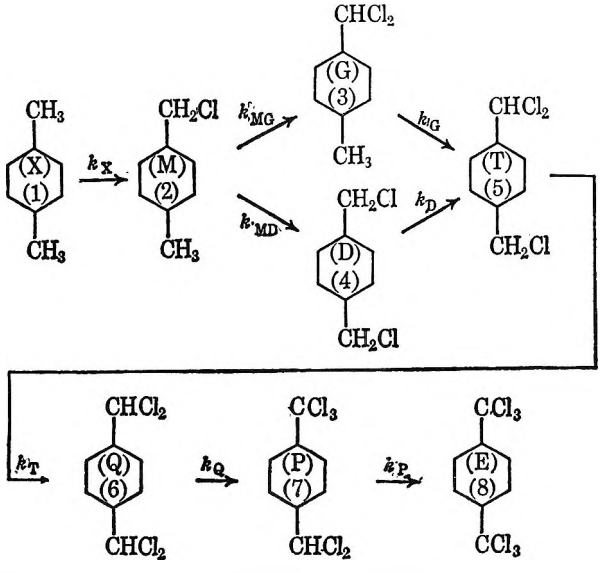

Experimental Section

Materials. *p*-Xylene, carbon tetrachloride, and diphenylmethane (internal standard) were commercial products of gas chromatographic purity; *p*-xylene in particular was free of *ortho* of *meta* isomers and of ethylbenzene. The gc conditions follow: 0.25 in. × 5.7 m column of 10% didecyl phthalate and 10% Bentone 34 on Chromosorb W (80–100 mesh); temperature, 130°; carrier gas, hydrogen at *ca.* 50 cc/min; thermal conductivity detector. Chlorine was taken from a cylinder and dried over concentrated H_2SO_4 before use.

α-Chloro-p-xylene (M) was prepared by chlorination with Cl_2, without ultraviolet irradiation, of a 500-ml CCl_4 solution of 26.5 g (0.25 mole) of *p*-xylene; after addition of *ca.* 0.5 mole of Cl_2 at 65–70° during 1 hr, the reaction mixture was washed with a $NaHCO_3$ solution and water, then dried, and the solvent was removed by evaporation. Distillation in a Todt column at *ca.* 20 mm pressure yielded a fraction boiling at 90–91°.

Anal. Calcd for C_8H_9Cl: C, 68.32; H, 6.45. Found: C, 67.84; H, 6.28.

α,α'-Dichloro-p-xylene (D) was isolated by crystallization from the distillation residue of the previous preparation. Recrystallized from ethanol, it had mp 100°.

Anal. Calcd for $C_8H_8Cl_2$: C, 54.88; H, 4.61. Found: C, 54.92; H, 4.45.

α,α-Dichloro-p-xylene (*G*). Monochloro-*p*-xylene (11 g) was treated with 10% KOH aqueous solution (100 ml), refluxing for 5 hr. The product had mp 52° (from petroleum ether (bp 75–120°), 7 g). It was oxidized to *p*-tolualdehyde with lead tetraacetate in pyridine.[5] The aldehyde was heated with the stoichiometric amount of PCl_5,[6] the reaction mixture was poured into iced water, and the *gem*-dichloro-*p*-xylene was filtered off and recrystallized from ethanol: mp 47°.

Anal. Calcd for $C_8H_8Cl_2$: C, 54.88; H, 4.61. Found: C, 55.20; H, 4.81.

(4) P. Beltrame and S. Carrà, *Tetrahedron Letters*, 3909 (1965).
(5) R. E. Partch, *ibid.*, 3071 (1964).
(6) L. Gattermann, *Ann.*, **347**, 353 (1906).

α,α,α′,α′-Tetrachloro-p-xylene (Q) was obtained by chlorinating a 1 *M* *p*-xylene solution in CCl_4 with Cl_2 under ultraviolet irradiation at 70°. After addition of about twice the stoichiometric chlorine (5 hr), the reaction mixture was treated as described, and a solid crystallized: mp 92–94° (from petroleum ether).

Anal. Calcd for $C_8H_6Cl_4$: C, 39.38; H, 2.47. Found: C, 39.08; H, 2.32.

α,α,α,α′,α′,α′-Hexachloro-p-xylene (*E*). After one of the kinetic runs, the solution was exhaustively chlorinated with excess chlorine, and after the usual treatment a solid was obtained: mp 109–110° (from petroleum ether).

Anal. Calcd for $C_8H_4Cl_6$: C, 30.71; H, 1.29. Found: C, 30.49; H, 1.08.

The products of the five preparations were of good gas chromatographic purity.

Analytical Method. Reaction mixtures were analyzed by gc (thermal conductivity detector) on two columns. Column 1 (0.25 in. × 2 m) contained 10% Apiezon L on Chromosorb W (30–60 mesh) and was used at 135° with hydrogen (*ca.* 400 cc/min) as carrier gas. Column 2 (0.25 in. × 1 m), filled with 20% Apiezon L on Chromosorb W (60–80 mesh), was used in the same thermal conditions (*ca.* 300 cc/min of H_2 as carrier gas). Retention times of the pure products were approximately (in minutes) (column 1) X = 0.79, M = 2.3, G = 5.4, D = 10, and diphenylmethane = 16; (column 2) G = 2.1, D = 3.9, diphenylmethane = 6.1, Q = 17, and E = 43. Two other peaks, well measurable on column-2 chromatograms, emerged with retention times 8.9 and 27 min, respectively. The former was attributed to *α,α,α′*-trichloro-*p*-xylene (T), the latter to *α,α,α,α′,α′*-pentachloro-*p*-xylene (P), as the only possible choice because of the timing of their appearance during the progress of the reaction, and taking into account Scheme I. The presence of other products, as revealed by gc, was always limited to very small amounts which were neglected. No reaction product had a retention time such as to produce overlap with the diphenylmethane peak. Diphenylmethane was introduced as an internal standard for quantitative analysis. Blanks of the pure compounds dissolved in CCl_4 at different concentrations with addition of known amounts of the standard gave the following molar calibration factors (diphenylmethane = 1.00): X = 1.28, M = 1.66, G = 1.19, D = 1.12, Q = 1.04 and E = 1.10. As these values were affected by large statistical deviations, and for lack of the exact factors for T and P, a normalization procedure was then preferred, giving a factor 1.5 to M and factor 1.0 to all other components.

A complication arose because some components (X and M) were analyzed only on column 1, other products (T, Q, P, and E) were analyzed on column 2, while G and D were analyzed on both columns. A scale factor, evaluated from the areas of the diphenylmethane peaks on the two chromatograms, was used in order to make comparable the results of the analyses of the same sample on different columns.

The analytical procedure was tested on a mixture of exactly weighed amounts of X, M, G, D, and Q; the average deviation was 10%.

Apparatus. The chlorination was carried out in a 350-cc cylindrical semibatch Pyrex reactor. Thermostated water was circulated into its jacket, and mechanical stirring was provided at 1000 rpm. The reactor was irradiated by means of an external 3600-A ultraviolet source (Quarzelampen Hanau) kept at a fixed (20 cm) distance. Chlorine, previously saturated with CCl_4, was introduced through a sintered-glass disk at the bottom of the reactor. The latter was equipped with an efficient condenser and a thermometer. Apart from an initial rise owing to the starting of the reaction, the temperature was constant ±0.2°.

A diagram of the apparatus is given in Figure 1.

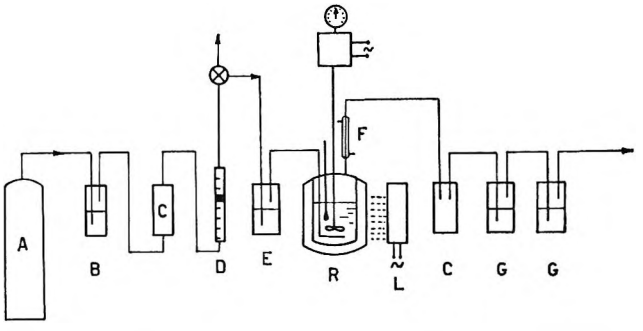

Figure 1. Apparatus diagram: A, Cl_2 cylinder; B, drying by concentrated H_2SO_4; C, empty vessels; D, variable-area flowmeter; E, CCl_4 saturator; R, reactor; F, reflux condenser; L, ultraviolet lamp; and G, absorption in 20% NaOH solution.

Kinetic Procedure. Having introduced 150 ml of a 0.5 *M* CCl_4 solution of *p*-xylene into the reactor, oxygen was removed from it by flushing for 0.5 hr from a line not indicated in Figure 1. A similar washing was effected with chlorine in the equipment from B to E. Eventually the chlorine flow was diverted into the reactor (t = 0). At time t a 1-ml sample was taken from the reacting solution and added to 1 ml of a CCl_4 solution containing a known amount of diphenylmethane; the resulting mixture was washed with 2 ml of $NaHCO_3$-saturated aqueous solution and then with water, dried with Na_2SO_4, and analyzed by gc.

Table I: Example of Kinetic Run (Temperature, 30°; Chlorine flow, 3000 cc/hr; C_X (t = 0) = 0.500 M)

Time, min	Mole/l.							
	C_X	C_M	C_G	C_D	C_T	C_Q	C_P	C_E
15	0.232	0.244	0.009	0.015	...	...	...	...
30	0.141	0.281	0.019	0.052	0.008	...	...	...
45	0.014	0.281	0.031	0.144	0.029	...	...	...
60	...	0.063	0.034	0.246	0.136	0.020	...	...
75	...	0.009	0.008	0.158	0.256	0.069	...	...
90	...	...	...	0.070	0.270	0.160	...	...
105	...	...	...	0.030	0.220	0.250	...	...
120	...	...	...	0.010	0.138	0.300	0.053	...
135	...	...	...	...	0.081	0.323	0.096	...
150	...	...	...	...	0.046	0.303	0.150	...
165	...	...	...	...	0.023	0.278	0.199	...
180	...	...	...	...	0.008	0.238	0.228	0.026

A blank has shown that the washing procedure does not affect the composition of a mixture of products (G, D, and Q). An example of kinetic run is given in Table I.

Results and Kinetic Treatment

The set of kinetic equations (1, where C_C is the chlorine concentration and C_X, C_M... refer to the organic compounds) derives from Scheme II, assuming that every reaction be first order with respect both to chlorine and to the organic substrate.

$$\frac{dC_X}{dt} = -k_X C_C C_X \tag{1a}$$

$$\frac{dC_M}{dt} = k_X C_C C_X - (k_{MG} + k_{MD}) C_C C_M \tag{1b}$$

$$\frac{dC_G}{dt} = k_{MG} C_C C_M - k_G C_C C_G \tag{1c}$$

$$\frac{dC_D}{dt} = k_{MD} C_C C_M - k_D C_C C_D \tag{1d}$$

$$\frac{dC_T}{dt} = k_G C_C C_G + k_D C_C C_D - k_T C_C C_T \tag{1e}$$

$$\frac{dC_Q}{dt} = k_T C_C C_T - k_Q C_C C_Q \tag{1f}$$

$$\frac{dC_P}{dt} = k_Q C_C C_Q - k_P C_C C_P \tag{1g}$$

$$\frac{dC_E}{dt} = k_P C_C C_P \tag{1h}$$

The concentration *vs.* time curve for each chlorinated compound, except E, shows a maximum. This corresponds to eq 2, each one valid at the given point of maximum.

$$\frac{k_{MG} + k_{MD}}{k_X} = \frac{C_X}{C_M} \text{ at the maximum of M} \tag{2b}$$

$$\frac{k_G}{k_{MG}} = \frac{C_M}{C_G} \text{ at the maximum of G} \tag{2c}$$

$$\frac{k_D}{k_{MD}} = \frac{C_M}{C_D} \text{ at the maximum of D} \tag{2d}$$

$$\frac{k_T}{k_D} = \frac{C_D}{C_T} + \frac{k_G}{k_D}\frac{C_G}{C_T} \text{ at the maximum of T} \tag{2e}$$

$$\frac{k_Q}{k_T} = \frac{C_T}{C_Q} \text{ at the maximum of Q} \tag{2f}$$

$$\frac{k_P}{k_Q} = \frac{C_Q}{C_P} \text{ at the maximum of P} \tag{2g}$$

A seventh equation (3) is provided by the ratio of (1c) and (1d)

$$\frac{dC_G}{dC_D} = \frac{k_{MG}C_M - k_G C_G}{k_{MD}C_M - k_D C_D} \tag{3}$$

that has an initial limit value ($C_G \to 0$, $C_D \to 0$) (eq 4)

$$\lim_{t\to 0}\left(\frac{dC_G}{dC_D}\right) = \frac{k_{MG}}{k_{MD}} \tag{4}$$

corresponding to the limit value of the ratio (C_G/C_D) when C_D and C_G tend to zero. Therefore, for each kinetic run the ratio C_G/C_D was plotted *vs.* C_D in order to extrapolate the initial value. Other plots were made reporting C_M *vs.* C_X, C_G *vs.* C_M, C_D *vs.* C_M, C_T *vs.* C_D, C_Q *vs.* C_T, and C_P *vs.* C_Q for a precise evaluation of the concentrations to be used in eq 2. The small value of $(C_G/C_T)_{max\ T}$ needed for eq 2e was evaluated from the concentration *vs.* time plot. Examples of the plots are shown in Figure 2. The method just described has the advantage of ignoring the chlorine

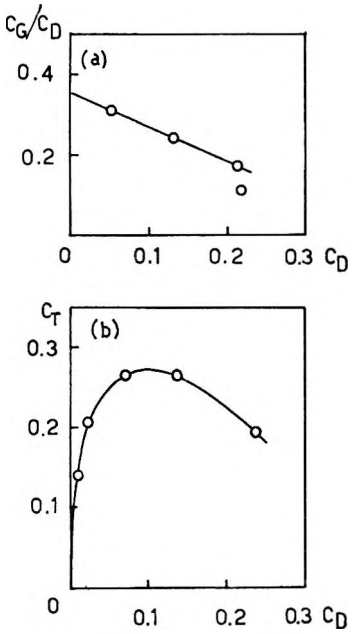

Figure 2. (a) Example of C_G/C_D *vs.* C_D plot (run at 50°; Cl_2 at 3000 cc/hr). (b) Example of C_T *vs.* C_D plot (same run).

concentration, which is variable during the course of the runs, although it gives only relative values of the rate constants.

Chlorinations have been performed mainly at 50°, covering low and high degrees of chlorination in a total of four runs. An additional run was carried at 30°. Relative rate constants, referred to k_X, are reported in Table II.

Table II: Relative Rate Constants

	Temp, °C	
	30°	50°
$k_X/k_X = K_{12}$	1	1
$k_{MG}/k_X = K_{23}$	0.075	0.085
$k_{MD}/k_X = K_{24}$	0.235	0.234
$k_G/k_X = K_{35}$	0.353	0.396
$k_D/k_X = K_{45}$	0.0749	0.0793
$k_T/k_X = K_{56}$	0.0277	0.0333
$k_Q/k_X = K_{67}$	0.00694	0.00843
$k_P/k_X = K_{78}$	...	0.00346

The progress of the reactions can be calculated, with the use of the relative constants, in the following way.

The variable chlorine concentration C_C may be expressed as

$$C_C = C_C^\circ f(t) \tag{5}$$

C_C° being the concentration at time zero. A pseudo-first-order rate constant, k_{12}, for the reaction of *p*-xylene can be defined as

$$k_{12} = k_X C_C^\circ \tag{6}$$

A set of relative rate constants, the same as in Table II, can now be introduced as

$$K_{23} = \frac{k_{MG}}{k_X} = k_{MG}\left(\frac{C_C^\circ}{k_{12}}\right);\quad K_{24} = k_{MD}\left(\frac{C_C^\circ}{k_{12}}\right);$$
$$K_{35} = k_G\left(\frac{C_C^\circ}{k_{12}}\right);\quad K_{45} = k_D\left(\frac{C_C^\circ}{k_{12}}\right);\quad K_{56} = k_T\left(\frac{C_C^\circ}{k_{12}}\right);$$
$$K_{67} = k_Q\left(\frac{C_C^\circ}{k_{12}}\right);\quad K_{78} = k_P\left(\frac{C_C^\circ}{k_{12}}\right) \tag{7}$$

while K_{12} is obviously unity. Substituting relations 5 and 7 into eq 1, the latter can be written in the general form

$$\frac{dC_i}{dt} = k_{12} f(t)\left[\sum_{j=1}^{m}{}'K_{ji}C_j - C_i\sum_{j=1}^{m}{}'K_{ij}\right] \tag{8}$$

where K_{ji} and K_{ij} are the relative rate constants, while m is the component number; the prime on the summation signs indicates that only the terms having $j \neq i$ are included. The first term in brackets refers to the formation of the ith component, and the second one to its disappearance. Eq 8 becomes

$$\frac{dC_i}{d\vartheta} = \sum_{j=1}^{m}{}'K_{ji}C_j - C_i\sum_{j=1}^{m}{}'K_{ij} \tag{9}$$

if one takes

$$\vartheta = k_{12}\int_0^t f(x)dx \tag{10}$$

Equation 9 has the typical form of the kinetic equations for the first-order competitive–consecutive reactions. The general solutions of eq 9 may be written[7] as

$$C_i = \sum_{r=1}^{m} a_{ir}Q_r e^{-\lambda_r\vartheta} = \sum_{r=1}^{m} A_{ir}e^{-\lambda_r\vartheta} \tag{11}$$

where the coefficients a_{ir} and λ_r are obtained solving a set of equations of the form

$$a_{ir}\left(\sum_{j=1}^{m}{}'K_{ij} - \lambda_r\right) - \sum_{j=1}^{m}{}'a_{jr}K_{ji} = 0 \tag{12}$$
$$r = 1, 2, \ldots m$$

while the values of Q_r are determined from initial conditions ($\vartheta = 0$).

Keeping r fixed, eq 12 represents a set of linear, homogeneous equations in the a_{ir} terms; the cor-

(7) A. A. Frost and R. G. Pearson, "Kinetics and Mechanism," John Wiley and Sons, Inc., New York, N. Y., 1956, p 160.

responding determinant of the coefficients must vanish as a condition for nontrivial solutions.

For the case under consideration it is

$$\begin{vmatrix} (K_{12}-\lambda) & 0 & 0 & 0 & 0 & 0 & 0 & 0 \\ -K_{12} & (K_{23}+K_{24}-\lambda) & 0 & 0 & 0 & 0 & 0 & 0 \\ 0 & -K_{23} & (K_{35}-\lambda) & 0 & 0 & 0 & 0 & 0 \\ 0 & -K_{24} & 0 & (K_{45}-\lambda) & 0 & 0 & 0 & 0 \\ 0 & 0 & -K_{35} & -K_{45} & (K_{56}-\lambda) & 0 & 0 & 0 \\ 0 & 0 & 0 & 0 & -K_{56} & (K_{67}-\lambda) & 0 & 0 \\ 0 & 0 & 0 & 0 & 0 & -K_{67} & (K_{78}-\lambda) & 0 \\ 0 & 0 & 0 & 0 & 0 & 0 & -K_{78} & -\lambda \end{vmatrix} = 0 \quad (13)$$

The eight solutions for λ are

$\lambda_1 = K_{12} = 1$; $\lambda_2 = K_{23} + K_{24}$; $\lambda_3 = K_{35}$; $\lambda_4 = K_{45}$; $\lambda_5 = K_{56}$; $\lambda_6 = K_{67}$; $\lambda_7 = K_{78}$; $\lambda_8 = 0$

For the runs at 50°, introducing the values of the relative rate constants from Table II and solving the set of equations (12), the appropriate a_{ir} coefficients were calculated. Then the initial conditions ($C_X^\circ = 0.5$, $C_M^\circ = C_G^\circ = \ldots = 0$) were taken into account to obtain the Q_r coefficients. If in eq 11 the A_{ir} coefficients are considered as elements of a square matrix, the terms $e^{-\lambda_r \vartheta}$ as elements of a column matrix, and C_i as elements of a row matrix, the final results at 50° can be expressed as

$$\mathbf{c} = \begin{vmatrix} 0.5 & 0 & 0 & 0 & 0 & 0 & 0 & 0 \\ -0.7342 & 0.7342 & 0 & 0 & 0 & 0 & 0 & 0 \\ 0.1033 & 0.8105 & -0.9138 & 0 & 0 & 0 & 0 & 0 \\ 0.1866 & -0.7167 & 0 & 0.5301 & 0 & 0 & 0 & 0 \\ -0.0576 & -0.9244 & 0.9977 & -0.9139 & 0.8982 & 0 & 0 & 0 \\ 0.0019 & 0.0991 & -0.0357 & 0.4294 & -1.2027 & 0.7580 & 0 & 0 \\ 0.0000 & -0.0027 & 0.0018 & -0.0477 & 0.3398 & -1.2858 & 0.9946 & 0 \\ 0.0000 & 0.0000 & 0.0000 & 0.0021 & -0.0353 & 0.5278 & -0.9946 & 0.5000 \end{vmatrix} \times \begin{vmatrix} \exp(-\vartheta) \\ \exp(-0.319\vartheta) \\ \exp(-0.396\vartheta) \\ \exp(-0.0793\vartheta) \\ \exp(-0.0333\vartheta) \\ \exp(-0.00843\vartheta) \\ \exp(-0.00346\vartheta) \\ 1 \end{vmatrix} \quad (14)$$

In this way it has been possible to calculate by computer the concentrations of *p*-xylene and of reaction products for 100 different ϑ values in the range 10^{-2}–10^3, practically covering the complete transformation from pure xylene to pure hexachloroxylene. At each ϑ value a chlorination degree (y) has been evaluated by the formula

$$y = \frac{1}{C_X^\circ} \sum_{i=1}^{m} C_i (n_{Cl})_i \quad (15)$$

$(n_{Cl})_i$ being the number of chlorine atoms in the ith component.

The calculated curves of C_i *vs.* y are reported in Figure 3. Experimental values of C_i, obtained as a function of time, were expressed as a function of y by means of eq 15 and then compared with the calculated curves (Figures 4–6).

Discussion

For each component of the reacting system the comparison of the calculated C_i–ϑ curve with the experimental C_i–t curve leads to an empirical relation between ϑ and t. Doing this for all the components and averaging, ϑ turns out to increase more than linearly with t, in the range examined. Because of eq 10, the differential of ϑ with respect to t is proportional to $f(t)$, *i.e.*, to C_C (eq 5). Therefore, the observed behavior of ϑ as a function of t means that the concentration of chlorine, as expected, is increasing from the beginning of the reaction up to nearly the end of it.

The ϑ *vs.* t curve for a typical run is reported in Figure 7. An approximate evaluation of $d\vartheta/dt$ shows that C_C has increased by a factor around 70 between t 10 min ($y = 0.68$) and t 160 min ($y = 5.6$). Not having experimentally determined any instantaneous value of chlorine concentration in the reacting solutions, the evaluation of the second-order rate constants k_X, k_{MG}, ...k_P was not feasible. However, the relative rate constants are by themselves sufficient, as it has been shown, to provide a complete pattern of the products distribution as a function of the chlorination level, at a given temperature. The agreement between calculated and experimental values of concentrations (Figures 4–6) is on the whole quite good, in spite of the difficulties of a gas chromatographic quantitative analysis. Such agreement proves that the evaluation

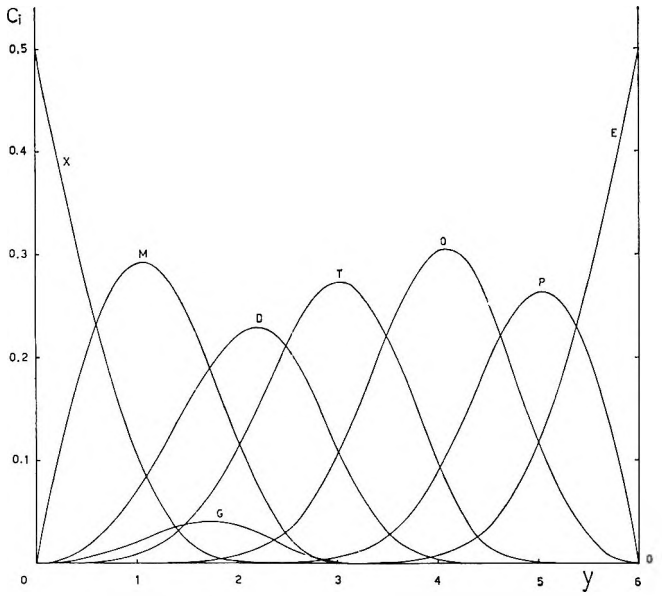

Figure 3. Calculated distribution of products as a function of the chlorination degree, at 50°.

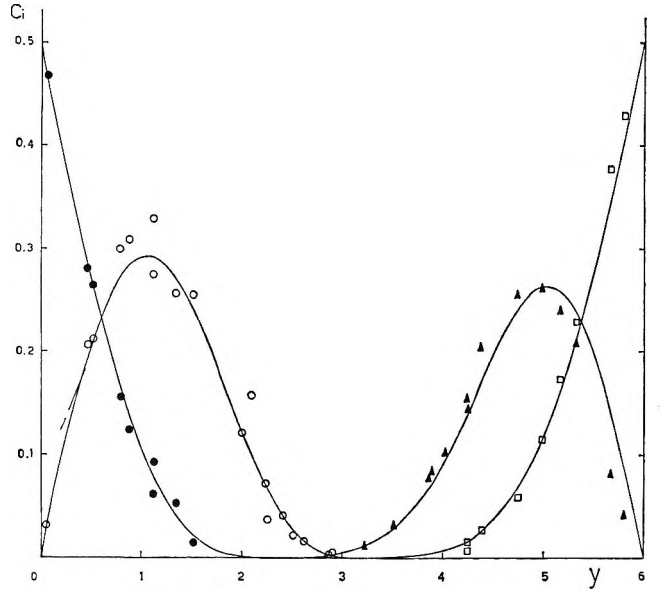

Figure 4. Comparison of the calculated curves and experimental data (50°) for X (●), M (○), P (▲), and E (□).

of K_{ij} constants through equations of the type (2) and (4) is satisfactory, even from a limited number of experiments, as already pointed out for the case of a system of consecutive reactions.[8]

Furthermore, the knowledge of the relative rate constants is useful for the elucidation of some aspects of the reaction mechanism. The accepted scheme for photochemical chlorination is based on the following propagation reactions.[9]

$$RH + Cl\cdot \xrightarrow{slow} R\cdot + HCl$$

$$R\cdot + Cl_2 \xrightarrow{fast} RCl + Cl\cdot$$

Accordingly, the rate-limiting step is the Cl· attack on C–H bonds, and the constants of Table II have to be modified by statistical factors in order to discuss the reactivity of the different kinds of bonds. Taking into account the number of hydrogen atoms available for each reaction of Scheme II, relative rate factors per C–H bond (f_r) were obtained for reactions at 50°. They are collected in Table III with regard to the group on which the attack is carried and to the substituent present in the *para* position.

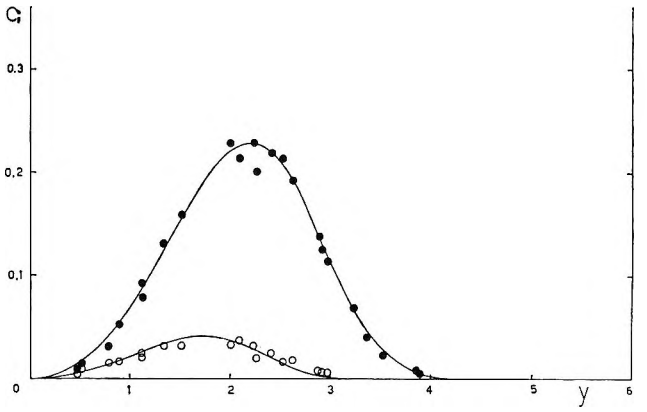

Figure 5. Comparison of calculated curves and experimental data (50°) for G (○) and D (●).

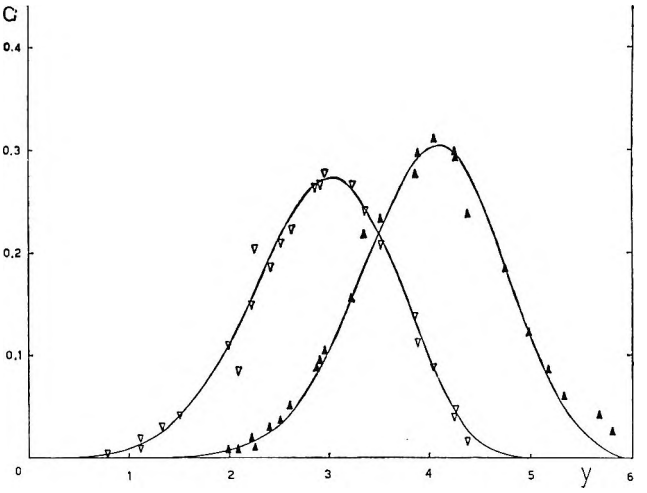

Figure 6. Comparison of calculated curves and experimental data (50°) for T (▽) and Q (▲).

(8) R. B. MacMullin, *Chem. Eng. Progr.*, **44**, 183 (1948).

(9) C. Walling, "Free Radicals in Solution," John Wiley and Sons, Inc., New York, N. Y., 1957, p 352 ff.

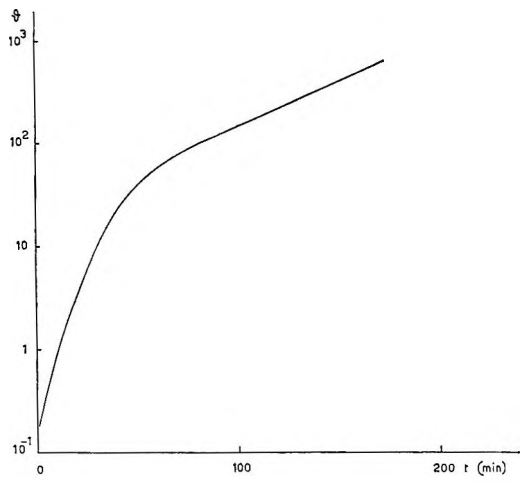

Figure 7. Diagram of the function ϑ *vs.* time for a run at 50° (Cl_2 at 3000 cc/hr).

Table III: Relative Rate Factors per C–H Bond (f_r) at 50°

Bond belonging to the group	Group present in the *para* position			
	CH_3	CH_2Cl	$CHCl_2$	CCl_3
CH_3	1	0.47	0.79	...
CH_2Cl	0.26	0.12	0.10	...
$CHCl_2$	...	...	0.025	0.021

The data in Table III show that both chlorine atoms in the α-position and chlorinated *para* substituents lower the reactivity of a side-chain C–H bond. This is in line with the electrophilic character of the chlorine atom. Obviously, the electron withdrawal by part of a Cl substituent is larger if it is adjacent to the reaction center than if it is on a *para* side chain. In fact, the relative reactivities of C–H bonds belonging to CH_3 and CH_2Cl groups differ by factors in the range 4–8; between CH_2Cl and $CHCl_2$ the factor is 4. On the other hand, the substitution of a Cl atom for hydrogen on the *para* group gives a reduction of rate around 2 for the first Cl, and a smaller lowering, by a factor 1.2, for subsequent substitutions, except when comparing α-chloro-*p*-xylene with α,α-dichloro-*p*-xylene. Apart from the last case, the negative inductive effect of chlorine appears to govern the rates of the reactions. For the parallel case of the liquid phase side-chain chlorination of toluene, f_r values have been found equal to 1, 0.25, and 0.087 (at 100°) and 1, 0.18, and 0.042 (at 40°) for C–H bonds included in CH_3, CH_2Cl, and $CHCl_2$ groups, respectively,[3] while values 1, 0.14, and 0.015 (at 15°) are given for the same bonds by other authors.[10] In different cases the C–H bond on a CH_2Cl group is attacked at a higher rate than that on a CH_3, as for instance in the liquid phase chlorination of trimethylacetic acid.[11] Due to the nonpolar character of solvent CCl_4, it is also reasonable to compare the f_r factors of Table III with results obtained in the gas phase for the chlorine atom attack on C–H bonds. For the series methane, methyl chloride, methylene dichloride, and chloroform,[12,13] the following f_r values at 50° can be derived: CH_4 = 1; CH_3Cl = 4.3; CH_2Cl_2 = 8.4; $CHCl_3$ = 2.5. On the other hand, a comparison of the chlorinations of *n*-butane, *n*-butyl chloride, and other butane derivatives with electron-withdrawing substituents in the 1-position[14] has shown that chlorine atoms (as well as other electronegative substituents) deactivate both α- and β-positions. For instance, at 78° the f_r values for the different positions are given as

	X—CH_2—	CH_2—	CH_2—	CH_3
X = H	1	3.6	3.6	1
X = Cl	0.8	2.1	3.7	1

It is usually suggested that the inductive effect of electronegative atoms or groups can be opposed by a mesomeric effect due to stabilization of the incipient free radical by conjugation. The latter appears to be prevailing in the methane series above, and also for the mentioned liquid phase chlorination of trimethylacetic acid. The inductive effect prevails in the *n*-butane derivatives, although the rate depression when X = Cl is larger for the β- than for the α-position because of the competing mesomeric effect.

The results on the *p*-xylene series (Table III) confirm that the additional conjugative stabilization due to chlorine is relatively unimportant in the case of aromatic side chains. It is also interesting to observe the effect of temperature variations on the relative rate constants of the chlorinations. Data in Table II indicate an increase of almost all K_{ij} constants going from 30 to 50°. This does not look accidental, although the statistical error of the K_{50}/K_{30} factors is certainly considerable owing to the narrow temperature range. Clearly, successive chlorinations after the first tend to have a higher activation energy, the increments $\Delta\Delta E^*$ being estimable by the formula

(10) G. Benoy and J. C. Jungers, *Bull. Soc. Chim. Belges*, 65, 769 (1956); *Chem. Abstr.*, 51, 9330*h* (1957).

(11) G. Benoy, *Tetrahedron*, 20, 1567 (1964).

(12) J. H. Knox, *Trans. Faraday Soc.*, 58, 275 (1962).

(13) G. C. Fettis and J. H. Knox, *Progr. Reaction Kinetics*, 2, 1 (1964).

(14) P. S. Fredricks and J. M. Tedder, *J. Chem. Soc.*, 144 (1960); H. Singh and J. M. Tedder, *ibid.*, 4737 (1964).

$$\Delta\Delta E^* = R\frac{T_1T_2}{T_2 - T_1}\ln\frac{K_2}{K_1} \qquad (16)$$

where indexes 1 and 2 are related to the two temperatures. Applying eq 16 to the data on toluene[3] at 40 and 100°, the values of $\Delta\Delta E^*$ for the chlorinations turn out to be 1.2 and 2.8 kcal/mole going from toluene to benzyl chloride and benzylidene chloride, respectively.

Mean values have been obtained from the data of Table II, considering K_{12} and K_{24} for the chlorination of CH_3 groups; K_{23}, K_{45}, and K_{56} for the attack on CH_2Cl groups, and finally K_{67} for the $CHCl_2$ group. The results for $\Delta\Delta E^*$ are 1.2 (average value) and 1.9 kcal/mole going from the attack on CH_3 to the one on CH_2Cl and $CHCl_2$, respectively. These figures are quite significant with respect to the low values of the activation energies for chlorine atom attack on aliphatic C–H bonds, ranging between 0 and 4 kcal/mole.[13]

Acknowledgment. We are indebted to the Italian Consiglio Nazionale delle Ricerche for financial aid.

The Ion-Exchange Properties of Zeolites. I. Univalent Ion Exchange in Synthetic Faujasite

by Howard S. Sherry

Research Department, Socony Mobil Oil Company, Inc., Paulsboro, New Jersey *(Received October 18, 1965)*

Ion-exchange isotherms describing the exchange of Li, K, Rb, Cs, Ag, and Tl(I) ions into the Linde Na–X type of synthetic faujasite are presented. All the alkali metal ion-exchange isotherms except the one for Li–Na exchange are sigmoidal and show selectivity reversals. The initial selectivity series is in the order Ag $\gg$ Tl > Cs $\geq$ Rb > K > Na > Li. Above approximately 40% replacement of sodium ions the selectivity series becomes Ag $\gg$ Tl > Na > K > Rb $\geq$ Cs > Li. Evidence is also presented to demonstrate that 16 out of 85 sodium ions per unit cell are not replaceable by Rb and Cs ions in Na–X. Ion-exchange isotherms for the exchange of Li, K, Rb, Cs, Ag, Tl(I), and NH_4 ions into the Linde Na–Y type of synthetic faujasite are also presented. These isotherms demonstrate that 16 out of the 50 sodium ions per unit cell cannot be replaced by Rb, Cs, Tl(I), and NH_4 ions. Furthermore, Rb–Na and Cs–Na ion exchange in zeolite Y gives non-sigmoidal isotherms which are compared to the sigmoidal isotherms found for these pairs of ions in zeolite X. In addition, Na–X is much more selective for Ag than is Na–Y. From these data and the structural data for these zeolites it is concluded that there is much ion binding in Na–X and little ion binding in Na–Y.

The ion-exchange properties of zeolites are of interest for several reasons. The pore size of these materials approaches, and in some cases is smaller than, the size of most monatomic ions, and the selectivity patterns exhibited by these materials are quite varied. For example, the synthetic zeolite Linde A exhibits the selectivity pattern[1] Na > K > Rb > Li > Cs, and

(1) R. M. Barrer, L. V. C. Rees, and D. J. Ward, *Proc. Roy. Soc.* (London), **A273**, 180 (1963).

clinoptilolite, phillipsite, erionite, and the Norton Company's synthetic mordenite all exhibit the selectivity pattern[2] Cs > K > Na. The latter selectivity series is the usual selectivity series observed in most commercially available cation-exchange resins in dilute solution.[3] However, both these selectivity patterns were predicted by Eisenman.[4]

Synthetic faujasite is of particular interest because this zeolite has two independent, though interconnecting, three-dimensional networks of cavities.[5,6] Cations are located in both networks of cavities.[7] One network consists of large cavities, sometimes called supercages, which have a diameter of about 13 A. They are linked in a tetrahedral, diamond-type lattice by sharing rings of 12 tetrahedra.[7] These rings have a free diameter of about 8 A.[7] The other network is formed by linking smaller cages, called sodalite cages,[7] in a tetrahedral, diamondlike lattice, through adjoining rings of 6 tetrahedra, thus forming secondary cavities which are hexagonal prisms, between sodalite cages.

The composition of the synthetic zeolite Linde 13-X, which is the synthetic faujasite used in this work, is given by the anhydrous unit cell formula $Na_{85}[(AlO_3)_{85}(SiO_2)_{107}]$. There are 85 sodium ions in a unit cell. Sixteen are located either in the hexagonal prisms, 1 in each of the 16 prisms per unit cell,[7] or in the sodalite cages, 2 in each of the 8 sodalite cages per unit cell.[8] It will be seen later that, for ion-exchange purposes, the disagreement is not important. Thirty-two of the sodium ions are located in the large cavities, very nearly in the plane of the rings of 6 tetrahedra which are shared by and, therefore, connect the supercages and the sodalite cages. The remaining 37 cations are either in several of many crystallographically equivalent positions or are in constant motion in the large cavities and cannot be located by X-ray techniques.

The composition of the synthetic zeolite Na–Y used in this work is given by the anhydrous unit cell formula $Na_{50}[(AlO_2)_{50}(SiO_2)_{142}]$. In this zeolite 16 cations per unit cell are located in the hexagonal prisms or sodalite cages.[8] The rest are located in the large cages. The SiO_2–AlO_2 framework of Linde Y is almost identical in structure with that of Linde X.

Study of synthetic faujasite provides an opportunity to vary the ion-exchange capacity *via* the isomorphous substitution of SiO_2 for $NaAlO_2$ while the configuration of the crystalline aluminosilicate backbone remains essentially constant. In an amorphous ion exchanger, which might be typified by Dowex-50, this is equivalent to varying the exchange capacity at constant cross-linking, polymer configuration, and water content. The crystalline system has the advantage that it is amenable to structural analysis, whereas the amorphous systems are not.

Faujasite is also unique because it has the most open framework of all known zeolite structures. The hydrated zeolite contains 264 molecules of H_2O per unit cell.[9] Thus, the average number of H_2O molecules per Na^+ ion is about 3 in Na–X. This value is 3.1 for the Li form of X and smoothly decreases, as the alkali metal series is descended, to 2 for Cs–X.[9] The internal molality is about 19 for Na–X. In Na–Y the water content is essentially the same as in Na–X.[10] There are approximately 5 water molecules per univalent ion and the internal molality is about 11.

The cations and water in the large cages may be thought of as a concentrated salt solution. Evidence that the ions in the supercages are hydrated has been enumerated by Baur[8] and will not be presented here. We will just add the additional statement that this zeolite does obey the Donnan membrane equilibrium.[11] The unusual and interesting feature of this system is that sites are located in the different networks of cavities. The sites in the large cages might be expected to exhibit the same selectivity series as that exhibited by commercially available resinous-type exchangers such as Dowex-50 in dilute or moderately concentrated solutions[3] because of the higher water content and more open structure, whereas the sites in the network of small cavities might be expected to exhibit a different selectivity series more characteristic of less open zeolites. Polyfunctionality is built into this crystal.

Experimental Section

All reagents used were Baker Analyzed reagent grade with the exception of RbCl and CsCl of 99.9% purity which were purchased from the Kawecki Chemical Co.

The Na–X used was Linde 13-X Lot No. 262. An average of three analyses is given in Table I on an anhydrous basis.

(2) L. L. Ames, Jr., *Am. Mineralogist*, **49**, 127 (1964).

(3) F. Helfferich, "Ion Exchange," McGraw-Hill Book Co., Inc., New York, N. Y., 1962.

(4) G. Eisenman, *Biophys. J.*, **2**, 259 (1962).

(5) G. Bergerhoff, H. Koyama, and W. Nowacki, *Experientia*, **12**, 418 (1956).

(6) G. Bergerhoff, W. H. Baur, and W. Nowacki, *Neues. Jahr. Mineral. Monatsh.*, 193 (1958).

(7) L. Broussard and D. P. Shoemaker, *J. Am. Chem. Soc.*, **82**, 1041 (1960).

(8) W. H. Baur, *Am. Mineralogist*, **49**, 697 (1964).

(9) R. M. Barrer and G. C. Bratt, *J. Phys. Chem. Solids*, **12**, 130 (1959).

(10) Determined by the author and many others in these laboratories.

(11) R. M. Barrer and A. S. Walker, *Trans. Faraday Soc.*, **60**, 171 (1964).

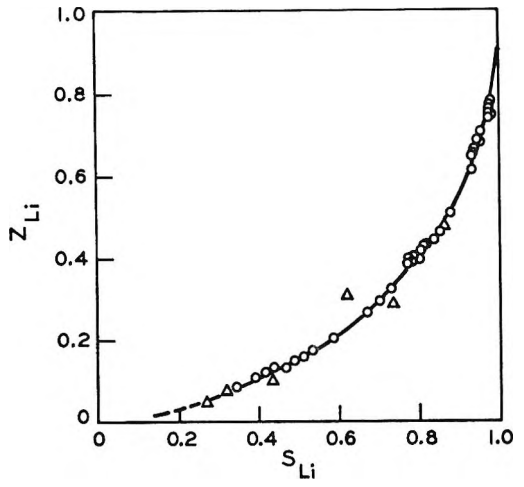

Figure 1. The ion-exchange isotherm for the Li–Na–X system at 0.1 total normality and 25°: O, $Li_S^+ + Na_Z^+$; △, $Na_S^+ + Li_Z^+$.

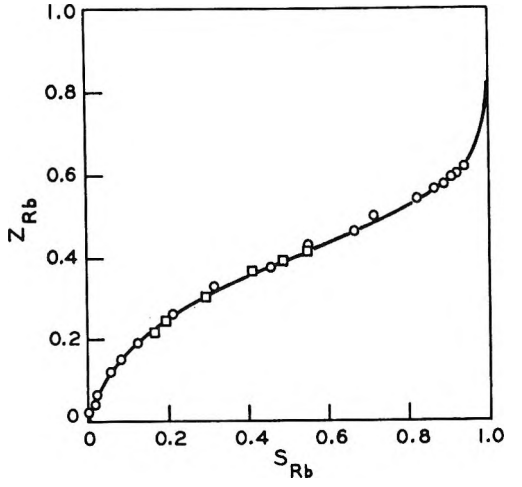

Figure 3. The ion-exchange isotherm for the Rb–Na–X system at 0.1 total normality and 25°: O, $Rb_S^+ + Na_Z^+$; □, $Na_S^+ + Rb_Z^+$.

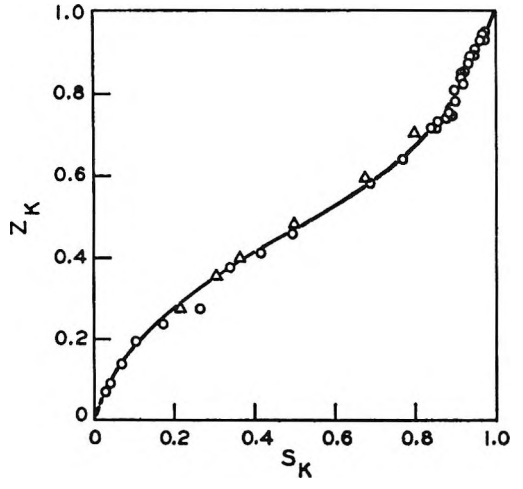

Figure 2. The ion-exchange isotherm for the K–Na–X system at 0.1 total normality and 25°: O, $K_S^+ + Na_Z^+$; △, $Na_S^+ + K_Z^+$.

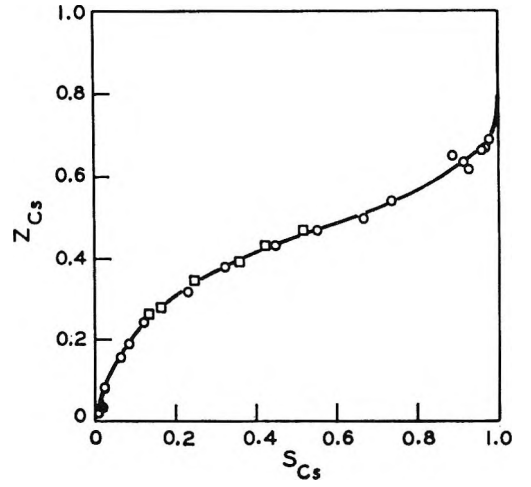

Figure 4. The ion-exchange isotherm for the Cs–Na–X system at 0.1 total normality and 25°: O, $Cs_S^+ + Na_Z^+$; □, $Na_S^+ + Cs_Z^+$.

Table I: Chemical Analyses of Zeolites Used in This Study

Zeolite	SiO_2	Al_2O_3	Na_2O
Na–X			
Wt %	46.8	32.2	21.0
Millimoles/gram	7.79	3.16	3.38
Na–Y			
Wt %	65.6	20.9	12.1
Millimoles/gram	10.92	2.05	1.96

The atom ratio of Na/Al in Na–X was 1.07 as received, probably due to NaOH occluded during synthesis, and the SiO_2/Al_2O_3 mole ratio was 2.46 ± 0.02. Batches of zeolite were washed with deionized water until the atom ratio of Na/Al was 1.00 ± 0.02 and then stored in desiccators over saturated NH_4Cl solution to maintain constant moisture content. When constant weight was reached, the moisture content was determined in duplicate by calcining samples for 5 hr at 815°. The same procedure of washing and storing over saturated NH_4Cl solution was used when other ion-exchanged forms of the zeolite were prepared.

The average of three analyses of the Na–Y used is also given in Table I. The atom ratio of Na/Al was 0.955 ± 0.045, and the SiO_2/Al_2O_3 mole ratio was 5.33. This zeolite was contacted four times for 2 hr each

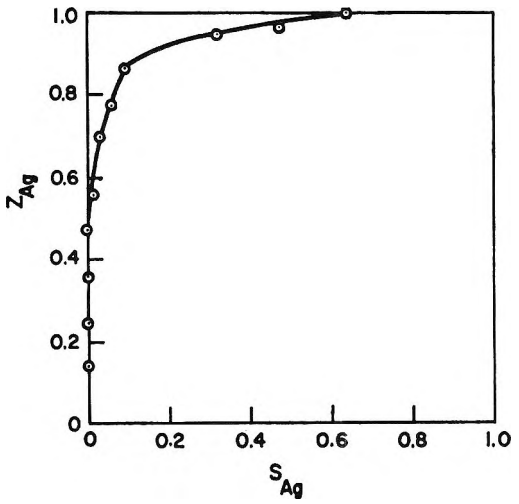

Figure 5. The ion-exchange isotherm for the Ag–Na–X system at 0.1 total normality and 25°: ⊙, $Ag_S^+ + Na_Z^+$.

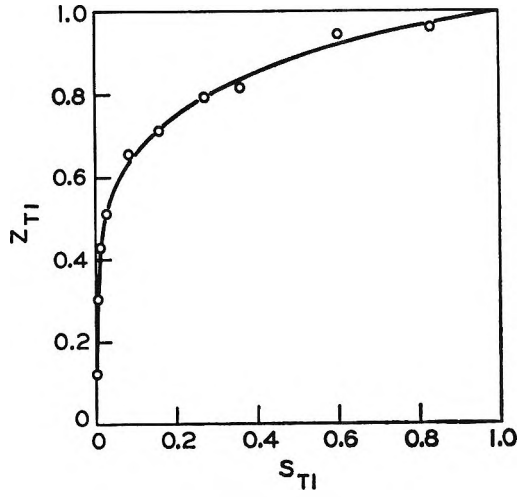

Figure 6. The ion-exchange isotherm for the Tl–Na–X system at 0.1 total normality and 25°: O, $Tl_S^+ + Na_Z^+$.

with 1.0 *M* NaCl solution and then stored in desiccators as described above for Na–X. Both zeolites had negligible amounts of crystalline impurities or amorphous material.

Equilibrations were performed in polyethylene bottles to which were added the appropriate quantities of zeolite and solution. The amounts of zeolite and solution used were measured by weighing the bottles before and after each addition. The bottles were agitated in a water bath for 24 hr. The temperature of the water bath was maintained at 25 ± 0.1°. Sodium isotope exchange showed that equilibrium was reached in less than 1 hr. After equilibration the phases were rapidly separated by filtration. The extent of exchange was determined by obtaining a complete chemical analysis of both phases, cation analysis of both phases, or cation analysis of the solution phase. In the latter case, the chemical analysis of the zeolite phase was calculated from the solution analyses before and after exchange and from the initial Na^+ and H_2O content of the zeolite phase.

Selected ion-exchanged samples of zeolite were submitted to X-ray analysis to ensure that the crystal structure was retained after exchange.

Results and Discussion

The ion-exchange isotherms for the Li–Na–X, K–Na–X, Rb–Na–X, Cs–Na–X, Ag–Na–X, and Tl–Na–X systems at 25° and 0.1 total normality are shown in Figures 1 through 6. In these figures Z_{Li}, Z_K, etc. represent the ratio of the equivalents of the ion of interest to the total equivalents of cations in the zeolite, or to the gram-atoms of aluminum in the zeolite. This is the equivalent fraction of the ion of interest. The concentrations in the solution, S_{Li}, S_K, etc., are also expressed in equivalent fractions.

The K–Na–X, Rb–Na–X, and Cs–Na–X isotherms show selectivity reversals. This is due to the fact that the univalent cations are located in three different kinds of crystallographic sites, each of which should exhibit different preferences for alkali metal ions. Let us assume, in the case of K^+, Rb^+, and Cs^+ exchange of Na–X, that the order of exchange of the sites is: (1) Exchange of the 37 cations per unit cell in the large cages which cannot be located by X-ray techniques. These ions probably are present in the large cages as hydrated ions.[8] (2) Exchange of the 32 cations per unit cell located near the rings of 6 tetrahedra which interconnect the supercages and the sodalite cages.[7] (3) Exchange of the 16 cations per unit cell which are located in either the hexagonal prisms[7] or the sodalite cages.[8]

The 37 sites which do not bind ions tightly and whose counterions probably exist as hydrated ions should prefer all of the alkali metal ions, except Li^+, to Na^+ from consideration of hydrated ionic radii[12] and coulombic interactions between the hydrated counterions and the anionic sites. Thus, the selectivity series Ag >> Tl > Cs > Rb > K > Na > Li is encountered below about 40% exchange. At the other two sets of cation positions, consideration of the lattice oxygen–counterion internuclear distances[7] leads to the conclusion that there are no water molecules interposed between the fixed anionic sites and the counterions. The selectivity of these sites for the counterions is

(12) E. R. Nightingale, Jr., *J. Phys. Chem.*, **63**, 1381 (1959).

the net result of the opposing effects of the free energy due to coulombic interactions between the partially dehydrated counterion and the negatively charged lattice of and the free energy of partial ion dehydration. On this basis, the selectivity series for the 32-fold set of sites located in the center, or slightly displaced from the center, of the rings of 6 tetrahedra separating the supercages from the sodalite cages which is observed in the region of 50% exchange, Ag >> Tl > Na > K > Rb ≥ Cs > Li, is entirely reasonable. It is one of the 11 selectivity series predicted by Eisenman.[4]

The selectivity for alkali metal ions exhibited by the set of 16 sites, located either in the hexagonal prisms or in the sodalite cages, cannot be interpreted solely on the basis of equilibrium selectivity for the following reason. It has not been possible to prepare pure Rb–X and Cs–X even when the exchange equilibria have been forced by contacting RbSCN and CsSCN with Ag–X at 22°. This result should be expected because the crystal radii of Rb^+ and Cs^+ are appreciably greater than the 2.4-A diameter openings to the network of small cavities.[13] This result is also consistent with the report that Cs^+ and Rb^+ penetrate sodalite with great difficulty and that only partial exchange was attained after 5 days of exchange of the Ag form of basic sodalite with RbCl and CsCl at 85°.[14] This crystalline aluminosilicate is composed wholly of sodalite cages, and an ion must diffuse through rings of 6 tetrahedra about 2.4 A in diameter in order to penetrate it. It is for this reason that we believe the isotherms for the Rb–Na–X and Cs–Na–X systems should terminate at the point $S = 1$, $Z = 0.82$, which corresponds to an X-type zeolite with 16 out of 85 Na^+ left in the unit cell. If we reject consideration of Cs^+ and Rb^+ selectivity in the network of small cavities for steric reasons, the equilibrium selectivity exhibited for the remaining 5 ions by the sites in the small cavities is Ag > Tl > Na > K > Li.

High selectivity for Ag^+ and Tl^+ exhibited by Linde X over the whole course of the exchange reaction is demonstrated in Figures 5 and 6. This is consistent with the high polarizability of Ag^+ and Tl^+ and indicates strong binding by all types of anionic sites.

We would like to stress the importance of properly expressing ionic concentrations and standard states in zeolites. We have used units of equivalent fractions and have calculated these fractions by calculating the ratio of the equivalents of the ion in question in the zeolite to the equivalents of total cations in the zeolite. This latter quantity was always equal to the gram-atoms of aluminum in the zeolite. This ratio is not synonymous with the ratio of the equivalents of the ion in question to the equivalents of exchange capacity which the zeolite has for that ion if the experimentally determined exchange capacity is not equal to the number of anionic AlO_2^- sites. When the latter method of calculating equivalent fractions is used, the exchange capacity should be reported so that it is made obvious that a point at $S = 1$, $Z = 1$ does not represent a completely exchanged zeolite. This becomes important when the free energy of exchange is calculated.

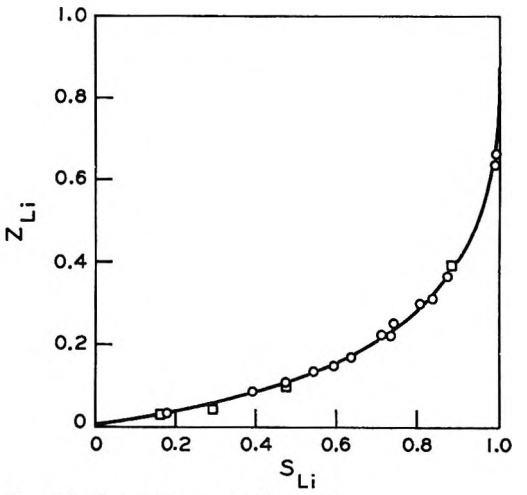

Figure 7. The ion-exchange isotherm for the Li–Na–Y system at 0.1 total normality and 25°: O, $Li_S^+ + Na_Z^+$; □, $Na_S^+ + Li_Z^+$.

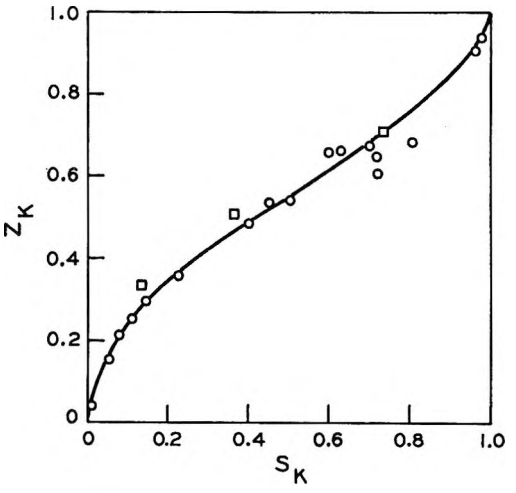

Figure 8. The ion-exchange isotherm for the K–Na–Y system at 0.1 total normality and 25°: O, $K_S^+ + Na_Z^+$; □, $Na_S^+ + K_Z^+$.

(13) T. Moellor, "Inorganic Chemistry," John Wiley and Sons, Inc., New York, N. Y., 1952.

(14) R. M. Barrer and J. D. Falconer, *Proc. Roy. Soc.* (London), **A236**, 227 (1956).

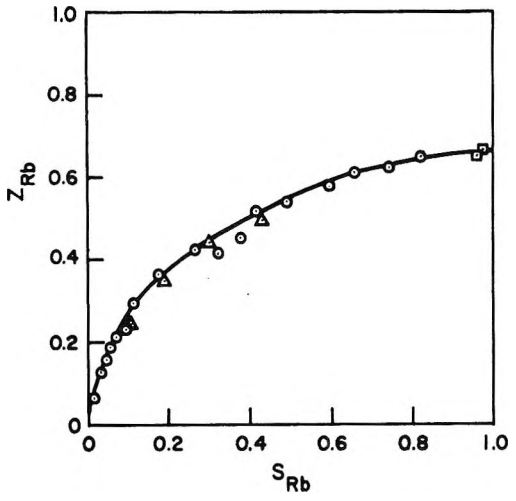

Figure 9. The ion-exchange isotherm for the Rb–Na–Y system at 0.1 total normality and 25°: ⊙, $Rb_S^+ + Na_Z^+$; △, $Na_S^+ + Rb_Z^+$.

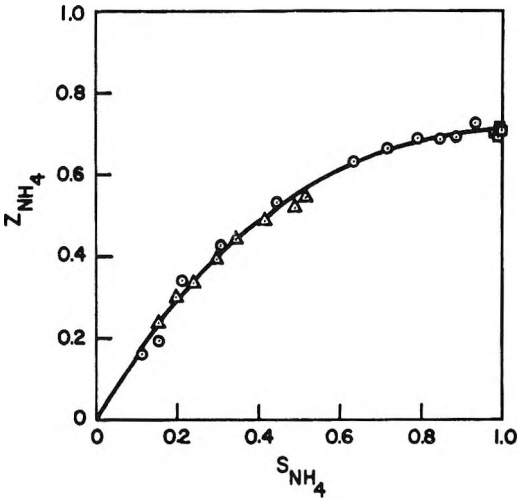

Figure 11. The ion-exchange isotherm for the NH_4–Na–Y system at 0.1 total normality and 25°: ⊙, $NH_{4S}^+ + Na_Z^+$; △, $Na_S^+ + NH_{4Z}^+$.

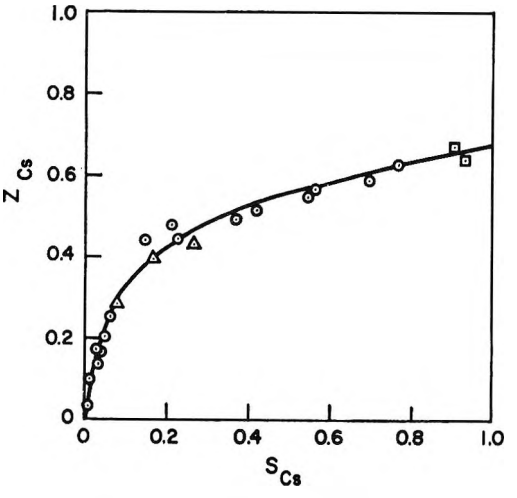

Figure 10. The ion-exchange isotherm for the Cs–Na–Y system at 0.1 total normality and 25°: ⊙, $Cs_S^+ + Na_Z^+$; △, $Na_S^+ + Cs_Z^+$.

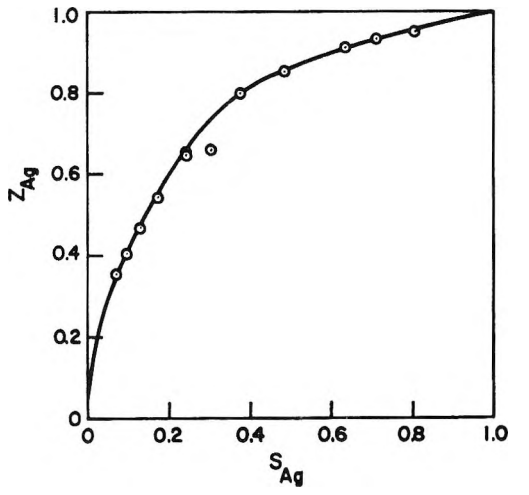

Figure 12. The ion-exchange isotherm for the Ag–Na–Y system at 0.1 total normality and 25°: ⊙, $Ag_S^+ + Na_Z^+$.

At this point in our work we realized that, if our interpretation of the sigmoidal isotherms which describe alkali metal ion exchange in Linde X is correct, the shape of the isotherms in Linde Y might be predicted. We reasoned that in Linde Y, the lower ion-exchange capacity and lower internal molality might lead to less ion binding. The sites in the large cages of Linde Y might all prefer Rb^+, Cs^+, NH_4^+, and K^+ to Na^+ and Na^+ to Li^+, a selectivity series characteristic of hydrated ions in the exchanger phase. Thus, nonsigmoidal isotherms should characterize the ion-exchange properties of the large cages.

The isotherms in Figures 7 to 13 demonstrate that over the first 68% of exchange the selectivity series is Tl > Ag > Cs > Rb > NH_4 > K > Na > Li. Most important to note is the nonsigmoidal nature of the Cs–Na–Y, Rb–Na–Y, NH_4–Na–Y, and Tl–Na–Y isotherms and the fact that, from the shapes of these isotherms, we can safely say that 32% of the Na^+ ions, or 16 per unit cell, are not replaceable by these 4 cations at 25°. The Linde-Y systems can be interpreted as follows.

(1) The nonsigmoidal shape of the isotherms below the 68% exchange level indicates no site heterogeneity in the large cages.

(2) The termination of the Rb, Cs, NH_4, and Tl–

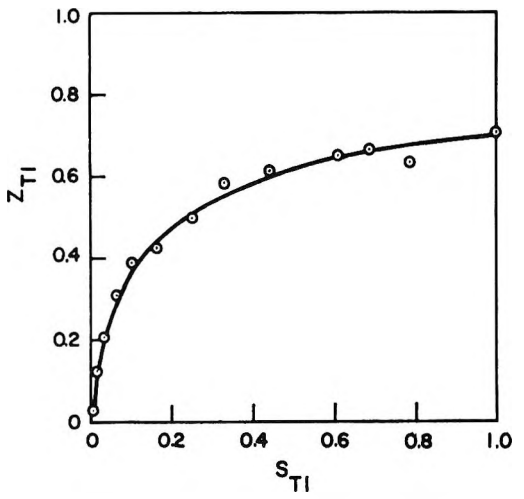

Figure 13. The ion-exchange isotherm for the Tl–Na–Y system at 0.1 total normality and 25°: ⊙, $Tl_S^+ + Na_Z^+$.

Na–Y isotherms at the point $S = 1$, $Z = 0.68$ indicates these ions are too large to penetrate the sodalite cages.

(3) The sodalite cages can be penetrated by Li^+, Na^+, Ag^+, and K^+ indicating that the rings of six Si–AlO_4 tetrahedra which are the windows between the large cages and the sodalite cages have an effective diameter, for the purpose of univalent ion exchange, of between 2.66 and 2.88 A at 25° if Pauling's crystal radii of the cations are used.

(4) The sites in the network of small cavities exhibit a selectivity pattern typical of a surface which binds ions tightly: Ag > Na > K > Li.

This last statement is consistent with the fact that there are 16 univalent cations and 32 water molecules per unit cell in the network of small cavities.[8] The cation–lattice oxygen internuclear distance also indicates direct coordination of the cation to the fixed negative charges[8] on the surface of the zeolite.

The isotherms for the Ag–Na–X and Ag–Na–Y systems shown in Figures 5 and 11 support these conclusions. The preference of the sodium–faujasite crystal for Ag^+ over Na^+ is sharply reduced as $NaAlO_2$ is replaced by SiO_2 (going from Linde X to Linde Y). This change is to be expected, if the binding of Ag^+ by the anionic surface decreases in the same direction and is consistent with the decrease in site density at constant water content in the unit cell.

We can summarize by stating that the 16 cations in the network of small cavities in Linde X and Linde Y form ion pairs with the fixed negative charges of the aluminosilicate backbone. The cations in the large cages, which comprise the majority, behave differently in Linde X and Y. In Linde X the majority of these cations are tightly bound to the fixed negative charges on the aluminosilicate backbone. X-Ray diffraction studies tell us that 32 of these cations are located near the center of the 32 rings of 6 AlO_4–SiO_4 tetrahedra which are the windows between the large cavities and sodalite cages.[7] Some of the remaining 37 cations may also be bound to the zeolite backbone. In Linde Y the majority of cations in the large cavities are probably completely hydrated, and we can think of the salt $NaAlO_2$ as being completely ionized.

Support for this view is found in the study of electrolyte imbibement by Linde X and Y made by Barrer and Walker.[11] Their data indicate that Na-X imbibes much more NaCl from NaCl solutions than does Na–Y. Consideration of ion-exchange capacity alone makes this result anomalous. However, this apparent anomaly can be explained by assuming extensive cation binding in the Na–X crystal and little cation binding in the Na–Y crystal.

As a result of the ion-exchange data, we predict that a determination of the complete crystal structure of hydrated Na–Y should show that the rings of 6 tetrahedra which are the windows between the large cages and the sodalite cages (a 32-fold set of sites) are empty of cations, or, if there are cations located near these rings, the univalent cation–lattice oxygen internuclear distances will be larger than in Linde X, large enough to support interposition of water molecules between the cation and the lattice oxygen atoms. In this latter case we are dealing with ionic atmosphere binding in the sense used by Strauss,[15] that is, the localization of hydrated cations by the electrostatic field of the negatively charged lattice.

If our interpretation of all of the isotherms encountered in univalent exchange of Linde X and Y is correct, sigmoidal isotherms should also be encountered in Linde 4-A. In this zeolite, which has 12 sodium ions per unit cell, 4 ions cannot be located and are probably completely hydrated when the zeolite is fully hydrated, and 8 are located near the center of six-membered rings of tetrahedra. These latter rings are the windows between large and small cavities. The lattice oxygen–sodium internuclear distances[16] indicate that the ions in the rings of 6 tetrahedra are bound to the surface through oxygen atoms.

This distribution of ion sites is strikingly similar to that encountered in Linde 13-X;[5-8] hence, we would predict sigmoidal Cs–Na, Rb–Na, and K–Na isotherms. Indeed, sigmoidal isotherms have been reported for these systems in Linde A.[1]

(15) U. P. Strauss and Y. P. Leung, *J. Am. Chem. Soc.*, 87, 1476 (1965).

(16) T. B. Reed and D. W. Breck, *ibid.*, 78, 5972 (1956).

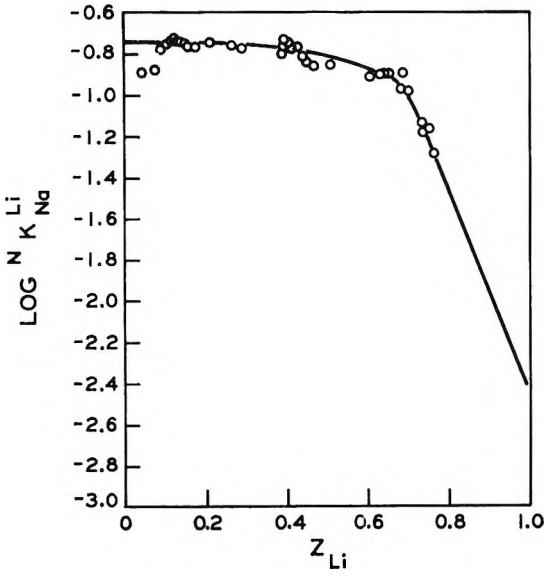

Figure 14. The rational selectivity coefficient for the Li–Na–X system at 0.1 total normality and 25° as a function of zeolite composition.

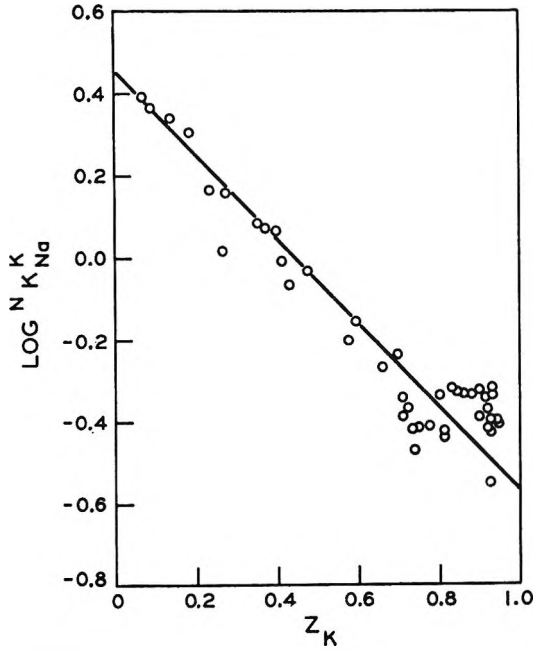

Figure 15. The rational selectivity coefficient for the K–Na–X system at 0.1 total normality and 25° as a function of zeolite composition.

A most interesting feature of the faujasite series is that Tl^+ will replace all of the cations in Na–X but will not replace 16 cations per unit cell in Na–Y. This is illustrated in Figures 6 and 13. This difference in behavior of Tl^+ in the more siliceous form of synthetic faujasite is attributed to the lattice contraction which occurs when SiO_2 replaces $NaAlO_2$. We have observed

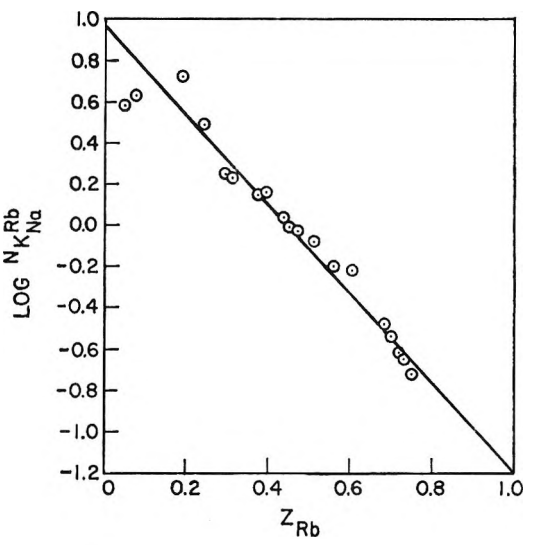

Figure 16. The rational selectivity coefficient for the Rb–Na–X system at 0.1 total normality and 25° as a function of zeolite composition.

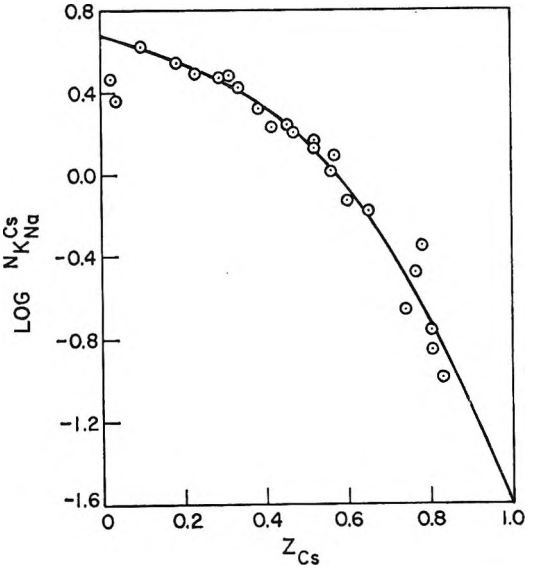

Figure 17. The rational selectivity coefficient for the Cs–Na–X system at 0.1 total normality and 25° as a function of zeolite composition.

that the lattice parameter, a_0, for this cubic unit cell can change by as much as 0.05 A. This lattice contraction must be sufficient to prevent Tl^+ from penetrating the sodalite cages of Na–Y.

We have calculated the free energy of exchange for the reaction $M_S^+ + Na_Z^+ \rightleftharpoons M_Z^+ + Na_S^+$, by using the method of Gaines and Thomas.[17] A modified

(17) G. L. Gaines and H. C. Thomas, *J. Chem. Phys.*, 21, 714 (1953).

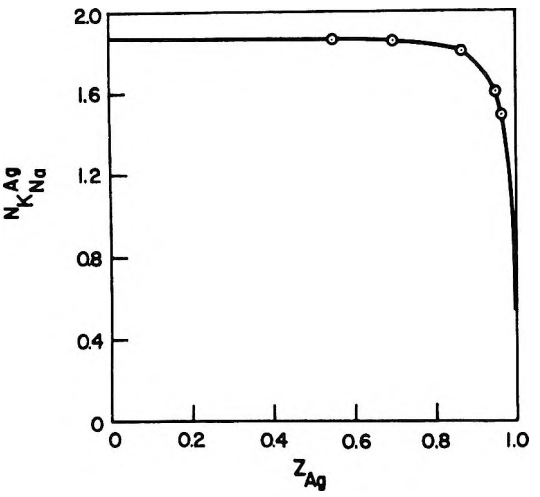

Figure 18. The rational selectivity coefficient for the Ag–Na–X system at 0.1 total normality and 25° as a function of zeolite composition.

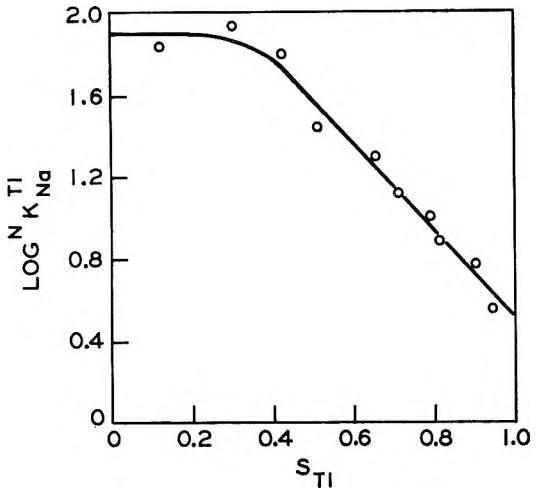

Figure 19. The rational selectivity coefficient for the Tl–Na–X system at 0.1 total normality and 25° as a function of zeolite composition.

form of their equation, which neglects salt imbibement and changes in water activity, was used

$$\Delta F^\circ_T = -2.303RT \times \left[\int_{Z=0}^{Z=1} \log {}^{N}K_{Na}^{M}\, dZ + 2\int_{Z=0}^{Z=1} \log \frac{(\gamma_\pm)_{Na}}{(\gamma_\pm)_M}\, dZ\right]$$

$$\Delta F^\circ_{298} = -1362 \times \int_{Z=0}^{Z=1} \log {}^{N}K_{Na}^{M}\, dZ - 2724\int_{Z=0}^{Z=1} \log \frac{(\gamma_\pm)_{Na}}{(\gamma_\pm)_M}\, dZ$$

In this equation the rational selectivity coefficient for the exchange of the metal ion in question into Na–X, ${}^{N}K_{Na}^{M}$, is defined as

$${}^{N}K_{Na}^{M} = \frac{Z_M S_{Na}}{Z_{Na} S_M}$$

and $\gamma_\pm$ is the mean molal activity coefficient. Use of this equation is justified because imbibement[11] of external electrolyte and changes in water activity[18] are negligible at a total ionic strength of 0.1 (the total normality was always maintained at 0.1). Activity coefficient ratios were calculated using Harned's rule[15] by assuming that the interaction coefficient for one ion is the negative of that for the other ion. This procedure is justified because the change in the activity coefficient ratio with change in solution composition is small.

The first integral in the free energy equation was graphically evaluated by calculating the area under the curve obtained by plotting the logarithm of the rational selectivity coefficient *vs.* ionic composition of the zeolite. These plots are shown in Figures 14 to 26. The rational selectivity coefficients for Rb and Cs ion exchange into Na–X and Na–Y and for Tl(I) and NH_4 ion exchange in Na–Y were calculated from normalized ion-exchange isotherms. The ordinate in the normalized

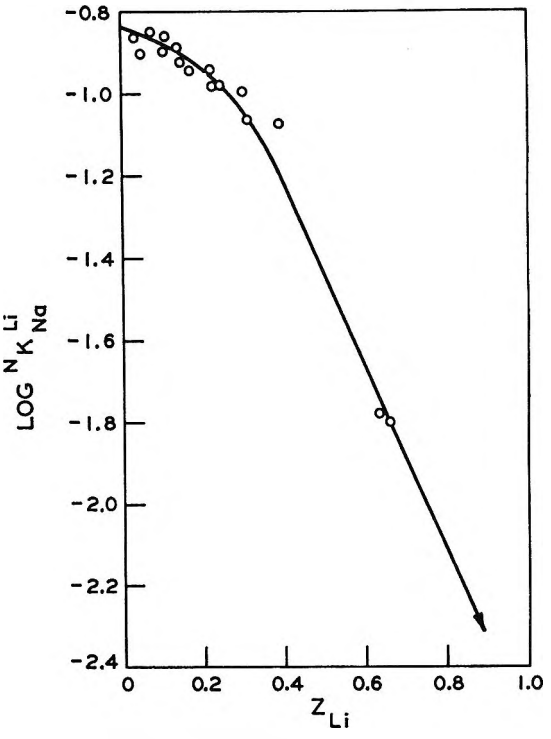

Figure 20. The rational selectivity coefficient for the Li–Na–Y system at 0.1 total normality and 25° as a function of zeolite composition.

(18) R. A. Robinson and R. H. Stokes, "Electrolyte Solutions," Butterworth and Co. Ltd., London, 1959.

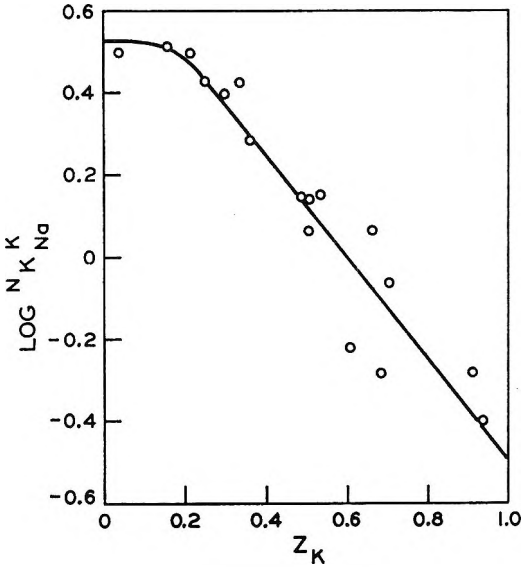

Figure 21. The rational selectivity coefficient for the K–Na–Y system at 0.1 total normality and 25° as a function of zeolite composition.

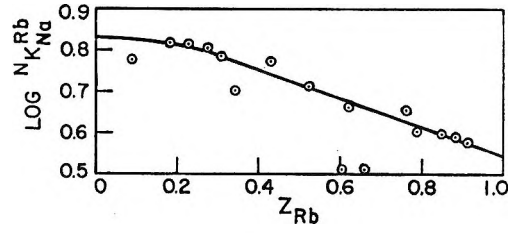

Figure 22. The rational selectivity coefficient for the Rb–Na–Y system at 0.1 total normality and 25° as a function of zeolite composition.

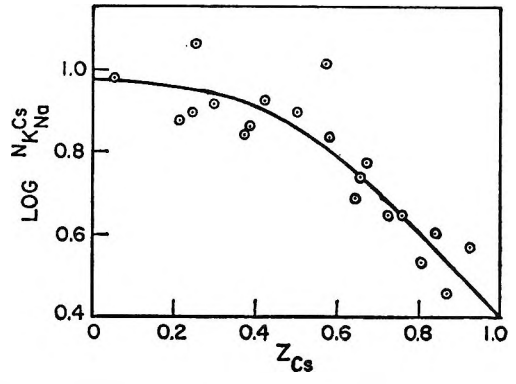

Figure 23. The rational selectivity coefficient for the Cs–Na–Y system at 0.1 total normality and 25° as a function of zeolite composition.

isotherms is the ratio of the equivalents of the ion of interest to the total equivalents of exchangeable cations. Thus, in the case of Rb and Cs ion exchange

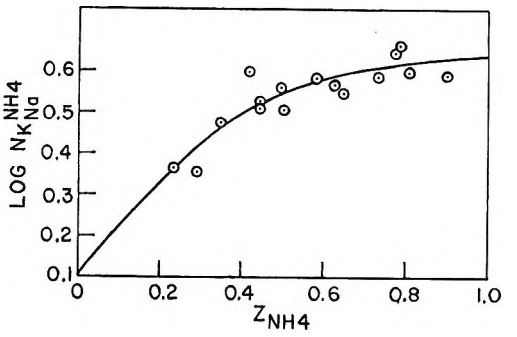

Figure 24. The rational selectivity coefficient for the NH_4–Na–Y system at 0.1 total normality and 25° as a function of zeolite composition.

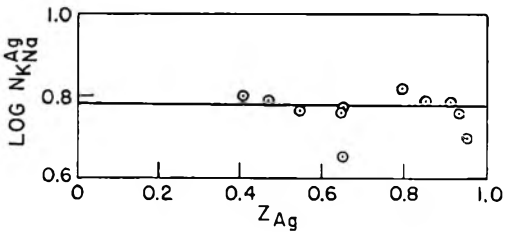

Figure 25. The rational selectivity coefficient for the Ag–Na–Y system at 0.1 total normality and 25° as a function of zeolite composition.

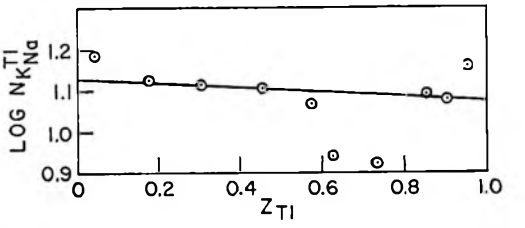

Figure 26. The rational selectivity coefficient for the Tl–Na–Y system at 0.1 total normality and 25° as a function of zeolite composition.

of Na–X, the total milliequivalents of exchangeable cations per gram of zeolite is 82% of the milliequivalents of Na per gram reported in Table I. In the case of Rb, Cs, Tl(I), and NH_4 ion exchange of Na–Y, the total milliequivalents of exchangeable cations per gram of zeolite is 68% of the milliequivalents of Na per gram of zeolite reported in Table I. The normalized isotherms all terminate at the point $S = 1$, $Z = 1$. The standard free energies of the ion-exchange reactions, which are listed in Table II, are, then, the differences between the free energy of the sodium form of the zeolite in pure water and the free energy of a zeolite in which all of the Na ions which can be replaced by a second ion have been replaced by that ion. This latter zeolite is also in pure water in its reference state.

Table II: Standard Free Energy of Exchange of Na–X and Na–Y at 25°

Reaction	$\Delta F°_{298}$, cal/equiv of zeolite
$Li^+ + Na–X$	1600 ± 200
$K^+ + Na–X$	140 ± 10
$Rb^+ + Na–X$	140 ± 10
$Cs^+ + Na–X$	87 ± 5
$Ag^+ + Na–X$	−2520 ± 20
$Tl^+ + Na–X$	−1840 ± 100
$Li^+ + Na–Y$	2700 ± 200
$K^+ + Na–Y$	−190 ± 30
$Rb^+ + Na–Y$	−1300 ± 30
$Cs^+ + Na–Y$	−1460 ± 100
$NH_4^+ + Na–Y$	−660 ± 60
$Ag^+ + Na–Y$	−1100 ± 20
$Tl^+ + Na–Y$	−1630 ± 30

The only known thermodynamic data to which the data in Table II can be compared are the data of Ames[2] on K^+ and Cs^+ exchange of Na–X at 25°. In this work, neither the exchange capacity of the zeolite nor the final state of the zeolite is reported for Cs^+, and it is difficult to compare our data. However, the Cs–Na–X isotherm is extrapolated through the point $S = 1$, $Z = 1$. If this point represents a pure Cs form of zeolite X, then we believe the extrapolation to be incorrect. If the composition in the zeolite is normalized so that the point $S = 1$, $Z = 1$ represents the zeolite $Cs_{0.82}Na_{0.18}X$ in equilibrium with pure 1.0 N CsCl, the extrapolation is correct. However, we report in Table II that the standard free energy of exchange of Na–X to $Cs_{0.82}Na_{0.18}X$ is 87 cal/equiv of Na–X using a normalized isotherm. Ames reports 600 cal. If we extrapolate our unnormalized Cs–Na–X isotherm to the point $S = 1$, $Z = 1$, we obtain close to 600 cal. Evidently, Ames has assumed that all of the sodium ions in Na–X are replaceable by cesium ions and has extrapolated an unnormalized Cs–Na–X isotherm to the point $S = 1, Z = 1$.

This problem should not exist in the K–Na–X system. In Table II, we report that the standard free energy of exchange of Na–X to K–X is 140 cal/equiv of zeolite; Ames reports −200 cal/mole of zeolite (presumably per equivalent of zeolite). We cannot account for this difference, unless the difference in total normality is the cause. The fact that Ames obtained his isotherm at a total normality of 1.0 may mean that imbibement of external electrolyte occurred.[11] Our ion-exchange isotherms do agree with the alkali metal ion selectivity series at the 50% exchange level reported by Barrer, Buser, and Grutter.[19]

Conclusions

The cation positions in synthetic faujasite are reasonably well defined, and we have interpreted selectivity reversals in terms of differing selectivities of the various types of sites for alkali metal ions. It is important to realize that all of the sites in a crystalline ion exchanger may not be accessible to all cations and that the ion-exchange capacity of zeolites can vary with the ingoing cation. Thus, extrapolation of an isotherm to 100% exchange is not always justifiable. Much confusion can result in the literature if ion-exchange capacities are not published along with the ion-exchange isotherms. We have found that we cannot put Rb^+ and Cs^+ into the small cavities of Ag–X by using concentrated solutions of the SCN salts at room temperature and have concluded that these ions are sterically hindered from entering these cages. Our results in the Linde-Y systems verify this.

The nonsigmoidal isotherms in the Rb–Na–Y and Cs–Na–Y systems and sigmoidal isotherms over the first 82% exchange in the Rb–Na–X and Cs–Na–X systems indicate extensive ion binding in the supercages of the Linde-X type of synthetic faujasite and little ion binding in the supercages of the Linde-Y type of synthetic faujasite.

Acknowledgments. The author wishes to express his appreciation to the Socony Mobil Oil Co., Inc., for its support and encouragement of this work. In particular, he wishes to thank Dr. L. J. Reid and Mr. A. B. Schwartz for many helpful discussions and Mr. J. F. Charnell for his X-ray analyses of many zeolite samples.

(19) R. M. Barrer, W. Buser, and W. F. Grutter, *Chimia* (Aarau), 9, 118 (1955).

The Critical Temperature and Coexistence Curve for Mercuric Chloride[1]

by J. W. Johnson, W. J. Silva, and Daniel Cubicciotti

Stanford Research Institute, Menlo Park, California 94025 *(Received October 20, 1965)*

The critical temperature of $HgCl_2$ has been determined as 972 ± 2°K and the critical density has been found by extrapolation to be 1.555 ± 0.006 g/cc. Mercuric chloride, as it undergoes critical transition during heating and cooling, exhibits many of the same features as does ethyl ether. The experimental densities of the two phases were fitted to a modified Guggenheim relation

$$\rho\ (\mathrm{g/cc}) = 1.555 + 1.473\left(\frac{972 - T}{972}\right) \pm 2.981\left(\frac{972 - T}{972}\right)^{1/3} \mp 1.000\left(\frac{972 - T}{972}\right)^{3}$$

In the last two terms the upper sign refers to the liquid phase and the lower to the vapor. Above 800°K the contribution of the last term becomes less than the average deviation and the relation assumes the standard form.

Introduction

Previous work in this laboratory[2-4] has been concerned with the thermodynamic parameters of vaporization of some electrically conducting molten salts between their normal boiling point and the vapor–liquid critical point. This is a report of the determination of the coexistence curve and critical temperature of mercuric chloride, a nonconducting molten salt.

Experimental Section

Baker's Analyzed reagent mercuric chloride was recrystallized from 0.05 *N* hydrochloric acid solution. The long, needlelike crystals were dried in a vacuum desiccator with continuous pumping for 72 hr; an ultimate pressure of 5×10^{-3} mm was maintained for the last 24 hr.

Mercury and chloride were determined on the same sample of the product by precipitating mercury as the sulfide and subsequently determining chlorine in the filtrate as silver chloride. The analytical results on three samples are given in Table I.

Melting and solidification of this preparation were observed to occur in the temperature range of 280.7 ± 0.5° in a sealed quartz capsule fitted with a reentrant thermocouple well. This value is to be compared with 279.5° reported by Yosim and Mayer[5] and 277° given in the NBS compilation.[6]

The furnace employed in this investigation was a modification of one described earlier.[2] The modification allowed the sample to be viewed by transmitted light and employed a nickel block with illumination and observation slits 3 mm in width to minimize radiation losses. Temperature control was maintained by a

Table I

	Wt % Hg	Wt % Cl
	73.88	26.12
	73.95	26.12
	73.84	26.16
Average	73.89	26.13
Theoretical	73.88	26.12

(1) This work was made possible by the support of the Research Division of the U. S. Atomic Energy Commission under Contract No. AT(04-3)-106.

(2) J. W. Johnson and D. Cubicciotti, *J. Phys. Chem.*, 68, 2235 (1964).

(3) J. W. Johnson, D. Cubicciotti, and W. J. Silva, *ibid.*, 69, 1989 (1965).

(4) J. W. Johnson, W. J. Silva, and D. Cubicciotti, *ibid.*, 69, 3916 (1965).

(5) S. J. Yosim and S. W. Mayer, *ibid.*, 64, 909 (1960).

(6) "Selected Values of Chemical Thermodynamic Properties," National Bureau of Standards Circular 500, U. S. Government Printing Office, Washington, D. C., 1952.

chromel–alumel thermocouple inserted in the block connected to a Wheelco controller. The temperature of the block was measured by a platinum—platinum–10% rhodium thermocouple previously calibrated against an NBS standard.

To establish the temperature in the interior of the sealed quartz tube, a calibration curve was determined based on the temperature indicated by the measuring thermocouple. A second platinum—platinum–10% rhodium couple, previously compared with the measuring thermocouple, was inserted into a length of quartz tubing having the same dimensions as the sealed tube, and the readings of the two couples at various positions and temperatures were compared. From these data a series of corrections to be applied to the reading of the measuring couple was obtained.

The liquid–vapor critical transition, *i.e.*, the disappearance of the liquid–vapor interface in the interior of the tube, was observed visually. The correction corresponding to the last observed position of the meniscus was applied to the indicated temperature to obtain the true temperature. The tubes used for the critical transition were either 2 or 3 mm i.d. × 6 mm o.d. × 4 cm long, approximately one-third filled with molten mercuric chloride at 300°.

The orthobaric liquid phase densities were determined by the float method employed in earlier work,[2,3] and additional measurements just above the melting point were made using a dilatometer. The quartz dilatometer consisted of a bulb section 2.5 cm long and a 5-mm bore which was sealed to a 2-mm bore tubing section. A fiduciary mark was inscribed on the stem just above the bulb section and the volume was determined as a function of height above this mark by calibration with mercury at room temperature. The volume at the reference mark was 0.4816 cc and the weight of $HgCl_2$ was 2.1069 g.

The vapor densities were obtained by the following method: the changes of the liquid and vapor volumes are measured as the total volume of a system which contains a fixed amount of mercuric chloride is reduced. For such a system the liquid and vapor volumes are related by the two equations

$$M = \rho_1 V_1' + \rho_2 V_2' \quad (1a)$$

$$M = \rho_1 V_1'' + \rho_2 V_2'' \quad (1b)$$

where M is the total mass of $HgCl_2$, $\rho_1 V_1$, $\rho_2 V_2$ denote the density and volume of the coexisting liquid and vapor phases, respectively, and the single and double prisms refer to different total volumes. The equation may be solved simultaneously to give

$$\rho_2/\rho_1 = -\frac{(V_1' - V_1'')}{V_2' - V_2''}; \quad \rho_2 = -\rho_1(\Delta V_1/\Delta V_2) \quad (2)$$

To obtain the variation in volume of the two phases, the following method was employed. On a quartz tube, sealed at one end, a reference mark was inscribed approximately 2 cm above the bottom, and the volume was determined at 1-mm intervals over a tube length of 5 cm. The tube was charged with $HgCl_2$, evacuated, and sealed off under vacuum at a distance 4.5 cm above the bottom. Although the calibration at the top of the tube was destroyed by the sealing process, it remained valid for a distance of at least 3.5 cm above the bottom.

The tube was inserted into the furnace in an upright position with the $HgCl_2$ in the calibrated portion of the tube. The height, and therefore the volume, of the liquid phase was determined at 25° intervals up to a temperature about 25° below the critical temperature by measuring the distance between the reference mark and the bottom of the liquid meniscus with a cathetometer graduated to 0.0001 cm. The tube was then removed from the furnace and inserted top end down and the volume of the vapor at the same temperatures was determined by measuring the distance between the reference mark and the bottom of the liquid meniscus. At this stage the measured volume of the liquid phase was smaller than the true liquid volume by the amount of liquid above the bottom of the meniscus, whereas the true vapor volume was greater than the measured vapor volume by the same amount.

The tube was then removed from the furnace and the $HgCl_2$ was distilled back to the bottom or calibrated section. A portion of the top end of the tube was sealed off, reducing the total volume by approximately 15% while the total mass of $HgCl_2$ remained constant. The above procedure was repeated for both liquid and vapor volumes and a new set of values determined at the same temperatures. Subtracting the second set of liquid and vapor volumes from the first set, obtained at the same temperature, eliminates the meniscus error, and substitution of these differences into eq 2, together with the known liquid density, ρ_1, allowed the vapor density, ρ_2, to be calculated.

At temperatures near the normal boiling point, this method is not very accurate because the difference in liquid volumes is quite small, but at higher temperatures it becomes quite useful. Two separate runs were made with 2- and 3-mm bore tubes. To check the results, the vapor density was measured at three temperatures by observing the disappearance of the liquid phase and determining the mass of $HgCl_2$ and the internal volume of the tube.

Results and Discussion

The liquid–vapor critical transition was observed in each of three tubes with increasing and decreasing temperatures. The results are given in Table II, along with tube dimensions and length of liquid column

Table II: Observation of Meniscus in Critical Region

Tube no.	Tube dimensions	Meniscus, T, °K — Disappearance	Meniscus, T, °K — Appearance	Length of liquid column, cm
1	3 mm × 6 mm × 4 cm	972.7 972.6	972.2 972.1	1.920
2	3 mm × 6 mm × 4 cm	972.8 972.6 972.7	972.2 972.1 972.1	2.202
3	2 mm × 6 mm × 4 cm	972.9 972.5	972.3 972.1	2.121

Accepted value 972 ± 2°K

at a temperature just below the critical transition. The temperature range over which the liquid–vapor interface disappears and reappears was not large but it is believed that the temperature of the appearance of the interface is probably closer to the true transition temperature. The critical temperature of 699 ± 2° derived from this work is 5° lower than the 704° reported by Rassow[7] and 4° lower than the 703° calculated by Rotinjanz and Suchhodsky[8] from the data of Prideaux.[9]

The visible changes in appearance of the system as the critical transition is approached from low temperatures and from high temperatures are completely different. With slowly rising temperature, the meniscus becomes quite flat about 3° below the critical transition and appears as a bright line due to reflection of the light off the interface. This line gradually fades into a thin gray cloud which becomes a gray band almost 1 mm thick extending across the tube. Then the band seems to shrink on the vapor side and the top portion of the tube appears to be collapsed due to the difference in light refraction across this band. As the temperature increases further, the gray band diffuses and the entire tube assumes a uniform, hazy appearance about 4° above the transition. The general impression is that the liquid phase just fades out into the supercritical fluid state.

On cooling the equilibrated supercritical fluid from about 5° above the transition, the hazy appearance begins to darken appreciably, then a reddish brown

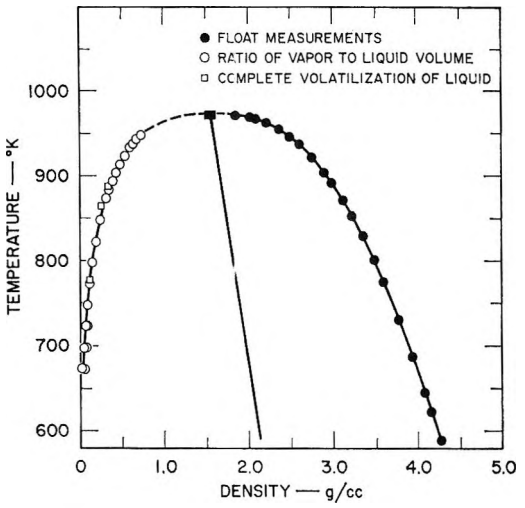

Figure 1. Coexistence curve for mercuric chloride.

band about 5 mm long appears in the middle of the tube, and in the center a black line then appears. Above and below this line small droplets form which are in violent motion. At this point the intensity of transmitted light increases markedly and the droplets appear as points of white light above and below the demarcation line. For some time this violent motion of the droplets in the vapor space and bubbles in the liquid space continue and then gradually subside to a quiescent liquid and vapor space separated by a clearly defined interface.

The appearance of the reddish brown cloud is not characteristic of mercuric chloride since Clark[10] describes the formation of a brown cloud with ethyl ether and goes on to say this changes to white and persists after the meniscus forms.

The orthobaric density data for the liquid and vapor phases of $HgCl_2$ are presented in Table III and shown as a coexistence curve in Figure 1. The extension of the average density line gives a critical density of 1.555 ± 0.006 g/cc at the critical temperature of 972°K. As was the case with the bismuth halides,[2,3] the experimental data can be fitted with the Guggenheim relation[11]

$$\rho = \rho_c + A\left(\frac{T_c - T}{T_c}\right) \pm B\left(\frac{T_c - T}{T_c}\right)^{1/3} \qquad (3)$$

where ρ_c and T_c are the critical density and tempera-

(7) H. Rassow, *Z. Anorg. Allgem. Chem.*, 114, 117 (1920).

(8) L. Rotinjanz and W. Suchhodsky, *Z. Physik. Chem.*, 87, 253 (1914).

(9) E. B. R. Prideaux, *J. Chem. Soc.*, 97, 2032 (1910).

(10) A. L. Clark, *Chem. Rev.*, 23, 1 (1938).

(11) E. A. Guggenheim, *J. Chem. Phys.*, 13, 253 (1945).

Table III: Orthobaric Densities of Mercuric Chloride

Liquid phase density, g/cc			Vapor phase density, g/cc				
T, °K	Obsd	Calcd	T, °K	Tube no. 1	Tube no. 2	Av	Calcd
588.6	4.261	4.260	673.2	0.013	0.049	0.031	0.025
622.0	4.157	4.159	698.2	0.039	0.063	0.051	0.038
645.5	4.070	4.084	723.2	0.060	0.075	0.068	0.056
687.0	3.924	3.942	748.2	0.083	0.090	0.086	0.080
730.5	3.772	3.778	773.2	0.105	0.115	0.110	0.107
775.0	3.590	3.597	776.7[a]	0.105	...	0.105	0.113
801.0	3.480	3.480	798.2	0.142	0.140	0.141	0.145
828.4	3.348	3.347	823.2	0.186	0.175	0.180	0.190
852.4	3.217	3.215	848.2	0.246	0.229	0.237	0.246
870.8	3.119	3.109	864.1[a]	0.256	...	0.256	0.287
891.1	2.981	2.978	873.2	0.318	0.296	0.307	0.313
903.5	2.896	2.887	883.2	0.354	0.331	0.343	0.348
921.7	2.747	2.744	888.8[a]	0.339	...	0.339	0.366
936.4	2.602	2.603	893.2	0.391	0.369	0.380	0.384
945.7	2.488	2.489	903.2	0.438	0.413	0.425	0.425
954.6	2.360	2.363	913.2	0.491	0.463	0.477	0.476
962.0	2.219	2.212	923.2	0.549	0.521	0.535	0.528
967.1	2.091	2.072	933.2	0.604	0.587	0.596	0.594
969.2[b]	2.024	1.989	938.2	0.632	0.621	0.626	0.632
971.2	1.855	1.855	943.2	...	0.668	0.668	0.673
			948.2	...	0.732	0.732	0.730
	Av dev	0.007				Av dev	0.008

[a] Density at temperature of complete vaporization of liquid. [b] Tube burst after float sank.

ture, respectively, A and B are coefficients adjusted to fit the data, and ρ is the density of liquid or vapor (upper sign for liquid and lower sign for vapor phase).

The parameters A, B, and ρ_c of eq 3 were obtained from the method of rectilinear diameters in the following manner. A smooth curve was drawn through the experimental densities and the average density of the two phases was obtained. A straight line was drawn through the averages. The slope of that line gave the constant A and the value of the average density extrapolated to 972°K (T_c) was taken as ρ_c. The differences of the liquid and vapor densities were taken from the curves at several temperatures between 900 and 950°K and an average value of B calculated from them. The resulting equation

$$\rho = 1.555 + 1.473\left(\frac{972 - T}{972}\right) \pm 2.981\left(\frac{972 - T}{972}\right)^{1/3} \quad (4)$$

fit the data well from 800 to 972°K. Below 800°K the calculated liquid densities are higher and the vapor densities lower than found experimentally. Another term was added to eq 4 to fit the entire range from 588 to 972°K.

$$\rho = 1.555 + 1.473\left(\frac{972 - T}{972}\right) \pm 2.981\left(\frac{972 - T}{972}\right)^{1/3} \mp 1.000\left(\frac{972 - T}{972}\right)^{3} \quad (5)$$

The contribution of the added term amounts to 0.061 g/cc at 588.6°K and becomes less than the average deviation, 0.008 g/cc, at 800°K. Equation 5 was used to determine the calculated values and average deviations shown in Table III.

The low-temperature liquid phase densities found in this work are smaller than those obtained by Prideaux[9] using a dilatometer method. To check this discrepancy, a dilatometer method was used to determine the liquid phase densities near the melting point. The experimental data are presented in Table IV, in which the run number associated with each entry refers to separate heating cycles of the same dilatometer. The data can be represented by the linear relation

$$\rho \text{ (g/cc)} = 6.105 - 3.13 \times 10^{-3}T \text{ (558–647°K)} \quad (6)$$

Table IV: Density of Liquid $HgCl_2$ from Dilatometer Measurements[a]

Run no.	Temp, °K	Obsd	Calcd	Run no.	Temp, °K	Obsd	Calcd
1	558.8	4.355	4.356	3	601.8	4.221	4.221
1	559.9	4.354	4.353	3	602.0	4.222	4.221
1	568.0	4.324	4.324	1	606.3	4.206	4.207
3	575.5	4.305	4.304	2	612.2	4.190	4.189
1	577.6	4.296	4.297	2	612.5	4.189	4.188
3	582.7	4.282	4.281	3	622.5	4.156	4.157
1	587.1	4.268	4.267	2	631.7	4.128	4.128
2	592.7	4.254	4.250	2	639.9	4.101	4.102
1	596.3	4.239	4.239	2	647.2	4.076	4.079
1	596.8	4.238	4.238	2	647.5	4.074	4.078

[a] Average deviation ±0.001 g/cc.

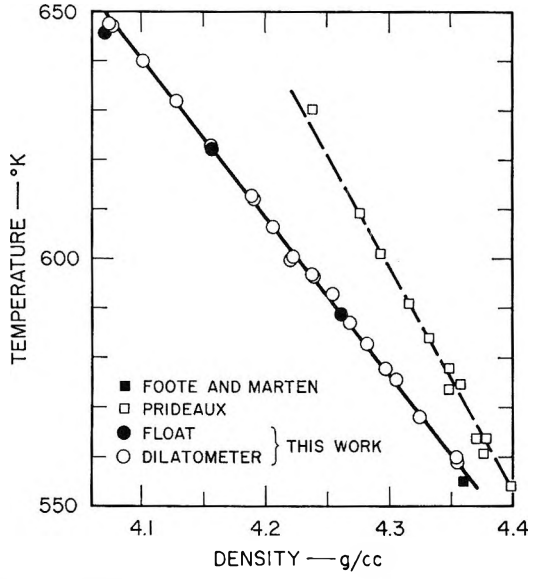

Figure 2. Dilatometer density data for molten mercuric chloride.

with an average deviation of ±0.001 g/cc for the 20 points. This differs considerably from the equation derived from Prideaux's[9] data

$$\rho \text{ (g/cc)} = 5.627 - 2.218 \times 10^{-3}T \text{ (553-630°K)} \quad (7)$$

Foote and Marten[12] report a density of 4.36 g/cc for molten mercuric chloride at 282°. A density of 4.368g/cc at 282° is given by eq 6 while eq 7 gives a value of 4.396 g/cc at this temperature. Figure 2 shows the relation of the dilatometer density data to densities determined by the float method in this investigation. We have no explanation for the discrepancy between the two sets of experimental data. Prideaux distilled his mercuric chloride in a stream of dry chlorine gas and states that the analyses for mercury and chlorine,

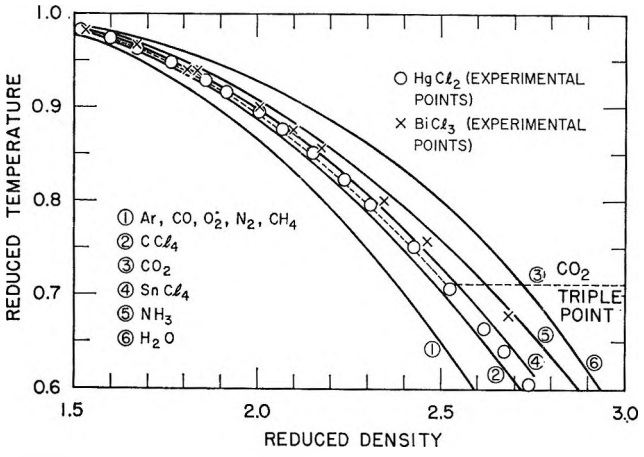

Figure 3. Comparison of liquid phase density of mercuric chloride with several liquids.

as the sulfide and silver salt, respectively, were satisfactory.

The similarity exhibited by the reduced coexistence curves of $HgCl_2$, $BiCl_3$, and $BiBr_3$, neglecting the correction term applied to $HgCl_2$ below 800°K, can be seen from a comparison of the coefficients of the temperature terms in the reduced density relation

$$\rho/\rho_c = 1 + a(1 - T/T_c) \pm b(1 - T/T_c)^{1/3} \quad (8)$$

for $HgCl_2$, $a = 0.947$, $b = 1.917$; for $BiCl_3$, $a = 1.048$, $b = 1.940$; for $BiBr_3$, $a = 0.999$, $b = 1.896$.

The relative position of $HgCl_2$ on a reduced density, reduced temperature plot compared to a number of fluids for which data are available in the literature is shown in Figure 3. It is interesting to note that CO_2, a linear molecule with a dipole moment of zero, like $HgCl_2$, falls on the same curve as $HgCl_2$, while the more spherically symmetric molecules CCl_4 and

(12) H. W. Foote and N. A. Marten, *Am. Chem. J.*, **41**, 451 (1909).

$SnCl_4$ lie on either side. Also, the reduced density of $BiCl_3$, a pyramidal molecule like NH_3, lies close to that of NH_3. (The data for $BiBr_3$ would lie just below those for $BiCl_3$. They were omitted for reasons of clarity.)

A linear dependence of $|\rho - \rho_c|$ on $(T_c - T)^{1/3}$ was found graphically for both the liquid and vapor down to a temperature about 50° below T_c. This is a much greater temperature range than the 10° found for N_2O.[13]

(13) D. Cook, *Trans. Faraday Soc.*, 49, 716 (1953).

A Study of the Bonding in the Hydrogen Molecule[1]

by Peter Politzer

Quantum Chemistry Group, Chemistry Department, Indiana University, Bloomington, Indiana
(Received October 21, 1965)

An analysis has been made of a number of hydrogen molecule wave functions in terms of the electrostatic forces operating within the molecule and the electronic density distributions. No correlation was found between the calculated energies and the degrees to which the functions satisfy the requirement that there be a zero resultant force upon each nucleus. Similarly, the energies do not directly reflect the extent to which charge density is concentrated at the midpoint of the bond in each case. Surprisingly, however, it was found from the most accurate wave function studied that the formation of the molecule from the free atoms involves a nearly constant increase in charge density at all points along the axis from one nucleus to the other.

In the hope of obtaining a better understanding of the nature of covalent bonding, a comparative study has been carried out of a number of different wave functions which have been proposed for the hydrogen molecule. These functions have been analyzed in terms of two properties: the attractive force which the electrons are found in each case to exert upon either nucleus and the manner in which the electronic distribution in the molecule differs from the hypothetical situation of two noninteracting hydrogen atoms at the same separation.

According to the Hellmann–Feynman theorem,[2,3] the electronic attractive force upon a nucleus can be calculated by classical electrostatics, using, however, the quantum mechanical electronic distribution. In the case of the hydrogen molecule, if the wave function describing the two electrons is $\psi(\mathbf{r}_1, \mathbf{r}_2)$, then the resulting force component along the molecular axis which acts upon nucleus A is given by

$$F_A = \int \rho \frac{\cos \theta_A}{r_A^2} \, d\tau \qquad (1)$$

where $\rho = 2\int \psi(\mathbf{r}_1, \mathbf{r}_2)\psi^*(\mathbf{r}_1, \mathbf{r}_2) \, d\mathbf{r}_2$, r_A is the radial distance from nucleus A, and θ_A is measured away from the molecular axis, at the nucleus. The right side of eq 1 can generally be expanded as a sum of integrals over the particular basis orbitals used in the wave function $\psi(\mathbf{r}_1, \mathbf{r}_2)$; there are formulas available

(1) This work was supported by grants from the National Science Foundation and the U. S. Air Force Office of Scientific Research.

(2) R. P. Feynman, *Phys. Rev.*, 56, 340 (1939).

(3) An interesting discussion of the Hellmann–Feynman theorem and some of its applications has been given by L. Salem, *Ann. Phys.* (Paris), 8, 169 (1963).

Table I: Summary of Force Analyses of Various H_2 Wave Functions (Values Given Are in Atomic Units)

Function	Energy	Attraction	Repulsion	% imbalance	Ref
Wang $\psi = 1s_A1s_B + 1s_B1s_A$	−1.13905	0.4033	0.5073	20.5	*a*
Weinbaum $\psi = 1s_A1s_B + 1s_B1s_A + \sigma(1s_A1s_A + 1s_B1s_B)$	−1.14796	0.4246	0.4888	13.1	*b*
Rosen $\psi = \varphi_A\varphi_B + \varphi_B\varphi_A$, $\varphi_A = 1s_A + \lambda 2p\sigma_A$	−1.1485	0.5011	0.4987	0.441	*c*
Floating orbital (based on Weinbaum function)	−1.1501	0.4882	0.4904	0.449	*d*
LCAO–SCF (all exponents equal)	−1.13211	0.5326	0.5102	4.39	*e*
LCAO–SCF–CI (all exponents equal)	−1.15661	0.4987	0.5102	2.25	*e*
LCAO–SCF (exponents varied)	−1.13349	0.5151	0.5088	1.24	*e*
LCAO–SCF–CI (exponents varied)	−1.15919	0.5185	0.5088	1.91	*e*
SCF (nine basis functions of type $\lambda^m\mu^n \exp(-0.75\lambda)$)	−1.13357	0.5127[f]	0.5102	0.490	*f*
Hagstrom (four-term truncated natural orbital expansion of 33-term CI function)	−1.169785	0.5121	0.5102	0.372	*g*
Experimental	−1.17444	0.5098	0.5098[h]	0.000	*i*

[a] S. C. Wang, *Phys. Rev.*, **31**, 579 (1928). [b] S. Weinbaum, *J. Chem. Phys.*, **1**, 593 (1933). The data used in this work were taken from improved unpublished calculations by Shull and Lowdin; see H. Shull, *J. Am. Chem. Soc.*, **82**, 1287 (1960). [c] N. Rosen, *Phys. Rev.*, **38**, 2099 (1931). [d] H. Shull and D. D. Ebbing, *J. Chem. Phys.*, **28**, 866 (1958). [e] S. Fraga and B. J. Ransil, *ibid.*, **35**, 1967 (1961). [f] J. Goodisman, *ibid.*, **39**, 2397 (1963). [g] S. Hagstrom and H. Shull, *Rev. Mod. Phys.*, **35**, 624 (1963). [h] This value is based on $R = 1.4006$ au, given by G. Herzberg and L. L. Howe, *Can. J. Phys.*, **37**, 636 (1959). [i] G. Herzberg, "Spectra of Diatomic Molecules," D. Van Nostrand Co., Inc., Princeton, N. J., 1950.

for the evaluation of such integrals.[4-6] All computations in this work were carried out on a CDC 3600 computer.

The results of these calculations for a number of different H_2 wave functions are given in Table I; there is also included one result which was taken from previously published work (see ref *f* in Table I).[7] At equilibrium, the net attractive force upon a nucleus due to the electrons should be exactly balanced by the repulsion due to the other nuclei; the extent to which this requirement is satisfied is indicated in each case.

If the exact H_2 wave function were used, there would of course be a perfect balance of the forces on each nucleus. However, there are also certain approximate wave functions which have the property of showing a balance at the calculated bond length;[8-12] among these are the "floating" functions, in which the atomic orbitals have been detached from their nuclei, and Hartree–Fock functions. These expectations are confirmed by the results obtained for the floating orbital function, for which the forces are seen to balance to within the precision of the functional parameters, and the SCF (self-consistent field) functions, these being close approximations to the Hartree–Fock.[13] It must

(4) R. F. W. Bader and G. A. Jones, *Can. J. Chem.*, **39**, 1253 (1961).

(5) S. Ehrenson and P. E. Phillipson, *J. Chem. Phys.*, **34**, 1224 (1961).

(6) M. J. Stephen, *Proc. Cambridge Phil. Soc.*, **57**, 348 (1961).

(7) Some of these forces were also computed by T. P. Das and R. Bersohn [*Phys. Rev.*, **115**, 897 (1959)], who examined a number of H_2 wave functions in terms of various electric and magnetic properties. It should be noted that they used a uniform bond length of 1.40 au.

(8) A. C. Hurley, *Proc. Roy. Soc.* (London), **A226**, 170, 179, 193 (1954).

(9) G. G. Hall, *Phil. Mag.*, **6**, 249 (1961).

(10) J. O. Hirschfelder and C. A. Coulson, *J. Chem. Phys.*, **36**, 941 (1962).

(11) C. A. Coulson and A. C. Hurley, *ibid.*, **37**, 448 (1962).

(12) C. W. Kern and M. Karplus, *ibid.*, **40**, 1374 (1964).

(13) Functions which include incomplete configuration interaction will not necessarily show a balance of forces, even though they may be based upon SCF solutions. This is discussed in ref *f* of Table I.

be noted, however, that this predicted balance of forces in the case of certain approximate functions is at the calculated bond length; there may be significant imbalance when the repulsion is given its actual value at the true bond length.

It is evident that no general correlation exists between the accuracies of the forces and the energies corresponding to the various wave functions. This is not surprising; the force depends upon the one-electron density, ρ, and this is not directly related to the energy. For instance, Hartree–Fock functions give good one-electron densities[9,14] despite their relatively poor energies. Another striking example of this lack of correlation is the Rosen function, which has only a fair energy but achieves a nearly exact balance of forces. This function gives an unexpectedly good charge distribution, as shall be discussed later in this paper.

The effect of bond formation upon the electronic distribution in a system of atoms can be studied by means of the function $\delta(\mathbf{r})$, which was introduced by Roux and co-workers[15–17] and has been discussed at length by Rosenfeld.[18] It is defined by

$$\delta(\mathbf{r}) = \rho(\mathbf{r}) - \rho^{F}(\mathbf{r}) \qquad (2)$$

Here $\rho(\mathbf{r})$ is the electronic density of the molecule at a point $\mathbf{r}$, as defined above, and $\rho^{F}(\mathbf{r})$ is the density which would result if the atoms could be brought together with no perturbing effect upon each other. Since $\delta(\mathbf{r})$ is a relatively small difference between two larger quantities, the values assigned to the latter are obviously critical; in the present work, $\rho^{F}(\mathbf{r})$ could fortunately be stated exactly, as the sum of the densities of two hydrogen atom 1s orbitals with effective Z equal to 1.00.

Figure 1 shows the δ function along the molecular axis for a group of H_2 wave functions. The free atom orbitals used in obtaining ρ^{F} were in each case taken to be separated by the particular calculated bond length. The Hagstrom and the Kolos–Roothaan[19,20] functions which are represented here are the seven-term natural orbital expansions, which have energies of -1.1713 and -1.1717 au, respectively. These values differ only slightly from the experimental energy of -1.1744 au, and the Kolos–Roothaan function shall therefore be taken to be a very close representation of the true wave function.

A certain pattern can be discerned in Figure 1. The Heitler–London function, in which the orbital exponents (effective nuclear charges) retain the 1.00 values of the free atoms, presents the usual simple qualitative description of the chemical bond—a pile-up of charge in the internuclear region. The next

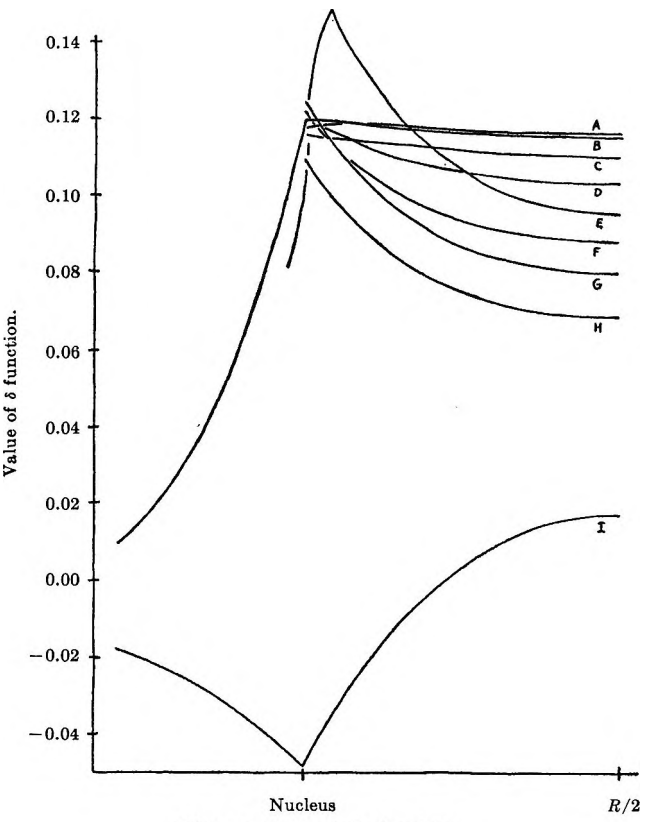

Figure 1. Variation of δ functions with distance along molecular axis. The distance is measured in units of the respective bond lengths. H_2 wave functions represented are: A, Hagstrom; B, Kolos–Roothaan; C, LCAO–SCF (variable exponents); D, Rosen; E, floating orbital; F, Coulson; G, Weinbaum; H, Wang; and I, Heitler–London. Only the Kolos–Roothaan and the Heitler–London δ functions are shown to the left of the nucleus; the others have essentially the same form as the Kolos–Roothaan.

six functions are still fairly uncomplicated in form and can readily be given physical interpretations, but they have orbital exponents greater than 1. This can be viewed as reflecting "promotion" of the atom prior

(14) M. Cohen and A. Dalgarno, *Proc. Phys. Soc.* (London), **77**, 748 (1961).

(15) M. Roux, S. Besnainou, and R. Daudel, *J. Chim. Phys.*, **218**, 939 (1956).

(16) M. Roux, *ibid.*, 754 (1958).

(17) M. Roux, M. Cornille, and L. Burnelle, *J. Chem. Phys.*, **37**, 933 (1962).

(18) J. L. J. Rosenfeld, "Electron Distribution and Chemical Binding," Technical Report No. 13, Institute of Theoretical Physics, University of Stockholm, April 1963.

(19) W. Kolos and C. C. J. Roothaan, *Rev. Mod. Phys.*, **32**, 219 (1960).

(20) E. R. Davidson and L. L. Jones, *J. Chem. Phys.*, **37**, 2966 (1962).

to bond formation.[21] Accordingly, these functions show a great increase in electronic density at the nuclei and a lesser increase in the region between them. Finally, with the very accurate Hagstrom and Kolos–Roothaan functions, in which nearly all electronic correlation has been taken into account, the internuclear density has been brought up to essentially the same level as at the nuclei.[22]

This is a surprising and significant result. The usual view of chemical bonding as involving a shift of electronic density into the region between the nuclei is clearly only part of the story—at least in the hydrogen molecule. There is a roughly equal buildup right at each nucleus, so that the total result is a nearly constant increase in charge density at all points along the axis from one nucleus to the other.

In Table II are presented the dissociation energies corresponding to the various H_2 wave functions and the respective values of $\delta(\mathbf{r})$ at the midpoint of the bond. It is seen that there is no direct relation between the two. This conclusion is contrary to a previous suggestion[18] (which was based upon an investigation of only three H_2 wave functions), but it seems quite reasonable once it is realized that the changes occurring near the nuclei during bond formation are as significant as those taking place in the internuclear region.

Table II: Comparison of Bond Properties for Various H_2 Wave Functions

Function	D_e, ev	δ (midpoint)
Heitler–London[a,b]	−3.156	0.0181
Coulson[b] (MO, variable exponent)	−3.488	0.0883
LCAO–SCF (exponents varied)	−3.632	0.1107
Wang	−3.784	0.0687
Weinbaum	−4.026	0.0802
Rosen	−4.041	0.1035
Floating orbital	−4.084	0.0953
Hagstrom	−4.662	0.1164
Kolos–Roothaan[c]	−4.672	0.1154
Experimental	−4.747	

[a] W. Heitler and F. London, *Z. Physik*, **44**, 455 (1927); Y. Sugiura, *ibid.*, **45**, 484 (1927). [b] C. A. Coulson, *Trans. Faraday Soc.*, **33**, 1479 (1937). [c] See ref 19 and 20.

Figure 2 shows a contour diagram of the δ function in two dimensions for the Kolos–Roothaan four-term wave function. This provides a very accurate picture of the change in electronic distribution which accompanies the formation of the hydrogen molecule.

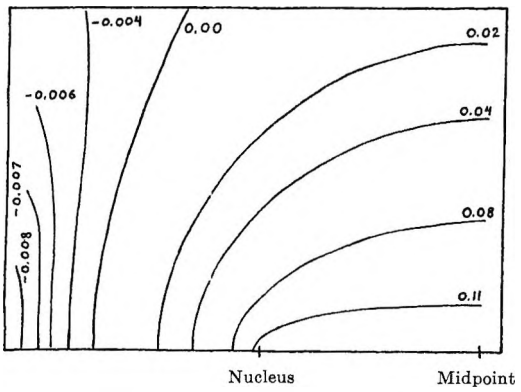

Figure 2. Two-dimensional δ function for Kolos–Roothaan H_2 wave function. Because of the symmetry of the molecule, the δ function at any point in space can be determined simply by rotating the above contours about the internuclear axis.

The curves plotted in Figure 1, as well as the force analyses discussed earlier, suggest that the LCAO–SCF and the Rosen functions give particularly good electronic density distributions.[23] This supposition was confirmed by comparing two-dimensional contour diagrams for the various δ functions. It seems, therefore, that the simple picture of the hydrogen molecule as being made up of two atoms slightly polarized toward each other is a reasonably valid one. This model is deficient of course in not taking proper account of the repulsive interactions between the electrons. It is not difficult to see one source of this deficiency, at least in the case of the Rosen function.[24] This function polarizes the atomic charge distributions directly toward each other along the molecular axis, whereas it is to be expected that the repulsion between the electrons would cause these polarized portions to shift somewhat away from each other and hence from the axis. This expectation is confirmed by the very significant effect which is observed when terms of π symmetry are added to the Hagstrom and Kolos–Roothaan natural orbital expansions; the energy is improved by nearly 0.3 ev (about 0.0109 au).[25]

Acknowledgments. The author is grateful to Pro-

(21) K. Ruedenberg, *Rev. Mod. Phys.*, **34**, 326 (1962).

(22) See also $\delta(r)$ for the five-term James–Coolidge function in ref 15.

(23) This is not surprising in the case of the SCF function, since it is known that Hartree–Fock solutions give good results for one-electron properties. (See ref 9 and 14.)

(24) This deficiency is inherent in the SCF function, which, by its very nature, cannot be energetically improved once it has reached the Hartree–Fock limit.

(25) J. O. Hirschfelder and J. W. Linnett [*J. Chem. Phys.*, **18**, 130 (1950)] proposed a modified version of the Rosen function which would take account of this "π character," but there is some question about the accuracy of their numerical results (see ref *d* in Table I).

fessor Harrison Shull for stimulating discussions and for his kind support. He also wishes to thank Dr. Darrell D. Ebbing and Dr. Norman T. Huff for their very useful comments regarding this work.

The Infrared Spectra of Carbon Dioxide Adsorbed on Zeolite X

by J. W. Ward[1] and H. W. Habgood

Contribution No. 323 from the Research Council of Alberta, Edmonton, Alberta, Canada
(Received October 21, 1965)

Spectra of carbon dioxide adsorbed on the Ca, Sr, and Ba forms of zeolite X showed no evidence of bent, or carbonate-like, structures such as were previously found for carbon dioxide adsorbed on LiX, NaX, and KX. This difference is believed to be due to the absence, in zeolites containing divalent cations, of any cations in the highly exposed type-III sites. Carbon dioxide on MgX did show some carbonate-like bands in the 1750–1300-cm^{-1} region but there was evidence that only partial replacement of monovalent cations had been achieved. The spectra of carbon dioxide on both group I-A and group II-A zeolites showed a strong band between 2375 and 2350 cm^{-1}, the frequency being higher the stronger the electrical field of the cation, which is believed to be due to a linear species held by an ion–dipole interaction. This band was accompanied (in most cases) by two pairs of weaker side bands symmetrically spaced about the central band.

A previous communication from this laboratory[2] described the infrared spectra of carbon dioxide adsorbed at low coverages on the lithium, sodium, and potassium forms of zeolite X. These spectra each included a band near 2350 cm^{-1} attributed to carbon dioxide adsorbed in a linear or near-linear configuration onto the exchangeable cations and at least two pairs of bands in the region 1750–1250 cm^{-1} ascribed to carbon dioxide chemisorbed in a bent configuration onto a surface oxygen to give a carbonate-like structure. The bands near 2350 cm^{-1} showed a slight dependence of frequency upon the nature of the cation while those ascribed to the bent forms varied widely from one cation to another. These observations have now been extended to the alkaline earth ion-exchanged forms of the zeolite and also to higher carbon dioxide coverages, and a number of unexpected results have been found.

Experimental Section

The procedures were similar to those reported previously. The various zeolites were prepared by ion exchange of the sodium form (Linde Lot No. 13916) using 5% solutions of the appropriate chlorides. LiX, KX, CaX, SrX, and BaX were essentially 100% exchanged while in the magnesium zeolite only 70% of the sodium was exchanged and the amount of magnesium taken up corresponded to 35% of the magnesium being added as $MgOH^+$ rather than as Mg^{2+}. A sample of RbX was also prepared but because of the small amount of material available, the degree of exchange was not determined.

The pellets were outgassed at 450–500°, and doses of carbon dioxide were added at room temperature up

(1) Research Council of Alberta Postdoctoral Fellow, 1962–1963.
(2) L. Bertsch and H. W. Habgood, *J. Phys. Chem.*, 67, 1621 (1963).

Table I: Observed Frequencies in Vicinity of ν_3 Band of Carbon Dioxide Adsorbed on Various Cationic Forms of Zeolite X

Zeolite	First band (strongest sites)	Additional bands in order of appearance (with displacement from initial band)
LiX	2365	
NaX	2351	2425 (+74), 2287 (−64); 2370 (+21), 2330 (−19)
KX	2349	2425 (+76), 2280 (−69); 2370 (+21), 2330 (−19)
RbX	2349	2415 (+66), 2280 (−69); 2340
MgX	2374	2403 (+29), 2305 (−69); 2290 (−84); 2350
CaX	2367	2433 (+66), 2300 (−67); 2350
SrX	2355	2422 (+67), 2288 (−67); 2370 (+15), 2335 (−20); 2350
BaX	2350	2415 (+65), 2285 (−65); 2375 (+25), 2320 (−30)

to an equilibrium pressure of a few millimeters. Spectra were obtained after each dose and occasionally several spectra were taken at various intervals up to 1 or 2 days to detect any slow processes. As in the previous work, a Perkin-Elmer 221G spectrometer was used.

Results

The frequencies of the observed absorption bands of carbon dioxide are listed in Tables I and II. Table I summarizes the observations between 2500 and 2200 cm^{-1} for both the group I-A and group II-A cationic forms of zeolite X, and Table II gives the bands observed below 2000 cm^{-1} for the group II-A forms. The bands between 1800 and 1300 cm^{-1} for carbon dioxide on LiX, NaX, and KX were described previously.

Of the group II-A zeolites, MgX behaves differently with carbon dioxide than do the others. Initial adsorption of a dose of 200 μ of carbon dioxide produced bands at 2374, 1734, and 1382 cm^{-1}. On standing up to 96 hr, the 2374-cm^{-1} band decreased in intensity, whereas the band at 1734 cm^{-1} increased in a manner analogous to that reported for group I-A zeolites. The band at 1382 cm^{-1} became more intense and split into a doublet, whereas after 23 hr a band at 1625 cm^{-1} was also observed. The adsorption of a further 400 μ of gas followed the same pattern. On increasing the pressure initially to 10 mm, a band comparable in intensity to that at 2374 cm^{-1} appeared at 2350–2345 cm^{-1}, together with weaker bands at 2403, 2305, and 2290 cm^{-1}. At this stage the presence of a small amount of CO_2 in the gas phase was detected. Expansion of the cell contents several times into a bulb of equal volume caused a decrease in the intensity of the 2350–2345-cm^{-1} band and a smaller decrease in the 1380–1360-cm^{-1} doublet; similar but more marked intensity decreases were observed on evacuation for 1 min to 150-μ pressure. On evacuation for 10 min to 10^{-3} mm, intensity changes were negligible except for the 2374-cm^{-1} band which decreased in absorbance from 0.74 after 1 min to 0.30 after 10 min. All bands were removed by evacuation overnight at room temperature.

Table II: Observed Frequencies below 2000 Cm^{-1} of Carbon Dioxide Adsorbed on Various Cationic Forms of Zeolite X

Zeolite						
MgX	1734	1700	1625	1382	1363	
CaX				1382		1270
SrX				1380		1265
BaX				1378		1265
RbX			1645	1382	1333	

The adsorption of carbon dioxide on Ca, Sr, and BaX followed a different form in that no discrete absorption bands in the 2000–1400-cm^{-1} region were observed. Occasionally, broad bands developed on adsorption of carbon dioxide but their appearance was not consistent, they appeared to have little effect on the rest of the spectrum, and they were easily removed by desorption. These bands are thought to be connected with possible changes in the solid. On the addition of 200 μ of carbon dioxide, a band appeared near 2350–2370 cm^{-1}, the frequency depending on the cation. As more carbon dioxide was added, the intensity of this band increased and new bands appeared equally spaced, 66 cm^{-1}, on either side of the main band. At the same time, two weak bands also appeared near 1380 and 1265 cm^{-1}. On further additions of carbon dioxide, other pairs of bands more or less equally spaced on either side of the ν_3 band also appeared. The development of the band system around 2350 cm^{-1} for BaX is shown in Figure 1. The principal side band on the low-frequency side is much sharper than that on the high-frequency side. The growth of the low-frequency side band at 2285 cm^{-1} as a function of amount of carbon dioxide adsorbed is shown in Figure 2. The total absorbance at the peak is plotted and the values for high coverage will be influenced by broadening of

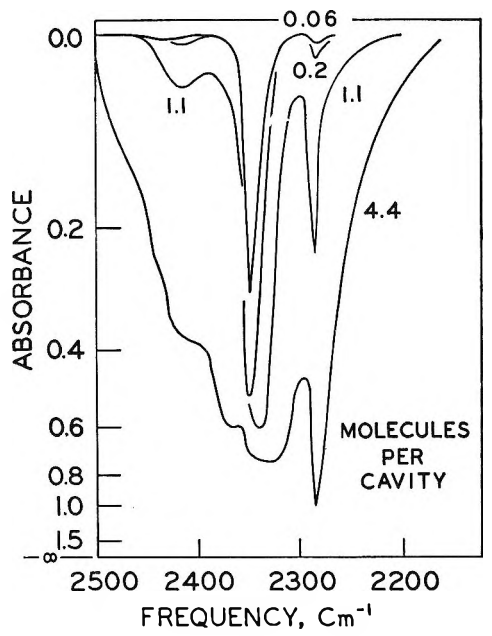

Figure 1. Spectra of carbon dioxide adsorbed on BaX (pellet density 19 mg/cm²; standard slit program 927 on PE 221 spectrometer) redrawn from observed spectra to correct for pellet background.

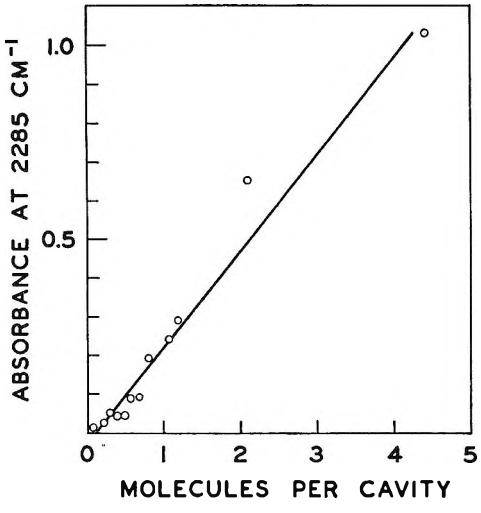

Figure 2. Maximum absorbance at 2285 cm^{-1}, sharp lower side band, against amount of carbon dioxide adsorbed by BaX.

the main band. Within this limitation, however, the growth of the band is linear with concentration. In all cases, reduction of the pressure produced a weakening of the bands in the reverse order of their appearance, and after continued evacuation at room temperature only the initially formed 2350–2375-cm^{-1} band was detectable; complete removal of this latter band required evacuation at temperatures up to about 200°.

The difference in behavior between the alkaline earth group X zeolites and the previously investigated LiX, NaX, and KX zeolites prompted an examination of RbX and the former three zeolites at higher pressure. During initial doses, RbX behaved analogously to LiX and KX. However, on further addition of CO_2, a pair of bands on either side of the main band at 2349 cm^{-1} appeared with frequencies of 2415 and 2280 cm^{-1}. Further addition of CO_2 produced a broad band at 2335–2345 cm^{-1}. Evacuation removed the bands in the 2400–2300-cm^{-1} region but left those between 1650 and 1300 cm^{-1} unaffected. These latter bands were removed by evacuation at elevated temperature. Similar results were obtained for NaX and KX, but with LiX, only the one band at 2365 cm^{-1} was observed. The development of side bands around the ν_3 band thus appears to be a general phenomenon accompanying the adsorption of carbon dioxide on all group I-A and group II-A X zeolites with the exception of LiX.

Chemisorption to carbonate-like species on group I-A zeolites was previously found to be accelerated by the presence of small amounts of water.[2] In a further examination of this effect, the spectrum of adsorbed D_2O was observed while carbon dioxide was added to a pellet of NaX. The use of D_2O instead of H_2O brought the water spectrum into a more convenient region. The pellet was dehydrated overnight at 500° under vacuum, cooled to 100°, and approximately 0.5 molecule of D_2O per cavity was added. A dose of carbon dioxide corresponding to approximately 0.5 molecule per cavity was introduced and the region 2800 to 2300 cm^{-1} was scanned. Chemisorption was complete within the approximately 1 min required for the first scan and the water spectrum showed significant changes due to the presence of carbon dioxide. Figure 3 shows the spectrum before and after the carbon dioxide admission; new bands were produced at 2682 and 2640 cm^{-1}; the sharp band at 2728 cm^{-1} was unchanged, but the broad band centered around 2500 cm^{-1} appeared to decrease in intensity. The strong bands at 1715 and 1365 cm^{-1}, attributed to the carbonate-like species, were similar in appearance to those observed on dry zeolite.[2] In this particular experiment the amount of carbon dioxide was sufficient that a small concentration of linearly adsorbed carbon dioxide was also present as indicated by the band at 2350 cm^{-1}.

Discussion

The adsorption of carbon dioxide on alkali and alkaline earth X zeolites appears to be of three different types: physical adsorption, chemisorption to a car-

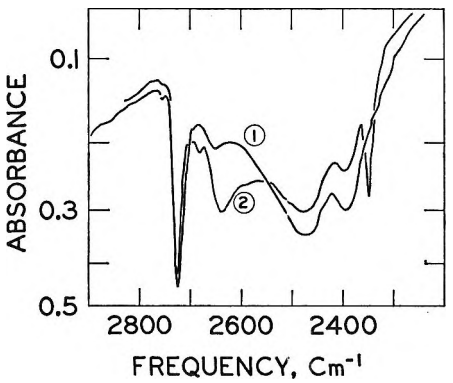

Figure 3. Spectrum of D_2O adsorbed on NaX (curve 1) showing the effect of added carbon dioxide (curve 2).

bonate-like species, and adsorption by an ion–dipole interaction. First, a band at or slightly below 2350 cm^{-1} observed at higher pressures can be attributed to the physical adsorption of carbon dioxide on the zeolite surface. The pressure dependence, ease of removal by evacuation, and proximity to the gas-phase carbon dioxide frequency are all consistent with this assignment.

Chemisorption of a bent carbon dioxide to form a carbonate-like species was previously postulated[2] to account for the appearance of a series of sharp bands in the 1750–1300-cm^{-1} region with LiX, NaX, and KX. These observations have been confirmed and extended to RbX which, with carbon dioxide, gives bands at 1645, 1382, and 1333 cm^{-1}, somewhat less well developed than those of KX but fitting into the series from LiX. With the exception of MgX, alkaline earth zeolites do not exhibit well-defined bands for carbon dioxide in this region. For MgX, several bands were observed in the 1750–1300-cm^{-1} region (*cf.* Table I) similar to those found with the alkali metal zeolites.

The apparent absence of carbonate-like species for carbon dioxide absorbed on alkaline earth zeolites is believed to result from the different distribution of cations in these forms as compared with the group I-A zeolites. In terms of the published structure[3] of the X zeolites and of calculations of the relative potential energies of the various sites,[4] it appears that sites of type II,[5] within the six-membered rings, are more stable than sites of type III, on the cavity walls. While type III sites have not yet been confirmed crystallographically, they can be assigned with reasonable probability. In the group I-A X zeolites some type III sites must be occupied by the cations; in the group II-A zeolites only half as many cations are present and these will probably be found only in sites of types I and II. It was apparent from the work with LiX, NaX, and KX zeolites that the carbonate-like structures were formed in intimate association with the cations. Cations in type III sites are less shielded than those in type II sites and have stronger electrical fields in their vicinity. It is reasonable to postulate that the carbonate-like species is associated with a cation in a type III site and that they are absent from CaX, SrX, and BaX because no type III sites are occupied. The apparent presence of a carbonate-like species with carbon dioxide on MgX may be due to a partial occupancy of type III sites resulting from the presence of a larger number of ions, either unexchanged Na^+ or $MgOH^+$ as indicated by the analysis. The MgX preparation was unusual also in that weak absorption bands were also observed in the OH stretching region (3740, 3690, and 3630 cm^{-1}) after outgassing at 480°, whereas under similar conditions no bands were found with the other zeolites.[6] These observations give some support to the presence of $MgOH^+$ but the situation is considered to be still uncertain.

The experiments involving D_2O suggest that the carbonate-like species may be stabilized by hydrogen bonding with adsorbed water. From the weakening of the broad 2500-cm^{-1} band and the production of new bands at 2682 and 2640 cm^{-1} it would seem that hydrogen bonding between water and carbon dioxide replaced hydrogen bonding of adsorbed water to surface oxygen.[2]

The third type of adsorption is that which gives rise to the strong band at low pressures between 2374 and 2349 cm^{-1}. The frequency of this band tends to be higher than that observed for the ν_3 vibration of the free molecule and the shift to higher frequencies is greatest for the more strongly polarizing cations, *e.g.*, Li^+, Ca^{2+}, and Mg^{2+}. Peri,[7] in the adsorption of carbon dioxide on silica–alumina aerogels, found a similar shift in frequency to 2375 cm^{-1}. With CaX, SrX, and BaX, the band intensity at a given pressure or coverage is time independent, whereas with MgX and group I-A X the intensity decreases with time paralleling the growth of the bands in the 1750–1300-cm^{-1} region.

(3) L. Broussard and D. P. Shoemaker, *J. Am. Chem. Soc.*, 82, 1041 (1960).

(4) P. E. Pickert, J. A. Rabo, E. Dempsey, and V. Schomaker, *Actes Congr. Intern. Catalyse, 3e, Amsterdam, 1964*, 714 (1965).

(5) D. W. Breck, *J. Chem. Educ.*, 41, 678 (1964).

(6) See J. L. Carter, P. J. Lucchesi, and D. J. C. Yates, *J. Phys. Chem.*, 68, 1385 (1964); H. W. Habgood, *ibid.*, 69, 1764 (1965); and J. B. Uytterhoeven, L. G. Christner, and W. K. Hall, *ibid.*, 69, 2117 (1965), for a discussion of the observation of discrete OH bands in the spectra of dehydrated zeolite X.

(7) J. B. Peri, *Actes Congr. Intern. Catalyse, 3e, Amsterdam, 1964*, 1110 (1965).

The displacement of a molecular vibration toward higher frequency is seldom observed. Interactions resulting from either solution or adsorption usually lead to a decrease in frequency. Little and Amberg[8] observed an increase in the vibrational frequency of adsorbed carbon monoxide; they discussed some of the factors which might lead to the increase and suggested a highly polarized structure for the adsorbed molecule. Considering the proximity of the observed band to the ν_3 vibration of carbon dioxide and also the sensitivity of the frequency of the band to the nature of the cation and the intense electric field gradients in the vicinity of the cation, analogy with the conclusions of Little and Amberg suggests linear adsorption by an ion–dipole interaction

$$M^+ + O{=}C{=}O \longleftrightarrow \overset{+}{M}\cdots\overset{\delta-}{O}{=}C{=}\overset{\delta+}{O}$$

Such a polarized structure with an increased electron density in the CO bonds should have an increased bond strength giving rise to an increase in frequency.

The asymmetry produced in the molecule by the mode of absorption suggested in the preceding paragraph would be expected to result in the ν_2 vibration becoming infrared active. For CaX, SrX, and BaX, the weak bands at 1380 and 1270 cm^{-1} vary in intensity in a manner roughly parallel to that of the band near 2350 cm^{-1}. It is therefore suggested that these bands are the ν_1 and $2\nu_2$ vibrations of carbon dioxide that are normally Raman active and observed in Fermi resonance at 1388 and 1285 cm^{-1}. In this respect also MgX behaves differently from the other alkaline earth zeolites. The intensity of the doublet observed at 1380 and 1362 cm^{-1} does not parallel the intensity of the 2374-cm^{-1} band and the assignment to a carbonate-type species seems more probable. No band is observed near 1270 cm^{-1}. The nature of the linear species of carbon dioxide adsorbed on CaX, SrX, and BaX thus appears to be somewhat different from that on MgX and the alkali metal X zeolites.

The pairs of bands appearing equally displaced on either side of the main ν_3 band are difficult to explain. The most pronounced pair and first to appear are spaced roughly 70 cm^{-1} from the main band and consist of a sharp low-frequency component and a much broader and weaker high-frequency component (see Table I and Figure 1). Three possible explanations may be suggested. One is that these bands represent adsorption on cations in different environments but symmetrical displacements would then hardly be expected. A second possibility is that the bands are the result of mechanical resonance between two carbon dioxide molecules adsorbed on the same cation or closely neighboring cations, but this is incompatible with the observed linear increase in band intensity with coverage (Figure 2). The third possibility is that the side bands represent combination frequencies of the ν_3 vibration of carbon dioxide and of the vibration of the whole molecule against the surface. Such combination frequencies are, indeed, to be expected but the displacement from the central band would also be expected to vary with different cations as does the frequency of the central band, because of the different strengths of binding to the surface. Thus, none of these possible explanations for the side bands is really satisfactory and further study is indicated.

(8) L. H. Little and C. H. Amberg, *Can. J. Chem.*, **40**, 1997 (1962).

The Surface Tension of Binary Liquid Mixtures[1]

by J. G. Eberhart

Sandia Corporation, Albuquerque, New Mexico *(Received October 21, 1965)*

An equation for the surface tension of binary liquid mixtures is presented which is based on the assumption that the surface tension, σ, is a linear function of the surface layer mole fraction. The condition for equilibrium between the surface layer and the bulk liquid phase provides a relationship between the surface and the bulk compositions and leads to an equation of the form $\sigma = (Sx_A\sigma_A + x_B\sigma_B)/(Sx_A + x_B)$, where σ_A and σ_B are the surface tensions of the two pure components, x_A and x_B are the bulk liquid mole fractions, and S is a function of temperature only, which gives the extent of surface layer enrichment in the component of lower surface tension. A statistical mechanical model is used to calculate the value of S for liquid hydrogen isotope and ortho–para mixtures.

Introduction

For almost all of the binary liquid mixtures on which surface tension measurements have been made, it has been found that the surface tension deviates negatively from a linear function of mole fraction. This behavior is usually explained qualitatively by the fact that the surface layer of the liquid is enriched in the component of lower surface tension, thereby minimizing the Helmholtz free energy of the mixture. Although surface tension is clearly not a linear function of the bulk liquid mole fraction, it is possible that it is a linear function of the surface layer mole fraction. A model based on this assumption is explored here.

The Surface Model

A liquid mixture of two components, A and B, is assumed to be in equilibrium with its own vapor. The liquid–vapor interface is treated here in the manner of Bakker,[2a] Verschaffelt,[2b] and Guggenheim[3] as a thin phase separated from the bulk liquid and vapor by two dividing surfaces which enclose the region of property variation normal to the interface. The bulk liquid phase is assumed to have mole fractions x_A and x_B, while the bulk vapor phase has mole fractions z_A and z_B. Although the interfacial or surface phase has a composition which varies in a direction normal to the dividing surfaces, it is assigned over-all mole fractions y_A and y_B which satisfy the material balance conditions for the system. For component A, for example, this condition is $n_A = n_Lx_A + n_Sy_A + n_Vz_A$, where n_A is the total number of moles of A in the three "phases," and n_L, n_S, and n_V are the number of moles of A and B in the liquid, surface, and vapor phases, respectively. Since, in general, n_S and n_V are very much smaller than n_L, it will be assumed that x_A is essentially equal to the over-all mole fraction of A, $n_A/(n_A + n_B)$. The surface tension, σ, is then assumed to be a linear function of the surface layer mole fraction, *i.e.*

$$\sigma = y_A\sigma_A + y_B\sigma_B \tag{1}$$

where σ_A and σ_B are the surface tensions of the pure components.

In order to relate the surface layer composition to the bulk liquid composition, the conditions for equilibrium between these two phases are employed, namely, that the chemical potential for each component is the same in the surface layer as it is in the bulk liquid. Then, by the usual argument

$$K_A = b_A/a_A, \quad K_B = b_B/a_B \tag{2}$$

where b and a are the activities in the surface layer and the bulk liquid, respectively, and K is a distribution constant which depends on temperature only. A sepa-

(1) This work was supported by the U. S. Atomic Energy Commission.

(2) (a) G. Bakker, "Handbuch d. Experimentalphysik," Vol. 6, Akademische Verlags-Gesellschaft, Leipzig, 1928; (b) J. E. Verschaffelt, *Bull. Classe Sci. Acad. Roy. Belg.*, 22, 373, 390, 402 (1936).

(3) E. A. Guggenheim, *Trans. Faraday Soc.*, 36, 398 (1940), or "Thermodynamics," North-Holland Publishing Co., Amsterdam, 1957, p 46.

ration factor, S, for the enrichment of the surface layer in A, the component of lower surface tension, is defined as

$$S = \frac{K_A}{K_B} = \frac{b_A/b_B}{a_A/a_B} = \frac{\delta_A/\delta_B}{\gamma_A/\gamma_B}\,\frac{y_A/y_B}{x_A/x_B} \qquad (3)$$

where δ and γ are surface layer and bulk liquid activity coefficients, respectively. It has been found that for the fractionation of isotope mixtures or mixtures of components with similar properties, between either two bulk phases[4] or one bulk phase and one adsorbed phase,[5] the activity coefficient quotient in eq 3 is unity to a very good approximation. By analogy to these results, the identification $(\delta_A/\delta_B)/(\gamma_A/\gamma_B) = 1$ is adopted as an additional assumption of the treatment for systems where A and B are similar in properties and leads to a simple relationship between surface layer and bulk liquid composition, namely

$$S = \frac{y_A/y_B}{x_A/x_B} \qquad (4)$$

where $S > 1$ for surface enrichment in A. Using eq 1 and 4, along with the conditions $x_A + x_B = 1$ and $y_A + y_B = 1$, σ can be expressed in terms of the bulk liquid composition of the mixture, namely

$$\sigma = \frac{Sx_A\sigma_A + x_B\sigma_B}{Sx_A + x_B} \qquad (5)$$

Equation 5 is of the same form as an empirical mixing rule suggested by Reshetnikov[6] for a variety of properties of binary mixtures and used by Lauermann, Metzger, and Sauerwald[7] to fit their surface tension data on the silver–tin alloy for tin mole fractions between 0.35 and 1.

Comparison with Experimental Data

In order to test eq 5 with experimental data, it is convenient to define ξ and r as

$$\xi = (\sigma - \sigma_A)/(\sigma_B - \sigma_A) \qquad (6)$$

$$r = x_B/x_A \qquad (7)$$

i.e., ξ is surface tension on a dimensionless scale varying from zero for pure A to unity for pure B, while r is the bulk mole ratio. Combining eq 5–7, it is found that

$$\xi = -S(\xi/r) + 1 \qquad (8)$$

Thus, if eq 5 is correct, a plot of ξ *vs.* ξ/r should be linear with an intercept of 1 and a slope of $-S$.

Surface tension data on a variety of alloy, fused-salt, organic, and inorganic liquid mixtures have been tested and found to fit eq 5. A few examples are discussed below. A liquid alloy system is shown in Figure 1 where the data of Fesenko, Eremenko, and Vasiliu,[8] on the copper–nickel system at 1550°, are plotted against the mole fraction of Ni. Figure 2 shows that ξ *vs.* ξ/r is linear with an intercept of 1 for this system and, from the slope, it is found that $S = 1.77$. This value of S was used in Figure 1 to calculate the curve drawn through the experimental points and again shows a good fit of the data to eq 5. Figure 3 shows the surface tension of the fused-salt $RbNO_3$–KNO_3 system at 350° as reported by Bertozzi and Sternheim.[9] An S value of 1.43 is required to fit this data. Figure 4 shows the surface tension data of Evans and Clever[10] for the isooctane–benzene system at 30°. For this system, S is found to be 3.12.

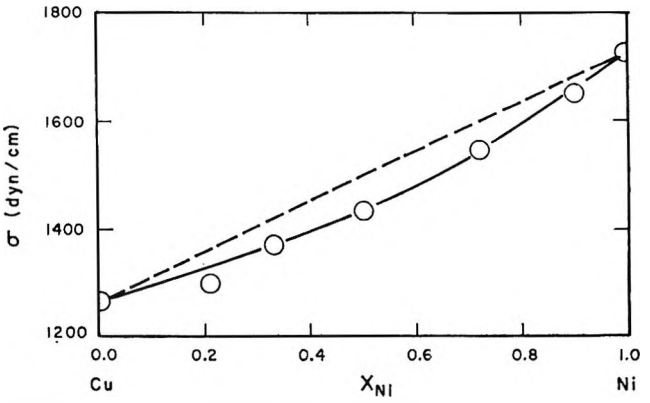

Figure 1. The surface tension of the copper–nickel liquid alloy at 1550°.

Although eq 5 accurately represents the surface tension–composition relationship for many binary liquid mixtures, there are also many binary mixtures whose surface tension cannot be accurately represented by this relationship. In general, these systems are composed of components whose properties would not be described as similar, and, in these cases, the activity coefficient ratio $(\delta_A/\delta_B)/(\gamma_A/\gamma_B)$ is undoubtedly a function of composition.

The Estimation of Surface Tension of Mixtures

A consequence of this model is that, if the surface tension is known for a mixture of A and B and for

(4) H. London, "Separation of Isotopes," George Newnes Ltd., London, 1961, pp 10, 42, 43.

(5) See, for example, C. M. Cunningham, D. S. Chapin, and H. L. Johnston, *J. Am. Chem. Soc.*, **80**, 2382 (1958), or D. White and E. N. Lassettre, *J. Chem. Phys.*, **32**, 72 (1960).

(6) M. A. Reshetnikov, *Dokl. Akad. Nauk SSSR*, **69**, 45 (1949).

(7) I. Lauermann, G. Metzger, and F. Sauerwald, *Z. Physik. Chem.* (Leipzig), **216**, 42 (1961).

(8) V. V. Fesenko, V. N. Eremenko, and M. I. Vasiliu, *Zh. Fiz Khim.*, **35**, 1750 (1961).

(9) G. Bertozzi and G. Sternheim, *J. Phys. Chem.*, **68**, 2908 (1964).

(10) H. B. Evans, Jr., and H. L. Clever, *ibid.*, **68**, 3433 (1964).

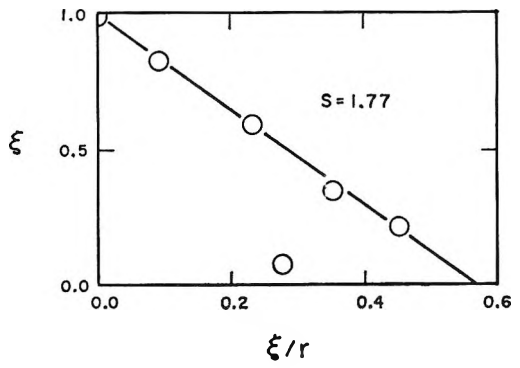

Figure 2. Plot for the determination of S for the liquid copper–nickel alloy at 1550°.

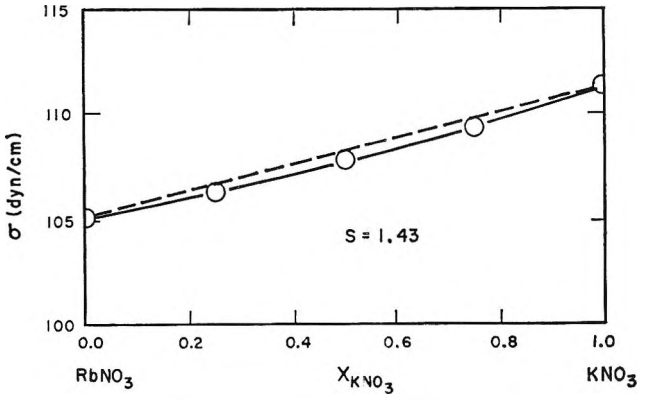

Figure 3. The surface tension of the rubidium nitrate–potassium nitrate fused-salt mixture at 350°.

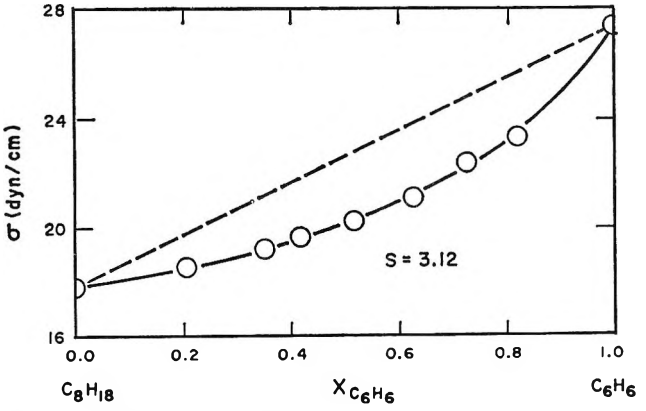

Figure 4. The surface tension of the isooctane–benzene liquid mixture at 30°.

another mixture of B and C at the same temperature, then the surface tension for a mixture of A and C can can be calculated at this temperature. This follows from eq 3, where it can be seen that

$$S(\mathrm{A,\ B})S(\mathrm{B,\ C}) = S(\mathrm{A,\ C}) \qquad (9)$$

This equation was tested with some of the surface tension data of Bertozzi and Sternheim[9] on fused alkali nitrate systems. The values of S for the various pairs of alkali nitrates were calculated as follows: $S(KNO_3, NaNO_3) = 2.11$, $S(RbNO_3, KNO_3) = 1.43$, $S(RbNO_3, NaNO_3) = 2.92$, $S(CsNO_3, KNO_3) = 1.43$, $S(CsNO_3, NaNO_3) = 2.93$, all at 350°. The product $S(CsNO_3, KNO_3)S(KNO_3, NaNO_3) = (1.43)(2.11) = 3.02$ agrees with $S(CsNO_3, NaNO_3) = 2.93$ within 3% which is less than the precision of the S determinations for these systems. Similarly $S(RbNO_3, KNO_3)S(KNO_3, NaNO_3) = (1.43)(2.11) = 3.02$, which agrees equally well with $S(RbNO_3, NaNO_3) = 2.92$.

It is possible to use eq 9 to estimate unknown surface tensions of binary mixtures. For example, Bertozzi and Sternheim measured the surface tension of all of the possible pairs of the four nitrates $CsNO_3$, $RbNO_3$, KNO_3, and $NaNO_3$, except for the $CsNO_3$–$RbNO_3$ pair. The S value for this pair can be estimated, however, using eq 9. One means of estimation is $S(CsNO_3, RbNO_3) = S(CsNO_3, KNO_3)/S(RbNO_3, KNO_3) = 1.43/1.43 = 1.00$. Another set of S values can alternatively be used, namely, $S(CsNO_3, NaNO_3)/S(RbNO_3, NaNO_3) = 2.93/2.92 = 1.00$. The two approaches give consistent results and predict a surface tension which varies linearly with bulk mole fraction.

In a more recent study, Bertozzi[11] also reported the surface tension of various binary mixtures of the alkali bromides. Although the data for each of the five pairs investigated are well fit by eq 5, the S values did not show consistency with eq 9.

Statistical Mechanics of Hydrogen Isotope Mixtures

Surface tension measurements have recently been made on the various liquid mixtures of H_2, HD, and D_2,[12,13] as well as the ortho–para mixtures of H_2.[14] These systems have sufficient simplicity that a statistical mechanical surface model can be used to calculate S for comparison with the values found empirically. For these mass or nuclear spin isotope mixtures, S can be calculated by replacing the mole fraction terms of eq 4 with partition functions, thus

$$S = (Q_A/Q_B)_{surf}/(Q_A/Q_B)_{liq} \qquad (10)$$

where Q is the total partition function for A or B in the surface layer or the liquid phase, and B is the heavier of the two isotopes. The total partition function is the product of partition functions for transla-

(11) G. Bertozzi, *J. Phys. Chem.*, **69**, 2606 (1965).

(12) V. N. Grigor'ev and N. S. Rudenko, *Zh. Eksperim. i Teor. Fiz.*, **47**, 92 (1964).

(13) V. N. Grigor'ev, *Zh. Tekhn. Fiz.*, **35**, 332 (1965).

(14) V. N. Grigor'ev, *Zh. Eksperim. i Teor. Fiz.*, **47**, 484 (1964).

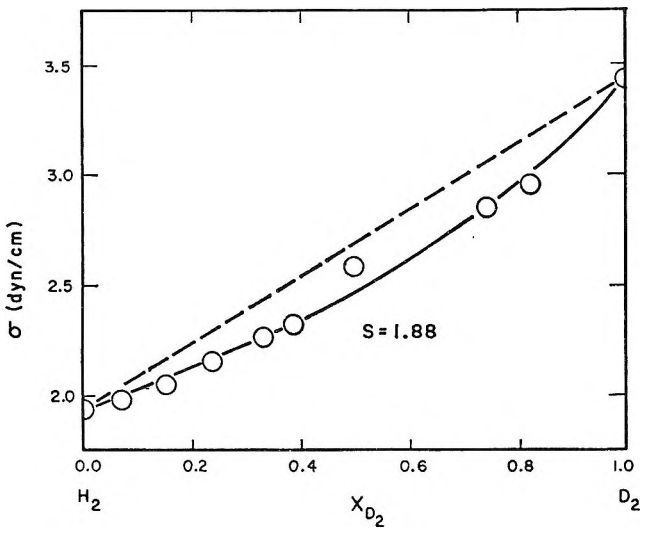

Figure 5. The surface tension of the hydrogen–deuterium liquid mixture at 20.4°K.

tional, rotational, vibrational, and electronic contributions. The rotational, vibrational, and electronic behavior of the hydrogen isotope molecules are assumed to be the same whether the molecule is in the liquid phase or the surface layer, and thus these partition functions cancel, leaving only the transitional partition functions in eq 10. The translational energy levels for a molecule in the liquid phase are assumed to be those of a particle in a three-dimensional box, while the translational energy levels for a molecule in the surface layer are assumed to be those of a particle in a two-dimensional rectangle.

The translational partition functions are, to a good approximation

$$Q_{\text{liq}} = \frac{(8\pi MkT)^{3/2}V}{h^3} \tag{11}$$

$$Q_{\text{surf}} = \frac{8\pi MkT\Omega}{h^2} \tag{12}$$

where M is the molecular mass, h is the Planck constant, k is the Boltzmann constant, V is the volume of the box, and Ω is the area of the rectangle. Substituting (11) and (12) into (10) then yields, after cancellation

$$S(\text{A, B}) = \sqrt{M_B/M_A} \tag{13}$$

Using the result of eq 15, the values of S for the binary mixtures H_2–D_2, H_2–HD, and HD–D_2 are predicted to be

$$\left.\begin{aligned} S(H_2, D_2) &= 1.41 \\ S(H_2, HD) &= 1.22 \\ S(HD, D_2) &= 1.15 \end{aligned}\right\} \tag{14}$$

while, for the ortho–para mixtures of H_2 and of D_2, the masses M_A and M_B are equal and

$$\left.\begin{aligned} S(p\text{-}H_2, o\text{-}H_2) &= 1 \\ S(o\text{-}D_2, p\text{-}D_2) &= 1 \end{aligned}\right\} \tag{15}$$

The H_2–D_2 system has been studied by Grigor'ev and Rudenko,[12] and the surface tension concentration dependence at 20.4°K is plotted in Figure 5 using their original data tabulation. The data was linearized as prescribed by eq 8 and was found to be fit by an S value in the range of 1.88 ± 0.20, a result which is not in close agreement with the prediction of eq 14.

Grigor'ev[13] has also studied the H_2–HD and the HD–D_2 systems and presents his results on a very small graph. Although his surface tension measurements cannot be read to their original accuracy, the concentration dependence is reproduced by S values which agree with those predicted above within ±0.05. The experimental results on the three mixtures are furthermore ranked by Grigor'ev[13] in order of decreasing deviation from linearity as H_2–D_2 > H_2–HD > HD–D_2, which agrees with the ranking of eq 14.

The surface tension of three different ortho–para hydrogen mixtures has also been determined by Grigor'ev[14] and was found to vary linearly from 1.90 dynes/cm for 2% o-H_2 to 1.95 dynes/cm for 75% o-H_2. A linear relationship implies that $S = 1$, which is in agreement with eq 15. The author is not aware of any surface tension measurements on D_2 at various ortho–para compositions.

Studies of Membrane Phenomena. II. Theoretical Study of Membrane Potentials

by Yonosuke Kobatake,[1] Yoshinori Toyoshima, and Noriaki Takeguchi

Laboratory of Neurobiology, National Institute of Mental Health, Bethesda, Maryland 20014, and Department of Polymer Science, Osaka University, Osaka, Japan *(Received October 22, 1965)*

In a recent paper dealing with membrane phenomena, we derived an equation for the membrane potential arising between two solutions of a uni-univalent electrolyte of different concentrations but at a constant temperature. This equation was shown to agree quite accurately with the available experimental data. This report is primarily concerned with a theoretical study of the membrane potential using a capillary model for the membrane, where the basic equation is derived on the basis of the thermodynamics of irreversible processes, subject to several external conditions. The equation thus obtained is substantially the same as that derived in the previous paper. It is shown that our equation for the membrane potential corresponds to the limiting case in which the charge density fixed on the capillary wall is high and that the earlier theories of Teorell and of Meyer and Sievers correspond to the opposite limiting case where the fixed charge density is extremely low.

Introduction

In part I of this series,[2] an equation was derived for the electric potential arising between two electrolyte solutions of different concentrations C_1 and C_2 which are separated by a charged membrane, and it was found that the equation agreed quite satisfactorily with experimental data available. The most crucial point in its derivation was to assume that the activities, a_+ and a_- of small ions in the membrane were represented by $a_+ = c_-$ and $a_- = c_-$, where c_- is the concentration of the coions in the membrane phase having the same sign as that of the ionizable group fixed on the membrane matrix. This assumption implies that in the direction of membrane thickness, the gradients of the chemical potential of positive and negative ions in the membrane are the same, *i.e.*, grad a_+ = grad a_-. It is shown, however, that this rather conventional assumption for the activity of each ionic species in the membrane phase is not necessary for the derivation of our equation of membrane potentials.

This paper will attempt to describe an improved derivation of the equation of membrane potentials, without introducing the empirical assumption described above, by using a capillary model for the membrane. The basic equation is derived by making use of the thermodynamics of irreversible processes; this equation is integrated between two bulk solutions across the membrane, under the assumption that the distributions of ions at a cross section of the capillary are governed by the Poisson–Boltzmann law. The equation thus obtained for the membrane potential is substantially the same as in the previous paper.[2] In addition, a theoretical explanation for the nonideal behavior of small ions in charged membranes is described in terms of the Poisson–Boltzmann distribution law.

Basic Equations

Membrane Model and Assumptions. The system considered is composed of a porous charged membrane separating two solutions of a simple uni-univalent electrolyte of different concentrations but at a constant temperature and pressure. A capillary model is used for the membrane. For simplicity of mathematical analysis, we replace the capillary by a fine slit com-

(1) Visiting Scientist, Department of Polymer Science, Osaka University, Osaka, Japan.

(2) Y. Kobatake, N. Takeguchi, Y. Toyoshima, and H. Fujita, *J. Phys. Chem.*, 69, 3981 (1965).

posed of two parallel plates placed 2δ apart in the y direction. The x axis is taken in the direction of the slit and the y axis perpendicular to it, with the y coordinate origin at the midpoint between the parallel walls. The origin of the x axis is placed on the membrane surface which is in contact with the solution of concentration C_1. It is assumed that 2δ is sufficiently small compared to the length of the slit, L, *i.e.*, the effective thickness of the membrane. Then the flows of all components in the slit may be considered to occur only in the direction of the slit. The value of x for the other membrane surface facing the solution of concentration C_2 is L. It is assumed that the bulk solutions are stirred vigorously so that the electric potential in each bulk solution is considered to be uniform. The charge density, σ, fixed on the slit wall is assumed to be constant and independent of the concentrations of the external electrolyte solutions with which the slit or membrane is in contact. The ion distribution in the slit is assumed to be governed by the Poisson–Boltzmann law, provided that the flows of ions and the solvent molecules passing through the slit are sufficiently slow.

Flow Equations. The thermodynamic force acting on each species is the negative gradient of its electrochemical potential, $\tilde{\mu}_k$, in the direction of the slit axis, x, provided that the aforementioned geometrical condition $\delta/L << 1$ is satisfied. The quantity $\partial\tilde{\mu}_k/\partial x$ may be written

$$\partial\tilde{\mu}_k/\partial x = (\partial\tilde{\mu}_k/\partial x)_{p,T} = e_k(\partial\varphi/\partial x) + RT(\partial \ln a_k/\partial x) \quad (1)$$

where φ, R, and T, are the electric potential, the gas constant, and the absolute temperature, respectively; e_k and a_k are the molar electric charge and the single-ion activity of species k (k = 0, +, −), respectively. Here, subscript 0 denotes the solvent species. In terms of the thermodynamics of irreversible processes, we may write the following expression for the flow flux $(j_k)_c$ of ionic species k relative to the wall of the vessel (subscript c) containing the given system[3]

$$(j_+)_c = -\left[(L_{++})_m - \frac{c_+}{c_0}(L_{+0})_m\right]\frac{\partial\tilde{\mu}_+}{\partial x} - \left[(L_{+-})_m - \frac{c_-}{c_0}(L_{+0})_m\right]\frac{\partial\tilde{\mu}_-}{\partial x} + c_+u_m \quad (2)$$

$$(j_-)_c = -\left[(L_{-+})_m - \frac{c_+}{c_0}(L_{-0})_m\right]\frac{\partial\tilde{\mu}_+}{\partial x} - \left[(L_{--})_m - \frac{c_-}{c_0}(L_{-0})_m\right]\frac{\partial\tilde{\mu}_-}{\partial x} + c_-u_m \quad (3)$$

when the system is in the mechanical equilibrium. Here c_k (k = 0, +, −) is the concentration of species k in moles/cc at a point considered, u_m is the local center of mass velocity, and $(L_{ki})_m$ (k, i = 0, +, −) are the phenomenological coefficients referred to the local center of mass and obey the Onsager reciprocal relations $(L_{ki})_m = (L_{ik})_m$ (k ≠ i). One should note that eq 2 and 3 refer to a particular stream line, not to the entire cross section of the slit, and also that the Onsager reciprocal relation holds strictly only for the mass-fixed phenomenological coefficients $(L_{ki})_m$.[3,4] The local center of mass velocity may be described in terms of the Navier–Stokes equation of motion as employed in a separate series of papers.[5] In this paper, however, the last terms in eq 2 and 3 are dropped out as a first approximation since the effect of the mass flow upon the membrane potential has been evaluated to be less than a few per cent, in the system studied.[2] Furthermore, it is assumed that the salt solution is dilute enough (*i.e.*, $C_0 >> C_k$ for k = + and −) so that the second term in each bracket given by $(c_k/c_0)(L_{k0})_m$ (k = +, −) in eq 2 and 3 is negligibly small compared to the first terms $(L_{ij})_m$ (i, j = +, −).

As noted above, we have assumed that the fluxes of all components occur only in the direction of the slit axis with the geometrical condition that $\delta/L << 1$, and hence the electrochemical potential of each component is considered to be constant in the direction of the y axis. Therefore, the flow flux (J_k) of species k (k = +, −) averaged over the cross section of the slit relative to the slit wall is defined by

$$J_k = \int_0^\delta (j_k)_c dy \Big/ \int_0^\delta dy$$

and is calculated to give

$$J_+ = -L_{++}(d\tilde{\mu}_+/dx) - L_{+-}(d\tilde{\mu}_-/dx) \quad (4)$$

$$J_- = -L_{-+}(d\tilde{\mu}_+/dx) - L_{--}(d\tilde{\mu}_-/dx) \quad (5)$$

In eq 4 and 5, L_{ki}'s (k, i = +, −) are the phenomenological coefficients averaged over the cross section of the slit, and they are defined by

$$L_{ki} = \int_0^\delta (L_{ki})_m dy \Big/ \int_0^\delta dy \quad (6)$$

It is easily shown that the Onsager reciprocal relation still holds for the L_{ki}'s. Hence, we have $L_{+-} = L_{-+}$. Using eq 4 and 5, we have the expressions for the reduced electric current density defined by $I^* = I/F =$

(3) D. D. Fitts, "Nonequilibrium Thermodynamics," McGraw-Hill Book Co., Inc., New York, N. Y., 1962, p 45.

(4) J. G. Kirkwood, R. L. Baldwin, P. J. Dunlop, L. J. Gosting, and G. Kegeles, *J. Chem. Phys.*, **33**, 1505 (1960).

(5) Y. Kobatake and H. Fujita, *ibid.*, **40**, 2212, 2219 (1964); **41**, 2965 (1964); *Kolloid-Z.*, **196**, 58 (1964).

$J_+ - J_-$ and the flow flux of the electrolyte component, $J_s = J_+ + J_-$, both relative to the slit wall as

$$I^* = -(L_{++} - L_{+-})(d\tilde{\mu}_+/dx) - (L_{--} - L_{-+})(d\tilde{\mu}_-/dx) \quad (7)$$

$$J_s = -(L_{++} + L_{+-})(d\tilde{\mu}_+/dx) - (L_{-+} + L_{--})(d\tilde{\mu}_-/dx) \quad (8)$$

where $|e_\pm|$ has been replaced by the Faraday constant, F.

Steady-State and Boundary Conditions. For the unidimensional flows considered above, the laws of conservation of mass and electric charge give the equations

$$dI^*/dx = 0 \text{ and } dJ_s/dx = 0 \quad (9)$$

when the flows are stationary. Hence we have $I^* =$ constant and $J_s =$ constant with respect to the axial direction x. In addition to these conditions, we can impose the condition $I^* = 0$ since in the present system no external electric field is applied across the membrane. Thus, the gradients of the electrochemical potential of the ionic species in the stationary state are represented in terms of J_s and L_{ki} (k, i = +, −) as

$$\frac{d\tilde{\mu}_+}{dx} = -\frac{(L_{+-} - L_{--})J_s}{2(L_{+-}^2 - L_{++}L_{--})} \quad (10)$$

$$\frac{d\tilde{\mu}_-}{dx} = \frac{(L_{++} - L_{+-})J_s}{2(L_{+-}^2 - L_{++}L_{--})} \quad (11)$$

where the Onsager reciprocal relation $L_{+-} = L_{-+}$ has been used. The integrations of the above equations between two bulk solutions across the membrane lead to

$$\Delta\tilde{\mu}_+ = -\frac{J_s}{2}\int_0^L \frac{L_{+-} - L_{--}}{L_{+-}^2 - L_{++}L_{--}}\,dx = F\Delta\varphi + RT \ln (a_2/a_1) \quad (12)$$

$$\Delta\tilde{\mu}_- = \frac{J_s}{2}\int_0^L \frac{L_{++} - L_{+-}}{L_{+-}^2 - L_{++}L_{--}}\,dx = -F\Delta\varphi + RT \ln (a_2/a_1) \quad (13)$$

In eq 12 and 13, a_1 and a_2 are the mean activities of the electrolyte components in the bulk solutions 1 and 2, and $\Delta\varphi$ is the difference of the electric potential between two bulk solutions, $\varphi_2 - \varphi_1$, *i.e.*, the membrane potential in question. From eq 12 and 13 the membrane potential $\Delta\varphi$ is represented by

$$\Delta\varphi = \frac{J_s}{4F}\int_0^L \frac{(L_{+-} - L_{--}) + (L_{++} - L_{+-})}{(L_{+-}^2 - L_{++}L_{--})}\,dx \quad (14)$$

On the other hand, introduction of eq 1 into eq 10 and 11 and rearrangement leads to

$$\frac{J_s}{2F(L_{+-}^2 - L_{++}L_{--})} = \frac{RT}{(L_{--} - L_{++})}\left(\frac{d \ln a_+}{dx} + \frac{d \ln a_-}{dx}\right) \quad (15)$$

As usual, defining the mobilities l_+ and l_- of positive and negative ions by

$$F(L_{++} - L_{+-}) = l_+\bar{c}_+ \quad (16)$$
$$F(L_{+-} - L_{--}) = -l_-\bar{c}_-$$

and eliminating J_s from eq 14 and 15, we have

$$\Delta\varphi = -\frac{RT}{F}\int_{a_1}^{a_2} \frac{l_+\bar{c}_+ - l_-\bar{c}_-}{l_+\bar{c}_+ + l_-\bar{c}_-}\left(\frac{da}{a}\right) \quad (17)$$

In the above equation a is the mean activity of the electrolyte component at a cross section of the slit defined by

$$(a_+a_-)^{1/2} = a \quad (18)$$

which becomes a_1 and a_2 at the two outsides of the membrane, and $\bar{c}_k$ (k = +, −) is the concentration of positive and negative ions averaged over the cross section of the slit defined by

$$\bar{c}_k = \int_0^\delta c_k dy \Big/ \int_0^\delta dy \quad (19)$$

The implication of eq 16 is that the mobilities of positive and negative ions are considered to be independent of the concentration of each ionic species. It is noted that the membrane potential given by eq 17 is represented in terms of the gradient of the activity of the electrolyte component instead of the gradient of the activity of each single ion a_+ and a_-.

Basic Equation in Terms of the Salt Concentration c. It is one of the unsolved problems in the field of electrolyte study to derive exact theoretical expressions for the activities of small ions in polyelectrolyte solutions or even in the charged capillary system considered here. However, in the theoretical system, since the distribution of ions at a cross section in the slit is assumed to be governed by the Boltzmann law, the product of concentrations of positive and negative ions at any point in the cross section is given by c^2, *i.e.*, $c_+c_- = c^2$ (this relation cannot hold for the concentrations averaged over the cross section of the slit, *i.e.*, $\bar{c}_+\bar{c}_- \neq c^2$), where c is a concentration of the electrolyte component at some point where the electrostatic potential is zero. In a real capillary system, such a point (where the static potential is considered to be zero) may or may not actually be present in the slit. On the other hand, as noted above, the activity

of each ionic species is constant in the y direction at a cross section of the slit, insofar as the flow fluxes are considered to be one-dimensional. This fact would make it possible to regard the solution in the cross section of the slit as one phase thermodynamically, which is equilibrated with the theoretical electrolyte solution of concentration c, within that cross section. Consideration of this rather hypothetical solution of concentration c at each cross section of the slit is actually equivalent to adopting the basic postulate of "local equilibrium" in the thermodynamics of irreversible processes.[6] It may be important to note that the distribution of c along the axial direction x of the slit is determined by the steady-state conditions of the system considered given by eq 9 and that the value of c at two sides of the membrane should coincide with C_1 and C_2, respectively. If the activity of ionic species k (k = +, −) in the cross section of the slit is denoted by $(a_k)_i$ and that in the hypothetical solution of concentration c is denoted by $(a_k)_0$, the following relation must be obeyed[7]

$$\frac{(a_+)_i(a_-)_i}{(a_+)_0(a_-)_0} = \exp[-p(\bar{v}_+ + \bar{v}_-)] \tag{20}$$

where $\bar{v}_k$ is the partial molar volume of the ionic species k, and p is the pressure difference between the membrane phase and the hypothetical solution, *i.e.*, $p = p_i - p_0$. It may be assumed that the external hypothetical solution behaves ideally, *i.e.*, we have

$$(a_+)_0(a_-)_0 = c^2 \tag{21}$$

This assumption is not unreasonable in the treatment of polyelectrolyte solutions or the capillary system considered here, but may be taken out if desired. Combining eq 18, 20, and 21, we have

$$a = c \exp(-p\bar{v}_s/2RT) \tag{22}$$

where $\bar{v}_s$ is the partial molar volume of the electrolyte component defined by $\bar{v}_s = (\bar{v}_+ + \bar{v}_-)/2$. Thus, we have

$$\mathrm{d} \ln a = \mathrm{d} \ln c - (\bar{v}_s/2RT)\mathrm{d}p \tag{23}$$

Introducing this equation into eq 17 and integrating under the external condition that no pressure difference is applied across the membrane, we have

$$\Delta\varphi = -\frac{RT}{F}\int_{c_1}^{c_2} \frac{l_+\bar{c}_+ - l_-\bar{c}_-}{l_+\bar{c}_- + l_-\bar{c}_-}\frac{\mathrm{d}c}{c} \tag{24}$$

Therefore, the problem has been reduced to that of knowing the expressions for the averaged concentrations $\bar{c}_+$ and $\bar{c}_-$ in the slit as functions of c. It may be worthwhile to note that eq 24 is considered to hold even in cases in which highly charged membranes are concerned since the nonideality of small ions in the membrane phase has already been taken into account.

Average Concentrations of Positive and Negative Ions in the Slit

Let us consider a negatively charged slit immersed in a solution of uni-univalent electrolyte of concentration c. At equilibrium, we can use the Boltzmann law for the distribution of ions. Introducing the reduced static potential ζ ($=F\psi/RT$) and the reduced distance μ ($=\kappa y$) with the Debye reciprocal radius κ of the ionic atmosphere defined by

$$\kappa = (8\pi F^2 c/\epsilon RT)^{1/2} \tag{25}$$

the Poisson–Boltzmann law is expressed by

$$\mathrm{d}^2\zeta/\mathrm{d}\mu^2 = \sinh \zeta \tag{26}$$

With the symmetry condition of the static potential at $\mu = 0$, we have the following equation for the surface potential, $-\zeta_0$, and the potential midway between the plates, $-u$, as a function of the plate distance, 2δ

$$\kappa\delta = 2e^{-u/2}[\mathrm{F}(e^{-u}, \pi/2) - \mathrm{F}(e^{-u}, \sin^{-1} e^{-(\zeta_0-u)/2})] \tag{27}$$

(where $\zeta_0 > 0$ and $u > 0$). In eq 27, $\mathrm{F}(k, \nu)$ is the elliptic integral of the first kind. The total countercharge (σ) of the double layer in half of the space between the two plates is given by

$$\sigma = (\epsilon RT\kappa/4\pi F)(2\cosh\zeta_0 - 2\cosh u)^{1/2} \tag{28}$$

By the use of these equations, the average concentration of negative "coions" in the slit defined by eq 19 is calculated to give

$$\bar{c}_- = \frac{2ce^{u/2}}{\kappa\delta}\{[\mathrm{F}(e^{-u}, \pi/2) - \mathrm{F}(e^{-u}, \sin^{-1} e^{-(\zeta_0-u)2}] - [\mathrm{E}(e^{-u}, \pi/2) - \mathrm{E}(e^{-u}, \sin^{-1} e^{-(\zeta_0-u)/2})]\} \tag{29}$$

where $\mathrm{E}(k, \nu)$ is the elliptic integral of the second kind. The difference $\bar{c}_+ - \bar{c}_-$ is shown to be given by

$$\bar{c}_+ - \bar{c}_- = |\sigma|/F\delta = \theta = \text{constant } (>0) \tag{30}$$

It is convenient to introduce the following reduced quantities: the reduced concentration of the outer solution, $\xi = (\kappa\delta)^2 = \lambda c$, the reduced coions and counterions concentration, $\xi_- = \lambda\bar{c}_-$ and $\xi_+ = \lambda\bar{c}_+$, the reduced fixed charge density, $\vartheta = \lambda\theta$, with $\lambda = 8\pi F^2\delta^2/\epsilon RT$. Along with these, we define $k = e^{-u}$

(6) D. D. Fitts, ref 3, Chapter 3.

(7) F. G. Donnan and E. A. Guggenheim, *Z. Physik. Chem.* (Leipzig), **A162**, 346 (1932).

and $\nu = \sin^{-1} e^{-(\xi_0 - u)/2}$. Then eq 27–30 are transformed to give

$$\xi^{1/2} = 2k^{1/2}[F(k, \pi/2) - F(k, \nu)] \quad (31)$$

$$\frac{4\xi}{k\vartheta^2} = \frac{\tan^2 \nu}{(1 - k^2 \sin^2 \nu)} \quad (32)$$

$$\xi_- = (\xi/k) - 2(\xi/k)^{1/2}[E(k, \pi/2) - E(k, \nu)] \quad (33)$$

and

$$\xi_+ = \xi_- + \vartheta \quad (34)$$

Elimination of the interparameters k and ν from the above equations leads to the average concentrations of positive and negative ions in the slit as functions of the salt concentration ξ, with ϑ characteristic of the system as a parameter. Figure 1 shows the relation between the average negative coions concentration ξ_-/ξ ($\equiv \bar{c}_-/c$) and ξ for various values of ϑ. In Figure 1 the values of ξ_-/ξ calculated by the Donnan equilibrium are also plotted for comparison. When ϑ is less than unity the solution of the Poisson–Boltzmann equation practically coincides with that of the Donnan equation. In the case in which ϑ is much larger than unity, the Donnan equation gives quite different values for ξ_-/ξ from those of the Poisson–Boltzmann equation, and the difference between them becomes large with increase of ϑ. It is important to note that the solution of the Poisson–Boltzmann law converges to a curve calculated from ϑ = infinity with increases of ϑ; this curve may be compared with the Donnan case, where the curves shift parallel by the amount $\log \vartheta$, when ξ_-/ξ is plotted against $\log \xi$. Numerically, the functional form of ξ_-/ξ can be represented approximately by the equation

$$\xi_-/\xi = \xi/(\xi + \tau) \text{ with } \tau \cong\cong 20 \quad (35)$$

when ϑ is larger than 10^2.

Equation for the Membrane Potential

Introducing eq 34 together with eq 35 into eq 24 and integrating between two bulk solutions having the reduced concentrations ξ_1 and ξ_2, we have

$$\frac{F\Delta\varphi}{RT} = \ln \frac{\xi_2}{\xi_1} - (1 - \alpha) \times \ln \frac{\xi_2^2 + \alpha\vartheta\xi_2 + \alpha\vartheta\tau}{\xi_1^2 + \alpha\vartheta\xi_1 + \alpha\vartheta\tau} + \alpha(1 - \alpha)\vartheta I \quad (36)$$

where α stands for $\alpha = l_+/(l_+ + l_-)$ and I is given by

$$I = [\alpha\vartheta(\alpha\vartheta - 4\tau)]^{-1/2} \times \left[\ln \frac{2\xi + \alpha\vartheta - [\alpha\vartheta(\alpha\vartheta - 4\tau)]^{1/2}}{2\xi + \alpha\vartheta + [\alpha\vartheta(\alpha\vartheta - 4\tau)]^{1/2}}\right]_{\xi_1}^{\xi_2} \quad (\text{for } \alpha\vartheta > 4\tau) \quad (37)$$

$$= 2[\alpha\vartheta(4\tau - \alpha\vartheta)]^{-1/2} \times \left[\arctan \frac{2\xi + \alpha\vartheta}{[\alpha\vartheta(4\tau - \alpha\vartheta)]^{1/2}}\right]_{\xi_1}^{\xi_2} \quad (\text{for } 4\tau > \alpha\vartheta)$$

$$= [-2/(2\xi + \alpha\vartheta)]_{\xi_1}^{\xi_2} \quad (\text{for } 4\tau = \alpha\vartheta)$$

When $(\alpha\vartheta/4)$ is much larger than τ ($\cong\cong 20$), eq 36 is simplified to give

$$\frac{F\Delta\varphi}{RT} = \ln (\xi_2/\xi_1) - 2(1 - \alpha) \ln \left(\frac{\xi_2 + \alpha\vartheta}{\xi_1 + \alpha\vartheta}\right) \quad (38)$$

Equation 38 is the same equation that was derived in our previous paper,[2] and equivalent to that in the earlier papers of Nagasawa[8] and of Kobatake,[9] provided that the effect of the mass flow in the membrane is neglected. Figure 2 shows the theoretical curves of eq 36 as a function of $\log (\xi_2/\alpha\vartheta)$ for various values of $\alpha\vartheta$, with a fixed concentration ratio $\gamma = \xi_2/\xi_1 = C_2/C_1$ and $\alpha = 1/2$ (corresponding to KCl or KI systems).[2] It is seen that eq 36 gives practically the same curve with eq 38 when $\alpha\vartheta$ is larger than 5×10^2 and that the Meyer, Sievers, and Teorell equation (the TMS theory) is an alternative limit of eq 38 in which ϑ tends to zero. It has been shown in our previous paper[2] that the experimental data available are represented quite satisfactorily by eq 38.

Discussion

Equation 24 has substantially the same form as that derived by Schlögl and Helfferich[10] and by Nagasawa.[8] As has already been shown in their earlier papers, if

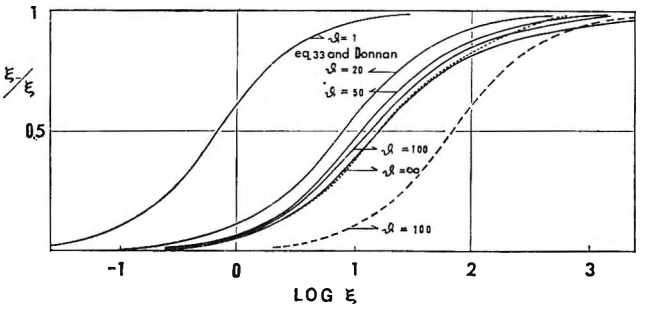

Figure 1. Theoretical relations between the average "coion" concentrations, ξ_-/ξ, and the logarithm of the salt concentration, $\log \xi$, for various values of the fixed charge density, ϑ: solid lines, eq 33; broken lines, the Donnan equilibrium; dotted line, eq 35 with $\tau = 17$.

(8) M. Nagasawa and I. Kagawa, *Discussions Faraday Soc.*, **21**, 52 (1956); M. Nagasawa, *Nippon Kagaku Zasshi*, **70**, 160 (1949); M. Nagasawa and Y. Kobatake, *J. Phys. Chem.*, **56**, 1017 (1952).

(9) Y. Kobatake, *J. Chem. Phys.*, **28**, 146, 442 (1958); *Progr. Theoret. Phys.* (Kyoto), *Suppl.*, **10**, 226 (1959).

(10) R. Schlögl and F. Helfferich, *Z. Elektrochem.*, **56**, 644 (1952).

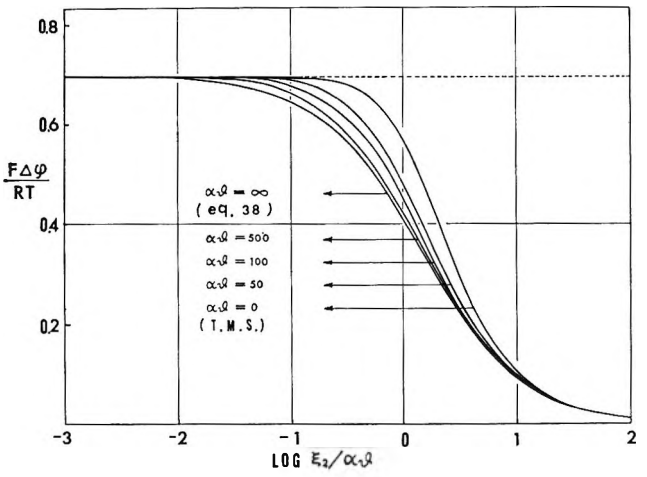

Figure 2. Relation between the reduced membrane potential $F\Delta\varphi/RT$ and log $\xi_2/\kappa\vartheta$ (eq 36) for various values of $\kappa\vartheta$, with a given ratio of concentrations $\gamma = \xi_2/\xi_1 = 2$ and $\alpha = 1/2$.

the Donnan equilibrium equation is used for the average concentrations of small ions in the membrane, instead of the Poisson–Boltzmann equation, eq 24 leads to the TMS theory. Thus, the crucial difference between the TMS theory and our equation for the membrane potential is in the evaluation of the average concentrations of small ions, $\bar{c}_+$ and $\bar{c}_-$, in the membrane phase. Therefore, it may be worthwhile to describe the general behavior of the solution of the Poisson–Boltzmann equation described above.

(1) *The Case of* $k << 1$ ($u >> 0$). This condition corresponds to the case in which the concentrations of the outer solutions are very dilute, and hence $\xi/\vartheta << 1$. In this case eq 33 is expanded to give

$$\xi_- = [\tan \nu_0(2\nu_0 + \sin 2\nu_0)/4\nu_0^2](\xi^2/\vartheta) + O(\xi^4) \quad (39)$$

where ν_0 stands for $(\pi/2) - \nu$, and is related to ϑ by the equation: $\tan \nu_0 = \vartheta/4\nu_0$. The coefficient for (ξ^2/ϑ) in eq 39, *i.e.*, $\tan \nu_0(2\nu_0 + \sin 2\nu_0)/4\nu_0^2$, is always less than unity and diminishes with an increase of ϑ. Only in the limit $\vartheta \to 0$, does the coefficient tend to unity, and ξ_- becomes equal to ξ^2/ϑ. This is equivalent to the Donnan equation for the case in which $\xi/\vartheta \ll 1$.

(2) *The Case of* $k = 1$ (*i.e.*, $u = 0$). Either $\kappa\delta \gg 1$ or $\xi/\vartheta \gg 1$; with the condition that $\vartheta/4\sqrt{\xi}$ is less than unity, eq 33 may be expanded to give

$$\xi_- = \xi - \frac{\vartheta}{2} + \frac{\vartheta^2}{16\sqrt{\xi}} + O(\vartheta^4/\xi^{3/2}) \quad (40)$$

This equation is compared to the expansion of the Donnan equation for the case in which $\xi/\vartheta \gg 1$, *i.e.*

$$\xi_- = \xi - \frac{\vartheta}{2} + \frac{1}{8}\left(\frac{\vartheta}{\xi}\right)^2 + O(\vartheta^2/\xi^2) \quad (41)$$

When ϑ tends to zero, eq 40 coincides with the Donnan equation (eq 41).

(3) δ *Tends to Zero with Constant* θ *and* c. With the limit of $\delta = 0$, the membrane phase may be regarded as thermodynamically one phase, with constant fixed charge density. In this case, eq 33 is approximated to give

$$\xi^2 = \vartheta\xi_-[1 + O(\xi^2)] + \xi_-^2 \quad (42)$$

At the limit $\delta = 0$, the reduced concentration ξ also becomes zero due to the definition of ξ, and hence eq 42 becomes $\xi^2 = \xi_-(\xi_- + \vartheta) = \xi_-\xi_+$, which leads to the Donnan equation. Thus, it may be concluded that our basic eq 33, combined with eq 31, 32, and 34 for the average concentration of the coions in the membrane, can be reduced to that of the Donnan equilibrium for the following three cases: (1) the membrane is regarded as thermodynamically one phase, which is realized as a limit of $\delta = 0$ at a given θ; (2) the membrane is very weakly charged with a given porosity, *i.e.*, $\theta \to 0$ for a constant δ; (3) the concentration of the outer salt solutions is much larger than the fixed charge density, *i.e.*, $c/\theta >> 1$. On the other hand, in the case in which the fixed charge density is very high, with an appropriate value of δ, eq 33 and 31 can be transformed to give

$$\xi = 4k[K(k)]^2 \quad (43)$$

$$\xi_-/\xi = [1 - 2(k/\xi)^{1/2}E(k)]/k \quad (44)$$

where $K(k)$ and $E(k)$ are the complete elliptic integrals of the first and second kinds. Elimination of the interparameter k from the two above equations gives the concentration dependence of ξ_-, which is independent of the charge density fixed in the membrane ϑ. In the above equations, when k tends to unity, which corresponds to θ becoming very large for a constant δ, eq 44 is approximated by

$$\xi_- = \xi - 2\xi^{1/2} \quad (45)$$

This equation holds for the case $\xi/\vartheta \geqq 10\vartheta$. Equation 35 gives almost the same numerical values with eq 43 and 44, as shown in Figure 1.

The difference between the solutions of the Poisson–Boltzmann equation and the Donnan equilibrium becomes more clear if the quantity $c^2/\bar{c}_+\bar{c}_- = \xi^2/\xi_+\xi_-$ is plotted against the concentration of the external solution. This quantity is unity for the case of the Donnan equilibrium, while the Poisson–Boltzmann equation gives a much smaller value than unity with a decrease of the salt concentration for a given value of ϑ, as shown in Figure 3. It has already been pointed out in our previous paper[2] that the typical data avail-

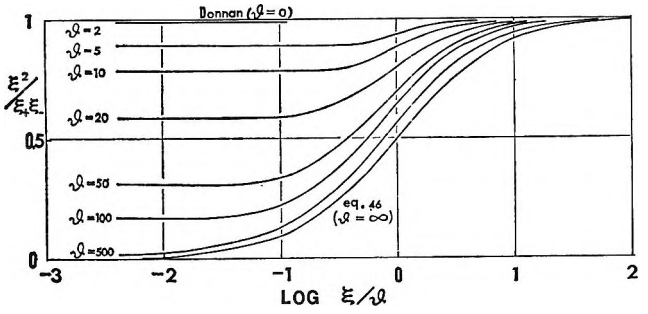

Figure 3. Relation between $\xi^2/\xi_+\xi_-$ and log ξ/ϑ for various values of ϑ.

able for the average concentration $\bar{c}_+$ and $\bar{c}_-$ in ion-exchange resins, or in a membrane equilibrated with a simple electrolyte solution, are well represented by

$$c^2/\bar{c}_+\bar{c}_- = c/(c + \theta) \equiv \xi/(\xi + \vartheta) \qquad (46)$$

It is seen from Figure 3 that there is no appreciable difference between the exact solutions of the Poisson–Boltzmann equation and eq 46 when ϑ is larger than 10^2. Equation 46 is equivalent to the assumption that $\bar{c}_+ = c - \theta$ and $\bar{c}_- = c$. This means that the coions are restricted by repulsion to the regions of the slit in which $F\psi/RT$ is low. These regions comprise the predominant parts of the slit, and therefore the average concentration of coions is not materially different from the concentration of the electrolyte in the bulk solution. This picture of the distribution of coions in the slit or membrane phase is essentially different from that of the Donnan equilibrium, in which the membrane phase is assumed to be one phase thermodynamically. This fact stems from the distribution of the fixed charges in the membrane, which is condensed on the capillary walls instead of uniformly distributed in the membrane phase. As a result, the local potential near the fixed charges becomes extremely high, and a larger proportion of the counterions is immobilized in the vicinity of the fixed charges; hence, both the Donnan equilibrium and the Debye–Hückel linearization approximation are not applicable. This is also true in a polyelectrolyte solution in which the behavior of the mobile ions is determined by the local high density of charges along the polymeric chain, as pointed out by Katchalsky, *et al.*[11] Hence, even in a membrane which is regarded as a polyelectrolyte gel, we may not describe membrane phenomena in terms of the Donnan equilibrium.

(11) A. Katchalsky, Z. Alexandrowicz, and O. Kedem, personal communication.

The Viscosity of Polymer–Diluent Mixtures

by G. C. Berry

Mellon Institute, Pittsburgh, Pennsylvania 15213 *(Received October 25, 1965)*

The empirical equation $\eta = (N_a/6)X_c(X/X_c)^a\zeta$ with $X = (\overline{s^2}/M)_0\varphi_2 Z/v_2$, is applied to data giving the dependence of the viscosity η on chain length Z and polymer concentration φ_2. It is shown that this equation, with $a = 1.0$ until $X > X_c$, and $a = 3.4$ for larger X, satisfactorily correlates the viscosity of several polymer–diluent systems provided the effect of φ_2 on the friction factor ζ is taken into account so that η is compared at constant ζ rather than at constant temperature. This can be accomplished through the dependence of the Vogel parameters α and T_0 on φ_2; the former are defined through the relation $\zeta = \zeta_0 \exp[1/\alpha(T - T_0)]$, with ζ_0 a constant. Data are examined for η as a function of Z, with φ_2 constant, and η as a function of φ_2, with Z constant. Finally, the relation of the parameters α and T_0 to free volume parameters is briefly discussed.

1. Introduction

The zero shear viscosity η of polymer–diluent systems has received extensive study by many investigators. The results of various empirical correlations[1-6] may be given by the empirical expression[1]

$$\eta = (N_a/6)X_c(X/X_c)^a\zeta \qquad (1)$$

where

$$X \equiv (\overline{s^2}/M)_0\varphi_2 Z/v_2$$

and

$$a = 3.4 \text{ for } X > X_c$$

$$a = 1.0 \text{ for } X < X_c$$

Here X_c is a constant (see below), $(\overline{s^2})_0$ is the unperturbed mean-square radius of gyration, M is the polymer molecular weight, Z is the number of *chain atoms* per molecule, φ_2 is the volume fraction of polymer, v_2 is the specific volume of polymer, N_a is Avogadro's number, and ζ is the friction factor per *chain atom*. The weight-average chain length is used here in X for polydisperse polymers.

Equation 1, although based on empirical correlation, has been given theoretical significance by Bueche,[5] and reduces exactly to Bueche's theoretical result when $X < X_c$. The inclusion of φ_2 in the parameter X accounts for the change in the number density of chains caused by the addition of diluent, as is discussed more fully below. This is in general, however, only a small part of the total change in η effected by the addition of diluent since the friction factor ζ usually depends strongly on the diluent concentration φ_2. In the following, the variation of η with φ_2 and Z will be discussed within the framework of eq 1 and certain formulations for the dependence of ζ on the φ_2 given below.

2. Constant φ_2, Variable Z

Many investigators[1-6] have noted that plots of η *vs.* Z (or M) *at constant* φ_2 obey eq 1. In this case, ζ may be considered constant at each φ_2 for $\varphi_2 < 1$ (except perhaps at low Z, where corrections to constant ζ can be made if necessary[4,7]), and slopes of 1.0 and 3.4 are observed in plots of log η *vs.* log $(\varphi_2 Z)$, below and above a critical value $(\varphi_2 Z)_c$, respectively, as illustrated in Figure 1 for some data on poly(vinyl acetate) in diethyl phthalate.[8] These data are plotted as iso-

(1) T. G Fox and V. R. Allen, *J. Chem. Phys.*, **41**, 344 (1964), and ref 1 to 8 contained therein.

(2) M. F. Johnson, W. W. Evans, I. Jordan, and J. D. Ferry, *J. Colloid Sci.*, **7**, 498 (1952).

(3) F. Bueche, *J. Appl. Phys.*, **24**, 423 (1953).

(4) T. G Fox, S. Gratch, and S. Loshaek, in "Rheology," Vol. 1, F. R. Eirich, Ed., Academic Press Inc., New York, N. Y., 1956, Chapter 12.

(5) F. Bueche, "Physical Properties of Polymers," Interscience Publishers, Inc., New York, N. Y., 1962, p 73.

(6) F. N. Kelley and F. Bueche, *J. Polymer Sci.*, **50**, 549 (1961).

(7) M. L. Williams, *J. Appl. Phys.*, **29**, 1395 (1958).

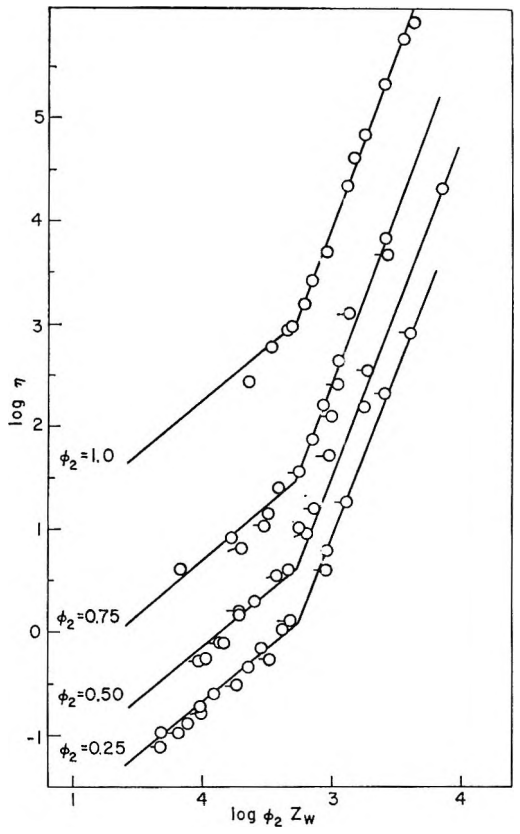

Figure 1. Log η *vs.* log ($\varphi_2 Z$) for poly(vinyl acetate) in diethyl phthalate,[6] O, and cetyl alcohol,[6] -o, at 396°K. Each set of curves was taken at constant ϑ_2, as indicated.

thermal viscosities *vs.* $\varphi_2 Z$; the correction to constant ζ described below has not been applied here. The solid lines are drawn with slope 1.0 and 3.4, appropriate to data corrected to constant ζ as discussed below; the lines provide good fit to the data except for that for low Z and $\varphi_2 = 1$, showing that ζ may be constant at each $\varphi_2 < 1$ for these purposes. The vertical separation in the curves is attributed to variation of ζ with φ_2.

It is seen in Figure 1 that the product $(\varphi_2 Z)_c$ is independent of φ_2 to within the uncertainty of the data, as is implied in writing down eq 1. This is at variance with a recent suggestion of Kelley and Bueche[6] in which $(\varphi_2^{6/5} Z)_c$, rather than $(\varphi_2 Z)_c$, is independent of φ_2 when data of this type are considered. The former implies that X_c decreases as $\varphi_2^{1/5}$. Unfortunately, this difference is too small to be definitively assessed from existing data (*e.g.*, $(\varphi_2^{6/5} Z)_c$ differs from $(\varphi_2 Z)_c$ by only 38% for φ_2 as low as 0.2, and typical uncertainties in the break point are ±10%). Thus, we use the simpler empirical result eq 1 with constant X_c in this study.

3. Constant Z, Variable φ_2

The analysis of η as a function of φ_2 *at constant* Z is more complicated because of the severe dependence of ζ on φ_2, but data of this type can also be correlated with eq 1, provided the variation of $\zeta(\varphi_2)$ is correctly included. Williams and later Williams, Landel, and Ferry[9] showed that the temperature dependence of η for many polymers can be represented by a version of the simple Vogel relation[10]

$$\zeta = \zeta_0 \exp[1/\alpha(T - T_0)] \qquad (2)$$

The empirical parameters α and T_0, which depend strongly on φ_2, will be related to free volume parameters below, but it is not necessary to do this at this stage. The parameter ζ_0 is presumed to be independent of Z, T, and φ_2. This, of course, implies that ζ_0 is also independent of the solvent although α and T_0 need not be so in general. The combined eq 1 and 2 can be expected to apply only above some ill-defined critical volume fraction φ_2^* above which all of the polymer coils overlap, as pointed out by Johnson, *et al.*[2] Below this limit, thermodynamic interactions can be expected to influence η inasmuch as they affect the polymer coil dimensions. For $\varphi_2 > \varphi_2^*$, η may be expected to be independent of the nature of the solvent so long as the product $\alpha(T - T_0)$ is independent of solvent (see below). A rough estimate for φ_2^* can be obtained from the value of φ_2 where polymer "spheres" of mean-square radius $\overline{S^2}$ form a hexagonal close-packed system. This criterion yields the estimate $\varphi_2^* \approx 2.22 v_2 M/(4\pi N_a(\overline{S^2})_0^{3/2})$, or $\varphi_2^* \approx (1/8)(10^{-4}M)^{-1/2}$ for typical values of the parameters in φ_2^*.

The parameters α and T_0 can be determined as functions of φ_2 from experimental $\eta(\varphi_2, T, Z)$ data by plotting the data at constant φ_2 and Z according to the expression

$$-\frac{T - T_r}{\ln \eta/\eta_r} = i + m(T - T_r) \qquad (3)$$

which may easily be derived from eq 2. Here T_r is an *arbitrary* reference temperature in the interval spanned by the data, η_r is the viscosity at T_r, and m and i are constants for any T_r. The ratio η/η_r has been used instead of the more appropriate ζ/ζ_r, but typically the temperature dependence of the parameters in X is so small compared to those in ζ that this makes no dif-

(8) H. Nakayasu and T. G Fox, Abstracts, Colloid Chemistry Division, 137th National Meeting of the American Chemical Society, Cleveland, Ohio, April 1960.

(9) M. L. Williams, *J. Phys. Chem.*, 59, 95 (1955); M. L. Williams, R. F. Landel, and J. D. Ferry, *J. Am. Chem. Soc.*, 77, 3701 (1955).

(10) H. Vogel, *Physik. Z.*, 22, 645 (1921).

ference although ζ/ζ_r could be used if necessary. The Vogel parameters can then be calculated as

$$T_0 = T_r - i/m \tag{4a}$$

and

$$\alpha = m^2/i \tag{4b}$$

Figure 2 shows T_0 and α *vs.* φ_2 for data on polystyrene (Z_w = 1340) in dibenzyl ether[11] and polystyrene (Z_w = 10,500) in diethylbenzene.[3] Data on poly(vinyl acetate) in diethyl phthalate[8] exhibit similar behavior.

Having determined the dependence of α and T_0, and hence ζ, on φ_2, we are now in a position to examine the effect of diluent on η. First, certain qualitative statements can be made by examining the general nature of the curves in Figure 2. Differentiation of eq 1 with respect to φ_2 at constant T and Z yields (assuming ζ_0, $\bar{s^2}$, and X_c to be independent of φ_2)

$$\frac{\partial \ln \eta}{\partial \ln \varphi_2} = a - \frac{1}{\alpha(T - T_0)}\left[\frac{\partial \ln (T - T_0)}{\partial \ln \varphi_2} + \frac{\partial \ln \alpha}{\partial \ln \varphi_2}\right] \tag{5}$$

The first term on the right-hand side of eq 5 is either 3.4 or 1.0 as $X > X_c$ or $X < X_c$, respectively. Reference to Figure 2 shows that the first term in the brackets is initially very large, decreasing with decreasing φ_2, whereas the second term in the brackets is small until φ_2 becomes very small. Thus, one expects an initially rapid decrease in η as diluent is added, followed by a region in which η decreases less rapidly with φ_2, according to the magnitude of a, which in turn depends on the magnitude of the parameter X relative to the constant X_c. Figure 3a shows that this is indeed the observed behavior for isothermal η when φ_2 is varied at fixed Z.

Turning to quantitative use of the information in Figure 2, we have used the empirically determined values of α and T_0 to construct Figure 3b in which log η is plotted against log ($\varphi_2 Z_w$), *at constant* ζ *rather than constant* T for a polystyrene fraction in dibenzyl ether (Z_w = 1340). Thus, the term

$$C = [1/\alpha(T - T_0)]_\varphi - [1/\alpha(T - T_0)]_\varphi$$

has been added to log η for each φ_2. *It is seen that the data transformed in this way describe straight lines with slopes 3.4 and 1.0, above and below the critical point* $(\varphi_2 Z)_c$, *respectively, and that satisfactory superposition is achieved with the curve for* $\varphi_2 = 1$ (corrected for variation in ζ for short chains by a similar method). Data on polystyrene in diethylbenzene also superpose satisfactorily with the curve for $\varphi_2 = 1$, but these data do not extend below $(\varphi_2 Z)_c$. Data for poly(vinyl acetate) in diethyl phthalate,[8] corrected to constant ζ in the same way, are displayed in Figure 4, where again satisfactory superposition is achieved.

The relation obtained by Kelley and Bueche, on the other hand, indicates that data of this type (constant

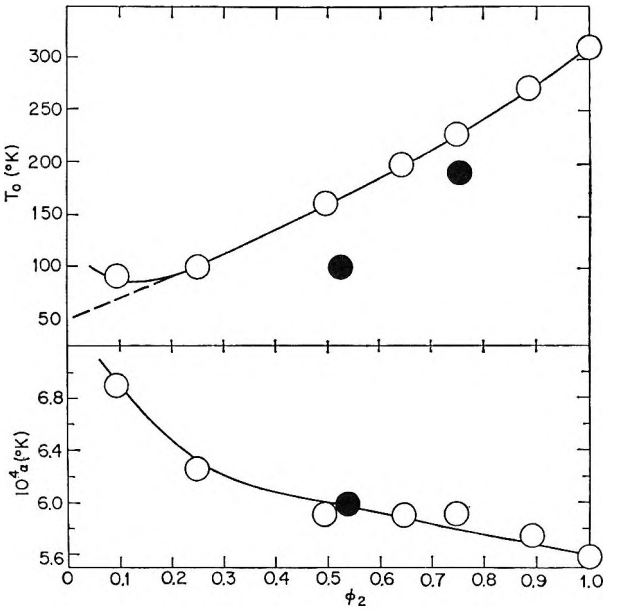

Figure 2. The Vogel parameters T_0 and α *vs.* φ_2 for polystyrene in dibenzyl ether,[11] O, and in diethyl benzene,[2] ●.

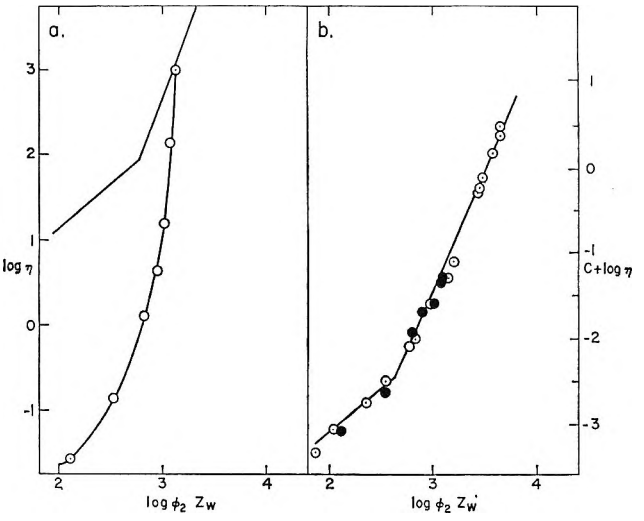

Figure 3. (a) Log η *vs.* log ($\varphi_2 Z_w$) at 217° for a polystyrene fraction in dibenzyl ether (Z_w = 1340) with $0.1 < \varphi_2 < 1.0$;[11] the intersecting straight lines represent the position of the curve for $\varphi_2 = 1$. (b) C + log η *vs.* log ($\varphi_2 Z_w$) for the same data and for data on fractions with $\varphi_2 = 1$, O. Here, C corrects the data to constant ζ.

(11) T. G Fox and A. R. Schultz, private communication.

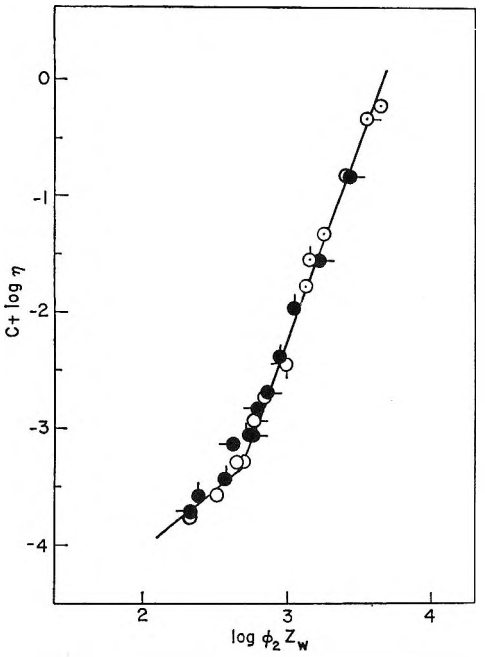

Figure 4. $C + \log \eta$ *vs.* $\log (\varphi_2 Z_w)$ for poly(vinyl acetate), open circles, and its concentrated solutions in diethyl phthalate, solid circles, where C corrects the data to constant ζ; Z_w = 2680, 1510, and 920 for pips right, up, and left, respectively.

Z, variable φ_2) should be plotted as $\log (\eta\varphi_2^{-1/2})$ *vs.* $\log (\varphi_2 Z)$ in order to achieve the superposition displayed in Figures 3b and 4. Unfortunately, there is sufficient latitude in the assignment of the parameter α and T_0 for typical data that this difference cannot be reliably evaluated from any data that have come to our attention.

Some data on poly(*n*-alkyl methacrylates) in diethyl phthalate[12] do not exhibit the behavior obtained above for polystyrene and poly(vinyl acetate). Here, α is observed to increase rapidly with decreasing φ_2, whereas T_0 decreases to a shallow minimum for $\varphi_2 \sim$ *ca.* 0.8 as φ_2 decreases, then becomes independent of φ_2. Furthermore, plots of $\log \eta$ *vs.* $\log \varphi_2 Z$ at constant $1/\alpha(T - T_0)$ and fixed Z do not exhibit the behavior seen in Figures 3b and 4 but show a shallow maximum as φ_2 decreases and then decreases rapidly with decreasing φ_2. Similar effects have been noted by Ferry and co-workers[13] in the reduction factors for dynamic mechanical properties of poly(alkyl methacrylates). The cause of this behavior must remain a matter for conjecture at present, but it may represent the effects of stereoregularity in the methacrylate polymers.

4. Free Volume Parameters

The free volume treatment of the temperature dependence of the viscosity leads to the relation[6,14–16]

$$\zeta = \zeta_0 \exp\{B/(f_g + \alpha_f(T - T_g))\} \quad (6)$$

Here B is proportional to the fractional void volume required for a segmental jump, f_g is the fractional free volume at the glass temperature T_g, and α_f is the expansion factor for the void volume. Simple comparison of eq 2 and 6 yields the relations

$$B = \alpha_f/\alpha \quad (7a)$$

and

$$f_g = \alpha_f(T_g - T_0) \quad (7b)$$

Williams, Landel, and Ferry suggested that approximately $B = 1$ and $\alpha_f \approx \alpha_l - \alpha_g$, where α_l and α_g are the expansion factors for the liquid and the glassy states, respectively. A more recent study on a simple liquid[17] has suggested that $\alpha_f \sim \alpha_l$, as was assumed by earlier investigators.[4,7] We shall employ the latter approximation here in calculating B and f_g as functions of φ_2. Thus, eq 7 can be used to compute B and f_g from the Vogel parameters T_0 and α provided T_g and α_l are known as functions of φ_2. Such data on polystyrene in dibenzyl ether[18] are displayed in Figure 5, with the corresponding Vogel parameters being given in Figure 2. These data indicate that B remains independent of φ_2 at a value of $B = 0.95$ over the interval spanned. In addition, f_g is essentially independent of φ_2 for $\varphi_2 > 0.5$ since $T_g - T_0$ varies little over the interval. These are entirely reasonable results, and they suggest that the viscous flow unit is essentially unchanged by the addition of diluent, at least until $\varphi_2 <$ *ca.* 0.2.

It has been reported that the glass temperature of polymer diluent mixtures depends only on φ_2 and is independent of the specific solvent.[18] If this observation is valid, eq 6 indicates that η should also be independent of the nature of the solvent at given φ_2, provided the free volume parameters B, f_g, and α_f are independent of solvent. Since B and f_g are expected to be essentially independent of φ_2, any specific solvent dependence must be attributed to $\alpha_f \approx \alpha_l$. Unfortunately, few studies of the dependence of α_l on φ_2 or solvent are known to us; the data displayed in

(12) F. Bueche, *J. Appl. Phys.*, **26**, 738 (1955); A. Teramoto, R. Okada, and H. Fujita, *J. Phys. Chem.*, **67**, 1228 (1963).

(13) J. W. Berge, P. R. Saunders, and J. D. Ferry, *J. Colloid Sci.*, **14**, 135 (1959).

(14) A. K. Doolittle, *J. Appl. Phys.*, **22**, 1471 (1951).

(15) F. Bueche, *J. Chem. Phys.*, **24**, 418 (1956).

(16) M. H. Cohen and D. Turnbull, *ibid.*, **31**, 1164 (1959).

(17) D. J. Plazek and J. Magill, to be published; see also abstract in *Rheol. Bull.*, **33**, No. 4, 6 (1964).

(18) T. G Fox, W. B. Schultz, and A. R. Schultz, private communication.

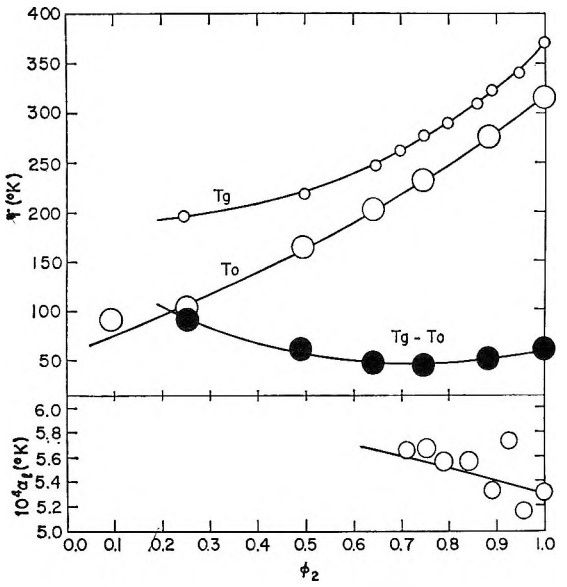

Figure 5. Free volume parameters for polystyrene in diethyl phthalate.[17]

Figure 5 suggest that α_1 depends on φ_2,[18] so it may also depend on solvent. These results also indicate that attempts to use the usual WLF equation to correlate the dependence of η on φ_2 will be successful only over the restricted interval for which $T_g - T_0$ is constant, for $0.5 < \varphi_2 < 1.0$ for polystyrene in dibenzyl ether, for example.

5. Conclusions

These calculations show that eq 1 and 2 can be used to predict adequately the effect of diluent addition on η for typical polymer–diluent systems. In particular, if the isothermal data are corrected to a constant value of ζ through the use of eq 2, then η is proportional to the parameter X for $X < X_c$ or to $X^{3.4}$ for $X > X_c$. Thus, data taken under different conditions of φ_2, T, and Z all superpose to yield a single curve when plotted as η at constant ζ *vs.* $X = (\bar{s}^2/M)_0\varphi_2 Z/v_2$. The parameters α and T_0 in eq 2 need only be viewed as empirical constants to be determined from the temperature dependence of η at constant φ_2 to effect the correction of the isothermal data to constant ζ.

We have not here dealt with the question of molecular weight heterogeneity, but the usual considerations may be expected to apply.[19,20] Thus, Z has been replaced by the weight-average value Z_w for polydisperse samples, and the friction factor ζ is expected to depend on the number-average chain length Z_n, chiefly through the dependence of T_0 on Z_n in terms of the parameters used here.

As a separate consideration, the parameters α and T^0 can be correlated with the parameter in the free volume treatment of the density dependence of the friction factor to yield reasonable results when applied to data on polymer–diluent systems. That is, the fractional void volume required for a segmental jump and the fractional free volume at the glass temperature T_g are essentially independent of concentration except when $\varphi_2 < 0.5$. This suggests that the effective viscous flow unit is essentially unchanged by the addition of diluent over a wide range of concentrations. Similarly, it is anticipated that these parameters will also be independent of Z at a given φ_2, except in the limit of very low Z, even though both T_g and T_0 will separately depend on Z_n for moderately low Z. Unfortunately, we are unaware of any data which give both $\eta(T)$ and T_g as functions of Z and φ_2.

Acknowledgments. It is a pleasure to acknowledge the cooperation of Dr. T. G Fox in making available the extensive data cited in ref 8, 11, and 18. This study was supported in part by the Research and Technology Division, Air Force Materials Laboratory, Wright–Patterson Air Force Base.

(19) P. J. Flory, *J. Am. Chem. Soc.*, **62**, 1057 (1940).
(20) V. R. Allen and T. G Fox, *J. Chem. Phys.*, **41**, 337 (1964).

Osmotic Coefficients of Concentrated Aqueous Urea Solutions from Freezing-Point Measurements

by R. H. Stokes[1]

Institute for Enzyme Research and Department of Chemistry, University of Wisconsin, Madison, Wisconsin
(Received October 25, 1965)

In order to resolve an inconsistency between published freezing-point data and other thermodynamic properties, the freezing points of aqueous urea solutions have been measured in the range 1–8 *M*. The new results are shown to be consistent with isopiestic vapor pressure measurements and thermal properties, but show that the equations of Gucker and Pickard for the apparent molar enthalpy cannot safely be used for extrapolation outside their experimental temperature range, especially at high concentrations.

Introduction

The thermodynamic properties of aqueous urea solutions are of interest in connection with models for the amide hydrogen bond[2-5] and with diffusion studies.[6,7]

It is appropriate here to comment on an erroneous view[4] that aqueous urea solutions are "nearly ideal." The molal osmotic coefficient, at 4 *M* and 25° is $\phi = 0.891$; the corresponding value for an ideal solution (*i.e.*, one with the water activity equal to the stoichiometric mole fraction of water) is $\phi = 0.965$. Calculations from the heat capacity and heat of dilution measurements of Gucker and Pickard[8] have shown that the departure from ideal behavior rapidly becomes more pronounced as the temperature is lowered. Both Gucker and Scatchard[9] were unable to reconcile the freezing-point data of Chadwell and Politi[10] with 25° isopiestic data and the thermal properties. The more recent freezing-point measurements of Cavallero and Indelli[11] agree adequately with the other data, but extend only to 0.6 *M*.

Accordingly, we report a new set of freezing-point measurements in the region 1–8 *M*, *i.e.*, up to near the eutectic point, from which we conclude that the work of Chadwell and Politi was in error.

Experimental Section

Since the freezing-point depressions of interest range from 1.8 to 11°, ordinary thermometric methods sensitive to 0.001° are suitable. We have used an American Instrument Co. quartz sheathed platinum resistance thermometer and a mercury-in-glass calorimeter thermometer, both calibrated by the National Bureau of Standards. The resistance thermometer was used at an immersion of about 15 cm; tests at other immersion depths showed that heat leakage along the stem and leads affected the reading by less than 0.001°. Tests with various thermometer currents showed that at the current used in the measurements (2.8 ma) the self-heating effect with this thermometer was less than 0.001°; the resistance bridge was a Leeds and Northrup Model G2. When using the mercury thermometer, the entire apparatus and the shivering operators were in a cold room held at approximately 2° in order to minimize emergent stem corrections. The mercury thermometer was not permitted to rise above

(1) On leave from University of New England, Armidale, N.S.W., Australia.

(2) J. A. Schellman, *Compt. Rend. Trav. Lab. Carlsberg, Ser. Chim.*, 29, 223 (1955).

(3) G. C. Krescheck and H. A. Scheraga, *J. Phys. Chem.*, 69, 1704 (1965).

(4) M. Abu-Hamidiyya, *ibid.*, 69, 2720 (1965).

(5) I. M. Klotz and J. S. Franzen, *J. Am. Chem. Soc.*, 84, 3461 (1962).

(6) J. G. Albright and R. Mills, *J. Phys. Chem.*, 69, 3120 (1965).

(7) R. H. Stokes, *ibid.*, 69, 4012 (1965).

(8) F. T. Gucker, Jr., and H. B. Pickard, *J. Am. Chem. Soc.*, 62, 1464 (1940).

(9) G. Scatchard, W. J. Hamer, and S. E. Wood, *ibid.*, 60, 3061 (1938).

(10) H. M. Chadwell and F. W. Politi, *ibid.*, 60, 1291 (1938).

(11) L. Cavallero and Indelli, *Gazz. Chim. Ital.*, 85, 993 (1955).

2° at any time in order to reduce bulb hysteresis error. It was found, however, that even if the thermometer was allowed to warm up to 25° before use, the zero-point depression resulting from hysteresis was only 0.005°. The equilibration vessel was a 20 × 2.5-cm glass tube fitted inside a 21 × 3.5-cm tube, which in turn was inside a dewar vessel containing an ice–salt mixture adjusted to slightly below the freezing point of the solution. The thermometer, the vertically moving mechanical helical stirrer of plastic-coated wire, and the passage for inserting the sampling needle passed through the stopper of the inner glass tube. The solution was placed in the central tube and frozen in a separate cooling bath until a suitable amount of ice had crystallized out before setting it in the apparatus. After about 10 min stirring, with temperature readings every minute, a long hypodermic needle was inserted through the stopper and down to the bottom of the solution tube. Further temperature readings were taken over 10 min; if the rate of change exceeded 0.001°/min, the dewar temperature was adjusted. When the temperature was sufficiently steady, stirring was stopped and about 15 sec was allowed for the ice crystals to float clear of the bottom of the tube. A 25-ml portion of the solution was then drawn off by means of the hypodermic syringe. Sampling was completed within 1 min of stopping the stirrer, so that temperature uncertainty during sampling was no more than 0.001°.

The samples were analyzed by density measurements at 25°, since the highly precise data of Gucker, *et al.*,[12] make possible accurate composition determination from density in this concentration range. The syringe and contents were warmed to 30° by warm water, then the syringe outlet was closed and the plunger pulled out a few centimeters, forming a vapor bubble. Vigorous shaking then degassed the solution sufficiently to prevent the formation of bubbles in the pycnometer. (This method of degassing solutions is highly recommended as it does not permit any significant loss of water vapor such as occurs if pumping is used.) The pycnometer (volume ~25 ml) was then filled directly from the syringe. A reproducibility of $\pm 1 \times 10^{-5}$ g ml^{-1} was obtained in the density measurements; vacuum corrections to all weighings were, of course, made. In the case of urea solutions, this precision in the density is equivalent to ±0.07% in the molality of a 1 *M* solution, and proportionately less at higher concentrations.

The urea used was of analytical reagent quality. For some of the measurements, material recrystallized from water (not heated above 60°), washed with cold ethanol, and dried on the filter pump and then at 55° to constant weight was used. This material gave results indistinguishable from the analytical reagent grade product. All solutions were used within a few hours of making up. Electrical conductivities were measured on each batch of material and showed negligible amounts of ionic impurities. Biuret tests were also negative. Solutions made up by weight from dried material were used to check the density measurement technique; molalities determined from the solution densities agreed to 0.1% or better with the weight compositions. Of some interest in connection with the purification of the urea was the observation that material recrystallized from absolute ethanol (temperature not above 60°) and dried to constant weight at 55° was apparently impure: solutions of this material when analyzed by density gave molalities some 0.6% lower than those based on the weights of dry solid and water, and the molal freezing point depressions ($\Delta T/m$) were 0.6 to 1% higher than those of the good material. It was thought possible that some contamination with urethane had occurred through reaction with the alcohol. It would seem advisable to avoid the use of hot alcohol in the purification of urea.

From the density of the samples withdrawn from the freezing-point apparatus, molarities (c) and subsequently molalities (m) were calculated from the equation[12] for 25°

$$d - d_0 = 1.59686 \times 10^{-2}c - 1.3958 \times 10^{-4}c^2 + 2.593 \times 10^{-6}c^3 \quad (1)$$

which is readily solved for c by successive approximations.

Results and Discussion

Table I gives the molalities and freezing points of the solutions studied. As the molal fp depression $\Delta T/m$ falls rather rapidly with increasing concentration, the arbitrary deviation function

$$x = \frac{\Delta T}{m} + 0.09488m - 0.005117m^2 \quad (2)$$

was used to represent the experimental results and to compare them with other work. Figure 1 shows that there are no systematic differences between the analytical reagent material and the recrystallized material, nor between the results from the platinum resistance thermometer and the mercury thermometer. The results of Cavallero and Indelli[11] are seen to be consistent with ours except for their two highest concentra-

(12) F. T. Gucker, Jr., F. W. Gage, and C. E. Moser, *J. Am. Chem. Soc.*, **60**, 2582 (1938).

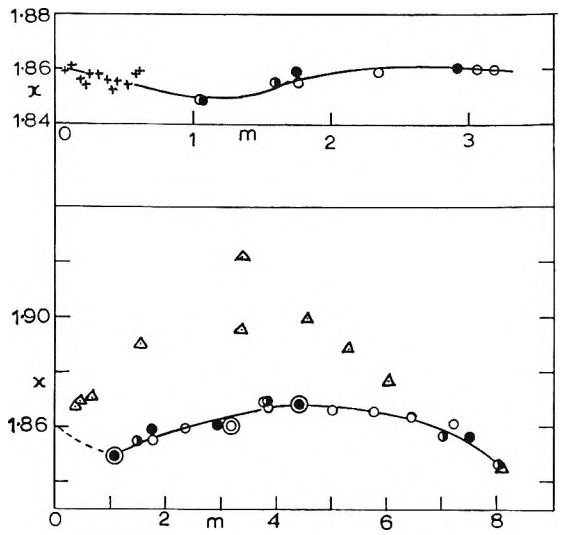

Figure 1. The deviation function x defined by eq 2 for the freezing points of aqueous urea solutions: ●, this work, platinum resistance thermometer, recrystallized urea; ◐, this work, platinum resistance thermometer, ACS grade urea; ○, this work, mercury thermometer, ACS grade urea; △, Chadwell and Politi (ref 10); +, Cavallero and Indelli (ref 11).

Table I: Freezing-Point Depressions for Aqueous Urea Solutions

m^a	ΔT^b	x^c	Notes
1.0425	1.830	1.849	*d*
1.0603	1.860	1.849	*e*
1.594	2.736	1.855	*f*
1.746	2.983	1.859	*e*
1.761	3.000	1.855	*d*
2.338	3.894	1.859	*d*
2.905	4.730	1.861	*e*
3.063	4.954	1.860	*d*
3.182	5.122	1.860	*d*
3.774	5.977	1.869	*d*
3.849	6.069	1.866	*d*
3.862	6.097	1.869	*f*
4.396	6.814	1.868	*e*
4.418	6.843	1.868	*d*
5.011	7.613	1.866	*d*
5.766	8.581	1.865	*d*
6.439	9.431	1.864	*d*
7.047	10.162	1.857	*f*
7.167	10.308	1.861	*d*
7.523	10.775	1.857	*e*
8.053	11.375	1.847	*f*

[a] m = moles of urea/kg of water. [b] ΔT is the freezing-point depression. [c] $x = \Delta T/m + 0.09488m - 0.005117m^2$. [d] Mercury thermometer; Mallinckrodt ACS grade urea. [e] Platinum resistance thermometer; recrystallized urea. [f] Platinum resistance thermometer; Mallinckrodt ACS grade urea.

tions. With the sole exception of their eutectic point results, the data of Chadwell and Politi[10] disagree with both ours and those of Cavallero and Indelli.[7] It is difficult at this distance in time to seek an explanation of the discrepancy; we are, however, satisfied that our results are more correct. As a check on the performance of our apparatus, we made a measurement on potassium chloride, obtaining $m = 0.9759$, $\Delta T = 3.189°$. From Scatchard's[13] very precise measurements on potassium chloride, the value of ΔT for this molality is 3.186°. From the internal consistency of our results we believe that osmotic coefficients derived from them should be reliable to ±0.001. Table II gives osmotic coefficients at round molalities, calculated from the equations[14]

$$\phi = -\frac{55.51}{m} \ln aw \qquad (3)$$

$$-\log aw = 0.004207\Delta T + 2.1 \times 10^{-6}\Delta T^2 \qquad (4)$$

These osmotic coefficients refer to solutions at their respective freezing points. Conversion to 0° or to 25° presents some difficulty in spite of the fact that thermal data are available down to 2°. Gucker and Pickard[8] give equations for the relative apparent molar enthalpy of aqueous urea at temperatures from 2 to 40°, based on their measurements of heats of dilution (Φ_{L_2}) at 25° and the heat capacity measurements of Gucker and Ayres.[15]

While the equation for 25° reproduces their heat of dilution measurements very well, we find that the equation for the relative partial molar heat capacity of the solute, obtained by differentiation of their expressions for Φ_{L_2} with respect to temperature, is

Table II: Freezing Points and Osmotic Coefficients at the Freezing Point for Aqueous Urea Solutions at Round Molalities

m	Fp, °C	ϕ_{Fp}	m	Fp, °C	ϕ_{Fp}
0.5	−0.9035	0.972	4.5	−6.951	0.8335
1.0	−1.760	0.947	5.0	−7.605	0.821
1.5	−2.583	0.927	5.5	−8.247	0.810
2.0	−3.375	0.909	6.0	−8.882	0.800
2.5	−4.137	0.892	6.5	−9.510	0.790
3.0	−4.871	0.875	7.0	−10.126	0.782
3.5	−5.588	0.861	7.5	−10.742	0.774
4.0	−6.282	0.847	8.0	−11.332	0.766

(13) G. Scatchard and S. S. Prentiss, *J. Am. Chem. Soc.*, **55**, 4355 (1933).

(14) R. A. Robinson and R. H. Stokes, "Electrolyte Solutions," 2nd ed, Butterworth and Co. Ltd., London, 1959, Chapter 8.

(15) F. T. Gucker, Jr., and F. D. Ayres, *J. Am. Chem. Soc.*, **59**, 2152 (1937).

less satisfactory in reproducing the heat capacity data, especially at low temperatures and high concentrations. In the extreme case, at 2° and 8 m, the equation gives $\Delta\Phi_{Cp_2} = 6.9$ cal mole^{-1} deg^{-1} in contrast with the experimental value of 12.2 cal mole^{-1} deg^{-1}. Furthermore, the equations yield values which with increasing molality reach a maximum and turn down again, in contrast to the monotone rise of the experimental values. Since the quantity required in converting the osmotic coefficient from 25° to other temperatures involves the *slope* of the curve of Φ_{L_2} *vs.* m, the use of these equations is clearly not acceptable at high concentrations. Any extrapolation below the lowest experimental temperature of the heat capacity data is even less desirable. Accordingly, we have preferred to compare the 25° isopiestic data with our freezing-point values in the following way.

The temperature dependence of the osmotic coefficient ϕ is given by

$$RT^2\frac{d\phi_{(T)}}{dT} = \frac{55.51\bar{L}_{1(T)}}{m} \quad (5)$$

where $\bar{L}_{1(T)}$, the relative partial molar enthalpy of the solvent in the solution at temperature T, is given by

$$\bar{L}_{1(T)} = \bar{L}_{1(298°)} + \int_{298°}^{T} (\bar{C}p_1 - \bar{C}p_1^0)dT \quad (6)$$

Using standard thermodynamic relations (6) transforms to

$$\bar{L}_{1(T)} = -\frac{m}{55.51}\left[\left(\frac{\partial\Phi_{L_2}}{\partial \ln m}\right)_{298°} + \int_{298°}^{T}\left(\frac{\partial\Phi_{Cp_2}}{\partial \ln m}\right)_T dT\right] \quad (7)$$

and hence (5) in terms of experimentally available thermal quantities becomes

$$RT^2\frac{d\phi}{dT} = -\left(\frac{\partial\Phi_{L_2}}{\partial \ln m}\right)_{298°} - \int_{298°}^{T}\left(\frac{\partial\Phi_{Cp_2}}{\partial \ln m}\right)_T dT \quad (8)$$

The first term on the right of (8) is evaluated from the equation of Gucker and Pickard,[8] which fits these data very well. The second we have evaluated by graphical differentiation. Normally, this method is not as good as analytical procedures, but in this case it happens that at high concentrations Φ_{Cp_2} becomes almost linear in ln m, so that the slope is readily determined. As a check, the slopes were also determined from graphs of Φ_{Cp_2} *vs.* m followed by multiplication by m, with good agreement with the first method. The integration in (8) was then made by graphical–tabular methods. Finally, eq 5 was integrated similarly to give $\phi_{(T)}$ in terms of $\phi_{298°}$. The recent extremely careful isopiestic vapor pressure measurements of Ellerton[16] were used as the source of the $\phi_{298°}$ values. By this method we have calculated $\phi_{(T)}$ for temperatures down to 2°, the lowest temperature at which the thermal data are available. The variation of Φ_{Cp_2} with temperature becomes increasingly rapid as the temperature is lowered, so that no great reliance can be placed on even short extrapolations. Hence, rather than attempt to guess values of Φ_{Cp_2} below 2° and thus estimate corrections to ϕ from the freezing points to 25°, we prefer to present the data as the temperature dependence of the osmotic coefficient (Figure 2). The lines extending below 2° in the figure seem to us to be reasonable extrapolations from the 25–2° data, and agree quite satisfactorily with the freezing-point data. There are possibly discrepancies of up to 0.003 in the osmotic coefficient at 2, 3, and 4 M. It is clear however, that there is no serious inconsistency between our freezing-point results, the 25° isopiestic data, and the thermal measurements. It must be concluded that the freezing-point data of Chadwell and Politi[10] were erroneous. Some of the discrepancy found by earlier investigators in the region above 4 M also seems to have arisen from the unsatisfactory fit of the equations of ref 8 to the heat capacity data of ref 4.

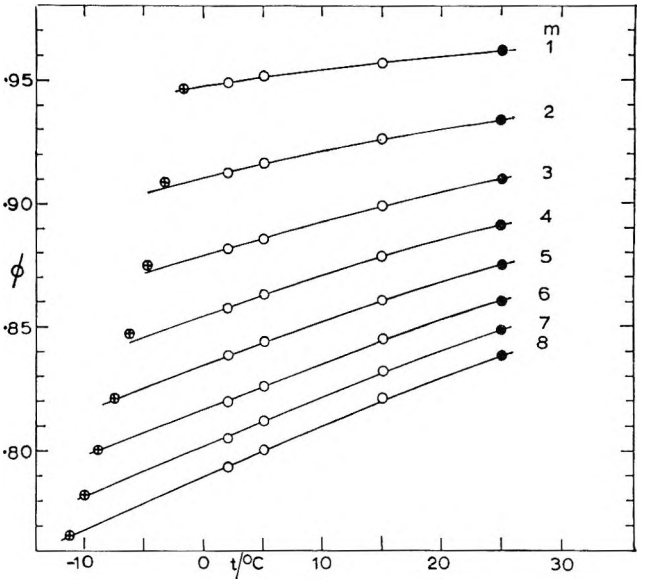

Figure 2. Osmotic coefficients of urea at various temperatures: ●, 25° isopiestic values; O, calculated from 25° isopiestic data and thermal properties of solutions as in text; ⊕, freezing-point data from Table II.

Acdnowledgment. The author is indebted to the University of Wisconsin for its hospitality, and to the

(16) H. J. Ellerton and P. J. Dunlop, to be published (private communication from P. J. Dunlop); see also ref 9.

U. S. National Science Foundation for the award of a Senior Foreign Scientist Fellowship during the tenure of which this work was done. This work was supported in part by Public Health Service Research Grant No. AM-05177 from the National Institute of Arthritis and Metabolic Diseases. Thanks are also due to Dr. R. A. Robinson of the National Bureau of Standards for the loan of a calibrated thermometer, and to Mrs. J. M. Stokes for extensive assistance with the experimental work.

Nuclear Magnetic Resonance Study of Molecular Complexes of Dimethylformamide with Aromatic Donors[1]

by Antonio A. Sandoval[2]

Department of Chemistry, University of Missouri at Kansas City, Kansas City, Missouri 64110

and Melvin W. Hanna[3]

Department of Chemistry, University of Colorado, Boulder, Colorado 80304 *(Received October 21, 1965)*

The complexes of dimethylformamide (DMF) with benzene, toluene, *p*-xylene, mesitylene, and durene have been studied by nmr spectroscopy. Equilibrium quotients for association and the chemical shifts of the two methyl groups in DMF in the pure complex have been determined. Contrary to an earlier suggestion, the complexes become stronger as the number of methyl substituents on the donor increases. The upfield shifts of the methyl protons in DMF in the pure complex become smaller, however, as the number of methyl groups on the donor is increased. This effect is very likely a measure of the decreased ring currents in the donor molecules as they become more substituted.

Introduction

It is now well established that, in certain cases, nmr spectroscopy can be used to study molecular complex equilibria.[4] The nmr method is especially valuable when it is applicable because it can give specific information about the geometry of the complex in solution.[5-7] Hatton and Richards, in studying solvent effects on the shifts of the two methyl proton resonances in dimethylformamide (DMF), have concluded that the DMF molecule must lie above the plane of the benzene ring with one methyl group approximately above the six-field axis of the benzene ring and the other methyl group off to one side.[5] Their postulated structure for the complex is

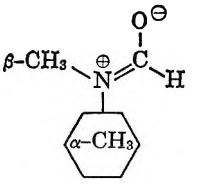

(1) Supported in part by the Directorate of Chemical Sciences, Air Force Office of Scientific Research, under Grant AF-AFOSR-216-65.

(2) NSF Summer Research Institute Participant.

(3) Alfred P. Sloan Fellow.

(4) M. W. Hanna and A. L. Ashbaugh, *J. Phys. Chem.*, **68**, 811 (1964).

(5) J. V. Hatton and R. E. Richards, *Mol. Phys.*, **5**, 139, 153 (1962).

(6) J. V. Hatton and W. G. Schneider, *Can. J. Chem.*, **40**, 1285 (1962).

In Hatton and Richards' work, the upfield shifts of the methyl groups in DMF were measured as DMF was diluted with aromatic hydrocarbon, and these shifts were extrapolated to infinite dilution. In analyzing these shifts it was pointed out that as the number of methyl groups on the aromatic hydrocarbon increased, the infinite dilution upfield shift decreased. This effect was rationalized by postulating that because of steric hindrance the complexes became weaker as the number of methyl groups on the donor increased. This would mean that the DMF molecule would lie farther away from the benzene ring and, consequently, would be less affected by the aromatic ring currents.

There are several reasons for investigating this hypothesis. First, if the aromatic hydrocarbon–DMF complexes are of the donor–acceptor type with the DMF molecule the acceptor, the strength of the complex would be expected to increase with methyl substitution on the donor.[8] Second, the nmr shift at infinite dilution of a species that is rapidly exchanging between the complexed and uncomplexed state is a function of the corresponding shift in the pure complex and of the equilibrium quotient[9] for association.[10] Thus, the shift at infinite dilution may decrease in a series of complexes either because the equilibrium quotient is decreasing or because the shift in the pure complex is decreasing. Third, in a study of complexes between TCNQ and methyl-substituted benzenes in these laboratories, it was found that the upfield shift of the protons on the acceptor (TCNQ) also decreased, but in this case the complexes were becoming stronger as the number of methyl groups increased.[4]

In the case of the TCNQ complexes it was postulated that a combination of the upfield shift due to the aromatic ring currents of the donor and a downfield shift due to an increasing paramagnetic shift might be responsible for this behavior.[4] It is also possible to explain these results by assuming that the ring currents on the aromatic donor *decrease* as the number of methyl groups increases. Martin has made this assumption plausible by showing that the aromatic ring currents must decrease whenever a substituent is introduced into the benzene ring.[11]

The purpose of the present research was to determine whether or not the equilibrium quotients (and presumably the strengths) of the complexes between DMF and methyl-substituted benzenes increase or decrease as the number of methyl substituents is increased. Furthermore, it was anticipated that information about the effect of substituents on the aromatic ring currents could be evaluated by studying the relative shifts of the α and β methyl groups in the pure complex.

Experimental Section

Materials. All chemicals used in this study were reagent grade (Eastman). Gas chromatographic analysis indicated no detectable impurities in these materials. All liquids were thoroughly dried over calcium hydride and in most cases distilled before use. Durene was sublimed.

Procedure. The appropriate amounts of donor were weighed into 10-ml glass-stoppered volumetric flasks. A 5-ml aliquot of a standard (0.06 *M*) solution of DMF in cyclohexane was added to each flask. These solutions were then made up to volume by the addition of cyclohexane. The density of each solution was measured with an accurately calibrated pycnometer. A series of 7–10 solutions was made for each aromatic compound studied.

Nuclear magnetic resonance spectra were taken on a Varian A-60 spectrometer. The cyclohexane resonance was used as an internal reference. Chemical shifts were measured by displaying the signal of interest and a modulation side band of the cyclohexane on the carefully calibrated 50-cps sweep of the A-60. A Hewlett–Packard Model 202-A low-frequency function generator and a Model 521-c electronic counter were used for the modulation source and frequency counter. Chemical shifts were reproducible to better than 0.3 cps, the uncertainty being determined by the line width. All measurements were made at 37.5 ± 0.5°, the temperature of the probe.

Results and Discussion

The nmr spectrum of DMF exhibits three absorptions with relative intensities of 1:3:3. The pair of strong lines appearing at τ 7.003 and 7.177 in the neat liquid arise from the absorption of the two methyl groups. These two methyl lines are distinguishable by their coupling constants with the formyl proton. The resonance line due to the methyl group which is

(7) W. G. Schneider, *J. Phys. Chem.*, **66**, 2653 (1962).

(8) See, for example, G. Briegleb, "Electronen-Donator-Acceptor-Komplexe," Springer-Verlag, Berlin, 1961, Chapter IX.

(9) The term equilibrium quotient Q represents the quotient of concentrations of products and reactants. The equilibrium constant K is equal to the product of Q and the appropriate quotient of activity coefficients $\gamma_{AD}/\gamma_A\gamma_D$. Equilibrium quotient is the more accurate term if activity coefficients are not evaluated or known, and will be used in the rest of this paper.

(10) See, for example, P. J. Berkeley, Jr., and M. W. Hanna, *J. Phys. Chem.*, **67**, 846 (1963).

(11) J. S. Martin, *J. Chem. Phys.*, **39**, 1728 (1963). This argument is based on a one-electron theory of molecular electronic structure. Martin showed that any magnetic resonance property depending on polarizabilities must be an even function of any perturbation. Thus the aromatic ring currents should decrease whether the substituent is electronegative or electropositive. R. McWeeny [*Mol. Phys.*, **1**, 811 (1958)] has shown that the aromatic ring currents are determined by the polarizabilities in the one-electron theory.

Table I: Equilibrium Quotients and Δ_{AD} Values for DMF Aromatic Complexes

Donor	Range of donor concentration, m, moles/kg	Max. Δ^{α}_{obsd}, cps	Max. Δ^{β}_{obsd}, cps	Δ^{α}_{AD}, cps	Δ^{β}_{AD}, cps	$\Delta^{\alpha}_{obsd}/\Delta^{\beta}_{obsd}$	Q^{α},[a] kg/mole	Q^{β},[b] kg/mole
Benzene	2.08–12.02	30.5	13.6	53 ± 3	20 ± 4	2.19 ± 0.05	0.126 ± 0.008	0.130 ± 0.006
Toluene	1.177–10.34	27.8	13.5	50 ± 3	20 ± 2	1.99 ± 0.06	0.136 ± 0.004	0.140 ± 0.006
p-Xylene	2.336–19.01	26.0	15.26	39.5 ± 0.5	19 ± 1	1.97 ± 0.03	0.202 ± 0.005	0.20 ± 0.01
Mesitylene	0.543–8.576	25.7	13.0	38 ± 4	19 ± 2	1.93 ± 0.01	0.21 ± 0.03	0.21 ± 0.06
Durene	1.919–3.771	18.6	10.6	34 ± 5	24 ± 7	1.75 ± 0.03	0.28 ± 0.06	0.28 ± 0.06

[a] The equilibrium quotient obtained from a plot of the data for the α methyl resonance [b] The equilibrium quotient obtained from a plot of the data for the β-methyl resonance calculated using the assumptions discussed in the text. In the ideal case Q^{α} should equal Q^{β}.

cis to the formyl proton appears downfield in the spectrum and is designated as the α-line. The resonance line due to the methyl group that is *trans* to the formyl proton appears upfield and is designated as the β line. When DMF is diluted with inert solvents such as cyclohexane, the α line experiences an upfield shift, whereas the β line experiences a downfield shift of equal magnitude. With cyclohexane as solvent, the doublet separation of the two lines has decreased to 2.60 cps at a concentration of 0.03 M.

When DMF is diluted with aromatic solvents, both the α and β lines experience an upfield shift. The shift of the α line is larger than the shift of the β line, however. At a certain concentration, the two lines coalesce and beyond this concentration the α line is found upfield.

It has previously been shown that nmr can be used to evaluate both the equilibrium quotient and the shift of the pure complex in systems in which a 1:1 complex is formed.[4] The appropriate equation for doing this is

$$\frac{1}{\Delta^{x}_{obsd}} = \frac{1}{\Delta^{x}_{AD}}\left(\frac{1}{Qm_D} + 1\right) \qquad (1)$$

where $\Delta^{x}_{obsd} = \delta^{x}_{obsd} - \delta^{x}_{0}$, δ^{x}_{obsd} is the observed shift of a particular resonance in acceptor–donor solutions, δ^{x}_{0} is the observed shift of the same line in a reference solution of acceptor, Δ^{x}_{AD} is the shift of the pure complex, Q is the equilibrium quotient for the reaction, acceptor + donor $\rightleftarrows$ complex, m_D is the molal concentration of donor, and $x = \alpha, \beta$.

This equation is valid provided that $m_D >> m_A$ and that the solutions are ideal or the ratio of activity coefficients $\gamma_{AD}/\gamma_A\gamma_D$ remains constant over the concentration range of the solutions studied.[12]

In this study, the relative shifts of the α and β methyl groups in DMF–aromatic solutions were evaluated using a 0.03 M solution of DMF in cyclohexane as the reference. The plots of $1/\Delta^{\alpha}_{obsd}$ and $1/\Delta^{\beta}_{obsd}$ *vs.* $1/m_D$ gave straight lines. The measured and calculated properties for these systems are summarized in Table I.

Equilibrium quotients, Q^{α} and Q^{β} were calculated from data for both the α and β methyl resonances. Due to the smallness of the observed shifts compared with the line width, the values of Q^{β} are considerably less precise than the values of Q^{α}. This lack of precision comes about because of the uncertainty in locating the intercept of a plot of the β methyl data. If the intercept for the β methyl data is taken so that the ratio of the intercepts $\Delta^{\alpha}_{AD}/\Delta^{\beta}_{AD}$ is the same as the average of the ratio of the experimental points, good agreement is obtained between Q_{α} and Q_{β}. This procedure is justified by the fact that the ratio $\Delta^{\alpha}_{obsd}/\Delta^{\beta}_{obsd}$ remains constant over the range of concentration used.

The important thing to notice about the values of Q is that they increase as the number of methyl substituents on the aromatic donor increases. Since there is little reason to believe that the entropy of formation of these complexes should be appreciably altered by increased methyl substitution, the increase in the values of Q implies an *increase* in the strength of the complex as the number of methyl substituents is increased. The postulate of Hatton and Richards that the DMF–aromatic donors become weaker as the number of methyl groups on the donor increase is, therefore, incorrect.

The chemical shift data in Table I show several important features. (1) The upfield shift of the α methyl protons in the pure complex becomes smaller as the complex becomes stronger. This is a similar result to that found for the TCNQ–aromatic complexes[4] and may be a general phenomenon characteristic of this series of donors. (2) The upfield shifts of the β methyl

(12) Equation 1 will often give a straight line plot even if these conditions are not met. A complete discussion of this point is given in P. J. Trotter and M. W. Hanna, *J. Phys. Chem.*, in press.

protons in the pure complex remain constant within experimental error. This means that whatever is responsible for the change in the α methyl proton shifts is not affecting the β protons. (3) The ratios $\Delta^{\alpha}_{obsd}/\Delta^{\beta}_{obsd}$ decrease as the number of methyl substituents on the donor increases.

These results seem to indicate that the chemical shift in the pure complex of the two methyl groups in DMF is made up of two contributions— an upfield contribution to the shift of both methyl groups which is independent of donor and an additional upfield contribution to the shift of the α methyl group which *decreases* as the number of methyl substituents increases. The constant contribution may be a reaction field or other intermolecular association effect.[13] There are several possible explanations for the decreasing upfield shift of the α methyl protons. One is that the aromatic ring currents decrease with increasing methyl substitution. This would be in accord with the theoretical predictions of Martin,[11] but is in disagreement with the magnetic susceptibility data recently tabulated by Bothner-By and Pople.[14] From crystal susceptibility data, the magnetic anisotropy of durene is more negative than that of benzene. If the magnetic anisotropy were due exclusively to the ring current effect, the crystal susceptibility data would indicate that the ring currents should increase in going from benzene to durene. It is also possible that molecular shape effects or changing electric fields with methyl substitution may account for the decreasing upfield shift.

To decide finally between the importance of various contributions to the shielding in complexes of this type, it will be necessary to have considerably more experimental and theoretical study of interactions between aromatic and dipolar or polarizable molecules.

(13) W. T. Raynes, A. D. Buckingham, and H. J. Bernstein, *J. Chem. Phys.*, **36**, 3481 (1962); L. Petrakis and H. J. Bernstein, *ibid.*, **37**, 2731 (1962).

(14) A. A. Bothner-By and J. A. Pople, *Ann. Rev. Phys. Chem.*, **16**, 43 (1965).

Kinetic and Thermodynamic Aspects of the Electrosorption of Benzene on Platinum Electrodes

by W. Heiland, E. Gileadi, and J. O'M. Bockris

The Electrochemistry Laboratory, The University of Pennsylvania, Philadelphia, Pennsylvania 19104
(Received October 27, 1965)

The electrosorption of benzene on platinum-plated gold electrodes from solutions of 1 *N* H_2SO_4 and H_3PO_4 has been studied by a radiotracer method. The adsorption follows a Frumkin-type isotherm with an interaction parameter r = 2–4 kcal/mole in the case of H_2SO_4 and 5 kcal/mole in the case of H_3PO_4. The benzene molecule is chemisorbed on the surface with probable loss of aromatic character. An average of nine water molecules is replaced by each adsorbed benzene molecule. The net heat of electrosorption is positive, $\Delta H \doteqdot 10$ kcal/mole. The net entropy of electrosorption is also positive, $\Delta S \doteqdot 50$ eu. The rate of adsorption is controlled by mass transfer to the electrode at low coverage. At intermediate coverage similar behavior is observed if adsorption equilibrium is only slightly disturbed. The adsorption peak and the whole θ *vs.* V curve shifts to more negative potential with increasing pH. This shift is associated with a shift of the potential of zero charge (pzc) of Pt with pH in the same direction.

Introduction

The growing interest in the kinetics of electrode reactions at solid electrodes and in the theory of electrocatalysis[1,2] requires a detailed understanding of adsorption at the electrode–electrolyte interface. Numerous studies of adsorption of neutral organic molecules on mercury have been reported[3] but methods for the study of electrosorption of neutral molecules on solid electrodes have only recently been developed.[4–7] A great deal of information can be obtained from gas phase adsorption studies,[8,9] in particular with respect to the nature of the surface and the type of bonding between the adsorbate and the surface atoms. It must be borne in mind, however, that electrosorption differs from gas phase adsorption in many important ways, as has been discussed recently elsewhere.[10]

Two radiotracer methods have been developed[4,7] and used[5,11–15] by Bockris and co-workers in recent years for the study of electrosorption of neutral molecules on solid electrodes. In a previous paper[15] a study of the electrosorption of ethylene on Pt electrodes from 1 *N* sulfuric acid solutions has been reported. Here, thermodynamic and kinetic phenomena related to the electrosorption of benzene on Pt from 1 *N* H_2SO_4, 1 *N* H_3PO_4, and mixtures of NaOH and Na_2SO_4 and of H_2SO_4 and Na_2SO_4 of constant SO_4^{2-} concentration and varying pH will be presented.

(1) J. O'M. Bockris and H. Wroblowa, *J. Electroanal. Chem.*, 7, 428 (1964).

(2) J. O'M. Bockris and S. Srinivasan, *Advan. Catalysis*, in press.

(3) A. N. Frumkin and B. B. Damaskin, "Modern Aspects of Electrochemistry," Vol. III, J. O'M. Bockris and B. E. Conway, Ed., Butterworth and Co. (Publishers) Ltd., London, 1964, Chapter 3.

(4) E. Blomgren and J. O'M. Bockris, *Nature*, 186, 305 (1960).

(5) H. Dahms, M. Green, and J. Weber, *ibid.*, 196, 1310 (1962).

(6) B. E. Conway, R. G. Barradas, and T. Zavidzky, *J. Phys. Chem.*, 62, 676 (1958).

(7) M. Green, D. A. J. Swinkels, and J. O'M. Bockris, *Rev. Sci. Instr.*, 33, 18 (1962).

(8) D. O. Hayward and B. M. T. Trapnell, "Chemisorption," Butterworth and Co. (Publishers) Ltd., London, 1964.

(9) G. C. Bond, "Catalysis by Metals," Academic Press Inc., New York, N. Y., 1962.

(10) E. Gileadi, *J. Electroanal. Chem.*, 11, 137 (1966).

(11) H. Wroblowa and M. Green, *Electrochim. Acta*, 8, 979 (1963).

(12) H. Dahsm and M. Green, *J. Electrochem. Soc.*, 110, 1075 (1963).

(13) J. O'M. Bockris and D. A. J. Swinkels, *ibid.*, 111, 736 (1964).

(14) J. O'M. Bockris, D. A. J. Swinkels, and M. Green, *ibid.*, 111, 743 (1964).

(15) E. Gileadi, B. T. Rubin, and J. O'M. Bockris, *J. Phys. Chem.*, 69, 3335 (1965).

Experimental Section

The Pt electrode consisted of a thin gold foil (2×10^4 A), electroplated with platinum from a chloroplatinic acid solution. The thickness of the Pt coating was approximately 2×10^3 A, and the resulting electrode had a roughness factor ranging from 50 to 100. The electrode was fixed over the window of an end-window proportional counter and placed in contact with the solution in the cell. The radiation entering into the counter through the electrode from C^{14}-labeled benzene molecules in solution was measured, and the surface concentration of benzene was calculated from the net count rate, by means of a calibration procedure as discussed elsewhere.[11] Details of electrode preparation, the cell, and the working procedure have been described in a recent publication.[15] A stock solution of radiolabeled benzene was prepared by dissolving approximately 1.5 mmoles of benzene (specific activity 1.7 mcuries/mmole) in 250 ml of water. Small amounts of this solution ranging from 0.05 to 10 ml were introduced into the cell. The final concentration in the cell was determined by withdrawing small samples of the solution after equilibrium adsorption had been reached, and measuring the benzene concentration in a liquid scintillation counter.

Results

1. Isotherms. Isotherms for electrosorption of benzene on Pt electrodes from 1 *N* H_2SO_4 and 1 *N* H_3PO_4 at three temperatures and at a potential of 0.5 v *vs.* nhe are shown in Figures 1 and 2, respectively. Partial coverage values, θ_{exptl}, were calculated assuming a maximum surface coverage of $\Gamma_m = 2.5 \times 10^{-10}$ mole/cm² of real surface area. This assumes that each benzene molecule on the surface occupies nine sites (*cf.* Discussion, section 2). The real surface area of the electrode was calculated from double-layer capacity measurements, as discussed previously.[15] Saturation behavior was observed only at the highest temperature (70°). The maximum coverage measured was essentially the same in both electrolytes ($\theta_{exptl,\,max} = 0.48$ in H_2SO_4 and $\theta_{exptl,\,max} = 0.52$ in H_3PO_4). For reasons to be discussed below, all coverage data have been normalized so that $\theta_{max} = 1.00$ in each electrolyte solution. All partial coverage data except Figures 1 and 2 are calculated on this basis.

2. Variation of Coverage with Potential. The isothermal variation of partial surface coverage θ with electrode potential is shown in Figures 3 and 4 for 1 *N* sulfuric and phosphoric acids, respectively. Measurements were made at 50° for three concentrations in each system. It is hard to determine accurately the potential of maximum adsorption owing to the relatively flat shape of the θ *vs.* *V* curve. Maximum adsorption occurs in the region of 0.4–0.5 v *vs.* nhe in

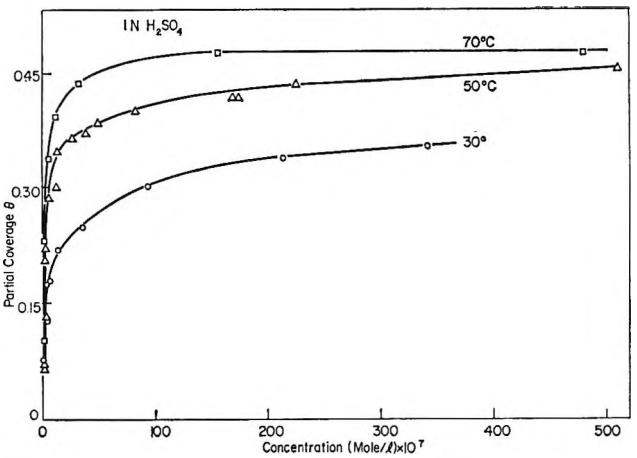

Figure 1. Adsorption isotherms at three temperatures in 1 *N* H_2SO_4; *V* = 0.5 v *vs.* nhe.

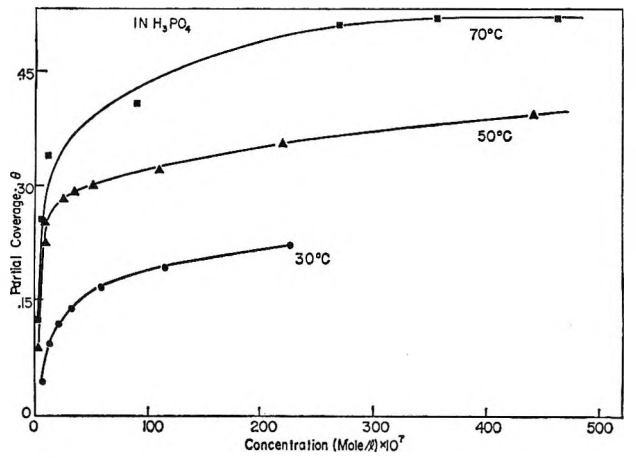

Figure 2. Adsorption isotherms at three temperatures in 1 *N* H_3PO_4; *V* = 0.5 v *vs.* nhe.

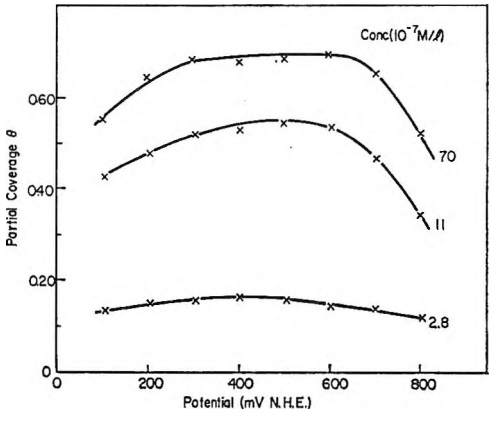

Figure 3. Coverage–potential relationship in 1 *N* H_2SO_4 at 50°.

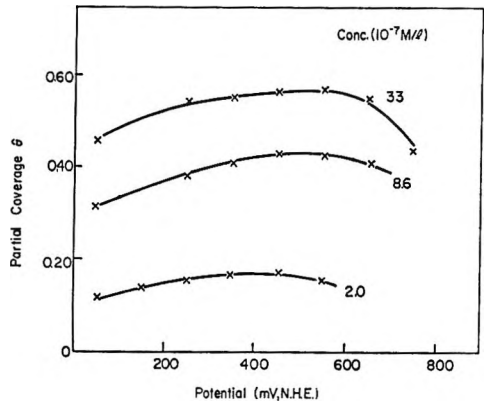

Figure 4. Coverage–potential relationship in 1 N H_3PO_4.

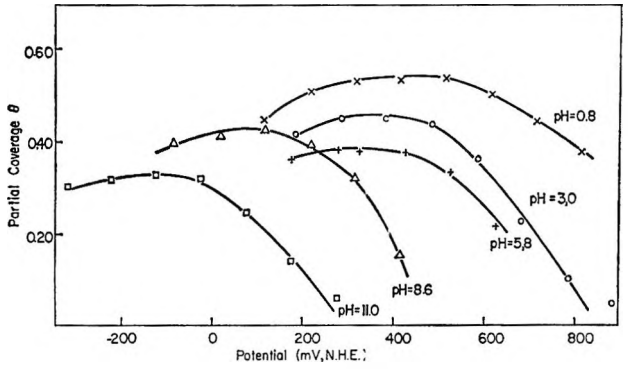

Figure 5. Coverage–potential plots as a function of pH at constant sulfate ion concentration. Potentials on the normal hydrogen scale.

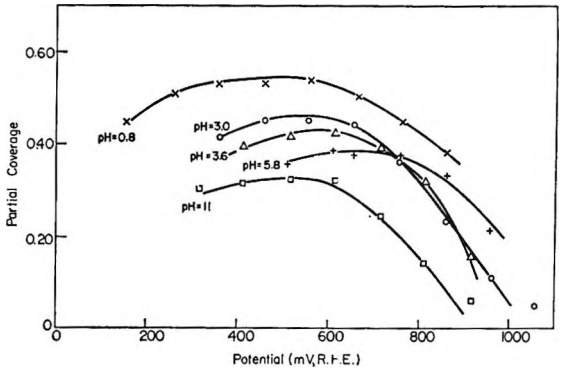

Figure 6. Coverage–potential plots as a function of pH at constant sulfate ion concentration plotted on the reversible hydrogen scale.

these systems. Normally the potential was changed from the most cathodic value (0.1 *vs.* nhe) to more positive potentials. When the direction of change of potential was reversed, a certain degree of hysteresis was observed in the θ *vs.* V plot above 0.6 *vs.* nhe.

3. Effect of pH on Adsorption. Electrosorption of benzene from mixtures of H_2SO_4 + Na_2SO_4 and NaOH + Na_2SO_4 covering the pH range 0.8–11 was studied. The variation of partial coverage with potential at various pH values is shown in Figure 5, plotted on the normal hydrogen scale, and in Figure 6, plotted on the reversible hydrogen scale. The curves are shifted to higher anodic potential, on the normal hydrogen scale, with decreasing pH, but are little affected by pH when plotted on the reversible hydrogen scale.

4. Kinetics of Adsorption. The kinetics of adsorption of benzene is represented in Figures 7–11 as plots of the net count rate (which is proportional to the

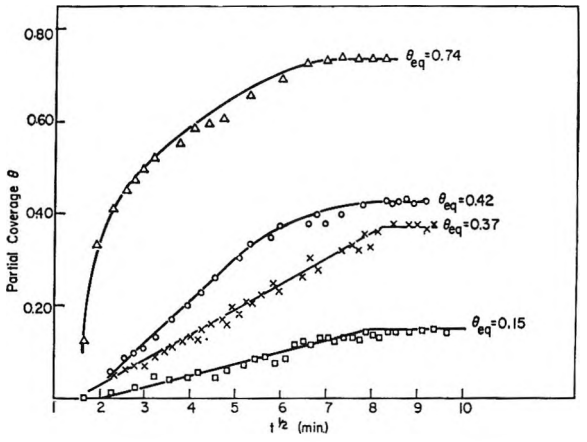

Figure 7. The rate of adsorption in 1 N H_2SO_4, 30°, at V = 0.1 v *vs.* nhe plotted as θ_t *vs.* $t^{1/2}$. Effect of introducing various amounts of benzene. The equilibrium coverage θ_{equil} at each concentration is shown.

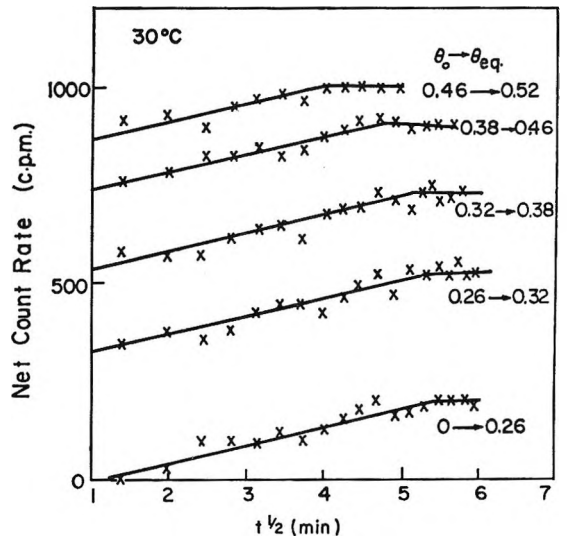

Figure 8. The rate of adsorption in 1 N H_2SO_4, 30°, at V = 0.5 v *vs.* nhe plotted as θ_t *vs.* $t^{1/2}$. Effect of incremental increase in concentration. The initial and final coverage (θ_0 and θ_{equil}) are shown for each experiment.

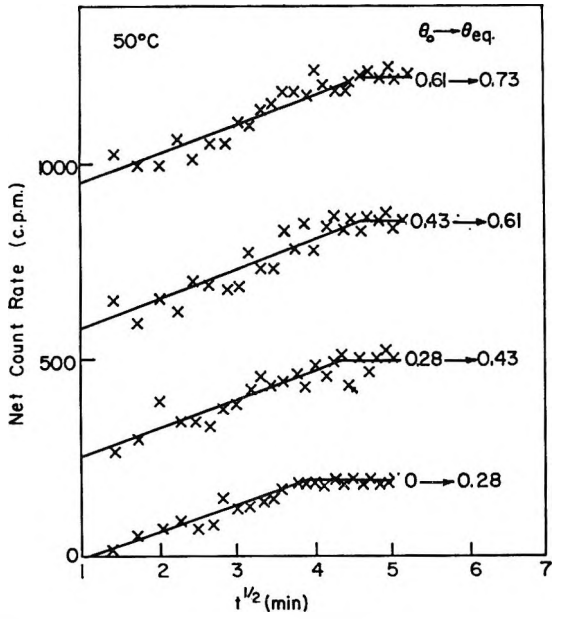

Figure 9. The rate of adsorption as shown in Figure 8 but at 50°.

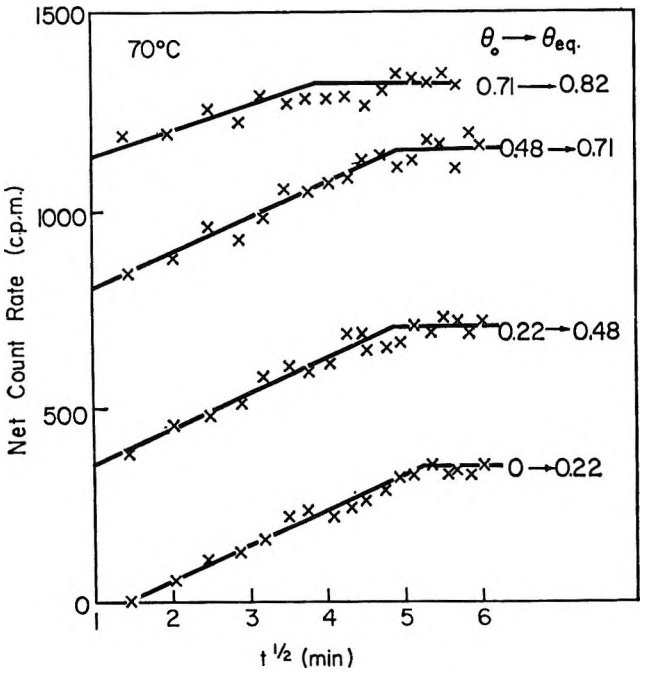

Figure 10. The rate of adsorption as shown in Figure 8 but at 70°.

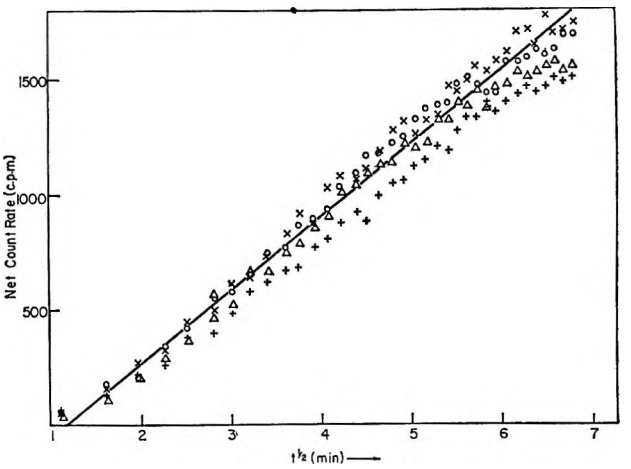

Figure 11. Effect of pH on the rate of adsorption. All measurements at 30°: +, V = 0.16 v at pH = 0.8; △, V = 0.36 v at pH 3.0; ×, V = 0.42 v at pH 8.6; and ○, V = 0.32 v at pH = 11 (all potentials on the reversible hydrogen scale).

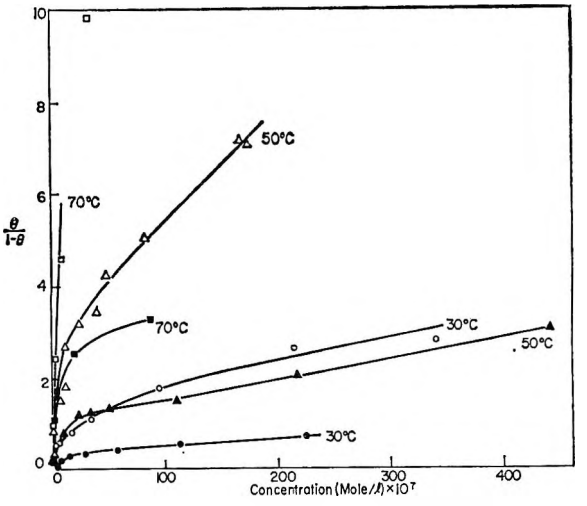

Figure 12. Plots of $\theta/(1-\theta)$ *vs.* concentration at three temperatures for H_2SO_4 and H_3PO_4.

partial surface coverage) *vs.* the square root of time. Figure 7 shows the effect of introducing various amounts of benzene into the solution which is initially free of benzene at a potential of 0.1 v *vs.* nhe. Figures 8–10 show the effect of temperature and of incremental increase in the concentration of benzene in solution at 0.5 v *vs.* nhe. In Figure 11 kinetic data obtained at various pH values are plotted. Below the potential at which oxygen adsorption has an effect, the variation of θ with time is essentially independent of potential.

Discussion

1. Nature of the Adsorption Isotherm. a. Saturation Coverage. The values of maximum coverage shown in Figures 1 and 2 of $\theta_{\text{exptl, max}} \doteq 0.5$ are in qualitative agreement with previously reported results for ethylene.[15] The possible causes for $\theta_{\text{exptl,max}}$ values substantially less than unity have been discussed recently.[15] The uncertainty in determination of real surface areas, the existence of crevices on the surface incapable of

accommodating a large organic molecule, and the occurrence of sites with a high energy of activation for adsorption or a low heat of adsorption have been suggested as the cause for lower θ_{max} values.

It is also possible that each benzene molecule adsorbed on the surface is surrounded by a ring of water molecules which act to some extent as a hydration shell in two dimensions. An interaction between benzene and water molecules may be expected in view of the well-known ability of water to form azeotropic mixtures with benzene. This model would give rise to $\theta_{max} = 1$ and would also be consistent with the mechanism observed for the anodic oxidation of benzene.[16]

For thermodynamic considerations, the value of θ_{max} should be taken as unity as long as a true saturation behavior is observed experimentally. This is shown to be the case for benzene from both sulfuric and phosphoric acids at 70° (Figures 1 and 2). A specific test for saturation was achieved by adding labeled benzene solution to the cell which had already contained 3×10^{-5} mole/l. of benzene at 70°. The count rate became constant after only 2 min. This time delay corresponds to mixing of the newly added benzene in the solution and a resulting increase in the solution background. The net count rate (*i.e.*, that owing to species adsorbed on the surface) did not change during this process. If further adsorption had taken place, the count rate would have increased slowly for about 10–15 min until a new equilibrium would have been established.

Further support for the normalization of θ values (based on the assumption of $\theta_{max} = 1.00$ in each solvent) is derived from a consideration of the adsorption isotherms (*cf.* section 1c below). Thus the θ *vs.* log c relationship is found to be linear for intermediate values of θ in agreement with the Temkin isotherm[17] only if the normalized values of θ are used.

Independent measurement of the kinetics of anodic oxidation of benzene and other unsaturated hydrocarbons on Pt electrodes[16,18] are consistent only with a high value for θ approaching unity.

b. Equilibrium Constant and Standard Free Energy. A plot of $\theta/(1 - \theta)$ *vs.* concentration is shown in Figure 12 for three temperatures and the two solutions studied. Unlike the behavior of ethylene[15] no linear relationships are observed, and the simple Langmuir isotherm is clearly not obeyed. At low concentration and coverage all isotherms reduce to that of Langmuir which may, therefore, be used as a good approximation as shown in Figure 13. The equilibrium constant for adsorption may thus be calculated. The results are given in Table I, together with the values of the

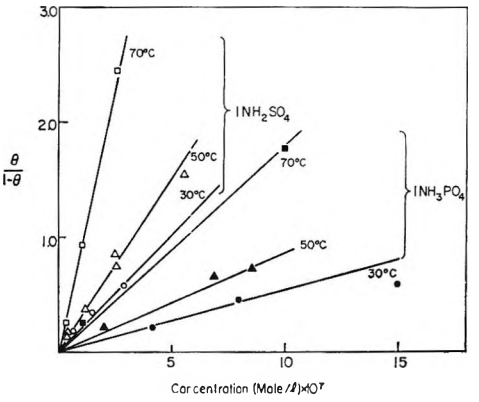

Figure 13. Plots of $\theta/(1 - \theta)$ *vs.* concentration at three temperatures for H_2SO_4 and H_3PO_4 in the low concentration range.

standard free energy of adsorption calculated for a standard state of $\theta = 0.5$ and $c = c_s$ where c_s is the concentration of benzene in a saturated solution. The standard state of $c = c_s$ is chosen here. In this way the standard free energy for the electrosorption of benzene can be compared to, *e.g.*, that of ethylene, the contributions owing to the differences in solubilities having been eliminated.

Table I: Equilibrium Constant and the Standard Free Energy for Electrosorption of Benzene at Various Temperatures

Temp, °C	K, ml/mole	c/c_s	Solubility c_s, mole/ml	ΔG_{ads}, kcal/mole
	Electrolyte: 1 *N* sulfuric acid			
30	2.1×10^9	4.8×10^4	2.3×10^{-5}	−6.5
50	3.1×10^9	9.0×10^4	2.9×10^{-5}	−7.3
70	9.4×10^9	3.4×10^5	3.6×10^{-5}	−8.7
	Electrolyte: 1 *N* phosphoric acid			
30	5.6×10^8	1.3×10^4	2.3×10^{-5}	−5.7
50	8.7×10^8	2.5×10^4	2.9×10^{-5}	−6.5
70	1.8×10^9	6.5×10^4	3.6×10^{-5}	−7.7

c. Deviations from Langmuir Behavior. It has been shown above (*cf.* Figure 12) that the θ *vs.* C relationship does not follow a simple Langmuir isotherm. It has been suggested[18] that for large molecules which occupy several sites on the surface an isotherm of the form of eq 1 may be used as a first approximation

(16) J. O'M. Bockris, H. Wroblowa, E. Gileadi, and B. J. Piersma, *Trans. Faraday Soc.*, **61**, 2531 (1965).

(17) M. I. Temkin, *Zh. Fiz. Khim.*, **15**, 296 (1941).

(18) H. Wroblowa, B. J. Piersma, and J. O'M. Bockris, *J. Electroanal. Chem.*, **6**, 401 (1963).

$$\frac{\theta}{(1-\theta)^n} = Kc \qquad (1)$$

where n is the number of sites occupied by each adsorbed species.

Application of eq 1 to the present experimental data did not give satisfactory agreement for any value of n between 1 and 10.

In Figures 14 and 15 the partial coverage is plotted as a function of log c, for adsorption of benzene from sulfuric and phosphoric acids, respectively. A linear relationship is observed at intermediate values of the coverage, in agreement with the Temkin isotherm,[17,19] eq 2, where r is the rate of change of the heat of adsorption with coverage. Departure from linearity is observed at about the same value of the coverage at all temperatures. However, since at high temperatures θ rises more rapidly with c, this allows for a shorter linear region in the θ *vs.* log c plot. For sulfuric acid the value of the parameter r decreases substantially with increasing temperature, while for phosphoric acid it is constant, within experimental error.

$$\theta = \frac{RT}{r} \ln Kc \qquad (2)$$

It has been shown by Gileadi and Conway[19,20] that the use of the logarithmic Temkin isotherm leads to erroneously high values of the parameter r except for very high values of r. Thus this parameter should preferably be calculated from the more general Frumkin isotherm,[21] which may be written in logarithmic form as eq 3. In Figure 16 the function of θ on the left-hand side of eq 3 is plotted *vs.* log c for various values of the parameter r. The expected slope of unity is only obtaine dfor $r \doteqdot 4$ kcal/mole. A similar analysis at the two higher temperatures gives $r = 3$ kcal/mole at 50° and $r \doteqdot 1.7$ kcal/mole at 70°. However, the accuracy of the value of r derived is lower at higher temperatures. For phosphoric acid a value of $r \doteqdot 5$ kcal/mole is obtained using eq 3, and the temperature variation is within experimental error. The values of r reported here are much lower than those observed in several instances in studies of adsorption from the gas phase,[8] probably owing to the leveling effect of the solvent, as discussed elsewhere.[10] The same order of magnitude of r values have been observed by Conway, *et al.*,[22] for adsorption of formate radicals in the formate decarboxylation reaction.

$$\log\left(\frac{\theta}{1-\theta}\right) + \frac{r\theta}{2.3RT} = \log Kc \qquad (3)$$

2. The Heat of Adsorption. The heat of electrosorption of benzene $\Delta H^\circ_{\theta=0}$ was obtained from the slope

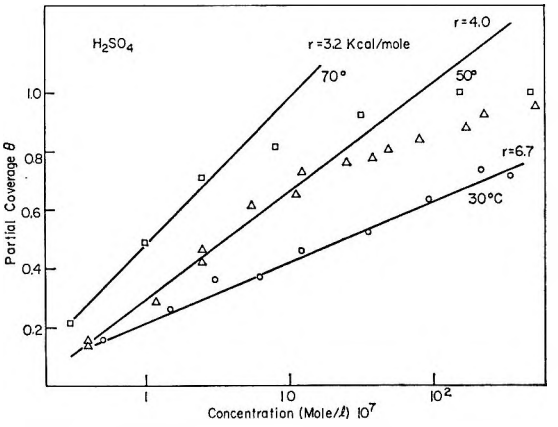

Figure 14. Plots of θ *vs.* log c for adsorption from 1 N H_2SO_4 at three temperatures. $V = 0.5$ v *vs.* nhe.

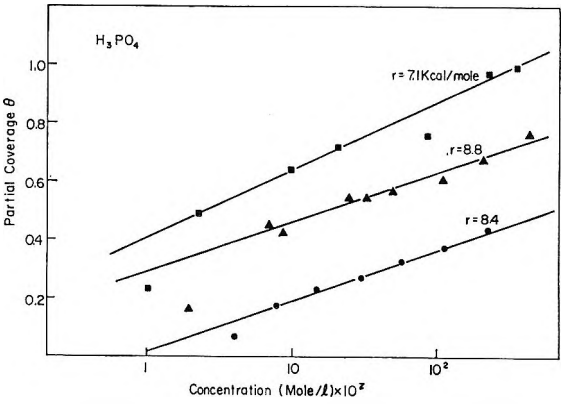

Figure 15. Plots of θ *vs.* log c for 1 N H_3PO_4 as in Figure 14.

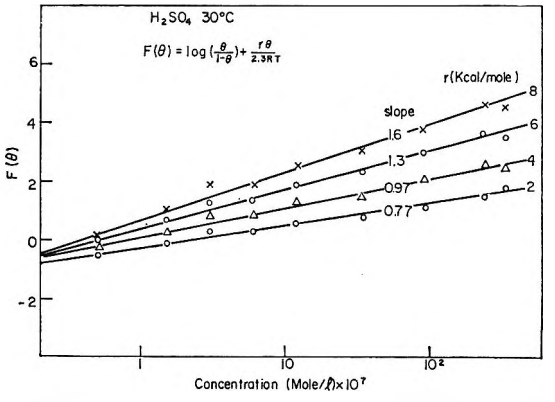

Figure 16. Plots of the Frumkin isotherm for various values of the parameter r: 1 N H_2SO_4, 30°, $V = 0.5$ v *vs.* nhe.

(19) E. Gileadi and B. E. Conway, "Modern Aspects of Electrochemistry," Vol. III, J. O'M. Bockris and B. E. Conway, Ed., Butterworth and Co. Ltd., London, 1964, Chapter 5.

(20) B. E. Conway and E. Gileadi, *Trans. Faraday Soc.*, **58**, 2493 (1962).

(21) A. N. Frumkin, *Z. Physik*, **35**, 792 (1926).

(22) B. E. Conway, E. Gileadi, and M. Dzieciuch, *Electrochim. Acta*, **8**, 143 (1963).

of a plot of $\Delta G_{\theta=0}/T$ *vs.* $1/T$ as shown in Figure 17. The slopes of the two curves for sulfuric and phosphoric acids are seen to be essentially the same. A positive enthalpy of adsorption of $\Delta H_{\theta=0} = 10$ kcal/mole is observed for both systems studied. This value refers to a partial coverage approaching zero, since it was calculated from the equilibrium constant (and hence the standard free energy) at limitingly low coverage. The isosteric heat of adsorption was calculated at various constant values of the coverage, and is plotted as a function of coverage in Figure 18. The extrapolated values for $\theta = 0$ are 6 and 9 kcal/mole for sulfuric and phosphoric acids, respectively. These are within experimental error of the value of 10 kcal/mole obtained above, when it is remembered that measurements were taken only at three temperatures, which gives rise to a high error in the numerical value of the isosteric heat of electrosorption.

Consider now the thermodynamic cycle involved in the electrosorption of benzene, assuming that each benzene molecule replaces n water molecules on the surface (Scheme I).

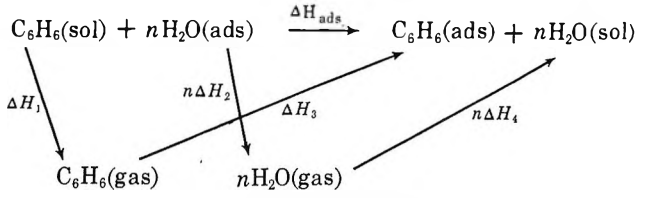

The value of ΔH_1 may be taken approximately equal to the heat of vaporization of benzene, 8 kcal/mole (the heat of solution is quite small and may be neglected); $\Delta H_4 = 9.6$ kcal/mole. Measurements of magnetization[23] and change of electric conductivity and of photoelectric sensitivity[24] upon adsorption of benzene on nickel in the gas phase indicate that six bonds are formed with the surface, and the aromatic character of benzene probably disappears. Qualitatively, the same results were obtained on platinum.[24] Since the mode of adsorption is probably similar to that for ethylene, *i.e.*, involves the breaking of the double bonds, the heat of adsorption may be estimated as being three times the value for ethylene, less the resonance energy of benzene. Thus, $\Delta H_3 = 3(-58) - (-40) = -134$ kcal/mole. For ΔH_2 a value of 22.6 kcal/mole has been used previously.[14,15] With these values and the experimental value of 10 kcal/mole for the heat of electrosorption[25] one finds $n = 10.5$. Since the value of n obtained in this manner is an average value it will not necessarily be an integer. The value of ΔH_3 used here is probably an upper estimate. In considering the adsorbed benzene molecule as an aggregate of three adsorbed ethylene molecules, it must

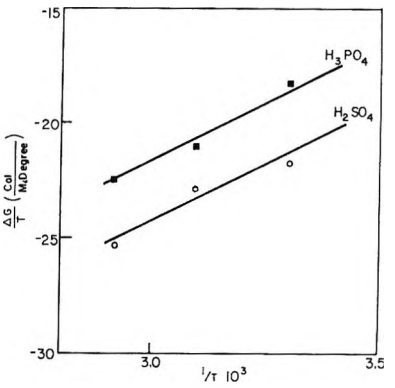

Figure 17. Plots of $\Delta G_{\theta=0}/T$ *vs.* $1/T$ for adsorption from sulfuric and phosphoric acid solutions.

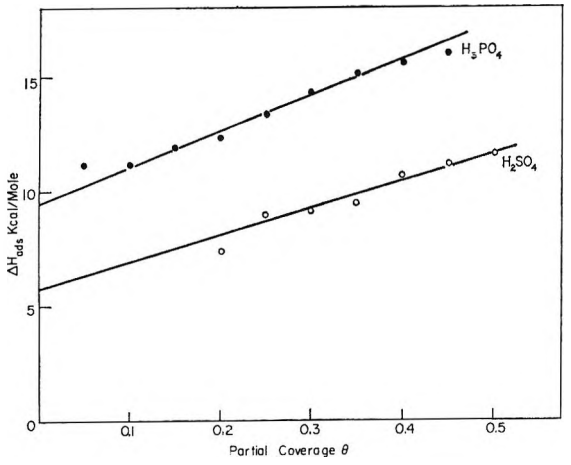

Figure 18. The isosteric heat of adsorption plotted as a function of coverage for adsorption from sulfuric and phosphoric acid.

be remembered that the pairs of carbon atoms are much more crowded in the former case than in the latter, and some loss of stability may result.[26]

The area of a benzene molecule is about 2.5–3 times that of an ethylene molecule. For the latter a value of $n = 4$ has been obtained[15] which would correspond to $n = 10$–12 for benzene, in agreement with the value arrived at above. On the other hand, on a purely geometrical consideration a value of $n = 7$ is obtained, which may be considered the lower limit.

(23) P. W. Selwood, *J. Am. Chem. Soc.*, 79, 4637 (1957).

(24) R. Suhrmann, G. Wedler, and G. Krieger, *Z. Elektrochem.*, 63, 155 (1959).

(25) Note that the value of n calculated here is not very sensitive to the experimentally obtained value for the heat of electrosorption. Taking, *e.g.*, $\Delta H_{ads} = 5$ kcal, one would have $n = 10.1$.

(26) A value of $\Delta H_3 = -30$ kcal/mole has been reported for adsorption of benzene from the gas phase on nickel. This would give rise to $n = 2.5$, which cannot be accepted on purely geometrical grounds.

Consideration of the entropy of electrosorption of benzene and ethylene (*cf.* below) gives consistency with values of $n = 8$–10 for benzene. It may thus be concluded that the number of water molecules replaced by one benzene molecule during electrosorption is $n = 9 \pm 2$.

3. The Entropy of Adsorption. Using the values obtained above for the standard free energy and the heat of adsorption, the entropies of electrosorption of benzene are 54 and 51 eu for H_2SO_4 and H_3PO_4 solutions, respectively, independent of temperature. The difference between these values is within experimental error. The positive entropy observed is consistent with the view that electrosorption is a replacement reaction, as discussed previously.[15,27,28]

A comparison of the entropy values for electrosorption of ethylene and benzene is of interest. One may write eq 4 and 5, where ΔS_1 and ΔS_2 are the observed

$$\Delta S_1 = \Delta S_B - n_1 \Delta S_W \quad (4)$$

$$\Delta S_2 = \Delta S_E - n_2 \Delta S_W \quad (5)$$

entropies of electrosorption of benzene and ethylene, respectively, ΔS_B and ΔS_E are the corresponding values for adsorption from solution, n_1 and n_2 are the number of water molecules replaced by a molecule of benzene or ethylene, and ΔS_W is the entropy of adsorption of water from bulk water. The entropy of adsorption of both organic molecules is probably low, if they retain two degrees of freedom of translation on the surface.[15] If it is taken as zero, one obtains $n_1/n_2 = 3.2$. For a value of $\Delta S_B = \Delta S_E = -10$ eu, one obtains $n_1/n_2 = 2.4$. These estimates are consistent with the ratio of the size of the two molecules and are also consistent with the above value of $n_1 = 9 \pm 2$, since for ethylene a value of $n_2 = 4$ has been obtained previously.[15]

In summary, the isothermal behavior of benzene at the electrolyte–platinum interface leads to the following conclusions. The benzene molecules is chemisorbed without dissociation. Approximately nine water molecules are replaced for each benzene molecule adsorbed. The high heat of adsorption of benzene is balanced by the heat of desorption of nine water molecules to give a small net positive heat of electrosorption. The negative free energy of electrosorption is mainly due to a large positive entropy, which in turn arises due to the gain in entropy upon desorption of nine water molecules. The adsorbed benzene molecules are probably bound to the surface by covalent bonds, as found in the gas phase.[23,24]

4. Potential–Coverage Relationship. The dependence of coverage on potential at constant temperature and bulk concentration is a phenomenon characteristic of electrosorption as opposed to chemisorption from the gas phase. The experimental behavior is shown in Figures 3 and 4 for adsorption from 1 *N* sulfuric and phosphoric acids, respectively, and in Figures 5 and 6 for adsorption from sulfate solutions of varying pH. The theory of the potential and charge dependence of coverage on mercury has been developed by Bockris, Devanathan, and Müller[27] and further extended for solid electrodes by Bockris, Swinkels, and Green,[13,14] on the basis of a "competition with water" model.

According to Bockris, *et al.*,[27] the isotherm may be written as

$$\frac{\theta}{1-\theta} = \frac{c_R}{c_W} \exp(-\Delta G^\circ_{X=0}/RT) \times \exp\left[-nZ\left(\frac{\mu X}{kT} - \frac{ZEm}{kT}\right)\right] \quad (6)$$

where

$$Z \equiv \tanh\left(\frac{\mu X}{kT} - \frac{ZEm}{kT}\right) \quad (7)$$

c_R and c_W are the concentrations of the organic and water, respectively, n is the number of water molecules replaced by one organic molecule on the surface, E is the energy of interaction between water molecules adsorbed, m is the coordination number, $\Delta G^\circ_{X=0}$ is the standard free energy of adsorption for the organic at zero field, and X is the field in the inner Helmholtz

$$X = 4\pi q_m/\epsilon \quad (8)$$

layer, given by eq 8, where q_m is the charge density on the metal and ϵ is the permitivity in the inner Helmholtz layer.

For the comparison of experiment with theory the following calculations were made. From eq 7 the value of the field X was calculated for a series of values of Z. From this the charge q_m on the metal was obtained according to eq 8, and from it the potential was computed assuming a constant value for the capacity. Equation 6 was then used to calculate θ as a function of the field, and hence of potential. The standard free energy $\Delta G^\circ_{X=0}$ was obtained by normalizing the curve at a single value of the coverage.

The degree of agreement between experiment and theory is shown for two bulk concentrations of benzene in Figure 19. The following numerical values have been used for this calculation: $\mu_{H_2O} = 1.83$ D.; $\epsilon = 6$; $E = 0.5\,kT$; $n = 8$; $m = 8$ and $C = 20\ \mu f/cm^2$ for a con-

(27) J. O'M. Bockris, M. A. V. Devanathan, and K. Müller, *Proc. Roy. Soc.* (London), **A274**, 55 (1963).

(28) B. E. Conway and R. G. B. Barradas, *J. Electroanal. Chem.*, **6**, 314 (1963).

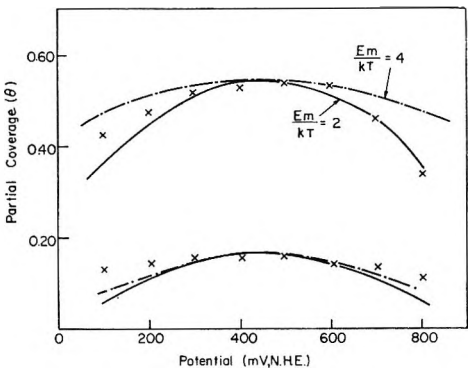

Figure 19. Experimental points and calculated curve for the potential dependence of electrosorption of benzene.

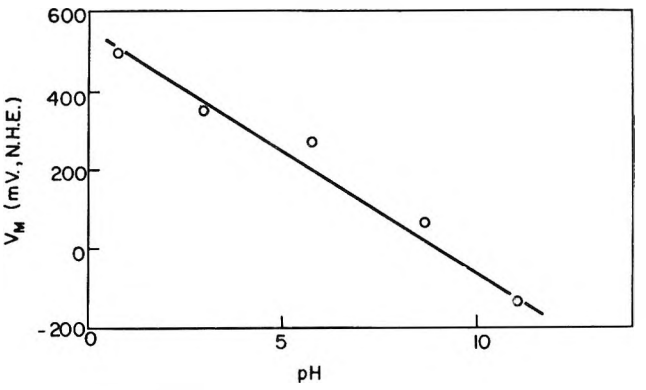

Figure 20. A plot of V_m, the potential of maximum adsorption on the normal hydrogen scale *vs.* pH.

centration of 2.8×10^{-7} *M*. $m = 4$ and $C = 10$ μf/cm^2 were taken for a concentration of 1.1×10^{-6} *M*.

Equation 6 is only applicable for low values of the coverage. A correction was here applied by making the coordination number m a function of coverage. This is justified qualitatively, since as the coverage by organic molecules increases, the number of water molecules in the neighborhood of a particular water molecule goes down.

The capacity has been assumed independent of the potential as a first approximation over the potential range where adsorption occurs.[16] A lower value of the capacity was taken at higher coverage corresponding to the direction of change of capacity with coverage by organic species observed on mercury.

5. The Effect of pH on Adsorption. Coverage–potential plots for electrosorption of benzene on Pt show two definite trends. The adsorption curves move to more cathodic potentials, on the normal hydrogen scale, with increasing pH, and the extent of adsorption is slightly lowered (Figure 5). The shift in the θ *vs.* V curves follows the shift in the reversible hydrogen potential. Thus, when plotted on the reversible rather than the normal hydrogen scale (Figure 6), the potential of maximum adsorption V_m is essentially independent of pH. A plot of V_m (*vs.* nhe) as a function of pH is linear with a slope of 60 mv as shown in Figure 20.

In the theory of organic electrosorption developed by Bockris, *et al.*,[10,13,14,27] maximum adsorption should occur at potentials somewhat cathodic to the potential of zero charge. In a recent publication[15] it has been shown that the potential of zero charge on Pt in 1 *N* sulfuric acid is 0.5–0.6 v *vs.* rhe while V_m is 0.4–0.5 v on the same scale. A dependence of the pzc of Pt on pH has been observed by Kheifets and Krasikov[29] and confirmed by recent measurements (by two independent methods) in this laboratory.[30] An average change of 60 mv/pH unit was observed, thus placing the potential of maximum adsorption at approximately the same rational potential, independent of pH, as expected from theory.[13]

6. The Rate of Electrosorption of Benzene. Plots of the net count rate, which is proportional to the partial coverage θ, are shown as a function of $t^{1/2}$ in Figures 7–11. Linear plots indicating diffusion-controlled rate of adsorption are obtained. Similar behavior has previously been observed for the rate of electrosorption of ethylene in the same system.[15] At low coverage, assuming a linear adsorption isotherm, the rate of change of coverage with time may be expressed as[15,31,32]

$$\frac{d\theta_t}{d(t^{1/2})} = \frac{2D^{1/2}}{\pi^{1/2}K\Gamma_{max}}(\theta_{equil} - \theta_0) \qquad (9)$$

where D is the diffusion coefficient, K the equilibrium constant for adsorption, Γ_{max} the limiting surface coverage, θ_{equil} the equilibrium value of θ at a given concentration, and θ_0 is the value of θ at $t = 0$. Figure 7 shows plots of θ_t *vs.* $t^{1/2}$ for $\theta_0 = 0$ and various values of θ_{equil}. The slope of the straight lines increases proportionally with θ_{equil} as expected (eq 9). For higher values of θ_{equil} a linear relationship is not obtained, since in this case the assumptions leading to eq 9 are not valid.

In Figures 8–10 similar plots are shown for three temperatures for increasing values of θ_0. The slopes of the θ_t *vs.* $t^{1/2}$ plots are found to be proportional, within experimental error, to the quantity (θ_{equil} —

(29) V. L. Kheifets and B. S. Krasikov, *Zh. Fiz. Khim.*, 31, 1992 (1952).

(30) E. Gileadi, S. D. Argade, and J. O'M. Bockris, *J. Phys. Chem.*, in press.

(31) P. Delahay and I. Trachtenberg, *J. Am. Chem. Soc.*, 79, 2355 (1957).

(32) W. H. Reinmuth, *Anal. Chem.*, 65, 473 (1961).

θ_0) in agreement with eq 9. The equilibrium constant K can be calculated from the slope of the lines in Figures 7–10 with known values of D and Γ_{max}. The results are shown in Table II together with the corresponding values obtained from equilibrium measurements.

Table II: Equilibrium Constant for Electrosorption of Benzene on Pt from Kinetic and Equilibrium Measurements

Temp, °C	$10^5 D$, cm²/sec	$10^{-9}K$, cm³/mole From kinetics	$10^{-9}K$, cm³/mole From equilibrium
30	0.66	1.2	2.1
50	1.0	1.8	3.1
70	1.5	1.8	9.4

Agreement between the two methods is obtained at 30 and 50° for this type of comparison, while at 70° the value of K obtained from kinetic measurement is too low.

An interesting problem arises upon close examination of Figures 8–10. The top lines in these figures are for relatively high values of both θ_0 and θ_{equil} where eq 9 would not be expected to apply and where substantial deviations are in effect found experimentally (*cf.* the two top curves in Figure 7). Nevertheless, a linear θ_t *vs.* $t^{1/2}$ plot is obtained. The explanation of this phenomenon probably lies in the fact that while θ_0 may be high and out of the region where a linear isotherm applies, the increment ($\theta_{equil} - \theta_0$) is small. Thus the equilibrium prevailing at $t = 0$ (corresponding to a certain finite bulk concentration and a value of θ_0) is only disturbed to a small extent, and the effect, *i.e.*, the increase of coverage from θ_0 to θ_{equil}, is linearly related to the driving force or affinity, which in this case is the incremental increase in solution concentration.

Conclusions

The electrosorption of benzene on Pt involves formation of strong bonds and probable loss of the aromatic character of the molecule. The net enthalpy of electrosorption observed is slightly endothermic (about 10 kcal/mole) owing to the fact that a large number of water molecules have to be replaced from the surface for each benzene molecule adsorbed. Energy and entropy considerations fix this number of $n = 9 \pm 2$, in agreement with the view that the present tracer method does indeed measure the adsorption of benzene and not of some radical formed as an intermediate of a possible reaction on the surface. A large positive entropy of electrosorption is observed as in the case of ethylene studied previously[15] and serves as the main driving force for the adsorption process.

The potential dependence of adsorption is consistent with present theories of adsorption of neutral organic molecules.[10,13,14,27] The potential of maximum adsorption, and with it the whole θ–V curve shifts with pH at constant sulfate ion concentration. The effect is due to a similar dependence of the potential of zero charge of Pt on pH which has been observed experimentally.

The kinetics of the adsorption process is shown to be diffusion controlled. The equilibrium constants calculated from the kinetic data are in fair agreement with results obtained from equilibrium measurements. Frumkin's adsorption isotherm applies with values of the interaction parameter r ranging from approximately 2 to 4 kcal/mole, depending on temperature in the case of adsorption from 1 N sulfuric acid, and about 5 kcal/mole (independent of temperature) for adsorption from 1 N phosphoric acid.

Acknowledgment. Financial support for this work by U. S. Engineer Research and Development Laboratory, Fort Belvoir, Virginia, under Contract No. DA44-009-AMC-469(7) is gratefully acknowledged.

Nuclear Spin Relaxation Phenomena of Adsorbed Molecules. Temperature-Dependence Studies of Benzene Adsorbed on Silica Gel

by D. E. Woessner

Socony Mobil Oil Company, Inc., Field Research Laboratory, Dallas, Texas *(Received November 1, 1965)*

The proton spin relaxation times have been measured as functions of temperature for a sample composed of three-fourths of a statistical monolayer of benzene adsorbed on silica gel. The data are interpreted by use of a generalization of previous theory in conjunction with the results of adsorption experiments. The benzene molecules rotate rapidly about a molecular axis, likely the hexad axis, even at 77°K. There is a broad distribution of temperature-dependent correlation times for this motion. There are three apparent transverse relaxation states which are characterized by different, temperature-dependent reorientation rates of the molecular rotation axis, and by different orientation distribution functions of this axis. Transitions occur among these states with changing temperature.

I. Introduction

Nmr relaxation phenomena are determined by the structure and motions of the physical system and, hence, adsorbed molecules can be studied effectively by means of relaxation measurements. In previous publications,[1,2] temperature-dependence studies of the proton relaxation phenomena of water adsorbed on silica gel have been presented together with several significant results deduced therefrom. Briefly, the protons exist in two different environmental states between which they transfer approximately 1000 times per second at room temperature. Below 0° the molecules reorient rapidly, much faster than in ice. The interaction of the nonspherical molecules with a surface causes this reorientation to be anisotropic.

In order to extend such studies to molecules which do not allow intermolecular proton transfer and thus which may yield different relaxation phenomena in the adsorbed state, measurements on the benzene–silica gel system have been initiated. A silica gel whose surface characteristics have been studied by a variety of techniques was employed so that relaxation phenomena may be interpreted in the light of other surface effects. Some of the pertinent surface characteristics will be described in the following section. In anticipating the results, one might look for rotation of the benzene molecule about its hexad axis as it is observed[3] in solid benzene.

An important part of this article is the extension and generalization of earlier relaxation theory.[1] The previous theory was applicable only to systems with local axial symmetry. This new work is applicable to all systems.

II. Experimental Section

A. Sample Preparation and Surface Characteristics. The sample of silica gel used in these measurements was obtained from the Mallinckrodt Chemical Works, St. Louis, Mo. It is precipitated gel of high purity (99.9% SiO_2, exclusive of water content) designated as Silicic Acid Special Bulky (SB). This material was used as received except for outgassing. The sample was outgassed at 210° for 24 hr after the residual pressure in the adsorption system reaches 10^{-6} torr. Spectroscopic grade benzene was distilled into the adsorption reservoir from a drying chamber utilizing Linde 5A Molecular Sieves until 100 mg of benzene/g of silica gel was adsorbed. The benzene was outgassed by repeated distillation under vacuum. The sample was sealed in a glass container.

This silica gel has been studied[4–8] by other tech-

(1) D. E. Woessner and J. R. Zimmerman, *J. Phys. Chem.*, **67**, 1590 (1963).

(2) D. E. Woessner, *J. Chem. Phys.*, **39**, 2783 (1963).

(3) E. R. Andrew and R. G. Eades, *Proc. Roy. Soc.* (London), **A218**, 537 (1953).

niques. From a BET treatment of nitrogen adsorption data a surface area of 353 m^2/g was obtained.[6] The outgassing treatment removes water molecules and leaves approximately seven OH groups per 100 A^2 of surface.[6,8] Infrared spectroscopic studies[5] indicate that the surface OH groups exist in several different states and are predominately hydrogen bonded. Outgassing at higher temperatures[6] causes a condensation of OH groups to form water. The hydroxyl group content suggests[6] that the surface has the cristobalite structure in which OH groups are paired. Hydrogen bonding and condensation demand a certain proximity between groups in order to occur. Heat of immersion studies[7] show a decrease of immersion heat with decrease of surface OH content. This agrees with the suggestion[9] that the OH group π-electron bond is a major interaction source. The coulombic interaction energies obtained from the immersion data agree[7] with values calculated from a model[10] in which a benzene molecule lies flat on the surface, situated over an OH group. Benzene adsorption studies[8] yield a BET surface area of only approximately one-half the nitrogen value. The site energy distribution[8] derived from the adsorption data is very broad and has an intense peak at 10.7 kcal/mole and also a weaker peak at 7 kcal/mole. The energy deduced from the BET treatment is 10.96 kcal/mole; hence the BET surface area corresponds to adsorption at the high-energy sites. The three-fourths statistical monolayer coverage then is composed of one-half monolayer on the high-energy sites and one-fourth monolayer either on the low-energy sites or distributed among the low-energy sites and multilayer formation on the high-energy sites.

B. Relaxation Time Measurements. The relaxation measurements were made by pulse techniques in the temperature range from 123 to 344°K at 25 Mc/sec and from 114 to 349°K at 50 Mc/sec. The longitudinal relaxation (T_1) was measured by use of repeated 180–90° pulse sequences; the transverse relaxation (T_2) was measured by use of 90–180° sequences. The electronic temperature control[2,11] and single-coil pulse system[12] are described elsewhere.

III. Experimental Results

A. Measurements Made at 25 Mc/Sec. Since the outgassing treatment leaves seven OH groups per 100 A^2, approximately 35% of the protons belong to these OH groups. The temperature dependence of the T_1 of these protons was measured for a sample prepared as above except that benzene was not added. The values obtained are 8.5 sec at 355°K, 5.1 sec at 298°K, 4.4 sec at 231°K, and 4.0 sec at 166°K.

Despite the fact that only 65% of the protons belong to benzene molecules, the longitudinal relaxation curves were generally single component. Only at temperatures lower than 143°K did a longer T_1 component appear, but the T_1 values were too close together to allow a reliable separation. In all cases, the relaxation curves were described by one relaxation time for the first two relaxation periods. These "initial slope" values are reported here. Evidently, processes such as cross relaxation[13] and molecular exchange[14] and unresolvable relaxation times occur so as to yield a weighted-average longitudinal relaxation rate at higher temperatures.

The measured T_1 values are presented in Figure 1. Since they are significantly less than the values for the OH protons alone, any relaxation contribution by trace paramagnetic impurities in the silica gel are inconsequential. There is a shallow T_1 minimum at 262°K. At low temperature, the data indicate a second T_1 minimum.

The transverse relaxation is much more complicated; as many as three transverse relaxation components are indicated over most of the temperature range employed. It is convenient for the subsequent interpretation to present the data in the order from high to low temperature. In the temperature range from 344 to 294°K, the transverse relaxation is two component. The shorter relaxation time component describes the relaxation of approximately one-third of the protons. Although this relaxation component may not follow exactly a simple $\exp(-t/T_2)$ decay law, it is approximated by it with $T_2 \approx 0.05$ msec. The signal-to-noise ratio for this small component at these high temperatures was insufficient to allow a detailed study of the decay law. The transverse relaxation time of the OH protons in the sample without benzene is of this magnitude, 0.035 msec at 50 Mc/sec. This component is due to the OH protons. The longer relaxation time

(4) S. Brunauer, D. L. Kantro, and C. H. Weise, *Can. J. Chem.*, **34**, 1483 (1956).

(5) R. S. McDonald, *J. Phys. Chem.*, **62**, 1168 (1958).

(6) J. W. Whalen, "Solid Surfaces and the Solid Gas Interface," Advances in Chemistry Series, No. 33, American Chemical Society, Washington, D. C., 1961, p 281.

(7) J. W. Whalen, *J. Phys. Chem.*, **66**, 511 (1962).

(8) J. W. Whalen, to be submitted for publication.

(9) A. V. Kiselev, *Proc. Symp. Colston Res. Soc.*, **10**, 195 (1958).

(10) A. V. Kiselev and D. P. Poshkus, *Dokl. Akad. Nauk SSSR*, **120**, 834 (1958).

(11) R. A. McKay, to be submitted for publication.

(12) D. E. Woessner and R. A. McKay, to be submitted for publication.

(13) N. Bloembergen, S. Shapiro, P. S. Pershan, and J. O. Artman, *Phys. Rev.*, **114**, 445 (1959).

(14) D. E. Woessner, *J. Chem. Phys.*, **35**, 41 (1961).

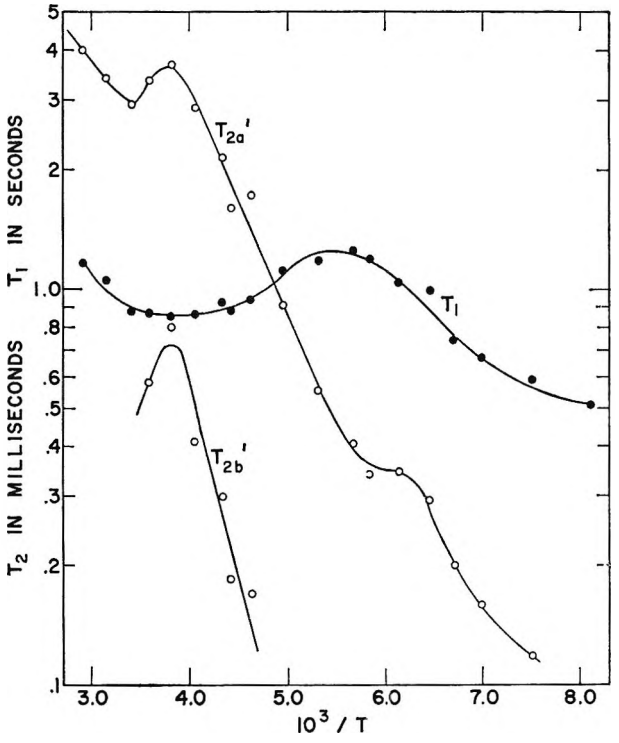

Figure 1. The temperature dependences of the 25-Mc/sec proton spin relaxation times of benzene adsorbed on silica gel at three-fourths of the statistical monolayer coverage.

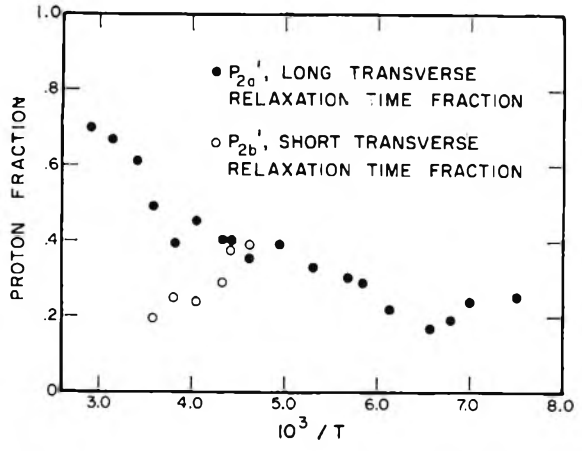

Figure 2. The temperature dependences of the experimental proton fractions described by simple exponential decay of transverse magnetization at 25 Mc/sec.

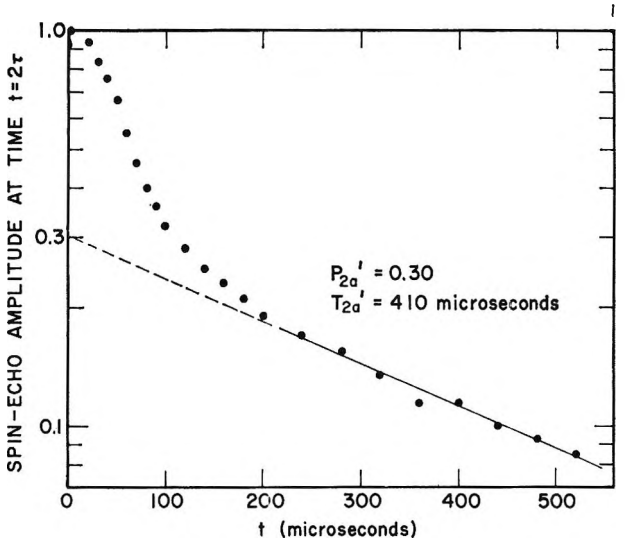

Figure 3. The 25-Mc/sec proton spin-echo amplitude at time, $t = 2\tau$, or the decay of the transverse magnetization, at 176.3°K, showing the long relaxation time component decaying at $P_{2a}' \exp(-t/T_{2a}')$.

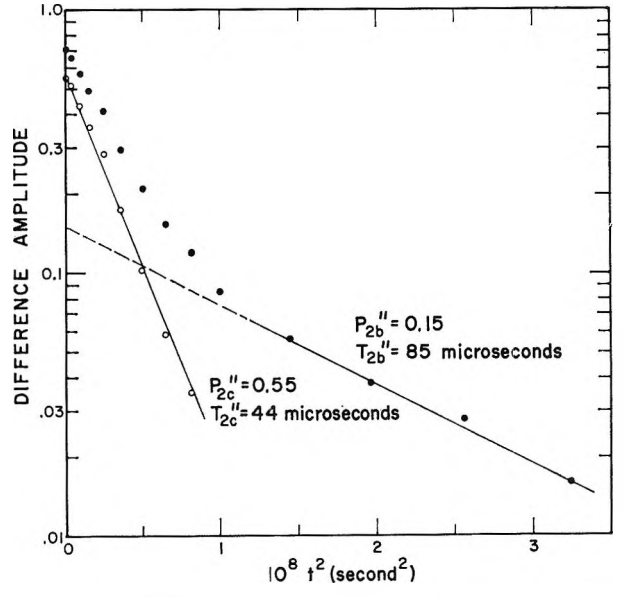

Figure 4. The difference curve obtained by subtracting the long relaxation time component from the experimental curve of Figure 3. The difference curve is plotted *vs.* t^2 and decomposed into two components to illustrate the gaussian character of the decay of two components of the transverse magnetism.

component, which is due to the benzene protons, does follow a simple $\exp(-t/T_{2a}')$ decay law.

The transverse relaxation curve of the benzene protons in the temperature range from 279 to 216°K follows the decay law $P_{2a}' \exp(-t/T_{2a}') + P_{2b}' \exp(-t/T_{2b}')$. This indicates that in this temperature range the benzene molecules exist in two different environmental states characterized by different relaxation times. The longer benzene relaxation time component follows the simple $\exp(-t/T_{2a}')$ decay at all temperatures except the lowest, 123.2°K. At this temperature, the data are inconsistent with this decay law. Figures 1 and 2

present the simple exponential decay relaxation times and proton fractions having those relaxation time values.

The complete transverse relaxation curves below 216°K become increasingly more complex. The relaxation component corresponding to the $P_{2b}' \exp(-t/T_{2b}')$ component at higher temperatures cannot be described by that simple decay law. After subtracting the $P_{2a}' \exp(-t/T_{2a}')$ component from the experimental curve, the resultant difference relaxation curve was analyzed by use of a gaussian curve, *i.e.*, by means of a semilogarithmic plot of amplitude *vs.* t^2. The difference curves in the temperature range from 188.4 to 149.6°K analyzed by this method are described by the gaussian decay law $P_{2b}'' \exp(-t^2/2T_{2b}''^2) + P_{2c}'' \exp(-t^2/2T_{2c}''^2)$. This indicates a third benzene relaxation state. Table I contains the parameters resulting from this treatment. Figures 3 and 4 show the decomposition on the observed transverse relaxation curve measured at 176.3°K. The difference curves for 143.2 and 133.2°K could not be described this way. The observed transverse relaxation curve for 123.2°K, however, could be described by the two-component gaussian curve; the resultant parameters are given in Table I also.

Table I: Proton Spin Transverse Relaxation Parameters Obtained from the Gaussian Decomposition of Transverse Relaxation Curves Measured at 25 Mc/Sec

Temp, °K	T_{2b}'', μsec	P_{2b}''	T_{2c}'', μsec	P_{2c}''
188.4	88	0.15	39	0.52
176.3	85	0.15	44	0.55
163.2	66	0.21	38	0.57
155.1	66	0.24	31	0.59
149.6	61	0.45	29	0.36
123.2	81	0.20	36	0.80

B. Measurements Made at 50 Mc/Sec. The measurements at 50 Mc/sec were performed approximately 1 year after the 25-Mc/sec measurements. The T_1 values are presented in Figure 5. Below 143°K, the multiple-component behavior was like that observed at 25 Mc/sec. A T_1 value of 0.55 sec was measured at 77°K. The subsequent T_1 values measured at higher temperatures were consistently lower than the values measured before the sample temperature was lowered to 77°K, as shown in Figure 5. The hysteresis was not apparent in the transverse relaxation phenomena. As before, there is a shallow T_1 minimum near room temperature, and a second T_1 minimum is inbicated at low temperatures.

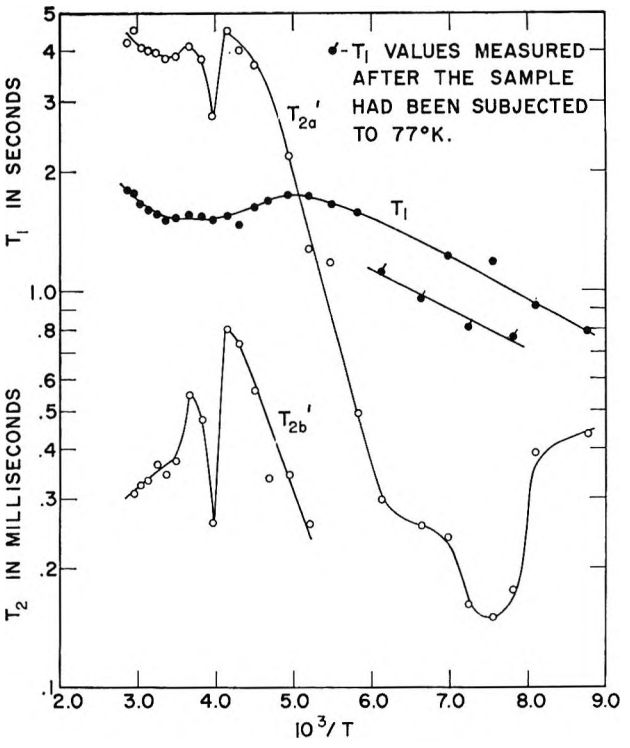

Figure 5. The temperature dependences of the 50-Mc/sec proton spin relaxation times of benzene adsorbed on silica gel at three-fourths of the statistical monolayer coverage.

The transverse relaxation behavior exhibits some differences compared to the earlier 25-Mc/sec measurements. How much is due to aging of the sample and how much is an artifact of the greater signal-to-noise ratio at 50 Mc/sec cannot be assessed. The long T_2 component for benzene protons was observed at all temperatures. The values $T_{2a}' = 0.19$ msec and $P_{2a}' = 0.20$ were measured at 77°K.

In the temperature range from 349 to 192°K, part of the protons follow the decay law $P_{2a}' \exp(-t/T_{2a}') + P_{2b}' \exp(-t/T_{2b}')$. Figures 5 and 6 present these values. At room temperature and above, a third relaxation component with a proton fraction of approximately 0.25 was observed. The experimental plots were not sufficiently detailed to yield a decay law for this component. This component relaxed most rapidly and apparently is due to the OH protons. Below room temperature, the third relaxation component increased in proton fraction and obeyed the gaussian decay law $P_{2c}'' \exp(-t^2/2T_{2c}''^2)$. This component included the OH protons and the protons of a fraction of the benzene molecules. The data for this component are presented in Figure 7.

Consider the transverse relaxation below 192°K. After subtracting the $P_{2a}' \exp(-t/T_{2a}')$ component, the resulting difference relaxation curves were ana-

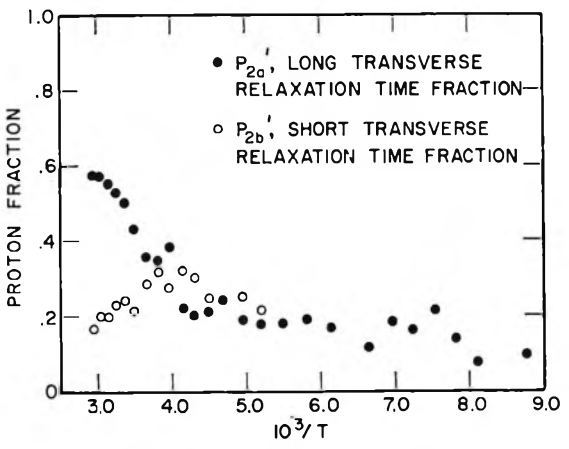

Figure 6. The temperature dependences of the experimental proton fractions described by simple exponential decay of transverse magnetization at 50 Mc/sec.

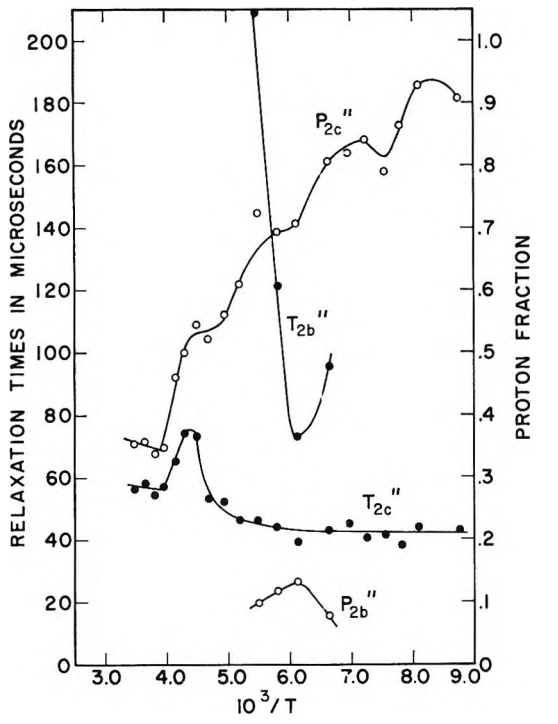

Figure 7. Proton spin relaxation parameters obtained from the gaussian decomposition of transverse relaxation curves measured at 50 Mc/sec.

lyzed by use of the gaussian decay law. The resultant parameters are given in Figure 7. Below 150°K, the difference curve was only one gaussian component. From 192 down to 150°K, the separation into two gaussian components instead of an exponential and a gaussian was not clear-cut. The latter separation was possible; it would have lowered the P_{2c}'' values but leave the T_{2c}'' values relatively unchanged. The gaussian choice T_{2b}'' was made because it allowed a continuation of the trend of increasing P_{2c}'' values with decreasing temperature and also the earlier 25-Mc/sec data support the gaussian curve.

IV. Interpretation and Discussion

A. Molecular Motion and Spin Relaxation in Solid Benzene. The relaxation phenomena reported here may be understood more easily after noting the relaxation phenomena in solid benzene.[3] At temperatures below 90°K, the second moment[15] of the proton magnetic resonance absorption line is constant, indicating a "rigid" lattice. In the temperature range between 90 and 120°K, the second moment decreases with temperature. From 120°K up to the melting point, the second moment remains almost constant. The decrease of the second moment between 90 and 120°K indicates reorientation of the molecules about their hexad axes in the crystal lattice. The spin-lattice relaxation is determined by this motion. At the resonance frequency employed, 23.4 Mc/sec, a T_1 minimum occurs at approximately 170°K. This indicates rapid motion; a T_1 minimum at 23.4 Mc/sec occurs when the correlation time describing the motion is 4.2×10^{-9} sec. From the temperature dependence of T_1, the activation energy for the reorientation process (the height of the potential energy barrier restricting reorientation) is found to be 3.7 kcal/mole.

The motion of adsorbed benzene molecules may be expected to resemble that of solid benzene molecules in its gross aspects. In the solid, the molecular geometry allows molecular reorientation about the hexad axis to experience a much smaller barrier than molecular reorientation about an axis in the plane of the molecule. In the adsorbed condition, the molecular geometry, π-electron distribution, and adsorption interaction taken together should have qualitatively similar effects on molecular reorientation.

B. Nuclear Spin Relaxation at Surfaces. The relaxation interactions for intramolecular, intermolecular, and C_6H_5–OH relaxation then are all produced by anisotropic motion at a surface. To a very good approximation, the relaxation, or at least the average relaxation, can be expressed as the appropriate average of the sums of pair interactions for the different protons. The surface interaction of the molecule makes necessary the recasting of the usual relaxation equations (which are set up in terms of the laboratory coordinate system) in terms of a local coordinate system associated with the surface itself. In general, the relaxation times depend on the orientation of the surface in the

(15) J. H. Van Vleck, *Phys. Rev.*, **74**, 1168 (1948).

applied magnetic field. However, for the powdered samples commonly used, there is an isotropic distribution of surface planes. The observed relaxation curves are then averages which are found by averaging the usual relaxation equations (which are set up in terms of the laboratory coordinate system) over this distribution. The following relaxation equations are the averages of the combined expressions resulting from several calculations.[1,16-18] This average is

$$1/T_1 = {}^1/_3\omega_p{}^2[\bar{j}(\omega_0) + 4\bar{j}(2\omega_0)] \quad (1)$$

for the longitudinal relaxation, where T_1 is the longitudinal relaxation time, *i.e.*, the time constant describing the decay of longitudinal magnetization towards the equilibrium value. The decay of the transverse magnetization is expressed as

$$f(t) = \exp\left\{-\omega_p{}^2\left[\int_0^t (t - \tau)\bar{G}(\tau)d\tau + {}^5/_6\bar{j}(\omega_0) + {}^1/_3\bar{j}(2\omega_0)\right]\right\} \quad (2)$$

In these equations

$$\bar{j}(\omega) = \int_{-\infty}^{\infty} \bar{G}(\tau)\exp(-i\omega\tau)d\tau \quad (3)$$

in which $\bar{G}(\tau)$ describes the physical motion by means of the reduced correlation function as given by

$$\bar{G}(\tau) = \langle F_0(t)F_0{}^*(t + \tau)\rangle/\langle|F_0(t)|^2\rangle \quad (4)$$

$$F_0(t) = (1 - 3\cos^2\theta(t))r^{-3}(t) \quad (5)$$

The time-dependent $\theta(t)$ is the angle between the magnetic field and the line of length $r(t)$ joining two nuclei. The quantity $\omega_p{}^2$ is the second moment of the resonance line expressed in angular units. It is related to the quantities in eq 4 as follows.

$$\omega_p{}^2 = {}^9/_{16}\gamma^4\hbar^2N^{-1}\sum_k|F_0(t)_{jk}|^2 = {}^9/_{16}\gamma^4\hbar^2\langle|F_0(t)|^2\rangle \quad (6)$$

In the derivation[17] of the integral used in eq 2, the assumptions are made that (a) at each instant the microscopic distribution of local magnetic fields generated by the surrounding proton magnetic moments through the sample is the same as for the rigid lattice (or no motion) and (b) the distribution of the local field values is gaussian. From resonance line-shape measurements it is found that this distribution is frequently gaussian, or nearly so.

It is instructive to review the characteristics of the relaxation expressions (1) and (2) before looking at the relaxation behavior for specific models of structure and motion. Ordinarily $\bar{G}(\tau)$ is of the form

$$\bar{G}(\tau) = \sum_i a_i \exp(-|\tau|/\tau_i) \quad (7)$$

in which the a_i are positive and the sum of the a_i is always unity. Applying this to eq 3 yields the expression

$$\bar{j}(\omega) = 2\sum_i a_i\tau_i/(1 + \omega^2\tau_i{}^2) \quad (8)$$

The contribution of a given τ_i to $\bar{j}(\omega)$ is a maximum when $\omega\tau_i = 1$. Consider the case where the τ_i values are widely separated. Then, if all the τ_i are varied over a wide range as by varying the temperature, the T_1 values will pass through successive minima. A T_1 minimum will occur when $\omega_0\tau_i = 0.6158$. The location of a T_1 minimum then serves to fix a τ_i value. Suppose all the τ_i values are identical. Then the absolute minimum T_1 value can be attained. It is directly proportional to ω_0, the angular resonance frequency. If the τ_i values are allowed to spread out somewhat, the minimum T_1 value is increased and the minimum in the T_1 *vs.* temperature curve is less sharp.[19,20] An abnormally large T_1 minimum value thus indicates a distribution of τ_i values. The absolute minimum T_1 value is easily computed with knowledge of $\omega_p{}^2$.

Such a minimum does not occur for the transverse relaxation. The transverse nuclear magnetization decays most rapidly when all the τ_i are infinite (*i.e.*, no physical motion). Any increase of motion causes the decay to be less rapid. When the τ_i values are long so that $\omega_0{}^2\tau_i{}^2 >> 1$, then the $\bar{j}(\omega)$ terms are relatively unimportant and the transverse relaxation is determined by the integral in eq 2. With this in mind, the substitution of eq 7 in eq 2 yields the equation

$$f(t) = \exp\left\{-\omega_p{}^2\sum_i a_i\tau_i{}^2[\exp(-t/\tau_i) - 1 + (t/\tau_i)]\right\} \quad (9)$$

If the τ_i values are long enough so that $\omega_p{}^2\tau_i{}^2 \gg 1$, then eq 9 reduces to

$$f(t) = \exp(-\omega_p{}^2t^2/2) \quad (10)$$

Since it is customary to use relaxation times, a relaxation time for a gaussian decay is defined by

$$f(t) = \exp(-t^2/2T_2{}''^2) \quad (11)$$

In this instance, $1/T_2{}''^2 = \omega_p{}^2$. Note that the τ_i values do not appear in these relaxation functions.

(16) R. Kubo and K. Tomita, *J. Phys. Soc. Japan*, **9**, 888 (1954).

(17) A. Abragam, "The Principles of Nuclear Magnetism," Oxford University Press, London, 1961, Chapters IV and X.

(18) D. E. Woessner, *J. Chem. Phys.*, **42**, 1855 (1965).

(19) K. Luszczynski and J. G. Powles, *Proc. Phys. Soc.* (London), **74**, 408 (1959).

(20) A. Odajima, *Progr. Theoret. Phys.* (Kyoto), *Suppl.*, **10**, 142 (1959).

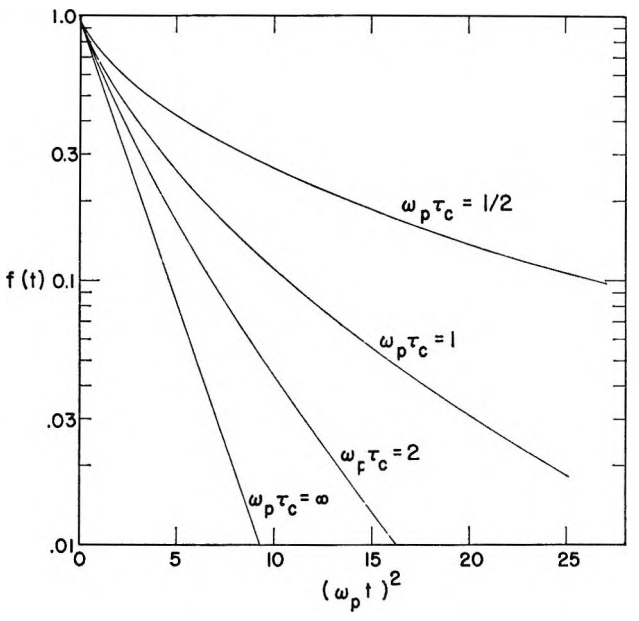

Figure 8. Theoretical transverse relaxation curves for intermediate values of $\omega_p\tau_c$ illustrating the exchange of relaxation behavior.

Suppose there is only one τ_i in the system, τ_c. For long τ_c values, eq 10 applies. For intermediate values such that $\omega_0^2\tau_c^2 \gg 1$ but $\omega_p^2\tau_c^2 \ll 1$ (note that $\omega_0 \gg \omega_p$), $f(t)$ becomes a simple exponential decay

$$f(t) = \exp(-t/T_2) \qquad (12)$$

in which $1/T_2 = \omega_p^2\tau_c$. A simple exponential decay means that all τ_i are sufficiently short so that $a_i\omega_p^2\tau_i^2 \ll 1$. In the transition region where $\omega_p\tau_c \sim 1$, the relaxation curve is more complex. Figure 8 contains the $f(t)$ curves calculated for several values of $\omega_p\tau_c$. Note the similarity of the curves for $\omega_p\tau_c = 1$ and $\omega_p\tau_c = {}^1/_2$ to the curve in Figure 4. This is unfortunate because the experimental curves for a system of several relaxation environments will be exceedingly difficult, if not impossible, to decompose for intermediate values of τ_i.

However, for a very broad distribution of τ_c values, only an insignificant fraction may exist in the transition region. Then the decay of transverse magnetization would be the sum of a rapid-decay gaussian component obeying eq 11 and a simple exponential decay obeying eq 12 with $1/T_2 = \omega_p^2\langle\tau_c\rangle_{av}$ in which the average is taken over only those τ_c values which are less than $1/\omega_p$.[21] The broad distribution of adsorption site energies for the sample may indicate that this situation prevails for the experiments described herein. Depending on the details of the distribution of $\tau_c < 1/\omega_p$, there may be multiple apparent T_2 values.

In order to apply the general equations to the anisotropic motion induced by the surface interaction, $\langle F_0(t)F_0^*(t+\tau)\rangle$ must first be expressed in terms of a local rectangular coordinate system

$$\langle F_0(t)F_0^*(t+\tau)\rangle = {}^4/_5\langle\{{}^1/_4(1-3n^2)(1-3n'^2) + 3(lnl'n' + mnm'n') + {}^3/_4[(l^2-m^2)(l'^2-m'^2) + 4lml'm']\}r^{-3}r'^{-3}\rangle = f_r(\tau) + f_s(\tau) + f_t(\tau) \qquad (13)$$

where l, m, and n are the direction cosines in the local coordinate system of the internuclear separation vector whose magnitude is r. The unprimed quantities are the initial values at time t, and the primed quantities are the values at time $t + \tau$. The fences ($\langle\rangle$) represent the average in the local coordinate system. This formulation is more general than the previous one[1] because no symmetry conditions are implicit. If the colatitude and azimuth angles of the internuclear vector in the local coordinate system are denoted by θ' and ϕ', respectively, then the direction cosines are the usual quantities

$$l = \sin\theta'\cos\phi',\ m = \sin\theta'\sin\phi',\ n = \cos\theta' \qquad (14)$$

Many times, it is natural to fix the local coordinate system to the surface so that the normal to the surface is parallel to a line described by $\theta' = 0$. This will be apparent later. The initial value (at $\tau = 0$) of $\langle F_0(t)\cdot F_0^*(t+\tau)\rangle$ is independent of motion. Motion merely separates it into a sum of functions which decrease with increasing τ values, as indicated by eq 7.

Many times, different protons experience greatly different relaxation environments. This can result in different protons having different relaxation phenomena. The observable nuclear magnetism is the sum of several components, each with different relaxation times. The preceding considerations of this section apply to protons in each relaxation environment, and calculations and data analysis must be carried out accordingly. The calculation of relaxation experienced by a given type of protons can be carried out by calculating separately the interaction caused by each type.

C. Theoretical Intramolecular Spin Relaxation in Benzene. Theoretically calculated relaxation phenomena for intramolecular interactions are useful for interpreting the observed quantities. Since magnetic dipolar interactions with protons in other molecules or surface OH groups always decrease the benzene relaxation times, such theoretical values serve to establish limits.

The nonspherical symmetry of the benzene molecule

(21) H. A. Resing, *J. Chem. Phys.*, **43**, 669 (1965).

together with its affinity for the silica gel surface should result in (a) the possibility that the molecular orientation distribution in a coordinate system attached to the surface may be anisotropic and (b) the molecule reorienting most rapidly about one of its axes. A general consequence of (a) is that $\langle 3\cos^2\theta(t) - 1\rangle$ may be nonzero; this causes a time-independent term to appear somewhere in the evaluation of eq 13.

In order to evaluate eq 13, the molecular motion together with the distribution of molecular orientation must be specified. Alternatively, comparison of calculations for preconceived models with experimental data can yield the significant aspects of these phenomena because the calculations are relatively insensitive to minor motional and orientational details. In order to illustrate the main features, we shall consider the relaxation for several extreme cases.

Calculate, first, the relaxation phenomena expected when all the τ_i in eq 7 are equal to τ_c. For isolated benzene molecules, the theoretical and experimental values[3] of ω_p^2 are both 2.22×10^9 sec^{-2}. For $\tau_c = \infty$, one finds that $T_1 = \infty$ and the transverse relaxation is a gaussian decay with $T_2'' = 21.2$ μsec. When $\omega_0\tau_c = 0.6158$, the absolute minimum T_1 value of 74.5 msec at a resonance frequency of 25 Mc/sec is obtained. In this situation, one cannot neglect the $\bar{j}(\omega)$ terms in eq 2. The transverse relaxation is a simple exponential decay with $T_2 = 46.5$ msec.

Calculate, next, the relaxation phenomena for an anisotropic model which yields relatively simple but illustrative results. This model is simply that the molecule reorients rapidly about one molecular axis and that this axis wobbles at a much slower rate. In order to describe the motion of the internuclear vector in the local coordinate system, one must define four angles: (a) Δ, the angle between the internuclear vector and the molecular reorientation axis, (b) ϕ, the azimuth angle of the internuclear vector about the molecular reorientation axis, (c) θ'', the angle between the molecular reorientation axis and the Z axis of the local coordinate system, and (d) ϕ'', the azimuth angle of the molecular reorientation axis in the local coordinate system. The value of $\langle F_0(t)F_0^*(t+\tau)\rangle$ may be evaluated by use of direction cosine transformations used in a previous calculation.[22] In order to obtain an explicit value, several assumptions are necessary. A reasonable assumption is that of axial symmetry so that $\langle\cos\phi\rangle = 0$ and $\langle\cos\phi''\rangle = 0$ for each molecule. For simplicity, one may assume that the azimuth angles fluctuate by stochastic diffusion such that $\langle[\phi(\tau) - \phi(0)]^2\rangle = 2\tau/\tau_m$ and $\langle[\phi''(\tau) - \phi''(0)]^2\rangle = 2\tau/\tau_w$. The molecular reorientation about its axis is described by ϕ and the wobble of this axis is described by θ'' and ϕ''. According to this model, the fluctuations of θ'' and ϕ'' are much slower than that of ϕ. Hence those fluctuation terms in (13) which contain ϕ will be predominantly determined by the fluctuations of ϕ, and functions of θ'' and ϕ'' in such terms may be considered to a good approximation as time independent. The results of this description are

$$f_r(\tau) = {}^1/_{20}r^{-6}(3\cos^2\Delta - 1)^2\langle(3\cos^2\theta'' - 1)^2\rangle\bar{f}_0(\tau) + {}^9/_{10}r^{-6}\sin^2 2\Delta\langle\sin^2\theta''\cos^2\theta''\rangle\exp(-|\tau|/\tau_m) + {}^9/_{40}r^{-6}\sin^4\Delta\langle\sin^4\theta''\rangle\exp(-4|\tau|/\tau_m) \quad (15)$$

$$f_s(\tau) = {}^3/_5 r^{-6}(3\cos^2\Delta - 1)^2\langle\sin^2\theta''\cos^2\theta''\rangle\bar{f}_1(\tau)\times\exp(-|\tau|/\tau_w) + {}^3/_{10}r^{-6}\sin^2 2\Delta[\langle(\cos^2\theta'' - \sin^2\theta'')^2\rangle + \langle\cos^2\theta''\rangle]\exp(-|\tau|/\tau_m) + {}^3/_{10}r^{-6}\sin^4\Delta[\langle\sin^2\theta''\cos^2\theta''\rangle + \langle\sin^2\theta\rangle]\exp(-4|\tau|/\tau_m) \quad (16)$$

$$f_t(\tau) = {}^3/_{20}r^{-6}(3\cos^2\Delta - 1)^2\langle\sin^4\theta''\rangle\bar{f}_2(\tau)\times\exp(-4|\tau|/\tau_w) + {}^3/_{10}r^{-6}\sin^2 2\Delta[\langle\sin^2\theta''\cos^2\theta''\rangle + \langle\sin^2\theta''\rangle]\exp(-|\tau|/\tau_m) + {}^3/_{40}r^{-6}\times\sin^4\Delta[\langle(1+\cos^2\theta'')^2\rangle + 4\langle\cos^2\theta''\rangle]\exp(-4|\tau|/\tau_m) \quad (17)$$

in which $\bar{f}_0(\tau)$, $\bar{f}_1(\tau)$, and $\bar{f}_2(\tau)$ are the reduced autocorrelation functions of $(3\cos^2\theta'' - 1)$, $\sin\theta''\cos\theta''$, and $\sin^2\theta''$, respectively. The first term in eq 15 gives rise to the nonzero value of $\langle 3\cos^2\theta(t) - 1\rangle$ mentioned previously. By making the simple assumption of a single exponential decay for the time-dependent part of $\bar{f}_0(\tau)$, this autocorrelation function becomes

$$\bar{f}_0(\tau) = a_r + (1 - a_r)\exp(-|\tau|/\tau_r) \quad (18)$$

where

$$a_r = \langle 3\cos^2\theta'' - 1\rangle^2/\langle(3\cos^2\theta'' - 1)^2\rangle \quad (19)$$

For this description, the τ_i values in $\bar{G}(\tau)$ consist of an infinite value, a group determined by the wobble of the molecular axis, and a distant group determined by the molecular rotation about this axis. The a_i values are determined by the orientation probability distribution function of this molecular axis.

This anisotropic model may be a reasonable approximation for adsorbed benzene molecules rotating rapidly about the molecular hexad axis. If the hexad axis does not wobble, then $\theta'' = 0$, and $\Delta = 90°$ for all proton pairs, and θ'' is time independent. This means that $a_r = 1$. The minimum T_1 value is 99.4 msec, only somewhat longer than for the previous case.

(22) D. E. Woessner, *J. Chem. Phys.*, 36, 1 (1962).

The transverse magnetization decay curve is gaussian with $T_2'' = 42.4$ μsec.

Consider the case where the hexad axis wobbles. If the wobble frequencies are small compared to ω_p, then the relaxation is nearly identical with the above. It is apparent from the two preceding calculations that wobble has relatively small effects on T_1. The main effects are on the transverse relaxation. The value of T_2'' will begin to increase when the wobble frequencies increase to the same order of magnitude as ω_p. When the wobble frequencies become large compared to ω_p, then the value of T_2'' again achieves a steady value which is determined by the average molecular orientation distribution. The orientation distribution of the molecular reorientation axis is not known. In order to illustrate the effects of wobble, a distribution must be assumed. A simple distribution function is given by the expression

$$p(\theta'')d\theta'' = (1 - \cos\alpha)^{-1} \sin\theta''d\theta'' \qquad (20)$$

in which θ'' takes values from 0 to the maximum wobble angle α. Some of the consequences of wobble with this distribution function are presented in Figure 9. For instance, when $\alpha = 52°$, the value of $a_r\langle(3\cos^2\theta'' - 1)^2\rangle = \langle 3\cos^2\theta'' - 1\rangle^2$ decreases to one-fourth of its value for no wobble so that T_2'' increases to 84.8 μsec. For $\alpha = 90°$, the molecular orientation distribution is isotropic and $a_r = 0$. In this paper, distributions yielding a very small or null value of $\langle 3\cos^2\theta - 1\rangle$ will be called "pseudo-isotropic"; some nonisotropic distributions can cause a near-zero value.

The relaxation times computed when the rotational axis lies in the plane of the molecule are not very different. For no wobble, $T_2'' = 36.2$ μsec and the minimum T_1 value is 136.5 msec. The effects of wobble would be similar to those just discussed.

D. Theoretical Nuclear Spin Relaxation Interaction between Benzene and Surface OH Group Protons. Since 35% of the protons belong to the surface OH groups, their relaxation effects on the benzene protons cannot be neglected arbitrarily. Also, the observations of single-component longitudinal relaxation with T_1 values much shorter than the OH protons alone indicate significant relaxation interaction between benzene and OH protons. The considerations of geometry and energy presented earlier suggest that the benzene molecules rotate rapidly about their hexad axes and that they lie generally parallel to the surface. In this section, a simple model based on this picture is used as the basis of an estimation of the relaxation interaction.

Each benzene proton experiences relaxation interaction with a number of OH protons. On the average,

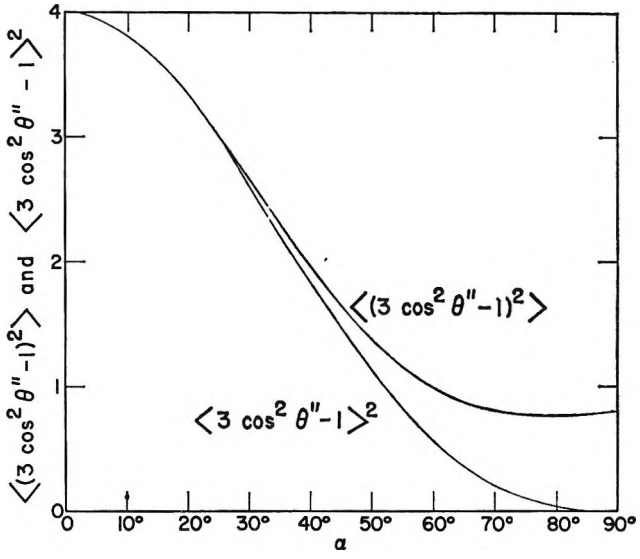

Figure 9. Anisotropic relaxation parameters calculated for the distribution function, $p(\theta'')d\theta'' = (1 - \cos\alpha)^{-1}\sin\theta''\,d\theta''$.

there are $^7/_3$ OH groups in the surface area covered by one benzene molecule. Furthermore, the calculated coulombic interaction between the benzene molecule and an OH group is not peaked sharply about the position in which the OH group is on the normal to the center of the benzene molecule. Therefore, even though the OH groups are paired, the assumption of a completely random surface distribution of OH groups with respect to a benzene molecule may be reasonable insofar as nuclear spin relaxation is concerned. The model used in the following calculations is rapid molecular rotational motion about their hexad axes which are normal to the surface (no wobble) and very slow molecular translational motion in which the average lifetime of a molecule on an adsorption site is long compared to $1/\omega_p$. Shorter lifetimes would decrease the relaxation rate.

The basic problem, then, is to calculate the relaxation interaction between a proton on a benzene molecule rotating rapidly about its hexad axis and an OH proton fixed in any surface position and then integrate over the random surface distribution of OH groups. The r value is time dependent. This greatly increases the complexity of the calculation. The relaxation interaction for this basic proton pair is not axially symmetric locally, and so the earlier formulation[1] would be incorrect.

The features of rapid rotation and no wobble mean that the τ_i values in eq 7 consist of an infinite value together with short values owing to the rapidity of the rotation. These short values are ineffective in transverse relaxation compared to the infinite value. The

lack of wobble means that eq 14 may be used directly. The dependence of r on the rotational angle of benzene causes functions related to elliptic integrals to appear in the evaluation of eq 13. These functions are very difficult to compute but they do not appear in the evaluation of the a_i value corresponding to $\tau_i = \infty$. Since the sum of the a_i is unity, the sum of the coefficients effective in spin-lattice relaxation can be found by subtracting the above a_i value from unity. The effective correlation time for spin-lattice relaxation is then approximately the value for molecular rotation. For τ values long compared to the short rotation values, the time-dependent components of $F_0(t + \tau)$ are uncorrelated with those of $F_0(t)$. The desired a_i value is then merely

$$a_\infty = \langle F_0(t)\rangle^2/\langle|F_0(t)|^2\rangle \quad (21)$$

The results for a given proton pair are as follows

$$\langle|F_0(t)|^2\rangle = {}^4/_5\langle r^{-6}\rangle \quad (22)$$

$$\langle F_0(t)\rangle^2 = {}^1/_5 f_0^2 + {}^3/_5 f_1^2 + {}^3/_5 f_2^2 \quad (23)$$

where

$$\langle r^{-6}\rangle = {}^1/_8 j^{-6}[3 + 2(1 - k^2) + 3(1 - k^2)^2]/(1 - k^2)^{5/2} \quad (24)$$

$$f_0 = (2/\pi j^5)\{[2b^2(2 - k^2)/(1 - k^2)^2 - j^2/(1 - k^2)]E(k) - [b^2/(1 - k^2)]K(k)\} \quad (25)$$

$$f_1 = (4/3\pi j^5)\{[2ab(1 + k^2)/(1 - k^2)k^2 - 2b(a + c)(2 - k^2)/(1 - k^2)^2]E(k) - [2ab/(1 - k^2)k^2 - b(a + c)/(1 - k^2)]K(k)\} \quad (26)$$

$$f_2 = (2/3\pi j^5)\{[3j^2/(1 - k^2) - 2b^2(2 - k^2)/(1 - k^2)^2 - 8a^2(2 - k^2)/(1 - k^2)k^4]E(k) + [b^2/(1 - k^2) + 16a^2/k^4]K(k)\} \quad (27)$$

in which

$$j^2 = (a + c)^2 + b^2 \quad (28)$$

$$k^2 = 4ac/j^2 \quad (29)$$

In this calculation, a is the distance from the center of the benzene molecule to a benzene proton (2.48 A), b is the distance from the OH proton to the plane of the benzene molecule, and c is the distance from the OH proton to the hexad axis of the benzene molecule. Since b is not known, it is approximated by the sum of the half-thickness of an aromatic molecule (1.70 A) and the covalent radius of the hydrogen atom (0.31 A). Also, $K(k)$ and $E(k)$ are the complete elliptic integrals of the first and second kind, respectively.

For a completely random continuous distribution of OH groups (no excluded area around a group), the probability density of finding an OH proton at a given c value is given by $N(c)dc = 2\pi Ncdc$, where N is the number of OH groups per square centimeter. The transverse relaxation of the benzene protons due to the OH protons is found by integrating eq 23 over this distribution to find the value of $a_\infty\omega_p'^2$ effective in the interaction. Graphical integration using the values $a = 2.48 \times 10^{-8}$ cm, $b = 2.01 \times 10^{-8}$ cm, and $N = 7 \times 10^{14}$ yields the value $a_\infty\omega_p'^2 = 3.20 \times 10^8$ sec^{-1}. The time-dependent intramolecular contribution for the rapid rotation is 5.55×10^8 sec^{-1}. The net decay of the benzene transverse magnetization is given by the sum of the contributions and yields a gaussian decay with $T_2'' = 33.8$ μsec. Any translational motion or wobble of the rotational axis would decrease the relaxation interaction.

The contribution of these OH groups to the benzene longitudinal relaxation (if it could be observed separately) can be estimated as follows. Graphical integration of eq 24, using the values and probability density given above, yields $\omega_p'^2 = 1.73 \times 10^9$ sec^{-2}. From this, $a_\infty = 0.185$, so that $(1 - a_\infty)\omega_p'^2 = 1.41 \times 10^9$ sec^{-2}; this is the effective interaction for longitudinal benzene proton relaxation. Since the effective correlation time is approximately that for intramolecular relaxation, this interaction leads to an OH proton contribution comparable to the intramolecular contribution itself. Then, since the relaxation effects are reciprocal, the OH proton T_1 should be comparable to the benzene proton T_1. The temperature-independent T_{2c}'' below 200°K of values which are consistent with isolated benzene molecules rotating rapidly about their hexad axes indicates a weaker interaction with OH protons. This may indicate a larger b value than that used in the computation.

The relaxation interaction between protons in different benzene molecules has not been considered since the calculations would be even more difficult and computer calculations would likely be necessary. However, these effects between layers of molecules are expected to be significantly less than those just considered because the nearest approach of protons in consecutive layers would be 3.4 A, considerably farther than the value considered above. Intermolecular relaxation between coplanar benzene molecules could be relatively more important, but they are expected to be dominated by intramolecular effects.

E. Nuclear Transfer Effects. Consider nuclei in two different environmental states so that they experience two different relaxation times (either T_1 or T_2). Assume that the relaxation is simple exponential

decay. Each of the relaxation curves for this composite system can be written in the form

$$F(t) = P_a' \exp(-t/T_a') + P_b' \exp(-t/T_b') \quad (30)$$

where T_a' and T_b' are the observable relaxation times corresponding to environmental states a and b, and P_a' and P_b' are the observable population fractions of nuclei having the corresponding relaxation times. Let b designate the environmental state having the shorter relaxation time. If nuclear magnetization does not transfer between the environmental states, the observed quantities are characteristic of the corresponding environmental states. Unprimed quantities designate these values. However, if transfer of nuclear magnetization does occur, the observed parameters are not characteristic of the individual environmental states. In general, transfer decreases the observable relaxation times. On the other hand, an increasing transfer rate increases P_a', which results in a corresponding decrease of P_b'. For sufficiently large transfer rates, P_a' becomes unity. Only one relaxation component is observed, and the relaxation is the weighted average as given by

$$1/T_{av} = P_a/T_a + P_b/T_b \quad (31)$$

Detailed discussions of these effects have been presented elsewhere.[1,14,23]

Several different processes can transfer nuclear magnetization. Two of these are actual molecular exchange and intermolecular proton transfer; these are effective for both longitudinal and transverse magnetization. Another is cross relaxation, which transfers longitudinal magnetization by means of nuclear magnetic spin–spin interactions.

F. Analysis of Relaxation Data. In the preceding sections, a general relaxation theory for relaxation at surfaces was presented and employed to calculate relaxation phenomena for several plausible models. In this section, the observed relaxation data will be analyzed on the basis of those results.

The observation of gaussian transverse relaxation is significant because it indicates that $\langle 3\cos^2\theta - 1\rangle$ is nonzero; this occurs in solids but not in liquids. However, the molecules must be rotating because the transverse relaxation is much too slow to allow nonrotating molecules. The value $T_2'' = 42.4$ μsec calculated for benzene molecules rotating about stationary hexad axes (stationary in the sense that the correlation time is long compared to $1/\omega_p$) is equal to the temperature-independent T_{2c}'' values measured below 200°K. The constancy of T_{2c}'' suggests that temperature-dependent phenomena such as wiggle of the rotational axis are insignificant for transverse relaxation of molecules in component c below 200°K. Hence, the molecules rotate about their hexad axes; rotation about other axes would yield shorter T_2'' values. Also, intermolecular and OH proton interactions contribute insignificantly to transverse relaxation since they would shorten T_2''. Since molecular residence lifetimes would be temperature dependent, the temperature independence of T_{2c}'' would suggest that the OH proton interaction is not made weaker by translational jumps between adsorption sites. Hence, b is sufficiently large and a_∞ is sufficiently small so that the OH proton interaction is sufficiently small so as to have negligible effect on T_{2c}''.

Since the OH protons are immobile in the context of relaxation effects, the motions effective in determining the relaxation times are those of the benzene molecules. The longitudinal relaxation is determined by the components of molecular motion at the resonance frequency and at twice this frequency. Hence, the high-frequency molecular motions, rotation about the hexad axis, are indicated by the longitudinal relaxation. Since a T_1 minimum serves to fix a τ_i value, the two T_1 minima indicated by the data suggest that there are at least two groups of benzene molecules which rotate rapidly but at greatly different rates.

The low-temperature T_1 minimum is due to the benzene molecules which reorient most freely. It is natural to associate these with the long transverse relaxation time component T_{2a}' since the longest transverse relaxation time indicates the greatest freedom of motion. Figures 2 and 6 show that approximately one-fifth of the protons belong to this group at temperatures below 160°K.

Since the benzene BET surface area is approximately one-half the nitrogen value, the three-fourths statistical monolayer adsorbed results in one-fourth statistical monolayer on weakly adsorbing sites. Then, since one-third of the benzene molecules are of this type, approximately 22% of the total protons would belong to this class. This value agrees with that given in the preceding paragraph. Accordingly, it is reasonable to identify these protons as belonging to component a of the transverse relaxation data.

Consider in more detail the low-temperature T_1 minimum. The experimental indication of multicomponent longitudinal relaxation below 143°K shows that some of the protons are relatively isolated; otherwise cross relaxation would result in single-component relaxation. The OH proton T_1 is lowered greatly upon introducing the benzene into the sample; this

(23) J. R. Zimmerman and W. E. Brittin, *J. Phys. Chem.*, **61**, 1328 (1957).

shows that longitudinal relaxation interactions do occur between OH and a fraction of the benzene protons. However, it seems reasonable that the OH protons interact the more strongly with protons of the strongly adsorbed molecules. This can occur to yield effective longitudinal relaxation but contribute relatively insignificantly to transverse relaxation so as to have little effect on T_2''; the calculation in section D shows that a_∞ can be small compared to the quantity $(1 - a_\infty)$. The relaxation interaction value computed for benzene and OH protons is a maximum value. If the van der Waals radius of the hydrogen atom (1.2 A), rather than the covalent radius, should be appropriate in the computation for weakly adsorbed molecules, the computed interaction would be very much less because it is generally proportional to the inverse sixth power of the distance between protons. Also, as discussed at the end of section D, the relaxation interaction between the protons in different benzene molecules should be much smaller than the intramolecular interaction. If all the longitudinal relaxation were due to intramolecular relaxation in weakly adsorbed benzene molecules rotating about their hexad axes, the net "initial slope" T_1 minimum value at 25 Mc/sec would be 99.4/0.22 = 452 msec. This value is consistent with the low-temperature minimum value suggested by Figure 1. A similar statement applies to the 50-Mc/sec data.

The high-temperature T_1 minimum must be due, therefore, to the protons in the more strongly adsorbed benzene molecules which would be expected to move less freely. These molecules have a broad distribution of correlation times for rotation about the hexad axis, as shown by the following. This broad T_1 minimum occurs around room temperature. The room-temperature T_1 values are 1.50 sec at 50 Mc/sec, 0.85 sec at 25 Mc/sec, and 0.336 sec at 9.5 Mc/sec. Since these values are directly proportional to the resonance frequency, as predicted by nuclear magnetic dipole–dipole relaxation theory, this is a true T_1 minimum in the context of that theory; it is not an artifact from any change of arrangement of the adsorbed molecules. If this T_1 minimum were due to a group of protons which had the same effective correlation time for rotation about the benzene hexad axis, the proton fractional population of this group would be 0.0994/0.85 = 0.117, neglecting the effects of OH protons. This is much less than any of the room-temperature population fractions observed at 50 Mc/sec. The OH protons are likely relaxed by protons in strongly adsorbed benzene molecules. Inclusion of OH proton interactions would increase the discrepancy. This excessive T_1 minimum value and the distribution of adsorption site energies indicate a broad distribution of rotational τ_i values for these molecules. The single-component longitudinal relaxation above 143°K may be the result of an insufficient difference between T_1 of weakly adsorbed molecules and the T_1 values of strongly adsorbed molecules and OH protons together with cross relaxation of benzene and OH protons. Alternatively, slow molecular transfer of molecules between the weakly and strongly adsorbing sites could yield the same T_1 for all benzene molecules but not affect transverse relaxation because T_1 is so much longer than T_2. Molecular residence times even as long as 0.1 sec would be short enough.

Since $T_1 >> T_2$, the transverse relaxation is determined by the slower motions. At 25 Mc/sec, a T_1 minimum occurs when $\tau_i = 3.9 \times 10^{-9}$ sec. For a rough comparison, assume rapid molecular rotation about the hexad axis while this axis undergoes isotropic rotational diffusion. Then, neglecting any intermolecular relaxation, the value $T_{2a}' = 3.68$ msec at 262°K (the 25-Mc/sec T_1 minimum) yields a correlation time of 6.1×10^{-7} sec for the axis motion. The smaller T_{2b}' values indicate correspondingly longer correlation times for the axis motion.

The transverse relaxation data indicate three apparent relaxation states for the benzene molecules. Their designation is somewhat arbitrary, as will be discussed later. Label these states a, b, and c to correspond to the experimental relaxation components. In all these states, any change of transverse relaxation times is in the same direction as the temperature change. State a is characterized by the greatest motion with a pseudo-isotropic orientation distribution at all temperatures employed so that the decay of the transverse magnetization is a simple exponential. State b is characterized by less motion and faster transverse relaxation. At the higher temperatures it has a pseudo-isotropic reorientation distribution which becomes anisotropic with appreciable wiggle of the molecular axis at lower temperatures to yield a gaussian decay of transverse magnetization. State c is characterized by an anisotropic orientation distribution function, with some wiggle of the molecular axis which decreases somewhat with temperature decrease. The wiggle is not very important; below 200°K the T_{2c}'' value is essentially constant with a value comparable to that for benzene molecules rotating rapidly about fixed hexad axes, 42.4 μsec. In all these states at the temperatures employed, the molecules are rotating rapidly about the molecular axis. The states differ in their rotational axis motions.

These relaxation states clearly do not correspond directly to those expected from the adsorption experi-

ments. The discrepancy can be explained as follows. The existence of a broad distribution of adsorption site energies can result in a distribution of T_2 values as well as of T_1 values. Designate by T_{2w} and T_{2s} the transverse relaxation times of weakly and a fraction of the strongly adsorbed molecules, respectively, and by T_{2c}'' the relaxation time of molecules with rotational axis correlation times greater than $1/\omega_p$. At any given temperature, distributions of T_{2w} and T_{2s} values can occur. The preceding discussion of T_1 minima suggests that the distribution of T_{2w} values is much narrower than the distribution of T_{2s} values. The values of P_{2a}' suggest that $T_{2a}' = T_{2w}$ at the lower temperatures, as indicated by the earlier discussion. At the high temperatures, the longest T_{2s} values of the strongly adsorbed molecules could be sufficiently great so that they are experimentally indistinguishable from the T_{2w} value. This would yield a state composed of some strongly adsorbed molecules along with the weakly adsorbed molecules so as to cause P_{2a}' to be greater than P_{2w}, and to decrease P_{2b}'. Since these longest T_{2s} values would likely be shorter than the T_{2w} value, the T_{2a}' value would be smaller than T_{2w}. Simultaneously, the measured T_{2b}' would be shortened because the longer T_{2s} values would be identified with state-a molecules. If the T_{2w} and T_{2s} values are close enough, or if their distributions overlap sufficiently, only single-component transverse relaxation would be observed. It should be emphasized that nuclear or molecular transfers between relaxation states have qualitatively the same effects.

The temperature dependence of the transverse relaxation can be explained in terms of these relaxation states and relaxation time distributions. Consider first the 50-Mc/sec data. At room temperature and above, all the benzene molecules are in states a and b with a pseudo-isotropic orientation distribution. As the temperature increases from room temperature, the slight decrease of T_{2b}' and P_{2b}' with simultaneous slight increase of P_{2a}' suggests that more of the strongly adsorbed molecules become identified with component a, as discussed in the preceding paragraph. This may be due to the distributions of T_{2w} and T_{2s} values, to molecular transfer, or to a combination of these effects. The simultaneous slight increase of T_{2a}' reflects the general increase of T_2 values with temperature. As the temperature decreases from room temperature, some of the strongly adsorbed molecules decrease their motion so as to enter state c. The T_2 values of the OH protons are sufficiently close to those of benzene state-c molecules so that both types of protons are included in the c relaxation component. Since the OH protons initially outnumber the benzene protons in this component, the early T_{2c}'' values do not give information on the T_2 of benzene c molecules. Down to about 242°K, values fluctuate somewhat, anticipating a transition at this temperature in which the strongly adsorbed molecules no longer exist in state a, and a jump in the number of benzene molecules in state c occurs. The value of T_{2a}' suddenly increases because it is no longer kept small by inclusion of the shorter (compared to T_{2w}) values from the larger of the T_{2s} values while the molecules with the shorter T_{2s} values now are in state c. Just below 242°K, the T_{2c}'' values are larger than at higher temperatures; and the curves from which T_{2c}'' was determined indicate unresolved multicomponent relaxation at 241 and 232°K. Evidently some of the molecules which now appear in state c still have appreciable wiggle of the rotational axis to yield longer relaxation times. With further temperature decrease, the values of T_{2a}' and T_{2b}' decrease because of decreased motion of the molecular rotational axis. The value of T_{2c}'' approaches a constant value indicative of at most only slight wiggle of the molecular axis but rapid rotation about this axis. The value should remain constant until the rate of rotation about the axis becomes comparable to ω_p. This evidently would occur below 77°K. At 182°K the motion of the rotation axis has sufficiently decreased for state-b molecules to cause gaussian behavior, T_{2b}''. With further temperature decrease, this motion decreases so that at 144°K all the strongly adsorbed molecules are in state c. The decrease of P_{2a}'' below 125°K together with the increase of T_{2a}'' values may indicate that part of the weakly adsorbed molecules have a shorter T_{2w} than the others. Evidently some rearrangement occurs at lower temperatures which increases P_{2a}' to 0.20 and returns T_{2a}' to 0.19 msec at 77°K; these values are close to those just above 125°K.

Consider now the 25-Mc/sec data. In contrast to the 50-Mc/sec data, the b component was not observed at room temperature and above. This may be the result of molecular transfer or strong overlap of relaxation times. The larger P_{2a}' values in the temperature range from 241 to 163°K together with smaller T_{2a}' values, compared to the later 50-Mc/sec data, may indicate that part of the strongly adsorbed molecules have sufficiently longer T_{2s} values to put them in the a component. Hence, part of the strongly adsorbed molecules exhibited greater motion than one year later when the 50-Mc/sec data were taken. The differences between the sets of data can be explained by this cause. The failure to observe T_{2a}' at 123.2°K may be due to the lower sensitivity compared to 50-Mc/sec experi-

ments; at 50 Mc/sec, the value of P_{2a}' was low, only 0.07.

These results indicate surprisingly great rotational motions of adsorbed benzene molecules. In contrast to clathrated benzene,[24] the rotational mobility at the lower temperatures is greater than for pure solid benzene. In contrast to experiments on benzene adsorbed on charcoal,[25] contributions to the benzene T_1 by paramagnetic impurities are insignificant so as to allow the observation of T_1 minima.

In a recent publication,[21] the existence of apparent two-phase transverse relaxation behavior caused by a broad distribution of correlation times has been emphasized. A detailed theory based on a log normal distribution of molecular residence times on adsorption sites was presented. The heterogeneity of adsorption sites in silica gel SB is such that the log normal distribution would not hold.

Acknowledgment. The author acknowledges the efforts of Mr. L. Bedell in preparing the sample and those of Mr. N. Kneten and Mr. J. Fagan in making most of the measurements. He also thanks Dr. J. R. Zimmerman for his active interest in this work and Dr. J. W. Whalen for useful discussions of the results of adsorption measurements.

(24) H. Nakajima, *J. Phys. Soc. Japan*, **20**, 555 (1965).

(25) H. A. Resing, J. K. Thompson, and J. J. Krebs, *J. Phys. Chem.*, **68**, 1621 (1964).

The Photoisomerization of Gaseous Methyl Isocyanide

by D. H. Shaw and H. O. Pritchard[1]

Chemistry Department, University of Manchester, Manchester 13, England *(Received November 1, 1965)*

Ultraviolet radiation at 2537 A causes methyl isocyanide vapor to isomerize to methyl cyanide without the intervention of radicals. The rate of isomerization is dependent on both pressure and temperature. The reaction is also catalyzed by methyl radicals and is photosensitized by mercury, nitrous oxide, carbon dioxide, and benzene.

The thermal isomerization of methyl isocyanide has been studied by Schneider and Rabinovitch[2] and was shown to be a typical unimolecular intramolecular reaction. We have found that although the reaction may be catalyzed in a number of ways, some of which involve radicals, the pure intramolecular isomerization can also be induced photochemically using radiation at 2537 A. The methyl cyanide produced is unaffected by 2537-A radiation, although it is decomposed by shorter wavelengths.[3]

Photolysis in the Absence of Added Gases. Methyl isocyanide was prepared by heating methyl iodide and silver cyanide in a sealed tube, and the resulting complex was decomposed using aqueous potassium cyanide.[4] After drying with magnesium sulfate, the product was purified by vapor phase chromatography and was stored *in vacuo* at −80° until required. No water, methyl iodide, or methyl cyanide could be detected in the final product.

The extinction coefficient of methyl isocyanide vapor was measured at 23 and 83° and was found to be about 0.3 ± 0.1 l. mole^{-1} cm^{-1} at both temperatures. The photochemical system consisted of a low-

(1) To whom correspondence should be addressed: Centre for Research in Experimental Space Science, York University, Toronto, Canada.

(2) F. W. Schneider and B. S. Rabinovitch, *J. Am. Chem. Soc.*, **84**, 4215 (1962).

(3) D. E. McElcheran, M. H. J. Wijnen, and E. W. R. Steacie, *Can. J. Chem.*, **36**, 321 (1958).

(4) E. G. J. Hartley, *J. Chem. Soc.*, 1296 (1916).

pressure spiral mercury discharge lamp, a 5-cm path length of deionized water to remove 1849-A radiation, and a 5 cm long, 5 cm diameter quartz reaction vessel maintained in an electrically heated furnace; provision was also made for monitoring the light output of the lamp.

In the preliminary experiments at 83°, the isomerization was found to be relatively fast and rather variable, but this was mainly due to mercury photosensitization. If extra mercury was added to the system, the rate of isomerization increased, and mercuric cyanide was deposited on the walls of the vessel. When stringent precautions were taken to exclude mercury from the reaction vessel, the rate of isomerization fell to a much lower but relatively much more reproducible figure. This limiting rate was not measurably reduced by the addition of a few millimeters of water and hydrocarbon mixture, or 0.1 mm of air, either of which should have removed any remaining mercury from the system.[5]

Under mercury-free conditions, it was necessary to illuminate any given sample for some 24 hr to obtain a measurable rate of isomerization—normally 0.5–5% decomposition; this is a direct consequence of the low extinction coefficient of CH_3NC at 2537 A. Analyses were performed at room temperature using a Perkin-Elmer gas chromatograph with a 4-m polyester column, thermistor detectors, and hydrogen as a carrier gas. In no experiment was there found any evidence of free-radical participation in the isomerization; *e.g.*, CH_4, C_2H_6, C_2N_2, HCN, etc. were never found, even in runs taken to quite high percentage decomposition.

The light intensity was measured using a ferrioxalate actinometer.[6] The cell was filled with actinometer solution and irradiated in position in the furnace. The measurement was then repeated with a Pyrex plate between the lamp and the cell, and the intensity at 2537 A was taken to be the difference of these two intensities. For all the runs discussed in this paper, the light intensity at the cell was 3.5×10^{14} quanta cm^{-2} sec^{-1} to within about 20%. Experiments with wire gauze filters showed that the rate of isomerization was directly proportional to the incident light intensity.

The variation in rate of isomerization over a 5000-fold pressure range at 83° is shown in Figure 1 and the results are also listed in Table I. Because of uncertainties inherent in determining the quantum yield for a molecule having such a low extinction coefficient, these yields are expressed as first-order rate constants for constant incident light intensity. While the experimental scatter is large, there is a definite trend

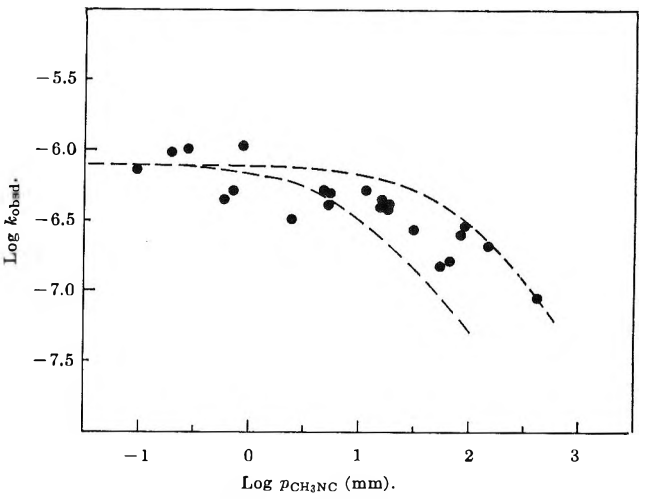

Figure 1. Variation of isomerization rate of CH_3NC with pressure.

in that the quantum yield falls by a factor of about 10 over the range of pressure studied. Thus, if the isomerization had an over-all quantum yield, Φ, of unity, the rate constant expressed in this way would be about 4×10^{-7} sec^{-1}. The results show therefore that the over-all quantum yield at the lowest pressures attainable appears to be about 2.

Table I: The Photoisomerization of CH_3NC at 83 ± 2° with an Incident Light Intensity of $(3.5 \pm 0.7) \times 10^{14}$ Quanta Cm^{-2} Sec^{-1}

Run no.	Pressure, mm	Time, hr	% conversion	$10^7 k_{obsd}$, sec^{-1}
5	0.094	20.5	5.32	7.43
2	0.193	17.0	5.81	9.86
11	0.270	20.5	7.37	10.4
16	0.607	17.0	2.73	4.55
19	0.707	17.0	3.14	5.23
13	0.860	17.0	6.43	10.9
21	2.38	20.5	2.37	3.24
3	4.75	17.0	3.18	5.27
12	5.11	21.0	3.14	4.23
20	5.12	18.5	3.31	4.98
4	11.6	20.0	3.74	5.31
10	15.9	17.0	2.66	4.40
6	16.5	19.0	2.69	4.00
1	17.0	16.5	2.31	3.95
9	31.3	18.0	1.75	2.81
15	54.4	18.0	1.01	1.53
17	65.8	20.25	1.20	1.64
7	80.9	18.0	1.68	2.59
8	90.6	18.5	1.98	2.97
18	151	18.5	1.38	2.11
14	426	18.0	0.57	0.92

(5) R. Pertel and H. E. Gunning, *J. Chem. Phys.*, **26**, 219 (1957).

(6) J. H. Baxendale and N. K. Bridge, *J. Phys. Chem.*, **59**, 783 (1955).

The simplest mechanism that can be written for such a process is

$$CH_3NC + h\nu \longrightarrow CH_3NC^*$$

where CH_3NC^* is in some unspecified electronically excited state 112 kcal above the ground state. This process takes place at a rate φI_{abs} where φ cannot exceed unity. (The existence of dimer molecules in CH_3NC vapor has been postulated,[2] but the fact that the optical density of a given mass of vapor does not change *at all* between 23 and 83° shows that if any dimer is present, it is certainly not the absorbing species. Furthermore, at the lower pressures, the time between collisions so exceeds the characteristic time for isomerization that we can rule out a process such as

$$CH_3NC^* + CH_3NC \xrightarrow{k_4'} CH_3NC' + CH_3NC''$$

in which CH_3NC^* shares its excitation energy with another molecule to produce two less excited but still potentially reactive molecules.)

$$CH_3NC^* \xrightarrow{k_1} CH_3CN^* \quad (1)$$

where CH_3CN^* is a molecule having approximately 122 kcal of excitation energy shared in some way between electronic and vibrational degrees of freedom.

$$CH_3NC^* + CH_3NC \xrightarrow{k_2} CH_3NC + CH_3NC \quad (2)$$

which, because $[CH_3CN] + [CH_3NC]$ is always a constant, is assumed to include deactivation by product molecules as well.

$$CH_3CN^* + CH_3NC \xrightarrow{k_3} CH_3CN + CH_3NC \quad (3)$$

again, assumed to include deactivation by product molecules.

$$CH_3CN^* + CH_3NC \xrightarrow{k_4} CH_3CN + CH_3NC^{**} \quad (4)$$

where CH_3NC^{**} can have up to 122 kcal of internal energy—however, for the sake of simplicity, it is assumed to react in the same way as CH_3NC^*. Thus we have a chain reaction, and the over-all quantum yield, Φ, is determined by the ratio of k_3 and k_4. One might also consider a branching chain mechanism including reaction k_4', which would be important at high pressures, and tend to maintain the isomerization rate above the simple falloff value. This would presuppose, however, that CH_3NC has at least one excited (triplet, see later) state lying somewhere between 38 kcal (E for thermal isomerization[2]) and 112 − 38 = 74 kcal above the ground state or that electronic energy in this molecule is readily convertible into vibrational excitation upon collision with another similar molecule. Furthermore, it is an experimental fact that the lifetime with respect to all decay processes of CH_3CN^* is considerably greater than CH_3NC^*—otherwise we should also have to consider the reverse of process 1 as being important, and there would be no falloff in the rate with increasing pressure. Excluding k_{-1} and k_4', therefore, a steady-state treatment of this reaction scheme gives eq 5. In all our experiments, ϵ is sufficiently small that I_{abs} is proportional to $[CH_3NC]$. Thus k_{obsd} tends to a horizontal line at low $[CH_3NC]$ but has a slope of −1 at high pressures. The ratio of k_1/k_2 may be deduced from the limiting behavior of plots of k^{-1}_{obsd} against $[CH_3NC]$ or k_{obsd} against $[CH_3NC]^{-1}$, and although the data is rather scattered, the limits of k_1/k_2 probably lie between 4×10^{17} and 3×10^{18} molecules cc^{-1}. The two lines shown in Figure 1 correspond to a choice of $k_3 = k_4$ so that $\Phi = 2$ at low pressures, and to the two most extreme possibilities for k_1/k_2, in each case with $\varphi = 1$. Following Weininger and Rice,[7] we take k_2 to be an efficiency factor, Q, times the collision rate Z_2, and from experiments described below, we are forced to conclude that Q is a function of temperature, *i.e.*, $Q(T)$. Thus, with σ for both CH_3NC and CH_3NC^* taken to be[2] 4.5 A, we have $k_2 = 3.8 \times 10^{-10} Q_{356}$ molecule^{-1} cc sec^{-1}, so that k_1 lies between $1.5 \times 10^8 Q_{356}$ and $1.1 \times 10^9 Q_{356}$ sec^{-1} at 356°K. If $1 > Q(T) \geq 0.01$, these are of a similar order of magnitude to the rate constants for the disruption of excited ethylene[8] and azoethane[9] molecules.

$$k_{obsd}[CH_3NC] = \frac{-d[CH_3NC]}{dt} = \frac{\varphi I_{abs}}{(k_3 + k_4)^{-1}k_3 + k_1^{-1}k_2[CH_3NC]} \quad (5)$$

Variation of Over-all Quantum Yield with Temperature. Experiments were also carried out at 15 mm total pressure at 23 and 101°, and, despite the scatter, there is a definite increase in rate with increasing temperature (the mean values of log k_{obsd} at 23, 83, and 101° are −7.36, −6.50, and −6.30, respectively). Expressed in Arrhenius terms, the "activation energy" for the photolysis certainly lies between 5 and 10 kcal/mole. A similar, but smaller, temperature effect has been noted previously in the photolysis of azo compounds.[9] A temperature coefficient of the magnitude we find cannot be explained in the way Cerfontain and Kutschke explained their results, and we are forced to

(7) J. L. Weininger and O. K. Rice, *J. Am. Chem. Soc.*, 74, 6216 (1952).

(8) H. M. Frey and I. D. R. Stevens, *J. Chem. Soc.*, 1700 (1965).

(9) H. Cerfontain and K. O. Kutschke, *Can. J. Chem.*, 36, 344 (1958).

conclude that, as I_{abs} remains unchanged, either k_1/k_2 or k_3/k_4 or both must change with temperature. Equation 5 is more sensitive to changes in k_2 than in k_3 or k_4, and the simplest assumption, therefore, is that k_2 must depend markedly on temperature through $Q(T)$. Since the work of Rabinovitch and his co-workers has shown that for polyatomic molecules, in direct contrast to diatomics, the deactivation rate goes down as the temperature goes up, this effect would be in the right direction. The variation of k_3 with temperature is probably very similar to k_2, but we have no knowledge at the present time of the way in which k_4 will behave. According to the mechanism we have chosen, experiments at very low pressure will eliminate the dependence on k_2, but in view of the experimental difficulties, no meaningful information could be obtained concerning k_3 and k_4.

Reaction of Methyl Radicals with Methyl Isocyanide. Cophotolysis of acetone with methyl isocyanide leads to an increased rate of isomerization, which could be due either to photosensitization (see below) or to a reaction of methyl radicals, or both. Reaction with methyl radicals was established by heating mixtures of methyl isocyanide and di-*t*-butyl peroxide[10] at 100°, when methyl cyanide was one of the major products. At the present time we do not know whether this reaction is an isomerization catalyzed by radicals, or whether it is simply an addition of a methyl radical to the carbon atom followed by ejection of the original methyl radical from the nitrogen end of the C–N bond.

Deactivation by Added Gases. A consequence of the mechanism we have proposed is that the rate of isomerization should be reduced by the addition of amounts of inert gases. Using about 1 mm of CH_3NC, at which pressure the isomerization has just about reached the low-pressure limiting rate, the addition of either argon or ethane caused the rate to fall. In both cases, k_{obsd} was reduced by a factor of 10 by the addition of about 200 mm of gas, and continued to fall with increasing gas pressure.

On the other hand, the addition of 20 mm of oxygen completely suppressed the isomerization. Oxygen is not normally regarded as an efficient deactivating molecule, except in those cases where the other molecule is in a triplet state.[11] This would suggest that the species CH_3NC^* and CH_3CN^* could be triplet molecules. Possibly, triplet CH_3NC^* could be formed by direct excitation of the ground state molecules but we feel this is unlikely. The extinction coefficient at 2537 A is low, only because this wavelength is on the extreme tail end of quite a strong absorption band, which therefore is likely to correspond to a singlet–

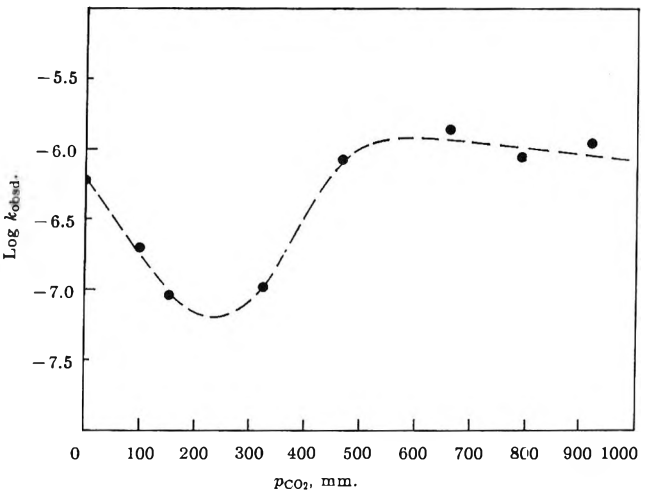

Figure 2. Variation of isomerization rate of 1 mm of CH_3NC with CO_2 pressure.

singlet transition. In the absence of any information about the available electronic states of the molecules CH_3NC and CH_3CN, we cannot speculate further.

Photosensitization by Added Gases. Figure 2 shows the variation of the rate of isomerization of 1 mm of CH_3NC in the presence of various pressures of CO_2. In the pressure range 0–200 mm the rate falls as expected, but instead of continuing to fall, it begins to rise and eventually settles down at a rate approximately twice the low-pressure limiting rate. We interpret the three regions of the graph as follows. (a) At 0–200 mm normal deactivation occurs as discussed above. (b) At 200–500 mm, if we assume that CO_2 has an extinction coefficient at 2537 A of around 10^{-3} l. mole^{-1} cm^{-1} (no experimental figure is available[12]), the absorption of radiation by CO_2 will begin to overtake the absorption by CH_3NC, and the rate of isomerization will rise if

$$CO_2^* + CH_3NC \longrightarrow CO_2 + CH_3NC^*$$

is a rapid process. (c) At 500–1000 mm the rate does not continue to rise, because at high pressures CO_2^* will be deactivated by

$$CO_2^* + CO_2 \longrightarrow CO_2 + CO_2$$

so that above about 500 mm, the increased rate of activation by absorption is balanced by the increasing collisional deactivation.

(10) G. O. Pritchard, H. O. Pritchard, and A. F. Trotman-Dickenson, *J. Chem. Soc.*, 1425 (1954).

(11) G. Porter and M. R. Wright, *Discussions Faraday Soc.*, **27**, 18 (1959).

(12) E. C. Y. Inn, K. Watanabe, and M. Zelikoff, *J. Chem. Phys.*, **21**, 1648 (1953).

The effect of adding N_2O is similar, except that the region (a) in which normal deactivation occurs is much less marked, and extends, at most out to 50 mm pressure. N_2O is known to absorb at 2537 A and also at longer wavelengths, but so far this absorption has been considered as resulting in dissociation of the molecule.[13] If the increased rate of isomerization of CH_3NC were due to catalysis by dissociation products of N_2O, the rate would continue to rise with N_2O pressure. We find, however, that the behavior is similar to that of CO_2, which we believe is a true photosensitization, and this in turn implies that N_2O must be excited to a nondissociating state N_2O^* by 2537-A radiation.

Addition of a few millimeters of benzene causes the rate of isomerization to increase by a factor of about 8, and further increase in benzene pressure does not cause any further rise. In this respect, the behavior is very similar to the effect of benzene on *cis–trans* isomerization about a double C–C bond.[14] Large pressures of oxygen do not photosensitize the isomerization.

It appears that photosensitization can take place by at least two distinct mechanisms, one chemical and the other physical. The chemical mechanism is important in many mercury-photosensitized decompositions, including that of CH_3NC and the xenon-photosensitized decomposition of fluorocarbons.[15] Physical photosensitization, which probably admits a wide variety of subclasses, is evidenced by the benzene-photosensitized *cis–trans* isomerizations,[14,16] by acetone-photosensitized decomposition of azomethane,[17] and by various examples discovered in this work, *i.e.*, the photosensitization of CH_3NC isomerization by CO_2^*, N_2O^*, $C_6H_6^*$, and CH_3CN^*. It seems likely that the occurrence of this second form of photosensitization is much more widespread than was hitherto imagined.

(13) M. Zelikoff, K. Watanabe, and E. C. Y. Inn, *J. Chem. Phys.*, **21**, 1643 (1953).

(14) R. B. Cundall, F. J. Fletcher, and D. G. Milne, *Trans. Faraday Soc.*, **60**, 1146 (1964).

(15) G. H. Miller and J. Dacey, *J. Phys. Chem.*, **69**, 1434 (1965).

(16) G. B. Kistiakowsky and C. S. Parmenter, *J. Chem. Phys.*, **42**, 2942 (1965).

(17) R. E. Rebbert and P. Ausloos, *J. Am. Chem. Soc.*, **87**, 1847 (1965).

Photolytic Processes in Perfluorocyclobutanone Vapor

by David Phillips

Department of Chemistry, University of Texas, Austin, Texas *(Received November 1, 1965)*

The photolysis of perfluorocyclobutanone in the vapor phase at 3130, 3340, 3660, and 4047 A has been investigated. Fluorescence and decomposition yields have been determined at the four wavelengths and the effects of pressure and temperature upon them studied. Two modes of decomposition occur at the shortest wavelengths and at high temperatures, one producing carbon monoxide and perfluorocyclopropane, the other producing tetrafluoroethylene. A mechanism is proposed which explains the results, and rate constants for reactions are determined. Results indicate that about 7 kcal mole^{-1} excess vibrational energy can be removed from the excited ketone by each collision with an unexcited ketone molecule.

Introduction

The photolysis of cyclic ketones has been reviewed by Srinivasan.[1] The only modes of reaction in the vapor phase which are common to the ketones with four, five, six, and seven carbon atoms are (a) decomposition to give carbon monoxide and a cyclic hydrocarbon and (b) a Norrish Type III[2] rearrangement to give a terminally unsaturated aldehyde.

Reaction b involves the migration of a hydrogen atom from one carbon atom to another. Reactions peculiar to individual ketones are also observed which again require hydrogen atom transfer.

It has been demonstrated recently that in the photolysis of perfluorocyclopentanone and perfluorocyclohexanone at 3130 A, the reactions analogous to those which involve hydrogen migration do not occur, the sole mode of decomposition being that which produces carbon monoxide and a cyclic fluorocarbon.[3]

The present work was undertaken to extend the comparison to perfluorocyclobutanone, which has been reported to decompose in the liquid phase upon irradiation with an ultraviolet lamp to give perfluorocyclopropane and carbon monoxide in a 1:1 ratio.[4] The photolysis of ordinary cyclobutanone at around 3130 A leads to the formation of ethylene, ketene, carbon monoxide, propylene,[5] and cyclopropane,[6] together with small amounts of an isomer, presumed to be 3-butenal.[7]

A recent study has confirmed these findings, although the 3-butenal was shown to be a very minor product.[8] This study showed the ratio C_2H_4/CO to be 1.7 ± 0.1 and to be independent of pressure and exciting wavelength, and to vary only slightly with temperature. The reaction scheme proposed was

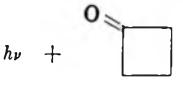

$$h\nu + \quad \longrightarrow \quad C_3H_6CO \qquad (1)$$

$$C_3H_6CO \xrightarrow{k_2} C_2H_4 + CH_2CO \qquad (2)$$

$$\xrightarrow{k_3} c\text{-}C_3H_6^* + CO \qquad (3)$$

$$\xrightarrow{k_4} H_2C{=}CH{\cdot}CH_2CHO \qquad (4)$$

$$c\text{-}C_3H_6^* \xrightarrow{k_5} CH_3CH{=}CH_2 \qquad (5)$$

$$c\text{-}C_3H_6^* + M \xrightarrow{k_6[M]} c\text{-}C_3H_6 + M \qquad (6)$$

C_3H_6CO is some excited intermediate, possibly a biradical. The asterisk indicates a highly vibrationally excited state.

The photolysis of perfluorocyclobutanone was not expected to produce products arising from reactions analogous to (4) and (5), since migration of a fluorine atom would be involved.

Experimental Section

Photolyses were carried out in quartz T-shaped cells

(1) R. Srinivasan, *Advan. Photochem.*, **1**, 83 (1963).
(2) R. G. W. Norrish, *et al.*, *J. Chem. Soc.*, 874 (1934); 1504 (1935).
(3) J. R. Majer and D. Phillips, unpublished work.
(4) D. C. England, *J. Am. Chem. Soc.*, **83**, 2205 (1961).
(5) S. W. Benson and G. Kistiakowsky, *ibid.*, **64**, 80 (1942).
(6) F. E. Blacet and A. Miller, *ibid.*, **79**, 4327 (1957).
(7) R. Srinivasan, *ibid.*, **81**, 5541 (1959).
(8) R. F. Klemm, D. N. Morrison, P. Gilderson, and A. T. Blades, *Can. J. Chem.*, **43**, 1934 (1965).

connected to a conventional grease-free high-vacuum system. For photolysis at 3130 A, a cell of volume 170 ± 1 ml was used. The group of lines around 3130 A was isolated by a standard arrangement of filters[9] from the spectrum emitted by a dc-operated Osram HBO 500-w high-pressure mercury arc. Owing to the high intensities emitted, it was found necessary to have continuously flowing solutions of potassium chromate and potassium biphthalate to avoid their deterioration and consequent fluctuations in incident intensity.

The approximately parallel beam of light traversing the reaction cell was focused by a lens onto the envelope of an RCA 935 phototube, whose output was recorded on an RCA W. V. 84-C sensitive dc microammeter. Meter readings were calibrated in terms of quanta per second using the ferrioxalate actinometer.[10] The number of quanta absorbed per milliliter per second was determined from the difference in meter readings with the cell empty and the cell full. This method gave the quantum yield for formation of carbon monoxide from acetone at 3130 A, 120° as 0.98. Temperatures above room temperature were maintained to ±1° by heating an aluminum block furnace surrounding the cell with a nichrome wire.

Photolyses at 3340, 3660, and 4047 A and all emission experiments were performed in a quartz cell of 6-cm length, 3-cm internal diameter with a 3-cm diameter T window. The total volume of the cell was 61 ± 1 ml. Wavelengths were selected by focusing light from the Osram lamp onto the entrance slits of a Bausch and Lomb 33-86-45 grating monochromator blazed at 3000 A. Most experiments were performed by use of 1-mm entrance and 1-mm exit slit widths, although sometimes 3-mm entrance and 1-mm exit slits were used. Emergent light was made approximately parallel and, after traversing the cell, was monitored on the same phototube and ammeter as before. When long irradiation times were used, the output from the RCA 935 phototube was recorded as a function of time on a Varian G.10 xy recorder, and any fluctuations in I_a were accounted for by graphical integration of the area under the curves.

Emission spectra were taken photographically using a Hilger and Watts quartz prism spectrograph Type E517 in conjunction with Kodak Type 103-0 plates. The optical density of the spots due to emission was taken from Jarrel-Ash recording microdensitometer tracings and plotted as a function of wavelength.

Emission measurements were taken by means of a 1P28 photomultiplier tube mounted in the T-piece of the reaction cell housing powered from a Kepco ABC dc power supply. Currents were displayed on the same RCA microammeter. A Corning CS-O-51 filter was placed between the cell and photomultiplier tube to eliminate background readings due to scattered incident light of wavelengths 3130, 3340, and 3660 A. Absolute quantum yields for emission were obtained by calibrating the photomultiplier tube with biacetyl at 4047 A. Q_E for biacetyl was taken as 0.145,[11] and readings were corrected for the different sensitivities of the photomultiplier tube to the emission from biacetyl and that from the ketone. The sensitivity of the RCA 935 phototube at different wavelengths was also taken into account in the measurement of quantum yields. The emission yield for 10 cm of acetone at 25° excited at 3130 A was found by this method to be 2.8×10^{-3}, compared with a published value of 2.6×10^{-3}.[12]

After photolysis, the contents of the cell were admitted to a trap cooled in liquid nitrogen, and any noncondensibles pumped through a Toepler pump into a McLeod gauge connected to a large volume, 1180 ml. As a check in several experiments, solid N_2 at −210° was first employed as a coolant, the McLeod reading taken, and then liquid N_2 substituted and pumping continued. In no case was there any change in McLeod reading upon substitution of liquid N_2. The noncondensible gas was assumed to be carbon monoxide.

When complete analysis was required, the liquid nitrogen was replaced by a powdered solid CO_2 coolant after the removal of the CO, and noncondensibles at this temperature were pumped off and frozen into a small capillary tube at liquid N_2 temperature. It was found that the reaction products could be quantitatively removed in this way and only a small amount of the parent compound distilled over. This greatly improved the vpc analysis. Analysis was carried out in an Aerograph Hy-Fi 600-C chromatograph at 205° using a 7.62 m long, 0.32-cm internal diameter copper column packed with 30–60 mesh silica gel, and a flame ionization detector. Good separation of fluorocarbons was obtained.

Occasionally, the capillary containing the products was introduced into a Consolidated CEC 21-102 mass spectrometer for analysis, or the products were frozen into an nmr tube containing Spectrograde n-hexane and sealed off. In two experiments the products were frozen into a tube containing 1 ml of conductivity water, and its pH was subsequently measured on a Beckman pH meter with micro electrodes.

(9) M. Kasha, *J. Opt. Soc. Am.*, **38**, 929 (1948).

(10) C. A. Parker, *Proc. Roy. Soc.* (London), **A220**, 104 (1953); C. G. Hatchard and C. A. Parker, *ibid.*, **A235**, 518 (1953).

(11) G. M. Almy and P. R. Gillette, *J. Chem. Phys.*, **8**, 37 (1940).

(12) G. W. Luckey and W. A. Noyes, Jr., *ibid.*, **19**, 227 (1951).

Materials

Perfluorocyclobutanone was very generously donated by Dr. D. C. England of E. I. du Pont de Nemours and Co. The compound is a pale yellow liquid boiling at 1°. The only impurities found to a small extent were products of photolysis, due to the very light-sensitive nature of the ketone. These could be removed by pumping on the compound frozen at solid CO_2 temperatures.

Perfluorocyclohexane, mp 51°, bp 52°, was obtained from the Pierce Chemical Co. Ltd. It contained no impurities detectable by vpc analysis on the silica gel column.

Perfluorocyclobutane as "Freon C-30" was obtained from Matheson Chemical Co. in a cylinder. No impurities were detectable by vpc analysis.

Tetrafluoromethane as "Freon 14" was obtained from Matheson Chemical Co. Vpc analysis showed it to be free of impurity.

Methyl fluoride was obtained in a cylinder from Matheson Chemical Co. It was distilled *in vacuo* and the middle third was retained. No impurities were detected in this fraction by vpc analysis.

Tetrafluoroethylene was prepared by heating Teflon to a temperature of 500° under vacuum, after Heicklen, *et al.*[13] The material contained higher fluorocarbons, but could be satisfactorally separated from them by removal from a liquid N_2–C_2H_5OH slush. This material contained about 3% impurity, but was considered sufficiently pure for column calibration.

Cyclopentane was Spectroquality obtained from Matheson Coleman and Bell. It contained a number of lower boiling impurities and was distilled *in vacuo*. The middle third was retained. This contained less than 2% impurities.

n-Hexane was Spectroquality from Matheson Coleman and Bell. It was distilled *in vacuo* and the middle third was retained. No impurities were observed by vpc analysis.

Biacetyl was obtained from Matheson Coleman and Bell. It was distilled on the line at low pressures and the middle third was retained. It was stored at room temperature.

Acetone was Spectroquality obtained from Matheson Coleman and Bell. It was distilled on the line at low pressure and the middle third was retained. Analysis on a dinonyl phthalate column at 50° showed this fraction to be pure.

Oxygen was prepared on the line by heating Analytical grade potassium permanganate, $KMnO_4$, and passing the gases through a liquid N_2 trap to remove water.

All compounds were degassed several times before use and with the exception of biacetyl were stored at liquid N_2 temperatures.

Results

The ultraviolet absorption spectrum of perfluorocyclobutanone in the vapor phase extends from 3000 to 4200 A with a maximum at 3800 A. There is banded structure on the long wavelength side resembling that of cyclobutanone. At the four wavelengths used in these experiments Beer's law was obeyed, and the molar extinction coefficients were determined to be $\epsilon_{4047} = 4.96$, $\epsilon_{3660} = 11.77$, $\epsilon_{3340} = 5.30$, and $\epsilon_{3130} = 1.55$ l. mole^{-1} cm^{-1}.

The large long-wavelength shift of the spectrum of perfluorocyclobutanone compared with cyclobutanone required a check that there was no isomeric impurity in the sample. An nmr analysis for F_{19} showed only two peaks in a 2-to-1 ratio, and the mass spectrometric cracking pattern was entirely typical of a cyclic ketone.

The emission spectrum of perfluorocyclobutanone extends from about 4000 to 5000 A and is a satisfactory mirror image of the absorption spectrum. The extent of the spectrum was found to be independent of exciting wavelength and of the presence of large pressures of oxygen. This identified the emission as singlet–singlet emission (fluorescence). From the overlap of absorption and emission spectra the O–O band was estimated to be at about 4050 A. The radiative lifetime of the fluorescent state was calculated from the integrated absorption to be 1.17×10^{-5} sec.[14]

The effect of pressure of perfluorocyclobutanone upon the fluorescence yields Q_λ, the ratio of number of molecules emitting to the number of quanta of light of wavelength λ absorbed, is shown in Figure 1. There is some evidence of quenching at 4047 A. A plot of the reciprocal of Q_{4047} against perfluorocyclobutanone concentration in moles per liter showed a linear position above a certain concentration whose equation given by the method of least mean squares was

$$1/Q_{4047} = (873 \pm 93)[\mathrm{K}] + 44.5 \pm 1.6 \qquad \text{(I)}$$

where [K] is the concentration of the ketone in moles per liter.

The emission yield at 3660 A, Q_{3660}, is apparently independent of pressure after an initial rise, whereas Q_{3340} rises approximately linearly with pressure from the origin. Q_{3130} also increases with increasing pressure from zero at zero pressure, but the relationship is not linear. A plot of log Q_{3130} against log [K] indicated that Q_{3130} varied as $[K]^{1.84}$.

(13) J. Heicklen, V. Knight, and S. A. Greene, *J. Chem. Phys.*, **42**, 221 (1965).

(14) M. Kasha, *Radiation Res. Suppl.*, **2**, 243 (1960).

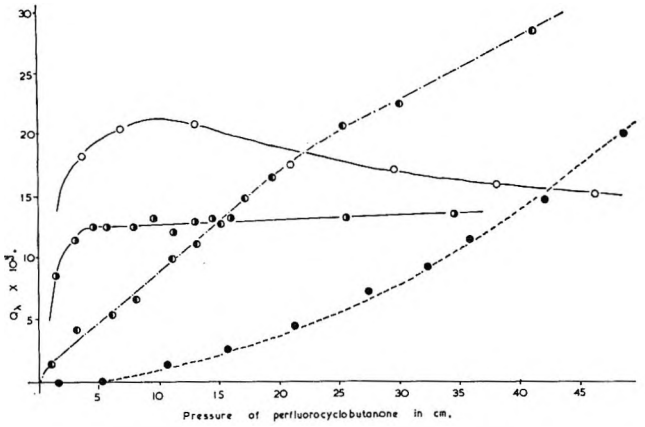

Figure 1. Effect of pressure of perfluorocyclobutanone on Q_f at 25°: O, 4047-A exciting wavelength, $y = 3$; ◑, 3660-A exciting wavelength, $y = 3$; ◐, 3440-A exciting wavelength, $y = 4$; ●, 3130-A exciting wavelength, $y = 5$.

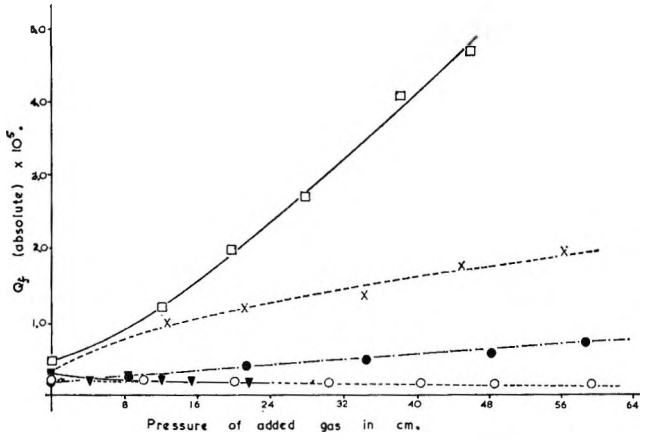

Figure 2. Effect of added gas upon Q_f at 3130 A, 25°: □, perfluorocyclobutane, ketone pressure 21.2 cm; X, tetrafluoromethane, ketone pressure 17.4 cm; ▼, cyclopentane, ketone pressure 17.0 cm; ●, methyl fluoride, ketone pressure 14.9 cm; O, oxygen, ketone pressure 14.5 cm.

The effect upon fluorescence yields excited by 3130- and 3340-A radiation of addition of foreign gases is shown in Figures 2 and 3, respectively. It can be seen that compounds containing large numbers of C–F bonds have the most pronounced effect upon the yields. Addition of large pressures of perfluorocyclobutane, tetrafluoromethane, methyl fluoride, or oxygen had no effect upon the fluorescence yields when excited by 4047- or 3660-A radiation, but addition of cyclopentane, *n*-hexane, and biacetyl at 3660 A and cyclopentane at 4047 A drastically reduced the yields. A plot of the reciprocal of Q_{3660} against concentration of biacetyl in moles per liter is shown in Figure 4. No sensitized triplet emission from the biacetyl was observed.

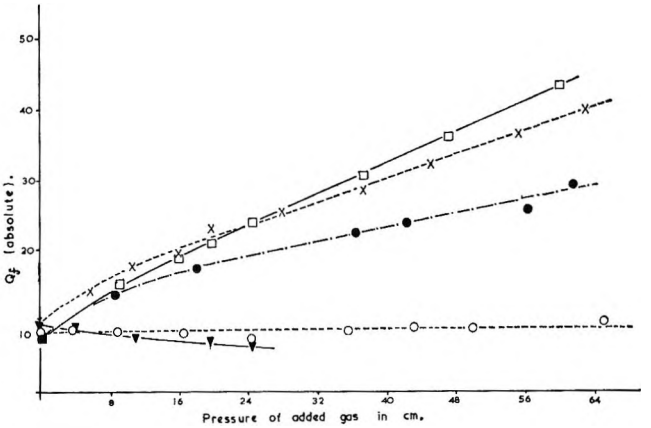

Figure 3. Effect of added gas upon Q_f at 3340 A, 25°: □, perfluorocyclobutane, ketone pressure 9.8 cm; X, tetrafluoromethane, ketone pressure 11.5 cm; ●, methyl fluoride, ketone pressure 9.2 cm; O, oxygen, ketone pressure 9.2 cm; ▼, cyclopentane, ketone pressure 11.3 cm.

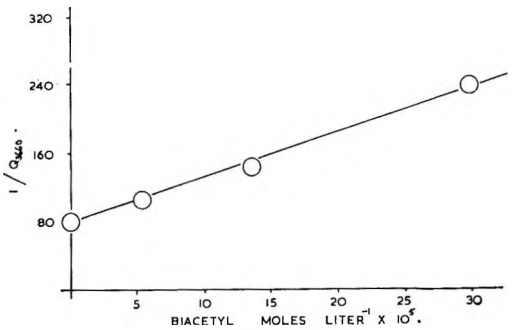

Figure 4. Effect of biacetyl pressure upon $1/Q_{3660}$. Pressure of C_4F_6O 25 mm, 25°.

Increase in temperature at all wavelengths caused a reduction in the value of the absolute fluorescence yield, as shown in Figure 5.

Decomposition

Vapor phase chromatographic analysis of photodecomposition products showed there were three peaks due to volatile fluorocarbons. The first of these was identified as tetrafluoroethylene by comparison of retention times with an authentic sample. The second was identified as perfluorocyclopropane by mass spectrometry and a comparison of its retention time with that found theoretically from a plot of log (retention time) against number of carbon atoms for the homologous series *c*-C_nF_{2n}. *c*-C_4F_8 and *c*-C_6F_{12} were used as reference compounds, and the theoretical retention time for $n = 3$ was found from the plot and found to be identical with that of the second peak in the analysis.

The small third peak obtained under some conditions

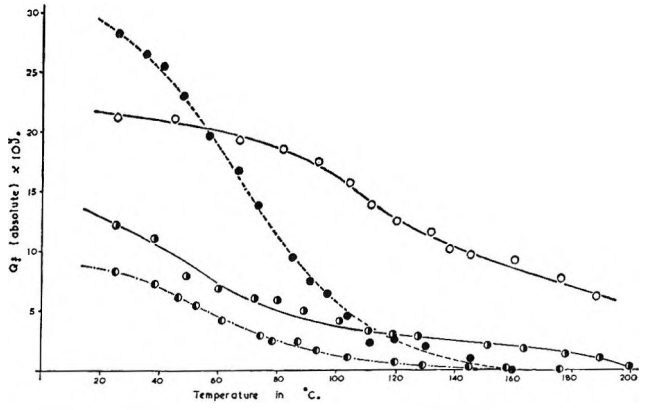

Figure 5. Effect of temperature upon Q_f excited at 3130, 3340, 3660, and 4047 A: ○, 4047 A, ketone pressure 9.6 cm, $y = 3$; ◑, 3660 A, ketone pressure 4.6 cm, $y = 3$; ◐, 3340 A, ketone pressure 9.8 cm, $y = 4$; ●, 3130 A, ketone pressure 16.3 cm, $y = 5$.

was tentatively identified as perfluoropropylene, since it appeared as a decomposition product of the pyrolysis of Teflon under vacuum at 450 to 480°, as reported by Heicklen,[13] and eluted from the silica gel column between perfluorocyclopropane and perfluorocyclobutane, as reported recently.[15] It was found in insufficient quantities to carry out a reliable mass spectrometric analysis.

A vpc analysis failed to show any peak that could be due to difluoroketene, CF_2CO, although it seems likely that under the column conditions used this material might polymerize. An attempt was made to demonstrate its presence by dissolving the products of reaction in 1 ml of distilled water and measuring the pH of the resulting solution. It was anticipated that any CF_2CO could hydrolyze to $CF_2H \cdot COOH$, which would cause a marked drop in pH. Although such a drop was indeed observed, the results could not be interpreted as showing the presence of CF_2CO since the parent ketone itself gave a very acidic hydrate, and the absolute separation of products from starting material could not be ensured.

Since no authentic sample of perfluorocyclopropane was available at the time the experiments were performed, quantum yields for its formation were determined by comparison of peak areas with that of one experiment at 4047 A, where it was assumed that carbon monoxide and c-C_3F_6 were formed in equal amounts. The same sensitivity of the vpc detector to perfluoropropene was assumed.

In experiments performed at 3130 A, carbon monoxide was the only product determined with one exception where complete analysis was effected. The quantum yield for formation of carbon monoxide, Φ_{CO}, was found to be independent of the number of quanta absorbed by the ketone over a fivefold range, and to vary only very slightly with concentration of ketone over a tenfold range. A least-mean-squares treatment of the data indicated the relationship

$$\Phi_{CO} = 0.402 \pm 0.013 + (3.10 \pm 1.26)[K] \quad \text{(II)}$$

where [K] is the concentration of perfluorocyclobutanone in moles per liter. It can be seen that the slope of this line is virtually zero. A single experiment with 176 mm of cyclopentane added to 14.4 mm of ketone at 25° had no apparent effect on the quantum yield for CO formation, but a series of runs adding c-C_4F_8 up to a pressure of 560 to 164 mm of ketone at 25° yielded the relationship

$$\Phi_{CO} = 0.40 \pm 0.03 + (4.6 \pm 1.9)[M] \quad \text{(III)}$$

where [M] is the concentration of c-C_4F_8 in moles per liter.

The single experiment where complete analysis was effected showed that within experimental error the sum of the yields of CO and C_2F_4 was unity and that the sum of the yields of c-C_3F_6 and C_3F_6 was approximately equal to the CO yield (Table I).

Over the temperature range 25 to 250°, the quantum yield of carbon monoxide showed no real trend with temperature at constant ketone pressure and absorption. A least-mean-squares treatment of the data indicated that

$$\Phi_{CO} = 0.409 \pm 0.015 + (0.32 \pm 0.12)T \times 10^{-3} \quad \text{(IV)}$$

where T is the temperature in °C.

The variation in quantum yields of products at different wavelengths with change in pressure of ketone is shown in Table I. The yield of CO at 3340 A is essentially independent of pressure, but at 3660 and 4047 A there is some reduction in CO yield with increase in pressure, although the trend in results at 3660 A may be more apparent than real. A plot of reciprocal of Φ_{CO} at 4047 A against concentration of perfluorocyclobutanone gave the relationship

$$1/\Phi_{CO} = 1.006 \pm 0.008 + (7.4 \pm 0.9)[K] \quad \text{(V)}$$

The effect of temperature upon quantum yields is shown in Figure 6. It can be seen that an increase in temperature tends to decrease the yield of CO to its value at 3130 A and correspondingly increase the yield of C_2F_4. Figure 6 also shows that at 3340 A, an increase in temperature favors the formation of per-

(15) M. B. Fallgatter and R. G. Hanrahan, *J. Phys. Chem.*, **69**, 2059 (1965); S. A. Greene and F. M. Wachi, *Anal. Chem.*, **35**, 928 (1960).

Table I: Variation of Product Yield with Pressure of Perfluorocyclobutanone at 25°

I_a, quanta ml^{-1} sec^{-1} × 10^{-11}	Time of irradiation, min	Pressure of C_4F_8O, cm	Φ_{CO}	$\Phi_{c\text{-}C_3F_6}$	$\Phi_{C_2F_4}$	$\Phi_{C_3F_6}$
			Wavelength 3130 A			
9.246	2785	29.7	0.417	0.356	0.551	0.109
			Wavelength 3340 A			
1.277	1145	4.7	0.506	0.405	0.420	0.063
4.917	1100	8.2	0.583	NA[a]	NA	NA
2.131	1080	10.0	0.596	0.391	0.485	0.052
6.487	3855	17.8	0.556	NA	NA	NA
3.688	1590	20.1	0.612	NA	NA	NA
4.686	1090	29.5	0.534	NA	NA	NA
7.130	1020	40.7	0.558	NA	0.403	NA
			Wavelength 3660 A			
0.869	1053	1.0	0.969	NA	NA	NA
3.032	1170	2.0	0.982	NA	NA	NA
51.137	150	2.5[b]	NA	1.005	0.022	0.018
80.311	300	4.7	0.896	NA	NA	NA
15.243	1020	4.8	0.945	NA	NA	NA
11.145	1305	6.15	0.921	0.999	0.045	0.000
13.210	150	10.2	0.902	NA	NA	NA
			Wavelength 4047 A			
2.631	1250	4.1	0.969	0.927	0.000	0.006
2.837	385	9.4	0.969	NA	NA	NA
5.953	965	10.5	0.956	NA	NA	NA
8.261	3960	12.4	0.949	NA	0.008	NA
9.462	1087	14.8	0.931	NA	0.000	0.000
12.719	990	20.3	0.940	NA	0.002	NA
17.734	1070	29.5	0.879	NA	0.002	0.003

[a] NA means not analyzed. [b] Contained 12 mm of O_2 in starting material.

fluoropropylene at the expense of perfluorocyclopropane.

Discussion

It is evident from the effects of both wavelength and temperature upon the results that the vibrational level of the first excited singlet state reached upon absorption is critical in determining the fate of the molecule. Before discussion of the mechanism of the reaction, it is necessary to determine whether or not a triplet state is involved. The existence of pressure effects upon fluorescence yields indicates that the mean lifetimes of the excited state or states are such that collisions can occur before reaction. Although reaction between a triplet state and oxygen may occur only in one collision or less per 1000, the complete lack of effect in this system of addition of very large pressures of oxygen is presumptive evidence that triplet states do not participate in emission or dissociation. However, if the mean lifetime of any triplet state were less than about 10^{-5} sec, then the use of oxygen in the present instance would not give evidence concerning the participation of a triplet state in decomposition.

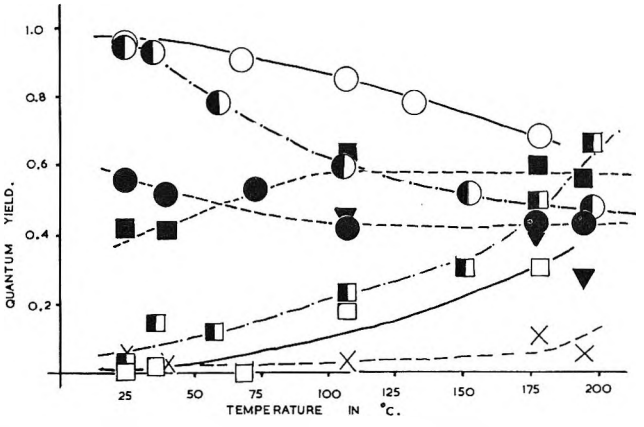

Figure 6. Effect of temperature upon product yields: O, average of CO and c-C_3F_6 yields; □, C_2F_4 yield; unshaded, 4047 A, ketone pressure 9.7 cm; half-shaded, 3660 A, ketone pressure 4.6 cm; shaded, 3340 A, ketone pressure 9.4 cm; O, CO yield; ∇, c-C_3F_6 yield; X, C_3F_6 yield.

With the same qualification, the lack of any sensitized triplet emission from biacetyl in this system is taken as evidence that no intermolecular triplet energy transfer between biacetyl and perfluorocyclobutanone occurs. It can be assumed, then, that the triplet state of the perfluorocyclobutanone is not populated under the conditions of these experiments.

The use of the Osram lamp, with resulting achromaticity of the incident radiation, makes the results difficult to interpret rigorously since several vibrational states of the upper singlet must be reached upon absorption. Thus in the mechanisms below, n refers to the group of levels initially reached upon absorption rather than a single level, and rate constants are the average of these for each level populated. Because of the very high quantum yields of decomposition even from the excited state produced with very little excess vibrational energy, there is a possibility that absorption is to two states, one a repulsive state leading to dissociation, the other a vibrational level or levels of the first excited singlet. However, there is no evidence of a continuum in the absorption spectrum, so the assumption is made that all processes occur from the first excited singlet.

The states ^1K_n formed by absorption (7) may decompose in two ways, (8) and (9), or lose vibrational energy by collision (10) to form the fluorescent state $^1K_0$. This state may also be quenched (12).

$$K + h\nu \longrightarrow {}^1K_n \tag{7}$$

$${}^1K_n \longrightarrow CO + c\text{-}C_3F_6 \tag{8}$$

$${}^1K_n \longrightarrow C_2F_4 + CF_2CO \tag{9}$$

$${}^1K_n + K \longrightarrow {}^1K_0 + K \tag{10}$$

$${}^1K_0 \longrightarrow h\nu_f + K \tag{11}$$

$${}^1K_0 + K \longrightarrow K + K \tag{12}$$

Now for absorption of 4047-A radiation, $k_9 = 0$, and the mechanism predicts that

$$1/\Phi_{CO} = 1 + \frac{k_{10}}{k_8}[K] \tag{VI}$$

This compares well with the experimentally obtained (V) and gives a value of 7.4 ± 0.9 mole^{-1} l. for k_{10}/k_8. The mechanism also predicts that for pressures of ketone such that $k_{12}[K] > k_{11}$

$$1/Q_{4047} = \frac{k_8k_{12}}{k_{10}k_{11}} + \frac{k_{12}}{k_{11}}[K] \tag{VII}$$

Comparison with the experimentally obtained (I) yields a value of 873 ± 93 mole^{-1} l. for k_{12}/k_{11}. Substitution of this value into the intercept from (I) gives a value of 20 ± 2 mole^{-1} l. for k_{10}/k_8, which is reasonably close to that obtained from (V) in view of the experimental difficulty of measuring small changes in CO quantum yields which are close to unity. The value of k_{10}/k_8 from the emission work is felt to be the more accurate. The self-quenching cross section for ketone molecules was calculated from k_{12}/k_{11} and the radiative lifetime to be 0.012×10^{-16} cm.[2] Since there is no apparent effect upon fluorescence yields of the addition of various foreign gases, the cross section for these molecules must be even smaller, whereas for cyclopentane, which strongly quenches the fluorescence, the cross section must be larger.

Absorption of a quantum of 3660-A radiation produces states with approximately 7.5 kcal mole^{-1} vibrational energy. From Table I, an approximate value for k_9'/k_8' of 0.03 ± 0.01 can be obtained, where the superscript denotes rate constants for the states formed by absorption of 3660-A light. Since $k_8' > k_9'$, eq VI should still hold, and a least-mean-squares treatment of the few data from Table I shows a plot of the reciprocal quantum yield for CO formation at 3660 A against concentration of ketone to be a straight line, whose slope gives a value for k_{10}'/k_8' of 20 ± 6 l. mole^{-1}.

The invariance of Q_{3660} with pressure above 50 mm of ketone is easily explained. The complete expression for Q_{3660} is

$$Q_{3660} = \frac{k_{10}'k_{11}[K]}{(k_{11} + k_{12}[K])(k_8' + k_9' + k_{10}'[K])} \tag{VIII}$$

From the value of k_{12}/k_{11} we know that at pressures above 50 mm, $k_{12}[K] > k_{11}$. Now if over the pressure range studied $k_{10}'[K] < k_8'$ and we know $k_9' < k_8'$, then

$$Q_{3660} = \frac{k_{10}'k_{11}}{k_8'k_{12}} \tag{IX}$$

Thus above 50 mm, Q_{3660} should be invariant with pressure which is as observed. Substitution of the asymptotic value of Q_{3660} from Figure 1 and the previously determined value of k_{12}/k_{11} into (IX) gives a value 11.3 ± 1.2 mole^{-1} l. for k_{10}'/k_8', which is again not too unfavorable a comparison with the previously obtained value when experimental difficulties are considered.

The marked effect of biacetyl and hydrocarbons on Q_{3660} requires that additional possible steps (13), (14), and (15) be added to the scheme.

$${}^1K_n + M \longrightarrow \text{products} \tag{13}$$

$${}^1K_n + M \longrightarrow {}^1K_0 + M \tag{14}$$

$${}^1K_0 + M \longrightarrow \text{products or } K + M \tag{15}$$

The complete expression for $1/Q_{3660}$ then becomes

$$1/Q_{3660} = \frac{(k_8' + k_9' + k_{13}[M] + k_{14}[M] + k_{10}'[K]) \times (k_{11} + k_{12}[K] + k_{15}[M])}{k_{11}(k_{10}'[K] + k_{14}[M])} \quad (X)$$

The observed linearity of the plot of $1/Q_{3660}$ against [M] for the case where [M] is biacetyl concentration in mole l.$^{-1}$ is predicted from X only if certain assumptions are made. The most likely of these is that $k_{13}[M]$ and $k_{14}[M]$ are vanishingly small compared with $k_{10}'[K]$, since the pressures of biacetyl added were very much smaller than that of the ketone present. Then

$$\frac{1}{Q_{3660}} = \frac{(k_8' + k_9' + k_{10}'[K])(k_{11} + k_{12}[K] + k_{15}[M])}{k_{10}'k_{11}[K]} \quad (XI)$$

From the slope of the line in Figure 6 k_{15}/k_{11} was found to be 7.98×10^3 mole^{-1} l., and the cross section for quenching of excited ketone molecules by biacetyl was found to be 0.086×10^{-16} cm^2.

From the results at 3340 and 3130 A, values of $k_9''/k_8'' = 0.79$ and $k_9'''/k_8''' = 1.50$ are obtained, where k'' refers to rate constants for the states produced upon absorption of 3340-A radiation, and k''' to those produced by 3130-A absorption. The two modes of decomposition must be supposed to be arising from the same initially formed state, since there is no effect of pressure upon the ratio of the modes.

The observed effect of pressure upon the fluorescence yields at the two shortest wavelengths cannot be explained by the simple mechanism above, since behavior like that at 3660 A would be predicted. Consideration of what the precise nature of reaction 10 is can offer an explanation for the observed results, however. Reaction 10 is usually only a convenient expression meaning collisional loss of vibrational energy, which in some instances takes place by a multistep cascade down the energy levels.[16,17] However, in some systems large quantities of vibrational energy can be lost in a single collision.[18] Let us suppose in this system that a single collision is sufficient to rob the states formed at 3660 A of all their excess vibrational energy and that this amount, 7.5 kcal, is about the maximum amount of energy that can be lost per collision. Since the states formed upon absorption at 3340 and 3130 A have 14.6 and 20.6 kcal mole^{-1} excess energy, respectively, on this simple basis removal of excess energy from the states at 3340 A would require two collisions and that from the states at 3130 A three collisions. To avoid the necessity of introducing many additional steps to the scheme above, for convenience we can suppose that the states formed by the first collision from those formed by 3130-A absorption are identical with those formed by 3340-A absorption and that these by collision form states identical with those formed by 3660-A absorption. Then with the knowledge that at pressures above 50 mm of ketone $k_{12}[K] > k_{11}$ and assuming again that over the pressure range studied $k_8 + k_9 > k_{10}[K]$ for all states, we can show that

$$Q_{3340} = \frac{k_{11}}{k_{12}} \frac{k_{10}'}{k_8' + k_9'} \frac{k_{10}''}{k_8'' + k_9''}[K] \quad (XII)$$

and

$$Q_{3130} = \frac{k_{11}}{k_{12}} \frac{k_{10}'}{k_8' + k_9'} \frac{k_{10}''}{k_8'' + k_9''} \frac{k_{10}'''}{k_8''' + k_9'''}[K]^2 \quad (XIII)$$

Thus Q_{3340} is predicted by this mechanism to vary linearly with pressure, and Q_{3130} to vary as the square of the pressure of perfluorocyclobutanone. This behavior is remarkably close to that observed. It can be seen that with the assumption that $k_8 + k_9 > k_{10}[K]$ for the two shortest wavelengths, no pressure effect upon quantum yields of decomposition would be anticipated, in agreement with observation. Rate constants and rate constant ratios are summarized in Table II.

The results obtained by increasing the temperature at the three shortest wavelengths can be explained easily on the basis of the mechanism above. In contrast to recent results on cyclopentanone,[8] it is clear that the ratio C_2F_4/CO varies with the amount of excess energy the excited ketone molecules possess. Increase in temperature will lead to an increase in the population of upper vibrational levels of the ground electronic state. Absorption from these levels will populate higher vibrational levels of the excited state than at 25°; thus one would anticipate that the ratio $\Phi_{CO}/\Phi_{C_2F_4}$ would approach its value at 3130 A. Figure 6 shows that despite scatter in the data this is substantially true. The promotion of the ketone to higher vibrational levels upon increasing the temperature would also be expected to decrease the fluorescence yield, since fewer molecules would be expected to reach the fluorescent state (Figure 5).

The appearance of perfluoropropene as a product is not easily explained. It is possible that under extreme conditions a fluorine migration could occur in perfluorocyclopropane giving the perfluoropropene by

(16) A. N. Strachan, R. K. Boyd, and K. O. Kutschke, *Can. J. Chem.*, **42**, 1345 (1964).

(17) G. B. Porter and B. T. Connelly, *J. Chem. Phys.*, **33**, 81 (1960).

(18) J. W. Simons, B. S. Rabinovitch, and D. W. Setser, *ibid.*, **41**, 800 (1964).

Table II: Rate Constants

Constant or ratio	Value obtained	Comment
k_{11}	8.55×10^4 sec^{-1}	From integrated absorption curve
k_{12}	7.46×10^7 l. mole^{-1} sec^{-1}	From (VII) and k_{11}
k_{15}	6.82×10^8 l. mole^{-1} sec^{-1}	From (XI) and k_{11}; subject to validity of assumptions
k_9'/k_8'	0.03	Ratio of $\Phi_{C_2F_4}/\Phi_{CO}$ at 3660 A
k_9''/k_8''	0.79	Ratio of $\Phi_{C_2F_4}/\Phi_{CO}$ at 3340 A
k_9'''/k_8'''	1.50	Ratio of $\Phi_{C_2F_4}/\Phi_{CO}$ at 3130 A
k_{10}/k_8	7.4 ± 0.9 l. mole^{-1}	From (VI) probably inaccurate
	20 ± 2 l. mole^{-1}	From (VII) more accurate
k_{10}'/k_8'	20 ± 6 l. mole^{-1}	From (VI) probably very inaccurate
	11.3 ± 1.2 l. mole^{-1}	From (IX) more accurate
$k_{10}''/(k_8'' + k_9'')$	11.85 l. mole^{-1}	From (XII) assumptions for calculation of these may not be valid, but results are useful guide to probable values
$k_{10}'''/(k_8''' + k_9''')$	1.94 l. mole^{-1}	From (XIII) assumptions for calculation of these may not be valid, but results are useful guide to probable values

a reaction analogous to (5).[8] However, there is evidence that perfluorocyclopropane decomposes by CF_2 ejection to give tetrafluoroethylene as the sole product. Although kinetic evidence suggests that in this system the C_2F_4 observed is formed by reaction 9, it is possible that some C_2F_4 is also formed by decomposition of excited perfluorocyclopropane molecules, especially since the CF_2CO was never found.

The present experiments offer little to determine whether or not a diradical intermediate is involved in the decomposition. One can only say either (a) a diradical is produced which does not react with oxygen or decomposes before collision can occur, or (b) a molecular elimination is the mechanism.

Acknowledgments. The author wishes to thank Dr. D. C. England of E. I. duPont de Nemours and Co. for his generous donation of the perfluorocyclobutanone. He is indebted to Dr. W. A. Noyes, Jr., for his encouragement and advice during the course of this work, and to colleagues for helpful discussions. Support from the Robert A. Welch Foundation and the Air Force Office of Scientific Research, Grant 778-65, is gratefully acknowledged.

Activity and Osmotic Coefficients of Four Symmetrical Tetraalkylammonium Fluorides in Aqueous Solutions at 25°[1]

by Wen-Yang Wen, Shuji Saito, and Chun-meei Lee

Chemistry Department, Clark University, Worcester, Massachusetts 01610 *(Received November 3, 1965)*

Osmotic and activity coefficients of four tetra-*n*-alkylammonium fluorides in aqueous solutions at 25° were determined by the gravimetric isopiestic comparison method for a concentration range of 0.1 to several molal. The mean molal activity coefficients, $\gamma_{\pm}$, of these fluorides were found to be strikingly high and in the increasing order: $(CH_3)_4NF < (C_2H_5)_4NF < (n\text{-}C_3H_7)_4NF < (n\text{-}C_4H_9)_4NF$. The $\gamma_{\pm}$ values of $(n\text{-}C_4H_9)_4NF$ are, in fact, higher than those of any 1–1 electrolytes reported in the literature in the same concentration range at 25°. Water-structure influences seem to play a significant role in determining the activity coefficients of these salts. The large values of $\gamma_{\pm}$ for these fluorides could be attributed to the structural repulsion or "structural salting out" of the cation and the anion against each other arising from the fact that the cation and the anion are structure-making in incompatible modes and therefore, with increasing concentration, compete against each other increasingly to influence the structure of water in different ways.

Introduction

Various tetra-*n*-butylammonium and tetraisopentylammonium salts are known to form hydrates with high water of crystallization.[2] Tetra-*n*-butylammonium fluoride forms a polyhedral clathrate hydrate with a stoichiometric composition of $(n\text{-}C_4H_9)_4NF \cdot 32.8H_2O$. Recently, McMullan, Bonamico, and Jeffrey[3] have reported a detailed X-ray structural analysis on this crystalline hydrate.

Even in liquid solutions, the interaction between this type of tetraalkylammonium salts and water is expected to be strong and to produce a considerable influence on the structure of the system. This expectation has been borne out in previous studies on various physical properties of aqueous solutions containing some of these salts.[4–7]

Measurements on the activity coefficients of various tetraalkylammonium salts have been reported,[8,9] but there seem to be none so far on the fluorides on this series.[10] In this paper we are reporting the osmotic and activity coefficients of four tetra-*n*-alkylammonium fluorides in water at 25° by the isopiestic method for the concentration range of 0.1 to several molal.

Experimental Section

Materials. The aqueous solutions of tetraalkylammonium fluorides, $(CH_3)_4NF$, $(C_2H_5)_4NF$, $(n\text{-}C_3H_7)_4NF$, and $(n\text{-}C_4H_9)_4NF$, were prepared in general by two

(1) Presented before the Division of Physical Chemistry, 148th National Meeting of the American Chemical Society, Chicago, Ill., Aug 30–Sept 4, 1964; see Abstracts, p 35V.

(2) D. L. Fowler, W. V. Loebenstein, D. B. Pall and C. A. Kraus, *J. Am. Chem. Soc.*, 62, 1140 (1940); R. McMullan and G. A. Jeffrey, *J. Chem. Phys.*, 31, 1231 (1959).

(3) R. K. McMullan, M. Bonamico, and G. A. Jeffrey, *ibid.*, 39, 3295 (1963).

(4) W.-Y. Wen, Ph.D. Thesis, University of Pittsburgh, 1957 (Microfilm no. 58-132).

(5) H. S. Frank and W.-Y. Wen, *Discussions Faraday Soc.*, 24, 133 (1957).

(6) J. N. Agar, *Advan. Electrochem. Electrochem. Eng.*, 3, 96 (1963).

(7) W.-Y. Wen and S. Saito, *J. Phys. Chem.*, 68, 2639 (1964).

(8) L. Ebert and J. Lange, *Z. Physik. Chem.*, A139, 584 (1928); J. Lange, *ibid.*, A168, 147 (1934).

(9) S. Lindenbaum and G. E. Boyd, *J. Phys. Chem.*, 68, 911 (1964).

(10) In their book ("The Physical Chemistry of Electrolytic Solutions," 3rd ed, Reinhold Publishing Corp., New York, N. Y., 1958), Harned and Owen have apparently misquoted the osmotic coefficient data of Ebert and Lange (ref 8). Graphs in Figure (12-9-2) of p 528 shown as the tetraalkylammonium fluorides are actually those of iodides.

Table I: Molalities of Isopiestic Solutions at 25°

Reference salt[a]	$(CH_3)_4NF$	Reference salt[a]	$(C_2H_5)_4NF$	Reference salt[a]	$(C_3H_7)_4NF$	Reference salt[a]	$(C_4H_9)_4NF$
0.1058	0.1039	0.1107	0.1050	0.1310	0.1223	0.1144	0.1052
0.1203	0.1167	0.2269	0.2058	0.2102	0.1897	0.1975	0.1746
0.2208	0.2101	0.3566	0.3120	0.3105	0.2703	0.3021	0.2560
0.2255	0.2137	0.6497	0.5319	0.4128	0.3479	0.3811	0.3141
0.3105	0.2887	0.8340	0.6572	0.5295	0.4315	0.4617	0.3696
0.5497	0.4890	1.163	0.8671	0.6024	0.4805	0.5437	0.4237
0.7187	0.6215	1.525	1.079	0.7197	0.5568	0.7522	0.5524
1.107	0.9045	1.889	1.275	0.9224	0.6802	0.8691	0.6210
1.630	1.252	2.293	1.478	1.165	0.8164	1.028	0.7083
2.124	1.553	2.512	1.589	1.314	0.8945	1.206	0.8032
2.383	1.705	2.938	1.782	1.594	1.035	1.313	0.8548
2.564	1.807	3.345	1.961	1.776	1.119	1.509	0.9523
2.795	1.935	3.671	2.101	1.943	1.196	1.606	0.9969
3.503	2.314	I	2.554	2.144	1.282	1.652	1.019
4.026	2.578	A	3.011	2.715	1.519	1.885	1.125
4.718	2.916	B	3.290	2.962	1.615	1.957	1.156
A	3.540	C	3.458	3.221	1.712	2.387	1.346
B	3.900	D	3.597	3.533	1.826	2.745	1.498
C	4.116	E	3.884	3.744	1.900	3.137	1.660
D	4.289	F	4.729	4.053	2.008		
E	4.665	G	5.078	I	2.262		
F	5.770	H	5.520	A	2.663		
G	6.242			C	3.070		
H	6.844			E	3.458		
				F	4.302		
				G	4.689		
				H	5.179		

[a] KCl unless otherwise specified; A, satd $(NH_4)_2SO_4$; B, satd NH_4Cl; C, satd NaCl; D, satd $NaNO_3$; E, satd $SrCl_2$; F, satd NH_4NO_3; G, satd NaBr; H, satd $Mg(NO_3)_2$; I, satd KCl.

methods. The first method was the double metathesis of a corresponding tetraalkylammonium iodide with Ag_2SO_4 and BaF_2 in water, and the completeness of the conversion was checked by the H_2O_2 test for iodide ion and $BaCl_2$ test for sulfate ion. The second method was the pH titration of a corresponding tetraalkylammonium hydroxide solution with HF solution. The tetraalkylammonium hydroxides were, in turn, prepared from the corresponding bromides by passing them through a column of an ion-exchange resin [Fisher Certified Rexyn 201 (OH)].

For $(n\text{-}C_4H_9)_4NF$ the crystalline hydrate $[(n\text{-}C_4H_9)_4NF{\cdot}32.8H_2O$, mp 25°] was prepared and purified by recrystallization from water. The first method (double metathesis) was found to be unsuitable for the preparation of $(C_2H_5)_4NF$, since it produced complexes of undetermined composition. In general, the second method (HF titration of the hydroxide) has yielded desired fluorides of higher purities.

The solutions of tetraalkylammonium fluorides so prepared were carefully analyzed for the cation content and the anion content—cations by gravimetric analysis using $NaB(C_6H_5)_4$ and the anion by gravimetric analysis using $CaCl_2$. The analyses of cations and the anion (F^-) agreed with each other to within 1% in all cases. This 1% precision was partly due to the difficulty of carrying out a very precise fluoride analysis.[11] The concentrations of the stock solutions were determined by the gravimetric analysis of the cations precipitated as $(C_nH_{2n+1})_4NB(C_6H_5)_4$ with a maximum error of 0.1%. All solutions for isopiestic measurements have been made up by diluting the stock solutions with doubly distilled water.

Reagent grade KCl was recrystallized with water and dried at 650° under nitrogen atmosphere.

Apparatus and Measurements. Osmotic and activity coefficients were determined by the gravimetric isopiestic comparison method with an apparatus similar to that employed by Owen and Cooke.[12] The details of the apparatus as well as the procedure of

(11) F. P. Treadwell and W. T. Stone, "Analytical Chemistry," 8th ed, Vol. II, John Wiley and Sons, Inc., New York, N. Y., 1935, p 416.

(12) B. B. Owen and T. F. Cooke, Jr., *J. Am. Chem. Soc.*, 59, 2273 (1937).

Table II: Osmotic and Activity Coefficients of Tetraalkylammonium Fluorides in Aqueous Solutions at 25°

Concn,	$(CH_3)_4NF$		$(C_2H_5)_4NF$		$(n\text{-}C_3H_7)_4NF$		$(n\text{-}C_4H_9)_4NF$	
m	ϕ	$\gamma_\pm$	ϕ	$\gamma_\pm$	ϕ	$\gamma_\pm$	ϕ	$\gamma_\pm$
0.1	0.945	0.795	0.976	0.836	0.976	0.859	1.004	0.904
0.2	0.957	0.776	1.000	0.858	1.014	0.883	1.045	0.955
0.3	0.974	0.778	1.028	0.887	1.051	0.925	1.089	1.025
0.4	0.992	0.787	1.057	0.924	1.090	0.982	1.138	1.115
0.5	1.012	0.802	1.086	0.966	1.133	1.051	1.189	1.220
0.6	1.034	0.823	1.119	1.016	1.178	1.135	1.243	1.336
0.7	1.055	0.846	1.150	1.073	1.225	1.224	1.297	1.468
0.8	1.075	0.873	1.182	1.130	1.273	1.327	1.350	1.618
0.9	1.096	0.902	1.216	1.192	1.323	1.449	1.404	1.785
1.0	1.120	0.931	1.250	1.258	1.374	1.580	1.458	1.940
1.2	1.166	0.998	1.320	1.404	1.483	1.902	1.562	2.409
1.4	1.215	1.077	1.397	1.596	1.596	2.316	1.660	2.895
1.6	1.262	1.171	1.472	1.816	1.707	2.822	1.778	3.595
1.8	1.312	1.276	1.550	2.092	1.824	3.470	...	...
2.0	1.363	1.385	1.629	2.405	1.946	4.295	...	...
2.5	1.489	1.728	1.840	3.49	2.237	7.390	...	...
3.0	1.617	2.170	2.057	5.18	2.527	12.62	...	...
3.5	1.744	2.75	2.298	7.87	2.788	20.85	...	...
4.0	1.879	3.50	2.516	11.90	2.986	33.25	...	...
4.5	2.011	4.48	2.736	17.72	3.180	49.9	...	...
5.0	2.134	5.64	2.962	26.97	3.359	80.1	...	...
5.5	2.257	7.10	3.192	41.85	...	...	...	...
6.0	2.382	9.01	...	...	...	...	...	...
7.0	2.627	14.40	...	...	...	...	...	...

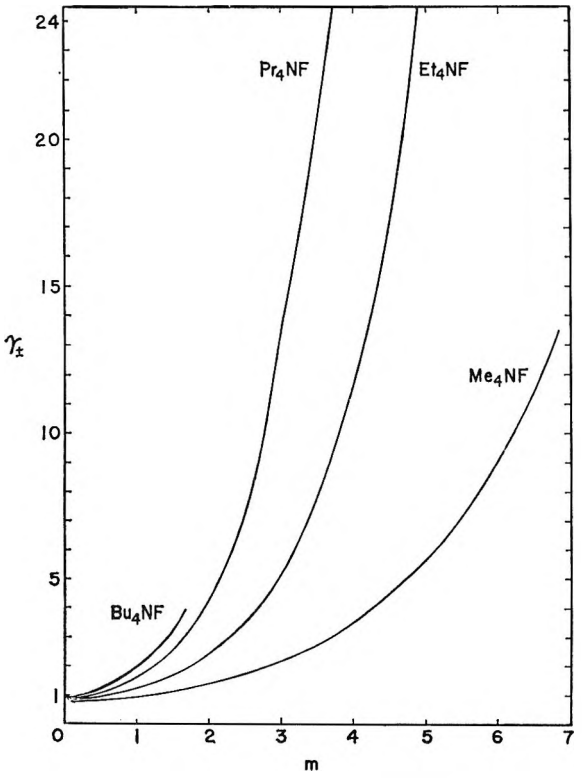

Figure 1. Mean molal activity coefficients, $\gamma_\pm$, of four symmetrical tetraalkylammonium fluorides in aqueous solutions at various molal concentrations, m, at 25°.

measurements have been described previously.[13] Our activity coefficient data are believed to be precise to within 0.5%.

Results and Discussion

The measured molalities of the isopiestic reference salts and tetraalkylammonium fluorides are given in Table I. From these data the osmotic coefficients, ϕ, and activity coefficients, $\gamma_\pm$, for the sample salts were calculated by the method previously described.[13] In the absence of data for concentrations less than 0.1 m our graphical extrapolation method[13] is likely to introduce some error. Consequently, ln $\gamma_\pm$ values so determined may be subject to a small constant correction when data on more dilute solutions become available, perhaps from the freezing-point depression method.[14] The osmotic and activity coefficients of the four tetraalkylammonium fluorides so obtained are given in Table II. For $(n\text{-}C_4H_9)_4NF$ the data are given for concentrations which extend up to about 1.6 m only, since, above this concentration, hydrate crystals with a stoichiometric composition of $(n\text{-}C_4H_9)_4NF \cdot 32.8H_2O$ would separate out from the solution at 25°.

(13) W.-Y. Wen and S. Saito, *J. Phys. Chem.*, 69, 3569 (1965).

(14) In very dilute solutions, however, the hydrolysis of the fluorides may become serious.

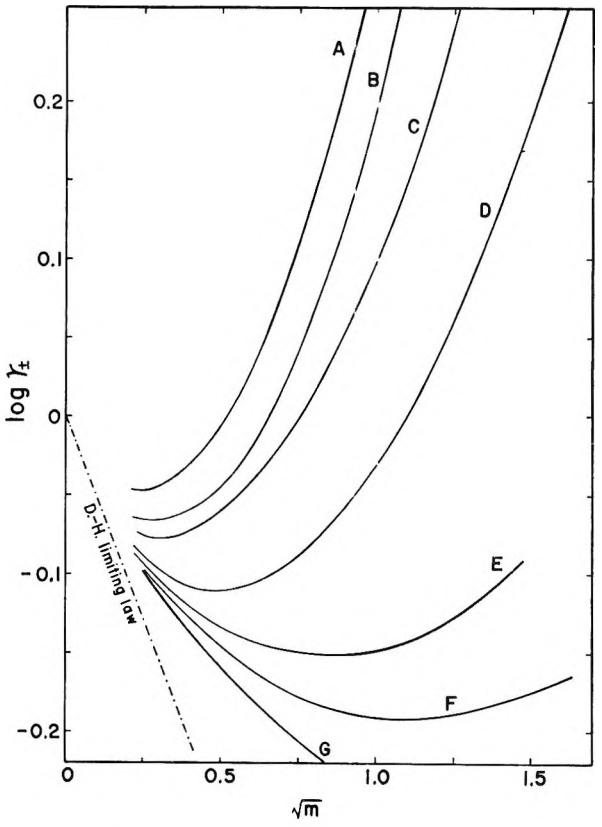

Figure 2. Plots of log $\gamma_{\pm}$ *vs.* $\sqrt{m}$ for fluorides in aqueous solutions at 25°: A, $(C_4H_9)_4NF$; B, $(C_3H_7)_4NF$; C, $(C_2H_5)_4NF$; D, $(CH_3)_4NF$; E, C_6F;[a] F, KF;[b] G, NaF.[b] ([a] H. T. Tien, *J. Phys. Chem.*, **67**, 532 (1963); [b] R. A. Robinson, *J. Am. Chem. Soc.*, **63**, 628 (1941)).

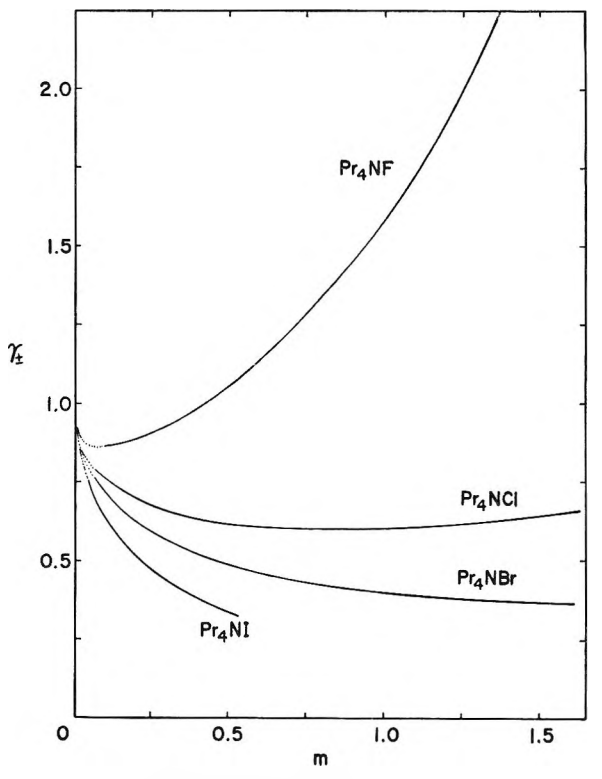

Figure 3. Mean molal activity coefficients, $\gamma_{\pm}$, of tetrapropylammonium fluoride, chloride, bromide, and iodide in aqueous solutions at various molal concentrations, m, at 25°.

Mean molal activity coefficients of the four salts are plotted against molalities in Figure 1 for the entire concentration range studied. In Figure 2 values of log $\gamma_{\pm}$ are plotted against $\sqrt{m}$ for the salts as well as some alkali fluorides in the dilute range for comparison. As can be seen from the tables and figures, the activity coefficients of fluorides with large tetraalkylammonium cations are strikingly large and in the increasing order

$$(CH_3)_4NF < (C_2H_5)_4NF < (n\text{-}C_3H_7)_4NF < (n\text{-}C_4H_9)_4NF$$

The $\gamma_{\pm}$ values for tetrapropyl- and tetrabutylammonium fluorides are, in fact, larger than for any 1–1 electrolytes reported in the literature in the same concentration range at 25°.

One possible way of explaining the remarkably high activity coefficients of these salts is in terms of the specific way in which the structure of water may be considered to be influenced by the ions. Such a structural influence may be discussed in analogy to and also as an extension of Hückel's concept of the electrostatic influence of ions upon water in moderately concentrated solutions.[15]

The self-energy of the charge on each ion, $e^2/2Db_i$, would increase when the ion is no longer in pure water but in a medium of lower dielectric constant D due to the presence of other ions. A lowering of D, produced by the addition of ions, thus has the effect of "salting out the ions" and causing an increase in the activity coefficient. This result corresponds to an effect of repulsive force between the ions. It adds a supplementary term in log $\gamma_{\pm}$ which is opposite in sign to the interionic attraction term.[16]

As suggested by Frank,[17] there will be an additional "medium effect" due to the specific way in which the structure of water is enhanced or disrupted by the ions. If an ion is a structure-maker or a structure-breaker, its free energy of hydration will also be influenced by the ease or difficulty with which the surrounding water can accommodate itself to such influences, and this will be changed if other ions are also changing the water

(15) E. Hückel, *Phys. Z.*, 26, 93 (1925).

(16) If a salt increased the dielectric constant of water, the "medium effect" would be reversed and there would be "salting in of the ions."

(17) H. S. Frank, *J. Phys. Chem.*, 67, 1554 (1963); *Z. Physik. Chem.*, 228, 364 (1965).

structure. There will be, therefore, a "structural salting in" or "structural salting out" of ions by each other and this will appear as a structural influence on log $\gamma_{\pm}$ in addition to the influence brought about by Hückel's "electrostatic salting in or salting out."

Returning to the very high activity coefficients of large tetraalkylammonium fluorides, let us examine the structural influences of the large cation and the small anion upon water. Both R_4N^+ and F^- are structure-making ions in a rough way of description, but they presumably make different kinds of water structures because they are basically different kinds of ions. F^- ion is small and may tend to immobilize water in a more-or-less radial pattern around it owing to its specific size and surface charge density. The R_4N^+ ion is large and tends to enhance the "cage-like" or "clathrate-like" structure of water owing to its hydrophobic properties. The cation and the anion are thus incompatible in their modes of structure making and can be expected to compete against each other to influence structure of water in different ways. Consequently, the presence of a cation and an anion in the vicinity of one another will cause a structural repulsion and result in "structural salting out." The "structural salting out" of cation and anion against each other must also be assumed to outweigh the effect of the "structural salting in" of cation by cation and of anion by anion. Thus, the strong "structural salting out" of R_4N^+ and F^- ions by each other is a possible cause of the very high activity coefficients of these salts in aqueous solutions.

In Figure 3 we have compared the activity coefficients of tetrapropylammonium fluoride, chloride, bromide, and iodide.[18] As shown in the figure, the curves are widely separated for different salts; particularly the $\gamma_{\pm}$ *vs.* m curve is very low-lying for the iodide in sharp contrast to the very high-lying one for the fluoride. The difference between $(C_3H_7)_4NF$ and $(C_3H_7)_4NI$ is enormous and demonstrates the diversity of structural effects exerted by the anions on a cation. The very low values of $\gamma_{\pm}$ for $(C_3H_7)_4NI$ may be explained by the concept of "structural salting in":[17] I^- ion, being a structure-breaker, makes water available, so to speak, for the self-salting in of the $(C_3H_7)_4N^+$ ion, plus the assumption that this effect outweighs the salting out of I^- ion by the cation.

Acknowledgments. This research is supported by the U. S. Department of the Interior, Office of Saline Water, through Grant No. 14-01-0001-306 and No. 14-01-0001-456.

(18) Data for the chloride, bromide, and iodide are those of Lindenbaum and Boyd, ref 9.

Thermochemistry of Charge-Unsymmetrical Binary Fused Halide Systems. II. Mixtures of Magnesium Chloride with the Alkali Chlorides and with Silver Chloride

by O. J. Kleppa and F. G. McCarty

Institute for the Study of Metals and Department of Chemistry, The University of Chicago, Chicago, Illinois 60637
(Received November 8, 1965)

The integral enthalpies of mixing of the liquid mixtures of magnesium chloride with the alkali chlorides and with silver chloride have been determined calorimetrically. The magnesium chloride–silver chloride system is slightly endothermic, while the alkali chloride systems are all exothermic, the negative enthalpy of mixing increasing sharply in the sequence Li < Na < K < Rb < Cs. For the mixtures of magnesium chloride with sodium, potassium, rubidium, and cesium chloride, the enthalpy of mixing changes linearly with the parameter $\delta_{12} = (d_1 - d_2)/d_1d_2$; d_1 and d_2 are the sums of the ionic radii of the two solution partners. This is consistent with the conformal solution theory of Davis for charge-unsymmetrical systems. The integral enthalpy data are discussed with respect to the asymmetry of the interaction parameter ($\Delta H^M/X(1 - X)$) and the deviations of this parameter from a linear dependence on composition. Relative partial enthalpies for magnesium chloride have been derived and have been compared with corresponding excess free energies reported in the literature. The new enthalpy data are interpreted to support the view, originally advanced by Flood and Urnes, that the alkali chloride–magnesium chloride mixtures contain the complex anionic species $MgCl_4^{2-}$. The stability of this species depends strongly on the alkali cation present, and increases from lithium to cesium.

Introduction

Among the binary mixtures formed by fused salts, the simplest ones have two solution partners of identical charge structure containing a common ion. The common ion may be an anion, as in NaCl–KCl, or a cation, as in NaBr–NaCl. In recent communications from this laboratory, the results of a comprehensive thermochemical investigation of binary halide mixtures of the former type have been reported.[1,2]

Somewhat more complex in character are mixed systems in which the two solution partners have different charge structures while they still contain a common ion. Among these systems, particular interest is attached to the mixtures of the divalent halides with the corresponding alkali halides. We have recently reported the results of a thermochemical study of the lead chloride–alkali chloride liquid mixtures.[3] In the present communication, our investigation of this type of solution system is extended to the mixtures of magnesium chloride with the alkali chlorides and with silver chloride.

The magnesium chloride–alkali chloride systems have in the past attracted considerable attention due to the possible existence of the complex $MgCl_4^{2-}$ in the melts. This possibility has been discussed in particular by Flood, Førland, and co-workers,[4,5] and very recently by Neil, *et al.*[6] The data reported in the present work

(1) L. S. Hersh and O. J. Kleppa, *J. Chem. Phys.*, **42**, 1309 (1965).

(2) L. S. Hersh, A. Navrotsky, and O. J. Kleppa, *ibid.*, **42**, 3752 (1965).

(3) F. G. McCarty and O. J. Kleppa, *J. Phys. Chem.*, **68**, 3846 (1964).

(4) H. Flood and S. Urnes, *Z. Elektrochem.*, **59**, 834 (1955).

(5) T. Førland in "Fused Salts," B. R. Sundheim, Ed., McGraw-Hill Book Co., Inc., New York, N. Y., 1964.

permit a look at this problem in the light of the enthalpy of mixing.

From the point of view of the present investigation, it is of particular interest that several of the magnesium chloride–alkali chloride systems also have been studied by means of emf formation cells.[6,7] This method, which was pioneered by Hildebrand and co-workers,[8] in principle may provide information on the enthalpy and entropy of mixing as well as on the free energy. However, it is generally recognized that the enthalpy and entropy data derived in this way often are of doubtful value. This certainly holds for the enthalpies and entropies for the magnesium chloride–alkali chloride systems given by Markov, *et al.*[7] On the other hand, free energies from emf work tend to be more accurate than the derived enthalpy and entropy data. In the present investigation, such free energy data will be compared with the corresponding enthalpies. This combination offers the best prospect of obtaining reliable information on the entropy of mixing.

Experimental Procedures and Materials

The calorimeter used in the present work is in many respects similar to one for work up to 500° which is described in some detail in the literature.[9] The modifications necessary for operation at temperatures up to about 800° have been discussed elsewhere.[1]

The calorimetric work reported here was carried out in the temperature range 730–810°. All experiments were of the simple liquid–liquid mixing type. They were performed in an atmosphere of dry pure nitrogen, using fused silica containers and break-off tubes.[9] Under the conditions of our experiments, the melt attacked the silica containers only slightly, and all containers could be used several times. Calibration was by the gold-drop method, based on the heat content equation for pure gold given by Kelley.[10] A small correction was applied for the pickup of heat by the falling gold wire.[1]

The magnesium chloride was prepared by removing the water from Mallinckrodt analytical reagent $MgCl_2 \cdot 6H_2O$. This salt was first heated very slowly to about 250° under rotary-pump vacuum. After the greater part of the water had been driven off in this manner, the salt was slowly brought up to the melting point and was melted down in a stream of dry HCl–N_2 mixture. The final product consisted of an agglomeration of quite coarse crystals of anhydrous $MgCl_2$. The product was neutral with respect to phenolphthalein when dissolved in water. In the form of small chunks it could be handled outside a drybox for short periods of time without gain in weight. The alkali chlorides and silver chlorides were of the same origin and quality as the salts used in our earlier work.[1,2]

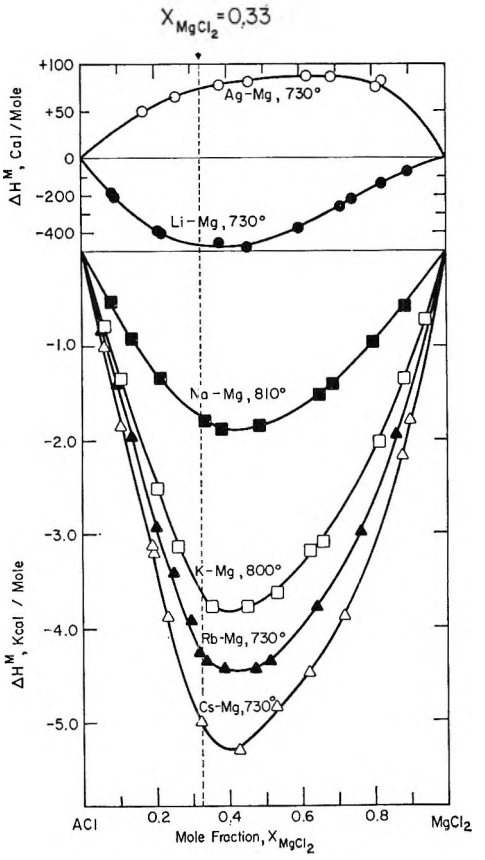

Figure 1. Molar enthalpies of mixing (ΔH^M) in liquid mixtures of magnesium chloride with silver chloride and with the alkali chlorides.

Results and Discussion

All experimental results obtained in the course of the present investigation are recorded in Table I. The columns in this table are: (1) mole fraction of magnesium chloride in the liquid mixture, (2) total number of moles in each experiment, and (3) molar enthalpy of mixing, ΔH^M. The product of the numbers in columns 2 and 3 will give the enthalpy of mixing actually observed in each individual experiment.

We give in Figure 1 a graph of ΔH^M *vs.* mole fraction for all the mixtures investigated. In order to discuss

(6) D. E. Neil, H. M. Clark, and R. H. Wiswall, *J. Chem. Eng. Data*, **10**, 23 (1965).

(7) B. F. Markov, I. K. Delimarskii, and I. D. Panchenko, *Zh. Fiz. Khim.*, **29**, 51 (1955).

(8) J. H. Hildebrand and E. J. Salstrom, *J. Am. Chem. Soc.*, **54**, 4257 (1932).

(9) O. J. Kleppa, *J. Phys. Chem.*, **64**, 1937 (1960).

(10) K. K. Kelley, U. S. Bureau of Mines Bulletin 584, U. S. Government Printing Office, Washington, D. C., 1960.

Table I: Molar Enthalpies of Mixing (ΔH^M) in Liquid Mixtures of Magnesium Chloride with Silver Chloride and with the Alkali Chlorides

Composition, X_{MgCl_2}	Total moles	ΔH^M, cal/mole
	$MgCl_2$–AgCl at 730°	
0.1714	0.1250	49
0.2589	0.1418	65
0.3789	0.1668	76
0.4599	0.1947	80
0.6200	0.1686	87
0.6871	0.0917	85
0.8095	0.1164	75
0.8264	0.1265	81
	$MgCl_2$–LiCl at 730°	
0.0828	0.1305	−182
0.0875	0.1293	−189
0.2097	0.1514	−380
0.2164	0.1202	−395
0.3783	0.1520	−444
0.4540	0.1725	−469
0.5962	0.1757	−370
0.7087	0.0811	−255
0.7422	0.2117	−215
0.8243	0.1270	−134
0.8938	0.1758	−70
	$MgCl_2$–NaCl at 810°	
0.0774	0.2443	−540
0.1353	0.1399	−918
0.2127	0.2863	−1339
0.3361	0.1822	−1773
0.3808	0.2489	−1870
0.4868	0.2168	−1839
0.6482	0.1462	−1510
0.6860	0.2353	−1404
0.7983	0.1322	−956
0.8834	0.1827	−586
	$MgCl_2$–KCl at 800°	
0.0608	0.1728	−792
0.1059	0.1502	−1342
0.2047	0.2041	−2497
0.2602	0.1815	−3105
0.3524	0.1636	−3735
0.4495	0.1749	−3735
0.5300	0.1088	−3587
0.6230	0.1262	−3147
0.6577	0.1630	−3062
0.8147	0.1935	−2006
0.8816	0.1216	−1348
0.9415	0.1674	−721
	$MgCl_2$–RbCl at 730°	
0.0551	0.1046	−820
0.0934	0.1121	−1394
0.1336	0.1180	−1959
0.2001	0.1048	−2915
0.2453	0.1310	−3392
0.2923	0.1436	−3909
0.3160	0.1495	−4241
0.3365	0.0750	−4338
0.3858	0.1365	−4426
0.4700	0.0939	−4423
0.5097	0.1555	−4345
0.6406	0.1640	−3768
0.7610	0.1042	−2974
0.8609	0.1220	−1946
	$MgCl_2$–CsCl at 730°	
0.0602	0.0950	−1017
0.1063	0.0997	−1849
0.1878	0.0586	−3112
0.1917	0.1105	−3192
0.2293	0.0929	−3862
0.3205	0.1311	−4984
0.4236	0.1242	−5288
0.5261	0.1004	−4823
0.6179	0.1017	−4466
0.7162	0.1466	−3864
0.8737	0.0720	−2166
0.8980	0.1169	−1798

in detail the variation of ΔH^M from system to system we give also in Figure 2 a corresponding plot of the experimental values of the interaction parameter, $\lambda = \Delta H^M/X(1 - X)$.

Note first the systematic dependence of λ on the size of the alkali metal cation, with values ranging from about −2 kcal/mole for lithium–magnesium to −20 kcal/mole for cesium–magnesium chloride. A similar trend has frequently been noted in the thermodynamic behavior of simple charge-unsymmetrical fused salt mixtures. Qualitatively, this trend may be rationalized in terms of the competition between the two cations for the common anion. In this competition the cation is aided by a small size, a high charge, and a high polarizability. In view of the similarity of the ionic radii of sodium and silver, the latter point explains the striking difference between the moderately exothermic sodium–magnesium chloride system and the slightly endothermic, in fact nearly ideal, silver–magnesium chloride.

Recently, a modified conformal solution theory for the heats of mixing in charge-unsymmetrical fused salt systems was developed by Davis,[11] on the basis of the model ionic melt of Reiss, *et al.*[12] Since the

(11) H. T. Davis, *J. Chem. Phys.*, **41**, 2761 (1964).

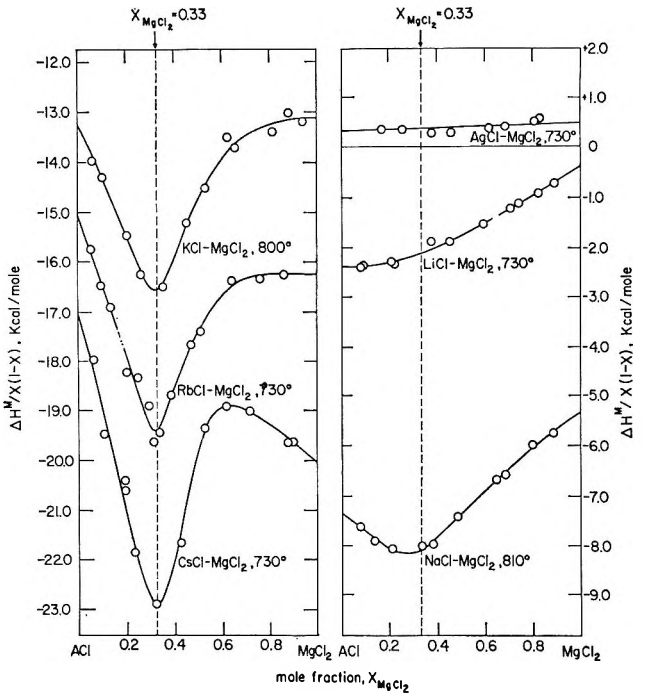

Figure 2. Interaction parameters ($\lambda = \Delta H^M/X(1 - X)$) in liquid mixtures of magnesium chloride with silver chloride and with the alkali chlorides.

Davis theory does not permit an explicit evaluation of the enthalpy of mixing for any chosen binary system, we shall not discuss it in detail.

However, according to Davis the interaction parameter, in a family of related systems such as that considered in the present work, should to a first approximation depend linearly on the parameter $\delta_{12} = (d_1 - d_2)/d_1d_2$, where d_1 and d_2 are the interionic distances which characterize the two salts. The linear relation between λ and δ_{12} has been found to hold fairly well for the alkaline earth nitrate–alkali nitrates,[11] and also, with the exception of the lead–lithium system, for the lead chloride–alkali chlorides.[3]

In Figure 3 we give a plot of λ against δ_{12} for the considered alkali chloride–magnesium chloride mixtures. Since λ varies with composition, we have selected for consideration the values at $X_{MgCl_2} = 0.33$. The figure contains both the actual experimental values ($\lambda_{A_2MgCl_4}$) and those obtained by linear interpolation of the two terminal values $[(^2/_3)\lambda_{ACl} + (^1/_3)\lambda_{MgCl_2}]$. With the obvious exception of the lithium–magnesium system, the predicted linear dependence of λ on δ_{12} clearly is confirmed. It is particularly interesting that the lines drawn through the experimental points in Figure 3 extrapolate to 0 at $\delta_{12} = 0$. In this respect the alkali chloride–magnesium chloride systems appear to be simpler than the charge-unsymmetrical systems

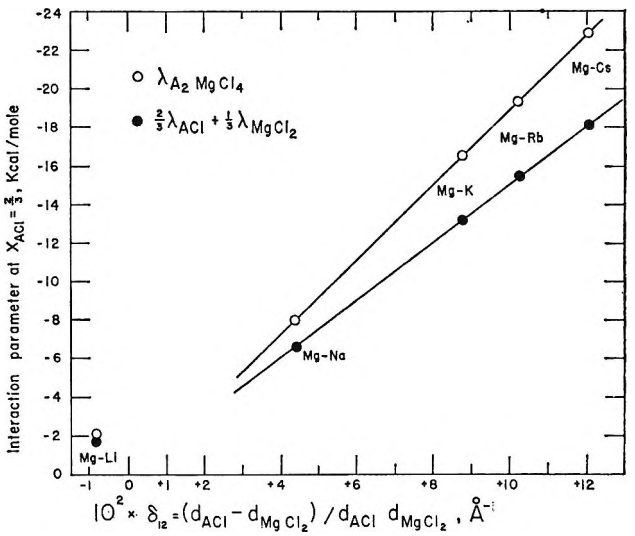

Figure 3. Dependence of the interaction parameter on the quantity $\delta_{12} = (d_1 - d_2)/d_1d_2$.

studied in previous work. In view of this observation, we may for the alkali chloride–magnesium chloride systems (again excepting lithium–magnesium) write the empirical relation, $\lambda = K(X)\delta_{12}$, where the coefficient $K(X)$, although it varies significantly with composition, is of the order of -150 kcal A/mole.

Figure 2 indicates that the variation of the interaction parameter within any one system involves two prominent features: (a) energetic asymmetry; generally λ takes on values in the magnesium chloride-rich region which are different from those in the alkali chloride-rich region ($\lambda_{ACl} \gtrless \lambda_{MgCl_2}$); (b) departures from linearity. This is particularly pronounced near $X_{MgCl_2} = 0.33$. Thus $\lambda_{A_2MgCl_4}$ often differs very significantly from $[(^2/_3)\lambda_{ACl} + (^1/_3)\lambda_{MgCl_2}]$.

The Davis theory for *charge-unsymmetrical* mixtures has not been developed to a point where it allows quantitative predictions to be made regarding energetic asymmetry. On the other hand, in evaluating the higher order terms in the theory of Reiss, *et al.*,[12] for charge-symmetrical systems, Blander[13] found that this theory predicts contributions to the energetic asymmetry which depend on the third power of δ_{12}. Hersh and Kleppa[1] found evidence for this kind of dependence in their study of the binary alkali halides. Without any attempt at theoretical justification we have tested this relation also for the considered alkali chloride–magnesium chloride systems in Figure 4.

(12) H. Reiss, J. L. Katz, and O. J. Kleppa, *J. Chem. Phys.*, **36**, 144 (1962).

(13) M. Blander, *ibid.*, **37**, 172 (1962). Actually, the predicted asymmetries are related to $\delta = (d_1 - d_2)/(d_1 + d_2)$. For moderate differences in ionic size the choice between the parameters δ and δ_{12} is not significant.

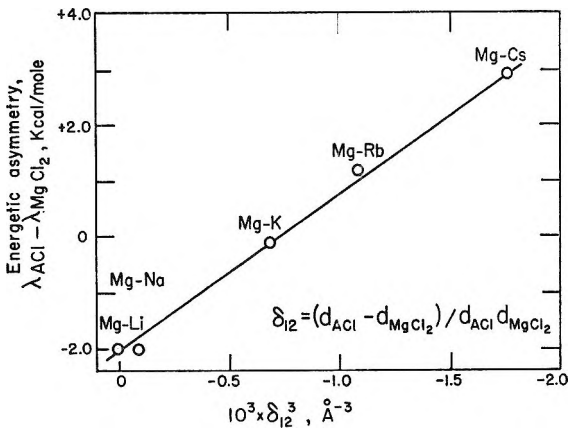

Figure 4. Dependence of the energetic asymmetry on the parameter $\delta_{12} = (d_1 - d_2)/d_1d_2$.

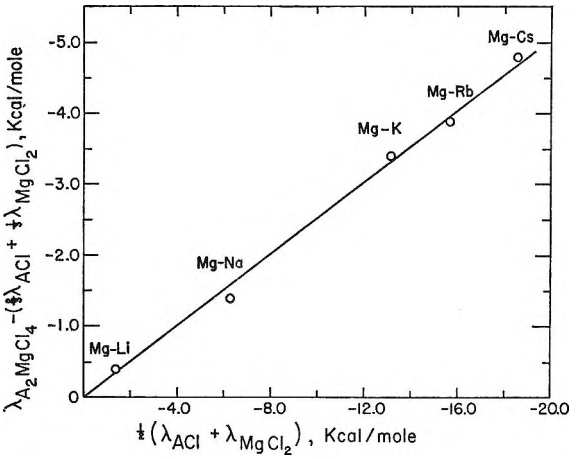

Figure 5. Dependence of the deviation of the interaction parameter at $X_{MgCl_2} = 0.33$ from linearity on its magnitude.

From an empirical point of view it is apparent that the energetic asymmetry indeed varies linearly with δ_{12}^3.

In the previously studied binary alkali halide and nitrate systems, departures of λ from a linear dependence on composition are small. Also, such departures, when present, are symmetrical in the mole fractions of the two components. Among the systems studied the largest departure was found in lithium–cesium chloride, with a value of about −500 cal at the 50:50 composition. In these charge-symmetrical systems the magnitude of the deviation of λ from linearity correlates with the square of the interaction parameter. This was attributed by Kleppa and Hersh[14] to short-range order in the cation "sublattice." The observed dependence on λ^2 is consistent with quasi-chemical theory.[15]

In charge-unsymmetrical systems the nature of the deviation of λ from linearity clearly has a different character. For example, in our recent work on the lead chloride–alkali chlorides we found the deviations to be somewhat more pronounced than in the binary alkali halides. Also, the deviations are unsymmetrical in the mole fractions of the two components. For cesium chloride–lead chloride, which was the only system with a nonlinear λ studied over the full range of liquid compositions, the maximum negative deviation of λ from linearity is about 1 kcal and occurs somewhere between 65 and 80 mole % cesium chloride.

In the considered mixtures involving magnesium chloride, the magnitude of the deviation is still greater. For example, the three systems containing potassium, rubidium, and cesium chloride all have sharp dips in λ near $X_{MgCl_2} = 0.33$. For the sodium- and lithium chloride containing systems the composition of maximum deviation cannot be pin-pointed as readily. However, even in these cases it is evident that the deviation is unsymmetrical in the mole fractions of the two components and that the maximum deviation occurs on the alkali chloride-rich side.

In the systems under consideration we also find a different relationship between the deviation from linearity and the magnitude of λ. This is illustrated in Figure 5, which gives a plot of $\lambda_{A_2MgCl_4} - [(2/3)\cdot\lambda_{ACl} + (1/3)\lambda_{MgCl_2}]$ *vs.* $1/2(\lambda_{ACl} + \lambda_{MgCl_2})$. It is apparent that a linear dependence is indicated.

In our earlier work on the lead chloride–alkali chloride mixtures, the unsymmetrical character of the deviation from linearity was interpreted to indicate the formation of complex species in the melt. However, the uncertainty in the location of the maximum deviation ruled out any attempt to draw firm conclusions regarding the most stable anionic configuration. In the considered systems this uncertainty in large measure is removed. In view of Figure 2 there can be little doubt that $MgCl_4^{2-}$ must be the most prominent complex species in the potassium, rubidium, and cesium chloride melts. By inference, we conclude that this species is of considerable importance also in sodium chloride–magnesium chloride, and to a lesser extent even in lithium chloride–magnesium chloride. These conclusions will be the subject of further discussion below.

Partial Molal Quantities. The new data reported above are all *integral* enthalpies. While no attempt was made in the present work to obtain *partial* enthalpies by direct measurements, the experimental

(14) O. J. Kleppa and L. S. Hersh, *J. Chem. Phys.*, **34**, 351 (1961).
(15) E. A. Guggenheim, "Mixtures," Oxford University Press, New York, N. Y., 1952.

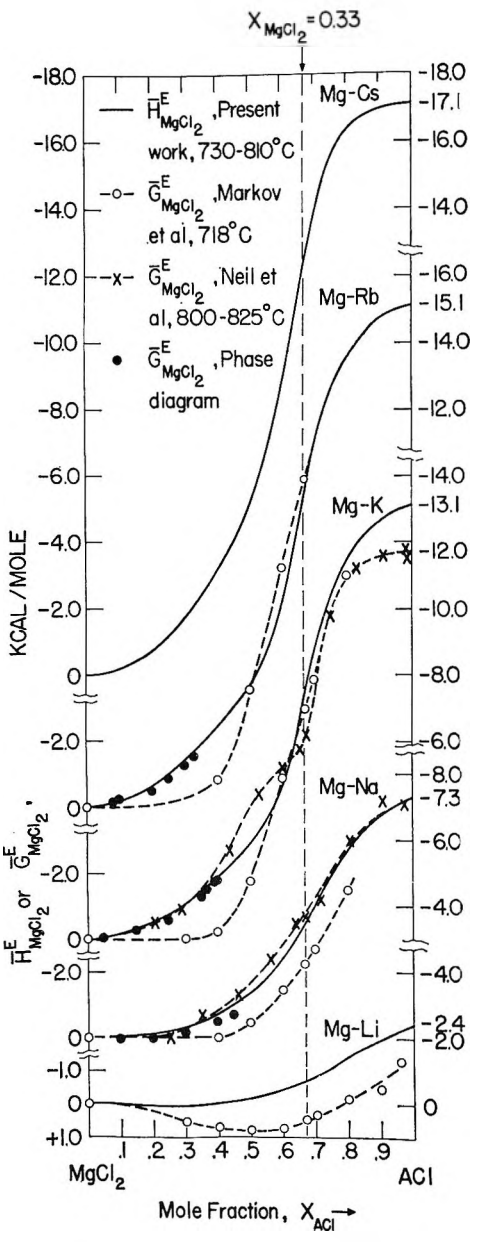

Figure 6. Partial excess enthalpies and partial free energies of magnesium chloride in its liquid mixtures with the alkali chlorides.

results on the whole are sufficiently precise and extensive to allow quite reliable smoothed curves to be drawn. From a large-scale version of Figure 1, fairly reliable relative partial enthalpies were derived by the method of intercepts. The resulting curves for magnesium chloride in its mixtures with the alkali chlorides are plotted against composition in Figure 6. This figure also contains partial excess free energies taken from the emf investigations of Markov, *et al.*,[7] and of Neil, *et al.*[6]

It is apparent that the agreement between the two emf studies is far from satisfactory. As an aid in our assessment of the relative merit of the two sets of data, we have included in Figure 6 the excess free energies calculated for magnesium chloride-rich mixtures from the phase diagrams of Klemm and co-workers.[16,17] These calculations are based on the known heat of fusion of magnesium chloride (10.3 kcal/mole).[18] It is assumed that this quantity does not depend on temperature and that solid solubility is negligible.

It will be noted that the agreement between the phase diagram values and the data of Neil, *et al.*, is quite good. However, the results of Markov and coworkers differ significantly. These values therefore will not be considered in the present discussion.

Figure 6 shows that for the two systems studied by Neil, *et al.*, there is extensive similarity between our own enthalpy data and the excess free energies. It accordingly may be concluded that the excess entropies in these two systems are not very large. This is true in particular for the mixtures involving sodium chloride, while those containing potassium chloride show somewhat greater differences. For the latter system the partial excess entropies for magnesium chloride at about 800° have been evaluated and are plotted against mole fraction in Figure 7. While it is difficult to assess the error in these entropy data, it is believed that they correctly reflect the general shape of the excess entropy curve. Note especially the positive values of $\bar{S}^E_{MgCl_2}$ for $X_{MgCl_2} > 0.4$ and the negative values for low magnesium chloride concentrations. Such a functional dependence of the *partial* entropy on composition corresponds to a fairly sharply defined local minimum in the *integral* entropy curve. In the considered system, this minimum clearly occurs at or near the composition $X_{MgCl_2} = 0.33$. In the partial enthalpy curves, as in the corresponding free energies, the composition $X_{MgCl_2} = 0.33$ is associated with an inflection point. This is barely noticeable in the lithium–magnesium system, but becomes more and more well defined as the alkali ion increases in size.

Qualitatively, the functional dependence of the partial quantities on composition near $X_{MgCl_2} = 0.33$ may be accounted for in terms of the high degree of local order associated with this composition, compared to neighboring compositions. More quantitatively, this problem may perhaps be discussed by a suitable

(16) W. Klemm and P. Weiss, *Z. Anorg. Allgem. Chem.*, **245**, 279 (1940).

(17) W. Klemm, K. Beyersdorfer, and J. Oryschkewitsch, *ibid.*, **256**, 25 (1948).

(18) National Bureau of Standards Circular 500, U. S. Government Printing Office, Washington, D. C., 1952.

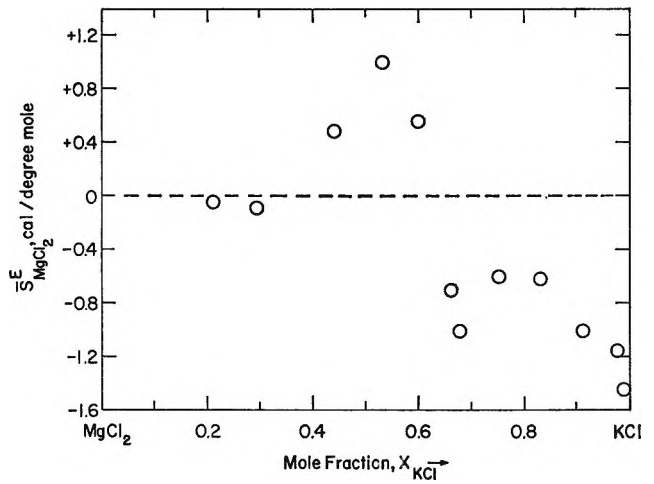

Figure 7. Partial excess entropy of magnesium chloride in its liquid mixtures with potassium chloride. From the partial enthalpies derived in the present work and the excess free energies of Neil, *et al.*

modification of the statistical theory for nearly ordered solid compounds developed by Wagner and Schottky[19] and by Ölander.[20] In the considered case, the "compound" refers to the liquid mixture of composition A_2MgCl_4, while the "degree of disorder" presumably may be related to the partial dissociation of the anionic species according to the equation

$$MgCl_4^{2-} \rightleftharpoons Mg^{2+} + 4Cl^-$$

However, from a chemical point of view it seems more natural to take this dissociation process as a starting point, as was done by Flood and Urnes[4] in their discussion of the cryoscopic behavior of the alkali chloride–magnesium chloride systems. For potassium and rubidium chloride as solvents, Flood and Urnes found that the freezing point depressions up to X_{MgCl_2} = 0.25–0.30 can be accounted for quantitatively by the assumption that the solution is an ideal Temkin mixture[21] of A^+, $MgCl_4^{2-}$, and Cl^-, *i.e.*, that all $MgCl_2$ is complexed to form $MgCl_4^{2-}$. In sodium chloride, on the other hand, there are deviations from this simple picture. These deviations were attributed to the dissociation of $MgCl_4^{2-}$ in the presence of the smaller sodium ion. A similar and still more pronounced deviation may be predicted for mixtures involving the even smaller lithium ion.

For solutions rich in magnesium chloride, on the other hand, Flood and Urnes were unable to account for the cryoscopic behavior in terms of an ideal Temkin mixture, now assumed to contain the ions A^+, Mg^{2+}, $MgCl_4^{2-}$, and Cl^-, since there are too few chloride ions present to complex all magnesium ions. The difference between the magnesium- and alkali-rich melts may readily be understood in view of the concentration dependence of ΔH^M indicated in Figure 1, and the observed dependence of the relative partial enthalpy of $MgCl_2$ on composition.

More recently, the existence of the complex species $MgCl_4^{2-}$ has been argued by Neil, *et al.*, who have used their free energy data to estimate the magnitude of the complex dissociation constant. For solutions containing 20 mole % magnesium chloride in sodium chloride and potassium chloride, Neil gives dissociation constants, according to the equation given above, of 2.3×10^{-2} and 1.8×10^{-3}, respectively, at 800–825°.[22] Using these values, and the ideal Temkin model, he goes on to calculate partial free energies for magnesium chloride over the complete range of liquid compositions.

With respect to the functional dependence of the partial free energy on composition near $X_{MgCl_2} = 0.33$, there is reasonable agreement between Neil's calculated values and experiment. Thus it is indicated that in a *qualitative* way the thermodynamic properties of the alkali chloride–magnesium chloride mixed systems may be accounted for fairly well by the postulation of the single complex species $MgCl_4^{2-}$. On the other hand, in a *quantitative* sense it undoubtedly is much too crude to assume a single, concentration-independent dissociation constant for each binary system. This is inconsistent both with the already mentioned analysis of the cryoscopic data and with the new enthalpy data reported in the present work.

Acknowledgments. This work was supported by the National Science Foundation (Grants GP-1993 and GP-5015) and by the Office of Naval Research (Nonr-2121 (11)). The work also has benefited from general facilities at the Institute for the Study of Metals provided by the Advanced Research Projects Agency.

(19) C. Wagner and W. Schottky, *Z. Physik. Chem.*, **B11**, 163 (1930).

(20) A. Ölander, *ibid.*, **A165**, 65 (1933).

(21) M. Temkin, *Acta Physicochim. URSS*, **20**, 411 (1945).

(22) These dissociation constants seem to be of a reasonable order of magnitude. In view of the partial heat data given in Figure 6, the corresponding dissociation constants for a cesium chloride medium should be of the order of 10^{-4} and for a lithium chloride medium 10^{-1}. This estimate is based on the assumption $\bar{G}^E \approx \bar{H}^E$.

The Effects of Temperature and Pressure on the γ-Radiation-Induced Isomerization of Cyclopentanone to 4-Pentenal in the Liquid Phase[1]

by D. L. Dugle and G. R. Freeman

Chemistry Department, University of Alberta, Edmonton, Alberta, Canada *(Received November 9, 1965)*

The radiation-induced isomerization of cyclopentanone to 4-pentenal in the liquid phase is inhibited by increasing the density of the liquid, either by lowering the temperature or by increasing the pressure. The volume of activation for the over-all reaction at 1 atm is 2.4 ml/mole, and it increases with increasing pressure. The effect of temperature, separated from the effect of density, on the isomerization reaction is relatively small. The effects of temperature and pressure on the benzene-sensitized isomerization of cyclopentanone are similar to their effects on the direct radiolysis reaction.

Introduction

One of the major products of the γ radiolysis of liquid cyclopentanone (CP) at room temperature is 4-pentenal (4P) and the 100-ev yield extrapolated to zero dose is $G_i(4P) = 0.83 \pm 0.10$.[2] During recent experiments we noticed that the yield of 4P decreased with decreasing temperature. However, as the temperature of CP decreases its density increases, and it was of interest to determine whether the change in 4P yield was simply a temperature effect or a density effect, or both. The yields of 4P from the direct and benzene-sensitized[2] radiolyses of CP have therefore been measured as functions of temperature and pressure.[3,4]

Experimental Section

The materials have been described earlier.[2,5] However, the cyclopentanone was triply distilled to reduce the 4-pentenal impurity to 0.002%.

The analyses were done on two gas chromatography columns. One column was 2.5 m of 25 wt % Ucon LB-1800-X on Celite at 110°. The other was 2.5 m of 25 wt % Carbowax 20M on Celite, temperature programmed from 50 to 130°. The hydrogen carrier gas flow rate was 100 cc/min in both cases.

Most of the samples were prepared by pipetting 0.7–2.0 ml of liquid into a vial and degassing it by three freeze–pump–thaw cycles followed by distillation while pumping on the condenser–receiver. The condenser–receiver was kept at −196° during the distillation. The sample was then distilled into the thoroughly evacuated irradiation cell, kept at −196°, and sealed off with a flame.

The cyclopentanone–benzene solutions used in the temperature studies were prepared by vaporizing 1.5 ml of the thoroughly degassed liquid solution into a 5000-cc bulb, mixing the vapors, then passing the vapors through a small orifice into the irradiation cell held at −196°. The filled cell was sealed off. Some of the samples were "annealed" at −79° for 14 hr before irradiation at the chosen temperature, but this had no observable effect on the results.

The temperature studies were made with Pyrex irradiation cells of 15-mm o.d. and 4-cc volume.

Special irradiation cells were made for the pressure studies. Several designs were unsatisfactory for various reasons; for example, Kovar seals crack under high pressure and polythene is slightly permeable to air and to the hydraulic fluid used (Esso Bayol 35). The construction of the type of cell that was successfully used is illustrated in Figure 1. The glass capil-

(1) This work was partially supported by the National Research Council of Canada.

(2) D. L. Dugle and G. R. Freeman, *Trans. Faraday Soc.*, 61, 1174 (1965).

(3) S. D. Hamann, "Physico-Chemical Effects of Pressure," Butterworth and Co. (Publishers) Ltd., London, 1957.

(4) P. W. Bridgman, "The Physics of High Pressure," G. Bell and Sons, London, 1958.

(5) D. L. Dugle and G. R. Freeman, *Trans. Faraday Soc.*, 61, 1166 (1965).

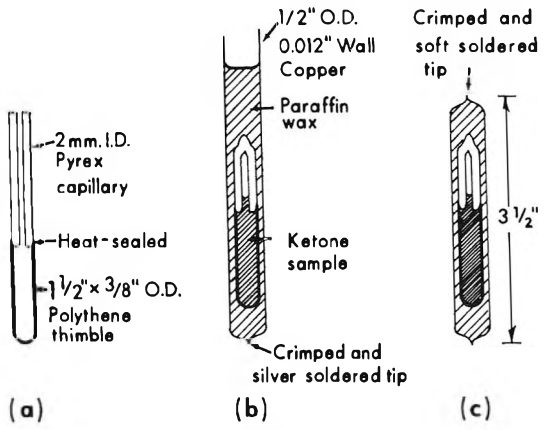

Figure 1. Irradiation cell construction: (a) polythene–glass thimble; (b) filled and sealed thimble, inserted into wax in copper tube; and (c) completed cell.

lary was cleaned with a hot solution of 1:3 (v/v) nitric acid–sulfuric acid, followed by many rinsings with doubly distilled water. The polythene was cleaned only with doubly distilled water because nitric acid treatment caused the results to be less reproducible. The polythene thimble was made of $^3/_8$ in. o.d. polythene tubing, with a $^1/_{16}$ in. thick wall. The thimble bottom was made by slowly drawing off a piece of the tubing, so that the end of the tube became sealed, using a gentle flame, then thickening the bottom by gently melting the polythene in the flame. The glass–polythene seal was made by fire polishing the end of a piece of glass capillary tubing, so the glass would not cut the polythene, then when the glass had cooled to just below the point where it would cause the polythene to burn, it was pushed into the top of the polythene thimble and allowed to cool. The glass–polythene cell shown in Figure 1a was attached to the vacuum rack and evacuated for at least 4 hr before filling. After filling with 0.70 ml of ketone or ketone–benzene solution, the cell was sealed off. It was then brought to room temperature and inserted into a thin-walled copper tube that contained just-molten paraffin wax (Figure 1b). During the insertion, it was necessary to warm the copper tube gently to remelt the wax to allow the glass–polythene cell to be inserted completely. The cell was then cooled with water; the tube was crimped off and sealed with soft solder. The corners of the ends of the completed cell were filed off enough to allow it to be placed in a reproducible position in the pressure chamber. After radiolysis, the cell was opened with a tube cutter and a glass knife.

The pressure transmission of this type of cell was checked by flattening an empty (no ketone) cell at 200 atm, the lowest measureable pressure obtainable with the apparatus.

The pressure chamber was a hardened steel cylinder with a 0.75-in. bore, $1^3/_8$-in. walls, and a Bridgman-type[4] closure. It was made by R. Cox and P. Bradbury of this department.

Pressures were produced by a gas-operated self-cycling intensifier pump (Haskel Engineering Model AO-602) and were measured by a calibrated Bourbon-type gauge (Aminco).

Aminco valves and fittings were used throughout the pressure line.

The irradiation dose rate for the pressure studies was 1.5×10^{18} ev/g hr, and the dose was 8×10^{19} ev/g. The temperature was about 25°.

The dose rate for the temperature studies was 4.6×10^{19} ev/g hr, and the dose was 2.8×10^{20} ev/g.

Results

Temperature Studies. The only pressure on these samples was their vapor pressure. The value of $G(4P)$ at 32° and 2.8×10^{20} ev/g was 0.68, which agrees with earlier measurements.[2] The ratio of the yield at temperature t to that at 32°, $G(4P)_t/G(4P)_{32}$, is plotted against t in Figure 2A for pure cyclopentanone. The value of the ratio decreases slowly as the temperature of the liquid is decreased below 32° and decreases rapidly in the vicinity of the freezing point of the ketone.

Values of $G(4P)_t/G(4P)_{32}$ are plotted *vs.* t in Figure 2B for the benzene-sensitized reaction. The solutions used were 0.025 and 0.192 electron fraction of cyclopentanone in benzene, and the values of $G(4P)$ at 32° were 0.59 and 1.42, respectively. The approximate temperatures at which these solutions formed slushes were measured and are indicated in Figure 2B. As in pure cyclopentanone, solidification of the solutions appears to coincide with the sharp decrease in 4P yield.

The density of CP was measured as a function of temperature, and the results are plotted in Figure 2A. The density increases by 11% when the ketone changes from liquid to solid at the freezing point at 1 atm pressure.

Pressure Studies. The yield of 4P from pure CP at 25°, 1 atm, and 8×10^{19} ev/g was $G(4P) = 0.80$, which agrees with the earlier measurements.[2] The log of the ratio[6] of the yield at pressure p to that at 1 atm, log $[G(4P)_p/G(4P)_1]$, is plotted against the pressure in Figure 3A. The yield of 4P decreases with increasing pressure, but the relative rate of decrease is

(6) Reference 3, Chapter 9.

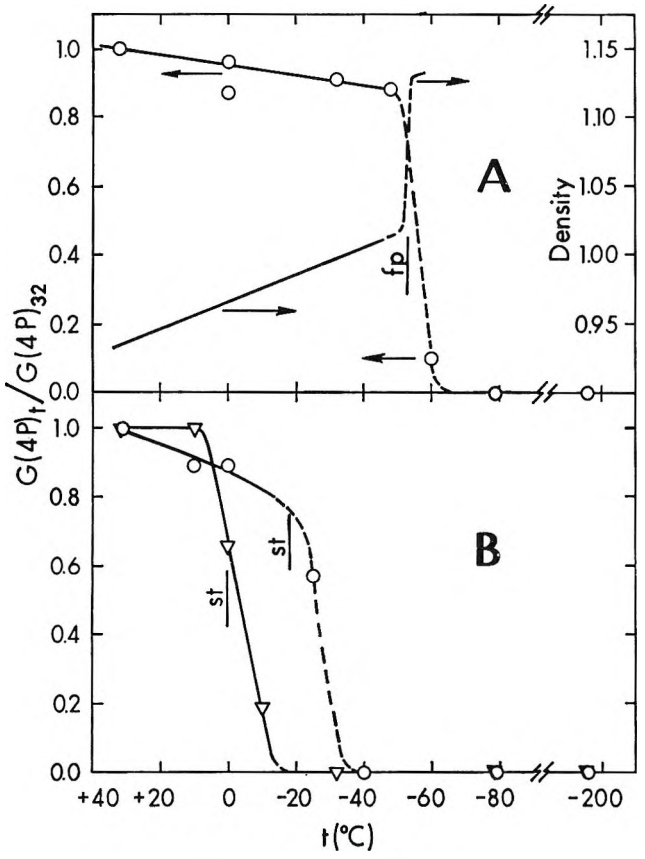

Figure 2. Variation of 4-pentenal yield with temperature. A: pure cyclopentanone; fp, freezing point. The density of cyclopentanone is also shown in this graph. B: cyclopentanone–benzene solutions; ▽, 0.025 electron fraction cyclopentanone; ○, 0.192 electron fraction cyclopentanone; st, approximate temperature at which the solution forms a slush.

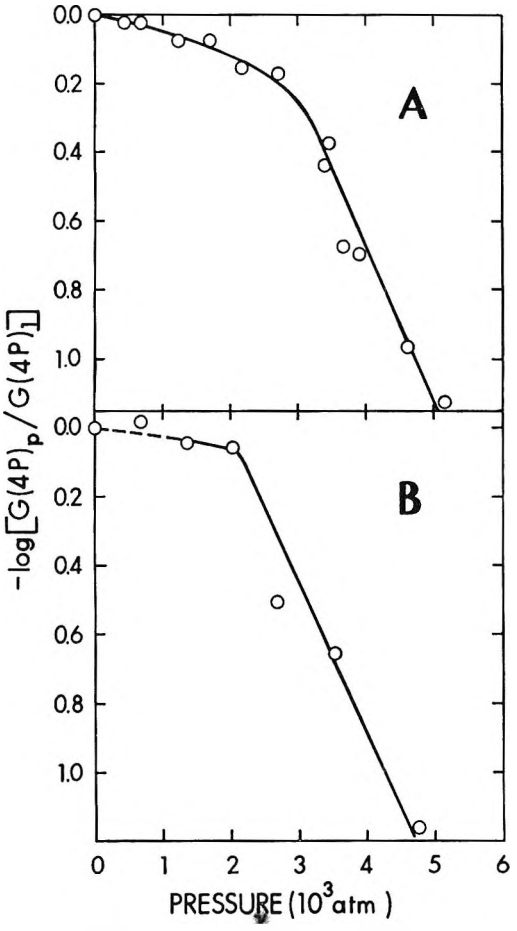

Figure 3. Variation of 4-pentenal yield with pressure: A, pure cyclopentanone; B, 0.192 electron fraction of cyclopentanone in benzene.

much greater at pressures greater than 3000 atm than it is at lower pressures.

The value $G(4P) = 1.44$ was obtained for a solution of 0.192 electron fraction of CP in benzene at 25°, 1 atm, and 8×10^{19} ev/g. The effect of pressure on this benzene-sensitized reaction is illustrated in Figure 3B. The effect was similar to that observed with pure CP, but the rapid decrease in $G(4P)$ began at a pressure about 1000 atm lower in the benzene solution than it did in the pure ketone.

Discussion

It is evident from Figures 2 and 3 that increasing the pressure has an effect on the 4P yields similar to that of lowering the temperature. It is thus possible that the effect is simply due to the change of the density of the medium in both sets of experiments. The relative 4P yields from the temperature experiments with pure CP are plotted against the density of the CP in Figure 4. The compressibility of CP is not known but it is probably very similar to that of isoamyl alcohol, which has been reported by Bridgman.[7] The dashed curve in Figure 4 represents the results from the pressure experiments with pure CP, assuming that CP has the same compressibility as does isoamyl alcohol. Isoamyl alcohol does not freeze under the present conditions of temperature and pressure,[7] although the results in Figure 3A indicate that cyclopentanone might begin to freeze at about 3200 atm and 25°. If so, the curve in Figure 4 should have a slightly less negative slope at densities greater than about 1.08 g/ml, such that the bottom end of the curve is shifted to roughly 1.18 g/ml.[8] A comparison of the results in Figures 2A and 3A indicates that if CP does freeze at 25° in the pressure range studied, the freezing occurs

(7) Reference 4, p 128.

(8) The fractional volume change on freezing at 5000 atm is roughly half that at 1 atm for a number of organic liquids: ref 4, p 196.

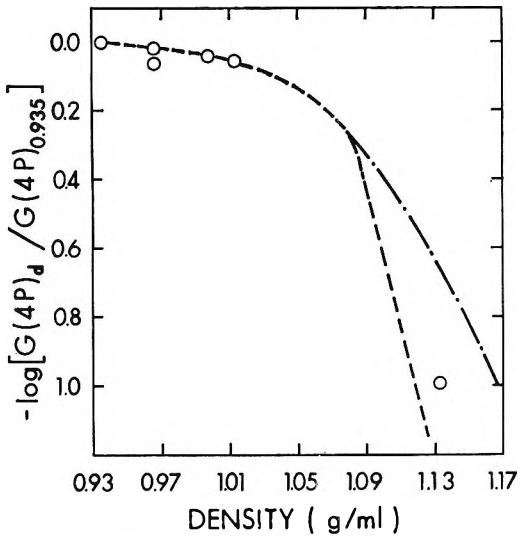

Figure 4. Variation of 4-pentenal yield with density of pure cyclopentanone. The density of cyclopentanone at 32° is 0.935 g/ml. O, temperature experiments; ---------, pressure experiments, assuming that the compressibility of cyclopentanone at 25° equals that of iscamyl alcohol at 20°; -·-·-, pressure experiments, assuming that the compressibility of cyclopentanone equals that of isoamyl alcohol, but that cyclopentanone freezes at 25° over the pressure range 3200–5160 atm.

gradually over a range of pressure rather than entirely at a given critical pressure (this would be a nonequilibrium situation). The dash–dot curve in Figure 4 roughly represents the results from the pressure experiments, assuming that the CP is entirely frozen at the highest pressure used (5160 atm).

Figure 4 indicates that, whether freezing occurs or not, the effect of density on the 4P yield is much greater than that of thermal energy (temperature, with the density effect separated out). This conclusion is supported by the results obtained with the benzene-sensitized isomerization. The decrease in the sensitized 4P yield is much more affected by solidification of the sample, with the consequent increase of sample density, than by temperature alone (Figure 2B). The fact that the rapid decrease in 4P yield in the 0.192 electron fraction CP–benzene solution begins at ∽2200 atm, compared to ∽3200 atm in pure CP, implies that the rapid decrease is due to solidification of the samples in both cases. Pure benzene at 22° freezes at about 850 atm.[9]

The small effect of temperature, separated from the effect of density, is not surprising because the excitation energy is supplied to the molecules by the radiation.

From the tangent at the origin of the curve in Figure 3A it was calculated that the volume of activation at 1 atm pressure[6] was $\Delta V^{\ddagger}_1 = 2.4$ ml/mole for the over-all radiation-induced isomerization of CP to 4P. The reaction mechanism can be represented as shown in eq 1–4. $I = 10^{-2}RG(CP^*)$, where R is the dose rate

$$CP \xrightarrow{I} CP^* \quad (1)$$

$$CP^* \longrightarrow 4P \quad (2)$$

$$\longrightarrow CP \quad (3)$$

$$CP^* + CP \longrightarrow 2CP \quad (4)$$

in electron volts per milliliter second. Similarly, $d[4P]/dt = 10^{-2}RG(4P)$. It may readily be shown that

$$G(4P) = k_2G(CP^*)/(k_2 + k_3') \quad (I)$$

where

$$k_3' = k_3 + k_4[CP] \quad (II)$$

Since[6]

$$-RT\partial(\ln k)/\partial P = \Delta V^{\ddagger} \quad (III)$$

we can write

$$-RT\frac{\partial}{\partial P}\{\ln G(4P)\} = -RT\frac{\partial}{\partial P}\{\ln G(CP^*) + \ln k_2 - \ln (k_2 + k_3')\} = \Delta V^{\ddagger}(\text{over-all reaction}) \quad (IV)$$

It is possible that each of $G(CP^*)$, k_2, and k_3' vary with pressure so we cannot interpret the observed $\Delta V^{\ddagger}$ (overall reaction) in detail. However, the molar volume of 4*P* (98.7 ml) is 10.0 ml greater than that of cyclopentanone at 20° and 1 atm. It is therefore probable that $\Delta V^{\ddagger}$(reaction 2) is positive. Reaction 4 is bimolecular, so $\Delta V^{\ddagger}$(reaction 4) is probably negative. We cannot say whether the volumes of activation of reactions 1 and 3 would be positive, negative, or zero.

$\Delta V^{\ddagger}$(over-all reaction) increases with increasing pressure and is 6.8 ml/mole at 2500 atm. In the pressure region from 3200 to 5160 atm it is about 26 ml/mole, although if freezing occurs in this pressure region the calculated value of $\Delta V^{\ddagger}$ is too high. An increase of the $\Delta V^{\ddagger}$ of a reaction with increasing pressure indicates that the compressibility of the transition state is less than that of the medium as a whole. In the present system, this might be attributed to one or more of the unimolecular reactions 1, 2, and 3. If it is due to reaction 1, then $\Delta V^{\ddagger}$(reaction 1) is positive; if due to reaction 2, $\Delta V^{\ddagger}$(reaction 2) is positive; if due to reaction 3, $\Delta V^{\ddagger}$(reaction 3) is negative.

The alignment of the molecules in the crystal might also contribute to the inhibition of the isomerization

(9) D. W. Brazier, private communication.

reaction by affecting one or more of reactions 1, 2, and 3. Furthermore, the formation of crystallites increases the probability of annihilation interactions between triplet excitons.[10-12] Triplet state CP molecules are precursors to about 70% of the 4P formed in pure CP and to about 90% of the 4P formed in the 0.192 electron fraction solution during radiolysis at 25° and 1 atm.[2]

Comment on the Isomerization Mechanism. Several papers have appeared recently in which the photoinduced isomerization of cyclic ketones to open-chain olefinic aldehydes (among other products) has been discussed.[13-15] If this isomerization of cyclic ketones follows the same reaction path in all the ketones studied, the question about whether the C–CO bond breaks (a) before, (b) at the same time as, or (c) after the H atom is transferred from the β-carbon to the carbonyl carbon has not yet been convincingly answered. The fact that the same ratios of the geometric isomers of the products are obtained from the vapor phase photolysis of either *cis*- or *trans*-2,6-dimethylcyclohexanone strongly supports the above mechanism a, in which the C–CO bond breaks first.[15] It may be shown, with the aid of molecular models, that the crowding together of molecules in the liquid phase would cause the product distributions to be very similar from all three of the above possible mechanisms. Thus, the results obtained from liquid phase photolyses by Srinivasan and co-workers[13] do not support one of the possible mechanisms more than the others. Furthermore, the absence of 5-hexen-2-one as a product from cyclohexanone[14] is not an argument against mechanism a because the formation of 5-hexene-2-one and of 4-hexenal are two quite different reactions, involving different bonds and orbitals. The formation of propylene and cyclopentanone from 2-*n*-propylcyclopentanone[14] is a Norrish type-II process which involves the side chain, and the presence of the C_5 ring in the ketone molecule is incidental to this reaction. The Norrish type-II process is sterically prevented from occurring in rings, and when simple C–C bond cleavage occurs as a result of photoexcitation, it is the C–CO bond that breaks, not the bond between the α- and β-carbon atoms. Thus 5-hexen-2-one is not a product to be expected, according to any of these mechanisms, from the photolysis of cyclohexanone.

If the above mechanism (a) applies, *i.e.*, if the C–CO bond breaks before the H atom is transferred (by disproportionation) to the carbonyl carbon, then the carbonyl group is in its ground electronic state during the H transfer. There are several possible routes from the $n \rightarrow \pi^*$ excited ketone molecule to the dissociated radical pair (*e.g.*, predissociation, intersystem crossing to the ground electronic state followed by dissociation of the resulting vibrationally excited molecule, etc.), but they all result in radicals in their ground electronic states.

If mechanism b or c applies, the $n \rightarrow \pi^*$ excited carbonyl group is involved in the transition state of the hydrogen atom transfer reaction (the lobes of the π^* orbital that are on the carbon atom are tilted away from the C=O bond and lean part way across the ring).

From this point of view it is difficult to understand, from any of the three mechanisms, why the photolysis of 3-methylcyclohexanone produced 3-methyl-5-hexenal but not 5-methyl-5-hexenal;[13] it is also difficult to explain the formation of 4-octenal but apparently not 2-*n*-propyl-4-pentenal from 2-*n*-propylcyclopentanone.[14]

(10) H. Sternlicht, G. C. Nieman, and G. W. Robinson, *J. Chem. Phys.*, **38**, 1326 (1963).

(11) R. A. Keller, *ibid.*, **42**, 4050 (1965).

(12) R. A. Keller and D. A. Breen, *ibid.*, **43**, 2562 (1965).

(13) R. Srinivasan and S. E. Cremer, *J. Am. Chem. Soc.*, **87**, 1647 (1965), and references therein.

(14) R. Srinivasan and S. E. Cremer, *J. Phys. Chem.*, **69**, 3145 (1965).

(15) R. L. Alumbaugh, G. O. Pritchard, and B. Rickborn, *ibid.*, **69**, 3225 (1965).

Association Constants in Molten Mixtures of Univalent and Divalent Nitrates. I. Silver Chloride in Mixtures of Potassium Nitrate with Calcium Nitrate or Strontium Nitrate[1]

by Jerry Braunstein and Judith D. Brill

Department of Chemistry, University of Maine, Orono, Maine *(Received November 10, 1965)*

Association constants of silver ion with chloride ion were measured potentiometrically in the mixed molten salt solvents, KNO_3–$Ca(NO_3)_2$ and KNO_3–$Sr(NO_3)_2$. The results are compared with those obtained in pure and mixed alkali metal nitrates and are discussed in terms of the reciprocal coulomb effect and the effective radius of the nitrate ion.

Introduction

Association constants of silver ion or cadmium ion with halide ions have been reported in a number of molten alkali nitrates and mixtures of alkali nitrates.[2] In a given solvent at a single temperature, the association constants of a cation with halide ions increase in the order Cl < Br < I. The effect of the solvent has been shown to depend on the relative sizes of the ions involved in the exchange reaction

$$MD + SX = MX + SD$$

where M refers to the solute cation (Ag^+ or Cd^{2+}), S the solvent cation (Li^+, Na^+, K^+, or Cs^+), X the solute anion (halide ion), and D the solvent anion (nitrate). In the solvents $NaNO_3$, KNO_3, $CsNO_3$, and their mixtures, the order of the association constants correlates with the calculated reciprocal coulomb effect.[2c,e] The calculated reciprocal coulomb effect takes into account the contribution to the energy of association of the change in coulombic energy on exchange of pairs of nearest-neighbor ions in the above reaction but not the long-range coulombic energy or the dispersion or polarization energy. In solvent mixtures containing lithium nitrate, the association constants are not consistent with the reciprocal coulomb effect unless a smaller "effective radius" (or distance of closest approach) is assumed for nitrate ions adjacent to lithium ions than for nitrate ions adjacent to the other alkali metal cations.

In this paper we present the results of potentiometric measurements of the association of silver ions with chloride ions in solvents consisting of 80 mole % potassium nitrate and 20 mole % calcium nitrate or strontium nitrate. We show that the effect of divalent solvent cations on the association constants is in the direction predicted by the reciprocal coulomb effect (destabilization), but a smaller effective radius of nitrate ion is indicated than the value (2.19 A) assumed previously.

Experimental Section

The electromotive force was measured of the concentration cell I by methods similar to those described

$$\mathrm{Ag}\left|\begin{matrix}\mathrm{AgNO_3}\\(\mathrm{K,S^{2+}})\mathrm{NO_3}\end{matrix}\right\|\begin{matrix}\mathrm{AgNO_3}\\(\mathrm{K,S^{2+}})\mathrm{NO_3}\\\mathrm{KCl}\end{matrix}\left|\mathrm{Ag}\right. \qquad \text{(I)}$$

previously.[3] The measurements in KNO_3–$Ca(NO_3)_2$ [and some of the measurements in KNO_3–$Sr(NO_3)_2$], however, were made with a silver electrode coated with silver iodide (by adding a small crystal of potassium

(1) This work was supported by the U. S. Atomic Energy Commission under Contract No. AT(30-1)-2873.

(2) (a) C. Thomas and J. Braunstein, *J. Phys. Chem.*, **68**, 957 (1964); (b) J. Braunstein, H. Braunstein, and A. S. Minano, *Inorg. Chem.*, **3**, 1334 (1964); (c) J. Braunstein and A. S. Minano, *ibid.*, **3**, 218 (1964); (d) J. Braunstein and R. E. Hagman, *J. Phys. Chem.*, **67**, 2881 (1963); (e) D. L. Manning, R. Bansal, J. Braunstein, and M. Blander, *J. Am. Chem. Soc.*, **84**, 2028 (1962); (f) J. Braunstein and R. M. Lindgren, *ibid.*, **84**, 1534 (1962); (g) D. L. Manning, J. Braunstein, and M. Blander, *J. Phys. Chem.*, **66**, 2069 (1962).

(3) M. Blander, F. F. Blankenship, and R. F. Newton, *ibid.*, **63**, 1259 (1959).

iodide to the melt). This lead to Nernst slopes over a larger range of silver concentrations and to more stable readings of the emf than could be obtained with bare electrodes, possibly by restricting access of oxygen to the silver electrode. Measurements in KNO_3 with bare electrodes and with silver electrodes coated with iodide indicated that the activity coefficients (and association constants) with and without iodide were in agreement within the experimental error (about 1 mv) at low enough (below 370°) temperatures to keep the solubility of silver iodide small. Reagent grade KNO_3, $Ca(NO_3)_2 \cdot 4H_2O$, $Sr(NO_3)_2$, KCl, and $AgNO_3$ from Mallinckrodt were used without further purification other than drying. Mixtures of KNO_3 and $Ca(NO_3)_2 \cdot 4H_2O$ were dried by bubbling helium through the melted mixture overnight at a temperature of about 250°. A series of measurements of the weight loss indicated a stoichiometric weight loss of the water of hydration of the $Ca(NO_3)_2 \cdot 4H_2O$ after about 4 hr of bubbling helium through the melt.

Results

In the absence of chloride, the electromotive force of the cell I followed the Nernst equation in the concentration of silver nitrate. When potassium chloride was added to the right-hand half-cell containing a fixed concentration of silver nitrate, the emf decreased. The stoichiometric activity coefficient of silver nitrate is given by the equation $\log \gamma_{AgNO_3} = F\Delta E/2.3RT$ where ΔE is the change of emf of the cell on addition of KCl. Figures 1 and 2 are plots of $-\log \gamma_{AgNO_3}$ as a function of the concentration of KCl at various fixed concentrations of $AgNO_3$ in the solvents $0.8KNO_3$–$0.2Sr(NO_3)_2$ at 350° and $0.8KNO_3$–$0.2Ca(NO_3)_2$ at 320°. These data and the data for the activity coefficients in $0.8KNO_3$–$0.2Ca(NO_3)_2$ are available from ADI (Table III).[4]

Concentration Units and Association Constants. The concentrations are reported as the ion mole ratios $R_{AgNO_3} = n_{AgNO_3}/[n_{KNO_3} + n_{Ca(NO_3)_2}]$ and $R_{Cl} = n_{Cl}/[n_{KNO_3} + 2n_{Ca(NO_3)_2}]$. At the low solute concentrations investigated ($<10^{-3}$ mole ratio), the ion ratios are numerically nearly equal to the ion fractions $N_{Ag^+} = n_{AgNO_3}/n_{cations}$, $N_{Cl} = n_{KCl}/n_{anions}$, where n_{AgNO_3}, n_{KCl}, etc., are the numbers of moles of $AgNO_3$, (K–Ca)Cl, etc. (The starred mole ratios $R_{Cl}^* = n_{Cl}/[n_{KNO_3} + n_{Ca(NO_3)_2}]$ in the figures were used for convenience in computations. The association constants were calculated in all cases using the ion mole ratios R_{Cl} and R_{Ag} which are virtually equal to the ion mole fractions.) In binary mixtures of molten salts of different charge types, the use of ion mole fractions (Temkin activities), based on a model of random mixing of all cations and random mixing of all anions, but no mixing of cations with anions has been shown to give better agreement of experimental results with the laws of dilute solutions than the use of equivalent fractions, *e.g.*, $X'_{M^+} = n_{M^+}/(n_{M^+} + 2n_{P^{2+}})$, which assume the introduction of vacancies with multiply charged ions as in mixed crystalline solids.[5-7]

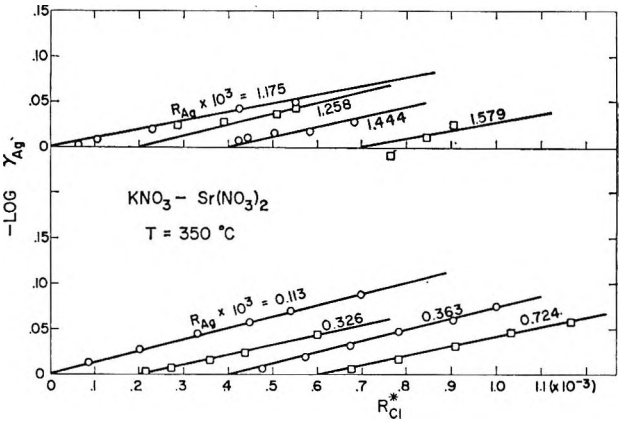

Figure 1. Activity coefficients (as $-\log \gamma_{AgNO_3}$) of silver nitrate *vs.* the concentration of chloride in molten $0.8KNO_3$–$0.2Sr(NO_3)_2$ at 350° at several fixed concentrations of silver nitrate.

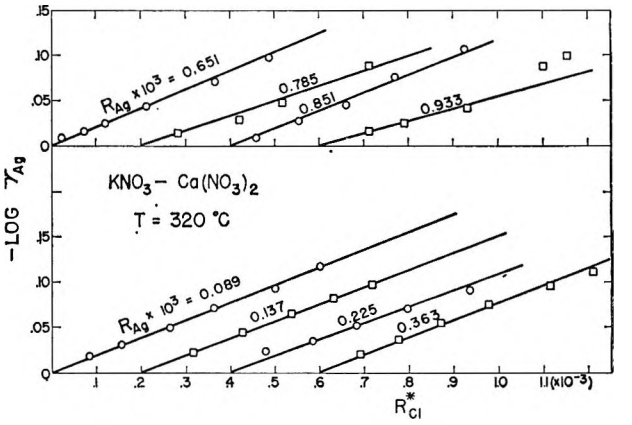

Figure 2. Activity coefficients of silver nitrate *vs.* the concentration of chloride in molten $0.8KNO_3$–$0.2Ca(NO_3)_2$ at 320° several fixed concentrations of silver nitrate.

(4) The data have been deposited as Document No. 8818 with the ADI Auxiliary Publications Project, Photoduplication Service, Library of Congress, Washington, D. C. A copy may be secured by citing the Document number and by remitting $1.25 for photoprints, or $1.25 for 35-mm microfilm. Advance payment is required. Make checks or money orders payable to: Chief, Photoduplication Service, Library of Congress.

(5) M. C. Bell and S. N. Flengas, *J. Electrochem. Soc.*, **111**, 569 (1964).

(6) (a) T. Førland, *Norg. Tek. Vitenskapsakad., Ser. 2*, **4** (1957); (b) T. Førland, *Discussions Faraday Soc.*, **32**, 122 (1962).

Table I: Association Constants, K_1, and Specific Helmholtz Free Energies of Association, $-\Delta A$

Nitrate solvent, mole %				Temp,	K_1, (moles/mole of solvent)$^{-1}$	$-\Delta A$, kcal/mole		
K	Ca	Sr	Li	°K		$Z = 4$	$Z = 5$	$Z = 6$
100[a]	0	0	0	623	553 ± 20	6.12	5.85	5.62
80	20	0	0	593	518 + 7 − 16	5.74	5.48	5.27
80	20	0	0	623	417 + 5 − 12	...	...	5.27
80	0	20	0	623	336 ± 23 − 32	5.50	5.23	5.01
67	0	0	33[b]	664	380 ± 25	...	...	5.5[b]
0	100	0	0					(3.9)[c]
0	0	100	0					(2.6)[c]

[a] Reference 2g. [b] Reference 2a. [c] Estimated by linear extrapolation of results in KNO_3 and KNO_3–$Ca(NO_3)_2$ or KNO_3–$Sr(NO_3)_2$.

The association constants are evaluated by considering the distribution of silver among the various possible associated species.[8]

$$n_{AgNO_3} = n_{Ag} + n_{AgCl} + n_{AgCl_2^-} + 2n_{Ag_2Cl^+} + \ldots \quad (1)$$

$$R_{AgNO_3} = \frac{n_{AgNO_3}}{n_{\text{solvent cations}}} = R_{Ag^+} + R_{AgCl} + \ldots \quad (2)$$

If the association constants are defined[8]

$$K_1 = \frac{R_{AgCl}}{R_{Ag^+} R_{Cl^-}} \quad (3)$$

etc., where R_{Ag^+} and R_{Cl^-} are the ion mole ratios of "free" or unassociated Ag^+ and Cl^-, and R_{AgCl} is the mole ratio of the associated species AgCl, eq 2 becomes

$$R_{AgNO_3} = R_{Ag^+} + K_1 R_{Ag^+} R_{Cl^-} + (\text{higher terms}) \ldots \quad (4)$$

Writing the activity coefficient of silver nitrate as $\gamma_{AgNO_3} = R_{Ag^+}/R_{AgNO_3}$, where R_{AgNO_3} is the stoichiometric mole ratio of silver nitrate, leads to the result

$$K_1 = \lim_{\substack{R_{Cl^-} \to 0 \\ R_{AgNO_3} \to 0}} \left(\frac{\partial \ln 1/\gamma_{AgNO_3}}{\partial R_{Cl}} \right)_{R_{AgNO_3}} \quad (5)$$

The graphical extrapolation of eq 5 is shown in Figure 3 and the results are shown in Table I.

Helmholtz Free Energies of Association. The specific Helmholtz free energies of association, ΔA, were calculated from the equation of the quasi-lattice model

$$K_1 = Z[\exp(-\Delta A/RT) - 1]$$

where Z is the quasi-lattice coordination number.[9] Table I summarizes the association constants and the specific Helmholtz free energies of association calculated for the values 4, 5, and 6 of the lattice coordination number Z. The previously reported results in potassium nitrate and 67% potassium nitrate–33% lithium nitrate also are shown in Table I.

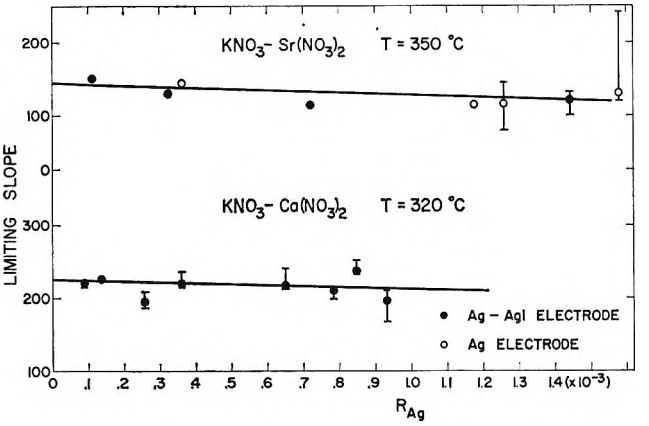

Figure 3. Extrapolation of the limiting slopes $[(\partial \log 1/\gamma_{AgNO_3}/\partial R_{Cl})]R_{Cl=0}$ to infinite dilution of silver nitrate.

The change of coulombic energy in the exchange of nearest neighbors taking place in the association reactions

$$Ag^+NO_3^- + K^+Cl^- \longrightarrow Ag^+Cl^- + K^+NO_3^-: \quad \Delta U_K$$

$$Ag^+NO_3^- + S^{z+}Cl^- \longrightarrow Ag^+Cl^- + S^{z+}NO_3^-: \quad \Delta U_z$$

is

$$\Delta U_z - \Delta U_K = \frac{Ne^2}{d} \frac{2\beta\alpha[1 + (\alpha + \beta)/2] - (z - 1)\alpha(1 + \alpha)}{(1 + \alpha)(1 + \beta)(1 + \alpha + \beta)} \quad (6)$$

(7) K. J. MacLeod and F. E. W. Wetmore, *Ann. N. Y. Acad. Sci.*, **79**, 873 (1960).

(8) J. Braunstein, M. Blander, and R. M. Lindgren, *J. Am. Chem. Soc.*, **84**, 1529 (1962).

(9) D. G. Hill, J. Braunstein, and M. Blander, *J. Phys. Chem.*, **64**, 1038 (1960).

This equation is an extension of one derived previously for univalent ions ($z = 1$).[2c] d is the sum of the radii of the ions K^+ and NO_3^-; α and β are the relative increments of the radii of the halide ion and of the solvent cation

$$\alpha = \frac{r_{Cl^-} - r_{NO_3^-}}{d}; \beta = \frac{r_S - r_K}{d}$$

If α and β are small, eq 6 may be approximated by

$$\Delta U_z - \Delta U_K \cong -(z - 1)\alpha\frac{Ne^2}{d} \qquad (7)$$

Values of $\Delta U_{Ca} - \Delta U_K$ were calculated from the Pauling radii of K^+, Ca^{2+}, Sr^{2+}, and Cl^- (1.33, 0.99, 1.13, and 1.81 A) together with the value $r_{NO_3^-} = 2.19$ A.[2c,10] With the further assumption (which has been shown to be valid in several other molten salt systems[2a,c]) that the specific Helmholtz free energy of association in the mixed molten salt solvent varies linearly with the composition (mole fraction) of the solvent mixture ($\Delta A_{12}(\text{mix}) = X_1\Delta A_1 + X_2\Delta A_2$), AgCl was estimated with (6) to be less stable in $0.8KNO_3$–$0.2Ca(NO_3)_2$ than in KNO_3 by 3.4 kcal/mole. The destabilization of AgCl in $0.8KNO_3$–$0.2Sr(NO_3)_2$, relative to KNO_3, was estimated to be 2.9 kcal/mole. From Table I, the experimental destabilization in $0.8KNO_3$–$0.2Sr(NO_3)_2$ is 0.6 kcal/mole and in $0.8KNO_3$–$0.2Ca(NO_3)_2$ is 0.4 kcal/mole.

A smaller radius of nitrate ion, *e.g.*, 1.85–1.90 A, would lead to much better agreement between the experimental solvent effect and the calculated reciprocal coulomb effect, and also would lead to more consistent results for the solvent effect in the univalent ntrates.[2a–c] However, the greater destabilization observed for strontium than for calcium cannot be explained with a single value of the radius of nitrate ion. We have reported previously that the solvent effect on the association of cadmium ion in mixtures of lithium nitrate and potassium nitrate indicated a smaller effective radius of nitrate ion in lithium nitrate than in potassium nitrate. The results reported in the present paper also would be consistent with a smaller effective radius of nitrate ion in calcium nitrate than in strontium nitrate. Kapustinskii[11] has suggested the value 1.89 A for the thermochemical radius of nitrate ion. Meschel and Kleppa,[12] from their data on enthalpies of solution of alkali halides in alkali nitrates, suggested the value 1.93 A (1.85 A in lithium nitrate). Calculations of the reciprocal coulomb effect for the solvents $0.8KNO_3$–$0.2Ca(NO_3)_2$ and $0.8KNO_3$–$0.2Sr(NO_3)_2$, using eq 6 and the assumed linearity of the solvent effect in solvent mixtures, are listed in Table II for several values of the effective radius of nitrate ion. Also listed are values of the solvent effect calculated with a smaller effective radius, $r'_{NO_3^-}$, for a nitrate ion adjacent to a divalent ion than for a nitrate ion adjacent only to univalent cations

$$0.2(\Delta U_{Ca} - \Delta U_K) = 0.2Ne^2\left[\frac{1}{r_K + r_{Cl}} + \frac{2}{r_{Ca} + r'_{NO_3}} - \frac{2}{r_{Ca} + r_{Cl}} - \frac{1}{r_X + r_{NO_3}}\right]$$

The observed solvent effect would be consistent with the reciprocal coulomb effect with an effective radius of nitrate ion of 1.88 A (1.86 A in calcium nitrate).

Table II: Experimental Solvent Effect and Calculated Reciprocal Coulomb Effect for Several Values of the Radius of Nitrate Ion

$r_{NO_3^-}$, A	$r'_{NO_3^-}$, A	$0.2(\Delta U_{Ca} - \Delta U_K)$, kcal/mole	$0.2(\Delta U_{Sr} - \Delta U_K)$, kcal/mole
2.19	2.19	3.4	2.9
1.90	1.90	0.89	0.75
1.90	1.88	0.57	0.46
1.90	1.86	0.24	0.24
1.88	1.88	0.70	0.59
1.88	1.86	0.37	0.30
1.86	1.86	0.50	0.42
		0.4[a]	0.6[a]

[a] Experimental value.

A value of the radius of nitrate ion smaller than the radius of bromide ion would be inconsistent with the direction of the solvent effect on the association of Ag^+ with Br^- for which the greater stability in KNO_3 (than in $NaNO_3$) indicates a smaller radius for the bromide ion than for the nitrate ion.[2e] Although consideration of the long-range coulombic effects, polarization, and dispersion are required for a complete treatment of the solvent effect, the present results appear to indicate a radius of nitrate ion less than 2.00 A.

(10) "Handbook of Chemistry," 9th ed, Handbook Publishers, Inc., Sandusky, Ohio, 1950, p 108.

(11) A. F. Kapustinskii, *Quart. Rev.* (London), **10**, 283 (1956).

(12) S. V. Meschel and O. J. Kleppa, *J. Phys. Chem.*, **68**, 3840 (1964).

A Mass Spectrometric Study of the Ionic Species in a Radiofrequency Discharge in Methane

by H. E. Evans and P. P. Jennings

Materials Division, Berkeley Nuclear Laboratories, Berkeley, Gloucestershire, England *(Received November 12, 1965)*

An investigation of the nature and distribution of the ionic species present in a radiofrequency discharge in methane is reported. The major ionic species in the discharge were $C_2H_5^+$, $C_2H_3^+$, $C_2H_4^+$, $C_3H_4^+$, $C_3H_5^+$, $C_3H_3^+$, and CH_5^+. The ion distribution is compared with that reported for electron beam experiments (140-v electrons) at similar pressures.

The nature and distribution of species in radiofrequency discharges in carbon dioxide, carbon monoxide, and oxygen have been recently examined.[1] The present study of radiofrequency discharges in methane has extended this work and has allowed a comparison between these observations and published work on electron bombardment (140-v electrons) studies at similar pressures.

Experimental Section

The apparatus and techniques used have been described in detail elsewhere. The radiofrequency discharge was excited by power from an induction heater operating at 0.5 Mc/sec applied to two electrodes surrounding the limbs of the discharge vessel. The discharge vessel was mounted above the top plate of a modified AEI MS2R single-focusing mass spectrometer, and ions were sampled directly into the source region. Gas was introduced into the vessel at up to 10 cc/min and the discharge was studied over the range 0.5 to 2.0 torr.

The mass scale was calibrated by using discharges in the rare gases helium, neon, argon, and krypton to provide reference points.

Phillips hydrocarbon provided high-purity methane (99.98 mole %). This was dried with P_2O_5 before use.

Results

Preliminary experiments showed that a radiofrequency discharge could be produced over the pressure range 0.5 to 2.0 torr in methane under our experimental conditions. This discharge produced a deposit of amorphous hydrocarbon on the walls of the vessel. A limited pressure-variation study showed that while the total ionization decreased with increasing pressure the relative importance of the major species was not changed. At that time the only published work at similar pressures was that of Wexler and Jesse[2] and Field, *et al.*[3] Since they used pressures of up to ~0.3 torr, it was decided to examine the discharge at 0.6 torr which allowed study of a stable discharge at a pressure close to that used by the previous workers. Since our experiments were carried out, Field and Munson[4] have reported further work extending their investigation to 2.0 torr. This has allowed further comparisons between discharge and electron-beam conditions. Table I gives the results of Wexler and Jesse and Field, *et al.*, at 0.2 torr, the results of the discharge study, and the results of Field and Munson at 0.34 and 0.91 torr. A correction for ^{13}C contributions has been made to all peaks where the ^{13}C contribution exceeds the limits of accuracy of the determination.

Discussion

A considerably greater proportion of the total ionization is carried by C_3 ions and above in the discharge experiments than in the electron-beam experiments, but comparison of the first two columns in Table I shows that quite wide variations occur between the results of two groups carrying out electron-beam experiments under similar conditions (the divergence

(1) H. E. Evans and P. P. Jennings, *Trans. Faraday Soc.*, 61, 2153 (1965).

(2) S. Wexler and N. Jesse, *J. Am. Chem. Soc.*, 84, 3425 (1962).

(3) F. H. Field, J. L. Franklin, and M. S. B. Munson, *ibid.*, 85, 3575 (1963).

(4) F. H. Field and M. S. B. Munson, *ibid.*, 87, 3289 (1965).

between the observed ion distributions reported for ethylene by these two groups is even greater).[5,6]

Table I

m/e	Ref 2 (0.2 torr)	Ref 3 (0.2 torr)	Ref 4 (0.34 torr)	This work (0.6 torr)	Ref 4 (0.91 torr)
12	0.01	0.03	0.007		
13	0.01	0.06	0.02		0.004
14	0.09	0.2	0.07		0.01
15	0.78	3.4	0.61	0.36	0.08
16	0.20	1.9	0.40	0.10	0.06
17	32.58	54.4	35.1	5.48	47.8
18		0.1		0.13	
19		0.2	0.22	2.1	0.38
24				0.003	
25	0.02			0.04	
26	0.08	0.2	0.05	0.13	
27	11.22	5.9	3.9	12.26	0.51
28	4.99	1.9	3.2	8.04	2.0
29	38.99	29.2	44.0	29.53	40.6
30	1.19	0.02		1.16	
31	0.26	0.004	0.08	0.60	0.12
32				0.05	
33				0.10	
35				0.007	
37				0.03	
38				0.05	
39	0.32	0.08	0.16	6.27	0.06
40	0.42	0.09	0.29	8.49	0.16
41	7.51	1.01	8.6	7.20	5.5
42	0.04			1.91	
43	0.61	0.06	0.47	2.64	0.71
44	0.29			0.17	
45	0.06			0.10	
46				0.007	
47	0.02			0.01	
50				0.74	
51	0.03			1.16	
52				1.57	
53	0.02			1.10	
54				0.59	
55	0.04	0.002	0.06	1.19	0.07
56	0.01	0.001		0.61	
57	0.06	0.002	0.05	0.52	0.13
58	0.01			0.06	
59				0.07	
60	0.003				
61	0.02			0.001	
62					
63	0.002			0.06	
64				0.12	
65	0.004			0.30	
66				0.32	
67	0.002			0.55	
68				0.24	
69	0.012	0.002	0.007	0.34	0.004
70				0.19	
Σ 71 to 100	0.052	0.004	0.006	3.16	0.004

Field, *et al.*,[3] suggested that the difference could be due to the greater ion path length in Wexler's apparatus giving greater reaction; however, we feel that the difference may be due to a difference in the residence time of products in the two systems and that the variation in the extent of reaction between the electron-beam experiments and the discharge experiment can be simply explained in terms of the greatly increased "dose rate" in the discharge.

Despite the increase in the importance of the higher ions in the discharge, a number of points of similarity occur between the two systems. In each case the dominant C_1 and C_2 ions are CH_5^+ and $C_2H_5^+$, and the $C_3H_5^+$ ion, dominant in the electron-beam experiment, is one of three ions of similar intensity in the discharge. Further, the concentrations of the C_1 ions are in the order $CH_5^+ >> CH_3^+ > CH_4^+$ in both systems and for all pressures and except at 0.91 torr the C_2 ions have concentrations in the order $C_2H_5^+ > C_2H_3^+ > C_2H_4^+ >> C_2H_6^+$.

A number of ions are present to a greater extent in the discharge than in the electron-beam system. We attribute the peaks with *m/e* ratios 18, 19, 32, and 33 to H_2O^+, H_3O^+, O_2^+, and HO_2^+ derived from water desorbed from the glass reaction vessel (Field and Munson[4] have recently commented on the importance of proton transfer to water), but as no appearance potential measurements could be made in the discharge this was not verified.

Similarly, the discharge shows a greater concentration of the $C_2H_7^+$, $C_3H_9^+$, $C_4H_{11}^+$, and $C_5H_{13}^+$ ions (0.6, 0.1, 0.5, and 0.03% of the total ionization) than has previously been reported. Munson and Field[7] observed an ion of mass 45 to 0.1% in the presence of propane but did not assign it definitely. However, in view of the presence of an ion of this mass in the discharge and, more important, the significant concentration of the homologous ion $C_4H_{11}^+$, we feel that protonated alkane ions probably do exist.

There was no sign of a variation in intensity between odd and even mass number ions in the discharge although such a variation was just apparent in the work of Field[3,5] and quite marked in the work of Wexler and Jesse.[2]

The low concentration of C^+, CH^+, and CH_2^+ ions in the electron-beam studies implies that these species have a high reactivity. While their absence from the discharge could be due to the same cause, it seems more likely that it is a feature of the discharge. The

(5) F. H. Field, *J. Am. Chem. Soc.*, **83**, 1523 (1961).
(6) S. Wexler and R. Marshall, *ibid.*, **86**, 781 (1964).
(7) M. S. B. Munson and F. H. Field, *ibid.*, **87**, 3294 (1965).

rather low effective electron energy in the discharge[1] implies that these ions are not formed by dissociation following electron impact. As formation of the ions from the corresponding radicals would require relatively low electron energies, we conclude that if the radicals are present they react rapidly giving a standing concentration below the limits of detection.

It is quite certain that reaction occurs in the discharge. Analysis shows the presence of C_2 and possibly C_3 saturated and unsaturated hydrocarbons and of a hydrocarbon deposit. In view of the dominance of product ions in the electron irradiation of ethylene[6] we suggest that the ion distribution we observe in the discharge is in part due to the formation of C_1, C_2, and possibly C_3 ions by a mechanism similar to that found in the electron-beam experiments, and in part due to other reactions, *e.g.*, ion–molecule reaction with unsaturated hydrocarbons, and ionization of high molecular weight products. This latter suggestion is supported by the observation that the concentration of higher ions increased over the first few minutes when a discharge was struck in a freshly cleaned reaction vessel.

Acknowledgment. We thank Mr. R. A. Mascall for his assistance with the experimental work; this paper is published by permission of the Central Electricity Generating Board.

Solubility in Water of Paraffin, Cycloparaffin, Olefin, Acetylene, Cycloolefin, and Aromatic Hydrocarbons[1]

by Clayton McAuliffe

Chevron Research Company, La Habra, California *(Received November 15, 1965)*

The solubilities in water at room temperature of 65 hydrocarbons have been measured using a gas–liquid partition chromatographic technique. For each homologous series of hydrocarbons, the logarithm of the solubility in water is a linear function of the hydrocarbon molar volume. Branching increases water solubility for paraffin, olefin, and acetylene hydrocarbons. The increased solubilities due to branching apparently are not due to a structural feature of the molecules, but to the higher vapor pressure of the branched-chain hydrocarbons compared with the corresponding paraffin or olefin hydrocarbon. The "structure" of water is such that, for the same hydrocarbon vapor pressure, approximately the same weight of a C_2 through C_9 paraffin hydrocarbon dissolves in water. For a given carbon number, ring formation increases water solubility. Increasing unsaturation of the hydrocarbon molecule, chain or ring, increases solubility of the hydrocarbon in water.

Introduction

Because of their relatively high solubility in water and ease of measurement by ultraviolet absorption in aqueous solution, the solubilities of benzene, toluene, xylenes, ethylbenzene, and isopropylbenzene have been determined by several investigators.[2-10] The solubilities of methane and ethane were determined by Winkler[11] in 1901 and substantiated by the work of

(1) Presented before the Division of Petroleum Chemistry, 148th National Meeting of the American Chemical Society, Chicago, Ill.

(2) L. J. Andrews and R. M. Keefer, *J. Am. Chem. Soc.*, 71, 3644 (1949).

Claussen and Polglase[12] and Morrison and Billett.[9] Claussen and Polglase also determined the solubilities of propane and *n*-butane; Morrison and Billett measured propane, *n*-butane, and ethene. However, the solubilities of only a few additional hydrocarbons have been reported. Führer[6] in 1924 measured *n*-pentane, *n*-hexane, *n*-heptane, and *n*-octane. The solubilities of *n*-hexane, *n*-heptane, and cyclohexane were determined by Durand.[10] Ethene,[13] propene,[14] and 2-methylpropene[13,15] solubilities in water are reported. With the exceptions cited, solubilities have not been measured for most of the paraffin, cycloparaffin, olefin, acetylene, and cycloolefin hydrocarbons reported here.

In this investigation, hydrocarbon solubilities in water were measured by the direct injection of hydrocarbon-saturated water into a gas chromatograph. The gas chromatographic technique has two principal advantages over previous methods of determining dissolved hydrocarbons in water. (1) The presence of impurities with high water solubility pose no problem unless the relative retention time of the impurity is the same as the hydrocarbon being measured. (2) The use of a hydrogen-flame ionization detector permits the measurement of relatively low concentrations of hydrocarbons in water.

A few preliminary results of the solubility measurements of selected paraffin, cycloparaffin, and aromatic hydrocarbons measured by the gas chromatographic technique were recently published.[16]

Experimental Section

Materials. The hydrocarbons were obtained either from Phillips Petroleum Co. (99+% purity) or from Columbia Chemical Co., Columbia, S. C. The hydrocarbons were used as received.

Equilibration of Hydrocarbon with Water. One atmosphere of the individual gaseous hydrocarbons was maintained over distilled water during equilibration. Gas was added to the equilibration vessel by displacing distilled water. A rubber balloon in the line from the gas cylinder to the equilibration bottle served as a reservoir. The bottle, three-fourths full of water, was vigorously hand shaken for 5 to 10 min to establish equilibrium between the gaseous hydrocarbon and water. The equilibrated solution was allowed to stand at least 30 min prior to analysis, to permit separation of undissolved gas phase from water.

From 10 to 20 ml of individual liquid hydrocarbons was added to 200 ml of distilled water in a 250-ml glass bottle. Saturated solutions of the liquid hydrocarbons in distilled water were prepared by either shaking the bottle vigorously on a reciprocal shaker for 1 hr, or stirring at least 1 day with a magnetic stirrer. Speed of stirring was adjusted so that the surface vortex was never greater than one-fourth the solution depth. In the case of vigorous shaking, the solution was allowed to stand for 2 days to permit separation of small hydrocarbon droplets; the aqueous phase was examined for the presence of emulsion under a phase-contrast microscope with a magnification of 1700×. No emulsions were found. If droplets were present, they were smaller than 0.2 μ. The same solubility values were obtained by stirring the solution. This fact supports the microscopic examination of the absence of emulsified hydrocarbon.

Because of greater convenience, most of the hydrocarbons were equilibrated with water by stirring on a magnetic stirrer. No attempt was made to regulate the temperature closer than 25 ± 1.5° maintained by the air-conditioning system in the laboratory.

Samples of the hydrocarbon-saturated water were obtained from beneath the hydrocarbon phase either by displacement of water through a tube, or by insertion of a hypodermic needle through a silicone rubber septum in a tubulation sealed near the bottom of the glass bottle.[17] A 50-μl sample of the hydrocarbon-saturated water was measured with a Hamilton syringe and injected into the fractionator of the gas chromatograph.

Fractionator. The fractionator, a modification of one reported by Zarrella, *et al.*,[18] separated the dissolved hydrocarbon from water. The fractionator was a 4.5-in. U-tube made from 6-mm glass tubing. One arm of the U-tube was attached to a modified $^1/_8$-in.

(3) L. J. Andrews and R. M. Keefer, *J. Am. Chem. Soc.*, **72**, 5034 (1950).

(4) R. L. Bohon and W. F. Claussen, *ibid.*, **73**, 1571 (1951).

(5) W. F. McDevit and F. A. Long, *ibid.*, **74**, 1773 (1952).

(6) H. Führer, *Chem. Ber.*, **57**, 510 (1924).

(7) D. S. Arnold, C. A. Plank, E. E. Erickson, and F. P. Pike, *Chem. Eng. Data Ser.*, **3**, 253 (1958).

(8) F. Franks, M. Gent, and H. H. Johnson, *J. Chem. Soc.*, 2716 (1963).

(9) T. J. Morrison and F. J. Billett, *ibid.*, 3819 (1952).

(10) R. Durand, *Compt. Rend.*, **226**, 409 (1948).

(11) L. W. Winkler, *Chem. Ber.*, **34**, 1408 (1901).

(12) W. F. Claussen and M. F. Polglase, *J. Am. Chem. Soc.*, **74**, 4817 (1952).

(13) R. W. Taft, Jr., E. L. Purlee, and P. Riesz, *ibid.*, **77**, 899 (1955).

(14) E. L. Purlee and R. W. Taft, Jr., *ibid.*, **78**, 5811 (1956).

(15) K. S. Kazanskii, S. G. Entelis, and N. M. Chirkov, *Zh. Fiz. Khim.*, **33**, 1409 (1959).

(16) C. McAuliffe, *Nature*, **200**, 1092 (1963).

(17) P. A. Witherspoon, personal communication.

(18) W. M. Zarrella, R. J. Mousseau, N. D. Coggeshall, M. S. Norris, and G. J. Schrayer, Preprint of presentation before Division of Petroleum Chemistry, 144th National Meeting of the American Chemical Society, Los Angeles, Calif., April 1963.

stainless steel Swagelok T-fitting by means of an O-ring joint. The second arm was attached by an O-ring joint to 1/8-in. stainless steel tubing. The O-ring joints were held together with ball-joint clamps. The O-ring joints permitted easy replacement of the glass U-tube. The Swagelok T-fitting was further modified to have a rubber septum as the water injection port. This assembly served as a sample loop of the gas chromatograph.

Approximately one-third of the U-tube was packed with 60–80 mesh firebrick, and the remaining two-thirds was packed with 8–20 mesh Ascarite. A small plug of glass wool was placed after the Ascarite to prevent solid particles from being carried into the chromatographic column by the helium gas flow. During analysis, helium gas flowed past the injection port and through the U-tube with helium passing first over the firebrick. The U-tube was immersed to just above the O-ring joints in boiling water. A 50-μl sample of water in the syringe was introduced through the injection port and onto the top of the firebrick. The firebrick permitted partial separation of the dissolved hydrocarbon from water. Ascarite prevented water from entering the chromatographic column. Three successive 50-μl water samples could be injected before it was necessary to replace the packing in the U-tube.

Chromatographic Analysis. The chromatographic column was 12 ft of 0.25-in. stainless steel tubing, packed with 25% SE 30 gum rubber on 30–60 mesh firebrick. Helium flow through the column was 65 cc/min, with the entire effluent passing into a hydrogen-flame ionization detector (Beckman). Depending upon the relative retention time of the hydrocarbon, the column was operated at approximately 60 (minimum attainable with hydrogen-flame burner in the oven compartment), 100, and 125°. The chromatograph was equipped with a 10-port valve (Consolidated Electrodynamic Corp.) which permitted attachment of the U-tube while an analysis was being made. The chromatograph also had a short precut column which permitted backflushing of heavier constituents.

Measurement of Hydrocarbon Concentration. The gas chromatographic technique of measuring the concentration of dissolved hydrocarbons in water has a principal advantage in that impurities do not interfere. Only in those instances where the impurity has the same relative retention time on the column as the hydrocarbon being measured will interference occur. Figure 1 demonstrates the ease with which the contributions by impurities can be eliminated. Figure 1 shows three superimposed chromatograms. The middle chromatogram was obtained by injecting pure 1-octene into the column, with an attenuation setting of 25,600; the top chromatogram was obtained at an attenuation of 256. Note that in the interval analyzed, no impurities are detectable in 1-octene, except for a small peak (256 attenuation) just prior to the emergence of 1-octene. However, after 1-octene was equilibrated with water and analyzed (bottom chromatogram), a number of impurity peaks became apparent. A measuring technique which would have included all organic constituents would have given a solubility for 1-octene very much higher than the true solubility.

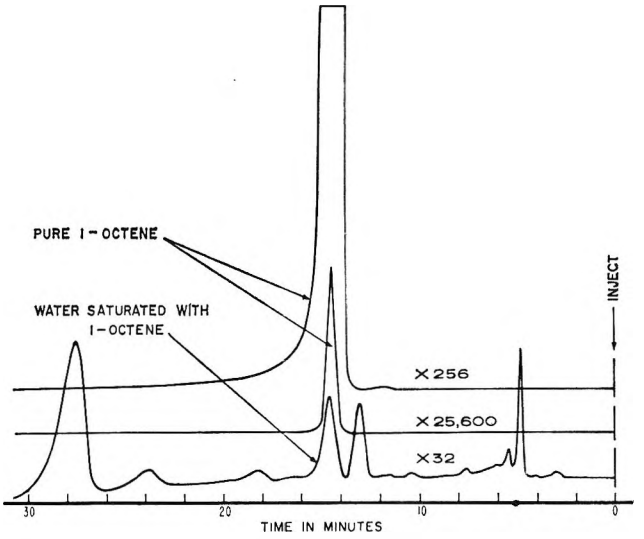

Figure 1. Gas chromatograms of 1-octene compared with chromatogram of water saturated with 1-octene.

The impurity peaks are either present in very small amounts in the original 1-octene and have very high water solubility, or the impurity peaks are formed during the equilibration of 1-octene with water either by oxidation, photoreactions, or by bacterial action. However, unless the impurity peaks interfere with the measurement of the hydrocarbon peak, their presence is of no significance. This assumes, of course, no interaction between the impurities and the hydrocarbon that would alter the solubility of the latter in water.

Although the effect of impurities becomes more pronounced the lower the solubility of the hydrocarbon, impurities can also be present and contribute to solubility measurements, by nonchromatographic techniques, of hydrocarbons having relatively high solubilities in water. Cyclopentane, when analyzed as a pure hydrocarbon on the chromatographic column, showed 0.2% impurity. After equilibration with water, the impurity peak was 25% of the cyclopentane area. Higher molecular weight hydrocarbons might also be present which would not be measured in the time interval used in the analysis.

Table I: Solubility in Water at Room Temperature of Paraffin and Branched-Chain Paraffin Hydrocarbons

Hydrocarbon	Solubility, g of hydrocarbon/10^6 g of water — This work	Lit.	Molar vol., ml/mole at 20°
Methane	24.4 ± 1.0[a]	21.7,[11] 22.8,[12] 21.5[9]	39
Ethane	60.4 ± 1.3	56.6,[11] 58.3,[12] 51.6[9]	55
Propane	62.4 ± 2.1	67.0,[12] 65.6[9]	88.1
n-Butane	(136)[b] 61.4 ± 2.6	72.7,[12] 67.2[9]	100.4
Isobutane	(165) 48.9 ± 2.1		104.3
n-Pentane	38.5 ± 2.0	360[6]	115.2
Isopentane	47.8 ± 1.6		116.4
2,2-Dimethylpropane	(54) 33.2 ± 1.0		122.1
n-Hexane	9.5 ± 1.3	140,[6] 36[10]	130.7
2-Methylpentane	13.8 ± 0.9		131.9
3-Methylpentane	12.8 ± 0.6		129.7
2,2-Dimethylbutane	18.4 ± 1.3		132.7
n-Heptane	2.93 ± 0.20	50,[6] 10[10]	146.5
2,4-Dimethylpentane	4.06 ± 0.29		148.9
n-Octane	0.66 ± 0.06	14[6]	162.6
2,2,4-Trimethylpentane	2.44 ± 0.12		165.1
2,2,5-Trimethylhexane	1.15 ± 0.08		181.3

[a] Standard deviation from mean. [b] Calculated solubility of liquid hydrocarbon at 25°.

A further advantage of the gas chromatographic technique is the unusually high sensitivity obtainable with hydrogen-flame ionization detectors. With the present technique, hydrocarbons in amounts as little as 0.1 ppm can be measured in 50 μl of water. In practice, because of impurities, it is usually not feasible to measure solubilities that are less than 1 ppm.

The concentration of hydrocarbon was determined by measuring the area under the chromatograph peak with a planimeter or an electronic integrator (Infotronics Model CRS-1). The hydrogen-flame ionization detector was calibrated by injecting 1.00 μl of a mixture of from eight to twelve carefully weighed pure liquid hydrocarbons. The injection of mixtures of known amounts of several liquid hydrocarbons were also used to determine the relative sensitivity of the detector to all hydrocarbons compared with *n*-heptane. The detector was found to be 1.16 times more sensitive to benzene than normal heptane and 1.14 times more sensitive to toluene. Detector sensitivity to other hydrocarbons was generally within ±5% of the value for *n*-heptane.

Results and Discussion

The solubilities in water at room temperature of paraffin and branched-chain paraffin hydrocarbons are shown in Table I. Previously measured solubilities are shown in Table I and the following tables where values are available. The last column in each table gives the molar volume of the individual hydrocarbons obtained from American Petroleum Institute Research Project 44[19] or calculated from data given by Doss.[20]

The solubilities of methane, ethane, propane, and *n*-butane are close to the values reported by Winkler,[11] Claussen and Polglase,[12] and Morrison and Billett.[9] However, the solubilities found for *n*-pentane, *n*-hexane, *n*-heptane, and *n*-octane are from 10 to 20 times lower than reported by Führer.[6] Durand's[10] values for *n*-hexane and *n*-heptane are much lower than Führer's but are still three to four times higher than observed in the present investigation.

The solubilities in water of olefin hydrocarbons are shown in Table II. Values for ethene and propene closely agree with previous work but the value for 2-methylpropene is lower. No other olefin solubilities were found in the literature.

For a given carbon number, the olefin hydrocarbons have considerably higher solubilities in water than do the paraffin hydrocarbons shown in Table I.

Table III shows the solubility in water at room temperature of the acetylene hydrocarbons. For a given carbon number, the acetylene hydrocarbons have much higher solubilities than the olefin hydrocarbons. As far as is known, solubilities of acetylene hydrocarbons in water at room temperature have not been measured.

The solubilities of cycloparaffin, cycloolefin, and aromatic hydrocarbons are listed in Table IV. Only one comparison value is available for cycloparaffins

(19) "Selected Values of Physical and Thermodynamic Properties of Hydrocarbons and Related Compounds," A.P.I. Research Project 44, Carnegie Press, Pittsburgh, Pa., 1953.

(20) M. P. Doss, "Physical Constants of the Principal Hydrocarbons," 4th ed, The Texas Co., New York, N. Y., 1943.

Table II: Solubility in Water at Room Temperature of Olefin Hydrocarbons

Hydrocarbon	Solubility, g of hydrocarbon/10^6 g of water — This work	Lit.	Molar vol., ml/mole at 20°
Olefins			
Ethene	131 ± 10[a]	134,[9] 131[13]	54.5
Propene	(2040)[b] 200 ± 27	183 at 30°[14]	81.9
1-Butene	(615) 222 ± 10		94.8
2-Methylpropene	(670) 263 ± 23	289,[13] 314[15]	94.4
1-Pentene	148 ± 7		109.5
2-Pentene	203 ± 8		107.0–108.2[c]
3-Methyl-1-butene	(156) 130 ± 14		111.8
1-Hexene	50 ± 1.2		125.0
2-Methyl-1-pentene	78 ± 3.2		123.4
4-Methyl-1-pentene	48 ± 2.6		126.7
2-Heptene	15 ± 1.4		138.7–140.0[c]
1-Octene	2.7 ± 0.2		157.0
Diolefins			
1,3-Butadiene	(1980) 735 ± 20		87.1
2-Methyl-1,3-butadiene	642 ± 10		100.0
1,4-Pentadiene	558 ± 27		103.1
1,5-Hexadiene	169 ± 6		118.7
1,6-Heptadiene	44 ± 3		134.0

[a] Standard deviation from mean. [b] Calculated solubility of liquid hydrocarbon at 25°. [c] Molar volume for *cis–trans* forms.

Table III: Solubility in Water at Room Temperature of Acetylene Hydrocarbons

Hydrocarbon	Solubility, g of hydrocarbon/10^6 g of water	Molar vol., ml/mole at 20°
Acetylenes		
Propyne	3640 ± 125[a]	60
1-Butyne	(5150)[b] 2870 ± 101	83
1-Pentyne	1570 ± 33	98.7
1-Hexyne	360 ± 17	114.8
1-Heptyne	94 ± 3	131.2
1-Octyne	24 ± 0.8	147.7
1-Nonyne	7.2 ± 0.5	164.1
Diacetylenes		
1,6-Heptadiyne	1650 ± 25	112
1,8-Nonadiyne	125 ± 3	147

[a] Standard deviation from mean. [b] Calculated solubility of liquid hydrocarbon at 25°.

and none for cycloolefins. Durand[10] measured the solubility of cyclohexane as 63 ppm, close to the value of 55 ppm measured in this investigation. A number of workers[2–10] have measured the solubilities of aromatic hydrocarbons, particularly benzene, toluene, and ethylbenzene. The measured solubilities for benzene and toluene closely agree with those reported by previous workers. However, the solubilities of *o*-xylene, ethylbenzene, and isopropylbenzene are somewhat lower than previously reported.

The data in Table IV show that as unsaturation of the ring structures increases, solubility in water increases.

Lindenberg[21] proposed a relationship between the logarithm of the solubility of hydrocarbons in water and the molar volume of the hydrocarbons. Using solubility data from the literature, he calculated constants for various saturated and aromatic hydrocarbons, as well as for chlorinated hydrocarbons. Rather than calculate constants, if the logarithm of the solubilities of the hydrocarbons in water is plotted against the molar volume of the hydrocarbons, a straight line is obtained.

Paraffin and Branched-Chain Paraffin Hydrocarbons. Figure 2 is a plot of the logarithm of the solubility in water of paraffin and branched-chain paraffin hydrocarbons *vs.* the molar volume of the hydrocarbons. A straight line has been drawn through the normal paraffin hydrocarbons having from four through eight carbon atoms. An excellent fit is shown.

Two values are shown in Figure 2 for *n*-butane, isobutane, and 2,2-dimethylpropane (neopentane). The lower value is the solubility measured for these gases at 1 atm pressure and 25°. The value at the point of the arrow represents the calculated solubility the hydrocarbon would possess in the liquid state, namely, the vapor pressure existing in contact with the liquid

(21) M. A. Lindenberg, *Compt. Rend.*, **243**, 2057 (1956).

Table IV: Solubility in Water at Room Temperature of Cycloparaffin, Cycloolefin, and Aromatic Hydrocarbons

Hydrocarbon	Solubility, g of hydrocarbon/10^6 g of water		Molar vol., ml/mole at 20°
	This work	Lit.	
Cycloparaffins			
Cyclopentane	156 ± 9[a]		94.1
Cyclohexane	55 ± 2.3	63[10]	108.1
Cycloheptane	30 ± 1.0		121
Cyclooctane	7.9 ± 1.8		135
Methylcyclopentane	42 ± 1.6		112.4
Methylcyclohexane	14.0 ± 1.2		127.6
1-*cis*-2-Dimethylcyclohexane	6.0 ± 0.8		140.9
Cycloolefins			
Cyclopentene	535 ± 20		88.2
Cyclohexene	213 ± 10		101.3
Cycloheptene	66 ± 4		116
1-Methylcyclohexene	52 ± 2		118.7
1,4-Cyclohexadiene	700 ± 16		93.6
4-Vinylcyclohexene	50 ± 5		130
Cycloheptatriene	620 ± 20		103
Aromatics			
Benzene	1780 ± 45	1740,[2] 1790,[4] 1775,[5] 1740,[7] 1730,[8] 1720,[9] 1450[10]	88.7
Toluene	515 ± 17	530,[2] 627,[4] 470,[b] 536[9]	106.3
o-Xylene	175 ± 8	204[2]	120.6
Ethylbenzene	152 ± 8	168,[3] 208,[4] 140,[6] 165[9]	122.4
1,2,4-Trimethylbenzene	57 ± 4		137.2
Isopropylbenzene	50 ± 5	73[3]	139.5

[a] Standard deviation from mean.

at 25°. The calculated values are shown in parentheses in the tables. The vapor pressures used throughout this paper were obtained from plots of vapor pressure *vs.* temperature for the various hydrocarbons obtained from the literature and compiled by Chevron Research Co. The chief source of vapor pressure data for the compilation was A.P.I. Project 44.[19] These data were supplemented with values from the literature. In general, experimental data were given preference over calculated or generalized data.

The solubilities of the branched-chain paraffin isomers are higher in all instances than for the normal paraffin hydrocarbons—the greater the branching, the higher the solubility. This is true also for the corrected solubilities to the liquid state for iso- and *n*-butane and neopentane. Note the reversal in solubilities of iso- and *n*-butane from that measured at 1 atm pressure and room temperature. Also, the solubility of neopentane is greater than isopentane; the sequence runs *n*-C_5, iso-C_5, neo-C_5.

The increased solubilities of the branched-chain paraffins apparently are not due to a structural feature of the molecules but to the higher vapor pressure (fugacity) of the branched-chain hydrocarbons. If the measured solubility of each normal or branched-chain paraffin hydrocarbon with a boiling point higher than 25° is divided by its vapor pressure in millimeters at 25° and multiplied by 760 mm, a predicted solubility at room temperature and 1 atm is obtained. The calculated values are shown underlined by the names of the hydrocarbons in Figure 2. With the exception of 2,4-dimethylpentane, the values range from 40 to 59 ppm. The lower values appear to be associated with the heavier hydrocarbons.

The solubilities of ethane, propane, iso-, and *n*-butane range from 49 to 62 ppm. Methane and neopentane, with solubilities of only 24 and 33 ppm at 1 atm pressure, are anomalous. The value of 31 for 2,4-dimethylpentane may be anomalous; however, the vapor pressure or the solubility may be in error. With these exceptions, it appears that to a first approximation the weight of a normal or branched-chain hydrocarbon which dissolves in water is proportional to the vapor pressure of the hydrocarbon. The "structure" of water is such that it will accommodate a given weight of a C_8 or C_9 paraffin hydrocarbon with almost as much ease as a corresponding weight of ethane or propane.

The size and configuration of methane and 2,2-dimethylpropane (neopentane) may be such that their

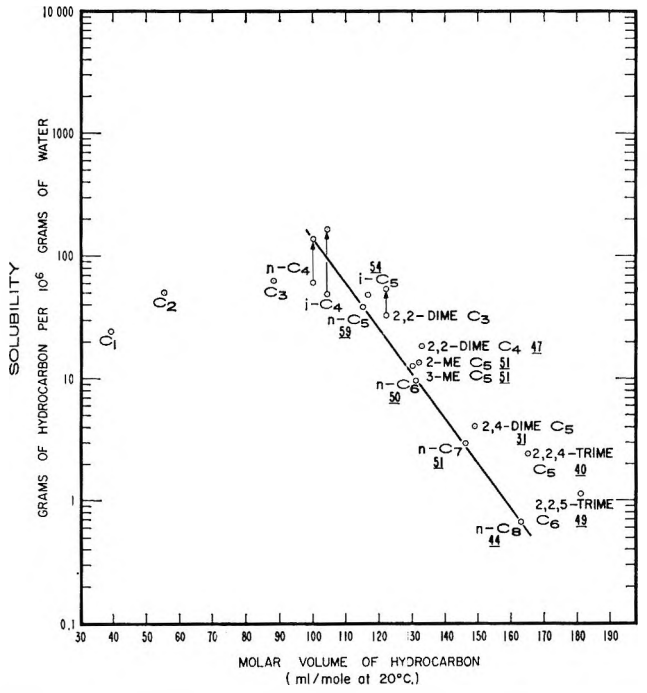

Figure 2. Solubility in water at 25° of paraffin hydrocarbons as a function of their molar volumes.

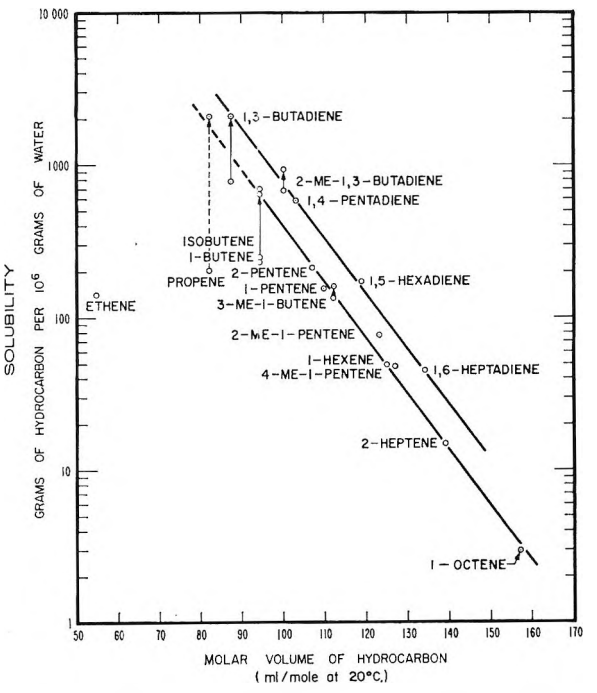

Figure 3. Solubility in water at 25° of olefin hydrocarbons as a function of their molar volumes.

association with water is different than for the other paraffin and branched-chain paraffin hydrocarbons, causing a decrease in observed solubility at 1 atm pressure and 25°.

The measurement of hydrocarbon solubilities by the gas chromatographic technique reported here is limited to concentrations above 0.1 ppm. If the relationship between the logarithm of the solubility of hydrocarbon in water *vs.* molar volume of the hydrocarbon is a continuous function, then the solubilities of C_9 and heavier hydrocarbons can be predicted by extrapolation of the line shown in Figure 2, or if accurate vapor pressures are available for C_9 and heavier hydrocarbons, their solubilities can be estimated from vapor pressures.

Olefin Hydrocarbons. The logarithm of the solubility in water of olefin and diolefin hydrocarbons plotted against molar volume of the hydrocarbons is shown in Figure 3. The solubility correction from gas at 1 atm to the liquid state at 25° has again been calculated for propene, isobutene, 1-butene, 3-methyl-1-butene, 1,3-butadiene, and 2-methyl-1,3-butadiene. The solubility correction from gas to liquid state for propene is probably not valid, inasmuch as the molar volume is not accurately known. The liquid density used to make the molar volume calculation was that of propene at its liquefaction temperature.

As was shown for the paraffin hydrocarbons, a straight line can be drawn through the straight-chain olefin and diolefin hydrocarbons. The solubility of 1-octene appears to be low, but the other straight-chain monoolefins closely fit the relationship postulated.

Availability of vapor pressures for the olefin hydrocarbons is more limited than for the paraffin hydrocarbons. Calculated solubilities at 1 atm and room temperature for 1-pentene, 1-hexene, and 1-octene are 186, 224, and 170 ppm. The measured values, Table II, for propene, 1-butene, and isobutene are 200, 222, and 236 ppm. Thus, as for the paraffin hydrocarbons, approximately the same weight of each monoolefin hydrocarbon dissolves in water at a constant vapor pressure.

As was the case for the paraffin hydrocarbons, branching of the olefin hydrocarbons increases water solubility. The same general solubility relationships exist for the olefin hydrocarbons as for the paraffin hydrocarbons, with the exception that the solubility for a given carbon number is higher.

Acetylene, Cycloparaffin, Cycloolefin, and Aromatic Hydrocarbons. If the solubility values for acetylene, cycloparaffin, cycloolefin, and aromatic hydrocarbons are plotted as for paraffin and olefin hydrocarbons, similar straight-line relationships are shown for each homologous series. 1-Nonyne and cycloheptane appear to have solubilities which are a little too high.

Cycloheptatriene has a solubility greater than

toluene. Its molar volume is less than toluene, and the cycloheptatriene value falls on the aromatic line. Cycloheptatriene, although not normally considered an aromatic hydrocarbon, differs from toluene only in having a seven-membered ring with a methylene carbon in the ring compared to a methyl group external to the six-membered benzene ring.

At constant vapor pressure, 760 mm, and 25°, benzene, toluene, *o*-xylene, ethylbenzene, and isopropylbenzene have calculated water solubilities of 1.5, 1.5, 2.0, 1.4, and 1.3 $\times$ 10^4 g/10^6 g of water.

With paraffin and olefin hydrocarbons, branching of the chain caused higher water solubility for a given number of carbon atoms in the molecule (Figures 2 and 3). In the case of cycloparaffins, cycloolefins, and aromatic hydrocarbons, addition of side chains on the ring structures has not increased water solubility for a given carbon number.

Water Solubility as Related to Hydrocarbon Type. The straight lines for each homologous series have been plotted in Figure 4 to show the relationship of water solubility *vs.* molar volume for the various classes of hydrocarbons. Using solubility data from the literature, Lindenberg[21] calculated constants from the relationship between the logarithm of the solubility of hydrocarbons in water and molar volume of the hydrocarbons. He concluded that all hydrocarbons gave a single constant. If plotted, this would mean that all hydrocarbons would fall on a single line. From Figure 4 it is obvious that all classes of hydrocarbons do not fall on a single line. Published data available to Lindenberg were limited. Further, Lindenberg used Fühner's solubilities for normal C_5–C_8, and, as shown in Table I, they are much too high.

In Figure 4 the solid lines represent the solubilities *vs.* molar volumes for the straight-chain hydrocarbons. The dashed lines represent the solubilities *vs.* molar volumes for hydrocarbons having ring structures. The solubilities for both chain and ring hydrocarbons increases as unsaturated bonds are added to the molecule. A single double bond increases the solubility of an olefin compared to the normal paraffin. A second double bond increases the solubility still further, and a single triple bond increases the solubility to a greater extent than two double bonds.

Ring closure increases water solubility. The addition of unsaturated bonds in the ring progressively increases water solubility through the sequence cycloolefin, cyclodiolefin, and aromatic hydrocarbons.

Figure 4 also demonstrates that although each class of hydrocarbons plot as a straight line when the logarithm of the solubility is plotted against molar volume, the ring structures have a different slope than do hydrocarbons with a straight-chain structure.

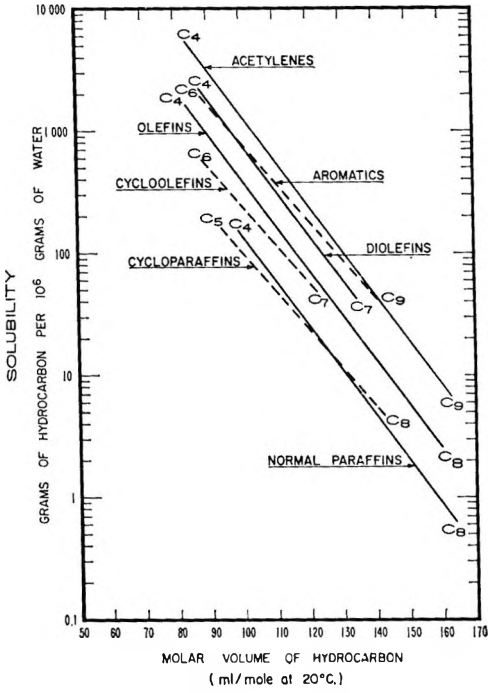

Figure 4. Comparison of the solubility in water of various types of hydrocarbons as a function of their molar volumes.

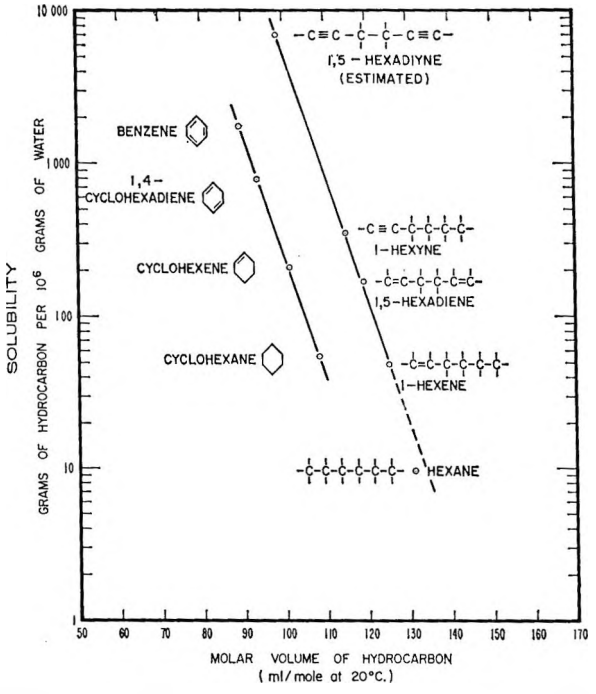

Figure 5. Solubility in water of various types of hydrocarbons, each with six carbon atoms in the molecule, as a function of their molar volumes.

The relationship of solubility *vs.* molar volume of different types of hydrocarbons having six carbon atoms in the molecule is shown in Figure 5. The addition of a single double bond to the molecule changes the molar volume of hexane to a lower value for 1-hexene and increases the water solubility appreciably. Two double bond additions to the six-carbon chain (1,5-hexadiene) further decreases the molar volume and increases water solubility. The addition of one triple bond further decreases the molar volume and likewise increases water solubility.

An additional decrease in molar volume is caused by the addition of a second triple bond to the molecule with a still greater increase in water solubility. The value for 1,5-hexadiyne is an estimated solubility. From Table III the solubility of 1,6-heptadiyne is 17.6 times greater than the solubility of 1-heptyne. The solubility of 1,8-nonadiyne is 17.4 times greater than 1-nonyne. If the solubility of 1,5-hexadiyne is 17.5 times higher than 1-hexyne, the solubility would be calculated to be 6700 ppm. A straight line can be drawn through the four olefin and acetylene hydrocarbons.

If ring closure occurs for hexane, a marked decrease in molar volume occurs and the solubility of cyclohexane increases to a greater extent than the addition of a double bond to the hexane molecule. As unsaturation occurs in the ring structure, progressing from cyclohexene to 1,4-cyclohexadiene to benzene, the molar volume of the liquid hydrocarbon decreases and the solubility correspondingly increases. Cyclohexene has a higher water solubility than does 1,5-hexadiene. 1,4-Cyclohexadiene has appreciably higher water solubility than 1-hexyne, but 1,5-hexadiyne has greater solubility than benzene.

A straight line can, again, be drawn through the four six-carbon ring structures. This line parallels the line drawn through the olefin and acetylene six-carbon hydrocarbons. Similar plots can be made using hydrocarbons having four, five, seven, and eight carbons in the various hydrocarbon structures. The C_6 hydrocarbons were plotted because more information is available.

Conclusions

For each homologous series of hydrocarbons, the logarithm of the solubility in water is a linear function of the hydrocarbon molar volume.

Branching increases water solubility for paraffin, olefin, and acetylene hydrocarbons, but not for cycloparaffin, cycloolefin, and aromatic hydrocarbons. The increased solubilities due to branching apparently are not due to a structural feature of the molecules, but to the higher vapor pressure of the branched-chain hydrocarbons compared with the corresponding paraffin or olefin hydrocarbon. Methane and neopentane are exceptions; their solubilities are lower than predicted.

On an equal hydrocarbon vapor pressure basis, approximately the same weight of paraffin and branched-chain paraffin hydrocarbon dissolves in water. Thus, the "structure" of water is such that it will accommodate a given weight of a C_8 or C_9 paraffin hydrocarbon with almost as much ease as a corresponding weight of ethane or propane. A similar relationship is shown for olefin and aromatic hydrocarbons.

For a given carbon number, ring formation increases water solubility.

Double bond addition to the molecule, ring or chain, increases water solubility. The addition of a second and third double bond to a hydrocarbon of given carbon number proportionately increases water solubility.

A triple bond in a chain molecule increases water solubility to a greater extent than two double bonds.

If the relationship between the logarithm of solubility in water and molar volume of the hydrocarbon for each homologous series is a continuous function, the solubilities of higher molecular weight hydrocarbons can be estimated by extrapolation.

A Spectrophotometric and Chronopotentiometric Study of the Lead–Lead Chloride and the Zinc–Zinc Chloride Systems[1]

by J. D. Van Norman, J. S. Bookless, and J. J. Egan

Brookhaven National Laboratory, Upton, New York *(Received November 16, 1965)*

The dissolution of lead and zinc in their respective molten chlorides was studied using both spectrophotometric and chronopotentiometric techniques. It was found that the amount of lead which dissolved in lead chlorides in contact with liquid Au–Pb alloys at 518 and 530° varied directly as the activity of lead in the alloy indicating formation of a soluble Pb_2^{2+} species. The solubility of pure lead in its chloride at 518° was evaluated chronopotentiometrically and was found to be 0.0057 mole %. The diffusion coefficient of Pb_2^{2+} was evaluated at 1.8×10^{-5} cm²/sec. In a similar manner it was found that zinc dissolved in its chloride at 500° to form the Zn_2^{2+} species. The solubility of zinc in its chloride was 0.019 mole % and the diffusion coefficient was 7.6×10^{-6} cm²/sec. The results of this investigation are compared with previously published results.

Introduction

The mode of dissolution of lead in its own molten chloride has been studied previously by two methods. First, Karpachev, Stromberg, and Jordan[2a] studied the emf of the cell

$$Pb|PbCl_2 + Pb(sat)||PbCl_2 + Pb|C$$

at 700°. When the amount of lead in the right-hand compartment was varied, a Nernst plot yielded an n value of 1 corresponding to the electrode reaction

$$Pb^{2+} + 1e = Pb^{+}$$

Thus the mode of dissolution was taken to be the formation of Pb^+ by the reaction

$$Pb^0 + PbCl_2 = 2PbCl \qquad (I)$$

Topol[2b] has tried to repeat these results without success. Because of the low solubility of lead in molten lead chloride, his results were inconclusive but tended more to an n value of 2 instead of 1.

Secondly, an anodic polarographic technique has been used[3] to measure the concentration of subhalide as a function of lead activity which was adjusted by the use of a series of liquid gold–lead alloys of known lead activity in equilibrium with the lead chloride mixture. It was found that the concentration of the subhalide varied linearly with the lead activity. This would be the case if lead dissolved in lead chloride according to the reaction

$$Pb + PbCl_2 = Pb_2Cl_2 \qquad (II)$$

If, however, the subhalide was formed by reaction I, the concentration would have depended upon the square root of the activity. Reactions I and II may also be written in the ionic form without altering the conclusions.

Because of the discrepancy existing between the two experiments, it was thought worthwhile to carry out further research on the Pb–$PbCl_2$ system. Thus both chronopotentiometry and spectrophotometry have been employed in this work to follow the concentration of dissolved subhalide with varying activities of lead.

It is known that solutions of lead dissolved in lead chloride take on a very dark coloration. The optical absorption of these solutions can be used as a measure of subhalide concentration. Assuming Beer's law, the law of mass action, and Henry's law to hold for

(1) This work was performed under the auspices of the U. S. Atomic Energy Commission.

(2) (a) S. Karpachev, A. Stromberg, and E. Jordan, *Compt. Rend. Acad. Sci. USSR*, **36**, 101 (1942); (b) L. E. Topol, *J. Phys. Chem.*, **67**, 2222 (1963).

(3) J. J. Egan, *ibid.*, **65**, 2222 (1961).

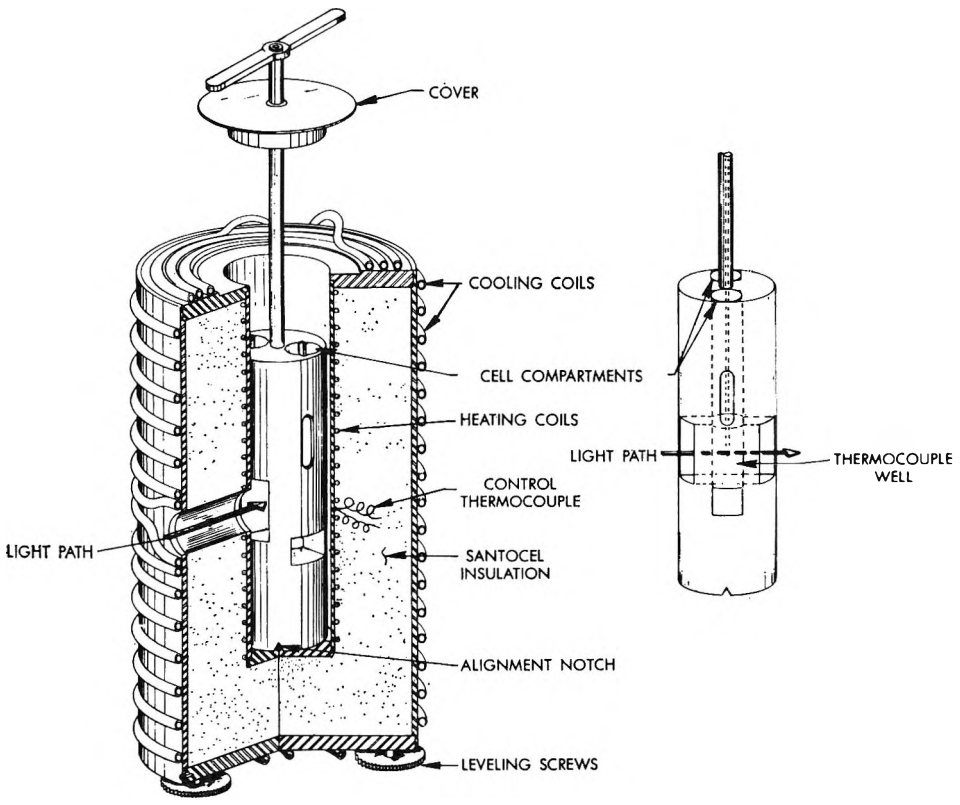

Figure 1. Furnace used for high-temperature spectrophotometry.

dilute solutions of subhalide, one obtains eq 1 for reaction I and eq 2 for reaction II, where A_s is the absorbance and A_s° is the absorbance of a solution at unit activity of lead.

$$A_s/A_s^\circ = a_{Pb}^{1/2} \quad (1)$$

$$A_s/A_s^\circ = a_{Pb} \quad (2)$$

In anodic chronopotentiometry, it is the quantity $i_0\tau^{1/2}$ which is proportional to concentration, since

$$i_0\tau^{1/2} = \frac{nF\pi^{1/2}D^{1/2}C}{2} \quad (3)$$

where i_0 is the current density, τ the transition time, D the diffusion coefficient, and C the concentration. Consequently, eq 4 holds for reaction I and eq 5 holds

$$i_0\tau^{1/2}/i_0\tau_{a_{Pb}=1}^{1/2} = a_{Pb}^{1/2} \quad (4)$$

$$i_0\tau^{1/2}/i_0\tau_{a_{Pb}=1}^{1/2} = a_{Pb} \quad (5)$$

for reaction II. This technique was used previously to study the Mg–$MgCl_2$ system.[4]

The solubility of lead in its molten chloride can also be determined using the chronopotentiometric technique developed for the Ag–AgCl and the Ag–AgBr systems.[5] This technique involved the addition of small known amounts of lead to lead chloride while monitoring the concentration of subhalide chronopotentiometrically. For each addition of lead, transition times are measured at various current densities. From eq 3 it can be seen that the product $i_0\tau^{1/2}$ is directly proportional to the concentration. Thus, a plot of this product *vs.* added lead will be a straight line until saturation is reached, at which point the product $i_0\tau^{1/2}$ becomes constant. Corbett and von Winbush[6] have measured the solubility of lead in its molten chloride at different temperatures, permitting a comparison of results. The diffusion coefficient, D, for the subhalide can be calculated from the slope of the previous plot.

The mode of dissolution of zinc in its chloride has never been determined. Topol[2b] was unable to secure stable potentials in emf cells. Corbett, von Winbush, and Albers[7] measured the solubility of zinc in its chloride. Therefore, the Zn–$ZnCl_2$ system was studied

(4) J. D. Van Norman and J. J. Egan, *J. Phys. Chem.*, **67**, 2460 (1963).
(5) J. D. Van Norman, *J. Electrochem. Soc.*, 112, 1126 (1965).
(6) J. D. Corbett and S. von Winbush, *J. Am. Chem. Soc.*, **77**, 3964 (1955).
(7) J. D. Corbett, S. von Winbush, and F. C. Albers, *ibid.*, **79**, 3020 (1957).

chronopotentiometrically and spectrophotometrically at 500° in the same manner as the Pb–$PbCl_2$ system.

Experimental Section

Materials. The lead chloride used in this investigation was reagent grade and was further purified by passing HCl gas through the powder while slowly raising the temperature above the melting point. Once the lead chloride was molten, HCl was bubbled through it for an additional 3 hr. The salt was then filtered through a fine quartz frit to remove any insoluble material. This purified salt was contacted for 24 hr at 520° with a piece of pure gold foil. The lead metal used was of 99.99% purity.

The zinc chloride used in the investigation was prepared by passing HCl over the metal (99.99% purity) at 700° and distilling the $ZnCl_2$ off. The distilled $ZnCl_2$ was collected in the molten state in a crucible and was later subjected to a stream of chlorine gas while in the molten state to purify the salt further. The zinc chloride so prepared was then contacted with liquid bismuth metal to remove any traces of dissolved zinc metal.

Apparatus and Measurements. The spectral measurements were taken using 2-mm quartz optical cells on a Cary Model 14 spectrophotometer with a special furnace compartment as shown in Figure 1. The entire assembly fitted into the sample compartment of the spectrophotometer. The steel core was 1.75 in. in diameter by 5.25 in. in height and could be rotated to obtain the spectra of two samples. The spectrum of pure $PbCl_2$ contacted with gold was taken as a background. Spectra were then taken of $PbCl_2$ contacted with various gold–lead alloys.

The chronopotentiometric measurements were taken in a cell similar to that used by Van Norman.[5] In the present investigation, an iridium electrode in contact with the molten salt served as the reference electrode. For some of the measurements on the zinc–zinc chloride system, a special Pyrex cap fitted over the quartz crucible to cut down on the amount of zinc chloride lost through volatilization.

Small amounts of lead were added to the purified lead chloride; after each addition, anodic chronopotentiograms were taken by passing a constant current between the two iridium electrodes while measuring the potential between them as a function of time. Once saturation was achieved, a large excess of lead was added and small weighed amounts of gold were successively added to vary the alloy composition. At the completion of an experiment the salt used was weighed: about 450 g.

In the case of the zinc–zinc chloride system, bismuth metal was used to remove initially any zinc dissolved in the pure zinc chloride. The solubility was then measured by successive additions of small amounts of zinc. A large excess of pure bismuth metal was added, and the composition of the Bi–Zn alloy was varied by adding known amounts of zinc to the system. The amount of zinc chloride used was about 300 g.

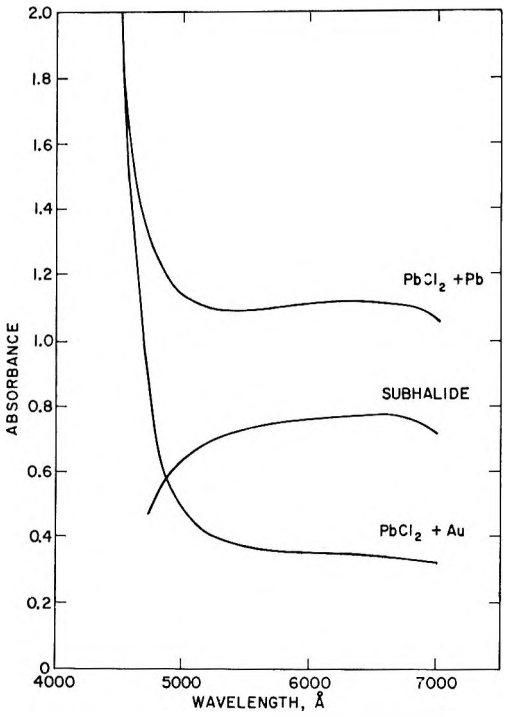

Figure 2. Absorption spectra at 530° of pure $PbCl_2$ equilibrated with Au and of $PbCl_2$ equilibrated with Pb. The curve labeled subhalide is the difference of the two.

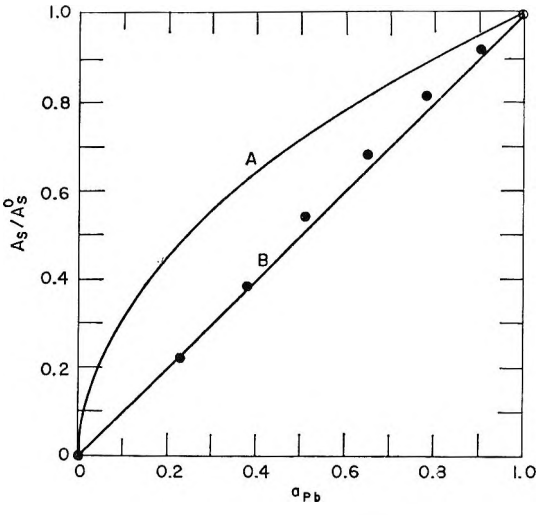

Figure 3. The relation between Pb activity and absorption due to subhalide in $PbCl_2$. Curve A is the theoretical curve for the formation of Pb^+, and curve B is for the formation of Pb_2^{2+}.

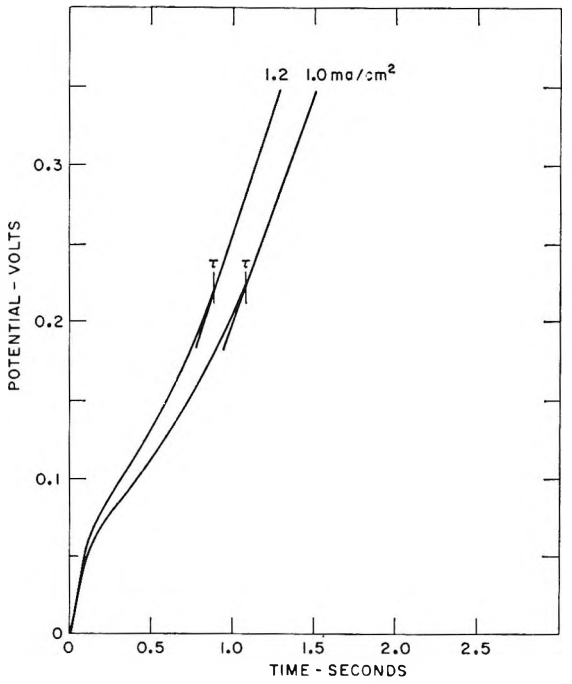

Figure 4. Typical anodic chronopotentiograms in the Pb–$PbCl_2$ system at 518°.

Results and Conclusions

Figure 2 shows the absorption spectra at 530° of pure $PbCl_2$ and of $PbCl_2$ equilibrated with lead. The curve labeled subhalide is the difference of the two. Similar spectra were obtained at various activities of lead in lead–gold alloys. Activities of lead were calculated from emf measurements published by Kleppa.[8] No experiments were performed below a lead activity of 0.3, where lead–gold alloys are solid at the temperature used. Figure 3 shows the plot of A_s/A_s° *vs.* a_{Pb} with the experimental points falling near the straight line, indicating that reaction II is correct and Pb_2^{2+} is the species formed. Absorbances were taken at 625 mμ.

Figure 4 shows typical anodic chronopotentiograms obtained for the Pb–$PbCl_2$ system at 518°. Transition times were measured in the same way as done previously.[5] Figure 5 shows a sample solubility plot for addition of small amounts of lead to lead chloride. The solubility so determined by two separate experiments was 0.0057 ± 0.0003 mole % lead in lead chloride at 518°. This result can be compared with the extrapolated value from the investigation of Corbett and von Winbush[6] of 0.0078 mole %. The diffusion coefficient, D, calculated from the slope of the solubility plots was $(1.8 \pm 0.3) \times 10^{-5}$ cm²/sec, quite comparable to other ions in fused salts. The density of

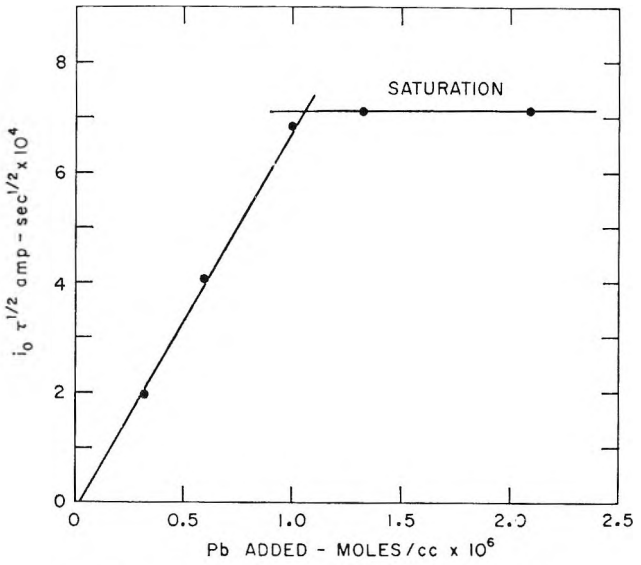

Figure 5. Plot of $i_0\tau^{1/2}$ *vs.* lead added to $PbCl_2$ at 518°.

lead chloride used in these calculations was 4.924 g/cc.[9]

Figure 6, a plot of $i_0\tau^{1/2}/(i_0\tau^{1/2})_{a_{Pb}=1}$ *vs.* a_{Pb}, shows that the amount of dissolved lead varies directly as the activity of lead in the metal phase indicating the formation of Pb_2^{2+}. The results of Karpachev, *et al.*, remain unexplained.

The anodic chronopotentiograms of zinc dissolved in zinc chloride at 500° were similar to those obtained for the Pb–$PbCl_2$ system, as were solubility plots. The solubility measured for the dissolution of zinc in its chloride at 500° for two separate experiments was 0.019 ± 0.002 mole %. This can be compared to the value obtained at 498° by Corbett, *et al.*, of 0.18, nearly a factor of ten higher. These workers recorded the loss of weight of the metal after contact with the salt. However, the low solubility measured in the present work could account for the instability of emf measurements reported by Topol.[2b] The diffusion coefficient for the zinc species in $ZnCl_2$ at 500° was calculated to be $(7.9 \pm 1.1) \times 10^{-6}$ cm²/sec. The density of $ZnCl_2$ used for these calculations was 2.294 g/cc.[9]

Figure 7, a plot of $i_0\tau^{1/2}/(i_0\tau^{1/2})_{a_{Zn}=1}$ *vs.* a_{Zn}, again shows a linear dependence indicating the formation on dissolution of zinc in its chloride of Zn_2^{2+} ions. Thus, zinc dissolves in its chloride in the same way that lead, mercury, magnesium, and cadmium do in their divalent chlorides. The activities of zinc in the zinc–bismuth alloys were calculated from emf data of

(8) O. J. Kleppa, *J. Am. Chem. Soc.*, 71, 3275 (1949).

(9) G. J. Janz, A. T. Ward, and R. D. Reeves, "Molten Salt Data," Technical Bulletin Series, Rensselaer Polytechnic Institute, Troy, N. Y., 1964.

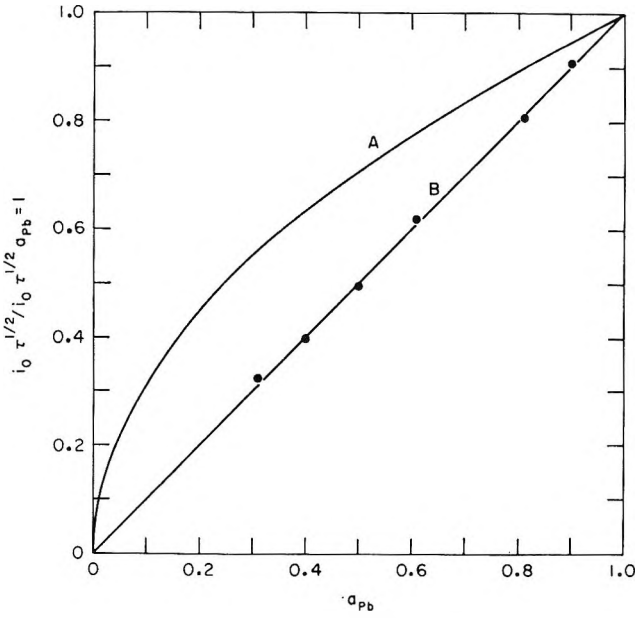

Figure 6. The relation between Pb activity and the product $i_0\tau^{1/2}/i_0\tau^{1/2}{}_{a_{Pb}=1}$ due to subhalide in $PbCl_2$. Curve A is the theoretical curve for the formation of Pb^+, and curve B is for the formation of Pb_2^{2+}.

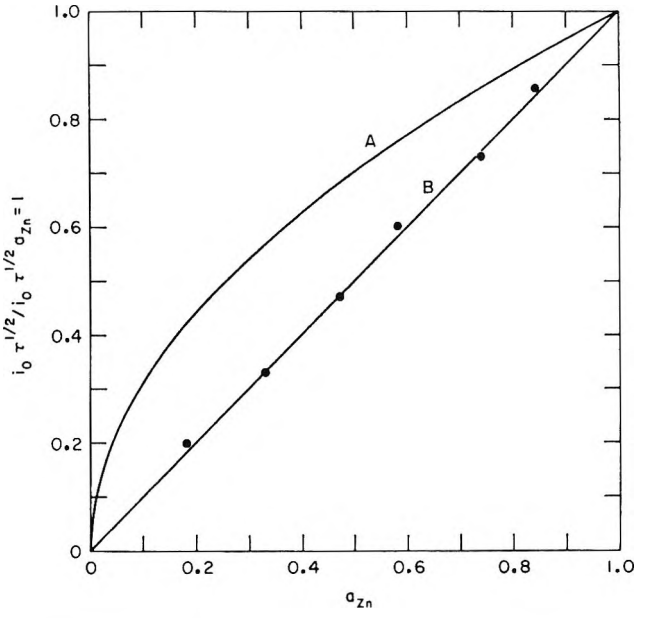

Figure 7. The relation between Zn activity and the product $i_0\tau^{1/2}/i_0\tau^{1/2}{}_{a_{Zn}=1}$ due to subhalide in $ZnCl_2$ at 500°. Curve A is the theoretical curve for the formation of Zn^+, and curve B for the formation of Zn_2^{2+}.

Kleppa.[10] Spectra taken of pure zinc chloride contacted with bismuth metal were the same as spectra of zinc chloride contacted with zinc metal, indicating that the zinc subhalide does not absorb in the spectral region studied, 700–300 mμ.

It should be mentioned that, although the findings of this investigation rule out the formation of Pb^+ and Zn^+ ions, other reactions besides reaction II are still possible. Thus, in the case of the Pb–$PbCl_2$ system, reactions III–V would also give the same

$$Pb + PbCl_2 = Pb \text{ atoms dispersed in } PbCl_2 \quad (III)$$

$$Pb + 2PbCl_2 = Pb_3Cl_4 \quad (IV)$$

$$Pb + 3PbCl_2 = Pb_4Cl_6, \text{ etc.} \quad (V)$$

results. The presence of lead atoms dispersed in lead chloride, although compatible with the results reported here, seems to be ruled out on other grounds, as pointed out by Bredig.[11] Also, on first thought, there does not seem to be any reason to postulate such complex ions as Pb_3^{4+} and Pb_4^{6+}. If, however, one considers an F center in solid sodium chloride with the electron in an anion vacancy being shared between the nearest neighbor Na^+ ions, one might represent this chemically as Na_6^{5+}. In this light perhaps the lead subhalide can be represented as Pb_4^{6+}.

In connection with the diffusion coefficients measured here, the work of Herzog and Klemm[12] should be mentioned. They studied the migration during electrolysis of the boundary between a pure lead chloride melt and a lead chloride melt containing dissolved lead. They found that the boundary moved toward the anode, not toward the cathode as one would expect for a positive species. They felt that the subhalide dissociated somewhat into Pb^{2+} ions and two electrons, the latter moving toward the anode. This could explain the fact that the diffusion coefficient of the subhalide, $(1.8 \pm 0.3) \times 10^{-5}$ cm²/sec, as measured in the present work is greater than the self-diffusion coefficient of lead ions in lead chloride, 1.05×10^{-5} cm²/sec at 518°,[13] since electron movement is involved in the diffusion of the subhalide.

They also found that the velocity of the boundary and thus the mobility of the subhalide varied during the course of an experiment. They believed this to be due to a change in concentration of the subhalide at the boundary. Their analysis showed that indeed one should expect a change in mobility with concentration of subhalide.

If the mobility of the subhalide does vary with con-

(10) O. J. Kleppa, *J. Am. Chem. Soc.*, **74**, 6052 (1952).

(11) M. A. Bredig, "Molten Salts," M. Blander, Ed., Interscience Publishers, Inc., New York, N. Y., 1964, p 421.

(12) V. W. Herzog and A. Klemm, *Z. Naturforsch.*, **16a**, 523 (1961).

(13) G. Perkins, Jr., R. B. Escue, J. F. Lamb, and J. W. Wimberley, *J. Phys. Chem.*, **64**, 1792 (1960).

centration, one would expect this to have an effect on the diffusion coefficient. In contrast to their findings there was no noticeable systematic variation of the diffusion coefficient with concentration in the experiments reported here. However, if one assumes that the subhalide dissociates into Pb^{2+} ions and an electron pair with the latter moving as an entity, then the mobility of the subhalide as well as the diffusion coefficient would remain constant. This may clearly be seen by applying Klemm's equations to electron pairs instead of electrons. Further experiments are probably needed to resolve this problem.

Acknowledgments. The authors wish to thank Mr. Raymond J. Heus for designing the spectrophotometer furnace. They also wish to acknowledge the encouragement of and helpful discussions with Dr. Richard H. Wiswall.

The Kinetics of Formate Ion Pyrolysis in Alkali Halide Matrices[1,2]

by K. O. Hartman and I. C. Hisatsune

Department of Chemistry, Whitmore Laboratory, The Pennsylvania State University, University Park, Pennsylvania 16802 *(Received November 16, 1965)*

The pyrolysis of the formate ion isolated in KCl, KBr, KI, and NaBr matrices was investigated from 500 to 620° by infrared spectroscopy. The infrared spectra of these pressed disks after heating showed that the formate ion was distorted as it went into solid solution with the matrix. The CO_2 valence angle in the distorted ion was estimated to be 136 ± 10° from the isotopic frequency product rule. The decomposition reaction of the formate ion in solid solution with KBr was found to be second order in formate with a rate constant of $2.0 \times 10^{10} \exp[(-50{,}700 \pm 3500)/RT]\ M^{-1}\ sec^{-1}$. Carbonate was obtained in 85% yield and traces of monomeric bicarbonate were also observed. The pyrolysis of formate-*d* showed a primary kinetic isotope effect, but no ^{13}C isotope effect was detected. Although the observed activation energy was independent of the matrix within experimental uncertainty, the rate constants were consistently higher in KI and NaBr matrices than in KBr and KCl matrices.

Introduction

Earlier we reported a kinetic study of the pyrolysis of calcium formate dispersed in a KBr matrix by infrared spectroscopy.[3] In the present investigation the pyrolysis of sodium formate in KCl, KBr, KI, and NaBr matrices was studied by the same experimental technique in order to test the reaction mechanism proposed earlier and to determine the effect of environmental changes on the decomposition kinetics of the formate ion.

Numerous, although fragmentary, studies have been reported in the literature on the thermal decomposition of undiluted sodium and potassium formates. For example, Levi and Piva[4] observed that the decomposition of sodium formate between 330 and 370° yielded an equimolar mixture of oxalate and carbonate. Above 500° they found the solid product to be ex-

(1) This work was supported by the National Science Foundation, Grant NSF-G17346, and by the Directorate of Chemical Sciences, Air Force Office of Scientific Research, Grant AF-AFOSR, 907-65.

(2) Abstracted in part from the Ph.D. Thesis of K. O. Hartman.

(3) K. O. Hartman and I. C. Hisatsune, *J. Phys. Chem.*, 69, 583 (1965).

(4) M. G. Levi and A. Piva, *Ann. Chem. Applicata*, 5, 271 (1915); *Chem. Abstr.*, 10, 2561 (1916).

clusively carbonate. Freidlin[5] confirmed these results and also showed that oxalate was the predominant solid product in the 390 to 430° temperature range. At a decomposition temperature below 330°, the main product reported by Takagi[6] was carbonate. Takagi also reported this reaction to be second order in formate. Other decomposition products observed by previous investigators were CO and H_2. Freidlin[5] postulated that formaldehyde was the precursor for these gases, and this molecule was in fact detected by Toyoda.[7]

In our study the formate ion was diluted with different alkali halide salts, and the mixtures were pressed into disks. These disks were heated in the 500 to 620° temperature range, and the decomposition of the solute was followed by observing the changes in the infrared spectrum of the disk. Carbonate was found to be the principal reaction product, but traces of bicarbonate were also observed. The reaction was second order in formate in contrast with the first-order rate observed earlier in calcium formate[3] decomposition. However, the kinetic results obtained in the present study were found to be consistent with the mechanism proposed before.

Experimental Section

Optical grade KCl, KBr (powdered), and KI crystals were from Harshaw. Reagent grade NaBr from Fisher was used directly. Sodium formate was a Baker Analyzed reagent and was recrystallized from water. Matheson Coleman and Bell was the source of potassium formate, and this was used without further purification. Sodium formate-*d* (99%) from Merck Sharp and Dohme of Canada and sodium formate-^{13}C (54%) from Bio-Rad Laboratories were also used directly. Sodium and potassium carbonates for intensity calibrations were Fisher reagent grade products.

The technique and apparatus for pellet fabrication and heating, the infrared spectrometers, the procedure for determining the reaction stoichiometry, and the method of obtaining the kinetic data all have been described before.[3] A conventional glass low-temperature cell with a cold finger adapted to hold a pressed disk was used to record the infrared spectrum of the sample at liquid nitrogen temperature.

The KBr matrix was used most extensively, and experimental results obtained with this matrix have the highest precision. In solid solution studies and in kinetic runs, recrystallized sodium formate was used most often as the source of the formate ion since exactly the same results were obtained when potassium formate was used instead. Solute concentrations ranged from about 0.1 to 5.0 mg of solute salt/g of matrix.

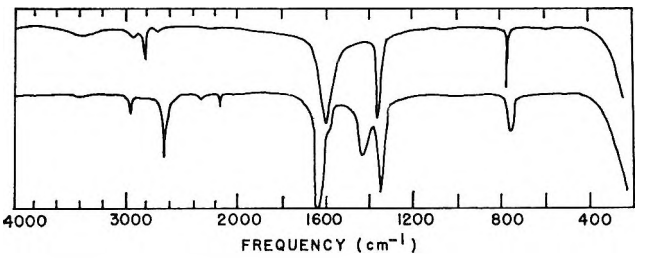

Figure 1. The infrared spectrum of sodium formate in a KBr matrix: upper spectrum, before heating; and lower spectrum, after heating for 2 min at 500°.

Results

A typical infrared spectrum of a KBr disk in which sodium formate had been dispersed by grinding is shown in Figure 1 (upper spectrum). Variation of the grinding time from 1 to 3 min or changing the pressure used to press the disk had no effect on the spectrum. A disk prepared by the freeze-dry method generally gave a sharper spectrum, but the frequencies of the bands in this spectrum were the same as those observed from a disk prepared by grinding a formate salt with the same cation as that of the matrix. Isotopic frequencies observed from sodium and potassium formates dispersed in KBr disks by grinding are summarized in Table I.

Table I: Sodium and Potassium Formate Frequencies (cm^{-1}) Observed in Unheated KBr Disks[a]

Mode[b]	$NaH^{12}CO_2$	$NaH^{13}CO_2$	$NaD^{12}CO_2$	$KH^{12}CO_2$
ν(C–H)	2832	2818	2131	2810
$\nu_\alpha(CO_2)$	1606	1560	1595	1590
ν_β(C–H)	1366	1365	1014	1368
$\nu_\sigma(CO_2)$	1366	1336	1331	1343
ν_ω(C–H)	1069	*c*	931	*c*
$\nu_\beta(CO_2)$	774	765	766	764

[a] Spectra recorded at 25°. [b] α = antisymmetric stretch, β = bending, σ = symmetric stretch, and ω = out-of-plane wag. [c] Not observed.

The infrared spectra of sodium formate dispersed by grinding in KCl, KBr, KI, and NaBr matrices were the same as long as these disks were not heated. However,

(5) L. Kh. Freidlin, *J. Appl. Chem. USSR*, **11**, 975 (1938).

(6) S. Takagi, *J. Chem. Soc. Japan*, **60**, 625 (1939); *Chem. Abstr.*, **36**, 6401 (1942).

(7) R. Toyoda, *Bull. Inst. Chem. Res., Kyoto Univ.*, **20**, 11 (1950).

when such disks were heated for a short time at temperatures above about 240°, they exhibited remarkable changes in their absorption spectra. An example of this heating effect on a typical KBr disk is shown in Figure 1. Here, the lower spectrum was obtained by heating at 500° for 2 min a KBr disk which gave initially the upper spectrum. In this new spectrum the changes in relative intensities and frequency shifts of the original formate bands are apparent, and in addition two new strong bands have appeared where none were present before. These new bands, however, were demonstrated to originate from the same chemical species, which produced the remaining three strong bands in the lower spectrum, by band optical density correlations over a wide range of solute concentrations and by the observation that the new bands and the other three strong bands all decayed with the same rate when the disk was heated at higher temperatures. That the new spectrum was due to a decomposition product of the normal formate ion was ruled out also by the following observations. If a heated disk was allowed to stand for a few weeks at room temperature or if it was ground in air and then repressed, the original formate spectrum was partially regenerated. If the disk was dissolved in water and freeze dried, the original spectrum was completely regenerated and the new bands disappeared. Reheating of the freeze-dried disk again yielded the new spectrum. Also, the new spectrum was generated even at 100° if the disk was heated for a few weeks. Thus, the new spectrum is still due to the formate ion, but one whose structure has been significantly altered by the matrix. The frequencies, together with their assignments, of isotopically substituted formate ions observed in heated KBr disks are summarized in Table II.

Table II: Frequencies (cm^{-1}) of Isotopically Substituted Formate Ions in Heated KBr Matrix[a]

Mode[b]	$H^{12}CO_2^-$	$H^{13}CO_2^-$	$D^{12}CO_2^-$
ν(C–H)	2666.2	2644.3	1995.6
$\nu_\alpha(CO_2)$	1632.9	1590.7	1621.9
ν_β(C–H)	1444.6	1444.6	1065.4
$\nu_\sigma(CO_2)$	1350.4	1329.5	1327.7
$\nu_\beta(CO_2)$	752.3	745.0	744.8

[a] All spectra recorded at −190°. [b] See footnote *b* of Table I. Out-of-plane mode not observed.

Since sodium formate melts at 255°, the new spectrum may have been due to formation of a potassium bromide–sodium formate eutectic mixture. Indeed, a eutectic melting at 233° was observed when the mole fraction of sodium formate in KBr was 0.91. However, if a sample with this mole fraction was heated above 250°, quenched to room temperature, mixed with more KBr, and pressed into a pellet, its spectrum was that of normal formate. None of the samples prepared from melts in which the mole fraction of sodium formate ranged from 0.85 to near 1.0 showed the shifted spectrum. On the other hand, KBr disks containing sodium formate in high dilution readily produced the shifted spectrum when they were heated for a few hours at 240°. In Table III the frequencies of $H^{12}CO_2^-$ in different heated matrices are listed. These same frequencies were obtained by heating either sodium formate or potassium formate in the matrices. Also, when a heated KBr–formate disk was diluted with KCl, pressed into a pellet, and then heated, its spectrum changed from that characteristic of the KBr matrix into one characteristic of the KCl matrix.

Table III: $H^{12}CO_2^-$ Frequencies (cm^{-1}) in Different Heated Matrices

Mode[a]	KCl[b]	KBr[b]	KI[b]	NaBr[c]
ν(C–H)	2683	2666.2	2643	2732
$\nu_\alpha(CO_2)$	1643	1632.9	1617	1633
ν_β(C–H)	1456	1444.6	1429	1448
$\nu_\sigma(CO_2)$	1357	1350.4	1344	1363
$\nu_\beta(CO_2)$	755	752.3	753	763

[a] See footnote *b* of Table I. [b] Spectrum recorded at −190°. [c] Spectrum recorded at 25°.

Prolonged heating of a formate–KBr disk at temperatures above 500° caused the solute to decompose, and carbonate was identified as the principal product in the matrix. The infrared spectrum of the carbonate produced by this decomposition was the same as that obtained from a heated KBr disk containing sodium or potassium carbonate. We also observed as a minor reaction product monomeric bicarbonate, whose infrared spectrum we have characterized and reported earlier.[8] Other weak infrared bands observed during the course of the pyrolysis reaction were due to trapped carbon dioxide and cyanate ion. The latter ion appeared as a common impurity in heated KBr disks containing solid chemical reagents.[8] Neither oxalate nor carbon monoxide was ever detected in our heated disks. However, our disks were generally much darker after heating than the previous calcium formate samples,[3] and hence CO was disproportionating into

(8) D. L. Bernitt, K. O. Hartman, and I. C. Hisatsune, *J. Chem. Phys.*, **42**, 3553 (1965).

CO_2 and carbon to a greater extent in the present studies.

The minor product bicarbonate was observed during pyrolysis in KCl, KBr, and KI matrices but not in NaBr disks. The concentration of this product was usually maximum after the first heating cycle and remained the same or decreased with further heating. The pyrolysis of formate-*d* produced bicarbonate-*d*, which decreased after the initial heating, and eventually a small amount of unlabeled bicarbonate was formed. Heated disks ground in an oxygen atmosphere and then reheated gave slightly more bicarbonate than those ground in air.

The stoichiometry of the decomposition reaction was analyzed by using the known initial concentrations of sodium formate and by determining the final carbonate concentrations from intensity calibration of its 880-cm^{-1}, nondegenerate, out-of-plane wag infrared band. In eight runs in which the initial sodium formate concentration ranged from 1.05 to 4.1 mg of solute/g of KBr, the mole ratio of formate to carbonate was 2.4 ± 0.23. This ratio corresponded to a carbonate yield of 85 ± 7%. When the initial solute concentration was less than 1.0 mg/g, the carbonate yield fell below 50%. However, in this case the relative amount of bicarbonate produced was higher even though the absolute concentration of this minor product was about the same as in higher concentration kinetic runs. Thus, the principal reaction at higher concentrations is

$$2HCO_2^- = CO_3^{2-} + H_2 + CO$$

The reaction order was determined from the slopes of log rate *vs* log concentration linear plots. The 752-cm^{-1} formate band was used for this purpose, and from five samples an order of 2.0 ± 0.1 with respect to formate was obtained. In general, the reciprocal of the formate concentration was a linear function of time over two to three reaction half-lives. However, two high concentration samples followed a first-order rate law through the first 40 to 60% of the reaction and then a second-order rate through the remainder.

The rate constants obtained from typical second-order plots of the KBr data are listed in Table IV. The 752-cm^{-1} formate band was used most extensively, and average deviations of the constants in two or three runs are also given in Table IV. The second-order rate constants for the decomposition in KCl, KI, and NaBr matrices are given in Table V. We have also listed here for comparison the calculated KBr constants for the corresponding temperatures. Only the 752-cm^{-1} band was used to study the kinetics in different matrices. One KBr disk having a solute concentration of 27.4 mg/g was studied by the isothermal thermogravimetric analysis at 570°. This study gave a second-order rate constant of 1.7×10^{-3} M^{-1} sec^{-1} which agreed well with 1.8×10^{-3} M^{-1} sec^{-1} calculated from the infrared data.

Table IV: Second-Order Rate Constants for HCO_2^- Decomposition in a KBr Matrix

Temp, °C	10^5k, M^{-1} sec^{-1}		
	752 cm^{-1} (HCO_2^-)[a]	2666 cm^{-1} (HCO_2^-)	880 cm^{-1} (CO_3^{2-})
497 ± 2	7.1 ± 0.3	9.0	7.5
512 ± 1	18 ± 4	15	15
533 ± 1	69 ± 5	73	62
578 ± 3	220 ± 40	250	220
614 ± 2	540 ± 60	650	420

[a] Average value from two or three kinetic runs.

Table V: Second-Order Rate Constants for HCO_2^- Decomposition in Different Matrices[a]

Temp, °C	10^5k, M^{-1} sec^{-1}			
	KCl	KBr	KI	NaBr
501 ± 1	14	10	56	70
548 ± 2	74	62	290	500
576 ± 2		220		1940
595 ± 2		330	1850	
600 ± 2	780	400		

[a] Rate constants from the 752-cm^{-1} formate band.

The Arrhenius activation energies and frequency factors calculated from kinetic data obtained in different matrices and with different infrared bands are summarized in Table VI. The 3.5-kcal/mole uncertainty in the activation energies is based on a 15% error in the reaction rate constants.

The kinetic isotope effects were also investigated. The activation energy and frequency factors for formate-*d* decomposition in a KBr matrix are given in Table VI while the observed k_H/k_D ratios are listed in Table VII. The carbon isotope effect was examined by using a formate sample containing 54% carbon-13 and by recording the spectrum with the sample cooled to liquid nitrogen temperature where the ^{12}C- and ^{13}C-formate C–O symmetric stretch bands were clearly resolved. However, at 550° no kinetic isotope effect was observed, as both isotopic bands decayed at the same rate.

Discussion

The sodium and potassium formate fundamental frequencies observed initially in unheated pressed

Table VI: Experimental Activation Energy and Frequency Factor

Frequency, cm^{-1}	Activation energy, kcal/mole	Frequency factor, M^{-1} sec^{-1}
Potassium Bromide Matrix		
752 (formate)	50.7 ± 3.5	2.0×10^{10}
2666 (formate)	51.7 ± 3.5	4.1×10^{10}
880 (carbonate)	49.5 ± 3.5	8.0×10^{9}
745 (formate-*d*)	54.5 ± 3.5	1.0×10^{12}
Different Matrices (752-Cm^{-1} Formate Band)		
Matrix		
KCl	53.0 ± 3.5	1.3×10^{11}
KI	51.7 ± 3.5	2.2×10^{11}
NaBr	54.3 ± 3.5	1.6×10^{12}

Table VII: Kinetic Isotope Effect

Temp, °K	k_H/k_D Formate ion in KBr[a]	k_H/k_D Calcium formate in KBr[b]
769 ± 2	1.80 ± 0.55	2.25
820 ± 2	1.52 ± 0.45	1.69
885 ± 2	1.24 ± 0.40	1.24
Temperature dependence	$\exp[(+3800 \pm 7000)/RT]$	$\exp(+7000/RT)$

[a] Observed, this study. [b] Calculated from data in ref 3.

disks (Table I) agree well with those reported by other investigators.[9] Moreover, these frequencies are not markedly different from those of salts with other cations[9b,10] or from the infrared and Raman frequencies of the aqueous ion.[11] Frequencies observed from our heated disks, however, are quite different from all previously reported values. Various experimental observations described in the Results section indicate that the new spectrum obtained from a heated disk must be due to the exchange of the cation of the original formate salt and to subsequent diffusion of the formate ion into the matrix forming a solid solution. The final frequencies observed in potassium halide matrices depend on the anion of the matrix as shown in Table III and are significantly different from those of potassium formate (Table I). In particular, the new CH bond stretch infrared band appears 144 cm^{-1} to the lower frequency of the original position while the bending mode of the same bond is shifted 77 cm^{-1} to a higher frequency. Also, comparison of the frequencies in Tables I and II shows that the symmetric A_1 modes are shifted to the red and the antisymmetric B_1 modes are shifted to the blue in the solid solution spectra of all isotopic formate ions.

The remarkable changes in the infrared spectrum produced by heating a formate–KBr disk suggest that the formate ion has become distorted as it formed a solid solution with the matrix. The shifted isotopic frequencies for the B_1 modes, however, can still be predicted quite well by the C_{2v} symmetry frequency product rule. Thus, the symmetry of the distorted ion appears to be C_{2v}, the same as in sodium formate single crystal.[12] The directions and magnitudes of frequency shifts in the CH bond stretching and bending mode infrared bands and the changes in relative intensities of the CO bond symmetric and antisymmetric stretch bands indicate that the CH bond has become weaker and the CO_2 valence angle has increased in the distorted ion. Both of these structural changes are consistent with the interpretation that the p character of the carbon hybrid atomic orbitals, which form the σ-bond frame of the ion, has changed. We expect that an increase in the p character of the CH bond carbon atomic orbital will cause the stretch and the bend frequencies to decrease and to increase, respectively. Conversely, a decrease in the p character of the CO bond carbon orbitals should produce a blue shift in the antisymmetric CO bond stretch infrared band and an increase in the CO_2 angle. The intensity of the antisymmetric stretch band should also increase relative to that of the symmetric mode. In the limit when the carbon orbital is pure sp hybrid, the CO_2 group dipole change with respect to symmetric stretch will be zero, and this vibration becomes forbidden in the infrared.

The CO_2 valence angle in the distorted formate ion can be calculated by equating the B_1 class frequency product rule value to its theoretical expression.[13] Different combinations of observed isotopic frequencies listed in Table II can be used for this purpose. With reasonable values of 1.09 and 1.25 A, respectively, for the C–H and the C–O bond distances, the best estimate of the valence angle was 136 ± 10°. Here, the lower limit in the angle was obtained by using di-

(9) (a) R. M. Hammaker and J. P. Walters, *Spectrochim. Acta*, **20**, 1311 (1964); (b) K. B. Harvey, B. A. Morrow, and H. F. Shurvell, *Can. J. Chem.*, **41**, 1181 (1963).

(10) J. D. Donaldson, J. F. Knifton, and S. D. Ross, *Spectrochim. Acta*, **20**, 847 (1964).

(11) K. Ito and H. J. Bernstein, *Can. J. Chem.*, **34**, 170 (1956).

(12) W. H. Zachariasen, *J. Chem. Phys.*, **1**, 634 (1933).

(13) G. Herzberg, "Infrared and Raman Spectra of Polyatomic Molecules," D. Van Nostrand Co., New York, N. Y., 1945, p 180. There is a typographical error in eq II-218. The mass factor in the last term on the right side of this equation should be $m_X m_Y$ instead of m_X^2.

rectly the observed product rule values in the calculation. The upper limit, on the other hand, was determined from corrected product rule values. Since there were deviations between the observed and calculated product rule values for the undistorted ion, it was assumed that similar deviations occurred in the distorted ion. Thus, deviations found in the normal ion were added to the experimental product rule values of the distorted ion for the same combination of isotopic frequencies.

The geometry of the distorted ion estimated above together with the observed frequencies allows us to calculate the vibrational force constants which can be compared to those of the normal ion. Such calculations showed that our assignment of the shifted spectrum was reasonable and that the differences between the force constants of the normal and distorted ions were consistent with our interpretation of the changes in structure. Interestingly, we found that the CH bond stretch force constant decreased by 11% and the bend constant increased by 11% when the formate ion was distorted. Also, the CO bond stretch constant increased by 13% while the CO_2 angle bend constant showed a 25% decrease.

The ease with which the formate ion diffused through our pressed disks, even at 100°, was indeed surprising. Evidently, the activation energy associated with this diffusion process must be very much smaller than the decomposition activation energies listed in Table VI. These reaction activation energies observed in different matrices are the same within experimental uncertainty, and the frequency factors are also similar to those observed for many second-order reactions in the gas phase.[14] In fact, one might deduce from these kinetic parameters that our decomposition is not occurring in the solid state but may be taking place in a liquid KBr–formate phase. However, this interpretation can be ruled out by the following arguments. The decomposition of undiluted formate occurs at a measurable rate at 300°, but the half-life of this reaction in the disk at about 500° is 100 hr. Since the solute is dispersed in the matrix initially as crystallites, it is not unreasonable to expect the concentration of the formate in the liquid KBr–formate phase, if it were produced at all, to be appreciable. Thus, such a large difference in the reaction half-lives of diluted and undiluted systems is not reasonable. Also, no shifted infrared spectrum was observed with samples prepared from high-concentration formate–KBr melts. The reaction half-life in the matrix at 500° is so long that we expect the KBr–formate liquid phase to be essentially in equilibrium with the surrounding solid KBr phase. The observed second-order rate is then unreasonable in view of the phase rule relationship between the two components at constant pressure and temperature.

Although the activation energies obtained in different matrices were the same within the estimated uncertainty, the rate constants in KI and NaBr were higher than those in KCl and KBr matrices as shown in Table V. If the same activation energy of 51 kcal/mole is used for all matrices, then the frequency factors in KI and NaBr matrices are larger than those in KBr and KCl by a factor of about seven. Similarly, the entropies of activation suggest differences in the two sets of matrices. The activation entropy, based on a standard state of 1 M, was -14 ± 5 cal/deg mole in KBr and KCl while it was -11 ± 5 cal/deg mole in KI and NaBr matrices.

A reaction mechanism similar to that proposed earlier for calcium formate decomposition[3] can satisfactorily account for the kinetic results obtained in the present investigation. In this mechanism two formate ions react to form the following transition complex, which

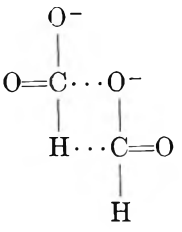

then decomposes into carbonate and formaldehyde. The inclusion of formaldehyde as the initial reaction product and as the source of CO and H_2 is consistent with Freidlin's postulate[5] and with Toyoda's observation.[7] The activation energy of 50.7 ± 3.5 kcal/mole observed here agrees well with 52.0 ± 3.0 kcal/mole obtained in calcium formate decomposition. We also observed a primary kinetic isotope effect in the present system, and the 3.8-kcal/mole temperature dependence of k_H/k_D is, within experimental error, the same as that in calcium formate system as shown in Table VII. Although the differences are well within our estimated error, both the activation energy and the temperature dependence of the kinetic isotope effect are larger in calcium formate than in the present system. This is reasonable since both the C–H stretch frequency and its deuterium isotope shift are larger in calcium formate than in formate–KBr solid solution system.

The yield of carbonate observed in the present study was generally low, and it was even more so when the

(14) See, for example, A. A. Frost and R. G. Pearson, "Kinetics and Mechanism," John Wiley and Sons, Inc., New York, N. Y., 1953, p 101.

formate in the matrix was in high dilution. The principal cause of this poor yield appears to be the side reaction which generated the bicarbonate ion. Since the maximum concentration of this by-product was observed after the first heating cycle of the disk and was about the same from one disk to another, oxygen and water trapped in the matrix may be involved in this side reaction. Observations in formate-*d* studies and in grinding experiments described in the Results section also support this interpretation. We suggested earlier that this side reaction may be the reverse of an unusual reaction encountered in the thermal reduction of bicarbonate to formate and that both of these reactions may involve the carbon dioxide anion free radical.[15] In order to test this hypothesis, we examined the esr spectra of formate disks during and after the decomposition reaction. These disks generally showed a weak but sharp signal with $g = 2.0028$, and similar signals were observed in the heated bicarbonate disks. This signal disappeared when the disk was dissolved in water and then freeze dried again. The intensity of this esr signal also decreased markedly or disappeared when the disk was ground in air. However, neither formate-*d* nor formate enriched in carbon-13 changed this esr spectrum. Thus, this radical, although unidentified, does not appear to be a significant intermediate in the side reaction or in the thermal reduction reaction. This negative result still does not rule out the possibility that CO_2^- radical may be involved in these reactions, because in another investigation carried out in our laboratory[16] we observed that the CO_2^- radical is not stable at the decomposition temperatures used in the present studies and also that this radical reacts with water to produce formate and bicarbonate ions.

Acknowledgments. We are grateful to Professor R. M. Hammaker for his generous gift of ^{13}C-enriched sodium formate, to Dr. F. E. Freeberg for thermal gravimetric analysis, to Mr. E. F. Reichenbecher for scanning the esr spectra, and to Dr. D. L. Bernitt for force constant analysis. We are pleased to acknowledge the financial support from the National Science Foundation and the Air Force Office of Scientific Research.

(15) I. C. Hisatsune and K. O. Hartman, *Science*, **145**, 1455 (1964).
(16) K. O. Hartman and I. C. Hisatsune, to be published.

The Crystal Structures of the Pyridinium Salts of the Group Vb Hexafluoride Anions[1]

by Richard F. Copeland,[2] Scott H. Conner, and Edward A. Meyers

Department of Chemistry, Texas A&M University, College Station, Texas 77843 *(Received December 10, 1964)*

The crystal structures of the pyridinium (PyH^+) salts of PF_6^-, AsF_6^-, and SbF_6^- have been determined. The unit cells are rhombohedral, $R\bar{3}m$-D_{3d}^5, with three molecules per cell when indexed on a hexagonal basis. The pyridinium rings in the three salts are statistically disordered with a distance between adjacent atoms in the ring, corrected for anisotropic thermal motion, of 1.376 ± 0.012, 1.381 ± 0.015, and 1.404 ± 0.021 A in the phosphorus, arsenic, and antimony salts, respectively. The fluorine atoms form, within experimental error, regular octahedra about the phosphorus, arsenic, and antimony atoms in their respective cells. For the model selected as best describing the thermal motion of the anions, the F_1–P–F_2 angle is 89.5° and the P–F bond distance is 1.593 A, the F_1–As–F_2 angle is 89.4° and the As–F bond distance is 1.777 A, and the F_1–Sb–F_2 angle is 86.2° and the Sb–F bond distance is 1.871 A. No hydrogen bonding was found in any of the three salts.

$PyH^+PF_6^-$ $a = 8.92$ A, $c = 8.78$ A

$PyH^+AsF_6^-$ $a = 9.13$ A, $c = 8.87$ A

$PyH^+SbF_6^-$ $a = 9.49$ A, $c = 8.93$ A

Introduction

The crystal structures of pyridinium hexafluorophosphate(V), hexafluoroarsenate(V), and hexafluoroantimonate(V) have been investigated as part of a study of amine salts of group Vb halide anions. Some structural work has been done on all of these hexafluoride anions. In particular, several reports of the determination of the structure of the hexafluoroantimonate(V) anion have been made, but in the most recent and accurate study,[3] the Sb–F bond distance is considerably different from that reported earlier.[4-6] In none of the reported structures of these group Vb hexafluoride anions has a relatively bulky organic cation been present, and it was thought that this might be of some interest, both for the packing of anions and cations within the unit cells and for the symmetry and structure of the group Vb hexafluoride anions. Neither nitrogen nor bismuth has been reported to form a hexafluoride anion.

Experimental Section

Crystals of pyridinium hexafluoroantimonate(V) were supplied by Dr. Albert C. Kunkle. The compound was crystallized[7] directly from a mixture of pyridine (Baker Chemical Co.) and 65% hexafluoroantimonic acid (Ozark-Mahoning Co., Tulsa, Okla.) in a polyethylene vessel in an ice bath. *Anal.* Calcd: F, 36.10; Sb, 38.69. Found: F, 36.20; Sb, 38.80. The density was 2.15 ± 0.06 g/cm^3.

(1) This paper was presented in part at the 19th Southwest Regional Meeting of the American Chemical Society, Dec 5–7, 1963, Houston, Texas.

(2) Submitted to the Graduate College of Texas A&M University in partial fulfillment of the requirements for the degree of Doctor of Philosophy, Aug 1965.

(3) J. H. Burns, *Acta Cryst.*, **15**, 1098 (1962).

(4) H. Bode, *Z. Anorg. Chem.*, **267**, 62 (1951).

(5) H. Bode and E. Voss, *ibid.*, **267**, 144 (1951).

(6) G. Teufer, *Acta Cryst.*, **9**, 539 (1956).

(7) A. C. Kunkle, Dissertation, Texas A&M University, 1963.

The single crystal selected for the study of this salt, a needle approximately 7 mm in length and 0.2 mm in diameter, was mounted in a thin-walled glass capillary and aligned on a Buerger precession camera. Intensity data for the $(h, 0, l)$, $(0, k, l)$, $(2h, \bar{h}, l)$, $(h, k, 4h + 2k)$, and $(h, k, 4h + 5k)$ zones were collected, using Zr-filtered Mo X-radiation and a precession angle of 30°. The intensities were measured using a Welch "Densichron 1" optical densitometer, Model 451-4, with a 0.012-in. aluminum aperture. The reflection spots were oval and regular in appearance. Earlier tests of "Densichron 1" measurements on oxalic acid dihydrate and pyridine hydrogen nitrate crystals had indicated that over-all reproducibility of between 5 and 6% in the observed structure factors was possible and that R factors in the range of 0.07–0.10 could be expected. The intensities were corrected for the Lorentz and polarization factors,[8] but no correction was made for absorption. The linear absorption coefficient, μ, is 30.67 cm^{-1} for pyridinium hexafluoroantimonate(V).

In later work short exposures of the $(h, 0, l)$ and $(0, k, l)$ zones were made on another crystal at temperatures as low as −110°. No evidence was found for any phase changes. After analysis of the data for pyridinium hexafluoroantimonate(V) had been carried out, samples of both pyridinium hexafluoroarsenate(V) and pyridinium hexafluorophosphate(V) were obtained from the Ozark-Mahoning Co., Tulsa, Okla.

Single crystals of pyridinium hexafluoroarsenate(V) suitable for X-ray study were obtained by recrystallization from aqueous hydrofluoric acid. Several needles about 0.3 mm in diameter were used in this study, and in all cases the needle axis was found to be parallel to the c axis of the crystal. Intensity data for the $(0, k, l)$, $(h, 0, l)$, $(\bar{h}, h, l)$, $(\bar{h}, 2h, l)$, and $(2\bar{k}, k, l)$ zones were collected at room temperature. The linear absorption coefficient, μ, for pyridinium hexafluoroarsenate(V) is 42.6 cm^{-1}. Efforts were made to obtain X-ray data at low temperatures, but four crystals in succession shattered in the vicinity of −30°, and it proved impossible to examine any one of the fragments.

Suitable crystals of pyridinium hexafluorophosphate(V) could not be obtained by recrystallization from aqueous mixtures and most alcoholic mixtures of solvents. Crystals were finally obtained from an amyl acetate–methanol mixture which had been allowed to stand for several days. The quality of the needles of pyridinium hexafluorophosphate(V) obtained in this way did not appear to be as good as that of the pyridinium hexafluoroarsenate(V) crystals, but a preliminary X-ray study indicated that the needles were indeed single crystals and that they would be satisfactory for the collection of intensity data. Data for pyridinium hexafluorophosphate(V) were collected at room temperature for the $(0, k, l)$, $(h, 0, l)$, $(\bar{h}, h, l)$, $(2h, \bar{h}, l)$, and $(\bar{h}, 2h, l)$ zones. For pyridinium hexafluorophosphate(V), μ is 5.4 cm^{-1}. The crystal was cooled to at least −120°, and it appears to decompose when warmed to the vicinity of 120°; between these temperatures no indication of a phase change was observed.

For all three compounds the structure was found to be rhombohedral. The reflections were indexed on the basis of a hexagonal cell, and the space group was identified as one of the following: R3-C_3^4, R$\bar{3}$-C_{3i}^2, R3m-C_{3v}^5, or R$\bar{3}$m-D_{3d}^5. In all of these rhombohedral space groups, with the choice of hexagonal axes, for each atom located at coordinates x, y, z there are similar atoms located at $x + {}^1/_3, y + {}^2/_3, z + {}^2/_3$ and $x + {}^2/_3, y + {}^1/_3, z + {}^1/_3$.[9] The unit cell dimensions for pyridinium hexafluoroantimonate(V) were found to be a = 9.49 A and c = 8.93 A; for pyridinium hexafluoroarsenate(V), they were found to be a = 9.13 A and c = 8.87 A; and for pyridinium hexafluorophosphate(V), they were found to be a = 8.92 A and c = 8.78 A. If it is assumed that there are three molecules per unit cell, the density of pyridinium hexafluoroantimonate(V) should be 2.26 g/cm³, compared to the value of 2.15 ± 0.06 g/cm³ measured by the flotation technique. Some fluctuations in the measured density of this compound were observed and attributed to imperfections in the material. For pyridinium hexafluoroarsenate(V), the density should be 2.09 g/cm³ compared to the measured density of 2.05 ± 0.03 g/cm³. For pyridinium hexafluorophosphate(V), the density should be 1.85 g/cm³ compared to the measured density of 1.84 ± 0.03 g/cm³.

Structure Determination and Refinement

Since there are only three formula weights per unit cell, the antimony, arsenic, and phosphorus atoms and the centers of the pyridinium rings must lie on special positions. These were taken to be (0, 0, 0), $({}^1/_3, {}^2/_3, {}^2/_3)$, and $({}^2/_3, {}^1/_3, {}^1/_3)$ for the antimony, arsenic, and phosphorus atoms in their respective cells and (0, 0, $1/2$), $({}^1/_3, {}^2/_3, {}^1/_6)$, and $({}^2/_3, {}^1/_3, {}^5/_6)$ for the centers of the pyridinium rings. The threefold axes of the crystal pass through these positions; since the ring itself does not possess a threefold axis of symmetry, the ring positions are disordered. Two of the four

(8) J. Waser, *Rev. Sci. Inst.*, 22, 567 (1951).

(9) "International Tables for X-ray Crystallography," Vol. I, "Symmetry Groups," The Kynoch Press, Birmingham, England, 1952, p 251 ff.

Table I: Pyridinium Hexafluoroantimonate(V) Structure Factors[a]

h	k	l	F_{obsd}	F_{calcd}	h	k	l	F_{obsd}	F_{calcd}	h	k	l	F_{obsd}	F_{calcd}
1	−2	0	187.1	187.9	2	−1	3	58.9	66.9	0	3	6	34.3	32.6
0	3	0	56.9	62.6	0	3	3	88.0	89.6	0	3	−6	30.0	33.9
2	−4	0	39.4	45.8	0	3	−3	89.9	95.5	−2	4	6	26.3	28.1
5	−4	0	51.8	54.2	−2	4	3	88.5	89.3	−1	5	6	19.1	23.5
0	6	0	49.9	48.7	7	−5	3	23.7	24.3	0	6	6	12.8	18.2
3	−6	0	47.3	45.3	0	6	3	24.0	23.0	0	6	−6	17.0	17.5
4	−8	0	22.5	25.4	0	6	−3	23.6	23.9	−3	6	6	15.7	18.9
10	−8	0	14.5	7.8	−3	6	3	41.4	44.6	−6	6	6	17.9	17.5
0	1	−1	146.0	132.9	−8	7	3	17.9	12.6	−2	7	6	17.5	15.2
0	2	1	113.8	122.0	−4	8	3	17.4	21.0	−4	8	6	8.4	10.3
4	−3	1	78.5	78.6	0	1	−4	78.9	81.7	0	1	−7	25.6	27.8
0	4	−1	75.0	79.2	0	2	4	70.6	70.6	3	−1	7	29.1	28.9
0	5	1	54.2	45.5	0	4	−4	53.9	52.3	0	2	7	28.1	30.9
−6	5	1	42.8	44.4	−1	4	4	50.5	50.5	0	4	−7	14.4	20.4
0	7	−1	16.6	19.8	−4	4	4	52.4	52.3	0	5	7	5.4	15.7
9	−7	1	17.1	13.8	6	−4	4	30.7	32.1	0	1	8	26.8	29.9
0	8	1	9.6	13.6	0	5	4	33.9	37.1	0	2	−8	20.2	22.5
0	1	2	189.6	180.8	−2	6	4	27.3	32.1	1	2	8	16.7	17.4
0	2	−2	110.5	111.9	0	7	−4	18.2	19.0	0	4	8	13.5	12.6
−1	3	2	73.5	77.8	−3	8	4	19.3	16.9	−3	4	8	14.1	14.2
0	4	2	64.5	51.1	−9	8	4	13.1	8.3	0	5	−8	16.1	11.8
0	5	−2	58.0	60.9	0	1	5	32.8	32.4	−1	6	8	13.6	9.9
−2	5	2	50.3	48.3	0	2	−5	50.4	54.1	0	0	9	17.7	11.5
−7	6	2	27.6	32.4	5	−3	5	38.8	41.1	1	1	9	15.5	13.2
8	−6	2	19.3	22.7	0	4	5	40.4	45.5	0	3	9	17.6	13.4
0	7	2	26.3	28.0	0	5	−5	29.3	24.7	0	3	−9	14.4	12.3
−3	7	2	30.7	32.9	0	0	6	66.6	68.8	0	1	−10	14.6	11.7
0	8	−2	15.2	14.9	1	1	6	50.7	49.7	0	2	10	17.9	9.0
0	0	3	19.7	19.3	4	−2	6	26.5	28.1	0	4	−10	16.1	6.2

[a] Only average values for equivalent reflections are tabulated.

possible space groups, R3 and R3m, were rejected as being structurally unlikely, and the refinement was begun in $R\bar{3}$.

The data, listed in Table I, for the (0, k, l) and (h, 0, l) zones of pyridinium hexafluoroantimonate(V) were analyzed by two-dimensional Fourier projection methods using an IBM 650 computer.[10] The signs used were determined by the Sb atoms, and the projections revealed the pyridine ring positions. Difference Fourier syntheses were then calculated, in which first the Sb atoms were removed and then the ring atoms as well. For the structure factor calculations required, scattering factor values given in the International Tables were used.[11] The atom scattering factor, f_{Sb}, was used for antimony, and an average scattering factor, $f = {}^5/_6 f_C + {}^1/_6 f_N$, was used for the ring atoms. Temperature and scale factors were adjusted for the difference Fourier syntheses.

The failure of the difference Fourier syntheses to indicate definite fluorine atom positions was unexpected. The data were reexamined, but no major discrepancies were found. In particular, there was no indication of additional weak reflections even on the most heavily exposed films, nor were there any obvious peculiarities in the background.

After an extended examination of various models, it was decided that the fluorine atom scattering was best described by a freely rotating regular octahedral "spherical rotor" of fluorine atoms about the antimony atom[12] with an Sb–F distance of 1.82 A. This model gave an over-all R of 0.099. This structure was proposed by us in an article to be published.

The data for pyridinium hexafluoroarsenate(V), listed in Table II, were collected and then analyzed by least-squares refinement,[13] using as a preliminary trial

(10) Professor L. H. Jenson of the University of Washington, Seattle, Wash., graciously supplied the programs used.

(11) "International Tables for X-ray Crystallography," Vol. III, The Kynoch Press, Birmingham, England, 1962, pp 202–212.

(12) W. H. Zachariasen, "Theory of X-ray Diffraction in Crystals," John Wiley and Sons, Inc., New York, N. Y., 1945, pp 223, 224.

(13) W. R. Busing, K. O. Martin, and H. A. Levy, "ORFLS, a FORTRAN Crystallographic Least-Squares Program," Oak Ridge National Laboratories Report ORNL-TM-305, Oak Ridge, Tenn, 1962.

Table II: Pyridinium Hexafluoroarsenate(V) Structure Factors[a]

h	k	l	F_{obsd}	F_{calcd}	h	k	l	F_{obsd}	F_{calcd}	h	k	l	F_{obsd}	F_{calcd}
−1	2	0	148.5	142.4	−1	2	3	35.5	38.5	−1	2	6	42.5	44.3
0	3	0	28.0	32.5	0	3	3	48.2	49.6	0	3	6	35.5	35.9
−2	4	0	16.8	19.8	0	3	−3	85.3	91.8	0	3	−6	28.5	30.2
0	6	0	48.0	48.9	−2	4	3	74.3	75.5	−2	4	6	22.4	27.6
−3	6	0	43.1	42.6	0	6	3	25.3	24.7	−8	4	6	11.3	14.4
−4	8	0	28.4	29.3	0	6	−3	21.3	22.5	0	6	6	24.0	23.7
0	9	0	12.9	14.8	−3	6	3	44.7	45.1	0	6	−6	21.0	22.6
−5	10	0	16.0	15.2	−4	8	3	20.5	26.0	−3	6	6	15.2	20.1
0	1	−1	102.5	95.8	0	1	−4	61.0	57.9	0	1	−7	23.2	23.8
0	2	1	71.7	70.0	0	2	4	44.5	45.8	0	2	7	31.1	31.2
0	4	−1	59.6	67.4	0	4	−4	51.4	51.1	0	4	−7	19.0	22.0
0	5	1	35.1	33.0	0	5	4	41.7	40.6	0	5	7	17.0	18.3
0	7	−1	17.3	20.8	0	7	−4	23.5	24.8	0	1	8	31.3	32.0
0	8	1	15.5	19.2	0	8	4	16.4	17.7	0	2	−8	19.6	23.4
0	1	2	155.9	145.9	0	1	5	14.8	11.6	0	4	8	17.5	17.1
0	2	−2	86.3	90.4	0	2	−5	42.7	45.1	0	5	−8	13.2	15.8
0	4	2	28.2	27.2	0	4	5	43.0	43.9	0	0	9	16.9	13.4
0	5	−2	56.7	59.6	0	5	−5	28.0	24.1	3	0	9	15.9	16.0
0	7	2	33.5	33.8	0	7	5	14.5	15.2	0	3	9	14.7	16.3
0	8	−2	22.9	20.8	0	8	−5	11.9	13.5	−1	1	10	19.3	15.4
0	0	3	40.6	41.1	0	0	6	55.9	56.4					

[a] Only average values for equivalent reflections are tabulated.

Table III: Pyridinium Hexafluorophosphate(V) Structure Factors[a]

h	k	l	F_{obsd}	F_{calcd}	h	k	l	F_{obsd}	F_{calcd}	h	k	l	F_{obsd}	F_{calcd}
−1	2	0	102.1	100.5	0	7	2	17.6	17.0	0	4	5	21.0	20.0
0	3	0	15.5	13.2	0	0	3	72.1	72.2	0	5	−5	10.8	6.8
−2	4	0	30.3	24.4	1	1	3	5.4	1.8	0	0	6	24.6	23.3
0	6	0	22.5	22.4	0	3	−3	53.6	59.6	−1	2	6	15.8	15.3
−3	6	0	16.2	14.5	−2	4	3	37.2	38.8	0	3	6	14.1	14.0
−4	8	0	13.1	14.4	−3	6	3	20.6	20.7	0	3	−6	7.5	8.3
0	1	−1	50.7	54.3	−6	6	3	8.6	3.1	−2	4	6	8.0	8.0
0	2	1	30.8	31.0	−4	8	3	8.9	8.8	0	6	6	12.1	12.0
0	4	−1	26.6	31.1	0	1	−4	19.4	19.4	0	6	−6	9.2	7.8
5	−5	1	7.9	8.3	0	4	−4	29.9	29.6	0	2	7	11.8	10.8
0	1	2	115.0	109.6	0	5	4	18.6	17.4	0	4	−7	5.8	7.1
0	2	−2	45.3	47.5	−7	7	4	8.8	8.7	0	5	7	5.5	5.9
0	4	2	21.6	21.7	0	1	5	28.4	26.7	0	1	8	14.9	15.7
0	5	−2	33.6	36.5	0	2	−5	11.0	13.5	0	2	−8	9.4	7.7

[a] Only average values for equivalent reflections are tabulated.

structure that found for pyridinium hexafluoroantimonate(V). Only the coordinates found for the antimony and the ring atoms were used at first. The spherical rotor model for the fluorine atoms, which had been used in the refinement of the antimony compound, was tested and eliminated as a possibility.

Fourier and difference Fourier projections[14] using the (h, 0, l) and (0, k, l) data gave fluorine atom positions which were successfully refined by least-squares methods. The hydrogen atom contributions were included in the final calculations, assuming an average ring atom to hydrogen atom distance of 1.08 A. The final R was 0.094 for the refinement using individual atom, isotropic temperature factors.

At this point the data for pyridinium hexafluoro-

(14) W. G. Sly, D. P. Shoemaker, and J. D. Van den Hende, "Two- and Three-Dimensional Crystallographic Fourier Summation Program for the IBM 7090 Computer," CBRL-22M-62, Esso Research and Engineering Co.–Massachusetts Institute of Technology, Cambridge, Mass., 1962.

phosphate(V) listed in Table III were analyzed by least-squares methods using the same trial structure which had been found for pyridinium hexafluoroarsenate(V). The refinement converged successfully to give a final R of 0.105 when individual atom, isotropic temperature factors were used.

The introduction of anisotropic temperature factors into the trial structures of both compounds was carried out, and it was observed that the coordinates of both the fluorine atoms and the ring atoms in pyridinium hexafluorophosphate(V) were very close to the special positions required by $R\bar{3}m$. Calculations were continued in which $R\bar{3}m$ symmetry was assumed, and the structures of both compounds refined satisfactorily. The anisotropic temperature factor, least-squares refinement in $R\bar{3}m$ gave an R factor of 0.071 for pyridinium hexafluoroarsenate(V) and 0.082 for pyridinium hexafluorophosphate(V). At this time the original draft of the pyridinium hexafluoroantimonate(V) paper was returned along with the comment by one of the referees that the "spherically rotating" model for SbF_6^- was probably not as good as a fixed fluorine atom model which he proposed on the basis of packing considerations. The data for pyridinium hexafluoroantimonate(V) were then reexamined, and the structure of this compound was found to be isomorphous with that of the other two compounds. The value found for R was 0.067. The configuration with fluorine atoms rotated 60° about the c axis from the final positions reported here, an attractive model from packing considerations, was examined and rejected. There is little difference between these two models in the antimony salt, but the structure chosen is definitely superior for the arsenic salt and greatly superior for the phosphorus salt.

The lengths calculated[15] for the Sb–F, As–F, and P–F bonds and the bonds between ring atoms in all three structures were shorter than comparable distances reported in other compounds. It has been recognized for some time that the presence of large anisotropic temperature factors may be accompanied by appreciable changes in bond distances,[16–18] and the anisotropic temperature factors found here were quite large. It was decided, therefore, to carry out additional least-squares refinements, using anisotropic temperature factors, and to calculate the effect of the Busing and Levy "riding motion" model of bond distance correction[19] upon the various bonds concerned. This is quite straightforward for the Sb–F, As–F, and P–F distances, but for the distances between atoms in the pyridinium ring it is considerably more complex. In this case, the distance which must be calculated is from the center of mass of the pyridinium group to the mean instantaneous position of one of the atoms in the ring; in addition, the anisotropic temperature factor, in this case, is the result of both translational and rotational movements, and these two factors cannot be readily separated. A convenient approximation which allows the use of the Busing–Levy "riding motion" model in the calculations may be made by assuming that the translational movement of the pyridinium group is the same as that of the central atom in the hexafluoride group. If this assumption is made, the calculated bond distances are much closer to similar bond distances reported in the literature, but they were still slightly shorter than would be expected on the basis of the standard deviations of the bond lengths.

Some work had been done earlier in this laboratory on the effect of the weighting system used for the structure factors in the least-squares refinement of coordinates.[20] This work was reexamined and revised slightly before being applied to the three structures under examination. Least-squares refinements were undertaken in an effort to find a self-consistent set of weights for the structure factors of each of the compounds. The reflections were arranged in several groups of about 20 reflections each by increasing magnitude of the structure factors, and a weight was calculated for each group. The weights found were then used in a least-squares refinement of the parameters of the structure, after which a new set of weights was calculated and the process was repeated until no significant changes occurred in either the weights or the structure parameters. Upon convergence of this process it was found that the calculated bond distances were in very satisfactory agreement with the values reported in the literature in all cases except in the pyridinium ring in the hexafluorophosphate(V) salt. Finally, a more thorough analysis of the thermal motions of the three salts was made.[16–13] The final sets of atomic coordinates and anisotropic temperature factor coefficients for all three compounds are given in Table IV, and the more important bond distances are reported in Table V.

Discussion of the Structures

The pyridinium ring was found to be, by symmetry,

(15) W. R. Busing, K. O. Martin, and H. A. Levy, "OR FFE, a FORTRAN Function and Error Program," Oak Ridge National Laboratories Report ORNL-TM-306, Oak Ridge, Tenn., 1964.

(16) D. W. J. Cruickshank, *Acta Cryst.*, 9, 747 (1956).

(17) D. W. J. Cruickshank, *ibid.*, 9, 754 (1956).

(18) D. W. J. Cruickshank, *ibid.*, 9, 757 (1956).

(19) W. R. Busing and H. A. Levy, *ibid.*, 17, 142 (1964).

(20) R. F. Copeland, Dissertation, Texas A&M University, 1965.

Table IV: Atomic Coordinates and Temperature Factors for $C_5NH_6^+XF_6^-$

		$C_5NH_6^+PF_6^-$	$C_5NH_6^+AsF_6^-$	$C_5NH_6^+SbF_6^-$
X	x	0.0	0.0	0.0
	y	0.0	0.0	0.0
	z	0.0	0.0	0.0
F	x	0.1593 ± 0.0014	0.1662 ± 0.0024	0.1510 ± 0.0035
	$y = {}^1/_2x$	0.0797	0.0831	0.0755
	z	0.1021 ± 0.0011	0.1126 ± 0.0011	0.1245 ± 0.0023
C or N	x	0.1516 ± 0.0012	0.1501 ± 0.0016	0.1455 ± 0.0022
	y	0.0	0.0	0.0
	z	0.5	0.5	0.5
H	x	0.2702	0.2675	0.2594
	y	0.0	0.0	0.0
	z	0.5	0.5	0.5
X	$\beta_{11} = \beta_{22} = 2\beta_{12}$	0.0160 ± 0.0012	0.0134 ± 0.0005	0.0262 ± 0.0006
	β_{33}	0.0157 ± 0.0009	0.0126 ± 0.0005	0.0203 ± 0.0005
	$\beta_{13} = \beta_{23}$	0.0	0.0	0.0
F	$\beta_{11} = 2\beta_{12}$	0.0368 ± 0.0032	0.0539 ± 0.0049	0.0493 ± 0.0054
	β_{22}	0.0523 ± 0.0025	0.0846 ± 0.0041	0.1809 ± 0.0130
	β_{33}	0.0445 ± 0.0015	0.0486 ± 0.0023	0.0533 ± 0.0027
	$\beta_{13} = 2\beta_{23}$	−0.0190 ± 0.0024	−0.0209 ± 0.0027	−0.0099 ± 0.0036
C or N	β_{11}	0.0268 ± 0.0027	0.0312 ± 0.0025	0.0346 ± 0.0032
	$\beta_{22} = 2\beta_{12}$	0.0418 ± 0.0035	0.0376 ± 0.0033	0.0489 ± 0.0051
	β_{33}	0.0203 ± 0.0013	0.0214 ± 0.0015	0.0238 ± 0.0020
	$\beta_{23} = 2\beta_{13}$	−0.0038 ± 0.0017	−0.0005 ± 0.0017	0.0051 ± 0.0024

Table V: Interatomic Distances and Angles[a]

	$C_5NH_6^+PF_6^-$	$C_5NH_6^+AsF_6^-$	$C_5NH_6^+SbF_6^-$
Bonds			
X–F[b]	$1.59_3 \pm 0.01_1$	$1.77_7 \pm 0.01_6$	$1.87_1 \pm 0.03_1$
C–C or N	$1.37_6 \pm 0.01_2$	$1.38_1 \pm 0.01_5$	$1.40_4 \pm 0.02_1$
C or N–H	Assumed to be 1.08 A for all three compounds		
Contacts[c]			
F_1–C_1 or C_2	3.38 ± 0.01	3.43 ± 0.03	3.59 ± 0.03
F_1–C_3 or C_4	3.53 ± 0.01	3.48 ± 0.03	3.40 ± 0.02
F_1–H_1 or H_2	2.44 ± 0.01	2.46 ± 0.02	2.60 ± 0.03
F_1–H_3 or H_4	3.76 ± 0.01	3.68 ± 0.02	3.61 ± 0.02
F_1–F_2	2.25 ± 0.01	2.50 ± 0.02	2.56 ± 0.03
C_1–C_3	4.03 ± 0.02	4.13 ± 0.02	4.26 ± 0.03
H_1–H_3	3.06 ± 0.01	3.12 ± 0.02	3.19 ± 0.02
F_1–F_3	2.27 ± 0.01	2.53 ± 0.02	2.73 ± 0.03
F_1–F_4	2.77 ± 0.01	2.55 ± 0.02	2.61 ± 0.03
Angle, deg			
F_1–X–F_2[b]	89.5 ± 0.6	89.4 ± 0.8	86.2 ± 1.3

[a] All distances are given in angstroms. [b] See Table VI for values for alternate models, and Figure 1 for identification of atoms. [c] All contact distances are based on the Cruickshank model assuming c^* rotation of the XF_6^- group and not on the uncorrected coordinates given in Table IV.

a regular hexagon with an average distance between adjacent atoms of $1.34_5 \pm 0.01_3$ A in the phosphorus compound, $1.37_1 \pm 0.01_5$ A in the arsenic compound, and $1.38_0 \pm 0.02_1$ A in the antimony compound. In view of the appreciable anisotropic thermal motion indicated by the temperature factors found in the least-squares analysis of the data, it was expected that these distances would be too short. Cruickshank's model[16–18] was used to calculate corrected bond distances. It was impossible to solve explicitly for all of the parameters required to describe the vibration and rotation of the ring; so it was assumed that the ring was rigid and that

the vibration of the center of mass was isotropic. The corrected ring bond distances were 1.376, 1.381, and 1.404 A for P, As, and Sb compounds, respectively.

Several determinations of the structure of pyridine[21,22] or pyridine-containing materials[23-25] have been carried out previously, and there is general agreement among the results, namely, that pyridine is a planar but not regular hexagonal ring with considerable variation in bond distances within the ring. The most reliable structure is probably that obtained in a microwave study.[21] The average ring–bond distance in the microwave structure is 1.377 ± 0.001 A, and this agrees precisely with the result obtained by an electron diffraction study.[22] This value also agrees well with the corrected distance in the P and As compound and is about one standard deviation from the value found for the Sb compound. The structures of various pyridinium salts give average ring distances that are less reliable than, but in essential agreement with, the value of 1.377 A used for comparison here. In the compounds studied here, these pyridine ring dimensions serve as an internal calibration scale for the dimensions of the XF_6^- groups, whose structures are less well documented.

The environment of all of the group Vb atoms is essentially the same, so only the coordination about the atom at the origin for each structure will be discussed. (Figures 1 and 2 show the general structure found for all three compounds.) Octahedrally located above and below the group Vb atom on the c axis are two sets of three fluorine atoms, and together these atoms form the XF_6^- group. Because the amplitude of thermal motion of the fluorine atoms is apparently very large and anisotropic, bond distance corrections must be applied in all three structures. The uncorrected values of the bond distances and F_1–X–F_2 angle of the XF_6^- groups are given in Table VI. If the Busing–Levy "riding motion" correction is applied,[19] the distances become considerably longer as also is shown in Table VI. No angular changes are made because of the fundamental assumption of the Busing–Levy treatment; that is, that the entire calculated displacement lies in the direction of the bond. The treatment given by Cruickshank[16-18] can be used to take into account rotations around different axes through the XF_6^- group. First, the vibrational motion is accounted for, as it is in the "riding motion" model, by the "rigid body" assumption that the vibration of the central atom and of the fluorine atoms is the same. From the equations that result, an estimate of the correction to be applied to the bond length because of rotation around the b axis, perpendicular to the bond, can be made. The remaining corrections

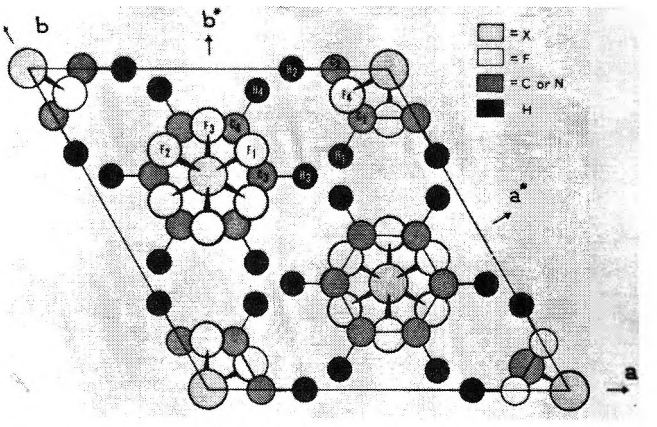

Figure 1. Projection of the structure along (001).

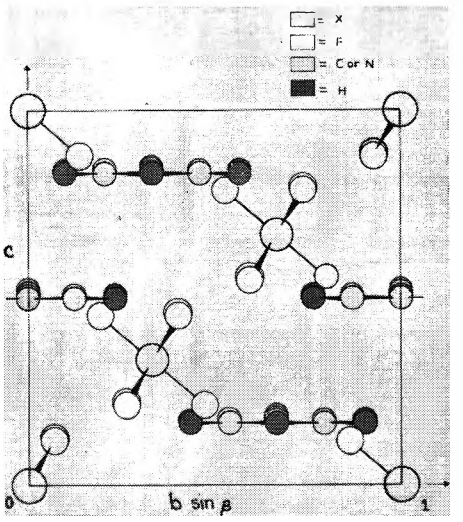

Figure 2. Projection of the structure along (100).

may be due to rotations around the a^* or c^* axes, but the relative contributions from these rotations cannot be assessed directly because of the limited number of independent thermal parameters that are available. Limiting values may be calculated, corresponding to rotations exclusively around the a^* and c^* axes, respectively. Because of the wide variations possible, the uncertainties in bond distances are quite large. The various calculated values are given in Table VI.

It is believed that the "best" values of the parameters are those associated with the largest bond angles,

(21) B. Bak, L. Hansen-Nygaard, and J. Rastrup-Anderson, *J. Mol. Spectry.*, **2**, 361 (1958).

(22) A. Almenningen, O. Bastiansen, and L. Hansen, *Acta Chem. Scand.*, **9**, 1306 (1955).

(23) Y. Takeuchi and R. Pepinsky, *Z. Krist.*, **109**, 29 (1950).

(24) C. Rerat, *Acta Cryst.*, **15**, 427 (1962).

(25) A. J. Serewicz, B. K. Robertson, and E. A. Meyers, *J. Phys. Chem.*, **69**, 1915 (1965).

Table VI: Bond Distances and Angles for Various Models of XF_6^-

	Uncorrected value	"Riding motion" value	Cruickshank		Lit. value
			a^* value	c^* value	
P–F[a]	$1.52_0 \pm 0.01_0$	$1.58_1 \pm 0.01_1$	1.588	1.59_3	$1.58 \pm ?$[26]
As–F[a]	$1.65_1 \pm 0.01_6$	$1.79_2 \pm 0.01_6$	1.762	1.77_7	1.80 ± 0.05[27]
Sb–F[a]	$1.67_1 \pm 0.02_4$	$1.91_8 \pm 0.03_1$	1.857	1.87_1	1.88 ± 0.007[3]
F–P–F[b]	88.8 ± 0.6	88.8 ± 0.6	88.1	89.5	90[1]
F–As–F[b]	87.2 ± 0.8	87.2 ± 0.8	84.2	89.4	88.7 ± 2.2[6]
F–Sb–F[b]	80.0 ± 1.3	80.0 ± 1.3	73.1	86.2	89.9 ± 0.2[21]

[a] Distances are given in angstroms. [b] Angles are given in degrees.

which correspond to rotation about the c^* axis. The reason for this belief is the following: within any given unit cell, the nitrogen atom will be located at one of the six ring sites for which only average values could be found. The negatively charged fluorine atom closest to this position cannot be expected to lie on the plane midway between the positively charged NH^+ group and the adjacent CH group. The twisting of the XF_6^- group toward the charged NH^+ group will produce the same effect as would a large rotation around the c^* axis. The corresponding rotation about a^* would probably not be as pronounced because of the close interatomic packing along the c axis. This would tend to make rotation about a^* much more difficult than rotation about c^*. In different unit cells, the location of the NH^+ group will change, and so will the sense of the rotation. The net result will be an apparently large anisotropic temperature factor corresponding to a large rotational movement of the fluorine atom, principally about the c^* axis.

The final bond distances and angles found here are in essential agreement with earlier results for these quantities, and the latter values are given in the final column of Table VI. There is good agreement between the length of the P–F bond found here, 1.59_3 A, and the value 1.58 A reported in α-KPF_6.[26] The same is true of the As–F bond of 1.77_7 A, compared to 1.80 ± 0.05 A calculated by Ibers[27] from Roof's data for $KAsF_6$.[28] Finally, the Sb–F distance of 1.87_1 A is in good agreement with that of 1.88 ± 0.007 A found by Burns.[3] The only serious difference in bond angles occurs with the Sb compound where a value of 86.2° has been found here, compared to 90° found by Burns. There have been suggestions made that electrostatic forces would be capable of producing distortions in bond angles. It appears more likely that the distortions found are only apparent, and that the large difference found for the F–Sb–F angle is due to the failure of the model for the extreme corrections required in this case. The final uncertainties in bond distances and angles cannot be readily assessed, but the least-squares estimates, particularly for the bond angles, are certainly too optimistic.

In the following discussion, the uncorrected bond distances given will be followed in parentheses by the distances calculated for the Cruickshank correction model, assuming rotation about the c^* axis.

In pyridinium hexafluorophosphate(V) there are pyridinium rings above and below the fluorine atoms of the PF_6^- with their centers at $z = +1/2$ and $z = -1/2$, respectively. Each of the six fluorine atoms is 3.56 ± 0.01 A (3.53 A) from two of the ring atoms in these two pyridinium rings and 3.79 ± 0.01 A (3.76 A) from the two hydrogen atoms attached to these ring atoms. In addition, there are three neighboring atoms at $z = 1/6$, with the ring centers at $x = 1/3$, $y = 2/3$ in their respective cells. Within each of these rings are located two ring atoms at 3.43 ± 0.02 A (3.38 A) from the nearest fluorine atom, and the two hydrogen atoms attached to these ring atoms are 2.52 ± 0.01 A (2.44 A) from the fluorine atom. Similar relations are found for the three neighboring rings located at $z = -1/6$, and with their centers at $x = 2/3$, $y = 1/3$ in their respective cells. The closest contact between carbon or nitrogen atoms in different rings is 4.05 ± 0.02 A (4.03 A), between hydrogen atoms in different rings is 3.08 ± 0.01 A (3.06 A), and between fluorine atoms in different PF_6^- groups is 2.92 ± 0.02 A (2.77 A).

In pyridinium hexafluoroarsenate(V) the ring atoms of the pyridinium rings at $z = \pm 1/2$ are 3.51 ± 0.03 A (3.48 A) from the nearest fluorine atom in the AsF_6^- at the origin, and the hydrogen atoms of these rings are 3.73 ± 0.02 A (3.68 A) from the nearest fluorine atoms. The two nearest ring atoms in the three pyridinium

(26) H. Bode and H. Clausen, *Z. Anorg. Allgem. Chem.*, **265**, 229 (1951).

(27) J. Ibers, *Acta Cryst.*, 9, 967 (1956).

(28) R. B. Roof, Jr., *ibid.*, 8, 739 (1955).

rings centered at $x = {}^1/_3$, $y = {}^2/_3$, $z = {}^1/_6$ and the three centered at $x = {}^2/_3$, $y = {}^1/_3$, $z = {}^1/_6$ are 3.49 ± 0.03 A (3.43 A) and the two hydrogen atoms are 2.55 ± 0.02 A (2.46 A) from the nearest fluorine atom. The closest contact between carbon or nitrogen atoms in different rings is 4.14 ± 0.02 A (4.13 A), between hydrogen atoms in different rings is 3.13 ± 0.02 A (3.12 A), and between fluorine atoms in different AsF_6^- groups is 2.81 ± 0.02 A (2.55 A).

In pyridinium hexafluoroantimonate(V) the ring atoms of the pyridinium rings at $z = \pm {}^1/_2$ are 3.42 ± 0.02 A (3.40 A), and the hydrogen atoms are 3.67 ± 0.02 A (3.61 A) from the nearest fluorine atom in the SbF_6^- at the origin, and the ring atoms in the pyridinium rings at $z = \pm {}^1/_6$ are 3.70 ± 0.03 A (3.59 A), and the hydrogen atoms in these rings are 2.76 ± 0.03 A (2.60 A) from the nearest fluorine atom. The closest contact between carbon or nitrogen atoms in different rings is 4.29 ± 0.03 A (4.26 A), between hydrogen atoms in different rings is 3.22 ± 0.02 A (3.19 A), and between fluorine atoms in different SbF_6^- groups is 3.09 ± 0.04 A (2.61 A).

All of the contact distances listed above are greater than the van der Waals contact distances[29a] with the possible exception of the shortest fluorine–hydrogen and fluorine–fluorine contacts. The F–H contact distance is 2.52 ± 0.01 A (2.44 A) in the hexafluorophosphate(V) salt, 2.55 ± 0.02 A (2.46 A) in the hexafluoroarsenate(V) salt, and 2.76 ± 0.03 A (2.60 A) in the hexafluoroantimonate(V) salt, as compared with the value of 2.55 A for the van der Waals fluorine–hydrogen contact. None of these distances is short enough to be a hydrogen bond,[29b] but the Cruickshank corrected models for PF_6^- and AsF_6^- give values intermediate between the hydrogen-bonded and van der Waals contact distance. If hydrogen bonding does occur in these salts, it would appear to be very weak. The fluorine–fluorine contact distances are not far from the van der Waals distance of 2.70 A, especially when the relative uncertainty in the fluorine atom positions is considered.

Perhaps the most striking feature in the structures of this set of compounds is the great similarity that they bear to each other. All three anions are regular within experimental error, although there is still some question about the SbF_6^- ion. Another feature is the very large anisotropic temperature factors found for the fluorine atoms. It has not been possible to handle such large, anisotropic temperature factors until quite recently, as is evidenced by the "spherically rotating SbF_6^-" structure originally proposed for pyridinium hexafluoroantimonate(V). At the time that this model was proposed, the programs available to us could handle atoms having an isotropic temperature factor, exp $\{-B[(\sin\theta)/\lambda]^2\}$, with $B < 10$. The best B for the fluorine atoms in SbF_6^- is about 22, and, in addition, this temperature factor is highly anisotropic. Prior to the availability of programs for the IBM 709, fixed atom models for the fluorine positions were systematically tested by rotating the fluorines about the c axis in both ordered and statistically disordered configurations. These models were uniformly unsatisfactory compared to the spherical or cylindrical rotor models. Ordered configurations were shown to be satisfactory only after larger, anisotropic temperature factors were calculated using the newer programs. It is possible that the disorder in the pyridinium ring might disappear at lower temperatures with the formation of a hydrogen bond and a shift to a lower symmetry crystal habit. Such a change might be very difficult to detect, however, because of "freezing in" of the statistical disorder observed in these room-temperature studies.

Acknowledgments. The financial support of The Robert A. Welch Foundation and funds from the Research Corporation used to purchase some of the equipment used in this work are gratefully acknowledged. The facilities of the Data Processing Center of the Texas A&M University System have been used extensively in the course of this research.

(29) L. Pauling, "The Nature of the Chemical Bond," Cornell University Press, Ithaca, N. Y., 1960: (a) p 257 ff; (b) p 449 ff.

Mechanism of Addition of Tritium to Oleate by Exposure to Tritium Gas

by C. T. Peng

Radioactivity Research Center and Department of Pharmaceutical Chemistry, University of California, San Francisco, California 94122 *(Received October 22, 1965)*

Formation of tritiostearate by exposure of oleate to tritium gas proceeds by a mixed radical and ion-molecule mechanism with 40% of the total addition caused by tritium atoms and 60% by ion molecules containing tritium. Argon sensitizes the addition by the formation of tritium argonium ion, ArT^+, and oxygen inhibits the reaction by scavenging both radicals and ions. Gross tritium incorporation in the reactant is temperature dependent, which is interpreted as the result of an equilibrium between tritium in the adsorbed phase and that in the gas phase. Labeling by tritium at cryogenic temperature is mainly decay induced. The activation energy for tritiation by addition is higher than by substitution and is of the same order of magnitude as those observed for addition of hydrogen atoms to unsaturates by others.

Labeling of organic molecules with tritium is frequently effected by the Wilzbach gas exposure method.[1] Under such conditions, addition of tritium atoms across the carbon–carbon double bond also occurs, giving rise predominantly to a saturated product of extremely high specific activity.[2–4]

Mechanisms of labeling by tritium substitution have been investigated in homogeneous systems of methane–tritium,[5] ethylene–tritium,[6] propane–tritium,[7] etc., and were found to involve decay-induced labeling and β labeling; the former is initiated by HeT^+ and the latter by electrons. In contrast, the mechanism of labeling by tritium addition remains relatively unknown. Although a free-radical mechanism has been postulated for the addition,[3,8] the presence of free radicals in the reaction mixture was not at a level readily confirmable by electron spin resonance measurement.[8]

We report here the effect of temperature and the activation energies of tritium labeling by substitution and by addition, and give evidence for an ion-molecule mechanism for the addition of tritium to an isolated –C=C– bond, based on the results obtained from a study of the methyl palmitate–methyl oleate–tritium system. The inclusion of methyl palmitate in the system as a reference compound is necessary to allow a comparion of the rates of addition and substitution.

Experimental Section

Methyl elaidate, methyl oleate, and methyl palmitate of greater than 99% purity, purchased from the Hormel Institute, University of Minnesota, and tritium gas from the Oak Ridge National Laboratory, all without further purification, were used for tritiation.

The mixture of fatty acid esters to be tritiated, consisting of either methyl palmitate and methyl oleate (28.66:71.34 wt %) (A) or methyl palmitate and methyl elaidate (27.03:72.97 wt %) (B), was deposited evenly onto 0.2 g of fine glass wool to provide a large surface area for contact with tritium gas in a 20-cc tritiation chamber.[9] According to the need, three to four such chambers were connected to one inlet. After evacuation to 10^{-3} mm or less, tritium gas was introduced by Toepler pumping. The individual chambers from one run, when sealed at the capillary and detached, contained approximately equal quantities of tritium and were separately maintained at different experimental temperatures for one

(1) K. E. Wilzbach, *J. Am. Chem. Soc.*, 79, 1013 (1957).

(2) H. J. Dutton and R. F. Nystrom, *Advan. Tracer Methodol.*, 1, 18 (1963).

(3) R. F. Nystrom, *ibid.*, 1, 46 (1963).

(4) E. P. Jones, L. H. Mason, H. J. Dutton, and R. F. Nystrom, *J. Org. Chem.*, 25, 1413 (1960).

(5) T. H. Pratt and R. J. Wolfgang, *J. Am. Chem. Soc.*, 83, 10 (1961).

(6) K. Yang and P. L. Gant, *J. Chem. Phys.*, 31, 1589 (1959).

(7) K. Yang and P. L. Gant, *J. Phys. Chem.*, 66, 1619 (1962).

(8) University of Illinois Report TID 14787, Feb 2, 1962.

(9) C. T. Peng, *J. Pharm. Sci.*, 52, 861 (1963).

predetermined length of time. In the first series of experiments, 0.5-ml portions of A were exposed to 4 curies of T_2 at 77, 193, 273, and 353°K for 2, 5, 12, and 28 days. In the second series, 0.3-ml portions of A and of B were exposed to 2.5 curies of T_2 at 77, 193, and 298°K for 6 days. In the third series, 0.3-ml portions of A were exposed to 3.3 curies of T_2 in the presence of argon or of oxygen at the above temperatures for 6 days. Exposure in the presence of nitric oxide was carried out with 3.0 curies of T_2 for 7 days. Argon and oxygen were passed through a molecular sieve column before being admitted to the tritiation chamber; nitric oxide (from the Matheson Co., Inc.) was introduced directly. Pressure of the added gas in the chamber was approximately 300 mm in all cases. In the fourth series of experiment, photosensitization with 2537-A Hg-resonance radiation was carried out in a quartz flask with a Hg lamp (250 w, Hanau) on 0.3 ml of A distributed evenly over 0.1 g of fine glass wool and 10 curies of T_2 for 30 min in the presence of finely dispersed mercury droplets. The isotropic light source was positioned approximately 10 cm away from the sample in order to avoid heat effect. After exposure, the unreacted tritium gas was removed under vacuum. A given amount of methyl stearate in *n*-heptane, approximating the amount of oleate present in the sample, was added prior to purification as a carrier for the tritiostearate formed by the addition reaction.

Analysis by gas radiochromatography was performed on samples before and after purification. Purification of the tritiated esters was carried out according to the procedure of Jones, *et al.*[4] Radioactivity of the samples was determined by liquid scintillation counting. The individual fatty acid esters were analyzed by gas chromatography with a hydrogen flame-ionization detector using a 0.25 in. × 6-ft column filled with 100–120 mesh Gas-Chrom P coated with 14% EGSS-X (a siliconated ethylene glycol succinate polyester from Applied Science Laboratories, Inc.) or with 90–100 mesh Celite coated with 15% diethylene glycol adipate polyester (Resoflex). The radioactivity of the effluent gas from the column was measured at a split ratio of 10:1 with a 275-cc high-temperature flow ion chamber connected to a critically damped vibrating reed electrometer; the sensitivity of this instrument was determined with a known sample of tritiated stearate. The area of the mass and radioactivity peaks, recorded with two synchronized potentiometers, was measured by planimetry for each individual ester.

Results

When the product of gross incorporated tritium activity and temperature of exposure of the system $C_{16:0}$–$C_{18:1}$–T[10] was logarithmically plotted *vs.* either the exposure in curie-days at 77, 193, 273, and 353°K or the reciprocal of temperature during exposure at 2-, 5-, and 12-day intervals, linear or approximately linear relationships with practically identical slopes were obtained. Based on these observations, an empirical equation relating the gross tritium incorporation, A, in millicuries, exposure, E, in curie-days, and temperature of exposure, T, in degrees Kelvin can be derived; thus

$$A = \frac{ET^{3/2}}{L} \qquad (1)$$

where L is a constant, characteristic of both the system and the compound under study. Figure 1 shows the plot of log A *vs.* log $(ET^{3/2})$ of all the systems investigated. Owing to the phase heterogeneity inherent in the reaction mixture and the uncertainty in the surface area available for tritium exposure, eq 1 is only approximate, and the scattering of the points is anticipated. However, over the extended range of temperature and duration of irradiation, points from similar systems fall along a straight line with an intercept equal to L on the horizontal axis.[11] For the $C_{16:0}$–$C_{18:1}$–T systems, an average value of 2.31×10^3 (from 1.72×10^3 to 2.90×10^3) for L was obtained. The presence of argon in the system caused a shift of the plot to the left from its normal position with $L = 0.80 \times 10^3$, while that of oxygen was shifted to the right with $L = 8.0 \times 10^3$. Systems containing nitric oxide yielded widely scattered points, presumably because nitric oxide is a very reactive gas and can induce profound changes in the system as indicated by the presence of a pronounced unidentified peak in the gas radiochromatogram. Samples which were unadulterated and have been exposed for 28 days at 77, 193, 273, and 353°K did not show a proportionate increase in the gross incorporated tritium activity and gave points that were positioned to the right of the normal plot with $L = 4.6 \times 10^3$. This shift indicates that on long exposure the rate of labeling is adversely affected by a change in the tritium concentration from dilution by hydrogen from exchange and other gaseous products from radiation decomposition. The composition at the

(10) The shorthand designation is from V. P. Dole, *et al.* [*J. Clin. Invest.*, **38**, 1544 (1959)]. The numeral before the colon indicates the number of carbon atoms in the fatty acid ester and that after is the number of double bonds present, namely, $C_{18:0}$ is for palmitate and $C_{18:1}$ is for oleate.

(11) The plots for different systems have unit slope and will pass through the origin provided that the scale of the horizontal or the vertical axis is adjusted with the corresponding log L term for each system according to eq 1, namely, $1 = \log A/[\log (ET^{3/2}) - \log L]$ or $1 = (\log A + \log L)/\log (ET^{3/2})$, respectively.

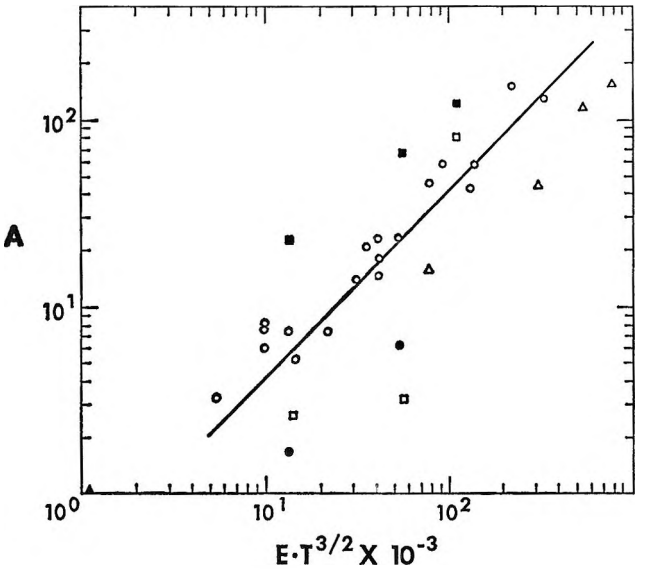

Figure 1. See text. ○, ■, □, and ● represent tritiated systems containing T_2, (T_2 + Ar), (T_2 + NO), and (T_2 + O_2), respectively. △ represents samples of $C_{16:0}$–$C_{18:1}$–T system exposed for 28 days and ▲, the Hg-photosensitized sample. Solid line is for the ○ points only.

gas–liquid or gas–solid interface may also have been altered, resulting in subsequent impediment of tritium and radical diffusion. From our limited data, the L value appears to be invariant toward slight fluctuations in tritium pressure and in the quantity of material being exposed.

Activation energies for tritium labeling by substitution and by addition for the $C_{16:0}$–$C_{18:1}$–T system are listed in Table I. These values were calculated from Arrhenius plots of log (specific activity) *vs.* $1/T$. The Arrhenius plots for tritiooleate and for tritiostearate have different slopes above and below 193°K, suggesting two different mechanisms of formation of these products. The activation energies of labeling of these two products in the temperature range of 77 to 193°K are of comparable magnitude as that of palmitate. Since labeling of palmitate occurs exclusively by substitution through replacement of a hydrogen atom by a tritium atom in the molecule, therefore it is reasonable to suggest that from the magnitude of the activation energy observed, the labeling of oleate in this particular temperature range may also follow a similar mechanism. In the absence of preferred addition of tritium to oleate, tritiostearate is also formed from oleate and tritium by the direct action of the latter, with a maximum probability of formation of 0.12, based on a random attachment of tritium atoms to 2 out of 17 carbon atoms in the alkenyl chain of oleate. The fact that this ratio was actually observed

Table I: Activation Energy for Addition and Substitution of Tritium

System	Reaction	Tritiated product	Temp, °K	E, kcal/mole
T + $C_{16:0}$	Substitution	$C_{16:0}$	77–273	0.4
T + $C_{18:1}$	Substitution	$C_{18:1}$	77–193	0.2
			193–353[a]	1.3
T + $C_{18:1}$	Addition	$C_{18:0}$	77–193[a]	0.3
			193–353	2.8

[a] See text for the reaction mechanism associated with this temperature range.

in the presence of oxygen at 77, 193, and 298°K lends credence to this proposed mechanism. As the low-temperature substitution, to be discussed later, is mediated by decay-induced labeling, it should have a low, if not zero, activation energy. Our results, shown in Table I, are in line with this argument.

At high temperatures, tritium addition to the –C=C– bond becomes predominant. But a finite probability also exists for a hydrogen atom elimination from the site of addition, thereby leading to the formation of a tritiooleate molecule. Formation of tritiooleate may occur in the condensed phase by disproportionation of the radicals formed from the addition of one tritium atom to an oleate molecule, but when the radicals are trapped at the surface, disproportionation with tritium atoms or other reactive species in the gas phase may become the only important mode of reaction. The plausibility of this explanation lies in its adequacy to account for the increased rate of formation of tritiooleate parallel to that of tritiostearate in this high-temperature range. The activation energy of addition of tritium to oleate given in Table I is in accord with the values reported for the addition of hydrogen atoms to unsaturates by others.[12–14]

The ratios of tritiostearate to tritiooleate formed under various experimental conditions (henceforth called the addition ratio) are given in Table II. The addition ratio increases with the temperature of exposure and reaches a limiting value of 14.5 at 298°K. Addition of tritium atoms to elaidate (*trans*-9-octadecenoate) is hindered at low temperatures, but at 298°K the difference in the rate of tritium addition to *cis* and *trans* –C=C– bond disappears. It may be noted that this observation is in accord with the findings

(12) M. D. Scheer and R. Klein, *J. Phys. Chem.*, **65**, 375 (1961).

(13) A. B. Callear and J. C. Robb, *Trans. Faraday Soc.*, **51**, 638 (1955).

(14) K. Yang, *J. Am. Chem. Soc.*, **84**, 3795 (1962).

Table II: Addition Ratio (Ratio of Tritiostearate to Tritiooleate) under Various Experimental Conditions

Tritiating system[a]	Temp of exposure, °K				
	77	193	273	298	353
T_2	2.04 ± 0.033[b]	2.94 ± 0.29	12.94 ± 0.43	...	14.0 ± 0.61
T_2	1.81	2.61	...	14.2	...
T_2 (B)	1.70	1.74	...	14.5	...
T_2 + Ar	3.34	8.14	...	12.4	...
T_2 + NO	0	0	...	8.3	...
T_2 + O_2[c]	0.12	0.11	...	0.12	...
T_2 (Hg-photosensitized)	...	...	...	5.4	...

[a] Mixture A was used in all systems unless indicated otherwise. [b] Average value plus or minus standard error from samples exposed to 4 curies of T_2 at 77, 193, 273, and 353°K for 2, 5, 12, and 28 days. [c] Samples were assayed on new gas chromatographic columns to avoid desorption of tritiostearate from the used column.

on the addition of hydrogen atoms to *cis*- and *trans*-2-butene at 296.5°K[14] and on the disproportionation of *sec*-butyl–*sec*-butyl radicals at 77°K into 2-butene, which was formed predominantly in the *trans* configuration.[15] The presence of argon enhanced the addition ratio only at cryogenic temperatures, but at 298°K the ratio approached the limiting value observed for the same system without argon. Oxygen inhibited the formation of tritiostearate by tritium addition to oleate at all temperatures and did not affect adversely the tritiation of palmitate and oleate. In contrast, the presence of nitric oxide in the $C_{16:0}$–$C_{18:1}$–T system completely eliminated the formation of both tritiostearate and tritiooleate at 77 and 193°K, while it sensitized the formation of both these labeled compounds with an addition ratio of 8.3 at 298°K. Mercury-photosensitized addition of tritium at 298°K yielded an addition ratio of 5.4.

Table III gives the G(T) value, namely, the number of tritium atoms incorporated per 100 ev absorbed, for some of the systems studied. The ratio of the G(T) values observed at 298 and 77°K for the T_2 system, at 298 and 193°K for the (T_2 + Ar) system, and at 193 and 77°K for the (T_2 + O_2) system agrees with the ratio calculated from the expression $(T_1/T_2)^{3/2}$ according to eq 1. The lowest G(T) value is 0.018 calculated for the decay-induced labeling based on the assumption that energy released per tritium decay is 5.7×10^3 ev. In the presence of argon the G(T) value is generally increased three- to fivefold for the reason that argon has a large ionization cross section and that the metastable argon atoms can cause more ionization of the reactant molecule to occur, thereby facilitating tritium labeling. At 298°K, the G(T) value for both the NO system and the Hg-photosensitized system is slightly increased but the presence of nitric oxide did not cause a similar increase at cryogenic temperatures. As can be seen in Figure 1, the tritiating systems with larger or smaller G(T) values than normal are invariably distributed to the left or the right of the normal plot, respectively, and with different L values.

Table III: G(T), Number of Tritium Atoms Incorporated per 100 ev Absorbed under Various Experimental Conditions

Tritiating system	Temp of exposure, °K				
	77	193	273	298	353
T_2[a]	0.046	0.11	0.35	...	0.35
T_2[b]	0.051	0.13	...	0.38	...
T_2 + Ar	0.18	0.51	...	1.05	...
T_2 + NO	0.015	0.019	...	...	...
T_2 + O_2	0.013	0.051	...	...	...
T_2 (Hg-photosensitized)	...	...	...	0.55[c]	...

[a] Average values from 2- and 5-day exposure samples of mixture A to 4 curies of tritium. [b] Values from 6-day exposure samples of mixture A to 2.5 curies of tritium. [c] This value is considerably lower than that obtained with other systems [F. Cacace, A. Guarino, and G. Montefinale, *Nature*, **189**, 54 (1961)]. The energy input for photosensitization was estimated to be approximately 1 w or below from the light source whose rating was 250 w owing to geometry and shading by glass wool. The dispersed Hg droplets appeared "oily" and were presumably covered with the fatty acid esters which further diminish the light intensity in the 2537-A region.

The stability of fatty acids toward β radiation during exposure to tritium has been noted.[16] Under pro-

(15) R. Klein, M. D. Scheer, and R. Kelley, *J. Phys. Chem.*, 68, 598 (1964).

(16) See ref 2, p 20.

longed exposure, radiation decomposition takes place yielding both short- and long-chain fatty acids of high specific activity with no apparent detectable mass peaks. Among all the systems studied, it is generally observed that the extent of decomposition is usually greater at 353°K than at 77°K. Composition by gas radiochromatographic analysis of the 28-day exposure samples at these two temperatures is given in Table IV. At the high temperature, long-chain saturated and unsaturated fatty acids are the predominant radiation decomposition products presumably formed by radical disproportionation and combination followed by hydrogen abstraction or hydride transfer. At the cryogenic temperature, reaction cage effect and restricted diffusion of free radicals diminish the extent of radiation decomposition, and unsaturation by hydrogen abstraction is also less favored. The decomposition products are mostly short-chain fatty acids formed by chain scission of the parent compound.

Table IV: Per Cent of Labeled Fatty Acid Esters Formed under Prolonged Irradiation with Tritium[a]

Ester[b]	Temp of exposure, °K: 77	353
$C_{12:0}$	1.43	...
$C_{13:0}$	1.47	...
$C_{14:0}$	3.28	0.01
$C_{15:0}$	1.97	...
$C_{15:1}$	...	0.48
$C_{16:0}$	12.10	2.06
$C_{16:1} + C_{17:0(iso)}$	1.78	0.79
$C_{17:0}$	0.73	...
$C_{17:1} + C_{18:0(iso)}$	...	0.39
$C_{18:0}$	52.26	82.76
$C_{18:1} + C_{19:0(iso)}$	24.94	5.91
$C_{19:0}$	...	3.05
$C_{18:2} + C_{20:0(iso)}$	...	1.86
$C_{18:3}$	...	0.81
$C_{21:0(iso)}$	...	0.32
$C_{22:0(neo)}$	...	0.29
$C_{21:1} + C_{22:0(iso)}$	...	1.03

[a] Mixture A was used. Exposure was 28 days. [b] See ref 10 for abbreviations. The iso and neo homologs are so designated.

The identity of the decomposition products listed in Table IV was determined by comparison of the retention times on two different columns with available known compounds and from plots of retention time *vs.* the number of carbon aroms.[17] The unsaturated products were identified by their absence in the gas radiochromatogram after bromination or hydrogenation; an example is given in Figure 2. The gaseous products and the short-chain fatty acids below laurate were neither determined nor identified.

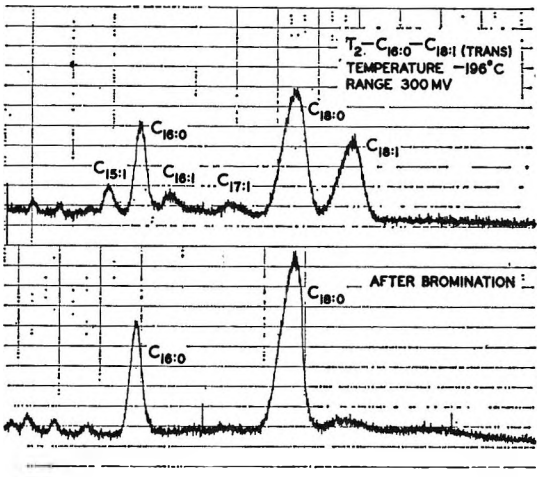

Figure 2. Gas radiochromatograms of a sample of tritiated fatty acid esters before and after bromination.

Discussion

Although the mechanism of tritiation in heterogeneous system is not well known,[18] by analogy to the model developed by Klein and Scheer[15,19] the probability is a surface reaction between the reactive tritium species generated either in the gas phase or at the gas–solid interface and the condensed reactant followed by diffusion into the interior of the latter. This model, however, assumes *a priori* the existence of an adsorption–desorption equilibrium of tritium between the surface of the condensed reactant, the wall of the container, and the gas phase which is temperature dependent. Diffusion of tritium to the interface where the primary reactions occur is also temperature dependent as evidenced by the variation of the coefficient of self-diffusion of hydrogen and deuterium with $T^{3/2}$.[20] Since diffusion is usually a rapid process, it is therefore unlikely that the depletion rate of tritium at the interface of the $C_{16:0}$–$C_{18:1}$–T system is diffusion controlled.

The primary reactions based on the findings for homogeneous systems[5-7] may involve decay-induced labeling and β labeling. In decay-induced labeling, the reactive species is HeT^+ formed from the reaction[6,7]

$$T_2 \longrightarrow HeT^+ + e^-$$

with a recoil energy of 1.65 ev and a $G(T)$ value of 0.018. Because of the immutability of radioactive

(17) J. W. Farquhar, W. Insull, P. Rosen, W. Stoffel, and E. H. Ahrens, *Nutr. Rev., Suppl.*, **17**, No. 8, 1 (1959).

(18) K. E. Wilzbach in "Tritium in the Physical and Biological Sciences," International Atomic Energy Agency, Vienna, 1962, p 3.

(19) R. Klein and M. D. Scheer, *J. Phys. Chem.*, **66**, 2677 (1962).

(20) J. O. Hirschfelder, R. B. Bird, and E. L. Spatz, *Chem. Rev.*, **44**, 205 (1949).

decay and the small magnitude of the $G(T)$ value, the decay-induced labeling is temperature independent and unimportant as a mechanism for tritiation under ordinary conditions.[21] At 77°K, when tritium addition in the $C_{16:0}$–$C_{18:1}$–T system is suppressed by the presence of oxygen, a $G(T)$ value of 0.013 is found, indicating that the decay-induced labeling is probably the exclusive mode for tritium incorporation. In the absence of oxygen, tritium addition occurs, but the $G(T)$ value for tritium incorporation by substitution in palmitate and oleate can be calculated to be 0.019[22] from the addition ratio and their relative specific activity, which is in approximate proportion to their weight fractions, showing that the labeling is again by the decay-induced mechanism. Thus, at the cryogenic temperature, when the molecules are in a state of lowest vibrational energy[23] and the molecular excitation energy from irradiation can be degraded thermally, decay-induced labeling becomes the dominant mode of tritiation.

In β labeling, the initiating step is the ionization of reactant molecules[5,7] and tritium.[24] The former on combination with electrons or negative ion molecules yield free radicals either directly or indirectly by dissociation; the reactions are depicted as

$$T_2 \xrightarrow{\sim} T_2^+ + e^-$$

$$T_2^+ + T_2 \longrightarrow T_3^+ + T$$

$$\mathrm{R{-}\underset{|}{\overset{|}{C}}{-}H} \xrightarrow{\sim} \mathrm{R{-}\underset{|}{\overset{|}{C}}{-}H^+} + e^- \longrightarrow \text{radicals}$$

$$\mathrm{R{-}\underset{|}{\overset{|}{C}}{-}H^+} + M^- \longrightarrow \mathrm{R{-}\underset{|}{\overset{|}{C}}{:}} + H^+$$

The temperature dependence of tritiation can be reasonably explained by a mechanism which involves a relative predominance of either a gas phase or an interface initiation of the reactive tritium species as a consequence of the adsorption-equilibrium established throughout the experiment in the tritiation chamber; the mechanisms are given in Scheme I,

Scheme I

Gas-phase initiation

$$T_2(g) \longrightarrow HeT^+ + e^-$$

$$e^- + T_2(g) \longrightarrow T_2^+ + 2e^-, \text{ etc.}$$

$$e^- + T_2(a) \longrightarrow T_2^+ + 2e^-, \text{ etc.}$$

$$e^- + M \text{ (or wall)} \longrightarrow M^* + e^- \text{ or } M^+ + 2e^-$$

$$(HeT^+, T_2^+, \text{etc.}) + M \longrightarrow \text{tritiation}$$

Interface initiation

$$T_2(a) \longrightarrow HeT^+ + e^-$$

$$e^- + M \longrightarrow M^* + e^- \text{ or } M^+ + 2e^-$$

$$HeT^+ + M \longrightarrow \text{tritiation}$$

where $T_2(g)$ = tritium in gas phase, $T_2(a)$ = tritium in adsorbed phase, M = reactant, and M* = reactant in the excited state. At 77°K, it is likely that the concentration of tritium in the adsorbed phase greatly exceeds that in the gas phase; hence, decay-induced labeling should predominate. With increasing temperature, the relative concentration of tritium in the gas phase increases and thus favors the β labeling.

It should be noted that from a mechanistic point of view, tritiation by substitution can be initiated by reactive species formed either from reactant molecules or from tritium, whereas tritiation by addition is only effected by the reactive species of tritium.

Radical meachanisms have been postulated for tritium incorporation by addition[3,8] and by substitution[5-7] in gas exposure, for the addition of hydrogen atoms to alkenes and other unsaturates[14] and for radiolysis of olefins.[25] The importance of ion-molecule mechanism has also been stressed for the latter.[26-28] Our results on tritium addition in the $C_{16:0}$–$C_{18:1}$–T system can best be explained on the basis of both mechanisms. Tritium atoms generated by quenching of $6(^3P_1)Hg^*$ atoms,[29] when acted upon the $C_{16:0}$–$C_{18:1}$–T system, gave an addition ratio of 5.4 *via* disproportionation.[30] Under these conditions, the reactive tritium species are entirely radicals. It is likely that molecular radicals formed from oleate and a tritium atom, when diffused away from the surface, can undergo disproportionation among themselves in the con-

(21) P. E. Riesz and K. E. Wilzbach, *J. Phys. Chem.*, **62**, 6 (1958).

(22) This value is higher than 0.013 given previously, probably owing to additional contribution from tritiooleate formed by disproportionation.

(23) L. P. Hammett, "Physical Organic Chemistry," McGraw-Hill Book Co., Inc., New York, N. Y., 1940, p 72.

(24) O. A. Schaeffer and S. O. Thompson, *Radiation Res.*, **10**, 671 (1959).

(25) R. A. Holroyd and G. W. Klein, *J. Phys. Chem.*, **69**, 194 (1965).

(26) C. D. Wagner, *Tetrahedron*, **14**, 164 (1961).

(27) P. C. Kaufman, *J. Phys. Chem.*, **67**, 1671 (1963).

(28) F. Collinson, F. S. Dainton, and D. C. Walker, *Trans. Faraday Soc.*, **57**, 1732 (1961).

(29) H. Niki, Y. Rousseau, and G. J. Mains, *J. Phys. Chem.*, **69**, 45 (1965).

(30) By analogy to the disproportionation of *sec*-butyl–*sec*-butyl radicals,[15] the 9-octadecenoate formed may have existed predominantly in the *trans* configuration. Analysis was not performed because the *cis* and *trans* forms could not be separated by gas chromatography on the packed columns used, although the individual forms when chromatographed alone showed slightly different retention times.

densed phase, but when trapped at the surface, they disproportionate with tritium atoms in the gas phase. The reactions are depicted below.

$$Hg^*(^3P_1) + T_2 \longrightarrow Hg(^1S_0) + 2T$$

$$R{-}CH{=}CH{-}R' + T \longrightarrow R{-}\underset{T}{C}H{-}CH{-}R'$$

a. At interface

$$R{-}\underset{T}{C}H{-}CH{-}R' + T \longrightarrow R{-}\underset{T}{C}H{-}\underset{T}{C}H{-}R' \quad \text{or}$$

$$R{-}CH{=}\underset{T}{C}{-}R' + HT$$

b. In condensed phase

$$2R{-}\underset{T}{C}H{-}CH{-}R' \longrightarrow R{-}\underset{H}{C}H{-}\underset{T}{C}H{-}R' + R{-}CH{=}\underset{T}{C}{-}R'$$

$$\text{or } R{-}\underset{T}{C}H{-}\underset{T}{C}H{-}R' + R{-}CH{=}CH{-}R'$$

$R = (CH_2)_7CH_3$

$R' = (CH_2)_7COOH$

Because of the large ionization cross section (by 75-v electron impact[31]), argon sensitizes the tritiating system by increasing the proportion of energy supplied to the tritium by the reaction[32]

$$Ar^+ + T_2 \longrightarrow ArT^+ + T$$

This formation of the tritium argonium ion, ArT^+, and the tritium atom elevates the $G(T)$ value of the $C_{16:0}$–$C_{18:1}$–T system at all temperatures of exposure. At 298°K, the addition ratio is 12.4, approaching that for the unsensitized system. When this is contrasted to the value of 5.4 obtained in mercury-photosensitized addition at 298°K, the increase can be attributed to a more selective electrophilic addition of tritium ions to the carbon–carbon double bond. The specificity of the tritium ion molecules for the π electrons may also account for the greater enhancement in the formation of tritiostearate, particularly at low temperatures, than of tritiopalmitate and of tritiooleate in the presence of argon. Oxygen inhibits the addition reaction by scavenging both radicals and ions. Since by virtue of its high affinity for electron attachment,[33] oxygen can form superoxide ion, O_2^-, and react with the tritium ions by charge neutralization. Such a mechanism can also adequately explain the relatively unperturbed tritium incorporation by substitution in palmitate and oleate in the presence of oxygen.

Nitric oxide promotes the combination of hydrogen atoms[34] but because of its own tendency to form nitrosonium ion, NO^+,[35] by charge transfer upon collision with other ion molecules, it cannot charge-neutralize reactive tritium ions. By contrast to mercury photosensitization, formation of tritiostearate by tritium addition at 298°K in the system containing nitric oxide is probably initiated solely by tritium ion molecules with an addition ratio of 8.3. The complete absence of tritiooleate and tritiostearate in the gas radiochromatogram in samples exposed at 77 and 193°K is anomalous, which is not easily explained and shall be further investigated.

The $C_{16:0}$–$C_{18:1}$–T system, if unperturbed, gives rise to tritiostearate by the mechanism of addition of both tritium atoms and tritium ion molecules to the double bond of oleate. The numerical value of the addition ratio of the unperturbed system at 298°K is almost identically the sum of the ratios of NO-scavenged and Hg-photosensitized systems, indicating about 60% participation by tritium ion molecules and 40% by tritium radicals in the addition reaction. This mechanism of mixed addition for tritium incorporation by unsaturates is not in contradiction with the

Scheme II

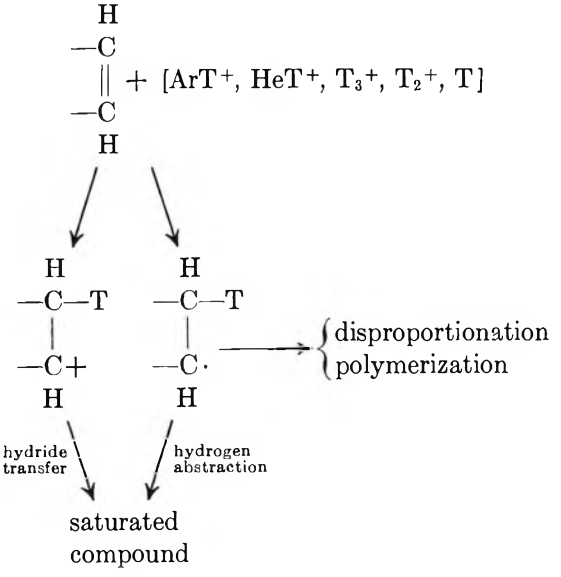

(31) F. W. Lampe, J. L. Franklin, and F. H. Field, *J. Am. Chem. Soc.*, **79**, 6129 (1957).

(32) A. Y. Mottlau, *J. Phys. Chem.*, **64**, 931 (1960).

(33) G. S. Hurst and T. E. Bortner, *Phys. Rev.*, **114**, 116 (1959).

(34) H. M. Smallwood, *J. Am. Chem. Soc.*, **51**, 1985 (1929).

(35) F. H. Field and J. L. Franklin, "Electron Impact Phenomena," Academic Press Inc., New York, N. Y., 1957, p 278.

exclusive radical mechanism postulated for the addition of hydrogen atoms to alkenes, since in such cases hydrogen atoms are generated thermally, and in the absence of ionizing radiation, ion formation is not energetically possible. An over-all mechanism of tritium addition can be thus depicted in Scheme II, with the reactive tritium species listed in the brackets. The formation of ion molecules as intermediates followed by hydride transfer would also account for the presence of more unsaturates observed in samples with high addition ratios.

Acknowledgment. The author is grateful to Professors W. D. Kumler and L. D. Tuck for helpful suggestions during the preparation of the manuscript and to one of the referees for the interpretation of the adsorption–desorption equilibrium of tritium treated in the Discussion.

Sorption of Nitrogen at Very Low Pressures by Molybdenum Films[1]

by R. A. Pasternak, N. Endow, and B. Bergsnov-Hansen

Stanford Research Institute, Menlo Park, California *(Received October 26, 1965)*

Nitrogen is adsorbed by clean molybdenum films in two well-defined states: one is stable to high temperatures; the other is stable only at temperatures below 130°K. For either state the amounts adsorbed at saturation are approximately independent of pressure. The sticking probability for both states is initially high, about 0.5; however, for the high-temperature state, it drops off rapidly with coverage, whereas for the low-temperature state it remains constant almost to saturation. The kinetic pattern for the former can be explained by molecular flow into the pores, and for the latter by surface diffusion of molecularly adsorbed nitrogen to the internal surfaces.

Introduction

Nitrogen is adsorbed by molybdenum in two well-defined states;[2] one is stable to high temperatures, the other only below 130°K. At least two states have been observed for nitrogen on other metals also. The high-temperature state has been studied extensively, whereas information on the properties of the low-temperature state is still rather limited. The present investigation was undertaken to establish in some detail the kinetics and the thermodynamics of nitrogen adsorption, particularly for this low-temperature state.

Experimental Section

Apparatus. The experimental apparatus is shown schematically in Figure 1. The pumping system (not shown) is of conventional design except that two three-stage glass oil-diffusion pumps are used in parallel in conjunction with a large Biondi trap[3] charged with activated alumina beads (A in Figure 1).

The electron beam evaporator (B), similar to one described previously,[4] has, as electron source, a 10-mil tungsten filament (a) which is kept at ground potential and heated by an ac current. The small tip of the molybdenum target (b), machined from electron beam melted stock, can be biased up to +3000 v; it approximates a point source for the metal vapors. A

(1) This research was supported by the Research Division of the U. S. Atomic Energy Commission.

(2) M. W. Roberts, *Trans. Faraday Soc.*, **59**, 698 (1963).

(3) M. A. Biondi, *Rev. Sci. Instr.*, **30**, 831 (1959).

(4) R. W. Berry, "Electron Bombardment Evaporation of Tantalum for Thin Film Components," Proceedings of Symposium on Electron Beam Technology, Allayad Electronics Corp., Cambridge, Mass., 1961.

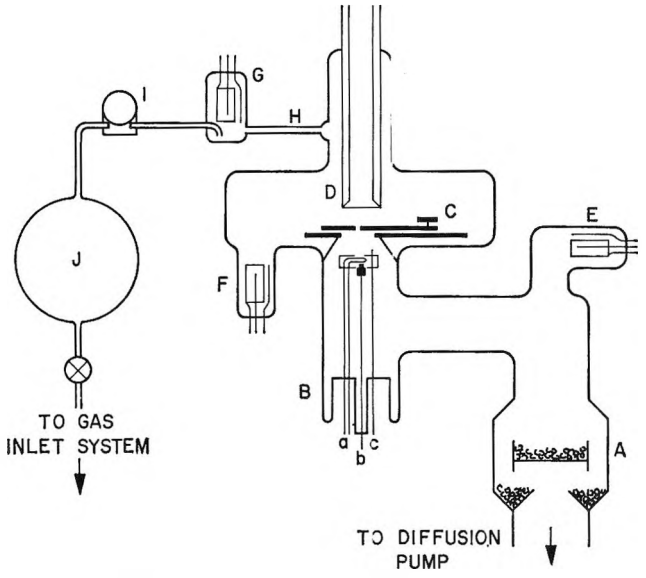

Figure 1. Schematic drawing of experimental unit: A, Biondi trap; B, electron beam evaporator (a, electron emitter; b, target; and c, cage structure); C, glass valve, D, substrate tube; E, F, and G, ion gauges: H, capillary; I, motor-driven valve; and J, gas reservoir.

cage structure (c) of molybdenum sheet is kept at −3 v with respect to the filament to improve focusing of the electron beam.

The sorption chamber (approximately 1000 cc) is separated from the evaporator by a magnetically operated ground-glass valve (C). The valve has three defined positions: fully open, fully closed, or with a small orifice with a calculated conductance of 230 cc of N_2/sec at 300°K. The flat end of a double-wall glass tube (D) located opposite the valve constitutes the substrate for film deposition. The desired substrate temperature is established by filling the tube with an appropriate constant-temperature fluid; dry nitrogen at room temperature is passed through the tube jacket to limit heating or cooling to the substrate itself. Three ion gauges measure the pressure: (E) close to the pump, (F) close to the sample film, and (G) at the upstream side of the glass capillary (H) (conductance of 100 cc of N_2/sec at 300°K) which is connected to the main chamber.

The motor-driven Granville–Phillips variable-leak valve (I) separates the sorption chamber from the gas reservoir (J). After baking of the system, the latter is filled with research grade nitrogen (impurities: $O_2 <$ 5 ppm, rare gases < 15 ppm), which is dried by cooling to 77°K.

Operational Features. Evaporation of the metal by electron bombardment and isolation of the evaporator from the sorption cell by means of the glass valve permit thorough degassing and premelting of the target; some metal is simultaneously evaporated onto the wall and acts as an excellent getter pump. The circular film deposited subsequently on the substrate is well defined by the circular hole in the cage structure and the aperture of the valve. Its area is about 6 cm^2 (comparable to that of filaments used in flash filament studies) and its thickness is quite uniform; electron microprobe analysis of one film showed that the variation was less than 5% except for an edge region about 1 mm wide.

The rate of adsorption is measured at constant pressure. The automatic controller maintains constant pressure in the sorption cell by adjusting the flow into the unit through the motor-driven valve. The pressure difference across the conductance (H) is a measure for the leak rate, *i.e.*, for the rate of sorption, and is recorded continuously; integration of the rate curve gives the total amount sorbed. With this constant-pressure approach, the effect of pressure on the sorption kinetics can be studied independently of other parameters, and effects arising from wall and ion gauge interaction with the gas are minimized. A detailed description of the constant-pressure technique has been given elsewhere.[5]

For the determination of the isotherm of the low-temperature state which is stable only below 130°K, a flash desorption technique similar to that used for filaments was employed; adsorbed gas was flashed off by filling the thermostat well with warm ethanol. Because of the small surface of the films, the resulting pressure increase was sufficiently small, less than 10^{-3} torr, to be measurable with the ultrahigh vacuum ion gauges.

Experimental Procedure. After standard bakeout at about 300°, degassing of the evaporator, premelting of the target, and evaporation of some metal (with the glass valve closed), a pressure in the 10^{-10}-torr range was reached in the cell. The substrate tube was then thermostated to the desired temperature and metal was evaporated onto it for about 30 min. The resulting film was annealed for 5 min at about 330°K. This short annealing time was chosen to keep film contamination to a minimum. The small conductance of the glass valve was then inserted, the desired film temperature was established, and the sorption run was started by activating the automatic leak valve. For the study of the reversible, low-temperature adsorption state, the control pressure could also be established first and

(5) R. Gibson, B. Bergsnov-Hansen, N. Endow, and R. A. Pasternak, Transactions, 10th National Vacuum Symposium, American Vacuum Society, Boston, Mass., 1963, p 88.

the film cooled afterwards; no significant difference was found.

The pressure during evaporation increased into the high (10^{-10} torr) or low (10^{-9} torr) range, depending somewhat on the history of the system. This increase is probably due to evolution of nitrogen from the previously deposited films in the evaporator. When evaporation was discontinued, the pressure again reached the low, 10^{-10}-torr range. The deposition rate of metal was approximately 1×10^{14} atoms/cm^2 sec, about 300 times the impingement rate of nitrogen molecules at 1×10^{-9} torr. Thus, provided that adsorbed gas is distributed uniformly throughout the bulk, contamination of the film during evaporation is quite small. Because of the low pressure during the time required to initiate the sorption run proper, the amount of gas adsorbed on the outer surface of the film cannot be significant either.

A large number of films were investigated by the described procedure. They were deposited either at 330 or at 77°K (called subsequently H and L films, respectively), and sorption was investigated at 300, 87 (liquid argon), and 77°K. Since the activity of the film decreased with time, the nitrogen data for a given film were in general taken all within 1 day. Subsequently, the adsorption isotherm of xenon on the films was determined *in situ*, and the surface area was derived by the method of Kaganer,[6] which is based on the theoretical treatment of Dubinin and Radushkevich.[7,8] As has been shown by Kaganer[6] and by Schram,[9] the surface areas obtained by this method are in approximate agreement with those obtained by the BET method. In the present study such a comparison could not be made because the relative pressures were below the range required for the BET method. The calculation of surface coverage was based on a molecular area of 25 A^2 for the adsorbed xenon atom. The surface areas as determined by physisorption decreased gradually with time, by a factor of about 2 over a period of 3 weeks. Since the areas quoted in Table I were obtained 1 or 2 days after the nitrogen sorption experiments, they are undoubtedly somewhat lower than the initial surface areas. The physisorption study has been presented in detail elsewhere.[10] Finally, the films were removed and their weights were determined by chemical analysis.

The conditions of preparation and of study for five films, which were studied more extensively, and the results obtained with them are summarized in Table I. Films 1 and 3 were prepared in sequence under closely similar conditions except for the deposition temperature; they, as well as film 5, will be discussed in some detail. Films 2 and 4 were studied at widely different times in the course of this study; data for them are listed to illustrate the reproducibility of the measurements. The data summarized in Table I and shown in the figures refer to a geometric area of 1 cm^2.

Results and Discussion

Segments of two films (1 and 3, see Table I) were studied by transmission electron microscopy and electron diffraction. The electron micrographs indicate that the L film 3 is spongy and uniform, whereas the H film 1 is quite dense, *i.e.*, probably has smaller pores than the former, and exhibits a few large crystallites with well-defined edges. The thickness of the H film was estimated from a surface replica of its edge to be about 400 A.

The electron diffraction patterns did not indicate any preferred orientation. The L film exhibited broader lines and a higher background than the H film.[11] From the line widths, average crystallite diameters of 80 and 120 A, respectively, were estimated.

A rough estimate of the film thickness and porosity can be made by assuming that the films consist of closely packed spheres of a diameter equal to the average particle size. A thickness of 670 A is calculated for either film, of the same magnitude as the measured value of 400 A, and the surface areas for films 1 and 3 are 0.3 and 0.4 cm^2/μg; these values agree closely with the values derived by xenon adsorption (0.35 and 0.50, see Table I). Thus, the specific surface areas of the two kinds of films are quite similar.

Irreversible Sorption at 300°K. Typical sticking probability curves for the two films are shown in Figures 2a and 2b. They agree closely except that the curve for the H film 1 approaches zero more gradually than that of the L film 3. For both films, the sticking probability has a high initial value of about 0.5, but then drops rather rapidly with coverage. Increase in sorption pressure, p, indicated by the arrows, does not

(6) M. G. Kaganer, *Dokl. Akad. Nauk SSSR*, **116**, 251 (1957).

(7) M. M. Dubinin and L. V. Radushkevich, *Proc. Acad. Sci. USSR*, **55**, 331 (1947).

(8) M. M. Dubinin, *Chem. Rev.*, **60**, 235 (1960).

(9) A. Schram, Transactions, The 9th National Vacuum Symposium, American Vacuum Society, Los Angeles, Calif., 1962, p 301.

(10) N. Endow and R. A. Pasternak, 12th National Symposium, American Vacuum Society, New York, N. Y., Oct 1, 1965; *J. Vacuum Sci. Tech.*, to be published.

(11) In the pattern of this film three additional very faint lines, characteristic for the compound Mo_2N, were found. We suspect that this compound was formed during film deposition at 330°K when the molybdenum atoms and adsorbed nitrogen may initially exhibit high mobility; the formation of a crystalline nitride does not seem likely during subsequent exposure to nitrogen at 300 and 77°K.

Table I: Sorption of Nitrogen on Molybdenum Films

Film no.	1	2	3	4	5
Deposition temp, °K	330	330	77	77	77
Weight, μg	50	25	52	*a*	54
Surface area, cm^2 (from xenon adsorption)	17	13	25	*a*	30
Surface area, $cm^2/\mu g$	0.35	0.5	0.5		0.55
Irreversible sorption at 300°K on virgin film					
Adsorption pressure × 10^8, torr	1.2	*b*	4.4	4.7	2.3[c]
Initial sticking probability, S_0	0.6		0.45	0.4	0.6[c]
Coverage × 10^{-14}, molecules	20		24	34	39[c]
Reversible sorption at 77 or 87°K					
Adsorption pressure × 10^8, torr	3–9000	2–2000	3–3000	0.6–25	0.6–400
Initial sticking probability, S_0	0.7	0.6	0.6	0.4	0.5
Coverage × 10^{-14}, molecules	12–20	10–16	26[d]	27[d]	37[d]

[a] Not measured. [b] Adsorption run miscarried. [c] Sorption on virgin film at 77°K. The coverage is the difference of the amounts shown in Figure 5. [d] Average value.

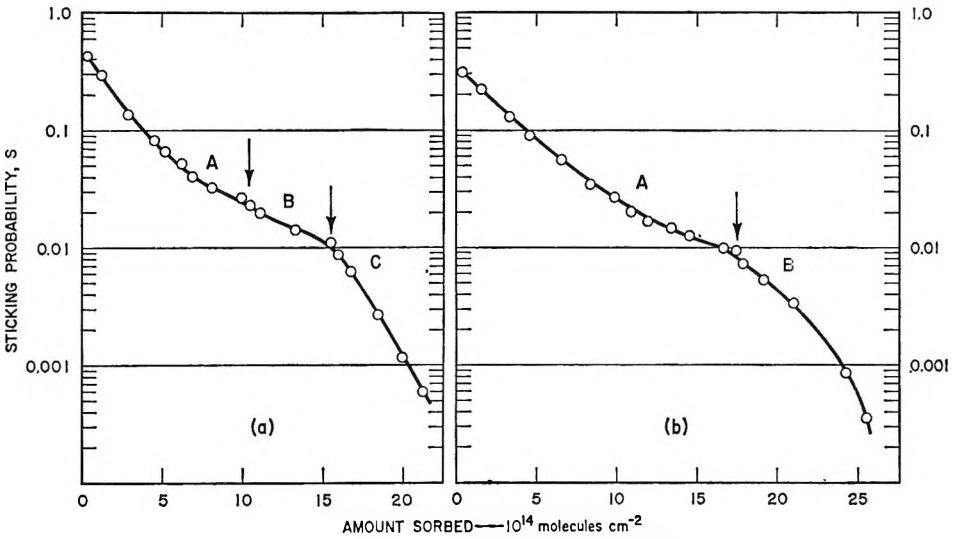

Figure 2. Sticking probability curves for adsorption of nitrogen on virgin film at 300°K: (a) H film 1 (deposited at 330°K+); control pressure (A) = 1.2 × 10^{-8} torr, (B) = 6.0 × 10^{-8} torr, and (C) = 3.3 × 10^{-7} torr; (b) L film 3 (deposited at 77°K); control pressure (A) = 4.4 × 10^{-8} torr, and (B) = 4.4 × 10^{-7} torr.

cause any significant discontinuity in the curves, *i.e.*, the rates of adsorption at a given coverage are proportional to pressure. Further pressure increase to 2 × 10^{-6} torr at the end of the runs did not result in additional gas uptake (within the limit of our experimental sensitivity in S of about 0.0005) nor were significant amounts of gas released when the pressure was reduced again by about two powers of ten. This sorption state is thus independent of pressure and irreversible at room temperature.

The saturation coverage per unit area of surface (defined here by xenon adsorption) is approximately 1 × 10^{14} molecules cm^{-2} for both films. This value is only about half that usually found on polycrystalline molybdenum or tungsten filaments. The discrepancy could be explained by assuming that the smallest pores are not accessible to nitrogen; however, the possibility that it is due to accumulated experimental errors and uncertainties cannot be excluded.

Initial sticking probabilities of the same magnitude as found here have been reported by Wagener[12] for nitrogen on a variety of metal films. (The sticking probabilities of nitrogen on molybdenum films reported originally by Roberts[2] are, according to a later

(12) S. Wagener, *J. Phys. Chem.*, 61, 267 (1957).

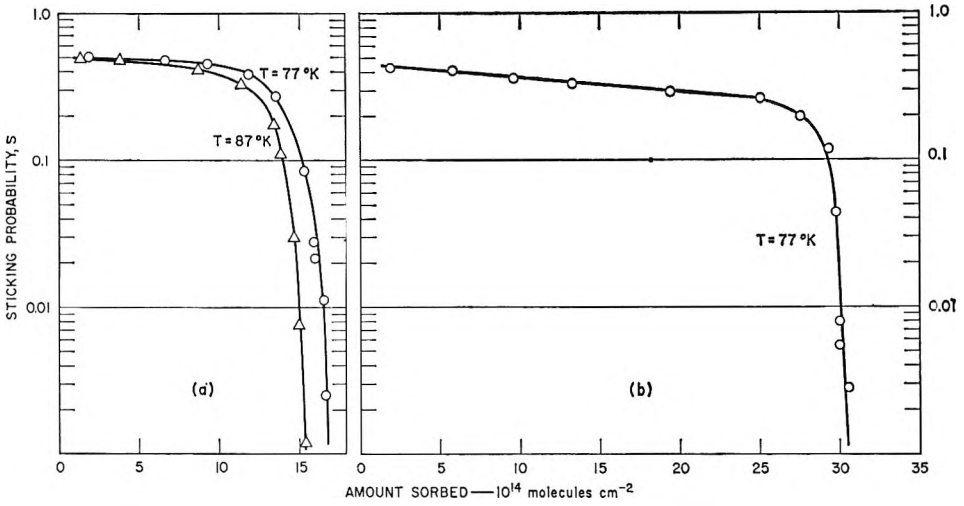

Figure 3. Sticking probability curves for reversible adsorption of nitrogen: (a) H film 1, control pressure = 4×10^{-8} torr; (b) L film 3, control pressure = 3×10^{-8} torr.

communication,[13] not significant because of experimental artifacts.) The sticking probabilities of nitrogen on filaments of polycrystalline molybdenum,[14] tungsten,[15-17] and niobium[18] are, at lower coverage, between 0.1 and 1.

The high initial sticking probabilities of filaments persist in general to beyond half coverage; in contrast, the sticking probabilities for the films decrease rapidly with coverage as observed in the present study. The primary adsorption step is undoubtedly the same on the films as on the filaments, as is indicated by the agreement in initial sticking probability, and thus the exposed surface of the film can be expected to adsorb nitrogen according to the same rate law as a smooth filament. However, the pore surfaces, representing more than 90% of the total film area, can be reached only by molecular flow through the capillary spaces; thus, the actual pressure seen by the internal surfaces is lower than that in the free gas phase, and the over-all sorption rate is reduced accordingly. Since nitrogen is undoubtedly adsorbed atomically in the high-temperature state and thus forms strong bonds with the metal atoms, surface diffusion is excluded as a mechanism for moving nitrogen into the pores.

Reversible Sorption at 77 and 87°K. On cooling the same films to liquid nitrogen or argon temperature, additional nitrogen is adsorbed which is desorbed again on warming the film. At 130°K (established with a liquid nitrogen–methylcyclopentane slush) no significant amounts of this nitrogen are retained.

Typical low-temperature sticking probability curves for films 1 and 3 are shown in Figures 3a and 3b. They are characterized by a high sticking probability of above 0.5, which decreases little until almost complete coverage is attained. The sticking probability curves at 87°K coincide, within the precision of the measurements, with those at 77°K, as is illustrated in Figure 3a.

The saturation amounts are shown as a function of pressure in Figure 4a for the L film 3 at 77°K, and in Figure 4b for the H film 1 at 77° and 87°K. For the L film no pressure dependence of the isotherm is observed; for the H film the amount sorbed increases slightly with pressure to approach a constant value. We suspect that in the latter case steady state was not quite reached during the experiments at the low pressures because of the smallness of the pores. Small pore sizes were suggested also by the electron micrograph of the H film. The flash desorption curves indicate the same; nitrogen is released by the H films more gradually than by L films. (Curve 4a also illustrates the general observation made for both H and L films that the amounts sorbed at the two film temperatures of 77 and 87°K do not differ significantly.)

Individual points of the isotherms are reproducible within about 20% when the measurements are all made in 1 day. However, the saturation amounts decline slowly over longer time intervals—to less than 5%

(13) C. S. McKee and M. W. Roberts, *Chem. Commun.* (London), No. 4, 59 (1965).

(14) R. A. Pasternak and H. U. D. Wiesendanger, *J. Chem. Phys.*, 34, 2060 (1961).

(15) J. A. Becker and C. D. Hartman, *J. Phys. Chem.*, 57, 157 (1953).

(16) P. Kisliuk, *J. Chem. Phys.*, 30, 174 (1959).

(17) G. Ehrlich, *ibid.*, 34, 29 (1961).

(18) R. A. Pasternak and R. Gibson, *Acta Met.*, 13, 1031 (1965).

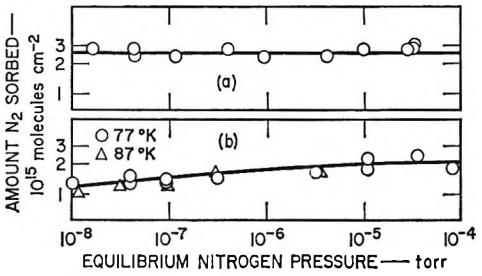

Figure 4. Isotherms for reversible adsorption of nitrogen: (a) L film 3; and (b) H film 1.

after approximately 3 weeks. This deactivation is chemical in nature, since it is not accompanied by a corresponding decrease in surface area (as defined by xenon adsorption).

This low-temperature sorption of nitrogen by molybdenum films cannot be physisorption; it must be a specific adsorption state for the nitrogen–molybdenum system with well-defined stability range and adsorption energy. This is indicated by the large amount adsorbed, which is of the magnitude of a monolayer, and by the approximate independence of the isotherm of pressure and temperature, within the range studied. Moreover, the small heat of adsorption ($-\Delta H$) of about 10 kcal/mole (estimated from the stability of this state), and the high, temperature-independent sticking probability suggest molecular rather than atomic adsorption. If adsorption was dissociative, attachment of the nitrogen atoms to the surface would be preceded by disruption or considerable stretching of the strong N–N bond (226 kcal/mole), since this bond is much shorter than the distance between adjacent adsorption sites on the molybdenum surface. Such a transition state would certainly have an enthalpy significantly higher than the initial state involving gaseous nitrogen or the final state involving adsorbed nitrogen, which differ by only the observed small heat of adsorption. Thus, the probability for atomic adsorption would undoubtedly be low and would be associated with a considerable activation energy.

The virtual independence of the sticking probability on coverage, contrasting pronouncedly with room temperature adsorption of nitrogen on virgin films, also points to molecular adsorption. This constancy can be explained if adsorption on the exposed surface occurs at a rate which is little dependent on coverage (as has been observed for low-temperature adsorption of nitrogen on tungsten filaments[17]), and the adsorbate is transported to the internal surfaces by fast surface diffusion. An estimate for surface mobility shows that such a mechanism demands a small binding energy between adsorbate and adsorbent, of the magnitude of the observed heat of adsorption. The number of surface jumps made by an adsorbed particle during the average time interval between impacts of gas molecules on the same site is

$$n = \frac{\nu_j}{\nu_a} = \frac{\nu_{oj}(-\Delta H/RT)}{\nu_{oa}p} \qquad (1)$$

where $\nu_j = \nu_{oj}(-\Delta H/RT)$ is the jump frequency and $\nu_a = \nu_{oa}p$ is the incidence rate. The frequency factor ν_{oj} is approximately 10^{13} sec^{-1} and ΔH, the heat of diffusion, is usually about one quarter of the binding energy ΔH_a.[19] The incidence rate at unit pressure ν_{oa} is about 10^6 $torr^{-1}$ sec^{-1} per site. By inserting the numerical values into eq 1, we obtain

$$n \approx 10^7 p^{-1} \exp\left(-\frac{\Delta H_a}{4RT}\right) \qquad (2)$$

At 77°K, a pressure of 10^{-7} torr, and a binding energy of 10 kcal/mole, which is indicative for molecular adsorption, n is about 10^7, and surface diffusion is sufficiently fast to move the gas adsorbing on the exposed surface into the pores. Formation of the strong atomic bond of about 130 kcal/g-atom would result in a completely immobile surface layer and, consequently, in a sticking probability curve similar to that observed for adsorption at 300°K.

Sorption on Virgin Films at Liquid Nitrogen Temperature. Film 5, which was deposited at 77°K and annealed at 330°K, was recooled to 77°K before exposing it to nitrogen. The resulting sticking probability curve is shown in Figure 5a. About half the amount originally adsorbed is released on warming the film and is readsorbed on recooling to 77°K; a sticking probability curve for this reversible sorption is shown in Figure 5b.

The sticking probability curve for the adsorption on the virgin film, curve 5a, is very similar to that of the subsequent reversible adsorption, although nitrogen probably adsorbs in both states. The approximate independence of the sticking probability on coverage indicates that the atomic adsorption layer at the internal surfaces is formed *via* the highly mobile molecular adsorption layer. Whether atomic adsorption on the exposed surface also proceeds through the molecular adsorption state cannot be established on the basis of the present data.

Subsequent low-temperature adsorption on this film is in all respects analogous to that on the other low-temperature films. The isotherm shows no sig-

(19) G. Ehrlich in "Structure and Properties of Thin Films," John Wiley and Sons, Inc., New York, N. Y., 1959, pp 425–475.

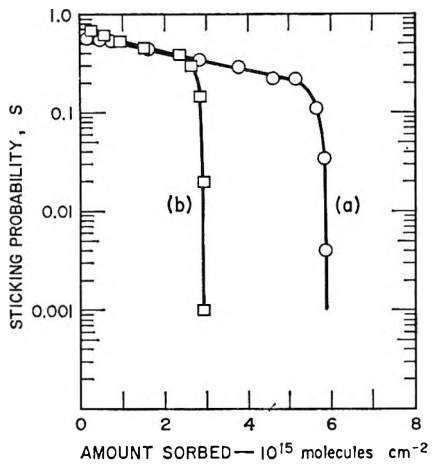

Figure 5. Sticking probability curves for adsorption of nitrogen at 77°K: film J, control pressure = 2×10^{-8} torr; (a) virgin film; and (b) film with preadsorbed nitrogen.

nificant pressure dependence and the amount is about equal to that adsorbed irreversibly.

Concluding Remarks. The low-temperature sorption state discussed here in some detail is not unique. Similar states have been observed for other nitrogen–metal[17,20–22] and for hydrogen–metal systems;[23–26] it seems likely that low-temperature sorption states also exist for oxygen on metals, but no reliable data have been published so far. This weakly bound state appears to be of quite general occurrence and may represent the physical reality of the intermediate state (often called the C state[27]) frequently postulated for explaining adsorption kinetics, in particular, the kinetics of catalytic reactions.

(20) O. Beeck, *Advan. Catalysis*, 2, 151 (1959).

(21) A. G. Nasini, G. Saini, and R. Ricca, *Actes Congr. Intern. Catalyse, 2e, Paris, 1960*, 241 (1961).

(22) T. A. Delchar and G. Ehrlich, *J. Chem. Phys.*, 42, 2686 (1965).

(23) R. J. Kokes and P. H. Emmett, *J. Am. Chem. Soc.*, 82, 1037 (1960).

(24) R. J. Kokes, *ibid.*, 82, 3018 (1960).

(25) R. A. Pasternak and N. Endow, to be published.

(26) T. Hickmott, *J. Chem. Phys.*, 32, 810 (1960).

(27) G. C. Bond, "Catalysis by Metals," Academic Press Inc., New York, N. Y., 1962, p 69.

NOTES

A Correlation of the Coefficients of Thermal Expansion of Metallic Solids with Temperature

by Y. A. Chang[1]

Inorganic Materials Research Division, Lawrence Radiation Laboratory, and Department of Mineral Technology, University of California, Berkeley, California (*Received October 14, 1965*)

One of the fundamental properties needed in the description of a solid is the coefficient of thermal expansion. Unfortunately, such data at the temperatures of interest are often lacking. The purpose of this note is to present a generalized correlation which expresses the reduced coefficient of thermal expansion as a function of the reduced Debye temperature for metallic solids. From this correlation, one can predict the coefficient of thermal expansion of a metallic solid at any temperature if the coefficient of thermal expansion is known at one temperature.

According to the Gruneisen relationship,[2] the coefficient of thermal expansion of a solid is proportional to its specific heat, and one thus expects that the temperature dependence of the coefficient of thermal expansion should be similar to that of the specific heat. This indeed is the case. The coefficient of thermal expansion goes to zero at absolute zero temperature and approaches a nearly constant value at high temperatures. However, this value differs for different metallic solids, depending on the melting points. It is hoped that plots of the reduced linear coefficient of thermal expansion, β_T/β_θ *vs.* the reduced Debye temperature, T/θ, may produce a universal curve common to all metallic solids. The term β_T is

(1) Aerojet-General Corporation, Sacramento, Calif.

(2) See N. F. Mott and H. Jones, "The Theory of the Properties of Metals and Alloys," Dover Publications, Inc., New York, N. Y., 1958.

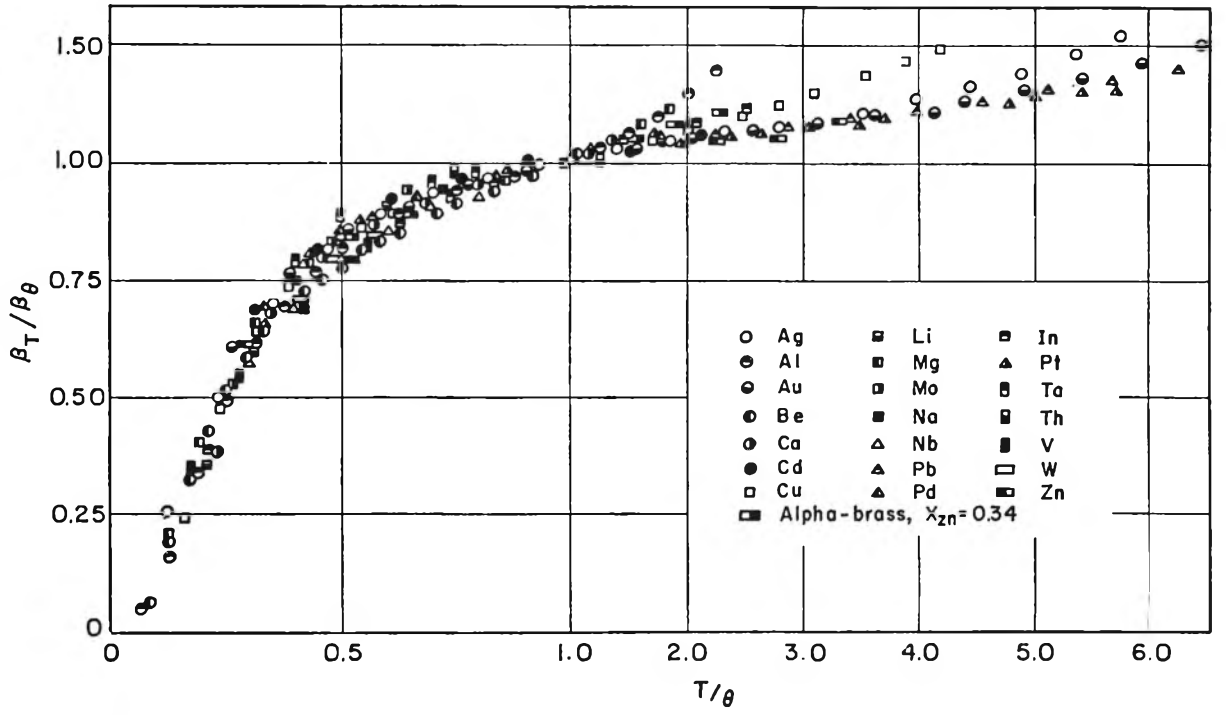

Figure 1. Reduced coefficient of thermal expansion of metallic solids (the scales of both the ordinate and the abscissa are compressed at temperatures higher than $T/\theta = 1.0$).

the linear coefficient of thermal expansion of a solid at any temperature, β_θ is the linear coefficient of thermal expansion at the Debye temperature, T is the absolute temperature, and θ is the Debye temperature, characteristic of a solid.

A plot of the reduced coefficient of thermal expansion *vs.* the reduced Debye temperature is made for 21 metallic elements and one α-brass with 34 atomic % zinc. As shown in Figure 1, all of these data fall close to the same curve except at temperatures higher than two-thirds of the absolute melting points. The deviation of the reduced coefficients of thermal expansion at high temperatures is perhaps due to the greater anharmonicity of lattice vibrations and the generation of vacancies in the lattice. It is noteworthy to point out that the linear coefficient of thermal expansion of beryllium with a Debye temperature of 1200°K and a melting point of 1556°K and lead with values of 88 and 601°K, respectively, agree rather well in this generalized correlation.

The Debye temperatures, the coefficients of thermal expansion at the respective Debye temperatures, and the references where thermal expansion data were obtained for these 22 metallic solids are summarized in Table I. For cubic solids, the linear coefficient of thermal expansion is the same in every direction, and for noncubic solids the average coefficients of thermal expansion obtained in the usual manner are used to obtain the curve in Figure 1.

Consequently, the values of the coefficient of thermal expansion of any metallic solid at any temperature may be obtained from Figure 1, when the Debye temperature and the coefficient of thermal expansion at one temperature are known. Values of the Debye temperature can be obtained either from the specific heat data or the Lindemann relationship which relates the Debye temperature of a solid as a function of its melting point, atomic volume, and atomic weight.[2] Recently, Gschneidner[3] has calculated the Debye temperature of many elements using the Lindemann relationship. The values of the Debye temperature calculated are in good agreement with those used in the present correlation.

The room temperature coefficient of thermal expansion of a metallic solid may be obtained from the relationship that the product of β and T_m, where β is the linear coefficient of thermal expansion at room temperature and T_m is the absolute melting point, is a constant. Gschneidner[3] has made an extensive compilation of the coefficients of thermal expansion at room temperature and the melting points of all the elements where data were available. He found the

(3) K. A. Gschneidner, Jr., *Solid State Phys.*, 16, 275 (1964).

Table I: Thermal Properties of Metallic Solids

Metallic solid	θ, °K	$\beta\theta \times 10^6$, °K^{-1}	References
Ag	215	18.2	*a–e*
Al	400	25.0	*a, b, d, f*
Au	194	13.4	*b, d, f*
Be	1200	22.9	*g, h*
Ca	220	20.8	*i*
Cd	165	29.3	*j*
Cu	325	16.9	*a, c, f, k, l*
In	120	27.5	*m, n*
Li	500	53.0	*o*
Mg	406	27.2	*b, c*
Mo	350	5.3	*d*
Na	240	66.5	*p*
Nb	250	7.1	*i*
Pb	88	24.9	*b, d, q*
Pd	300	11.7	*d*
Pt	230	8.70	*c, d*
Ta	252	6.40	*d*
Th	200	10.3	*i*
V	450	9.5	*i*
W	310	4.6	*r*
Zn	180	28.1	*j, s*
Cu–Zn (66:34)	290	18.9	*l, t*

[a] R. M. Buffington and W. M. Latimer, *J. Am. Chem. Soc.*, **48**, 2305 (1926). [b] H. Ebert, *Z. Physik*, **47**, 712 (1928). [c] H. Esser and H. Easterbrock, *Arch. Eisenhuettenwes.*, **14**, 341 (1941). [d] F. C. Nix and D. MacNair, *Phys. Rev.*, **61**, 74 (1942). [e] K. E. Salimaki, *Ann. Acad. Sci. Fennicae*, **AVI**, No. 56, 40 (1960). [f] F. C. Nix and D. MacNair, *Phys. Rev.*, **60**, 597 (1941). [g] P. Gordon, *J. Appl. Phys.*, **20**, 908 (1949). [h] A. Owen and T. L. Richards, *Phil. Mag.*, **22**, 304 (1936). [i] H. D. Erfling, *Ann. Phys.*, **41**, 467 (1942). [j] E. Gruneisen and E. Goens, *Z. Physik*, **29**, 241 (1924). [k] R. O. Simmons and R. W. Balluffi, *ibid.*, **108**, 278 (1957). [l] P. D. Merica and L. W. Schad, National Bureau of Standards Bulletin No. 14, U. S. Government Printing Office, Washington, D. C., 1919, p 571. [m] J. Graham, A. Moore, and G. V. Raynor, *J. Inst. Metals*, **84**, 86 (1955). [n] C. A. Swenson, *Phys. Rev.*, **100**, 1607 (1955). [o] F. E. Simon and R. Bergmann, *Z. Physik. Chem.*, **138**, 255 (1930). [p] S. Seigel and S. L. Quimby, *Phys. Rev.*, **54**, 76 (1938). [q] A. R. Stokes and A. J. C. Wilson, *Proc. Roy. Soc.* (London), **A53**, 658 (1941). [r] P. Hidnert and W. T. Sweeny, National Bureau of Standards Scientific Paper No. 20, U. S. Government Printing Office, Washington, D. C., 1925, p 483. [s] A. Owen and E. L. Yates, *Phil. Mag.*, **17**, 113 (1934). [t] H. W. Altman, T. Rubin, and H. L. Johnson, TR264-28, Cryogenic Laboratory, Department of Chemistry, Ohio State University, Columbus, Ohio, 1954.

product βT_m to be 0.0186 ± 0.0080 for all the elements. However, when he considered only those elements crystallized either with a face-centered cubic, body-centered cubic, or hexagonal close-packed structures, the product was found to be 0.0197 ± 0.0051. The uncertainty of ±0.0051 corresponded to a per cent error of only 26% instead of 43% when all the elements were considered.

In short, the correlation shown in Figure 1 with the well-known relationship that the product βT_m is a constant may be used to estimate the thermal expansion coefficient of any metallic solid, elements as well as alloys, at any temperature when experimental data are not available. Moreover, from the findings for metallic solids, it is anticipated that similar correlations also exist for nonmetallic solids.

Acknowledgment. The author is indebted to the U. S. Atomic Energy Commission and the Office of Scientific Research of the U. S. Air Force for their support of this work. He also wishes to thank Prof. R. Hultgren for his interest in this work and R. Orr for some helpful suggestions.

The Interaction between Maleic Anhydride and Electronically Excited Anthracene[1]

by Robert Livingston, Rosario Maria Go, and T. G. Truscott

Division of Physical Chemistry, Institute of Technology, University of Minnesota, Minneapolis, Minnesota
(Received October 26, 1965)

The Diels–Alder addition of maleic anhydride to anthracene is accelerated by exposure to light of 3650 A.[2] The quantum yield of this process increases with increasing concentration of maleic anhydride, and (in dioxane) is approximately 0.03 for 0.5 *M*. Simons[2] attributed the photochemical reaction to a diffusional interaction between a molecule of maleic anhydride and one of anthracene in its first excited singlet state. Since these reactants form a weakly stable complex in solution, an alternative explanation for the photochemical reaction is that the absorption of a photon by this complex can result in the intramolecular formation of the Diels–Alder adduct. In relation to this problem, we have measured the quenching of the fluorescence and of the triplet state of anthracene by maleic anhydride, in air-free dioxane.

Experimental Section

Materials and Methods. Fisher's zone-refined anthracene was used without further purification. Maleic

(1) Sponsored by the U. S. Army Research Office (Durham).
(2) J. P. Simons, *Trans. Faraday Soc.*, **56**, 391 (1960).

anhydride was sublimed three times under vacuum before use. The purification of dioxane was similar to that described by Simons.[2]

The intensity of fluorescence was measured with a Photovolt (Model 520) photometer. The exciting light of 3650 A was isolated from the radiation of a GE AH4 arc by a suitable interference and cutoff filter. The collimated beam of exciting light was incident upon a 1-cm² Pyrex cell containing the solution or solvent. Fluorescent light, emitted at right angles to the incident beam, passed through a filter which excluded light of wavelengths shorter than 4200 A before striking the photomultiplier. All solutions contained 2×10^{-4} M anthracene and were measured at room temperature. The method of measuring the rate of decay of the triplet states of anthracene (in the presence and in the absence of maleic anhydride) has been described.[3] The solutions used for fluorescence measurements were partially deoxygenated by bubbling tank N_2 through them: those used in the flash-photolytic experiments were carefully degassed by the usual freeze–thaw technique.[3]

Results and Discussion

As shown in Figure 1, $(I_0/I) - 1$ is directly proportional to the concentration of maleic anhydride up to concentrations of 0.1 M. The quantity I_0/I is the ratio of the intensities of anthracene fluorescence in solutions free from and containing maleic anhydride, under otherwise identical conditions. At higher concentrations, there is a marked positive deviation from the Stern–Volmer law, presumably due to internal filter action of the nonfluorescent anthracene–maleic anhydride complex. The straight line corresponds to a quenching constant of 67 M^{-1}. Combining this with the actual mean lifetime, 6.2×10^{-9} sec (measured by Berlman[4] in air-free cyclohexane) we obtained a bimolecular quenching constant of 1.1×10^{10} M^{-1} sec^{-1}. This value suggests that the quenching is a diffusionally limited bimolecular reaction.

Measurements of the rates of decay and of the relative yields of the anthracene triplet were made in the presence and absence of maleic anhydrides. All measurements were made at room temperature, using 7.0×10^{-5} M anthracene dissolved in carefully deoxygenated dioxane. The addition of 0.012 M maleic anhydride reduced the yield of triplet-state anthracene by a factor of 0.61. This result can be compared to the values of the mean lifetime, τ, and the bimolecular quenching constant, k_Q, of the fluorescent state. Unless the quenching of fluorescence produces the triplet state, the quantum yield of the triplet should be

$$\phi_\tau = \frac{\alpha\tau^{-1}}{\tau^{-1} + k_Q[Q]}$$

where α is the fraction of the spontaneous nonradiative transitions which result in the formation of the triplet. The ratio of the yields in the presence of 0.012 M maleic anhydride and in its absence is then

$$\frac{\phi_\tau}{\phi_\tau(\max)} = \frac{\tau^{-1}}{\tau^{-1} + k_Q[Q]} = \frac{1.6 \times 10^8}{1.6 \times 10^8 + 1.1 \times 10^{10} \times 1.2 \times 10^{-2}} = 0.55$$

This agrees, within the limits of experimental uncertainty, with the directly observed value of 0.61 and confirms the postulate that the quenching of fluorescence does not result appreciably in the formation of the triplet state.

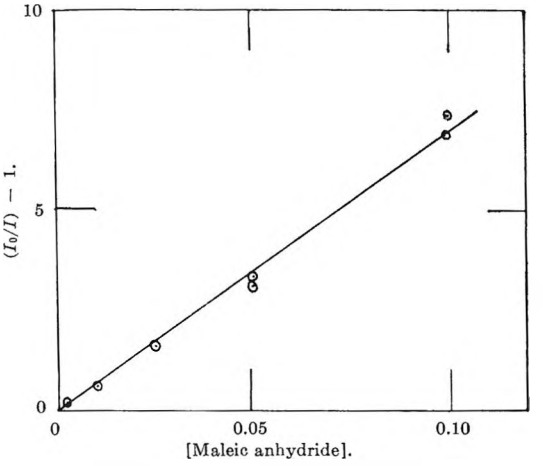

Figure 1. Quenching of the fluorescence of anthracene by maleic anhydride.

The addition of maleic anhydride at a concentration of 1.5×10^{-4} M to 7×10^{-5} M anthracene increased the rate of the first-order decay of the anthracene triplet by about 10%. Since this increase was not much greater than the uncertainty of the measurements, the experiment was repeated using 1.2×10^{-2} M maleic anhydride. In this experiment, the average values of the first-order rate constant for the unquenched and quenched solutions were 230 and 1220 sec^{-1}, which correspond to a bimolecular rate constant for the quenching reaction of 8.2×10^4 M^{-1} sec^{-1}. This should be considered a maximum value, since the sample of purified maleic anhydride may have contained a trace of a strongly quenching impurity.

(3) G. Jackson, R. Livingston, and A. Pugh, *Trans. Faraday Soc.*, 56, 1635 (1960).

(4) I. B. Berlman, *J. Chem. Phys.*, 37, 1888 (1962).

Based on spectrophotometric measurements, Simons[2] reported a value of 0.05 M^{-1} for the equilibrium constant

$$K = [AM]/[M][A]$$

and values of the extinction coefficients at 3650 A for complexed and free anthracene of 3100 and 820 M^{-1} cm^{-1}, respectively. We have made a few preliminary measurements which are in general agreement with these values. If these values are correct and the complex is nonfluorescent, the constant corresponding to static quenching is 0.2 M^{-1}, which is much smaller than the experimental value of 67 M^{-1}.

The present observation, that maleic anhydride quenches the fluorescent state much more efficiently than the triplet state, supports Simon's view that the triplet state of anthracene is not involved in this photochemical reaction. Indeed, the opposite assumption, that only the triplet state leads to the formation of the adduct, results in the erroneous prediction that the quantum yield should have a maximum value at a relatively low concentration of maleic anhydride. If the present values for the quenching constants and for the (oxygen-dependent) mean lifetime of the triplet state are used, the quantum yield would have a maximum value for 0.02 M maleic anhydride. Accordingly, we shall assume that the triplet state is not detectably involved in the reaction. The remaining plausible reaction steps may be written as follows, where MA represents the weak complex and AM the Diels–Alder adduct.

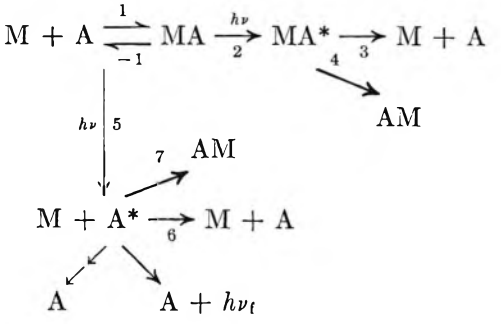

For intuitive and not very convincing reasons, Simons[2] assumed that step 4 is negligible compared to step 3. Tentatively accepting this postulate and using a quantum yield of 0.03 for a maleic anhydride concentration of 0.5 M (*cf.* Figure 2, ref 1), the bimolecular quenching constant ($k_6 + k_7$) of 1.1×10^{10} M^{-1} sec^{-1} indicates that only about 3% of the quenching encounters result in the formation of the stable adduct. The opposite assumption, that only light absorbed by the complex, MA, is photochemically active, leads to the value

$$\frac{k_4}{k_3 + k_4} = \phi\left(1 + \frac{\epsilon_A}{\epsilon_{MA} K [M]}\right) = 0.03\left(1 + \frac{820}{3100 \times 0.05 \times 0.5}\right) = 0.34$$

More likely, both steps 4 and 7 contribute to the chemical reaction. Unfortunately, it is not possible to compare this prediction to the experimental data, since the actual quantum yields at different concentrations of maleic anhydride were not reported (*cf.* Figure 3, ref 2).

Carbon-13 Chemical Shifts of Carboxyl Species from Acetic, Benzoic, and Mesitoic Acids in Sulfuric Acid and Oleum Solutions[1]

by Daniel D. Traficante

The Frank J. Seiler Research Laboratory, Office of Aerospace Research, U. S. Air Force Academy, Colorado

and Gary E. Maciel

The Department of Chemistry, University of California, Davis, California *(Received October 11, 1965)*

The nature of species present in solutions of carboxylic acids in sulfuric acid and oleum media has been the subject of a considerable amount of research.[2-7] Several experimental methods including cryoscopy and ultraviolet, infrared, and nuclear magnetic resonance spectroscopy have been employed, and it has been concluded that the protonated carboxyl species $RC(OH)_2^+$ and the "acylium ion" RCO^+ are the important cations in these strongly acidic media. Deno and coworkers[4] have reported the results of an extensive proton magnetic resonance study of several carboxylic acids including acetic and mesitoic (2,4,6-trimethyl-

(1) Reproduction in whole or in part is permitted for any purpose by the U. S. Government.

(2) R. J. Gillespie and J. A. Leisten, *Quart. Rev.* (London), **8**, 40 (1954).

(3) W. M. Schubert, J. Donohue, and J. D. Gardner, *J. Am. Chem. Soc.*, **76**, 9 (1954).

(4) N. C. Deno, C. V. Pitman, and M. J. Wisotsky, *ibid.*, **86**, 4370 (1964).

(5) R. Stewart and K. Yates, *ibid.*, **82**, 4059 (1960).

(6) G. E. Maciel and D. D. Traficante, *J. Phys. Chem.*, **69**, 1030 (1965).

(7) D. Cook, "Friedel-Crafts and Related Reactions," Vol. I, G. A. Olah, Ed., Interscience Publishers, Inc., New York, N. Y., 1963, Chapter IX.

benzoic) acids over the range of sulfuric acid strengths for which the transformations $RCO_2H \rightarrow RC(OH)_2^+ \rightarrow RCO^+$ were observed. In a recent paper[6] we reported results of a natural abundance C^{13} magnetic resonance study of the protonation of acetic and benzoic acids and their ethyl esters in concentrated sulfuric acid. While the results conclusively identified the carbonyl oxygen atom as the position of protonation, the relatively high solution concentrations (mole ratio of solute:H_2SO_4 was 1:6) necessary for observation of a signal markedly influences the effective acidity of the medium.[8] Furthermore, using this technique we were unable to observe signals due to acylium ions. A previous report of the C^{13} chemical shift of the $CH_3C^{13}O^+SbF_6^-$ complex, determined by the INDOR (internuclear double resonance) method, has appeared,[9] but there appears to be an appreciable mutual inconsistency in the reported data. Because of the theoretical interest in the C^{13} chemical shifts of acylium ions and the need for further characterization of the carboxylic species present in H_2O–H_2SO_4–SO_3 media, we have measured the C^{13} chemical shifts of C^{13}-carboxyl-labeled acetic, benzoic, and mesitoic acids in dilute solutions in such media with compositions covering the ranges of major interest.

Experimental Section

Materials. Trifluoroacetic acid was an Eastman White Label sample. Triethyl orthoacetate (bp 58° (23 mm)) and diethyl sulfate (bp 81° (3 mm)) were redistilled Eastman Practical materials. Acetyl fluoride was prepared by the reaction of sodium fluoride with acetyl chloride according to a modification of the method of Tullock and Coffman[10] using dimethylformamide as the solvent. The product boiled at 19.8°.

The carbon-13-enriched (57 atom % C^{13}) acetic and benzoic acids were used directly as obtained from Volk Radiochemical Co. Ethyl benzoate was prepared by the general procedure of Clinton and Laskowski[11] and was purified by collection from a gas chromatography column.[12] The infrared spectrum of the collected ester was identical with that obtained from the corresponding nonlabeled ester. The mesitoic acid carboxyl C^{13} was prepared by the method of Schmid and Banholzer[13] for the analogous C^{14} compound and was recrystallized from aqueous ethanol, mp 150–152° (lit[3] mp 151–153°).

The sulfuric acid solutions were prepared in a glove box filled with dry nitrogen, by mixing the appropriate amounts of 68.52% oleum[14] (technical grade) and 94.32% sulfuric acid[14] (reagent grade), both from Baker and Adamson.

C^{13} Magnetic Resonance Measurements. The C^{13} nmr spectra were obtained at 35° at a frequency of 15.085 Mc/sec, using dispersion mode, rapid passage conditions as previously described.[15,16] The shifts reported here may be considered internally self-consistent to about ±0.2 ppm.

Results and Discussion

Carbon-13 chemical shifts of the carboxyl carbon atom of acetic, benzoic, and mesitoic acids in sulfuric acid media of various compositions were determined and are collected in Tables I, II, and III. The solutions represented by these data were each about 0.5% carboxylic acid by weight, corresponding to less than 1 mole % of solute for each solution. In a few cases, solutions with about four times this solute concentration were studied and additional signals of low intensity were observed in some instances.

Acetic Acid. It is of interest to view the C^{13} chemical shift data of Table I in terms of the pertinent conclusions of Deno and co-workers[4] based on proton magnetic resonance measurements. In agreement with previous cryoscopic studies, they concluded that acetic acid exists predominantly in the protonated form in 100% H_2SO_4 and that in 85% H_2SO_4–15% SO_3 it exists half in the form of the acylium ion and half as the protonated carbonyl species. Their results indicate that the major shift of the equilibrium

$$CH_3C(OH)_2^+ + SO_3 \rightleftharpoons CH_3CO^+ + H_2SO_4 \quad (1)$$

occurs between 87% H_2SO_4–13% SO_3 and 83% H_2SO_4–17% SO_3. Their plot of the weight-average shift[17] *vs.* per cent SO_3 shows a sharp incline between 10 and 20% SO_3, and its apparently zero slope between 20% SO_3 and 65% SO_3 implies the presence of only acylium ion in oleum solutions in this composite range. Our data in Table I are only partially consistent with these conclusions. The −65.3-ppm shift in 100% H_2SO_4 is assigned to the species $CH_3C(OH)_2^+$ in agreement with

(8) N. C. Deno, N. Friedman, and J. Mockers, *J. Am. Chem. Soc.*, 86, 5676 (1964).

(9) G. A. Olah, W. S. Tolgyesi, S. J. Kuhn, M. E. Moffatt, I. J. Bastien, and E. B. Baker, *ibid.*, 85, 1328 (1963).

(10) C. W. Tullock and D. D. Coffman, *J. Org. Chem.*, 25, 2016 (1960).

(11) R. O. Clinton and S. C. Laskowski, *J. Am. Chem. Soc.*, 70, 3135 (1948).

(12) An 8 ft × 0.75 in. silicone gum rubber (methyl) column GE SE-30 at 70° was employed.

(13) H. Schmid and K. Banholzer, *Helv. Chim. Acta*, 37, 1706 (1954).

(14) Determined by titration with standardized sodium hydroxide.

(15) P. C. Lauterbur, *J. Am. Chem. Soc.*, 83, 1838 (1961).

(16) G. E. Maciel and D. D. Traficante, *ibid.*, 88, 220 (1966).

(17) J. A. Pople, W. G. Schneider, and H. J. Bernstein, "High-Resolution Nuclear Magnetic Resonance," McGraw-Hill Book Co., Inc., New York, N. Y., 1947, Chapter 10.

Table I: C^{13} Chemical Shifts of Acetic Acid Carboxyl C^{13} in Sulfuric Acid Solutions, Ppm with Respect to Benzene

Expt no.[a]	% H_2O–% H_2SO_4–% SO_3						
	0–100–0	0–95–5	0–90–10	0–85–15	0–80–20	0–75–25	0–60–40	0–32–68
1	−65.3 →		NS[b]					
2	−65.1 ←		NS					
3	→			NS				
4	→				NS →	NS		
5							−23.6 ←	−23.5
6						NS →	−23.6	
7						NS[c]		
8	−65.4 ←	NS	→					−23.4[d]

[a] Arrows indicate the sequence of operations on each sample. The absence of an arrow indicates that the datum was obtained on a solution freshly prepared at the stated sulfuric acid concentration. [b] No signal observed. [c] No signal was observed even when the amount of acetic acid employed was increased by a factor of 4. [d] In a sample containing four times the normal amount of "acetic acid" another weak signal at −32 was observed.

Table II: C^{13} Chemical Shifts of Benzoic Acid Carboxyl C^{13} in Sulfuric Acid Solutions Ppm with Respect to Benzene

Expt no.[a]	% H_2O–% H_2SO_4–% SO_3							
	2–98–0	0–100–0	0–98–2	0–94–6	0–90–10	0–80–20	0–65–35	0–32–68
9	−54.3	→					−51.2[b]	
10		−54.3	→		−51.8 →	−51.7		
11		−54.2						
12								−26.2
13			→	−54.5 →	−52.6[b]			
14		−54.4	←					−26.3[c]

[a] Arrows indicate the sequence of operations on each sample. The absence of an arrow indicates that the datum was obtained on a solution freshly prepared at the stated sulfuric acid concentration. [b] Weak, broad signal. [c] In a sample containing four times the normal amount, a weak signal at −11 ppm was also observed.

Table III: C^{13} Chemical Shifts of Mesitoic Acid Carboxyl C^{13} in Sulfuric Acid Solutions, Ppm with Respect to Benzene

Expt no.[a]	% H_2O–% H_2SO_4–% SO_3							
	15–85–0	9–91–0	5–95–0	3–97–0	0–100–0	0–90–0	0–65–35	0–32–68
15	−57.3[b]	→		−60.0 ←		−32.2		
16		−59.2[c] ←			NS ←			
17				NS →	−32.3			
18							−32.2[d] ←	−32.4
19	−57.9							
20					→	−32.2		
21		−59.5						

[a] Arrows indicate the sequence of operations on each sample. The absence of an arrow indicates that the datum was obtained on a solution freshly prepared at the stated sulfuric acid concentration. [b] A weak signal at 3.0 ppm was also observed. [c] A weak signal at −54.2 ppm was also observed. [d] A weak signal at −26.7 ppm was also detected.

our earlier paper[6] and with the interpretation of Deno and co-workers.[4] Also, the failure to observe a signal in the range of SO_3 concentrations from 10 to 20% could be considered consistent with a possible broadening effect of the weight-average signal of the equilibrating system represented by eq 1.[17] However, the failure to observe signals in the solutions which contain 25% excess SO_3 would require a different explanation since, in this range of oleum compositions, the species present according to previous conclusions[4] would be presumably the same as that giving the sharp signal corresponding to a −23.5-ppm shift at 40 and 68% excess SO_3. Furthermore, it seems unlikely that this high-field shift could be due to the CH_3-

CO^+ ion since it is about 41 to 54 ppm higher than one would estimate from the data of Olah and co-workers.[9] These investigators reported the C^{13} shift of the complex $CH_3C^{13}O^+SbF_6^-$ in anhydrous HF from an INDOR experiment at −30.9 ppm relative to $CF_3C^{13}O_2H$ or −45.4 ppm relative to $CH_3C^{13}OF$. From our data on these reference compounds these correspond to −64.7 and −77.8 ppm, respectively, with respect to benzene. While the acylium ion in an H_2SO_4–SO_3 medium need not give an identical shift to the complex studied by Olah and co-workers, a 41 to 54 ppm difference seems unlikely, and we conclude that the species observed with solutions in 40 and 68% SO_3 is not the acylium ion. The inability to observe a signal at 5, 10, 15, 20, and 25% SO_3 may be due to rapid equilibria between interconvertible species. On the basis of the data of Deno and co-workers[4] we are forced to conclude also that whatever the identity of this "high-field" species may be, it must have a proton chemical shift almost identical with that of the acylium ion. It is also worth noting that a comparison of experiments 1, 2, 6, and 8 indicates that the equilibria are largely reversible, at least to the extent indicated by the intensities of the primary resonance peaks.

Benzoic Acid. Aside from cryoscopic[2] and C^{13} magnetic resonance data[6] which demonstrated the existence of the protonated carboxyl species of benzoic acid in 5% H_2O–95% H_2SO_4 and 100% H_2SO_4 solutions, the benzoic acid species in H_2SO_4–SO_3 systems have been rather poorly characterized. However, the data in Table II can be understood by analogy with results obtained with the other two acids. Thus, the peak at −54.3 ppm which occurs in all the solutions studied with less than 6% SO_3 is attributed to the protonated carboxyl species. The resonance at about −51.5 ppm which is observed in solutions with oleum compositions ranging from 90% H_2SO_4–10% SO_3 to 65% H_2SO_4–35% SO_3 is attributed to the acylium ion, and the broad character and position of the signal in the 94% H_2SO_4–6% SO_3 solution is attributed to the effect of rapid equilibrium between these two species. The broadness of the signal obtained with the solution in 65% H_2SO_4–35% SO_3 may be due to a broadening effect of an appreciable concentration of a species with which the acylium ion is in rapid, reversible equilibrium and to which the value −26.2 ppm is assigned for the solution in 32% H_2SO_4–68% SO_3. Presumably the latter species is analogous to the acetic acid species responsible for the −23.5 shift in the solutions with highest SO_3 concentrations. As in the acetic acid case, comparison of the results from experiments 10 and 14 indicated the predominant reversibility of these systems.

Mesitoic Acid. The shifts reported in Table III are readily interpreted in terms of data previously obtained by proton nmr and ultraviolet spectroscopic methods[3,4] Both types of study have shown that mesitoic acid exists predominantly as the protonated carboxyl species in about 91% H_2SO_4–9% H_2O, as the acylium ion in 100% H_2SO_4 and as a one-to-one equilibrium mixture of these two species in 97% H_2SO_4. Accordingly, we assign the value −59.3 ppm to the protonated carboxyl species and −32.2 ppm to the acylium ion and note that the latter appears to be the predominant species for all of the oleum compositions studied. We attribute our inability to detect a signal in the solution in 3% H_2O–97% H_2SO_4 to the broadening effect of the rapid equilibrium between acylium ion and the protonated carboxyl species.

The Unknown, "High-Field Species." The peaks occuring at −23.5 and −26.2 ppm in solutions of acetic and benzoic acids, respectively, in the oleum solutions with highest SO_3 concentrations apparently betray similar species which heretofore have gone unnoticed or at least unreported. From the present results one notes that their formation is reversible to at least a major degree. Their relative algebraic proximity suggested that perhaps they might be due to a common species; however, an experiment in which both acids were dissolved in 32% H_2SO_4–68% SO_3 gave two lines, at −26.3 and −23.1 ppm, rather than the single line one might have expected from this hypothesis. Further work will be required to characterize these new species adequately.

Acknowledgment. The authors gratefully acknowledge helpful discussions with Professor A. T. Bottini and the assistance of Mr. Paul Ellis with some of the experiments.

The Reaction of Oxygen Atoms with Iodine[1]

by D. I. Walton and L. F. Phillips

Chemistry Department, University of Canterbury, Christchurch, New Zealand *(Received November 2, 1965)*

In a previous study of the reaction of iodine with atomic nitrogen[2] it was observed that a solid film, having the physical properties expected for I_2O_5,

(1) This work was supported by Grant AF-AFOSR-264-65 from the U. S. Air Force Office of Scientific Research.

(2) C. G. Freeman and L. F. Phillips, *J. Phys. Chem.*, 68, 362 (1964).

was slowly deposited on the wall of the reaction vessel near the iodine inlet. This was attributed to the presence of a trace of oxygen in the prepurified nitrogen and, hence, of atomic oxygen in the active nitrogen stream leaving the discharge. The present work was undertaken with the aim of establishing the chemical nature of the wall deposit, and of finding whether the extent of oxide formation can be used as a quantitative measure of the oxygen atom concentration.

The first of these aims is complicated by the fact that a number of different oxides of iodine are known,[3] but the results show that although other oxides appear to be formed as well, I_2O_5 accounts for the bulk of the solid material. As far as the second aim is concerned it appears that at moderate pressures, in the type of apparatus used here, the rate of oxide production is too dependent on such factors as the total gas pressure, the surface-to-volume ratio of the reaction vessel, and the form of the iodine inlet jet, for the reaction to be considered as a means of estimating oxygen atom concentrations while other methods[4] are available. The results suggest, however, that at very low oxygen atom pressures and when the mean free path in the gas is relatively large the efficiency of trapping oxygen atoms in the oxide layer should approach unity. Under these conditions, which occur, for example, in the upper atmosphere, the rate of solid oxide formation might provide a very convenient measure of the oxygen atom flow rate.

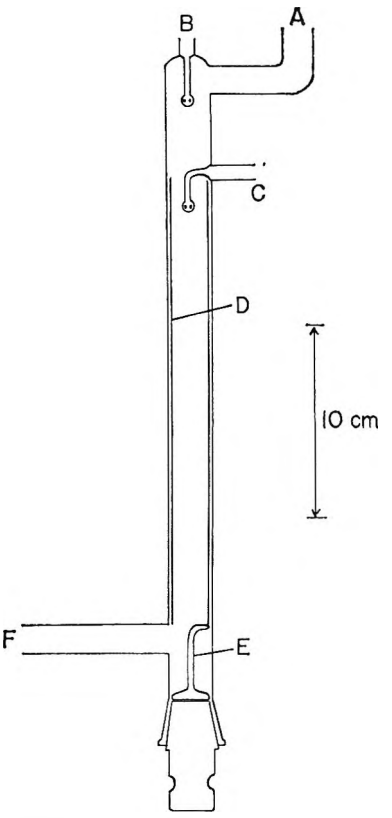

Figure 1. Diagram of the reaction vessel. See Experimental Section.

Experimental Section

A diagram of the apparatus used for most of the measurements is given in Figure 1. Nitrogen or oxygen passes through a microwave discharge and enters the reaction vessel at A. Nitric oxide or NO_2 can be introduced through the titration inlet, B, while iodine, carried in a stream of argon, enters through jet C. The removable Pyrex sleeve, D, on which the solid is deposited, is held in position by the glass support, E. Tube F leads to a McLeod gauge and to a cold trap and rotary vacuum pump. Provision is made for electrically heating the iodine saturator, the tube leading from the saturator, and the reaction tube. The pressure in the reaction tube is typically between 0.5 and 5 torr, with a linear flow velocity of between 3 and 6 m sec^{-1}.

Welding grade dry argon, Matheson prepurified nitrogen, and a selected cylinder of commercial oxygen were used. A discharge through this oxygen gave no perceptible "air afterglow" in the reaction tube.[4] The gases were dried at −80° before use. Matheson nitric oxide was purified by distillation from soda asbestos; NO_2 was prepared by reaction of purified NO with excess oxygen, further purified by trap to trap distillation, and stored at *ca.* 100 torr or less in order to keep the proportion of N_2O_4 low. The other chemicals used were analytical reagent grade.

In a typical experiment, oxygen atoms from discharged O_2 were titrated visually with NO_2 at jet B. The NO_2 flow was then cut off, and iodine was introduced through jet C. After 5 min, the discharge was turned off, sleeve D was removed, and the deposit was washed into a standard flask with cold distilled water. Aliquots of the resulting iodic acid solution were treated with excess KI solution in the presence of dilute sulfuric acid, and the liberated iodine was immediately titrated with thiosulfate. One tenth of the original iodate solution generally gave a titer of about 1.5 ml with 0.05 *M* thiosulfate. The reaction was also carried out with oxygen atoms prepared, in absence of O_2, by titrating nitrogen atoms with nitric oxide.[5]

(3) R. C. Brasted, "The Halogens," Vol. 3, "Comprehensive Inorganic Chemistry," M. C. Sneed, J. L. Maynard, and R. C. Brasted, Ed., D. Van Nostrand Co., Inc., New York, N. Y., 1954.

(4) F. Kaufman, *Progr. Reaction Kinetics*, **1**, 3 (1961).

(5) J. E. Morgan, L. Elias, and H. I. Schiff, *J. Chem. Phys.*, **33**, 930 (1960).

Results

The deposit generally formed as a yellow ring surrounding the iodine inlet jet, with heaviest deposition directly opposite the holes in the jet and bands of interference colors extending some way along the removable sleeve. X-Ray powder photographs[6] of the solid showed a large amount of background haze (I_2O_5 is commonly amorphous) together with the lines listed for I_2O_5 and some other lines (most intense, d = 4.67, 5.72) which may have been due to other iodine oxides.

The reaction is accompanied by a small and rather weak visible flame in the region of mixing of iodine and atomic oxygen. The flame spectrum[7] appears as a continuum with maximum intensity at about 5500 A and a short wavelength limit at about 5000 A, often with superimposed absorption bands of molecular iodine.

The amount of atomic oxygen trapped in the wall deposit has been calculated on the assumption that the solid is essentially pure I_2O_5. Some typical results, showing the fraction of atomic oxygen in the gas phase that becomes trapped in the deposit, as a function of iodine flow at different total gas pressures, are given in Figure 2. These results are for discharged oxygen; essentially similar results have been obtained with O from the reaction of N and NO.

The results of Figure 2 show that the fraction of the atomic oxygen which forms I_2O_5 decreases markedly with increasing gas pressure. This fraction also decreases when the diameter of the reaction vessel is increased and when the walls of the vessel are heated. The results in Table I show that the fraction increases appreciably when the oxygen atom concentration is reduced. Some deposit always forms on the iodine inlet jet and can cause partial or complete blocking of the small (0.2 mm) holes in the jet. The efficiency of I_2O_5 production then changes in an unreproducible manner, which indicates that the way the reactants are mixed is also important. The maximum observed efficiency of I_2O_5 production was slightly less than 50%.

Table I: Variation of the Fraction of O Trapped as I_2O_5 with O Atom Flow Rate (O Atoms Were Produced by Adding Small Amounts of NO to Active Nitrogen; P = 1.05 torr total)

$[O]_{gas}$, μmole/sec	$[O]_{wall}$, μmole/sec	$[O]_{wall}/[O]_{gas}$
0.145	0.064	0.44
0.232	0.105	0.45
0.410	0.167	0.41
0.554	0.204	0.37
0.682	0.254	0.37

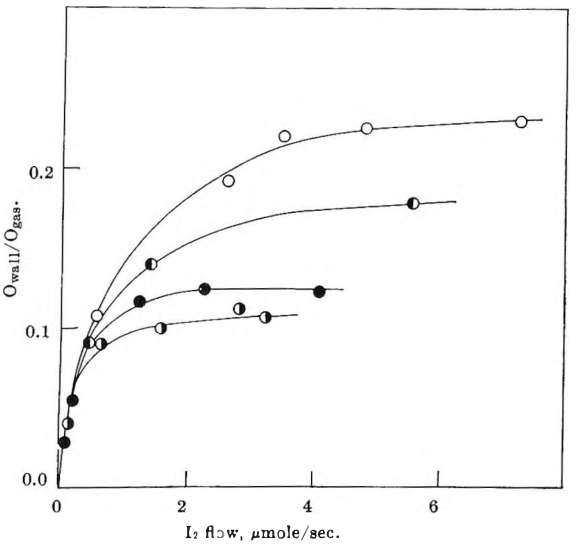

Figure 2. Efficiency of trapping O on the wall as a function of iodine flow and total gas pressure: ○, 0.75 torr; ◐, 1.65 torr; ●, 2.7 torr; and ◑, 3.4 torr; T_{wall}, 35°.

Discussion

Apart from I_2O_5, the stable oxides of iodine which are likely to be important in the present system are I_2O_4 (a yellow solid, slightly soluble in water, decomposing to I_2O_5 and I_2 at 135° and to iodic acid and iodine in hot water[3]) and I_4O_9 (a light-colored hygroscopic powder prepared by allowing iodine to react with ozonized oxygen, decomposing to I_2O_5, I_2, and O_2 at 75° and dissolving in water to give iodine and iodic acid[3]). Probably both of these oxides are present to some extent, in view of the yellow color, the fact that a brown discoloration is produced when the yellow deposit is dissolved in water, and the observation that the solid material is sometimes hygroscopic. However, a wall deposit, albeit a white one, is still produced at temperatures above which I_2O_4 and I_4O_9 are stable, and it seems reasonable to regard the bulk of the material as I_2O_5. If I_2O_4 were formed exclusively, the present estimates of the amount of atomic oxygen trapped would be only 4% too large, while if pure I_4O_9 were formed, these estimates would be only 1% too large.

The results strongly support the hypothesis that competition occurs between the wall reaction and homogeneous recombination of oxygen atoms in the gas phase. A detailed mechanism can be written as follows.

(6) We are indebted to Dr. B. R. Penfold of this department for use of the X-ray diffraction equipment.

(7) C. G. Freeman, B.S. Honors Project, University of Canterbury, 1963.

$$O + I_2 \longrightarrow IO + I \quad (1)$$

$$O + IO \longrightarrow O_2 + I \quad (2)$$

together with

$$I + \text{wall} \longrightarrow I(\text{wall}) \quad (3)$$

and

$$I_2 + \text{wall} \rightleftharpoons 2I(\text{wall}) \quad (4)$$

followed by

$$O + I(\text{wall}) \longrightarrow IO(\text{wall}) \quad (5)$$

$$IO + I(\text{wall}) \longrightarrow IOI(\text{wall}) \quad (6)$$

and so on. Molecular oxygen takes no part in the reaction, and it is assumed that an oxygen atom cannot escape once it has become bound on the wall. Ternary recombination processes are too slow to be significant here. Iodine very readily forms a monatomic layer on glass,[8] so it is reasonable to regard [I(wall)] as essentially constant, at least when the plateau of solid formation has been reached as at high iodine flows in Figure 2. The ratio of the rates of loss of O atoms by homogenous and wall reaction is now given by

$$\frac{2k_1k_2[O][I_2]}{[I(\text{wall})](k_5k_6[I(\text{wall})] + k_2k_5[O] + k_1k_6[I_2])} \quad (7)$$

This ratio varies inversely with the fraction that is plotted in Figure 2. It tends to zero as [O] tends to zero, increases with increasing temperature because of decreasing [I(wall)], and varies directly with pressure and size of the reaction vessel because k_5 and k_6 refer to processes that are limited by the rate of diffusion to the wall.

The weak reaction flame that has been observed can be accounted for by the process[9]

$$I(^2P_{1/2}) + I(^2P_{3/2}) \longrightarrow I_2 + h\nu \quad (8)$$

It is necessary for one of the iodine atoms to be in an excited state as shown, which implies that excited iodine atoms (21.7 kcal/mole) are produced during the reaction. This is most likely to occur in step 2, since reaction 1 is not sufficiently exothermic and ternary reactions such as

$$O + O + I_2 \longrightarrow O_2 + I + I^* \quad (9)$$

are expected to be too slow to account for a visible flame, in view of the very low efficiency of the light-emitting process (8).

(8) J. S. Campbell, R. L. Moss, and C. Kemball, *Trans. Faraday Soc.*, **56**, 1481 (1960).

(9) A. G. Gaydon, "The Spectroscopy of Flames," Chapman and Hall, London, 1957.

cis–trans Isomers of Acyclic Semidiones

by Glen A. Russell and Robert D. Stephens[1]

Department of Chemistry, Iowa State University, Ames, Iowa
(Received November 22, 1965)

Aliphatic semidiones $RC(O\cdot)=C(O^-)R$ can be prepared in numerous cyclic and acyclic systems.[2] When acyclic semidiones are examined by esr spectroscopy under conditions of high signal amplification, a minor radical anion can be detected in addition to C^{13} satellites of the major radical. In Figure 1, the esr spectra of the disproportionation products of acetoin in basic solution are shown. The formation of semidione under these conditions can be rationalized as

$$2CH_3COCHOHCH_3 \xrightarrow[CH_3SOCH_3]{KOC(CH_3)_3} CH_3COCOCH_3 + CH_3CH(OH)CH(OH)CH_3$$

$$CH_3COCOCH_3 + CH_3C(O^-)=C(O^-)CH_3 \rightleftharpoons 2CH_3C(O\cdot)=C(O^-)CH_3$$

The major radical, whose peaks are off scale in Figure 1, has a 1:6:15:20:15:6:1 spectrum with a^H = 5.6 gauss and is assigned the *trans* structure, I, R = CH_3.[2c] Natural abundance of C^{13} at the carbonyl carbon atom leads to the C^{13} satellites, a^C = 4.5 gauss,

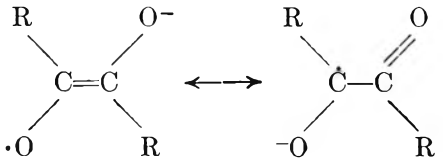

I

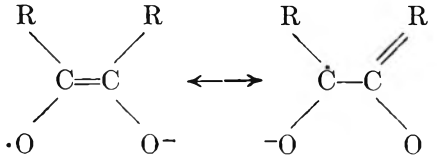

a b

II

shown in Figure 1. Spin density at the carbonyl carbon is estimated to be 0.28 from the equation[3]

$$a^H = \rho_C 40 \cos^2 \theta$$

(1) National Institutes of Health Postdoctoral Fellow, 1965.

(2) (a) G. A. Russell and E. T. Strom, *J. Am. Chem. Soc.*, **86**, 744 (1964); E. T. Strom, G. A. Russell, and R. D. Stephens, *J. Phys. Chem.*, **69**, 2131 (1965); (b) H. C. Heller, *J. Am. Chem. Soc.*, **86**, 5346 (1964); (c) G. R. Luckhurst and L. E. Orgel, *Mol. Phys.*, **7**, 297 (1963).

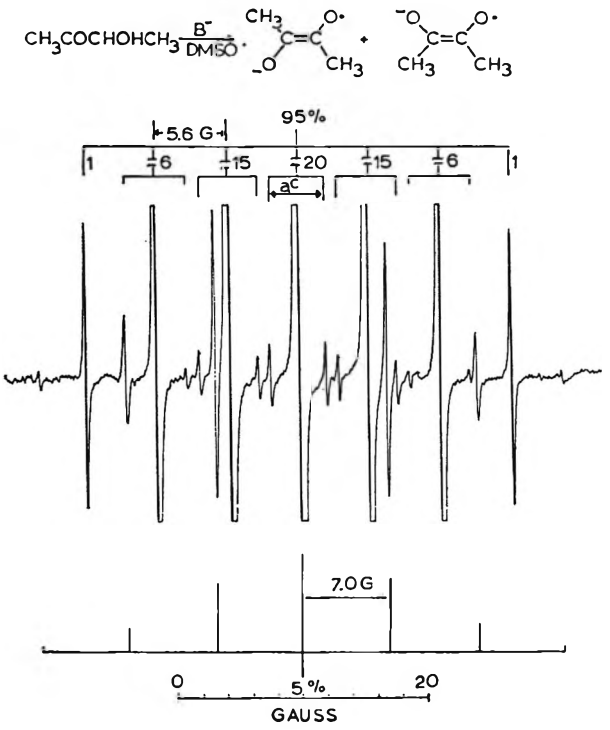

Figure 1. First-derivative esr spectrum, ~9500 Mcps, of products of spontaneous disproportionation of acetoin (0.05 *M*) in dimethyl sulfoxide containing 0.1 *M* potassium *t*-butoxide at 28°.

wherein $\cos^2\theta$ is taken as 0.5 for a freely rotating methyl group.

The minor radical apparently has a seven-line spectrum, a^H = 7.0 gauss, of which the outermost six lines are in a 1:6:15:15:6:1 intensity ratio. The center lines of the minor and major radicals coincide because of identical g values. We believe the minor radical, which is present at a concentration of 5 ± 1% of the total radical anion concentration, is due to the *cis* structure, II. A thermodynamic equilibrium is suggested from the fact that electron transfer with diketone should be a facile process.

$$\mathrm{I} \underset{+e}{\overset{-e}{\rightleftharpoons}} \mathrm{CH_3COCOCH_3} \underset{-e}{\overset{+e}{\rightleftharpoons}} \mathrm{II}$$

Carbonyl carbon spin density in II is calculated to be 0.35. This indicates a less coplanar structure for II than for I, as would be expected from an elementary consideration of repulsion of the negatively charged oxygen atoms. The lowered coplanarity of II relative to I results in a more substantial contribution of structure IIb than Ib to the respective resonance hybrids. This repulsion also contributes to the free energy difference of about 2 kcal/mole between I and II.[4] The higher spin density on the carbonyl carbon atoms of II may also reflect a partial bond (1,4-π overlap) between the oxygen atoms. Other examples of *cis–trans* isomers of semidiones are listed in Table I.

Table I: Analysis of Esr Spectra of Acyclic Semidiones $RC(O\cdot)=C(O^-)R$ at 25–28° in Dimethyl Sulfoxide Solution (Hyperfine Splitting Constants in gauss)

R	a^H (*cis*)[a]	a^H (*trans*)[a]	*trans*/*cis*	a^C (*trans*)
CH_3	7.0	5.6	20	4.5
CH_3CH_2	6.0	4.9	20	4.4
$CH_3CH_2CH_2$	5.6	4.6	30	4.4
$(CH_3)_2CH$	...	2.0	>100	...
$(CH_3)_2CHCH_2$	5.3	4.3	45	4.4

[a] Hydrogen atoms α to the dicarbonyl system.

Acknowledgment. The work was supported by grants from the National Science Foundation and the Petroleum Research Fund.

(3) M. C. R. Symons, *J. Chem. Soc.*, 277 (1959). H. C. Heller and H. M. McConnell, *J. Chem. Phys.*, **32**, 1535 (1960), suggested the equation $a^H = (B\cos^2\theta + B')\rho_{CCH}$. Recent results [G. A. Russell and K. Y. Chang, *J. Am. Chem. Soc.*, **87**, 4381 (1965)] concerning bridged bicyclic semidiones indicate that B' must be quite small (<1 gauss) if the Heller and McConnell equation applies. The value of B = 40 gauss has been estimated for the *m*-xylene radical anion [J. R. Bolton and A. Carrington, *Mol. Phys.*, **4**, 497 (1963)] by E. T. Strom, G. A. Russell, and R. Konaka, *J. Chem. Phys.*, **42**, 2033 (1965), and is somewhat smaller than the value of B = 2(29.25) used earlier.[2a] Using ρ_C = 0.28 for I leads to a resonance hybrid composed of 56% Ib and 44% Ia, *i.e.*, 44% double-bond character between the carbonyl carbon atoms in I. The double-bond character decreases to 30% for II.

(4) When ion pairing and chelation are important, the *cis* structure is favored: ref 2c and N. L. Bauld, *J. Am. Chem. Soc.*, **84**, 4345 (1962). The spectrum given in Figure 1 is observed at low potassium ion concentrations or in the presence of quaternary alkylammonium ions. Further investigation by Dr D. C. Lini has shown that at $[K^+]$ = 0.2 *M* the *trans*/*cis* ratio is 88/12 while at a concentration of $[Na^+]$ = 0.2 *M* the ratio is 76/24. Addition of 0.1 *M* lithium perchlorate to a solution giving the spectrum of Figure 1 reduces the *trans*/*cis* ratio nearly to zero. The *cis* radical anion shows a well-resolved hyperfine splitting (1:1:1:1 quartet) by a single lithium ion, a^{Li} = 0.60 gauss, with very little change in $a_{CH_3}^H$. These effects and the effect of temperature on the *trans*/*cis* ratio are being investigated in detail.

Radical Cations Derived from α-Diketones

by Glen A. Russell, Erach R. Talaty, and Maria C. Young

Department of Chemistry, Iowa State University, Ames, Iowa 50010
(Received November 22, 1965)

Treatment of α-diketones with 98% sulfuric acid and sodium dithionite gives rise to paramagnetic intermediates that we believe to be the radical cations I.

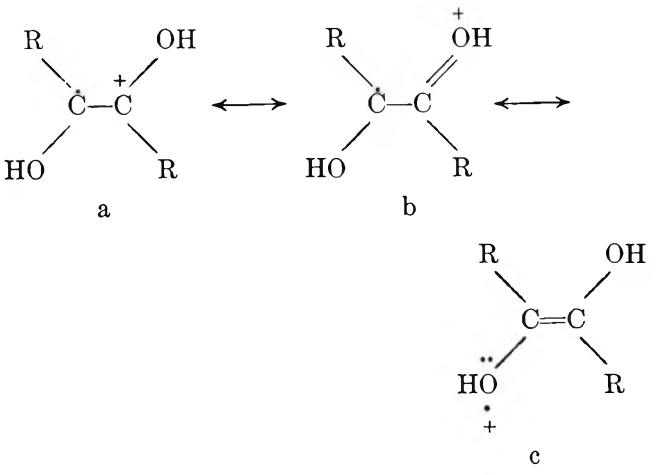

I

In Figure 1 are given the esr spectra of the radical cations derived from cyclohexane-1,2-dione (II) and 4-*t*-butylcyclohexane-1,2-dione (III). The spectra of II and III are similar to those of the corresponding

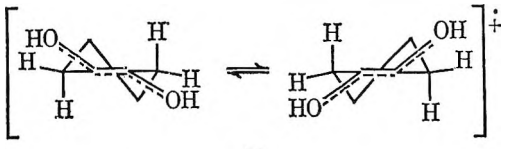

II

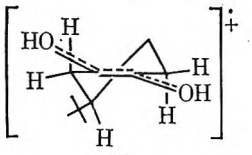

III

radical anions (RC(O·)=C(O⁻)R).[1] However, the hyperfine splitting constants for hydrogen atoms α to the dicarbonyl system are much smaller for the radical cations in sulfuric acid than for the radical anions in dimethyl sulfoxide solution: a^H = 3.03 gauss for II; a^H = 9.83 for cyclohexane-1,2-semidione radical anion; a^H = 4.04, 2.02 for III; a^H = 13.02, 6.64 for 4-*t*-butylcyclohexane-1,2-semidione radical anions.[2] This indicates a lowered carbonyl carbon spin density in the cations than in the anions (IV). Apparently structure Ic contributes more to the cation than structure IVb to the anion.

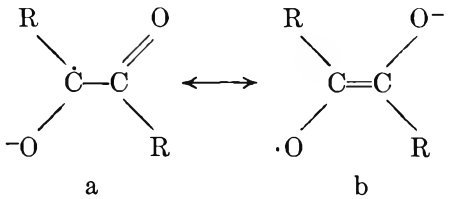

IV

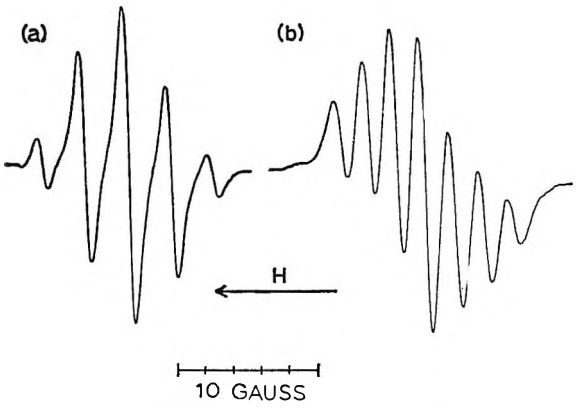

Figure 1. First-derivative esr spectrum of radical cations formed by treatment of (a) cyclohexane-1,2-dione and (b) 4-*t*-butylcyclohexane-1,2-dione with 98% sulfuric acid containing a trace of sodium dithionite ($Na_2S_2O_4$). Fortuitous overlap occurs in (b) since $a^H_{axial} = 2a^H_{equatorial}$. Spectra obtained at ~9.5 Gc/sec with 100 kc/sec field modulation at 28°.

The equivalence of the four hydrogen atoms in II is consistent with a rapid time averaging between two equally populated half-chair conformations.[1] For III a considerable conformational preference is indicated. Presumably the preferred conformation involves the equatorial 4-*t*-butyl substituent.

Phenylglyoxal and 1-phenylpropane-1,2-dione give rise to radical cations under these conditions. The hyperfine splittings are a doublet, 3.14 gauss, and a 1:3:3:1 quartet, a^H = 2.05 gauss, respectively. The lines are broad, and hyperfine splitting by the aromatic hydrogens has not been resolved. The hyperfine splittings of the corresponding hydrogen atoms in the radical anions are 6.88 and 3.43, respectively.[1,3]

Biacetyl yields a heptet, Figure 2, with roughly a 1:6:15:20:15:6:1 intensity ratio. We believe that the radical cation (I, R = CH_3) probably has a *trans* structure from elementary considerations of charge repulsion. The hyperfine splitting constant for the biacetyl radical cation changes very little from 98% (concentrated) sulfuric acid (a^H = 2.17 gauss) to 65 vol % sulfuric acid (a^H = 2.14 gauss). However, the concentration of this radical cation is much less in 65% sulfuric acid, and in 50 vol % sulfuric acid no esr signal could be detected 2 min after preparation of an 0.08 *M* solution of biacetyl in presence of sodium

(1) G. A. Russell and E. T. Strom, *J. Am. Chem. Soc.*, 86, 744 (1964); E. R. Talaty and G. A. Russell, *ibid.*, 87, 4867 (1965).

(2) Hyperfine splitting by the ring hydrogen atoms is the same in *p*-benzosemiquinone radical anion and cation: J. R. Bolton and A. Carrington, *Proc. Chem. Soc.*, 385 (1961).

(3) G. A. Russell, R. D. Stephens, and E. R. Talaty, *Tetrahedron Letters*, 1139 (1965).

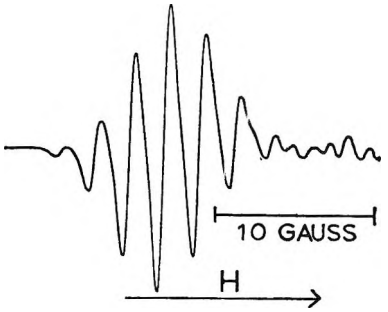

Figure 2. First-derivative esr spectrum of the paramagnetic reduction product of 5 mg of biacetyl in 0.75 ml of concentrated sulfuric acid solution to which had been added 22 mg of sodium dithionite. The low-field multiplet is attributed to the biacetyl radical cation. The high-field multiplet increases in relative intensity as the sulfuric acid is diluted with water.

dithionite. In 98% sulfuric acid, the esr signal shows little decay in 30 min.

A biacetyl radical cation has been reported by Steven and Ward from oxidation of acetoin by titanous ion in acidified hydrogen peroxide (pH ~1).[4] In view of the present results it seems most likely that Steven and Ward actually observed the radical anion (IV, R = CH_3) (reported[4] a^H = 8.5 and 9.8 gauss for two septets) which is known to exist in *cis* and *trans* structures in dimethyl sulfoxide solution (a^H (*cis*) = 7.0, a^H (*trans*) = 5.6 gauss).[5] If this is the case, the conjugate acid of a semidione (Vb) must be considered to be a quite strong acid. Alternately, Steven and Ward may have observed some time-averaged species such as Va–Vb.

$CH_3C(O\cdot)=C(O^-)CH_3 \rightleftharpoons$

a

$CH_3C(O\cdot)=C(OH)CH_3 \rightleftharpoons$

b

$CH_3\dot{C}(OH)-\overset{+}{C}(OH)CH_3$

c

V

We have not seen hyperfine splitting by hydroxyl hydrogen atoms in the semidione radical cations,[6] possibly because of exchange of solvent protons with hydroxyl hydrogen atoms or possibly because of the width of the esr lines involved. The broad esr lines may reflect exchange broadening as well as hydroxyl hydrogen exchange. The lack of significant change in $a_{CH_3}^H$ for the biacetyl radical cation as the solvent is varied from 98 to 65% sulfuric acid suggests that the

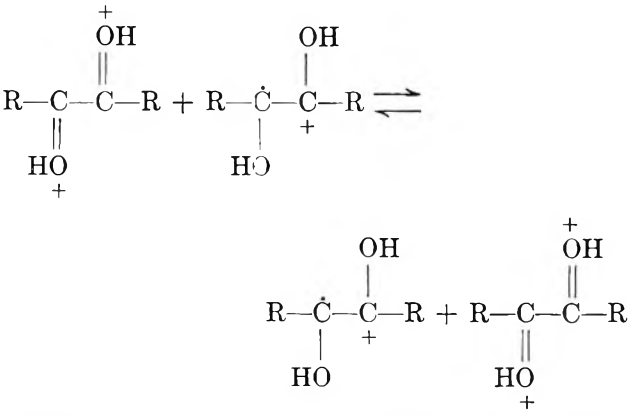

paramagnetic species is not the time-averaged mixture Vb–Vc.

Empirical spin densities can be calculated for the carbonyl carbon atoms of the biacetyl radical anion and cation by the equation[5] $a^H = \rho_C B \cos^2\theta$, wherein $\cos^2\theta$ is taken as equal to 0.5 for a freely rotating methyl group. A value of $B = 40$ seems most appropriate for radical anions.[6] For radical cations a larger value of B is indicated.[7] This leads to empirical estimates of $\rho_C = 0.28$ for the carbonyl carbon atom for the *trans* radical anion in dimethyl sulfoxide and $\rho_C \ll 0.1$ for the radical cation in sulfuric acid.

Acknowledgment. This work was supported by grants from the National Science Foundation and the Petroleum Research Fund.

(4) J. R. Steven and J. C. Ward, *Chem. Commun.*, 273 (1965).

(5) G. A. Russell and R. D. Stephens, *J. Phys. Chem.*, 70, 1320 (1966).

(6) Hydroxyl hydrogen splitting is routinely observed in *p*-benzosemiquinone radical cations in sulfuric acid solution: J. R. Bolton and A. Carrington, *Proc. Chem. Soc.*, 174 (1961), and ref 2; *Mol. Phys.*, 5, 161 (1962); J. R. Bolton, A. Carrington, and J. dos Santos-Veiga, *ibid.*, 5, 465 (1962).

(7) See, for example, R. Hulme and M. C. R. Symons, *J. Chem. Soc.*, 1120 (1965). Values of $B \cos^2\theta$ (uncorrected for delocalization of the electron onto methyl) in the range of 50 gauss are indicated for cations with approximately +0.2 charge density on the carbon atom bearing the methyl substituent.

Intrinsic Viscosity and Flexibility of Rodlike Detergent Micelles

by D. Stigter

Western Regional Research Laboratory,[1] Albany, California 94710

(Received October 4, 1965)

This note extends a previous treatment[2] to the viscosity of large, flexible micelles. In general the in-

trinsic viscosity, $[\eta]$, of detergent micelles may be expressed as

$$[\eta] = 2.5FSE/d \quad (1)$$

where d is the micelle density, F is a flexibility factor, S is a shape factor, and E corrects for the electroviscous effect which has been discussed[3] for charged spheres surrounded by a Gouy–Chapman ionic atmosphere. The dimensionless factors F, S, and E are equal to unity for rigid, spherical, or uncharged particles, respectively.

$[\eta]$ refers to a "kinetic micelle," that is, to the particle enveloped by the shear surface of the micelle. Accordingly, the density, d, is the weight of micellar detergent per unit volume of kinetic micelles and d has units, say grams per milliliter, if one expresses the detergent concentration in grams of detergent per milliliter of solution in the experimental determination of $[\eta]$. It is evident that, if F, S, and E are known, experimental data on $[\eta]$ may be used to evaluate d and, hence, to locate the shear surface. Such calculations have been made[2] for the relatively small micelles of sodium dodecyl sulfate where the assumption of rigid, spherical micelles, $F = S = 1$, is adequate. E was evaluated with the electrophoretic micelle charge. We found[2] that the shear surface envelops the ionic heads of the micellized detergent ions and leaves no room for extra hydration, solid icelike water, or the like, at the micelle surface.

We now turn to micelles of dodecyl ammonium chloride in aqueous sodium chloride solutions. Light scattering[4] shows that the micelles in this system are so large that a spherical shape is no longer plausible. Therefore, we assume that the micelles have an ellipsoidal hydrocarbon core. The core density[2] is 0.802 g/ml. In addition, we assume that the shear surface is 2.8 A from the surface of the micelle core, that is, at a distance equal to the length of the hydrated ionic head of the micellized detergent ion. Retaining the assumption of micelle rigidity, $F = 1$, we calculate the shape factor, S, for prolate and for oblate ellipsoids[5] (rods and disks). E is derived from electrophoretic results, as before.[2] The experimental turbidity and viscosity data[4] are replotted assuming the best smooth curve of cmc *vs.* ionic strength. The micellar weights are corrected for the dissymmetry[6] of light scattering with factors appropriate for cylindrical micelles. This correction is significant only for large micelles.

In Figure 1 $[\eta]/E$ is compared with $2.5FS/d$. The theoretical models fail to explain the experimental data. There are differences up to a factor of 4 with disks and as large as a factor of 50 with rods. In the case of rods the discrepancy is reduced somewhat (by a factor between 1 and 1.6) when the prolate ellipsoidal model is replaced by that of a stiff cylinder with the same minor axis and the same volume.

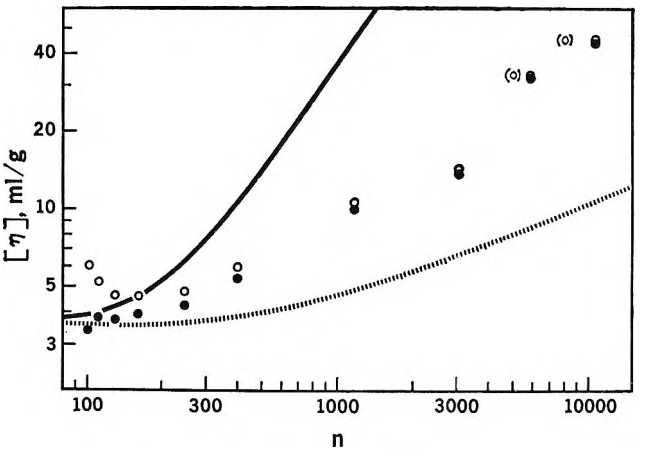

Figure 1. Intrinsic viscosity of dodecyl ammonium chloride micelles in aqueous sodium chloride solutions *vs.* association number n: O, $[\eta]$ from experimental viscosity data;[4] ●, $[\eta]/E$ with $[\eta]$ from experiment;[4] (O), n values uncorrected for dissymmetry of light scattering; ——, $[\eta]/E = 2.5FS/d$ calculated for rigid, prolate ellipsoidal micelles, $F = 1$; and ·····, $[\eta]/E = 2.5FS/d$ calculated for rigid, oblate ellipsoidal micells, $F = 1$.

The lack of agreement in Figure 1 cannot be attributed to uncertainties in n or in $[\eta]/E$ which are of the order of 20%. Hence a change of model is indicated. One might introduce rigid micelles with three different major dimensions (plank). However, recent data on micelle compressibility[7] provide good evidence that micelles are liquid. In addition, light scattering[8] and small-angle X-ray scattering[9] suggest that large micelles are rods rather than planks. It is likely, therefore, that in the systems under discussion the micelles behave as flexible rods.

It is interesting to investigate how flexible the micelles are and whether the flexibility is independent

(1) A laboratory of the Western Utilization Research and Development Division, Agricultural Research Service, U. S. Department of Agriculture.

(2) D. Stigter, Proceedings of the IVth International Congress on Surface-Active Substances, Brussels, Sept 1964, Vol. B/IV.2, in press.

(3) F. Booth, *Proc. Roy. Soc.* (London), **A203**, 533 (1950).

(4) L. M. Kushner, W. D. Hubbard, and R. A. Parker, *J. Res. Natl. Bur. Std.*, **59**, 113 (1957).

(5) H. L. Frisch and R. Simha in "Rheology," Vol. I, F. R. Eirich, Ed., Academic Press Inc., New York, N. Y., 1956, Chapter 14.

(6) P. Doty and R. F. Steiner, *J. Chem. Phys.*, **18**, 1211 (1950).

(7) T. Sasaki and K. Shigehara, ref 2, Vol. B/IV 13, in press.

(8) P. Debye and E. W. Anacker, *J. Phys. Colloid Chem.*, **55**, 644 (1951).

(9) F. Reiss-Husson and V. Luzzatti, *J. Phys. Chem.*, **68**, 3504 (1964).

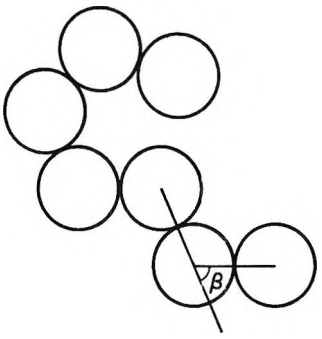

Figure 2. Model of flexible rod.

of micelle size. To this end we apply the theory of the viscosity of short-chain polymers by Peterlin.[10]

The model is a collection of N touching spheres. The flexibility is given by the angle β between the lines connecting the centers of successive pairs of spheres (see Figure 2). Peterlin[10] plots $[\eta]$ as a function of N for several values of $\alpha = \cos \beta$, varying from $\alpha = 1$ (completely stiff, straight chain) to $\alpha = 0$ (maximum flexibility). The parameter F in our eq 1 is the ratio of two $[\eta]$ values obtained from Peterlin's graphs.

$$F(N,\alpha) = [\eta]_{N,\alpha}/[\eta]_{N,\alpha=1} \quad (2)$$

We have compared the data on micelles also with Hearst's expression for the intrinsic viscosity of weakly bending rods.[11] The derivation is based on the pearl-necklace model described above. However, the flexibility parameter is the ratio, λ, of the diameter of the spheres and the Kuhn statistical length of the chain of spheres. In this case the stiff rod and the completely flexible chain are characterized by $\lambda = 0$ and $\lambda = \infty$, respectively. For the model of N touching spheres, we find for the flexibility factor, F, from eq 28 of Hearst's paper[11]

$$F(N,\lambda) = 1 - \lambda(N - 1)[\ln (N - 1) - 1.70]/[16 \ln (N - 1) - 24.52] \quad (3)$$

In the application of eq 2 and 3, N is set equal to the axis ratio of the prolate ellipsoidal micelle.

In Figure 3 F is plotted *vs.* N for the experiments on micelles and for the two different theories. It appears that the Hearst theory does not apply. Firstly, for $\ln (N - 1) < 1.70$, that is, for $N < 6.47$, it follows from eq 3 that $F > 1$. This unrealistic result shows that the theory is not designed for short chains. Furthermore, eq 3 is linear in λ which makes the theory suitable only for small values of λ, that is, relatively stiff chains, as stated explicitly by the author.[11]

Peterlin's theory[10] is not subject to the foregoing limitations. However, the model does not allow flexibility for $N \leq 2$. This may explain the trend toward lower N values where the family of full curves in Figure 3 gradually deviates from the experimental points. Apart from this discrepancy the open circles follow, within experimental error, the line for $\alpha = 0.4$, that is, $\beta = 66.4°$. This is the actual angle in the two-dimensional model pictured in Figure 2. It is evident that the average radius of curvature of the long axis of the micelle is not much larger than the diameter of the micelle. This result indicates a very flexible structure and supports the notion that detergent micelles are liquid. It would be of interest to investigate how well flexible micelle rods fit the light-scattering[8] and small-angle X-ray scattering[9] data.

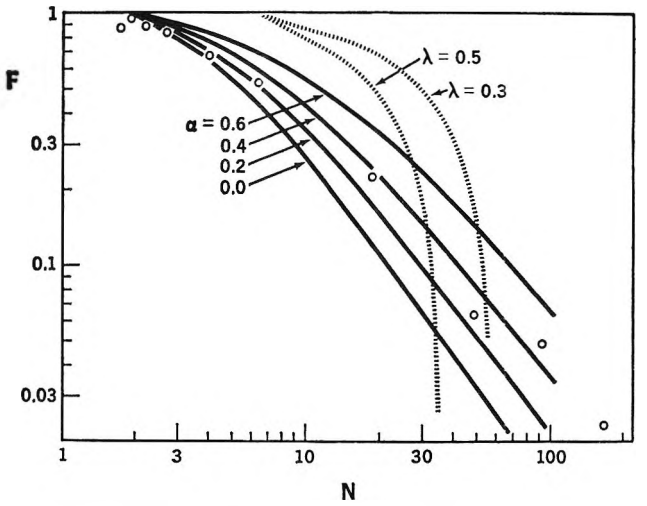

Figure 3. Flexibility factor, F, *vs.* micelle size (axis ratio) for dodecyl ammonium chloride micelles: O, $F = [\eta]d/(2.5SE)$ with $[\eta]$ from experiment;[4] ▬▬▬, Peterlin theory, eq 2; and ▪▪▪▪▪▪▪▪▪▪, Hearst theory, eq 3.

Finally, we remark that for large ionic micelles the rod is the shape with the maximum surface-to-volume ratio and, hence, with the minimum electrical free energy. The latter condition might be a significant one for optimum shape of ionic micelles. Note that bending a cylinder does not change its surface-to-volume ratio. Thus, bending a micelle leaves its surface free energy constant while it increases the entropy of the micelle as a whole. Of course, in concentrated micellar solutions, such as are used for small-angle X-ray scattering,[10] the interaction between micelles might favor an arrangement of straight rod-like micelles.

(10) A. Peterlin, *J. Chim. Phys.*, **47**, 669 (1950); *J. Polymer Sci.*, **8**, 173 (1952).

(11) J. E. Hearst, *J. Chem. Phys.*, **40**, 1506 (1964).

The Heat of Reaction of Nitrogen Trifluoride and Hexafluoroethane

by G. C. Sinke

Thermal Research Laboratory, Dow Chemical Co., Midland, Michigan *(Received October 15, 1965)*

Published work on the thermochemistry of hexafluoroethane is limited to one investigation[1] in which C_2F_6 reacted with elemental potassium to form potassium fluoride and amorphous carbon. A recent paper[2] called attention to discrepancies in the energy relationships involved in the dissociation of C_2F_6 to CF_3 radicals. The heat of reaction of NF_3 and C_2F_6 has been measured in an attempt to resolve the discrepancies. The method developed should be useful for other volatile fluorocarbons.

Experimental Section

Materials. Commercial technical grade NF_3 was purified by low-temperature distillation. A combination of infrared spectroscopy, mass spectroscopy, and gas chromatography indicated the product was at least 99.9 mole % pure. Commercial C_2F_6 was found to contain a trace of air which was removed by condensing the C_2F_6 in liquid nitrogen and pumping. No other impurities were detected. Commercial "ultrapure" hydrogen was stated by the supplier to be 99.995% pure. No impurities were detected by infrared and mass spectroscopy.

Procedure. A conventional Parr platinum-lined combustion bomb of 348-ml volume was employed. The bomb cylinder and head were dried at 110° for 1 hr, assembled, connected to a vacuum line, and evacuated while still hot. After cooling to room temperature, the bomb was surrounded by a constant-temperature water bath and pumped until a pressure of about 1 μ was achieved. The bomb was then charged with 800.0 mm of hydrogen as measured by a Wallace & Tiernan precision dial manometer which could be read to 0.1 mm. Hexafluoroethane and nitrogen trifluoride were contained in small stainless steel cylinders which were weighed on a 200-g capacity analytical balance. The cylinders were connected to the vacuum line and the bomb was successively charged with C_2F_6 to a total pressure of about 1270 mm and NF_3 to a total pressure of about 2300 mm. The bomb valve was closed except when charging and sample remaining in the connecting lines was recondensed in the cylinders with liquid nitrogen. The cylinders were reweighed to obtain the exact amounts of sample charged.

The bomb was placed in a conventional combustion calorimeter and the charge was fired by discharging a condenser through a fine platinum fuse wire. The condenser voltage before and after firing was a measure of the ignition energy. The calorimeter was calibrated with National Bureau of Standards benzoic acid 39h. An average of 0.55 g of acid was used and the bomb charged with 1 ml of water and 30.3 atm of oxygen. Under these conditions the standard sample was calculated to have a heat of combustion of 6317.5 thermochemical cal/g of mass. The calorimeter equivalent was 3407.10 cal/deg with a standard deviation of 0.42 cal/deg for five experiments.

After the calorimetry was completed, the gaseous reaction products were passed over 85% KOH pellets and the scrubbed gases were examined by infrared and mass spectroscopy. Only traces (less than 0.05%) of the original NF_3 and C_2F_6 were found, indicating complete reaction of hydrogen to HF, C_2F_6 to CF_4, and excess NF_3 to N_2 and F_2. Because the thermochemistry of HF vapor is poorly defined, comparison experiments were run in which NF_3 and H_2 mixtures were exploded to give the same final amount of HF in the bomb.

A washer of Teflon fluorocarbon used on the insulated ignition post was slightly attacked by fluorine. In the comparison experiments, the extent of this attack was determined by mass spectrometer analysis of the CF_4 in the reaction products; in the C_2F_6 experiments an average value was obtained by weighing the washer before and after the series of five runs.

Results

The results for five comparison runs are given in Table I. The calorimeter equivalent adjusted for changes in the bomb contents was 3403.54 cal/deg. The correction for fluorine attack on Teflon was taken as 2.474 cal/mg.[3] All runs were adjusted to a standard quantity of 0.9600 g of NF_3 using an enthalpy of dissociation under constant volume conditions of 411.4 cal/g.[4] Results for the hexafluoroethane experiments are given in Table II. The adjusted calorimeter equivalent was 3403.79 cal/deg and all runs were again adjusted to a standard of 0.9600 g of NF_3 above that required for reaction with C_2F_6. The assumption was made that the final state of the comparison experi-

(1) F. W. Kirkbride and F. G. Davidson, *Nature*, **174**, 79 (1954).

(2) E. Tschuikow-Roux, *J. Phys. Chem.*, **69**, 1075 (1965).

(3) E. S. Domalski and G. T. Armstrong, *J. Res. Natl. Bur. Std.*, **69A**, 137 (1965).

(4) D. D. Wagman, W. H. Evans, I. Halow, V. B. Parker, S. M. Bailey, and R. H. Schumm, National Bureau of Standards Technical Note 270-1, U. S. Government Printing Office, Washington, D. C., Oct. 1, 1965.

Table I: Results of Comparison Experiments

Mass of NF_3, g	Ignition energy, cal	Washer correction, cal	Adjustment to 0.96 g of NF_3, cal	Corrected temp rise, °C	Calories per expt.
0.9621	0.24	24.74	0.86	0.49399	1657.19
0.9698	0.21	29.69	4.03	0.49488	1658.47
0.9382	0.22	23.30	−8.97	0.49740	1660.43
0.9746	0.22	16.33	6.01	0.49143	1662.06
0.9757	0.18	16.33	6.46	0.49103	1661.19
					Av 1659.87

Table II: Results of Hexafluoroethane Experiments

Mass of C_2F_6, g	Mass of NF_3, g	Washer correction, cal	Ignition energy, cal	Adjustment to 0.96 g of NF_3, cal	Δt, °C	$-\Delta Er/M$, cal/g
1.1701	1.3769	21.53	0.21	6.42	0.75203	756.0
1.1702	1.3523	21.53	0.20	−3.70	0.75604	758.9
1.1625	1.3448	21.53	0.21	−5.72	0.75578	761.5
1.1481	1.3407	21.53	0.20	−5.39	0.74940	752.4
1.1727	1.3511	21.53	0.20	−4.57	0.75365	749.6
						Av 755.7

ments was thermally equivalent to the final state in the C_2F_6 experiments. The calorimeter starting temperature was selected so that the final temperature in each series was 25.00°. In the C_2F_6 series, however, CF_4 and additional N_2 were present as well as HF vapor. The comparison experiments therefore did not exactly duplicate the final state in the C_2F_6 experiments. Further work on this aspect of the method is planned. The effect of the additional gases on the thermal state of the HF vapor is probably small.

Employing atomic weights of 12.0111 and 18.9984 for carbon and fluorine, respectively, there is derived for the reaction

$$C_2F_6(g) + {}^2/_3NF_3(g) \longrightarrow 2CF_4(g) + {}^1/_3N_2(g)$$

$$\Delta Er_{298} = -104.3 \text{ kcal/mole}$$

Calculating to constant pressure conditions

$$\Delta Hr_{298} = -103.9 \text{ kcal/mole}$$

The over-all uncertainty is estimated as ±1 kcal/mole.

Conclusions

Although accurate heats of formation for fluorocarbons cannot be computed because of the uncertainty in the true value for aqueous HF, a consistent set based on the most recent selections at the National Bureau of Standards[4] allows some comparisons to be made. The selected enthalpies of formation (all in kcal/mole) are −29.8 for $NF_3(g)$, −221 for $CF_4(g)$, and −164.5 for $CHF_3(g)$. Tschuikow-Roux[2] selected 102 ± 2 kcal as the most reliable value for the CF_3–H bond dissociation energy, which gives for the enthalpy of formation of CF_3 radical −114.6 ± 2.5 kcal/mole. The present work yields an enthalpy of formation of C_2F_6 of −318.2 ± 2 kcal/mole. From these data is calculated a CF_3–CF_3 bond dissociation energy of 89 ± 4.5 kcal. Tschuikow-Roux[5] measured 93 ± 4 kcal by direct observation of the dissociation of C_2F_6 in a shock tube, in agreement within experimental error. Other work listed by Tschuikow-Roux[2] leading to much higher or lower values now appears to be in error.

Acknowledgment. This work was supported by the United States Air Force under Contract No. AFO4-(611)-7554(4).

(5) E. Tschuikow-Roux, *J. Chem. Phys.*, **43**, 2251 (1965).

Schmidt Number Correction for the Rotating Disk

by John Newman

Department of Chemical Engineering, University of California, Berkeley, California *(Received October 13, 1965)*

According to Levich,[1,2] the rate of mass transfer to a rotating disk is given by

Table I: Comparison of Values for $i(1 - t)/nF(c_\infty - c_0)\sqrt{\Omega\nu}$

		Eq 5		Gregory and Riddiford		Levich	
Sc	"Exact"[a]		ϵ[b]		ϵ[b]		ϵ[b]
100	0.026874	0.026892	0.069	0.026970	0.36	0.028799	7.16
200	0.017188	0.017194	0.038	0.017226	0.22	0.018137	5.52
500	0.009471	0.009472	0.015	0.009488	0.18	0.009850	4.00
800	0.006964	0.006965	0.010	0.006975	0.16	0.007200	3.39
1000	0.006016	0.006017	0.009	0.006024	0.14	0.006205	3.13
1200	0.005338	0.005338	0.007	0.005346	0.15	0.005495	2.94
1400	0.004824	0.004824	0.005	0.004830	0.14	0.004958	2.79

[a] "Exact" refers to a numerical evaluation of eq 1, and thus is still subject to error. [b] ϵ is per cent deviation.

$$\frac{i}{nF} = \frac{D}{1 - t}\left.\frac{dc}{dy}\right|_{y=0} = \frac{D(c_\infty - c_0)/(1 - t)}{\int_0^\infty \exp\left\{\int_0^y \frac{v_y}{D}\,dy\right\}\cdot dy} \quad (1)$$

where

$$v_y = \sqrt{\Omega\nu}\left[-0.51023\frac{\Omega}{\nu}y^2 + {}^1/_3\left(\frac{\Omega}{\nu}\right)^{3/2}y^3 - 0.10265\left(\frac{\Omega}{\nu}\right)^2 y^4 + \ldots\right] \quad (2)$$

i is the current density, t is the transference number, c is the concentration of the reactant, y is the distance from the disk, Ω is the rotation speed, ν is the kinematic viscosity of the fluid, F is Faraday's constant, and n is the number of electrons produced when one reactant ion or molecule reacts. Equation 1 applies to two cases: (a) when the reactant is an ion in a solution with excess indifferent electrolyte or the reactant is a neutral molecule; then $t = 0$, and D is the diffusion coefficient of the reactant ion or molecule; (b) when the reactant is one of two ionic species in the solution; then D is the diffusion coefficient of the salt.

For large Schmidt numbers, Levich[1,2] neglected all but the first term in eq 2, so that with this approximation eq 1 yields

$$\frac{i(1 - t)}{nF(c_\infty - c_0)\sqrt{\Omega\nu}} = 0.6205Sc^{-2/3} \quad (3)$$

where $Sc = \nu/D$. For a Schmidt number of 1000, accurate evaluation of eq 1 gives a value about 3% lower than eq 3.

Gregory and Riddiford[3] evaluated eq 1 numerically and fitted the results empirically with the equation

$$\frac{i(1 - t)}{nF(c_\infty - c_0)\sqrt{\Omega\nu}} = \frac{0.554Sc^{-2/3}}{0.8934 + 0.316Sc^{-0.36}} \quad (4)$$

This representation agrees with eq 1 within 1% for $Sc > 250$ according to Gregory and Riddiford, although Table I shows that the agreement actually is better.

It should be noted that if one expands the exponential in eq 1 for large Schmidt numbers and integrates analytically, then one obtains

$$\frac{i(1 - t)}{nF(c_\infty - c_0)\sqrt{\Omega\nu}} = \frac{0.62048Sc^{-2/3}}{1 + 0.2980Sc^{-1/3} + 0.14514Sc^{-2/3}} \quad (5)$$

where terms of order Sc^{-1} have been neglected in the denominator. This expression adequately approximates eq 1 for $Sc > 100$, in which region the maximum deviation is about 0.1%. Thus an analytic approach yields a result essentially no more complicated than that of Gregory and Riddiford and at the same time does not sacrifice accuracy. The results of these several formulas are compared in Table I.

(1) V. Levich, *Acta Physicochim. URSS*, **17**, 257 (1942).
(2) V. G. Levich, "Physicochemical Hydrodynamics," Prentice-Hall, Inc., Englewood Cliffs, N. J., 1962.
(3) D. P. Gregory and A. C. Riddiford, *J. Chem. Soc.*, 3756 (1956).

The Acid-Catalyzed Oxygen Exchange of Acetylacetone in Dioxane–Water Solutions Measured by Oxygen-17 Nuclear Magnetic Resonance

by Z. Luz and Brian L. Silver

The Weizmann Institute of Science, Rehovoth, Israel
(*Received November 16, 1965*)

Rates of oxygen isotope exchange are usually studied using ^{18}O as tracer.[1] This almost always requires sepa-

(1) D. Samuel and B. L. Silver, *Advan. Phys. Org. Chem.*, **3**, 123 (1965).

ration of the exchanging species at known times and subsequent isotopic analysis by mass spectrometry. Often a practical separation procedure would be much longer than the reaction half-life. In such cases a spectroscopic method not requiring chemical separation would be preferable. Infrared spectroscopy could in principle be used but is limited by the difficulty of accurately determining the intensities of the relevant absorption bands.[2] Oxygen-17 spectroscopy provides a means of overcoming these drawbacks, ^{17}O being the only stable oxygen isotope with a magnetic moment. Oxygen exchange may be conveniently studied by following the changes with time of the intensity of the relevant absorption peaks during the exchange reaction. An additional advantage of the nmr method lies in the possibility of studying the exchange of two or more chemically nonequivalent oxygen atoms in the same molecule, or of studying the simultaneous exchange with solvent of two interconvertible isomers. As an example of the latter case, we have studied the oxygen exchange of both the keto and enol forms of acetylacetone in dioxane–water solutions containing varying amounts of acid.

The ^{17}O nmr spectrum of neat acetylacetone enriched to about 4 atom % ^{17}O was examined. It consisted of two lines at −274 and −566 ppm from $H_2{}^{17}O$ as an external standard, with relative integrated intensities of approximately 4 to 1. The larger line at −274 ppm is attributed to the enol form and has been observed previously[3] at natural abundance of ^{17}O. The smaller line has a chemical shift falling in the region typical for carbonyl groups[3] and is assigned to the keto form. In dioxane–water mixtures the ratio of the intensities of the keto to enol resonances increases with increasing fraction of water in the solvent due to a shift in the position of the equilibrium between the two isomers. The addition of dioxane–water mixtures to acetylacetone results in a high-field shift of the keto resonance. This is typical of the behavior of the carbonyl–^{17}O resonance in the presence of hydrogen-bonding solvent.[4]

Experimental Section

Spectra were recorded on a Varian DP 60 spectrometer operating at 8.13 Mcps, the probe temperature being 25 ± 2°. The derivatives of the absorption lines were recorded and the peak-to-peak height taken as an arbitrary measure of intensity. Next 0.5 ml of acetylacetone was dissolved in 2.5 ml of a mixture of dioxane–$H_2{}^{17}O$ (1.5 to 1.0 by volume) containing varying amounts of HCl, and the increases in intensity of the nmr peaks were recorded at known intervals of time until no further significant changes in intensity were observed. The first recording of the spectrum was possible within 0.75 min from the preparation of the sample. In the mixtures used in these experiments the ratio of the enol to the keto form at equilibrium is 1.65 as determined from the proton nmr. The water contained 6 atom % ^{17}O and was obtained from the separation plant of this institute.

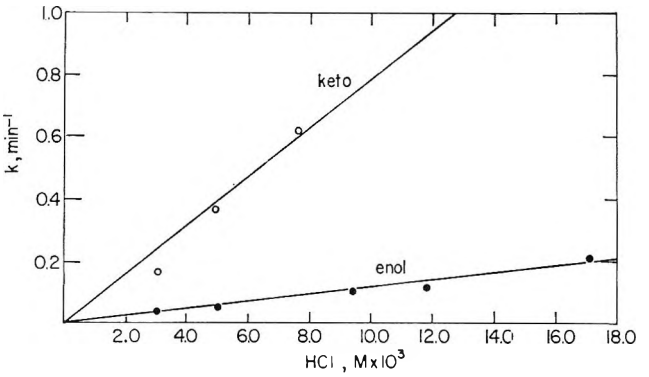

Figure 1. First-order rate constant for oxygen exchange of acetylacetone in dioxane–water mixture as a function of HCl concentration. The composition of the solution is given in the text; $t = 25 \pm 2°$.

Results and Discussion

The analysis of the kinetics of exchange is complicated by the fact that together with exchange there is an interconversion of the keto and enol forms, the rate of which is of the same order of magnitude as the exchange. It was found that in contrast to the rate of tautomerism,[5] the exchange is acid catalyzed. The half-life for tautomerism is about 1 min as determined from the proton nmr of the methyl line.[6] To circumvent the difficulties caused by tautomerism, we studied the exchange at acidities high enough to ensure that the half-life for exchange was less than 10 min. The first-order rate constant for exchange was then derived from the initial slope of the plot of the peak intensity against time. The results are plotted as a function of acid concentration in Figure 1. It may be seen that the exchange rate of the keto form is much larger than the observed rate for the enol form. Both rates are acid catalyzed with apparent acid catalysis constants,

(2) A. Lapidot, S. Pinchas, and D. Samuel, *Proc. Chem. Soc.*, 109 (1962); *J. Chem. Soc.*, 1128 (1963).

(3) S. S. Dharmatti, K. J. S. Rao, and R. Vijayaraghavan, *Nuovo Cimento*, 11, 656 (1959); H. A. Christ, P. Diehl, H. R. Schneider, and H. Dahn, *Helv. Chem. Acta*, 44, 865 (1961).

(4) H. A. Christ and P. Diehl, *Helv. Phys. Acta*, 36, 170 (1963).

(5) R. P. Bell and O. M. Lidwell, *Proc. Roy. Soc.* (London), A176, 88 (1940).

(6) S. Peller, Z. Luz, and B. L. Silver, unpublished results.

derived from the plots, of $k_H^{keto} = 1.3$ l. mole^{-1} sec^{-1}, and $k_H^{enol} = 0.2$ l. mole^{-1} sec^{-1}. Since even at the highest acidities the rate of tautomerism is comparable with the exchange rate, it is possible that a large part of the observed enol exchange rate is due to prior exchange of the keto form and subsequent tautomerism. In this case, the actual rate of oxygen exchange of the enol form will be considerably lower than the figure quoted above. A rigorous analysis of the exchange kinetics could be made in principle, but would necessitate a large number of runs and a correspondingly large amount of ^{17}O enriched water. However, the large difference in exchange rates of the keto and enol forms is demonstrated.

The commonly accepted mechanism for oxygen exchange of a carbonyl group involves the nucleophilic attack of the oxygen atom of a water molecule on the carbon atom of the protonated carbonyl group to give a tetrahedral intermediate.[1] The keto form has two carbonyl groups available for protonation, while the enol has formally only one carbonyl group, and therefore, other factors being neglected, there is twice as great a chance of the keto form being protonated and subsequently exchanging. The actual ratio of the rates is at least 6:1. Presumably, electronic effects play an important part in determining the relative rates; in particular, the carbonyl group in the enol form will be less susceptible to protonation than the keto carbonyl group, since it is already internally hydrogen bonded.

COMMUNICATIONS TO THE EDITOR

Comment on the Article "On the Theory of the Dielectric Dispersion of Spherical Colloidal Particles in Electrolyte Solution"[1]

Sir: Spherical colloidal particles suspended in an electrolyte solution display a dispersion of very high dielectric constants at low frequencies.[2] A mechanism due to the polarization of the counterion atmosphere was shown to account very well for the observed experimental facts.[3] The underlying model theory has recently been criticized by Schurr[1] for not taking into account the surface conductivity due to free charge carriers as introduced by O'Konski.[4] We would like to make clear that this "free" surface conductivity λ can be neglected as far as the subject of the criticized paper is concerned, that is, the low-frequency dielectric dispersion of spherical colloidal particles suspended in a fairly well conducting electrolyte solution.

It had already been pointed out[2,5] that the "free" surface conductivity cannot explain the low-frequency dielectric dispersion since it results in relatively small dielectric increments which display a dispersion at far higher frequencies. Therefore, the effect of λ was not taken into account in the above-mentioned model theory, but only the complex conductivity due to bound counterions. Schurr has included the "free" surface conductivity in his calculations, thus obtaining a somewhat more general theory. His result differs from that of ref 5 only by the fact that the conductivity inside the particle κ_i is replaced by an apparent conductivity $\kappa_i + 2\lambda/R$ (R = radius of the sphere). This might be of significance for certain other phenomena, but not for the phenomenon in question. Since the quantity $2\lambda/R$ can be assumed to be small in comparison with the external conductivity κ_a, it will have no noticeable effect on the low-frequency dielectric dispersion as may be seen from eq 26 and 27 in ref 5.

Schurr has suggested dielectrophoretic measurements of the dipole moments of the particles to test the theories. According to him, there should be an extremely large difference in these dipole moments (almost five orders of magnitude in one case) depending on which of both model theories is applied. Such a big difference in the dipole moments would indeed be very remarkable in view of the fact that the over-all dielectric increment is virtually the same. It can be shown, however, that this big difference does not exist. In order to calculate the dipole moments for his model Schurr used the true surface charge density as deter-

(1) J. M. Schurr, *J. Phys. Chem.*, **68**, 2407 (1964).

(2) H. P. Schwan, G. Schwarz, J. Maczuk, and H. Pauly, *ibid.*, **66**, 2626 (1962).

(3) G. Schwarz, *ibid.*, **66**, 2636 (1962).

(4) C. T. O'Konski, *ibid.*, **64**, 605 (1960).

(5) H. P. Schwan, *Advan. Biol. Med. Phys.*, **5**, 183 (1957).

mined from the divergence of the dielectric displacement vectors. In the case of the model of ref 3 he took into account only the charge density due to the bound counterions and not the true surface charge density as he consequently should have done. In that case he would have found little difference in the dipole moments. They then differ only by the missing $2\lambda/R$ in the apparent conductivity of the inner conductivity of the sphere. We may point out, however, that the apparent dipole moment of the particle is not only due to the true surface charges but also to "apparent" surface charges ("apparent" surface charges are, for instance, responsible for the dipole moment of a purely dielectric sphere in a purely dielectric medium[6]). In the case of interest here the apparent dipole moment as seen in the electrolyte solution can easily be obtained from the equation for the outside electric potential ψ_a which is simply a supposition of the potential of the external field and the potential of the apparent dipole moment of the sphere (eq 13 in ref 1, eq 34 in ref 3).

(6) C. J. F. Böttcher, "Theory of Electric Polarization," Elsevier Publishing Co., Amsterdam, 1952.

DEPARTMENT OF BIOMEDICAL ENGINEERING
MOORE SCHOOL
UNIVERSITY OF PENNSYLVANIA
PHILADELPHIA, PENNSYLVANIA
G. SCHWARZ
H. P. SCHWAN

RECEIVED AUGUST 24, 1965

Shapes of Critical Isotherms

Sir: The conditions which characterize the liquid–vapor critical point on the P–V–T surface for a pure substance are: $(\partial P/\partial V)_{T_c} = 0$, $(\partial^2 P/\partial V^2)_{T_c} = 0$, ..., $(\partial^n P/\partial V^n)_{T_c} \lesseqgtr 0$. If the critical isotherm is to be a continuously differentiable function, thermodynamic stability requires n to be an odd integer in the first nonzero derivative.[1] For a van der Waals or classical fluid, the familiar value of n is 3.

The thermodynamic similarities of single- and two-component systems have been discussed by Rice.[2] The corresponding conditions for a critical-solution point in a two-component system may be expressed as derivatives of the chemical potential with respect to mole fraction; *i.e.*, $(\partial\mu_1/\partial x_1)_{T_c,P} = 0$, $(\partial^2\mu_1/\partial x_1^2)_{T_c,P} = 0$, ..., $(\partial^n\mu_1/\partial x_1^n)_{T_c,P} \gtreqless 0$, or in terms of the Gibbs free energy of mixing: $(\partial^2 G/\partial x_1^2)_{T_c,P} = 0$, $(\partial^3 G/\partial x_1^3)_{T_c,P} = 0$, ..., $(\partial^{n+1} G/\partial x_1^{n+1})_{T_c,P} \gtreqless 0$.

There have been several experimental and theoretical investigations to find the order of the first nonvanishing derivative.[3-9] From their careful measurements of the compressibility of xenon in the critical region, Habgood and Schneider[5] found the critical isotherm considerably flatter than that corresponding to a van der Waals fluid. The function $(\partial^2 P/\partial V^2)_{T_c}$ *vs.* density has an inflection at or very near the critical density indicating that $(\partial^4 P/\partial V^4)_{T_c}$ must vanish if the isotherm is continuous. The third derivative was shown to be small, and they suggested that it may also vanish. Zimm,[4] from an analysis of his light-scattering data in the critical-solution region of the system perfluoromethylcyclohexane + carbon tetrachloride, found evidence that the third derivative of the chemical potential, $(\partial^3\mu_1/\partial x_1^3)_{T_c,P}$, tends toward zero.

Recent experiments in our laboratory on the volume of mixing, V, for the system perfluoro-*n*-heptane + isooctane (2,2,4-trimethylpentane)[10] and the enthalpy of mixing, H, for the system perfluoro-*n*-hexane + *n*-hexane[11] show that the third derivatives $(\partial^3 V/\partial x_1^3)_{T_c,P}$ and $(\partial^3 H/\partial x_1^3)_{T_c,P}$ also vanish in the neighborhood of their respective critical-solution points. ($T_c = 23.7°$, $x_{C_7F_{16}} = 0.374$; $T_c = 22.64°$, $x_{C_6F_{14}} = 0.370$.)

Partial molar volumes for perfluoro-*n*-heptane and isooctane were determined at several concentrations through the critical-solution region and at infinite dilution using a technique similar to that of Shinoda and Hildebrand.[12] The enthalpy of mixing for the second system was determined using an improved diphenyl ether calorimeter. The data in both studies were sufficiently precise to justify four coefficients in analytical functions of the form $y = x_1 x_2 \sum_{m=0} a_m (x_1 - x_2)^m$.

The results that bear upon the subject of this letter are shown in Figures 1 and 2 where the second derivatives of the analytical functions for the volume and enthalpy of mixing *vs.* the mole fraction of fluorocarbon show maxima at or very near the critical-solution compositions of these systems. Rowlinson[13,14] has specu-

(1) J. S. Rowlinson, "Liquids and Liquid Mixtures," Butterworth and Co. Ltd., London, 1959, Chapter 3.

(2) O. K. Rice in "Thermodynamics and Physics of Matter," F. D. Rossini, Ed., Princeton University Press, Princeton, N. J., 1955.

(3) O. K. Rice, *Chem. Rev.*, **44**, 69 (1949), and references therein.

(4) B. H. Zimm, *J. Chem. Phys.*, **19**, 1019 (1951); *J. Phys. Colloid Chem.*, **54**, 1306 (1950).

(5) H. W. Habgood and W. G. Schneider, *Can. J. Chem.*, **32**, 98 (1954).

(6) B. Widom and O. K. Rice, *J. Chem. Phys.*, **23**, 1250 (1955).

(7) B. Widom, *ibid.*, **41**, 1633 (1964).

(8) D. S. Gaunt, M. E. Fisher, M. F. Sykes, and J. W. Essam, *Phys. Rev.*, **14**, 713 (1964).

(9) M. E. Fisher, *J. Math. Phys.*, **5**, 944 (1964).

(10) S. D. Furrow, M.S. Thesis, University of Maine, 1962.

(11) S. D. Furrow, Ph.D. Thesis, University of Maine, 1965.

(12) K. Shinoda and J. H. Hildebrand, *J. Phys. Chem.*, **62**, 295 (1958).

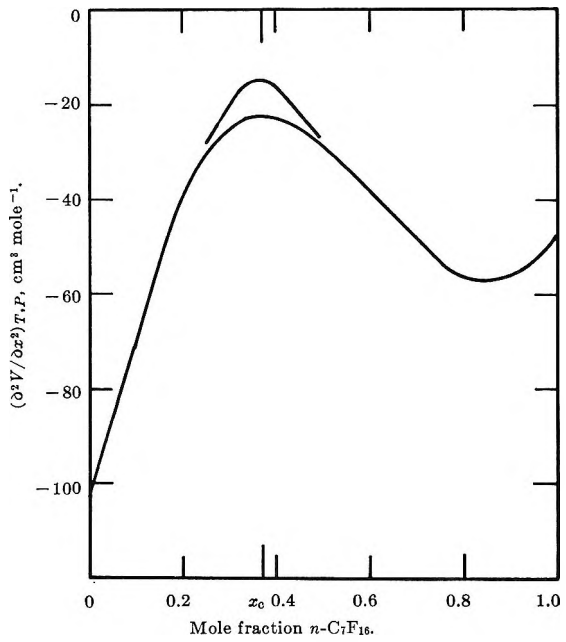

Figure 1. Shape of the volume of mixing function for the system n-C_7F_{16} + isooctane at 23.7° (0.06° above the critical-solution temperature): upper curve is calculated from 25 determinations of partial molar volumes between 0.36 and 0.52 mole fraction n-C_7F_{16}; lower curve incorporates values of the partial molar volumes at infinite dilution.

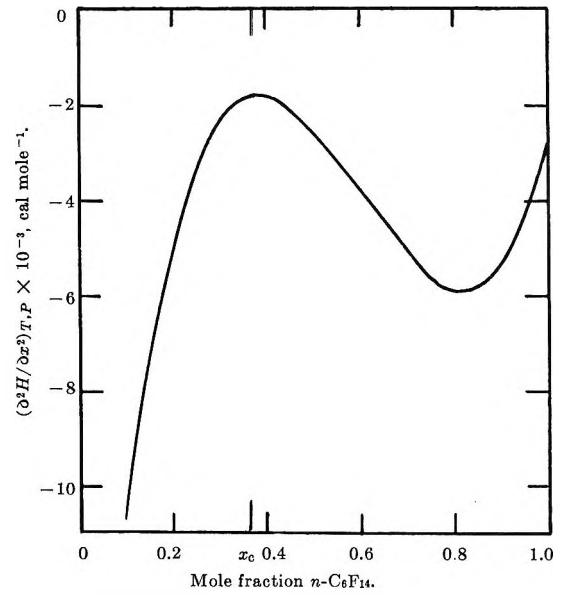

Figure 2. Shape of the enthalpy of mixing function for the system n-C_6F_{14} + n-C_6H_{14} at the critical-solution temperature, 22.64°, from measurements of the enthalpy of mixing at 26.94° and enthalpy differences between these temperatures.

lated that the second derivatives should also vanish at the critical-solution point. Although these data show this tendency, this condition is not firmly resolved. The third derivatives, however, clearly vanish. The exact composition at which they vanish will, of course, always remain subject to experimental uncertainty.

The relations between the third and fourth derivatives of the Gibbs free energy and the third derivatives of volume and entropy of mixing are shown in eq 1 and 2. Equation 3 holds along the critical-solution line.

$$d(\partial^3 G/\partial x^3)_{T,P} = (\partial^4 G/\partial x^4)_{T,P}dx + (\partial^4 G/\partial x^3 \partial P)_T dP + (\partial^4 G/\partial x^3 \partial T)_P dT \quad (1)$$

$$d(\partial^3 G/\partial x^3)_{T,P} = (\partial^4 G/\partial x^4)_{T,P}dx + (\partial^3 V/\partial x^3)_{T,P}dP - (\partial^3 S/\partial x^3)_{T,P}dT \quad (2)$$

$$0 = (\partial^4 G/\partial x^4)_{T_c,P}dx + (\partial^3 V/\partial x^3)_{T_c,P}dP - (1/T_c)(\partial^3 H/\partial x^3)_{T_c,P}dT \quad (3)$$

The vanishing of the third derivatives for the volume and enthalpy of mixing at or near the critical-solution point strengthens the argument for the vanishing of the fourth derivative of the function for the Gibbs free energy of mixing. By analogy, the argument that $(\partial^3 P/\partial V^3)_{T_c}$ for a single component vanishes is also strengthened. There is considerable evidence that the critical isotherm is not continuously differentiable.[6-9] By analogy with the results for single-component fluids, however, it is highly probable that $(\partial^5 G/\partial x^5)_{T_c,P}$ also vanishes. Widom and Rice[6] in an analysis of experimental data for xenon, hydrogen, and carbon dioxide found the degree of the critical isotherm to be 4.2 ± 0.2, slightly larger than 4. Recent calculations[8] for the three-dimensional Ising model, which is analogous to the lattice gas, result in an estimated value of 5.2 ± 0.2 for the degree of the critical isotherm.

(13) J. S. Rowlinson, "Conference on Phenomena in the Neighborhood of Critical Points," Washington, D. C., April 1965.

(14) J. S. Rowlinson, private communication.

CHEMISTRY DEPARTMENT
UNIVERSITY OF MAINE
ORONO, MAINE 04473

R. D. DUNLAP
S. D. FURROW

RECEIVED JANUARY 10, 1966

Barium Ion Exchange of the Synthetic Zeolite Linde 4-A

Sir: There have been several reports that ion exchange of the synthetic zeolite, Linde 4-A, with barium ion destroys the crystal structure.[1,2] We have begun to study the thermodynamics of exchange of alkaline

Table I: Composition of Some Zeolite Samples

Samples	% wt[a]				Atoms per unit cell[a]			
	Na	Ba	SiO_2	Al_2O_3	Na	Ba	Si	Al[b]
Linde 4-A Lot No. 47077	16.0	...	41.3	36.1	11.8	...	11.6	12
Ba–A	2.14	31.8	32.6	28.4	2.00	4.99	11.7	12
Na–A from Ba–A	15.5	0.78	41.8	35.8	11.5	0.10	11.9	12

[a] Composition of the anhydrous unit cell. [b] Composition of unit cell is based on the assumption that there are 12 aluminum atoms per unit cell.

earth cations into Linde 4-A. One of the important points we had to verify was whether or not the zeolite retained its structural integrity during exchange. This was done by measuring its sorptive properties and obtaining an X-ray powder diffraction pattern. A numerical value of the degree of crystallinity of all our samples of Na–A and Ba–A was assigned by comparing the intensity of the 34.1° (2θ) peak, measured with a standard X-ray diffractometer, to the intensity of the peak obtained using Linde 4-A Lot No. 4353 (in the case of Na–A) and Linde 5-A Lot No. 5104 (in the case of Ba–A), as standards.

We prepared a sample of Ba–A which was 83.2% in the barium form. The remainder of the cations were sodium ions. The analyses of this material and the material from which it was prepared, Linde 4-A, Lot No. 4077, are shown in Table I. The sorptive properties and relative crystallinities of the Linde 4-A starting material, and the Ba–A prepared from it, are tabulated in Tables II and III, respectively. The samples were activated by calcining for 2 hr in a stream of dry air at 350° and then water or *n*-hexane was brought into contact with the samples at 20 mm partial pressure and room temperature. The sample of Na–A sorbed no *n*-hexane, in agreement with other investigators.[1] We had expected that the sample of Ba–A would have an appreciable capacity to adsorb *n*-hexane as reported by others for Ca–A;[1] however, it did not. Furthermore, its capacity to adsorb water is essentially zero. X-Ray powder diffraction patterns and relative crystallinity data obtained using these two samples indicate that the Linde 4-A was quite crystalline whereas the calcined and rehydrated Ba–A was amorphous. The relative crystallinity data are shown in Table III.

We suspected that dehydration under the conditions we used was responsible for the loss in crystallinity of the Ba–A crystals. An X-ray powder diffraction pattern was taken of a sample of Ba–A which had never been dehydrated for verification. The pattern was very weak and the relative crystallinity listed in Table III was correspondingly low. Despite the low intensity of all the lines, every major line of the Ca–A[1] pattern was present. We felt the low intensity of the pattern obtained from this sample was due to the high absorption coefficient of barium for X-rays.

Table II: Sorptive Properties of Zeolite Samples

Sample	g of H_2O sorbed[a]/g of activated zeolite	g of *n*-hexane sorbed[a]/g of activated zeolite
Linde 4-A Lot No. 47077	0.237	...
Ba–A	0.003	0.011
Na–A reexchanged from Ba–A	0.237	

[a] At room temperature and 20 mm partial pressure of sorbate.

Table III: Relative X-Ray Crystallinity of Zeolite Samples

Sample	% crystallinity
Linde 4-A Lot No. 47077, never calcined	90[a]
Ba–A, calcined and rehydrated	Amorphous[b]
Ba–A, never calcined	15[b]
Na–A, reexchanged from uncalcined Ba–A, calcined, and rehydrated	85[a]
Na–A, reexchanged from uncalcined Ba–A, never calcined	90[a]

[a] Ratio of intensity of 34.1° (2θ) peak of sample to that of Linde 4-A Lot No. 4353 times 100%. [b] Ratio of intensity of 34.1° (2θ) peak of sample to that of Linde 5-A Lot No. 5104.

In order to verify our suspicions we reexchanged a sample of Ba–A which had never been dehydrated with NaCl solution until it was essentially in the pure sodium form (see Table I). The water adsorption data and relative crystallinities shown in Tables II and III indicate that the Na–A obtained by reexchange of Ba–A is identical with the Linde 4-A starting ma-

(1) D. W. Breck, W. C. Eversole, R. M. Milton, T. B. Reed, and T. L. Thomas, *J. Am. Chem. Soc.*, **78**, 5963 (1956).

(2) R. M. Barrer and W. M. Meier, *Trans. Faraday Soc.*, **54**, 1074 (1958).

terial. Powder diffraction patterns of both materials are identical. We therefore conclude that barium ion exchange of Linde 4-A does not cause the crystals to become amorphous. It is the very calcination required to activate the zeolite for sorption which causes the Ba–A crystals to collapse and be amorphous to X-rays. This structure collapse is reflected in the lack of water sorption capacity shown in Table II for Ba–A. The loss in stability of the dehydrated Linde A structure in the barium form is probably due to the large internuclear distances which must be expected between the barium ion and the oxygen atoms of the lattice and concomitant large charge separation.

Previous reports of the decomposition of Linde A caused by barium exchange[1,2] must have been based on X-ray studies of calcined samples. Although calcination does destroy the crystal lattice, any ion-exchange studies involving Linde 4-A and $BaCl_2$ at moderate temperatures in aqueous solution will be valid because the system is reversible.

RESEARCH DEPARTMENT HOWARD S. SHERRY
SOCONY MOBIL OIL COMPANY, INC.
PAULSBORO, NEW JERSEY

RECEIVED JANUARY 20, 1966

On the Reaction of Vibrationally Excited Cyclopropane[1]

Sir: The photolysis of ketene in the presence of an excess of ethylene is known to produce vibrationally excited cyclopropane.[2] In such a system the vibrational energy-rich cyclopropane undergoes isomerization to propene or collisionally deenergizes to normal cyclopropane depending upon the total pressure of the system. Thus far very little is known about the formation of vibrationally excited cyclopropane by direct molecular split in a photochemical reaction. We wish to report that one of the primary processes in the photolysis of tetrahydrofuran leads to the formation of excited cyclopropane.

$$CH_2{=}C{=}O \xrightarrow{h\nu} CH_2{:} + CO \qquad (1)$$

$$CH_2{:} + C_2H_4 \longrightarrow \triangle^* \qquad (2)$$

$$\triangle^* \xrightarrow{k_{iso}} CH_3{-}CH{=}CH_2 \qquad (3)$$

$$\triangle^* + M \xrightarrow{\beta} \triangle \qquad (4)$$

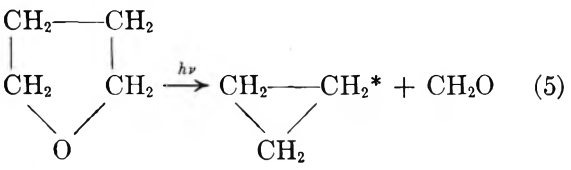

$$CH_2{-}CH_2 \xrightarrow{h\nu} CH_2{-}CH_2{}^* + CH_2O \qquad (5)$$

A Hanovia S500 mercury full arc was used as a light source. Since tetrahydrofuran absorbs[3] strongly in the region 2100–1800 A, the effective wavelength was in the 2100–1900-A region. Products were analyzed gas chromatographically on a 25-ft silver nitrate–ethylene glycol (25% by weight on Chromosorb) column. Unless otherwise stabilized by collision, the excited cyclopropane formed in reaction 5 will isomerize to propene. The result of a series of runs at different pressure and at 120° are shown in Figure 1. Included in the same figure are the results obtained by Frey and Kistiakowsky in the photolysis of the ketene–ethylene system,[2] where the fractional yield of cyclopropane was plotted against the initial pressure of the reactant.

From the thermochemical data,[4] reaction 5 is 28 kcal/mole endothermic. Since energy absorbed in the system is of the order of 143 kcal/mole, an excess energy of ~115 kcal/mole is available to be carried over to the products as vibrational energy. The data given in Figure 1 undoubtedly demonstrate this. Two notable features are obvious from the data. First, the highest pressure required to stabilize all of the cyclopropane is much less than that required in the ketene–ethylene system. Second, the fractional yield at high pressure (0.72 to be compared with 0.60 obtained by Frey and Kistiakowsky) is less than unity. This might imply the formation of additional propene by secondary reaction.

If it is assumed that the degradation of vibrational energy of excited cyclopropane occurs on every collision, then the rate constant for the isomerization step (3) is given by

$$k_{iso} = \frac{P_i - P_\alpha}{\Delta_i}\beta$$

where P_i = yield of propene at pressure i, P_α = yield of propene at high pressure, Δ_i = yield of cyclopropane at pressure i, and β = collisional rate constant. At 120° the average value for $k_{iso} = 6.01 \times 10^7$ sec^{-1}. This value is to be compared with 1.11×10^{10} sec^{-1}

(1) Supported, in part, by the U. S. Atomic Energy Commission.

(2) H. M. Frey and G. B. Kistiakowsky, *J. Am. Chem. Soc.*, **79**, 6373 (1957); H. M. Frey, *Proc. Roy. Soc.* (London), **A251**, 575 (1959).

(3) L. W. Pickett, *et al.*, *J. Am. Chem. Soc.*, **73**, 4865 (1951).

(4) J. D. Cox, *Tetrahedron*, **18**, 1337 (1962).

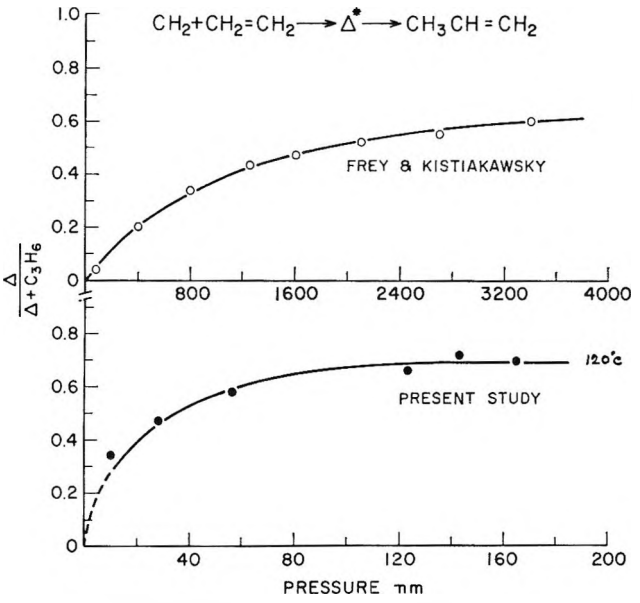

Figure 1. Fractional yield of cyclopropane in the decomposition of tetrahydrofuran, as a function of pressure.

obtained by Frey and Kistiakowsky in their system. In this system the average lifetime of the vibrationally excited cyclopropane is of the order of 10^{-7} sec. This lifetime is about three orders of magnitude longer than that obtained by Frey and Kistiakowsky in their system. However, our value is similar to the average lifetime of a reacting molecule in the thermal isomerization of cyclopropane[5] at 445°.

An estimate of the energy content of the vibrationally excited cyclopropane may be obtained from the Rice, Ramsperger, and Kassel[6] equation for unimolecular reaction where the rate constant is given by

$$k_{iso} = \left[\frac{E_e - E_{act}}{E_e}\right]^{S-1} A$$

Substituting $k_{iso} = 6.01 \times 10^7$ sec^{-1}, $S = 13$, $E_{act} = 65$ kcal, and $A = 10^{15.17}$ sec^{-1} into the above equation, the energy of the excited cyclopropane molecule was found to be $E_e = 86$ kcal. This value is much lower than a recently estimated[7] value of 103 kcal/mole for the photochemical system ethylene + methylene (from ketene). The lower energy content of cyclopropane in the present system is indicative of the fact that energy stabilization by collision occurs at a much lower pressure (Figure 1) than that required in the methylene and ethylene system. The longer lifetime is also another indication of lower energy content. In summary it appears, therefore, that photolysis of tetrahydrofuran yields energy-rich cyclopropane but in an energy state which is not as "hot" as that produced by the chemical reaction of methylene with ethylene.

Acknowledgment. The author is thankful to Dr. K. O. Kutschke for his interest in this work.

(5) B. S. Rabinovitch, *et al.*, *J. Am. Chem. Soc.*, 81, 1981 (1959).
(6) L. S. Kassel, "Kinetics of Homogeneous Gas Reactions," Chemical Catalog Co., New York, N. Y., 1932.
(7) H. M. Frey, *J. Am. Chem. Soc.*, 80, 5005 (1958).

RADIATION RESEARCH LABORATORIES B. C. ROQUITTE
MELLON INSTITUTE
PITTSBURGH, PENNSYLVANIA

DIVISION OF PURE CHEMISTRY
NATIONAL RESEARCH COUNCIL
OTTAWA, CANADA

RECEIVED JANUARY 31, 1966

Cation Exclusion from Gels[1]

Sir: In his comment on an earlier note of Tien,[2a] Maatman[2b] concludes that there ". . . seems to be no need to postulate . . . ion exclusion from small pores in alkali metal cation–silica gel systems," and he cites as evidence the invasion of even the smallest pores of silica gels by the large hydrated Al^{3+} ion. However, the argument may be spurious, for the mechanism of ion exclusion probably does not entail simply the mismatch of ion and pore sizes. The structure of liquid water is different near a gas–water, liquid–water, or solid–water interface than in the bulk water. The water region near the interface will thus incorporate or exclude ion species relative to the bulk solution in accord with the effect of these species on water structure. For example, the surface electrical conductivity of aqueous electrolytic solutions is less than the bulk conductivity due to enhanced water structure and/or ion exclusion.[3,4] If there are charge sites on the surfaces of the pores, the situation will be further complicated by ion exclusion arising from the electric double layer.[5] In a system of great surface area, such as a gel, where the amount of water near a surface is comparable to the amount distant from a surface, the effects of interface-produced perturbations of the concentration of ionic constituents should become ap-

(1) This work was supported in part by the Office of Naval Research.
(2) (a) H. T. Tien, *J. Phys. Chem.*, 69, 350 (1965); (b) R. W. Maatman, *ibid.*, 69, 3196 (1965).
(3) S. Bordi, *Ann. Chim.* (Rome), 48, 327 (1958).
(4) S. Bordi and F. Vannel, *ibid.*, 54, 710 (1964).
(5) L. Dresner, *J. Phys. Chem.*, 69, 2230 (1965).

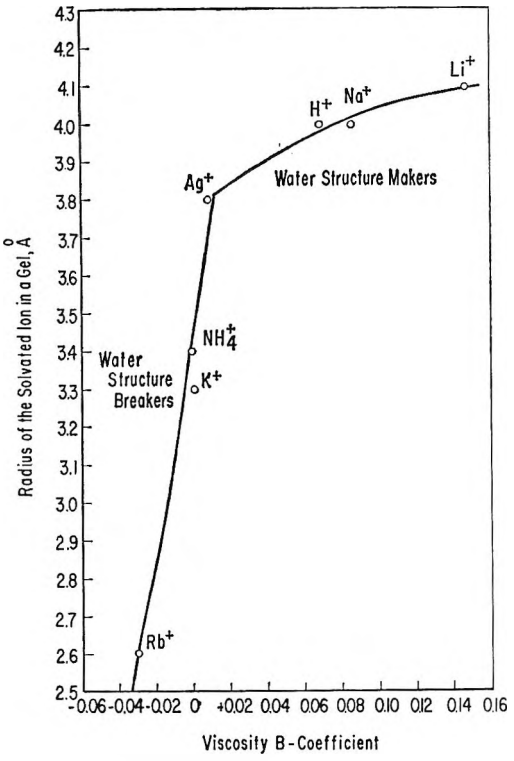

Figure 1. Dependence of ion exclusion on the viscosity B coefficient.

preciable. McConnell, *et al.*,[6] tabulate values for the radii of hydrated cations *inside* silica gels derived from ion-exclusion measurements. If one interprets these "radii" as being some kind of a measure of ion exclusion, one might expect them to be related to the water-structure-altering capabilities of the cations as reflected in the B coefficient in the viscosity equation of Jones and Dole.[7] In Figure 1 the cationic radii given by McConnell, *et al.*,[6] are plotted *vs.* the cationic B coefficients at 25° given by Gurney.[8] Not only does the expected correlation obtain but the structure makers and structure breakers form two distinct curves, and the dependence of exclusion of the B coefficient is much greater in the latter case, as expected.

The phenomena discussed above probably play a role in the perturbation of the ionic constituents of sea water in marine sediments.[9]

(6) B. L. McConnell, K. C. Williams, J. L. Daniel, J. H. Stanton, B. N. Irby, D. L. Durgger, and R. W. Maatman, *J. Phys. Chem.*, **68**, 2941 (1964).

(7) G. Jones and M. Dole, *J. Am. Chem. Soc.*, **51**, 2950 (1929).

(8) R. W. Gurney, "Ionic Processes in Solution," McGraw-Hill Book Co., Inc., New York, N. Y., 1953, Chapter 9.

(9) R. Siever, K. C. Beck, and R. A. Berner, *J. Geol.*, **73**, 39 (1965).

ARTHUR D. LITTLE, INC. R. A. HORNE
CAMBRIDGE, MASSACHUSETTS

RECEIVED FEBRUARY 3, 1966

Argon Sensitized Radiolysis of Liquid Propane[1]

Sir: We wish to report evidence for very efficient liquid phase ionic reactions in the argon-sensitized radiolysis of liquid propane. The gas phase radiolysis of propane has received quite detailed study,[2-6] and the reactions of ionic species have been shown to be of major importance by careful isotopic experiments.[2a] Mass spectrometric studies of dissociative charge exchange of rare gas ions with propane have established the resulting gas phase ion distributions.[7] Rare gas sensitized radiolysis of propane has been interpreted on the basis of the charge-exchange distributions and has largely corroborated the importance of ionic reactions. The extensive gas phase data provide guidelines for assessing the importance of ionic reactions in the liquid. In analogy to Futrell's conclusion[2b] about the gas phase we may anticipate that a sensitive indicator of ionic processes will be ethane which is formed by hydride transfer.

In our laboratory we have succeeded in preparing solutions of argon and other rare gases with propane; these components are miscible over at least 0.5 to 0.1 mole fraction of propane. All samples were exposed to cobalt-60 γ irradiation at a dose rate of 0.602 ± 0.04 Mrad/hr to H_2O. A typical exposure time was 100 min. Analysis for all initial components and resulting products, except H_2, was accomplished by gas chromatography.

In Table I we compare the product yields from liquid propane at −130° with those from an argon–propane liquid mixture also at −130°. Results are given for oxygen scavenged and for unscavenged systems. It can be inferred from the nearly total disappearance of products greater than C_3 that O_2 is an efficient scavenger under these conditions. The yields are based on the total energy absorbed by the mixture. The exposure dose to the mixture and the pure liquid was the same, but because of energy transfer the "effective" dose to the propane in the mixture was about 9 times that for the pure liquid. Higher doses to the pure

(1) This work was supported by the Petroleum Research Fund.

(2) (a) P. Ausloos and S. Lias, *J. Chem. Phys.*, **36**, 3162 (1962); earlier references given therein; (b) J. H. Futrell and T. O. Tiernan, *ibid.*, **37**, 1964 (1962).

(3) S. G. Lias and P. Ausloos, *ibid.*, **37**, 877 (1962).

(4) I. B. Sandoval and P. Ausloos, *ibid.*, **38**, 2454 (1963).

(5) P. Ausloos, S. Lias, and I. B. Sandoval, *Discussions Faraday Soc.*, **36**, 66 (1963).

(6) L. W. Sieck, N. K. Blocker, and J. H. Futrell, *J. Phys. Chem.*, **69**, 888 (1965).

(7) (a) J. H. Futrell and T. O. Tiernan, *J. Chem. Phys.*, **39**, 2539 (1963); (b) E. Pettersonn and E. Lindholm, *Arkiv Fysik*, **24**, 39 (1963); (c) V. Cermak and Z. Herman, *Nucleonics*, **19**, 106 (1961).

liquid show that the product distribution observed in the argon–propane mixtures is distinctive of the mixture rather than of a higher dose to propane.

Table I: Product Yields per 100 Ev (G) for Propane and Propane–Argon Liquid Mixtures at −130°, Scavenged and Unscavenged[a]

	C_3H_8:Ar:O_2			
	1:0:0	1:0:0.04	1:13:0	1:13:0.10
	←1.17 Mrads→		←0.80 Mrad→	
CH_4	0.51	0.33	1.01	0.94
C_2H_4	0.48	0.35	0.35	0.31
C_2H_6	0.37	0.16	1.25	0.83
C_2H_2	0.07	0.04	0.10	0.08
C_3H_6	2.5	0.75	0.43	0.13
ΣC_4–C_5[b]	1.56	0.16	0.59	<0.02

[a] All data presented are averages of at least two separate samples. [b] Individual products were analyzed but are no pertinent to the main conclusions.

The G values of individual products in Table I show some striking characteristics resulting from energy transfer from argon to propane. Yields of ethane and methane have increased dramatically and selectively and are much higher than in pure propane. Thus, the large majority of propane decomposition arising from energy transfer produces ethane and methane. This selectivity is characteristic only of argon–propane mixtures. In xenon–propane mixtures energy transfer is indicated by the enhancement of *all* product yields; in fact, general enhancement is the usual result of studies of this kind.[8] The oxygen-scavenged argon–propane mixtures still exhibit large yields of methane and ethane. This suggests that these products arise *via* ionic or excited molecule reactions.

In the gas phase ethane is mainly produced by reaction 1 and methane is a product of reaction 2.[2] Other nonradical reaction possibilities exist which

$$C_2H_5^+ + C_3H_8 = C_2H_6 + C_3H_7^+ \quad (1)$$

$$C_3H_8^+ = C_2H_4^+ - CH_4 \quad (2)$$

form methane and ethane ($C_2H_4^- + C_3H_8 = C_2H_6 + C_3H_6^+$), but (1) and (2) are the major reactions. The large and *selective* yields of ethane and methane that we observe in oxygen-scavenged argon–propane mixtures strongly indicate that reactions 1 and 2 occur *efficiently* in the liquid.

If the above conclusion is valid, the main mechanism of energy transfer must be charge exchange. The charge-exchange mass spectrum of propane with argon tells one the ion abundances observed in the gas phase. In the liquid much less fragmentation should occur, and one would expect the charge-exchange fragmentation pattern for *liquid* propane with argon to be more like the gas phase pattern for propane with krypton or xenon than like the gas phase pattern for propane with argon. In the gas phase xenon charge-exchange spectrum, $C_2H_5^+$ and $C_2H_4^+$ comprise 87% of the ions. These two ions are just those we postulate for reactions 1 and 2. Further experiments with other rare gases and with isotopic labeling are in progress.

(8) D. R. Davis, W. F. Libby, and L. Kevan, *J. Am. Chem. Soc.*, **87**, 2766 (1965).

(9) National Science Foundation Predoctoral Fellow.

DEPARTMENT OF CHEMISTRY
UNIVERSITY OF KANSAS
LAWRENCE, KANSAS

R. D. KOOB[9]
LARRY KEVAN

RECEIVED FEBRUARY 7, 1966

Photosensitization in the Gas Phase with Hexafluorobenzene

Sir: For many years the sensitizer most often used in gas phase photochemical studies has been mercury or another volatile metal. In the past few years, however, some organic molecules have been increasingly utilized in this role. This shift may perhaps be traced to the advent of flash photolysis,[1] which has facilitated the identification of the triplet states of many organic molecules.

There are several advantages in the use of organic molecules as sensitizers, of which the most important is probably the wide range of energies available from such excited molecules. It is somewhat surprising, then, that only two organic molecules have been used in this role with any frequency. Thus, there is a considerable body of literature on the use of benzophenone in the liquid phase, as developed by Hammond and his collaborators.[2–4] Although benzene photosensitization has not been as widely accepted, it has been used successfully both in the gas phase[5,6] and in liquids.[7]

We have been interested for several years in the photolytic and photosensitized decompositions of small

(1) G. Porter, *Proc. Chem. Soc.*, 291 (1959).

(2) G. S. Hammond and W. M. Moore, *J. Am. Chem. Soc.*, **81**, 6334 (1959).

(3) G. S. Hammond and P. A. Leermakers, *ibid.*, **83**, 2395 (1961).

(4) G. S. Hammond, P. A. Leermakers, and N. J. Turro, *ibid.*, **83**, 2396 (1961).

(5) R. B. Cundall and T. F. Palmer, *Trans. Faraday Soc.*, **56**, 1211 (1960).

(6) G. P. Semeluk and I. Unger, *Nature*, **198**, 853 (1963).

(7) J. T. Dubois and F. Wilkinson, *J. Chem. Phys.*, **38**, 2541 (1963).

halogenated organic molecules.[6] The use of mercury in such studies introduces considerable experimental difficulties because it reacts directly with halogens,[8] hence our interest in organic sensitizers. We have had some success in sensitizing the decomposition of chloroform and methylene chloride with benzene irradiated with 2537 A. The irradiation times, however, are inordinately long (72 hr with chloroform and 96 hr with methylene chloride), and complications are introduced because the benzene itself is attacked by the radicals produced.

We have recently explored the possibility of using hexafluorobenzene excited with 2537 A as a photosensitizer in the decomposition of dichloromethane and have obtained most encouraging results.[9] As for benzene sensitization, the primary chemical process is a carbon–hydrogen bond cleavage, but irradiation times can be reduced to less than 5 hr, and there is no evidence for any chemical participation by hexafluorobenzene in the resulting radical reaction.

Both the photolytic and sensitized (with benzene or hexafluorobenzene) decompositions of dichloromethane proceed analogously to the decompositions of chloroform.[6] Thus, the photolysis with 1849-A radiation can be explained by the sequence

$$CH_2Cl_2 + h\nu \longrightarrow CH_2Cl + Cl$$

$$Cl + CH_2Cl_2 \longrightarrow HCl + CHCl_2$$

The main organic products are $C_2H_4Cl_2$, $CHCl_2$–CH_2Cl, and $C_2H_2Cl_4$ which arise from combinations of the two organic radicals. The benzene-sensitized decomposition appears to proceed *via* a carbon–hydrogen bond break, followed by a sequence of reactions analogous to those which have been considered in the sensitized decomposition of chloroform, the major organic product being $C_2H_2Cl_4$. The hexafluorobenzene-photosensitized reaction also proceeds through a carbon–hydrogen bond split, but in this case there are no product molecules derivable from the sensitizer. A mechanism which adequately explains the observed products is

$$C_6F_6^* + CH_2Cl_2 \longrightarrow C_6F_6 + CHCl_2 + H$$

$$H + CH_2Cl_2 \longrightarrow H_2 + CHCl_2$$

$$H + CH_2Cl_2 \longrightarrow HCl + CH_2Cl$$

$$2CHCl_2 \longrightarrow C_2H_2Cl_4$$

$$CH_2Cl + H \longrightarrow CH_3Cl$$

where $C_6F_6^*$ is the excited sensitizing species. It is not possible at this time to identify which excited state transfers the energy. Phillips at the University of Texas is currently investigating hexafluorobenzene and informs us[10] that at 2537 A the fluorescent quantum yield is about 10^{-3}. This suggests that almost all excited (singlet) molecules of hexafluorobenzene convert the absorbed energy to some other state which does not fluoresce. Obviously, one possibility is that this other state is the triplet and that this is the energy-transfer agent.

The advantages of using C_6F_6 as a sensitizer are threefold. (a) The excited state of C_6F_6 has a much larger reaction cross section than does C_6H_6, so that reaction times are much shorter. In addition, the extinction coefficient at 2537 A of C_6F_6 is approximately twice that for C_6H_6. (b) C_6F_6 is not decomposed at wavelengths greater than 2300 A. (c) C_6F_6 is not significantly attacked by radicals, or H atoms, near room temperature under these conditions.

We hope in the near future to publish a more detailed account of the photolysis and sensitized decomposition of CH_2Cl_2.

(8) C. R. Masson and E. W. R. Steacie, *J. Chem. Phys.*, **19**, 183 (1951); H. E. Gunning, *Can. J. Chem.*, **36**, 89 (1958).

(9) A. K. Basak and G. P. Semeluk, unpublished results.

(10) D. Phillips, private communication.

CHEMISTRY DEPARTMENT
UNIVERSITY OF NEW BRUNSWICK
FREDERICTON, NEW BRUNSWICK, CANADA

A. K. BASAK
G. P. SEMELUK
I. UNGER

RECEIVED FEBRUARY 15, 1966

Quadrivalent Arsenic

Sir: Electrochemical evidence has been obtained in support of the existence of the arsenic(IV) oxidation state. The basis for this identification comes from the study of the irreversible voltammograms of millimolar As(III) and As(V) solutions in 1.0 *M* perchloric acid. The foot of the anodic wave corresponding to the reduction of As(III), when analyzed on a Tafel plot, shows a distinct and reproducible inflection (see Figure 1). This effect is characteristic of electrode reactions involving a sequence of two consecutive one-electron-transfer steps[1]

$$As(III) \longrightarrow As(IV) + e$$

$$As(IV) \longrightarrow As(V) + e$$

The over-all reaction is

$$As(III) \longrightarrow As(V) + 2e$$

(1) P. Delahay, "Double Layer and Electrode Kinetics," Interscience Publishers, Inc., New York, N. Y., pp 178–180.

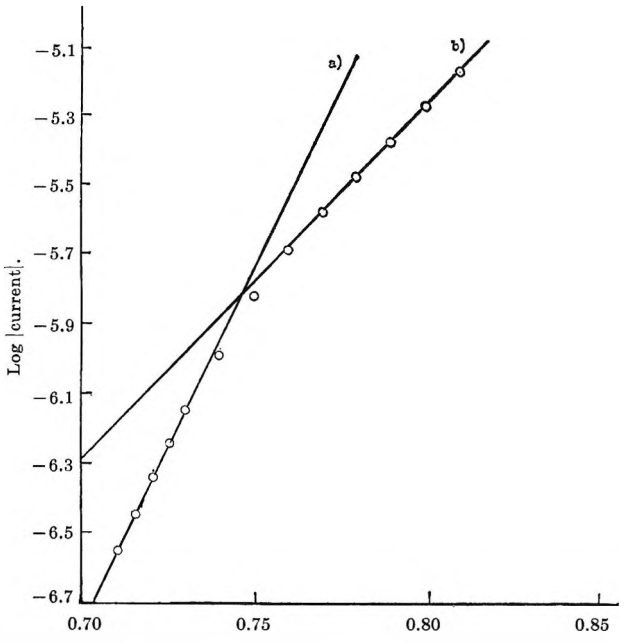

Figure 1. A typical Tafel plot of the foot of the anodic voltammetric wave of 10^{-3} M As(III) in 1.0 M perchloric acid. The symmetry factors $(1 - \beta)$, calculated in the usual manner: slope $= n(1 - \beta)F/2.3RT$, of each of the linear portions are 1.2 and 0.6, respectively. n, the number of electrons transferred in the rate-determining step, is taken to be unity.

Kinetic equations describing this mechanism in the form of current–voltage curves obtainable at microelectrodes were derived by Vetter,[2] in terms of exchange currents, and Catherino and Jordan,[3] in terms of specific rate constants. Hurd[4] studied the properties of Vetter's equation *via* the application of computer techniques and established a set of criteria for identifying such a mechanism operationally.

Listed below are the experimental observations and a brief discussion of the manner in which they satisfy the established criteria.

I. The most important characteristic of the mechanism is illustrated in Figure 1, which shows two discrete linear portions which occur below the limiting current.

II. The second criterion involves the relationship between the exchange currents of the oxidation and the reduction processes. Since As(V) was not electroreducible anywhere in the range of potentials accessible for study, the ratio of the hypothetical exchange currents obtainable from the anodic waves to that from the reduction wave approaches infinity. The properties of the equation require that the wave having the two linear logarithmic portions must occur on that wave having the larger exchange current. This was the case under the experimental conditions.

III. The last criterion involves the agreement between the symmetry factors. The equation characteristic of the mechanism requires that the symmetry factor determined from that linear portion of the Tafel plot occurring at low currents be greater than 1.0 but less than 2.0 and the linear portion occurring at larger currents be greater than 0 but less than 1.0. A series of ten determinations yielded the following symmetry factors for the linear portion at higher and at lower currents, 1.3 ± 0.1 and 0.6 ± 0.1, respectively.

The electrochemical experiments described herein when taken together with the kinetic evidence obtained from measurements made of the reaction in homogeneous media[5,6] provide a convincing argument for the existence of the As(IV) intermediate.

Acknowledgment. This investigation was supported in part by a grant from the Horace H. Rackham School of Graduate Studies of the University of Michigan. The author also acknowledges the facilities made available by the Computing Center at the University.

(2) K. J. Vetter, *Z. Naturforsch.*, 7a, 328 (1952); 8a, 823 (1953).
(3) H. A. Catherino and J. Jordan, *Talanta*, 11, 159 (1964).
(4) R. M. Hurd, *J. Electrochem. Soc.*, 109, 327 (1962).
(5) R. Woods, I. M. Kolthoff, and E. J. Meehan, *J. Am. Chem. Soc.*, 86, 1698 (1964).
(6) M. Daniels, *J. Phys. Chem.*, 66, 1473 (1962).

DEPARTMENT OF CHEMISTRY
THE UNIVERSITY OF MICHIGAN
ANN ARBOR, MICHIGAN
HENRY A. CATHERINO

RECEIVED FEBRUARY 18, 1966

Measurement of Contact Angle between Thin Film and Bulk of Same Liquid

Sir: The surface tension of a liquid at equilibrium is generally considered to be uniform and its surface smooth as a consequence. However, as the thickness of a liquid layer decreases, intermolecular forces come into action and give rise to a "disjoining" pressure which should correspond to a change in surface tension and to the existence of a contact angle between a thin film and the bulk of liquid. Alternately, one may consider that intermolecular forces pull molecules out of the region between the film and the bulk until the resultant forces become normal to the surface, when the proper contact angle is established.

A qualitative observation of such a contact angle for a multimolecular film supported by a solid was

discussed by one of us a long time ago.[1] More recently, a qualitative observation for the interface between two liquids has been made on a microscopic scale[2] and its significance discussed.[3] Independently of these last reports, our attention was drawn to this phenomenon by the establishment in this laboratory[4] of conditions under which the "second" black film having a thickness of some 44 A is formed from solutions of ionic surfactants in the presence of salts and is not only indefinitely stable but, once nucleated, can show an impressive tendency to form at the expense of thicker films as measured by the kinetics of film thinning. It seems likely, therefore, that along the line where such a film meets the bulk surface, intermediate thicknesses will disappear and a contact angle will form. As described below, we have been able not only to observe the existence of such a contact angle but also to measure its value, which is not negligible. It may be noted that Drude[5] already tried to find such a phenomenon by comparing the curvature of the black and thicker portions of the same soap bubble but failed to find any effect. He may have dealt, however, with the ordinary or "first" black film having a greater thickness.

A small bubble of air clinging to a Teflon orifice was carefully brought from below into the surface of a solution containing 0.05% sodium dodecyl sulfate and 0.4 *M* NaCl and filling to overflow a cell protected from evaporation. Observation was from above in reflected light by means of a crude schlieren system and a low-power microscope which permitted sensitive detection of any departure from horizontality on the surface. At first, the surface curved upward when the bubble top crossed its level. After some time, however, when the second black film was formed, the surface around the bubble became exactly horizontal for a certain position of the bubble. It could be made to curve upward or downward by raising or lowering the bubble by as little as 0.01 mm and would return immediately to the original flatness when the bubble was returned to its position from any displacement. The diameter of the base of the calotte (spherical segment film) in equilibrium with the horizontal surface was 0.5 to 0.6 mm depending on the diameter of the bubble. A clear change in the curvature of the surface during the spread of the black film after its nucleation could often be observed.

Concurrent observations were made with a horizontal microscope fitted with a screw micrometer eyepiece. The difference between the second black and thicker films could be clearly observed, including the change of curvature of the calotte when the second black film spread and the contact angle with the bulk surface. By comparison with schlieren observations, the characteristic appearance of the surface when it was exactly horizontal was learned, and measurement of diameter, d, of the base of the calotte and of its height, h, under these conditions gave the contact angle θ as $2h/d = \cot(\theta/2)$. The average of several measurements on each of several bubbles at 23.5 ± 1° gave $\theta = 8°\ 50'$ with a maximum deviation of 0.5°. This corresponds to 1.2% difference in surface tension between the film and the bulk for this solution and, as the bulk surface tension is 29.5 dynes/cm, to a difference $\Delta G = 0.4$ erg/cm² between the free energies of the two surfaces of the same solution and to a disjoining pressure of 1.5×10^6 dynes/cm² or 1.5 atm.

Acknowledgment. This work was supported in part by the National Science Foundation.

(1) D. H. Bangham and R. I. Razouk, *Trans. Faraday Soc.*, **33**, 1459 (1937).

(2) G. D. M. MacKay, Ph.D. Thesis, McGill University, 1962 (quoted in ref 3).

(3) H. M. Princen, Thesis, Utrecht, 1965.

(4) M. N. Jones, K. J. Mysels, and P. C. Scholten *Trans. Faraday Soc.*, in press.

(5) P. Drude, *Ann. Phys.*, **43**, 158 (1891).

DEPARTMENT OF CHEMISTRY
UNIVERSITY OF SOUTHERN CALIFORNIA
LOS ANGELES, CALIFORNIA 90007

KAROL J. MYSELS
H. F. HUISMAN
RASHAD I. RAZOUK

RECEIVED MARCH 1, 1966